

Advances in Civil Engineering

# Ground Control of High-Stress Mining Roadways: From Experiments to Cases

Lead Guest Editor: Zizheng Zhang

Guest Editors: Zhijie Zhu, Xianjie Hao, and Zhixiong Zeng







---

# **Ground Control of High-Stress Mining Roadways: From Experiments to Cases**



Advances in Civil Engineering

---

# **Ground Control of High-Stress Mining Roadways: From Experiments to Cases**

Lead Guest Editor: Zizheng Zhang

Guest Editors: Zhijie Zhu, Xianjie Hao, and  
Zhixiong Zeng





---

Copyright © 2021 Hindawi Limited. All rights reserved.

This is a special issue published in "Advances in Civil Engineering." All articles are open access articles distributed under the Creative Commons Attribution License, which permits unrestricted use, distribution, and reproduction in any medium, provided the original work is properly cited.







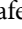
# Chief Editor

Cumaraswamy Vipulanandan, USA













## Associate Editors

Chiara Bedon , Italy  
Constantin Chaliotis , Greece  
Ghassan Chehab , Lebanon  
Ottavia Corbi, Italy  
Mohamed ElGawady , USA  
Husnain Haider , Saudi Arabia  
Jian Ji , China  
Jiang Jin , China  
Shazim A. Memon , Kazakhstan  
Hossein Moayedi , Vietnam  
Sanjay Nimbalkar, Australia  
Giuseppe Oliveto , Italy  
Alessandro Palmeri , United Kingdom  
Arnaud Perrot , France  
Hugo Rodrigues , Portugal  
Victor Yepes , Spain  
Xianbo Zhao , Australia

## Academic Editors

José A.F.O. Correia, Portugal  
Glenda Abate, Italy  
Khalid Abdel-Rahman , Germany  
Ali Mardani Aghabaglou, Turkey  
José Aguiar , Portugal  
Afaq Ahmad , Pakistan  
Muhammad Riaz Ahmad , Hong Kong  
Hashim M.N. Al-Madani , Bahrain  
Luigi Aldieri , Italy  
Angelo Aloisio , Italy  
Maria Cruz Alonso, Spain  
Filipe Amarante dos Santos , Portugal  
Serji N. Amirkhanean, USA  
Eleftherios K. Anastasiou , Greece  
Panagiotis Ch. Anastasopoulos , USA  
Mohamed Moafak Arbili , Iraq  
Farhad Aslani , Australia  
Siva Avudaiappan , Chile  
Ozgur BASKAN , Turkey  
Adewumi Babafemi, Nigeria  
Morteza Bagherpour, Turkey  
Qingsheng Bai , Germany  
Nicola Baldo , Italy  
Daniele Baraldi , Italy

Eva Barreira , Portugal  
Emilio Bastidas-Arteaga , France  
Rita Bento, Portugal  
Rafael Bergillos , Spain  
Han-bing Bian , China  
Xia Bian , China  
Huseyin Bilgin , Albania  
Giovanni Biondi , Italy  
Hugo C. Biscaia , Portugal  
Rahul Biswas , India  
Edén Bojórquez , Mexico  
Giosuè Boscato , Italy  
Melina Bosco , Italy  
Jorge Branco , Portugal  
Bruno Briseghella , China  
Brian M. Broderick, Ireland  
Emanuele Brunesi , Italy  
Quoc-Bao Bui , Vietnam  
Tan-Trung Bui , France  
Nicola Buratti, Italy  
Gaochuang Cai, France  
Gladis Camarini , Brazil  
Alberto Campisano , Italy  
Qi Cao, China  
Qixin Cao, China  
Iacopo Carnacina , Italy  
Alessio Cascardi, Italy  
Paolo Castaldo , Italy  
Nicola Cavalagli , Italy  
Liborio Cavaleri , Italy  
Anush Chandrappa , United Kingdom  
Wen-Shao Chang , United Kingdom  
Muhammad Tariq Amin Chaudhary, Kuwait  
Po-Han Chen , Taiwan  
Qian Chen , China  
Wei Tong Chen , Taiwan  
Qixiu Cheng, Hong Kong  
Zhanbo Cheng, United Kingdom  
Nicholas Chileshe, Australia  
Prinya Chindaprasirt , Thailand  
Corrado Chisari , United Kingdom  
Se Jin Choi , Republic of Korea  
Heap-Yih Chong , Australia  
S.H. Chu , USA  
Ting-Xiang Chu , China

Zhaofei Chu , China  
Wonseok Chung , Republic of Korea  
Donato Ciampa , Italy  
Gian Paolo Cimellaro, Italy  
Francesco Colangelo, Italy  
Romulus Costache , Romania  
Liviu-Adrian Cotfas , Romania  
Antonio Maria D'Altri, Italy  
Bruno Dal Lago , Italy  
Amos Darko , Hong Kong  
Arka Jyoti Das , India  
Dario De Domenico , Italy  
Gianmarco De Felice , Italy  
Stefano De Miranda , Italy  
Maria T. De Risi , Italy  
Tayfun Dede, Turkey  
Sadik O. Degertekin , Turkey  
Camelia Delcea , Romania  
Cristoforo Demartino, China  
Giuseppe Di Filippo , Italy  
Luigi Di Sarno, Italy  
Fabio Di Trapani , Italy  
Aboelkasim Diab , Egypt  
Thi My Dung Do, Vietnam  
Giulio Dondi , Italy  
Jiangfeng Dong , China  
Chao Dou , China  
Mario D'Aniello , Italy  
Jingtao Du , China  
Ahmed Elghazouli, United Kingdom  
Francesco Fabbrocino , Italy  
Flora Faleschini , Italy  
Dingqiang Fan, Hong Kong  
Xueping Fan, China  
Qian Fang , China  
Salar Farahmand-Tabar , Iran  
Ilenia Farina, Italy  
Roberto Fedele, Italy  
Guang-Liang Feng , China  
Luigi Fenu , Italy  
Tiago Ferreira , Portugal  
Marco Filippo Ferrotto, Italy  
Antonio Formisano , Italy  
Guoyang Fu, Australia  
Stefano Galassi , Italy


Junfeng Gao , China  
Meng Gao , China  
Giovanni Garcea , Italy  
Enrique García-Macías, Spain  
Emilio García-Taengua , United Kingdom  
DongDong Ge , USA  
Khaled Ghaedi, Malaysia  
Khaled Ghaedi , Malaysia  
Gian Felice Giaccu, Italy  
Agathoklis Giaralis , United Kingdom  
Ravindran Gobinath, India  
Rodrigo Gonçalves, Portugal  
Peilin Gong , China  
Belén González-Fonteboa , Spain  
Salvatore Grasso , Italy  
Fan Gu, USA  
Erhan Güneyisi , Turkey  
Esra Mete Güneyisi, Turkey  
Pingye Guo , China  
Ankit Gupta , India  
Federico Gusella , Italy  
Kemal Hacıfendioglu, Turkey  
Jianyong Han , China  
Song Han , China  
Asad Hanif , Macau  
Hadi Hasanzadehshooiili , Canada  
Mostafa Fahmi Hassanein, Egypt  
Amir Ahmad Hedayat , Iran  
Khandaker Hossain , Canada  
Zahid Hossain , USA  
Chao Hou, China  
Biao Hu, China  
Jiang Hu , China  
Xiaodong Hu, China  
Lei Huang , China  
Cun Hui , China  
Bon-Gang Hwang, Singapore  
Jijo James , India  
Abbas Fadhil Jasim , Iraq  
Ahad Javanmardi , China  
Krishnan Prabhakan Jaya, India  
Dong-Sheng Jeng , Australia  
Han-Yong Jeon, Republic of Korea  
Pengjiao Jia, China  
Shaohua Jiang , China



MOUSTAFA KASSEM , Malaysia  
Mosbeh Kaloop , Egypt  
Shankar Karuppanan , Ethiopia  
John Kechagias , Greece  
Mohammad Khajehzadeh , Iran  
Afzal Husain Khan , Saudi Arabia  
Mehran Khan , Hong Kong  
Manoj Khandelwal, Australia  
Jin Kook Kim , Republic of Korea  
Woosuk Kim , Republic of Korea  
Vaclav Koci , Czech Republic  
Loke Kok Foong, Vietnam  
Hailing Kong , China  
Leonidas Alexandros Kouris , Greece  
Kyriakos Kourousis , Ireland  
Moacir Kripka , Brazil  
Anupam Kumar, The Netherlands  
Emma La Malfa Ribolla, Czech Republic  
Ali Lakirouhani , Iran  
Angus C. C. Lam, China  
Thanh Quang Khai Lam , Vietnam  
Luciano Lamberti, Italy  
Andreas Lampropoulos , United Kingdom  
Raffaele Landolfo, Italy  
Massimo Latour , Italy  
Bang Yeon Lee , Republic of Korea  
Eul-Bum Lee , Republic of Korea  
Zhen Lei , Canada  
Leonardo Leonetti , Italy  
Chun-Qing Li , Australia  
Dongsheng Li , China  
Gen Li, China  
Jiale Li , China  
Minghui Li, China  
Qingchao Li , China  
Shuang Yang Li , China  
Sunwei Li , Hong Kong  
Yajun Li , China  
Shun Liang , China  
Francesco Liguori , Italy  
Jae-Han Lim , Republic of Korea  
Jia-Rui Lin , China  
Kun Lin , China  
Shibin Lin, China

Tzu-Kang Lin , Taiwan  
Yu-Cheng Lin , Taiwan  
Hexu Liu, USA  
Jian Lin Liu , China  
Xiaoli Liu , China  
Xuemei Liu , Australia  
Zaobao Liu , China  
Zhuang-Zhuang Liu, China  
Diego Lopez-Garcia , Chile  
Cristiano Loss , Canada  
Lyan-Ywan Lu , Taiwan  
Jin Luo , USA  
Yanbin Luo , China  
Jianjun Ma , China  
Junwei Ma , China  
Tian-Shou Ma, China  
Zhongguo John Ma , USA  
Maria Macchiaroli, Italy  
Domenico Magisano, Italy  
Reza Mahinroosta, Australia  
Yann Malecot , France  
Prabhat Kumar Mandal , India  
John Mander, USA  
Iman Mansouri, Iran  
André Dias Martins, Portugal  
Domagoj Matesan , Croatia  
Jose Matos, Portugal  
Vasant Matsagar , India  
Claudio Mazzotti , Italy  
Ahmed Mebarki , France  
Gang Mei , China  
Kasim Mermerdas, Turkey  
Giovanni Minafò , Italy  
Masoomah Mirrashid , Iran  
Abbas Mohajerani , Australia  
Fadzli Mohamed Nazri , Malaysia  
Fabrizio Mollaioli , Italy  
Rosario Montuori , Italy  
H. Naderpour , Iran  
Hassan Nasir , Pakistan  
Hossein Nassiraei , Iran  
Satheeskumar Navaratnam , Australia  
Ignacio J. Navarro , Spain  
Ashish Kumar Nayak , India  
Behzad Nematollahi , Australia

Chayut Ngamkhanong , Thailand  
Trung Ngo, Australia  
Tengfei Nian, China  
Mehdi Nikoo , Canada  
Youjun Ning , China  
Olugbenga Timo Oladinrin , United Kingdom  
Oladimeji Benedict Olalusi, South Africa  
Timothy O. Olawumi , Hong Kong  
Alejandro Orfila , Spain  
Maurizio Orlando , Italy  
Siti Aminah Osman, Malaysia  
Walid Oueslati , Tunisia  
SUVASH PAUL , Bangladesh  
John-Paris Pantouvakis , Greece  
Fabrizio Paolacci , Italy  
Giuseppina Pappalardo , Italy  
Fulvio Parisi , Italy  
Dimitrios G. Pavlou , Norway  
Daniele Pellegrini , Italy  
Gatheeshgar Perampalam , United Kingdom  
Daniele Perrone , Italy  
Giuseppe Piccardo , Italy  
Vagelis Plevris , Qatar  
Andrea Pranno , Italy  
Adolfo Preciado , Mexico  
Chongchong Qi , China  
Yu Qian, USA  
Ying Qin , China  
Giuseppe Quaranta , Italy  
Krishanu ROY , New Zealand  
Vlastimir Radonjanin, Serbia  
Carlo Rainieri , Italy  
Rahul V. Ralegaonkar, India  
Raizal Saifulnaz Muhammad Rashid, Malaysia  
Alessandro Rasulo , Italy  
Chonghong Ren , China  
Qing-Xin Ren, China  
Dimitris Rizos , USA  
Geoffrey W. Rodgers , New Zealand  
Pier Paolo Rossi, Italy  
Nicola Ruggieri , Italy  
JUNLONG SHANG, Singapore

Nikhil Saboo, India  
Anna Saetta, Italy  
Juan Sagaseta , United Kingdom  
Timo Saksala, Finland  
Mostafa Salari, Canada  
Ginevra Salerno , Italy  
Evangelos J. Sapountzakis , Greece  
Vassilis Sarhosis , United Kingdom  
Navaratnarajah Sathiparan , Sri Lanka  
Fabrizio Scozzese , Italy  
Halil Sezen , USA  
Payam Shafigh , Malaysia  
M. Shahria Alam, Canada  
Yi Shan, China  
Hussein Sharaf, Iraq  
Mostafa Sharifzadeh, Australia  
Sanjay Kumar Shukla, Australia  
Amir Si Larbi , France  
Okan Sirin , Qatar  
Piotr Smarzewski , Poland  
Francesca Sollecito , Italy  
Rui Song , China  
Tian-Yi Song, Australia  
Flavio Stochino , Italy  
Mayank Sukhija , USA  
Piti Sukontasukkul , Thailand  
Jianping Sun, Singapore  
Xiao Sun , China  
T. Tafsirojjaman , Australia  
Fujiao Tang , China  
Patrick W.C. Tang , Australia  
Zhi Cheng Tang , China  
Weerachart Tangchirapat , Thailand  
Xiixin Tao, China  
Piergiorgio Tataranni , Italy  
Elisabete Teixeira , Portugal  
Jorge Iván Tobón , Colombia  
Jing-Zhong Tong, China  
Francesco Trentadue , Italy  
Antonello Troncone, Italy  
Majbah Uddin , USA  
Tariq Umar , United Kingdom  
Muahmmad Usman, United Kingdom  
Muhammad Usman , Pakistan  
Mucteba Uysal , Turkey







Ilaria Venanzi , Italy  
Castorina S. Vieira , Portugal  
Valeria Vignali , Italy  
Claudia Vitone , Italy  
Liwei WEN , China  
Chunfeng Wan , China  
Hua-Ping Wan, China  
Roman Wan-Wendner , Austria  
Chaohui Wang , China  
Hao Wang , USA  
Shiming Wang , China  
Wayne Yu Wang , United Kingdom  
Wen-Da Wang, China  
Xing Wang , China  
Xiuling Wang , China  
Zhenjun Wang , China  
Xin-Jiang Wei , China  
Tao Wen , China  
Weiping Wen , China  
Lei Weng , China  
Chao Wu , United Kingdom  
Jiangyu Wu, China  
Wangjie Wu , China  
Wenbing Wu , China  
Zhixing Xiao, China  
Gang Xu, China  
Jian Xu , China  
Panpan , China  
Rongchao Xu , China  
HE YONGLIANG, China  
Michael Yam, Hong Kong  
Hailu Yang , China  
Xu-Xu Yang , China  
Hui Yao , China  
Xinyu Ye , China  
Zhoujing Ye, China  
Gürol Yildirim , Turkey  
Dawei Yin , China  
Doo-Yeol Yoo , Republic of Korea  
Zhanping You , USA  
Afshar A. Yousefi , Iran  
Xinbao Yu , USA  
Dongdong Yuan , China  
Geun Y. Yun , Republic of Korea


Hyun-Do Yun , Republic of Korea  
Cemal YİĞİT , Turkey  
Paolo Zampieri, Italy  
Giulio Zani , Italy  
Mariano Angelo Zanini , Italy  
Zhixiong Zeng , Hong Kong  
Mustafa Zeybek, Turkey  
Henglong Zhang , China  
Jiupeng Zhang, China  
Tingting Zhang , China  
Zengping Zhang, China  
Zetian Zhang , China  
Zhigang Zhang , China  
Zhipeng Zhao , Japan  
Jun Zhao , China  
Annan Zhou , Australia  
Jia-wen Zhou , China  
Hai-Tao Zhu , China  
Peng Zhu , China  
QuanJie Zhu , China  
Wenjun Zhu , China  
Marco Zucca, Italy  
Haoran Zuo, Australia  
Junqing Zuo , China  
Robert Černý , Czech Republic  
Süleyman İpek , Turkey

# Contents


## **Surrounding Rock Stresses on a Working Face-End Roof under Mining Influence**

Kang Wang , Xinglong Huang, Haibo Li, Feng Zhang , Jiazhen Li , and Zhijie Zhu   
Research Article (11 pages), Article ID 9915008, Volume 2021 (2021)

## **Analysis on Influence Factors of Roadway Instability in High-Stress, Steeply Inclined Extra-Thick Coal Seam**

Hai Rong , Liting Pan, Xiaoyan Li, Ming Wang, Zeliang Qu, Mengsheng Lu, and Kaipeng Guo  
Research Article (17 pages), Article ID 4676685, Volume 2021 (2021)


## **Deformation Mechanism and Surrounding Rock Control in High-Stress Soft Rock Roadway: A Case Study**

Yuwen Gao, Chen Wang , Yong Liu, Yuyang Wang, and Lianchang Han  
Research Article (15 pages), Article ID 9950391, Volume 2021 (2021)












## **Investigation on Surrounding Rock Stability Control Technology of High Stress Roadway in Steeply Dipping Coal Seam**

Honglin Liu , Chen Xu, Hongzhi Wang, Guodong Li, and Sanyang Fan  
Research Article (11 pages), Article ID 5269716, Volume 2021 (2021)


## **Height of the Fractured Zone in Coal Mining under Extra-Thick Coal Seam Geological Conditions**

Dequan Sun, Xiaoyan Li, Zhijie Zhu , Yang Li, and Fang Cui  
Research Article (9 pages), Article ID 9998545, Volume 2021 (2021)


## **Evolution Analysis of Microseismic Events before and after Mining through Large-Scale Weak Zone with High Confined Water**

Jing Jia , Xianjie Hao , Guanghui Zhao , Yubao Li , Xiaoyu Chuai , Lei Huang , Guangyao Pan , Yingnan Wei , Kai Chen , Ruilai Huang , and Rongcheng Zhan   
Research Article (12 pages), Article ID 6915221, Volume 2021 (2021)

## **Mechanism and Control of Cable Breakage in a Roadway with Thick Top Coal in a Rockburst Mine**

Ying Xu , Xiekang Zhou, and Weimei Gong  
Research Article (12 pages), Article ID 2275820, Volume 2021 (2021)






## **Study on the Effect of Soft and Hard Coal Pore Structure on Gas Adsorption Characteristics**

Xun Zhao , Tao Feng, Ping Wang, and Ze Liao  
Research Article (10 pages), Article ID 1425227, Volume 2021 (2021)


## **Study on the Lagging Support Mechanism of Anchor Cable in Coal Roadway Based on FLAC<sup>3D</sup> Modified Model**

Xiangyu Wang , Guanghui Wang , Bowen Wu , and Shuaigang Liu   
Research Article (12 pages), Article ID 9919454, Volume 2021 (2021)


## **Analysis on the Influence Degree of Deformation Control Factors of Deep-Buried Roadway's Fractured Surrounding Rock Using Orthogonal Design**

Ke Li , Weijian Yu , Youlin Xu , Ze Zhou , Mengtang Xu , and Wei Liang  
Research Article (11 pages), Article ID 9981539, Volume 2021 (2021)

**The Stability Factors' Sensitivity Analysis of Key Rock B and Its Engineering Application of Gob-Side Entry Driving in Fully-Mechanized Caving Faces**

Hong-Sheng Wang , Hai-Qing Shuang, Lei Li, and Shuang-Shuang Xiao  
Research Article (11 pages), Article ID 9963450, Volume 2021 (2021)

**Research on the Reasonable Coal Pillar Width and Surrounding Rock Supporting Optimization of Gob-Side Entry under Inclined Seam Condition**

Li-li Jiang, Zeng-qiang Yang , and Gang-wei Li  
Research Article (13 pages), Article ID 7145821, Volume 2021 (2021)


**Exploration and Practice of Pressure Relief by Slotting Coal Seams with a Diamond Wire Saw**

Zhu Tang , Shuqing Li , Fei Huang , Shouqing Huang, and Kangxu Cai  
Research Article (7 pages), Article ID 9961326, Volume 2021 (2021)


**Grouting Technique for Gob-Side Entry Retaining in Deep Mines**

Xianyang Yu , Zhihong Sun, Min Deng, and Jinlin Xin  
Research Article (9 pages), Article ID 5343937, Volume 2021 (2021)







**Research and Application of Open-Off Cut Roof Cutting Pressure Releasing Technology**

Xingen Ma , Manchao He, Weidong Li, Yilong Wang, Lifeng Li, Xiaohu Sun, Yongyuan Li, Leiyu Gu, and Xingfeng Sha  
Research Article (14 pages), Article ID 9989213, Volume 2021 (2021)


**Large-Scale Model Test of a Micropile Group for Landslide Control**

Xueling Liu, Jinkai Yan , Lei Liu, and Bing Han  
Research Article (11 pages), Article ID 6687124, Volume 2021 (2021)






**Risk Early Warning Evaluation of Coal Mine Water Inrush Based on Complex Network and Its Application**

Yanhui Li , Jianbiao Bai , Wei Yan , Xiangyu Wang , Bowen Wu , Shuaigang Liu , Jun Xu, and Jiaxin Sun  
Research Article (13 pages), Article ID 9980948, Volume 2021 (2021)

**Pile-Soil Stress Ratio and Settlement of Composite Foundation Bidirectionally Reinforced by Piles and Geosynthetics under Embankment Load**

Binhui Ma , Zhuo Li, Kai Cai, Meng Liu, Minghua Zhao, Bingchu Chen, Qiunan Chen, and Zhiyong Hu  
Research Article (10 pages), Article ID 5575878, Volume 2021 (2021)

**Study on Dynamic Evolution of Roof Crack and Support Timing of Secondary Tunneling for Large Section Open-Off Cut in Deep Mines**

Shuaigang Liu , Jianbiao Bai , Xiangyu Wang , Bowen Wu , Guanghui Wang , Yanhui Li , and Jun Xu  
Research Article (16 pages), Article ID 9918470, Volume 2021 (2021)

# Contents







## **Mining-Induced Redistribution of the Abnormal Stress under the Close Bearing Coal Pillar for Entry Design**

Xudong Liu, Wenlong Shen , Jianbiao Bai , Rui Wang , Jizhong Kang, and Xiangyu Wang   
Research Article (13 pages), Article ID 5595372, Volume 2021 (2021)





## **Instability Analysis and Reinforcement Support Technology of Coal-Rock Interbed Roadway in Gaojiazhuang Coal Mine**

Chaolin Liu and Guohua Zhang   
Research Article (17 pages), Article ID 5542830, Volume 2021 (2021)


## **Distribution Law of Mining Stress of the Gob-Side Entry Retaining in Deep Mining Thin Coal Seam**

Tao Qin , Kai Ren , Chen Jiang , Yanwei Duan , Zhi Liu , and Lei Wang   
Research Article (9 pages), Article ID 5589948, Volume 2021 (2021)

## **An Innovative Elastoplastic Analysis for Soft Surrounding Rock considering Supporting Opportunity Based on Drucker-Prager Strength Criterion**

Rui Wang , Xu-dong Liu , Jian-biao Bai , Shuai Yan , and Jun Xu  
Research Article (9 pages), Article ID 5555839, Volume 2021 (2021)

## **Theoretical Analysis on Distribution Pattern of Plastic Zone in Surrounding Rock of High-Gas-Coal Roadway**

Chao Yuan , Liming Cao, Lei Fan, and Jianqiang Guo  
Research Article (17 pages), Article ID 6684243, Volume 2021 (2021)



## **Study on Pressure Relief Effect of Rock Mass with Different Borehole Parameters**

Chao Peng  and Wanrong Liu   
Research Article (15 pages), Article ID 5558673, Volume 2021 (2021)

## **Numerical Analysis of the Width Design of a Protective Pillar in High-Stress Roadway: A Case Study**

FuZhou Qi , ZhanGuo Ma, Ning Li , Bin Li, Zhiliu Wang, and WeiXia Ma  
Research Article (18 pages), Article ID 5533364, Volume 2021 (2021)


## **Properties of Gobi Aggregate and Sulfide-Rich Tailings Cemented Paste Backfill and Its Application in a High-Stress Metal Mine**

D. Q. Deng , Y. H. Liang , and F. C. Huangfu  
Research Article (12 pages), Article ID 6624915, Volume 2021 (2021)



## **A Study of the Anchorage Body Fracture Evolution and the Energy Dissipation Rule: Comparison between Tensioned Rock Bolts and Torqued Rock Bolts**

Bowen Wu , Xiangyu Wang , Jianbiao Bai , Shuaigang Liu , Guanghui Wang, and Guanjun Li  
Research Article (14 pages), Article ID 5542569, Volume 2021 (2021)

## **Study on Safety Control of Large-Section Roadway with High Stress and Broken Surrounding Rock**

Wen-qing Peng , Hao Zhu, Qi Wang, and Gang Peng  
Research Article (12 pages), Article ID 6686208, Volume 2021 (2021)

**Partitioning Control Mechanism and Engineering Practice of Rebuilding Bearing Arch in Surrounding Rock under High Ground Stress**

Mengtang Xu , Ke Li , and Youlin Xu

Research Article (9 pages), Article ID 6667182, Volume 2021 (2021)

## Research Article

# Surrounding Rock Stresses on a Working Face-End Roof under Mining Influence

Kang Wang <sup>1</sup>, Xinglong Huang,<sup>2,3</sup> Haibo Li,<sup>2,3</sup> Feng Zhang <sup>1,2,4</sup>, Jiazhen Li <sup>1</sup>,  
and Zhijie Zhu <sup>1,2</sup>

<sup>1</sup>Mining Engineering School, Liaoning Technical University, FuXin 123000, China

<sup>2</sup>Engineering Laboratory of Deep Mine Rockburst Disaster Assessment, Jinan 250104, China

<sup>3</sup>Shandong Bureau of Coal Geology, Jinan 250104, China

<sup>4</sup>Department of Mining Engineering, Shanxi Institute of Technology, Yang Quan 045000, China

Correspondence should be addressed to Feng Zhang; [ln\\_zns@163.com](mailto:ln_zns@163.com)

Received 9 March 2021; Revised 6 May 2021; Accepted 5 October 2021; Published 10 November 2021

Academic Editor: Quoc-Bao Bui

Copyright © 2021 Kang Wang et al. This is an open access article distributed under the Creative Commons Attribution License, which permits unrestricted use, distribution, and reproduction in any medium, provided the original work is properly cited.

The evolution process of the surrounding rock failure mechanism is studied because of spalling and roof fall accidents at the top corner of longwall top coal caving faces affected by mining and the difficulty of moving the advanced end support. Methods are proposed to improve the stability of surrounding rocks at the top corner of the end including cutting at the top corner of the end, reinforcing the anchor cable, changing the stress distribution of surrounding rocks at the top corner of the end, and transferring the stress concentration area of surrounding rocks to the deeper rock. Field observations of the surrounding rocks at the top corner of the 15107 fully mechanized caving face show that the stress value of the surrounding rocks at the corner between the roof of the return airway and the coal wall of the working face is 28.9 MPa when the surrounding rocks are in a stable state without mining. The stress value of surrounding rocks at the top corner of the end is 32.3 MPa when it is affected by mining, which results in spalling and roof fall. The surrounding rocks are in a stable state when the maximum stress of the surrounding rocks at the top corner of the reinforced anchor cable's back-end is 26.1 MPa. The results show that cutting of the surrounding rocks at the top corner of the end and the reinforcement of the anchor cable can avoid the spalling and roof fall when the top corner of the end is affected by mining and can ensure that the end support advances and working face moves forward.

## 1. Introduction

The roof of the working face-end area of the longwall top coal caving (LTCC) face is affected by many factors such as the forward movement of the working face and the effect of the abutment pressure during the mining, which makes it more difficult to ensure the stability of the roof of the face-end [1]. In the western part of Turkey, Basarir et al. predicated the stresses around main and tail gates during top coal caving by numerical analysis [2]. In Slovenia, Jeromel et al. studied the multilevel longwall top coal caving process by numerical simulations and in situ measurements during coal excavation at different locations in the Velenje Coal Mine [3]. Zang et al. studied the formation and failure process of the triangle hanging plate at the face-end of LTCC by using theoretical

analysis, numerical simulation, and field measurement and analyzed the protective effect of the triangle hanging plate to the weak area [4]. Summarizing studies about the stability of the face-end of LTCC, it is generally believed that instability of the face-end can lead to a lower recovery ratio [5–8]. In recent years, experts such as Wang et al., Liu, and Jin et al. [9, 10, 12] proposed to use end support to maximize the strength and area of roof control, to reduce the influence of periodic weighting on the roof fracture, and to enhance the adhesion of surrounding rocks at the top corner of the end to control the stability of the end roof. However, these methods only enhance the support strength of external surrounding rocks and the cohesion of near-distance coal at the top corner of the roadway end from the surface and do not change the stress distribution of surrounding rocks and the failure range of



surrounding rocks with mining from the source. Problems such as support movement and maintenance difficulties caused by spalling and roof falling of the end roof affected by mining still cannot be solved under the existing production and support conditions.

Taking the 15107 working face of Erjing Coal Mine as the engineering background, this paper expounds on the failure mechanism and the evolution process of surrounding rocks at the top corner of a fully mechanized caving face under the influence of mining through theoretical analysis and numerical simulation. We examine changing the original stress distribution of surrounding rocks at the top corner of the end to transfer the stress concentration area of the top corner to the deep and to enhance the antimining disturbance ability of the surrounding rocks at the top corner of the end. Industrial field tests verify the feasibility and rationality of the method.

## 2. Evolution Process of the Failure Mechanism of Surrounding Rocks at the Top Corner of the End

**2.1. Engineering Background.** The 15107 working face of Erjing Coal Mine is located in the northwest wing of the 15# coal I mining area and is deeply buried with complex geological structures. The working face adopts top coal caving mining technology for a coal thickness of 5 m and a mining and caving ratio of 1.083. The intake and return air roadways are rectangular, and the anchor cable and advanced end support are used to maintain the roof. The existing support methods can basically control the deformation of the roadway roof and two sides. However, the coal wall at the top corner of both ends is loose and unstable because it is affected by the mining of the working face and periodic weighting of the roof. Coal wall bearing capacity of the overlying roof strata is gradually lost. The broken roof and serious subsidence cause spalling and roof fall and difficulty in moving the advanced end support when the working face passes the head and tail of the machine, which will affect the advancing speed of the working face (Figure 1).

**2.2. Stress Analysis of Surrounding Rocks at the Top Corner of the End.** Lateral pressure of the roadway is biaxially unequal and variable under the influence of mining, especially for geological conditions with deep burial and complex structures. At present, it is impossible to theoretically derive the stress solution of roadway surrounding rocks under the condition of unequal lateral pressure. However, under the assumption that the lateral pressure is equal, the analytical formula of roadway surrounding rock stress is solved

according to the elastic-plastic theory. The stress distribution of surrounding rocks and the plastic failure zone are approximately analyzed, along with actual mechanical parameters.

Because the height and width of a roadway are far less than the length of a roadway, the stress calculation of a rectangular roadway is transformed into a plane rectangular strain problem. The analytical formula of surrounding rock stress is obtained by using complex variable function theory and elastic-plastic mechanics theory with and without support [11–17].

According to the complex variable function method, the expression of the stress value of roadway surrounding rocks under the plane strain problem is

$$U = \operatorname{Re} \left[ \bar{z} \Phi(z) + \int \psi(z) dz \right]. \quad (1)$$

In the formula,  $\Phi(z)$  and  $\Psi(z)$  are two analytic functions of complex variable  $z = x + iy$ .  $\operatorname{Re}$  represents the real part of the complex number,  $z$  is the complex sum of the complex variable  $Z$ , and  $U$  is the Airy stress function.

**2.2.1. The Surrounding Rock Stress of the Roadway Is Not Subject to Support Resistance.** The roadway's external surrounding rocks in the direction of  $\alpha$ -angle with the  $x$ -axis are subjected to uniform pressure  $p$ , and the roadway's internal surface is not stressed. As shown in Figure 2, the stress of the external surrounding rocks is consistent, which meets the following relationship:

$$\begin{cases} \bar{X} = \bar{Y} = X = Y = 0, \sigma_1 = p, \sigma_2 = 0, \\ B = \frac{1}{4} (\sigma_1 + \sigma_2) = \frac{p}{4}, \\ B' + iC' = -\frac{1}{2} (\sigma_1 - \sigma_2) e^{-2i\alpha} = -\frac{p}{2} e^{-2i\alpha}, \\ B' - iC' = -\frac{p}{2} e^{-2i\alpha}, \end{cases} \quad (2)$$

where  $p$  denotes the stress of surrounding rocks,  $X$  is the surface force in the  $x$ -direction of the roadway, and  $Y$  is the surface force in the  $y$ -direction of the roadway.  $\sigma_\theta + \sigma_\gamma = 4\operatorname{Re}\Phi(\xi)$  is the stress value of the roadway side; in the roadway side,  $\sigma_\gamma = 0$  and  $\sigma_\theta = \xi = \cos\theta + i\sin\theta$  after simplification can be obtained.

Assume surrounding rock stress of the roadway without support resistance is  $\sigma'_\theta$ .

$$\sigma'_\theta = \frac{(1-s)16pc_0^2 + (1-s)16pc_1^2 + 32pc_0c_1(1-s)c_1 + (1+s)c_0/c_2 - c_0 - (1-s)144pc_2^2 + (1-s)72pc_0c_2 \cos 4\theta - [(1-s)40pc_0c_1 + 64pc_0^2(1-s)c_1 + (1+s)c_0/c_2 - c_0 - 96pc_0c_2(1-s)c_1 + (1+s)c_0/c_2 - c_0] \cos 2\theta}{[64c_0^2 + 16c_1^2 + 144c_2^2 + 32(3c_1c_2 - 2c_0c_1) \cos 2\theta - 192c_0c_2 \cos 4\theta]} \quad (3)$$

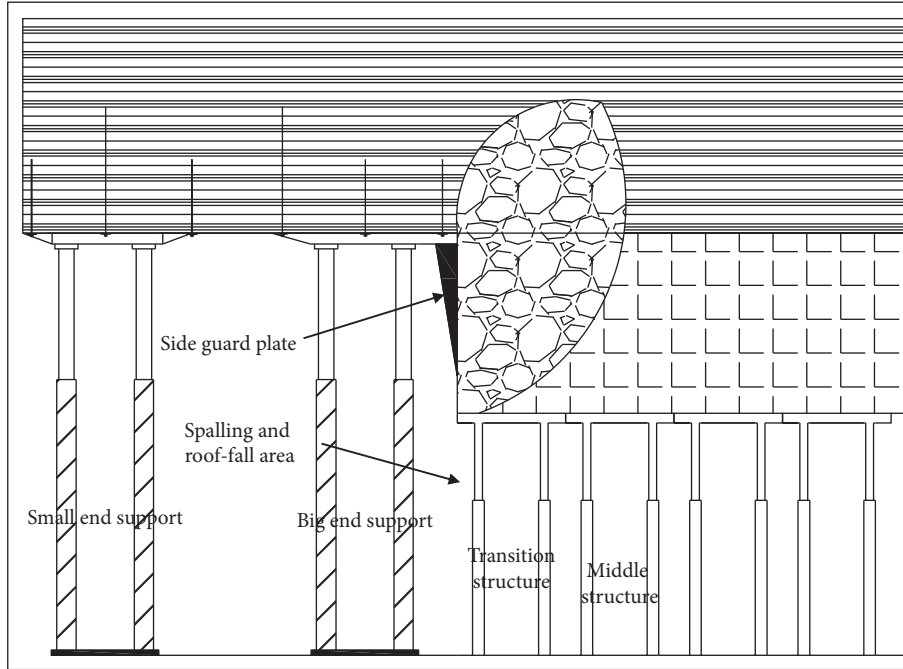


FIGURE 1: Spalling and roof fall area.

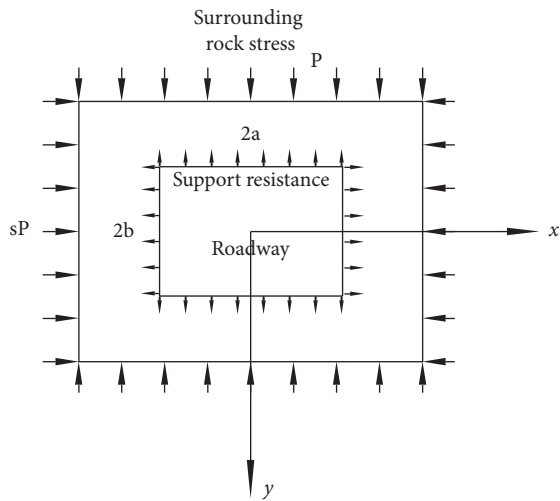


FIGURE 2: The mechanical model of rectangular roadway analysis.

where  $c_0$ ,  $c_1$ , and  $c_2$  represent three coefficients of the mapping function,  $\mu$  denotes the strain constant,  $s$  is the lateral pressure coefficient of the roadway, and  $\theta$  is the angle.

2.2.2. *The Stress of the Roadway Surrounding Rocks Is Only Subject to Support Resistance.* The surrounding rocks of the roadway are only supported by the resistance provided by the support body. The support resistance is uniformly distributed, and the roadway surface is not subjected to any shear force. The internal support resistance is shown in Figure 2, which meets the following relationship:

$$\begin{cases} \bar{X} = \bar{Y} = X = Y = 0, \sigma_1 = p, \sigma_2 = 0, \\ B = \frac{1}{4}(\sigma_1 + \sigma_2) = 0, \\ Bt + iCt = -\frac{1}{2}(\sigma_1 - \sigma_2)e^{-2i\alpha} = 0, \\ Bt - iCt = 0. \end{cases} \quad (4)$$

Because  $\sigma_\theta + \sigma_y = 4\text{Re}\Phi(\xi)$ ,  $\sigma_y = 0$ .

Assume surrounding rock stress of the roadway without support resistance is  $\sigma'_\theta$ .

$$\sigma''_\theta = \frac{[(1 + \mu)X/8\pi\cos\theta - (1 + \mu)Y/8\pi\sin\theta + G\cos2\theta - F\sin2\theta][3c_2\cos4\theta + c_1\cos2\theta - 2c_0]}{9c_2^2 + c_1^2 + 4c_0^2 + 6c_1c_2 - 12c_0c_2\cos4\theta - 4c_0c_2\cos2\theta} + \frac{4[(1 + \mu)X/8\pi\sin\theta - (1 + \mu)Y/8\pi\cos\theta + G\sin2\theta + F\cos2\theta][3c_2\sin4\theta + c_1\sin2\theta]}{9c_2^2 + c_1^2 + 4c_0^2 + 6c_1c_2 - 12c_0c_2\cos4\theta - 4c_0c_2\cos2\theta} \quad (5)$$

From the derivation of (3) and (5), it can be concluded that the stress calculation formula of the roadway under the combined action of surrounding rock stress  $\sigma_\theta''$  is

$$\sigma''_\theta = \sigma'_\theta + \sigma''_\theta \quad (6)$$

Since the pressure measurement coefficient of roadway surrounding rocks of the adjacent 15105 working face is 0.4,

the pressure measurement coefficient of the 15107 fully mechanized caving face is 0.4 using the engineering analogy method. Combined with the geological data of the 15107 fully mechanized caving face, Mathcad 14 software [18] is used to analyze the overall assignment using formula (6) and illustrated in Figure 3.

The stress concentration area of roadway surrounding rocks mainly exists in the top and bottom corners of the roadway, as shown in Figure 3, and the stress value reaches the maximum at the top and bottom corners, which is close to 30 MPa. The roadway is in a temporary stable state.

As shown in Figure 4, when the vertical stress  $Y$  is constant, with the increase of lateral pressure coefficient  $s$ , the horizontal stress  $X$  increases, and the stress at the top corner of the end increases gradually. When the horizontal stress  $X$  is constant, the vertical stress  $Y$  increases with the decrease of the lateral pressure coefficient  $s$ , and the stress at the top corner of the end decreases gradually. According to the above analysis, the roadway stress is mainly affected by the lateral pressure coefficient  $s$ . When the geological and mining conditions are certain, the lateral pressure coefficient  $s$  is mainly affected by mining disturbance.

When the end of the working face is disturbed by mining, the stress  $\sigma_\theta$  at the top corner of the two ends is several times of that under static pressure, and the top corner stress  $\sigma_\theta$  increases with the decrease of the distance between the shearer and the end. When the shearer continues to cut coal in the direction of the end and the surrounding rocks' stress  $\sigma_\theta$  at the top corner of the end reaches a certain critical value, the roof begins to loosen, becomes less stable, and shows fracture failure, and spalling and roof fall accidents occur.

**2.3. Numerical Simulation of the Failure Evolution Process of Surrounding Rocks at the Top Corner of the End.** FLAC3D was used to simulate the variation of stress in the plastic zone of surrounding rocks at the top corner of the 15107 fully mechanized caving face before and after mining [19–29]. The buried depth of the coal seam is 740 m, the model size is 80 m × 50 m × 60 m, the overlying load is 18.5 MPa, and the horizontal stress is 7.4 MPa. The basic parameters of rock mechanics are shown in Table 1.

Figure 5 illustrates two stress states and plastic zone distribution characteristics of surrounding rocks. The stress concentration area of the roadway surrounding rock is at the top and bottom corner when the working face is not mined. The top corner stress has reached 27.5 MPa. The stress is balanced at the four corners of the roadway, the plastic zone has a butterfly distribution, and the roadway is in a stable state.

The top corner stress of the roadway increases from 27.5 MPa to 36.6 MPa in a stable state when the working face is mined. The stress concentration area has narrowed, the surrounding rock has formed shear failure, and the coal body is less stable at the top corner of the end. It is concluded that the rib spalling and roof caving have appeared at the top corner of the end, and the surrounding rock is in an unstable state.

### 3. Control Scheme of Surrounding Rocks at the Top Corner of the End

**3.1. Control Scheme.** When spalling and roof fall appear at the end of a fully mechanized caving face, normally, the failure mechanism of surrounding rocks is mitigated by cutting the coal wall near the top corner of the working face. The original stress distribution is changed at the top corner of the end so that the stress concentration area in the surrounding rocks is released at the top corner of the end, and the stress concentration area at the top corner of the end is transferred to the deeper rock. After cutting, the top is supplemented with an anchor cable to strengthen the support strength at the top corner of the end and reduce the probability of coal wall roof instability. Spalling and roof fall accidents must be reduced to ensure the movement of the advanced end support and the mining of the working face.

For the anchor machine to work smoothly after cutting, the wind pick is used to cut at 1 m from the roof, and the width and height are 1 m. After cutting, adding the metal mesh, and patching the anchor cable ( $\phi 17.8 \text{ mm} \times 8300 \text{ mm}$ ) to strengthen support, anchor cable spacing is 0.5 m, row spacing is 1 m, each row is 2 m, and square gasket is 250 mm × 250 mm. When cutting once a day, each cutting length is 4 m to ensure a day of production cycle progress as shown in Figure 6.

**3.2. Simulation Test of the Control Scheme.** FLAC3D was used to simulate the stress change of the plastic zone of surrounding rocks of the 15107 fully mechanized caving face when it was mined after cutting and reinforcing anchor cables, as shown in Figure 7.

Figure 7 illustrates that when the original stress concentration area of the surrounding rock at the top corner of the end of the air return cross-heading is released, stress concentration area is transferred to the deep part of the top corner of the end, and the maximum stress value at the top corner of the end is also maintained at 27.5 MPa in a stable state. Under the conditions of Figure 7, there is no plastic failure in the surrounding rocks at the top corner, and there are no spalling or roof fall accidents, so the working face can move forward normally.

### 4. Field Test

The KSE-II-1 borehole stress meter was used to arrange two monitoring stations along the top corner of the return air roadway in the 15107 fully mechanized caving face. Three measuring points were arranged in each monitoring station, as shown in Figure 8. Measuring point 1 was 0.5 m from the exposed coal wall of the top corner with an elevation angle of 30°. The distance between measuring point 2 and measuring point 1 was 1 m, and the distance between measuring point 2 and measuring point 3 was 2 m. The first monitoring station is set at 20 m in front of the working face to monitor the stress change of the surrounding rock at the top corner of the end. The second monitoring station is set at 50 m in front of the working face, which is used to monitor the change of the

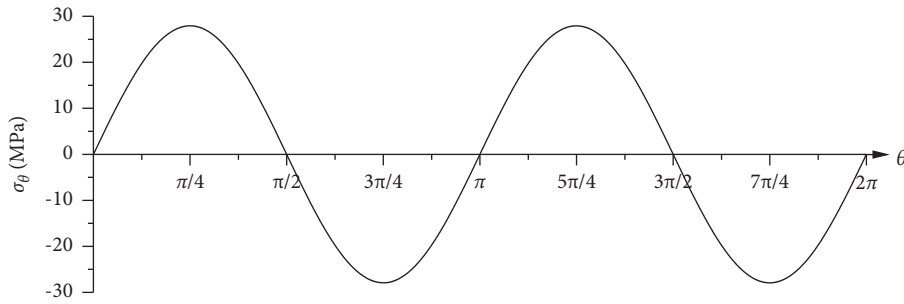


FIGURE 3: Stress distribution of the roadway.

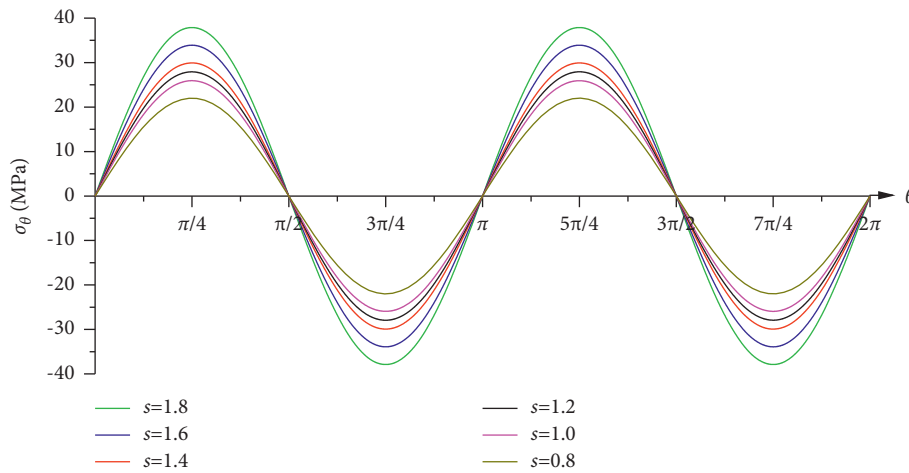


FIGURE 4: The stress distribution of the roadway with the change of lateral pressure coefficient.

TABLE 1: Basic parameters of rock mechanics.

Lithology	Internal friction angle (°)	Cohesion (MPa)	Tensile strength (MPa)	Elastic modulus (GPa)	Poisson's ratio ( $\mu$ )	Density ( $\text{kg}\cdot\text{m}^{-3}$ )
Mudstone	33.0	4.50	0.93	6.20	0.12	2597
Sandy shale	33.6	10.08	1.03	3.00	0.15	2577
Shale	33.4	10.11	1.20	10.60	0.11	2653
Limestone	36.0	12.32	3.41	23.60	0.12	2682
Coal	29.5	2.11	2.60	4.20	0.22	1420
Fine sandstone	33.4	10.12	1.95	18.60	0.21	2582
Sandy mudstone	33.0	4.50	0.93	6.20	0.12	2597
Mudstone	33.0	4.26	1.05	5.00	0.26	2753

top corner stress of the end when it is not mined and when it is mined after cutting and reinforcing anchor cables.

Observations from two monitoring stations are calculated and summarized in previous research. The stress changes of the same measuring point in different measuring points and different states were compared and analyzed, and the stress changes of the same measuring point under the influence of mining were compared and analyzed.

- (1) The stresses of the surrounding rock at measuring points 1, 2, and 3 of the first monitoring station were compared and analyzed when the working face was

not mined, mined, and mined after cutting and reinforcing with anchor cables, as shown in Figure 9.

- (i) Figure 9(a) illustrates that measuring points are affected by the original rock stress at the top corner of the end. The maximum stress value is 28.9 MPa, the stress is relatively concentrated, and there are no spalling and roof fall. When it is mined, the surrounding rock stress concentration area at the top corner of the end is released. Surrounding rock stress value is very low, but spalling and roof fall accidents may occur.



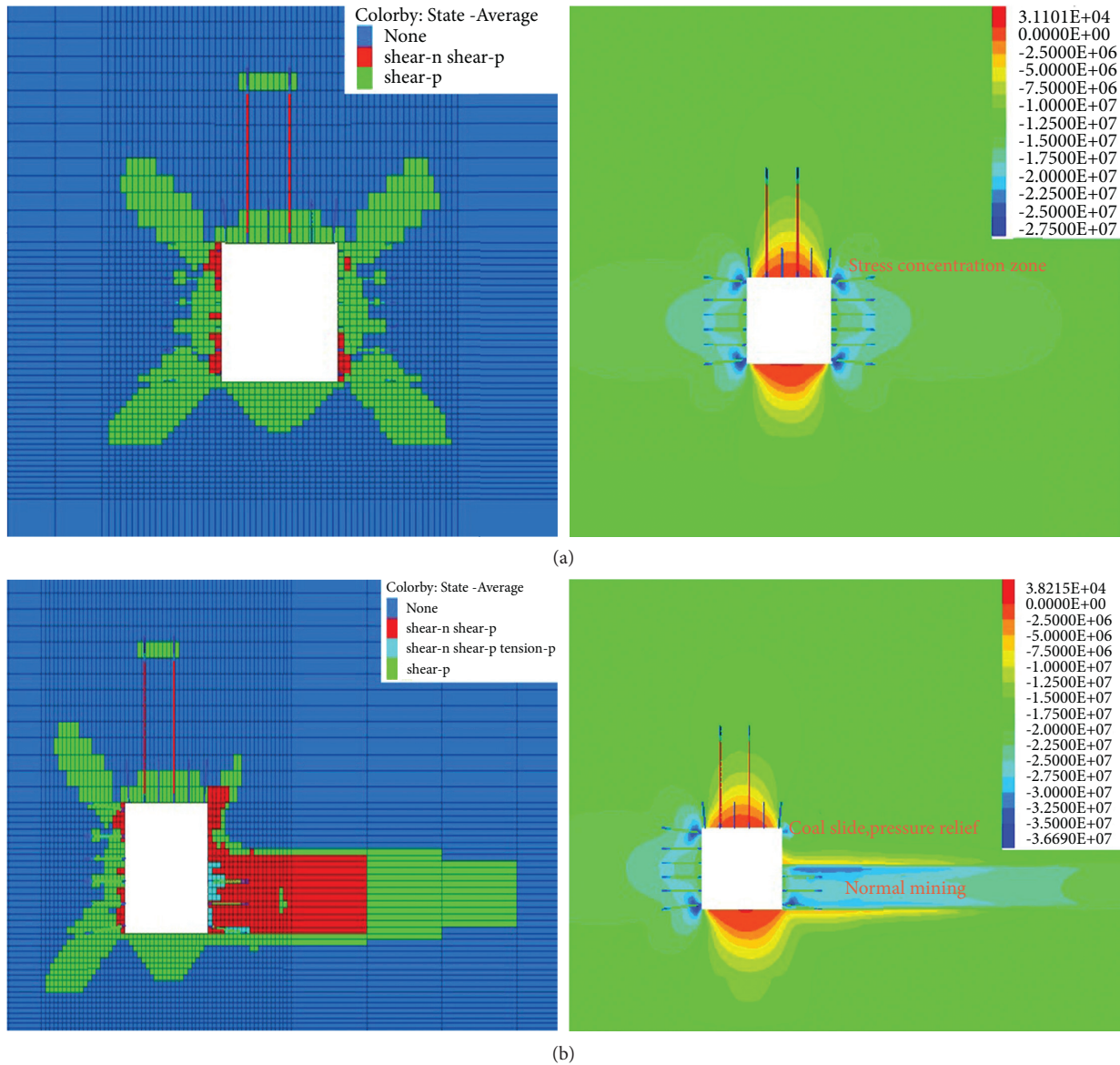


FIGURE 5: Distribution of the plastic zone and stress of surrounding rocks at the top corner of the end before and after mining: (a) stress distribution of roadway surrounding rocks without mining; (b) stress distribution of roadway surrounding rocks after mining.

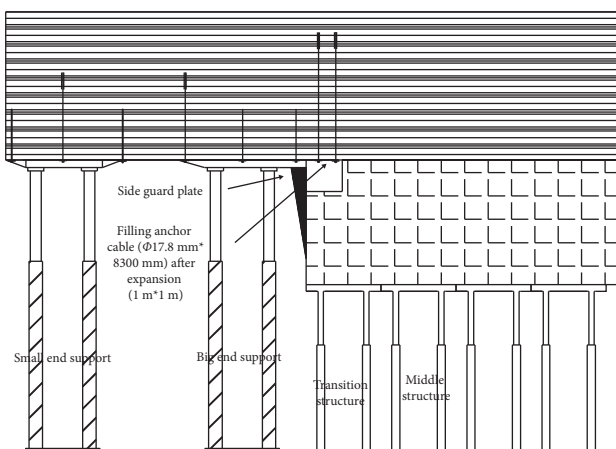


FIGURE 6: Cutting the repair cable.

When it is mined after cutting and reinforcing with an anchor cable, the surrounding rock stress at the top corner of the end has been released, the stress value is low, and the surrounding rock tends to be stable.

- (ii) Figure 9(b) shows that when the rock face is not mined, the stress value of measuring point 2 is 32.5 MPa at the top corner of the end, and the coal wall is loose, unstable, and wrapped by the external coal body, which is temporarily in a stable state. When it is mined, the stress value is 38.3 MPa at the top corner of the end, so coal loses stability, and spalling and roof caving occur. After the reinforcement of the anchor cable by cutting, the stress at measuring point 2 is released, the stress concentration area is

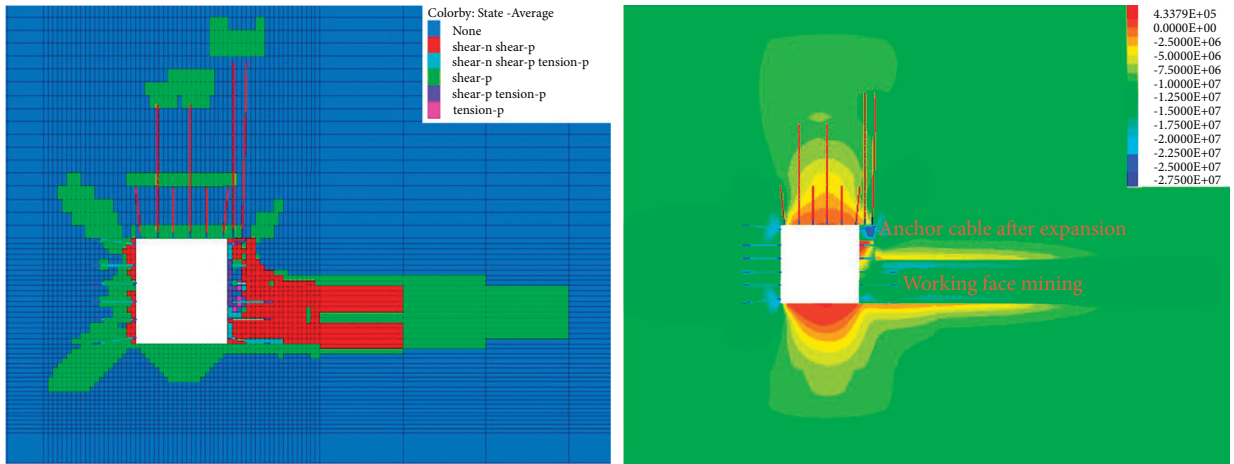


FIGURE 7: Distribution of the plastic zone and stress at the top corner of the end during mining after cutting and reinforcing anchor cables.

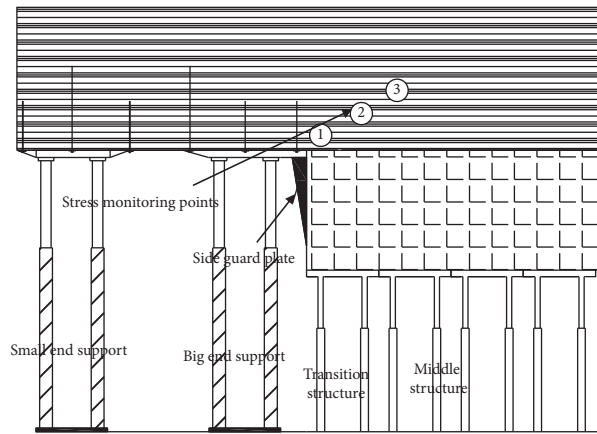


FIGURE 8: Distribution of measuring points.

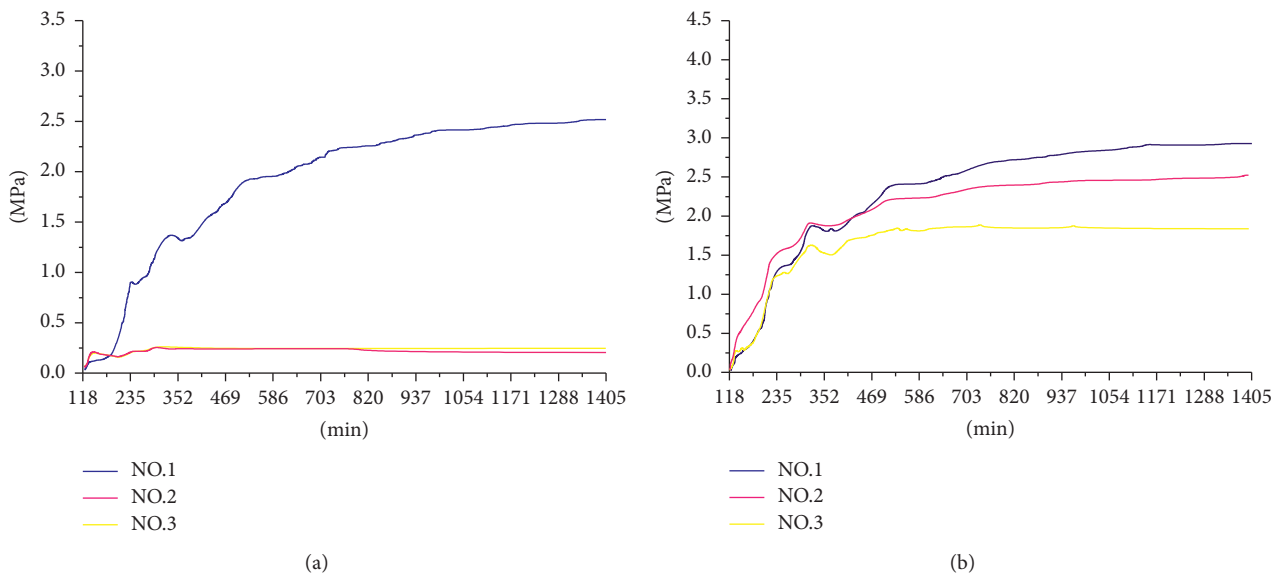
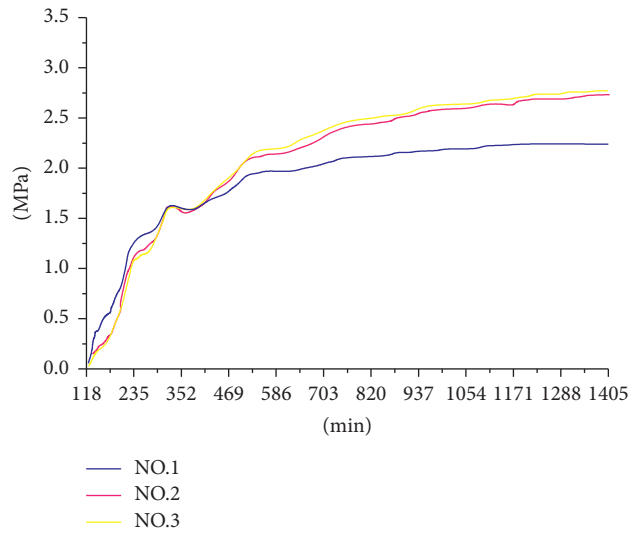


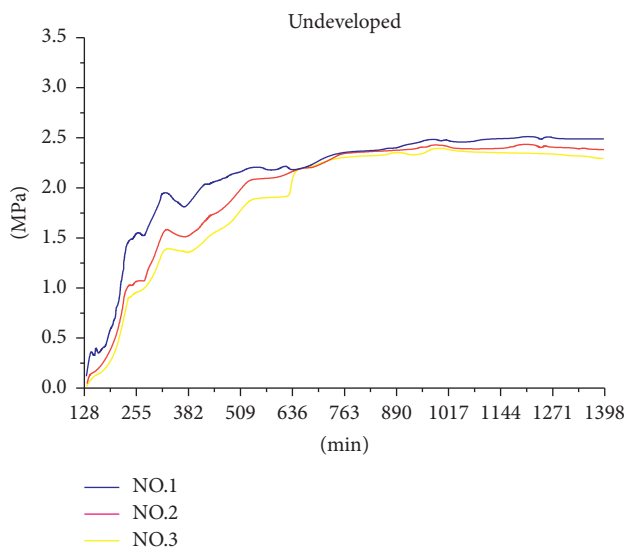
FIGURE 9: Continued.



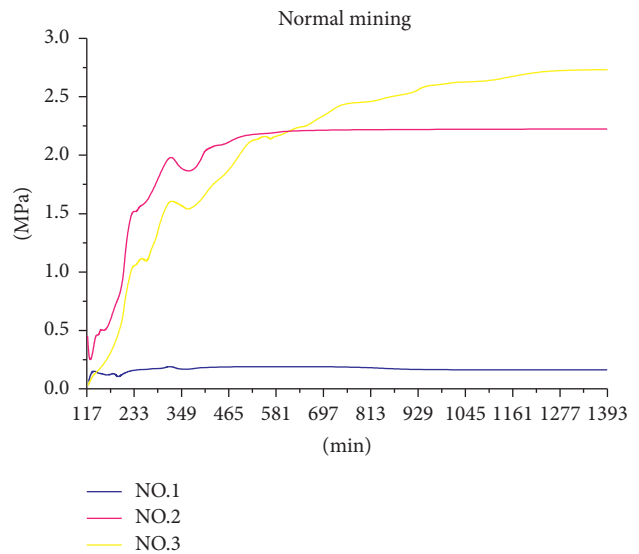


(c)

FIGURE 9: Stress curves of three measuring points at the top corner of the end under three conditions: (a) stress variation curves of measuring point 1 under three states; (b) stress variation curves of measuring point 2 under three states; (c) stress variation curves of measuring point 3 under three states



(a)



(b)

FIGURE 10: Continued.

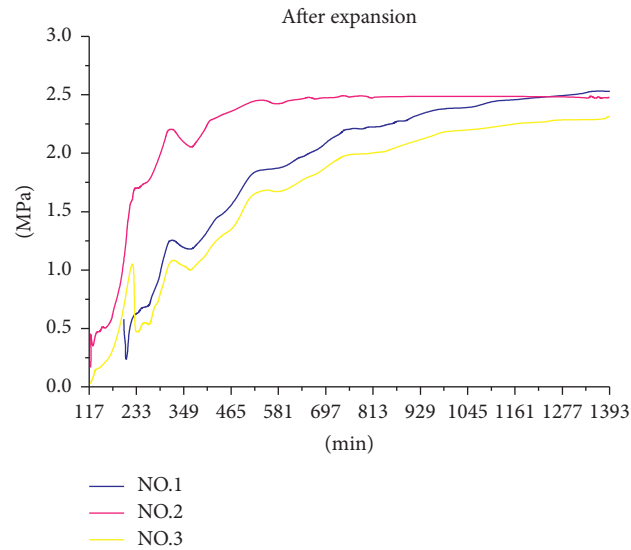


FIGURE 10: Stress variation of three measuring points under three states: (a) stress variation diagram of three measuring points at the top corner of the roadway before mining; (b) stress variation diagram of three measuring points at the top angle of the roadway end in normal mining; (c) stress variation diagram of three measuring points at the top corner of the end in mining after cutting and reinforcement of the anchor cable.

transferred to the deep rock, and the surrounding rock at the top corner of the end tends to be stable.

- (iii) Figure 9(c) shows that the stress concentration of the top corner at the end of the working face at measuring point 3 reaches 31.5 MPa without mining and with normal mining, which is gradually reduced compared with measuring point 2. However, because of mining, rib spalling and roof fall accidents are prone to occur. Compared with the stress of measuring point 1 and measuring point 3, the stress at measuring point 3 increases gradually after cutting and reinforcing the anchor cable. Cable reinforcement releases the stress concentration area at the top corner of the end, transfers the stress to the deep rock, and controls the surrounding rock at the top corner of the end.
- (2) The stresses of the surrounding rock at measuring points 1, 2, and 3 of the second monitoring station were compared and analyzed when the working face was not mined, mined, and mined after cutting and reinforcing with an anchor cable, as shown in Figure 10.
- (i) Figure 10(a) shows that the stress of measuring points 1, 2, and 3 at the top corner of the end decreases gradually without mining. The stress concentration area is formed at measuring point 1, and the surrounding rock stress at measuring point 1 is the highest, close to 28.9 MPa, which is in a critical state. At 28.9 MPa, mining of the working face is prone to spalling and roof fall accidents.
- (ii) Figure 10(b) shows that, compared with no mining, the stresses at measuring points 1 and 2 at the top corner of the end have been greatly reduced, indicating that spalling and roof fall accidents may occur at the working face. The stress concentration area is released, and the stress at measuring point 3 exceeds 32.3 MPa, indicating that the spalling and roof fall accidents continue to expand to the deep rock.
- (iii) Figure 10(c) shows that when mining is carried out after cutting and reinforcing the anchor cable, the stress values of measuring points 1, 2, and 3 are all within 26.1 MPa, and the stress area is relatively concentrated. The stress concentration area of the measuring point around the top corner of the end is released to a certain extent, and there are no spalling or roof fall accidents, so the top corner of the end is controlled during mining.

## 5. Conclusions

Elastic-plastic mechanics, complex variable function theory, and Mathcad 14 software were used to analyze the stress of surrounding rocks at the top corner of the end. FLAC3D numerical simulation software was used to analyze the stress change of surrounding rocks and the failure of the plastic zone at the top corner of the end before and after the mining of a fully mechanized caving face. With the model, we simulate the evolution process of the failure mechanism of surrounding rocks at the top corner of the end.

The stress of roadway surrounding rocks under unequal lateral pressure is analyzed using elastic-plastic mechanics,

complex variable function theory, and Mathcad 14 software. It is concluded that the stress concentration area of roadway surrounding rocks is at the top and bottom corner of the roadway, and the maximum stress value is close to 30 MPa. We analyzed the influence of lateral pressure coefficient on roadway stress. The stress of the roadway increases with the increment of lateral pressure coefficient.

FLAC3D numerical simulation and field monitoring of the KSE-II-1 borehole stress meter were carried out using the failure evolution process of surrounding rocks at the top corner of a fully mechanized caving face. It is concluded that the stress of surrounding rocks is 28.9 MPa when the top corner of the end is stable, and the stress of surrounding rocks is 32.3 MPa when the rib spalling and roof fall occur under the influence of mining.

The stress distribution of the top corner of the end is changed after cutting and reinforcing the anchor cable, and the original stress concentration area is released and transferred to the deep rock. Under the influence of mining, the surrounding rock stress at the top corner of the end is maintained at 26.1 MPa, which is in a stable state.

## Data Availability

The data used to support the findings of this study are available from the corresponding author upon request.

## Conflicts of Interest

The authors declare that they have no conflicts of interest.

## Acknowledgments

This work was supported by Scientific and Technological Innovation Programs of Higher Education Institutions in ShanxiShanxi (2020L0724) and the Engineering Laboratory of Deep Mine Rockburst Disaster Assessment Open Project (LMYK2021009).

## References

- [1] Y. Z. Wu, "Stabilization principle and technique control of face-end support at fully-mechanized coal caving face," *Coal*, vol. 9, no. 107, pp. 25–28, 2008.
- [2] H. Basarir, I. Ferid Oge, and O. Aydin, "Prediction of the stresses around main and tail gates during top coal caving by 3D numerical analysis," *International Journal of Rock Mechanics and Mining Sciences*, vol. 76, pp. 88–97, 2015.
- [3] G. Jeromel, M. Medved, and J. Likar, "An analysis of the geomechanical processes in coal mining using the Velenje mining method," *Acta Geotechnica Slovenica*, vol. 7, pp. 31–45, 2010.
- [4] C. W. Zang, J. F. Xia, H. C. Li, and J. G. Zhu, "Study on rational support strength of roof at face-end area of fully mechanized caving face," *Safety In Coal Mines*, vol. 46, no. 6, pp. 50–53, 2015.
- [5] D. Z. Kong, W. Jiang, Y. Chen, Z. Song, and Z. Ma, "Study of roof stability of the end of working face in upward longwall top coal," *Arabian Journal of Geosciences*, vol. 10, pp. 184–194, 2017.
- [6] M. Khanal, D. Adhikary, and R. Balusu, "Preliminary study—geotechnical studies for introducing longwall top coal caving in Indian mines," *Journal of Mining Science*, vol. 50, no. 4, pp. 719–732, 2014.
- [7] J. Likar, M. Medved, M. Lenart, V. Malenković, G. Jeromel, and E. Dervarič, "Analysis of geomechanical changes in hanging wall caused by longwall multi top caving in coal mining," *Journal of Mining Science*, vol. 48, pp. 135–145, 2012.
- [8] W. Lawrence, "A method for the design of longwall gateroad roof support," *International Journal of Rock Mechanics and Mining Sciences*, vol. 46, pp. 789–795, 2004.
- [9] T. Jin, K. X. Zhang, Z. Y. Qin, and M. G. Fan, "Stability analysis and control of face end in fully-mechanized coal winning face," *Coal Technology*, vol. 11, pp. 29–32, 2015.
- [10] Z. J. Liu, "Analysis and control of falling and leaking mechanism of broken roof end," *Energy AND Energy Conservation*, vol. 11, pp. 172–173, 2015.
- [11] S. C. Li, S. C. Zhuo, and W. H. Xie, "Natural boundary element method for the stress field of circular roadway's surrounding rocks," *Journal of China Coal Society*, vol. 29, no. 6, pp. 672–675, 2004.
- [12] X. B. Wang, Y. S. Pan, and Y. J. Li, "Effect of confining pressure on distributions of horizontal and vertical stresses around rectangular roadway and broken rock zone," *Chinese Journal of Underground Space and Engineering*, vol. 2, no. 6, pp. 962–970, 2006.
- [13] M. Y. Fattah, M. J. Hamoud, F. A. Salman, and A. Raheem, "Complex variable solution of elastic tunneling problems," *International Journal of the Physical Sciences*, vol. 5, no. 13, pp. 1999–2013, 2010.
- [14] N. I. Muskhelishvili, *Some Basic Problems of Mathematical Theory of Elasticity*, Noordhoff, Groningen, The Netherlands, 2nd edition, 1963.
- [15] L. Yuan, Z. N. Gao, and X. R. Meng, "Viscoelastic analysis of stress concentration coefficient in rectangular roadway based on complex variable function," *Safety In Coal Mines*, vol. 44, no. 2, pp. 196–199, 2013.
- [16] R. F. Wang, K. X. Zhang, W. L. Shen, and H. Cui, "Research on grouting strengthening in control of stress concentration in deep tunnel surrounding rocks," *Coal Technology*, vol. 35, no. 1, pp. 65–68, 2016.
- [17] A. Bobet, "Drained and undrained response of deep tunnels subjected to far-field shearloading," *Tunnelling and Underground Space Technology*, vol. 25, pp. 21–31, 2010.
- [18] G. S. Zheng, *MATHCAD2000 Practical Tutorial*, National Defense Industry Press, Beijing, China, 2000.
- [19] D. Y. Chen, *Numerical Simulation on Pre-stressed Bolt Support of Underground Project*, Shandong University of Science and Technology, Qingdao, China, 2005.
- [20] Y. Wu, *Research on the Roadway Support under the Influence of Mining*, Inner Mongolia University of Science and Technology, Baotou, China, 2015.
- [21] L. Tian, "Simulation analysis of FLAC3D in support of numerical tunnel," *Inner Mongolia Coal Economy*, vol. 1, pp. 92–97, 2014.
- [22] Q. B. Meng, L. J. Han, W. G. Qiao, D. G. Lin, and L. C. Wei, "Numerical simulation of cross-section shape optimization design of deep soft rock roadway under high stress," *Journal of Mining and Safety Engineering*, vol. 29, no. 5, pp. 650–656, 2012.
- [23] Y. G. Gao, *Study on Rapid Modeling Method of FLAC3D Model Based on AutoCAD File*, Xi'an University of Science and Technology, Xi'an, China, 2012.
- [24] Y. H. Shan, Q. Y. Shang, L. K. Xie, and G. Guo, "Numerical simulation on deep laneway surrounding rocks deformation based on FLAC3D," *Morden Mining*, vol. 517, pp. 28–29, 2012.

- [25] D. Lin, Y. Yang, C. H. Wang, and G. R. Xu, "Pressure behavior and analysis of rock damage in roadway by the first mining based on FLAC3D simulation," *Science Technology and Engineering*, vol. 11, no. 15, pp. 3407–3412, 2011.
- [26] P. R. Dawson and D. E. Munson, "Numerical simulation of creep deformations around a room in a deep potash mine," *International Journal of Rock Mechanics and Mining Sciences*, vol. 20, no. 1, pp. 33–42, 1983.
- [27] M. Xiao, D. X. Ding, and Y. G. Mo, "Numerical simulation of surrounding rocks stability of soft rock roadway based on FLAC3D," *Mining R & D*, vol. 27, no. 1, pp. 73–75, 2007.
- [28] Z. Zhang, M. Deng, X. Wang, W. Yu, F. Zhang, and V. D. Dao, "Field and numerical investigations on the lower coal seam entry failure analysis under the remnant pillar," *Engineering Failure Analysis*, vol. 115, 2020.
- [29] Z. Zhang, M. Deng, J. Bai, S. Yan, and X. Y. Yu, "Stability control of gob-side entry retained under the gob with close distance coal seams," *International Journal of Mining Science and Technology*, vol. 31, no. 2, pp. 321–332, 2020.

## Research Article

# Analysis on Influence Factors of Roadway Instability in High-Stress, Steeply Inclined Extra-Thick Coal Seam

Hai Rong <sup>1,2</sup>, Liting Pan,<sup>1</sup> Xiaoyan Li,<sup>2,3</sup> Ming Wang,<sup>2,3</sup> Zeliang Qu,<sup>2,3</sup> Mengsheng Lu,<sup>2,3</sup> and Kaipeng Guo<sup>1,4</sup>

<sup>1</sup>College of Mining, Liaoning Technical University, Fuxin, Liaoning Province, China

<sup>2</sup>Engineering Laboratory of Deep Mine Rockburst Disaster Assessment, Jinan, Shandong Province, China

<sup>3</sup>Shandong Province Research Institute of Coal Geology Planning and Exploration, Jinan, Shandong Province, China

<sup>4</sup>State Key Laboratory of Mining Disaster Prevention and Control Co-Founded by Shandong Province and the Ministry of Science and Technology, Shandong University of Science and Technology, Qingdao, China

Correspondence should be addressed to Hai Rong; ronghai1988@163.com

Received 8 April 2021; Accepted 18 August 2021; Published 13 September 2021

Academic Editor: Emanuele Brunesi

Copyright © 2021 Hai Rong et al. This is an open access article distributed under the Creative Commons Attribution License, which permits unrestricted use, distribution, and reproduction in any medium, provided the original work is properly cited.

In order to solve the problem of roadway support safety in coal mining under high stress conditions and to improve safe and efficient production in coal mines, the control countermeasures of the surrounding rock stability and the optimization scheme of support are put forward and the model and numerical simulation of roadway bolt support system are established. Based on bolt support theory and instability mechanism of the coal rock dynamic system, this paper puts forward the evaluation of support effect and the optimization parameters of bolt support, and the scheme of mine pressure monitoring and the corresponding support optimization system are established. The roof fall accident and the bolt and cable of support have been broken in the Wudong coal mine, the phenomenon of bolt pulling out in the roadway. The causes of roof fall are analyzed and the solutions are put forth, judging the influence of different factors on roadway support. In view of the roof fall accident in the North Lane of the east wing of the +575 level 43 #coal seam in the north mining area of the Wudong coal mine, the cause analysis and support suggestions are made. And, according to the performance of the bolting material and anchoring agent, the laboratory theoretical research was carried out. Through the experiment, it is concluded that the FRP bolt with a diameter not less than 27 mm is the first choice for the side support of the working face in the mining roadway, then ribbed steel bolt with a diameter not less than 20 mm for the nonworking face, and the length of the anchor rod not less than the range of the loose circle. Therefore, full-length anchoring should be carried out in roadway support, the anchorage length of the anchor cable should be increased, and the integrity of the roof should be improved, so as to reduce the amount of roadway roof separation and improve the support effect.

## 1. Introduction

Because of the different geological dynamic environment, the stress distribution characteristics and energy accumulation degree of coal bodies in different areas in the mining field are different; therefore, there are stress rising areas and coal rock mass areas with high degree of energy accumulation [1]. Under the influence of mining engineering activities, it will cause a redistribution of stress, forming a stress rising area, causing deformation of coal and rock mass and destruction, even leading to the release of energy. It

leads to roadway instability and roof fall accidents, leading to rock bursts. Aiming to identify the reasons of roadway instability and deformation and supporting technology, Tan et al. [2] proposed two new indexes, namely, impact energy velocity index of coal rock combination and impact energy velocity index of unloading confining pressure. The evaluation system of coal rock burst tendency is established according to the types of rock burst, and the synchronous integration technology of drilling construction and early warning is developed aiming at the problem of rock burst monitoring and prevention in deep mining of coal mines.

Pan et al. [3] based on the dynamic response of the surrounding rock and support of roadway established the mechanical model of “stress surrounding rock support.” It is proposed that the support of the roadway against the impact of ground pressure should be from the static dynamic angle, the starting stress condition of rock burst under roadway support is that the far-field stress is greater than the critical stress, and the energy condition of stopping is that the energy absorbed by the surrounding rock and the energy absorbed by support is greater than that of the far field. Dou et al. [4] studied the energy and stress conditions of rock burst induced by the superposition of dynamic load and static load, and the principle of rock burst induced by superposition of dynamic and static loads is put forward. Jiang et al. [5] studied the mechanism and law of rock burst in coal mine, which are deformation and failure law and mining stress distribution of the deep intermittent coal body, spatiotemporal evolution of energy field. Hou et al. [6] put forward the strength strengthening theory of the surrounding rock. It is considered that bolt support can improve the mechanical parameters and properties of rock mass in anchorage zone, and then improve the bearing capacity of the surrounding rock; at the same time, the bolt and the rock mass in the anchorage zone form a bearing structure, jointly maintaining the stability of roadway. Dong et al. [7] put forward the theory of the surrounding rock loose zone. It is considered that after roadway excavation, the loose circle of the surrounding rock exists in the surrounding rock, and the main load of support is the interaction between the deformation generated in the formation of loose circle and the support body. According to the thickness of loose circle, the support mechanism and the corresponding support parameters are determined. Ran et al. [8] determined the combined support form of “front beam + bolt + anchor cable + metal mesh” in rectangular roadway, based on the theory of the surrounding rock loose zone. Pan [9] believed that the principle of rock burst initiation is that elastic brittle single structure breaks through material strength limit, material instability, as a result of the dynamic instability of engineering structure. Liu et al. [10] using the orthogonal numerical simulation method, the variation laws of plastic zone volume, roof and floor movement and two-side convergence under different bolt lengths, preloads, and top angle bolt installation angles are systematically studied, the multi-index orthogonal design matrix analysis method of roadway bolt support is proposed, the supporting scheme of supporting engineering is optimized, and the field industrial test is carried out, Finally, the multifactor analysis of the roadway support and multi-index evaluation of the support effect are realized. Zuo et al. [11] considered that the roadway should be supported from the whole space, and the theory of equal strength beam support in deep coal mine roadway is put forward; it is considered that according to the different damage degree of surrounding rock of the roadway, support with different length bolts should be provided, so that the surrounding rock of the roadway is evenly stressed. Zhang et al. [12] combined fuzzy mathematics with extenics, and the parameters of roadway support are optimized. Thus, the problem of roadway

support is effectively solved. Cai et al. [13] analyzed the mineral composition by XRD and SEM, and researched the physical and mechanical properties of the weakly cemented soft rock. Secondly, using the research methods of field investigation and physical simulation experiment, this paper studies the roadway failure and deformation mechanism and control technology and puts forward the coupling control technology of the “inverted trapezoidal” anchor mesh cable beam support structure with high strength and high pre-load + straight wall cutting arch roadway section + full section shotcrete. Li [14] studied the instability mechanism of weakly bonded roof systematically, and the long anchor cable is proposed as the leading factor, that is, multilevel roof control technology involving long anchor and short anchor cables. Meng et al. [15] adopted the optimization of roadway cross section shape and double-layer anchorage balanced arch structure to solve the problem of roadway surrounding rock stability control in extremely weak stratum. Wang et al. [16] taking the weak cemented soft rock roadway of the Yi li No. 1 mine as the research object, based on the analysis of deformation and failure of surrounding rock of the roadway, and optimization of support parameters by numerical simulation, put forward the scheme of anchor mesh cable coupling support. Huang [17] used physical simulation and FLAC 3D numerical calculation; combining with the theory of self-stable balance ring, the optimal section of straight wall with arc and reverse arch is determined, supported by “anchor cable + steel ladder + metal mesh grouting.” Yang et al. [18] adopted a combination of mechanical analysis and numerical simulation for proposing a supporting system with the core of “high strength anchor net, beam and cable + shotcrete sealing + floor anchor grouting”. Sun [19] using artificial intelligence, indoor experiment, theoretical analysis, engineering investigation proposed the research method of combining numerical calculation and field tests. The rheological model of coal is established, the rheological parameters of roadway coal are inverted, and the rheological mechanism of roadway is revealed; the control measures of grouting by rotary injection to strengthen the loose coal body are put forward, and it makes an important contribution to the research and treatment of loose coal roadway rheology. Sun [20] established the fracture mechanics model of overburden; using mts-815 rock mechanics test system and fatigue damage test of sandstone under cyclic loading by acoustic emission system, the disaster mechanism of overburden fault is studied; deformation and failure law of surrounding rock in deep roadway, mechanical behavior of rock under cyclic loading, energy dissipation and fatigue damage characteristics, and the influence factors and deformation mechanism of surrounding rock deformation under dynamic disturbance are analyzed, and the control scheme of surrounding rock deformation is put forward. Fan et al. [21] put forward the combined support technology of “bolt mesh shotcreting active support + 36U steel support + full face bolt grouting” based on X-ray diffraction experiment, scanning electron microscope, physical test, and field monitoring of rock mechanics; the field monitoring results show that the improved support scheme can effectively control the deformation of surrounding rock and the



expansion of plastic zone, and ensure the long-term stability and safety of the roadway. Chen [22] established the mechanical model of surrounding rock stress and deformation of straight wall arch roadway in steep seam, combined with the theory of complex variable and conformal transformation and influence of mining intensity and dip angle; the analytical solutions of stress and deformation of surrounding rock under different mining intensities and dip angle are obtained by genetic algorithm, and the influence of mining intensity and dip angle on the instability mode of large dip angle roadway is revealed from the perspective of mechanics. Su et al. [23] used the physical similarity simulation test method, the deformation and failure characteristics and stress evolution law of layered rock roadway with different support methods are studied, and the arching characteristics of layered rock roadway are analyzed from the perspective of pressure arch. Chu et al. [24] further studied the distribution of stress and strain before and after roadway support in the contact zone between ore and rock by numerical simulation. Through on-site deformation monitoring data and physical and mechanical parameters of ore and rock, the tensile failure volume is calculated from the plastic zone. Comparative analysis of shear failure volume and total volume of bolt support, shotcrete support, application effect of combined bolting, and shotcreting support is performed. Finally, the paper puts forward the partition support method for the mine rock contact zone roadway. Yu et al. [25] studied the asymmetric deformation and failure of Soft Rock Roadway after excavation, and the asymmetric control technology of strengthening support for weak structure is put forward. Wang et al. [26] systematically analyzed the variation characteristics of stress, displacement, and plastic zone of the surrounding rock before and after deep soft rock roadway support are simulated. Guo and Song [27] through field measurement, mineral composition and water quality analysis, surrounding rock disintegration and mechanical properties test, and numerical simulation studied the instability characteristics and mechanism of the water drenching roof roadway in the transportation roadway. Thus, the influencing factors of roadway instability under the water drenching roof in the gob with accumulated water are obtained. Yao et al. [28] explored the roof instability mechanism of water-rich coal seam from micro and macro aspects: due to roof cracks caused by disturbance of roadway excavation, the hydraulic connection between the immediate top aquifer and the basic top aquifer is formed. Because silty mudstone is composed of hydrophilic minerals and the microstructure fracture is developed, it is easy to expand after absorbing water; under the action of three-dimensional stress, disintegration damage occurs. At the same time, the bearing capacity of the support is weakened, resulting in instability of the roadway roof. Zheng et al. [29] analyzed the mechanism of buckling of layered floor by mechanical theory, by establishing the mechanical model of the layered floor of the roadway with equal spacing bottom anchor; the mechanical criterion of heave instability of layered floor is established, with the help of the proposed mechanical criterion, and the stability of the floor is determined and evaluated, The rock strata which are the first to

disintegrate leading to the failure of the support system are obtained. Li et al. [30] aiming at the problem of surrounding rock deformation and instability of thin-layered soft floor roadway, the buckling instability mechanism and control technology of thin-layered soft floor roadway are studied in detail by integrating theoretical analysis, mechanical calculation, numerical simulation, underground test, and field measurement methods. According to Lu and Yao [31], the bedded rock mass in the floor is regarded as a transversely isotropic continuum. According to the overburden load distribution characteristics of coal seam, the analytical solution of floor stress at any point after coal mining is derived, and the influence of the anisotropy of the deformation parameters on the stress distribution is analyzed. Xu et al. [32] discussed the fracture instability mechanism and control technology of narrow coal pillar through the combination of theoretical analysis, numerical simulation, and field measurement and put forward the support scheme of fully mechanized top coal caving goaf roadway of the "high-strength bolt support+roof anchor cable channel steel composite structure+coal pillar side anchor cable reinforcement" and carried out field application. Following discussion on the failure mechanism of narrow coal pillar and its control technology, the supporting scheme of "high strength bolt support+roof anchor cable channel steel composite structure+coal pillar side anchor cable reinforcement" is put forward and applied on-site. Zhang et al. [33] analyzed the dynamic process of structural damage of roadway roof caused by the key block breaking and rotating process under the condition of gob side entry driving in mining face, and put forward the pre-stressed combined support technology, and carried out the field engineering practice. Hao et al. [34] used field measurement, theoretical analysis, and numerical simulation, and the instability mechanism and main influencing factors of mining roadway are discussed. According to the physical and mechanical properties and stress characteristics of surrounding rock of test roadway, the targeted solutions are put forward. Vazaios et al. forecasted the hazard of rockburst and coal and gas outburst in roadway at different mining depths based on the finite-discrete element method and other methods [35, 36].

About roadway support, the research mainly focuses on the occurrence conditions of near horizontal and gently inclined coal seams, and there are few domestic reports on the causes of roadway instability and deformation and supporting technology under the condition of high stress and steep inclination. The north mining area of the Wudong coal mine in Shenhua Xinjiang is a high-stress steeply inclined coal seam. The extension direction of mining roadway is nearly perpendicular to the direction of maximum principal stress, and it is strongly compressed by in situ stress. It has an important influence on the stability of roadway; occasionally, roof fall accidents of different degrees occur, for example:

On April 17, 2017, a roof fall accident occurred at the south of the top of the North roadway of the east wing of +575 horizontal 43# coal seam in the north mining area of Wudong mine. The roadway was filled with coal and rock slag, which had a serious impact on the safety production of

the mine. In this paper, the geological dynamic conditions are analyzed, along with fault structure division, on-site monitoring, laboratory experiment, and numerical simulation. In this paper, the causes of roadway instability and roof fall in Wudong high-stress steeply inclined extra-thick coal seam are analyzed in detail and some suggestions are given. It provides the basis and direction for further optimization of roadway support in the Wudong coal mine, and technical support and security for safe and efficient production at the mine. It provides important support for the technical progress and sustainable development of mines with similar conditions.

## 2. Analysis of Support Problems in the Wudong Mine Field

*2.1. General Situation of Mine.* The Wudong coal mine is located to the east of Zhungeer coalfield, northwest limb of the Bogda mountain anticline, north of Yaomengshan Lucaogou reverse fault. The Wudong coal mine is located in the Bogda mountain fault zone system, high in the south and low in the north. The maximum elevation is 934 m, minimum is 739.20 m, and the maximum relative height difference is 130 m. Generally, the height difference is 60 m. It lies between the north foot of Bogda mountain and the southeast edge of Junggar basin. Most of the structures in the area are NE trending, and the Mesozoic strata constitute asymmetric linear tight folds. The Wudong minefield belongs to the piedmont hilly belt at the north foot of Bogda; small valleys crisscross, the large-scale gullies are mainly north-south, there is little outcrop in the area, and most of them are covered by Quaternary loess and sandy loam. Due to the long history of coal mining in the working area, most of the surface collapse pits in the goaf are developed; according to rough statistics, there is one collapse per 100 m on average, every 200 m of the mine shaft. The Wudong mining area is located in the southeast of Zhunnan coalfield, it belongs to piedmont secondary tectonic unit, it is distributed in the northeast direction, and it is basically consistent with the distribution direction of the Tianshan latitudinal structural system. The minefield is located in the north and south wings of the Badaowan syncline, a secondary fold in the Piedmont depression of Urumqi. Large structures in the mining area include Qidaowan anticline, Badaowan syncline, Wanyaogou thrust fault, and Baiyangnangou anticline.

The south mining area of the Wudong coal mine is located in the south wing of the Badaowan syncline, and it comprises 32 coal-bearing beds. The main coal seam is B1 + 2 and B3 + 6 coal. The maximum thickness of B1 + 2 coal seam is 39.45 m, minimum thickness is 31.83 m, and the average thickness is 37.45 m. The maximum thickness of B3 + 6 coal seam is 52.3 m, minimum thickness is 35.39 m, and the average thickness is 48.87 m. The dip angle of coal seam is 87 degrees, and it belongs to steep coal seam. The two groups of coal are separated by a rock wall, the dyke gradually thinned from west to East, and the variation range is between 53 m and 110 m. The main minable coal seams in the north mining area are coal seams 43 and 45. The pseudo roof of the

coal seam is carbonaceous mudstone or mudstone, and the thickness is about 1 m~3 m. The direct roof is siltstone or sandy mudstone; the main roof is siltstone, fine sandstone, or medium sandstone, the pseudo floor of the coal seam floor is carbonaceous mudstone or mudstone; and the direct bottom is siltstone. The occurrence characteristics of coal seams in the Wudong coal mine are shown in Figure 1. Because of this natural factor, roadway instability deformation and roof fall accidents often occur in the process of mining in the north mining area.

*2.2. Factors of Tectonic Stress Field in the Minefield.* Judging from the rate of crustal activity, the criteria for judging strong active faults are: since the middle late Pleistocene, it is active and strong in Holocene, the average fault activity rate is  $v > 1$  mm/a, and the historical earthquake magnitude is  $M \geq 7$ . The criteria for moderately judging active faults are as follows: it has been active since the middle late Pleistocene, and the Holocene activity is relatively strong,  $0.1 \text{ mm/a} \leq v \leq 1 \text{ mm/a}$ ,  $5 \leq M < 7$ . The criteria for judging weak active faults are: It has been active since the middle late Pleistocene, and the Holocene activity is relatively strong, when  $V < 0.1 \text{ mm/a}$ ,  $M < 5$  [37]. The northern edge of the Bogda fault is in a strong compression state, as shown in Figure 2. The study area is a thrust nappe structure, and its basic structure is roughly divided into the root thrust fault zone, central detachment layer, and front compression uplift zone. From the rate of crustal activity in the Tianshan area, the northern edge of the Bogda fault in the Wudong minefield is in a strong compression state. Under the influence of this dynamic state, a large amount of elastic deformation energy is accumulated in the region. The direction of maximum principal stress is NNW and NW, the difference between the maximum principal stress and the minimum principal stress is large, the horizontal force gradient is large, and the effect of extrusion stress is obvious. The number of earthquakes in the Wudong mine field is increasing with every passing year; it shows that the geological dynamic conditions are more and more active, and the energy of rock mass in the mining area also increases with every passing year.

The Wudong minefield inherits the action characteristics of the regional stress field. In situ stress is dominated by horizontal compressive stress, the maximum principal stress direction is N27.8°W. The mining roadway in the Wudong coal mine is mainly arranged along the strike direction of the coal seam; the strike direction of the roadway is N59°E, and the angle between the maximum principal stress and the strike of roadway is 94 degrees, near vertical. As shown in Figure 3, the mining roadway in the Wudong coal mine is strongly affected by in situ stress. It has an important influence on the stability of roadway support.

*2.3. Structural Fracture Factors in the Minefield.* Application of geo dynamic zoning method to grade I-V fault structure division in the Wudong mine field and the geological dynamic conditions are analyzed, faults are determined by geological dynamic zoning, and the

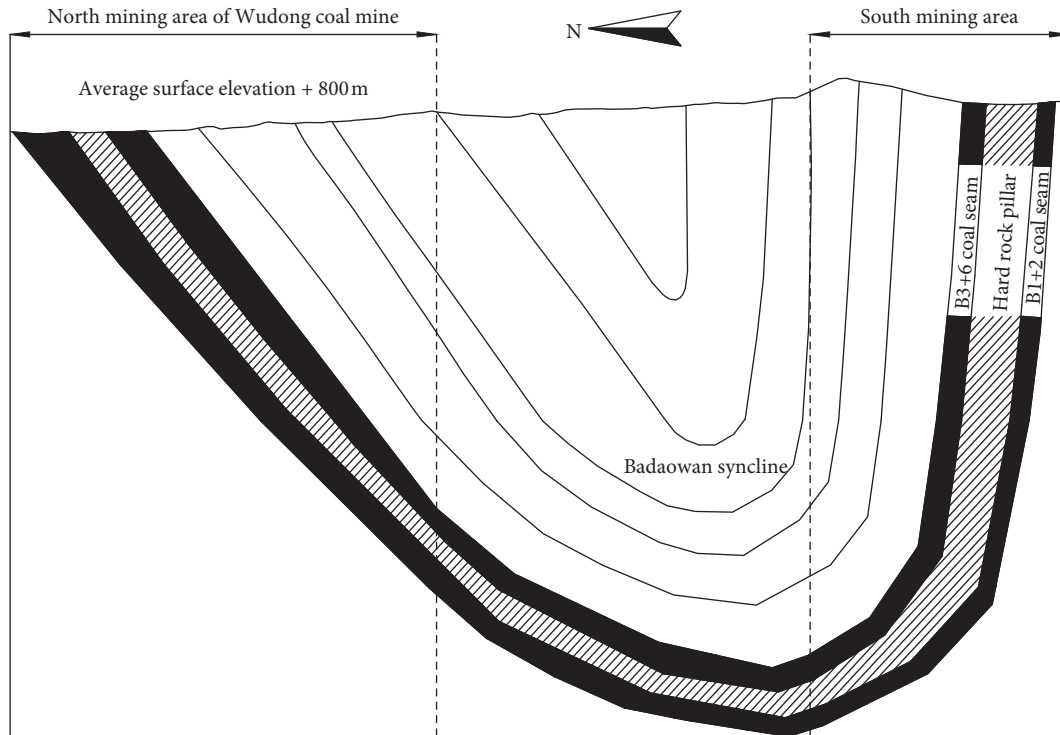


FIGURE 1: Geological profile of the Wudong coal mine.

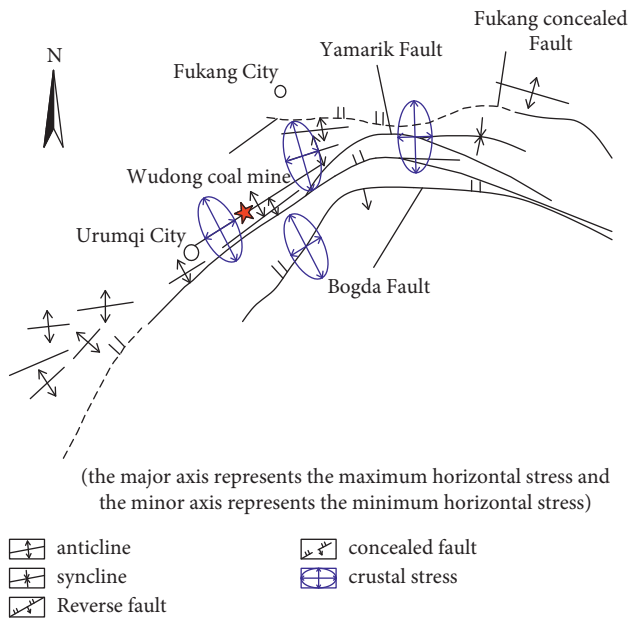


FIGURE 2: Structural stress distribution of the bogda fault zone system.

characteristics of regional geological dynamic state are revealed. The activity of fracture means the change of dynamic system so as to cause the accumulation and increase of energy. The movement of fault structure makes the stress structure of coal and rock mass redistributed, and the stress and energy in the crust are released. Take grade V fracture diagram as an example; in this paper, the roof fall area of the North roadway and roadway in the east wing of the +575 level 43 # coal seam in the

north mining area of the Wudong coal mine is combined with the V-level fault map, as shown in Figure 4.

As can be seen from Figure 5, the roof fall area is affected by V-5 active fault. It occurs nearly 180 m away from V-5 active fault, as shown in Figure 5. The activity of V-5 active fault provides power source and energy basis for coal and rock mass in the roof fall area. Besides, there are intersection points between the North Lane in the east wing of coal seam +575 and V-5 fault and iv-3 fault, respectively. The intersection points are 434 m and 2278 m in the North Lane of the east wing of the +575 coal seam. Therefore, there is a risk of roof fall at the intersection.

**2.4. Experimental Study on Stress Analysis of the Bolt Body and Anchoring Agent.** Tensile strength of bolt is one of the most important indexes of bolt mechanical properties. At present, the anchor material used in the Wudong coal mine is hbr335. For this reason, we carried out the pull-out experiment of threaded bolt in the Wudong coal mine. The phenomenon of bolt sliding appeared in the experiment, and as a result, the drawing force has a small change. The experimental process is shown in Figure 6. The experimental results are shown in Table 1.

It can be seen from the experimental results that mechanical parameters of rebar bolt body in the Wudong coal mine, namely, pull-out force of 189 kN, tensile strength of 601 MPa, and elongation of rod body by 20.61%, meet the support material standard of the Wudong coal mine. Therefore, the material and property of bolt body in the Wudong coal mine is not the cause of roof fall of supporting roadway in the Wudong coal mine.

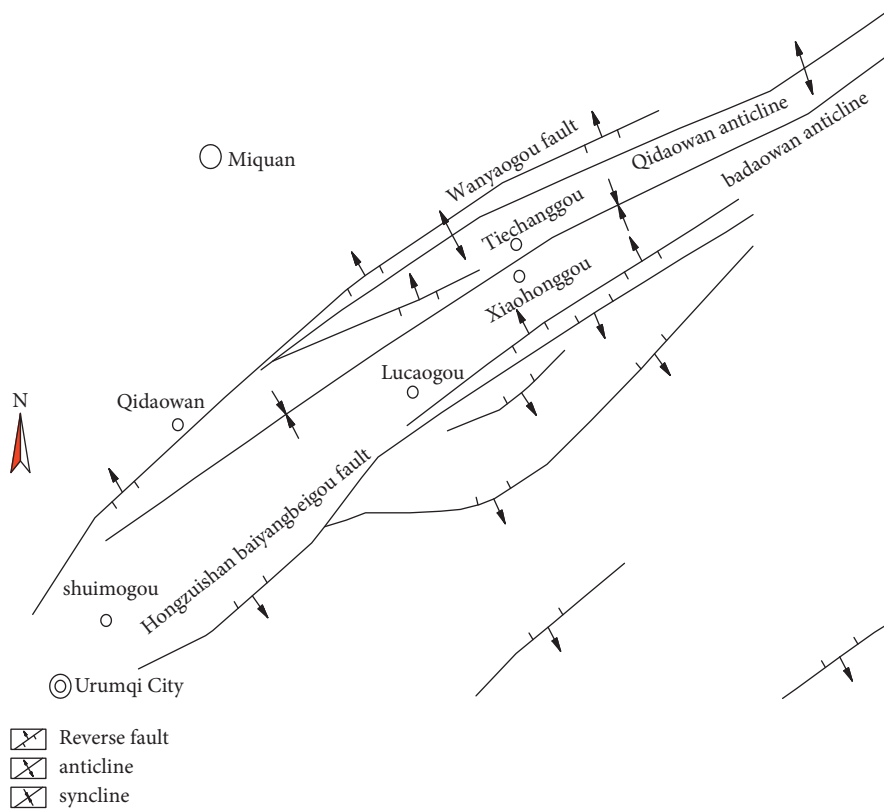


FIGURE 3: Characteristics of in situ stress in the Wudong minefield.

The length of anchor also has a certain influence on the supporting effect, in order to master the bolt supporting effect of different bolt lengths. The anchorage performance of  $1\text{ m} \times 1\text{ m} \times 1\text{ m}$  concrete blocks with 150 mm and 300 mm anchorage length was tested in the laboratory. During the experiment, ZY portable bolt drawing instrument and dial indicator were used to apply pressure and test bolt displacement, respectively. The experimental process is shown in Figure 7. Drawing force of screw steel bolt (anchorage 150 mm) is shown in Figure 8. Drawing force of screw steel bolt (anchorage 300 mm) is shown in Figure 9.

Summary of pull-out force of bolt with different anchorage lengths is shown in Table 2. On analyzing the experimental results, it is found that when the anchor length is 150 mm, the pull-out force of the bolt can reach more than 60 kN; when the anchorage length is 300 mm, the anchor force increased by 50%, thereby increasing the length of bolt in roadway support. It is suggested that full-length anchorage should be used in roadway support. It can significantly improve the quality of bolt support.

The resin anchoring agent has excellent performance. It has the characteristics of “double fast and one high.” “Double fast and one high” refers to fast strength growth, fast curing time (adjustable speed), and high strength. The mechanical parameters of anchoring agent used in the Wudong coal mine are tested. The results are shown in Table 3. In order to test its anchoring performance, a cylindrical specimen with a height diameter ratio of  $2 \pm 0.2$  and a specification of 50 mm were made with a self-made mold and mine anchoring agent (MSCKa23-35) as the 50 mm long  $\times$  50 mm wide  $\times$  50 mm

high cube specimens are used for uniaxial compression and shear tests, respectively. Cylindrical specimens with height diameter ratio of  $2 \pm 0.2$  and Cube Specimens with size of  $50\text{ mm} \times 50\text{ mm} \times 50\text{ mm}$  (length  $\times$  width  $\times$  height) were made for uniaxial compression and shear tests, respectively. The processes are shown in Figures 10 and 11, respectively.

According to the experimental results, the compressive strength of anchorage agent in the Wudong coal mine is consistent with the standard of more than 60 MPa in the inspection requirements. So, the anchoring agent is not the main reason that affects the supporting effect of the Wudong coal mine.

### 3. Monitoring Equipment and Scheme of the Experiment

#### 3.1. Detection of the Roadway Surrounding Rock Structure

**3.1.1. Monitoring Equipment.** YTJ20 type strata detection recorder is mainly used to monitor the +575 level 43 # coal seam in the north mining area of the Wudong coal mine, as shown in Figure 12.

**3.1.2. Monitoring Scheme and Result Analysis.** Two test drillings are arranged in the North Lane of coal seam 43 in the north mining area of the Wudong coal mine: one for each roof, and one for each of the two sides of the tunnel. The results of field data acquisition with YTJ 20 type strata detection recorder show that:



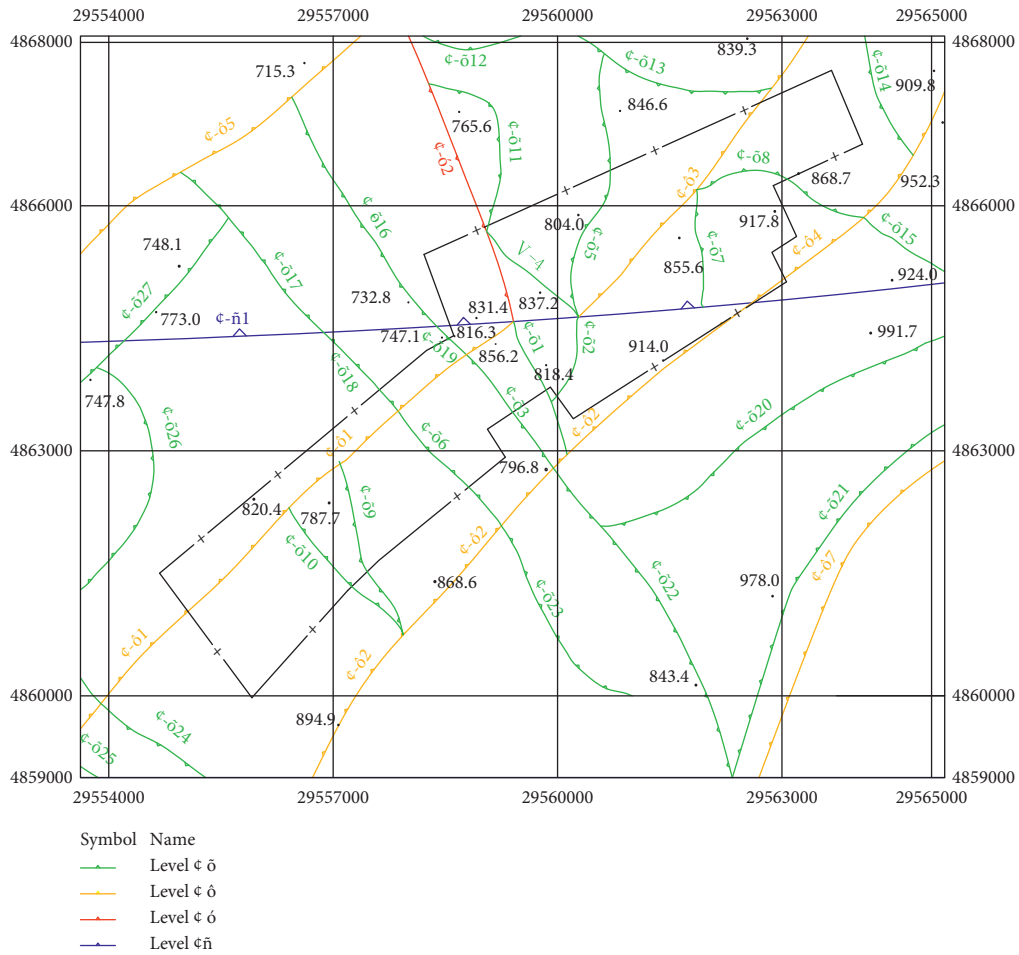


FIGURE 4: Grade V fault map of the Wudong minefield.

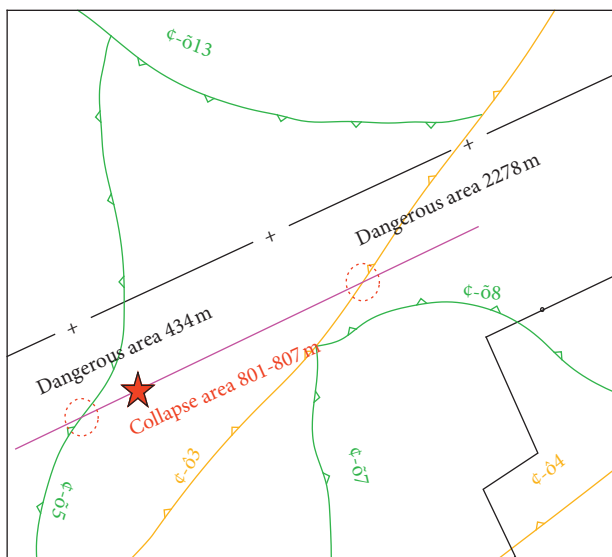


FIGURE 5: Relationship between roof fall area and fault location.

The surrounding rock structure of the 1# roadway at the test drilling site is relatively broken. There are fracture phenomena in different depths of coal wall. The fracture in parallel boreholes is more serious. As the drilling goes deeper,

the fracture phenomenon improves. The fissures of the surrounding rock are relatively developed. There are cracks both in parallel drilling and 45° drilling. The roof is relatively complete; there is no obvious breakage and separation in the roof drilling. As shown in Figure 13, the 2# actual detection depth of the detection surface is 3.7 m–6.6 m. The coal side is also relatively broken and the fracture development of the rock wall is not obvious relative to the 1# detection point, but there is a phenomenon of coal rock interbedding. The roof of the test drilling is also relatively complete, and there is no obvious breakage and separation in the roof drilling, as shown in Figure 14. During the detection of surrounding rock structure, the north mining area is in a stopping state. Therefore, it is not affected by mining.

Judging from the detection results, in the north mining area of the Wudong coal mine, the two sides of the North Lane in the +575 level 43 coal seam are relatively broken. Therefore, more attention should be paid to the detection of the two sides of the roadway. Select the appropriate support scheme in the broken area.

3.2. Test and Analysis on the Loose Zone of Roadway Surrounding Rock. Before roadway excavation. The rock mass is in a state of natural stress equilibrium, the natural

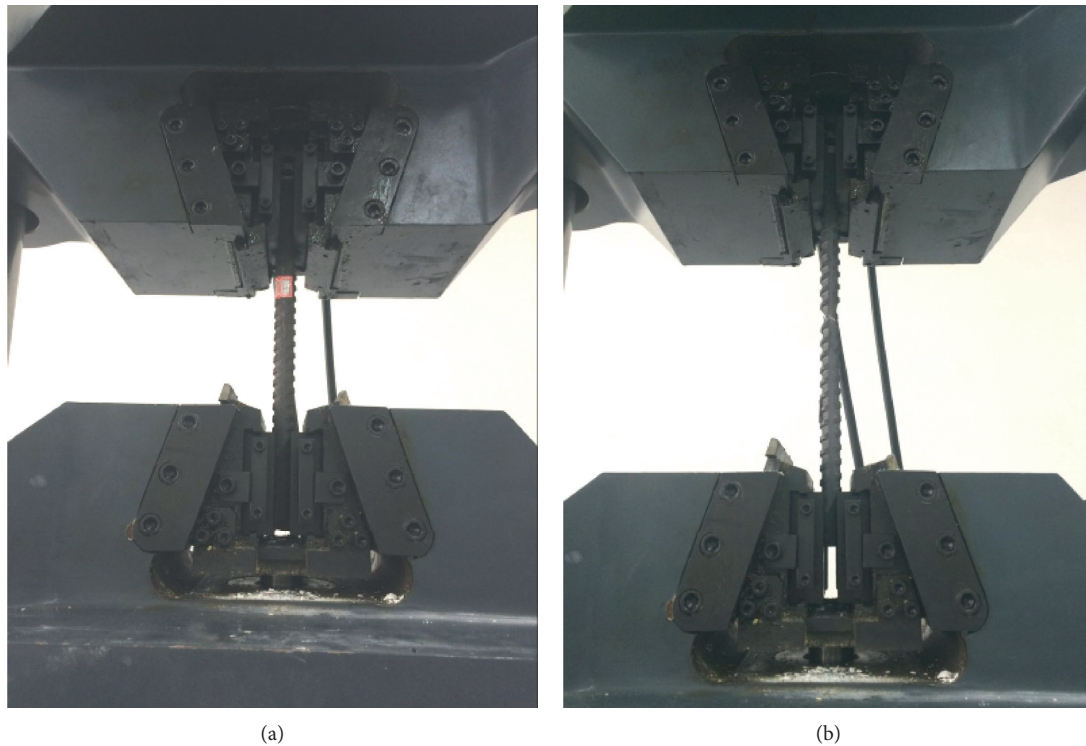


FIGURE 6: Drawing process of bolt body. (a) Rod body installation. (b) Broken rod. (c) Failure mode of the rod.

TABLE 1: Drawing test results of deformed steel bars.

Number	Original length of stretching section (mm)	Stretch length (mm)	Rod diameter (mm)	Elongation of rod (%)		Pull-out resistance (kN)	
				Actual measurement	Mean value	Actual measurement	Mean value
1#	205.50	39.28	20.05	19.11		188	
2#	203.20	42.40	20.10	20.86	20.61	185	189
3#	201.56	44.10	20.08	21.87		194	



FIGURE 7: Pull-out test of different bolts.

stress is the original rock stress. After roadway excavation, the stress is redistributed to the surrounding rock of the roadway. There is a stress change area in the surrounding rock. Stress concentration occurs in this area. The stress concentration around the roadway is the most serious. When the stress exceeds the strength limit or yield limit of

the surrounding rock mass, the rock mass around the roadway is destroyed first, or ruptures, and a certain range of loose area is formed around the roadway.

In this paper, the change of wave spectrum parameters, such as wave velocity, wave amplitude, wave form, and spectrum, is detected in the process of acoustic signal propagation in rock mass. Through these changes, we can indirectly understand the physical and mechanical properties and structural characteristics of rock mass media and the change of sound wave propagation velocity in rock mass, and the loose range of surrounding rock around roadway can also be obtained indirectly. Using BA-II ultrasonic rock crack detector to test the rock loose zone of +575 horizontal roadway in North Mining Area, three test positions were selected in the North roadway of coal seam 43, namely, in the heading roadway, which are 1340 m, 1370 m, and 1400 m, respectively. In order to ensure the reliability of the test, three boreholes were drilled in each place with spacing of 1.5 m, as shown in Figure 15.

According to the field observation results, the anchoring end of the bolt in the roof fall area of the North Lane of the east wing of the +575 level 43 # coal seam in the north



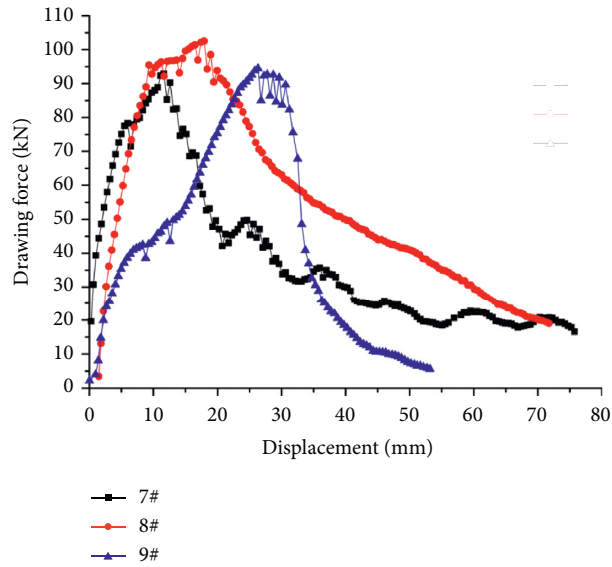


FIGURE 8: Drawing force of screw steel bolt (anchorage 150 mm).

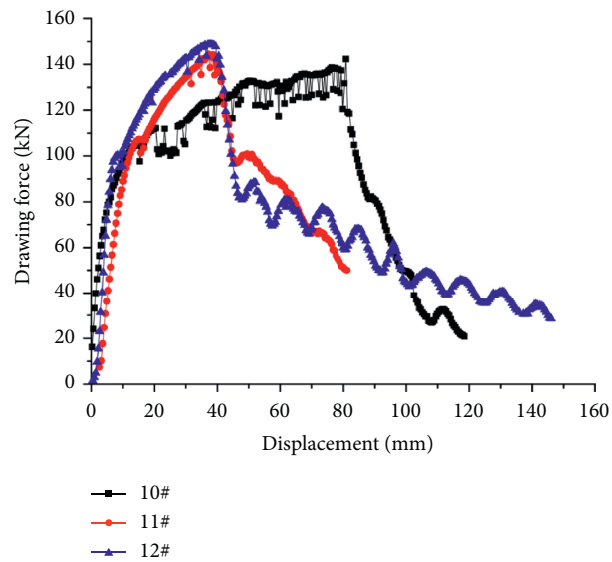


FIGURE 9: Drawing force of screw steel bolt (anchorage 300 mm).

TABLE 2: Summary of pull-out force of bolt with different anchorage lengths.

Type	Number	Design anchorage length (mm)	Actual anchorage length (mm)	Rod diameter (mm)	Failure load (kN)	Mean value (kN)
Screw thread steel	1	150	161	20	93.0	96.7
	2		178		102.5	
	3		164		94.5	
	4	300	285		142.3	145.1
	5		278		144.2	
	6		293		148.9	

mining area of the Wudong coal mine is located at the coal rock joint. It is in the area of weak rock stratum. At present, the length of the bolt used in the Wudong coal mine is 2500 mm. When the bolt is supporting, the exposed length of

the anchor rod is 100 mm. The length of anchoring into the surrounding rock is 700 mm. If the 2500 mm long bolt meets the actual requirements, the thickness of the loose ring should be less than 1700 mm, as shown in Figure 16. Test

TABLE 3: Summary of mechanical parameters of anchoring agent used in the Wudong coal mine.

Type	Compressive strength (MPa)	Elastic modulus (GPa)	Poisson's ratio	Cohesion (MPa)	Internal friction angle (°)
Anchoring agent (MSCKa23-35)	62.02	13.03	0.26	9.42	33.97



FIGURE 10: Process of uniaxial compression test and failure specimen. (a) Specimen installation. (b) Failure specimen.

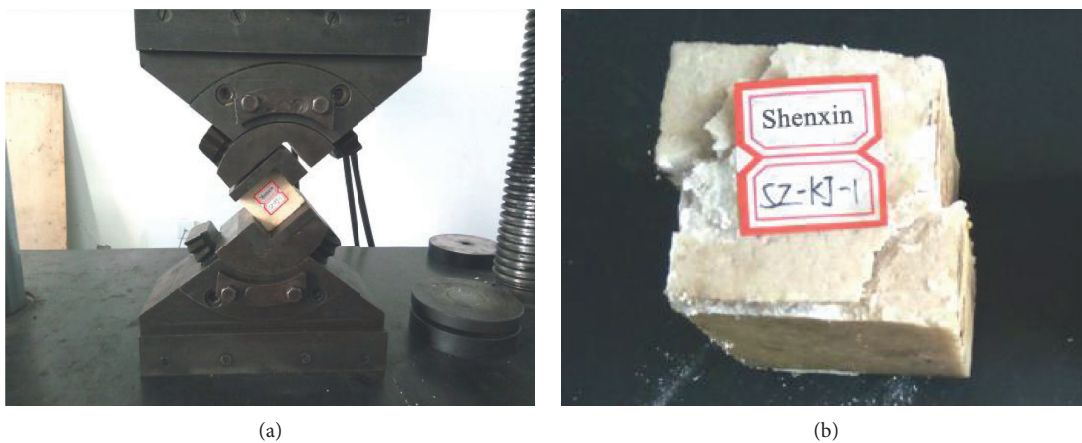


FIGURE 11: Shear test process and failure specimen. (a) Specimen installation. (b) Shear angle 58 degrees.

result. The range of loose circle in the North Lane of 43 # coal seam at +575 level is 1600 mm–2000 mm. The average is 1775 mm. The length of the bolt meeting the roof fall area of the North roadway in the east wing of the +575 coal seam is at least 2575 mm.

The unreasonable selection of bolt length and the location of bolt end in soft rock are the main contributory factors for roof fall accidents. In order to make the coal mine more safe and efficient for mining, we should carry out the exploration of weak strata. We should reasonably select the length of the anchor rod, ensure the support effect and quality of the anchor rod, and ensure that the detection work and reinforcement support work are carried out simultaneously. At the same time, we should also pay attention to the quality of bolt body and anchoring agent.

*3.3. Numerical Simulation Study on the Influence of Working Face Mining on the Mining Roadway.* According to the purpose, the numerical calculation model of +525 m mining level up to the surface range in the north mining area of the Wudong coal mine is established. This paper analyzes the influence of horizontal stress and vertical stress of +575 coal seam on horizontal mining, and the influence of adjacent coal seam mining on mining roadway.

*3.3.1. Influence Analysis of +575 Horizontal Mining in 43# Coal Seam.* The stress distribution of the strike surrounding rock in 43 # coal seam +575 horizontal working face after mining can be known. The maximum advance stress is 8 m in front of the working face. In order to analyze the influence



FIGURE 12: Y TJ20 type rock exploration recorder.

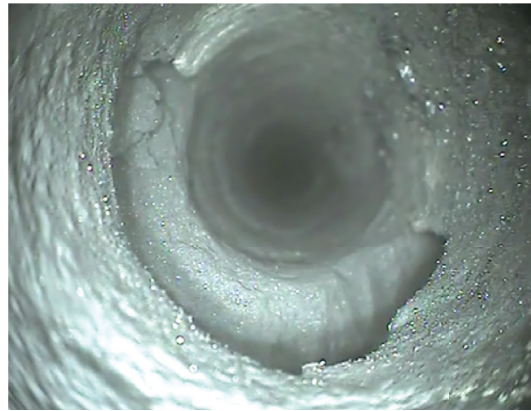


FIGURE 13: 1# detection of parallel boreholes in face of coal support.



FIGURE 14: 2 # parallel drilling of coal side of test drilling.

depth of mining face in the floor direction, the vertical stress and horizontal stress data of the floor at 8 m in front of the working face are extracted when the working face is 100 m.

In order to analyze the influence of upper slice mining on lower slice mining roadway, extract the strike stress data of lower layer +550 horizontal mining roadway. Also, make the

vertical stress and horizontal stress distribution curve before and after the working face, as shown in Figures 17 and 18.

It can be seen from Figure 17 that after working face mining, the vertical stress behind the working face (under the goaf) decreases. Formation of pressure relief zone is seen when the working face advances 50 m. The maximum leading vertical stress is 10.9 MPa, the peak point is 15 m away from the coal wall, and the stress concentration factor is 1.6. When the working face advances 100 m, the maximum leading vertical stress is 10.1 MPa, the peak point is 15 m away from the coal wall, and the stress concentration factor is 1.5. When the working face advances 150 m, the maximum leading vertical stress is 10.7 MPa, the peak point is 15 m away from the coal wall, and the stress concentration factor is 1.6. When the working face advances 200 m, the maximum leading vertical stress is 10.4 MPa, the peak point is 15 m away from the coal wall, and the stress concentration factor is 1.6. It can be seen from the vertical stress distribution curve of the lower-layered roadway after upper-layered mining. After the working face is mined, the leading influence range of the lower slicing roadway is 130 m.

It can be seen from Figure 18 that after working face mining, the horizontal stress behind the working face (under

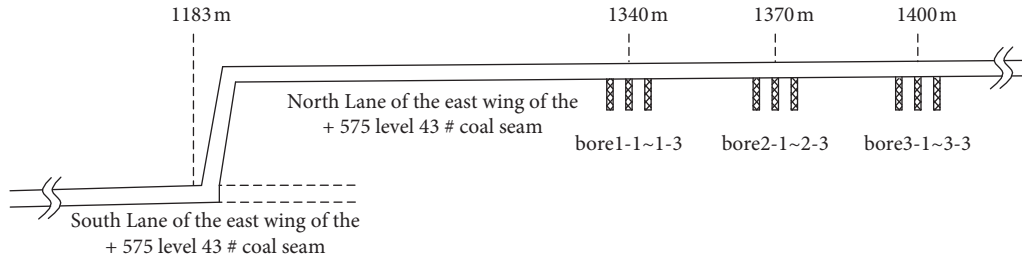


FIGURE 15: Layout of measuring holes in 43 coal seam.

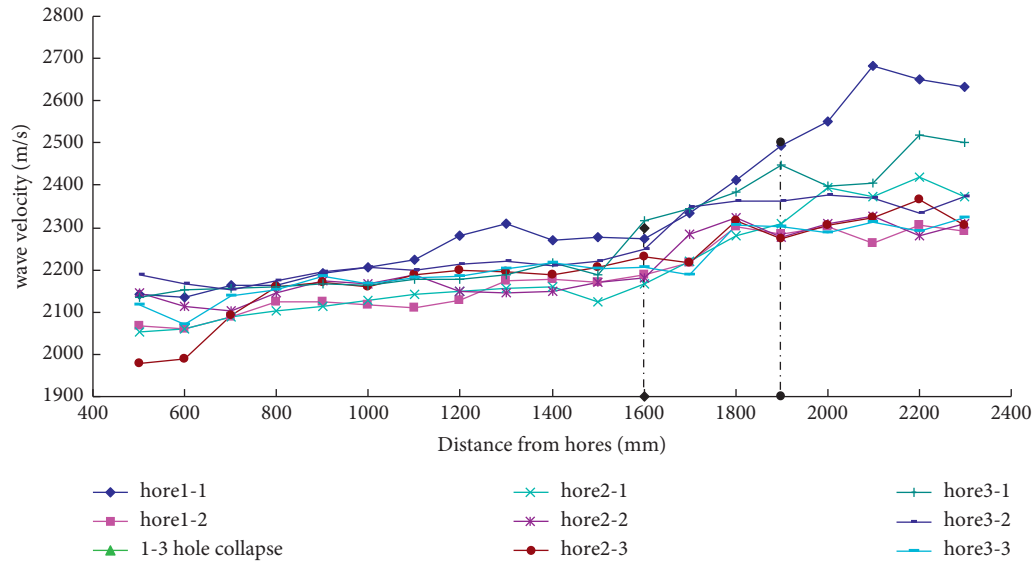


FIGURE 16: Test curve of surrounding rock loose zone in north roadway of 43 # coal seam in the east wing of +575 level.

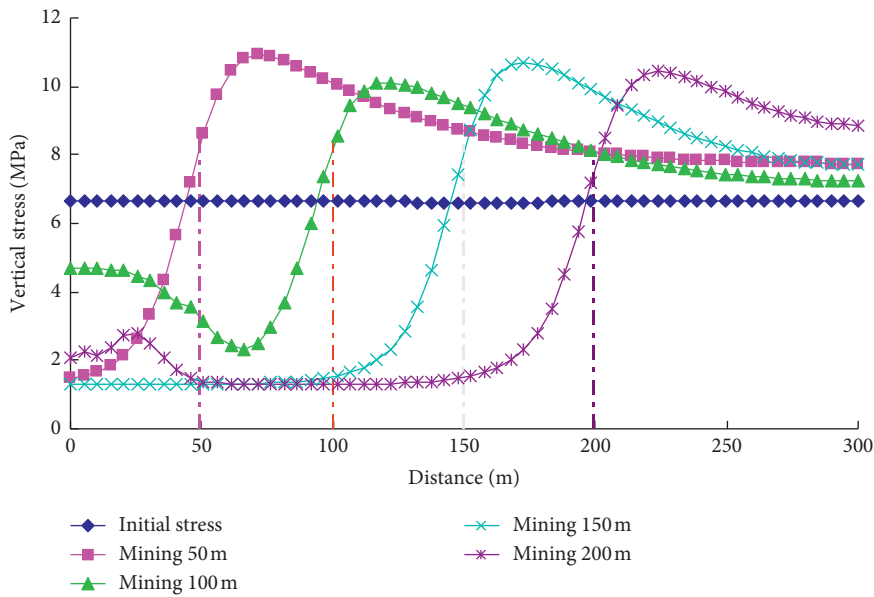


FIGURE 17: Vertical stress distribution of strata strike in roadway of lower slice after upper slice mining.

the goaf) decreases. Formation of pressure relief zone is seen when the working face advances 50 m. The maximum leading horizontal stress is 11.1 MPa and the peak point is

20 m away from the coal wall. The stress concentration factor is 1.1. When the working face advances 100 m, the maximum leading horizontal stress is 11.0 MPa, the peak point is

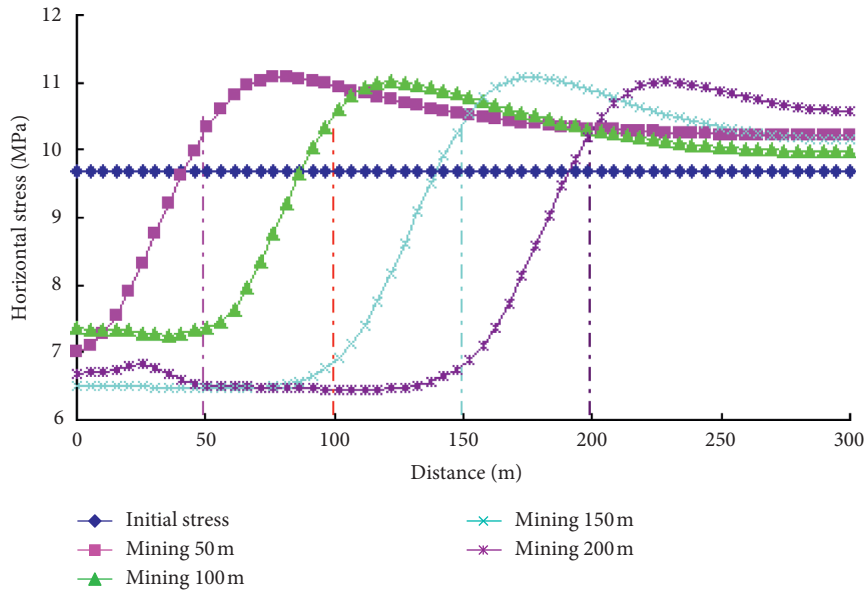


FIGURE 18: Horizontal stress distribution along the strike of roadway in the lower slice after upper slice mining.

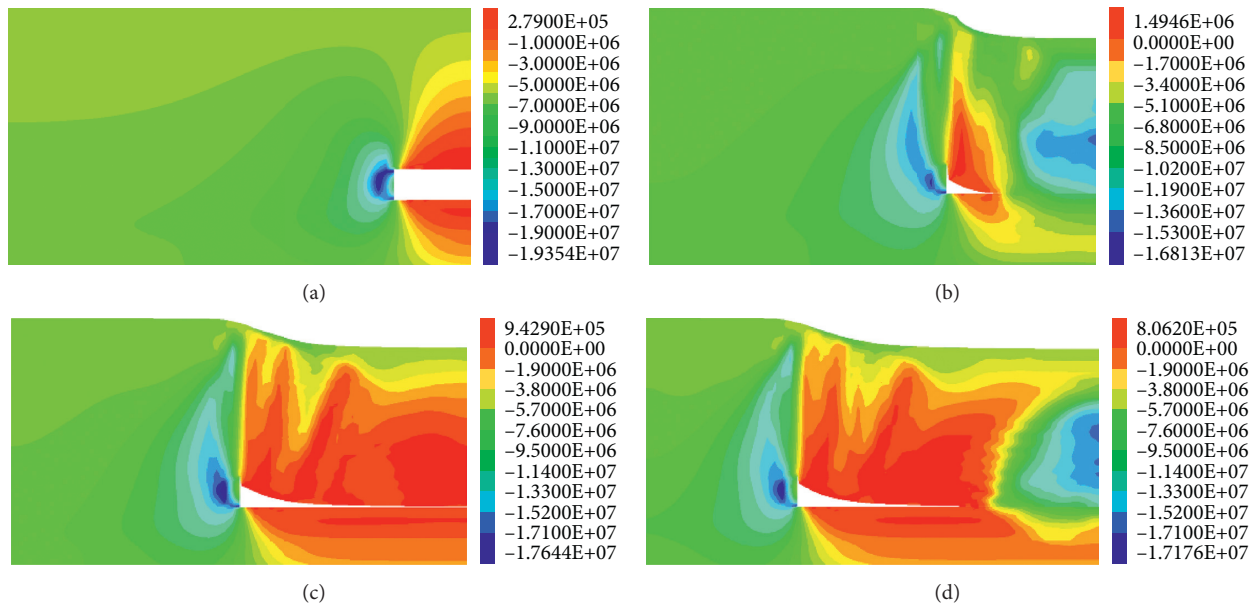


FIGURE 19: Vertical stress distribution of strike surrounding rock with different advancing distances. (a) Advance 50 m. (b) Advance 100 m. (c) Advance 150 m. (d) Advance 200 m.

20.0 m away from the coal wall, and the stress concentration factor is 1.1. When the working face advances 150 m, the maximum leading horizontal stress is 11.1 MPa, the peak point is 20 m away from the coal wall, and the stress concentration factor is 1.1. When the working face advances 200 m, the maximum leading horizontal stress is 11.0 MPa, the peak point is 20 m away from the coal wall, and the stress concentration factor is 1.1. From the distribution curve of horizontal stress in advance, it is seen that after the working face is mined, the leading influence range of the lower slicing roadway is 130 m. Therefore, when driving in the lower layered roadway, the distance between the direction of

driving in the upper layered roadway and the direction of driving in the lower layered roadway should be 130 m, and the mine pressure observation and dynamic pressure prevention measures should be strengthened.

3.3.2. Study on the Influence of Working Face Mining on the Mining Roadway. After advancing different distances of +550 level 43 # coal seam working face in north mining area of the Wudong coal mine, the vertical stress and horizontal stress distribution of the surrounding rock along the coal seam strike are shown in Figures 19 and 20. The advanced



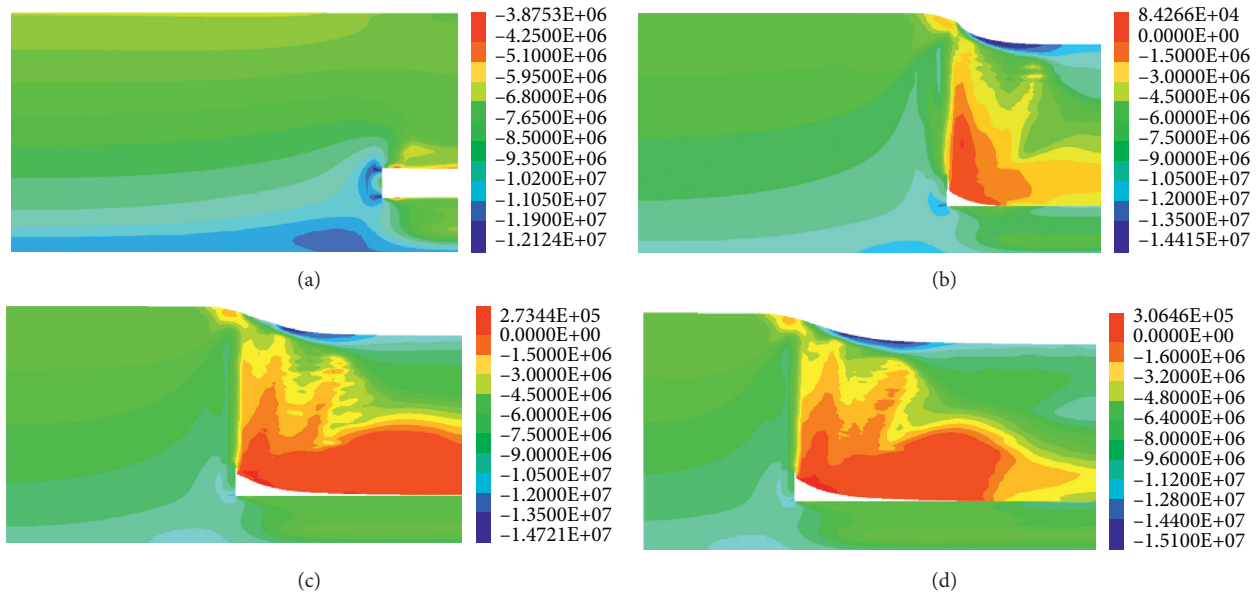


FIGURE 20: Horizontal stress distribution of strike surrounding rock with different advancing distances. (a) Advance 50 m. (b) Advance 100 m. (c) Advance 150 m. (d) Advance 200 m.

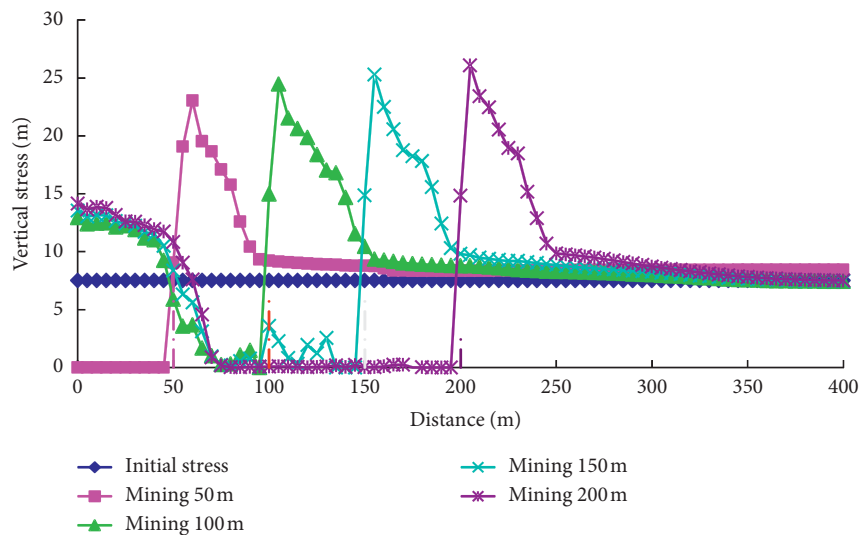


FIGURE 21: Vertical stress distribution of strike after mining in +550 horizontal working face.

vertical stress and horizontal stress curves of working face are shown in Figures 21 and 22.

It can be seen from Figures 19 and 21 that after mining of 43 # coal seam working face, in front of the working face, the vertical stress concentration is formed in the direction of the roof and floor. The stress concentration in the range of 5 m to 15 m in front of the working face is particularly significant. The distribution of high stress area is uniform along the layer height. The high stress area is mainly distributed in the middle and lower part along the stratification height, the roof overburden behind the working face collapses, and the stress reduction area (pressure relief area) is formed in a

certain range of the bottom plate. Under the action of broken surrounding rock, the vertical stress increases gradually. The stress reduction zone (pressure relief zone) is formed in a certain range of the bottom plate. At different advancing distances of the working face, the variation range of the maximum vertical stress is small. From the advanced vertical stress curve, the influence range of vertical stress after mining is 90 m.

It can be seen from Figures 20 and 22, after mining of 43 # coal seam working face, horizontal stress concentration is formed in front of the working face. The stress concentration in the range of 5 m to 15 m in front of the working face is

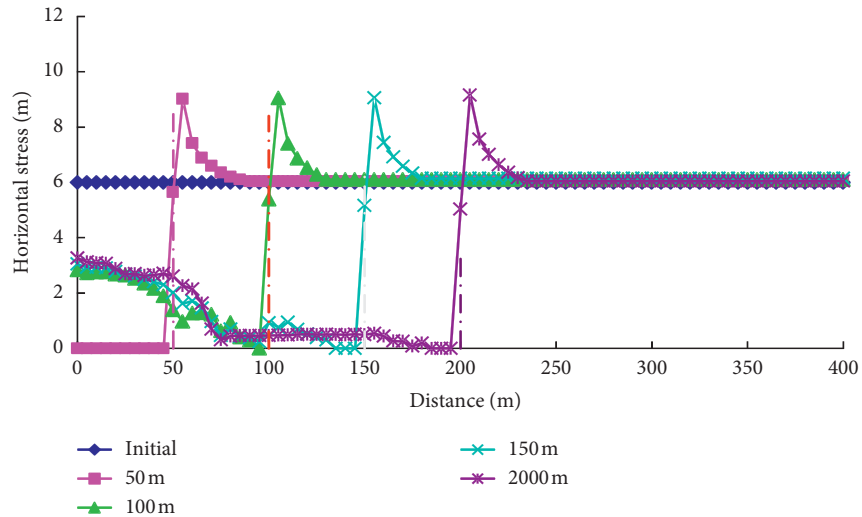


FIGURE 22: Distribution of strike horizontal stress in +550 horizontal working face after mining.

particularly significant, the high stress area is mainly distributed in the middle and lower parts along the delamination height, roof overburden is caving behind the working face, and the stress reduction zone (pressure relief zone) is formed in a certain range of the bottom plate.

At 200 m, the maximum leading horizontal stress is 9.1 MPa, the peak point is 5 m away from the coal wall, and the stress concentration factor is 1.5. At different advancing distances of the working face, the change range of the maximum value of the leading horizontal stress is small. From the advanced horizontal stress curve, after mining, the leading influence range of horizontal stress is 75 m.

To sum up, it can be seen from the analysis, after working face mining, the maximum value of leading vertical is 26.0 MPa and the stress concentration factor is 3.5. The maximum leading horizontal stress is 9.1 MPa and the stress concentration factor is 1.5. The leading influence distance is 110 m, and the peak point is 5 m–10 m away from the coal wall. Within 45 m of the advanced working face, the vertical stress concentration factors are greater than 1.5, and the mining roadway of the working face should strengthen the advance support in this range.

## 4. Conclusions and Suggestions

### 4.1. Conclusion

- (1) The angle between the maximum principal stress and the strike of mining roadway is nearly vertical in the Wudong coal mine, and mining roadway is strongly affected by in situ stress; it is an important reason for the difficulty of roadway support in the Wudong coal mine.
- (2) The drawing experiment of bolt body in the Wudong coal mine shows that the mechanical parameters of the bolt meet the inspection standard. Considering the influence of the strength and elongation of the bar material on the supporting effect, HRB500 thread steel can be used for roadway support in the Wudong

coal mine. The anchoring agent has good performance and should be stored in a suitable environment to avoid failure. The length of anchor should be increased or full-length anchorage should be adopted.

- (3) The test results of loose ring show that the bolt length of the roadway side in the Wudong coal mine is 2500 mm, the thickness of the loose ring should be less than 1700 mm, and the effective length of the anchor should be larger than the size of the loose circle. The length of the bolt meeting the roof fall area of the North roadway in the east wing of the 43 # coal seam at +575 level should be at least 2575 mm. It can squeeze and reinforce the broken surrounding rock and improve the supporting effect of roadway surrounding rock.
- (4) According to the numerical simulation of north mining area, the vertical stress and horizontal stress of the surrounding rock along the coal seam strike are simulated and analyzed. After mining, the maximum value of advanced vertical is 26.0 MPa. The stress concentration factor is 3.5 and the maximum horizontal stress is 9.1 MPa. The stress concentration factor is 1.5 and the leading influence distance is 110 m. The peak point is 5 m–10 m away from the coal wall. The vertical stress concentration factor is greater than 1.5 within 45 m of advanced working face. It is concluded that the working face mining will have a certain impact on the roadway, and the mining roadway of working face should strengthen the advance support in this range.

### 4.2. Suggestions

- (1) It is suggested that the length of the bolt should be increased in roadway support in the Wudong coal mine. Full-length anchorage shall be adopted as far as possible to improve the anchoring effect of the

roadway. It can improve the formula of the anchoring agent, reduce its viscosity, use special installation equipment, reduce the difficulty of manual installation, and improve the installation efficiency.

- (2) Under the condition of high stress and steep incline, in the production process of coal mine, with the development of the working face, it is necessary to detect the surrounding coal and rock mass structure and monitor the mine pressure from time to time, and timely adjust and update the support scheme.

## Data Availability

The data used to support the findings of this study are available from the corresponding author upon request.

## Conflicts of Interest

The authors declare that they have no conflicts of interest.

## Acknowledgments

This research was financially supported by the National Natural Science Foundation of China (Grant No. 51904145), Engineering Laboratory of Deep Mine Rockburst Disaster Assessment Open Project (Grant No. LMYK2020006), Liaoning Natural Science Foundation Program Guidance Plan (Grant No. 2019-ZD-0045), Liaoning Provincial Department of Education Project (Grant No. LJ2019JL007), and the State Key Laboratory of Mining Disaster Prevention and Control, Cofounded by Shandong Province and the Ministry of Science and Technology (Grant No. MDPC201806).

## References

- [1] H. Rong, H. W. Zhang, and B. Liang, "Instability mechanism of coal rock power system," *Acta coalae Sinica*, vol. 7, pp. 1663–1671, 2017.
- [2] Y. L. Tan, W. Y. Guo, and H. Q. Xin, "Research on key technology of rock burst monitoring in deep mining of coal mine," *Acta coalae Sinica*, vol. 44, no. 1, pp. 160–172, 2019.
- [3] Y. S. Pan, Q. X. Qi, and A. W. Wang, "Theory and technology of three-stage support for roadway with rock burst in coal mine," *Acta coalae Sinica*, vol. 45, no. 5, pp. 1585–1594, 2020.
- [4] L. M. Dou, J. He, and Y. Cao, "Superposition principle of static and dynamic load and its prevention in coal mine," *Acta coalae Sinica*, vol. 40, no. 7, pp. 1469–1476, 2015.
- [5] Y. D. Jiang, Y. S. Pan, and F. X. Jiang, "Mechanism and prevention of rock burst in coal mining in China," *Acta coalae Sinica*, vol. 39, no. 2, pp. 205–213, 2014.
- [6] C. J. Hong, "Research on key technology of surrounding rock control in deep roadway," *Journal of China University of mining and technology*, vol. 46, no. 5, pp. 970–978, 2017.
- [7] F. T. Dong, H. W. Song, Z. H. Guo, S. M. Lu, and S. J. Liang, "Support theory of surrounding rock loose zone in roadway," *Acta coalae Sinica*, vol. 1, pp. 21–32, 1994.
- [8] J. L. Ran, H. S. Wang, and T. C. Li, "Support technology of rectangular Roadway Based on surrounding rock loose circle theory," *Coal mine safety*, vol. 50, no. 7, pp. 135–139, 2019.
- [9] J. F. Pan, "Study on the theory of rock burst starting and its complete set of technology system in coal mine," *Acta coalae Sinica*, vol. 44, no. 1, pp. 173–182, 2019.
- [10] H. Y. Liu, J. P. Zuo, and D. J. Liu, "Optimization of roadway bolt support based on orthogonal matrix analysis," *Journal of mining and safety engineering*, vol. 38, no. 1, pp. 84–93, 2021.
- [11] J. P. Zuo, J. H. Wen, and S. Y. Hu, "Theoretical model and simulation study of equal strength beam support in deep coal mine roadway," *Acta coalae Sinica*, vol. 43, no. S1, pp. 1–11, 2018.
- [12] M. L. Zhang, Y. D. Zhang, and M. Ji, "Optimization of roadway support parameters based on fuzzy extension comprehensive evaluation method," *Journal of mining and safety engineering*, vol. 33, no. 6, pp. 972–978, 2016.
- [13] J. L. Cai, M. Tu, and H. L. Zhang, "Study on deformation instability mechanism and surrounding rock control technology of mining roadway in Jurassic weak cemented soft rock," *Journal of mining and safety engineering*, vol. 37, no. 6, pp. 1114–1122, 2020.
- [14] Y. L. Li, *Deformation and Instability Mechanism and Control Technology of Layered Roof in Large Section Coal Roadway of Zhaozhuang Mine*, China University of Mining and Technology, Beijing, China, 2017.
- [15] Q. B. Meng, L. J. Han, and W. G. Qiao, "Numerical simulation research on Optimization Design of section shape of deep high stress soft rock roadway," *Journal of mining and safety engineering*, vol. 29, no. 5, pp. 650–656, 2012.
- [16] W. M. Wang, X. Gao, and J. D. Jing, "Research on bolt mesh cable coupling support technology in weak cemented soft rock roadway," *Coal Science and Technology*, vol. 42, no. 1, pp. 23–26, 2014.
- [17] Q. X. Huang, Q. Guo, and J. Cao, "Failure mechanism and support technology of soft rock roadway with large deformation," *Journal of Xi'an University of Science and Technology*, vol. 39, no. 6, pp. 934–941, 2019.
- [18] R. S. Yang, Y. Zhu, and Y. L. Li, "Floor Heave Mechanism and control measures of layered floor in weak cemented soft rock roadway," *Journal of mining and safety engineering*, vol. 37, no. 3, pp. 443–450, 2020.
- [19] Y. T. Sun, *Study on Rheological Mechanism of Deep Loose Coal Roadway and Control Measures*, China University of Mining and Technology, Beijing, China, 2020.
- [20] Y. D. Sun, *Study on Instability Mechanism and Control of Roadway Surrounding Rock under Dynamic Load of Overburden Fracture in Deep Mining*, Liaoning University of Engineering and Technology, Shenyang, China, 2020.
- [21] Y. Q. Fan, Y. C. Liu, and M. Z. Zhao, "Distribution law of stress and displacement of surrounding rock in weak cemented soft rock roadway and supporting technology," *Coal engineering*, vol. 52, no. 4, pp. 84–91, 2020.
- [22] L. Chen, *Study on Fracture Evolution and Instability Mechanism of Surrounding Rock of Roadway in Steep Coal Seam under the Influence of Mining*, China University of Mining and Technology, Beijing, China, 2020.
- [23] S. L. Su, X. W. Gu, and L. Zhang, "Physical simulation test research on bearing characteristics of deep layered rock roadway," *China mining*, vol. 29, no. 1, pp. 123–128, 2020.
- [24] Y. Y. Chu, G. F. Ren, and C. Zou, "Study on instability analysis and control method of mine rock contact zone roadway," *Journal of Wuhan University (Natural Science Edition)*, vol. 52, no. 11, pp. 975–980, 2019.
- [25] Y. Yu, J. B. Bai, and X. Y. Wang, "Asymmetric deformation and failure characteristics and stability control of soft rock

- roadway,” *Journal of mining and safety engineering*, vol. 31, no. 3, pp. 340–346, 2014.
- [26] L. G. Wang, X. X. Miu, J. T. Dong, and X. N. Tan, “Numerical simulation of bolt grouting support in deep soft rock roadway,” *Geotechnical mechanics*, vol. 6, pp. 983–985, 2005.
- [27] Y. X. Guo and X. M. Song, “Study on instability mechanism of roof roadway under water drenching in Gob with accumulated water,” *Coal Science and Technology*, vol. 47, no. 11, pp. 36–43, 2019.
- [28] Q. L. Yao, X. H. Li, and Q. F. Chen, “Study on instability and failure characteristics and classification of water bearing sandstone roof roadway,” *Journal of China University of mining and technology*, vol. 42, no. 1, pp. 50–56, 2013.
- [29] W. X. Zheng, Q. W. Bu, and C. Wang, “Mechanical mechanism of deformation and instability of layered floor in Roadway with equal spacing bottom anchor,” *Coal mine safety*, vol. 50, no. 9, pp. 212–215, 2019.
- [30] C. M. Li, G. X. Xie, and Y. D. Lin, “Deformation control mechanism and support practice of surrounding rock with thin layered weak floor in Roadway,” *Journal of mining and safety engineering*, vol. 34, no. 5, pp. 948–954, 2017.
- [31] H. F. Lu and D. X. Yao, “Study on stress distribution and failure depth of layered rock mass in mining floor,” *Journal of rock mechanics and engineering*, vol. 33, no. 10, pp. 2030–2039, 2014.
- [32] Q. Y. Xu, Q. G. Huang, and G. C. Zhang, “Mechanism and control technology of fracture instability of narrow coal pillar in coal roadway affected by severe mining of fully mechanized top coal caving,” *Journal of mining and safety engineering*, vol. 36, no. 5, pp. 941–948, 2019.
- [33] N. Zhang, X. H. Li, and M. S. Gao, “Pre tension support and engineering application of gob side entry driving in mining face,” *Journal of rock mechanics and engineering*, vol. 12, pp. 2100–2105, 2004.
- [34] D. Y. Hao, Y. Z. Wu, and H. J. Chen, “Instability mechanism and control of mining roadway in short distance Extra Thick Coal Seam Under Goaf,” *Journal of coal*, vol. 44, no. 9, pp. 2682–2690, 2019.
- [35] I. Vazaios, M. S. Diederichs, and N. Vlachopoulos, “Assessment of strain bursting in deep tunnelling by using the finite-discrete element method,” *Journal of Rock Mechanics and Geotechnical Engineering*, vol. 11, no. 1, pp. 12–37, 2019.
- [36] L. R. E. Sousa, T. Miranda, R. L. E. Sousa, and J. Tinoco, “The use of data mining techniques in rockburst risk assessment,” *Engineering*, vol. 3, no. 1, pp. 552–558, 2017.
- [37] Code of China, *GB 50021-2001. Code for Geotechnical Engineering Investigation*, Code of China, Ministry of Construction of the People’s Republic of China, Beijing, China, 2002.

## Research Article

# Deformation Mechanism and Surrounding Rock Control in High-Stress Soft Rock Roadway: A Case Study

Yuwen Gao,<sup>1</sup> Chen Wang ,<sup>1</sup> Yong Liu,<sup>1</sup> Yuyang Wang,<sup>1</sup> and Lianchang Han<sup>2</sup>

<sup>1</sup>School of Mining, Guizhou University, Guiyang 550025, China

<sup>2</sup>Guizhou Panjiang Refined Coal Co., Ltd., Panzhou 553529, China

Correspondence should be addressed to Chen Wang; [cwang@gzu.edu.cn](mailto:cwang@gzu.edu.cn)

Received 4 April 2021; Accepted 29 May 2021; Published 25 August 2021

Academic Editor: Zizheng Zhang

Copyright © 2021 Yuwen Gao et al. This is an open access article distributed under the Creative Commons Attribution License, which permits unrestricted use, distribution, and reproduction in any medium, provided the original work is properly cited.

Stability control for soft and broken surrounding rock of roadways is one important segment of mining support. Taking 1412 Roadway of a mine in Guizhou province as a research background, this paper studies the large deformation of surrounding rock and the failure of bolts and cables. The deformation and failure mechanism are analyzed by related theoretical analysis and field survey. Then, the feasibility of the composite controlling scheme, bolts and cables + grouting + steel tube concrete support, is verified by theoretical analysis, numerical simulation, and industrial test. Following results can be obtained: main reasons leading to the deformation of surrounding rock and the failure of cables and bolts in the roadway are low strength and poor self-stability of surrounding rock, complex stress environment, low support resistance, and lack of reinforced support in crucial supporting sites; the control scheme can reduce the surrounding rock deformation by 40%, which meets the requirements of field application so that this practice can provide some guidance for other similar projects.

## 1. Introduction

Deformation and failure control of surrounding rock in soft rock roadway are always regarded as a difficult problem within worldwide underground engineering. With the depletion of coal resources in shallow bed, the mining depth increases incrementally and the number of soft rock roadway with high stress as well. Besides, unfavorable conditions such as high in situ stress and strong disturbance, soft and broken surrounding rock increase the difficulty of surrounding rock deformation and failure control [1–3].

For roadways with the loose and broken surrounding rock, traditional control techniques including anchor note, bolting shotcrete, cable anchor, u-steel yieldable support, concrete, and reinforced concrete hardly work to maintain the roadway stability especially under the influence of high stress and strong disturbance [4–6]. Compared with traditional support materials, the concrete-filled steel tube support is better than them in mechanical properties. Take an example, the support has three times bearing capacity of U-steel support under the same volume of steel. In recent

years, concrete-filled steel tube support has been applied on the field to control the deformation in soft rock roadway [7, 8]. Li et al. [9] proposed and applied “high-strength concrete-filled steel tube” supporting scheme to control the surrounding rock deformation in Chaganmuer mine so that the deformation and destruction had been effectively controlled; Liu et al. [10] used the closed-end composite supporting scheme “anchor net spray + oval concrete-filled steel tube supports + steel fiber concrete + reinforcement cable” to address the problem of deformation control in Qingshuiying coal mine large-section soft rock roadway; Wang et al. [11] applied “elliptical concrete-filled steel tube supports + deep-shallow cross grouting reinforcement” composite supporting scheme to reduce surrounding rock deformation in the Xingdong mine, and the scheme has worked effectively; Gao et al. [12] proposed and applied high-strength composite support technology based on concrete-filled steel tube support to successfully control surrounding rock deformation and failure.

In short, the advantages of concrete-filled steel tube support have been confirmed in several soft rock roadways



in China [13–15]. Nevertheless, this technology has not been utilized to soft and broken swelling rock roadways influenced by high stress and strong disturbance.

According to the on-site survey, 1412 Roadway belongs to a soft and broken swelling rock roadway influenced by high stress and strong disturbance. And, deformation and destruction of the surrounding rock were serious, which restricts normal production. Based on the analysis of the surrounding rock deformation characteristics and mechanism, the composite supporting scheme, bolts and cables + grouting + steel tube concrete support, has been put forward and verified by the industrial test. In brief, this scheme can provide a reference for the surrounding rock control under similar conditions.

## 2. Engineering Background

With depth of embedment between 650 m and 850 m, 1412 Roadway is located at an intersection of many roadways in 17# coal seam. Coal seam group consisting of 16#, 17#, and 18# coal seam is a close-distance coal seam group. Besides, the adjacent coal seams of 17# coal seam have been hollowed out one after the other. In addition, the superposition of disturbed stress field and primary stress field formed by multiple disturbances makes the roadway stress environment complicated. And, the surrounding rock lithology is dominated by mostly weak rock such as mudstone, shale, fine sandstone, and silty mudstone. When such rocks are exposed with water, it easily generates great swelling pressure. Furthermore, the phenomenon of stress concentration appears serious. The local vertical stress exceeds 20 MPa, which belongs to the high-stress soft rock roadway.

For the original supporting scheme, “anchor net + cable + bolt-shotcrete” had been adopted. The bolt adopts left spiral rigid bolt with diameter 22 mm and length 2000 mm. The distance between adjacent rows of the bolt is 800 mm. The specification parameters of the initial cable, respectively, are diameter 22 mm and length 6000 mm. The distance between adjacent rows of the cables is 1200 mm. The hanging net is diamond-shaped metal net, and the thicknesses of the sprayed concrete are 150 mm. The dimension of original roadway section, respectively, is net width 5500 mm, wall height 860 mm, arch height 2750 mm, and clear height 3610 mm.

## 3. Analysis of Deformation Characteristics and Mechanism

*3.1. Deformation and Failure Characteristics of Surrounding Rock.* Through the field investigation and records about 1412 Roadway, these deformation characteristics can be obtained:

- (1) The surrounding rock has great deformation and rapid deformation rate. The initial convergence speed is up to 60 mm/day after roadway excavation. And, the maximum deformation amount among the roof, the floor heave, and the two sides, respectively, come to 1155 mm, 580 mm, and between 1500 mm and 2200 mm.

- (2) Clay mineral will be expanded, and mudding occurs when it exposes to water, which aggravates rock deformation. The studied roadway surrounding rock contains a large number of clay minerals including montmorillonite and illite. Therefore, the surrounding rock sharply causes softening and mudding phenomenon with water.
- (3) The supporting components are seriously ineffective. In key parts such as the roof, the shoulder socket, and the two sides of roadway, the failure of bolts and cables frequently happened. The failure features mainly perform breakage, slippage, exfoliated nut, pallet bending, and fracturing. And, the metal mesh pockets appeared to have tear and local rock fall.
- (4) The surrounding rock expresses loose and broken in a wide range. Using YTJ-20 rock formation drilling detector to drill the surrounding rock at field, the detection result presents the range of loose circle which is between 2.3 m and 4.2 m, which is beyond anchorage range of the bolts. Hence, the bolts are difficult to play an active support role. Figure 1 shows part deformation characteristics of the roadway.

*3.2. Mineral Composition Analysis and Mechanical Properties' Test.* Using the PANalytical multifunctional powder X-ray diffractometer in room for the composition analysis of the surrounding rock, the mineral compositions are shown in Table 1.

Using the HDH-1 point load test instrument to conduct a point load test in this roadway, the average uniaxial compressive strength of the floor rock and roof rock, 1.23 MPa, can be obtained. The above results present that the strength of the surrounding rock is extremely low.

### 3.3. Deformation and Failure Mechanism of Surrounding Rock

- (1) The surrounding rock has such characteristics of low strength and poor self-stability. The major lithology of the surrounding rock is dominated by soft rocks such as mudstone, shale, fine sandstone, and silty mudstone. Mudstone, fine sandstone, and other mineral mainly consist of quartz. Besides, there is a higher content of clay minerals, including plagioclase and albite, in the surrounding rock. These clay minerals are easy to expand when exposed to water, which produces huge swelling pressure and aggravates roadway deformation. Furthermore, the fracture and joints of the surrounding rock developed, resulting in surrounding rock loose and broken with low bearing capacity.
- (2) The roadway was significantly affected by repeated mining. And, the stress environment is complex. The mining effect mainly comes from the mining of the close coal seam group. Besides, the roadway is located near the intersection of various roadways. The superposition of the disturbed stress field, formed by multiple disturbances, and the primary stress field

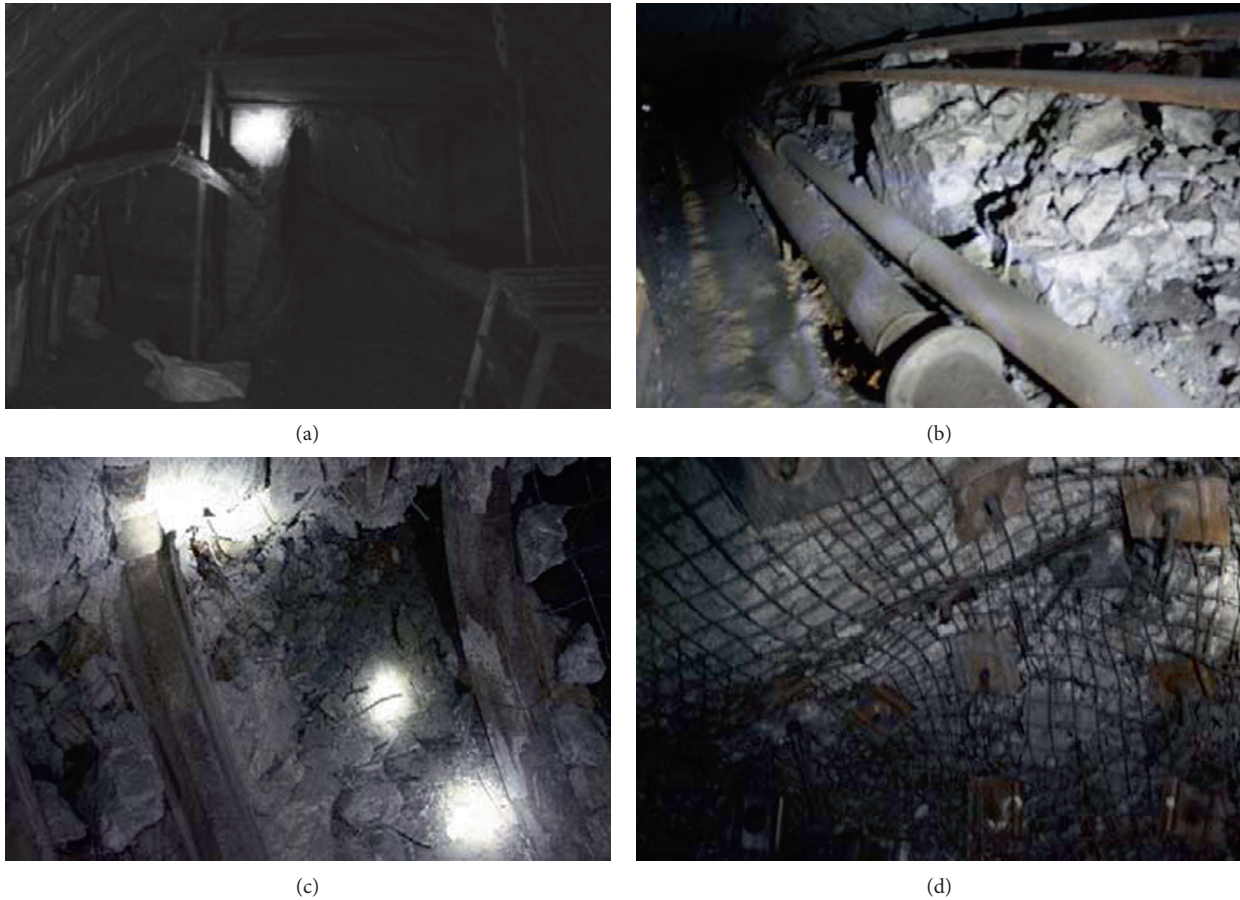


FIGURE 1: Roadway deformation figure under original support. (a) Section deformation. (b) Large deformation of section. (c) Broken surrounding rock. (d) Pallet bending.

TABLE 1: Mineral composition and content.

Mineral composition	Content (%)
Clay mineral	70.4
Quartz	18.1
Plagioclase	8.4
Albite	3.1
Montmorillonite	33
Kaolinite	42
Illite	12
Chlorite	13

contributes to the more complicated stress environment. Furthermore, the phenomenon of stress concentration has intensified.

- (3) The primal supporting parameters are unreasonable. The length of the original support bolt is 2.0 m, and the distance between adjacent rows is 800 mm. The length of the anchor cable is 6 m, and the distance between adjacent rows is 1200 mm. Owing to the range of loose circles exceeded the length of original bolts, the active bearing capacity of the bolts and the cables was not fully utilized. With unreinforced

support, vital parts such as bottom corners, shoulder, and roof have serious damage.

- (4) The mudding phenomenon of surrounding rock is serious. The roof and the two sides had serious seepage. Long-term contact between surrounding rock and water causes the strength and the bearing capacity of the surrounding rock decrease. Secondly, water leads to expansion and sliming of the surrounding rock which contains a large number of montmorillonite and kaolinite. Thereby, the self-supporting capacity of the surrounding rock becomes low.
- (5) There was unreinforced support on the floor and the bottom corner. After excavation, the floor was opening and unsupported, which belongs to the weakest link of support. In addition, the effect of water dripping from roof and water accumulation on floor contributed to that the floor undergoes significant swelling deformation and rheological deformation. The floor has seriously deformed and the roof and two sides as well. Eventually, the supporting structure became unstable and damaged.

## 4. Deformation and Failure Control Technology of Surrounding Rock

*4.1. Control Principles of Roadway Surrounding Rock Deformation.* In order to effectively control the deformation and destruction of 1412 Roadway and to choose the optimal supporting scheme, following supporting principles should be complied:

Governing sequence: Govern floor → Govern two sides → Govern roof. Furthermore, the shoulder corner is also a vital position which should be supported.

Active supporting improves integrity of the surrounding rock; thus, let surrounding rock give full play to the active bearing performance. There are some aspects that should be specifically considered:

- (1) Strengthen support for critical parts: instability and deformation of the roadway start from crucial positions which determines the stability of the overall structure. When there are weak links in the surrounding rock, it is frequently the breakthrough point of deformation and destruction. And, the malignant expansion of weak links will eventually lead to instability and deformation over time. Therefore, these critical parts should be reinforced to avoid stress concentration, so as to improve the overall performance of the surrounding rock and control the instability and the deformation.
- (2) Strengthen support on the floor: the type of floor heave is squeezing fluidity floor heave in 1412 Roadway. Shearing damage occurs in the unsupported floor strata under the action of high stress, which causes cracks and gaps in the floor. Otherwise, the invasion of water will aggravate the destruction. Therefore, bolts will be used to cut off pressure transmission of the two sides. Furthermore, the hardening grouting concrete can provide a large amount of bearing capacity. And, the stress state of the floor is transformed from the two-direction stress state to three-direction stress state. In other words, the ultimate strength of the floor rock is improved. The bearing range of stress is gradually enlarged. And, the floor heave can be effectively controlled.
- (3) Use strong bolts and high prestressed cables: at the initial stage of roadway support, the cables and the bolts undertake main carrying work. By increasing the initial pretightening force of supporting components, it can form an effective prestressed load-bearing structure and that exerts the characteristics of bolts and cables rapidly increase resistance, strong initial support, and high working resistance. In addition, it can likewise restrain discontinuous deformation and expansion of surrounding rock within anchorage scope such as separation, sliding, and crack propagation. In other words, the measure ensures the integrity of surrounding rock and improves the rock's active bearing capacity.

- (4) Implement full-section grouting behind wall and strengthen the carrying capacity of surrounding rock: full-section grouting not only can seal or even fill the water flowing fracture in the surrounding rock but also prevent the erosion of water and strengthen the strength of surrounding rock. Secondly, grouting can penetrate into fractures of broken surrounding rock under the action of high-pressure pump. Besides, grouting can fill or even close larger fractures. The consolidated permeable slurry can form a network skeleton structure, so as to improve the strength of surrounding rock. The cables and bolts are arranged inside the grouting layer, which is conducive to prestressed diffusion and improving the stress state. The stress state of surrounding rock transforms from two-direction stress to three-direction stress. After the roadway is widened to the designed section, the bolts and cables, concrete-filled steel tube support, and concrete coordinate with the surrounding rock to form a collaborative supporting system, which achieves a hierarchical coordinated load-bearing layer.

In other words, the first bearing layer is made of concrete-filled steel tube support and hardened concrete. The combination of these supports cannot only resist high strength pressure but also moderate pressure relief. For the stress environment where pressure around the roadway is large and uneven, the layer can provide great bearing capacity.

The arching effect of high-strength bolts improves the stress state of shallow surrounding rock, transforms anchoring area from the load body into the bearing body, and restricts the destruction and deformation of shallow surrounding rock. The influenced layer is named the second bearing layer.

The high prestressed anchor cable anchored in the stable rock layer effectively links shallow broken surrounding rock and deep stable surrounding rock. Therefore, this and the arching action of anchor bolts together form the third bearing layer, which controls the deformation of surrounding rock.

*4.2. Deformation Control Strategy and Parameter Determination of Surrounding Rock.* Derived from the above analysis, the support theory of high stress soft rock roadway, and field experience, a preliminary design of composite supporting scheme "anchor cables and bolts + grouting + concrete-filled steel tube support" is designed, as follows:

- (1) The original roadway adopts straight wall semicircular arch roadway, which cannot provide any support for the floor. The deformation first occurs from weak link in the support, that is, the place where stress is concentrated. Using horseshoe-shaped roadway section as roadway section not only avoids weak links but also improves stress state of the surrounding rock.



- (2) The prestress of the original bolt and the support strength of the initial proposal are lower. It has been tested that the surrounding rock within 1.7 m was severely broken. In order to give full play to the restriction of the bolts on the shallow surrounding rock's deformation and destruction, the length of bolts is extended to 2500 mm. The anchor bolt adopts ultraintense thread steel bolt with diameter 22 mm. The distance between adjacent rows of bolt is 800 mm. There are 15 bolts arranged in each row of the roadway, and each bolt uses 3 rolls of K2335 resin medicine (fixative). In addition, since the floor heave type is a squeezing fluidity floor heave, the inclination angle of the bolt which is arranged at corner should be set between 20° and 30° to cut off the stress transmission between the two sides. The bolt screws must be tightened by plum blossoms with diameter 34 mm. Tightening torque is between 150 N·m and 200 N·m. The anchor bolt is lapped at the overlap of steel mesh. The length and width of the steel mesh are, respectively, 1800 mm and 980 mm. The anchoring section length takes 1500 mm. And, the overlap length of the steel mesh fetches 100 mm. The cables adopt prestressed cable with diameter 21.6 mm and length 7000 mm. The distance between adjacent rows of the cables has 1200 mm. And, each row is arranged with 7 anchor cables. Moreover, each anchor cable uses 5 anchoring agents. The pre-tightening force of the cable is not less than 150 N·m. The exposed length of the cable is between 150 mm and 250 mm after tightening.
- (3) For maintaining the stability of the roadway with high stress and intense surrounding pressure, the surrounding rock not only needs bearing capacity from itself but also needs external supporting force. In this paper, concrete-filled steel tube support is selected as a crucial part of the active support. The concrete-filled steel tube support has same shape as the roadway section and uses 20# seamless steel pipes with diameter 194 mm and wall thickness 10 mm. The specification of casing selects diameter 219 mm and length 100 mm. And, a set of concrete-filled steel tube support is erected every 500 mm. Using HBTS-15 concrete pump, C40 concrete was injected into inner of the support from bottom to top. The mixing ratio of cement, water, and sand fetches 1 : 0.39 : 1.29 in C40 concrete. The pressure value of the transfer pump gets to about 5 MPa, which can be adjusted according to the actual situation, but the maximum pressure cannot exceed 6 MPa. Due to the deep loose and broken range of surrounding rock, the arching effect of bolt hardly works. Therefore, a 500 mm gap between roadway and support for high-pressure grout was left when erecting the concrete-filled steel tube supports. The slurry under the action of high pressure penetrates in the deep surrounding rock to improve the integrity. The grouting pressure value takes 6 MPa, and the wind pressure is controlled at

0.15 MPa to 0.18 MPa. After the bolts and cables are laid, the bottom grout is conducted, and then, the support has erected. Secondly, reinforced mesh and noncombustible material cloth are laid behind the support. The mixing ratio of cement and sand takes 1 : 3 in cement mortar. And, the mixture must be mixed evenly with accelerator which accounts 3% to 5% of the cement amount. Besides, the storage time of the mixture with accelerator cannot get past twenty minutes. The composite supporting scheme is shown in Figure 2.

## 5. Check Bearing Capacity of the Composite Support Scheme

5.1. *Calculate Support Resistance of the Concrete-Filled Steel Tube Support.* The support resistance of the concrete-filled steel tube support can be calculated through the following formula:

$$\sigma_0 = \frac{\varphi_0 N_0}{DR_S}, \quad (1)$$

$$R_S = k_m \sqrt{\frac{S_S}{\pi}},$$

where  $S_S$  presents the area enclosed by the concrete-filled steel tube support,  $m^2$ ,  $\varphi_0$  represents the reduction factor, taking 0.80, and  $N_0$  represents the ultimate bearing capacity of the concrete-filled steel tube short columns. Due to the steel tube adopted diameter 194 mm and thickness 10 mm,  $N_0$  takes 3186.4 kN;  $D$  represents the spacing of the support, taking 0.5 m;  $k_m$  is the section correction factor, taking 1.05 [16]. The section area is 14.84  $m^2$ . Bring each parameter into formula (3), it can be obtained that  $\sigma_0$  is 2.24 MPa.

5.2. *Calculate Support Resistance of Grouting Body.* The support resistance of hardened concrete can be calculated through the following formula [17]:

$$P_c = \frac{2\tau_c d_c}{R_c \sin 2\gamma}, \quad (2)$$

$$R_c = k_m \sqrt{\frac{S_c}{\pi}},$$

where  $\tau_c$  represents shear strength of grout,  $\tau_c = 0.15f_c$ ,  $f_c$  represents the designed compressive strength of grout, taking 12 MPa,  $d_c$  represents thickness of the grouting body, taking 500 mm,  $\gamma$  represents the shearing slip angle, taking 33°, and  $S_c$ , area enclosed by the grouting body, is 18.07  $m^2$ . Bringing each parameter into formula (2), it can be obtained that  $P_c$  is 0.782 MPa.

5.3. *Calculate Support Resistance of Bolt and Cable.* Computed mechanical model of the superimposed bearing layer is shown Figure 3.

Calculate the effective length of the bolt and cable [18]:

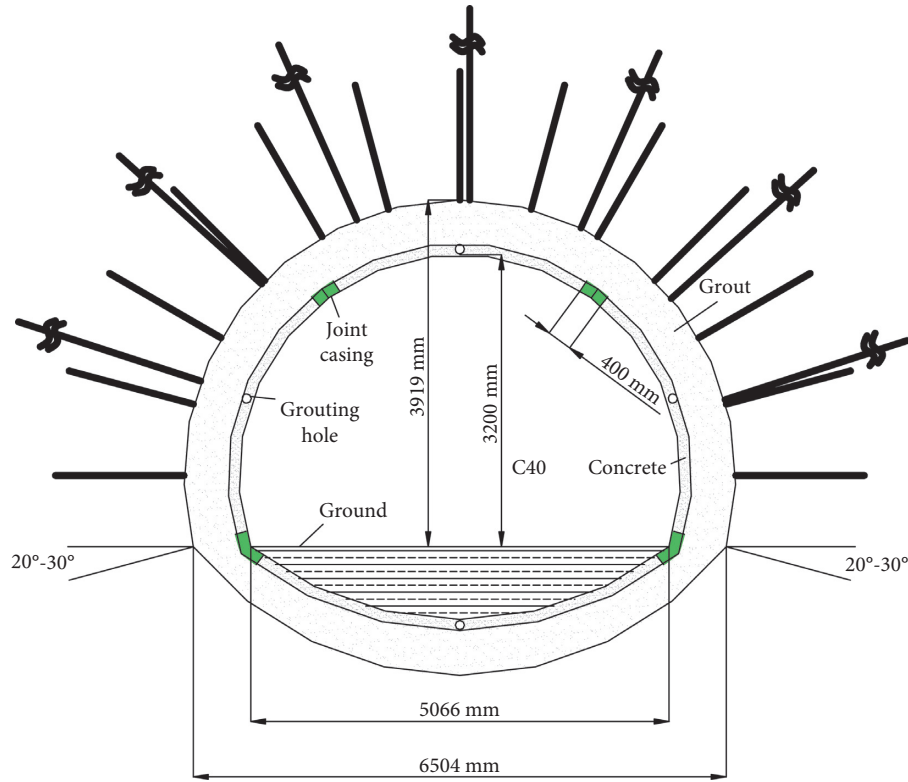


FIGURE 2: Composite support schematic.

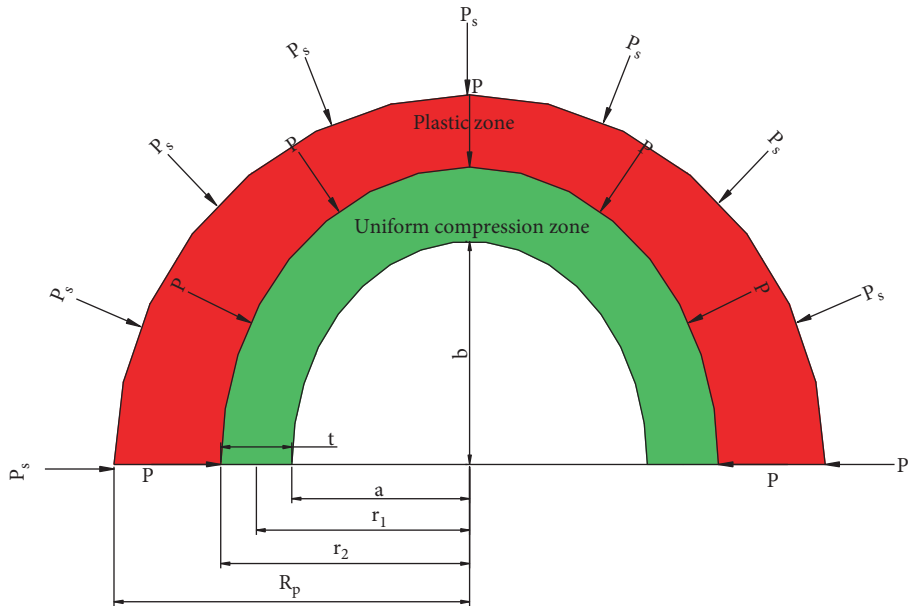


FIGURE 3: Mechanical model of the arched compression zone.

$$t_1 = \frac{L_1 \tan \beta - D_1}{\tan \beta},$$

$$t_2 = \frac{L_2 \tan \beta - D_2}{\tan \beta},$$

(3)

where  $L_1$  is the effective length of bolt,  $L_1 = L'_1 - L_a - L_b$ ,  $L'_1$  is a length of the bolt, taking 2.5 m,  $L_a$  is an exposed length of the bolt, taking 0.15 m,  $L_b$  is an end length of the bolts, taking 0.5 m,  $\beta$  is the control angle of the cable and the bolt in the ruptured surrounding rock, taking 45°,  $L_2$  is the effective length of the cable,  $L_2 = L''_2 - L_c - L_d$ ,  $L''_2$  is a length of the



cable, taking 7 m,  $L_c$  is an exposed length of the cable, taking 0.2 m,  $L_d$  is an end length of the cable, taking 2.5 m,  $h_c$  is thickness of the grouting body, taking 0.5 m, and  $D_1$  and  $D_2$ , respectively, presents the distance between adjacent rows of the bolt and cable, taking 0.8 m and 1.2 m. Bringing each parameter into formula (5), it can be obtained that  $t_1$  and  $t_2$  are, respectively, 1.05 m and 3.10 m. The model of the bearing layer structure is shown as Figure 4.

The radial axial force provided by the cable and bolt can be calculated by the following formula:

$$\begin{aligned}\sigma_s &= \frac{F_s}{D_2 * D_2}, \\ \sigma_g &= \frac{F_g}{D_1 * D_1},\end{aligned}\quad (4)$$

where  $F_s$  is the pulling force of the cable and  $F_g$  is the pulling force of the bolt. According to the specification of the selected bolt and cable, it can be obtained that  $F_s$  and  $F_g$  are, respectively, 454 kN and 127 kN. By calculating,  $\sigma_s$  and  $\sigma_g$  are, respectively, 0.31 MPa and 0.20 MPa.

The relationship between tensile force of a bolt and weight of the rock mass it bears is as follows:

$$F_g > \rho * D_1^2 * g * L_1' * 1.8 = 41.6 \text{ KN}, \quad (5)$$

where  $\rho$  is the density of strata passed by the bolt, taking  $2600 \text{ kg}\cdot\text{m}^{-3}$ ,  $g$  presents acceleration of gravity, taking  $10 \text{ N/kg}$ , and 1.8 represents the safety factor.

It can be seen from the above equation that the tensile force is greater than the rock mass gravity, so the bolt spacing is reasonable.

#### 5.4. Check Bearing Capacity of Uniform Compression Zone.

This paper focuses on the elliptic section in the upper half of the roadway, so the hyperbolic section in the lower part will not be discussed. On the horseshoe roadway section, the stress state of the upper half of the surrounding rock can be equivalent to the stress state of the upper surrounding rock of the elliptical roadway under the same load.

In this paper, the ratio of long axis to short axis is 1.26, which is high elliptical roadway. The plastic area boundary of high elliptical roadway is close to circular, so the boundary of the plastic area in the upper half of the roadway in this paper is equivalent to semicircle [19].

Based on the principle of the arched compression zone, the mechanical model of elliptical roadway under stress in original rock is established, as shown in Figure 3.

The boundary outside the plastic zone, that is, the boundary inside the elastic zone, meets the following equation [20]:

$$\begin{aligned}\sigma_{\theta(p)} + \sigma_{\rho(p)} &= 2P_0, \\ \sigma_{\theta(p)} &= \frac{1 + \sin \varphi}{1 - \sin \varphi} \sigma_{\rho(p)} + \frac{2c \cos \varphi}{1 - \sin \varphi}.\end{aligned}\quad (6)$$

The following equation can be obtained from the above equations:

$$\sigma_{\rho(p)} = (1 - \sin \varphi)P_0 - c \cos \varphi, \quad (7)$$

where  $P_0$  represents the initial ground stress,  $\varphi$  represents the internal friction angle,  $c$  represents cohesion, and  $R_p$  is the radius of the surrounding rock plastic area. According to the experimental results and field measurement,  $\varphi$  takes  $27^\circ$ ,  $c$  is 0.37 MPa,  $R_p$  is 6700 mm, and  $P_0$  is 17.24 MPa. Bringing each parameter into the formula, it can be obtained that  $\sigma_{\rho(p)}$  is 9.08 MPa.

The load  $P$  acting on the uniform compression zone formed by bolts and cables can be obtained by using the Jager and Cook formulas [20, 21]

$$P = P_s \left( \frac{r_2}{R_p} \right)^{2 \sin \varphi / (1 - \sin \varphi)}. \quad (8)$$

The elliptic equation can be expressed in the form of polar coordinates, as shown in the following:

$$\rho = \frac{ab}{\sqrt{b^2 \cos^2 \theta + a^2 \sin^2 \theta}}, \quad (9)$$

$$r_2 = \frac{ab}{\sqrt{b^2 \cos^2 \theta + a^2 \sin^2 \theta}} + t, \quad (10)$$

$$P_s = \sigma_{\rho(p)}, \quad (11)$$

where  $\theta$  is the angle between the stress and the horizontal axis. Since the number of cables used in this roadway is fewer, the effective length of the bolt is taken as the width of the uniform compaction zone:

$$t = t_1. \quad (12)$$

Bringing formulas (7) and (10) into formula (8), the following equation can be obtained:

$$P = P_s \left( \frac{ab + t_1 \sqrt{b^2 \cos^2 \theta + a^2 \sin^2 \theta}}{R_p \sqrt{b^2 \cos^2 \theta + a^2 \sin^2 \theta}} \right)^{2 \sin \varphi / (1 - \sin \varphi)}. \quad (13)$$

The schematic diagram of the force on the arch formed by the uniform compression zone is shown in Figure 5.

Under the action of only considering the supporting force, the radial stress in the uniform compression zone upper part can be calculated by the following complex variable function method to shortcut calculation.

Through the mapping function, the shadow part in the  $Z$  plane will be mapped to the shadow part in the corresponding complex plane [22]. Curve  $L$  and points  $A, B, C,$  and  $D$  in the  $z$  plane are mapped to complex plane curve  $L'$  and points  $A', B', C',$  and  $D'$ , respectively. The mapping relationship and schematic diagram are shown in Figure 6.

$$\begin{aligned}z &= w(\zeta) = R \left( m\zeta + \frac{1}{\zeta} \right), \\ R &= \frac{a+b}{2}, \\ m &= \frac{a-b}{a+b},\end{aligned}\quad (14)$$

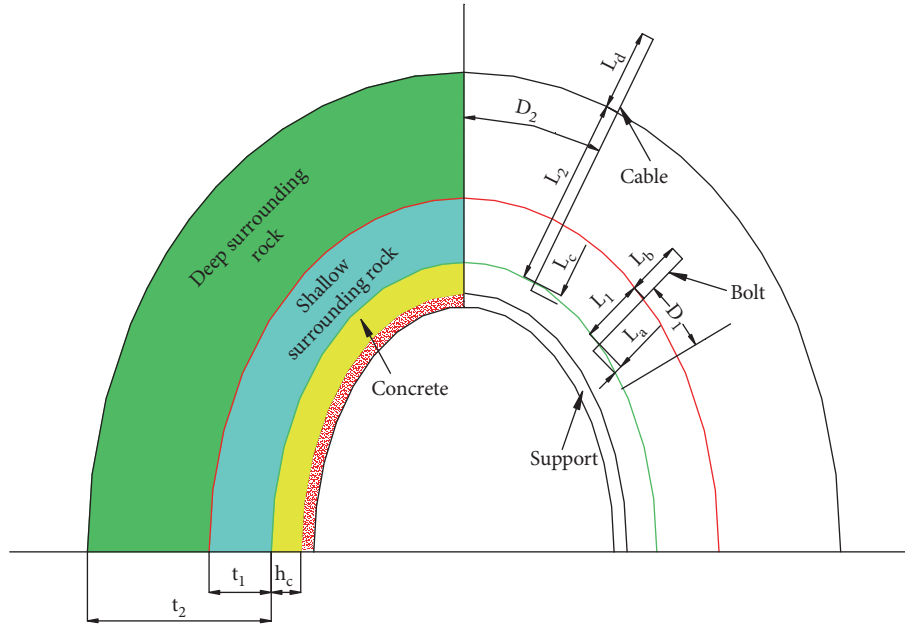


FIGURE 4: Model of the bearing layer structure.

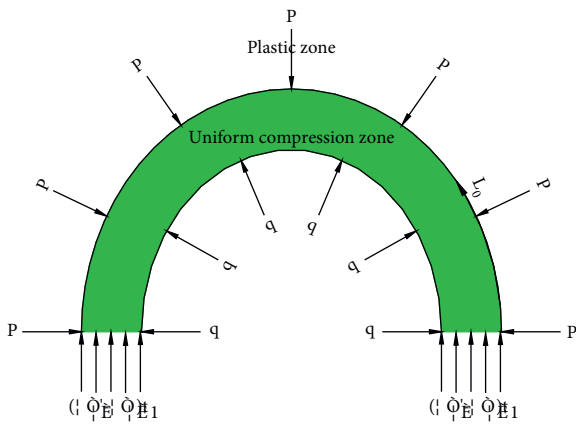


FIGURE 5: Force diagram of the arch.

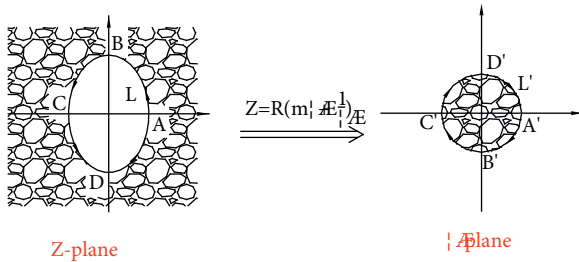


FIGURE 6: Mapping diagram. where a and b are the semilong axis and semishort axis of an ellipse, respectively.

Assuming that the roadway after support following the basic hypothesis of elasticity, the stress function can be expressed as follows:

$$U = \frac{1}{2} [\bar{z}\chi(z) + z\overline{\chi(z)} + \theta(z) + \overline{\theta(z)}], \quad (15)$$

where  $z$  represents point coordinates in the complex plane and both  $\chi(z)$  and  $\theta(z)$  are analytic functions.

When considering only the effect of support force on roadway surrounding rocks, the following equation is met on the roadway boundary:

$$f_0 = i \int_L (\overline{T_x} + i\overline{T_y}) ds - \frac{X + iY}{2\pi} \ln \sigma - \frac{1 + \nu'}{8\pi} \cdot (X - iY) \frac{w(\sigma)}{w(\sigma)} \sigma - 2Bw(\sigma) - (B' - iC') \overline{w(\sigma)},$$

$$\chi(\zeta) = \frac{1}{2\pi i} \int_{L'} \frac{f_0 d\sigma}{\sigma - \zeta},$$

$$\theta'(\zeta) = \frac{1}{2\pi i} \int_{L'} \frac{f_0 d\sigma}{\sigma - \zeta} - \zeta \frac{\zeta^2 + m}{m\zeta^2 - 1} \chi'(\zeta),$$

$$\sigma_p + \sigma_\theta = 4\text{Re} \left[ \frac{\chi'(\zeta)}{w'(\zeta)} \right],$$

(16)

where in hole edge,  $\overline{T_x}$  represents surface force component of  $x$  direction,  $\overline{T_y}$  represents surface force component of  $y$  direction,  $X$  and  $Y$  represent, respectively, boundary resultant force of  $x$  and  $y$  directions,  $B$ ,  $B'$ , and  $C'$  are real constants, and  $\sigma$  represent the points which locate the boundary of the unit circle on the complex plane  $\zeta$ .

Since the hole edge pressure is self-balanced and the stress at infinity is 0, there is  $X = Y = B = 0$  and  $B' - iC' = 0$ :

$$f_0 = -q \int_L (dx + idy) = -qR \left( \frac{1}{\zeta} + m\zeta \right),$$

$$\chi(\zeta) = -qRm\zeta, \quad (17)$$

$$\theta l(\zeta) = -qR(1+m^2) \frac{\zeta}{1-m\zeta}$$

According to the actual situation,  $\sigma_\rho$  is  $-q$ :

$$\sigma_\theta = q \frac{1 - (3m^2 + 2m \cos 2\theta)}{1 + (m^2 - 2m \cos 2\theta)}. \quad (18)$$

Under the action of only considering original rock stress, the calculation formula of circumferential stress around high elliptical roadway is as follows:

$$\sigma_{\theta'} = P_0 \frac{2m'}{\cos^2 \theta' + m'^2 \sin^2 \theta'}, \quad (19)$$

$$m' = \frac{b}{a},$$

where  $\theta l$  is the angle between the stress and the vertical axis.

On the arch structure formed by the uniform compression zone, the arch's stress distribution and roadway section are symmetrical about  $Y$  axis. Therefore, if the resultant force in  $Y$  direction under unit length is greater than 0, the support scheme can ensure the roadway safe:

$$ds = \sqrt{(a \sin \alpha)^2 + (b \cos \alpha)^2} d\alpha, \quad (20)$$

where  $ds$  represents an arc length differential length unit,  $\alpha$  represents the angle, and  $L_0$  represents the arc length of  $P$  acting on the uniform compression arch.

Under the action of the original rock stress, the  $Y$ -direction resultant force under unit length of the outer plane on the uniform compression zone can be obtained by the following equation:

$$Y_p = \int_{L_0} P \sin \alpha ds. \quad (21)$$

Equations (20) and (13) are brought into equation (21) to obtain the following equations:

$$Y_p = \int_0^\pi P_s \left( \frac{ab + t_1 \sqrt{(a \sin \alpha)^2 + (b \cos \alpha)^2}}{R_p \sqrt{(a \sin \alpha)^2 + (b \cos \alpha)^2}} \right)^{2 \sin \varphi / (1 - \sin \varphi)} \sin \alpha \sqrt{(a' \sin \alpha)^2 + (b' \cos \alpha)^2} d\alpha \quad (22)$$

$$= -2P_s \int_0^{\pi/2} \sqrt{a'^2 + (b'^2 - a'^2) \cos^2 \alpha} \left( \frac{ab + t_1 \sqrt{a^2 + (b^2 - a^2) \cos^2 \alpha}}{R_p \sqrt{a^2 + (b^2 - a^2) \cos^2 \alpha}} \right)^{2 \sin \varphi / (1 - \sin \varphi)} d \cos \alpha,$$

where  $a$  takes 3.252 m,  $b$  is 3.919 m,  $a'$  is 4.302 m, and  $b'$  is 4.969 m. Bringing each parameter into (25), it can be obtained that  $Y_p$  is  $3.548 \times 10^4$  KN.

Without considering the increment of tangential stress along the radial direction, the radial force under unit length of the arch formed by the uniform compression zone under the action of original rock stress can be obtained:

$$Y_{\theta'} = 2\sigma_{\theta'} t_1. \quad (23)$$

Bringing each parameter into formula (23), it can be obtained that  $Y_{\theta'}$  is  $6.008 \times 10^4$  KN.

In this case, one end of the bolts and cables and grouting body are directly acted on the innermost side of the uniform compression belt, so the supporting force provided by them can be directly superimposed. For the steel tube concrete support, it has no direct action on the uniform compression zone, but the grouting body they act on can be regarded as an elastomer. So, it is not difficult to obtain the equivalent

supporting force acting on the uniform compression zone. The sum of the forces acting on the uniform compression zone by the above components is  $q$ :

$$\sqrt{\frac{b^2 - a^2}{a^2}} = k,$$

$$\sqrt{\frac{(b - h_c)^2 - (a - h_c)^2}{(a - h_c)^2}} = k_1,$$

$$m_e = \frac{a - b}{a + b - 2h_c},$$

$$P_e = \frac{\sigma_0(a - h_c)1/k_1 \left[ k_1 \sqrt{1 + k_1^2} + \ln \left| k_1 + \sqrt{1 + k_1^2} \right| \right] - 2\sigma_0(1 - 3m_e^2 + 2m_e \cos 2\theta/1 + m_e^2 - 2m_e \cos 2\theta)h_c}{a1/k \left[ k \sqrt{1 + k^2} + \ln \left| k + \sqrt{1 + k^2} \right| \right]} \quad (24)$$

Bringing each parameter into formula (23), it can be obtained that  $P_e$  is 1.70 MPa:

$$q = P_e + \sigma_s + \sigma_g + P_c, \quad (25)$$

$$Y_q = \int_0^\pi q \sin \alpha \sqrt{(a \sin \alpha)^2 + (b \cos \alpha)^2} d\alpha, \quad (26)$$

$$= -2q \int_0^{\pi/2} \sqrt{a^2 + (b^2 - a^2) \cos^2 \alpha} d \cos \alpha,$$

$$\sqrt{\frac{b^2 - a^2}{a^2}} = k \rightarrow Y_q = 2qa \frac{1}{k} \int_0^k \sqrt{1 + x^2} dx = qa \frac{1}{k} \left[ k \sqrt{1 + k^2} + \ln \left| k + \sqrt{1 + k^2} \right| \right]. \quad (27)$$

Bringing formulas (24) and (25) into formula (27), it can be obtained that  $Y_q$  is  $2.084 \times 10^4$  KN.

Without considering the increment of tangential stress along the radial direction, the radial force of the arch formed by the uniform compression zone under the action of support force can be obtained:

$$Y_\theta = 2\sigma_\theta t_1. \quad (28)$$

Bringing each parameter into formula (28), it can be obtained that  $Y_\theta$  is  $4.41724 \times 10^3$  KN:

$$\sum Y = Y_{\theta_t} + Y_q - Y_\theta - Y_p = 4.102 \times 10^4 \text{ KN} > 0. \quad (29)$$

Above all, the ultimate bearing capacity of the design scheme is higher than the required load of the roadway, which meets the requirements of roadway support. It means that the superimposed bearing structure meets design requirements.

## 6. Numerical Simulation Analysis

**6.1. Model Establishment.** The numerical model of the roadway is shown in Figure 7, based on FLAC3D simulation software. Considering the boundary effect, the length of the outer boundary and the horizontal direction have more than 8 times the radius of the roadway. The size is 60 m \* 20 m \* 40 m with a total of 67282 units and 91550 nodes. The model adopts the strain softening model. At same time, the uniform load 11.74 MPa is applied at the top of the model. In the process of tunnel excavation, for the bottom boundary, it is prohibited to move in any directions. For the top boundary, it is free. For other boundaries, it is forbidden to move in any directions, except vertical direction. In the supporting process, the bolts and the cables adopt the cable unit. And, concrete-filled steel tube support adopts the beam unit. The material parameters of the roadway surrounding rock are shown in Table 2.

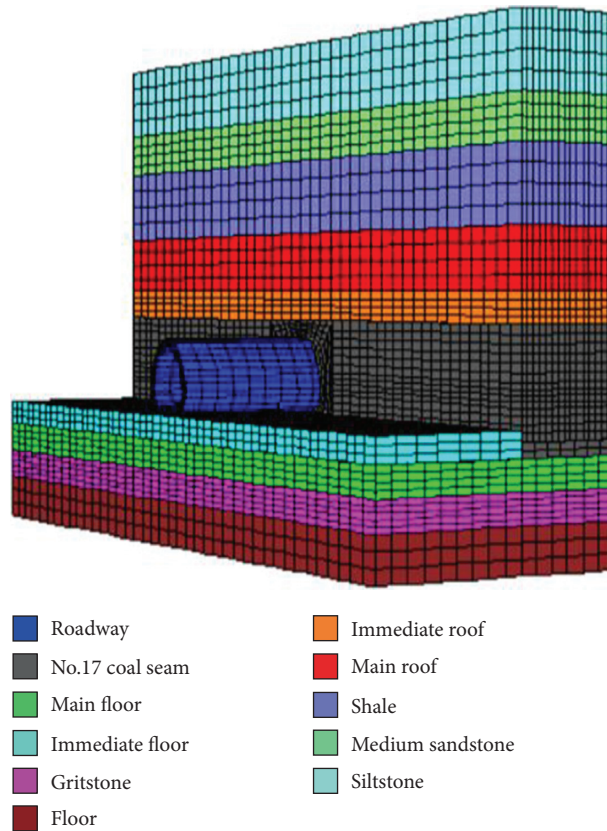


FIGURE 7: Numerical model of the roadway.

TABLE 2: Rock material parameters.

Rock	Density (kg-m <sup>-3</sup> )	Shear modulus (GPa)	Bulk modulus (GPa)	Cohesion (MPa)	Interfriction angle	Tensile strength (MPa)
Mudstone	2100	0.27	0.53	0.55	25	0.80
Shale	2600	3.3	5.10	2.00	37	2.00
Siltstone	2200	0.47	0.91	0.81	25	1.00
Medium sandstone	2550	0.60	1.00	0.82	32	1.10
Fine sandstone	2600	0.67	1.18	0.80	30	1.15
Coal	1650	0.19	0.42	0.57	24	0.65
Gritstone	2520	0.60	1.00	0.82	32	1.14

6.2. Result Analysis. Figure 8 shows a comparison of the numerical simulation cloud chart between the roadway without bracing and the roadway with the concrete-filled steel tube support bracing.

6.2.1. Roadway Excavation without Support. After excavation, due to no support measures have been taken, the roadway changed from the three-direction stress state before excavation to the two-direction stress state. This change prompts the roadway instability and deformation. The displacement of roadway surface increases with the excavation time. As shown in Figure 8(a), the maximum subsidence of the roof reaches 300 mm. The maximum size of bottom heave reaches 250 mm. And, the deformation convergence rate reaches 15.32%. Furthermore, the plastic

zone of the roadway has great distribution range. The original roadway cannot maintain normal work. Thereby, support should be applied immediately after the excavation of the roadway.

6.2.2. Applying Support. After excavation of the roadway and anchoring the cables and bolts, the concrete-filled steel tube supports are erected in time. There is a gap of 500 mm between the support and the surrounding rock. After the supports are erected, concrete will be sprayed between the surrounding rock and the supports. At the initial stage of support, the bolts and cables play a main supporting role to maintain the stability of the roadway. As the concrete gradually solidified, the supporting role of the concrete and concrete-filled steel tube supports gradually appears.



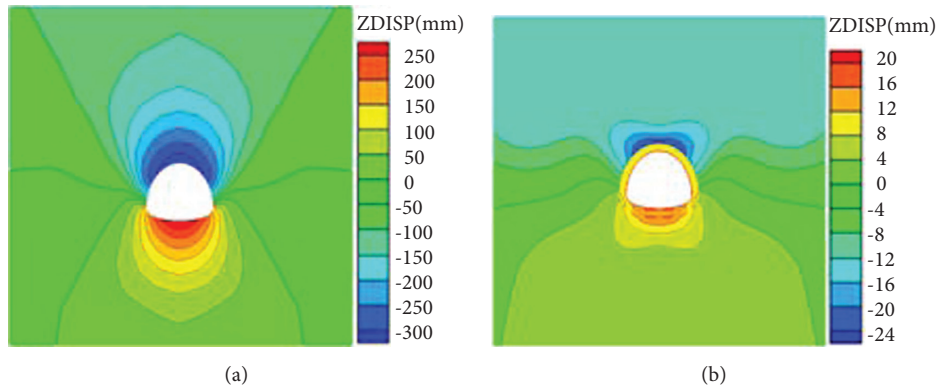


FIGURE 8: Roadway surrounding rock displacement contour.

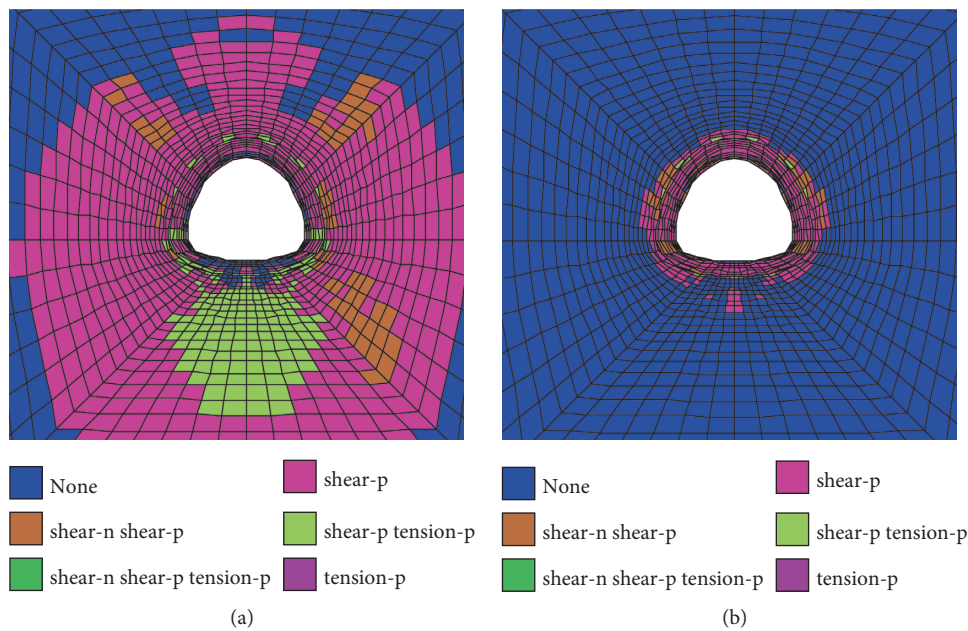


FIGURE 9: Plastic zone diagram of roadway surrounding rock.

Meanwhile, the deformation gradually decreases and eventually tends to stabilize. As shown in Figure 8(b), the maximum subsidence of the roof reaches 24 mm. The maximum deformation of the floor reaches 20 mm. At the same time, it can be obtained by the plastic zone figure, Figure 9, that the range of the plastic zone significantly reduces. And, the deformation of the surrounding rock is within a controllable extent.

## 7. Engineering Application

**7.1. Construction Procedure.** The construction procedure of support: (1) widen the roadway section to the designed section; (2) use the cables and bolts for temporary support; (3) install the concrete-filled steel tube supports without filled concrete, lay metal mesh, and noncombustible material cloth, and ensure that there is a gap of 500 mm between the support and the roadway; (4) spray cement mortar with a

spray powder to fill the gap; (5) pour C40 concrete into the concrete-filled steel tube supports.

**7.2. Field Measurements.** After the completion of supports, the displacement deformation of the floor, roof, and two sides is monitored by the cross-distribution point method. The specific monitoring methods are as follows: monitored every 2 days from the outset to 15th day after detection; monitored every 5 days from 15th day to 40th day after detection; monitored every 10 days from 40th day to 90th day after detection. The monitoring data is shown in Figure 10.

Monitoring results present that the surrounding rock deformation can be divided into three stages:

**7.2.1. Rapid Deformation Stage.** Within 15th day after the roadway repair is completed, the deformation of the

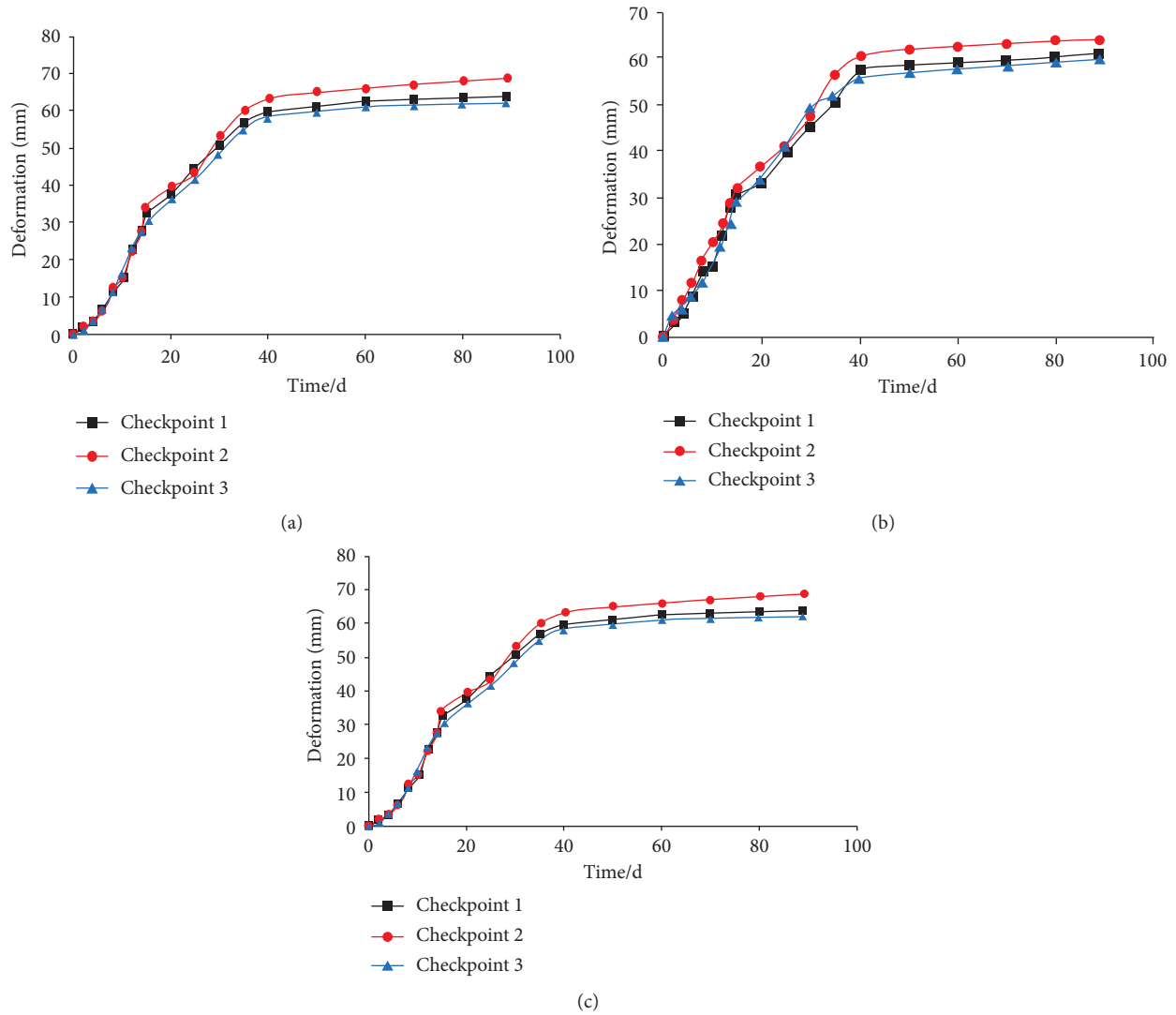


FIGURE 10: Surrounding rock deformation monitoring graph. (a) Deformation curve of the roof. (b) Deformation curve of the floor. (c) Deformation curve of the two sides.

surrounding rock expresses intense. The maximum deformation among the roof, floor, and two sides reaches, respectively, 34.23 mm, 32.12 mm, and 37.58 mm. At this stage, the concrete has not hardened. Therefore, the concrete-filled steel tube supports cannot undertake a supporting role. In other words, the bolts and cables jointly prevent the surrounding rock deformation.

**7.2.2. Slow Deformation Stage.** Within 15th day to 45th day after roadway support, the maximum deformation among the roof, floor, and two sides, respectively, reaches 63.55 mm, 60.46 mm, and 68.45 mm. During the period, the concrete gradually hardens. Hence, the supporting action of concrete-filled steel tube support begins to appear. The deformation velocity of the surrounding rock decreased.

**7.2.3. Tend to a Stabilized Stage.** After 45th day from the roadway support, the deformation speed decreased



FIGURE 11: 1412 Roadway after support.

obviously. And, the deformation gradually stabilizes. The final deformation among the roof, floor, and two sides reaches, respectively, 69.22 mm, 64.11 mm, and 72.45 mm.

At this stage, the concrete is completely hardened. Thus, the coordination with the concrete and concrete-filled steel tube support provides main bearing capacity, which limits the deformation of the surrounding rock. Meanwhile, the bolts and cables also exert their arch action and suspension action. Figure 11 is the scene figure after the roadway support is completed.

## 8. Conclusions

- (1) By means of field investigation and laboratory tests, 1412 Roadway is verified as a typical high-stress soft rock roadway. The instability and deformation basically are caused by low strength, poor self-stability, high stress and complicated stress environment of surrounding rock, lower support resistance of the supporting members and failure to strengthen support for fatal parts.
- (2) Combined with the deformation characteristics and the deformation mechanism of the roadway, this paper analyzes and puts forward the composite supporting scheme “cables and bolts + grouting + concrete-filled steel tube support.” According to the theoretical calculations and numerical simulations, it has been certified that the ultimate load of the designed composite support scheme is greater than that of the surrounding rock. It means that the scheme can provide sufficient force to maintain the stability of the roadway.
- (3) The underground detection shows that the surrounding rock deformation tends to stabilize after supporting 45th day. The maximum deformation among the roof, floor, and two sides of roadway is less than 100 mm, which is within a controllable range. On the whole, it has successfully solved that the difficulty of 1412 Roadway with large deformation and hard support.

## Data Availability

The data used to support the findings of this study are available from the corresponding author upon request.

## Conflicts of Interest

The authors declare that there are no conflicts of interest regarding the publication of this paper.

## Acknowledgments

This work was financially supported by National Natural Science Foundation of China (nos. 51904081 and 51964008), Guizhou Provincial Science and Technology Foundation (Qian Ke He Zhi Cheng [2020]4Y042), and Guizhou Provincial Science and Technology Foundation (Qian Ke He Ji Chu-ZK[2021] Yiban 264).

## References

- [1] M. He, H. Xie, S. Peng, and Y. -D. Jiang, “Study on rock mechanics in deep mining engineering,” *Chinese Journal of Rock Mechanics and Engineering*, vol. 24, no. 16, pp. 2803–2813, 2005.
- [2] R. Yang, Y. Li, D. Guo et al., “Deformation reasons and support technology of deep and high-stress soft rock roadway,” *Journal of Mining & Safety Engineering*, vol. 34, no. 6, pp. 1035–1041, 2017.
- [3] M. He, Jinghaihe, and X. Sun, *Soft Rock Engineering Mechanics*, pp. 47–62, Science Press, Beijing, China, 2002.
- [4] H. Zhang, H. Li, Z. Li et al., “Research on surrounding rock deformation mechanism and support technology of deep soft rock roadway,” *Mining and safety engineering*, vol. 32, no. 6, pp. 955–962, 2015.
- [5] Q. Meng, L. Han, J. Zhang, S. Wen, F. Zhang, and H. Li, “Research and application of deep high-stress broken soft rock roadway support technology,” *Journal of Central South University: Natural Science Edition*, vol. 47, no. 11, pp. 3861–3872, 2016.
- [6] Q. Meng, L. Han, W. Qiao et al., “Numerical simulation of bolt-grouting support mechanism in deep soft rock roadway,” *The Journal of Mining and Safety Engineering*, vol. 33, no. 1, pp. 27–34, 2016.
- [7] Y. Gao, X. Li, J. Wang et al., “Numerical simulation analysis of grouting hole reinforcement technology for concrete filled steel tubular support,” *Tunnel construction*, vol. 31, no. 4, pp. 426–430, 2011.
- [8] Y. Gao, B. Wang, J. Wang et al., “Concrete filled steel tubular support for deep soft rock roadway Performance test and application of supporting structures,” *Journal of rock mechanics and engineering*, vol. 29, no. S1, pp. 22–27, 2010.
- [9] X. Li, R. Yang, Y. Gao et al., “High strength concrete filled steel tubular support technology for large section soft rock inclined shaft,” *Journal of Coal*, vol. 38, no. 10, pp. 1742–1748, 2013.
- [10] K. Liu, Y. Gao, and F. Zhang, “Composite support technology of concrete-filled steel tube support in large section extremely soft rock roadway,” *Journal of Mining and Safety Engineering*, vol. 34, no. 2, pp. 243–250, 2017.
- [11] J. Wang, F. Chen, G. Liu et al., “Application of Concrete-filled Steel tube support in the repairing of 1000m-deep roadway,” *Tunne Construction*, vol. 33, no. 9, pp. 774–778, 2013.
- [12] Y. Gao, K. Liu, X He et al., “Steel tube concrete support applied to dynamic pressure roadway in kilometers deep mine,” *Coal Science and Technology*, vol. 43, no. 8, pp. 7–12, 2015.
- [13] S. Wang, Z. Lei, and G. Liu, “Design and application of concrete-filled steel tube support,” *Journal of North China University of Science and Technology*, vol. 9, no. 1, pp. 50–54, 2012.
- [14] X. Zhang and W. Yan, “Application of concrete-filled steel tube support in deep well support of Huafeng Coal Mine,” *Coal mine machinery*, vol. 32, no. 7, pp. 194–196, 2011.
- [15] K. Peng, Z. Dong, X. Li, and Q. Zhu, “Study on soft rock roadway support technology in coal seam scouring zone,” *Comprehensive utilization of resources in China*, vol. 29, no. 7, pp. 47–49, 2011.
- [16] M. He, H. Yuan, H. Jing et al., *The Theory and Practice of Bolt Support in Chinese Coal Mines*, pp. 114–115, Science Press, Beijing, China, 2004.
- [17] W. Gao, *Rock Mechanics*, pp. 149–160, Peking University Press, Beijing, China, 2010.

- [18] W. Yu, Q. Gao, and C. Zhu, "Study of strengthen theory and application of overlap arch bearing body for deep soft surrounding rock," *Chinese Journal of Rock Mechanics and Engineering*, vol. 29, no. 10, pp. 2134–2142, 2010.
- [19] W. Yueguang, "Calculation of elastic-plastic problems of elliptical roadways by perturbation method," *Engineering Mechanics*, no. 2, pp. 93–102, 1990.
- [20] M. Cai, M. He, and D. Liu, *Rock Mechanics and Engineering*, Science Press, Beijing, China, 2002.
- [21] M. Oda, "Permeability tensor for discontinuous rock masses," *Géotechnique*, vol. 35, no. 4, pp. 483–495, 1985.
- [22] Z. Xu, *Brief Course on Elastic Mechanics*, Higher Education Press, Beijing, China, 5th edition, 2018.

## Research Article

# Investigation on Surrounding Rock Stability Control Technology of High Stress Roadway in Steeply Dipping Coal Seam

Honglin Liu <sup>1,2</sup>, Chen Xu,<sup>3</sup> Hongzhi Wang,<sup>1,2</sup> Guodong Li,<sup>1,2</sup> and Sanyang Fan<sup>3</sup>

<sup>1</sup>College of Geology and Mines Engineering, Xinjiang University, Urumqi 830046, China

<sup>2</sup>Key Laboratory of Environmental Protection Mining for Minerals Resources at Universities of Education Department of Xinjiang Uygur Autonomous Region, Xinjiang University, Urumqi 830047, China

<sup>3</sup>Xinjiang Hongxin Coal Industry Co., Ltd, China National Coal Group Corporation, Changji 831200, China

Correspondence should be addressed to Honglin Liu; liuhonglin@xju.edu.cn

Received 8 April 2021; Revised 4 June 2021; Accepted 29 June 2021; Published 18 August 2021

Academic Editor: Zizheng Zhang

Copyright © 2021 Honglin Liu et al. This is an open access article distributed under the Creative Commons Attribution License, which permits unrestricted use, distribution, and reproduction in any medium, provided the original work is properly cited.

There are a large amount of steeply dipping coal seams deposited in China, the safe and effective extraction of which are the challenge for coal operators due to the complicated geological characteristics, in particular, when the underground roadway is excavated in the steeply dipping coal seams with limited seam distance. The Universal Distinct Element Code (UDEC) was adopted in the present research to explore the stress distribution of surrounding rock of the roadway. Based on the numerical simulation, the damage coefficient was proposed and then used to classify the roof conditions into four groups. After that, the asymmetric support technique was proposed and put into practical applications. It is indicated that the stress concentration on the floor is the main feature of the extraction of steeply dipping coal seams. Moreover, the distributions of the maximum vertical stress and horizontal stress which are much different from each other mainly attributed to the effect of the large dip angle. This research also verified the feasibility of using the asymmetric and partition support technique to maintain the integrity of the surrounding rock, as from the case study conducted at the 12032 longwall coal face of Zhongwei coal mine.

## 1. Introduction

The development of the mining industry in Xinjiang, one of the largest coal fields in China, is currently in the rapid and sustainable progress. The large thickness and shallow depth are the two attractive features of the coal seams in Xinjiang, which make it the ideal mining field to build the huge coal mines. Different from its counterparts exposed in other coal fields, however, the steeply dipping coal seam accounts for over 25%; the proven reserves in China attributed to the unique diagenetic environment [1, 2]. It has been well noted that the extraction of steeply dipping coal seams is difficult due to its unique geo-mechanical condition. The movement of the overlying strata upon the steeply dipping coal seam is much different with the increase of the dip angle. In particular, the large abutment pressure applied on the surrounding rock will significantly affect the stability of the roadway. This situation will be more serious when the

adjacent coal seams with close distance are extracted [3, 4]. How to effectively control the unexpected deformation of surrounding rock and maintain the integrity of the roadway is now the hot research topic to be considered either from the insight of the underground coal operators or the scientific scholars.

Various studies have been conducted to obtain an in-depth understanding of the underground pressure distribution characteristics during the excavation of steeply dipping coal seam. As reported by Wu et al. [5–7], the excavation of upper coal seam will significantly affect the stability of the “R-S-F” system of the lower coal seam. Their research also indicated that both the underground pressure and the migration law of the steeply dipping coal seam is much different from other coal seams with small dip angle. The development and establishment of the asymmetrical structure is closely related to the stability of the longwall, which agrees well with the research carried out by Tu et al.



[8, 9]. Based on the geological and mining condition of Huainan mining zone, Yang and Kong studied the mutual superposition and evolution mechanism of underground pressure during the excavation of the steeply dipping coal seams as well [10–12]. It can be found from their research that the failure mechanism and stress distribution of the mining floor will be affected with the increase of the dip angles. In general, most studies did pay attention to the stress distribution and deformation failure of the surrounding rock with the excavation of two-layer coal seams.

Against this background, this paper presents a comprehensive research to obtain a better understanding on the mechanical mechanism and deformation characteristics of the surrounding rock for the roadway located in the steeply dipping coal seam. It starts with a concise introduction about the research area, followed by the detailed numerical modelling of the excavation procedure of the roadway in the steeply dipping coal seams. This paper ends up with the field investigation to verify the proposed controlling technique. The meaningful research outcomes can be used as the guideline for other underground coal mines in Xinjiang coal fields where there are similar geological and mining conditions.

## 2. Geological and Mining Conditions of the Research Area

Zhongwei Coal Mine, which is operated by Henan Energy and Chemical Industry Group Co., Ltd., is located in Baicheng, Xinjiang. The single-entry longwall operation is adopted to excavate the IV13 coal seam. The coal seam featured with its large dips ranging from 25° to 50°, with the average value of 35°. Except for the large dip angle, the variable thickness of the IV13 coal seam is the other concern to be accounted for. As depicted in Figure 1, the normal thickness of the IV13 coal seam is within 0.87 to 10.92 m, with the average thickness of 3.67 m. Note that the IV13 coal seam has to be mined separately (see Figure 1(a)). For ease of reference, these split coal seams are termed as IV13<sup>a</sup> and IV13<sup>b</sup>, respectively. Currently, the upper subsection termed IV13<sup>a</sup> has been totally extracted and the preparation of 12032 longwall is still in progress.

As the first longwall located in the lower subsection (i.e., IV13<sup>b</sup>), the strike length and the trend length of the 12032 longwall are 691 m and 161.7 m, respectively. The ground elevation is +2730~+2900 m and the elevation of 12032 longwall is +2315 ± 2400 m. As depicted in Figure 1(b), the coal resource around the 12032 longwall has been completely extracted. The 2.07 m thickness IV13<sup>b</sup> coal seam is fully excavated. More detailed information about surrounding rock is shown in Table 1.

## 3. Numerical Modelling of the Excavation of Steeply Dipping Coal Seams

**3.1. Setup of the Numerical Model.** The redistribution of the underground pressure will result in the development of fissures of surrounding rock, generally associated with the large deformation of the excavated zone [13, 14].

Considering that the distribution and transmission law of surrounding rock is the foundation to further investigate the damage process of the surrounding rock, the two-dimensional numerical program, Universal Distinct Element Code (UDEC), was applied to simulate the extraction progress of coal resource in the 12032 longwall.

As shown in Figure 2, the length and height of the UDEC Trigon model are 250 m and 150 m, respectively. Herein, both the coal seam and surrounding rocks are all simply defined with the dip angle of 35°, equivalent to the average dip angle of the coal seam. The boundaries of the numerical model were fixed according to the practical conditions. Note that the vertical stress applied on the upper boundary is 7.2 MPa based on the average mining depth of 300 m. The Mohr–Coulomb yield criterion was given to the interface, while the elastic model was applied for block element [15, 16]. Four monitoring lines were distributed along the floor of IV13<sup>a</sup> coal seam to record the value of stress. The uniform space between each monitoring line is 1 m.

Different from the conventional finite element modelling method (FEM), the critical parameters for the UDEC Trigon model cannot be directly obtained from the calibration of experimental tests. Thus, the micromechanical parameters of layered polygonal block and contact interface were obtained from existing open literature [17–21]. The values of these critical input parameters including the internal friction angle ( $\phi$ ), the cohesive force ( $C$ ), and the tensile strength ( $T$ ) of the contact surface are summarized in Table 1. In addition, the micromechanical parameters of polygonal block are also shown in Table 1.

**3.2. Stress Distribution of Floor.** In accordance with the practical mining process, the upper coal seam (i.e., IV13<sup>a</sup>) was firstly excavated with a 15 m-width coal pillar left. Figure 3 presents the stress Mises distribution around the gob and the floor of the coal pillar. Herein, the stresses including the vertical stress, horizontal stress, and shear stress were plotted in Figure 4, the values of which were obtained from the embedded monitoring lines mentioned earlier.

As can be seen from Figures 3 and 4, there is an obvious stress concentration under the coal pillar after the excavation of the IV13<sup>a</sup> coal seam, whereas, the monitored stresses around the gob floor exhibit somewhat reduction. For ease of reference, the ratio between the monitored stress and the in situ stress is defined as stress concentration factor (SCF). Note that the initial horizontal stress and vertical stress are 10.8 MPa and 9.0 MPa, respectively. The maximum vertical stress was obtained from the center line of the coal pillar (larger buried depth side) with the value of 25.2 MPa (SCF = 2.8). It can also be found that the peak value of the horizontal stress is 22.7 MPa (SCF = 2.1), which is obtained from the upper side of the center line. If the vertical distance between the floor and the coal pillar is within 4.0 m, both the vertical stress and the horizontal stress concentration coefficients will experience the gradually increase with the enlargement of the vertical distance.

With the increased horizontal distance apart from the center line in the coal pillar, both the vertical stress and the

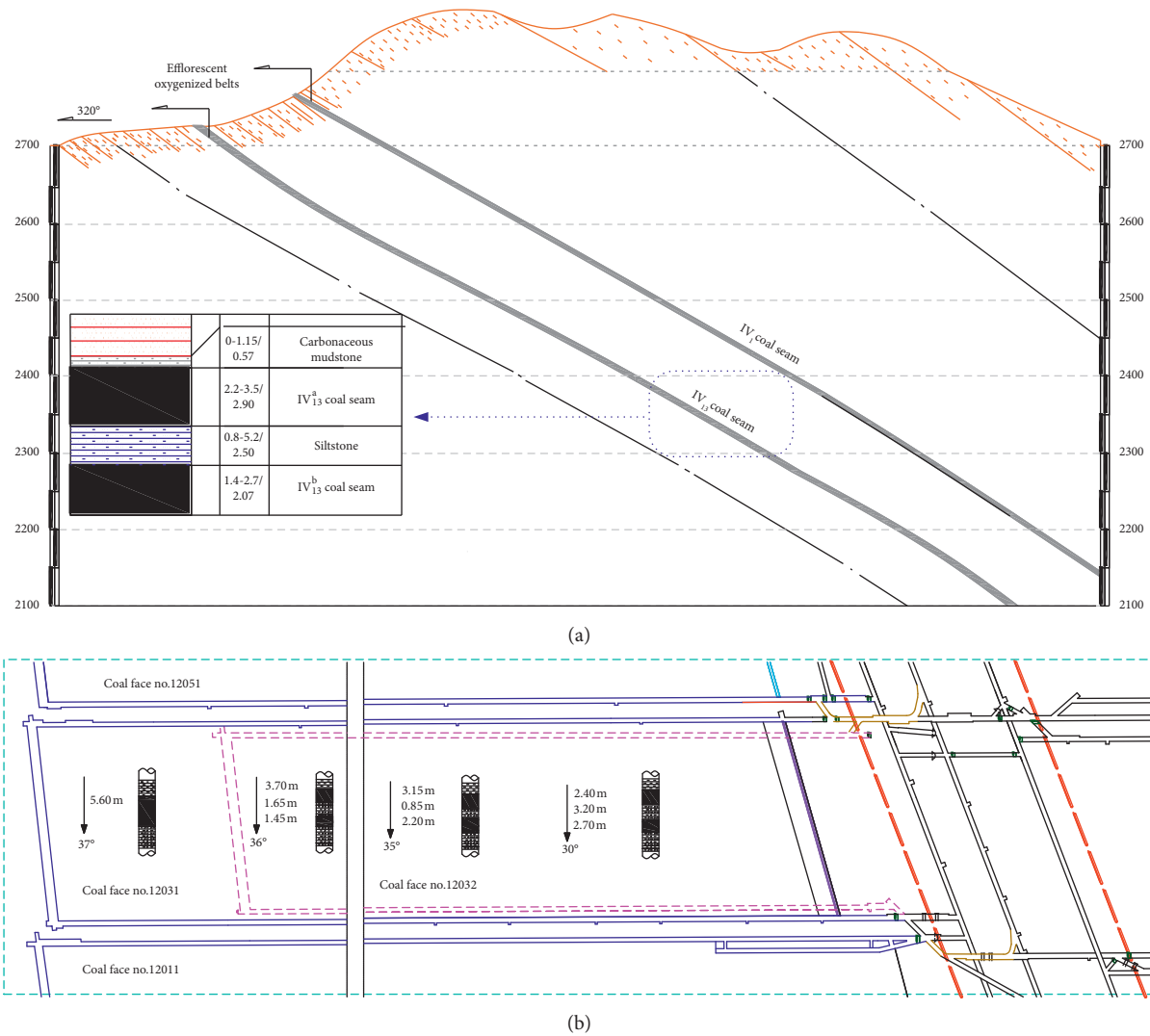


FIGURE 1: Geological survey of research object: (a) geological section of coal seam no. IV13 and (b) roadway layout of 12032 coal face.

TABLE 1: Micromechanical parameters of each layered rock of the model.

Lithology	Block parameters				Contact surface parameters		
	Density (kg·m <sup>-3</sup> )	Elastic modulus (GPa)	Bulk modulus (GPa)	Shear modulus (GPa)	Friction angle (°)	Cohesion (MPa)	Tensile strength (MPa)
Carbonaceous mudstone	2 500	5.30	24.40	9.70	18	1.5	0.5
Coal seam	1 300	2.60	11.50	4.60	14	0.8	0.32
Mudstone	2 500	3.80	24.40	9.70	18	1.3	0.4
Sandstone	2 500	10.04	28.70	9.50	21	0	0

horizontal stress experience the obvious decline, which are approximately in accordance, with a normal distribution, with each other. However, the attenuation speed for vertical stress and horizontal stress is much different. In detail, the attenuation trend of the vertical stress nearby the upper side of the central line is more obvious compared to its counterpart. Differently, the attenuation of the horizontal stress nearby the upper side of the central line seems to be significant.

It is interesting that the peak shear stresses recorded from each side are much different from each other. The peak shear stress upon the center line with the smaller mining depth is generally larger than that obtained from the other side. In particular, the value of SCF will also experience the reduction with the increase of the depth, when the distance between the floor and the coal pillar is within 4 m.

Based on the above discussions, it can be summarized that there exists the stress concentration on the floor of the

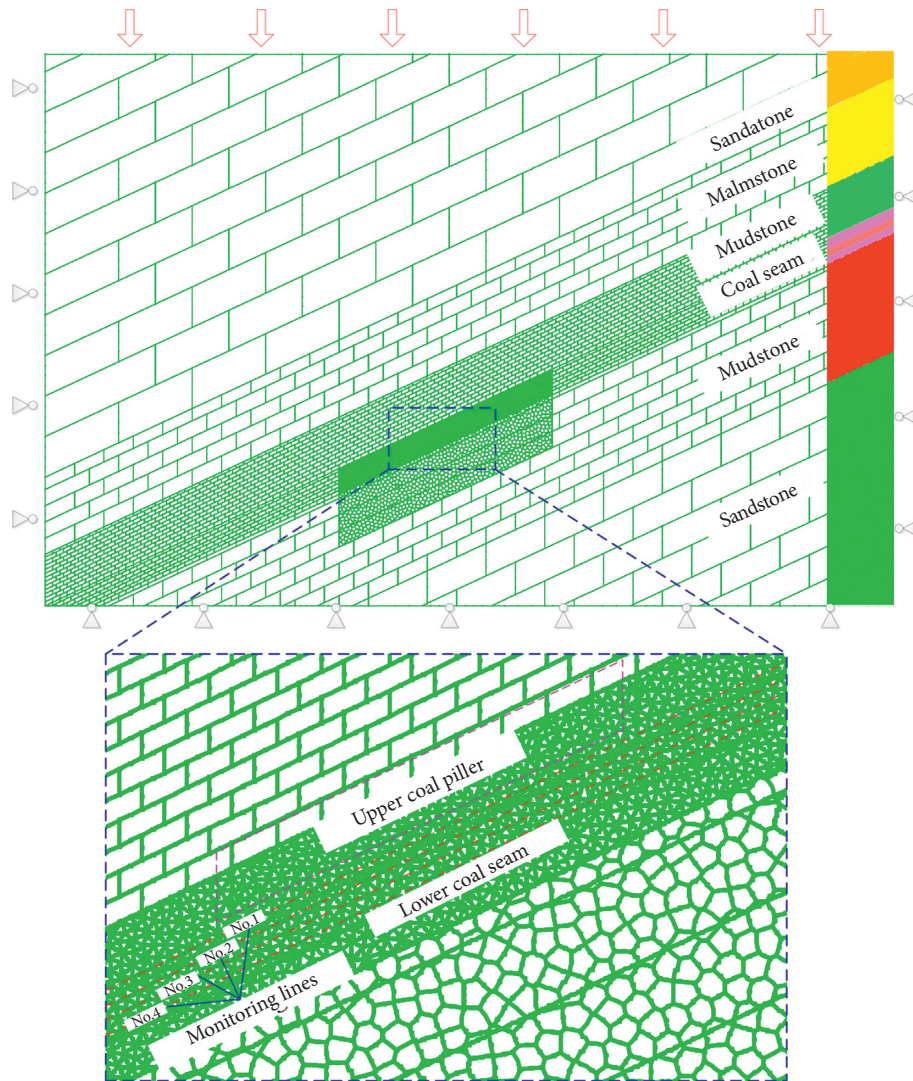


FIGURE 2: Numerical calculation model.

residual coal pillar. The maximum vertical stress is generally below the centerline of the coal pillar, while the maximum horizontal stress is above the centerline of the coal pillar. In general, the peak shear stress above the centerline of the coal pillar is generally larger than that obtained from the other side.

#### 4. Damage Regulation of the Floor

**4.1. Definition of the Damage Coefficient.** A large number of laboratory tests have revealed that the microstructure will affect the mechanical properties of intact rock and coal mass [22–24]. Although the coal/rock mass are heterogeneity in natural from the microscopic insight, it can still be evaluated and presented by the Weibull statistical distribution. Herein, the damage coefficient is defined with the following considerations: (1) it should sufficiently reflect the characteristics of rock mass damage and (2) it is feasible to obtain the value by the actual measurement technique.

In this research, the damage coefficient was adopted in the respect of the numerical simulation. That is, the ratio

between the contact length (e.g., shear or stretch) of the failed block and the total length of all blocks is used to evaluate the development density and penetration of fractures in coal/rock masses.

**4.2. Damage Characteristics of the Floor.** Figure 5 presents the damage characteristics of floor rock after the excavation of the upper IV13<sup>a</sup> coal seam, in which the types of the failure are marked in different colors. It is apparent that the floor rock is featured with the shear failure. Moreover, many shear cracks and tensile cracks were observed from the affected zone within 6 m apart from the central line of the coal pillar. With the increase of the distance, apart from the coal pillar, the number of cracks nearby the edge of coal pillar exhibit a significantly decrease. In addition, the floor is generally dominated by the tension cracks. The tensile cracks are widely distributed around the edge of the coal pillar within the 20 m zone. Both the number of cracks and the crack penetration experience the reduction when the distance apart from the center line is over 20 m.



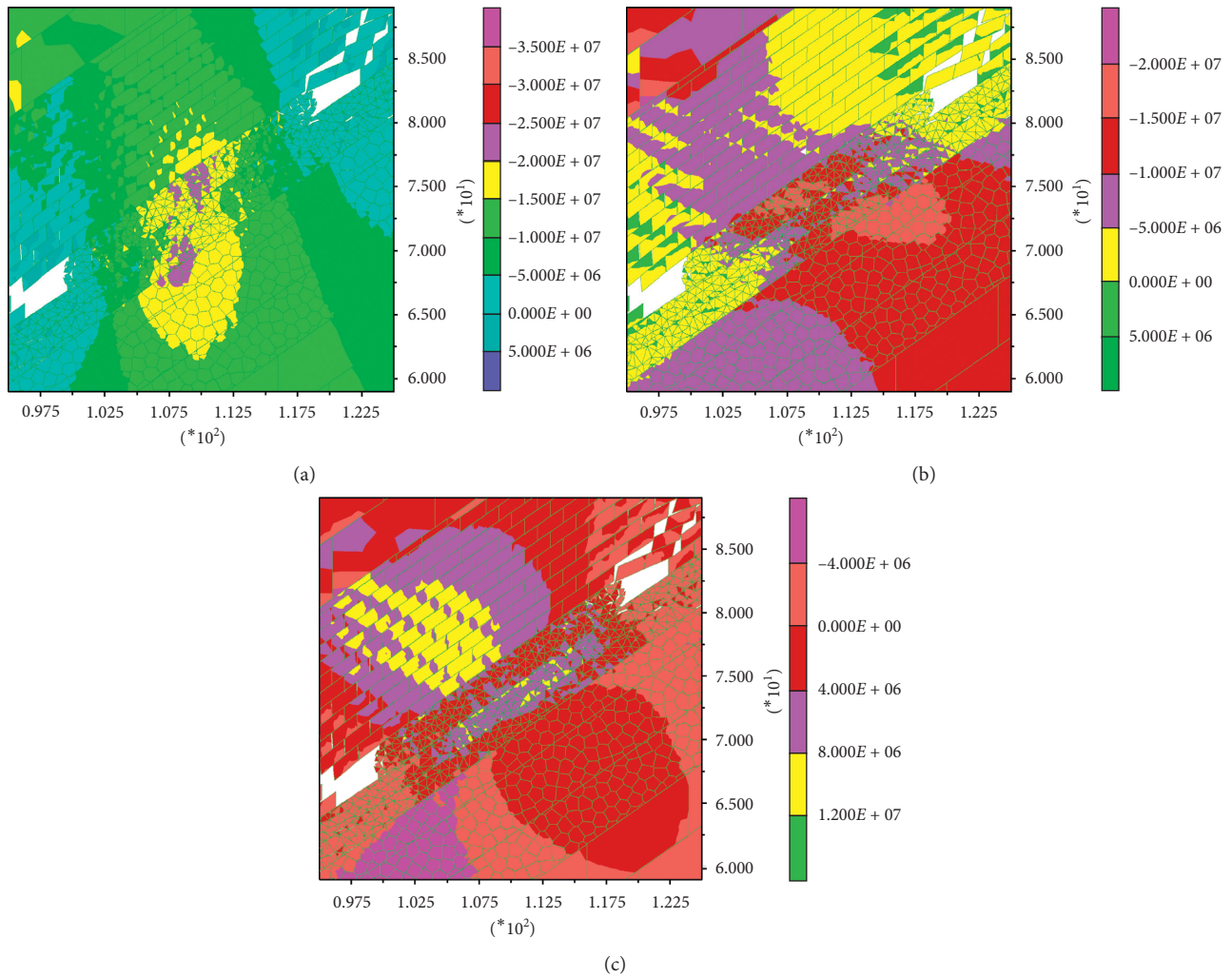


FIGURE 3: Stress distribution characteristics in the floor of goaf and coal pillar: (a) vertical stress, (b) horizontal stress, and (c) shear stress.

With the consideration of the rock damage at different locations (e.g., coal pillar, floor, and lower coal seam), the additional monitoring line was arranged along the perpendicular side to the surrounding rock. The distribution of the damage coefficient can be found from Figure 6, in which the values of the damage coefficient were theoretically calculated according to its definition. It can be seen from Figure 6 that the damage coefficient of the floor under the coal pillar ranges from 12% to 50%. In addition, the damage coefficient of the surrounding rock above the center line is generally larger than its counterpart. Because the compressive strength of coal seam is much smaller than that of surrounding rock, the damage of the lower coal seam seems to be serious than that of the floor, which is about 19~64%, as shown in Figure 6.

### 5. Classification of the Roof Conditions Based on the Damage Coefficient

The predicted distances between the IV13<sup>a</sup> and IV13<sup>b</sup> coal seams in the 12302 longwall are listed in Tables 2 and 3, the values of which are obtained from the actual exposure of the

strata as well as the exploration data. Compared with the predicted values (e.g., 0.85–3.90 m), the damaged depth of surrounding rock (e.g., 1.50–3.50 m) are generally larger, indicating that most surrounding rocks are damaged due to the mining activities. Thus, the roof of the roadway can be correspondingly classified into four groups, as listed in Table 4.

Type I (broken and loose roof): the coal pillar is failed with the shear slip at its bottom edge, mainly attributed to the combined effects of the abutment pressure and the front strata pressure. The roof will be completely crushed if the distance between two coal seams is within 1.5 m. The main feature of this type roof is its loose structural after the drilling of the roadway in the lower coal seam.

Type II (crack-extended roof): under the combined influence of front strata pressure and the abutment pressure, there will be lots of cracks and fissures. However, the integrity of the roof can be sustained when the distance between the coal seams ranges from 1.5 m to 2.5 m.

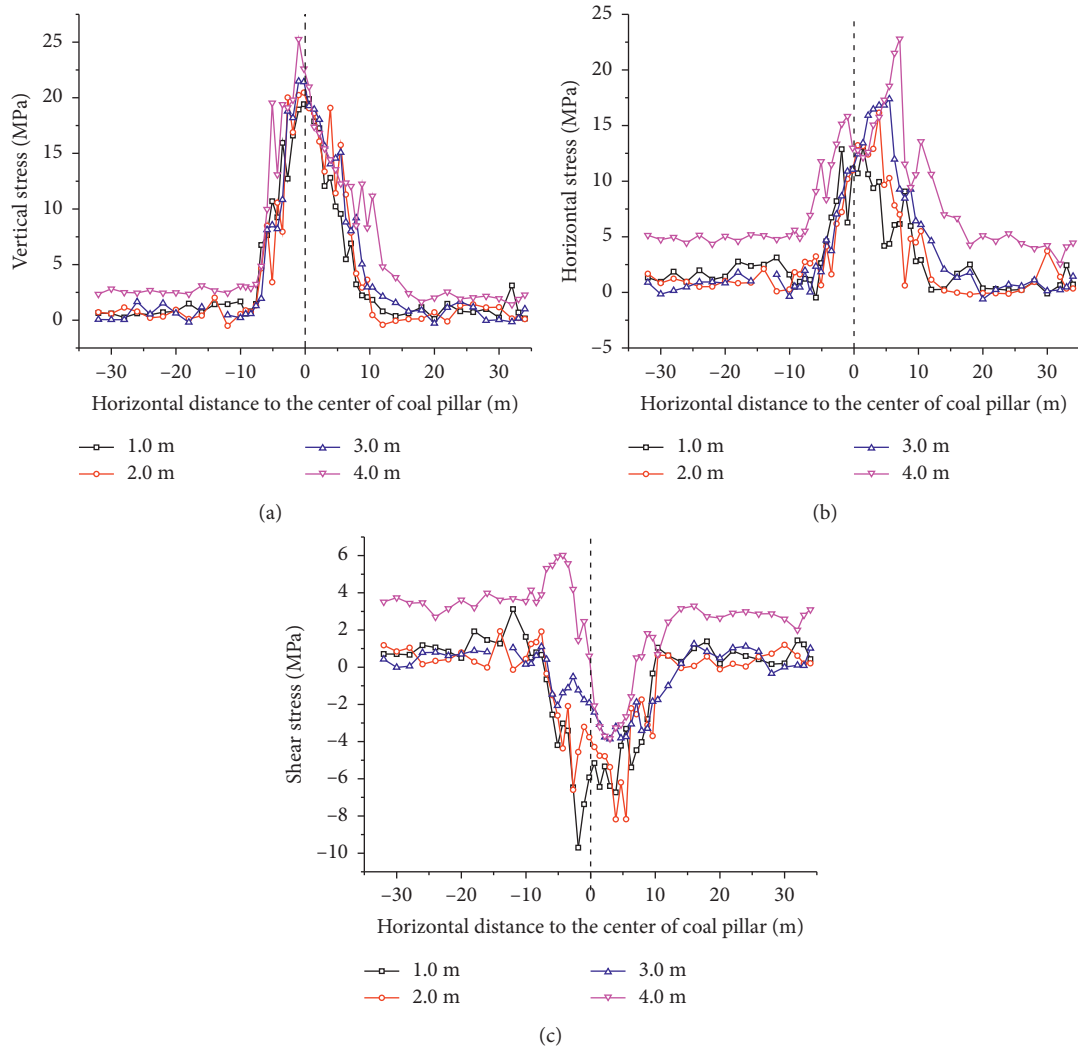


FIGURE 4: Stress distribution in different depths of floor: (a) vertical stress distribution of floor and (b) horizontal stress distribution of floor.

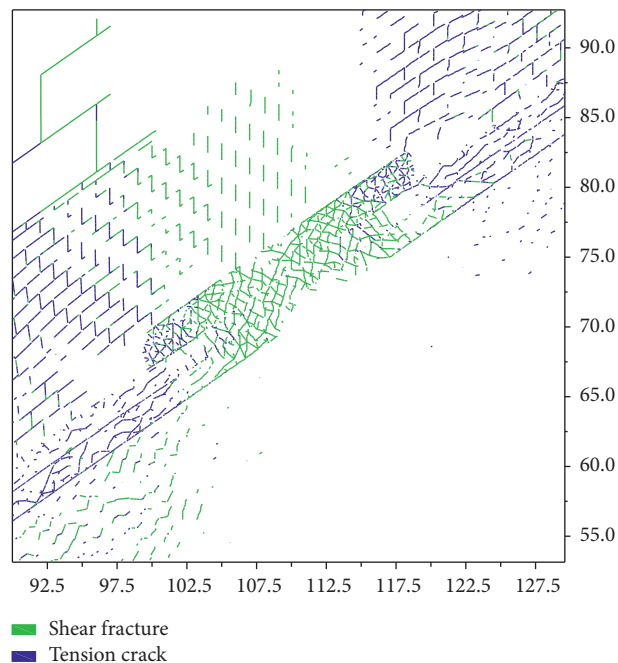


FIGURE 5: Damage characteristics of floor rock.



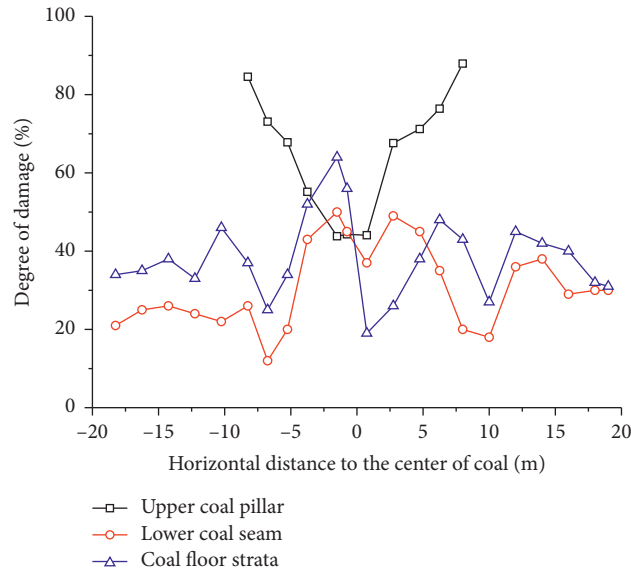


FIGURE 6: Damage distribution law of floor strata.

TABLE 2: The distance between roof and upper coal seam of 12032 haulage roadway.

Distance to open-off cut $L$ (m)	0–55	55–200	200–235	235–310	310–465	465–620	620–710
Roadway length $l$ (m)	55.0	145.0	35.0	75.0	155.0	55.0	90.0
Roof thickness $H$ (m)	1.50–1.75	0.85–1.50	1.50–2.00	2.00–2.50	2.50–3.00	3.00–3.50	3.50–3.90
Roof classification type	II	I	II	II	III	III	IV

TABLE 3: Speculates the distance between the roof of the 12032 tailgates and the upper coal seam.

Distance to open-off cut $L$ (m)	0–40	40–155	155–230	230–325	325–390	390–660	660–690
Roadway length $l$ (m)	40.0	115.0	75.0	95.0	65.0	270.0	30.0
Roof thickness $H$ (m)	2.20–2.50	2.50–2.80	2.00–2.50	2.50–3.20	2.20–2.50	2.50–3.50	3.50–3.70
Roof classification type	II	II	II	III	II	III	IV

TABLE 4: Classification of coal roof types.

Classification type	Characteristics of roof types	Thickness between coal seams (m)
I	Broken loose roof	$H \leq 1.5$
II	Crack through roof	$1.5 < H \leq 2.5$
III	Fractured roof	$2.5 < H \leq 3.5$
IV	Partially complete roof	$H > 3.5$

Type III (fissures developed roof): there are number of fissures and cracks existing in the surrounding rock which attributed to the mining activities. However, these fissures and cracks are not perforated. In this case, the interface between the coal seam and surrounding rocks is not strong enough, resulting in the reduction of the strength of the surrounding strata. If the distance between each coal seam falls into 2.5 m to 3.5 m, the excavation of the lower coal seam may result in the repeated unloading and destruction of the interlayer rock mass.

Type IV (relative intact roof): if the distance between the coal seams is larger than 3.5 m, the influence of the excavation of the lower coal seam will not significantly affect the intact of the upper coal seam. In this case, there is no dangerous for the roof controlling.

## 6. Filed Study

6.1. *Asymmetric and Partition Support Technique.* With the consideration of the variable thickness of overlying strata, the asymmetric and partition support technique was

TABLE 5: The main support forms of mining roadway.

Classification type	Characteristics of roof types	Roof support form	Support form of roadway side
I	Broken loose roof	Hydraulic expansion bolt + shed support	Shed support + anchor cable support
II	Crack through roof	Short bolt + Anchor cable	Short bolt + short anchor cable
III	Fractured roof	Bolt + Anchor cable	Bolt + short anchor cable
IV	Partially complete roof		

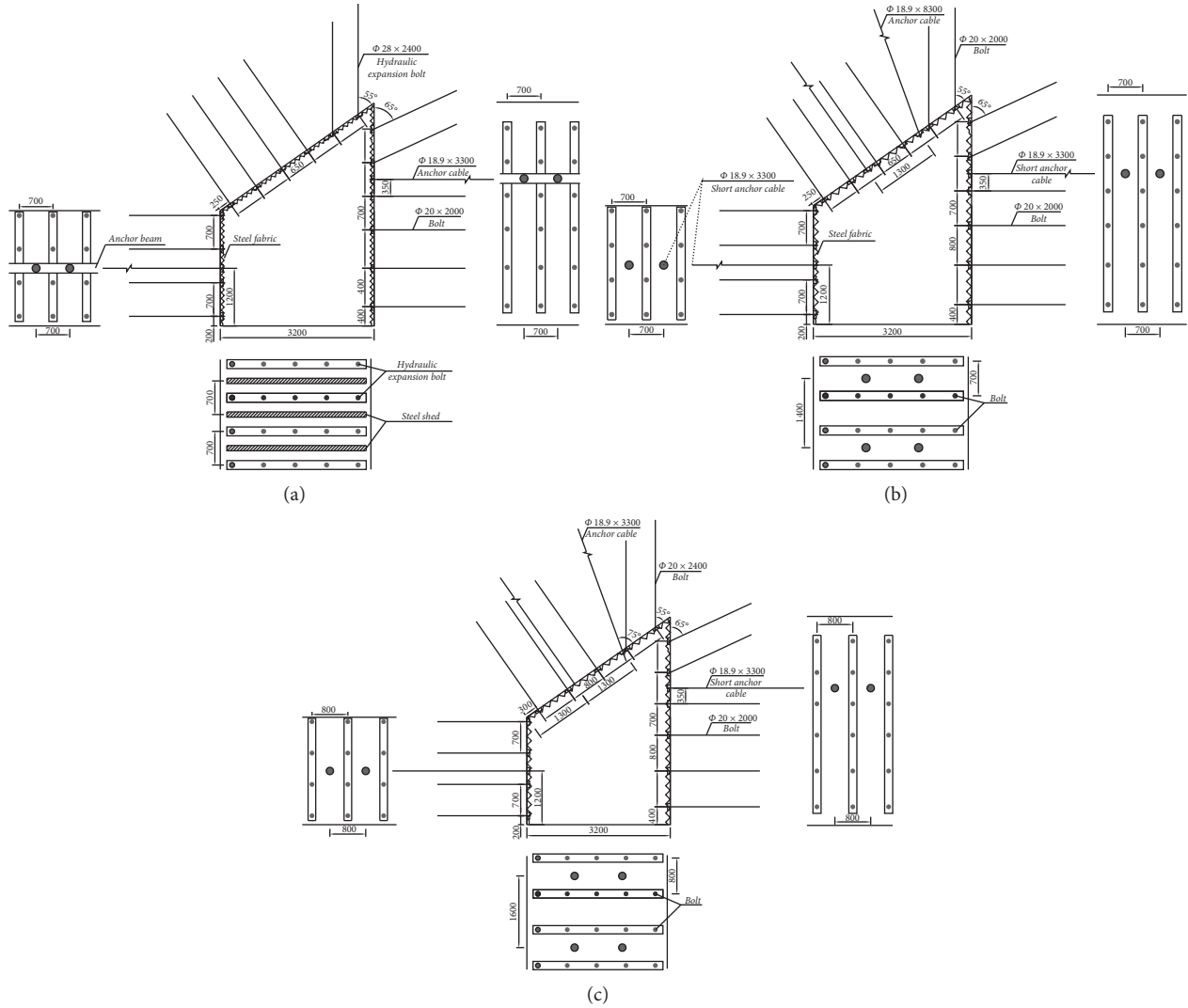


FIGURE 7: Support section of the roadway: (a) class-I roof roadway, (b) class-II roof roadway, and (c) class-III/IV roof roadway.

currently proposed based on the classification of the roof conditions and the values of the damage coefficient discussed above. The support forms and critical parameters of the 12032 Longwall mining roadway are shown in Table 5 and Figure 7, in which different support patterns are presented in detail.

6.2. Verification of the Proposed Support Technique. To verify the feasibility of proposed support technique in controlling the integrity of the roadway surrounding rock, the case study was conducted at the 12032 longwall. The width and the

center height of the trapezoidal roadway is 3.6 m and 2.8 m, with 10.08 m<sup>2</sup> cross-sectional area. Based on the classification of the roof conditions, the partition support technique was applied. More detailed information about the support parameters are presented below:

- (1) Type-I roof condition: the hydraulic expansion bolts and I-sectional steel frame are applied. In addition, the high-strength rebar bolts together with the  $\phi 18.9 \text{ mm} \times 3300 \text{ mm}$  cables combined with the beam are adopted to control the deformation of the roadway ribs. The row space for bolts and steel frame

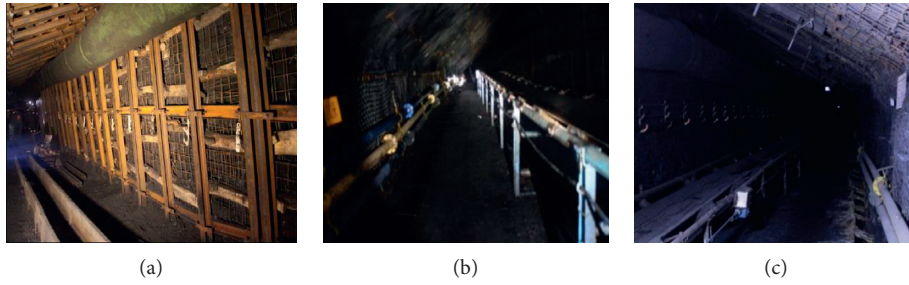


FIGURE 8: The effect of roadway support in 12032 longwall: (a) class-I roof roadway, (b) class-II roof roadway, and (c) class-III/IV roof roadway.

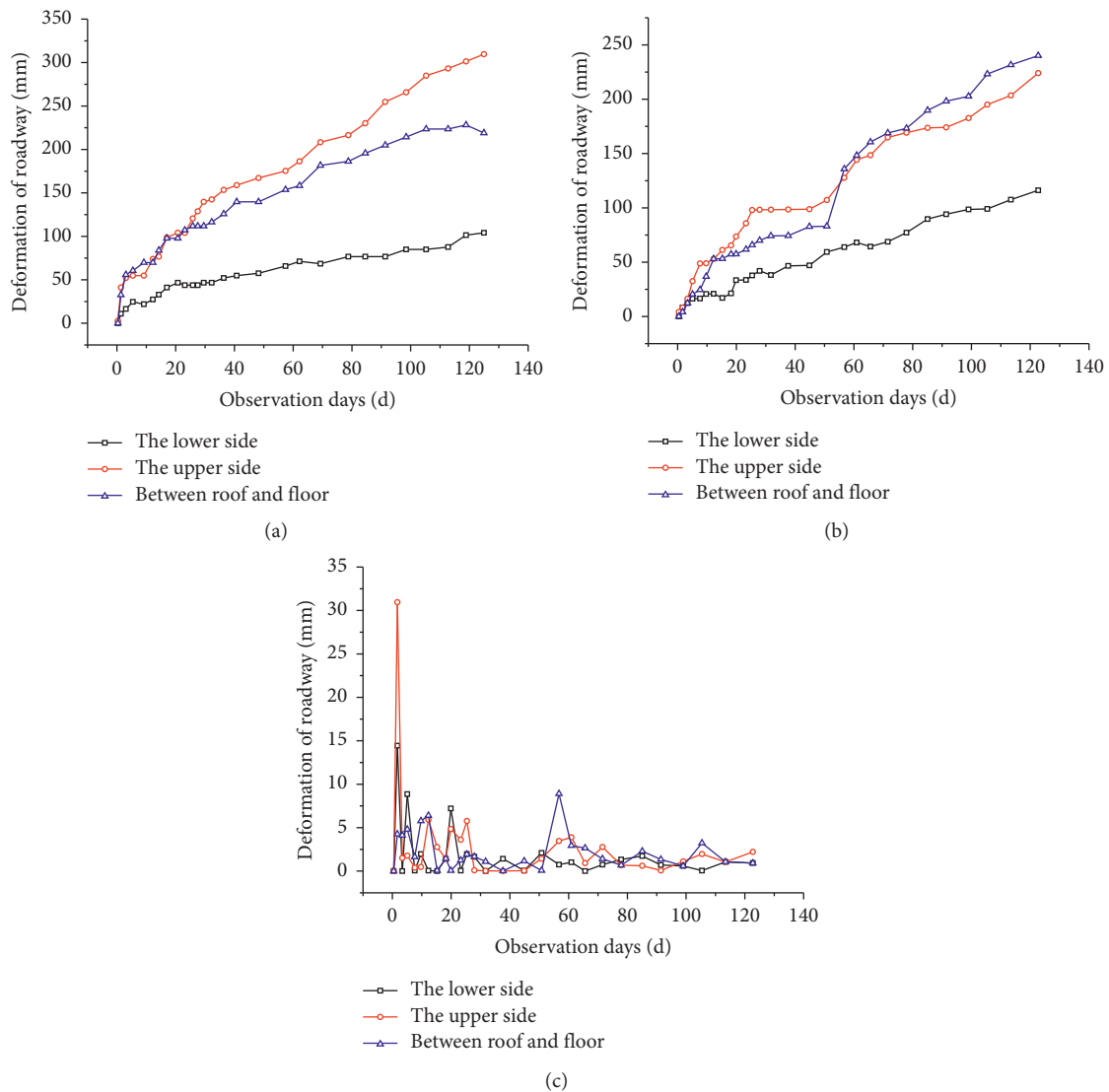


FIGURE 9: Monitoring results of roadway deformation in 12032 longwall: (a) class-I roof roadway, (b) class-II roof roadway, and (c) class-III/IV roof roadway.

is with the constant value of 700 mm. Note that the line space between the bolts in the roof and the ribs are 650 mm and 700 mm, respectively.

(2) Type-II roof condition: the roof is supported by high-strength rebar bolts and the  $\phi 18.9 \text{ mm} \times 8300 \text{ mm}$  cables with the additional

pressure release apparatus, and the row space and line space of roof support are 700 mm and 650 mm, respectively. The high-strength bolts and the  $\phi 18.9 \text{ mm} \times 3300 \text{ mm}$  cables are also used to maintain the stability of the roadway ribs. The same value of the line space and row space (i.e., 700 mm) for rib supports are adopted.

- (3) Type III/IV roof conditions: the high-strength rebar bolts and cables were used as the primary support. Different from the above support design, the larger value (800 mm) of the row space was adopted for roof support. In addition, the value of the line space for rib support also increased to 800 mm and 700 mm, respectively.

As depicted in Figures 8 and 9, the deformation of surrounding rock with type-I roof condition is 219 mm in axial direction and 412 mm along the horizontal direction, respectively. The values of this mentioned deformation are 224 mm and 356 mm for the roadway with the type-II roof. The deformation of the roof, floor, and ribs is with the smaller values when the support technique was adopted for the roadway with type-II roof condition. It indicated that the proposed partition support technique is effective and feasible in sustaining the integrity of surrounding rock.

## 7. Conclusion

This paper presents a comprehensive research on the stability controlling of the roadway driven in the steeply dipping coal seam with close distance. The detailed numerical simulation was carried out via the Universal Distinct Element Code (UDEC) based on the concise analysis of the geological and mining conditions of the research area, followed by the classification of the roof conditions with the consideration of the damage coefficient. The case study was then conducted and the feasibility of the proposed asymmetric and partition support technique was verified. The following conclusions can be obtained from this research:

- (1) There is a stress concentration on the floor of the residual coal pillar. The maximum vertical stress is generally below the centerline of the coal pillar, while the maximum horizontal stress is above the centerline of the coal pillar. Moreover, the peak shear stress above the centerline of the coal pillar is generally larger than that obtained from the other side.
- (2) The roadway roof are classified into four groups based on the actual exposure of the strata, which are broken and loose roof, crack-extended roof, fissures developed roof, and relative intact roof, respectively.
- (3) It is feasible to use the asymmetric and partition support technique to maintain the stability of the surrounding rock, as verified by the case study conducted at the 12032 longwall.

Note that the surrounding rock of the roadway is a heterogeneous material in nature, which is not well accounted for in the present research. To obtain the in-depth understanding about the deformation characteristic of

surrounding rock of steeply dipping coal seam, the further research with the consideration of initial cracks in surrounding rock should be well considered.

## Data Availability

The research data used to support the findings of this study are currently under embargo while the research findings are commercialized. Requests for data, 12 months after publication of this article, will be considered by the corresponding author.

## Conflicts of Interest

The authors declare that they have no conflicts of interest.

## Authors' Contributions

H. L. and C. X. conceptualized the study; H. L. and H. W. carried out formal analysis; H. L. and G. L. investigated the study; H. L., C. X., and S. F. wrote and prepared the original draft; H. L. and H. W. reviewed edited the manuscript; H. L. and G. L. supervised the study.

## Acknowledgments

The authors would like to thank the technical support from ZhongWei coal mine in sampling and on-site investigation. The research was financially supported by the Natural Science Foundation of Xinjiang Uyghur Autonomous Region (2019D01C023), Natural Science Foundation of China (51964043 and U1903216), and PhD Research Startup Fund of Xinjiang University (no. BS620321027).

## References

- [1] D. S. Zhang, H. L. Liu, G. Fan, and X. Wang, "Connotation and prospection on scientific mining of large Xinjiang coal base," *Journal of Mining & Safety Engineering*, vol. 32, no. 1, pp. 1–6, 2015.
- [2] J. Ning, J. Wang, T. Bu, S. Hu, and X. Liu, "An innovative support structure for gob-side entry retention in steep coal seam mining," *Minerals*, vol. 7, no. 5, p. 75, 2017.
- [3] S. Liu, K. Yang, C. Tang, and X. Chi, "Rupture and migration law of disturbed overburden during slicing mining of steeply dipping thick coal seam," *Advances in Civil Engineering*, vol. 2020, Article ID 8863547, 11 pages, 2020.
- [4] H. L. Liu, W. X. Cao, C. F. Shan et al., "Similar simulation experimental study on fracture characteristics of overburden strata under mining with large dip angle," *Journal of Xinjiang University (Natural Science Edition in Chinese and English)*, vol. 37, no. 3, pp. 301–308, 2020.
- [5] Y. P. Wu, "Study on dynamics controlling basis of system "R - S - F"" in *Steeply Dipping Seam Mining* Xi'an University of Science and Technology, Xi'an, China, 2003.
- [6] W. Lv, Y. Wu, L. Ming, and J. Yin, "Migration law of the roof of a composited backfilling longwall face in a steeply dipping coal seam," *Minerals*, vol. 9, no. 3, p. 188, 2019.
- [7] H. W. Wang, *Research on Evolution of Stress and Structural Stability of Surrounding Rock in the Longwall Mining of Steeply Dipping Seam*, Xi'an University of Science and Technology, Xi'an, China, 2014.

- [8] H. S. Tu, S. H. Tu, C. Zhang, L. Zhang, and X. G. Zhang, "Characteristics of the roof behaviors and mine pressure manifestations during the mining of steep coal seam," *Archives of Mining Sciences*, vol. 62, no. 4, pp. 871–891, 2017.
- [9] H.-s. Tu, S.-h. Tu, D.-f. Zhu, D.-y. Hao, and K.-j. Miao, "Force-Fracture characteristics of the roof above goaf in a steep coal seam: a case study of xintie coal mine," *Geofluids*, vol. 2019, Article ID 7639159, 11 pages, 2019.
- [10] J. P. Xiao, K. Yang, S. Liu, and B. Zhou, "Study on breaking mechanism of overlying strata in deeply inclined coal seam," *Journal of Safety Science and Technology*, vol. 15, no. 3, pp. 75–80, 2019.
- [11] X. Y. Kong, K. Yang, and W. Lu, "Floor failure mechanism and engineering application of downward mining of the large dip angle coal seam group," *Chinese Journal of Underground Space and Engineering*, vol. 36, no. S2, pp. 394–400, 2015.
- [12] K. Yang, X. Y. Kong, W. Lu, and S. Liu, "Study of strata pressure behaviors with longwall mining in large inclination and thick coal seam under closed distance mined gob," *Chinese Journal of Rock Mechanics and Engineering*, vol. 9, no. S2, pp. 4278–4285, 2015.
- [13] Z. Zhang, M. Deng, X. Wang, W. Yu, F. Zhang, and V. D. Dao, "Field and numerical investigations on the lower coal seam entry failure analysis under the remnant pillar," *Engineering Failure Analysis*, vol. 115, Article ID 104638, 2020.
- [14] Z. Zhang, M. Deng, J. Bai, S. Yan, and X. Yu, "Stability control of gob-side entry retained under the gob with close distance coal seams," *International Journal of Mining Science and Technology*, vol. 31, no. 2, pp. 321–332, 2021.
- [15] F. Q. Gao, D. Stead, and H. Kang, "Numerical simulation of squeezing failure in a coal mine roadway due to mining-induced stresses," *Rock Mechanics and Rock Engineering*, vol. 48, no. 4SI, pp. 1635–1645, 2015.
- [16] F. Q. Gao, *Simulation of Failure Mechanisms Around Underground Coal Mine Openings Using Discrete Element Modelling*, Simon Fraser University, Burnaby, Canada, 2013.
- [17] M. Ju, X. Li, Q. Yao, S. Liu, S. Liang, and X. Wang, "Effect of sand grain size on simulated mining-induced overburden failure in physical model tests," *Engineering Geology*, vol. 226, pp. 93–106, 2017.
- [18] F. Q. Gao and D. Stead, "The application of a modified Voronoi logic to brittle fracture modelling at the laboratory and field scale," *International Journal of Rock Mechanics and Mining Sciences*, vol. 68, pp. 1–14, 2014.
- [19] T. Kazerani and J. Zhao, "Micromechanical parameters in bonded particle method for modelling of brittle material failure," *International Journal for Numerical and Analytical Methods in Geomechanics*, vol. 34, no. 18, pp. 1877–1895, 2010.
- [20] W.-d. Wu, J.-b. Bai, X.-y. Wang, S. Yan, and S.-x. Wu, "Numerical study of failure mechanisms and control techniques for a gob-side yield pillar in the s coal mine, China," *Rock Mechanics and Rock Engineering*, vol. 52, no. 4, pp. 1231–1245, 2019.
- [21] Z. Zhang, M. Deng, J. Bai, X. Yu, Q. Wu, and L. Jiang, "Strain energy evolution and conversion under triaxial unloading confining pressure tests due to gob-side entry retained," *International Journal of Rock Mechanics and Mining Sciences*, vol. 126, Article ID 104184, 2020.
- [22] L. Zhang and H. H. Einstein, "Using RQD to estimate the deformation modulus of rock masses," *International Journal of Rock Mechanics and Mining Sciences*, vol. 41, no. 2, pp. 337–341, 2004.
- [23] C. Zhang, S. H. Tu, and L. Zhang, "Study of stress sensitivity of coal samples with different mining damage in overlying strata," *Journal of China University of Mining & Technology*, vol. 47, no. 3, pp. 502–511, 2018.
- [24] Y. J. Yang, D. C. Wang, M. F. Guo et al., "Study of rock damage characteristics based on acoustic emission tests under triaxial compression," *Chinese Journal of Rock Mechanics and Engineering*, vol. 33, no. 1, pp. 98–104, 2014.



## Research Article

# Height of the Fractured Zone in Coal Mining under Extra-Thick Coal Seam Geological Conditions

Dequan Sun,<sup>1,2</sup> Xiaoyan Li,<sup>1,2</sup> Zhijie Zhu ,<sup>1,3</sup> Yang Li,<sup>1,2</sup> and Fang Cui<sup>1,2</sup>

<sup>1</sup>Engineering Laboratory of Deep Mine Rockburst Disaster Assessment, Jinan 250104, China

<sup>2</sup>Shandong Provincial Research Institute of Coal Geology Planning and Exploration, Jinan 250104, China

<sup>3</sup>Mining Engineering School, Liaoning Technical University, Fuxin 12300, China

Correspondence should be addressed to Zhijie Zhu; zhuzhijie@lntu.edu.cn

Received 30 March 2021; Accepted 29 July 2021; Published 11 August 2021

Academic Editor: Hui Yao

Copyright © 2021 Dequan Sun et al. This is an open access article distributed under the Creative Commons Attribution License, which permits unrestricted use, distribution, and reproduction in any medium, provided the original work is properly cited.

The height of the fractured zone caused by coal mining is extremely significant for safely mining under water, water conservation, and gas treatment. At present, the common prediction methods of overburden fractured zone height are only applicable to thin and medium-thick coal seams, not suitable for thick and extra-thick coal seams. In order to determine the overburden fractured zone distribution characteristics of extra-thick seam mining, failure process analysis method of overlying strata was proposed based on key strata theory. This method was applied to 15 m coal seam of Tongxin coal mine, and fractured zone height was determined to be 174 m for 8100 panel. EH4 electromagnetic image system and borehole televiewer survey were also conducted to verify the theory results. The distribution of the electrical conductivity showed that the failure height was 150–170 m. Observation through the borehole televiewer showed that the fractured zone height was 171 m. The results of the two field test methods showed that the fractured zone height was 150–171 m, and it was consistent with the theory calculation results. Therefore, this failure process analysis method of overlying strata can be safely used for other coal mines.

## 1. Introduction

The deformation and failure are changed by the mining process. After coal is mined out, overlying strata will deform and break, and the overlying strata can be classified to caved zones, fractured zones, and continuous bending zones. The fractures formed in the overburden are the channels for mine water inrush. Thus, the development process of fractures in the overburden is the basis for determining the occurrence, and predicting and formulating control measures for mine water inrush [1]. At the same time, in order to properly lay out the mine and to efficiently drain the methane gas, it is also extremely important to accurately determine the fracture characteristics of the overburden [2, 3]. At present, the commonly used guide height prediction methods in my country are the empirical formulas given in the «Code for Building, Water, Railway, and Main Roadway Coal Pillar Setting and Compression Coal Mining», but these formulas are only applicable to thin coal

seams and medium-thick coal seams. For thick and extra-thick coal seams, there is no suitable theory for determining overlying failure height.

Some scholars at home and abroad have conducted a lot of research on the failure height of thick coal seams. Liu et al. studied overburden failure characteristics in deep thick loose seam and thick coal seam mining [4]. Wang al. used microseismic monitoring system, ground penetrating radar, and borehole televiewer system, and the height of water flowing fractured zone of fully mechanized top caving was monitored [5]. van Schoor applied in-mine electrical resistance tomography (ERT) to map potholes and other disruptive features ahead of mining [6]. Kidybinski and Babcock used a two-dimensional finite element method of stress analysis to study the development of the fracturing process within the roof rock of a longwall face in a coal mine [7]. Palchik studied the fractured zones caused through the change in natural gas emission during longwall coal excavation [8]. Mills et al. measured shear movements in the

overburden strata ahead of longwall mining [9]. Ju et al. studied the effect of sand grain size on simulated mining-induced overburden failure in physical model tests [10]. Sun et al. used distributed optical fiber sensing to detect overburden deformation and failure in a mining face [11]. Application of magnetotelluric method to the detection of overburden failure height in shallow seam mining is done [12]. Chen et al. used RFPA software to simulate the whole process of overburden deformation and caving during mining and determined the fractured zone height [13]. Wang applied microseismic monitoring method to determine the fractured zone height [14]. Wang et al. studied the process of overburden failure in steeply inclined multiseam mining: insights from physical modelling [15]. Liu et al. used numerical simulation software FLAC3D to investigate overburden failure characteristics in deep thick loose seam and thick coal seam mining [4]. Xu et al. analyzed the overburden migration and failure characteristics after mining shallow buried coal seams with thick loose layer based on actual measurement data and simulation results [16]. Peng et al. analyzed main controlling factors of overburden failure in coal mining under thick coal seam geological conditions [17]. Yang et al. studied the evolution characteristics of two-zone failure mode of the overburden strata under shallow buried thick seam mining using physical modelling and on-site observation [18]. Judging from the research progress at home and abroad, few people have established mechanical model of overlying rock structure to analyze the overburden failure height.

In this paper, 8100 panel of Tongxin coal mine in China was selected as a research object. Failure process analysis method of overlying strata was proposed based on key strata theory. EH4 electromagnetic image system and borehole televiewer survey were conducted to verify the theory results. The results can provide a guidance for mining safety and economy.

## 2. Geology and Mining Conditions

The Tongxin Minefield is located in the north east of the Datong Coalfield, China, and it belongs to the east wing of the Datong syncline. The basic structure is a monoclinic structure that strikes N10~55°E, tendency northwest, high in the east and low in the west. The stratum dip is generally 3~10°. In the southeast and the south, the stratum dip near the coal seam outcrop is steep, generally 30~80°, and it is upright and inverted locally. The dip angle of the formation to the northwest quickly becomes flat. The mine field structure is simple. There are few faults in the minefield, and there are two normal faults. The faults are spread along the NNE direction and tend to the northwest. There are two larger folds in the minefield, namely, the Diaowozui syncline and the Hanjiayao anticline, and there are second-order small folds associated with them.

Panel 8100 of No. 3~5 seam was selected for this study. Its average thickness was 15.3 m, and the dip is 2°~3°. The thickness of the coal seam varies a little. The roof strata above No. 3~5 seam are shown in Table 1, and hard strata account for a large part. The panel width along the dip direction was

193 m, and the panel length along the strike direction was 1406 m. The top coal caving method was used to extract the full seam thickness with mining height 3.9 m at the bottom of the seam and the remaining 11.4 m on the top by natural caving. The gob of No. 14 seam located 190 m above the No. 3~5 seam covered about half of the panel length. The width of the section coal pillar was 38 m, and the speed of mining face was 5.6 m every day. Shield type low-level top coal caving hydraulic support was used in this longwall face, and its type was ZF15000/27.5/42.

## 3. Determination of Failure Height of Overlying Strata Based on Key Strata Theory

**3.1. Determination of Key Strata.** For the hard roof group structure with different thickness, the bearing capacity of the roof of each stratum should be clarified to determine the bearing capacity of the roof group structure. The bearing capacity of the multistrata roof composite structure satisfies the following relationship [19, 20]:

$$(q_n)_m = \frac{E_m h_m^3 \sum_{i=m}^n h_i \gamma_i}{\sum_{i=m}^m E_i h_i^3}, \quad (1)$$

where  $(q_n)_m$  is the load imposed by the roof of the  $n$ th stratum on the roof of the  $m$ th strata;  $m, n, i$  are No. of roof rock stratum;  $E_m$  is the elastic modulus of the  $m$ th strata MPa;  $h_m, h_i$  are the thickness of the  $m$ th strata and the  $i$ th strata, m;  $\gamma_i$  is the volume-weight of the  $i$ th strata kN/m<sup>3</sup>.

In the process of deformation of the key strata, simultaneous deformation happens to the overlying strata controlled, while the lower strata are not deformed. Thus, the load it bears no longer needs to be borne by the lower rock. If the  $n$ th strata are the roof of the key strata, the following relationship shall be satisfied [21, 22]:

$$(q_n)_m < (q_{(n-1)})_m, \quad (2)$$

where  $(q_n)_m$  is the load kNimposed by the  $n$ th strata on the  $m$ th strata;  $(q_{(n-1)})_m$  is the load kNimposed by the  $(n-1)$ strata on the  $m$ th strata.

At the same time, the key strata need to meet the strength conditions. If the failure span of the lower hard stratum is less than that of the upper hard stratum, the strength criterion of the key strata is [23]

$$l_{(n+1)} > l_1, \quad (3)$$

where  $l_{(n+1)}$  is the failure span of the  $n+1$ strata, m;  $l_1$  is the failure span of the  $l$ th strata, m.

**3.2. Failure Process Analysis of Upper Overlying Strata.** Fixed beam mechanical model is used to estimate limited span of hard stratum [24]:

$$l_G = h \sqrt{\frac{2\sigma_t}{q}}, \quad (4)$$

where  $h$  is the thickness of the strata,  $\sigma_t$  is the ultimate tensile strength of the strata, and  $q$  is the strata load.

TABLE 1: Characteristics of overlying strata.

No.	Lithology	Elastic modulus (GPa)	Tensile strength (MPa)	Bulk force (kN/m <sup>3</sup> )	Thickness (m)
1	Sandy mudstone	18.35	5.47	26.31	3.2
2	K3 sandstone	36.21	7.68	25.44	5.3
3	Medium sandstone	29.57	6.14	26.73	7.7
4	Fine sandstone	35.54	7.81	27.12	2.1
5	Siltstone	23.64	4.97	26.45	5.3
6	4 coal	4.20	1.27	10.36	2.1
7	Siltstone	23.35	4.25	25.78	2.4
8	Kernstone	20.32	4.82	24.21	4.3
9	Fine sandstone	35.62	8.20	25.62	14.8
10	Conglomerate	28.43	4.34	27.35	12.9
11	Kernstone	19.98	5.24	23.89	3.5
12	Conglomerate	28.74	4.34	27.10	12.0
13	Medium sandstone	29.62	7.01	25.52	13.7
14	Siltstone	23.48	4.45	24.58	3.2
15	Fine sandstone	35.21	7.93	27.17	10.7
16	Conglomerate	28.64	4.23	26.95	4.6
17	Fine sandstone	36.01	7.87	26.51	10.3
18	Siltstone	23.17	4.52	25.20	10.5
19	Sandy mudstone	18.46	5.81	25.98	6.9
20	Conglomerate	28.42	3.92	27.15	5.1
21	Sandy mudstone	18.56	4.14	26.51	2.9
22	Fine sandstone	36.12	8.11	26.82	10.7
23	Kernstone	21.31	5.34	25.24	14.3
24	Fine sandstone	35.87	8.64	27.54	6.2
25	Kernstone	20.12	5.42	25.37	25.4

For the weak strata, the limited span at the maximum horizontal tensile strain [25] is

$$l_R = h \sqrt{\frac{8E\epsilon_{\max}}{3q}}, \quad (5)$$

where  $E$  is the elastic modulus of the strata, and  $\epsilon_{\max}$  is the maximum horizontal tensile strain of the strata.

The maximum deflection of the weak strata [25] is

$$\omega_{\max} = \frac{5ql^4}{384EI}, \quad (6)$$

where  $l$  is the limited failure span of the rock strata;  $I$  is the moment of inertia of the section.

The free space height underneath the rock strata [26] is

$$\Delta_i = M - \sum_{j=1}^{i-1} h_j (k_j - 1), \quad (7)$$

where  $\Delta_i$  is the free space height underneath the  $i$ th strata;  $M$  is the coal seam mining height;  $h_j$  is the thickness of the  $j$ th strata;  $k_j$  is the residual frosting coefficient of the  $j$ th strata.

The critical mining length at failure [27, 28] is

$$L = \sum_{i=1}^m h_i \cot \varphi_q + l + \sum_{i=1}^m h_i \cot \varphi_h, \quad (8)$$

where:  $m$  is the number of strata between coal seam roof and the lower part of the strata;  $h_i$  is the thickness of the  $i$ th strata;  $\varphi_q$  and  $\varphi_h$  are the front and rear fracture angles of the strata, respectively.

The overlying strata failure process is affected by the tensile strength of the key strata, the antistrain ability of the soft rock strata, the free space height beneath the rock formation and the propulsion distance of the working face, etc. The evolvement of overlying strata failure can be judged by the relationship between the failure of key strata and the soft rock and the free space height beneath them. Specific judgments are shown in Figure 1.

### 3.3. Analysis of Overlying Strata Failure of Tongxin Coal Mine.

Since the Jurassic mined-out area is located about 190 m above the 8100 working face, the calculated scope of the key strata ends with the Jurassic mined-out area. There are 25 strata between the 8100 working face and the Jurassic coal seam, among which hard sandstone and conglomerate predominate. According to identification conditions of the key strata, each key stratum of overlying strata above the 8100 working face is identified combined with formulas (1)–(3), with the results shown in Table 2.

According to the identification results of the key strata and the identification formulas (4) to (8), and according to the overlying strata failure height identification process (Figure 1), the development of overlying strata failure is determined (Table 3), when the working face advanced to different positions. It can be seen from the table that the inferior key strata I and the inferior key strata II are broken when the working face advances to 55 m and 109 m, and the controlled strata above them are destroyed. Overlying strata have a failure height of 32 m and 143 m. When the face is advanced to 193 m, the key strata III are broken. Overlying

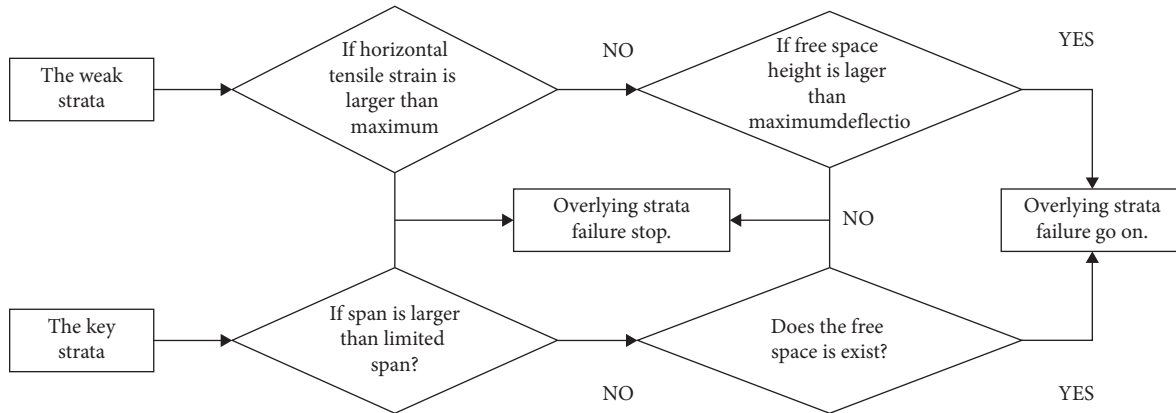


FIGURE 1: Judgment flow chart for height of fractured zone.

TABLE 2: Identification results of key strata.

No.	Lithological characters	Thickness (m)	Key strata	Failure span (m)	Distance from roof of coal seam (m)
Y25	Kernstone	25.4	Main key strata	104.18	174.6
Y22	Fine sandstone	10.7	Inferior key strata III	76.82	143.5
Y9	Fine sandstone	14.8	Inferior key strata II	67.44	32.4
Y2	K3 sandstone	5.3	Inferior key strata I	52.18	3.2

TABLE 3: Initial failure of each key strata with advancement of the working face.

Advancement of face (m)	Failure height of overlying strata (m)	Initial failure of key strata
55	32	Y2 (inferior key strata I)
109	143	Y9 (inferior key strata II)
193	174	Y22 (inferior key strata III)

strata fracture develops to the bottom of the main key strata, and overlying strata have a failure height of 174 m. As the face continues to advance, the fracture zone develops to the lower part of the main key strata, because the tendentious suspension and exposure span of the main key strata are less than its limit span.

#### 4. Survey of Water Conducting Fractured Zone Height by Electromagnetic Image System

**4.1. Survey Schemes.** The EH4 continuous conductivity imaging system uses artificial emission signals to compensate for the deficiencies of certain frequency bands of natural signals to obtain high-resolution resistivity imaging.

EH4 electromagnetic imaging system was used in panel 8100 to classify the fractured and caved zones of the overburden by utilizing the different electrical conductivity characteristics of various strata. The survey was performed in three stages: (1) premining of intact overburden in May 2011; (2) postmining of mined-out gob in August 2011; and (3) postmining after movement of overburden had stabilized in May 2012. Two survey lines were laid out in panel 8100 (see Figure 2). Survey line #1 was located in area of panel 8100, where no mining would be performed, while survey line #2 was located above the gob of panel 8100. The length of survey line #1 was 160 m, containing nine measuring points. Survey line #2 was oriented at N21°W. It was 340 m long and

contained 18 measuring points. In the second and third stages of surveys, survey was repeated along survey lines #1 and #2. When the second stage of survey was performed, the panel had been mined out for one month. When the third stage of survey was performed, the panel had been mined out for 10 months.

**4.2. Analysis of Survey Data.** Figure 3 shows the two-dimensional Earth resistivity inversion of survey line #1 at each stage (double black dashed line is the seam position). According to the resistivity distribution, resistivity was higher, and there was little change in the area surrounded by red dotted line, and this area can be inferred to be a caving zone. The blue dashed line was the boundary of high and low resistivity, so the area between blue dashed line and red dotted line was a fracture zone. It can be seen from Figure 3(a) that the resistivity contours are smooth and continuous; there is little abnormal change of electrical conductivity density and no dislocation. The distribution of resistivity contours is layered except some fluctuations in shallow layers. The results confirmed that this area was not affected by coal mining, and the overburden was undisturbed. Similarly, it can be seen from Figure 3(b) that there were closed contour lines of abnormal electrical resistivity in an area bounded in the horizontal direction between 80 m and 180 m and in the vertical direction between +800 m and +880 m (the red dotted line). This abnormal area coincides

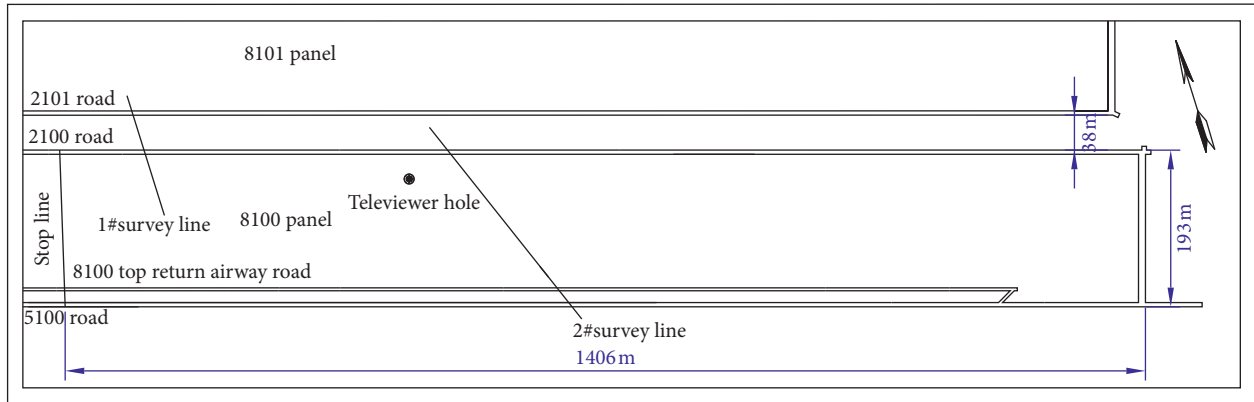


FIGURE 2: Panel layout.

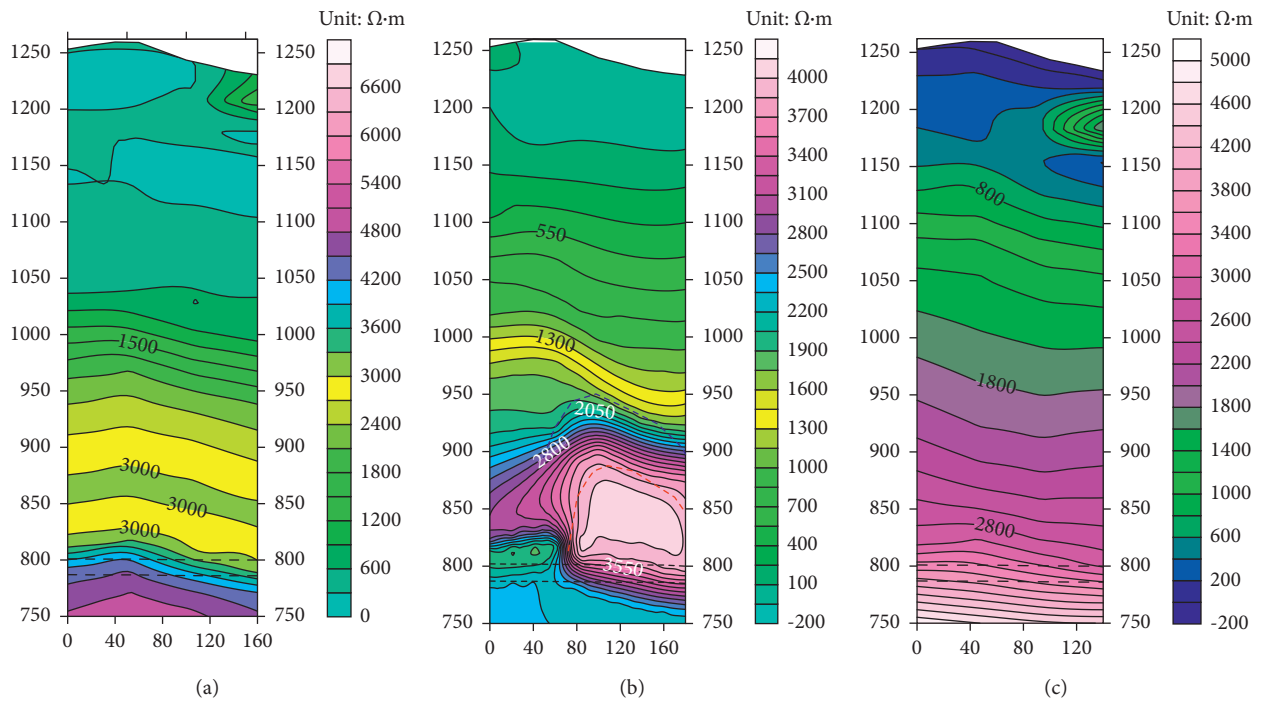


FIGURE 3: EH-4 two-dimensional inversion profiles of survey line #1. (a) The first stage (May 2011). (b) The second stage (August 2011). (c) The third stage (May 2012).

with the dimensions of panel 8100 shown in Figure 1. Therefore, it can be inferred that this high resistance anomaly area was the caved zone about 80 m high. The blue dashed line was the boundary of the fractured zone. It was about 150 m high. The continuous deformation zone covered the area from the boundary line of the fractured zone to ground surface. Again it can be seen from Figure 3(c) that high resistivity was distributed within a certain distance above the coal seam (double black dashed line is the seam position). Within this area, the resistivity contours were smooth, continuous, and layered, indicating that overburden movement had reached a steady state after one year of mining. Loose rocks and fractures are the cause of high electrical resistance. Resistivity contours are restored to the

smooth layered distribution found in premining condition after overburden strata movement ceased and became compacted.

Figure 4 shows the two-dimensional earth resistivity inversion of survey line #2 at each stage (double black dashed line is the seam position). It can be seen from Figure 4(a) that there was a closed contour line bounded in the horizontal direction between 80 m and 300 m and in the vertical direction between +800 m and +900 m (the red dotted line). The abnormal area was matched with the dimensions of panel 8100 shown in Figure 1. Therefore, it can be inferred that this high resistance anomaly area was the caved zone about 100 m high. The blue dashed line was the boundary of the fractured zone. It was about 170 m high. The continuous



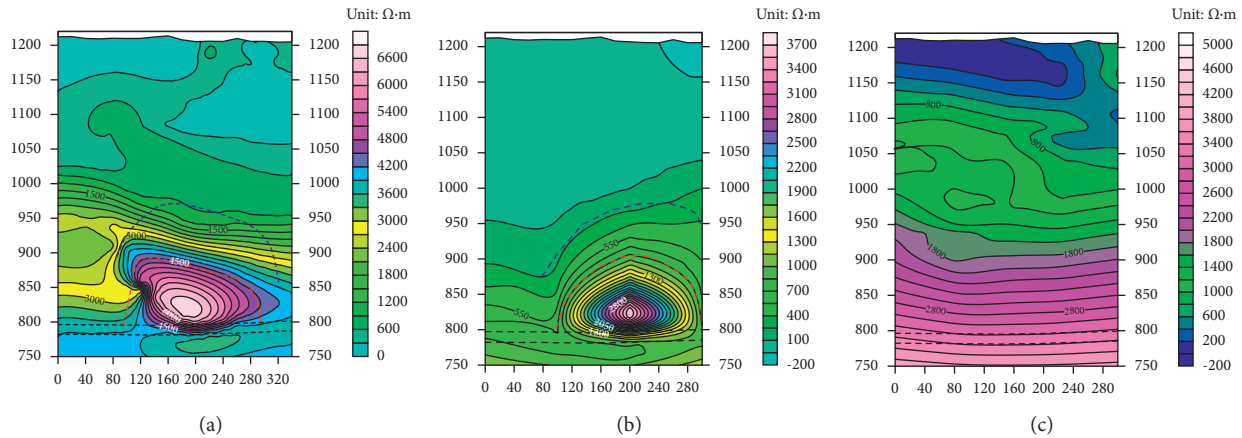


FIGURE 4: EH-4 two-dimensional inversion profiles of survey line #2. (a) The first stage (May 2011). (b) The second stage (August 2011). (c) The third stage (May 2012).

deformation zone covered the area from the boundary line of the fractured zone to the ground surface. The abnormal region in Figure 4(b) is consistent with the region in Figure 4(a). There was a closed contour line in the horizontal direction between 80 m and 300 m and in the vertical direction between +800 m and +900 m. So, it can be inferred that the caved zone is about 100 m high, and the fractured zone is about 170 m high. It can be seen from Figure 4(c) that resistivity contours were smooth, continuous, and layered, indicating that overburden movement had reached a steady state after one year of mining. Loose rocks and fractures are the cause of high electrical resistance. Resistivity contours are restored to the smooth layered distribution found in premining condition after overburden strata movement ceased and became compacted.

Table 4 is the summary of the EH4 geophysical survey results. The caved and fractured zones height at Tongxin mine was 150–170 m after mining of panel 8100 or 10 to 12 times of mining height (mining height = 15 m).

## 5. Determination of Fractured Zone Height of Water Conductivity by Borehole Televier

The fractured zone height of water conductivity of panel 8100 was determined by using the JL-IDOI (A) Drilling TV Smart Imager (Figure 5) in July 2011. The surface borehole was located in the gob of panel 8100 about 456 m from the panel stop line. The distance between the borehole and 2100 transport road was 32 m (Figure 1). The vertical distance between borehole mouth and coal seam floor was 437.5 m, and the bottom end of the borehole was 60 m above the coal seam roof. The data collected by the borehole televier were used to analyze the fractures in various strata, and finally, the caved and fractured zones were determined.

Analysis of the images as viewed from the borehole televier indicated that the observation segments can be divided into four parts (Figure 6). The first part was the tiny fissure zone. It was 159–171 m from the coal seam floor. In this region, the fine sandstone is more or less intact with localized microcracks. This region was located within the

TABLE 4: EH4 survey results showing the height of the two zones in the gob.

Survey line	Caved zone height (m)	Fractured zone height (m)
1	80	70
2	100	70

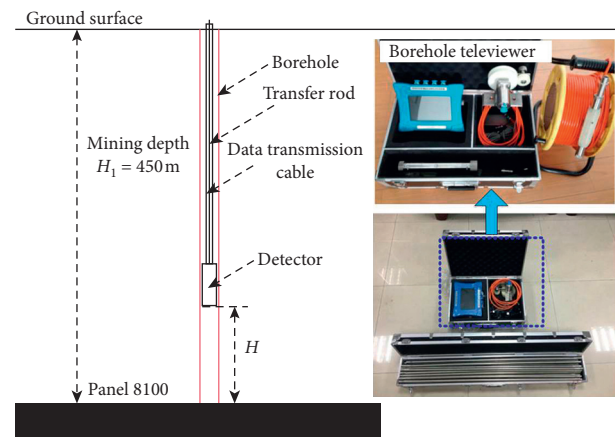


FIGURE 5: Borehole televier survey for roof strata.

fractured zone. The second part was the visible fractured zone, being located 90–159 m from the coal seam floor. There were visible crisscross cracks with bed separations. The third part was bed separation fractured zone, being located 60–90 m from the coal seam floor. In this region, broken rock, bed separation, and intact rocks alternated. This part bordered the caved zone. The fourth part was the badly broken zone, being located 0–60 m from the coal seam floor. Based on the above analysis, the caved zone height was about 90 m, that of the fractured zone was 81 m, and the height of overburden failures was 171 m (Figure 7).

In the «code for coal pillar setting and coal mining under pressure in buildings, water bodies, railways and main roadways», overlying failure height can be determined by

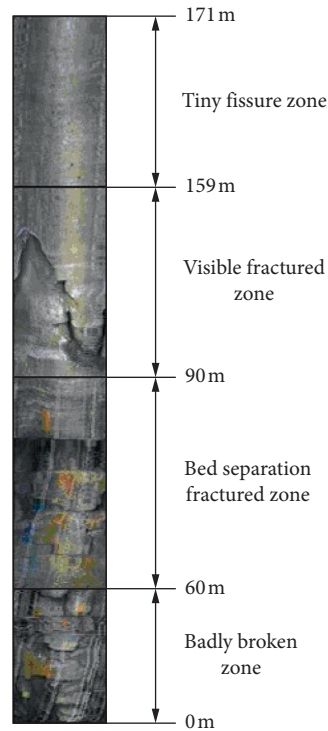


FIGURE 6: Damage characteristics of the hole wall.

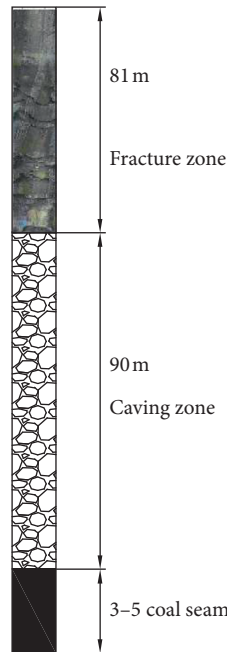


FIGURE 7: Caved and fractured zone heights.

(9) and (10) for thick coal seam under hard roof. The final calculation is based on the maximum value. Mining height is 15.3 m, and overlying failure heights are 66.25 m, 85.05 m, and 127.34 m calculated by (9) and (10). Therefore, overlying failure height was 127.34 m based on the code.

According to the above calculated results, the overburden failure height of the extra-thick coal seam was higher

than that of the conventional thickness coal seam. It might be caused by the key strata.

$$H_{li} = \frac{100 \sum M}{1.2 \sum M + 2.0} \pm 8.9, \tag{9}$$

$$H_{li} = 30 \sqrt{\sum M} + 10. \tag{10}$$

TABLE 5: Comparison of overlying failure height determined by different methods.

Methods	Overlying failure height (m)
Key strata theory	174
EH4 electromagnetic imaging system	150–170
Borehole televiewer	171
«Code for coal pillar setting and coal mining under pressure in buildings, water bodies, railways and main roadways»	127.34

Overlying failure heights determined by different methods are shown in Table 5. For theory calculation, EH4 electromagnetic imaging system, and borehole televiewer, the heights are nearly on the same level. So, the height of 170–174 m can be safely used. But the height calculated by the code is much lower than that of other methods. The equations proposed from many coal mines 20 years ago were outdated in the code, and the data was not complete for new mining methods, and new roof conditions and new mining height were applied in recent years.

The distance between panel 8100 in the No. 3–5 seam and the overlying No 14 seam was 190 m, more than the height of overburden failure zone. Therefore, cracks in the No. 3–5 seam did not connect to those in the No. 14 seam. The determination of the damage height of the overlying rock in the Tongxin Mine is of great significance to the prevention of mine water inrush accidents and gas control in the goaf of multiple coal seams and is beneficial to ensuring the safe production of the mine.

## 6. Conclusion

In China, there are few theories that can determine overlying failure height for thick and extra-thick coal seams. In order to understand the overburden movements of the longwall top coal caving mining, the key strata theory, EH4 geophysical survey, and borehole televiewer observation were applied to study this issue. The conclusions in this paper can be summarized as follows:

- (1) The key strata controlling some overlying strata can affect overburden failure process. Applying key strata theory, the failure height was determined of 174 m.
- (2) Through EH4 geophysical survey and borehole televiewer survey, the failure height was 150–171 m. The value is nearly the same as the key strata theory; therefore, the theory can be safely used for determination of overburden failure.
- (4) The failure zone does not approach upper goaf, and the gas in the upper goaf will not threaten the mining of the 8100 working face. The determination of the damage height of the overlying rock in the Tongxin Mine is of great significance to the prevention of mine water inrush accidents and gas control in the goaf of multiple coal seams and is beneficial to ensuring the safe production of the mine.

## Data Availability

No data were used in the study.

## Conflicts of Interest

The authors declare no conflicts of interest.

## Acknowledgments

This research has been supported by the Shandong Province Deep Rock Burst Disaster Assessment Engineering Laboratory Open Project (LMYK2021001) and Liaoning Revitalization Talents Program (XLYC1807064).

## References

- [1] L. M. Dou, J. He, S. Gong, and Y. F. Song, "A case study of micro-seismic monitoring: goaf water-inrush dynamic hazards," *Zhongguo Kuangye Daxue Xuebao/Journal of China University of Mining and Technology*, vol. 41, no. 1, pp. 20–25, 2012.
- [2] M. H. Loke, J. E. Chambers, D. F. Rucker, O. Kuras, and P. B. Wilkinson, "Recent developments in the direct-current geoelectrical imaging method," *Journal of Applied Geophysics*, vol. 95, pp. 135–156, 2013.
- [3] B. Poulsen, M. Khanal, A. M. Rao, D. Adhikary, and R. Balusu, "Mine overburden dump failure: a case study," *Geotechnical & Geological Engineering*, vol. 32, no. 2, pp. 297–309, 2014.
- [4] W. Liu, L. Pang, B. Xu, and X. Sun, "Study on overburden failure characteristics in deep thick loose seam and thick coal seam mining," *Geomatics, Natural Hazards and Risk*, vol. 11, no. 1, pp. 632–653, 2020.
- [5] X. Wang, Q. Qin, and C. Fan, "Failure characteristic and fracture evolution law of overburden of thick coal in fully mechanized sub-level caving mining," *Sains Malaysiana*, vol. 46, no. 11, pp. 2041–2048, 2017.
- [6] M. van Schoor, "The application of in-mine electrical resistance tomography (ERT) for mapping potholes and other disruptive features ahead of mining," *Journal of the South African Institute of Mining and Metallurgy*, vol. 105, no. 6, pp. 447–451, 2005.
- [7] A. Kidybinski and C. O. Babcock, "Stress distribution and rock fracture zones in the roof of longwall face in a coal mine," *Rock Mechanics*, vol. 5, no. 1, pp. 1–19, 1973.
- [8] V. Palchik, "Formation of fractured zones in overburden due to longwall mining," *Environmental Geology*, vol. 44, no. 1, pp. 28–38, 2003.
- [9] K. W. Mills, O. Garratt, B. G. Blacka, L. C. Daigle, A. C. Rippon, and R. J. Walker, "Measurement of shear movements in the overburden strata ahead of longwall mining," *International Journal of Mining Science and Technology*, vol. 26, no. 1, pp. 97–102, 2016.
- [10] M. Ju, X. Li, Q. Yao, S. Liu, S. Liang, and X. Wang, "Effect of sand grain size on simulated mining-induced overburden failure in physical model tests," *Engineering Geology*, vol. 226, pp. 93–106, 2017.

- [11] B. Y. Sun, P. S. Zhang, R. X. Wu, and L. Q. Guo, "Dynamic detection and analysis of overburden deformation and failure in a mining face using distributed optical fiber sensing," *Journal of Geophysics and Engineering*, vol. 15, no. 6, pp. 2545–2555, 2018.
- [12] D. Yang, W. Guo, and Y. Tan, "Application of magnetotelluric method to the detection of overburden failure height in shallow seam mining," *Arabian Journal of Geosciences*, vol. 11, no. 13, 2018.
- [13] R. H. Chen, H. B. Bai, and M. M. Feng, "Determination of the height of water flowing fractured zone in overburden strata above fully-mechanized top-coal caving face," *Journal of Mining & Safety Engineering*, vol. 23, no. 2, pp. 220–223, 2006.
- [14] H. Wang, "Research on microseism monitor in height of water flowing fractured zone of cover rock," *Express Information of Mining Industry*, no. 3, pp. 27–29, 2006.
- [15] H. Wang, Y. Qin, H. Wang, Y. Chen, and X. Liu, "Process of overburden failure in steeply inclined multi-seam mining: insights from physical modelling," *Royal Society Open Science*, vol. 8, no. 5, Article ID 210275, 2021.
- [16] Z. Xu, Q. Li, and X. Li, "Overburden migration and failure characteristics in mining shallow buried coal seam with thick loose layer," *Advances in Materials Science and Engineering*, vol. 2020, Article ID 9024751, 12 pages, 2020.
- [17] L. Pang, W. Liu, and Y. Qin, "Analysis of main controlling factors of overburden failure in coal mining under thick coal seam geological conditions," *Geotechnical & Geological Engineering*, vol. 39, no. 4, 2020.
- [18] D. Yang, W. Guo, and Y. Tan, "Study on the evolution characteristics of two-zone failure mode of the overburden strata under shallow buried thick seam mining," *Advances in Civil Engineering*, vol. 2019, Article ID 9874769, 9 pages, 2019.
- [19] J. Ju and J. Xu, "Structural characteristics of key strata and strata behaviour of a fully mechanized longwall face with 7.0m height chocks," *International Journal of Rock Mechanics and Mining Sciences*, vol. 58, pp. 46–54, 2013.
- [20] J. Xu, W. Zhu, and X. Wang, "New method to predict the height of fractured water-conducting zone by location of key strata," *Journal of China Coal Society*, vol. 37, no. 5, pp. 762–769, 2012.
- [21] Y. Yuan, S. Tu, X. Zhang, and B. Li, "Dynamic effect and control of key strata break of immediate roof in fully mechanized mining with large mining height," *Shock and Vibration*, vol. 2015, Article ID 657818, 11 pages, 2015.
- [22] T. Kuang, Z. Li, W. Zhu et al., "The impact of key strata movement on ground pressure behaviour in the Datong coalfield," *International Journal of Rock Mechanics and Mining Sciences*, vol. 119, pp. 193–204, 2019.
- [23] H. Han, J. Xu, X. Wang, J. Xie, and Y. Xing, "Method to calculate working surface abutment pressure based on key strata theory," *Advances in Civil Engineering*, vol. 2019, Article ID 7678327, 20 pages, 2019.
- [24] K. Wang, T. Kang, H. Li, and W. Han, "Study of control caving methods and reasonable hanging roof length on hard roof," *Chinese Journal of Rock Mechanics and Engineering*, vol. 28, no. 11, pp. 2320–2327, 2019.
- [25] X. J. Lin and M. G. Qian, "Method to distinguish key strata in overburden," *Journal of China University of Mining & Technology*, vol. 29, 2000.
- [26] J. Cheng, G. Zhao, and S. Li, "Predicting underground strata movements model with considering key strata effects," *Geotechnical and Geological Engineering*, vol. 36, 2017.
- [27] C. Xu, G. Yang, H. Sun et al., "Key strata inducing dynamic disasters based on energy condition: criterion and application," *Geofluids*, vol. 2021, Article ID 6672020, 10 pages, 2021.
- [28] W. Lu, C. He, and X. Zhang, "Height of overburden fracture based on key strata theory in longwall face," *PLoS One*, vol. 15, Article ID e0228264, 2020.

## Research Article

# Evolution Analysis of Microseismic Events before and after Mining through Large-Scale Weak Zone with High Confined Water

Jing Jia <sup>1</sup>, Xianjie Hao <sup>2,3,4</sup>, Guanghui Zhao <sup>4</sup>, Yubao Li <sup>1</sup>, Xiaoyu Chuai <sup>1</sup>,  
Lei Huang <sup>4</sup>, Guangyao Pan <sup>4</sup>, Yingnan Wei <sup>4</sup>, Kai Chen <sup>4</sup>, Ruilai Huang <sup>4</sup>,  
and Rongcheng Zhan <sup>4</sup>

<sup>1</sup>Hebei Coal Research Institute, Xingtai, Hebei 054099, China

<sup>2</sup>Beijing Key Laboratory for Precise Mining of Intergrown Energy and Resources,  
China University of Mining and Technology (Beijing), Beijing 100083, China

<sup>3</sup>Key Laboratory of Safety and High-Efficiency Coal Mining, Ministry of Education (Anhui University of Science and Technology),  
Huainan 232001, China

<sup>4</sup>School of Energy and Mining Engineering, China University of Mining and Technology (Beijing), Beijing 100083, China

Correspondence should be addressed to Xianjie Hao; haoxianjie@cumtb.edu.cn and Guanghui Zhao; zqt1900101063g@student.cumtb.edu.cn

Received 9 April 2021; Revised 7 July 2021; Accepted 15 July 2021; Published 3 August 2021

Academic Editor: Youjun Ning

Copyright © 2021 Jing Jia et al. This is an open access article distributed under the Creative Commons Attribution License, which permits unrestricted use, distribution, and reproduction in any medium, provided the original work is properly cited.

The existence of large-scale weak zone will have a great adverse impact on coal mining in high confined aquifer. Taking the Wutongzhuang Coal Mine which is threatened by high-pressure water as an example, this paper studies the difference between the microseismic events before and after mining and analyzes the influence of the large size weak zone on the coal mining on the confined aquifer. The research results show that the microseismic characteristics of the large soft weak belt are small number of events, the spatial distribution of events is concentrated, and the energy level is large. The amplitude of microseismic events is higher, and the proportion of large events in microseismic events is larger than that of small events; the characteristics of microseismic events caused by mining face mining are that the number of events is more, the distribution of events is loose, the distribution of roof and floor is more, the energy level is less, the amplitude is smaller, and the proportion of small and medium events in microseismic events is larger than that of large events. Due to the joint influence of large-scale weak zone of floor and mining, the floor in the middle area of working face is affected by mining, the number of microseismic events in each aquifer increases suddenly, the karst fissures between the aquifers are further developed, and there is a trend of transfixion. Therefore, measures such as floor grouting should be taken to reinforce the large-scale weak zone before mining.

## 1. Introduction

Mine water disaster is one of the five major disasters in coal mines in China [1]. Coal mine water inrush accidents account for a large proportion of coal mine disasters, causing heavy losses to the country and people's lives and property [2]. According to statistics, about 60% of coal mines in China are affected by confined water to varying degrees, and the area and the severity of water disaster rank first among major

coal-producing countries in the world [3]. Take Wutongzhuang Coal Mine as an example. It is typical coal mining on confined water in the "three underground and one water-borne circumstances" special mining [4]. In recent years, with the increase of mining depth, the Wutongzhuang Coal Mine has been more and more threatened by high-pressure o.l. water [5, 6]. Even if water disaster prevention measures are taken, water inrush accidents still occur [7]. Therefore, studying the mining of coal seam on confined water and



avoiding the occurrence of water inrush from the floor are an urgent problem to be solved [8].

China is a country that started to study coal mining on high confined water relatively early in the world and has achieved a lot of results. Xie et al. [9] started from the mechanism of hydraulic fracturing and analyzed the permeability changes to infer the risk of water inrush from the floor and introduced the concept of damage. Xu et al. [10] studied the mining failure of coal mining floor under high confined water and the formation and evolution of water inrush channels through on-site monitoring and numerical simulation. Li and Xu [11] established a physical model to prevent water inrush disasters from the collapse column using the comprehensive methods of theoretical analysis, similar simulation, and digital simulation. Zhao et al. [12] put forward the key technology of advanced treatment of o.l. water damage in the ground area, and it has been widely used. Dong et al. [13] and Wang et al. [14] put forward the idea of using a weathering zone at the top of the Ordovician limestone which has better water blocking performance as a water-repellent layer, and they conducted a study on its availability and established a criterion for the thickness of the rock section on top of Ordovician limestone. Xu et al. [15] used borehole ultrasonic detection, core indoor ultrasonic transmission, and point load test methods to study the damage and destruction degree of the floor rock before mining working face in the upper and lower coal seams of the confined water, and they obtained the rock elastic modulus. The density, lithology, and completeness of rock mass show a nonlinear positive correlation. Ma [16] combined method of transient electromagnetic method and radio wave perspective method to comprehensively detect the internal water-conducting structure of the working face under the effect of high confined water and achieved good results. Wei et al. [17] and others used numerical simulation and similar simulation methods to analyze the degeneration characteristics of the roadway under the effect of high confined water. Chen et al. [18] used the knowledge of mechanics combined with the "drilling double-ended side leakage plugging device" to study the evolution of cracks in the mining rock mass under high confined water. Xu and Gao [19] established a mechanical model to theoretically analyze the mechanism of water inrush from a working face cross-fault under high confined water conditions. Wang et al. [20] analyzed the failure law of complex rock during UCA mining and proposed a method for predicting the danger zone of support fractured water inrush. Yu et al. [21] used the fractal dimension method to partition the structural complexity of the study area and evaluated the risk of water inrush from the deep coal seam floor by mining above the confined aquifer in the mining area. Duan and Zhao [22], by analyzing some water inrush cases, put forward four main factors that affect water inrush from coal seam floor and established a mechanical model for the homogeneously broken and weak rock layer of the floor water-insulating layer. Li [23] introduced the development history of various geophysical prospecting technologies such as underground electrical methods, transient electromagnetics, electrical

perspective, radio wave tunnel perspective, and channel wave seismic in China and discussed the development direction of the discipline.

The microseismic monitoring method has been widely used in coal mines. In recent years, many scholars have made a series of achievements in the field of microseismic events. Ge and Han [24] proposed an imaging method for reverse-time migration of the structure below the microseismic zone. Lou et al. [25] used microseismic monitoring methods to analyze and study the stress conditions in the goaf and the rearrangement of the fracture zone. Wang et al. [26] proposed a source-independent objective function based on convolving reference traces, which avoids the cycle jump phenomenon caused by unknown sources and improves the accuracy of estimating the location of the seismic source. Hao et al. [27, 28] studied the fracture characteristics of coal under dynamic load through uniaxial compression tests and studied the influence of bedding cleats on it, and they found in subsequent studies that microseismic events occur when the coal bedding dip is  $45^\circ$  at most. Hao et al. [29] used a quantitative analysis method to construct three physical models and combined numerical simulation to analyze the influence of the main principal stress directions on the long axis of the tunnel on the stability of the underground tunnel. Zheng et al. [30], based on the limit equilibrium method and genetic algorithm, proposed a new method for stability assessment of ABRs considering seismic inertial forces. The effects of seismic and mechanical properties of rock strata on the failure mechanism of ABRs are discussed. Zhang et al. [31] proposed a new method based on VMD to distinguish between coal and rock fracture and blasting vibration microseismic signals by processing the signal. Chen et al. [32] evaluated the effect of hydraulic fracturing by analyzing the number of microseismic events and energy changes caused by high-pressure hydraulic fracturing. The Brune model and grid search method were used to calculate the source parameters, and the relationship between  $M_0$  and other source parameters was analyzed. The relationship between  $M_w$  (moment magnitude) and  $M_L$  (local magnitude) of microseisms induced by hydraulic fracturing is obtained. Amad et al. [33], through the joint inversion of source location and distance tensor, reconstructed the space and role of (micro) seismic events and constructed a full-waveform technology. Estay et al. [34] obtained the  $b$  value of seismic activity related to mining by studying the time decay law of seismic activity after rockburst and large-magnitude events occurred in the aftershock sequence of the mine. Liu et al. [35] proposed a microseismicity-based method for the dynamic estimation of the potential rockburst scale during tunnel excavation.

In summary, it can be seen that there are a large number of results in exploration, mechanical models, and similar simulations in high-pressure water mining. However, there are few studies on the microseismic characteristics of excessively large-sized weak zones before mining. Therefore, this paper uses the data collected by the microseismic monitoring system to study the difference between the large-scale weak zone near the F702-11 fault in the front

floor before and after the mining of Wutongzhuang Coal Mine 182703 working face, and it analyzes the impact of large-size weak zones on coal mining above confined aquifers and provides technical guidance for coal mine safety production.

## 2. Project Profile

Wutongzhuang Coal Mine is located in Handan City, Hebei Province. It is one of the main mines of Jizhong Energy Fengfeng Group, with a design production capacity of 3.0 Mt/a. The hydrogeological conditions are extremely complex, and the ground temperature of the mine affected by the geological structure is higher than that of other mines in the group [36, 37].

The 182703 working face is located in the seventh mining area, the east is the designed 182704 working face, the west is the 182702 mined area, the south is the F2-2 fault, and the north is the south belt transportation lane with no other excavation condition. The No. 2 coal seam is mined at the working face, the coal bulk density is  $1.35 \text{ t/m}^3$ , the mining area is  $145071 \text{ m}^2$ , the industrial reserves are 0.722 Mt, and the recoverable reserves are 0.686 Mt. The strike length of the working face is 683 m, with an average of 683 m; the inclination length is 94 m ~ 252 m, with an average of 212 m; the inclination of the working face is  $1^\circ \sim 36^\circ$ , with an average of  $25^\circ$ ; the maximum coal seam thickness is 4.2 m, the minimum is 3.0 m, and the average is 3.69 m. The buried depth of the working face is about 660 meters, and the direct top lithology is sandy shale, which is brittle and compact.

## 3. Distribution of Large-Size Weak Zones in the Working Face

According to the data provided by the Wutongzhuang Coal Mine Geology Department, in the 182703 working face, there are many weak zones dominated by faults, and the fault occurrence is shown in Table 1. Figure 1 shows the distribution of abnormal weak bands on the working face measured by the transient electromagnetic method. Figure 2 shows the cross-sectional view of the weak fault zone in the working face.

## 4. Comparative Analysis of Microseismic Events before and after Mining

### 4.1. Construction of the Microseismic Monitoring System

**4.1.1. Layout of the Microseismic Monitoring System.** There are 11 geophones arranged in the upper and lower tunnels and 2 underground monitoring substations for a total of 15 channels on the 182703 working surface of Wutongzhuang Mine. Among them, 3# and 7# are three-component detectors, the others are single-component detectors, 1#~5# detectors are located in the lower groove, and 6#~11# detectors are located in the upper groove. There are 24-bit digital microseismic acquisition substations, respectively, in the 182703 transportation roadway and the 182703 return airway, with a sampling frequency of 5 kHz.

The monitoring layout is shown in Figure 3. In order to avoid the influence of the loose circle of the roadway, the geophones are buried at a depth of 6 m and the spacing is about 100 m.

**4.1.2. Transmission and Processing of Microseismic Monitoring Data.** The microseismic monitoring data is continuously collected in real time, and the underground optical fiber is directly transmitted to the surface switch of Xingdong Coal Mine and transmitted to the microseismic monitoring and monitoring center of the Academy of Coal Science through the Jizhong Energy LAN (Figure 4).

The 182703 working face monitoring system was set up in April and began to collect data. The working face started mining on May 17th. We compared the number of events, energy, amplitude, and spatial distribution in the microseismic monitoring data collected from April 1st to April 10th and May 18th to May 27th to analyze the impact of mining work on microseisms.

**4.2. Comparative Analysis of the Number of Microseismic Events before and after Mining.** Figure 5 shows the statistics of the number of events before and after mining. From April 1st to April 10th, before mining, there were a total of 340 events collected. The number of events on April 10 was the least, with 15 events, and the number of events on April 3 was the most, with 55 events, with an average of 34 events per day. From May 18 to May 27 after the mining, there were a total of 820 microseismic events collected, of which the number of events on May 19 was the least, with 47 events, and the number of events on May 24 was the most, with 132 events, with an average of 82 events per day. After querying the data of the mine, it was concluded that the increase in microseisms on May 24 was caused by the roof first weighting.

From the comparison of the data in Figure 5, in terms of quantity, it can be seen that the number of microseismic events affected by mining activities has increased significantly in May.

**4.3. Comparative Analysis of Microseismic Energy before and after Mining.** Figure 6 shows the comparison of microseismic energy before and after mining. Figure 6 shows that, from April 1st to April 10th, before mining, the minimum energy was 4691 J on April 8, the maximum energy was 4614966 J on April 5, and the average daily energy was 1002882 J. After mining from May 18 to May 27, the lowest energy was 2801 J on May 21, the highest energy was 658864 J on May 27, and the average daily energy was 119664 J. It can be seen that the energy in April is an order of magnitude higher than that in May, so it can be concluded that before the working face was mined in April, the cause of the microseismic event was due to the existence of a weak zone in front of the working face, which was affected by the geological tectonic movement of the coal mine, causing a large microseismic event, so the energy is huge. The microseismic event in May is caused by mining activities, although the number is large, but the energy is much smaller than the energy generated by the weak zone.

TABLE 1: Occurrence characteristics of weak zone in 182703 working face.

Construct name	Trend	Tendency	Dip angle (°)	Type	Falling head (m)
F702-10	N5°E	SW	65	Normal fault	2
F702-11	N58°W	SE	70	Normal fault	1.2
F703-12	N18°E	SE	80	Normal fault	7.2
F703-13	N24°E	SE	80	Normal fault	2.7
F703-15	N44°E	SE	67	Normal fault	6
F703-16	N50°E	SE	55	Normal fault	3.5

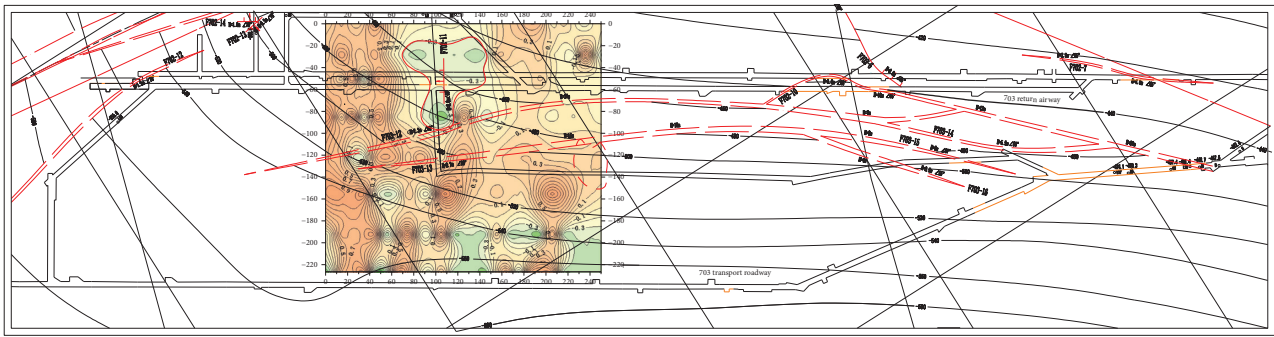


FIGURE 1: Distribution range of weak zone in 182703 working face.

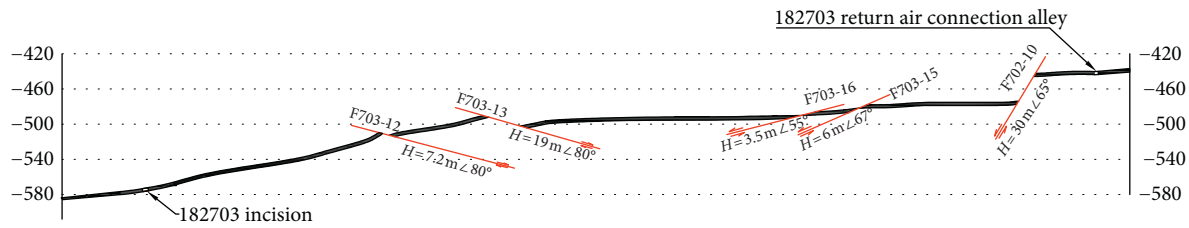


FIGURE 2: Fault profile in working face.

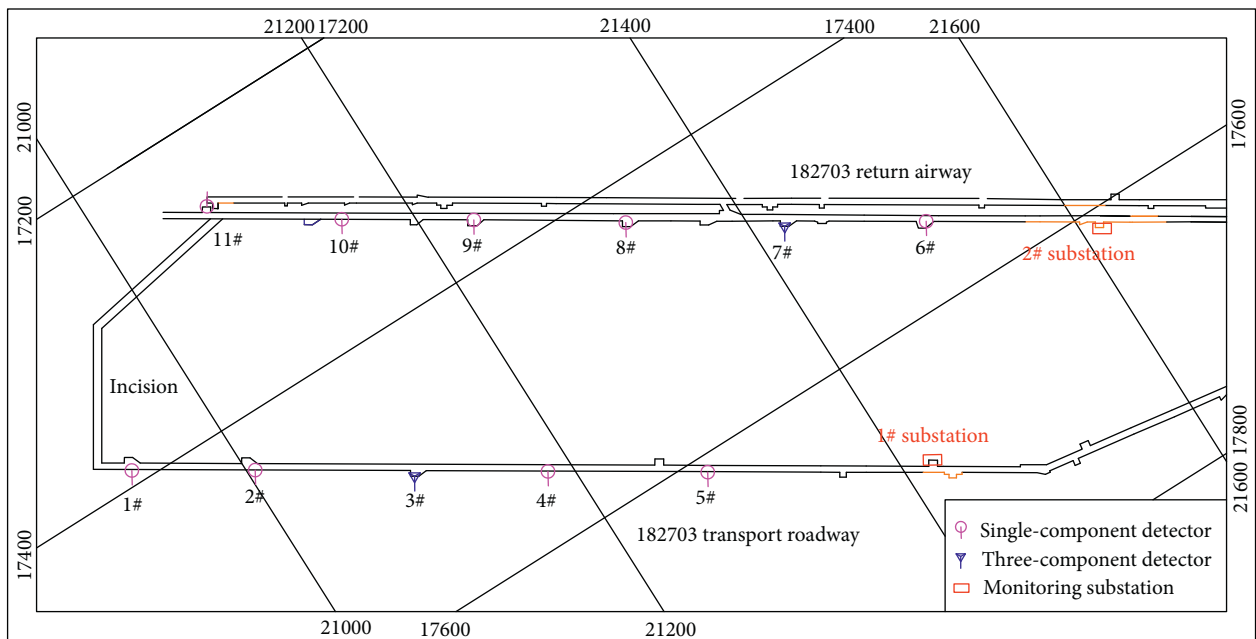


FIGURE 3: Microseismic monitoring layout of 182703 face in Wutongzhuang Mine.



FIGURE 4: Microseismic monitoring center.

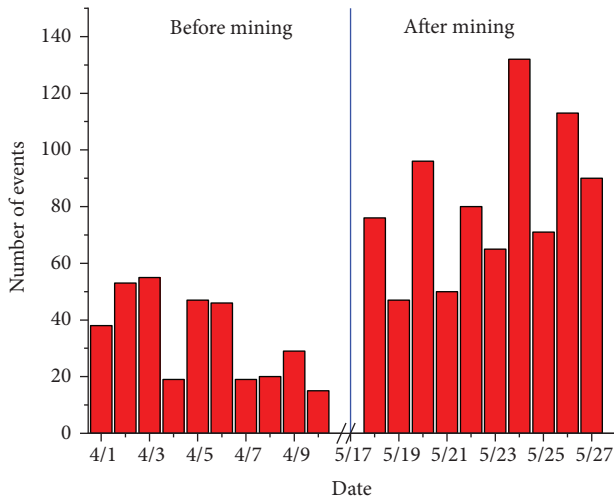


FIGURE 5: Comparison chart of the number of microseismic events before and after mining.

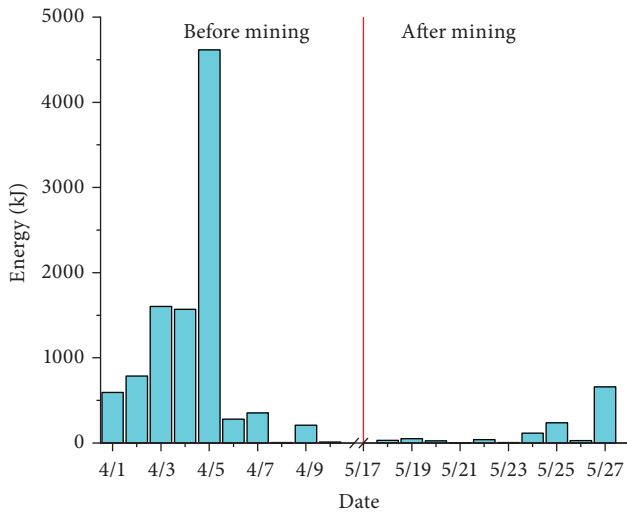


FIGURE 6: Energy comparison graph of microseismic events before and after mining.

Figure 7 is a graph of cumulative energy and cumulative events. It can be seen from Figure 7 that the cumulative number of microseismic events is higher after mining, but in terms of cumulative energy of microseisms, the large-size weak zone was affected by the geological tectonic movement resulting in the dislocation of the large-size weak zone before

mining, which caused a large microseismic event, resulting in a surge in energy, which was an order of magnitude higher in energy data than after mining.

It can be seen from the comparison diagrams of Figures 5–7 that the microseismic events monitored in April were caused by the large-scale weak zone in front of the working face that was affected by the movement of geological tectonic movement and caused the large microseismic event. Its manifestation is large energy and small number of events. The microseismic events monitored in May are microruptures caused by the mining activities. The manifestation is low energy and large numbers of microseismic events.

#### 4.4. Comparison of the Amplitude of Microseismic Events before and after Mining.

Figure 8 is a comparison diagram of the amplitude of microseismic events before and after mining. It can be seen that, from April 1st to April 10th, before mining, there was a microseismic event with a minimum amplitude of 0.8597 on April 1st and a maximum microseismic amplitude of 4.2951 on April 7th with an average amplitude of 2.0751, and the microseismic amplitude distribution was more even. From May 18th to May 27th, after mining, there was a microseismic event with a minimum amplitude of 0.0934 on May 23rd and a microseismic event with a maximum amplitude of 4.8481 on May 18th, with an average amplitude of 1.3903, and there were more small amplitude events. Therefore, it can be seen from the comparison diagram of the amplitude of the microseismic event that before the working face was mined in April, the large-scale weak zone was affected by the geological tectonic movement and caused a large microseismic event. Although the number of events is small, the energy and amplitude are relatively large. In May, the working face was affected by the continued mining activities to cause small ruptures. There were many microseismic events, but most of them were small events with small amplitude and low energy.

#### 4.5. Analysis of the Spatial Distribution of Microseismic Events before and after Mining

##### 4.5.1. Distribution Characteristics of Microseismic Events in Each Aquifer.

Figures 9 and 10 are, respectively, the spatial distribution of microseismic events. The sphere in the figure represents the microseismic event, the size of the sphere represents the amplitude of the microseismic event, and the black curved surface is the No. 2 coal seam. By comparing the spatial distribution map of microseismic events before and after mining, it can be seen that the microseismic events before mining are mainly floor events, and the distribution range of the events is concentrated between -400 and -650 meters. Although the microseismic events caused by mining activities are still mainly floor events, the roof events have obviously increased. From the distribution range, it can be seen that the distribution range of microseismic events after mining is mainly concentrated between -400 and -800 meters, but there are still a small number of microseismic



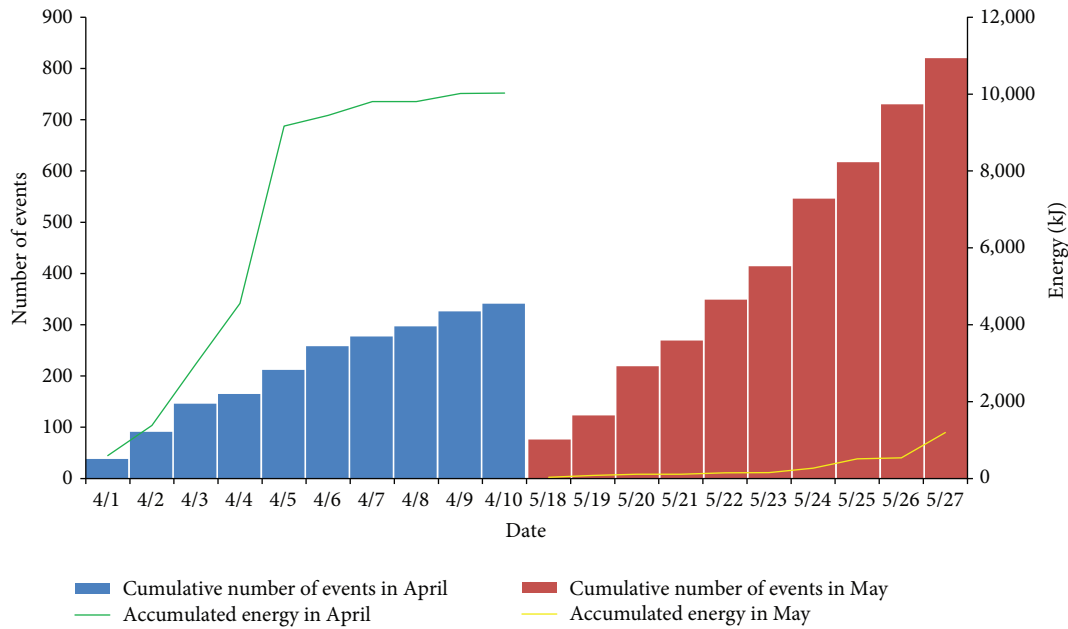


FIGURE 7: Comparison of cumulative number of microseismic events and accumulated energy before and after mining.

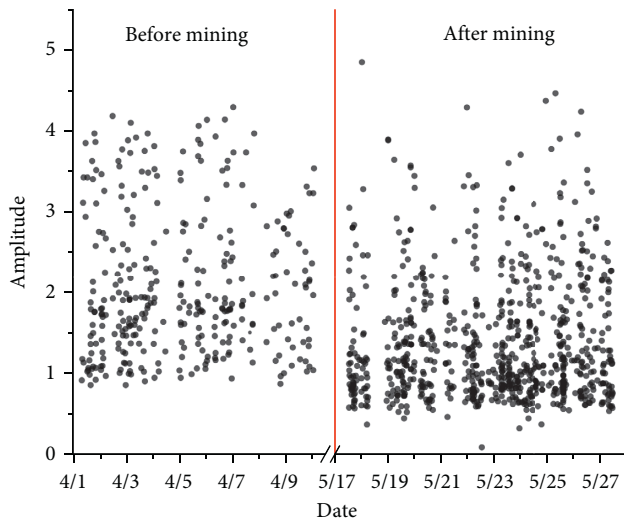


FIGURE 8: Comparison chart of microseismic events before and after mining.

events extending to the top  $-200$  meters and the bottom  $-1000$  meters. Therefore, the distribution of microseismic events caused by mining is wider, with a large number of microseismic events on the floor and the roof, but the magnitude of the microseismic events is smaller than that of the large-scale weak band movement.

The microseismic event distribution diagram (Figures 11–14) was established through the microseismic data collected by the microseismic monitoring system. From Figure 11, it can be seen that the microseismic events generated by tectonic activities in April were distributed in the middle of the area on the plane, and the events that occurred in the Ordovician limestone were mainly concentrated in the area of the F702-11 fault and extending to

F2-2 fault area, the distribution range of events that occurred in the Ordovician limestone is relatively concentrated. It can be seen from Figure 12 that the number of events that occurred in the Ordovician limestone after mining in May increased significantly compared to Figure 11, and they were mainly distributed near the F702-11 fault area. However, the number of events that occurred in the Ordovician limestone was more dispersed than that in May, from the shallow part of 2# coal to the Yeqing layer mainly concentrated near the transport roadway and the return air trough and extending to the open-off cut. The distribution of events is relatively concentrated. The analysis reason is that, from the shallow part of 2# coal to Yeqing layer mainly affected by mining pressure, Ordovician limestone interval is mainly affected by the o.l. water pressure.

Figures 13 and 14 are cross-sectional views perpendicular to the transport roadway and the return air trough. From Figures 13 and 14 it can be seen that microseismic events occur in all aquifers, but the proportion of events that occurred in the Ordovician limestone in the distribution of microseismic events in May has increased significantly compared to the proportion of events that occurred in the Ordovician limestone in the distribution of microseismic events in April, and the proportion of occurrences of microseismic events in the floor of Shanfuqing-the floor of Daqing has decreased. At the same time, combining the microseismic events of each aquifer in Figure 15, it can be seen that the large-scale weak zone was distorted by the geological tectonic movement in April, which mainly occurred in the floor of Yeqing-the floor of Fuqing area, which caused a significant increase in the proportion of microseismic events in this area, and after the mining in May, since no tectonic activity has occurred so far, it is only affected by mining activities, so the distribution of microseismic events in each aquifer is relatively even.



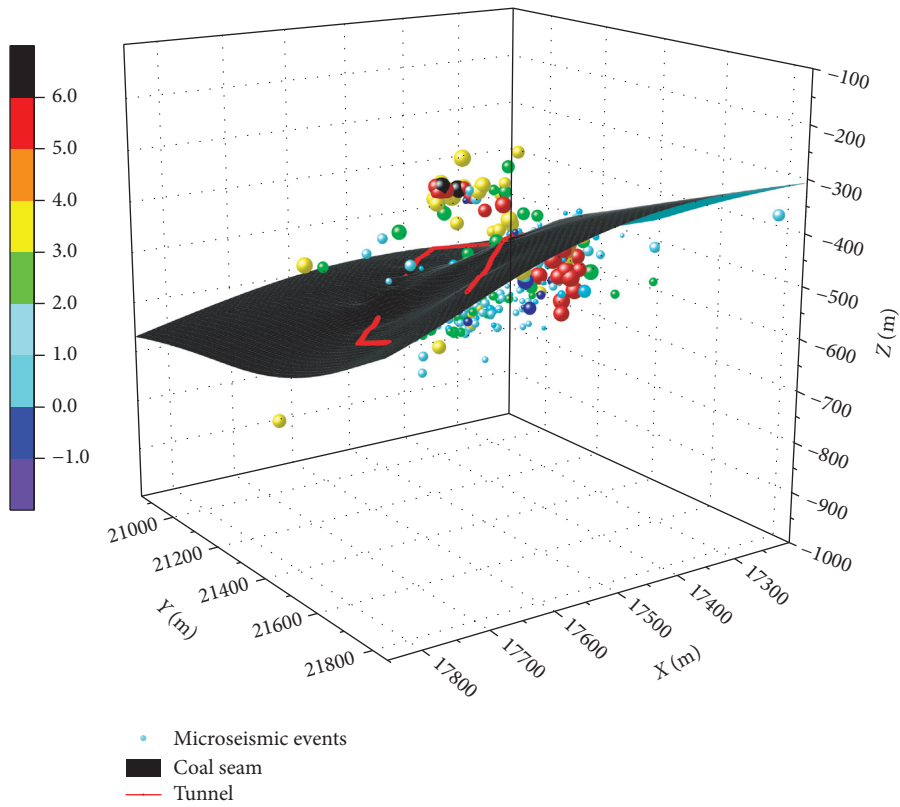


FIGURE 9: Spatial distribution map of microseismic events before mining.

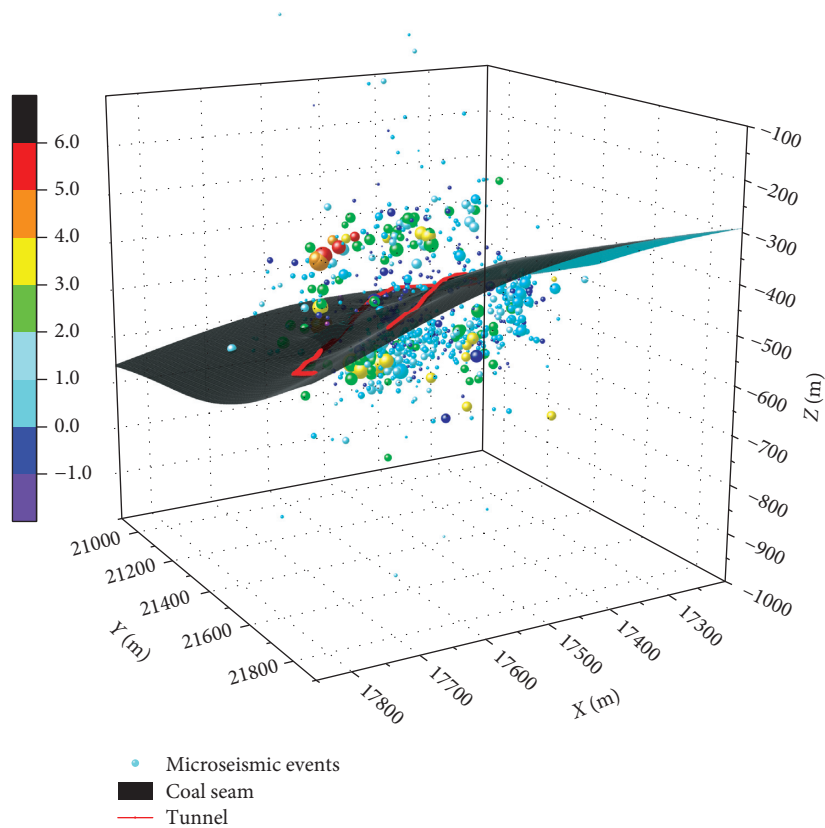


FIGURE 10: Spatial distribution map of microseismic events after mining.

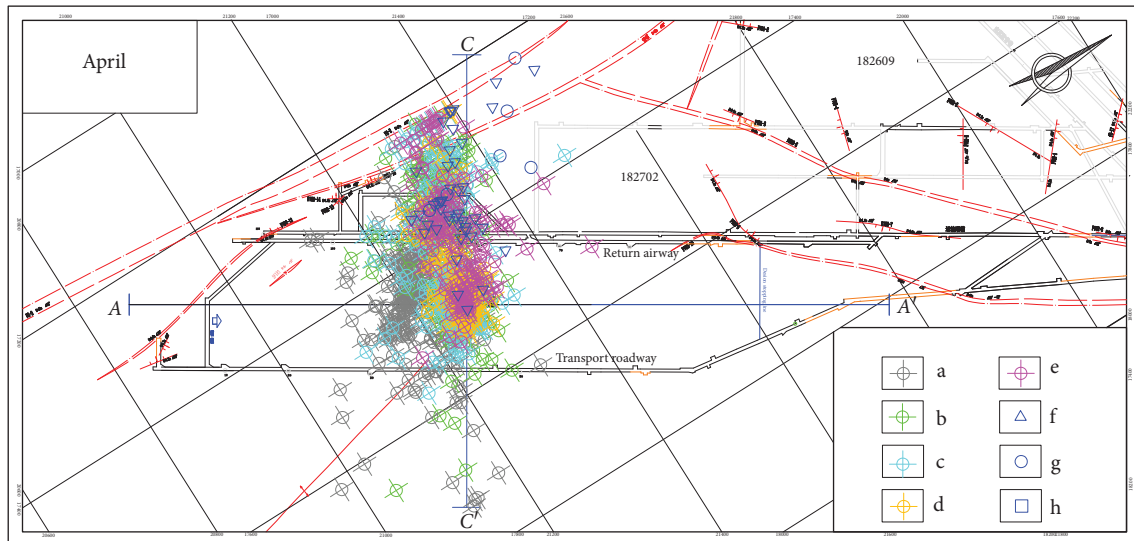


FIGURE 11: Distribution plan of microseismic events in April. a: shallow of 2# coal; b: floor of 2# coal-floor of Yeqing limestone; c: floor of Yeqing limestone-floor of Fuqing limestone; d: floor of Fuqing limestone-floor of Daqing limestone; e: floor of Danqing limestone-roof of Ordovician limestone; f: Ordovician limestone (0–50 m); g: Ordovician limestone (51–150 m); h: Ordovician limestone (150 m-deep part).

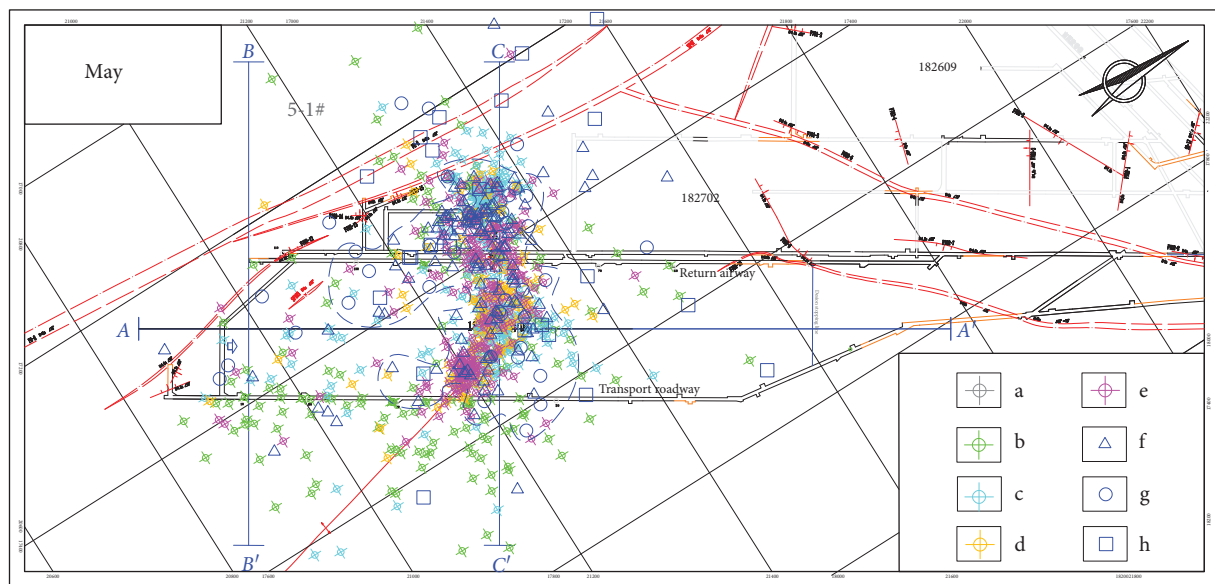


FIGURE 12: Distribution plan of microseismic events in May. a: shallow of 2# coal; b: floor of 2# coal-floor of Yeqing limestone; c: floor of Yeqing limestone-floor of Fuqing limestone; d: floor of Fuqing limestone-floor of Daqing limestone; e: floor of Danqing limestone-roof of Ordovician limestone; f: Ordovician limestone (0–50 m); g: Ordovician limestone (51–150 m); h: Ordovician limestone (150 m-deep part).

4.5.2. *The Relationship between the Variation of Water Pressure in Different Aquifers and Microearthquakes.* The water pressure of aquifers with different depths is different, which leads to different microseismic monitoring data. According to the water pressure data collected by the mine hydrological monitoring unit, there is a clear difference in water pressure between the Yeqing limestone aquifer and the mountain blue limestone aquifer. The water pressure of the Yeqing limestone aquifer ranges from 1.6 to 7.1 MPa. The water pressure of the rock aquifer ranges from 1.3 to 8.8 MPa. According to the microseismic profile, it can be seen that the number of microseismic events in the

mountain bladder limestone aquifer is more than that of the Yeqing limestone aquifer, which can indicate that there is a certain connection between water pressure and microseismic events, and the increase in water pressure will lead to the increase in the number of microseismic events.

4.6. *Microseismic Characteristics When Passing through the Grouting Abnormal Area.* There are two abnormal grouting areas on the working face. When the working face passes through the abnormal grouting area, the microseismic monitoring data has changed significantly compared with

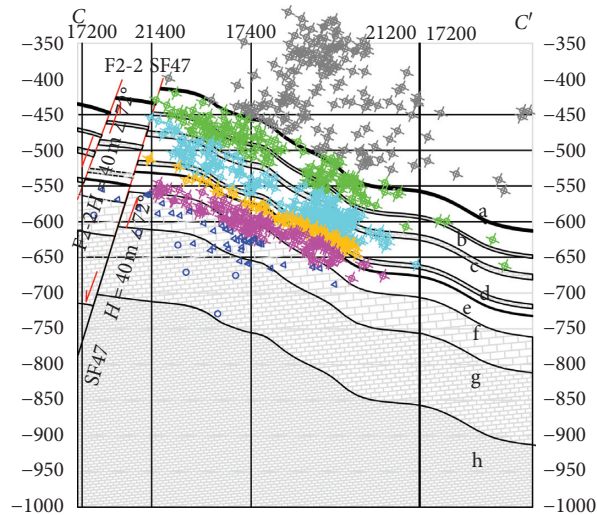


FIGURE 13: Distribution profile of microseismic events in April. a: 2# coal seam; b: Yeqing limestone; c: Shanfuqing limestone; d: Daqing limestone; e: 9# coal seam; f: Ordovician limestone; g: Ordovician limestone (50 m); h: Ordovician limestone (100 m).

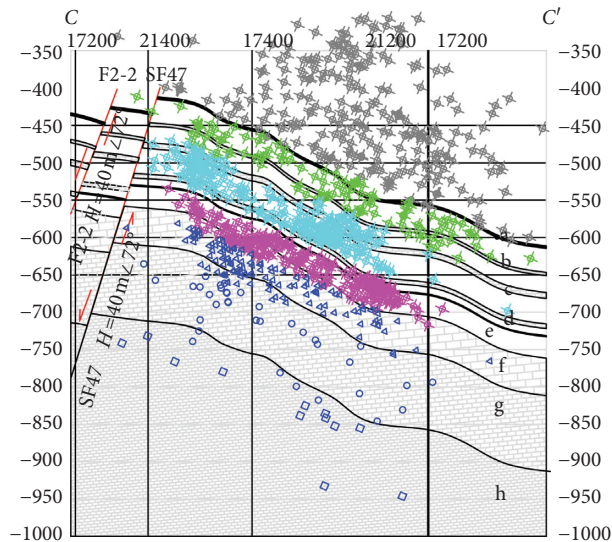


FIGURE 14: Distribution profile of microseismic events in May. a: 2# coal seam; b: Yeqing limestone; c: Shanfuqing limestone; d: Daqing limestone; e: 9# coal seam; f: Ordovician limestone; g: Ordovician limestone (50 m); h: Ordovician limestone (100 m).

the normal grouting area. When the working face passes the 1# grouting anomaly zone, the accumulated energy of microseismic events from June 26th to July 10th, 2019, is 16575760 J, of which the minimum energy of the microseismic event on July 9th is 7322 J and the maximum energy of July 5th is 13242289 J. The average is 1105051 J. When the working face passes the 2# grouting abnormal area, the accumulated energy of microseismic events from September 6th to September 20th, 2019, is 29697036 J, of which the lowest energy on September 6th is 1906 J and the highest energy on September 15th is 7154687 J, with an average of 1979802 J. Therefore, it can be seen that when the working

face gradually approaches and passes through the grouting abnormal area, the number of microseismic events will increase significantly. However, from the perspective of the energy of microseismic events, most of the increased microseismic events (when the working face approaches the grouting abnormal area) are mining activities. The roof collapse event caused by the incident is manifested as a large number of small energy events; when passing through the grouting abnormal area, the surrounding rock deep in the floor ruptures, resulting in microseismic events, manifested in the form of large energy and large number of events.

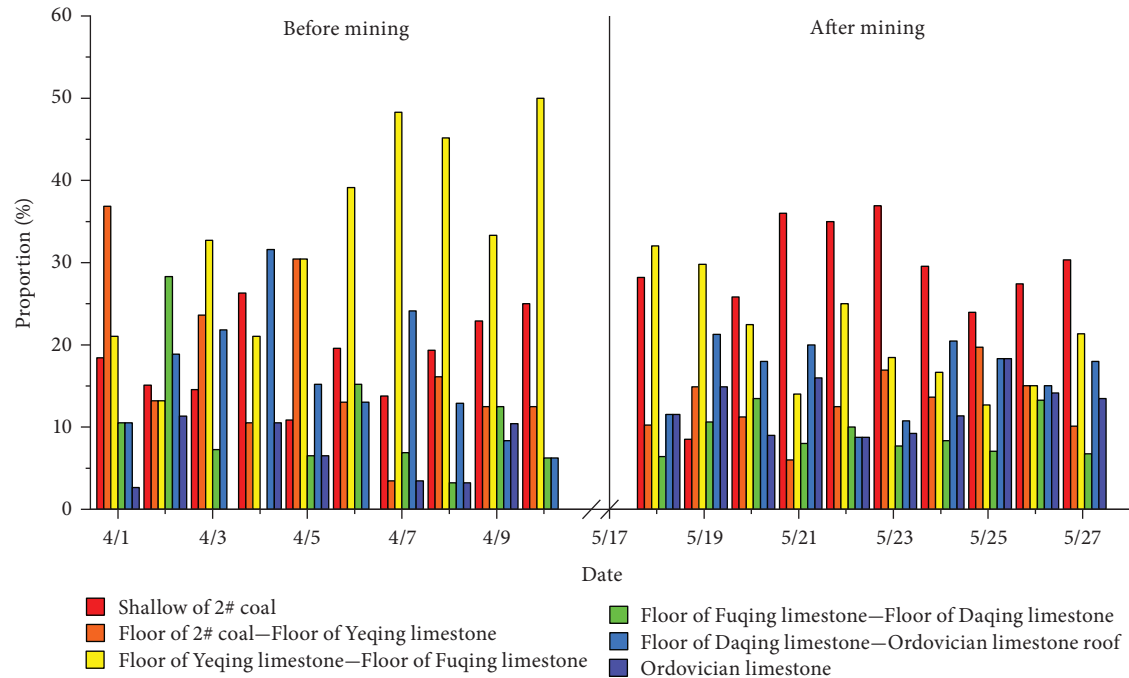


FIGURE 15: The proportion of microseismic events in each aquifer.

## 5. Conclusion

Through the quantitative processing of the data collected by the microseismic monitoring system, a spatial distribution diagram of microseismic events, a comparison diagram of the number of events, and a comparison diagram of amplitudes have been established, combined with the actual measurement before and after mining in the Wutongzhuang Coal Mine. The following can be concluded:

- (1) There is a large-scale weak zone in the floor of Yeqing-the floor of Fuqing area in front of the working face, and the cause of its dislocation is geological tectonic movement.
- (2) When the large-scale weak zone under the floor of the working face is misaligned, the microseismic feature is that the number of events is small, the event spatial distribution is concentrated, the energy magnitude is high, the amplitude is high, and the proportion of large events in microseismic events is greater than that of small ones. The characteristics of microseismic events caused by working face stopping are the following: the number of events is large, the distribution of events is relatively loose, the roof and floor are more distributed, but the energy level is small, the amplitude is also small, and the proportion of small and medium events in microseismic events is greater than that of large ones.

It can be seen that there is a weak zone dominated by faults under the floor of Wutongzhuang Coal Mine 182703 working face. When it is misaligned by the influence of geological tectonic movement, it will trigger a large microseismic event, which is different from the microseismic event caused by mining activities.

The microseismic event caused by the weak zone dislocation has a large energy level and is more dangerous to the mine. It will aggravate the changes in the stability of the floor aquifer during the mining and increase the possibility of water inrush from the coal floor. Therefore, measures such as floor grouting should be taken in time to enhance coal mine safety.

At the same time, it should also be noted that there is no tectonic activity caused by mining at the current working face excavation. Therefore, this article only compares and analyzes the microseisms caused by tectonic activity and those caused by mining. If there is tectonic activity caused by mining, it is inferred that the slight earthquake may be more severe.

## Data Availability

The data used to support the findings of this study are available from the corresponding author upon request.

## Conflicts of Interest

The authors declare that they have no conflicts of interest.

## Acknowledgments

This work was supported by the National Natural Science Foundation of China (51804309), Yue Qi Young Scholar Project (2019QN02) and Distinguished Scholar Project (2017JCB02) from China University of Mining and Technology (Beijing), and Joint Fund of State Key Laboratory of Coal Resources and Safe Mining and Beijing Outstanding Young Scientist Program (Grants nos. SKLCRSM20LH01 and BJWZYJH01201911413037).



## References

- [1] M. G. Qian, X. X. Liao, J. L. Xu et al., *The Key Layer Theory of Rock Formation Control*, China University of Mining and Technology Press, Xuzhou, China, 2003.
- [2] H. W. Jin, S. L. Yu, G. Xu et al., “Quantitative evaluation method of water hazard risk in coal mine,” *Journal of Safety Science and Technology*, vol. 16, no. 4, pp. 107–113, 2020.
- [3] Q. Wu, “Progress, problems and prospects of prevention and control technology of mine water and reutilization in China,” *Journal of China Coal Society*, vol. 39, no. 5, pp. 795–805, 2014.
- [4] Y. D. Jiang, K. K. Lu, Y. X. Zhao et al., “Similar simulation test for breakage law of working face floor in coal mining above aquifer,” *Chinese Journal of Rock Mechanics and Engineering*, vol. 30, no. 8, pp. 1571–1578, 2011.
- [5] Q. B. Zhao, “Ordovician limestone karst water disaster regional advanced governance technology study and application,” *Journal of China Coal Society*, vol. 39, no. 6, pp. 1112–1117, 2014.
- [6] X. X. Miao and H. B. Bai, “Water-resisting characteristics and distribution rule of carbonate strata in the top of Ordovician in North China,” *Journal of China Coal Society*, vol. 36, no. 2, pp. 185–193, 2011.
- [7] Z. L. Zhang, Y. F. Gao, J. Wu, and S.-M. Wei, “Discussion on the technical system of solid prevention and control on mine flooding,” *Journal of China Coal Society*, vol. 38, no. 3, pp. 378–383, 2013.
- [8] P. D. Zhang, W. Yan, W. Q. Zhang et al., “Study on factors influencing groundwater inrush induced by backstopping of a coal seam with a hidden fault,” *Journal of Mining & Safety Engineering*, vol. 35, no. 4, pp. 765–772, 2018.
- [9] X. H. Xie, B. Y. Su, Y. F. Gao et al., “Numerical study on water inrush above a confined aquifer in coal mining using hydrofracturing,” *Chinese Journal of Rock Mechanics and Engineering*, vol. 24, no. 6, pp. 987–993, 2005.
- [10] Z. M. Xu, Y. J. Sun, S. Y. Gong et al., “Monitoring and numerical simulation of formation of water inrush pathway caused by coal mining above confined water with high pressure,” *Chinese Journal of Rock Mechanics and Engineering*, vol. 31, no. 8, pp. 1698–1704, 2012.
- [11] J. B. Li and Y. C. Xu, “Mechanical model of the collapse column water inrush prevention considering the confined water seepage and its application,” *Journal of China University of Mining & Technology*, vol. 45, no. 2, pp. 217–224, 2016.
- [12] Q. B. Zhao, B. W. Zhao, Y. G. Fu et al., “Research on key technology to control Ordovician limestone water disaster on surface region of deep mining depth mine,” *Coal Science and Technology*, vol. 44, no. 8, pp. 14–20, 2016.
- [13] S. N. Dong, H. Wang, and W. Z. Zhang, “Judgement criteria with utilization and grouting reconstruction of top Ordovician limestone and floor damage depth in North China coal field,” *Journal of China Coal Society*, vol. 44, no. 7, pp. 2216–2226, 2019.
- [14] H. Wang, A. K. Luo, S. N. Dong et al., “Utilizability research on the top layer of Ordovician limestone as aquiclude of coal seam floor,” *China Coal*, vol. 44, no. 1, pp. 34–38, 2018.
- [15] Y. C. Xu, P. F. Li, W. Y. Guo et al., “Study on the damage of floor rock mass before mining in lower coal seam working face above the confined water,” *Metal Mine*, no. 10, pp. 119–125, 2019.
- [16] S. J. Ma, “Research on comprehensive geophysical prospecting technology for long coal face with high confined water,” *Mining Safety & Environmental Protection*, vol. 44, no. 6, pp. 65–68, 2017.
- [17] S. Y. Wei, X. M. Chen, and Y. C. Xu, “Research on roadway stabilization passing fault fractured zone above high water pressure of quifer,” *Coal Science and Technology*, vol. 41, no. S2, pp. 8–10, 2013.
- [18] J. T. Chen, Q. Wu, L. M. Yin et al., “Law of crack evolution in floor rock mass above high confined water,” *Coal Science and Technology*, vol. 46, no. 7, pp. 54–60, 2018.
- [19] Y. C. Xu and Y. B. Gao, “Theoretical analysis on working face cross-fault under high water pressure condition,” *Safety in Coal Mines*, vol. 46, no. 9, pp. 192–195, 2015.
- [20] X. Wang, W. Zhu, J. Xu, H. Han, and X. Fu, “Mechanism of overlying strata structure instability during mining below unconsolidated confined aquifer and disaster prevention,” *Applied Sciences*, vol. 11, no. 4, Article ID 1778, 2021.
- [21] H. T. Yu, S. Y. Zhu, and Y. Chen, “Comparative analysis of water inrush from the deep coal floor by mining above the confined aquifer,” *Journal of Mining Science*, vol. 55, no. 3, pp. 407–413, 2019.
- [22] H. F. Duan and L. J. Zhao, “New evaluation and prediction method to determine the risk of water inrush from mining coal seam floor,” *Environmental Earth Sciences*, vol. 80, no. 1, pp. 1–13, 2021.
- [23] Y. B. Li, “The new development of coal mine geophysical prospecting in China,” *China Mining Magazine*, vol. 21, no. S1, pp. 449–451, 2012.
- [24] Q. Ge and L. Han, “Direct imaging structure beneath the source using microseismic data,” *Chinese Journal of Geophysics-Chinese Edition*, vol. 62, no. 10, pp. 3988–3999, 2019.
- [25] J. F. Lou, F. Q. Gao, J. H. Yang et al., “Characteristics of evolution of mining-induced stress field in the longwall panel: insights from physical modeling,” *International Journal of Coal Science and Technology*, 2021.
- [26] H. Wang, Q. Guo, T. Alkhalifah et al., “Regularized elastic passive equivalent source inversion with full-waveform inversion: application to a field monitoring microseismic data set,” *Geophysics*, vol. 85, no. 6, pp. KS207–KS219, 2020.
- [27] X. J. Hao, W. S. Du, and Y. X. Zhao, “Dynamic tensile behaviour and crack propagation of coal under coupled static-dynamic loading,” *International Journal of Mining Science and Technology*, vol. 30, no. 5, pp. 659–668, 2020.
- [28] X. J. Hao, Y. N. Wei, and K. Yang, “Anisotropy of crack initiation strength and damage strength of coal reservoirs,” *Petroleum Exploration and Development*, vol. 48, no. 1, pp. 243–255, 2021.
- [29] X. J. Hao, Q. Zhang, and Z. W. Sun, “Effects of the major principal stress direction respect to the long axis of a tunnel on the tunnel stability: physical model tests and numerical simulation,” *Tunnelling and Underground Space Technology*, vol. 114, no. 7, Article ID 103993, 2021.
- [30] Y. Zheng, C. Chen, T. Liu et al., “A new method of assessing the stability of anti-dip bedding rock slopes subjected to earthquake,” *Bulletin of Engineering Geology and the Environment*, vol. 80, no. 4, pp. 1–18, 2021.
- [31] X. L. Zhang, R. S. Jia, X. M. Lu et al., “Identification of blasting vibration and coal-rock fracturing microseismic signals,” *Applied Geophysics*, vol. 15, no. 2, pp. 280–289, 2018.
- [32] D. Chen, N. Li, and E. Y. Wang, “Reliability assessment of the hydraulic fracturing process in coal mine based on the analysis of micro-seismic source parameters,” *Natural Resources Research*, vol. 16, 2021.
- [33] A. A. S. Amad, A. A. Novotny, and B. B. Guzina, “On the full-waveform inversion of seismic moment tensors,” *International Journal of Solids and Structures*, vol. 202, pp. 717–728, 2020.



- [34] R. Estay, J. Vallejos, C. Pavez, and M. Brönnner, "A comparison of characteristic parameters of mining related and tectonic seismic aftershock sequences," *International Journal of Rock Mechanics and Mining Sciences*, vol. 128, p. 11, 2020.
- [35] G. F. Liu, Q. Jiang, G. L. Feng, D. F. Chen, B. R. Chen, and Z. N. Zhao, "Microseismicity-based method for the dynamic estimation of the potential rockburst scale during tunnel excavation," *Bulletin of Engineering Geology and the Environment*, vol. 80, no. 5, pp. 3605–3628, 2021.
- [36] Y. Q. Guan, "Preliminary research on genesis of geothermal abnormalism in Wutongzhuang mine," *Coal Geology of China*, vol. 14, no. 3, pp. 37–39, 2002.
- [37] J. J. Zhao and Q. L. Liu, "Analysis on the geothermal origin in Wu Tong–ZhuangMine," *Hebei Coal*, no. 3, pp. 14–15, 2010.

## Research Article

# Mechanism and Control of Cable Breakage in a Roadway with Thick Top Coal in a Rockburst Mine

Ying Xu <sup>1</sup>, Xiekang Zhou,<sup>1</sup> and Weimei Gong<sup>2</sup>

<sup>1</sup>School of Mines, China University of Mining and Technology, Xuzhou 221116, China

<sup>2</sup>Shandong Tian'an Mining Group CO., Ltd., Jining 273155, China

Correspondence should be addressed to Ying Xu; [kdxuying@163.com](mailto:kdxuying@163.com)

Received 9 April 2021; Accepted 31 May 2021; Published 12 June 2021

Academic Editor: Zizheng Zhang

Copyright © 2021 Ying Xu et al. This is an open access article distributed under the Creative Commons Attribution License, which permits unrestricted use, distribution, and reproduction in any medium, provided the original work is properly cited.

Because top coal is not stable, a roadway with thick top coal often appears to mine pressure problems, such as bolt failure, cable breakage, and roof caving. In particular, these problems are more serious in rockburst mines. Based on a cable breakage case of No. 3 roadway in Xingcun coal mine, the paper analyzed the stress and elastic energy evolution law of surrounding rock and stress state of cable in the 3# roadway by means of the numerical simulation method. Thus, the cable breakage mechanism of the roadway with thick top coal in rockburst mine was revealed. Then, because surrounding rock grouting can reduce the stress concentration of surrounding rock and cable, surrounding rock grouting technology was proposed as control technology of cable breakage. Finally, parameters of surrounding rock grouting were designed and applied in the No. 3 roadway. The field results showed that surrounding rock grouting technology can be one of the solutions for cable breakage of roadway with thick top coal in rockburst mine. The research results of this paper can provide certain theoretical and practical value for mine pressure control of roadway.

## 1. Introduction

In China, with the increase of coal seam mining depth and intensity, there are more and more rockburst mines. According to statistics of the China National Administration of Mine Safety, there are currently about 138 rockburst mines. In these rockburst mines, the problem of mine pressure is more serious. Through the research and implementation of occurrence mechanisms, hazard pre-evaluation, real-time monitoring, and early warning, comprehensive prevention, and control, most rockburst problems are gradually being resolved [1–6]. However, due to unclear mechanisms and inadequate control technology of rockburst under complex conditions, there are still some rockburst phenomena, events, and accidents.

According to the consequences of damage, rockburst can be divided into general rockburst (rockburst phenomenon), destructive rockburst (rockburst events), and accidental rockburst (rockburst accidents). Many engineers and scholars pay more attention to the last two rockburst types because of their more severe damage and more casualties.

For instance, Zhu et al. [7] analyzed the rockburst accident in the first section of the working face of No. 3 and No. 4 mining area of layer 17, 3rd level north mining zone in Junde coalmine. Wu et al. [8] studied the occurrence of dynamic disasters during the horizontal sublevel mining of a steeply inclined and extremely thick coal seam in the Wudong coal mine. Yang [9] investigated rockburst accidents in some typical coal mines, and the behavior and predisposing factors of rockburst were analyzed. Li [10] analyzed several rockburst events and accidents of roadway floor in the Huating coalfield. Li et al. [11] studied the influence of geological and mining technology factors on the rockburst formation based on the analysis on the occurrence characteristics of rockburst in Qianqiu coal mine. Tian [12] researched the occurrence mechanism and prevention of rockburst of Xinzhouyao mine in Datong combining the mining condition and what type of rockburst happened. But the frequent occurrence of general rockburst (rockburst phenomenon) may be a precursor or gradually cause the occurrence of destructive rockburst (rockburst events) and accidental rockburst (rockburst accidents). Therefore, the

occurrence mechanism, characteristics, and prevention technology of general rockburst should also receive more attention, for example, high energy microseismic activity [13, 14], coal crack with firecrackers or thunder sound [15, 16], and breakage of bolt or cable [17, 18].

Cable breakage occurred frequently in the No. 3 roadway in Xingcun coal mine of Shandong Tian'an Mining Group CO., Ltd., during the roadway excavation. The paper aims at addressing the cause and solution of the case of general rockburst (rockburst phenomenon). Firstly, based on the analysis of stress and elastic energy evolution law of surrounding rock and stress state of cable, cable breakage mechanism was revealed. After that, grouting technology and parameters of cable breakage control were designed and applied in the No. 3 roadway. The research results can provide certain theoretical and practical value for mine pressure control of roadway, especially in rockburst mines.

## 2. A Case of Cable Breakage

*2.1. Situation of Roadway.* Xingcun coal mine, located in Jining city, is mining No. 3 coal seam with about 8.5 meters thick. Because of depth of more than 1100 m and many faults, initial ground stress is very high (Table 1). In addition, according to the appraisal report of rockburst tendency, the No. 3 coal seam and its roof have a weak rockburst tendency. So Xingcun coal mine is determined as a rockburst mine. The mine pressure on the working face and roadway appears to be severe. Particularly, there were several rockburst events in the past.

In the recent roadway excavation project, cable breakage occurred in the No. 3 exploration roadway in the seventh mining area of the Xingcun coal mine. The roadway adopted a straight wall circular arch section with 4300 mm width, 3000 mm straight wall height, and 700 mm circular arch height (Figure 1). Because it was driven along the floor of the coal seam, its roof was reserved with about 4.8 m top coal.

The support form of the No. 3 exploration roadway was bolt and cable support. The bolt was made of KMG500 heat-treated threaded steel with 22 mm diameter, 2400 mm length, and 180 kN anchoring force. The spacing and row spacing of bolts were 800 mm. In particular, 400 Nm pretightening torque was imposed on the bolts. The cable was a constant resistance cable of the H-MS-500-08 model with diameter of 22 mm, length of 8000 mm, constant resistance of 350 kN, and allowable deformation of 300 mm–500 mm [19, 20]. The spacing and row spacing of the cable was 800 mm. 250 kN pretightening force was imposed on the cable.

*2.2. Situation of Cable Breakage.* According to the field observations data that lasted for a month during the No. 3 roadway excavation, it was found that 34 cases of cable breakage (Figure 2) occurred in the range of 10 m–30 m from the heading of roadway and 9 cases of cable breakage occurred in the range of 30 m outside the heading. Among the 34 cases, all of them were roof cable, 15 cases on the arch of the roof, 12 cases on the right side of the roof, and 7 cases

on the left side of the roof. Among the 9 cases, 6 cases, 2 cases, and 1 case of cable breakage occurred on the arch of roof, the left side of the roof, and the right side of the roof, respectively.

In addition, the cable breakage had the following characteristics:

- (1) When a fully mechanized excavating machine was driving or coal cracked with firecrackers or thunder sound, which were two sources of dynamic load, the cable breakage occurred.
- (2) From the analysis of the shape and characteristics of the cable breakage, it can be judged as a “tension-shear” breakage.
- (3) The cable breakage was mainly concentrated between 1.5 m and 3.5 m away from the anchorage of the cable.
- (4) The constant resistors of cable were deformed and the constant resistance displacement was 0~200 mm which was less than the allowable deformation of cable.

*2.3. Deformation of Top Coal.* During the No. 3 roadway excavation, the top coal and rock of the roof were drilled and peeped at 15 m behind the heading of the roadway. From the peeping images of the boreholes (Figure 3), it can be seen that the top coal between 1.6 m and 4.0 m had poor integrity, severe separation, loose and broken parts, and well-developed fissures; vertical fissures between 4.0 m and 4.8 m were developed in the top coal. But the rock of the roof in 4.8 m~6.2 m had better integrity. In general, the thick top coal of the No. 3 roadway was damaged and loose, but the rock above top coal was more stable. In other words, the thick top coal of roadway was mainly deformed and difficult to control surrounding rock, which was like other thick top coal roadways in other coal mines [21, 22].

## 3. Cable Breakage Mechanism

*3.1. Stress Evolution Law of Roof.* The cable stress was the foundation of cable breakage. Therefore, the mechanism of cable breakage can be revealed by clarifying the causes and changes of cable stress. According to the interaction between anchor cable and surrounding rock [23], the reason for cable stress was the deformation of surrounding rock. Therefore, this paper firstly analyzed the stress evolution law of surrounding rock by numerical simulation method.

A three-dimensional numerical simulation model of the No. 3 roadway was established using FLAC3D software (Figure 4). The horizontal width, strike length, and vertical height of the model were  $X \times Y \times Z = 50 \text{ m} \times 30 \text{ m} \times 47.5 \text{ m}$ . For the accuracy of calculation, the grids of adjacent roadways were densely divided, and other grids were relatively sparse. The total number of nodes was 226,414 and the total number of units was 214,800. The front, rear, left, right, and top surfaces of the model used a stress boundary, and initial ground stresses (Table 1) were applied on the surfaces. The bottom surface used displacement boundaries. The

TABLE 1: Initial ground stress of Xingcun coal mine.

Measuring point	Depth (m)	$\sigma$ Maximum principal stress			$\sigma$ Intermediate principal stress			$\sigma$ Minimum principal stress		
		Value (MPa)	Direction (°)	Inclination (°)	Value (MPa)	Direction (°)	Inclination (°)	Value (MPa)	Direction (°)	Inclination (°)
No. 1	-1186	68.46	152.86	8.35	49.63	-115.07	13.86	35.23	-147.35	-73.73
No. 2	-1156	68.65	153.87	10.26	54.69	65.57	7.16	34.92	121.25	-77.44

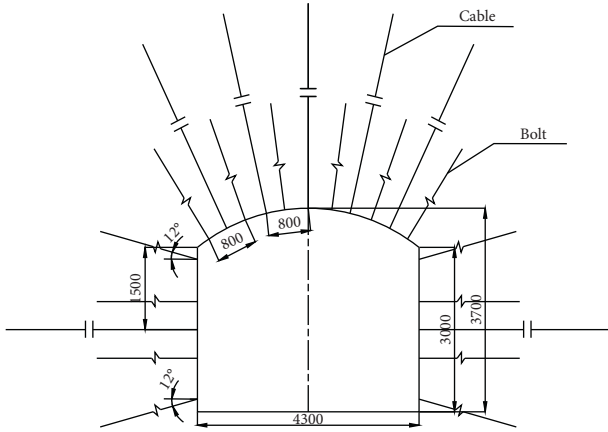


FIGURE 1: Section size and support parameters of No. 3 exploration roadway (unit: mm).

Mohr-Coulomb constitutive model was used for the constitutive relationship of coal and rock, and Table 2 showed their mechanical parameters.

The excavation of the roadway made the surrounding rock lose the original equilibrium state and caused the stress redistribution within a limited range; that is, the stress in the surrounding rock had a continuous change process in time and space [24]. For the stress evolution in space, the surrounding rock within 10 meters above the roadway arch was selected for stress monitoring. For the stress evolution in time, the roadway advancing was simulated by the step-by-step excavation method, and the step advancing distance was 3 m.

According to the numerical simulation results (Figure 5), horizontal stress evolution law was as follows:

- (1) When the roadway was excavated forward 3 m, the horizontal stress peak in the same cross-section of the roof was 35.45 MPa. When the roadway was excavated forward 9 m, the peak stress was 38.54 MPa. When the roadway was excavated forward 18 m, the peak stress was 39.42 MPa. In a word, horizontal stress peak in the same cross-section of the roof had a tendency to increase with the roadway excavation.
- (2) When the roadway was excavated forward 6 m, horizontal stress peak was located at 2.5 m in the top coal. When the roadway was excavated forward 15 m, horizontal stress peak was located at 3.0 m in the top coal. In a word, horizontal stress peak shifts to deep with the roadway excavation.

In addition, according to the numerical simulation results (Figure 6), vertical stress evolution laws were as follows: when the roadway was advanced for 3 m, the vertical stress

peak was 64.69 MPa. When the roadway was advanced for 9 m, the vertical stress peak was 57.35 MPa. When the roadway was advanced for 18 m, the vertical stress peak was 55.43 MPa. In a word, with the roadway advancing, the vertical stress peak at the same position of the roadway roof gradually decreases.

From the perspective of the evolution law of horizontal and vertical stress on the roof of the roadway, as the roadway excavation, the horizontal stress peak increased and finally tended to balance and shifted to the deep. Particularly the horizontal stress peak no longer spread to the deep when it was transferred to a depth of about 3 m in top coal. But the vertical stress peak gradually decreases as the roadway advances and eventually tends to balance. This causes the stress difference between the horizontal and vertical stress to gradually increase as the roadway excavation continues. The maximum stress difference occurred at about 3.5 m in depth in top coal, which was about the place of cable breakage.

**3.2. Elastic Energy Evolution Law of Roof.** The change of elastic energy in the surrounding rock of roadway was the main cause of rockburst phenomenon, incident, or accident in a roadway [25–28]. The elastic energy of surrounding rock of roadway is

$$E_0 = \frac{[\sigma_1^2 + \sigma_2^2 + \sigma_3^2 - 2\mu(\sigma_1\sigma_2 + \sigma_1\sigma_3 + \sigma_3\sigma_2)]}{2E}, \quad (1)$$

where  $E$  is the modulus of elasticity,  $\mu$  is Poisson's ratio,  $\sigma_1$  is the maximum principal stress,  $\sigma_2$  is the intermediate principal stress, and  $\sigma_3$  is the minimum principal stress.

Based on the numerical simulation model shown in Figure 4, the elastic energy evolution law of the roof was obtained (Figure 7). The following can be seen:

- (1) The elastic energy of the shallow surrounding rock was released instantly after the roadway was excavated, and the elastic energy accumulated in the deep coal and rock. In particular, the elastic energy accumulation range was between 3 m and 4 m in depth in the top coal.
- (2) As the roadway excavation, the elastic energy in the range of 10 m in depth of roof was released, and when the roadway advanced distance changed from 3 m to 6 m, the elastic energy released at the area around 3.5 m in depth in the top coal was the largest. The position was exactly the place of cable breakage.

**3.3. Cable Stress Distribution.** The force of the cable that exceeded the ultimate strength of the anchor cable was the most direct cause of cable breakage. Based on the numerical





FIGURE 2: Cable breakage of No. 3 exploration roadway.

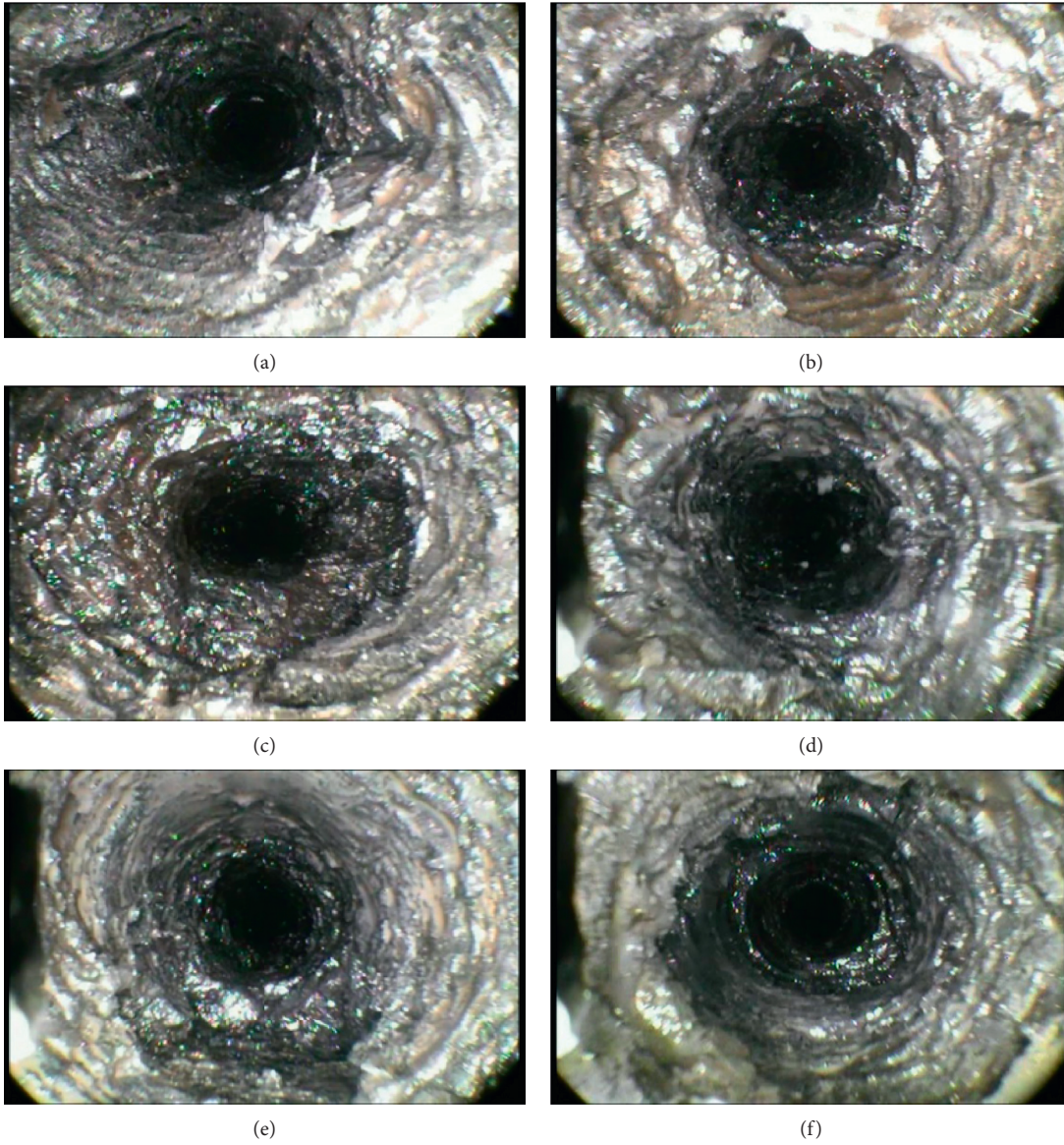


FIGURE 3: Continued.





(g)

FIGURE 3: Borehole peep image under different borehole depths. (a) 1.6 m. (b) 2.5 m. (c) 3.1 m. (d) 4.0 m. (e) 4.3 m in depth. (f) 4.8 m in depth. (g) 6.2 m in depth.

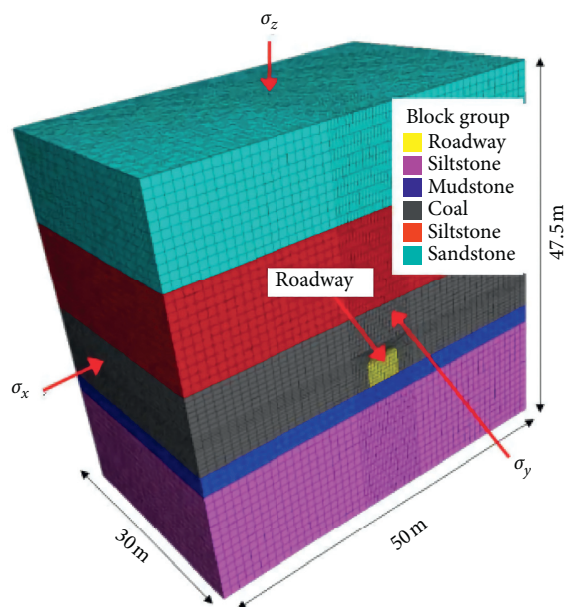


FIGURE 4: Three-dimensional numerical simulation model of the No. 3 roadway.

simulation model shown in Figure 4, cable stress distribution under different excavation distances of roadway was obtained (Figure 8). The following can be seen:

- (1) Whether the roadway excavation distance was 3 m, 6 m, 9 m, and 12 m, the cable stress increased first and then decreased from the surface to the deep part of the top coal and the rock, and the concentrated part of the larger axial force of the cable was within the range of 2 m~4 m.
- (2) When the roadway was advanced for 3 m, 6 cables with an axial force greater than  $1.4 \times 10^6$  MPa appeared. When the roadway advanced for 9 m, 12 cables with an axial force greater than  $1.4 \times 10^6$  MPa appeared. When the roadway advanced for 12 m, there were 14 cables with an axial force greater than  $1.4 \times 10^6$  MPa, which was 2 times more than that which appeared when the roadway advanced for 9 m. In a word, as the roadway advanced, more and more

cables with an axial force greater than  $1.4 \times 10^6$  MPa appeared.

- (3) Because the length of the bolt was 2.4 m which was in the top coal range, bolt stress was uniform and little change as the roadway excavation. In other words, the bolts of the roof were not broken, but the cable was broken. The roadway scene also proved the phenomenon.

Through the above analysis of stress distribution, elastic energy distribution, and cable stress, cable breakage mechanism was revealed: in the process of roadway excavation, the stress was constantly redistributed and the stress was constantly shifting to the deep part of the roof. The vertical stress dropped at about 3.5 m in depth in top coal of the roadway with a large descending gradient, and the horizontal stress reached its peak. Especially when the surrounding rock in the load-bearing area suddenly broke, due to the large amount of elastic energy that accumulated here, the surrounding rock in this area would be dislocated instantly, and the cable would be broken in the area where the axial force was concentrated.

## 4. Control of Cable Breakage

*4.1. Control Mechanism of Surrounding Rock Grouting.* Surrounding rock grouting technology can allow the grout to penetrate the fissures in the surrounding rock, thereby improving the integrity, elastic modulus, and strength of the surrounding rock. In addition, it can transform the two-dimension force-bearing fractured structural surface due to the influence of excavation or mining into three-dimension force-bearing [29–31]. The following was a comparative analysis on the stress distribution of surrounding rock, the elastic energy of surrounding rock, and stress distribution of cable before and after surrounding rock grouting.

*4.1.1. Comparison of Horizontal Stress Evolution.* The mechanical parameters of the top coal and the rock with grouting were set larger than that without grouting in the numerical simulation model shown in Figure 4. Figure 9 was a comparison of the calculation results of horizontal stress

TABLE 2: Mechanical parameters of coal and rock.

Lithology	Density/kg·m <sup>-3</sup>	Bulk modulus/GPa	Shear modulus/GPa	Friction/°	Cohesion/MPa	Tensile strength/MPa
Sandstone	2620	20.5	12.5	39	13	2.5
Siltstone	2640	16.1	10.2	35	12	1.9
Coal	1800	14.3	8.2	38	8	1.2
Mudstone	2490	15.6	8.8	36	11	2.2
Siltstone	2660	18.2	11.2	35	12	1.9

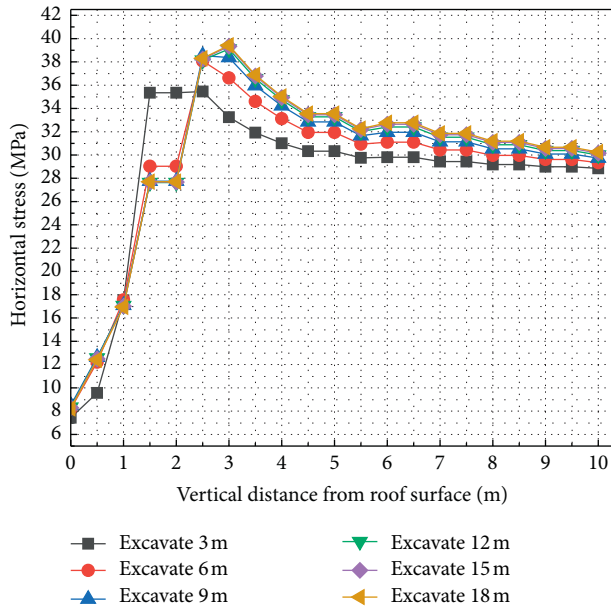


FIGURE 5: Horizontal stress distribution under different excavation distance.

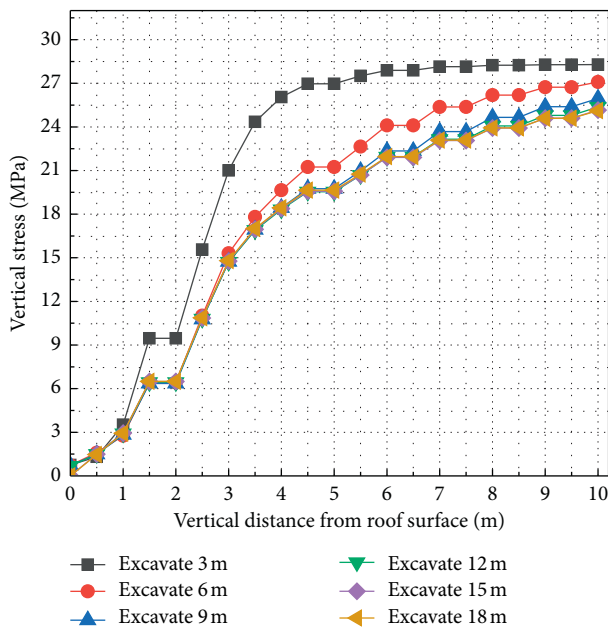


FIGURE 6: Vertical stress distribution under different excavation distance.

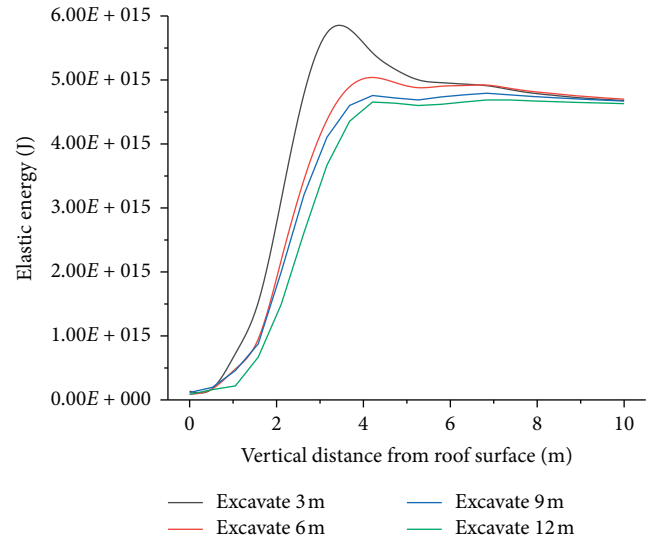


FIGURE 7: Elastic energy distribution under different excavation distance.

evolution. After surrounding rock grouting, the horizontal stress in the range of 0.5 m~3.5 m of the roof was relatively uniform. In addition, as the roadway excavation continues, the horizontal stress of the roof surface was continuously decreasing, which was consistent with the evolution law before surrounding rock grouting, but the difference was that the stress value of the roof surface did not appear to be greatly reduced and approached lower value but gradually approached the higher stress value after surrounding rock grouting.

4.1.2. Comparison of Vertical Stress Evolution. Figure 10 shows a comparison of the calculation results of vertical stress evolution. Whether it was grouted or not, as the roadway excavation continues, the vertical stress within 10 m above the roof surface gradually decreased as a whole. But compared to that without surrounding rock grouting, the vertical stress drops evenly within the range of 3 m~4 m of roof after surrounding rock grouting, and there was no instantaneous sharp drop in the vertical stress. Another aspect, regardless of whether there is surrounding rock grouting or not, as the roadway excavation continues, the vertical stress of the surrounding rock within 1 m above the roof surface was gradually decreasing, but there was no situation that the vertical stress tended to be of very low value without surrounding rock grouting. For example, at the part 1 m deep of the top coal, the vertical stress without

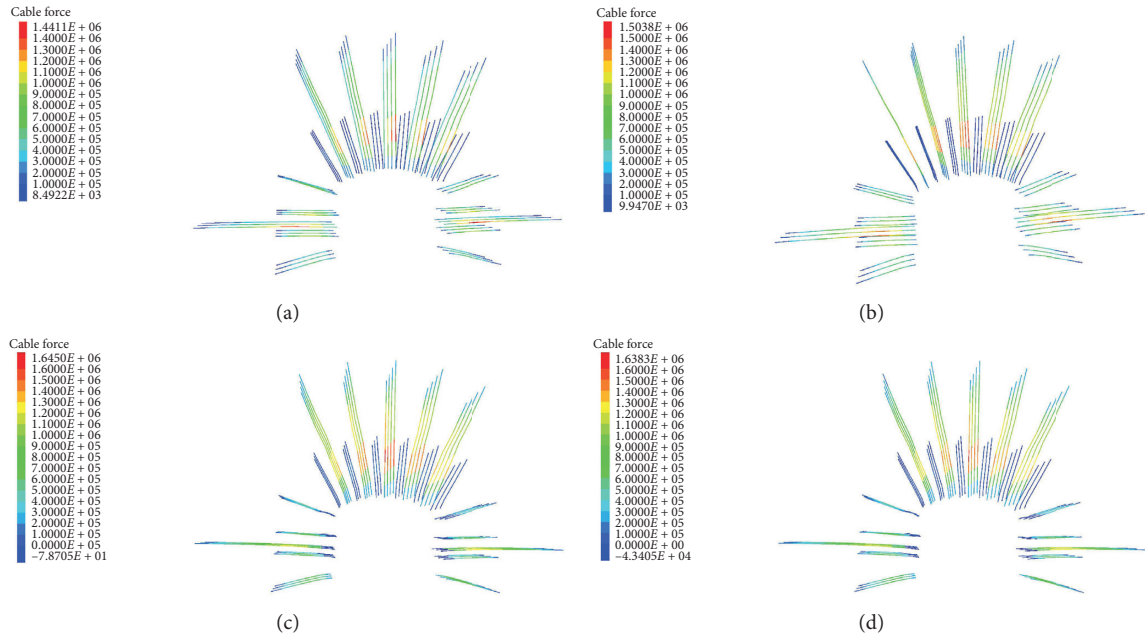


FIGURE 8: Stress condition of cable under different excavation distance. (a) Excavate 3 m. (b) Excavate 6 m. (c) Excavate 9 m. (d) Excavate 12 m.

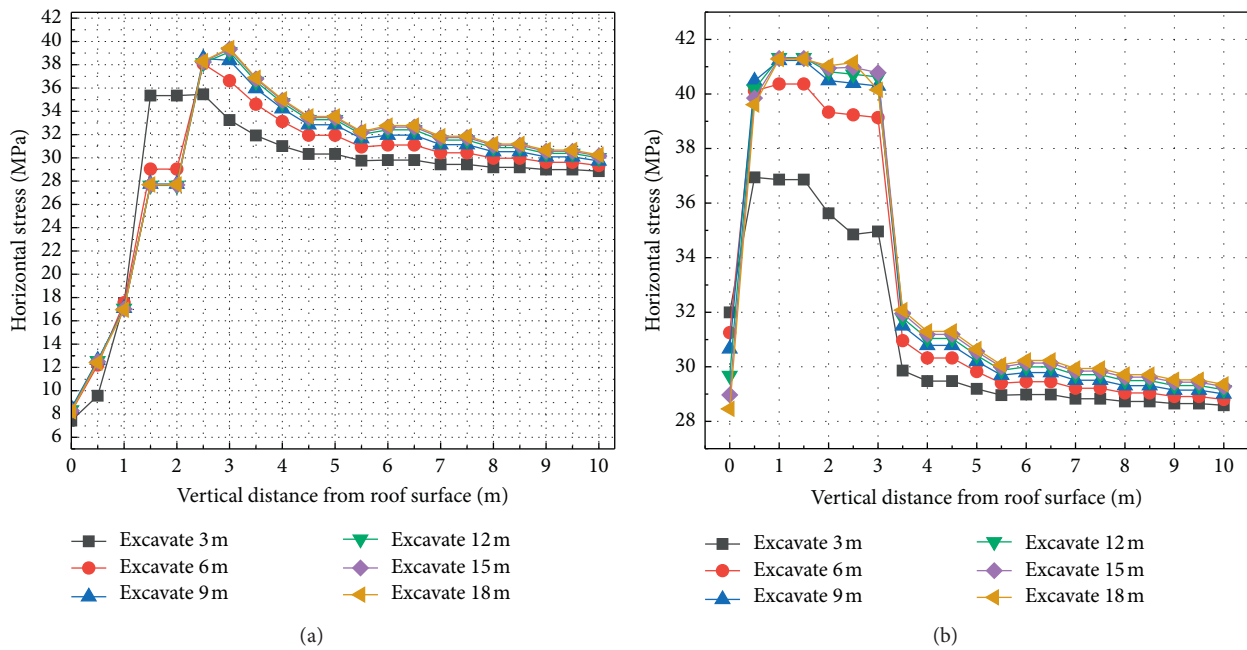


FIGURE 9: Horizontal stress evolution under different excavation distance without and with surrounding rock grouting. (a) Without surrounding rock grouting. (b) With surrounding rock grouting.

surrounding rock grouting was about 3 MPa, and the vertical stress was at 9 MPa after surrounding rock grouting.

4.1.3. Comparison of Elastic Energy Evolution. Figure 11 was a comparison of the calculation results of the elastic energy. When the roadway surrounding rock was not grouted, as the roadway excavation, the elastic energy of the surrounding rock within 1 m of the shallow part of the roof tended to

zero, and a large amount of elastic energy accumulated within 3 m~4 m of the roof. After the surrounding rock was reinforced by grouting, although the surrounding rock energy was dissipated within 1 m of the shallow part of the roof, the elastic energy dissipation in this range was less compared to that without surrounding rock grouting. In addition, the elastic energy distribution of the surrounding rock was even within the range of 1.8 m~3 m of the roof, and the peak value was reduced compared to that without

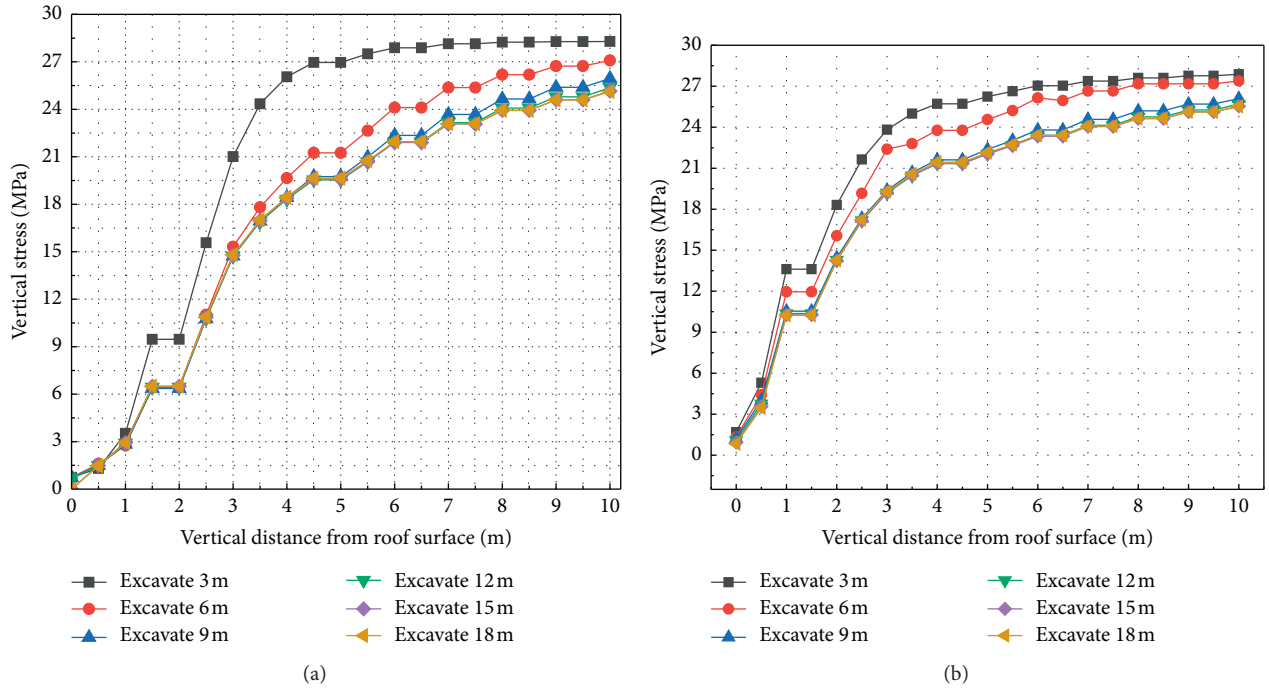


FIGURE 10: Vertical stress evolution under different excavation distance without and with surrounding rock grouting. (a) Without surrounding rock grouting. (b) With surrounding rock grouting.

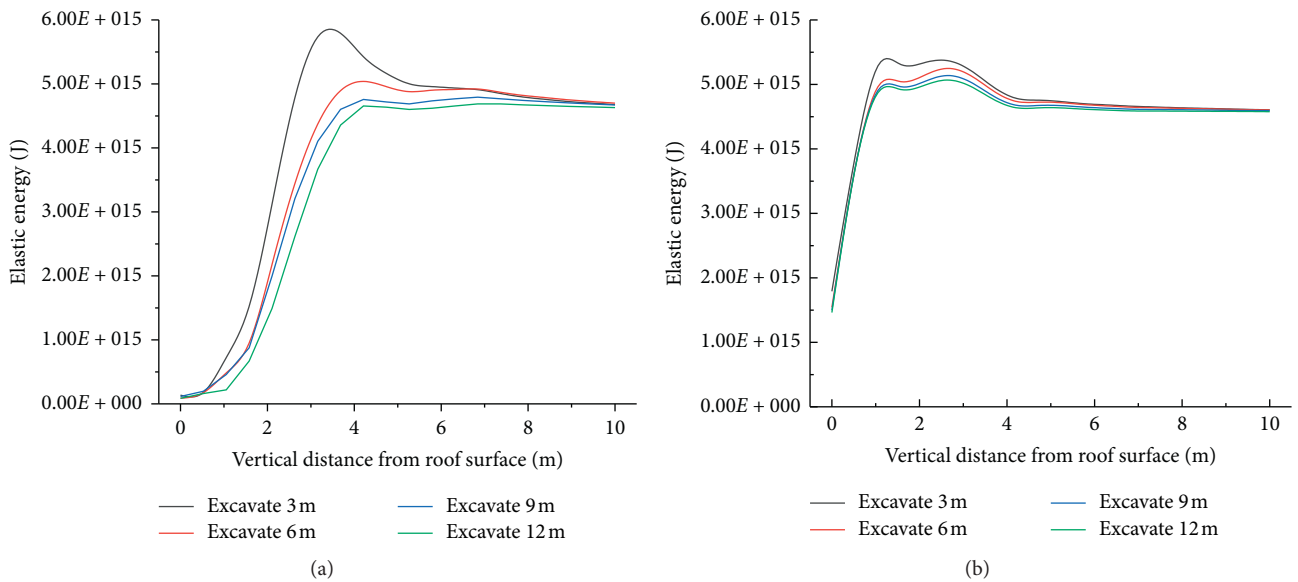


FIGURE 11: Elastic energy evolution under different excavation distance without and with surrounding rock grouting. (a) Without surrounding rock grouting. (b) With surrounding rock grouting.

surrounding rock. As the roadway excavation, the degree of the elastic energy dissipation in this range was smaller and even than that without surrounding rock grouting.

**4.1.4. Cable Stress Distribution after Surrounding Rock Grouting.** Cable stress distribution after surrounding rock grouting under different roadway excavation distance was

obtained (Figure 12). Compared with that without surrounding rock grouting (Figure 8), the following can be seen:

- (1) After the surrounding rock was grouted, the cable was uniformly stressed in the middle, and there was no axial force concentration, and the value was smaller than that without surrounding rock grouting.



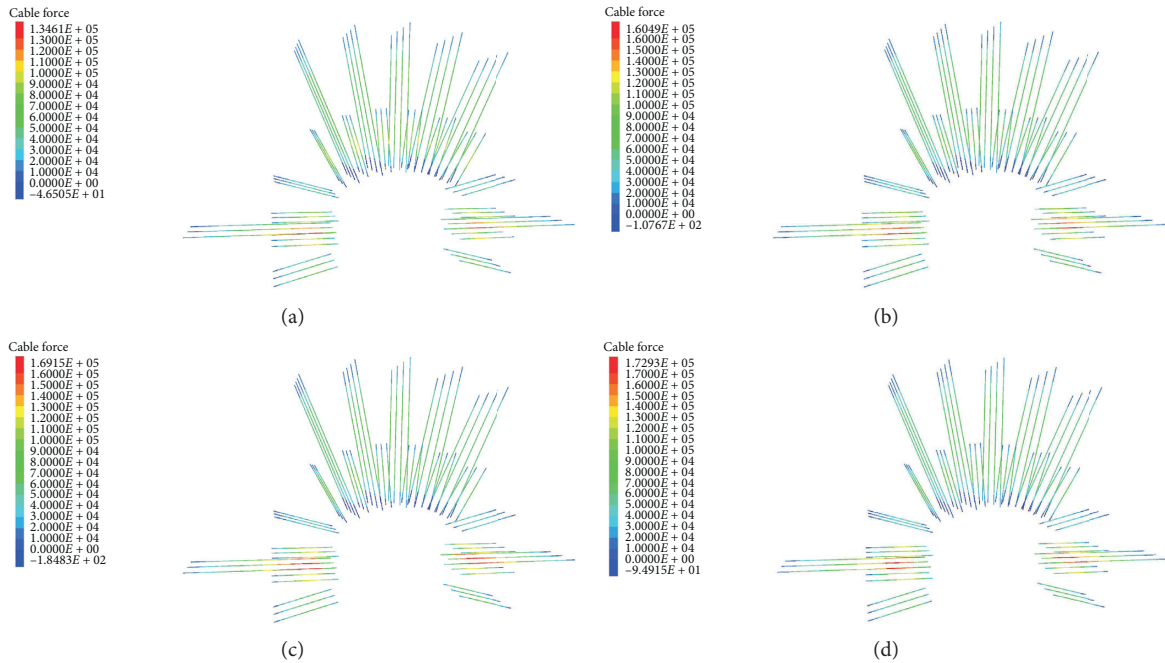


FIGURE 12: Cable stress distribution under different excavation distance with surrounding rock grouting. (a) Excavate 3 m. (b) Excavate 6 m. (c) Excavate 9 m. (d) Excavate 12 m.

(2) After the surrounding rock was grouted, the cables with larger axial force were rib cables, but the maximal axial stress value of the rib cables was still smaller than that without surrounding rock grouting.

Through the above analysis, surrounding rock grouting can reduce the stress concentration of surrounding rock and cable. So surrounding rock grouting technology was proposed as control technology of cable breakage.

#### 4.2. Parameters of Surrounding Rock Grouting

**4.2.1. Grouting Material.** According to the above borehole peeking results of the No. 3 roadway, it can be seen that the top coal of the roadway was loose and broken, and cracks were developed. So cement-based grouting material can be selected for surrounding rock grouting of the roadway [32]. Particularly, the grouting material had a wide source and low price. The water-cement ratio was 0.8 : 1.

**4.2.2. Grouting Hole Design.** The reasonable design of surrounding rock grouting holes can effectively shorten the work, reduce the number of grouting materials, and increase the utilization rate of the grout. The grouting method of the No. 3 roadway used a combination of shallow hole grouting and deep hole grouting (Figure 13). The length of the shallow hole grouting pipe was 2600 mm (in the range of the fissure development zone), the radius was 15 mm, and the spacing and row spacing were 1300 mm. The length of the deep hole grouting pipe was 4800 mm (in the range of the small fissure zone), the radius was 10 mm, and the spacing and row spacing were 1300 mm.

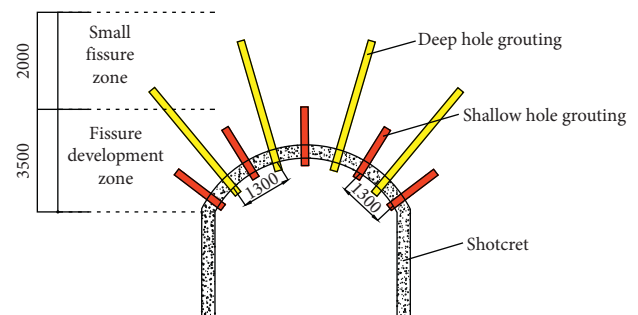


FIGURE 13: Schematic diagram of grouting hole design (unit: mm).

**4.2.3. Grouting Pressure.** The pressure selected for surrounding rock grouting was to ensure that the grout can penetrate the fissures of the surrounding rock, but the grouting pressure should not be too high or too small [33]. If the grouting pressure was too high, problems such as roof falling will easily occur. If the grouting pressure was too small, the grout cannot be diffused in the surrounding rock due to insufficient power, and the grouting cannot achieve the expected effect of reinforcement. So the shallow hole grouting of the surrounding rock of the No. 3 roadway used 1 MPa grouting pressure, and the deep hole grouting used 1.5 MPa grouting pressure.

**4.2.4. Shotcrete.** The cement of concrete strength grade C20 was used to shoot out the surface of the No. 3 roadway to close the fissure on the surface of the surrounding rock of the roadway to ensure that the injected grout will not flow out and to improve the grouting efficiency and effect. The water-cement ratio was 0.5, and the thickness of the shotcrete was 60 mm.



### 5. Application

In order to verify the control effect of surrounding rock grouting technology on cable breakage, the design parameters were applied to the new excavation section of No. 3 roadway in Xingcun coal mine and the displacement of the surrounding rock and the cable force were monitored.

In the early stage of roadway excavation, the surface displacement of the surrounding rock near the heading of the roadway changes quickly. When the excavation distance was about 20 m from the heading, the surface displacement of the roadway started to converge stably. The convergence displacement of the two ribs was stabilized at about 53 mm, and the convergence displacement of the roof and floor was stabilized at about 97 mm (Figure 14). The deformation of the roadway was small.

In order to check the integrity of the surrounding rock of the roadway after grouting, deep base point displacement meters were used to monitor the displacement of the surrounding rock of the roadway at different depths. The first measuring point was arranged at a distance of 5 m from the heading of the roadway, and the next measuring point was arranged every 20 m of the roadway. There were 3 measuring points in total, and the average value of the displacement value of the same depth measured by each measuring point was regarded as the final result. Figure 15 showed that when the measuring point was close to the heading, the displacement of each depth of the roof of the roadway increased faster and finally stabilized gradually. According to the data, the amount of separation in the deep part of the surrounding rock of the roadway was smaller, and the shallow part was slightly larger. But after a certain period of time, they all tend to be stable, and the maximum displacement was on the surface of the roadway. The maximum displacement of the roof was 38 mm.

For the monitoring of the force of cable, the force of each part of the cable decreased first, then increased, and then stabilized (Figure 16). The axial force of the cable on the roof arch was the largest, and the maximum was 190.6 kN. The axial force of cable at the corner of the roadway was the next, and the maximum was 171.5 kN, and the anchoring force of the cable at the rib was the smallest, and the maximum was 151 kN. The axial force value of all the cable did not exceed the ultimate strength of the cable. More importantly, there was no cable breakage.

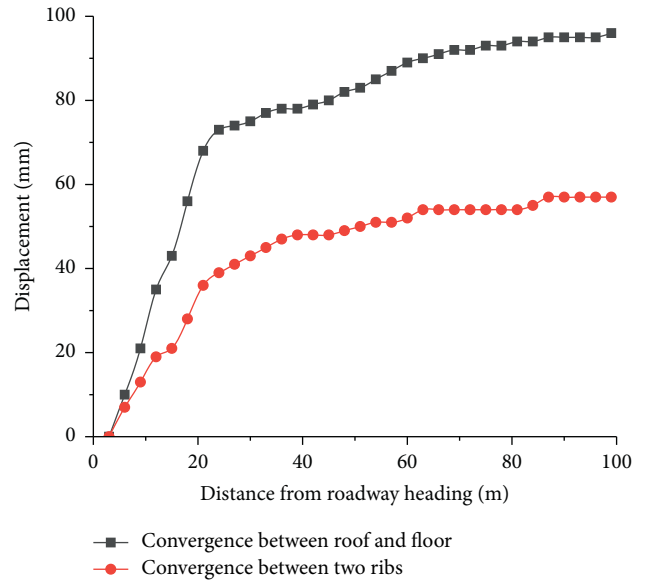


FIGURE 14: Convergence displacement of roadway surrounding rock surface in the No. 3 roadway.

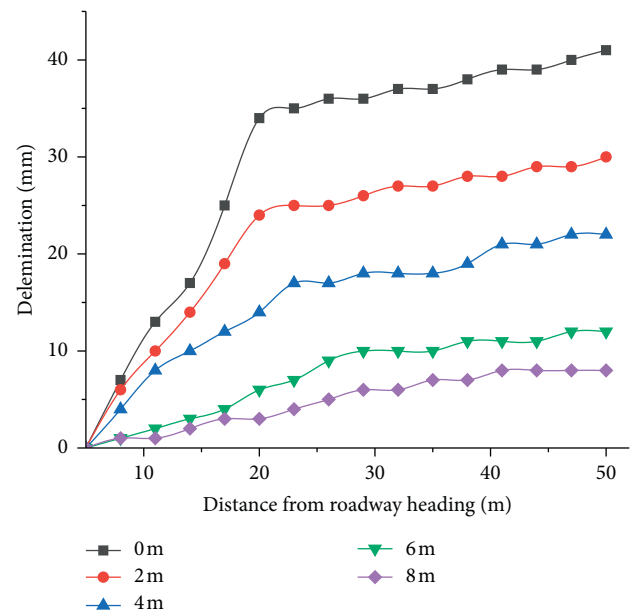


FIGURE 15: Displacement of surrounding rock at different depth in the No. 3 roadway.

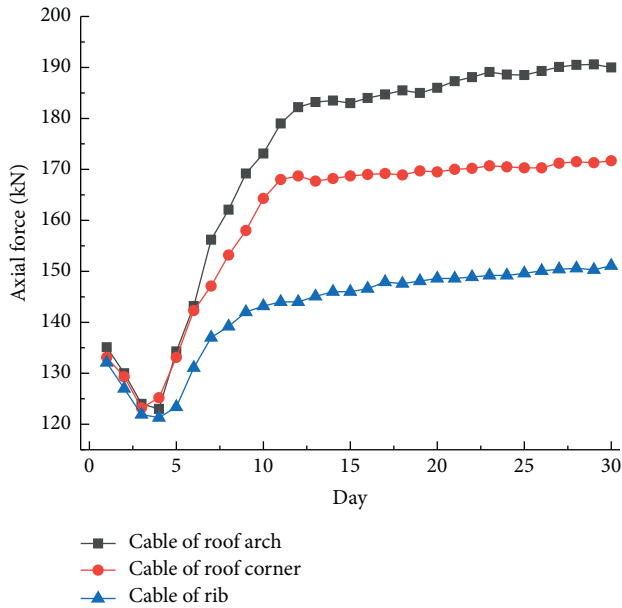


FIGURE 16: Axial force of the cable in the No. 3 roadway.

## 6. Conclusion

The study was mainly focused on the mechanism and control of the case of cable breakage in the No. 3 exploration roadway in Xingcun coal mine. The main conclusions in this paper are summarized as follows:

- (1) When the roadway was excavated forward, there was a stress adjustment process in which the horizontal stress continuously increases and the vertical stress continuously decreases in the surrounding rock. The location of the largest difference between the horizontal stress and the vertical stress was about the position where the maximum axial force and breakage of cable occurred.
- (2) When the roadway was excavated forward, the elastic energy of the surrounding rock was released from shallow part to deep part of roof and accumulated in the top coal at a depth of 3 m-4 m. The top coal and its accumulated elastic energy were the main factors of cable breakage.
- (3) When the roadway was affected by dynamic load, a large amount of accumulated elastic energy in the top coal was released, and then the cable was broken at the position of maximum axial force.
- (4) The surrounding rock grouting technology can make top coal improve the stress and elastic energy distribution, which was conducive to the uniform force of the cable and the prevention of cable breakage. The results of the field measurements of the No. 3 roadway showed there was no cable breakage phenomenon and guaranteed the normal use of the No. 3 roadway.

## Data Availability

The data used to support the findings of this study are included within the article.

## Conflicts of Interest

The authors declare that they have no conflicts of interest.

## Acknowledgments

The financial support by the Fundamental Research Funds for the Central Universities (2020ZDPYMS16) and A Project Funded by the Priority Academic Program Development of Jiangsu Higher Education Institutions for this work are gratefully acknowledged.


## References

- [1] Q. Qi and L. Dou, *Theory and Technology of Rockburst*, China University of Mining and Technology Press, Xuzhou, China, 2008.
- [2] L. Dou, S. Wang, S. Gong et al., "Cloud platform of rock-burst intelligent risk assessment and multi-parameter monitoring and early warning," *Journal of China Coal Society*, vol. 45, no. 6, pp. 2248–2255, 2020.
- [3] Q. Qi, S. Zhao, H. Li et al., "Several key problems of coal bump prevention and control in china's coal mines," *Safety in Coal Mines*, vol. 51, no. 10, pp. 135–143, 2020.
- [4] F. Jiang, Y. Liu, Y. Zhang, J. Wen, W. Yang, and J. An, "A three-zone structure loading model of overlying strata and its application on rockburst prevention," *Chinese Journal of Rock Mechanics and Engineering*, vol. 35, no. 12, pp. 2398–2408, 2016.
- [5] S. Wang, W. Ju, J. Pan, and C. Lu, "Mechanism of energy partition evolution of excavation roadway rockburst in coal seam under tectonic stress field," *Journal of China Coal Society*, vol. 44, no. 7, pp. 2000–2010, 2019.
- [6] Y. Pan, L. Dai, G. Li et al., "Study on compound disaster of rockburst and roof falling in coal mines," *Journal of China Coal Society*, vol. 46, no. 1, pp. 112–122, 2021.
- [7] S. Zhu, Y. Ma, F. Jiang et al., "Mechanism of rockburst in the bottom coal seam of super high seam with overall slippage and instability," *Journal of Mining & Safety Engineering*, vol. 38, no. 1, pp. 31–40, 2021.
- [8] Z. Wu, P. Pan, S. Zhao et al., "Study on the mechanism of rockbursts caused by "roof-rock pillar" in mining steeply-inclined and its prevention and treatment," *Journal of China Coal Society*.
- [9] Y. Yang, *Mechanism and Prevention Technology of Coal Bumps for Highly-Stressed Coal in Deep Mining Under Dynamic Disturbance*, China University of Mining & Technology, Beijing, China, 2016.
- [10] P. Li, *Study on Bursting Mechanism of Gateways Floor and Protection Methods in Huating Coal Field*, University of Science and Technology Beijing, Beijing, China, 2015.
- [11] B. Li, W. Xiangzhi, and Y. Ren, "Analysis on occurrence characteristics and causes of rockburst in qianqiu coal mine," *Coal Engineering*, vol. 46, no. 1, pp. 83–86, 2014.
- [12] L. Tian, *Research on the Occurrence Mechanism and Prevention of Compression Type Rockburst in Xinzhouyao Mine*, Liaoning Technical University, Fuxin, China, 2013.
- [13] C. Dong, E. Wang, and L. Nan, "Analysis of microseismic source parameters and focal mechanism in qianqiu coal mine," *Journal of China Coal Society*, vol. 44, no. 7, pp. 2011–2019, 2019.
- [14] X. Tian, Z. Li, and D. Song, "Study on microseismic precursors and early warning methods of rockbursts in a working face,"

- Chinese Journal of Rock Mechanics and Engineering*, vol. 39, no. 12, pp. 2471–2482, 2020.
- [15] X. Du, Y. Jiang, and T. Wang, “Temporal and spatial distribution of rockburst in China,” *Safety in Coal Mines*, vol. 48, no. 8, pp. 186–189, 2017.
- [16] J. Wang, B. Li, and T. Zhang, “Research of action range and mechanism of coal-gun phenomenon in drifting process,” *Industry and Mine Automation*, vol. 33, no. 7, pp. 39–41, 2010.
- [17] H. Jing, J. Wu, Q. Yin et al., “Particle flow simulation of rockburst and roof fall of deep coal roadway under dynamic disturbance,” *Chinese Journal of Rock Mechanics and Engineering*, vol. 39, pp. 3475–3487, 2020.
- [18] A. Wang, Y. Pan, and B. Zhao, “Numerical analysis on the failure mechanism of bolted rock structure under impact load,” *China Earthquake Engineering Journal*, vol. 39, no. 3, pp. 417–424, 2017.
- [19] M.-C. He, J. Wang, X.-M. Sun, and X.-J. Yang, “Mechanics characteristics and applications of prevention and control rockbursts of the negative poisson’s ratio effect anchor,” *Journal of China Coal Society*, vol. 39, no. 2, pp. 214–221, 2014.
- [20] G. Zhang, E. Wang, and L. Xu, “Mechanical characteristics of high constant resistance and large deformation anchor rope in coal mines,” *Chinese Journal of Rock Mechanics and Engineering*, vol. 35, no. 10, pp. 2033–2043, 2016.
- [21] L. Lei, *Research on the Catastrophe Mechanism and Control Technology of Roadway with Large Cross Section and Top Coal*, China University of Mining and Technology, Xuzhou, China, 2013.
- [22] Y. Peng, J. Yang, J. Cheng et al., “Deformation mechanism and control technology of large section gateway with top coal in coal mine,” *Journal of Mining Science and Technology*, vol. 2, no. 5, pp. 439–448, 2017.
- [23] J. Hu, M. He, Z. Li et al., “Numerical study on NPR cable-rock interaction using 3D discrete-continuous coupling method,” *Engineering Mechanics*, vol. 37, no. 7, pp. 27–34, 2020.
- [24] Z. Zhang, *The Study on Temporal and Spatial Evolution Characteristics of Surrounding Rock Stress Shell of Deep Roadway and Supporting Mechanism*, China University of Mining & Technology, Beijing, China, 2018.
- [25] S.-T. Zhu, F.-X. Jiang, X.-Y. Wang et al., “Energy accumulation characteristics and rockburst mechanism of surrounding rock at heading face of extra-thick coal seam,” *Chinese Journal of Geotechnical Engineering*, vol. 41, no. 11, pp. 2071–2078, 2019.
- [26] J. Yang, *Study on Evolutionary Mechanism of Energy Field and Support Mechanism of Energy-Absorbing Bolt in Deep Roadway*, University of Science and Technology Beijing, Beijing, China, 2020.
- [27] Y. Hui, X. Zhang, B. Li et al., “Macro-micro mechanical response and energy mechanism of surrounding rock under excavation disturbance,” *Journal of China Coal Society*, vol. 45, no. S1, pp. 60–69, 2020.
- [28] Y. Zhao, Y. Jiang, and S. Tian, “Investigation on the characteristics of energy dissipation in the preparation on the characteristics of energy dissipation in the preparation process of coal pumps,” *Journal of China Coal Society*, vol. 35, no. 12, pp. 1979–1983, 2010.
- [29] C. Hou, X. Wang, J. Bai et al., “Basic theory and technology study of stability control for surrounding rock in deep roadway,” *Journal of China University of Mining & Technology*, vol. 50, no. 1, pp. 1–12, 2021.
- [30] H. Kang, P. Jiang, B. Huang et al., “Roadway strata control technology by means of bolting-modification-destressing in synergy in 1000 m deep coal mines,” *Journal of China Coal Society*, vol. 45, no. 3, pp. 845–864, 2020.
- [31] A. Fahimifar and M. Ranjbaria, “Analytical approach for the design of active grouted rockbolts in tunnel stability based on convergence-confinement method,” *Tunnelling and Underground Space Technology*, vol. 24, no. 4, pp. 363–375, 2009.
- [32] D. Ma, “Experimental research on optimum proportioning of coal cement grouting materials,” *Coal*, vol. 25, no. 8, pp. 40–42, 2016.
- [33] C. Hou, *Ground Control of Roadways*, China University of Science and Technology Press, Xuzhou, China, 2013.

## Research Article

# Study on the Effect of Soft and Hard Coal Pore Structure on Gas Adsorption Characteristics

Xun Zhao <sup>1,2,3</sup> Tao Feng,<sup>1,2</sup> Ping Wang,<sup>1,2</sup> and Ze Liao<sup>1,2</sup>

<sup>1</sup>School of Resource, Environment and Safety Engineering, Hunan University of Science and Technology, Xiangtan 411201, China

<sup>2</sup>Work Safety Key Lab on Prevention and Control of Gas and Roof Disasters for Southern Coal Mines,

Hunan University of Science and Technology, Xiangtan 411201, Hunan, China

<sup>3</sup>Guizhou Coal Mine Design Research Institute Co.Ltd., Guiyang 550025, China

Correspondence should be addressed to Xun Zhao; 247651516@qq.com

Received 9 April 2021; Accepted 28 May 2021; Published 12 June 2021

Academic Editor: Zhijie Zhu

Copyright © 2021 Xun Zhao et al. This is an open access article distributed under the Creative Commons Attribution License, which permits unrestricted use, distribution, and reproduction in any medium, provided the original work is properly cited.

In order to grasp the effect of soft and hard coal pore structure on gas adsorption characteristics, based on fractal geometry theory, low-temperature nitrogen adsorption and constant temperature adsorption test methods are used to test the pore structure characteristics of soft coal and its influence on gas adsorption characteristics. We used box dimension algorithm to measure the fractal dimension and distribution of coal sample microstructure. The research results show that the initial nitrogen adsorption capacity of soft coal is greater than that of hard coal, and the adsorption hysteresis loop of soft coal is more obvious than that of hard coal. And the adsorption curve rises faster in the high relative pressure section. The specific surface area and pore volume of soft coal are larger than those of hard coal. The number of pores is much larger than that of hard coal. In particular, the superposition of the adsorption force field in the micropores and the diffusion in the mesopores enhance the adsorption potential of soft coal. Introducing the concept of adsorption residence time, it is concluded that more adsorption sites on the surface of soft coal make the adsorption and residence time of gas on the surface of soft coal longer. Fractal characteristics of the soft coal surface are more obvious. The saturated adsorption capacity of soft coal and the rate of reaching saturation adsorption are both greater than those of hard coal. The research results of this manuscript will provide a theoretical basis for in-depth analysis of the adsorption/desorption mechanism of coalbed methane in soft coal seams and the formulation of practical coalbed methane control measures.

## 1. Introduction

Coal is a kind of porous solid medium with developed pore structure. The abundant pore structure in the coal body is not only a place for gas storage, but also a channel for gas production. The adsorption state of gas in coal makes the mechanical properties of gas-containing coal different from non-adsorption media. Gas-containing coal is a multi-phase porous medium with temporal and spatial variability, which is composed of pore fluid, matrix pores and micro-fractures. The distribution and connectivity of coal pore directly affect the migration and diffusion of gas. In the process of coal seam mining or gas drainage, the coal seam stress field, fissure field, and gas seepage field change. Fracture

expansion and penetration of coal and rock mass caused by mining unloading will change the interaction between coal and gas.

The natural pore and fissure structural characteristics of coal determine that coal has good gas adsorption capacity and storage performance. In recent years, scholars have conducted a lot of research on coal pore structure and gas adsorption characteristics. Bing et al. [1] studied the pore structure and adsorption characteristics of outburst coal and found that micropores with a pore size of 3–5 nm in outburst coal are the main gas adsorption space. Xue et al. [2] used a variety of test methods to study and found that for the same coal grade, as the degree of structural deformation increases, open pores gradually transform into fine bottleneck pores,

and the adsorption capacity increases, but the coal porosity decreases. Yuan et al. [3, 4] used nitrogen adsorption method and mercury injection method to study the pore structure of coal and obtained the pore characteristics of coal adsorption and migration; Sitprasert et al. [5] used multi-scale methods to study physical adsorption in micropores; Rigby et al. [6] studied the gas adsorption law of irregular meshes. Zhang et al. [7] used the low-temperature liquid nitrogen method to study the influence of structural deformation on the nano-scale pore structure of coal and found that ductile deformed coal has more complex pore structure and a higher fractal dimension than brittle deformed coal. An et al. [8] conducted a fractal study on the pore characteristics of high coal rank coals and found that the pore fractal dimension is negatively correlated with coal metamorphism, porosity, macropore content, and volume median pore size, and has a negative correlation with mesopore content and adsorption pore content. Mercury removal efficiency and ash yield are positively correlated. Jiang et al. [9] used the mercury intrusion method to determine the characteristic parameters of the ultrafine pore structure of coal and found that as the hardness of the coal increases, the fractal dimension of pores continues to decrease. Wang et al. [10] used small-angle rays combined with scanning electron microscopy to find that coal pores are mostly spheres at low coal ranks, and generally ellipsoids with high coal ranks. Klimenko et al. [11] used the conditional moment model to study the fractal characteristics of the transportation, storage, and adsorption processes in the pores of CO<sub>2</sub> porous media. However, there are relatively few systematic studies on the pore characteristics of soft coal bodies. A large number of studies have shown that the pore distribution of porous media satisfies self-similarity and conforms to the fractal law [12, 13]. Harpalant et al. [14–18] showed that the coal body will produce expansion stress and deformation after adsorbing gas. There are few systematic research results on the influence of soft coal pore structure on gas adsorption performance.

A typical soft coal body has a smaller consolidation coefficient and a larger initial dispersion rate. This manuscript takes typical soft coal seams and contrasting hard coals as the research objects. Using scanning electron microscope, low-temperature nitrogen adsorption test and isothermal adsorption test, combined with fractal geometry theory, the pore structure characteristics of soft coal and hard coal and their influence on gas adsorption characteristics are studied. In order to quantitatively characterize the pore distribution characteristics of soft coal and hard coal, the mechanical properties of soft coal and the gas flow law in soft coal are studied. The research results of this manuscript will provide a theoretical basis for in-depth analysis of the adsorption/desorption mechanism of coalbed methane in soft coal seams and the formulation of practical coalbed methane control measures.

## 2. Experimental

**2.1. Experimental Apparatus.** The self-developed high/low-temperature pressure swing adsorption-desorption

experimental system is shown in Figure 1. The experimental equipment mainly consists of an adsorption system, a gas desorption system, a refrigeration system, an electrical control system, and a computer data acquisition and processing system. The gas adsorption experiment adopts the pressure range is 0–8 MPa. The working temperature is 0–40°C.

The low-temperature nitrogen adsorption test uses the ASAP-2020 specific surface and pore size analyzer produced by Micromeritics. The pore volume is less than 0.0001 cm<sup>3</sup>/g, the pore size analysis range is 0.35 to 500 nm, and the specific surface area analysis range is 0.0005 to 5000 m<sup>2</sup>/g. The pore size classification method defined by the International Union of Pure and Applied Chemistry (referred to as IUPAC) is used. Using the SIGMA scanning electron microscope produced by Zeiss, the acceleration voltage range of the instrument is 0.1–30 kV, and the magnification range is 12–500 kX. It can analyze the microstructure of powder, block, and film samples.

**2.2. Sample Preparations.** The soft coal sample used in the test was taken from the Lvtang Coal Mine (LT) in Bijie District, Guizhou, China, and the hard coal used was taken from the Quanlun Coal Mine (QL) in Qinglong County, Xingyi City. The geographical location of the LT and QL is shown in Figure 2.

Each coal sample is not less than 1 kg. According to the China Coal Industry Standard [19] to prepare the coal sample for proximate analysis and gas adsorption experiment, the humidification process for coal samples is shown in Figure 3.

The data of proximate analysis of coal samples, coal hardness coefficient, and initial gas diffusion velocity of coal are shown in Table 1. Select a small coal sample with a flat cross section with a particle size of 1 to 2 cm<sup>3</sup> for low-temperature nitrogen adsorption test. It should be handled with care during operation. Table 1 data display that the firmness coefficient of soft coal is significantly lower than that of hard coal, and the initial rate of dispersal is greater than that of hard coal.

**2.3. Experimental Methods.** Coal sample gas desorption process simulation was conducted by employing the experimental device shown in Figure 3. The gas desorption environment of the sample was always maintained at a temperature of 30 ± 1°C and a gas outlet pressure of 0.1 MPa during the measurement process, and gas desorption of the coal sample could be considered to be an isothermal and isostatic desorption process. The experiment is conducted following the steps:

- (1) The experimental coal sample is loaded into the coal sample tank.
- (2) The coal sample tank and the reference tank are fully degassed using a vacuum pump.
- (3) When the vacuum in the experimental system reaches 25 kPa, gas is introduced into the reference tank. When the gas pressure is stable, the coal sample tank and the reference tank are connected to conduct gas adsorption.



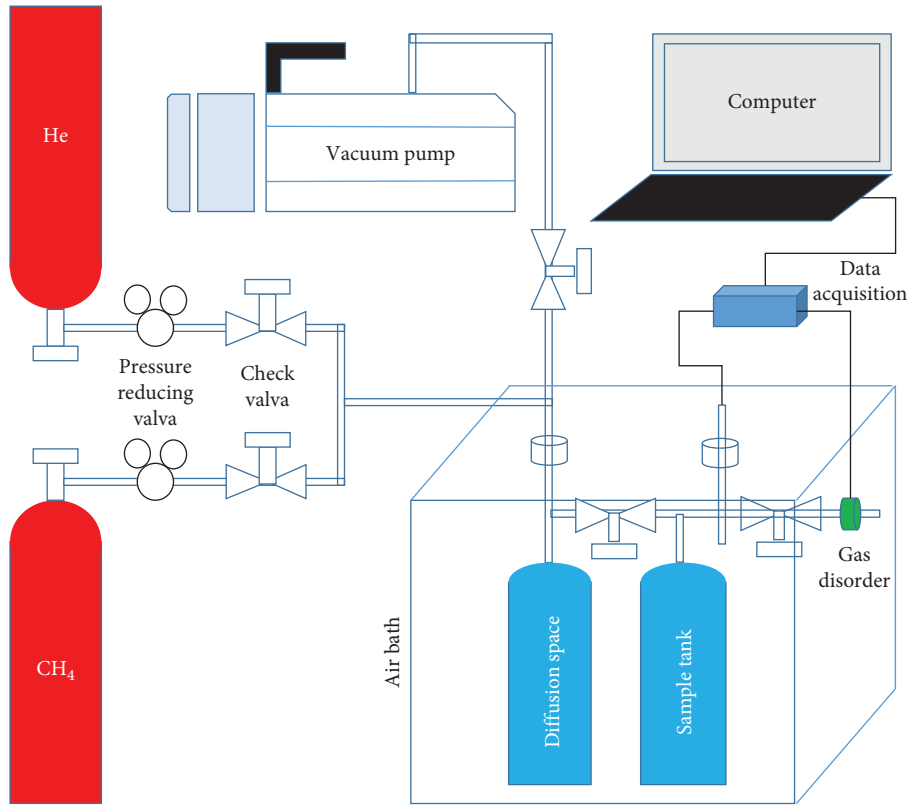


FIGURE 1: Schematic diagram of the experimental platform for the high-low temperature coal gas desorption and adsorption experiments.

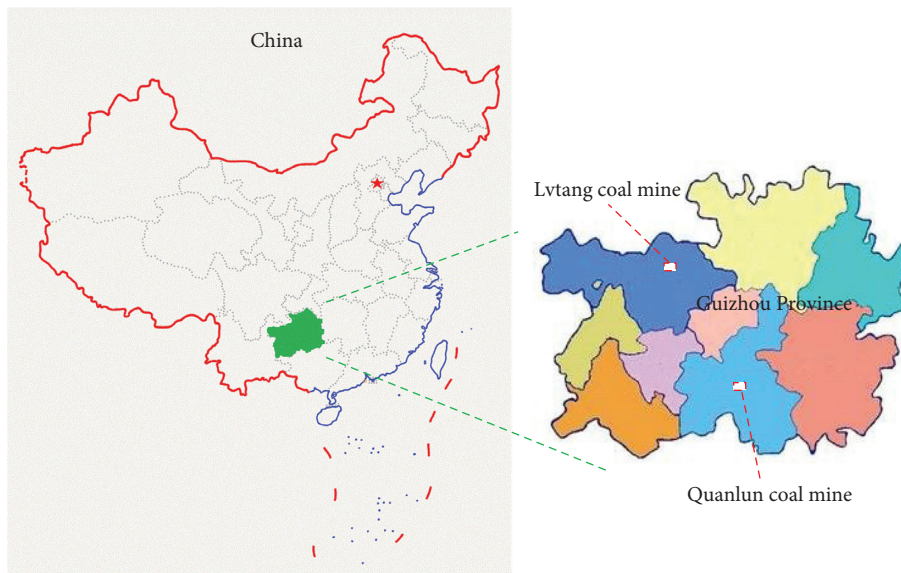


FIGURE 2: Geographical location of the LT and QL coal mine.

- (4) As gas adsorption balance in the coal sample is reached, the gas inlet valve is first closed, and the gas outlet valve is opened second to conduct the gas desorption experiment.
- (5) After the experiment is completed, the measured gas desorption amount is converted into volume in the standard state.

### 3. Experimental Results

**3.1. Pore Microstructure Analyses.** The coal sample from the Lvtang coal mine showed a microscopic breccia structure when observed under a microscope, as shown in Figure 4(a). Its characteristic is that the coal body is broken into particles of different sizes, some of which have more obvious edges and corners. The particles on the coal surface are mostly

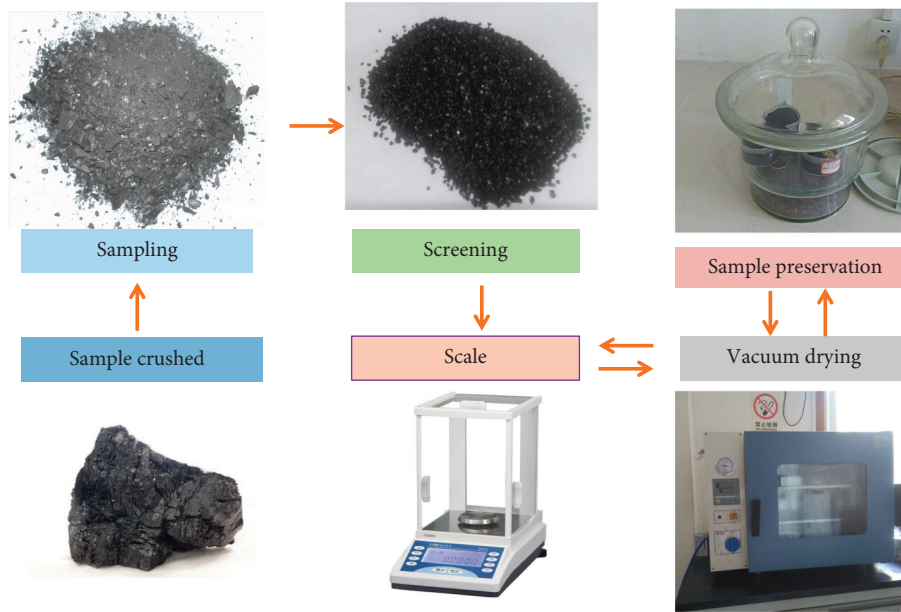


FIGURE 3: Humidification process for the coal samples.

TABLE 1: Experiment and proximate analysis data of coal samples.

Coal type	Coal mine	Mark as	$M_{ad}$	$A_{ad}$	$V_{daf}$	$f$	$\Delta P$
Soft coal	Lvtang	LT-1	0.73	10.98	12.1	0.1912	19.8
		LT-2	0.83	12.1	15.1	0.1622	20.6
Hard coal	Quanlun	QL-1	6.54	7.24	36.11	0.6742	11.4
		QL-2	5.98	6.65	35.25	0.6982	13.8

$M_{ad}$  is moisture content on air-dry (ad) basis, %;  $A_{ad}$  is ash content on air-dry (ad) basis, %;  $V_{daf}$  is volatile matter content on dry-ash-free (daf) basis, %;  $f$  is coal hardness coefficient, dimensionless;  $\Delta P$  is the initial gas diffusion velocity of coal, mmHg.

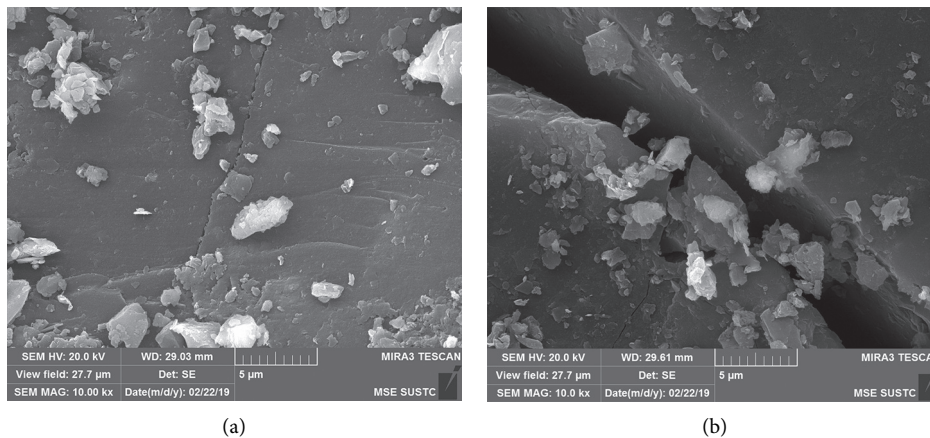


FIGURE 4: The microstructure of the coal sample. (a) Lvtang coal sample. (b) Quanlun coal sample.

irregular polyhedrons with sharp edges and corners. It shows that the coal sample has poor plasticity and high brittleness. At the same time, it can be seen that a large number of irregular pores are developed on the surface of the coal sample, and the size of the pores is different. The existence and density of the pores indicate that the coal has a certain

gas storage capacity. In addition, the existence of a large number of holes reduces the mechanical strength of coal, which is one of the reasons why soft coal is easily broken.

The surface of the coal sample in Quanlun Coal Mine is relatively flat, and a large, dominantly developed fissure can be seen to develop stably in the longitudinal direction. The

fissure penetrates the entire coal surface in the visible range, as shown in Figure 4(b). The surface of the coal sample is distributed with some inorganic components such as point-like and pile-like clay materials. On the one hand, the presence of inorganic components increases the strength of the coal and acts as the skeleton of the coal; on the other hand, it destroys the uniformity of the coal and softens when exposed to water, which directly reduces the anti-destructive ability of the coal body itself.

**3.2. Specific Surface Areas and Pore Volume Characteristics.** Two sets of soft coal experiment coal samples from LT and two sets of hard coal experiment coal samples from QL were selected, and a total of 4 sets of nitrogen adsorption tests were carried out. The pore volume characterization method adopts the BJH method, and the specific surface area characterization method adopts the BET method and the Langmuir method. The pore structure characteristics of the soft and hard coal surface are analyzed from different angles. The results of the low-temperature nitrogen adsorption test are shown in Table 2.

It can be seen from Table 2 that the BET specific surface area values of soft and hard coal are all smaller than the corresponding Langmuir specific surface area values. This is because the calculation methods of the two models are different. The Langmuir model assumes that the gas adsorption on the coal surface is limited to a single layer, while the BET model believes that the gas adsorption on the coal surface can be multilayer adsorption. That is, when the gas reaches the saturated adsorption capacity, the adsorption capacity of the BET model is greater than that of the Langmuir model. In addition, single-layer adsorption capacity referred to by Langmuir theory is the saturated adsorption capacity, while the single-layer adsorption capacity referred to by the BET theory is only a theoretical value. The Langmuir saturated adsorption capacity is not equal to the maximum adsorption capacity, but corresponds to the closed point of the adsorption loop on the adsorption isotherm. The appearance of adsorption loops on the adsorption isotherm indicates that there are mesopores or microporous pores in the test object. However, the adsorption in the mesopores appears as capillary condensation. According to theory of Langmuir, it is an adsorbate liquefaction process and cannot be regarded as an adsorption process. Therefore, the Langmuir theoretical model is not suitable for explaining the adsorption behavior of the adsorbate in the mesopores. For porous media, especially materials with more micropores and mesopores, the BET model is more suitable for characterizing the specific surface area. The BET specific surface area of soft coal ranges from 10.4158 to 14.3245 m<sup>2</sup>/g, and the BJH pore volume ranges from 0.006117 to 0.008416 cm<sup>3</sup>/g. The specific surface area and pore volume of soft coal are 2.33 times and 1.79 times larger than those of hard coal, respectively. Specific surface area and pore volume are important indicators to characterize the ability of coal to absorb gas. The larger the value, the larger the gas absorption volume of coal. The average pore diameter of soft coal is smaller than that of hard coal, indicating that the inner surface area of the pores of soft coal is larger in unit

volume, so that the pore surface provides more gas adsorption sites.

**3.3. Relationship between Adsorption/Desorption Curve and Pore Structure Characteristics.** The shape of the different relative pressure sections of the adsorption isotherm reflects the physical characteristics of the coal surface and the relationship between the coal and gas. The relative pressure can evaluate the performance of the coal reservoir, especially the permeability of the coal. The low-temperature nitrogen adsorption/desorption curve of a typical soft and hard coal sample is shown in Figure 5.

It can be seen from Figure 5 that when the relative pressure is zero, the nitrogen adsorption capacity of soft and hard coal is greater than zero. It shows that a certain volume of nitrogen has been adsorbed in the micropores, and the adsorption capacity of soft coal at the starting point is greater than that of hard coal. It can be seen that soft coal has a larger micropore area than hard coal. This is because the gas is preferentially adsorbed in the micropores of the coal. The more micropores contained in the coal, the stronger the superposition of the adsorption potential energy in the micropores. As a result, nitrogen adsorption capacity increases faster. When the relative pressure is between 0 and 0.2, the adsorption curve shows an upward convex trend. It shows that the force between the surface of the coal body and the nitrogen molecules is strong [20]. When the relative pressure is between 0.5 and 1, soft and hard coal have different adsorption hysteresis loops. And the hysteresis range of soft coal is larger than that of hard coal. The size of the hysteresis ring reflects the connectivity of coal pores. It shows that the pore connectivity of soft coal is better than that of hard coal [21]. Compared with hard coal, the hysteresis loop of soft coal is more obvious in the desorption process. This shows that it is very likely that a large amount of gas will escape in a short time when mining soft coal seams. Major outburst prevention and stress control measures should be taken to mine and ease the pressure during mining. When the relative pressure is higher than 0.9, the adsorption curve rises sharply, and the rise rate of the soft coal adsorption curve is obviously greater than that of the hard coal adsorption curve. The opening degree of coal pores is related to the rate of rise of the adsorption line. The faster the rise, the greater the opening degree of the pores.

**3.4. Fractal Geometric Characteristics of Coal Surface.** The fractal dimension can be used to characterize the fractal characteristics of the pore surface of coal, and its numerical value can be obtained from low-temperature nitrogen adsorption test data. Calculating and analyzing from different angles, taking the adsorption capacity at the inspection point, the relationship between fractal dimension and adsorption capacity is as follows [22]:

$$\ln Q = (D_f - 3) \ln \left( \ln \frac{P_0}{P} \right) + C, \quad (1)$$

where  $P$  is nitrogen partial pressure, MPa;  $Q$  is the adsorption capacity when the equilibrium pressure is  $P$ , cm<sup>3</sup>/g;

TABLE 2: Coal sample nitrogen adsorption test results.

Coal type	Coal mine	Mark as	BET specific surface area ( $\text{m}^2 \cdot \text{g}^{-1}$ )	Langmuir specific surface area ( $\text{m}^2 \cdot \text{g}^{-1}$ )	BJH pore volume ( $\text{cm}^3 \cdot \text{g}^{-1}$ )	Average pore size (nm)
Soft coal	Lvtang	LT-1	12.2148	14.2310	0.008416	6.1773
		LT-2	14.3245	16.2412	0.007415	6.2112
Hard coal	Quanlun	QL-1	6.2271	8.1648	0.004452	14.8725
		QL-2	4.3718	6.2147	0.003674	15.5149

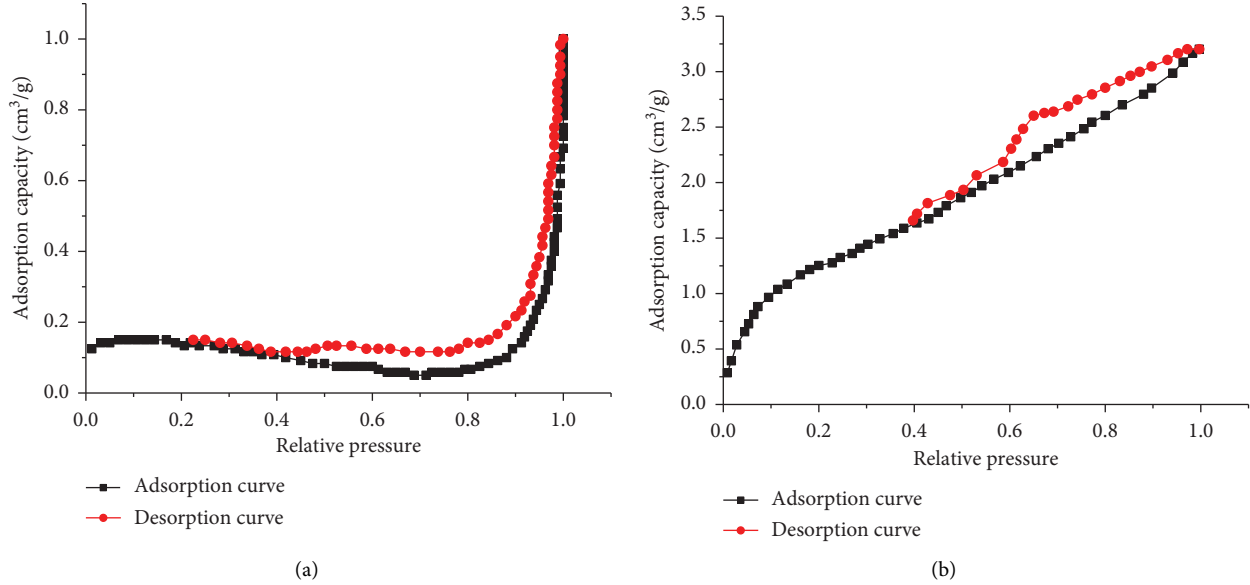


FIGURE 5: Low-temperature nitrogen adsorption/desorption curve of coal sample. (a) Soft coal. (b) Hard coal.

$P_0$  is saturated vapor pressure of gas adsorption, MPa;  $D_f$  is fractal dimension, which characterizes the fractal characteristics of coal pore surface, dimensionless; and  $C$  is constant, dimensionless.

Taking the specific surface area of coal as an investigation point, the relationship between fractal dimension and specific surface area is as follows [23]:

$$\ln A = (D_f - 2) \ln \left( \ln \frac{P_0}{P} \right) + C, \quad (2)$$

where  $A$  is specific surface area of coal surface,  $\text{m}^2/\text{g}$ ; other parameter symbols have the same meaning as above.

In the low-temperature nitrogen adsorption experiment, a straight line can be obtained by plotting  $\ln Q$  and  $\ln A$  against  $\ln(\ln P_0/P)$ , and the fractal dimension can be obtained from the slope of the straight line. According to formula (1) and (2), the size of the fractal dimension of the coal sample surface can be calculated, and the calculation results are shown in Table 3.

The data in Table 3 shows that the calculation results of formula (1) and (2) are slightly different, and the calculation result of formula (1) is slightly larger than that of formula (2). This difference may be due to the micropores or mesopores in the coal. The difference in the pore size of the micropores or mesopores results in the difference in the adsorption potential of the micropores for nitrogen, so that nitrogen molecules cannot completely and effectively fill all mesopores. The

scoring dimension results of the two calculation formulas reflect the characteristics of coal pore structure to a certain extent. It can be seen from Table 3 that the calculation results of the surface fractal dimension of soft coal are between 2.12 and 2.35, the calculation results of the surface fractal dimension of hard coal are between 1.43 and 1.62, and the average surface fractal dimension of soft coal is 1.47 times that of hard coal. The larger the fractal dimension, the rougher the surface and the larger the specific surface area of coal pores. This also reflects that soft coal has more developed pores than hard coal.

**3.5. Characteristics of Coal Gas Adsorption.** Constant temperature adsorption experimental data of soft and hard coal are shown in Table 4, and the constant temperature adsorption test curve is shown in Figure 6.

Comprehensive analysis of Table 4 and Figure 6 can be drawn that, under the same experimental conditions, the soft coal adsorption constants  $a$  and  $b$  are both larger than the hard coal adsorption constants. Soft coal has a larger saturated adsorption capacity than hard coal, and at the same time soft coal reaches the saturated adsorption capacity faster. It shows that the gas adsorbs and stays on the pore surface of the soft coal for a long time, the gas coverage is high, and the soft coal has a stronger ability to adsorb gas.

TABLE 3: Calculation results of the surface fractal dimensions of coal samples.

Coal mine	Mark as	Relative pressure $P/P_0$ range	Formula (1) fractal dimension calculation	Formula (2) fractal dimension calculation
Lvtang	LT-1	0.15–0.96	2.34	2.23
	LT-2	0.17–0.97	2.35	2.25
Quanlun	QL-1	0.44–0.99	1.58	1.43
	QL-2	0.43–0.99	1.62	1.55

TABLE 4: Results of constant temperature adsorption experiment of the coal sample.

Coal mine	Mark as	Adsorption constants $a$	Adsorption constants $b$	Fitting curve	$R^2$
Lvtang	LT-1	18.7513	2.6515	$Q = 49.7169P/(1 + 2.6515P)$	0.9991
	LT-2	18.5424	2.5425	$Q = 47.1457P/(1 + 2.5427P)$	0.9992
Quanlun	QL-1	18.1	0.44	$Q = 7.74P/(1 + 0.35P)$	

The adsorption constants  $a$  and adsorption constants  $b$  are important indicators of the ability of coal to absorb gas, which conform to the Langmuir adsorption formula:  $Q = (abP)/(1 + bP)$ . Here,  $a$  is the value reflects the maximum adsorption capacity of the coal,  $\text{cm}^3/\text{g}$ ;  $b$  is the value represents the rate at which the coal reaches its saturated adsorption capacity,  $\text{MPa}^{-1}$ ;  $Q$  is gas adsorption capacity under a certain pressure,  $\text{cm}^3$ ;  $P$  is the gas pressure of the coal seam,  $\text{MPa}$ .

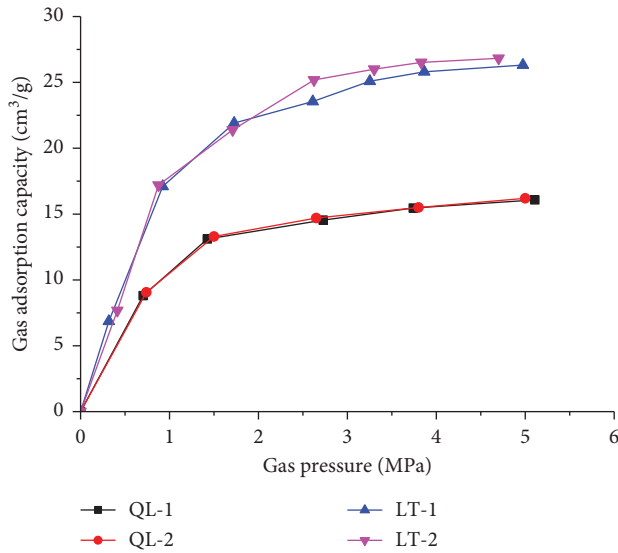


FIGURE 6: Constant temperature adsorption curve of soft and hard coal.

## 4. Discussion

### 4.1. The Influence of Pore Type on Gas Adsorption

**4.1.1. The Superposition of Adsorption Potential Energy in the Micropores.** The abundant pore structure in the coal body is not only a place for gas storage, but also a channel for gas migration and diffusion. In particular, the presence of micropores greatly increases the surface area of the coal body. Since the size of the micropores is similar to the size of the gas molecules, the gas molecules are surrounded by the micropores. The adsorption force field in the micropores produces a superposition effect, so that the adsorption potential energy is greatly enhanced compared with the adsorption potential energy on the flat pore wall surface. Under low relative pressure, it has stronger adsorption attraction for gas molecules. Studies have shown that the adsorption potential is greatly enhanced in circular pores less than six molecular diameters and in slit pores less than

two molecular diameters. The relationship between micropore adsorption volume and adsorption potential energy can be expressed as [24]

$$\begin{cases} \varphi = \varphi_0 \cdot e^{-K\varepsilon^2}, \\ \varepsilon = \ln \frac{P}{P_0}, \end{cases} \quad (3)$$

where  $\varphi$  is adsorption volume,  $\text{cm}^3$ ;  $\varphi_0$  is maximum adsorption volume,  $\text{cm}^3$ ;  $K$  is constant related to the micropore structure, dimensionless; and  $\varepsilon$  is adsorption potential energy,  $J$ .

In formula (3),  $\varepsilon^2$  reflects the superposition of the adsorption potential field on the micropore wall.

**4.1.2. Diffusion in Mesopores.** The analysis of mesopores is closely related to the nitrogen adsorption/desorption curve, and the specific form of the adsorption hysteresis ring corresponds to different mesopore structures. The large range of the hysteresis ring indicates that the corresponding pores are smooth and the pores have high air permeability, which is conducive to the migration and diffusion of gas. The diffusion of gas in mesopores satisfy Fick diffusion, and the diffusion rate can be expressed as

$$\frac{dQ}{dt} = -D_0 \cdot A_g \cdot \frac{dc}{dx}, \quad (4)$$

where  $dQ/dt$  is gas diffusion rate,  $\text{kg/s}$ ;  $D_0$  is gas diffusion coefficient,  $\text{m}^2/\text{s}$ ;  $A_g$  is the gas diffusion area in the channel,  $\text{m}^2$ ; and  $dc/dx$  is gas concentration gradient,  $\text{kg}/(\text{m}^3 \cdot \text{m})$ .

In formula (4), “-” means that the direction of gas diffusion in the channel is opposite to the direction of the gas concentration gradient.

**4.2. The Effect of Adsorption Residence Time on Gas Adsorption.** The time from when the gas molecules hit the surface of the coal body to when they leave the surface and return to the gas phase is called the adsorption residence time. If the adsorption residence time is much longer than



the molecular vibration period, it can be considered that adsorption has occurred. The inner surface area of the pores of soft coal is larger, it provides more gas adsorption sites, and the adsorption site gas coverage is high. Soft coal has a stronger adsorption potential for gas, and the adsorption residence time of gas on the surface of soft coal is longer than that of hard coal, so the amount of gas adsorption is greater. The gas coverage of coal pore surface can be expressed as

$$\theta = \frac{a}{a_m}, \quad (5)$$

where  $\theta$  is the gas coverage on the surface of coal pores, ( $^\circ$ );  $a$  is the number of gas molecules adsorbed on the coal surface, unit; and  $a_m$  is the number of gas molecules covering the monolayer of  $1 \text{ cm}^2$  coal surface, unit.

The relationship between the number of gas molecules and the adsorption residence time  $\tau$  can be expressed as

$$\begin{cases} a = n \cdot \tau, \\ n = \frac{N_A P}{(2\pi MRT)^{1/2}}, \end{cases} \quad (6)$$

where  $n$  is the number of gas molecules that collide on the surface of the coal body in a unit time, unit;  $N_A$  is Avogadro's constant, which is  $6.02 \times 10^{23} \text{ mol}^{-1}$ ;  $P$  is gas pressure, MPa;  $M$  is the relative molecular mass of adsorption, dimensionless;  $R$  is the ideal gas constant, which is  $8.314 \text{ J}/(\text{mol}\cdot\text{K})$ ;  $T$  is the thermodynamic temperature,  $\text{K}$ ; and  $\tau$  is adsorption residence time,  $\text{S}$ .

**4.3. The Influence of Fractal Characteristics on Gas Adsorption.** The difference in the fractal characteristics of the coal surface reflects the change of the coal pore structure. The pore size of the soft coal gradually decreases with the increase of the fractal dimension of the coal surface. The change curve of the calculation result using formula (1) is shown in Figure 7.

The larger the fractal dimension, the higher the surface roughness of the coal and the increase of pores per unit volume. The radius of the pore channel decreases, which increases the pore volume and specific surface area. The gas adsorption sites provided by the pore surface of the coal increase, and the gas adsorption capacity is enhanced.

According to the theory of fractal geometry, there is the following relationship between the pore radius and the cumulative number in coal [25]:

$$\begin{cases} N \propto r^{-D_f}, \\ N = A_2 \cdot r_m^{D_f} \cdot (\lambda^{D_f} - 1) \cdot (r_0^{-D_f} - r_m^{D_f}), \\ \lambda = \frac{r_0}{r_m}, \end{cases} \quad (7)$$

where  $N$  is the total number of pores per unit volume of coal, unit;  $r$  is the radius of the pores in the coal,  $\text{nm}$ ;  $A_2$  does not significantly include the proportional coefficient of  $D_f$ ;  $r_m$  is maximum radius of the pore,  $\text{nm}$ ;  $r_0$  is minimum radius of

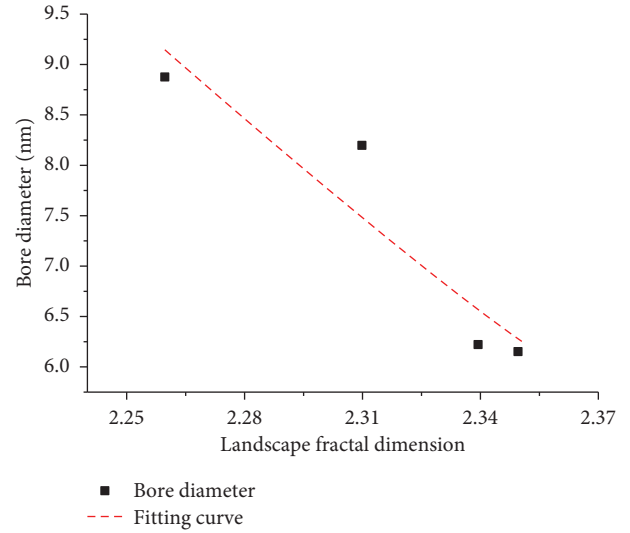


FIGURE 7: The relationship curves between aperture and fractal dimension.

pore,  $\text{nm}$ ; and  $\lambda$  is the ratio of the minimum and maximum pore radius.

From formula (7), the distribution density function of the pore radius in the coal body can be obtained:

$$Y(r) = AD_f r^{-(1+D_f)}. \quad (8)$$

From formula (8), the average radius of pores in the coal body can be obtained as

$$\bar{r} = \frac{D_f}{1-D_f} r_m \frac{1-\lambda^{1-D_f}}{\lambda^{-D_f}-1}. \quad (9)$$

Analyzing formula (9), it can be obtained that the average radius of coal pores depends entirely on the fractal dimension  $D_f$  of the coal, the upper and lower limits  $r_m$  and  $r_0$  of the pore distribution in the coal, and the total number of pores in the porous medium per unit volume  $N$ .

In addition, upper and lower limits  $r_m$  and  $r_0$  of the pore distribution in the coal body and the total number  $N$  of pores per unit volume of porous media are constant. Then, the average radius  $\bar{r}$  of the pore gradually decreases with the increase of the fractal dimension  $D_f$ .

## 5. Conclusion

In this paper, a self-developed adsorption/desorption device is used to test the gas adsorption and desorption performance of soft coal and hard coal under low-temperature conditions, combined with scanning electron microscope and low-temperature nitrogen adsorption experiment to test the pore characteristics of experimental soft coal and hard coal. Analyze the microscopic pore and fracture structure and connectivity of typical soft coal, use the box dimension algorithm to measure the fractal dimension of the microstructure of the coal sample, and compare and analyze the relevant characteristics of hard coal. And we got the following conclusions:

- (1) The results of the low-temperature nitrogen adsorption test calculated that the BET specific surface area of soft coal ranges from 10.4158 to 14.3245 m<sup>2</sup>/g, and the BJH pore volume ranges from 0.006117 to 0.008416 cm<sup>3</sup>/g, both of which are larger than those of hard coal. It shows that soft coal has more pores than hard coal, and the inner surface of the pores is larger. Particularly, the number of micropores and the superposition of the adsorption potential energy existing in the micropores make the adsorption potential energy of soft coal to gas greater.
- (2) According to the nitrogen adsorption test data, the fractal characteristics of the pore surface of soft and hard coal are calculated, and the average fractal dimension of the surface of soft coal is more than double that of hard coal. It shows that the surface roughness of soft coal is high, there are many pores per unit volume, and the inner surface of the pores can provide more adsorption sites. The gas adsorption site coverage on the surface of the soft coal body is high, and the adsorption residence time is long. Therefore, soft coal has a stronger ability to absorb gas than hard coal.
- (3) Compared with hard coal, soft coal exhibits a larger adsorption hysteresis loop in the nitrogen adsorption test. It shows that the pore connectivity of coal is better than that of hard coal. When mining soft coal seams, it is more likely to cause a large amount of gas escape in a short time. When mining, the main prevention and control measures should be taken to extract and relieve pressure [26].

## Data Availability

All the data generated or published during the study are included within the article; no other data were used to support this study.

## Conflicts of Interest

The authors declare that they have no conflicts of interest regarding the publication of this paper.

## Acknowledgments

This work was supported by the Guizhou Province Science and Technology Support Program Funding Project ([2021] General 349), the project supported by an Open-End Fund of the Work Safety Key Lab on Prevention and Control of Gas and Roof Disasters for Southern Coal Mines (E21822), and a youth project supported by the National Natural Science Foundation of China (51804114).





## References

- [1] L. Bing, Z. Guocheng, S. Zhimin, and R. Jiangang, "Analysis on coupling relationship between pore structure of deformed coal and CH<sub>4</sub> adsorption-desorption characteristics," *International Journal of Earth Sciences and Engineering*, vol. 7, no. 1, pp. 90–98, 2014.
- [2] G. Xue, H. Liu, and W. Li, "Deformed coal types and pore characteristics in hancheng coalmines in eastern weibe coalfields," *International Journal of Mining Science & Technology*, vol. 22, no. 5, pp. 681–686, 2012.
- [3] Q. Yuan, X. L. Ge, S. P. Zhou, and R. G. Deng, "Study on the variation of fractal and multifractal characteristics of coal particles in the ultra-fine pulverizing process," *Advanced Materials Research*, vol. 347-353, pp. 3653–3657, 2011.
- [4] T. Yin, D. Liu, Y. Cai, Y. Zhou, and Y. Yao, "Size distribution and fractal characteristics of coal pores through nuclear magnetic resonance cryoporometry," *Energy & Fuels*, vol. 31, no. 8, pp. 7746–7757, 2017.
- [5] C. Sitprasert, Z. H. Zhu, F. Y. Wang, and V. Rudolph, "A multi-scale approach to the physical adsorption in slit pores," *Chemical Engineering Science*, vol. 66, no. 22, pp. 5447–5458, 2011.
- [6] S. P. Rigby, R. S. Fletcher, and S. N. Riley, "Characterisation of porous solids using integrated nitrogen sorption and mercury porosimetry," *Chemical Engineering Science*, vol. 59, no. 1, pp. 41–51, 2004.
- [7] X. Zhang, H. Yao, W. Li, X. Wang, and J. Yan, "Fractal characteristics of nano-scale pore structure of structural coal in Hancheng mining area," *Coal Geology and Prospecting*, vol. 42, no. 5, pp. 5–8, 2014.
- [8] S. An, S. Sang, Y. Li et al., "Pore fractal characteristics of high coal-grade reservoirs in the southern Qinshui Basin," *China Coal Geology*, vol. 23, no. 2, pp. 17–21, 2011.
- [9] B. Jiang, B. Lin, H. Wu et al., "Study on the characteristics of ultramicro pore structure and fractal law of coal and rock," *Journal of Hunan University of Science and Technology*, vol. 25, no. 3, pp. 15–18, 2010.
- [10] G. Wang, Y. Qin, J. Shen et al., "Dynamic-change laws of the porosity and permeability of low-to medium-rank coals under heating and pressurization treatments in the eastern junggar basin, China," *Journal of Earth Science*, vol. 29, no. 3, pp. 133–141, 2018.
- [11] A. Y. Klimenko, D. N. Saulov, and P. Massarotto, "Conditional model for sorption in porous media with fractal properties," *Transport Porous Media*, vol. 92, pp. 745–765, 2012.
- [12] D. Kong, S. Pu, Z. Cheng et al., "Coordinated deformation mechanism of the top coal and filling body of gob-side entry retaining in a fully mechanized caving face," *International Journal of Geomechanics*, vol. 21, no. 4, Article ID 04021030, 2021.
- [13] Y. Yao, D. Liu, D. Tang et al., "Fractal characterization of adsorption - pores of coals from north: an investigation on CH<sub>4</sub> adsorption capacity of coals," *International Journal of Coal Geology*, vol. 73, pp. 27–42, 2008.
- [14] S. Harpalant and G. L. Chen, "Influence of gas production induced volumetric strain on permeability of coal," *Geotechnical and Geological Engineering*, vol. 15, no. 4, pp. 303–325, 1997.
- [15] H. GaoM. Masakutsan et al., "Statistical distribution characteristics of pyriding transport in coal particales and a series of new phenomenological models for overshoot and non-overshoot solvent swelling of coap particals," *Energy and Fuels*, vol. 13, no. 2, pp. 518–528, 1999.
- [16] S. Zhou and B. Lin, *Theory of Coal Seam Gas Occurrence and Flow*, Coal Industry Press, Beijing, China, 1999.

- [17] C. O. Karacan, "Heterogeneous sorption and swelling in a confined and stressed coal during CO<sub>2</sub> injection," *Energy and Fuels*, vol. 17, no. 6, pp. 1595–1608, 2003.
- [18] C. O. Karacan, "Swelling-induced volumetric strains internal to a stressed coal associated with CO<sub>2</sub> sorption," *International Journal of Coal Geology*, vol. 72, no. 3-4, pp. 209–220, 2007.
- [19] F. Wang, Y. Liang, X. Li et al., "Orthogonal experimental study on multifactor conditions for gas desorption in coal," *Advances in Civil Engineering*, vol. 2019, pp. 1–12, 2019.
- [20] A. D. Swann, "Analytical solutions for determining naturally fractured reservoir properties by well testing," *Society of Petroleum Engineers Journal*, vol. 16, no. 3, pp. 117–122, 1976.
- [21] J. E. Warren, P. J. Root, "The behavior of naturally fractured reservoirs," *Society of Petroleum Engineering*, vol. 3, no. 3, pp. 245–255, 1963.
- [22] G. I. Barenblatt, I. P. Zheltov, and I. N. Kochina, "Basic concepts in the theory of seepage of homogeneous liquids in fissured rocks [strata]," *Journal of Applied Mathematics & Mechanics*, vol. 24, no. 5, pp. 1286–1303, 1960.
- [23] K. Jeffrey, J. Jacek, M. Sharon, and P-R. Javier, "Unified method to the total pore volume and pore size distribution of hierarchical zeolites from argon adsorption and mercury intrusion," *Langmuir*, vol. 31, no. 4, pp. 1242–1247, 2015.
- [24] J. Sobczyk, "A comparison of the influence of adsorbed gases on gas stresses leading to coal and gas outburst," *Fuel*, vol. 115, no. 1, pp. 288–294, 2014.
- [25] E. B. Louw, G. D. Mitchell, J. Wang et al., "Constitution of drop-tube generated coal chars from vitrinite-rich and inertinite-rich South African coals," *Energy & Fuels*, vol. 30, no. 1, pp. 112–120, 2016.
- [26] L. Han, Y. Lin, and K. Chen, "Proximate analysis of coal," *National standards of People's Republic of China*, vol. 99, pp. 1–9, 2008.

## Research Article

# Study on the Lagging Support Mechanism of Anchor Cable in Coal Roadway Based on FLAC<sup>3D</sup> Modified Model

Xiangyu Wang <sup>1,2</sup>, Guanghui Wang <sup>1,2</sup>, Bowen Wu <sup>1,2</sup> and Shuaigang Liu <sup>1,2</sup>

<sup>1</sup>School of Mines, China University of Mining & Technology, Xuzhou 221116, China

<sup>2</sup>State Key Laboratory of Coal Resources and Safe Mining, Xuzhou 221116, China

Correspondence should be addressed to Guanghui Wang; [guanghuiwang@cumt.edu.cn](mailto:guanghuiwang@cumt.edu.cn)

Received 2 April 2021; Revised 7 May 2021; Accepted 20 May 2021; Published 7 June 2021

Academic Editor: Zhijie Zhu

Copyright © 2021 Xiangyu Wang et al. This is an open access article distributed under the Creative Commons Attribution License, which permits unrestricted use, distribution, and reproduction in any medium, provided the original work is properly cited.

Aiming at the broken failure of anchor cable in the mining roadway roof during the mining process, the lagging support scheme of anchor cable is proposed. Based on the results of indoor anchor cable pull-out test, the Cable element in FLAC<sup>3D</sup> is modified to realize the extension breaking of anchor cable in the calculation process. Furthermore, the minimum principal stress and volume strain rate mutation point are used as the failure criteria of the anchor cable. Through the comparative analysis of five anchor cable lagging support schemes of 6208 transport tunnel in Wangzhuang Mine Coal, the results demonstrate that the lagging support reduces the initial support resistance of the supporting structure. With the increase of lagging time, the ability of anchor cable to adapt to deformation increases gradually. When the lagging time reaches the gentle area of roadway deformation, its ability to adapt to deformation remains stable. Finally, it was determined that the support should start at 10–15 m of the anchor cable lagging head of the 6208 transport tunnel. Industrial tests show that the lagging support scheme ensures that the anchor cable can withstand a certain deformation, and the support body has no broken failure, which effectively controls the large mining-induced deformation of surrounding rock.

## 1. Introduction

With the continuous development of coal mining technology, roadway support technology has developed from passive support to active support. A large number of engineering practices have proved that the combined support technology of bolt and cable can effectively improve the stability of surrounding rock [1–4]. With the increase of coal mining depth, the deep complicated geomechanical environment makes the rock mass exhibit obvious nonlinear large deformation mechanical properties [5, 6]. With the increase of the load acting on the supporting structure, coupled with the superposition of dynamic loads such as mining, mine earthquake, and rock burst, the stress and deformation of the supporting body can easily exceed its limit value. The broken failure becomes more and more prominent, which seriously affects the stability of roadway surrounding rock [7–12].

According to many field observation results of roadway support, most of the bolts are anchored in the shallow surrounding rock within 2 m of the roadway, and their elongation rate is large. Generally, they will not break due to tensile deformation. Most anchor cables are anchored in the deep surrounding rock within 5–8 m of the roadway. Because the relative displacement between the deep and shallow surrounding rocks is relatively large, but the elongation of the anchor cable is small, the anchor cable is more prone to broken failure [13, 14].

In order to adapt to the deformation characteristics of deep surrounding rock, the coupling support relationship between anchor cable and roadway surrounding rock should be satisfied, which usually shows the coupling of strength, stiffness, and force [15]. (1) Strength coupling: the surrounding rock of the roadway has a large deformation energy, so it is difficult to prevent the deformation of the surrounding rock by bolt and anchor cable alone. Therefore,

bolt and anchor cable should be used to support the surrounding rock without damaging the bearing strength of the surrounding rock. (2) Stiffness coupling: in view of deformation, the surrounding rock of the roadway is mainly broken due to the incongruous deformation. The coupling between the stiffness of the supporting body and the surrounding rock is the basis to ensure that the surrounding rock will not be destroyed. However, the deformation limit of bolt and anchor cable supporting structure should be considered to ensure its stiffness, so that it will not break and fail. (3) Force coupling: the force of bolt and anchor cable in roadway support is interrelated, and the coupling effect of force will directly affect the stability of surrounding rock.

In fact, the supporting time is very important in the strength, stiffness, and force coupling mechanism of bolt and anchor cable support structure. The supporting time choice will affect the bearing state of the whole supporting system, which determines the overall supporting effect. For many years, many scholars have found that reasonable supporting time is particularly important to control the deformation of surrounding rock in the study of bolt and anchor cable coupling support [16–18]. Based on the modified nonlinear rheological Nishihara model, Yu et al. [19] obtained the best secondary supporting time in Jinchuan mining area through reverse analysis and proposed the bolt and anchor cable combined support technology. Meng et al. [20] analyzed the coupling deformation mechanism of supporting structure and surrounding rock, revealed the relationship between plastic zone expansion and stress release rate, and finally determined the optimal supporting time. According to the deformation monitoring data of roadway in Xingdong Mine, Liu and Li [21] obtained the optimal supporting time of each supporting element in the combined support scheme. Yu et al. [22] and Wu et al. [23] established a piecewise linear strain softening model to analyze the influence of different anchoring methods and different secondary support time on the stability of roadway in soft rock and finally put forward a reasonable design principle of support scheme. Previous studies have not well analyzed and verified the reasonable time of anchor cable lagging support from the perspective of the coupling force of the supporting body and its supporting effect. In order to adapt to the large deformation of surrounding rock without breaking and to enhance the complementarity of supporting between bolt and anchor cable, the scheme of installing anchor cables at a certain distance in lagging tunneling head is put forward in this paper.

Up to now, numerical simulation has made great contributions to the study on deformation and support of surrounding rock. The anchor cable structural element in FLAC<sup>3D</sup> has obvious advantages in simulating the working state of bolt and anchor cable [24, 25]. However, because the axial force of the Cable element will maintain the ultimate load even after reaching its tensile strength, the bolt in the model will not fail when it is stretched [26]. Currently, few scholars consider the tensile failure of bolt and anchor cable in simulation calculation, so it is not accurate to use it to further study the supporting law of anchor cable.

Therefore, based on the pull-out test of solid anchor cable, FISH language is used to modify the anchor cable

structural element in FLAC<sup>3D</sup> to achieve the simulation of the anchor cable breaking effect under extension deformation. Meanwhile, based on the modified anchor cable structure element, the law of the force action of the anchor cable lagging support on the supporting structure is studied, the influence law of surrounding rock support effect is revealed, and reasonable anchor cable lagging support scheme is determined.

## 2. FLAC<sup>3D</sup> Anchor Cable Element Modification Based on Pull-Out Test

The Cable element built into FLAC<sup>3D</sup> can simulate the stress and deformation of the anchor cable with small deformation, which cannot be used to reveal the extended failure process of the anchor cable in large deformation. Based on the deformation behavior characteristics of the measured anchor cable in the tensile process, Fish language is used to modify the Cable element, so that the simulation results are closer to the reality.

*2.1. Pull-Out Test of Mechanical Properties for Anchor Cable.* MZ-II anchor cable installation and LW-1000 horizontal tensile testing machine are used in test. The structure characteristics and working principle of horizontal tensile testing machine are shown in Figure 1. The machine is mainly composed of host, control cabinet, measurement and control system, servo oil source, and other parts.

In the test, a mine-used steel strand anchor cable with a diameter of 17.8 mm was selected as the research object, which was anchored inside the seamless steel pipe with an inner diameter of 26 mm and an anchoring length of 800 mm. A mine-used steel strand anchor bolt with a diameter of 20 mm was selected as the research object, which was anchored inside the seamless steel pipe with an inner diameter of 30 mm and an anchoring length of 600 mm. The relevant parameters of the test anchor cable are shown in Table 1, the test results are shown in Table 2, and the load-displacement curve of the anchor cable is shown in Figure 2.

The test results show that the tensile strength of this type of anchor cable is 1591 MPa, the maximum tensile force that it can bear is about 400 kN, and its elongation is only 3.5%–4%. The maximum force that the bolt can withstand is about 180 kN, and the elongation is about 16%–18%. Based on the mechanical parameters and deformation law of this kind of anchor cable, the cable structural element in FLAC<sup>3D</sup> will be modified.

*2.2. Fish Language Optimization of Cable Element.* Based on the mechanical behavior characteristics of anchor cable, the state of Cable element is divided into three categories: (1) elastic stage: it fails to reach the maximum load that it can bear, and the deformation and stress are both less than the maximum. The structural element will continue to deform in elastic stage and then enter the plastic stage. (2) Plastic stage: in this stage, the force of Cable element is equal to the maximum load it can bear, but the deformation does not reach the critical value, and it will continue to deform in this



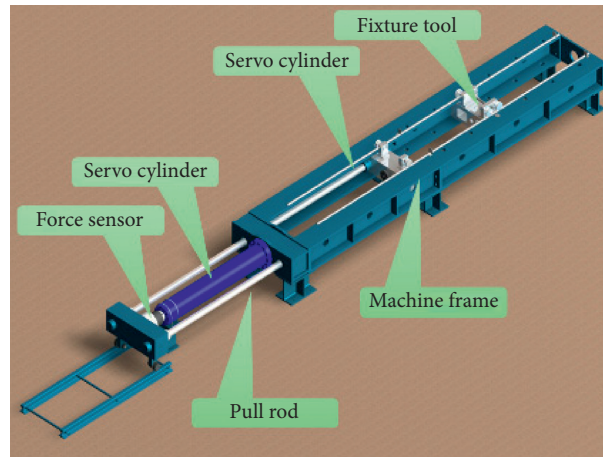


FIGURE 1: Structure of horizontal tensile testing machine.

TABLE 1: Mechanical properties test scheme of cable bolt.

	Length (m)	Diameter (mm)	Anchor length (mm)	Diameter of anchor hole (mm)
Bolt	2.2	20	600	30
Cable	2.5	17.8	800	28

TABLE 2: Experimental results of cable bolt pull-out test.

Variable/unit	Bolt/value	Cable/value
Tensile strength ( $R_m$ )/MPa	561	1591
Maximum force ( $F_m$ )/kN	176.2	395.62
Upper yield strength ( $R_{eH}$ )/MPa	409	1532
Upper yield force ( $F_{eH}$ )/kN	128.46	381.21
Lower yield strength ( $R_{eL}$ )/MPa	402	1524
Lower yield force ( $F_{eL}$ )/kN	128.43	379.13

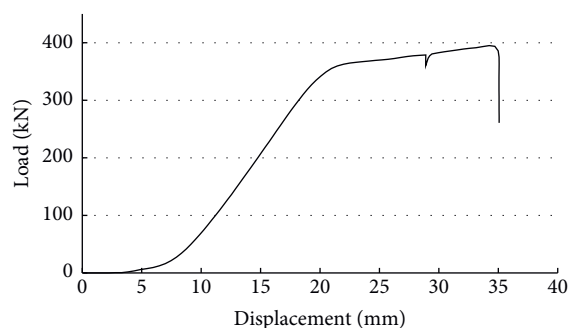


FIGURE 2: Load-displacement curve of cable bolt pull-out test.

stress state. (3) Failure stage: the deformation of the structural element exceeds the maximum deformation it can withstand, and it will break and fail. The optimized force model of Cable element is shown in Figure 3.

When the anchor cable enters the yielding state and its axial deformation reaches the specified breaking criterion, the anchor cable will enter the breaking state. After breaking, the axial force of the anchor cable drops to zero, and the axial restraint on the deformation of the surrounding rock is lost.

In  $FLAC^{3D}$ , except for the anchorage section, the interaction between Cable element and surrounding rock is realized through the connection between nodes at its ends and solid elements, which can be used to simulate the role of tray and nut in the actual support. This kind of node can be removed from modified Cable element through programming, and the specific process is shown in Figure 4.

**2.3. Simulation Test of Modified Structural Element.** In order to test the effectiveness of the modified scheme, the tensile simulation experiment of anchor bolt was carried out in  $FLAC^{3D}$ . The experimental object is the left-hand screw bolt with a diameter of 20 mm, the theoretical breaking load is 180 kN, and the breaking elongation is 16%. The established tensile test model of the bolt is displayed in Figure 5. The total length of the bolt model is 2 m, and the fixed section and the anchor section are both 0.5 m. The bolt is divided into 20 elements, with 0.1 m in length. The element number (CID) is 1 to 20 from right to left, and the monitoring element is element 10.

The experiment tests include the original model test and two modified model tests. During the test, a speed of  $1e-5$  was applied to the left side of the model for calculation. The displacement and force of element 10 are continuously monitored, and experiment results are shown in Figure 6.

The modified model realizes the tensile failure when the Cable element reaches the maximum elongation in the calculation process. With the increase of displacement, the load presents a trend of fluctuating decrease, which is obviously different from the change rule of the vertical line of the load in the pull-out test results. The reason is that the numerical experiment monitors the force change of the small element in the cable structural element, and there is a certain lag and

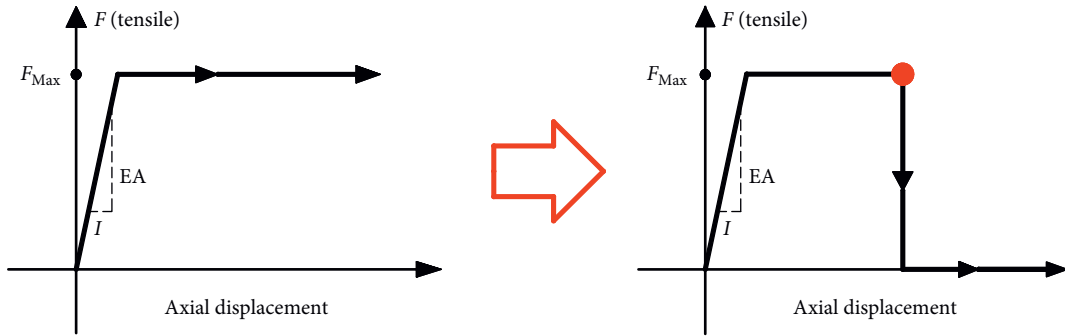


FIGURE 3: Anticipated result of cable unit modification.

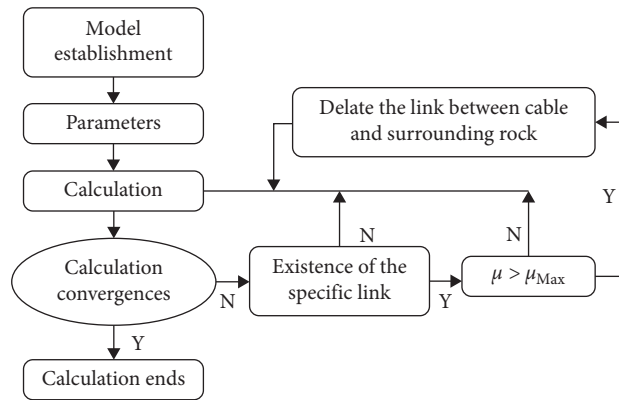


FIGURE 4: Flowchart of revised plan for the anchor cable unit.

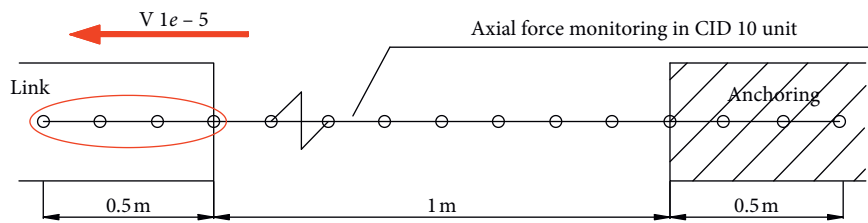


FIGURE 5: Simulation experiment of Cable element modification model.

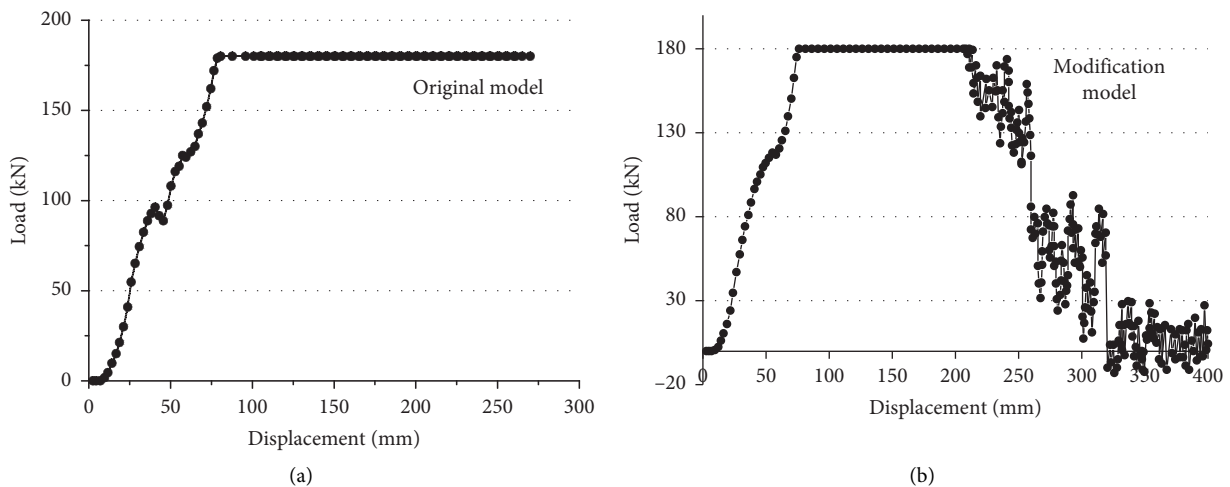


FIGURE 6: Comparison of the load-displacement curves between the original model and the modified model. (a) Original model. (b) Modified model.

fluctuation in the monitoring of the force change. The modification method is to equate the failure behavior of anchor cable by removing the connection point (link point) between the end of cable structural element and solid element. The released structural element no longer interacts with the solid element (surrounding rock), so this fluctuating load drop will not affect the simulation results. Meanwhile, this equivalent simulation method can realize the continuous action of the structural elements in the anchorage section, which is in good agreement with the actual situation. Therefore, it is considered that this modification scheme is feasible and can simulate the action law of anchor cable deformation failure on the surrounding rock of the roadway more truly.

### 3. Mechanical Effect of Anchor Cable Lagging Supporting Time under Mining Dynamic Pressure

*3.1. Establishment of Numerical Calculation Model and Parameters Determination.* The supporting time of anchor cable lagging support needs to consider many factors, such as roadway surrounding rock properties, joint structure, and support parameters. In this study, taking roadway driving along goaf at 6208 working face of Wangzhuang Coal Mine for example. Because the upper section 6207 transportation along the roadway uses the same support parameters, the relative movement of the roof and floor of the roadway is relatively large, and the roof squeeze transfer machine appears. Circumstances, along with a certain amount of anchor cable breakage, seriously affected safe and efficient production. The modified numerical analysis model is used to study the time of anchor cable lagging support. In Wangzhuang Coal Mine, one side of 6208 transport tunnel is a solid coal bank, and the other side is adjacent to the mined area of 6207 working face. The width of coal pillars for roadway protection is 7.6 m. The plan sketch of the mining engineering is shown in Figure 7. The length, width, and height of the numerical model are 200 m, 130 m, and 66 m, respectively. The bottom boundary of the model is fixed in the vertical direction, while the two sides and front-rear boundaries are fixed in the horizontal direction. Using the numerical model parameter modification method of Zhang et al. [27, 28] and based on the laboratory results, the physical and mechanical parameters of each rock layer in the model are finally determined, as shown in Table 3. The mechanical parameters of the anchor cable are selected from the experimental parameters; that is, the elastic modulus of the anchor is 200 GPa, the diameter is 20 mm, the length is 2.2 m, the breaking load is 180 kN, and the anchoring length is 0.6 m. The diameter of the anchor cable is 17.8 mm, the length is 6.0 m, the breaking load is 400 kN, and the anchoring length is 1.2 m. The roof is arranged with 6 anchor rods with a distance of 800 mm, and the roof is arranged with 2 anchor cables with a distance of 1.8 m.

*3.2. Simulation and Monitoring Programs.* In order to determine the reasonable time of anchor cable support, based on the property that the deformation amount and

deformation rate of surrounding rock are significantly different with the increase of the distance from the tunneling face, taking the distance from the tunneling face as the index, five kinds of anchor cable lagging support schemes were determined, as shown in Table 4. This scheme can be used to simulate the supporting effect of surrounding rock in different deformation periods, that is, the severe deformation period, gentle period close to surrounding rock deformation, and gentle period completely entering into the surrounding rock deformation. The bolt/mesh/anchor combined support in the model is shown in Figure 8. The mechanical behavior of the anchor cable under advanced support stress in the mining face and its influence on the stability of the roadway in five schemes are simulated, respectively.

Without support conditions, the leading support pressure distribution of the working face and the deformation law of the roadway roof are shown in Figure 9. The leading support pressure of the working face first increases and then decreases. The peak value is 14 MPa, and the peak point is 18 m away from the working face. The peak value area is about 12~22 m from the working face, and the severe influence area is about 0~35 m. In order to study the influence of the deformation behavior of surrounding rock on the supporting structure when the anchor cable lagged support, 3 measuring points at a depth of 2 m in the roof were set up before and after the peak zone of the leading support pressure. The measuring points are used to monitor the failure time of anchor cable and the change rule of supporting effect. The 3 measuring points are 15 m, 20 mm, and 25 m away from the working surface in sequence.

*3.3. Determination Condition of Anchor Cable Failure.* In order to accurately reflect the failure time of the anchor cable and the change of the support effect before and after the failure, the minimum principal stress ( $\sigma_{\min}$ ) and the volume strain rate (VSR) of the surrounding rock within 2 m of the shallow part of the roadway when the anchor cable fails are proposed as the determination indicators for the failure. In order to prove the validity of the determination indicators, model tests were carried out. The numerical model is shown in Figure 10. High in situ stress is applied to the model to make the surrounding rock of the roadway deform greatly until the anchor cable extends and fails. The minimum principal stress and the volumetric strain rate of the surrounding rock within 2 m of the roadway roof were monitored continuously during the calculation process.

The numerical simulation results are shown in Figure 11. The figure reveals that the minimum principal stress and volume strain rate within 2 m of the roadway roof monitored before and after the failure of the anchor cable have obvious abrupt changes, which are in one-to-one correspondence with the time of the failure of the anchor cable. When the modified model is not adopted (Figure 11(a)), the anchor cable does not fail in the process of roadway deformation and has always played a supporting role for the surrounding rock. When the modified model is not adopted (Figure 11(b)), the anchor cable does not fail in the process of roadway deformation and has always played a supporting

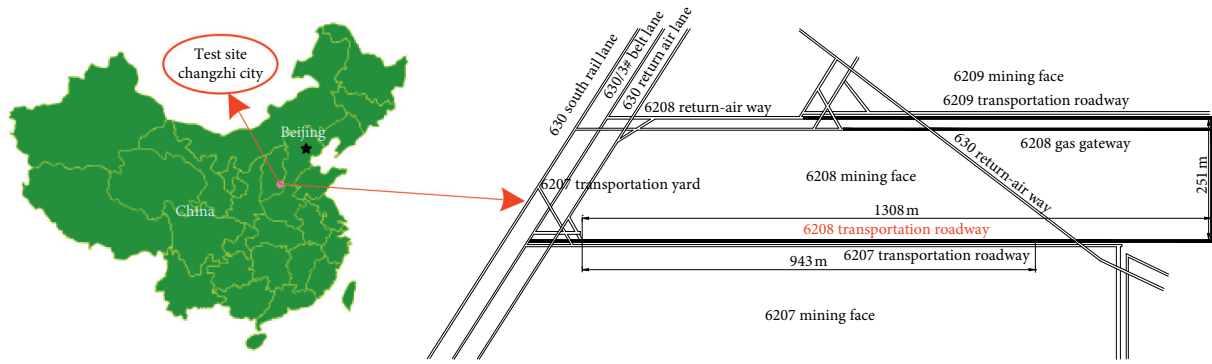


FIGURE 7: Schematic diagram of 6208 roadway engineering plane in Wangzhuang coal mine.

TABLE 3: Mechanical parameters used in the model.

Stratum	Thickness (m)	Density ( $\text{kg}\cdot\text{m}^{-3}$ )	Elastic modulus (GPa)	Poisson's ratio	Cohesion (MPa)	Interior friction angle ( $^{\circ}$ )
Fine sandstone	28	2550	10.5	0.29	7.5	39
Mudstone	6	2400	7.0	0.33	4.5	35
Coal	6	1400	5.3	0.30	2.5	30
Mudstone	6	2400	7.0	0.33	4.5	35
Medium grained sandstone	20	2500	9.0	0.30	6.5	37

TABLE 4: Comparison scheme of cable delayed supporting.

Scheme	Scheme I	Scheme II	Scheme III	Scheme IV	Scheme V
Lag distance (m)	Timely support	5	10	15	20
Deformation period	Severe deformation	Severe deformation	Tending to be slowly	Beginning to be slowly	Slow deformation period

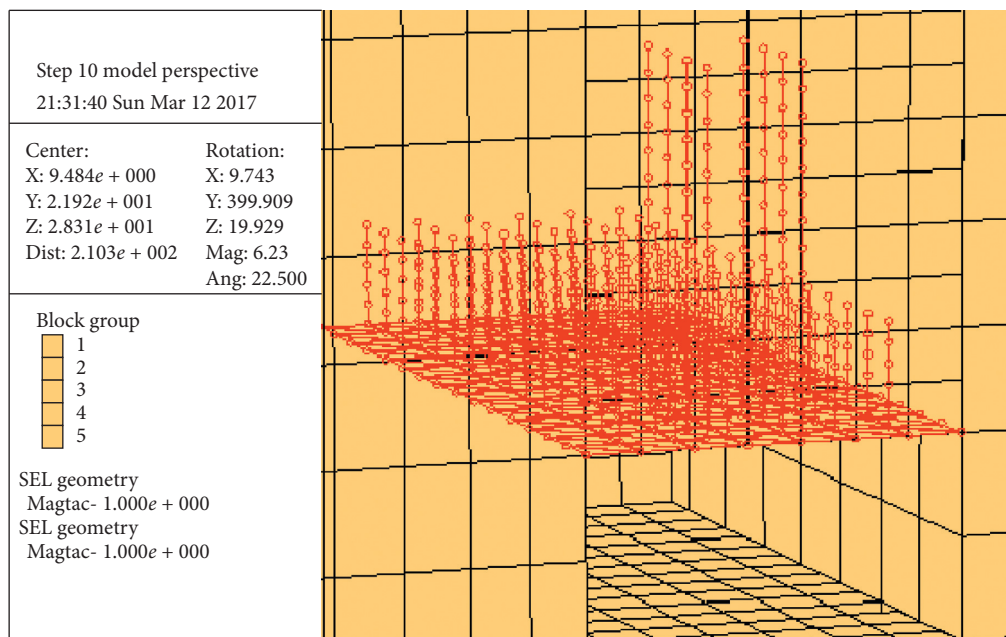


FIGURE 8: Schematic diagram of bolt-mesh-anchor cable supporting in the model.

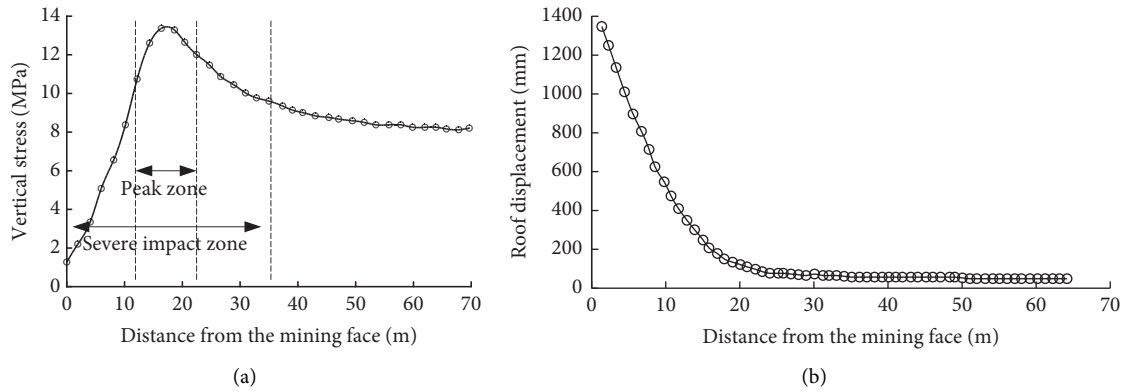


FIGURE 9: The behavior of advanced strata pressure in mining period. (a) Advancing support pressure distribution. (b) Roadway deformation.

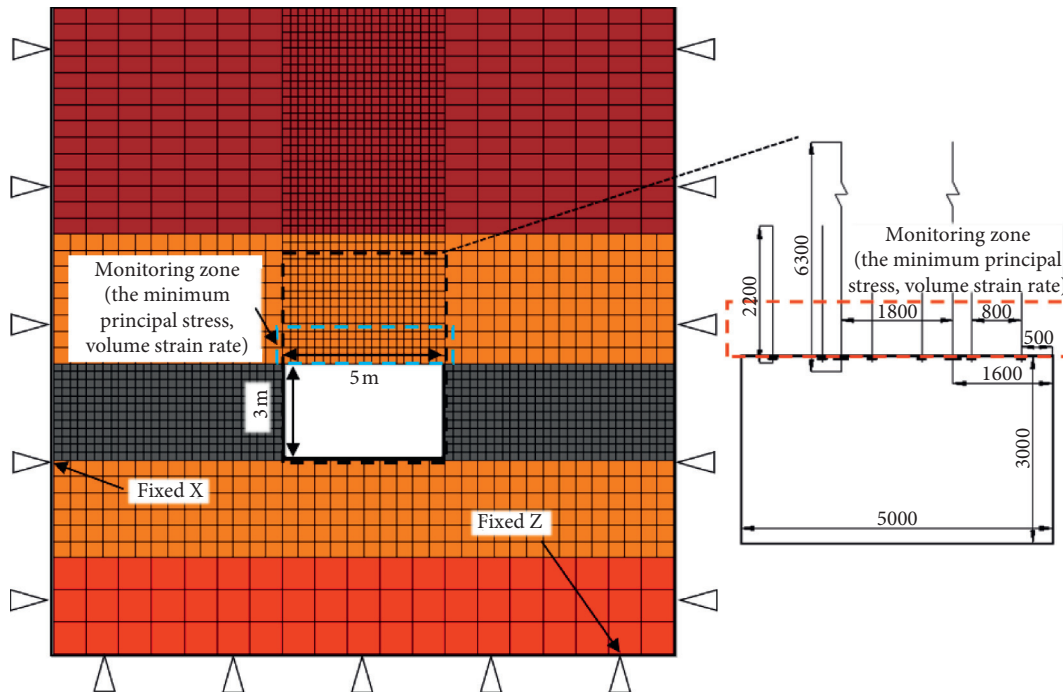


FIGURE 10: Test model of judgment index.

role for the surrounding rock. In the later stage when the deformation of surrounding rock is stable, the minimum principal stress within the monitoring range changes around 1.55 MPa, while the volume strain rate keeps around 0, and both tend to be stable without large fluctuations. However, after adopting the cable modified model (Figure 11(b)), the deformation of roadway surrounding rock drives the extension of structural elements, and the anchor cable fails. The failure of anchor cable can also be verified by intuitively displaying the force of Cable element in the FLAC<sup>3D</sup> model. With the failure of the anchor cable, the minimum principal stress of surrounding rock in the monitoring area will suddenly decrease and the volumetric strain rate will suddenly increase. The sudden failure of the anchor cable causes the supporting resistance provided by the supporting structure to suddenly disappear, and the internal stress state

of the surrounding rock changes, causing a sudden change in volume strain rate of the surrounding rock. This one-to-one characterization relationship is verified, and the feasibility of the two failure determination indicators, the minimum principal stress and volume strain rate, is determined.

3.4. Variation Law of Failure Criterion of Anchor Cable in Front of Mining Working Face. During the stopping of working face, the variation rules of anchor cable failure determination indexes under the five lagging support schemes are shown in Figure 12. It is found that the failure time of several anchor cable lagging schemes is obviously different due to the different supporting time and coupling stress state in the early stage. With the increase of the lagging distance of anchor cable support, the ability of the anchor



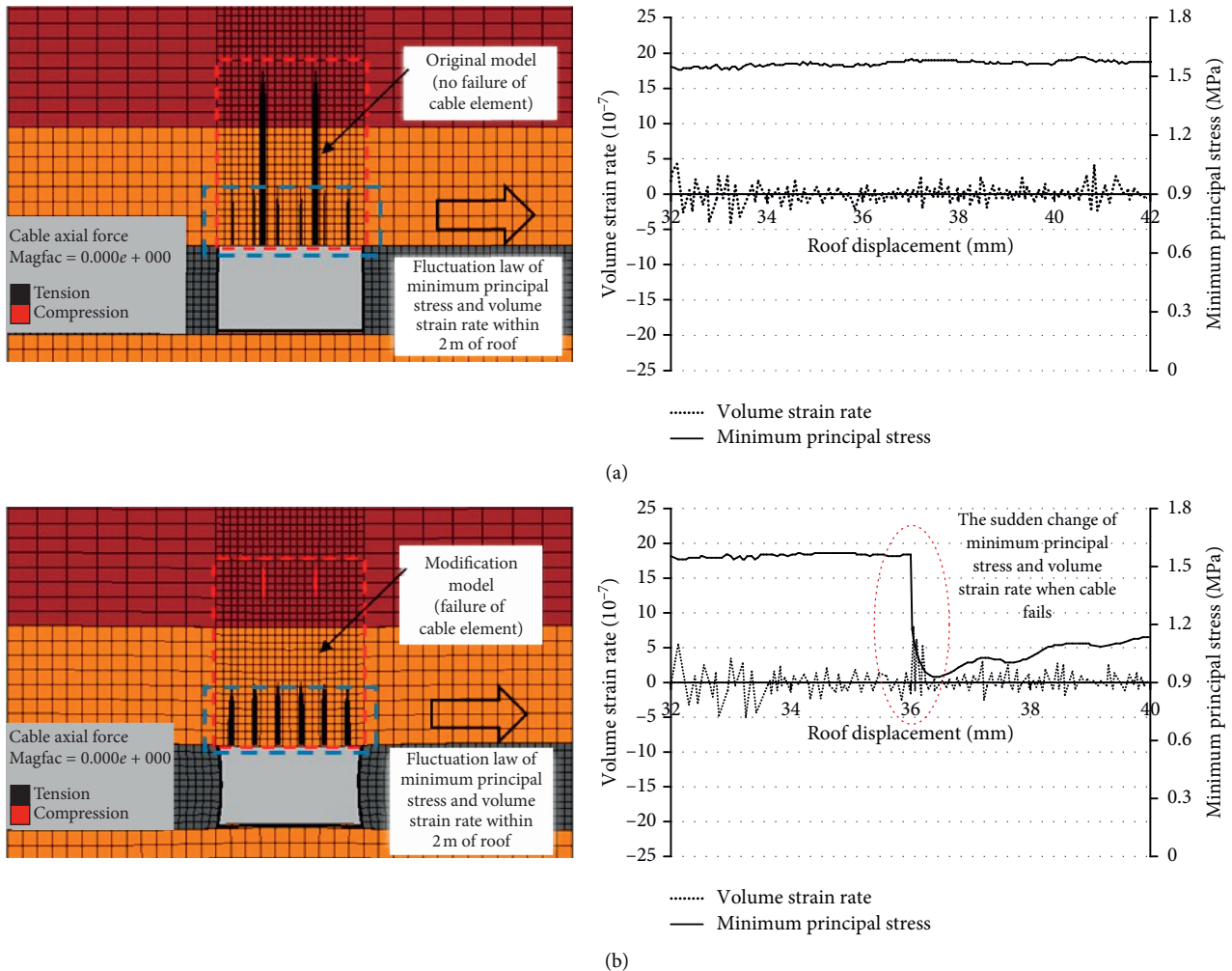


FIGURE 11: Variation of index. (a) Variation of assessment index before anchor Cable element is failure. (b) Variation of assessment index after anchor Cable element is failure.

cable to adapt to deformation gradually increases. In schemes 3, 4, and 5, the adaptability of anchor cable to deformation is significantly improved compared with schemes 1 and 2. When the lagging time of the anchor cable is a gentle area of roadway deformation (schemes 4 and 5), the ability increment of the anchor cable to adapt to deformation has been reduced.

The lagging support of the anchor cable significantly improves the deformation bearing capacity, but the different supporting time leads to the different coupling stress conditions of the supporting body. The initial resistance of the supporting structure is significantly different, which is reflected in the mechanical phenomenon in the figure that the minimum principal stress increases with deformation. For scheme 3, there is no anchor cable failure at the position of the 20 m measuring point, but it also shows that the maximum working resistance cannot be reached in time during the initial deformation process of the roof under the advanced supporting pressure. Due to the certain hysteresis of the anchor cable, the initial axial force of the anchor cable decreases, and the reduction of the minimum principal

stress in the surrounding rock at the initial stage of the surrounding rock deformation caused by this is not strong. Therefore, scheme 3 is considered to be feasible. It can be seen from schemes 4 and 5 that when the anchor cable lagging support is completely located in the gentle period of roadway deformation, the initial minimum principal stress in the surrounding rock is significantly reduced. The supporting body needs a long process of surrounding rock deformation to reach its maximum support resistance, so the supporting effect of the supporting structure cannot be fully exerted in the early stage, which is not conducive to the deformation control.

Therefore, considering the improvement of the deformation bearing capacity of the anchor cable by different schemes and the supporting capacity of the anchor cable in the early stage of roadway deformation, the lagging support time of the anchor cable is the best when it is close to the stable period of the surrounding rock deformation of the roadway. It is determined that the lagging support time of anchor cable in 6208 transport tunnel in Wangzhuang Coal Mine is within 10–15 m behind the head.

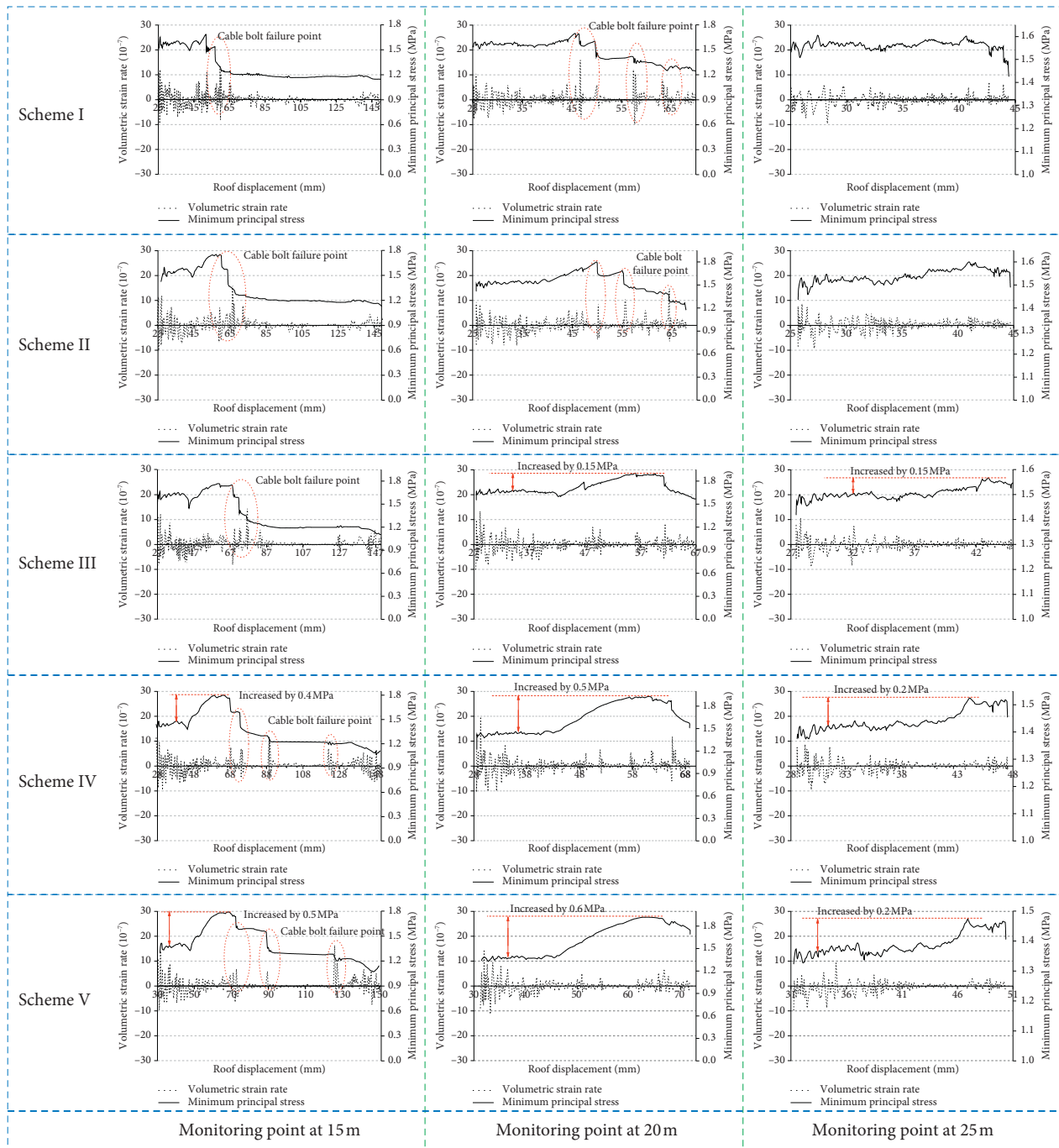


FIGURE 12: Change of the failure judgment index for the cables during the advancing of the working face.

#### 4. Industrial Tests

In order to verify the effectiveness of the optimization support scheme of 6208 tunnel in Wangzhuang Coal Mine, three groups of surface displacement and anchor cable stress measurement stations are set up. The monitoring scheme is shown in Figure 13. In the process of tunneling and mining, the bolt dynamometer is used to monitor the strain of the load-measuring bolt and the load-measuring cable, and then

the stress state is calculated according to the mechanical parameters of the bolt and the cable. The monitoring results of the 1# comprehensive measuring station are shown in Figure 14.

After raising the prestress of the bolt and adopting lagging support for the anchor cable, roof anchor bolt and cable show good coupling and cooperative stress relationship (Figure 14). In the later stage of tunneling, the coupling force range is basically reached. Meanwhile, the reasonable

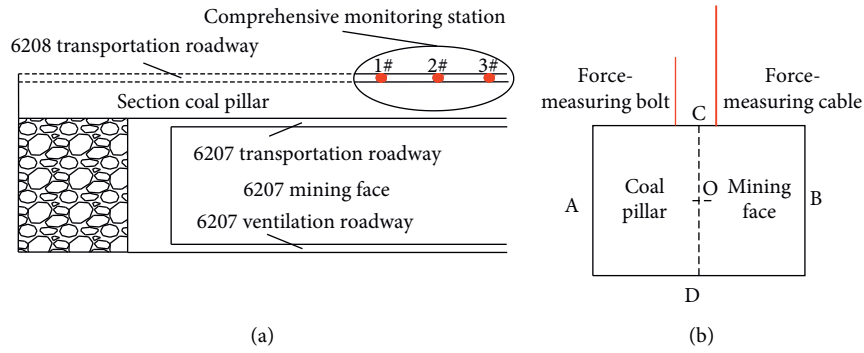


FIGURE 13: Integrated station layout.

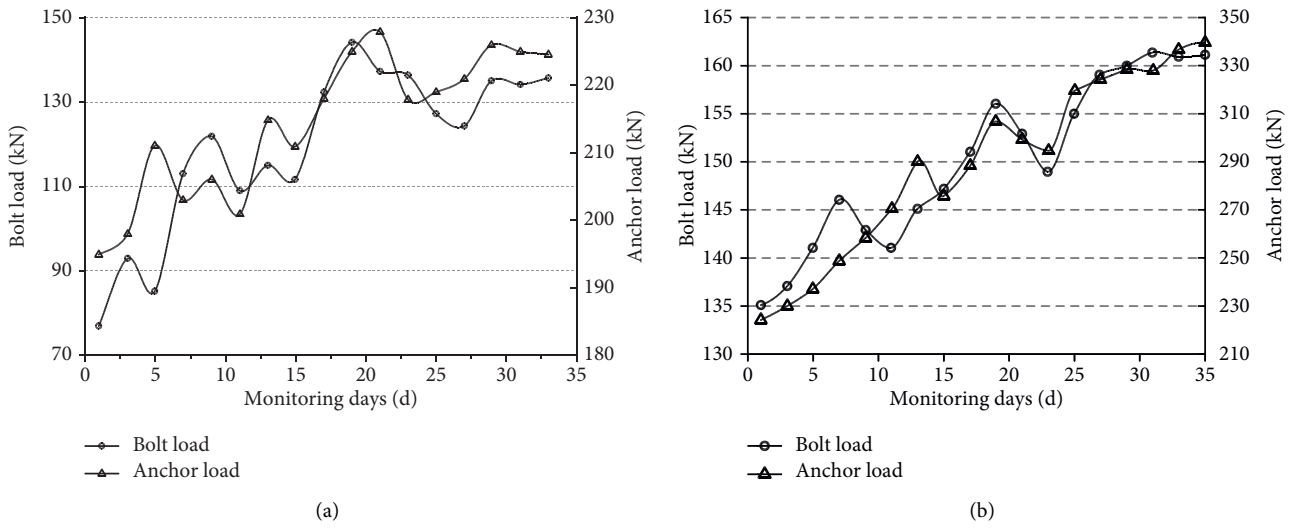


FIGURE 14: Force change of bolt and cable. (a) The period of drilling. (b) The period of mining.

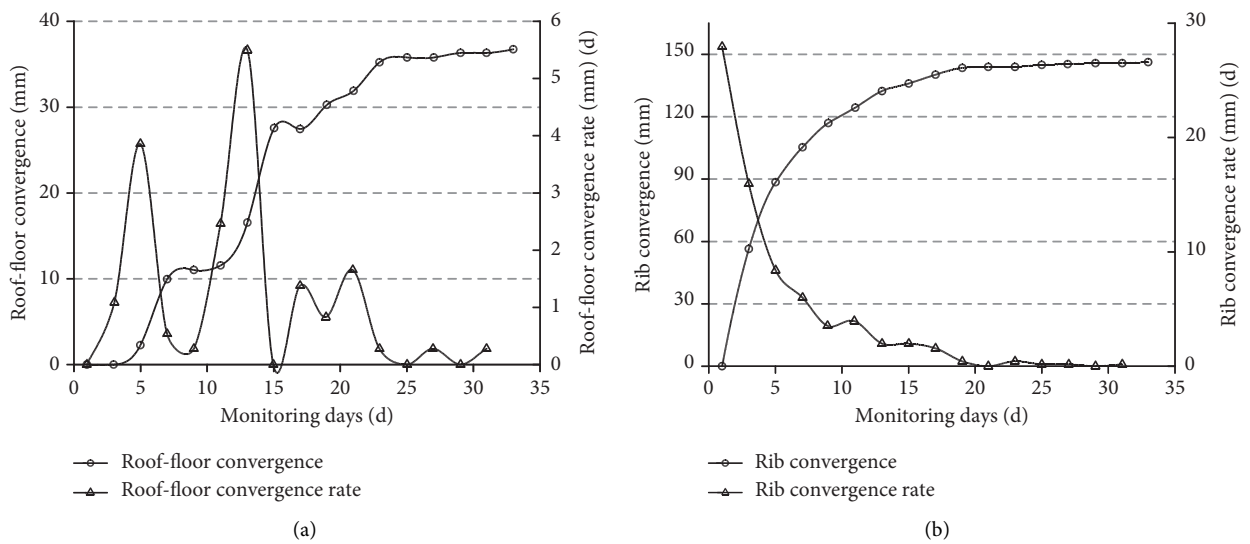


FIGURE 15: Continued.

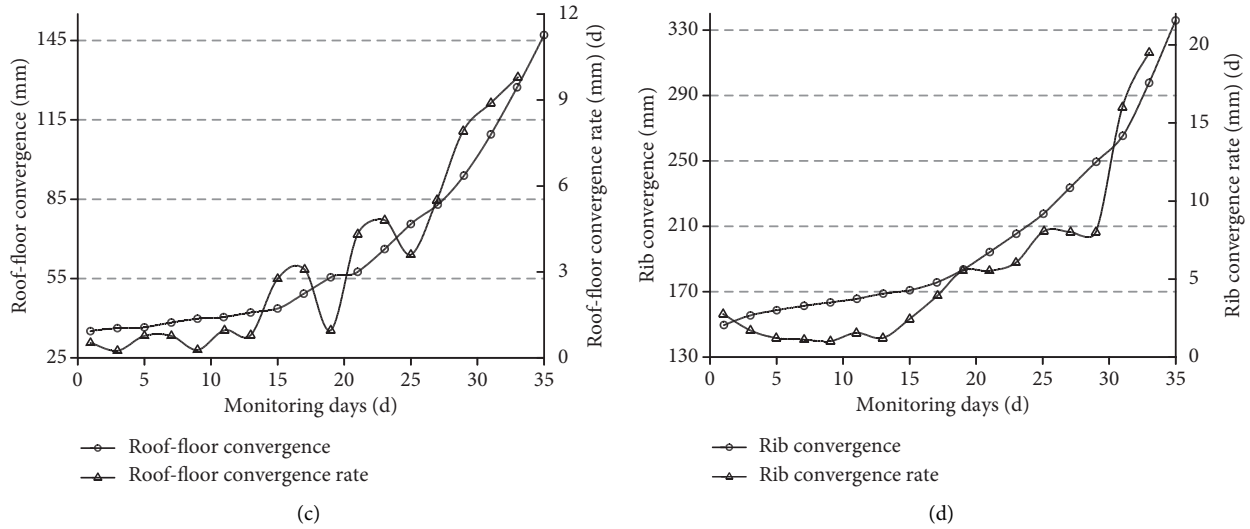


FIGURE 15: Evolution of the surface displacement around the roadway. (a) Displacement of roof and floor during excavation. (b) Displacement of two sides during excavation. (c) Displacement of roof and floor during extraction. (d) Displacement of two sides during extraction.

lagging support also ensures that the anchor cable can withstand a certain deformation during mining without broken failure, which ensures the safe use of the roadway.

The surface displacement of surrounding rock is shown in Figure 15. After adopting the optimized support scheme, the deformation of the surrounding rock of the roadway has been well controlled. In the mining and stopping stages, the final relative approaching quantities of roof and floor are 37 mm and 147 mm, respectively, and the corresponding relative approaching quantities of roadway sides are 149 mm and 330 mm, respectively, in the two stages. In view of the overall control effect of surrounding rock, the roadway surrounding rock is in a relatively stable state, and its deformation is effectively controlled.

## 5. Conclusion

In mining engineering, the failure of anchor cable of the mining roadway roof induces by mining is very serious; therefore, solving the failure of anchor cable is very important to maintain the stability of roadway. As a result, a solution for anchor cable lagging support is proposed in this study. Moreover, based on the modified Cable element in FLAC<sup>3D</sup>, the real breaking effect of anchor cable in the calculation process is realized. Through the simulation analysis of five anchor cable lagging support schemes of 6208 transport tunnel in Wangzhuang Mine Coal, industrial tests are carried out, and the feasibility of the scheme is verified successfully. The main conclusions are as follows:

- (1) Based on the results of indoor anchor cable pull-out test, the deformation behavior of anchor cable is obtained. Then, the deformation property of Cable element in FLAC<sup>3D</sup> is modified so that the extension breaking effect of anchor cable can be realized in the calculation process.

- (2) The minimum principal stress and volumetric strain mutation point are used as the mechanical criterion for the failure of anchor cable. It is proved that with the increase of anchor cable support lagging time, the ability of anchor cable to adapt to deformation increases gradually, the increase rate decreases gradually, and the initial support resistance decreases gradually.
- (3) According to the modified numerical model, it is determined that the lagging time of the anchor cable along the 6208 transport tunnel in Wangzhuang Coal Mine is within 10–15 m of lagging head. The industrial test verifies the feasibility of the scheme and ensures the safe use of the roadway.

## Data Availability

The data used to support the findings of this study are available from the corresponding author upon request.

## Conflicts of Interest

The authors declare that they have no conflicts of interest regarding the publication of this paper.

## Acknowledgments

This research was financially supported by the National Key Research and Development Program of China through contract no. 2020YFB1314200.

## References

- [1] C. J. Hou, *Ground Control of Roadways*, China University of Mining and Technology Press, Xuzhou, China, 2013.
- [2] A. Mirzaghobanali, H. Rasekh, N. Aziz, G. Yang, S. Khaleghparast, and J. Nemcik, "Shear strength properties of

- cable bolts using a new double shear instrument, experimental study, and numerical simulation,” *Tunnelling and Underground Space Technology*, vol. 70, pp. 240–253, 2017.
- [3] Z. Wen, E. Xing, S. Shi, and Y. Jiang, “Overlying strata structural modeling and support applicability analysis for large mining-height stopes,” *Journal of Loss Prevention in the Process Industries*, vol. 57, pp. 94–100, 2019.
  - [4] C. Zhang, Z. Zhu, S. Zhu et al., “Nonlinear creep damage constitutive model of concrete based on fractional calculus theory,” *Materials*, vol. 12, no. 9, p. 1505, 2019.
  - [5] Z. Zhang, M. Deng, J. Bai, X. Yu, Q. Wu, and L. Jiang, “Strain energy evolution and conversion under triaxial unloading confining pressure tests due to gob-side entry retained,” *International Journal of Rock Mechanics and Mining Sciences*, vol. 126, no. 4, Article ID 104184, 2020.
  - [6] S. Liu, J. Bai, X. Wang, B. Wu, and W. Wu, “Mechanisms of floor heave in roadways adjacent to a goaf caused by the fracturing of a competent roof and controlling technology,” *Shock and Vibration*, vol. 2020, Article ID 5632943, 17 pages, 2020.
  - [7] Y. Zhao, Y. Wang, W. Wang, W. Wan, and J. Tang, “Modeling of non-linear rheological behavior of hard rock using triaxial rheological experiment,” *International Journal of Rock Mechanics and Mining Sciences*, vol. 93, pp. 66–75, 2017.
  - [8] W. D. Ortlepp and T. R. Stacey, “Performance of tunnel support under large deformation static and dynamic loading,” *Tunnelling and Underground Space Technology*, vol. 13, no. 1, pp. 15–21, 1998.
  - [9] M. He, W. Gong, J. Wang et al., “Development of a novel energy-absorbing bolt with extraordinarily large elongation and constant resistance,” *International Journal of Rock Mechanics and Mining Sciences*, vol. 67, pp. 29–42, 2014.
  - [10] P. Wang, L. S. Jiang, J. Q. Jiang, P. Q. Zheng, and W. Li, “Strata behaviors and rock-burst-inducing mechanism under the coupling effect of a hard thick stratum and a normal fault,” *International Journal of Geomechanics*, vol. 18, no. 2, Article ID 04017135, 2018.
  - [11] Y. Liu, P. Zheng, and P. Wang, “Multi-factors influence of anchorage force on surrounding rock under coupling effect of creep rock mass and bolt/cable,” *Geomatics, Natural Hazards and Risk*, vol. 12, no. 1, pp. 328–346, 2021.
  - [12] Q. Wu, X. Li, L. Weng, Q. Li, Y. Zhu, and R. Luo, “Experimental investigation of the dynamic response of prestressed rockbolt by using an SHPB-based rockbolt test system,” *Tunnelling and Underground Space Technology*, vol. 93, Article ID 103088, 2019.
  - [13] E. Y. Dong, W. J. Wang, N. J. Ma, and C. Yuan, “Analysis of anchor space-time effect and research of control technology considering creep of surrounding rock,” *Journal of the China Coal Society*, vol. 43, no. 5, pp. 1238–1248, 2018.
  - [14] H. P. Kang, J. Lin, and B. C. Zhang, “Study on small borehole pretensioned cable reinforcing complicated roadway,” *Chinese Journal of Rock Mechanics and Engineering*, vol. 22, no. 3, pp. 387–390, 2003.
  - [15] Y. L. Lu, L. G. Wang, B. Zhang, and Y. Y. Li, “Optimization of bolt-grouting time for soft rock roadway,” *Rock and Soil Mechanics*, vol. 33, no. 5, pp. 1395–1401, 2012.
  - [16] L. D. Yang, J. P. Yan, Y. Z. Wang, and Q. Y. Wang, “Study on time-dependent properties and deformation prediction of surrounding rock,” *Chinese Journal of Rock Mechanics and Engineering*, vol. 24, no. 2, pp. 212–216, 2005.
  - [17] H. Lin, “Study of soft rock roadway support technique,” *Procedia Engineering*, vol. 26, pp. 321–326, 2011.
  - [18] H. P. Kang, J. Lin, and M. J. Fan, “Investigation on support pattern of a coal mine roadway within soft rocks—a case study,” *International Journal of Coal Geology*, vol. 140, pp. 31–40, 2015.
  - [19] W. Yu, B. Pan, F. Zhang, S. Yao, and F. Liu, “Deformation characteristics and determination of optimum supporting time of alteration rock mass in deep mine,” *KSCE Journal of Civil Engineering*, vol. 23, no. 11, pp. 4921–4932, 2019.
  - [20] Q. B. Meng, L. J. Han, and Q. Wang, “Optimization analysis of grouting timing in deep and high stress soft rock roadway,” *Journal of Central South University (Science and Technology)*, vol. 48, no. 10, pp. 2765–2776, 2017.
  - [21] H. T. Liu and J. Q. Li, “Research on timeliness of coordination support of bolting-mesh-shotcreting-grouting in deep roadway,” *Journal of China Coal Society*, vol. 40, no. 10, pp. 2347–2354, 2015.
  - [22] W. Yu, G. Wu, and B. An, “Investigations of support failure and combined support for soft and fractured coal-rock tunnel in tectonic belt,” *Geotechnical and Geological Engineering*, vol. 36, no. 6, pp. 3911–3929, 2018.
  - [23] G. S. Wu, W. J. Yu, Z. Lu, and Z. Tang, “Failure law and mechanism of the rock-loose coal composite specimen under combined loading rate,” *Advances in Civil Engineering*, vol. 2018, Article ID 2482903, 10 pages, 2018.
  - [24] J. Nemcik, S. Ma, N. Aziz, T. Ren, and X. Geng, “Numerical modelling of failure propagation in fully grouted rock bolts subjected to tensile load,” *International Journal of Rock Mechanics and Mining Sciences*, vol. 71, pp. 293–300, 2014.
  - [25] L. Jiang, A. Sainoki, H. S. Mitri, N. Ma, H. Liu, and Z. Hao, “Influence of fracture-induced weakening on coal mine gateroad stability,” *International Journal of Rock Mechanics and Mining Sciences*, vol. 88, pp. 307–317, 2016.
  - [26] S. Yan, Y. Song, J. Bai, and D. Elmo, “A study on the failure of resin end-anchored rockbolts subjected to tensile load,” *Rock Mechanics and Rock Engineering*, vol. 52, no. 6, pp. 1917–1930, 2019.
  - [27] Z. Zhang, M. Deng, X. Wang, W. Yu, F. Zhang, and V. D. Dao, “Field and numerical investigations on the lower coal seam entry failure analysis under the remnant pillar,” *Engineering Failure Analysis*, vol. 115, Article ID 104638, 2020.
  - [28] Z. Z. Zhang, M. Deng, J. B. Bai, S. Yan, and X. Y. Yu, “Stability control of gob-side entry retained under the gob with close distance coal seams,” *International Journal of Mining Science and Technology*, vol. 31, no. 2, pp. 321–332, 2020.



## Research Article

# Analysis on the Influence Degree of Deformation Control Factors of Deep-Buried Roadway's Fractured Surrounding Rock Using Orthogonal Design

Ke Li <sup>1,2</sup>, Weijian Yu <sup>1,3</sup>, Youlin Xu <sup>2</sup>, Ze Zhou <sup>2</sup>, Mengtang Xu <sup>2</sup> and Wei Liang<sup>2</sup>

<sup>1</sup>School of Resource & Environment and Safety Engineering, Hunan University of Science and Technology, Xiangtan, Hunan 411201, China

<sup>2</sup>College of Mining, Guizhou Institute of Technology, Guiyang, Guizhou 550003, China

<sup>3</sup>Hunan Provincial Key Laboratory of Safe Mining Techniques of Coal Mines, Hunan University of Science and Technology, Xiangtan, Hunan 411201, China

Correspondence should be addressed to Weijian Yu; ywjlah@163.com

Received 1 April 2021; Accepted 23 May 2021; Published 7 June 2021

Academic Editor: Zhijie Zhu

Copyright © 2021 Ke Li et al. This is an open access article distributed under the Creative Commons Attribution License, which permits unrestricted use, distribution, and reproduction in any medium, provided the original work is properly cited.

It is a complex issue to select the support structure parameters for a deep-buried roadway with fractured surrounding rock; especially when the support structure parameters need to be adjusted, the influence degree of support structure parameters on roadway deformation needs to be determined. The deformation of deep-buried roadway's fractured surrounding rock development was investigated using multi-index orthoplan in this paper. According to the coal mine field investigation, support structure's failure often occurs, and some need to be repaired many times. Through the roadway surrounding rock drilling, it was found that the stress of the surrounding rock was relieved, resulting in the cavity and separation of the stratum layer. The two sidewalls' development and roof fractures are mainly tangential, and the original rock state appears only beyond 6.3~8.2 m. The length of bolts, the row distance between bolts, the length of cables, and the row distance of U-shaped steel were selected as control factors in the multi-index orthogonal design, and roadway's deformation values were taken as the test indexes. According to the orthoplan, nine numerical simulation schemes were designed, and FLAC<sup>3D</sup> was used for establishment. The range analysis method was used to analyze the test results. The results show that the control factors' influence order on the total deformation of the roadway is as follows: row spacing between U-shaped steel > bolt length > cable length > row spacing between bolts, the influence order on the deformation of the roadway floor is as follows: row spacing between U-shaped steel > row spacing between bolts > bolt length > cable length, same as the left sidewall and right sidewall, and the influence order on the roadway roof's deformation is as follows: row spacing between U-shaped steel > bolt length = cable length > row spacing between bolts, which provide a reference for the support design of deep-buried roadways with fractured surrounding rock, especially the adjustment of the supporting structure.

## 1. Introduction

With the shallow resource mined out, the coal mining gradually shifts to the deep. The factors such as significant buried depth, high-stress environment, complex structure, broken surrounding rock, and aquifer influence are superimposed, bringing about more challenges to the maintenance of coal mine roadway [1]. The deep-buried soft rock roadway's maintenance difficulty gradually becomes

the bottleneck of building high-efficiency mines. Choosing the appropriate supporting method is challenging to solve urgently in the coal mine site.

In the Yunnan-Guizhou plateau of Southwest China, coal mines are greatly affected by geological structure. Under the vigorous promotion of many scholars and engineers, bolts (cables), section steel, shotcrete (grouting), and other support technologies are widely used in coal mine field [2, 3]. The exploration of support structure mechanism and its

bearing mechanism with surrounding rock has always been the focus of academic research and engineering practice. Many significant achievements have emerged and solved many engineering and technical problems. Batugin et al. [4] developed a combined support technology for adjacent roadways and analyzed for a rock bolt and anchor cable mechanism based on the external staggered split-level panel layout's spatial structure. Yu et al. [5] and Wu et al. [6] proposed a combined control scheme based on the bearing system of the "long-short" bolt (cable) and the controlled grouting reinforcement of the "internal-external" structure. Gong et al. [7] and Li et al. [8] considered that the radial stress had a greater effect on the spalling failure under the three-dimensional stress condition than the axial stress. Zhang et al. [9] established a mechanical model concerning roof separation within and outside the anchorage zone above the backfill area of gob-side entry retaining and derived a formula to calculate the roof separation, whose influence factors and law were also obtained. Zuo et al. [10, 11] analyzed the stress distribution and failure mechanism of surrounding rock for deep underground project based on brittle constitutive model and slippage destruction theory and considered that excavation unloading would cause the growth of the shear stress, which leads to the local irreversible (plastic) slip or break, and the surrounding rock will be divided into blocks with a certain scale; the frictions between the blocks decide the value of the rest strength. Zhang et al. [12] built a mechanical model of roadway stress based on the nonconstant pressure force state and the cracks revolution mechanisms of floor roadway surrounding rock. Li et al. [13] presented a discontinuous elastoplastic model for the plane strain to depict rock shear strain localization phenomenon and considered that the discontinuous model could profoundly describe the postpeak shear localization phenomenon of the deep rock mass. Huang et al. [14] considered that the large deformation of roadways includes the large deformation of the whole movement caused by the large structure instability of the overlying strata and the large deformation of the movement of the fractured rock mass in the loosening circle. Yan et al. [15] proposed a model for end-anchored rock bolts loaded in tension by implementing a novel tensile failure criterion as part of a 3D continuum numerical modeling package. Zhu et al. [16] developed a parametric asymmetric Voronoi block generation program by Python and established the roadway's numerical model by combining the results of exploration test, micro properties calibration, tension and shear test of rock bolt, and bearing characteristics of timber.

Due to the complexity of fractured rock mass, control technology of roadway with fractured surrounding rock has not yet formed a mature system. At present, the combination of passive support and active support is mainly used, such as steel, bolts, cables, and grouting scheme [12, 17]. However, due to the significant difference in the rock mass, both the stability of rock mass and the control of surrounding rock should be adopted to local conditions [18, 19]. Coal mine's sedimentary environment and structural environment are complex in the Yunnan-Guizhou Plateau of Southwest China. Most of the rock engineering encountered is low

strength fractured rock mass, which has low integrity and poor overall strength and is easy to cause large deformation or instability.

The orthogonal design is used to carry out multiple combinations of supporting structure parameters to determine the influence degree of supporting structure parameters on the supporting effect, which provides a reference for the support design of deep-buried roadway with fractured surrounding rock, especially the adjustment of supporting structure.

## 2. Engineering Background

*2.1. Basic Information.* Wanshun coal mine in Tongzi County, Guizhou Province, is located in the northeast of Songkan syncline. The mining elevation is  $+1200 \sim \pm 0$  m, and the maximum mining depth is 1500 m. There are three minable coal seams, which are numbered C5, C3, and C1, respectively. The coal seams' inclination angle is  $65^\circ \sim 90^\circ$ , the coal seams above the elevation of  $+700$  m in the minefield are inverted, and the coal seams are upright in the range of  $+500$  m  $\sim$   $+700$  m. Movable coal seams are all present in the Permian Longtan Formation ( $P_{3l}$ ), and the upper strata of  $P_{3l}$  are in the Permian Changxing Formation ( $P_{3c}$ ), belonging to medium to thickly layered limestone with suture structure and thinner layered marl, with well-developed joints and fissures. The underlying strata of  $P_{3l}$  are in the Permian Maokou Formation ( $P_{2m}$ ), which is a strong aquifer.

*2.2. Roadway Layout.* Wanshun coal mine is the second mining area. There are four raises in the mining area located in  $P_{3c}$  and marl of Yulongshan member of Yelang Formation ( $T_{1y}^2$ ). To eliminate the risk of gas outburst in the coal seam and shorten the service life of headentries and tailentries in coal mining face, before crossheadings enter the coal seam, main transportation and ventilated roadways are arranged in  $P_{3c}$  between raises and coal seam. After the danger of gas outburst is eliminated, the crossheadings will be constructed from main roadways to coal seam every 200 m, and the headentries and tailentries are arranged after exposing coal seam. According to the field investigation, the second mining area's surrounding rock, which is now arranged in  $T_{1y}^2$ , is relatively stable and deformed. The surrounding rock joints and fissures of the raise and concentrated roadway in  $P_{3c}$  are developed (Figure 1). The 550 main roadway arranged in  $P_{3c}$  and 40 m away from C5 was considered an engineering background. The roadway layout is shown in Figure 2.

*2.3. Roadway Support and Deformation.* The 550 main roadway has a semicircular arch section, with a clear width of 3.6 m, a wall height of 1.4 m, an arch height of 1.8 m, a section of  $10.0 \text{ m}^2$ , and a buried depth of 700 m. The original support method of the roadway is bolting with wire mesh and shotcrete. The bolts adopt resin anchored steel anchor rod, the diameter of the bolts is 18 mm, the length is 2.2 m, and the row distance between the bolts is  $900 \times 900$  mm.

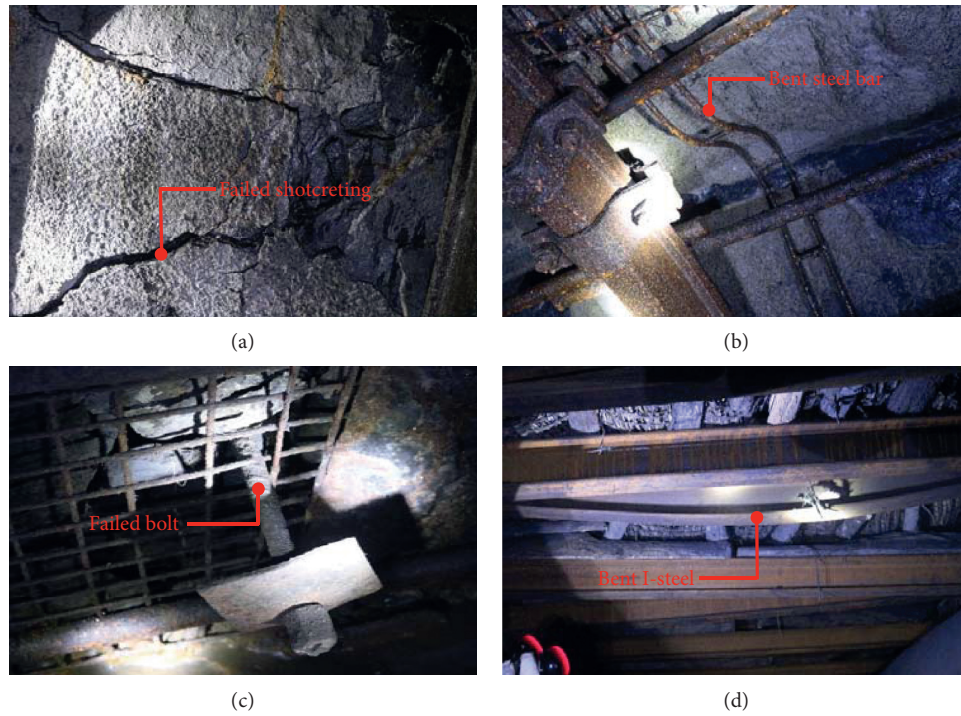


FIGURE 1: Current status of the support structure.

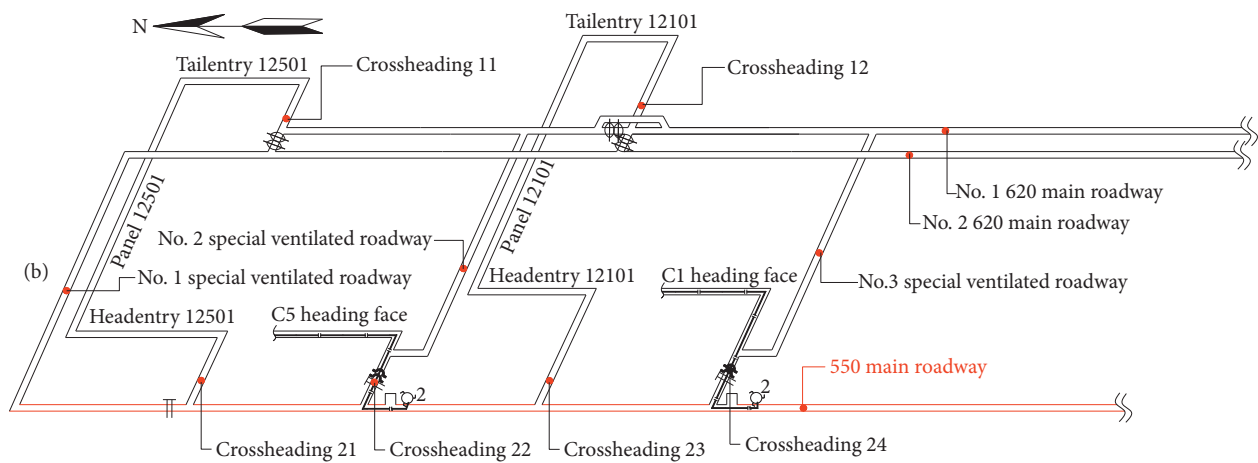


FIGURE 2: Schematic diagram of the roadway layout.

According to the field investigation, the roof subsidence is close to 1.0 m, and the arch wall on the far coal side cracks and falls seriously in the spray layer (as shown in Figure 1(a)). The roadway has been repaired many times. The steel ladder and bolts were repaired for the second time. The roadway continued to deform, most of the bolts failed, and the steel ladder was squeezed and deformed (as shown in Figure 1(b)), whereafter part of the roadway was changed to I-steel + bolt + cables, but the bolts and cables failed in an extensive range (as shown in Figure 1(c)). The I-steel was bent, and the roadway deformation was still not effectively controlled. At present, some sections have been forced to use retractable U-shaped steel flexible supports for support, and

the roadway is still undergoing continuous and rapid deformation (as shown in Figure 1(d)).

### 3. Analysis of Fractures and Mining Impact

3.1. *Surrounding Rock Fragmentation.* To observe the two sidewalls and roof's damage of 550 main roadway after excavation, measurement point was arranged at a distance of 100 m from the raise of the second mining area, and three boreholes were constructed on the two sidewalls and the roof. Observed by CXK12 stratascope, the borehole depth is 15 m. The peeking result shows that primary fissures dominate the surrounding rock with small extension length,

no voids, and a small amount of fragmentation within 2 m of the shallow part. The results of stratascope are shown in Figure 3.

Peeping data from the measurement point show that the roof of the roadway deforms significantly; within 1.8 m, it is completely broken and broken, and there are large cavities and separations at 3.6 m, 5.0 m, 6.2 m, 8.0 m, etc., and it presents the original rock state only after 8.2 m. The right sidewall was broken within 1.3 m, and disturbed fissures developed within the range of 1.6~5.0 m, but no cavity or separation layer was produced. The left sidewall is broken and damaged within 1.8 m, and, after 1.8 m, fissures develop at 2.4 m, 2.7 m, 3.0 m, etc., and there are radial fractures. After 6.3 m, the original rock state appears. The fractures in the two sidewalls and the roof are dominated by the tangential direction, expanding to form voids and separation layers.

### 3.2. Damage Scope of the Mined-Out Area

- (1) If the damage depth of the goaf exceeds the location of the roadway, that is, the roadway is arranged in the crack zone or collapse zone, the surrounding rock of the roadway will lose stability as a whole, and the roadway will be in a large deformed and broken environment for a long time. The existing common coal mine support technology cannot control its long-term deformation and destruction. Therefore, if the roadway is in the goaf's damage range, the roadway location should be changed, and the roadway should be rearranged, and the roadway deformation problem should not be solved from the perspective of support.

The coal seam within the range of +500 m ~ +550 m within the minefield is close to upright, and the formation above +550 m is inverted. Therefore, the research object belongs to the coal seam floor above +550 m and the roof of the coal seam below +500 m. The methods of actual measurement of the destruction depth of the roof and floor of the goaf mainly include the liquid leakage method, micro-seismic monitoring method, strain measurement method, and double-ended water plugging method of drilling holes. At present, the mined-out area of a mining area has been closed, and its destruction depth cannot be measured. This paper adopts the theoretical calculation method to calculate the destruction depth after considering the safety margin.

- (2) Depth of damage to the floor: according to the regression analysis of the measured data, Sun et al. [20] obtained the floor failure depth equation:

$$h_1 = 0.1105L + 0.006H + 0.4514F - 0.0085\alpha, \quad (1)$$

where  $h_1$  is the depth of floor failure, m;  $L$  is the panel's slope length, which is 100 m;  $H$  is the coal mining depth, which is 750 m;  $F$  is the

Protodyakonov coefficient; and  $\alpha$  is the coal seam inclination, which is  $90^\circ$ . The calculation result of equation (1) differs from the actual measured value by  $\pm 15\%$ . In this paper, the surplus coefficient is 20%. From this calculation, the damage depth of the mine floor is 16.3 m.

- (3) Depth of roof damage: the caving zone and fracture zone in the goaf of steep coal seams generally present a uniform ear shape or asymmetrical arch up and down, and the height of the fracture zone is calculated using the following statistical equation [21]:

$$h_2 = \frac{100Mh}{7.5h + 293} \pm 7.3, \quad (2)$$

where  $h_2$  is the fracture zone's height, m;  $M$  is the mining thickness, which is 2 m; and  $h$  is the section's vertical height. The vertical height of the research mine section is not fixed, and the maximum is 100 m. Calculated by equation (2), the fracture zone's height in the goaf is in the range of 11.9 m to 26.5 m.

The calculation results of equations (1) and (2) are smaller than the distance between the 550 main roadway and the C5 coal seam. Therefore, the 550 main roadway is not within the crack zone or collapse zone of the goaf.

## 4. Orthogonal Experimental Design

Many factors influence the effect of roadway support in underground coal mines, such as the layer position of the roadway layout, the environment of considerable buried depth, the structural environment, the water content of the formation, and the support engineering. For the above influencing factors, only the support engineering can be very convenient. Therefore, based on the original support plan, this article used the orthogonal test method to determine the degree of influence of the support structure parameters on the roadway support effect.

The combined support plan of bolt + anchor cable + shotcrete + wire mesh + U-shaped steel was adopted. Technical standards require the shotcrete in this scheme, and there is not much room for optional wire mesh parameters, so it is determined that the bolt length, row spacing between bolts, cable length, and row spacing between U-shaped steel are the control factors. The deformation of the roadway is used as the test index. The level values of the main control factors of the scheme are shown in Table 1.

If all combinations of four factors, three levels of each factor, are to be examined, the number of tests to be performed is  $3^4 = 81$ . It is a hefty workload. The selective test is carried out by orthogonal design, and only nine tests are required. The orthogonal test is given in Table 2.

The numerical models of roadway support in the above nine tests are shown in Figure 4, and the parameters of each support scheme marked in the figure correspond to each test scheme in Table 2.



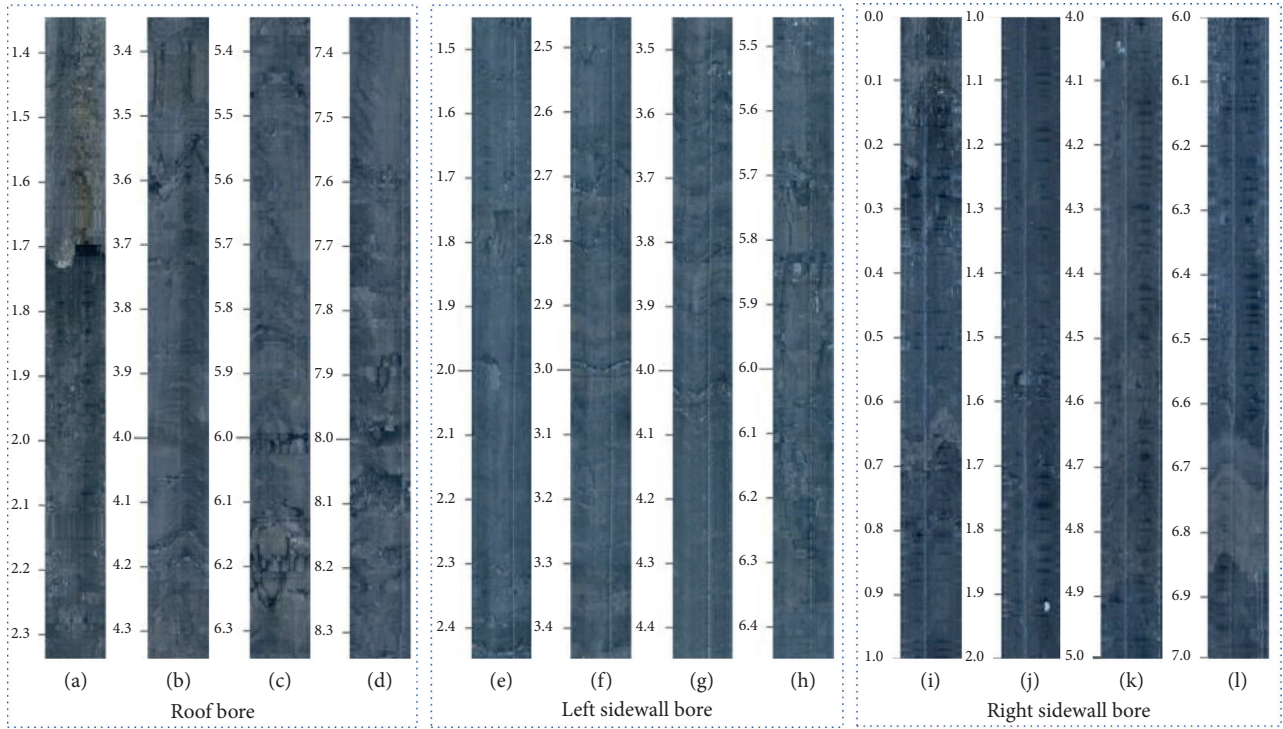


FIGURE 3: Chart of borehole netting.

TABLE 1: The level value of the main control factors.

Main control factors	Level 1	Level 2	Level 3
Bolt length (m)	2.0	2.5	3.0
Row spacing between bolts (m × m)	0.6 × 0.6	0.8 × 0.8	1.0 × 1.0
Cable length (m)	5	7	9
Row spacing in U-shaped steel (m)	0.4	0.7	1.0

TABLE 2: The orthogonal table of control factors  $L_9 (3^4)$ .

No.	Main control factors			
	Bolt length ( $L_b$ , m)	Row spacing between bolts ( $D_b$ , m × m)	Cable length ( $L_c$ , m)	Row spacing in U-shaped steel ( $D_u$ , m)
T <sub>1</sub>	2.0	0.6 × 0.6	5	0.4
T <sub>2</sub>	2.0	0.8 × 0.8	7	0.7
T <sub>3</sub>	2.0	1.0 × 1.0	9	1.0
T <sub>4</sub>	2.5	0.6 × 0.6	7	1.0
T <sub>5</sub>	2.5	0.8 × 0.8	9	0.4
T <sub>6</sub>	2.5	1.0 × 1.0	5	0.7
T <sub>7</sub>	3.0	0.6 × 0.6	9	0.7
T <sub>8</sub>	3.0	0.8 × 0.8	5	1.0
T <sub>9</sub>	3.0	1.0 × 1.0	7	0.4

## 5. Numerical Simulation

**5.1. Calculation Model and Scheme.** The damage of 550 main roadway located in  $P_3c$  is simulated based on  $FLAC^{3D}$ , and the model size is  $x \times y \times z = 150 \text{ m} \times 20 \text{ m} \times 150 \text{ m}$ . The extrusion module of  $FLAC^{3D}$  is used to build the model. The number of zones in the model is 838,400, and the number of nodes is 868,936. The Mohr-Coulomb constitutive

model was used. The model includes  $P_3l$ ,  $P_3c$ , and  $P_2m$ . Considering the formation inversion, the lower stratum and coal seam's dip angle is  $80^\circ$ , and the upper part is  $100^\circ$  in the model. The upper part of the model is the bearing boundary, the buried depth of the top of the model is about 650 m, the surface force of 15.9 MPa is loaded on the top of the model, and the other five surfaces of the model are fixed by *Fix* command. The origin of the model is located in the



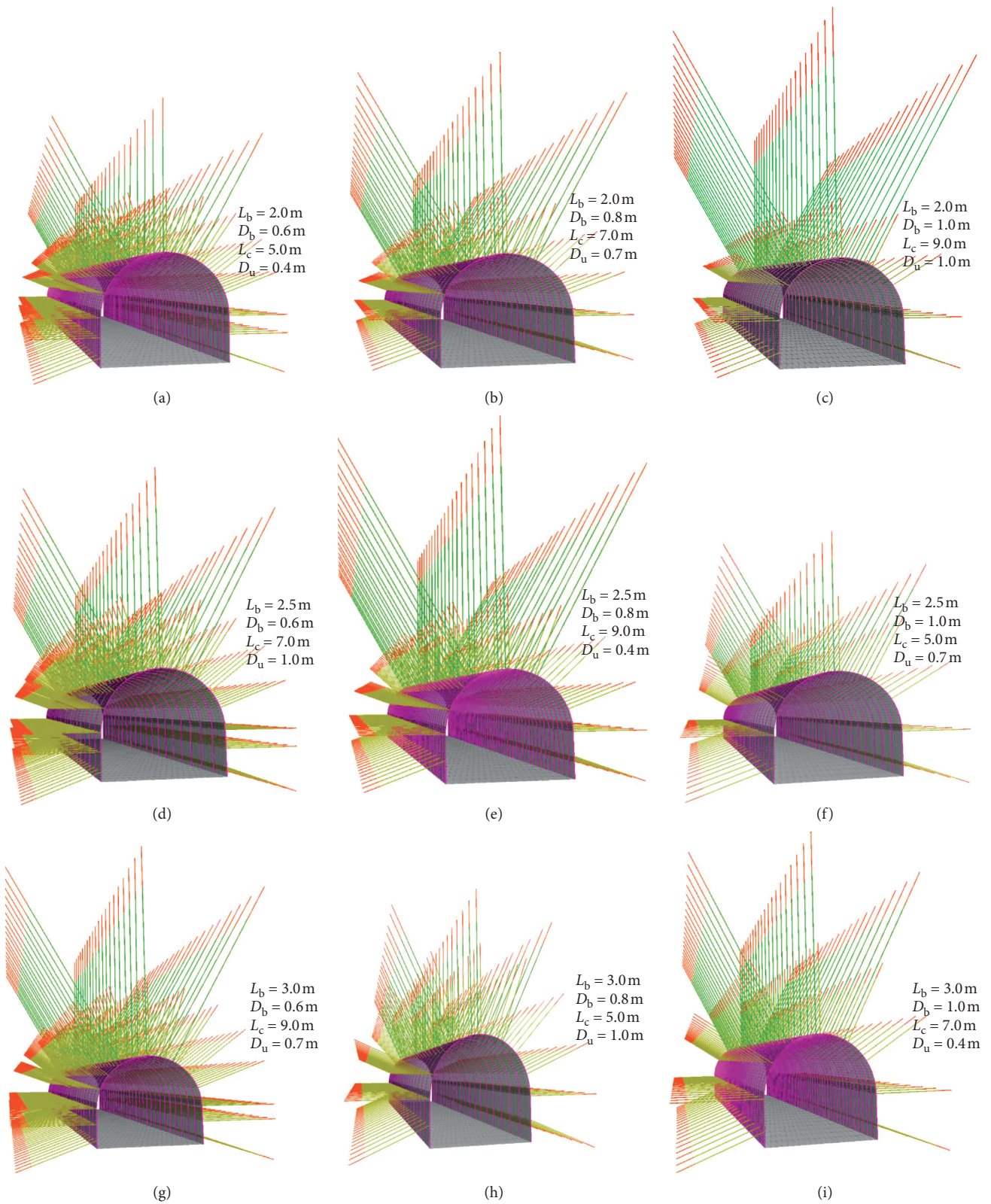


FIGURE 4: Numerical model of supporting structures. (a)  $T_1$ . (b)  $T_2$ . (c)  $T_3$ . (d)  $T_4$ . (e)  $T_5$ . (f)  $T_6$ . (g)  $T_7$ . (h)  $T_8$ . (i)  $T_9$ .

middle of the roadway. The positive value of stress and strain indicates that the direction points to the positive direction, and the negative value indicates that the

direction points to the negative direction. The numerical model is shown in Figure 5, and the mechanical parameters of the strata are shown in Table 3.

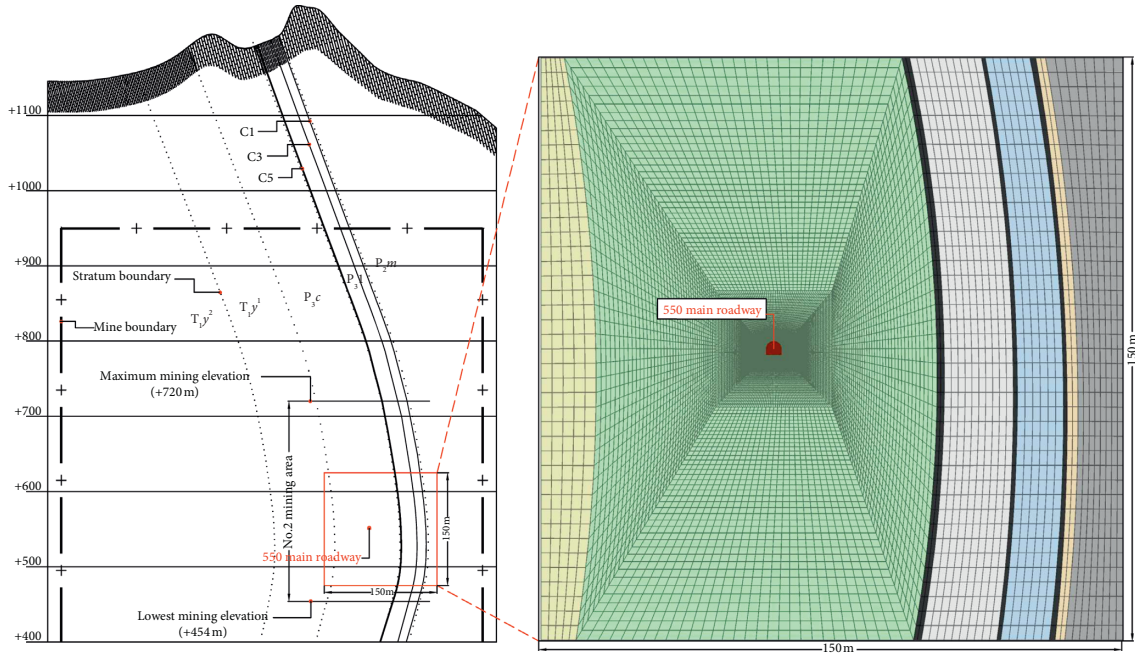


FIGURE 5: Numerical model.

TABLE 3: Rock lithology and mechanics parameters of the numerical model.

Strata and main lithology	Density (kg·m <sup>-3</sup> )	Bulk modulus (GPa)	Shear modulus (GPa)	Internal friction angle (°)	Cohesion (MPa)	Tensile strength (MPa)
T <sub>1y</sub> <sup>1</sup> Mudstone/sandstone	2720	2.6	2.1	31	2.5	2.9
P <sub>3c</sub> Bedded limestone	2700	2.8	1.5	29	1.8	1.5
P <sub>3l</sub>	C5 coal	1 480	1.0	25	0.8	1.2
	C5 coal floor	2 720	2.4	29	2.1	1.2
	C3 coal	1 510	0.7	24	1.2	1.0
	C1 coal roof	2 600	1.7	31	1.5	1.9
	C1 coal	1 540	0.6	25	0.9	1.0
P <sub>2m</sub> Layered limestone	2 710	3.8	2.5	30	2.8	2.8

TABLE 4: Numerical calculation parameters of liner.

Young's modulus (GPa)	Poisson's ratio	Cohesion (MPa)	Friction angle (°)	Thickness (m)	Normal stiffness (10 <sup>8</sup> N·m <sup>-3</sup> )	Shear stiffness (10 <sup>8</sup> N·m <sup>-3</sup> )
25	0.2	3	50	0.12	8	8

TABLE 5: Numerical calculation parameters of the bolt/cable.

Element	Young's modulus (GPa)	Cross-sectional area (10 <sup>-4</sup> m <sup>2</sup> )	Perimeter (10 <sup>-2</sup> m)	Cohesive strength (10 <sup>5</sup> N·m <sup>-1</sup> )	Stiffness (10 <sup>7</sup> N·m <sup>-2</sup> )	Tensile yield strength (kN)
Bolt	200	3.8	9.42	4.3	2.40	228
Cable	195	3.8	9.42	1.7	1.12	607

TABLE 6: Numerical calculation parameters of U-section steel.

Young's modulus (GPa)	Poisson's ratio	Cross-sectional area ( $10^{-4}$ m <sup>2</sup> )	Second moment of the $y$ -axis ( $10^{-8}$ m <sup>4</sup> )	Second moment of the $z$ -axis ( $10^{-8}$ m <sup>4</sup> )
200	0.3	45.69	1245	929

5.2. *Selection of Supporting Structure Parameters.* Structural element liner in FLAC<sup>3D</sup> is used to simulate reinforced wire mesh and shotcrete, and the calculation parameters are shown in Table 4 [22]. The bolts and cables are simulated by structural element cable, and the calculation parameters are shown in Table 5 [22–24]. Structural element beam is used to simulate U29 U-shaped steel, and the calculation parameters are shown in Table 6 [21, 22]. The bolts' and cables' outer end is connected with the reinforced wire mesh in a node-node way to ensure its coordinated deformation. Their internal end is connected with the zone body in a node-zone way.

5.3. *Numerical Simulation Calculation Results.* FLAC<sup>3D</sup> was used to calculate the above nine examination schemes. During the calculation, the deformation of the roadway was monitored. The monitoring points are arranged at 5 m, 10 m, and 15 m in the model's  $y$ -direction. Each monitoring point monitors the roof, floor, and sidewalls of the roadway. After taking the average of the four deformations of the two gangs, the data in Table 7 are obtained. The deformations in the roadway's four directions are added to obtain the roadway's total deformation, which serves as the orthogonal test analysis index.

## 6. Analysis of Orthogonal Test Results

For the results of orthogonal experiments, there are two methods: range analysis and variance analysis. The range analysis method is simple and straightforward, and the calculation workload is small. The variance analysis can estimate the test error's size and judge whether the investigated factors' influence on the test results is significant. The purpose of this article is to propose a support structure that is prioritized to be adjusted or optimized when controlling roadway deformation. The test indicators to be investigated include roof deformation, floor deformation, two-side deformation, and total deformation. The range analysis method is used to compare the test data. Take the analysis of total deformation as an example, and the processing results are shown in Table 8.

In Table 8,  $K_i$  is the sum of the deformation of the same level of the main control factors,  $K_i = \sum_{j=1}^3 y_{ij}$ ,  $y_{ij}$  are the test results of the same level,  $k = 1, 2, 3$ ;  $k_i$  is the arithmetic mean of the test results obtained when the factor in any column is set to level  $i$ ,  $k_i = K_i/s$ , where  $s$  is the number of occurrences of each level in any column;  $R_m$  is the range of the  $m$ -th factor,  $m = 1, 2, 3, 4$ .

Table 8 is a range analysis of the influence of various factors on the roadway's total deformation. From the calculation results, it can be known that the degree of influence of the four supporting structure parameters on the

deformation is  $D_u > L_b > L_c > D_b$ . Using the same calculation and analysis method, the above four influencing factors are used to make a range analysis of the roadway roof deformation, floor deformation, and deformation of the two sides. The results are shown in Table 9.

From the calculation results in Table 9, it can be seen that the control factors' order of the influence on the total deformation of the roadway is as follows: row spacing between U-shaped steel > bolt length > cable length > row spacing between bolts; the order of influence on the roadway floor's deformation is as follows: row spacing between U-shaped steel > row spacing between bolts > bolt length > cable length, same as the left sidewall and right sidewall; and the order of influence on roadway roof deformation is as follows: row spacing between U-shaped steel > bolt length = cable length > row spacing between bolts.

## 7. Discussions

- (1) The stability control of deep-buried underground engineering structure is a hot topic in current academic research, and it is also a problematic issue. As it has many influencing factors, some of which are related to the geological environment, some are related to the geological structure, which humans cannot control. There are also some influencing factors, such as selecting supporting materials and selecting supporting structure parameters. In particular, the series of conclusions drawn in this article is based on the site geological conditions of the Wanshun coal mine. These structures are not necessarily applicable to all deep-buried mines. The purpose of this article is to propose a research method, especially for deep mine undergrounds. When the deformation of the roadway's surrounding rock creates an acceptable range, it needs to be adjusted. When adjusting, it is necessary to distinguish the primary and secondary relationship of the factors affecting the roadway's deformation, analyze the influence degree of different support structure parameters, and maximize control of the roadway's surrounding rock's deformation.
- (2) The conclusions are subject to specific conditions. Only under the conditions described in this paper or similar conditions will the conclusions be applicable. If the conditions change, the conclusions will be different. This paper provides a solution when the deformation of roadway at the coal mine site cannot be controlled, and the support parameters need to be adjusted. That is, the orthogonal test method is used to rank the influence degree of the adjustable parameters



TABLE 7: Monitoring values of roadway deformation.

Test number	Roof (mm)	Floor (mm)	Left sidewall (mm)	Right sidewall (mm)	Total deformation (mm)
T <sub>1</sub>	30	91	51	49	221
T <sub>2</sub>	43	90	55	52	240
T <sub>3</sub>	75	93	62	57	287
T <sub>4</sub>	55	93	57	54	259
T <sub>5</sub>	30	89	51	49	219
T <sub>6</sub>	35	89	55	52	231
T <sub>7</sub>	44	91	53	49	237
T <sub>8</sub>	56	92	57	54	259
T <sub>9</sub>	31	89	52	50	222

TABLE 8: Range analysis of the main control factors.

No.	Control factor				Total deformation (mm)
	Bolt length	Row spacing between bolts	Cable length	Row spacing in U-shaped steel	
T <sub>1</sub>	1 (2.0)	1 (0.6×0.6)	1 (5.0)	1 (0.4)	221
T <sub>2</sub>	1	2 (0.8×0.8)	2 (7.0)	2 (0.7)	240
T <sub>3</sub>	1	3 (1.0×1.0)	3 (9.0)	3 (1.0)	287
T <sub>4</sub>	2 (2.5)	1	2	3	259
T <sub>5</sub>	2	2	3	1	219
T <sub>6</sub>	2	3	1	2	231
T <sub>7</sub>	3 (3.0)	1	3	2	237
T <sub>8</sub>	3	2	1	3	259
T <sub>9</sub>	3	3	2	1	222
K <sub>1</sub>	748	717	711	662	
K <sub>2</sub>	709	718	721	708	
K <sub>3</sub>	718	740	743	805	
k <sub>1</sub>	249.3	239.0	237.0	220.7	
k <sub>2</sub>	236.3	239.3	240.3	236.0	
k <sub>3</sub>	239.3	246.7	247.7	268.3	
R <sub>m</sub>	13.0	7.7	10.7	47.7	

TABLE 9: The range of calculation results for each factor.

Item	Control factor				The order of control factors
	Bolt length	Row spacing between bolts	Cable length	Row spacing in U-shaped steel	
Roof, R	9.3	4.0	9.3	31.7	$D_u > L_b = L_c > D_b$
Floor, R	1.0	1.3	0.3	3.0	$D_u > D_b > L_b > L_c$
Left sidewall, R	2.0	2.7	1.0	7.3	$D_u > D_b > L_b > L_c$
Right sidewall, R	1.7	2.3	0.3	5.7	$D_u > D_b > L_b > L_c$
Total deformation, R	13.0	7.7	10.7	47.7	$D_u > L_b > L_c > D_b$

for comparison. Under the minimum adjustment work, the best support effect can be obtained.

- (3) The orthogonal test with four factors and three levels was chosen in the paper, and no empty column was set. In this case, the variance analysis cannot be performed. To reduce the calculation amount in numerical simulation, this paper considers four control factors, and each control factor sets three levels. However, there are still many factors that can be considered, such as different buried depths, different anchor cable layout schemes, the layout of the roadway floor bolts, and whether to use grouting reinforcement. More research on these needs to be done later.

## 8. Conclusions

- (1) The deformation of the surrounding rock mass roadway with deep-buried fissures was investigated on site, and it was found that the support of this type of roadway is complex, the failure of the support structure often occurs, and some require multiple repairs. Peeping through drilling holes in the surrounding rock of the roadway, it is found that, due to the excavation of the roadway, the stress of the surrounding rock mass is relieved, resulting in cavities and separation, and the development of the cracks in the two sidewalls and the roof is mainly tangential.

- (2) The multi-index orthogonal design was adopted to carry out various combinations of supporting structure parameters to determine the degree of influence of the supporting structure parameters on the supporting effect. The bolt length, row spacing between bolts, cable length, and row spacing between U-shaped steel are selected as the main control factors, and the total deformation of the roadway roof, floor, two sidewalls, and the roadway is used as the examination index. Nine numerical simulation schemes were designed based on orthogonal experiments, and a numerical model consistent with the geological conditions of the coal mine site was established using FLAC<sup>3D</sup>. Numerical calculations were carried out to simulate the ground pressure conditions under the condition of deep burial at the site.
- (3) The test results were analyzed by range analysis. It was found that the control factors' influence order on the total deformation of the roadway is as follows: row spacing between U-shaped steel > bolt length > cable length > row spacing between bolts; the influence order on the deformation of the roadway floor is as follows: row spacing between U-shaped steel > row spacing between bolts > bolt length > cable length, same as the left sidewall and right sidewall; and the influence order on the roadway roof's deformation is as follows: row spacing between U-shaped steel > bolt length = cable length > row spacing between bolts.

## Data Availability

The data used to support the findings of this study are included within the article.

## Conflicts of Interest

All the authors declare that they have no conflicts of interest.

## Acknowledgments

This research was supported by the National Natural Science Foundation of China (nos. 51974117, 51764010, and 51874109), Science and Technology Project for Outing and Young Talents of Guizhou (Talents of Science Platform in Guizhou; no. [2019] 5674), New Talent Training Project of Guizhou Institute of Technology (no. GZLGXM-02), Hunan Provincial Natural Science Foundation of China (no. 2020JJ4027), Guizhou Provincial Science and Technology Support Program (no. QKHZC[2021]General 347), and Scientific Research Foundation for High-Level Talents in Guizhou Institute of Technology (no. XJGC20190633). Professor Xueling Du from Guizhou Institute of Technology had provided a lot of valuable opinions on this article. The authors would like to express their sincere thanks to Professor Du.

## References

- [1] H. Kang, "Support technologies for deep and complex roadways in underground coal mines: a review," *International Journal of Coal Science & Technology*, vol. 1, no. 3, pp. 261–277, 2014.
- [2] Z. Zhang, J. Bai, Y. Chen, and S. Yan, "An innovative approach for gob-side entry retaining in highly gassy fully-mechanized longwall top-coal caving," *International Journal of Rock Mechanics and Mining Sciences*, vol. 80, pp. 1–11, 2015.
- [3] M. Kanji, M. C. He, and L. R. Sousa, *Soft Rock Mechanics and Engineering*, Springer, Berlin, Germany, 2020.
- [4] A. Batugin, Z. Q. Wang, Z. H. Su, and S. S. Sidikovna, "Combined support mechanism of rock bolts and anchor cables for adjacent roadways in the external staggered split-level panel layout," *International Journal of Coal Science & Technology*, pp. 1–15, 2021.
- [5] W. Yu, G. Wu, B. Pan, Q. Wu, and Z. Liao, "Experimental investigation of the mechanical properties of sandstone-coal-bolt specimens with different angles under conventional triaxial compression," *International Journal of Geomechanics*, vol. 21, no. 6, Article ID 04021067, 2021.
- [6] G. Wu, W. Yu, J. Zuo, and S. Du, "Experimental and theoretical investigation on mechanisms performance of the rock-coal-bolt (RCB) composite system," *International Journal of Mining Science and Technology*, vol. 30, no. 6, pp. 759–768, 2020.
- [7] F. Gong, W. Wu, T. Li, and X. Si, "Experimental simulation and investigation of spalling failure of rectangular tunnel under different three-dimensional stress states," *International Journal of Rock Mechanics and Mining Sciences*, vol. 122, Article ID 104081, 2019.
- [8] S.-c. Li, H.-t. Wang, Q. Wang et al., "Failure mechanism of bolting support and high-strength bolt-grouting technology for deep and soft surrounding rock with high stress," *Journal of Central South University*, vol. 23, no. 2, pp. 440–448, 2016.
- [9] Z. Zhang, M. Deng, J. Bai, X. Yu, Q. Wu, and L. Jiang, "Strain energy evolution and conversion under triaxial unloading confining pressure tests due to gob-side entry retained," *International Journal of Rock Mechanics and Mining Sciences*, vol. 126, Article ID 104184, 2020.
- [10] J. P. Zuo and J. Y. Shen, *The Hoek-Brown Failure Criterion—from Theory to Application*, Springer, Singapore, 2020.
- [11] J. Li, N. J. Ma, and Z. W. Ding, "Heterogeneous large deformation mechanism based on change of principal stress direction in deep gob side entry and control," *Journal of Mining and Safety Engineering*, vol. 35, no. 4, pp. 670–676, 2018.
- [12] H. Zhang, J. Cao, and M. Tu, "Floor stress evolution laws and its effect on stability of floor roadway," *International Journal of Mining Science and Technology*, vol. 23, no. 5, pp. 631–636, 2013.
- [13] W. P. Li, M. Y. Wang, P. X. Fan, and H. J. Deng, "Study of deformation and failure model for deep rock mass and its numerical method," *Chinese Journal of Rock Mechanics and Engineering*, vol. 30, no. 6, pp. 1250–1257, 2011.
- [14] B. X. Huang, N. Zhang, H. W. Jing et al., "Large deformation theory of rheology and structural instability of the surrounding rock in deep mining roadway," *Journal of China Coal Society*, vol. 45, no. 3, pp. 911–926, 2020.
- [15] S. Yan, Y. Song, J. Bai, and D. Elmo, "A study on the failure of resin end-anchored rockbolts subjected to tensile load," *ROck Mechanics and Rock Engineering*, vol. 52, no. 6, pp. 1917–1930, 2019.



- [16] D. Zhu, Y. Wu, Z. Liu, X. Dong, and J. Yu, "Failure mechanism and safety control strategy for laminated roof of wide-span roadway," *Engineering Failure Analysis*, vol. 111, Article ID 104489, 2020.
- [17] H. Yu, Z. Niu, L. Kong, C. Hao, and P. Cao, "Mechanism and technology study of collaborative support with long and short bolts in large-deformation roadways," *International Journal of Mining Science and Technology*, vol. 25, no. 4, pp. 587–593, 2015.
- [18] P. Nikolenko, S. Epshtein, V. Shkuratnik, and P. Anufrenkova, "Experimental study of coal fracture dynamics under the influence of cyclic freezing–thawing using shear elastic waves," *International Journal of Coal Science & Technology*, 2020.
- [19] R. Wang, J.-b. Bai, S. Yan, Y.-b. Song, and G.-d. Wang, "An improved numerical simulation approach for the failure of rock bolts subjected to tensile load in deep roadway," *Geofluids*, vol. 2020, Article ID 8888390, 21 pages, 2020.
- [20] J. Sun, L. G. Wang, F. R. Tang, and Y. F. Shen, "Microseismic monitoring failure characteristics of inclined coal seam floor," *Rock and Soil Mechanics*, vol. 32, no. 5, pp. 1589–1595, 2011.
- [21] X. T. Feng, *Rock Mechanics and Engineering Volume 4, Excavation, Support and Monitoring*, CRC Press, Boca Raton, FL, USA, 2016.
- [22] ITASCA Consulting Group Inc., *Help and Documentation*, ITASCA Consulting Group Inc., Minneapolis, MIN, USA, 2019.
- [23] W. J. Yu, K. Li, Q. H. Lu, H. X. Guo, and S. H. Du, "Engineering characteristics and deformation control of roadways in fractured rock mass," *Journal of China Coal Society*, pp. 1–12, 2021.
- [24] F. Q. Gao, *Simulation of Failure Mechanisms Around Underground Coal Mine Openings Using Discrete Element Modelling*, Simon Fraser University, Burnaby, Canada, 2013.

## Research Article

# The Stability Factors' Sensitivity Analysis of Key Rock B and Its Engineering Application of Gob-Side Entry Driving in Fully-Mechanized Caving Faces

Hong-Sheng Wang <sup>1</sup>, Hai-Qing Shuang,<sup>2</sup> Lei Li,<sup>1</sup> and Shuang-Shuang Xiao<sup>1</sup>

<sup>1</sup>School of Energy Engineering, Xi'an University of Science and Technology, Xi'an, Shaanxi 71005, China

<sup>2</sup>School of Safety Science and Engineering, Xi'an University of Science and Technology, Xi'an, Shaanxi 710054, China

Correspondence should be addressed to Hong-Sheng Wang; [cumtwhs@xust.edu.cn](mailto:cumtwhs@xust.edu.cn)

Received 29 March 2021; Accepted 4 May 2021; Published 25 May 2021

Academic Editor: Zizheng Zhang

Copyright © 2021 Hong-Sheng Wang et al. This is an open access article distributed under the Creative Commons Attribution License, which permits unrestricted use, distribution, and reproduction in any medium, provided the original work is properly cited.

To reveal the critical factors of the main roof influencing stability of surrounding rocks of roadways driven along goaf in fully-mechanized top-coal caving faces, this paper builds a structural mechanics model for the surrounding rocks based on geological conditions of the 8105 fully-mechanized caving face of Yanjiahe Coal Mine, and the stress and equilibrium conditions of the key rock block B are analyzed, and focus is on analyzing rules of the key rock block B influencing stability of roadways driven along goaf. Then, the orthogonal experiment and the range method are used to confirm the sensitivity influencing factors in numerical simulation, which are the basic main roof height and the fracture location, the length of the key rock block B, and the main roof hardness in turn. It is revealed that the basic main roof height and its fracture location have a greater influence on stability of gob-side entry driving. On the one hand, the coal wall and the roof of roadways driven along goaf are damaged, and the deformation of surrounding rocks of roadways and the vertical stress of narrow coal pillars tend to stabilize along with the increase of the basic main roof height. On the other hand, when the gob-side entry is located below the fracture line of the main roof, the damage caused by gob-side entry is the most serious. Therefore, on-site gob-side entry driving should avoid being below the fracture line of the main roof. At last, industrial tests are successfully conducted in the fully-mechanized top-coal caving faces, 8105 and 8215, of Yanjiahe Coal Mine.

## 1. Introduction

Adoption of the narrow coal pillar gob-side entry driving technique can efficiently increase recycling efficiency of coal resources and control effect of surrounding rocks of roadways. The technique has been widely used in China, but stability of surrounding rocks of roadways driven along goaf has limited further development of the technique [1–17]. Research has shown that there are multiple factors that influence the stability. References [1–17] are the Chinese scholars' findings. Among them, Bai et al. [1, 2] built an arch-shaped triangular block structural mechanism model for surrounding rocks based on stress conditions of the working face; Li [3, 4] analyzed influence of big and small structures of roadways driven along goaf in fully-mechanized top-coal

caving face on stability of surrounding rocks; Zhang et al. [5, 6] analyzed deformation features of surrounding rocks of gob-side entry retaining in the fully-mechanized coal face with top-coal caving and influence of multiple factors on deformation and stress of gob-side entry retaining with entry-in packing in the top-coal mining face; Wang et al. [7, 8] discussed influence of three different fracture locations of the overlaying main roof of roadways driven along goaf on stability of surrounding rocks of the roadway and rational width of the narrow coal pillar based on the fracture line location of key rock B in the main roof; Zhu et al. [9] studied the main factors affecting the deformation of the filling body; Xie [10] adopted UDEC simulation to analyze rules of six factors, such as support technique and influencing stability of surrounding rocks of gob-side entry retaining in top-coal

mining faces; Zhang et al. [11, 12] analyzed four different Chinese coal mining sites and evaluated the influencing factors; Meng and Li [13] studied parameters' sensitivity of bolt support in gob-side entry driving and found that the main influence parameters were bolt pretightening force and bolt interval; Yuan et al. [14] studied the dynamic effect and control mechanism of key strata in the immediate roof; Bai et al. [15] studied the stress state and the deformation failure mechanism of the heading adjacent to the advancing working face roof structure; Li et al. [16] studied the in situ stress distribution characteristics of the rock mass near different slope angles' hillslope surfaces; Wang et al. [17] studied the stability of the concrete artificial side introduced to stabilize a gob-side entry.

The above analysis suggested that stability of the key rock block B could directly influence stability of the large structure of roadways driven along goaf and indirectly influence the stress environment of the small structure. The former mainly adopted theoretical analysis and quantitative experiments to analyze stability of the large structure of roadways driven along goaf, while the latter mainly analyzed influence of factors, such as support parameters, on stability of surrounding rocks of roadways based on numerical simulation. Few of them analyzed sensitivity of major factors of the main roof on stability of surrounding rocks of roadways driven along goaf in fully-mechanized top-coal caving faces. In view of the research gap, this paper built a structural mechanics structure for surrounding rocks of the key rock block B to quantitatively analyze influence of main roof factors on stability of surrounding rocks. Based on mining technical conditions of Yanjia Coal Mine in Binchang Mining Area, four factors of the main roof are confirmed. Combining the orthogonal experimental scheme, the author analyzes sensitivity of the four main roof factors and conducts a univariate analysis of the two factors with a stronger sensitivity. Research findings are successfully applied to the 8105 working face and further promoted in the 8215 working face. Therefore, research results of this paper can contribute to popularization of gob-side entry driving technique under similar geological conditions.

## 2. Mechanical Analysis of the Key Rock Block B in the Main Roof

*2.1. Building of the Key Rock Block B Mechanical Model.* Currently, the narrow coal pillar gob-side entry driving technique is prevailing in China. After the overlaying rock of the goaf in the working face of the former sector stabilizes, the roadway driven along goaf starts. Figure 1 shows the structure of the fracture line of the main roof surrounding rock structure within the coal wall during gob-side entry in a fully-mechanized top-coal caving face.

Below is the stress analysis of the key rock block B [18]: the resultant force of shear force and horizontal thrust of the key rock block A on the key rock block B is  $R_{AB}$  and  $T_{AB}$ , respectively; the resultant force of vertical shear force and horizontal thrust of the key rock block C on the key rock block B is  $R_{BC}$  and  $T_{BC}$ , respectively; the dead load of the soft stratum above the block B is  $F_R$ ; the dead load resultant force

of the block B is  $F_Z$ ; the support force of the goaf waste rock for the block B is  $F_G$ ; the support force of the damaged immediate roof in the section without top-coal caving for the block B is  $F_D$ ; the support force of the immediate roof in the narrow coal pillar for the block B is  $F_S$ ; the support force of the immediate roof of the physical coal wall for the block B is  $F_M$ ; the rotation angle of the block B is  $\theta$ . The stress situations of block B are shown in Figure 2. To put the surrounding rock structure of the block B in an equilibrium state, the block B should achieve equilibrium of stress horizontally and vertically after its stability. Besides, there is no allowance for slipping and rotation.

(1) Vertical:

$$\begin{aligned} \sum F_y &= 0, \\ R_{AB} + F_M + F_D + F_G - 2R_{BC} - F_R - F_Z &= 0. \end{aligned} \quad (1)$$

(2) Horizontal:

$$\begin{aligned} \sum F_x &= 0, \\ T_{AB} - 2T_{BC} \cos \alpha &= 0, \end{aligned} \quad (2)$$

where  $\alpha$  stands for the base angle of the key rock block B ( $^\circ$ ).

(3) Conditions for the key rock blocks B and A to lose stability are as follows [19]:

$$\begin{aligned} T_{AB} \tan \varphi &\geq R_{AB}, \\ \frac{T_{AB}}{L_1 a} &\leq \eta \sigma_c, \end{aligned} \quad (3)$$

where  $\tan \varphi$  stands for the friction factor between the two rock blocks,  $(T_{AB}/L_1 a)$  stands for the average crushing stress between the two rock blocks, MPa,  $\eta$  stands for the special coefficient of the stress analysis between the two rock blocks, and  $\sigma_c$  stands for the compressive strength of the rock block B, MPa.

*2.2. Analysis of Factors Influencing Stability of the Key Rock Block B.* Based on structural stress analysis of the key rock block B, it can be seen that the length of the block B can directly influence the area of the immediate roof that it covers after rotary subsidence. Since the dead load of the soft stratum is above the key rock block B,  $F_R$ , the dead load of the key rock block B,  $F_Z$ , will cause different degrees of contact with the immediate rock or the goaf waste rocks; the value of  $F_G$ ,  $F_D$ ,  $F_S$ , and  $F_M$  is thus decided. During the rotary subsidence process, if the block B does not contact the immediate rock and the goaf waste rocks, or it does contact them but generate no compression, the immediate roof or the goaf waste rocks cannot provide support stress for the main roof. When the block B contacts the two and generates compression, the latter will provide support stress for the main roof. The value of the stress is closely related to the compression rate of the immediate roof and the goaf waste

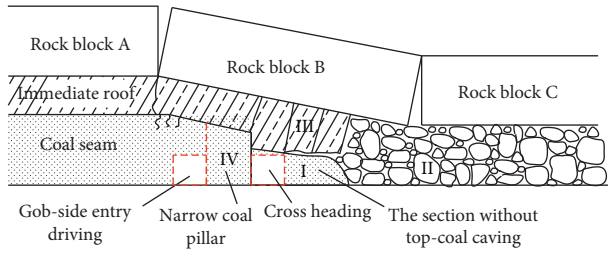


FIGURE 1: Surrounding rock structural mechanics model during gob-side entry in a fully-mechanized top-coal caving face.

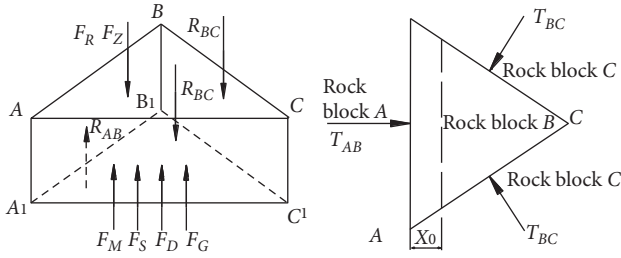


FIGURE 2: Structural stress of surrounding rocks of the key rock block B.

rocks, and the compression rate has a close bearing on thickness, strength, and swell factor of the immediate roof and the coal strata and the mechanical strength of goaf waste rocks.

When the fracture line location of the main roof is different [8], the horizontal stress remains the same, but the vertical stress of the key rock block B changes. See the following:

- (1) When the fracture line of the main roof is within the physical coal wall,  
Under the condition, the vertical stress changes as follows:

$$R_{AB} + F_M + F_D + F_G + F_S - 2R_{BC} - F_R - F_Z = 0. \quad (4)$$

- (2) When the fracture line of the main roof is outside the narrow coal pillar,  
Under the condition, there is no  $F_M$  on the block B vertically, and the stress changes as follows:

$$R_{AB} + F_D + F_G - 2R_{BC} - F_R - F_Z = 0. \quad (5)$$

- (3) When the fracture line of the main roof is just above the roadway,

Under the condition, there is no  $F_M$  and  $F_S$  on the block B vertically, and the stress changes as follows:

$$R_{AB} + F_D + F_G + F_S - 2R_{BC} - F_R - F_Z = 0. \quad (6)$$

To sum up, different fracture line locations of the main roof will directly influence the value of the vertical stress on the block B. Besides, during the rotary subsidence process, different compression ratios with the immediate roof can result in different value of support stress. Therefore, there are

many factors influencing stability of the block B. It is hard to accurately and quantitatively describe its value theoretically and in practices. It is necessary to turn to the numerical simulation to analyze influence of factors of the basic roof on stability of surrounding rocks in gob-side entry in fully-mechanized top-coal caving faces.

### 3. Confirmation of Sensitivity of Major Factors of the Main Roof

**3.1. Confirmation of Influencing Factors.** The working face of Yanjiahe Coal Mine features a single-wing main roadway belt layout. In order to efficiently connect working faces and efficiently control deformation of the surrounding rock of roadways, the narrow coal pillar gob-side entry is adopted, and favorable technical and economic efficacy is achieved [20–23], but geological conditions of Yanjiahe Coal Mine are complex, and the working face mine pressure behaviors and drill peeping analysis show that storage condition changes of the main roof are huge [2, 3]. Based on geological conditions of Yanjiahe Coal Mine, rules of four factors, including the main roof height and strength, the length of the key rock block B, and the fracture location of the main roof, in influencing stability of surrounding rocks of roadways driven along goaf is analyzed.

**3.2. Orthogonal Experiment.** The orthogonal experimental scheme is adopted to analyze different degrees of influence of four factors of the main roof on stability of surrounding rocks of roadways driven along goaf. The experimental scheme and the four factors are shown in Tables 1 and 2. Under the same bolt support, the deformation of surrounding rocks of roadways is an index to measure influence of different factors on stability of surrounding rocks of roadways. According to the orthogonal experimental scheme, the sensitivity of the four factors is ranked in order, and the two of them with a greater sensitivity are selected for the univariate analysis as to their influence on stability of surrounding rocks of roadways.

**3.3. Modeling.** Based on geological conditions of the 8105 fully-mechanized top-coal caving face, the authors adopt UDEC2D4.0 to build the numeric calculation model [21, 24, 25]. The constitutive relation between the rock block and the surrounding rocks features a Mohr–Coulomb model. The physical mechanical parameters of the rock mass are shown in Table 3. The belt cross-heading fracture surface of 8105 is 4000 mm × 3000 mm; and, the combined support featuring high-intensity deformed steel bar resin bolt + high preload + cable reinforcement + roof bolting with bar and wire [18, 22] is adopted. During the simulation process, the neighboring caving faces are first excavated and balanced; and, then comes the gob-side entry driving. The whole process should lay out corresponding stress and displacement monitoring points.

TABLE 1: Experimental factors and levels.

Level	Factor			
	Main roof height (m)	Main roof hardness (MPa)	Length of the key rock block B (m)	Fracture position of the main roof (m)
1	0	Soft/25	16	Inside the coal wall 2 m
2	5	Medium-hard/35	18	Right above the roadway
3	10	Hard/45	20	Outside the coal wall 2 m

3.4. *Analysis of the Orthogonal Experimental Scheme.* The “cross-measurement method” is adopted to measure deformation of surrounding rocks. Then, the range method is used to comparatively analyze the deformation of four factors under three levels. The deformation of surrounding rocks is shown in Table 2.

From Table 2, it can be seen that the range of the four factors influencing overall stability of surrounding rocks of roadways, including the main roof height and hardness, the length of the key rock block B, and the fracture location, based on the orthogonal univariate analysis is 393.54 mm, 29.19 mm, 84.20 mm, and 93.03 mm, respectively; the range of the four factors influencing stability of surrounding rocks on two ribs of roadways is 173.09 mm, 54.59 mm, 3.96 mm, and 29.02 mm, respectively; and, the range of four factors influencing stability of the roof-to-floor surrounding rocks is 220.45 mm, 25.40 mm, 80.24 mm, and 90.18 mm, respectively.

Thus, the degree of influence of the four factors of the main roof on stability of surrounding rocks of roadways driven along goaf can be ranked as follows: the main roof height > the main roof fracture location > the length of the key rock block B > the main roof hardness. The degree of influence of the four factors on surrounding rocks on two ribs of roadways can be ranked as follows: the main roof height > the main roof hardness > the main roof fracture location > the length of the key rock block B. The degree of influence of the four factors on the roof-to-floor surrounding rocks can be ranked as follows: the main roof height > the main roof fracture location > the length of the key rock block B > the main roof hardness. It can be seen that the main roof height and the main roof fracture location are two factors with a greater sensitivity.

## 4. Sensitivity Univariate Analysis of the Main Roof

4.1. *Simulation Scheme.* In order to further analyze the influence of the main roof height and its fracture location on stability of roadways driven along goaf, the univariate analysis is adopted. The simulation scheme is shown in Table 4. The main roof hardness is set to be medium-hard, and the length of the key rock block B is set to be 18 m.

### 4.2. Univariate Analysis Scheme

4.2.1. *Influence of the Main Roof Height on Stability of Surrounding Rocks of Roadways.* The average value of the deformation of surrounding rocks of roadways and the vertical stress value before and after coal pillar driving of nine schemes included in Table 2 are shown in Figure 3.

From Figure 3, it can be seen that the coal pillar stress before driving is larger than that after driving. Before the roadway driving, the overlaying strata of neighboring caving faces is basically stable, the key rock block B is in an equilibrium state, and the stress on the coal wall is concentrated. In Schemes 1–3, Schemes 4–6, and Schemes 7–9, the vertical stress scope in the central position of the narrow coal pillar is 7.41~9.43 MPa. This suggests that the influence of the main roof height and the fracture location on the coal pillar stress before the roadway driving is not significant. After the roadway driving, the stress of surrounding rocks of roadways needs to be redistributed, and the stress peak value transfers to the inside of the coal. At the moment, the coal pillar is in the stress declining area. In Schemes 1–3, Schemes 4–6, and Schemes 7–9, the average vertical stress of the coal pillar is within the range of 4.36~5.03 MPa, 1.56~2.67 MPa, and 2.07~2.38 MPa, respectively. This suggests that, when the main roof height is 0 m, the narrow coal pillar has a greater support stress,  $F_S$ , for the key rock block B. Along with the increase of the main roof height, the support stress of the main roof in the section without coal and the goaf waste rocks for the key rock block B is  $F_D$  and  $F_G$ , respectively, thus reducing the compression of the key rock block B on the immediate roof above the coal pillar.

From Figure 3, it can be seen that the relative deformation on the two ribs of the roadway in Schemes 1–9 is 151.50%, 141.45%, 136.04%, 163.12%, 143.72%, 131.24%, 168.07%, 76.96%, and 146.21% of the roof-to-floor relative deformation. Thus, it can be judged that deformation on two ribs dominates in roadways driven along goaf in fully-mechanized top-coal caving faces. The relative deformation on two ribs in Schemes 1–3, Schemes 4–6, and Schemes 7–9 is 274.95~322.25 mm, 315.01~368.86 mm, and 295.57 mm~390.31 mm, respectively; the deformation is small in Schemes 1–3. The deformation in Schemes 4–6 and Schemes 7–9 is almost the same. After roadways driven along goaf, the surrounding rocks of roadways obtain timely support. The surrounding rocks’ stress is quickly redistributed. Relying on bolt and cable support, surrounding rocks of roadways form a small structure. With the rotary subsidence of the key rock block B, the support stress provided by the immediate roof and the physical coal wall right above the narrow coal pillar,  $F_S$  and  $F_M$ , increases and the stress of the narrow coal pillar and the physical coal wall concentrates, thus resulting in expansion and deformation of surrounding rocks.

4.2.2. *Influence of the Main Roof Fracture Location on Stability of Surrounding Rocks of Roadways.* The deformation of surrounding rocks of roadways in Schemes 1~3,



TABLE 2: Orthogonal experimental scheme and simulation results.

Serial number	Factors							Total deformation of surrounding rocks (mm)	Rib-to-rib relative deformation (mm)	Roof-to-floor relative deformation (mm)
	Main roof height	Main roof hardness	Length of the key rock block B	Fracture location						
1	1	1	3	2	479.7	288.97	190.73			
2	2	1	1	1	880.29	515.70	364.59			
3	3	1	2	3	775.7	447.07	328.63			
4	1	2	2	1	455.28	282.25	173.03			
5	2	2	3	3	755.02	445.23	309.79			
6	3	2	1	2	849.82	482.32	367.50			
7	1	3	1	3	413.1	259.00	154.10			
8	2	3	2	2	893.39	388.55	504.84			
9	3	3	3	1	741.64	440.42	301.22			
Average value	449.36	711.90	658.79	740.97						
1										
Average value	842.90	686.71	742.99	692.40						
2										
Average value	789.05	682.71	679.54	647.94						
3										
Range	<b>393.54</b>	<b>29.19</b>	84.20	93.03						
Average value	276.74	417.25	391.54	386.61						
1										
Average value	449.83	403.27	395.50	412.79						
2										
Average value	456.60	362.66	396.13	383.77						
3										
Range	<b>173.09</b>	54.59	<b>3.96</b>	29.02						
Average value	172.62	294.65	267.25	354.36						
1										
Average value	393.07	283.44	347.49	279.61						
2										
Average value	332.45	320.05	283.41	264.17						
3										
Range	<b>220.45</b>	<b>25.40</b>	80.24	90.18						

Total deformation of surrounding rocks

Rib-to-rib relative deformation

Roof-to-floor relative deformation

TABLE 3: Physical mechanical parameters of the rock mass.

Lithology	Bulk modulus (GPa)	Shear modulus (GPa)	Internal friction angle (°)	Cohesion (MPa)	Thickness (m)
Coarse-grained sandstone	11	9	36	4.0	7
Sandy mudstone	16	12	32	3.5	20
Siltstone	20	16	33	6.0	10
Siltstone	20	16	33	6.0	6
No. 5 <sup>-1</sup> coal seam	8	6	28	1.5	3
Mudstone	6	5	28	4.0	2
Sandy mudstone	16	12	32	3.5	2
No. 5 <sup>-2</sup> coal seam	8	6	28	1.5	2
Mudstone	6	5	28	4.0	3
Sandy mudstone	16	12	32	3.5	3
Siltstone	20	16	33	6.0	3
Sandy mudstone	16	12	32	3.5	8
Siltstone	20	16	33	6.0	4
No. 7 coal seam	8	6	28	1.5	2
Mudstone	6	5	28	4.0	2
Sandy mudstone	16	12	32	3.5	1.5
No. 8 coal seam	8	6	28	1.5	7
Sandstone	12	10	38	7.0	28.5

TABLE 4: Simulation scheme.

Main roof height (m)	Main roof fracture location		
	Inside the coal wall 2 m	Outside the narrow coal pillar 2 m	Right above the roadway
0	Scheme 1	Scheme 2	Scheme 3
5	Scheme 4	Scheme 5	Scheme 6
10	Scheme 7	Scheme 8	Scheme 9

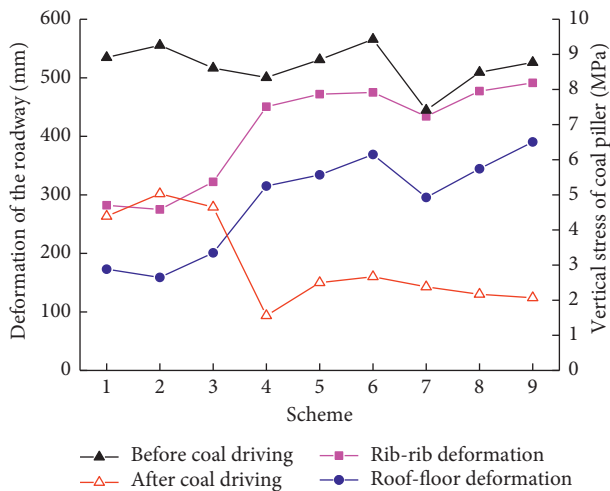


FIGURE 3: Display of relative deformation of surrounding rocks of roadways and vertical stress of the coal pillar.

Schemes 4~6, and Schemes 7~9 is shown in Figures 4(a)–4(c), respectively.

From Figure 4, it can be seen that deformation of surrounding rocks of roadways driven along goaf mainly happens in the physical coal wall and the roof side. Under the same height but different basic roof fracture locations, the deformation of surrounding rocks of roadways is different. Below is a detailed analysis.

When the main roof height is 0 m, the deformation of the coal wall side, the roof side, the coal pillar side, and the floor side in roadways shown in Schemes 1–3 is 241.40 mm, 117.29 mm, 40.85 mm, 55.73 mm, 210.84 mm, 109.53 mm, 64.11 mm, 49.40 mm, 214 mm, 152.12 mm, 108.25 mm, and 48.76 mm, respectively.

At the moment, there is no immediate roof above the coal strata, thus resulting in no goaf waste rock support force,  $F_G$ , for the key rock block B. When the basic main roof fracture location is right above roadways, the key rock block B will rotate and sink directly on the roof side of the roadway and the side of the narrow coal pillar. Under the condition, the deformation of surrounding rocks of roadways is larger than that under the other two conditions.

When the main roof height is 5 m, the deformation of the physical coal wall side, the roof side, the coal pillar side, and the floor side is 360.9 mm, 229.73 mm, 89.68 mm, 85.23 mm, 386.14 mm, 248.3 mm, 85.87 mm, 85.87 mm, 343.56 mm, 277.26 mm, 131.39 mm, and 91.6 mm, respectively.

When the main roof height is 10 m, the deformation of the physical coal wall side, the roof side, the coal pillar side, and the floor side is 338.99 mm, 219.34 mm, 95.11 mm, 76.24 mm, 365.29 mm, 263.28 mm, 111.97 mm, 81.28 mm, 364.9 mm, 318.25 mm, 126.38 mm, and 72.06 mm, respectively. At the moment, there is an immediate roof between the coal strata and the main roof. After roadway driving and rotary subsidence of the key rock block B, the block B might receive the stress from the main roof,  $F_D$ ,  $F_S$ ,  $F_M$ , and  $F_G$ . Through the immediate roof, it will function on the coal

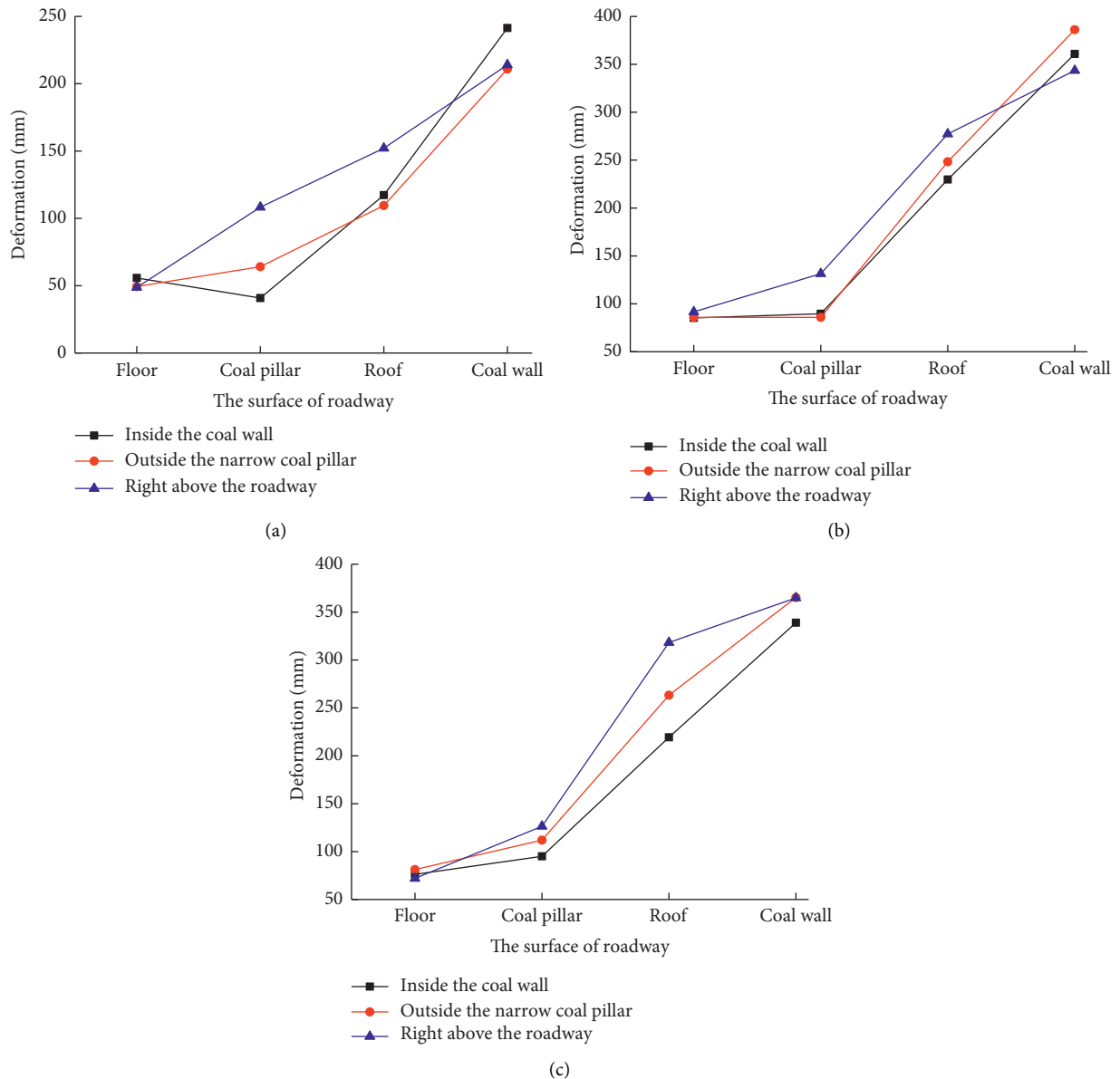


FIGURE 4: Deformation of surrounding rocks of roadways when the main roof fracture location is different. (a) The main roof height is 0 m. (b) The main roof height is 5 m. (c) The main roof height is 10 m.

pillar, the roadway roof, the physical coal wall, and the goaf to achieve an equilibrium state. When the main roof fracture location is right above roadways, the compression rate between the narrow coal pillar and the immediate roof right above roadways is relatively large, and the stress concentration is high. Consequently, the deformation of surrounding rocks of the narrow coal pillar side and the roof side becomes larger than that under the above two conditions.

Therefore, in order to reduce the stress concentration degree of the narrow coal pillar side and right above roadways, it is necessary to avoid laying gob-side entry driving right below the main roof fracture location. In this way, the bolt or the cable will control deformation of surrounding rocks of roadways more easily.

## 5. Engineering Application Analysis

Based on the above research, engineering application analysis is conducted on two fully-mechanized top-coal caving faces, namely, 8105 and 8215.

**5.1. 8105 Fully-Mechanized Top-Coal Caving Face.** 8105 track transport roadway drives along the 8104 goaf. It is necessary to master the main roof fracture line location on the 8105 top-coal caving face. Therefore, the 8103 track transport roadway and the 8105 belt transport roadway lay the probing drills on the 8102 goaf and the 8106 goaf. Measurement shows that the basic main fracture line is located within the physical coal wall, which is 3.42~3.87 m away from the goaf

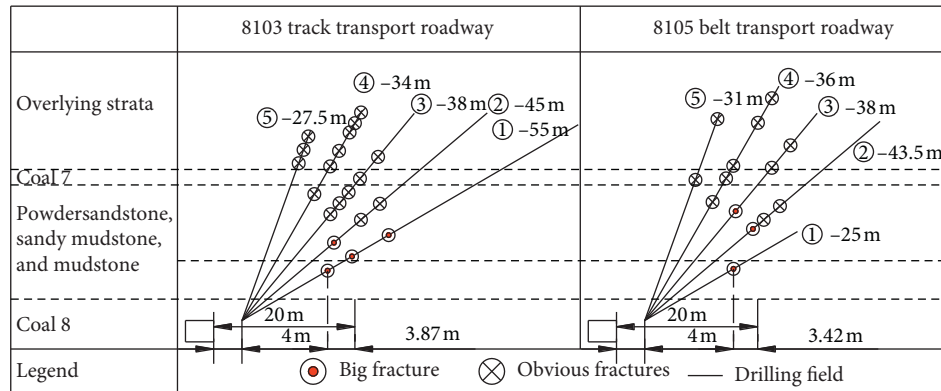


FIGURE 5: Probing results of the main roof fracture location.

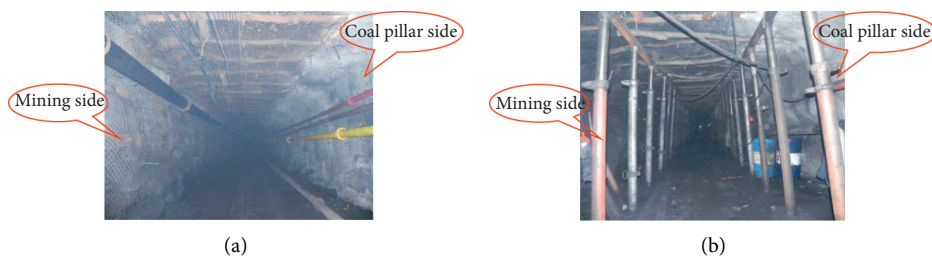


FIGURE 6: Control effects of surrounding rocks on the belt cross-heading of the 8105 caving face. (a) One year late after driving. (b) Influenced by mining.

boundary. Therefore, the coal pillar width should not be within the range of 3.42~3.87 m [8, 22]. (See Figure 5) The numerical simulation analysis is adopted to analyze changing rules of surrounding rock deformation and coal pillar and seam floor vertical stress under different coal pillar width. Finally, the reasonable width of the coal pillar is 6.5 m. After 20 days of roadway driving, the surrounding rocks are basically stable, and the maximum roof-to-floor and two-rib displacement is 118 mm and 65 mm, respectively. Influenced by the caving face excavation, the maximum roof-to-floor and two-rib displacement is 200~420 mm and 380~600 mm, respectively. The control effect of surrounding rocks of roadways is shown in Figure 6.

**5.2. 8215 Fully-Mechanized Top-Coal Caving Face.** The 8215 track transport roadway drives along the 8214 goaf boundary, and the coal pillar width of the coal section is 8.0 m. Six monitoring stations are laid out to monitor surrounding rocks of roadways. After 20 days of roadway driving, the surrounding rocks are basically stable, the bolt and cable working conditions are favorable, and the maximum roof-floor and two-rib displacement amount of six monitoring stations is 100~160 mm and 80~100 mm, respectively. Influenced by excavation, the maximum roof-floor and two-rib displacement amount is 220~460 mm and 340~620 mm, respectively. The stress variation rules of the coal monitored by the monitoring station 2 are shown in Figure 7. 064Y, 065Y, and 066Y in Figure 7 represent the surrounding rock stress 4 m within the narrow coal pillar,

5 m within the physical coal wall, and 10 m within the physical coal wall.

From Figure 7, it can be seen that the stress 4 m within the coal pillar is low and changes within the range of 0.1~0.2 MPa. The stress 5 m within the physical coal wall is large. If not influenced by excavation, it changes within the range of 0.1~0.6 MPa, and if influenced by excavation, it changes within the range of 0.7~0.8 MPa. The stress 10 m within the physical coal wall is relatively large. If not influenced by excavation, the change is within the range of 0.1~0.8 MPa; if influenced by excavation, the peak stress value can reach 10.9 MPa. Results suggest that, if the coal is not influenced by excavation, the surrounding rock stress is relatively small; if influenced by excavation, the surrounding rock stress is transferred to be within the physical coal wall. However, the roadways driven along goaf far always in the stress decline area, which is beneficial to the surrounding rock control of roadways.

Changing rules of the surrounding rock deformation and the coal stress suggest that roadways, influenced by excavation, are efficiently controlled, thus meeting requirements of the working face stopping [20, 23]. In order to master the main roof fracture line of the 8215 caving face, probing drills are laid by the 8215 track transport roadway to the overlying strata on the 8214 goaf, and the probing results are shown in Figure 8.

From Figure 8, the large fractures concentrate above the coal pillar near the goaf. Their distance away from the coal pillar margin is short, namely, 1.22 m, 3.42 m, and 4.15 m, respectively. Areas with obvious fractures are gradually away from Coal 8, and they are mainly distributed near the upper

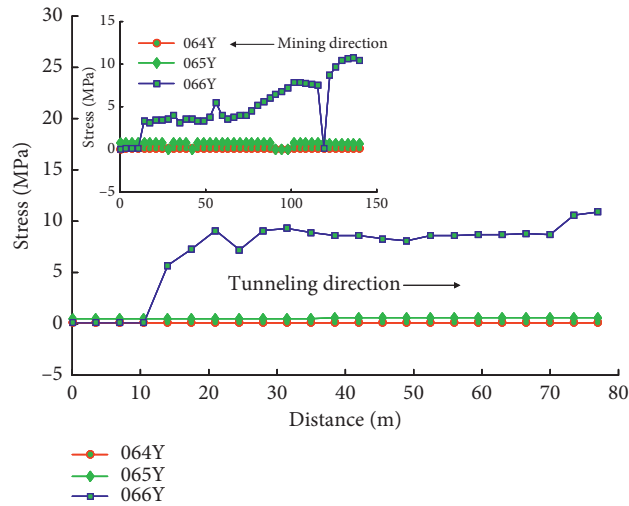


FIGURE 7: Changing rules of the coal stress.

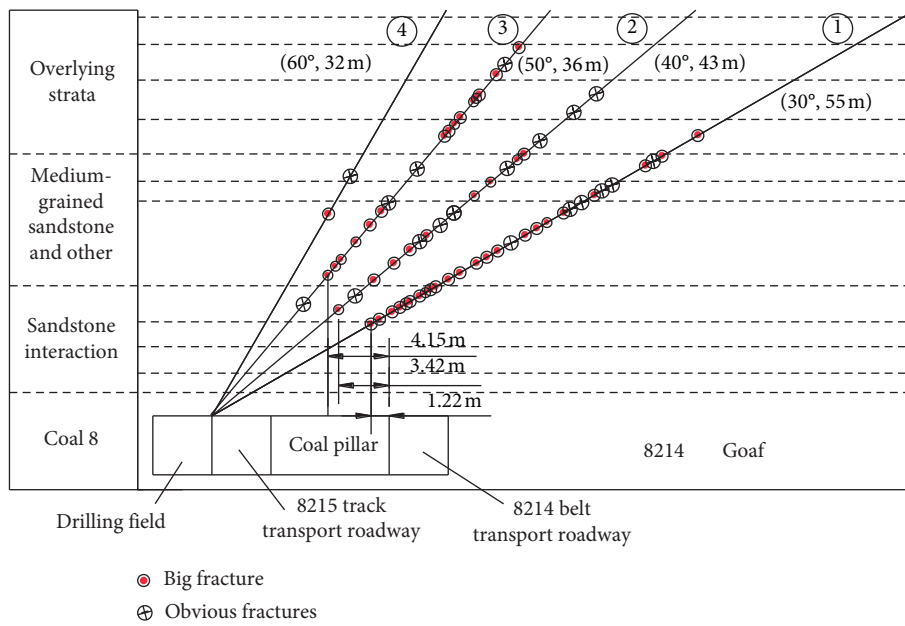


FIGURE 8: Probing results of the main roof fracture location.

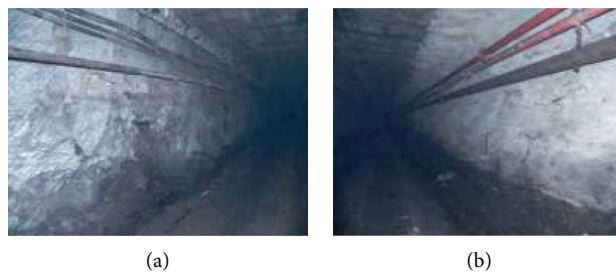


FIGURE 9: Surrounding rock control effect of the 8215 rail transportation roadway ten months late after driving. (a) Mining side. (b) Coal pillar side.



right of the coal pillar in goaf and far away from the coal pillar margin. It suggests that it is reasonable to set the coal pillar to be 8.0 m, which can avoid putting the roadway right under the basic fracture line, and the surrounding rock control effects are shown in Figure 9.

## 6. Conclusions

This paper builds the structural mechanics model of the key rock block B, points out that equilibrium of the key rock block B should meet conditions not to lose equilibrium horizontally and vertically, qualitatively analyzes the influence of the main roof factors on stress of the key rock block B, and places particular emphasis on stress-changing rules of the key rock block B vertically under three different fracture locations of the main roof.

Based on mining technical conditions of Yanjiahe Coal Mine in Binchang Mining Area, four factors of the main roof are confirmed, including the main roof height and hardness, the length of the key rock block B, and the main roof fracture location. The orthogonal experiment is used to set nine plans; the range method is employed to confirm the sensitivity order of the main roof, which is as follows: the main roof height > the main roof fracture location > the length of the key rock block B > the main roof strength.

The univariate method is adopted to analyze the influence of the main roof height and the fracture location on stability of surrounding rocks of roads in fully-mechanized caving faces. It is found that surrounding rock deformation during roadways driven along goaf happens in the physical coal wall and the roof side. The deformation of surrounding rocks of roadways and the vertical stress of the narrow coal pillar tend to stabilize along with the increase of the main roof height. Meanwhile, the roadway driving right below the basic fracture line should be avoided.

The engineering application effects suggest that the narrow coal pillar layout is reasonable on the 8105 and 8215 caving face, which can avoid putting the main roof fracture location right above the roadway. The surrounding rocks of the driving roadways are in a low-stress environment, and the surrounding rocks of the roadways are efficiently controlled. All these have guaranteed safe and efficient stopping of caving faces.

## Data Availability

The data used to support the findings of this study are included within the article.

## Conflicts of Interest

The authors declare that there are no conflicts of interest regarding the publication of this paper.

## Authors' Contributions

Hong-sheng Wang conceived of the research. Hong-sheng Wang and Hai-qing Shuang analyzed the data and wrote the

paper. Lei Li and Shuang-shuang Xiao participated in the design of the study and verified the results. All authors have read and approved the final manuscript.

## Acknowledgments

This work was supported by the National Natural Science Foundation of China (no. 51974231) and National Basic Research Program of China (973 Program) (no. 2015CB251600).

## References

- [1] J. B. Bai, W. J. Wang, and C. J. Hou, "Control mechanism and support technique about gateway driven along goaf in fully mechanized top coal caving face," *Journal of China Coal Society*, vol. 25, no. 5, pp. 478–481, 2000.
- [2] Z. Zhang, J. Bai, Y. Chen, and S. Yan, "An innovative approach for gob-side entry retaining in highly gassy fully-mechanized longwall top-coal caving," *International Journal of Rock Mechanics & Mining Sciences*, vol. 80, no. 12, pp. 1–11, 2015.
- [3] C. J. Hou and X. H. Li, "Stability principle of big and small structures of rock surrounding roadway driven along goaf in fully mechanized top coal caving face," *Journal of China Coal Society*, vol. 26, no. 1, pp. 1–7, 2001.
- [4] X. H. Li, "Deformation mechanism of surrounding rocks and key control technology for a roadway driven along goaf in fully mechanized top-coal caving face," *Journal of Coal Science Engineering*, vol. 9, no. 1, pp. 28–32, 2003.
- [5] D. S. Zhang, X. B. Mao, and W. D. Ma, "Testing study on deformation features of surrounding rocks of gob-side entry retaining in fully-mechanized coal face with top-coal caving," *Chinese Journal of Rock Mechanics and Engineering*, vol. 21, no. 3, pp. 331–334, 2002.
- [6] D. S. Zhang, L. Q. Ma, and X. X. Miao, "Factor analysis on deformation of gob-side entry retaining with entry-in packing in top-coal caving mining face," *Journal of China University of Mining Technology*, vol. 35, no. 1–6, pp. 331–334, 2006.
- [7] H. S. Wang, *Research on the Creep Character and its Stability Control Technology of Gob-Side Entry's Narrow Side*, China University of Mining and Technology, Xuzhou, China, 2011.
- [8] H. S. Wang, D. S. Zhang, S. G. Li, L. Wang, and L. Z. Wang, "Rational width of narrow coal pillar based on the fracture line location of key rock B in main roof," *Journal of Mining and Safety Engineering*, vol. 31, no. 1, pp. 10–16, 2014.
- [9] C. Q. Zhu, X. X. Miao, and Z. Liu, "Mechanical analysis on deformation of surrounding rock with road-in packing of gob-side entry retaining in fully-mechanized sub-level caving face," *Journal of Coal Science and Engineering*, vol. 14, no. 1, pp. 24–28, 2008.
- [10] W. B. Xie, "Influence factors on stability of surrounding rocks of gob-side entry retaining in top-coal caving mining face," *Chinese Journal of Rock Mechanics and Engineering*, vol. 23, no. 18, pp. 3059–3065, 2004.
- [11] N. Zhang, L. Yuan, C. L. Han, J. H. Xue, and J. G. Kan, "Stability and deformation of surrounding rock in pillarless gob-side entry retaining," *Safety Science*, vol. 50, no. 4, pp. 593–599, 2012.
- [12] N. Zhang, C. Liu, and P. Yang, "Flow of top coal and roof rock and loss of top coal in fully mechanized top coal caving mining of extra thick coal seams," *Arabian Journal of Geosciences*, vol. 9, no. 6, pp. 1–9, 2016.

- [13] C. Meng and X. H. Li, "Analysis and application of parameters sensitivity of bolt support in gob-side entry driving," *China Coal*, vol. 39, no. 3, pp. 45–49, 2013.
- [14] Y. Yuan, S. H. Tu, X. G. Zhang, and B. Li, "Dynamic effect and control of key strata break of immediate roof in fully mechanized mining with large mining height," *Shock & Vibration*, vol. 2015, no. 4, 11 pages, Article ID 657818, 2015.
- [15] J. B. Bai, W. L. Shen, G. L. Guo, X. Y. Wang, and Y. Yu, "Roof deformation, failure characteristics, and preventive techniques of gob-side entry driving heading adjacent to the advancing working face," *Rock Mechanics and Rock Engineering*, vol. 48, no. 6, pp. 2447–2458, 2015.
- [16] B. X. Li, Y. Li, W. S. Zhu, C. Li, and Z. X. Dong, "Impact of in situ stress distribution characteristics on jointed surrounding rock mass stability of an underground cavern near a hillslope surface," *Shock and Vibration*, vol. 2017, no. 1, 10 pages, Article ID 2490431, 2017.
- [17] H. S. Wang, D. S. Zhang, L. Liu et al., "Stabilization of gob-side entry with an artificial side for sustaining mining work," *Sustainability*, vol. 8, no. 7, pp. 1–17, 2016.
- [18] J. B. Bai, *Control Mechanism about Gateway Driven along Goaf*, China University of Mining and Technology press, Beijing, China, 2006.
- [19] M. G. Qian, X. X. Miao, and F. L. He, "Analysis of key block in the structure of voussoir beam in longwall mining," *Journal of China Coal Society*, vol. 19, no. 6, pp. 557–563, 1994.
- [20] H. Q. Shuang, H. S. Wang, S. G. Li, X. Z. Zhang, L. Z. Wu, and Y. J. Dong, "Reasonable width optimization of narrow coal pillar in roadway driven along goaf of fully mechanized caving face," *Coal Engineering*, vol. 47, no. 2, pp. 18–21, 2015.
- [21] H. S. Wang, X. Z. Zhang, L. Z. Wu, S. G. Li, and Y. J. Dong, "Surrounding rock control technology of roadway in "isolated island" fully mechanized coal face," *Coal Technology*, vol. 30, no. 8, pp. 83–84, 2011.
- [22] H. S. Wang, S. G. Li, X. Z. Zhang, L. Z. Wu, Y. J. Dong, and H. Q. Shuang, "Analysis on stability of narrow coal pillar influenced by main roof fracture structure of gob-side roadway," *Coal Science and Technology*, vol. 42, no. 2, pp. 19–22, 2014.
- [23] H. Q. Shuang, *Study on Stability Analysis and Control Technology about Roadway Driving along Goaf at Fully Mechanized Top Coal Caving*, Xi'an University of Science and Technology, Xian, China, 2015.
- [24] W. Jiang, W. J. Ju, Z. L. Wang, Z. Zhang, and M. Shi, "Characteristics of overburden stress distribution and rational pillar width determination of gob-side roadway with thick and hard basic roof in fully mechanized top coal caving workforce," *Journal of Mining and Safety Engineering*, vol. 37, no. 6, pp. 1142–1151, 2020.
- [25] X. J. Meng, "Solid coal rib support technology of fully-mechanized mining along gob-side entry driving based on main roof fracture location," *Coal Science and Technology*, vol. 48, no. 1, pp. 61–68, 2020.

## Research Article

# Research on the Reasonable Coal Pillar Width and Surrounding Rock Supporting Optimization of Gob-Side Entry under Inclined Seam Condition

Li-li Jiang,<sup>1</sup> Zeng-qiang Yang<sup>2</sup>,<sup>3</sup> and Gang-wei Li<sup>3</sup>

<sup>1</sup>School of Civil Engineering, Chongqing Vocational Institute of Engineering, Jiangjin, Chongqing 402260, China

<sup>2</sup>School of Transportation Engineering, Jiangsu Vocational Institute of Architectural Technology, Xuzhou, Jiangsu 221116, China

<sup>3</sup>State Key Laboratory of Mining Response and Disaster Prevention and Control in Deep Coal Mines, Anhui University of Science and Technology, Huainan, Anhui 232001, China

Correspondence should be addressed to Zeng-qiang Yang; zengqiang5@126.com

Received 8 April 2021; Accepted 7 May 2021; Published 19 May 2021

Academic Editor: Zizheng Zhang

Copyright © 2021 Li-li Jiang et al. This is an open access article distributed under the Creative Commons Attribution License, which permits unrestricted use, distribution, and reproduction in any medium, provided the original work is properly cited.

In order to study the optimal coal pillar width and surrounding rock control mechanism of gob-side entry under inclined seam condition, the 130205 return air entry adjacent to 130203 gob in Yangchangwan No. 1 well is taken as a typical engineering background. By means of engineering background analysis, theoretical analysis based on inside and outside stress field, numerical simulation by FLAC<sup>3D</sup> software, and in situ industrial test and relevant monitoring methods, the optimal coal pillar width and surrounding rock control technology are obtained. The results show that the influence range of inside stress field is about 12.2~12.8 m based on theoretical calculation result; under the influence of 10 m coal column, the overall deformation of the roadway is relatively small and within the reasonable range of engineering construction, so the width of the coal pillar along the return air roadway is set to 10 m which is more reasonable; the cross-section characteristics of special-shaped roadway lead to asymmetric stress distribution and fragmentation of surrounding rock, and then the asymmetric surrounding rock control technology under the coupling effect of roof prestressed anchor + high-strength single anchor cable + truss anchor cable support is proposed. The monitoring results of this support method are effective for the maintenance of gob-side entry, and the study conclusions provide new guidance for the surrounding rock control mechanism of gob-side entry under inclined seam conditions.

## 1. Introduction

During the underground coal seam mining process, coal pillar mining is usually realized in the form of open-cut tunneling. Scholars determine the reasonable size of coal pillar through theoretical calculation, numerical simulation, and engineering test and arrange the tunnel in the stress reduction zone, when the coal pillar is in the yielding state but still has the bearing capacity, and can keep the tunnel stable if it is reasonably supported [1–3]. If the width of the coal pillar is not reasonable; it may cause dynamic pressure disaster in the process of roadway boring. Therefore, choosing a reasonable width of coal pillar can improve the coal resource recovery rate and reduce the cost of roadway support under the premise of ensuring roadway safety.

Wilson [4] carried out an analysis on the stability factors of soft rock retrieval roadway and discussed comprehensively the mechanism of roadway soft rock damage under the influence of coal column width and workface retrieval. Bai et al. [5] analyzed the stability of narrow coal pillars along the air-excavated roadway by numerical simulation methods to arrive at a reasonable range of coal pillar widths under specific geological conditions. Xie et al. [6] revealed the effect of coal pillar width change on the distribution and change law of surrounding rock stress and pointed out that the reasonable width of the coal pillar in the guard lane should be less than the critical width of the transfer of stress within the solid coal of the lane gang to the coal pillar. He and Zhang [7] proposed a systematic asymmetric support theory by analyzing the deformation characteristics of the

surrounding rock along the hollow roadway in large sections. Hou and Li [8] studied the stability principle of the size structure of the surrounding rock along the air-digging lane. Zha et al. [9, 10] analyzed the influence of the basic top fracture location on the narrow coal pillar protection lane and studied the selection criteria of reasonable coal pillar width based on this. Li et al. [11], in order to improve the accuracy of the numerical model calculation, set the mining area as a strain hardening model and the coal column as a strain-softening model according to the mechanical properties of the coal rock body.

In previous studies, vertical stress was used as one of the criteria for determining the stability of the surrounding rock, while usually the crustal movement is dominated by horizontal movement, and it is inherently wrong to ignore the influence of horizontal stress and shear stress to evaluate the stability of the surrounding rock. The second invariant of deviatoric stress ( $J_2$ ) as a unit of characterization of the magnitude of shear stress and distortion appears to be more relevant for determining the degree of shear damage and integrity of the rock mass. It can be expressed by the combination of the maximum principal stress ( $\sigma_1$ ), the intermediate principal stress ( $\sigma_2$ ), and the minimum principal stress ( $\sigma_3$ ), as follows:

$$J_2 = \frac{1}{6} [(\sigma_1 - \sigma_2)^2 + (\sigma_2 - \sigma_3)^2 + (\sigma_3 - \sigma_1)^2]. \quad (1)$$

Many scholars have used the second invariant of deviatoric stress to study the mechanical characteristics of surrounding rock, and some research results have been obtained [12, 13]. In this paper, taking 130205 backwind road of Yangchangwan coal mine as the engineering background, on the basis of theoretical analysis, the influence of coal seam inclination on the roadway surrounding rock is fully considered, and FLAC3D numerical simulation is used to derive the distribution of the main deflection stress and deformation mechanism of the roadway surrounding rock, which provides the basis for the reasonable selection of coal pillar width.

## 2. Engineering Situations

130205 working face is located in the eastern part of the well field of Yangchangwan No.1 well, the adjacent 130203 working face in the upper part of the 130205 working face has been mined out, and a 20 m width of coal pillar was left to protect the 130205 return air entry. The burial depth of 130205 working face is about 587.1~726.7 m, and the average burial depth is 656.9 m. Its primary mineable coal bed is the No.2 coal seam, the thickness of this coal seam is about 8.2~10.7 m, and the average thickness of this coal seam is 8.4 m. The layout plan of 130203 fully mechanized working face is shown in Figure 1.

## 3. Theoretical Analysis of Narrow Coal Pillar Width

*3.1. Relationship between the Position of the Basic Top Breaking Line and the Width of the Coal Column.* With the advance of the upper section of the working face, the basic top of the edge of

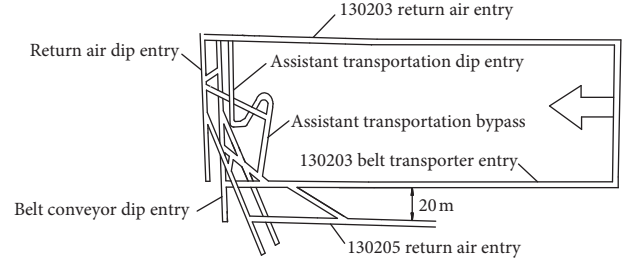


FIGURE 1: 130203 fully mechanized working face layout plan.

the mining area breaks until it touches the gangue, gangue to the basic top to form a preliminary support role, and the adjacent blocks bite each other to form an articulated structure, which is relatively stable by the horizontal thrust of the adjacent rock blocks [14–16]. According to the “internal-external stress field” mine pressure theory that was put forward by Song et al. [17], the break line again divides the lateral coal body into 2 parts, one of which is the internal stress field determined by the weight of the moving rock beam, and the other is the external stress field associated with the overall force of the overlying rock, where a new plastic and elastic zone is again formed within the external stress field, as shown in Figure 2. The mechanical model can be obtained by simplifying Figure 2, as shown in Figure 3.

From Figure 3, the support pressure in the internal stress field at a distance  $x$  from the edge of the coal wall is shown as follows:

$$\sigma_y = G_x \cdot y_x, \quad (2)$$

where  $G_x$  is the stiffness of the coal seam at a distance  $x$  from the coal wall in the internal stress field ( $Pa$ ) and  $y_x$  is the compression of the coal body at a distance  $x$  from the coal wall in the internal stress field ( $m$ ).

Reducing this to a linearly varying process, the geometric relationship yields as follows:

$$y_x = \frac{y_0}{x_0 / \cos(\theta - \psi)} \cdot \left( \frac{x_0}{\cos(\theta - \psi)} - \frac{x}{\cos(\theta - \psi)} \right), \quad (3)$$

$$G_x = \frac{G_0}{x_0} x, \quad (4)$$

where  $y_0$  is the maximum compression at the coal wall at the edge of the mining area ( $m$ );  $\theta$  is the dip angle of the coal seam, set at  $13^\circ$  according to the mine data;  $\psi$  is the break angle between the rock seams when the key block B breaks, which is  $5^\circ \sim 7^\circ$  according to the actual measurement;  $x_0$  is the size of the internal stress field range of this coal seam ( $m$ ).

Combining equations (2) and (3), the support stress component of the internal stress field in the direction perpendicular to the coal bed roof can be obtained as follows:

$$\int_0^{x_0 \cdot \cos(\theta - \psi)} \sigma_y = G_0 y_0 x_0 \left( \frac{\cos^2(\theta - \psi)}{2} - \frac{\cos^3(\theta - \psi)}{3} \right). \quad (5)$$

The direction of the supporting stress of the internal stress field is vertical downward, so the magnitude of the

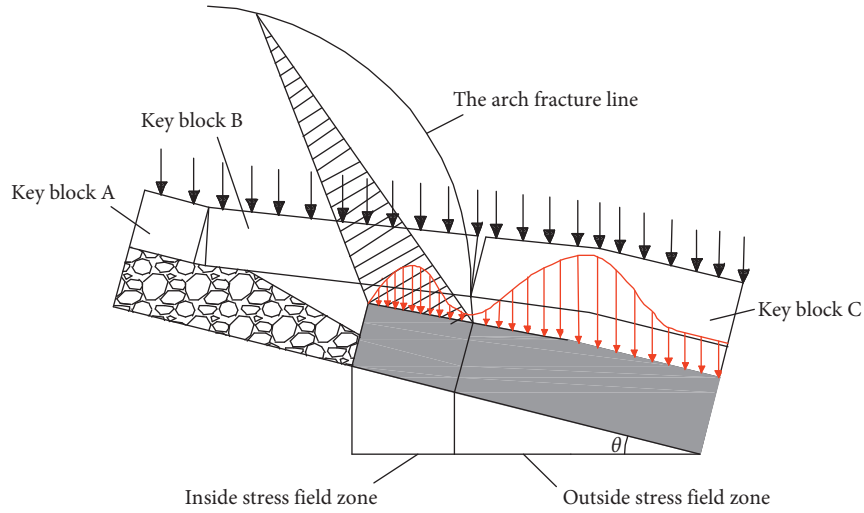


FIGURE 2: Lateral abutment stress distribution along dip direction in coal mass adjacent to gob.

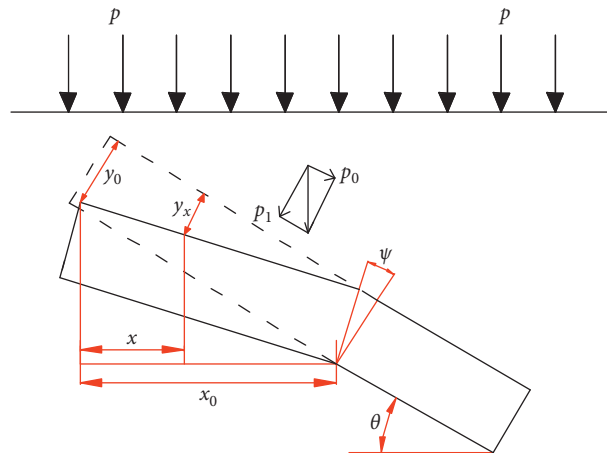


FIGURE 3: The basic roof fracture structure and stress condition above coal mass adjacent to gob.

supporting stress within the range of the internal stress field is shown as follows:

$$\frac{G_0 y_0 x_0 \cdot ((\cos^2(\theta - \psi)/2) - (\cos^3(\theta - \psi)/3))}{\cos \psi} \quad (6)$$

The support stress within the internal stress field is approximated as the weight of the basic top rock layer in the range of the internal stress field when incoming pressure occurs, i.e.,

$$\frac{G_0 y_0 x_0 \cdot ((\cos^2(\theta - \psi)/2) - (\cos^3(\theta - \psi)/3))}{\cos \psi} = LC_0 M \gamma, \quad (7)$$

where  $L$  is the length of the working face of the upper section ( $m$ );  $C_0$  is the incoming pressure step of the working face ( $m$ );  $M$  is the thickness of each transfer rock beam ( $m$ );  $\gamma$  is the average capacity of each transfer rock beam ( $kN/m^3$ ). From the beginning of the collapse of the direct top until the end of the

gange process, as the deformation of the coal seam and the direct top is synchronized, the geometric relationship can be obtained as follows:

$$\frac{y_0}{x_0 / \cos(\theta - \psi)} = \frac{\Delta h}{L' / \cos(\theta - \psi)} = \frac{h - m_z (K_p - 1)}{L' / \cos(\theta - \psi)}, \quad (8)$$

where  $\Delta L$  is the maximum sinkage when the direct top touches the gange stability ( $m$ );  $L'$  is the span of the direct top hinge rock beam ( $m$ );  $h$  is the mining height of the seam ( $m$ );  $m_z$  is the collapse height of the broken direct top ( $m$ );  $K_p$  is the broken expansion coefficient of the basic top rock.

The stiffness  $G_0$  of the coal body in the plastic state can be expressed by the envelope theory as follows:

$$G_0 = \frac{E}{2(1 + \nu)\xi}, \quad (9)$$

where  $E$  is the modulus of elasticity of coal body ( $Pa$ );  $\nu$  is Poisson's ratio;  $\xi$  is the influence coefficient, which is related to the fracture development in the coal body.



The magnitude of the internal stress field can be obtained by combining the above equations as follows:

$$x_0 = \sqrt{\frac{12LC_0M\gamma(1+\nu)\zeta L' \cos \psi}{E[h - m_z(K_p - 1)] \cdot [3 \cos^2(\theta - \psi) - 2 \cos^3(\theta - \psi)]}} \quad (10)$$

According to the geological data of the mine and field measurements, it is known that  $L = 170$  m,  $C_0$  is 32~35 m,  $M = 12.8$  m, and  $\gamma = 27$  kN/m<sup>3</sup>,  $\nu = 0.27$ ,  $\xi = 0.8$ ,  $L' = 18\sim 21$  m,  $E = 2.5$  GPa,  $h = 4.5$  m,  $m_z = 4.1$  m,  $K_p = 1.7$ , and  $\theta = 13^\circ$ . The internal stress field can be found in the range of 12.2 to 12.8 m. The internal stress field is in a low stress range; if the roadway is arranged within the internal stress field range by using the roadway along the air boring, it can effectively improve the mechanical state of the roadway surrounding rock, improve the stability of the roadway, and reduce the roadway maintenance cost.

**3.2. Preliminary Determination of Coal Pillar Width of Inclined Coal Seam.** Usually, the basic top fracture line is located in the coal wall at 0~14 m. When the fracture line is located in the coal wall at 9~14 m, generally 1~5 m coal pillar is used to arrange the roadway along the empty roadway within the fracture line; at this time, the sum of the width of the roadway along the empty roadway and the width of the narrow coal pillar is less than the width of the “internal stress field”, so that the roadway is in the low stress area. However, in addition to the support pressure factor, the influence of the size of the stable area inside the narrow coal column and the influence of the sheet gang, water accumulation in the mining area, and uneven strength of the coal body on the stability of the narrow coal column should also be considered.

- (1) Yangchangwan coal mine No.2 coal seam belongs to the inclined coal seam, above the mining area gangue along the coal seam tendency to have downward pressure on the coal pillar, and there is a certain range of plastic damage area at the coal wall, the coal pillar internal fissure is developed, and stability is poor, so leaving 1~5 m coal pillar cannot ensure that the coal pillar can exist in the elastic core area of the main bearing capacity
- (2) Because the combustion point of No.2 coal is relatively low, it is especially important to reduce the degree of fissure development in the coal column in order to prevent the spontaneous combustion of residual coal caused by the leakage of wind from the return air tunnel to the mining area

Considering the role of the coal pillar to block gangue, waterproof, fire prevention, gas, etc., the protective coal pillar is at least set at 3~5 m. In order to meet the normal working design of the shaft width of 5 m, the width of the coal pillar is initially set at 8~10 m. The 8~10 m protective coal pillar is left and the roadway is arranged within 2~3 m below the basic top fracture line, which effectively avoids the

huge load transmitted down by the arch foot and keeps the surrounding rock of the roadway relatively stable after digging.

## 4. Numerical Simulation

**4.1. Establishment of the Numerical Simulation Model.** According to the production geological condition of 130205 working face, a FLAC<sup>3D</sup> numerical model is established, as shown in Figure 4. The model is fixed at the two boundaries of the X and Y axes and the bottom boundary of Z axis, a self-weight load of 17.625 MPa is applied directly above the model Z axis, and the lateral pressure coefficient is set to 1.2, which is confirmed by in situ stress test results. The rock parameters were obtained by evolutionary analysis based on the measured results. The coal seam model was set as the Mohr-Coulomb strain-softening model [18, 19], and the rock mechanical parameters of the coal seam and surrounding rocks are listed in Table 1.

### 4.2. The Second Invariant of Deviatoric Stress Field Distribution

**4.2.1. Distribution of Second Invariant of Deviatoric Stress in Coal Pillar Affected Area of the Roadway Surrounding Rock.** The second invariant of deviatoric stress represents the magnitude of the shear force and deformation of the rock body, which can objectively reflect the essential characteristics of the deformation and damage of the surrounding rock caused by the excavation of the roadway [13, 20]. It is more comprehensive than the previous use of only the support pressure (vertical stress) as a measure. The weight of the overlying rock in the mining void area of the middle and upper section of the inclined coal seam is transferred to the side of the coal pillar by means of a fracture arch, so the width of the coal pillar is crucial to the mechanical state of the surrounding rock along the empty roadway. The simulation studies the second invariant of deviatoric stress cloud at  $Y = 80$  m cut for coal column widths of 5, 8, 10, 12.5, 15, and 20 m, respectively, as shown in Figure 5.

**4.2.2. Coal Seam Tendency Second Invariant of Deviatoric Stress Distribution State.** By monitoring the magnitude of  $\sigma_1$ ,  $\sigma_2$ , and  $\sigma_3$  stresses at the location of the coal pillar and solid coal midline, the second invariant of deviatoric stress under the influence of different coal pillars is calculated and plotted, as shown in Figure 6.

From Figure 6(a), the following can be seen:

- (1) The peak value of the second invariant of deviatoric stress shows a trend of increasing first and then decreasing. For the coal pillar in the section of 5~12.5 m, with the increase of the width of the coal pillar, the peak value of the second invariant of deviatoric stress in the coal pillar shows a “positive correlation” growth. For the coal pillar in the 12.5~20 m section, the curve shape changes from “single peak” to “double hump” as the width of the coal pillar increases, and the peak of the second

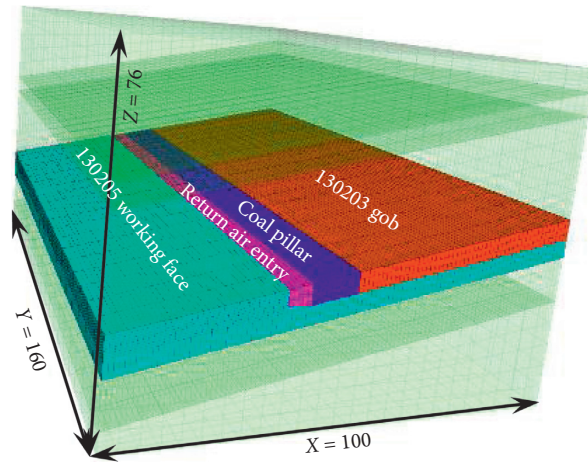


FIGURE 4: The establishment of a three-dimensional numerical model by FLAC3D software.

TABLE 1: Testing result of coal samples about physical and mechanical properties.

Types	Density (g·cm <sup>-3</sup> )	Bulk modulus (GPa)	Shear modulus (GPa)	Cohesion (MPa)	Internal friction angle (°)	Thickness (m)
Fine sandstone	2.70	13.3	10	10.2	37	5.0
Medium sandstone	2.34	12.3	9.1	5.2	37	13.0
Fine sandstone	2.70	13.3	10	10.2	37	5.0
Siltstone	2.65	9.1	7.8	7.2	34	5.0
Carbon mudstone	2.54	8.4	5.7	8.0	36	1.5
2# coal	1.30	5.0	2.1	1.68	28	8.5
Siltstone	2.65	9.1	7.8	7.2	34	5.0
Mudstone	2.25	6.8	4.8	6.2	26	2.0
Fine sandstone	2.70	13.3	10	10.2	37	5.0

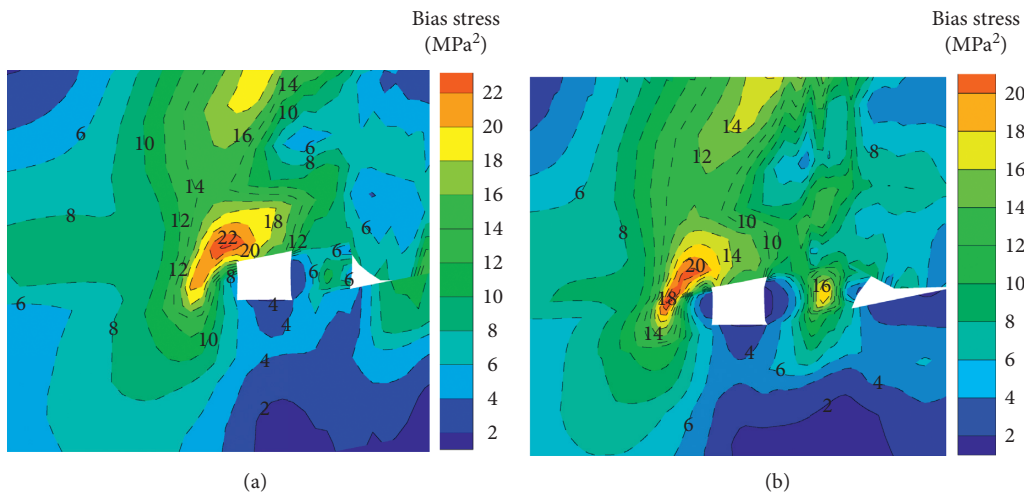


FIGURE 5: Continued.

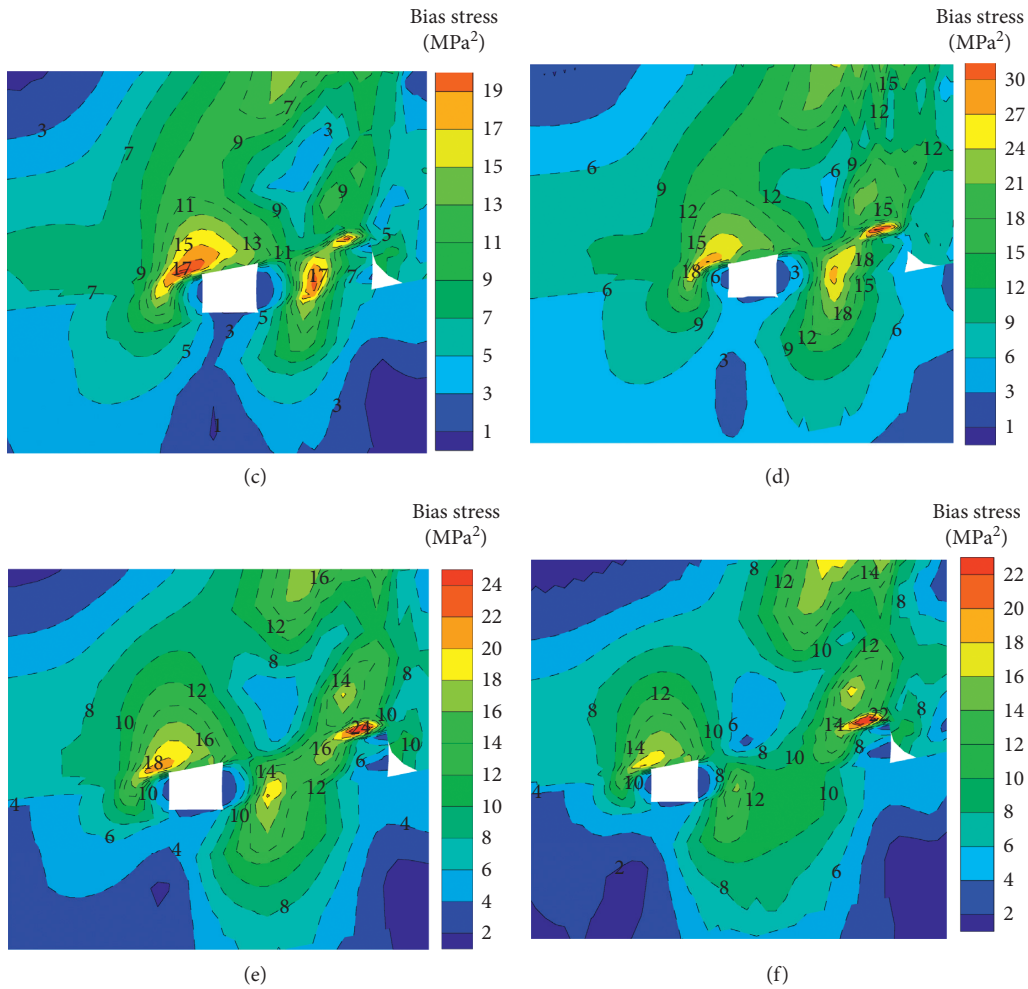


FIGURE 5: The second invariant of deviatoric stress cloud in the surrounding rock of the roadway under different width coal pillars. (a) 5 m coal pillar, (b) 8 m coal pillar, (c) 10 m coal pillar, (d) 12.5 m coal pillar, (e) 15 m coal pillar, and (f) 20 m coal pillar.

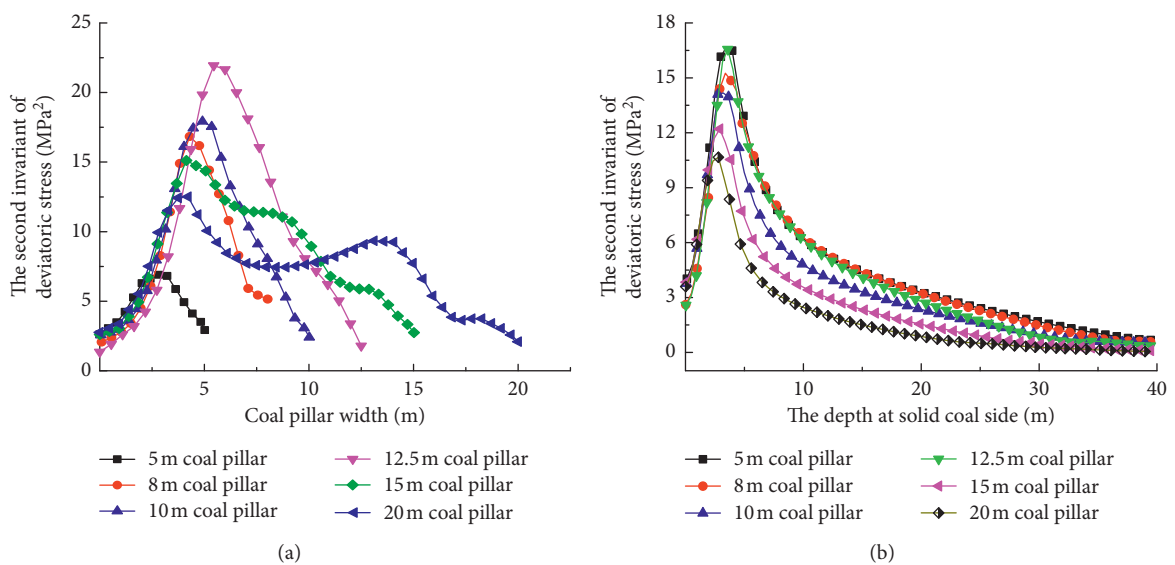


FIGURE 6: The second invariant of deviatoric stress distribution curves in the two coal girders of the roadway under different width coal pillars. (a) Coal pillar side. (b) Solid coal side.

invariant of deviatoric stress in the coal pillar shows a “negative correlation” with the width of the coal pillar

- (2) The peak location of the second invariant of deviatoric stress also shows a trend of increasing and then decreasing

For the coal pillars in the 5~12.5 m section, as the width of the pillar increases, the location of the peak appears at a linear increase from the horizontal distance of the roadway, with the peak location shifting away from the roadway. For the coal column in the 12.5~20 section, the hump shape starts to appear when the coal column equals 15 m. At this time, the peak of the hump is almost equal, which is called the “positive trapezoid” shape here. Thus, within this range of coal pillars, the shape of the second invariant of deviatoric stress distribution undergoes a transformation from single hump - orthotropic shape-double hump, and the interior of large coal pillars is more complete, which also indirectly reveals the reason for the feasibility of traditional large coal pillars.

From Figure 6(b), the following can be seen:

- (1) The overall second invariant of deviatoric stress in the solid coal shows the “asymmetric” characteristic of increasing first and then decreasing, and the coal pillars of different widths have a tendency to converge within 40 m of the surrounding rock on the side of the solid coal. The magnitude of the second invariant of deviatoric stress in the coal body 40 m away is almost 0, and the coal body in this range is approximately in the original rock stress zone
- (2) Overall, with the increase of the width of the left coal pillar, the peak of the second invariant of deviatoric stress within the solid coal decreases and the stress has a tendency to transfer from the solid coal side to the coal pillar side. As the width of the coal column increases, the corresponding peak position of the solid coal side as a whole shows a negative linear correlation law with it

**4.2.3. Characteristics of Top Plate’s Second Invariant of Deviatoric Stress Distribution.** In order to analyze the distribution characteristics of the second invariant of deviatoric stress in the surrounding rock of the tunnel roof, a total of 3 monitoring lines were set up, each line set up a monitoring point at 0.5 m interval, each line has a total of 40 monitoring points, and the roof monitoring line was laid out as Figure 7, using the formula which is shown in equation (1) to find out the second invariant of deviatoric stress and postprocessed to obtain curve in Figure 8.

The following pattern can be derived from Figure 8:

- (1) When the coal column is stable and the width of the coal column is small, the shallow surrounding rock above the roof of the roadway has a higher second invariant of deviatoric stress, and with the increase of the surrounding rock depth, the stress increases

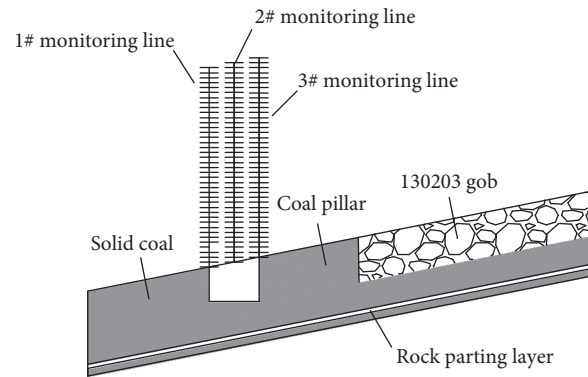


FIGURE 7: Monitoring point arrangement plan in the roof of the roadway.

again after the second invariant of deviatoric stress decreases to a certain minimal value, and a higher stress concentration zone appears, and the wider the coal column is, the smaller the peak of this influence zone is

- (2) When the coal column is stable and the width of the coal column is large, the shallow surrounding rock above the roof of the roadway has a low value of the second invariant of deviatoric stress compared with the narrow coal column, the shallow surrounding rock is more stable and does not form a strong shear stress concentration area, and the integrity of the roof of the roadway is better under this large coal column. As the depth of the surrounding rock increases, due to the distance from the mining area, the influence of stress in the adjacent mining area is relatively small, and there is an overall “negative exponential” relationship between the value of the second invariant of deviatoric stress and the increase in the depth of the surrounding rock
- (3) The different horizontal distance between the three monitoring lines and the mining area directly affects the size and location of the peak of the second invariant of deviatoric stress. It can be seen that ① the degree of damage to the surrounding rock on the top plate monitoring line 3 is much greater than that on the monitoring line 1, and the shear fragmentation of the shallow part of the top plate shows significant asymmetric characteristics; ② the surrounding rocks of the three monitoring lines under different width coal pillars differ greatly in the peak value of the second invariant of deviatoric stress due to the influence of adjacent mining areas. When the coal pillar width is 5~8 m, the minimum peak second invariant of deviatoric stress under the influence of 8 m coal pillar is 12.42 MPa when monitoring the surrounding rock of line 1 under the influence of adjacent mining area, which is 9.74% lower than the peak at 5 m coal pillar. When the width of the coal pillar is 5~10 m, the minimum peak of the second invariant

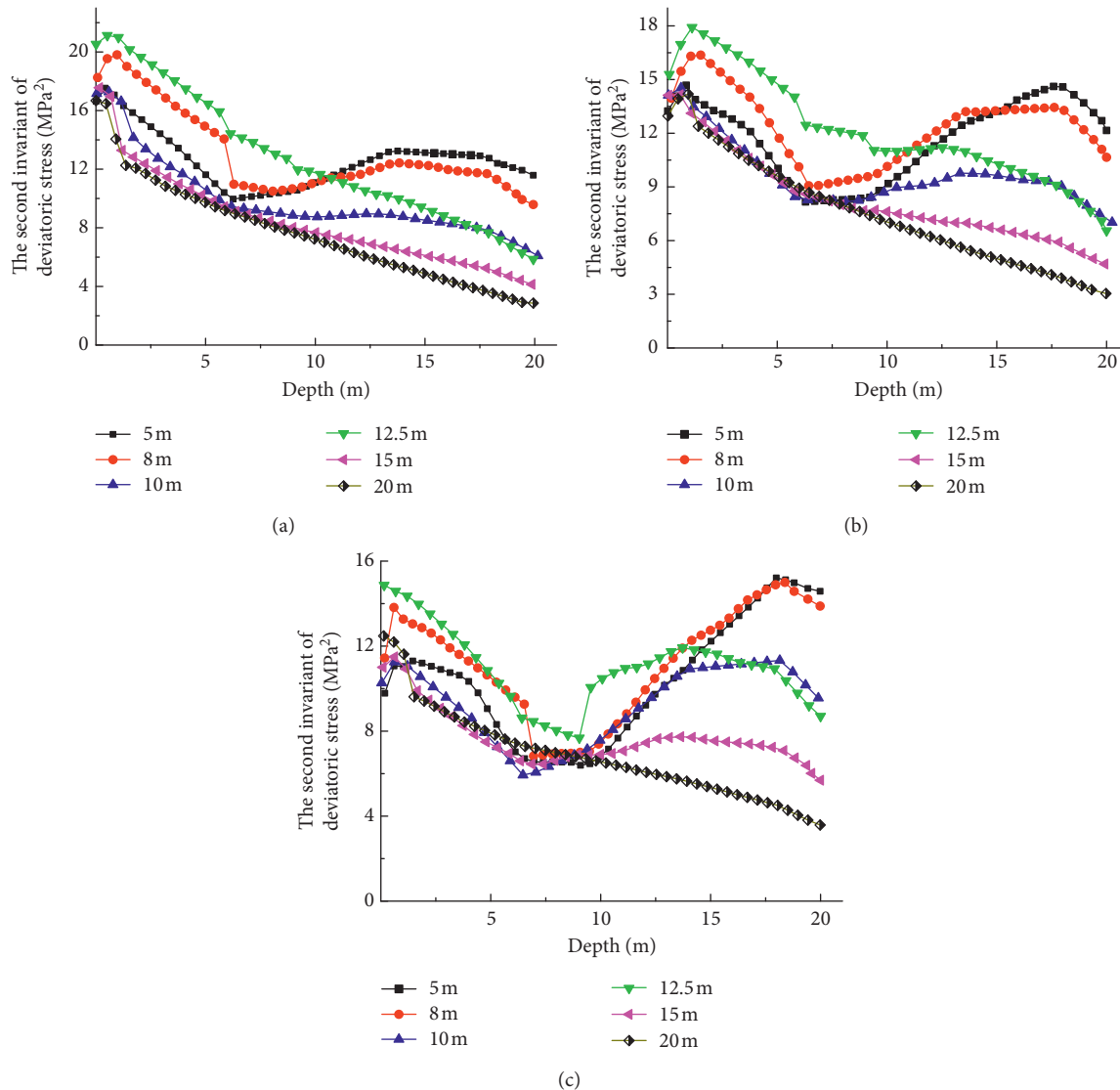


FIGURE 8: The second invariant of deviatoric stress curve by top slab surrounding rock monitoring line. (a) 1<sup>#</sup> monitoring line. (b) 2<sup>#</sup> monitoring line. (c) 3<sup>#</sup> monitoring line.

of deviatoric stress under the influence of 10 m coal pillar is 9.31 MPa in the surrounding rock of monitoring line 2 by the adjacent mining area, which is 36.28% lower than the peak of 5 m coal pillar; the minimum peak of the second invariant of deviatoric stress under the influence of 10 m coal pillar is 11.32 MPa in the surrounding rock of monitoring line 3, which is 25.58% lower than the peak of 5 m coal pillar; ③ under the influence of 10 m coal pillar, the surrounding rock of monitoring line is less influenced by the upper section of mining area, and shear damage is not big; from the safety point of view, choosing this width coal pillar is more conducive to the stability of the roof

### 4.3. Deformation Characteristics of the Tunnel Surrounding Rock

**4.3.1. Displacement Distribution State within the Coal Column.** In order to investigate the reasonableness of the width of the coal pillar left between 130205 along the empty road and the upper section of the mining area, the characteristics of the horizontal displacement distribution within the coal pillar of different widths were selected as the object of study, as shown in Figure 9. The following can be seen:

- (1) In the side close to the mining area, the displacement of the coal body to the mining area is more obvious, and it can be seen from Figure 9(b) that when the width of the coal column is less than 5 m, there is a



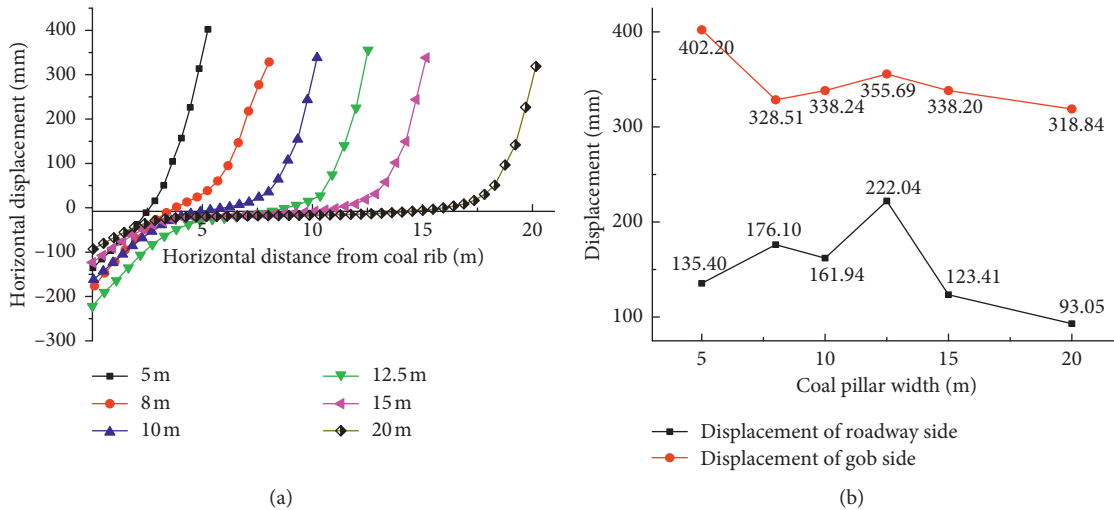


FIGURE 9: Horizontal displacement distribution curves under coal column of different widths. (a) Coal pillar midline displacement curve. (b) Maximum displacement value on both sides of the coal column.

large displacement of the coal column along the direction of the coal seam inclination on the side of the mining area, and at this time, the coal column is broken seriously and thrown down to the mining area. Under the influence of 8 m and 10 m coal pillar, the displacement of coal pillar to the mining area is greatly relieved compared with 5 m coal pillar, and then with the increase of coal pillar width, although it can reduce the degree of breakage within the coal pillar, its overall effect is not obvious

- (2) From Figure 9(b), it can be seen that under the influence of 12.5 m coal pillar, the maximum displacement of 222.04 mm is generated on the side of the mining area, the minimum displacement is 93 mm at 20 m coal pillar, and the overall displacement curve approximately forms a “single hump” shape
- (3) As seen in Figure 9(a), when the coal column width is 10 m, continuous 0 mm displacement points start to appear within the coal column. The elastic nucleus zone without displacement is extremely important to the stability of the coal column. The elastic nucleus zone has strong stability under the mutual extrusion of the surrounding coal body, which can effectively avoid gas protrusion and wind leakage and other disasters and facilitate the management and maintenance of the roadway

Therefore, the necessity of narrow coal pillars for the stability of the roadway can be seen. The elastic core zone with very small displacement starts to appear within the 10 m coal pillars, the elastic core zone plays the main bearing role for the overlying rock layer, and its width is inseparable from the stability of the dug tunnel and the high maintenance cost at a later stage. Therefore, the width of the coal pillar is initially set at 10 m from the

consideration of the internal stability of the coal pillar alone.

4.3.2. *Deformation Law of the Surrounding Rock along the Air Dug Tunnel.* The monitoring points are set up at the two helpers of the roadway, the two ends of the top and bottom plates, and the midline, respectively, and the displacement curve shown in Figure 10 is obtained, which shows the following:

- (1) The sinkage of the roof slab: as the width of the coal pillar increases, the sinking amount of roof monitoring point on the side of the coal pillar is always larger than that on the side of solid coal. Therefore, it is necessary to reasonably arrange anchor support near the roof of the coal pillar, so that it can form a “small structure” with a shallow surrounding rock to fully improve the residual strength of the surrounding rock and improve the stress environment of the surrounding rock
- (2) Bottom drum volume: 130205 backwind lane bottom slab is loose and soft; in the process of stress distribution of surrounding rock caused by lane excavation to the new balance of stress, the bottom slab coal keeps bulging into the lane space, compared to the direct bottom as the lane bottom slab will form a larger bottom drum volume
- (3) The displacement of the coal pillar gang: from the overall view of the curve, the displacement of the coal pillar gang is most obvious at the midline, the displacement of the shoulder angle of the coal pillar gang is small and does not change significantly, and the overall displacement of the bottom angle of the coal pillar gang shows a trend of increasing first and then decreasing

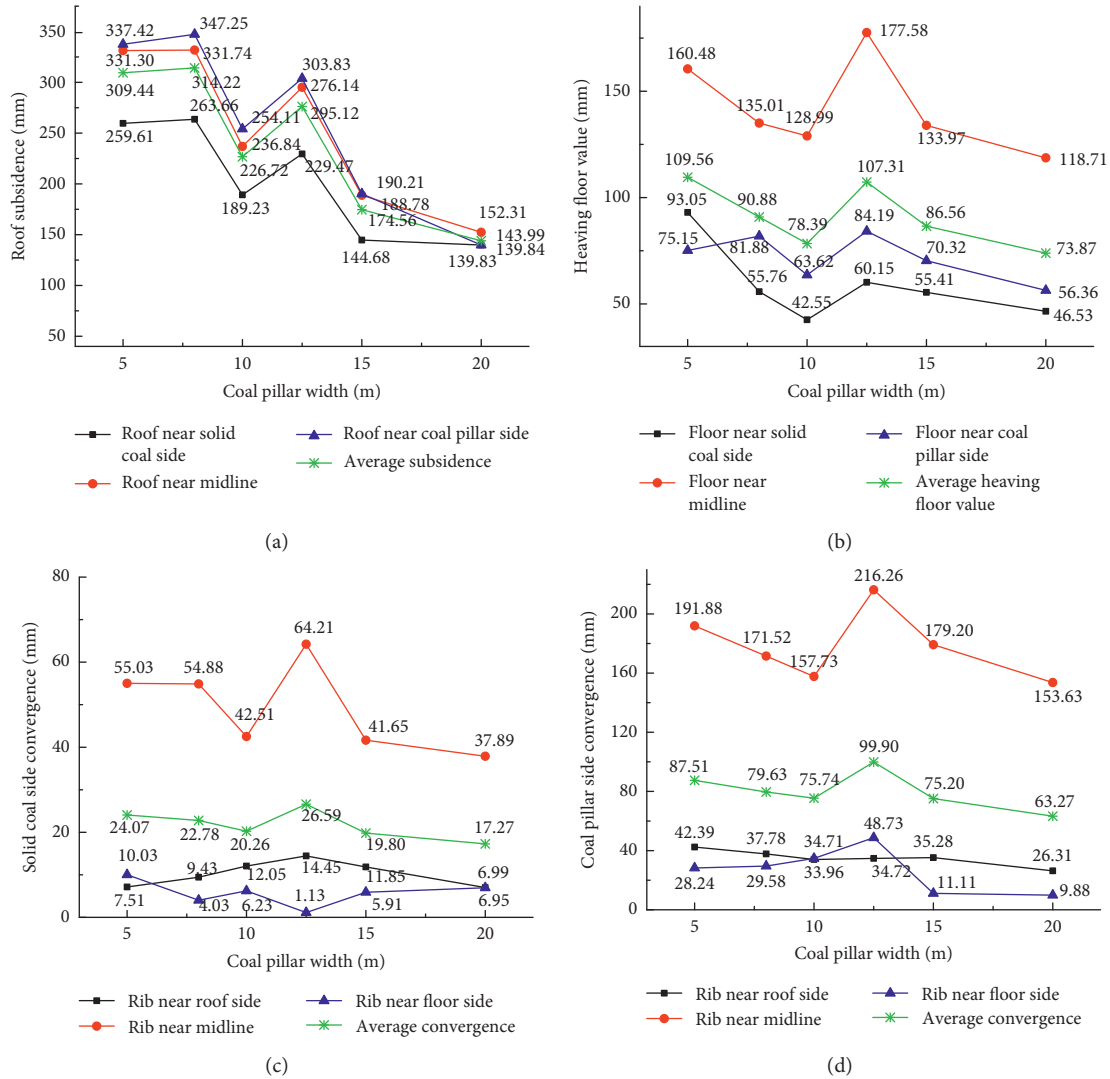


FIGURE 10: Variation of the displacement of the surrounding rock of the roadway under different width coal pillars. (a) Top plate sinkage. (b) Bottom drum volume. (c) Coal pillar gang approach amount. (d) Solid coal gang approach amount.

(4) The amount of solid coal gang migration: from the average displacement data, the influence of coal pillar width on the solid coal gang is not significant, under the influence of 12.5 m coal pillar, the displacement of the solid coal gang reaches the maximum 17.73 mm, under the influence of 15~20 m large coal pillar, the displacement decreases, and under the influence of 20 m coal pillar, the average displacement of the solid coal gang reaches the minimum 9.29 mm

In summary, the variation of coal pillar width along the air dug tunnel has a greater impact on the amount of roof sinking, bottom bulge, and coal pillar gang displacement in the 130205 return tunnel. Under the influence of 10 m coal column, the overall deformation of the roadway is relatively small and within the reasonable range of engineering construction, which can fully meet the basic roadway transportation, ventilation, and pedestrian requirements, the internal coal column is more

stable and the stress carried above the coal column is relatively small, and the roadway roof is less affected by the superimposed stress of the adjacent mining area, so the width of the coal column along the air dug roadway is set to 10 m which is more reasonable.

### 5. Roadway Rock Control Technology and Practice

5.1. Rock Control Technology along the Empty Roadway. Based on the numerical simulation results and combined with the actual mine production requirements, the causes of maintenance difficulties in the 130205 return airway can be summarized as follows:

- (1) The coal pillar plays an extremely important role in supporting the overlying rock as the support point of the fracture arch from the time the roadway is dug until the coal pillar is stabilized. Because the coal body has strain-softening characteristics, so in the

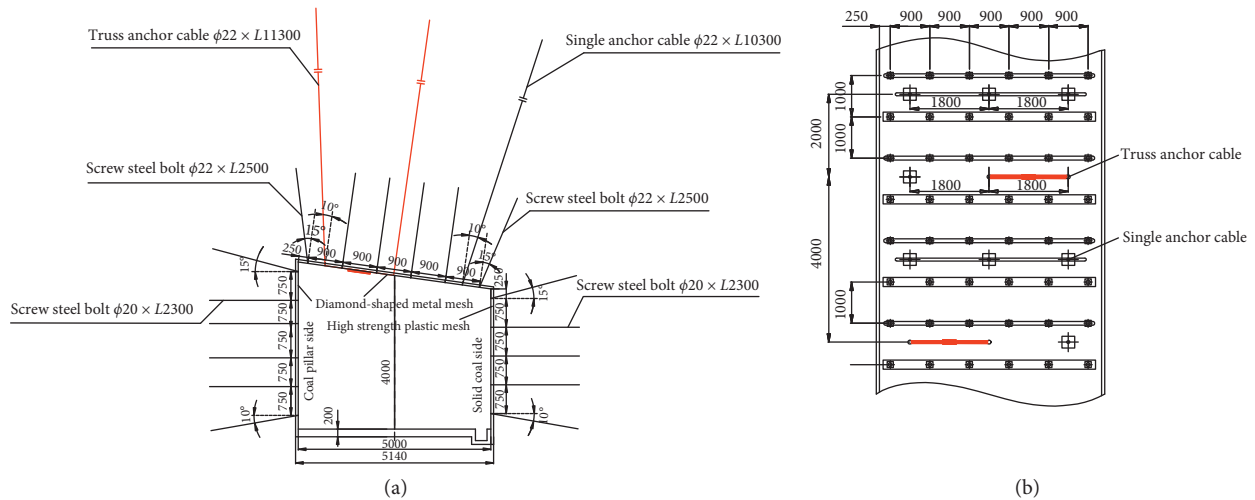


FIGURE 11: Scheme of rock support system in the roadway. (a) Front view. (b) Top view.

subsequent 130205 working face of the recovery process, by the influence of superimposed support pressure, coal column stability again greatly reduced, may lead to destabilization of the roadway occurred in large deformation, and even cause serious economic losses

- (2) No.2 coal seam thickness distribution is more uneven, and there is more gangue layer in the direct bottom; in view of this special geological structure design along the coal seam mid-waist line boring, forming a special roadway structure with coal body as the bottom plate, coal seam bottom plate coal quality is softer, so the stability of the bottom plate along the empty roadway compared with other similar roadway needs to pay more attention to consider

In response to the above problem, the “new prestressed truss anchor cable + single anchor cable + anchor rod + net + slurry spray” support method is adopted in 130205 section backwind flat road, and concrete hardened base plate is used to limit the coal body projection of the base plate. This asymmetric support system effectively reduces the maximum tensile stress of the coal rock body in the middle area of the roadway and improves the strength and resistance of the coal rock body [21–23]. This asymmetric support system can effectively reduce the maximum tensile stress in the central part of the roadway and improve the strength and resistance to deformation.

5.2. *Parameters of Return Air Tunnel Support System.* The stability of the surrounding rock of the retrieval tunnel is equally inseparable from the interaction between the support and the surrounding rock, and Figure 11 shows the flat section of the shaped section support along the hollow tunnel.

From Figure 11, the following can be seen:

- (1) The roof anchors are  $\phi 22 \text{ mm} \times L2500 \text{ mm}$  left-hand threaded steel anchors, each anchor is 900 mm apart,

the distance between the corner anchors on the side of the coal pillar gang and the coal pillar gang is 250 mm, the anchors near the two gangs are inclined  $15^\circ$  to the outside, and the rest of the anchors are arranged perpendicular to the roof. The truss anchor cable adopts two  $\phi 22 \text{ mm} \times L11300 \text{ mm}$  high-strength low relaxation prestressing steel strands, and the anchor cable near the gang is inclined  $10^\circ$  to the outside, and there is another single anchor cable near the solid coal gang with the specification of  $\phi 22 \text{ mm} \times L10300 \text{ mm}$

- (2)  $\phi 20 \text{ mm} \times L2300 \text{ mm}$  threaded steel anchor rods were used in the solid coal gang, 5 anchor rods were arranged in a row, the distance between rows of anchor rods is  $750 \text{ mm} \times 1000 \text{ mm}$ , the upper anchor rods are 250 mm from the top plate, the anchor rods near the top plate were inclined upward by  $15^\circ$ , the anchor rods near the bottom plate are inclined downward by  $10^\circ$ , and the rest were arranged perpendicular to the gang
- (3) The coal pillar gang uses  $\phi 20 \text{ mm} \times L2300 \text{ mm}$  threaded steel anchor rods, 6 anchor rods are arranged in a row, the distance between rows of anchor rods is  $750 \text{ mm} \times 1000 \text{ mm}$ , the upper anchor rods are 250 mm from the top plate, the anchor rods near the top plate are inclined upward by  $15^\circ$ , the anchor rods near the bottom plate were inclined downward by  $10^\circ$ , and the rest were arranged perpendicular to the roadway gang

5.3. *Numerical Simulation Analysis of Support.* 130205 along the empty roadway roof staggered with truss anchor cable and single anchor cable joint support form greatly enhances the surrounding rock support difficult area of the bearing performance and the use of numerical simulation method to analyze the support form under the roadway surrounding rock pressure characteristics, as shown in Figure 12. Although the distribution of the second invariant of deviatoric

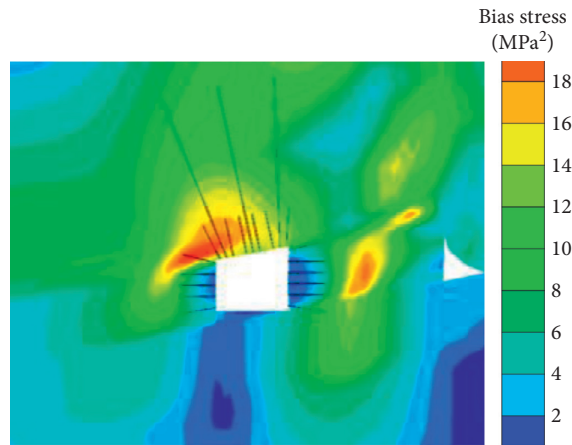


FIGURE 12: Cloud diagram of the second invariant of deviatoric stress distribution for the effect of rock support in the roadway.

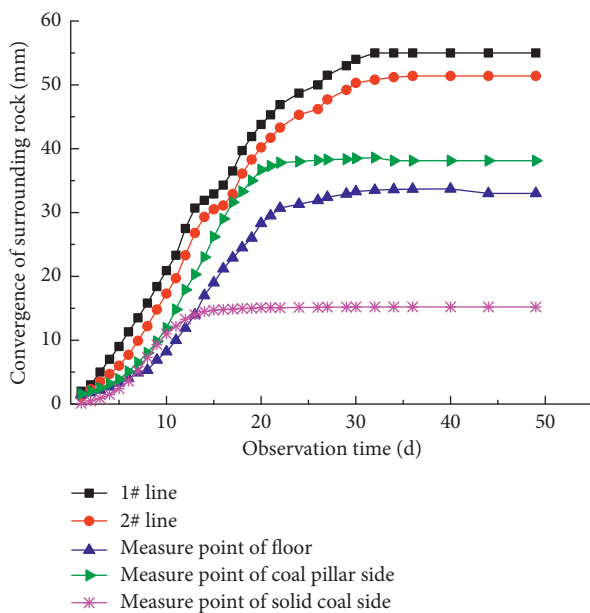


FIGURE 13: Field mine pressure observation results.

stress in the shallow surrounding rock of the roof still shows asymmetry, its overall distribution is relatively uniform, the stress concentration area at the shoulder nest of solid coal is relieved, and the range of low stress area on the gang side of coal pillar is also reduced. According to the reciprocal influence relationship between the top plate and gang deformation of the roadway, the coupling effect of its asymmetric support can alleviate the roadway deformation, thus effectively limiting the harmful deformation damage of the surrounding rock, achieving the uniformity of non-uniform load, and thus maintaining the roadway stability.

## 6. Mineral Pressure Observation and Analysis of Results

This return airway is continuously observed for the convergence of the tunnel surrounding rock while it is dug. Two

lines are set up at the top plate to monitor the convergence of the surrounding rock after tunneling, line 1 is 0.8 m near the coal pillar side, line 2 is 0.8 m near the solid coal side, and the monitoring points of the gang and bottom plate are all at their midline locations. The curve of the surrounding rock change after tunneling is shown in Figure 13. It can be seen that the process of surrounding rock stabilization after roadway boring is a dynamic process until the equilibrium state, the top and bottom plates and coal pillar gangs tend to stabilize at about 30 d roadway deformation, and the solid coal gangs tend to stabilize at 20 d after roadway boring. The maximum deformation of the top plate 1 line is 55 mm, the maximum deformation of the top plate 2 line is 51 mm, the maximum displacement of the coal pillar gang is 38 mm, and the maximum displacement of the solid coal gang is 15 mm. Monitoring results, this support method is effective for the maintenance of the roadway.

## 7. Conclusion

- (1) Usually, the roadway is arranged within the internal stress field, so that the surrounding rock of the roadway is in a low stress state, which greatly improves the mechanical environment of the surrounding rock. In this paper, this paper establishes a simple mechanical model of inclined coal seam and derives the formula of the influence range of "internal stress field" in inclined coal seam
- (2) Using FLAC3D simulation technology, it is concluded that along the coal seam inclination direction, with the increase of coal pillar width, the second invariant of deviatoric stress curve in the coal pillar shows the transformation from single hump shape to positive trapezoid shape to double hump shape, the solid coal stress gradually shifts to the coal pillar side with the increase of coal pillar width, and the reasonable coal pillar width is usually less than the width of the coal pillar when the extreme value of the second invariant of deviatoric stress appears
- (3) The top plate surrounding rock on the side of coal pillar has a high second invariant of deviatoric stress compared with the top plate on the side of solid coal, and the top plate surrounding rock has asymmetric destructive property; in the inclined coal seam, it is usually taken as reasonable narrow coal pillar width at the minimum fluctuation value of the second invariant of deviatoric stress
- (4) The internal integrity of the coal pillar directly determines the stability degree along the empty roadway. With the compaction of coal gangue in the mining area after the working face, the fissures on both sides of its narrow coal pillar are also gradually developed, its bearing capacity continues to decrease, and the existence of a certain range of elastic core area in the middle of the coal pillar is crucial to the stability of the coal pillar and the roadway
- (5) A new type of truss anchor cable joint support method is proposed for asymmetric control of the



roadway, with high-strength anchors placed in each row of the roof and gang to reinforce the coal body, and the top plate is staggered with a single anchor cable and truss anchor cable to enhance the bearing capacity of the difficult area of support, thus improving the stress environment of the surrounding rock and preventing the malignant collapse of the coal pillar gang roof and shoulder sockets

## Data Availability

All data used to support the findings of this study are included within the article, and there are not any restrictions on data access.

## Conflicts of Interest

The authors declare no conflicts of interest.

## Acknowledgments

The work was supported by the Engineering Laboratory of Deep Mine Rockburst Disaster Assessment Open Project (LMYK2020005) and the National Natural Science Foundation of China (Nos. 51574243, 51404269, and 51674253).

## References

- [1] Z. Zhang, J. Bai, Y. Chen, and S. Yan, "An innovative approach for gob-side entry retaining in highly gassy fully-mechanized longwall top-coal caving," *International Journal of Rock Mechanics and Mining Sciences*, vol. 80, pp. 1–11, 2015.
- [2] Z. Yang, C. Liu, S. Tang, L. Dou, and J. Cao, "Rock burst mechanism analysis in an advanced segment of gob-side entry under different dip angles of the seam and prevention technology," *International Journal of Mining Science and Technology*, vol. 28, no. 6, pp. 891–899, 2018.
- [3] Z. Zheng, Z. Q. Yang, H. Z. Zhu et al., "Study on reasonable coal-pillar width and surrounding-rock control of gob-side irregular roadway in inclined seam," *Journal of Mining & Safety Engineering*, vol. 36, no. 2, pp. 223–231, 2019.
- [4] A. H. Wilson, "The stability of underground workings in the soft rocks of the coal measures," *International Journal of Mining Engineering*, vol. 1, no. 2, pp. 91–187, 1983.
- [5] J. B. Bai, C. J. Hou, and H. F. Huang, "Numerical simulation study on stability of narrow coal pillar of roadway driving along goaf," *Chinese Journal of Rock Mechanics and Engineering*, vol. 23, no. 20, pp. 3475–3479, 2004.
- [6] G. X. Xie, K. Yang, and Q. M. Liu, "Study on distribution laws of stress in inclined coal pillar for fully-mechanized top-coal caving face," *Chinese Journal of Rock Mechanics and Engineering*, vol. 25, no. 3, pp. 545–549, 2006.
- [7] F. L. He and G. C. Zhang, "Asymmetric failure and control measures of large cross-section entry roof with strong mining disturbance and fully-mechanized caving mining," *Chinese Journal of Rock Mechanics and Engineering*, vol. 35, no. 4, pp. 806–818, 2016.
- [8] C. J. Hou and X. H. Li, "Stability principle of surrounding rock structure in fully mechanized driving along next goaf," *Journal of China Coal Society*, vol. 26, no. 1, pp. 1–7, 2001.
- [9] W. H. Zha, X. Li, X. Z. Hua et al., "Impact and application on narrow coal pillar for roadway protecting from fracture position of upper roof," *Journal of China Coal Society*, vol. 39, no. S2, pp. 332–338, 2014.
- [10] Z.-Q. Yang, C. Liu, G.-A. Wang, G.-W. Li, and F.-S. Li, "Structural characteristics analysis of overlying rocks and prevention measures with a long-wall face passing across abandoned roadways: a case study," *Shock and Vibration*, vol. 2021, Article ID 6665341, 15 pages, 2021.
- [11] T. Li, T. T. Mei, G. Q. Li et al., "Mechanism study of coal and gas outburst induced by rockburst in "three-soft" coal seam," *Chinese Journal of Rock Mechanics and Engineering*, vol. 30, no. 6, pp. 1283–1288, 2011.
- [12] J. G. Guo, W. G. Wang, F. L. He et al., "Main roof break structure and surrounding stability analysis in gob-side entry with fully-mechanized caving mining," *Journal of Mining & Safety Engineering*, vol. 36, no. 3, pp. 446–454+464, 2019.
- [13] G. .C. Zhang, L. J. Chen, Z. J. Wen et al., "Squeezing failure behavior of roof-coal masses in a gob-side entry driven under unstable overlying strata," *Energy Science & Engineering*, vol. 8, 2020.
- [14] Z.-q. Yang, H.-m. Wang, D.-q. Sun, X.-j. Ma, M.-b. Xu, and N.-x. Si, "Study on occurrence mechanism of coal pillar in L-Shaped zone during fully mechanized mining period and prevention technology," *Shock and Vibration*, vol. 2021, Article ID 6638009, 15 pages, 2021.
- [15] M. B. Wold, L. D. Connell, S. K. Choi et al., "The role of spatial variability in coal seam parameters on gas outburst behaviour during coal mining," *International Journal of Coal Geology*, vol. 75, no. 1, pp. 1–14, 2008.
- [16] C. Liu, Z. Yang, P. Gong et al., "Accident analysis in relation to main roof structure when longwall face advances toward a roadway: a case study," *Advances in Civil Engineering*, vol. 2018, Article ID 3810315, 11 pages, 2018.
- [17] G. C. Zhang, F. L. He, L. S. Jiang et al., "Analytical analysis and field observation of break line in the main roof over the goaf edge of longwall coal mines," *Mathematical Problems in Engineering*, vol. 2016, Article ID 4720867, 11 pages, 2016.
- [18] Z. Yang, L. Dou, C. Liu, M. Xu, Z. Lei, and Y. Yao, "Application of high-pressure water jet technology and the theory of rock burst control in roadway," *International Journal of Mining Science and Technology*, vol. 26, no. 5, pp. 929–935, 2016.
- [19] W. H. Peng and A. H. Lu, "Numerical simulation of layered crack and failure of roadway surrounding rock under the action," *Journal of Mining & Safety Engineering*, vol. 25, no. 2, pp. 213–216, 2008.
- [20] G. A. Zhu, L. M. Dou, Z. L. Li et al., "Mining-induced stress changes and rock burst control in a variable-thickness coal seam," *Arabian Journal of Geosciences*, vol. 5, no. 9, pp. 365–376, 2016.
- [21] Z. Z. Zhang, M. Deng, J. B. Bai et al., "Strain energy evolution and conversion under triaxial unloading confining pressure tests due to gob-side entry retained," *International Journal of Rock Mechanics and Mining Sciences*, vol. 126, pp. 1–10, 2020.
- [22] M. G. Qian, P. W. Shi, and J. L. Xu, *Mining Pressure and Strata Control*, pp. 105–125, China University of Mining and Technology Press, Xuzhou, China, 2010.
- [23] L. Li, J. B. Bai, and X. Y. Wang, "Ration position and control technique of roadway driving along next goaf in fully mechanized top coal caving face," *Journal of China Coal Society*, vol. 37, no. 9, pp. 1564–1569, 2012.



## Research Article

# Exploration and Practice of Pressure Relief by Slotting Coal Seams with a Diamond Wire Saw

Zhu Tang <sup>1,2,3</sup> Shuqing Li <sup>1,2</sup> Fei Huang <sup>1,2</sup> Shouqing Huang<sup>1,4</sup> and Kangxu Cai<sup>1,2</sup>

<sup>1</sup>Hunan Provincial Key Laboratory of Safe Mining Techniques of Coal Mines, Work Safety Key Laboratory on Prevention and Control of Gas and Roof Disasters for Southern Coal Mines, Hunan University of Science and Technology, Xiangtan 411201, Hunan, China

<sup>2</sup>School of Resource Environment and Safety Engineering, Hunan University of Science and Technology, Xiangtan 411201, Hunan, China

<sup>3</sup>School of Mines and Civil Engineering, Liupanshui Normal University, Liupanshui 553004, Guizhou, China

<sup>4</sup>Guizhou Pan Jiang Coal and Electricity Refco Group Ltd., Guiyang 550081, Guizhou, China

Correspondence should be addressed to Shuqing Li; 2793997437@qq.com

Received 20 March 2021; Accepted 6 May 2021; Published 13 May 2021

Academic Editor: Xianjie Hao

Copyright © 2021 Zhu Tang et al. This is an open access article distributed under the Creative Commons Attribution License, which permits unrestricted use, distribution, and reproduction in any medium, provided the original work is properly cited.

To safely and economically eliminate the threat of high geostress in the coal mining process, based on the engineering case study of pressure relief by slotting residual coal pillars at a mine in the Kailuan mining area, a method of pressure relief by slotting coal seams with a wire saw was explored, and numerical simulation was carried out. The results show that the wire saw can cut coal seams in a large area, with a cutting efficiency and slotting depth greater than those of hydraulic slotting; a stress concentration zone forms in front of the wire saw coal cutting working face and a stress reduction zone and a stress recovery zone form behind. The pressure relief range varies, increasing at first and then decreasing. The exploration and practice of pressure relief by slotting coal seams with a diamond wire provides theoretical guidance and practical reference for pressure relief by slotting coal seams.

## 1. Introduction

High geostress during coal mining is a great threat to coal mine production safety, and slotting pressure relief is an effective method to release high geostress in coal seams [1–4]. Based on the principle of water hammer pressure breaking coal by high-pressure water jet impact, high-pressure water jet seam slotting equipment and technology have been developed and applied under certain conditions [5–7]. The high-pressure water jet pressure in use is 60~100 MPa, and the diameter of the nozzle is 2~2.5 mm. When coal rocks with a firmness coefficient  $f$  of 0.3~1 are cut under these conditions, an annular slot with the slot height of 2~6 cm and the slot depth of 1.5~2.5 m can be obtained [8]. In practice, due to the limited influence range of hydraulic slotting, to realize large-area pressure relief by slotting coal seams, it is often necessary to drill multiple boreholes and cut multiple intermittent slots in the coal seams to carry out joint pressure relief, which requires a

great deal of manpower and is very costly. To find a safe and economical method for large-area coal seam slotting, a diamond wire saw (DWS) is used to replace the high-pressure water jet to cut coal seams for pressure relief. In this paper, a method of slotting coal seams with a wire saw is proposed. Through numerical simulation and the practice of pressure relief by cutting coal pillars with a wire saw, the changes in the vertical stress of coal rocks and the range of pressure relief during the advancing process of the working face with wire saw coal cutting are studied, aiming to provide theoretical guidance for pressure relief by slotting coal seams with a wire saw.

## 2. Engineering Practice of Coal Seam Slotting

*2.1. Proposed Slotting Coal Seams with a DWS Method for Pressure Relief.* When a mine in the Kailuan mining area was in the deep mining stage, under the influence of high geostress and remnant pillar, the coal rock impact dynamic

instability was severe. A total of 47 dynamic failures were documented above the mining depth of  $-530$  m, and the other dynamic failures occurred in the normal mining working face below the mining depth of  $-630$  m. At this mine, the false roof of the residual coal pillars consisted of dark gray mudstone. The immediate roof consisted of relatively hard laminated gray siltstone and medium-grained sandstone. The direct floor was composed of hard sandy mudstone and siltstone. The hard floor was composed of fine- and medium-grained sandstone, which was hard and relatively brittle. On this basis, to explore a safe and economical method for relieve the pressure of the residual coal pillars and reduce and eliminate the threat of high geostress, the Hunan University of Science and Technology and Kailuan Group jointly developed a set of equipment for slotting coal seams with a wire saw and carried out a pressure relief by cutting coal pillars with a single wire between the T3150 air channel and T2051 North driving roadway No. 2.

### 2.2. Effect and Process of Slotting Coal Seams with a Wire Saw.

Wire saw cutting is an advanced cutting method that is simple to perform and has a high flexibility [9–12]. The principle of slotting coal seams with wire saw is as follows. The wire saw machine drives the diamond beaded rope to move at high speed in the coal seam. The diamond particles on the wire saw continuously grind the coal body. The wire saw machine moves on the track to drive the beaded rope to feed, and the wire saw continuously cuts the coal seam inward. After slotting the coal seam, a narrow and long slot space similar to the goaf is formed inside the coal seam. It is generally believed that Hertz fracture and volume break are the main ways of diamond particles cutting fractured rock mass [13–15].

A slotting system with a wire saw generally consists of a wire saw machine, a guide device, a string bead wire, and a control and auxiliary system. A working face can be constructed by cutting drilling and wire return drilling in the coal seam, as shown in Figure 1. The preparation work before slotting mainly includes equipment installation, wire winding, and reeving. There are three steps for operation. Step 1: the first group guide device is installed in one side of the roadway, and the wire saw machine and the second group guide device are installed in the other side of the roadway. Step 2: the string bead wire is reeved through the borehole. The string bead wire is wound through the driving wheel, and the device of the wire saw machine is guided in turn. The tension of the string bead wire is adjusted. Then, the string bead wire with a joint is fastened. Step 3: the wire saw machine is started, and the rotational speed of the driving wheel is adjusted. Next, the auxiliary system is started to spray water to cool the string bead wire and suppress the dust. Finally, the advancing speed of the wire saw on the track is controlled to cut the coal seams along the advancing direction from the start of drilling. The operating parameters of coal seam wire saw slotting are shown in Table 1. Engineering practice shows that the wire saw can cut the coal seam in a large area, with the linear cutting speed reaching  $15$  m/s and the cutting efficiency reaching  $80$  m<sup>2</sup>/h.

After cutting the coal pillars with the wire saw, there is a long narrow slot space left with a seam height of  $15$  mm and a seam depth of  $30$  m. The statistics indicate that both the working efficiency and seam depth after coal seam slotting with a wire saw are better than those after hydraulic seam slotting. The following numerical simulation focuses on the variation in vertical stress and pressure relief range in the advance of the working face when cutting coal seams with a wire saw.

## 3. Numerical Simulation of Pressure Relief by Wire Saw Slotting

To ensure the accuracy of numerical simulation and the solving efficiency, considering the practice of coal seam wire saw slotting engineering, we used the ratio function of FLAC<sup>3D</sup> and applied the domain decomposition method to form a three-dimensional model composed of dense, transitional and loose grid areas, with dimensions of  $100$  m  $\times$   $10$  m  $\times$   $18$  m,  $528,000$  grid cells, and  $580,860$  grid points, as shown in Figure 2(a). The dense grid around the slot in the model is partially enlarged, as shown in Figure 2(b).

A Mohr–Coulomb constitutive model was adopted. A  $10$  MPa vertical stress was applied on the upper boundary. Rolling boundary conditions were adopted on the front and back boundary, left and right boundary, and lower boundary. The horizontal stresses of the front, back, left, and right of the model were considered hydrostatic pressures. Lying in the middle part of the coal seam, the wire saw coal slotting working face advanced by  $0.8$  m each time from the start slotting position along the coal seam direction. The rock mechanics properties of each layer are shown in Table 2.

**3.1. Vertical Stress Distribution.** The vertical stress distribution during the advancement of the wire saw coal slotting working face is shown in Figure 3. According to Figure 3, when the wire saw coal slotting working face advanced by  $0.8$  m, two stress concentration zones,  $A_1$  and  $A_2$ , were formed on the left and right coal walls of the slot, respectively, and the vertical stress of the coal pillars approximately  $1$  m above and below the slot was released.

When the working face advanced by  $11.2$  m, the vertical stress  $7$  m above and  $9$  m below the slot was released, the range of the stress reduction zone B was greatly extended, the vertical stress in the stress reduction zone was reduced to approximately  $0$  MPa, the stress release rate was up to  $100\%$ , the two stress concentration zones  $A_1$  and  $A_2$  formed, the vertical stress in the stress concentration zone was increased to approximately  $30$  MPa, and the stress concentration factor became three.

When it advanced by  $22.4$  m, the stress recovery zone C formed in the middle of the slot, the vertical stress in the stress recovery zone returned to approximately  $6$  MPa, and the original stress reduction zone was divided into  $B_1$  and  $B_2$ , which were close to the  $A_1$  side of the stress concentration zone and the  $A_2$  side of the stress concentration zone, respectively. When it advanced by  $33.6$  m, the range

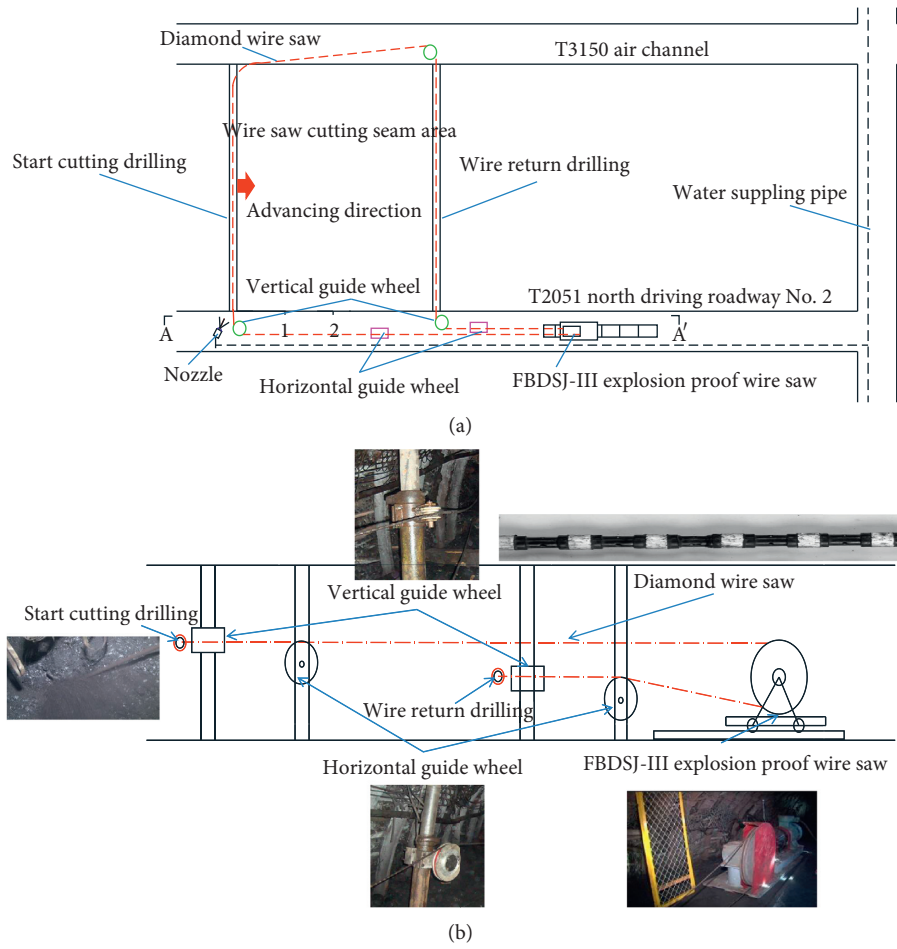


FIGURE 1: Schematic diagram of the test system and site layout for cutting coal pillars with DWS. (a) Layout chart and (b) A-A' side view.

TABLE 1: Operating parameters of the cutting system with DWS.

Type	$W$	$v$	$\Phi$	$h$	$d$
Parameter	37	15	11.5	15	0.8

$W$  = power, KW;  $v$  = linear velocity,  $\text{ms}^{-1}$ ;  $\Phi$  = diameter, mm;  $h$  = slot height, mm;  $d$  = advanced distance, m.

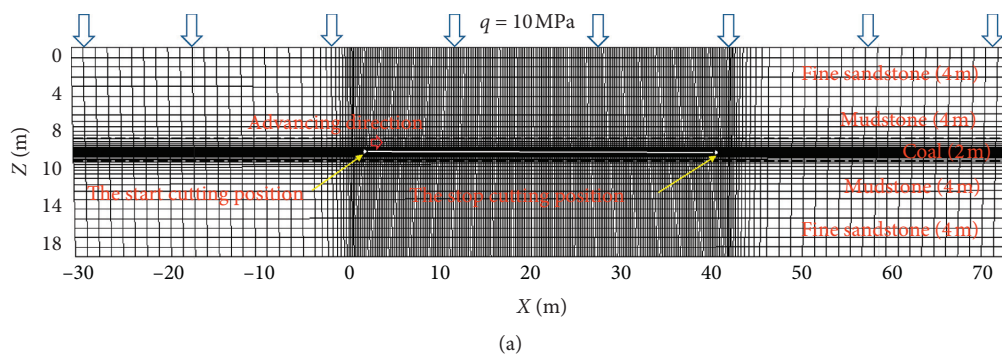
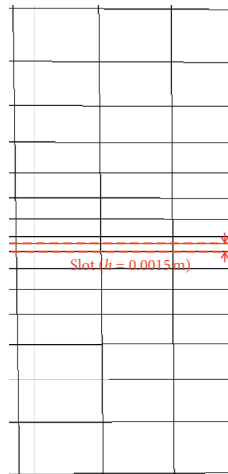


FIGURE 2: Continued.



(b)

FIGURE 2: The FLAC<sup>3D</sup> numerical simulation model.

TABLE 2: Rock mechanics properties.

Type	$H$	$\gamma$	$E$	$\mu$	$c$	$t$	$\varphi$
Fine sandstone	4	2560	8.83	0.27	5.8	3.5	38
Mudstone	4	2150	5.51	0.31	3.5	2.8	30
Coal	2	1400	3.28	0.26	1.8	0.8	24
Mudstone	4	2150	5.51	0.31	3.5	2.8	30
Fine sandstone	4	2560	8.83	0.27	5.8	3.5	38

$H$  = thickness, m;  $\gamma$  = unit weight,  $\text{kgm}^{-3}$ ;  $E$  = Young's modulus, GPa;  $\mu$  = Poisson's ratio;  $c$  = cohesive forces, MPa;  $t$  = tensile strength, MPa;  $\varphi$  = angle of internal friction,  $^\circ$ .

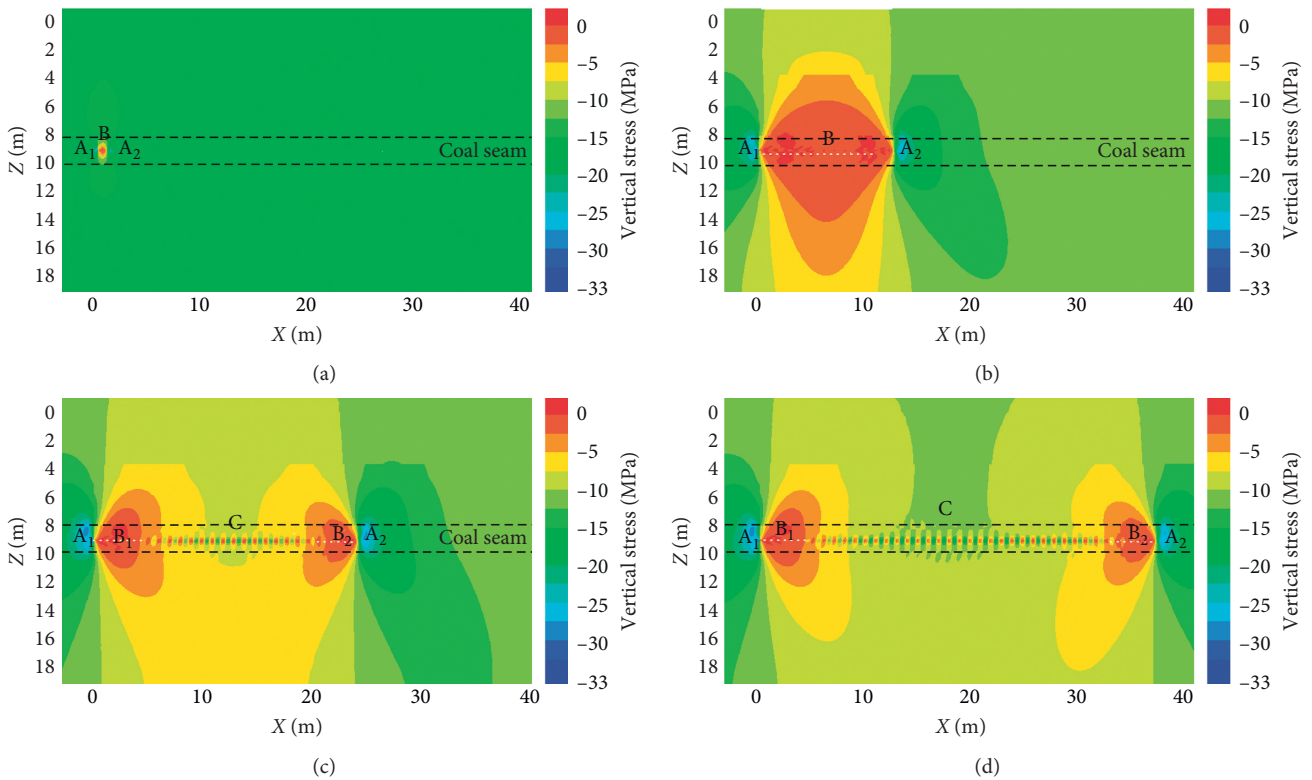


FIGURE 3: Vertical stress distribution of different slot depths. (a)  $L = 0.8$  m, (b)  $L = 11.2$  m, (c)  $L = 22.4$  m, and (d)  $L = 33.6$  m.

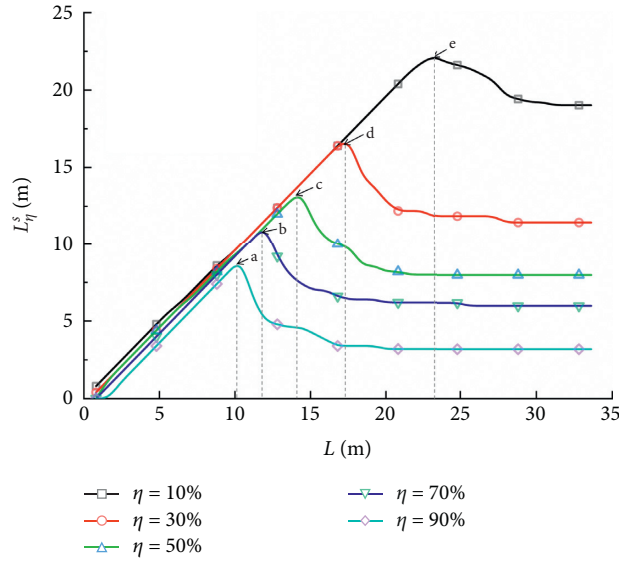


FIGURE 4:  $L_{\eta}^s$  at different slot depths.

of the stress recovery zone C extended, the vertical stress in the stress recovery zone returned to approximately 8 MPa, and the changes in the stress of the stress concentration zone and the stress reduction zone on both sides were not obvious.

**3.2. Vertical Stress Release and Stress Release Range.** For the purpose of exploring the coal rock stress release and the changes in the pressure relief range, formula (1) presents the calculation method of the stress release rate. The FISH language in FLAC<sup>3D</sup> software was used to analyze the 10%, 30%, 50%, 70%, and 90% vertical stress release at the top 0.7 m of the slot, as shown in Figure 4.

$$\eta = \frac{\sigma^{i'} - \sigma^i}{\sigma^i} \times 100\%, \quad (1)$$

where  $\sigma^i$  is the initial stress value of grid cells  $i$ , MPa;  $\sigma^{i'}$  is the stress value of grid cells  $i$  after pressure relief, MPa; and  $\eta$  is the stress release ratio of grid cells  $i$ , %.

In Figure 4, the ordinate indicates the pressure release range  $L_{\eta}^s$  and the abscissa denotes the advancement distance of the wire saw coal slotting working face (slot depth). a, b, c, d, and e are the critical points at which the pressure relief range of the wire saw slotting changes from increasing to decreasing when the stress release rate is 10%, 30%, 50%, 70%, and 90%, respectively. Figure 4 shows that when  $\eta = 10\%$ , the wire saw coal slotting working face advances from 0.8 m to 23.2 m and  $L_{10}^s$  increases from 0.8 m to 22.2 m. When the working face advances from 23.2 m to 31.2 m,  $L_{10}^s$  is reduced from 22.2 m to 19 m. Thereafter,  $L_{10}^s$  does not change with increasing  $L$ .

When  $\eta = 30\%$ , the wire saw coal slotting coal working face increases from 0.8 m to 17.6 m, and  $L_{30}^s$  increases from 0.4 m to 16.8 m. When the working face advances from 17.6 m to 28 m,  $L_{30}^s$  is reduced from 16.8 m to 11.4 m. Thereafter,  $L_{10}^s$  does not change with increasing  $L$ .

At  $\eta = 50\%$ , the wire saw coal slotting working face advances from 0.8 m to 14.4 m, and  $L_{30}^s$  increases from 0.4 m to 16.8 m. When the working face advances from 14.4 m to 21.6 m,  $L_{30}^s$  is reduced from 13.4 m to 8 m. Thereafter,  $L_{10}^s$  does not change with increasing  $L$ .

When  $\eta = 70\%$ , the wire saw coal slotting working face advances from 0.8 m to 12 m and  $L_{30}^s$  increases from 0 m to 11.2 m. When the working face advances from 12 m to 25.6 m,  $L_{30}^s$  is reduced from 11.2 m to 6 m. Thereafter,  $L_{10}^s$  does not change with increasing  $L$ .

At  $\eta = 90\%$ , the wire saw coal slotting working face advances from 0.8 m to 10.4 m and  $L_{30}^s$  increases from 0 m to 9 m. When the working face advances from 10.4 m to 20 m,  $L_{30}^s$  is reduced from 9 m to 3.2 m. Thereafter,  $L_{10}^s$  does not change with increasing  $L$ .

During the advancement of the wire saw coal slotting working face, with the increase in  $L$ ,  $L_{\eta}^s$  increases first and then reduces to a certain stable value. The relationship between  $L_{\eta}^s$  and  $L$  is fitted, as shown in Table 3.

## 4. Discussion

In the practice of slotting coal seams with wire saws, a 30 m slotting depth cut by a single wire has been realized. Under normal circumstances, the efficiency of coal seam wire saw slotting reaches 80 m<sup>2</sup>/h. Compared with those of the existing hydraulic slotting approaches, the depth and efficiency of coal seam wire saw cutting are approximately 5 times greater and equivalent, respectively. The advancing distance of wire saw slotting affects the pressure relief effect of wire saw slotting. When the working face advances from 0.8 m to approximately 10 m, the degree and range of pressure relief by slotting coal seams with a wire saw both increase significantly. After that, stress recovery occurs in the middle of the slot due to roof and floor contact, and the range of stress recovery increases with the continuous advancement of the working face, but the range of pressure



TABLE 3: Fitted formulas.

$\eta$ (%)	Fitted formulas	$R^2$
10	$I_{10}^s = 1.106 \times 10^{-5} L^5 - 9.122 \times 10^{-4} L^4 + 0.025 L^3 - 0.286 L^2 + 2.197 L - 1.2814$	0.99
30	$L_{30}^s = 1.118 \times 10^{-8} L^8 - 1.472 \times 10^{-6} L^7 + 7.773 \times 10^{-5} L^6 - 0.0021 L^5 + 0.0308 L^4 - 0.2426 L^3 + 0.963 L^2 - 0.6585 L + 0.4716$	0.98
50	$L_{50}^s = -3.768 \times 10^{-9} L^8 + 6.453 \times 10^{-7} L^7 - 4.454 \times 10^{-5} L^6 + 0.0016 L^5 - 0.0313 L^4 + 0.3317 L^3 - 1.786 L^2 + 5.225 L - 3.509$	0.97
70	$L_{70}^s = -1.1707 \times 10^{-8} L^8 + 1.633 \times 10^{-6} L^7 - 9.2547 \times 10^{-5} L^6 + 0.0027 L^5 - 0.0439 L^4 + 0.3775 L^3 - 1.613 L^2 + 3.959 L - 2.44$	0.95
90	$I_{90}^s = -4.7243 \times 10^{-9} L^8 + 5.8536 \times 10^{-7} L^7 - 2.7663 \times 10^{-5} L^6 + 5.892 \times 10^{-4} L^5 - 0.0042 L^4 - 0.0356 L^3 + 0.5932 L^2 - 1.2196 L + 0.734$	0.91

$\eta$  = vertical stress release ratio, %;  $L$  = slot depth, m.

relief by slotting coal seams with a wire saw decreases to a certain extent. This analysis shows that wire saw slotting is similar to mining a very thin “protective layer” in coal seams, delaying and controlling the roof and floor contact of the slot, which may allow the wire saw slotting to produce a better pressure relief effect than hydraulic slotting. In addition, in practice, when a high-pressure water jet is used to slot hard coal seams, the difficulty of cutting will be higher, and the slotting depth will be smaller. As the Mohs hardness of the objects cut by the wire saw is generally higher, wire saw slotting may have more advantages in slotting hard coal rocks, which may be more conducive to wire saw slotting operation and its pressure relief effect.

## 5. Conclusions

- (1) Wire saw slotting can cut a long and narrow slot in a coal seam, and its cutting efficiency and slotting depth are better than those of hydraulic slotting.
- (2) A stress concentration zone forms in front of the wire saw coal slotting working face, while the stress reduction zone and the stress recovery zone form behind the working face. In the advancing process of the wire saw coal slotting working face, the stress release range varies, increasing at first and then decreasing to a certain stable range with the increase in the advancing distance of the working face.
- (3) Partial stress recovery occurs after the roof and floor contact in the middle of the slot, which is the critical condition for the range of the pressure relief effect of wire saw slotting to change from increasing to decreasing. According to the actual situation, the creep and deformation characteristics of overlying coal rocks over the coal slot cut by a wire saw can be further explored.

## Data Availability

All the data generated or published during the study are included within the article; no other data were used to support this study.

## Conflicts of Interest

The authors declare that they have no conflicts of interest regarding the publication of this paper.

## Acknowledgments


This study was funded by the National Natural Science Foundation of China (51974121 and 51804115), Open Research Fund Program of Hunan Province Key Laboratory of Safe Mining Techniques of Coal Mines (E21723), and Project of Liupanshui Science and Technology (52020-2018-03-06).

## References

- [1] M. G. Qian and T. C. Liu, *Mine Pressure and its Control*, China University of Mining and Technology Press, Beijing, China, 1991.
- [2] L. M. Dou and X. Q. He, *Theory and Technology of Rock Burst Prevention*, China University of Mining and Technology Press, Xuzhou, China, 2001.
- [3] Y. S. Zhao, *Multi-field Coupling of Porous Media and its Engineering Response*, Science Press, Beijing, China, 2010.
- [4] A. Q. Lin, W. Yang, H. J. Wu et al., “A numeric analysis of the effects different factors have on slotted drilling,” *Journal of China University of Mining and Technology*, vol. 39, no. 2, pp. 153–157, 2010.
- [5] C. C. Li, “Application of high pressure hydraulic slotting in pressure relief and permeability enhancement of coal roadway,” *IOP Conference Series: Earth and Environmental Science*, vol. 526, no. 1, Article ID 012159, 2020.
- [6] B. Q. Lin, F. W. Meng, and H. B. Zhang, “Regional gas control based on drilling-slotting-extracting integration technology,” *Journal of China Coal Society*, vol. 36, no. 1, pp. 75–79, 2011.
- [7] F. Huang, Y. Y. Lu, X. C. Liu et al., “Breakage mechanism of transverse isotropic rock subjected to high-pressure water JET,” *Chinese Journal of Rock Mechanics and Engineering*, vol. 33, no. 7, pp. 1229–1335, 2014.
- [8] Y. J. Zhang and S. S. Guo, “Theoretical model of annular slotting depth for high pressure water jet and its application,” *Journal of China Coal Society*, vol. 44, no. 1, pp. 126–132, 2019.
- [9] Y. X. Lu, Y. Li, and H. Huang, “Study on sawing forces of diamond wire saw in concrete cutting,” *Diamond and Abrasives Engineering*, vol. 31, no. 6, pp. 47–50, 2011.
- [10] S. S. Rajpurohit, R. K. Sinha, P. Sen, and S. Singh, “Influence of physico mechanical properties of Indian dimension stones on cutting rate of diamond wire saw,” *Arabian Journal of Geosciences*, vol. 11, no. 18, 2018.
- [11] Z. Yang, “Structure and material properties of soft tissues,” *Finite Element Analysis for Biomedical Engineering Applications*, vol. 31, no. 2, pp. 45–48, 2019.
- [12] G. S. Huang, “Practice and application of wire saw cutting ore in underground mining of mirabilite mine in Qi Li well, Hengyang city, Hunan Province,” *Modern Chemical Research*, vol. 11, pp. 59–61, 2020.
- [13] F. C. Frank and B. R. Lawn, “On the theory of hertzian fracture,” *Proceedings of the Royal Society of London. Series A, Mathematical and Physical Sciences*, vol. 299, no. 1458, pp. 291–306, 1967.
- [14] L. Baochang, Z. Zupei, S. Youhong et al., “Research into the sawing trajectory and mechanism of diamond wire saw,” *Diamond and Abrasives Engineering*, vol. 132, no. 4, pp. 17–21, 2002.
- [15] H. Guoqin, H. Hui, G. Hua et al., “Influences of sawing parameters on forces and energy in wire sawing of granite,” *Journal of Mechanical Engineering*, vol. 45, no. 3, pp. 234–239, 2009.

## Research Article

# Grouting Technique for Gob-Side Entry Retaining in Deep Mines

Xianyang Yu <sup>1,2</sup>, Zhihong Sun,<sup>1,2</sup> Min Deng,<sup>1,2</sup> and Jinlin Xin<sup>1,2</sup>

<sup>1</sup>Hunan Provincial Key Laboratory of Safe Mining Techniques of Coal Mines, Hunan University of Science and Technology, Xiangtan 411201, China

<sup>2</sup>Work Safety Key Lab on Prevention and Control of Gas and Roof Disasters for Southern Coal Mines, Hunan University of Science and Technology, Xiangtan 411201, China

Correspondence should be addressed to Xianyang Yu; 1010092@hnust.edu.cn

Received 8 April 2021; Accepted 4 May 2021; Published 13 May 2021

Academic Editor: Zhijie Zhu

Copyright © 2021 Xianyang Yu et al. This is an open access article distributed under the Creative Commons Attribution License, which permits unrestricted use, distribution, and reproduction in any medium, provided the original work is properly cited.

The retained rib displacement accounts for roughly 80% of rib-to-rib convergence in gob-side entry retaining in deep coal mines, which shows significant nonsymmetrical feature and long-term rheological phenomenon. Affected by mining-induced stress, cracks spread widely, and broken zones expand beyond the anchoring range. Without grouting and supplementary support in retained rib, the surrounding rock-support load-bearing structure will be in a postpeak failure state, and the anchoring force of the bolting system will be greatly attenuated. After grouting, the compressive strength of grouting geocomposite specimen is significantly higher than the postpeak residual strength of the intact coal specimen, and it is partially restored compared to that of the intact coal specimen. The ductility of the fractured coal specimen increases after grouting, and it has stronger elasticity and plasticity. Broken rock block can become a whole with coordinated bearing capacity, and its stability is improved after grouting. The grouting technique could restore the integrity and strength of the fractured retained coal rib, repair the damaged bolting structure, and make the surrounding rock and supporting structure become an effective bearing structure again. The research result shows that it is feasible to restore the bearing capacity of the retained coal rib by grouting technique.

## 1. Introduction

Gob-side entry retaining is a technique to maintain the original roadways along the gob edges after coal mining. Gob-side entry retaining can improve the coal recovery rate, reduce the excavation rate, and reduce the probability of rock burst, which is an important technology to achieve continuous mining without coal pillars. Its technical advantages and economic benefits are significant [1–3]. Under the rapid development of surrounding rock control theories, coal mining equipment, support techniques, and support materials, gob-side entry retaining has been successfully applied under various conditions [4–9].

Under the influence of high in situ stress and mining-induced stress, it is difficult to maintain the retained roadway in deep coal mines [7, 10]. During the long-term rotation and subsiding of the main roof above the retained roadway, the original cracks in the surrounding rock gradually expand, and new cracks appear at the same time. The

surrounding rock is loose, is broken, and has a large amount of deformation and long-term rheology [11]. In this process, the loose and broken surrounding rock of the retained coal rib is the weakest part of the whole roadway, and large-deformation often occurs in this part, which may even affect the stability of the whole roadway [12, 13]. Maintaining the bearing capacity of the retained coal rib has an important effect on the overall stability of the surrounding rock of the retained roadway.

In this paper, the surrounding rock deformation characteristics of retained roadway are monitored and summarized. The temporal and spatial development of the cracks in retained coal rib and its influence on bolting support structure are tested and analyzed. The effect of grouting reinforcement on the strength of fractured coal is tested, and the principle of grouting reinforcement to restore the bearing capacity of surrounding rock is proposed. The technique of restoring the load capacity of the fractured coal by grouting has been successfully applied to some filed cases.

## 2. Surrounding Rock Deformation Characteristics

The surrounding rock deformation observation site is located in the tail roadway of 1252 (1) panel in the Panyidong Mine, which is retained after coal mining. The panel layout is 264 m wide by 1728 m long. The elevation of the panel is  $-823$ – $-738$  m, and the ground elevation is  $+21.5$ – $+22.1$  m. The average thickness of the coal seam is 2.3 m, and the dip angle is  $3^{\circ}$ – $9^{\circ}$ . The main roof is medium-fine sandstone with a thickness of 0–11.0 m. The immediate roof is composed by mudstone, sandy mudstone, and 11–3 coal seam, with a thickness of 0–8.4 m. The surrounding rock deformation of retained roadway is shown in Figure 1. The surrounding rock deformation presents the following characteristics:

- (1) Roadway deformation presents a significant non-symmetrical feature, which is mainly caused by the retained coal rib deformation and the floor heave. The retained coal rib deformation accounts for 85% of the rib-to-rib convergence; and the floor heave accounts for 79% of the roof-to-floor convergence.
- (2) The roadway surrounding rock is in a state of high-speed deforming for a long time under the disturbance of the main roof rotation and subsiding, and it still shows a long-term rheological phenomenon after the main roof structure is stabilized. In deep mines, the retained roadway surrounding rock is loosened and broken under the influence of the mining-induced stress before and after the working face, and its bearing performance is significantly reduced. Surrounding rock has a strong rheological property, which has lower speed and sustained deformation. If proper reinforcement support is not adopted, the damaged area of the roadway will further increase, and even completely lose stability.

## 3. Cracks Development in Retained Coal Rib

**3.1. Observation Plan.** The development of cracks in coal and rock is one of the characteristics of its stability, and it has always been a research hotspot in the stability of roadway surrounding rock [14, 15]. Affected by times excavation and mining disturbances, the retained coal rib is loose and broken and deforms in a large area during the service process. The internal cracks of the surrounding rock will develop, and its bearing capacity is reduced. The expansion of the cracks leads to the debonding of the bonding interface between the anchoring agent and the surrounding rock and gradually extends to both sides of the cracks, which causes the axial stress of the bolting structure to decrease exponentially [16, 17]. This paper uses the observation results of the borescope to reflect the stability of the surrounding rock of the retained coal rib. Studying the development of cracks in the retained coal rib can provide an evaluation of its stability status and optimize the timing of grouting and other reinforcement methods [18, 19].

In order to observe the development of the cracks in the retained coal rib along with the advancement of the working

face, holes with a depth of 6 m were drilled at the positions of 50 m, 30 m, 10 m, and 5 m in front of the working face, at the working face, and 10 m, 20 m, 40 m, 60 m, 100 m behind the working face along the coal seam inclination. In order to quantitatively describe the development of cracks in the holes, referring to other research results, coal bodies and cracks are divided into the following four categories [20]. Various kinds of typical cracks are shown in Figure 2.

- (a) *Small Crack.* The crack is original crack or newly developed with aperture less than 2 mm
- (b) *Medium Crack.* Affected by the mining-induced stress, the aperture of the cracks in the coal rib has increased to 2–5 mm
- (c) *Large Crack.* When the coal rib is relatively broken, multiple cracks are connected to each other and gradually expand, and the aperture reaches more than 5 mm
- (d) *Broken Zone.* Affected by mining-induced stress, a large number of cracks in the surrounding rock of the large-deformation roadway are interconnected with each other, and the range of the broken zone is greatly expanded

**3.2. Development of the Cracks and Its Influence on Anchoring System.** After the borescope was completed, the development of the cracks in the boreholes was sketched, and the result is shown in Figure 3. In order to facilitate statistics and analysis, every 500 mm width of the broken zone is equivalent to a small crack, a medium crack, and a large crack. Figure 4 shows the final statistical results of the cracks in the drilling hole. The development of cracks in the retained coal rib along with the working face is as follows:

- (1) Outside of the mining-induced stress area, the cracks in coal rib are generated within a depth of about 1 m from the surface. The causes of cracks are mostly the original small cracks, mining-induced stress caused by roadway excavation, and weathering of coal on the roadway surface.
- (2) With the advancement of the working face, the roadway surrounding rock fracture gradually penetrated into the coal body. Within the range of 0–30 m in front of the working face, the high mining-induced stress section, the cracks in coal rib are generated within a depth of about 0–2.8 m from the surface. The greatly fluctuating mining-induced stress caused a large number of new cracks in the retained coal rib and caused the original cracks to expand further. However, it is worth noting that because the roadway adopts the active strong bolting support method, and the main roof above the roadway has not broken or rotated and subsided, the range of the broken zone in coal rib has not been greatly expanded at this time.
- (3) In the 0–40 m mining-induced stress-affected section behind the working face, both the ranges of cracks and the width of the broken zones have increased

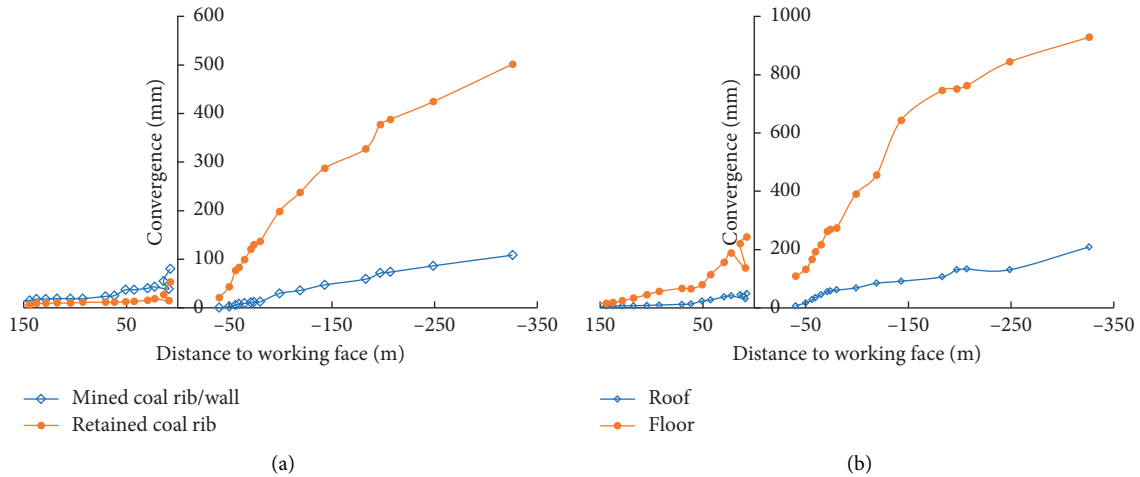


FIGURE 1: Surrounding rock convergence. (a) Rib/wall convergence. (b) Roof/floor convergence.

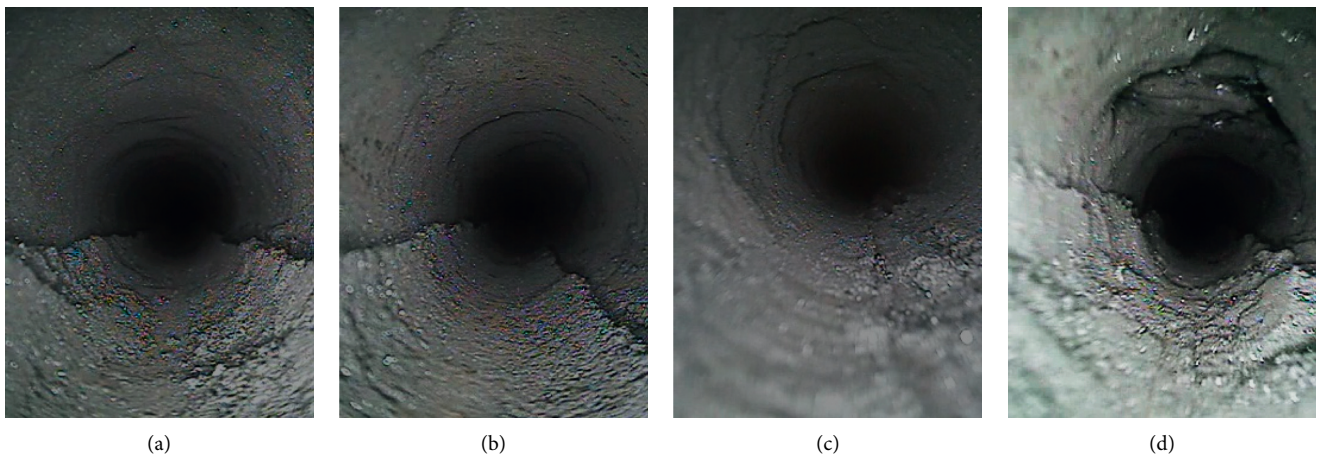


FIGURE 2: Typical cracks in borehole images. (a) Small crack. (b) Medium crack. (c) Large crack. (d) Broken zone.

significantly, and the broken zone has also begun to appear inside the retained coal rib. After the main roof breaking, rotating, and subsiding, stress concentration occurs in the retained rib, which causes the shallow part of the coal rib to be crushed and squeezed out. At the same time, it also causes the weakening and failure of the bolting structure. At this time, the surrounding rock-supporting load-bearing structure is already in a postpeak failure state. The roadway surrounding rock needs strengthening supporting in time; otherwise, there will be slow and continuous plastic flow in the future.

- (4) Beyond 100 m behind the working face, retained coal rib cracks extend beyond 6 m depth. It is often found that the broken zone is in the deep part of the surrounding rock, and the cracks width is further increased. At this stage, the surrounding rock of the roadway has been in a loose and broken state, the anchoring force of the bolting system has been greatly attenuated or has been lost, and the roadway is in a state of plastic flow under low supporting force.

#### 4. Mechanical Properties of Grouted Fractured Coal Mass

Grouting can bond the broken surrounding rock, improve the overall mechanical properties of the surrounding rock, weaken the stress concentration between the rock blocks, and make the broken surrounding rock reform a bearing structure. By comparing the stress-strain curves of the intact coal mass and the fractured coal mass grouting geocomposite, the mechanical properties of grouted postpeak coal can be obtained, and the effect of grouting reinforcement can be analyzed.

*4.1. Experimental Device and Plan.* The experiment was carried out on the MTS 815.03 testing machine and the self-made pressure-bearing grouting device. The self-made pressure-bearing grouting device can produce the fractured coal mass grouting geocomposite specimen by  $\Phi 50 \text{ mm} \times 100 \text{ mm}$ , as shown in Figure 5.

The first step of the experiment was a conventional uniaxial compression experiment, which mainly measured



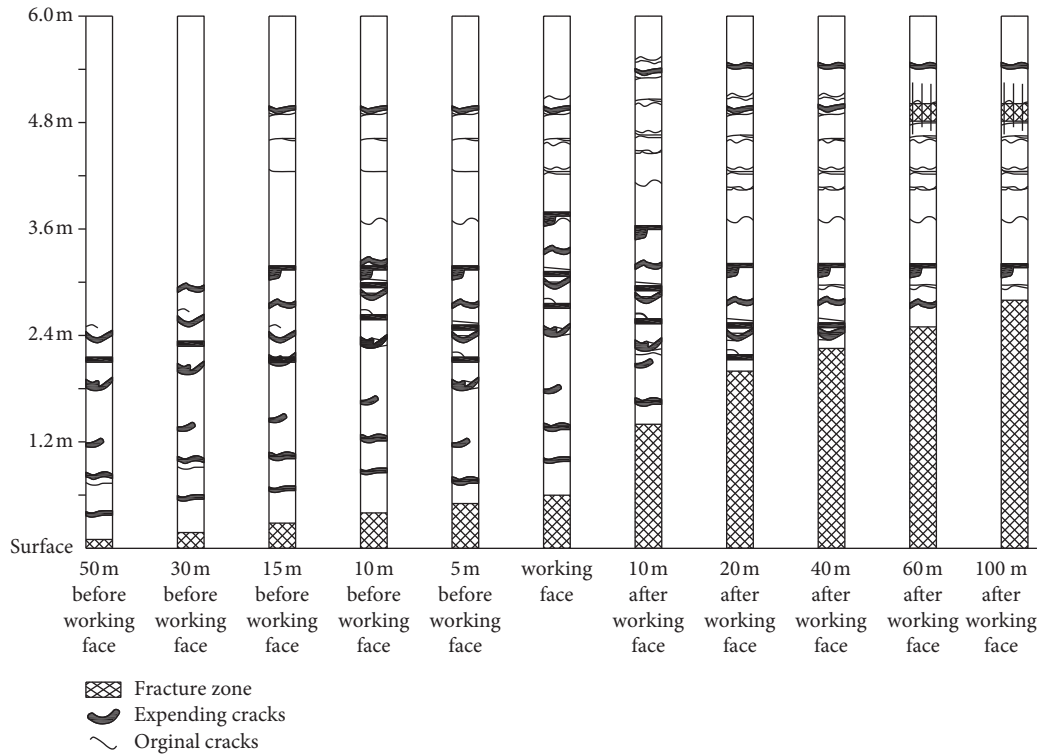


FIGURE 3: Sketch of cracks and fractures zones in retained coal rib around working face.

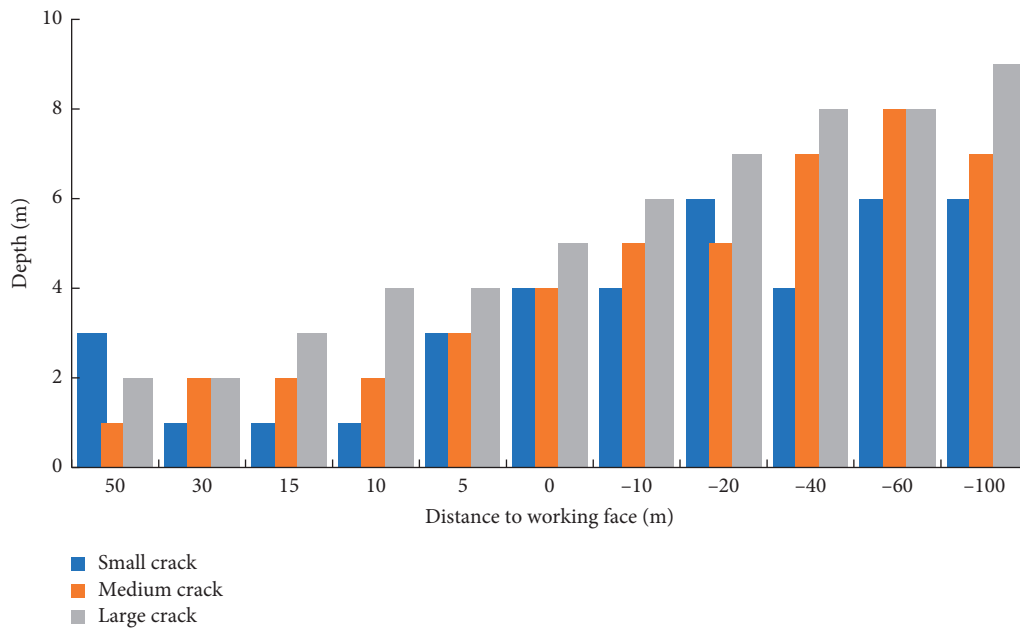


FIGURE 4: Statistical graph of cracks development in boreholes around working face.

the compressive strength and stress-strain curve of the intact coal mass specimen to obtain the mechanical parameters of the intact coal mass specimen. The second step was to prepare the grouting geocomposite specimen. Stirring the cement slurry evenly according to the three water-cement ratios of 0.7, 0.8, and 1.0. Put the specimen that has been fractured in the previous step of the experiment into the

pressure-bearing grouting device, and then pour the cement slurry to submerge the specimen. After closing the device cap, start the grouting pump to grout until the pressure reaches 2 MPa, and then stop pressurizing. Maintain the pressure until the slurry condenses. Cure at room temperature for 2 to 3 weeks until the cement slurry reaches its maximum strength. Then, trim the grouting geocomposite

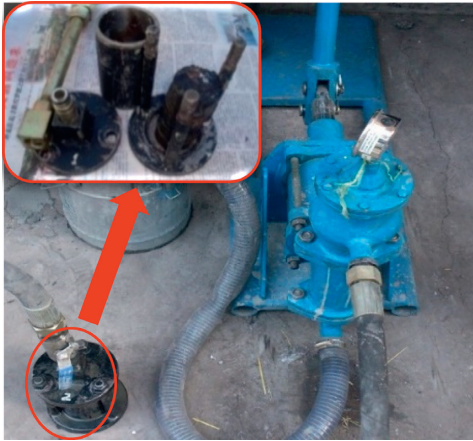


FIGURE 5: Pressure-bearing grouting device.

specimen to make them meet the experimental requirements, as shown in Figure 6.

**4.2. Experiment Result and Data Analysis.** The ratio of the grouting geocomposite specimen strength to the residual strength of the intact specimen is defined as the consolidation coefficient; the ratio of grouting geocomposite specimen strength to the compressive strength of the intact specimen is defined as the recovery coefficient. In this experiment, the mechanical properties of coal specimen with different P. O42.5 Portland cement water-cement ratios before and after grouting are obtained, as shown in Table 1. Figure 7 shows the stress-strain and Poisson's ratio-strain during the whole loading process of the grouting geocomposite specimen under the condition of 0.8 water-cement ratio. Analyzing the experimental results, we can get the following conclusions:

- (1) After grouting, the compressive strength of the grouting geocomposite specimen is significantly higher than the postpeak residual strength of the intake coal specimen, and it is partially restored compared to that of the intact coal specimen. When the water-cement ratio is 0.7, 0.8, and 1.0, the average consolidation coefficient and recovery coefficient of the grouting geocomposite specimen are 2.84, 2.55, and 1.24 and 35.33%, 31.43%, and 40.12%, respectively.
- (2) During the whole process from the beginning of the compression to the failure the grouting geocomposite specimen, there is no stress sudden decrease stress after failure of the specimen. It shows that the ductility of the fractured coal specimen increases after grouting, and it has stronger anti-deformation ability and plasticity.
- (3) After the specimen is fractured, the rock blocks slip and move along the fracture surface, the lateral deformation increases rapidly, and its Poisson's ratio  $\mu$  increases rapidly. Poisson's ratio  $\mu$  of the grouting geocomposite specimen is smaller than that of the intact specimen, which indicates that the broken

rock block can become a whole with coordinated bearing capacity, and its stability is improved after grouting.

## 5. The Principle of Retained Coal Rib Bearing Capacity Recovered

**5.1. The Principle of Bearing Capacity Recovered.** Affected by times excavation and mining disturbances, the original cracks in the retained coal rib are activated, extended and merged, and eventually became internal and surface broken zones. This leads to progressive interface debonding of the anchoring system, which is one of the main forms of bolt support system failure in deep coal mines [16, 17]. In this situation, the large rib to rib deformation is unavoidable, and large-scale plastic zones and even broken zones appear and develop.

After grouting, the cracks in the retained coal rib are cemented and filled, the cohesion, internal friction angle, and elastic modulus of the retained coal rib are significantly improved, and the stress concentration in the retained coal rib is greatly weakened. The grouting technique has restored the integrity and strength of the fractured coal rib, repaired the damaged anchoring structure, and made the surrounding rock and supporting structure become an effective bearing structure again [21]. Use the coordinated bearing capacity of bolts and cables to support the surrounding rock. Bolts are used to maintain the shear strength and integrity of the surrounding rock in the shallow surrounding rock. Anchor cables are used to fully utilize the load-bearing capacity of large rock masses with relatively light damage in the deep rock. Under the triple reinforced support of grouting, bolt, and cable, the retained coal rib can effectively resist the impact of mining-induced stress, avoid the continued expansion of cracks, and significantly improve the stability. The stability of retained coal rib has been significantly improved.

**5.2. Grouting Opportunity.** Research shows that there is an optimal grouting opportunity for grouting in dynamic stress roadway surrounding rock [22–25]. If the grouting is carried out too early, an effective grouting diffusion path has not been formed inside the surrounding rock, and the reinforcement effect will be poor. Under the influence of mining-induced stress, the surrounding rock and supporting structure of the roadway will deform or even be damaged. If the grouting is carried out too late, large-scale loosening and destruction of the surrounding rock of the roadway have appeared, and the bolting and supporting structure have been damaged. At this time, simply relying on grouting can no longer prevent the instability of the roadway.

According to the crack development in retained coal rib and its influence on the bolting structure, grouting can be carried out in the section affected by strong mining-induced stress before and after the working face, in which grouting can achieve the best results at this time. In this section, a large number of cracks have been formed in coal rib, and the broken zone has not been extended beyond the bolting

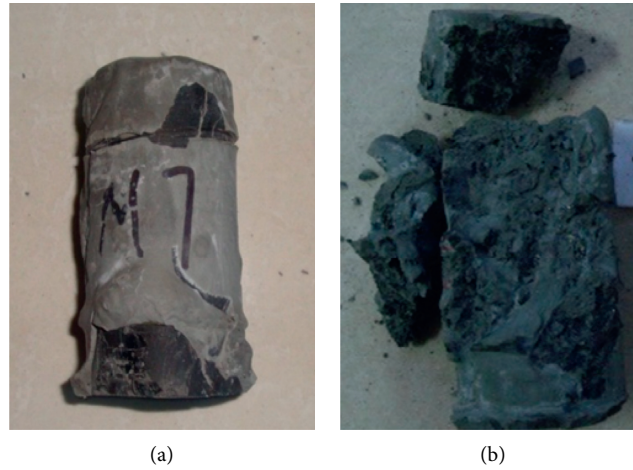


FIGURE 6: Grouting geocomposite specimen (a) and its broken pieces (b).

TABLE 1: Mechanical properties of coal specimen before and after grouting.

No.	Water-cement ratio	Intact specimen UCS (MPa)	Intact specimen residual strength (MPa)	Grouting geocomposite specimen UCS (MPa)	Consolidation coefficient	Recovery coefficient (%)
1		19.50	2.84	8.19	2.88	41.98
2	1.0	24.63	2.50	7.52	3.01	30.54
3		16.01	2.04	5.36	2.63	33.48
4		11.45	2.73	5.33	1.95	46.54
5	0.8	26.74	-	0.54	-	2.01
6		22.92	3.32	10.49	3.16	45.76
7		19.19	5.37	8.83	1.64	46.02
8	0.7	16.51	5.80	4.65	0.80	28.19
9		8.30	2.98	3.83	1.29	46.14

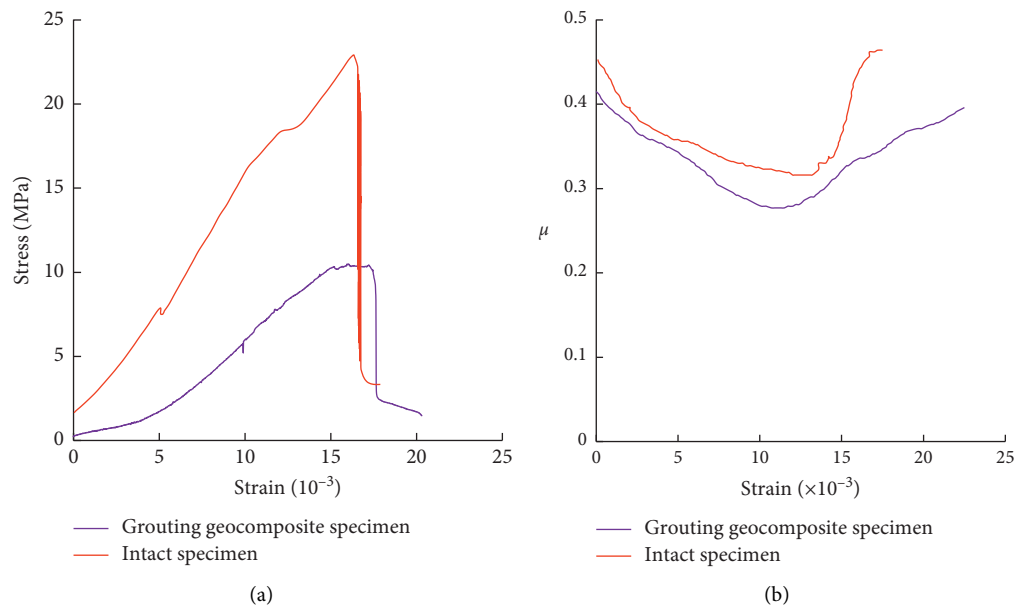


FIGURE 7: Mechanical properties of coal specimen before and after grouting. (a) Typical stress-strain curve. (b) Typical Poisson's ratio-strain curve.

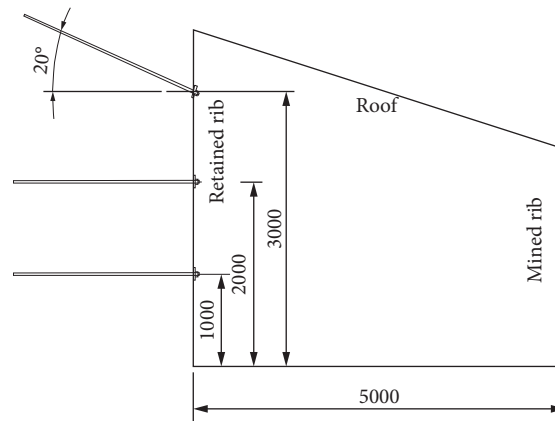


FIGURE 8: Grouting bolts layout.

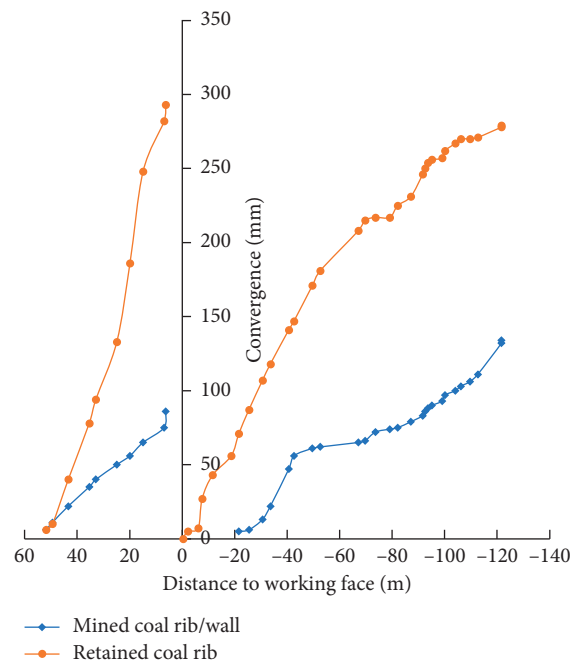


FIGURE 9: Curve of retained roadway ribs displacement.

range. At this time, the interaction between the bolting structure and the surrounding rock is in a critical state, and the bolting system has exerted its maximum supporting effect. Grouting in the strong mining stress affecting section could repair damaged surrounding rock and bolting structure and rebond the broken zones of the surrounding rock. The broken surrounding rock bonded by grouting reforms a bearing unit, which greatly increases the resistance-increasing speed of bolts and cables in large-deformation roadways.

## 6. A Field Case

**6.1. Working Panel Situation and Roadway Initial Support.** The tail roadway of 12418 panel in the Xieqiao Mine was retained after coal mining. The panel layout is 212.8 m wide by 826.9 m long. The elevation of the panel is -579 ~ -598.8 m,

and the ground elevation is +18.3 ~ +27.1 m. The average thickness of the coal seam is 3.08 m. The main roof of the coal seam is composed of siltstone, medium-fine sandstone, and sandstone, with an average thickness of 5.85 m. The immediate roof is composed by cemented fracture mudstone, sandy with a thickness of 4.56 m.

The roadway has a trapezoidal shape with a width × height dimension of 5.0 × 3.0 m, and it was supported by bolts, meshes, and cables. The roof was supported by 7 bolts, the diameter and length of the bolts were 20 mm and 2500 mm, and the layout is 800 × 1000 mm. High prestressed anchor cable beams were constructed on the top plate, the diameter and length of the steel strand were 17.8 mm and 6300 mm, and the layout was “2-2-0-2-2”. The retained rib was supported by 5 bolts, the diameter and length of the bolts were 20 mm and 2500 mm, and the layout was 780 × 1000 mm. The mined rib was supported by 54 bolts, the diameter and length



FIGURE 10: Roadway at 160 m after working face.

of the bolts were 18 mm and 2000 mm, and the layout was  $730 \times 1000$  mm. The width of the filling wall is 3.0 m. The wall is made of ready-mixed concrete, and the main components are cement, fly ash, and sand and gravel aggregates and additives. The measured final setting strength is 25–30 MPa.

**6.2. Grouting and Supplementary Support in Retained Coal Rib.** When the roadway was not affected by the mining-induced stress, a row of anchor cable beams was carried out along the roadway direction on the retained rib to control its rapid deformation during the mining. The distance between the anchor cable beam and the roadway floor was 2.5 m, and the diameter and length of the steel strand were 17.8 mm and 4300 mm, respectively. The drill hole was inclined upward by  $40^\circ$ . Quick-hardening sulphoaluminate cement was adopted for grouting cement, the compressive strength of which can reach 30 MPa in one day and 42.5 MPa in three days. Grouting was carried out 20–30 m in front of the working face with a water-cement ratio of 0.8. Three grouting bolts were arranged in each row in the retained rib, the length of the bolts is 2600 mm, and the distance between the bolts was 1.0–2.0 m. The hole sealing length of the grouting holes needs to be 1.0 m, and the grouting pressure was 1.0–1.5 MPa. The layout of grouting bolts is shown in Figure 8.

**6.3. Retained Roadway Deformation.** Grouting and supplementary support in retained roadway have controlled the surrounding rock deformation, as shown in Figures 9 and 10. In front of the working face, the rib-to-rib convergence was only 300 mm, which provided a foundation for the stability of the retained roadway behind the working face. The retained roadway within the section of 0–40 m behind the working face was strongly affected by mining-induced stress. The influence of mining-induced stress in the section of 40–90 m behind the working face gradually weakened, and the deformation speed of the retained rib and wall began to slow down. Outside the section of 100 m behind the working face, the roof rotated and subsided to a stable state. At this time, the deformation speed of the retained roadway gradually decreased and entered a stable

period. After that, the deformation of the retained coal rib is less than 1 mm per day. Grouting and supplementary support kept the surrounding rock of the roadway intact, and the width and height of the roadway were about 3.6 m and 2.5 m respectively.

## 7. Conclusion

- (1) The retained roadway deformation presents a significant nonsymmetrical feature. The retained coal rib deformation accounts for most of the rib-to-rib convergence in deep mines.
- (2) If proper support method is not adopted, the cracks in the retained rib will gradually increase, and the range of the broken zone will expand from the surface beyond the bolting range. Without grouting and supplementary support in retained rib, the surrounding rock-supporting load-bearing structure will be in a postpeak failure state, and the anchoring force of the bolting system will be greatly attenuated.
- (3) After grouting, the compressive strength of the grouting geocomposite specimen is significantly higher than the postpeak residual strength of the intake coal specimen, and it is partially restored compared to that of the intact coal specimen. The ductility of the fractured coal specimen increases after grouting, and it has stronger elasticity and plasticity. Broken rock block can become a whole with coordinated bearing capacity, and its stability is improved after grouting.
- (4) The grouting technique could restore the integrity and strength of the fractured coal rib, repair the damaged bolting structure, and make the surrounding rock and supporting structure become an effective bearing structure again. The research result shows that it is feasible to restore the bearing capacity of the retained coal rib by grouting technique.

## Data Availability

All the data generated or published during the study are included within the article; no other data were used to support this study.

## Conflicts of Interest

The authors declare that they have no conflicts of interest.

## Acknowledgments

The authors gratefully acknowledge the funding for this work provided by the National Natural Science Foundation of China (no. 51904102) and Open Foundation of Hunan Provincial Key Laboratory of Safe Mining Techniques of Coal Mines, China (no. E21733).



## References

- [1] Z. Z. Zhang, M. Deng, J. B. Bai, X. Y. Yu, Q. H. Wu, and L. S. Jiang, "Strain energy evolution and conversion under triaxial unloading confining pressure tests due to gob-side entry retaining," *International Journal of Rock Mechanics and Mining Sciences*, vol. 126, Article ID 104184, 2020.
- [2] Z. Z. Zhang, M. Deng, X. Y. Wang, W. J. Yu, F. Zhang, and V. D. Dao, "Field and numerical investigations on the lower coal seam entry failure analysis under the remnant pillar," *Engineering Failure Analysis*, vol. 115, Article ID 104638, 2020.
- [3] N. Zhang, C. L. Han, J. G. Yu, and X. G. Zheng, "Theory and practice of surrounding rock control for pillarless gob-side entry retaining," *Journal of China Coal Society*, vol. 39, no. 08, pp. 1635–1641, 2014.
- [4] Z. Zhang, M. Deng, J. Bai, S. Yan, and X. Yu, "Stability control of gob-side entry retaining under the gob with close distance coal seams," *International Journal of Mining Science and Technology*, vol. 31, no. 2, pp. 321–332, 2021.
- [5] N. Zhang, H. Chen, and Y. Chen, "An engineering case of gob-side entry retaining in one kilometer-depth soft rock roadway with high ground pressure," *Journal of China Coal Society*, vol. 40, no. 03, pp. 494–501, 2015.
- [6] F. Ju, Z. W. Chen, Q. Zhang, P. Huang, Y. Yu, and L. X. Lan, "Surrounding rock stability control in gob-side entry retaining with solid backfilling in coal mining technology," *Journal of Mining & Safety Engineering*, vol. 32, no. 06, pp. 936–942, 2015.
- [7] X. M. Sun, X. Liu, G. F. Liang, D. Wang, and Y. L. Jiang, "Key parameters of gob-side entry retaining formed by roof cut and pressure releasing in thin coal seams," *Chinese Journal of Rock Mechanics and Engineering*, vol. 33, no. 07, pp. 1449–1456, 2014.
- [8] H. P. Kang, D. L. Niu, Z. Zhang, J. Lin, Z. H. Li, and M. J. Fan, "Deformation characteristics of surrounding rock and supporting technology of gob-side entry retaining in deep coal mine," *Chinese Journal of Rock Mechanics and Engineering*, vol. 29, no. 10, pp. 1977–1987, 2010.
- [9] Y. L. Tan, F. H. Yu, J. G. Ning, and T. B. Zhao, "Adaptability theory of roadside support in gob-side entry retaining and its supporting design," *Journal of China Coal Society*, vol. 41, no. 02, pp. 376–382, 2016.
- [10] N. Zhang, Z. Y. Zhang, H. Wu, and P. Cao, "Technology and application of reparation in deep gob-side entry retaining," *Chinese Journal of Rock Mechanics and Engineering*, vol. 33, no. 03, pp. 468–474, 2014.
- [11] P. F. Jiang, J. Zhang, and B. Hu, "Mechanical and deformation characteristics of gob-side entry retaining surrounding rock and support methods," *Journal of Mining & Safety Engineering*, vol. 33, no. 01, pp. 56–62, 2016.
- [12] S. R. Xie, L. Xu, G. C. Zhang, S. J. Li, S. Gong, and L. G. Yang, "Subsidence broken of deep gob-side entry retaining surrounding rock structure with large mining height and its control," *Rock and Soil Mechanics*, vol. 36, no. 02, pp. 569–575, 2015.
- [13] Z. Z. Zhang, J. B. Bai, Y. Chen, and M. Li, "Investigation and application analysis of unbalanced bearing characteristics of gob-side entry retaining," *Rock and Soil Mechanics*, vol. 36, no. 09, pp. 2665–2673, 2015.
- [14] C. Wang, Z. S. Du, N. C. Zhang, and D. Y. Qian, "Study on surrounding rock control for mining roadway of the overlying protected seam in ascending de-stressed mining," *Journal of Mining and Safety Engineering*, vol. 29, no. 02, pp. 220–225, 2012.
- [15] J. Zhu, R. H. Wang, and B. Lin, "Research on the phenomenon of multiple fracturing and fracture apertures of surrounding rock mass in deep roadway," *Journal of China Coal Society*, vol. 35, no. 06, pp. 887–890, 2010.
- [16] I. W. Farmer, "Stress distribution along a resin grouted rock anchor," *International Journal of Rock Mechanics and Mining Sciences & Geomechanics Abstracts*, vol. 12, no. 11, pp. 347–351, 1975.
- [17] B. Benmokrane, A. Chennouf, and H. S. Mitri, "Laboratory evaluation of cement-based grouts and grouted rock anchors," *International Journal of Rock Mechanics and Mining Sciences & Geomechanics Abstracts*, vol. 32, no. 7, pp. 633–642, 1995.
- [18] S. C. Li, H. P. Wang, Q. H. Qian et al., "In-situ monitoring research on zonal disintegration of surrounding rock mass in deep mine roadways," *Chinese Journal of Rock Mechanics and Engineering*, vol. 27, no. 08, pp. 1545–1553, 2008.
- [19] X. H. Li, S. Liang, Q. L. Yao, Q. D. Zhai, and L. Zhang, "Analysis on fissure evolving law and roof falling mechanism in roadway with mudstone roof," *Journal of China Coal Society*, vol. 36, no. 06, pp. 903–908, 2011.
- [20] X. Y. Yu, N. Zhang, H. Wu, and B. Y. Li, "A dynamic roof fall risk index for coal mine roadways," *Disaster Advances*, vol. 6, no. 5, pp. 8–15, 2013.
- [21] Q. Wu, L. Chen, B. Shen, B. Dlamini, S. Li, and Y. Zhu, "Experimental investigation on rockbolt performance under the tension load," *Rock Mechanics and Rock Engineering*, vol. 52, no. 11, pp. 4605–4618, 2019.
- [22] Y. L. Lu, L. G. Wang, B. Zhang, and Y. J. Li, "Optimization of bolt-routing time for soft rock roadway," *Rock and Soil Mechanics*, vol. 33, no. 05, pp. 1395–1401, 2012.
- [23] W. J. Wang, G. Peng, and J. Huang, "Research on high-strength coupling support technology of high stress extremely soft rock roadway," *Journal of China Coal Society*, vol. 36, no. 02, pp. 223–228, 2011.
- [24] H. Wu, X. K. Wang, W. J. Yu et al., "Analysis of influence law of burial depth on surrounding rock deformation of roadway," *Advances in Civil Engineering*, vol. 2020, Article ID 8870800, 2020.
- [25] X. Wu, S. Wang, C. Tian, C. Ji, and J. Wang, "Failure mechanism and stability control of surrounding rock of docking roadway under multiple dynamic pressures in extrathick coal seam," *Geofluids*, vol. 2020, Article ID 8871925, 16 pages, 2020.

## Research Article

# Research and Application of Open-Off Cut Roof Cutting Pressure Releasing Technology

Xingen Ma <sup>1,2</sup>, Manchao He,<sup>2</sup> Weidong Li,<sup>1</sup> Yilong Wang,<sup>1</sup> Lifeng Li,<sup>3</sup> Xiaohu Sun,<sup>1</sup> Yongyuan Li,<sup>1</sup> Leiyu Gu,<sup>1</sup> and Xingfeng Sha<sup>1</sup>

<sup>1</sup>Huaneng Coal Technology Research Co., Ltd., China Huaneng, Beijing 100070, China

<sup>2</sup>State Key Laboratory for Geomechanics & Deep Underground Engineering, China University of Mining & Technology, Beijing 100083, China

<sup>3</sup>School of Architecture and Civil Engineering, Guizhou University of Engineering Science, Bijie, Guizhou 551700, China

Correspondence should be addressed to Xingen Ma; 294185559@qq.com

Received 14 March 2021; Accepted 25 April 2021; Published 12 May 2021

Academic Editor: Zizheng Zhang

Copyright © 2021 Xingen Ma et al. This is an open access article distributed under the Creative Commons Attribution License, which permits unrestricted use, distribution, and reproduction in any medium, provided the original work is properly cited.

The first weighting control is one of the difficult problems that cannot be avoided in the safe and efficient production of longwall mining face. To optimize the existing pressure releasing technology of open-off cut, the open-off cut roof cutting pressure releasing (OCRCPR) technology is put forward on the basis of roof cutting pressure releasing gob-side entry retaining (RCPRGER) technology. Firstly, the mechanism of the technology and the design method of related key parameters are summarized. Then the pressure releasing effect of OCRCPR and the stress environment change under this technology are analyzed by mechanics calculation and numerical simulation, respectively, which verify the feasibility of the OCRCPR technology from the theoretical level. Finally, a test mining face is taken as an example to implement the field test. The field test results show that the OCRCPR can effectively shorten the first weighting step and weaken the first weighting strength and has a good pressure releasing effect.

## 1. Introduction

In 1950s, the world first longwall mechanized mining coal was established in Britain. This mining technology has the advantages of high mining efficiency, high resource recovery rate, and convenient production continuity. Since China began to learn the longwall mining method from the Soviet Union during the First Five-Year Plan period, after many years of experiment and promotion, combined with the coal seam occurrence conditions in China, the longwall mining technology with Chinese characteristics has been developed [1].

However, in the process of longwall mining operation, the weighting control of the main roof is one of the unavoidable problems about safety [2]. In particular, the first weighting of the working face is the most violent strata behavior process which is difficult to control. For quite some time, many researchers have studied the mechanism of rock pressure in this process and have got a lot of achievements in

the prediction of first weighting step, the analysis of the main roof instability process, the prevention and control of roof leakage and wall caving and so on. For examples, Dai Xingguo has established the calculation method of main roof first weighting step according to the damage limit analysis of plate structure [3, 4]. Huang Qingxiang analyzed the stability of roof structure and its control ways during the first weighting period based on the “S-R” theory [2]. Existing research results give many references for the prevention and control of first weighting in longwall face, but its prevention and control strategy mainly is weighting forecast in advance and passive support reinforcement, which has not really changed the weighting structure of the main roof and has great limitations in practical application.

In recent years, with the deepening of theoretical research and the improvement of practical level, the roof presplitting blasting technology of open-off cut appeared in the prevention and control of working face first weighting [5–7]. Existing presplitting blasting technologies on open-off

cut roof realize the prevention and control of first weighting to a certain extent by actively changing the shape and structure of roof, but there are still many shortcomings in the process of field implementation: first, the direction of presplitting blasting is difficult to control, the efficiency of roof breaking is low, and it is easy to cause damage to the original support of open-off cut; second, the implementation process is complicated, as it often needs to carry out the blast on open-off cut roof after the hydraulic supports, which will affect the mining progress at the initial stage.

Therefore, taking a test working face as an example, this paper draws lessons from the theory of roof cutting entry retaining (RCPRGER) put forward by academician He Manchao and studies the open-off cut roof cutting (OCRCPR) technology based on tension blasting [8]. The research results can further optimize the means of prevention and control of first weighting in longwall face, improve the pressure releasing efficiency of first weighting, and expand the application scope and advantages of longwall mining.

## 2. The OCRCPR Technology

Existing RCPRGER technology can change the retained entry roof structure actively through the presplitting blasting and take use of the gangue collapsed from lower layers of goaf roof to realize the entry retaining without coal pillar or material, as shown in Figure 1(b) [9, 10]. Based on above, in order to reduce the first weighting strength of main roof artificially on the strike direction, the OCRCPR technology is put forward, and the roof structure of open-off cut can also be changed actively by presplitting blasting, as shown in Figure 1(c).

*2.1. Open-Off Cut Pressure Releasing Mechanism and Related Design.* In the mining early stage of traditional longwall working face, the one end of goaf roof is supported by the coal wall on strike section, and the other end is supported by the hydraulic supports of working face and the coal wall in front of open-off cut, showing a fixed beam state (as shown in Figure 2) [11, 12]. Therefore, the length of roof suspension behind working face is usually longer before the first weighting, and the first weight strength is also usually greater, which is easy to cause damage to the hydraulic supports and other equipment of the working face.

When using OCRCPR technology to carry out the presplitting roof cutting on the open-off cut roof along the inclination direction of mining face, in the mining early stage, the goaf roof presents a cantilever beam structure on the strike direction, and the goaf roof is only supported by the hydraulic supports and the front coal wall (as shown in Figure 3). At this time, compared with the roof uncut condition, the first weighting step of working face will be greatly shortened, and the first weighting strength can also be greatly reduced.

Referring to the practical experience, the formula of roof cutting height preliminary design is shown as Formula (1). When there are more than one strata layer about cutting roof, the roof bulking coefficient can be got through

weighted calculation based on thickness of each layer as follows [13]:

$$H_F = \frac{(H_M - \Delta H_1 - \Delta H_2)}{(K - 1)}, \quad (1)$$

$$K = \sum_{i=1}^n K_i \frac{D_i}{H_M}, \quad (2)$$

where  $H_F$  is the cutting height,  $H_M$  is the coal seam mining height,  $\Delta H_1$  is the roof subsidence volume,  $\Delta H_2$  is the floor heave volume,  $K$  is the bulking coefficient,  $n$  is the number of rock layers in the roof cutting range,  $n \geq 1$ ,  $D_i$  is the thickness of each rock layer,  $1 \leq i \leq n$ , and  $K_i$  is the bulking coefficient of each rock layer,  $1 \leq i \leq n$ .

The roof cutting angle design of open-off cut includes three cases: backward inclination, forward inclination, and vertical inclination, as shown in Figure 4. (a) Under the same roof cutting height, the amount of gangue in the roof cutting range is larger under backward inclination condition, which is conducive to the filling of the goaf. Therefore, choosing the backward inclination roof cutting design can reduce the cutting height to a certain extent under the thick coal seam. (b) Forward inclination design is more conducive to roof collapse within the cutting range, so when the thickness of coal seam is small and the cutting height is low, roof collapse can be promoted earlier through the design of this scheme. (c) The advantage of vertical roof cutting is easy to construct. Usually the space behind supports in the open-off cut is limited, and the vertical cutting has a lower space demand and whose construction adaptability is better.

*2.2. Bidirectional Concentrated Tension Blasting Technology.* In the OCRCPR technology, the directional roof presplitting is also realized by the bidirectional concentrated tension blasting technology. This blasting technology can make the explosive blasting energy directional transmit, and the principle of bidirectional concentrated tensile blasting is shown in Figure 5 [14, 15].

In the field application of this study, the pipe size of blasting is  $\phi 36.5 \text{ mm} \times 1500 \text{ mm}$ , and pipes can be connected one by one. The best blasting parameters can be determined by field blasting test.

## 3. Effect Analysis of Roof Cutting Pressure Releasing

The schematic diagram of entry retaining technology with roof cutting is shown in Figure 1(b). To further study the pressure releasing effect of open-off cut roof cutting on above, this section uses two methods, mechanical calculation and numerical simulation, to analyze the first weighting of mining face and the stress environment.

### 3.1. Calculation about First Weighting

*3.1.1. Open-Off Cut Roof Uncut Condition.* Under the open-off cut roof uncut condition, the first weighting process of roof is shown in Figure 2 [16, 17]. Because the tendency

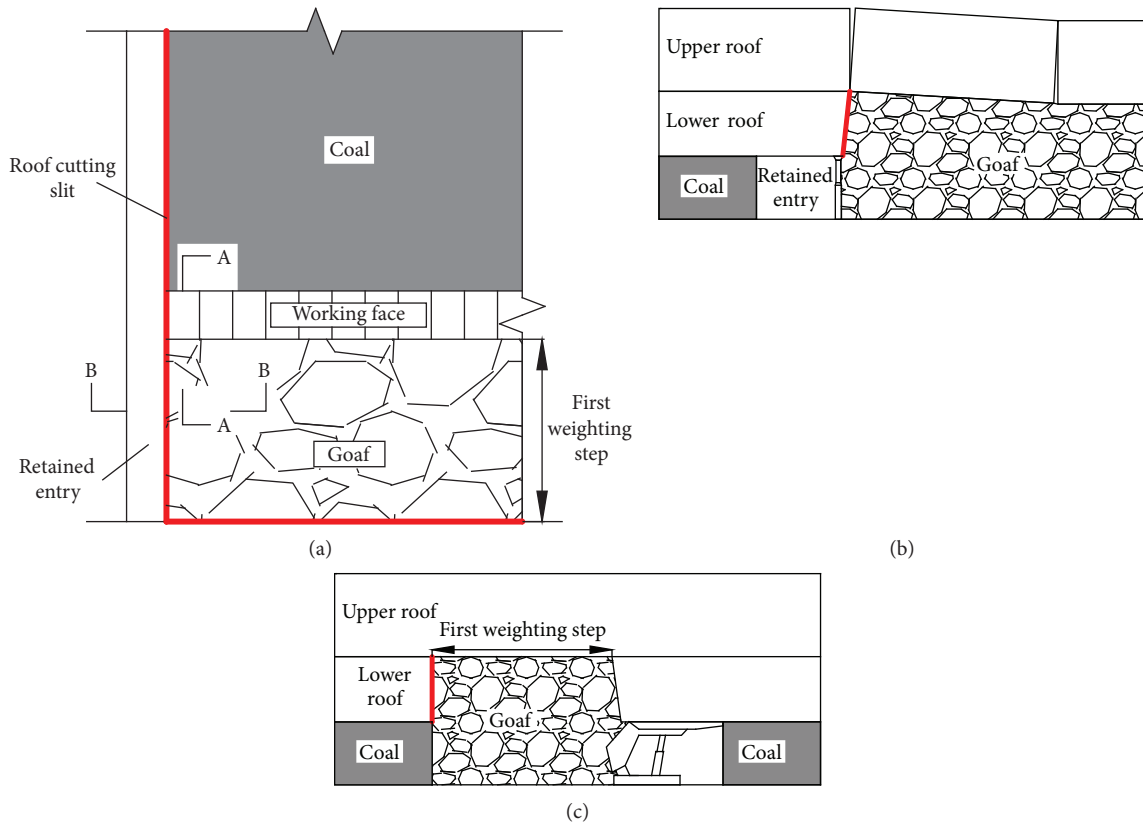


FIGURE 1: Schematic diagram of roof cutting in retained entry and open-off cut: (a) plane of roof cutting in retained entry and open-off cut; (b) section map of entry retaining roof cutting (section B-B); (c) section map of open-off cut roof cutting (section A-A).

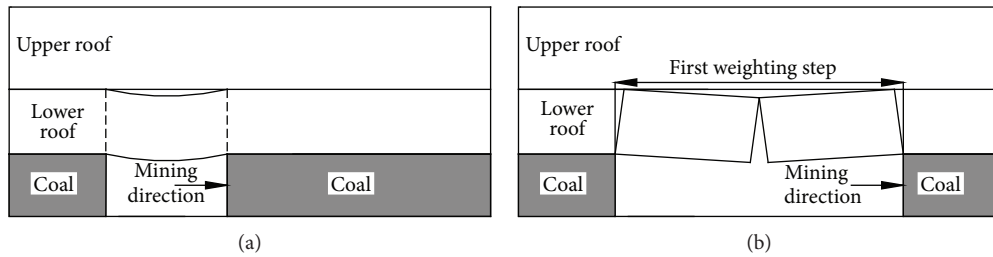


FIGURE 2: Working face first weighting under traditional condition: (a) roof structure before first weighting; (b) roof structure at first weighting.

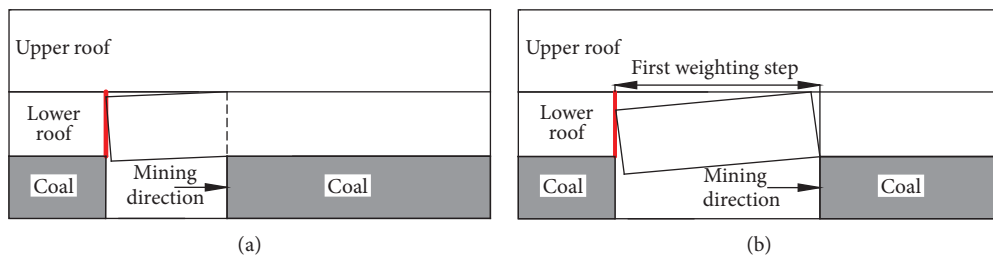


FIGURE 3: Working face first weighting under open-off cut roof cutting condition: (a) roof structure before first weighting; (b) roof structure at first weighting.

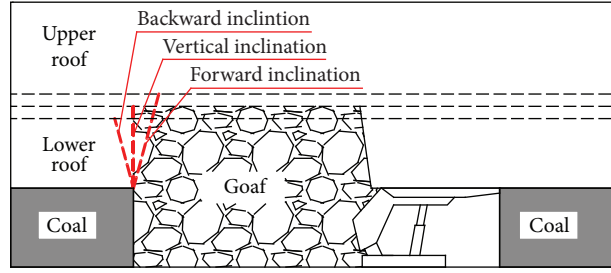


FIGURE 4: Roof cutting angle design of open-off cut.

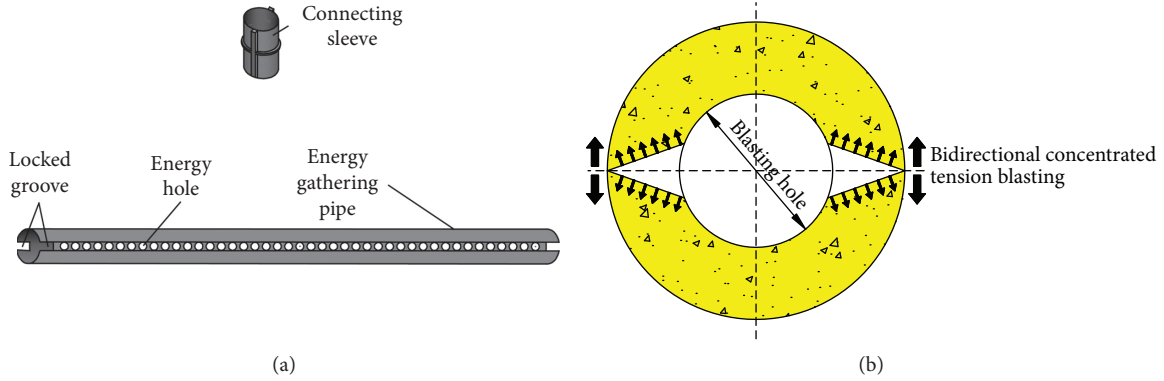


FIGURE 5: Devices and principle of bilateral cumulative tensile blasting: (a) energy gathering pipe and connecting sleeve; (b) mechanism model (Figure 5 is reproduced from Xingen Ma et al.).

length of working face is much longer than the weighting step of strike direction, the lower roof before collapse at the mining early stage can be seen as a fixed beam state, whose stress analysis is shown in Figure 6.

According to the stress analysis above, the following can be got:

$$\begin{cases} R_1 = R_2 = \frac{qL}{2}, \\ M_1 = M_2 = -\frac{1}{12}qL^2, \\ M_x = R_1x - \frac{qx^2}{2} + M_1 = \frac{q}{12}(6Lx - 6x^2 - L^2). \end{cases} \quad (3)$$

At both ends of the fixed beam (when  $x=0$  or  $x=L$ ),  $M_{\max} = -qL^2/12$ ; at the middle of the fixed beam (when  $x=L/2$ ),  $M = qL^2/24$ . The normal stress at any point is

$$\sigma = \frac{My}{J_z}, \quad (4)$$

where  $M$  is the moment of the section where the point is located,  $y$  is the distance from the point to the center axis, and  $J_z$  is the end distance of the symmetrical center axis. Because the bending moment is the highest at both ends of the fixed beam, the tensile stress is also the highest at there:

$$\sigma_{\max} = \frac{qL^2}{2h^2}. \quad (5)$$

When  $\sigma_{\max} = R_T$ , that is, when the normal stress of the stratum reaches its ultimate tensile strength, the stratum will be fractured. At this time, the ultimate span of the roof (first weighting step) is

$$L = h\sqrt{\frac{2R_T}{q}}, \quad (6)$$

where  $L$  is the first weighting step,  $h$  is the thickness of rock beam,  $R_T$  is the tensile strength of rock beam, and  $q$  is the uniform load of rock beam and its overlying rock mass.

When the working face is weighting, the main stress of hydraulic support is from the gravity of the falling lower roof. According to this, the weighting strength can be estimated according to the following formula:

$$P = \frac{Lh\rho}{l_y} = \frac{h^2\rho}{l_y} \sqrt{\frac{2R_T}{q}}, \quad (7)$$

where  $\rho$  is the density of rock beam and  $l_y$  is the support length of single hydraulic support.

**3.1.2. Open-Off Cut Roof Cutting Condition.** Under the open-off cut roof cutting condition, the first weighting process of roof is shown in Figure 3 [17]. At this time, the lower roof before collapse at the mining early stage can be



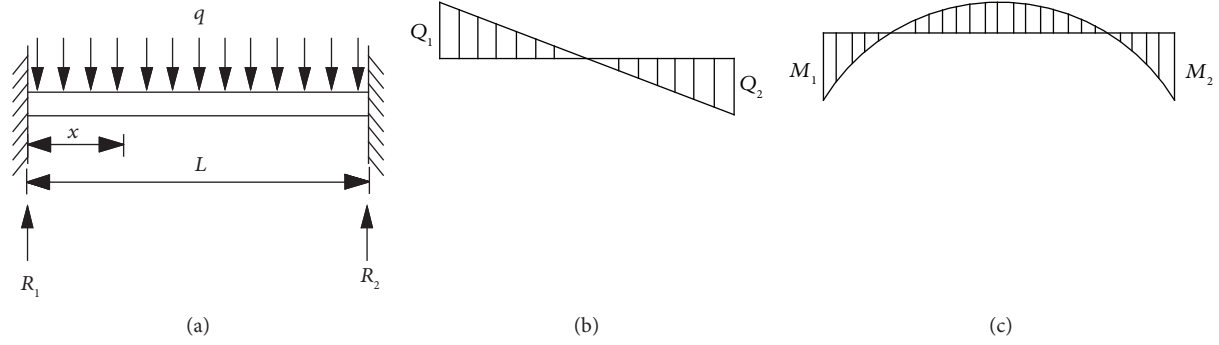


FIGURE 6: Stress analysis of fixed beam: (a) mechanical model; (b) shear stress diagram; (c) bending moment diagram.

seen as a cantilever beam state, whose stress analysis is shown in Figure 7.

According to the stress analysis above, the bending moment on any section of the cantilever beam is

$$M_x = -\frac{1}{2}(ql - x)^2. \quad (8)$$

The maximum bending moment occurs at the fixed position of the beam, namely,

$$M_{\max} = M_1 = -\frac{qL^2}{2}. \quad (9)$$

The tensile stress here is the maximum:

$$\sigma_{\max} = \frac{3qL^2}{2h^2}, \quad (10)$$

when  $\sigma_{\max} = R_T$ , that is, when the normal stress of the stratum reaches its ultimate tensile strength, the stratum will be fractured. At this time, the ultimate span of the roof (first weighting step) is

$$L = h\sqrt{\frac{R_T}{3q}}. \quad (11)$$

The weighting strength can be estimated as follows:

$$P = \frac{Lh\rho}{l_y} = \frac{h^2\rho}{l_y} \sqrt{\frac{R_T}{3q}}. \quad (12)$$

We can see that the structure of lower roof changed from fixed beam to cantilever beam in the mining early stage after the open-off cut roof cutting, and then the first weighting step became shorter and first weighting strength became weaker.

**3.2. Stress Evolution Analysis of Surrounding Rock.** Based on the geological conditions of test mining face, the surrounding rock stress evolution process with or without open-off cut roof cutting at the mining initial stage will be simulated by using FLAC 3D numerical simulation software [18, 19]. Modeling size is  $200\text{ m} \times 170\text{ m} \times 50\text{ m}$ , including roof 30 m, coal seam 3 m, and floor 17 m. In this model, working face simulation strike length is 160 m, simulation tendency length is 130 m, and simulation entry width is 5 m,

as shown in Figure 8. The parameters of each stratum in this model are shown in Table 1, the cutting height is designed as 7.7 m, and the vertical roof cutting is adopted [20].

The numerical simulation results of key section are shown in Figure 9. When mining to footage 0 m, the stress distribution with roof cutting is asymmetrical. Compared with the symmetrically stress distribution under open-off cut roof uncut condition, the peak value of stress concentration in advance is slightly higher. When mining to footage 10 m, the goaf roof collapse under the open-off cut roof cutting condition is more sufficient than that under the roof uncut condition, and the stress peak value in advance of mining face begins to be less than that of roof uncut condition. When mining to footage 20 m and 40 m, the roof collapse shape is basically stable under the two conditions, and the stress peak value under the open-off cut roof cutting condition is more smaller than that under roof uncut condition. The relationship between the stress concentration peak value and the mining footage under the two conditions in the early mining stage is further sorted out as shown in Figure 10, which shows that the peak values are all equal to 31.0 MPa under two conditions when mining to 6.8 m; the stress concentration peak value under open-off cut roof cutting is slightly higher before mining to 6.8 m; the stress concentration peak value under open-off cut roof cutting is smaller after mining to 6.8 m, and the difference increases gradually with the working face advancing within the first weighting step.

Through the above analysis, the open-off cut roof cutting can cut off the support to goaf roof of coal pillar behind the open-off cut, and then the advanced stress concentration strength of working face is higher at initial mining stage. But with the mining, the goaf roof is easier to collapse under the roof cutting condition, and the advanced stress concentration strength of working face turns to be smaller than that of roof uncut condition.

## 4. Field Condition and Cut Top Design

On the basis of the above mechanism and effect analysis through theoretical calculation and numerical simulation, taking 8304 mining face of Tashan coal mine as an example, the field test of OCR CPR technology is carried out to verify the feasibility and practicability.

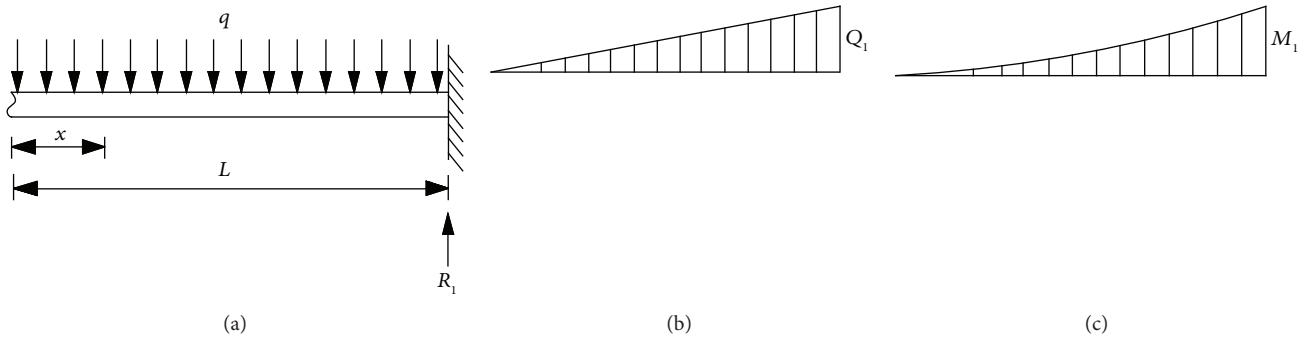


FIGURE 7: Stress analysis of cantilever beam: (a) mechanical model; (b) shear stress diagram; (c) bending moment diagram.

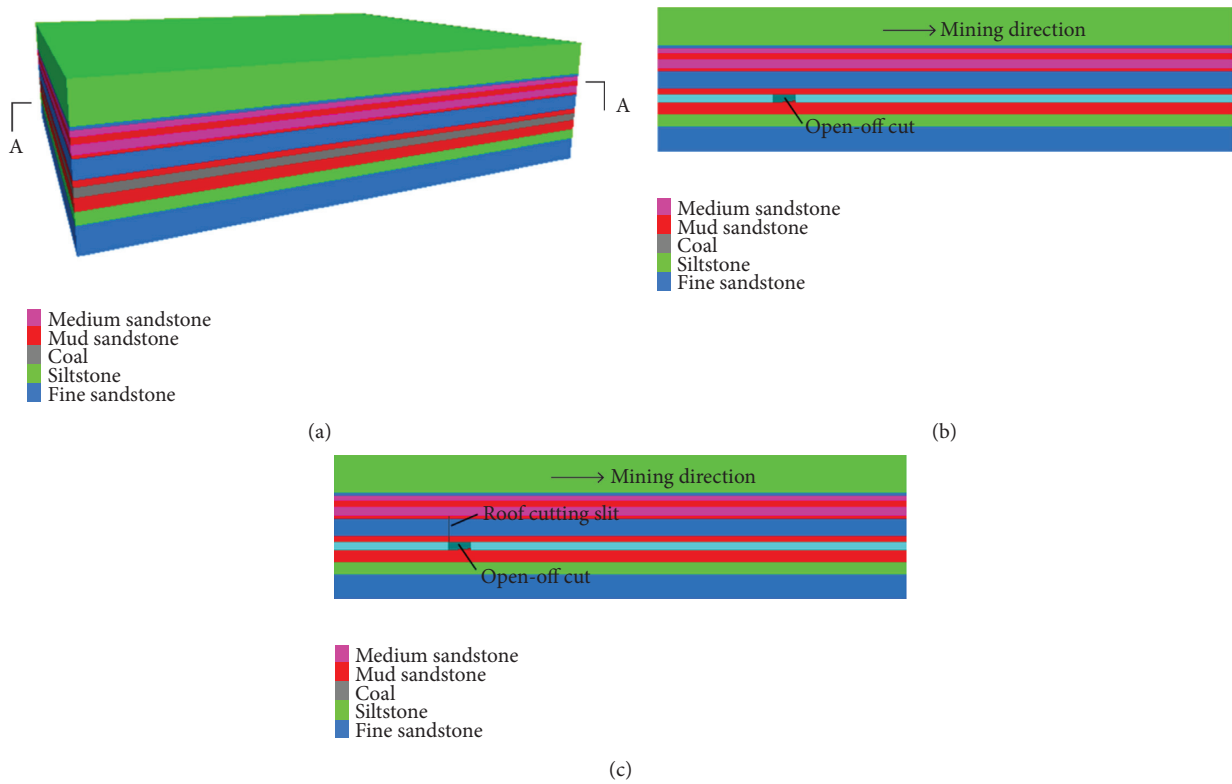


FIGURE 8: Numerical simulation model: (a) three-dimensional model; (b) A-A section under open-off cut roof uncut condition; (c) A-A section under open-off cut roof cutting condition.

TABLE 1: Physical and mechanical parameters of each rock layer.

Lithology	Density/kN/m <sup>3</sup>	Tensile strength/MPa	Internal friction angle/°	Cohesion/MPa	Bulk modulus/GPa	Shear modulus/GPa
Medium sandstone	25	8.4	33	2.6	11.49	7.26
Mudstone	23	3.2	28	0.2	0.20	0.15
Coal	13	3.3	29	0.2	0.35	0.18
Siltstone	23	4.3	32	0.8	2.11	1.86
Fine sandstone	24	7.3	32	1.0	3.81	3.05

4.1. *Engineering Overview.* The key information of test mining face is shown in Table 2 and Figure 11 [21].

As test working face, 8304 working face adopts comprehensive mechanized mining method, and its planned

daily mining speed is 10 m. The auxiliary haulage entry of this working face is designed to be retained by roof cutting and still used as auxiliary haulage entry for 8305 working face. In order to reduce the working face first weighting

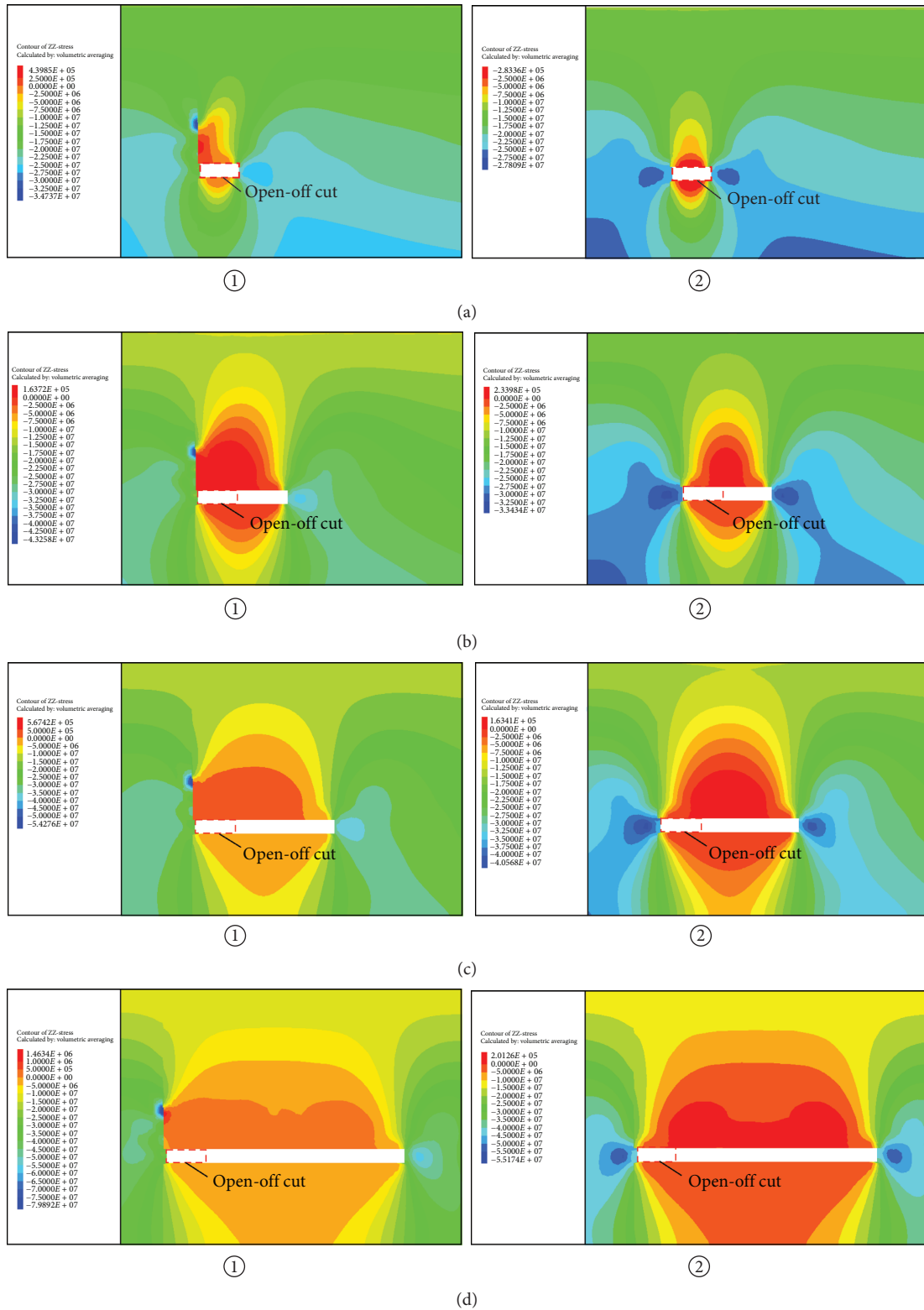


FIGURE 9: Numerical simulation results: (a) mining to footage 0 (m) ① open-off cut roof cutting condition; ② open-off cut roof uncut condition; (b) mining to footage 10 (m) ① open-off cut roof cutting condition; ② open-off cut roof uncut condition; (c) mining to footage 20 (m) ① open-off cut roof cutting condition; ② open-off cut roof uncut condition; (d) mining to footage 40 (m) ① open-off cut roof cutting condition; ② open-off cut roof uncut condition.

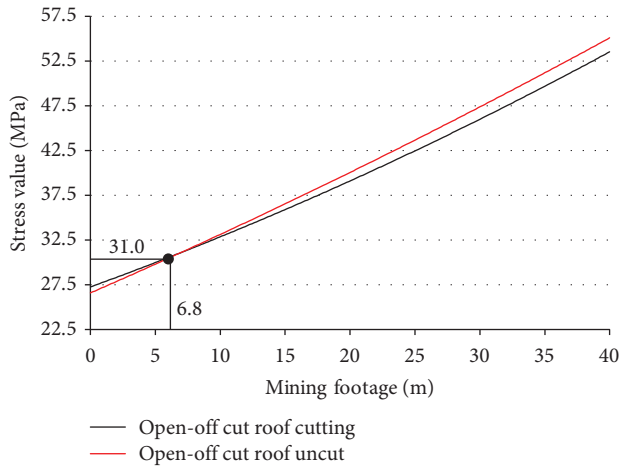


FIGURE 10: Comparison of stress concentration peaks in advance of working face.

strength and promote the rapid stability of retained entry initial section, the OCRCPR test is carried out on 8304 working face.

**4.2. Open-Off Cut Roof Cutting Design.** The roof cutting height can be calculated to be 7.5 m according to Formula (1) without considering the roof subsidence and floor heave (taking the roof bulking coefficient as 1.41). Comparing with the roof lithological column, the cutting height is adjusted to 7.7 m [21]. Because the test mining face is medium-thick coal seam working face, the vertical roof cutting design with stronger adaptability and lower construction difficulty is selected. The roof cutting line is arranged at the intersection of the coal pillar behind the open-off cut and whose roof is along the tendency direction of working face. In order to facilitate the construction, after the open-off cut is penetrated and the hydraulic support is arranged, a 1.5 m wide passage is set up behind the hydraulic supports, and the specific roof cutting design is shown in Figure 12.

**4.3. Open-Off Cut Roof Cutting Process.** Based on the above design, the hydraulic support with model ZZS10000/20/38 is selected for 8304 working face, and the sectional dimension of the open-off cut is set as 8.0 m × 3.1 m. After the penetration of open-off cut, the hydraulic supports need to be installed firstly, and an enough space should be left behind supports for blasting holes drilling. Then the marking line of the roof cutting is drawn on the open-off cut roof according to design, which serves as the baseline of the blasting holes drilling and roof presplitting blasting (as shown in Figure 13). To ensure the cutting effect of bidirectional concentrated tension blasting, the marking line should be kept as straight as possible along the working face tendency direction.

After the roof cutting height, angle, and position all determined, the roof cutting blasting parameters, including explosive charge weight, blasting hole spacing, and blasting hole amount at single initiation, all need to be further got

through field blasting test [22, 23]. The field blasting test is divided into three steps as shown in Figure 14 [15]. The first step is to carry out single hole blasting test, namely, blasting one hole each time with different explosive charge weight to determine the reasonable charge of a single hole. The second step is to carry out interval hole blasting test, namely, blasting holes each time with different hole spacing and leaving peephole to judge the reasonable spacing. The third step is to carry out continuous hole blasting test, namely, through the harmful gas monitoring to determine the blasting hole amount at single initiation. Through field test, it is determined that the single blasting hole charge structure in 8304 working face is 4 + 3 + 3 + 2, four energy gathering pipes are filled in each blasting hole, and the sealing length of each hole is 1.7 m (as shown in Figure 15). The common presplitting effect in peephole is shown as Figure 16, and the average single hole crack rate detected in site is 83.6%.

## 5. Engineering Application Analysis

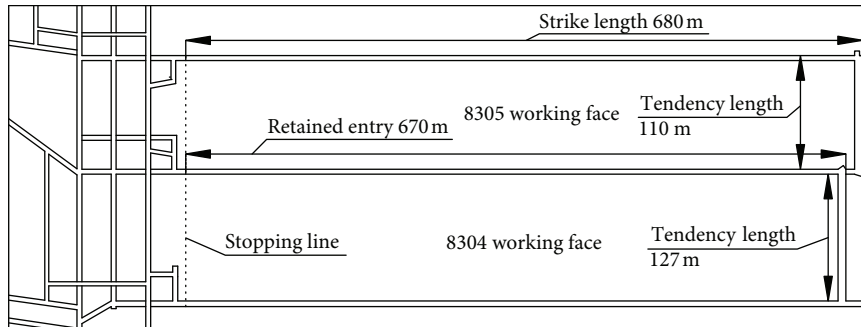
**5.1. Roof Initial Collapse.** The 8304 working face not only uses the OCRCPR technology to weaken the first weighting but also uses the entry retaining technology with roof cutting. The roof cutting range of open-off cut is the 107 m section near entry retaining side, and another 20 m section without roof cutting is set as the control section (as shown in Figure 17). On one hand, open-off cut roof cutting on the entry retaining side can reduce the first weighting step and strength, which is good for the rapid stability of retained entry initial section; on the other hand, the retained entry can also provide an observation condition for the goaf roof collapse.

Based on the mining experience of the same mining field, it is inferred that the first weighting step of 8304 working face should be within 50-70 m. Therefore, the initial caving of the goaf roof is observed in the retained entry at footage 10 m. When it is behind the working face 20 m, the goaf roof collapse at retained entry side is shown in Figure 18(a). At this time, the immediate roof has collapsed with large areas, but the gangue pile has not yet reached the goaf roof. When it is behind the mining face 40 m, the goaf roof collapse at retained entry side is shown in Figure 18(b). At this time, gangue pile has reached the goaf roof with bulking, and the gangue wall has been formed basically. In the initial mining stage, the open-off cut roof cutting and the entry roof cutting influence the goaf roof collapse at same time. So the goaf roof collapse process at this time does not have the representativeness of the whole mining face in the inclination direction. However, in the further mining and entry retaining process, the gangue wall all formed within the range 35-42 m behind the working face, and the OCRCPR can promote the roof collapse in the early mining stage and basically eliminate the problem that the goaf roof is difficult to collapse in the early mining stage.

**5.2. Monitoring and Analysis of First Weighting.** In addition to the direct observation of the roof collapse in the retained entry, this study also verifies the pressure releasing effect to

TABLE 2: Basic parameters of 8304 working face.

Coal seam thickness/average (m)	1.80–3.55/3.1	Depth (m)	367–411
Mining height (m)	3.1	Dip angle/average (°)	2~6/4
Strike length (m)	670	Tendency length (m)	127
Immediate roof/thickness (m)	Mudstone/1.47	Immediate floor/thickness (m)	Mudstone/3.2
Main roof/thickness (m)	Fine sandstone/3.88	Main floor/thickness (m)	Siltstone/3.1



(a)

Columnar	Thickness (m)	Lithology
	1.38	Siltstone
	0.50	Fine sandstone
	1.30	Medium sandstone
	1.23	Mudstone
	2.89	Medium sandstone
	0.80	Mudstone
	5.46	Fine sandstone
	1.44	Mudstone
	3.10	Coal

(b)

FIGURE 11: Layout and roof lithologic histogram of 8304 working face.

working face first weighting of the open-off cut roof cutting through the pressure monitoring shown as Figures 17 and 19 [24–26].

The monitoring results of weighting step are shown in Figure 20. Overall, the periodic weighting step is shorter than the first, and that of the retained entry side is longer than the other side. Affected by the roof cutting of open-off cut and entry, the first weighting step of the retained entry side is also smaller. In order to further highlight the pressure releasing effect of open-off cut, the difference between first weighting step and periodic weighting step is arranged in Figure 20(b). The difference between first and periodic

weighting step is smaller in the roof cutting range of open-off cut, and the difference is larger in the roof uncut range of open-off cut.

Similarly, the monitoring results of weighting strength are shown in Figure 21. Overall, the periodic weighting strength is lower than the first, and the periodic weighting strength of the retained entry side is smaller. The difference between first weighting strength and periodic weighting strength is arranged in Figure 21(b). The difference between first and periodic weighting strength is smaller in the roof cutting range of open-off cut, and the difference is larger in the roof uncut range of open-off cut. To sum up, the



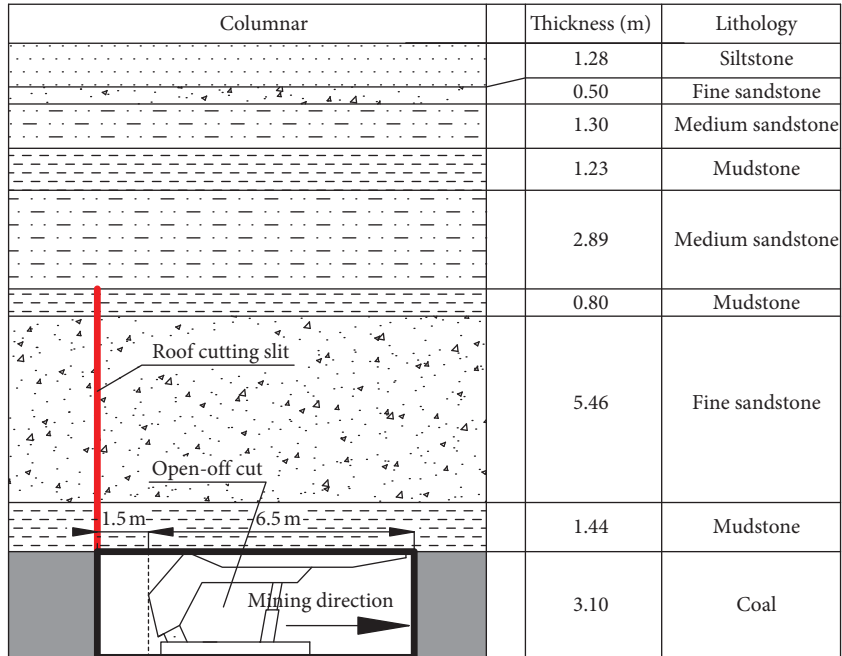


FIGURE 12: Open-off cut roof cutting design of 8304 working face.

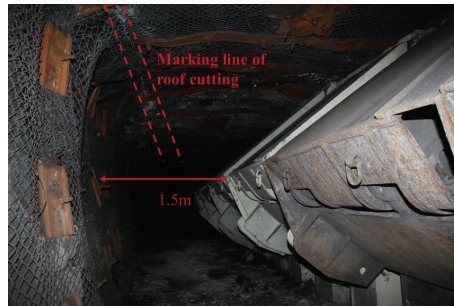
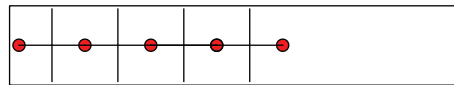
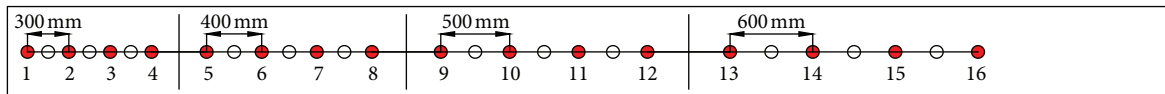


FIGURE 13: Open-off cut roof cutting scene of 8304 working face.



● Blasting hole

(a)



○ Peephole  
● Blasting hole

(b)

FIGURE 14: Continued.

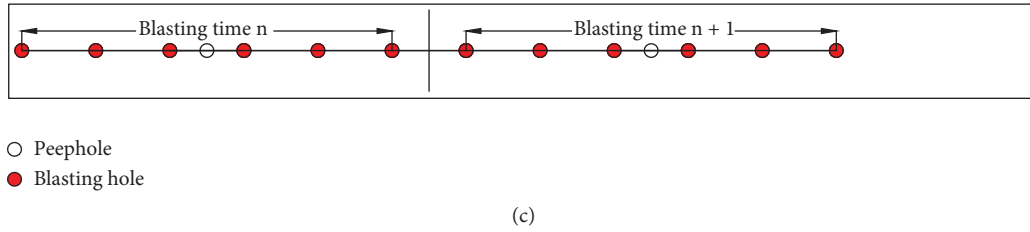


FIGURE 14: Blasthole layout of blasting test: (a) single hole blasting test; (b) interval hole blasting test; (c) continuous hole blasting test (Figure 14 is reproduced from Xingen Ma et al.).

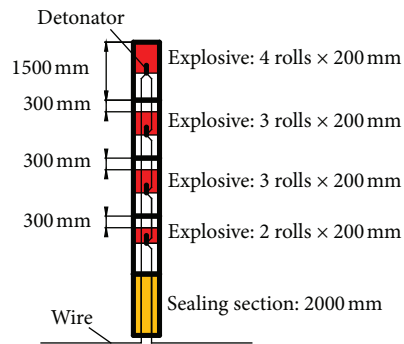


FIGURE 15: Charge structure of explosive rolls.

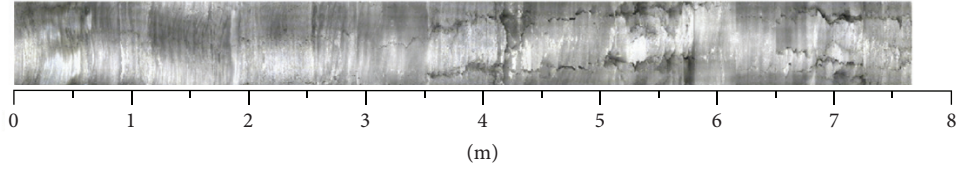


FIGURE 16: Fissure map of roof cutting blasting.

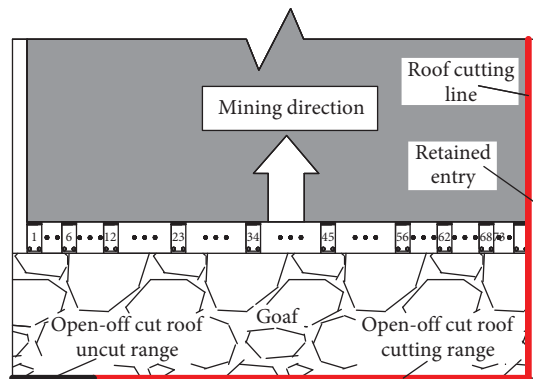


FIGURE 17: Monitoring scheme.



FIGURE 18: Gangue collapse process at 10 m footage: (a) behind working face 20 m; (b) behind working face 40 m.

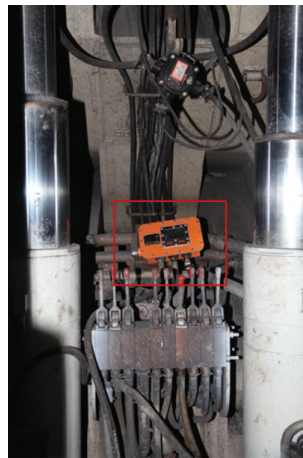


FIGURE 19: Monitoring equipment for hydraulic support.

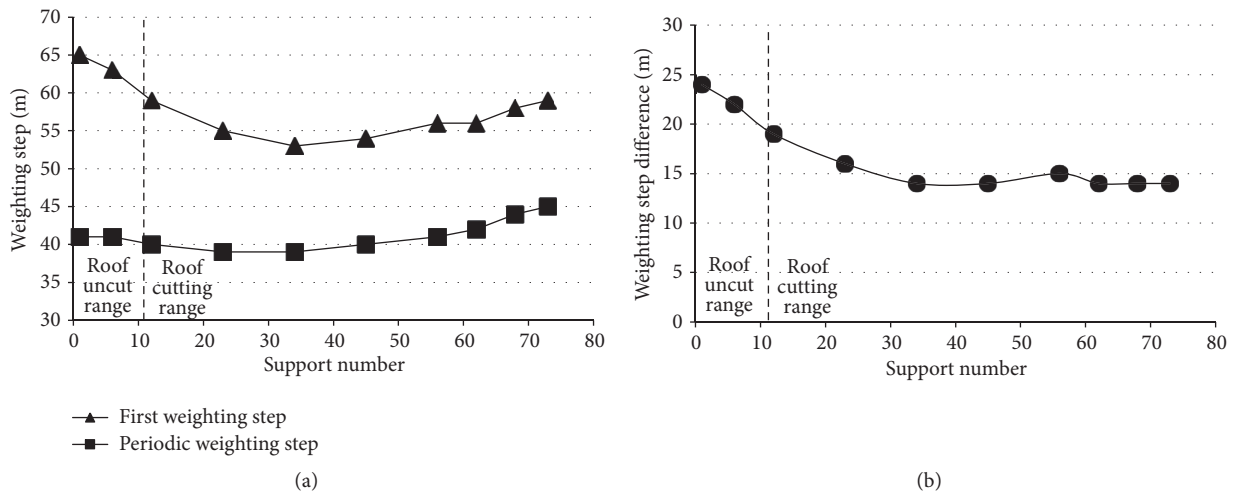


FIGURE 20: Monitoring result of weighting step: (a) weighting step statistics; (b) weighting step difference.

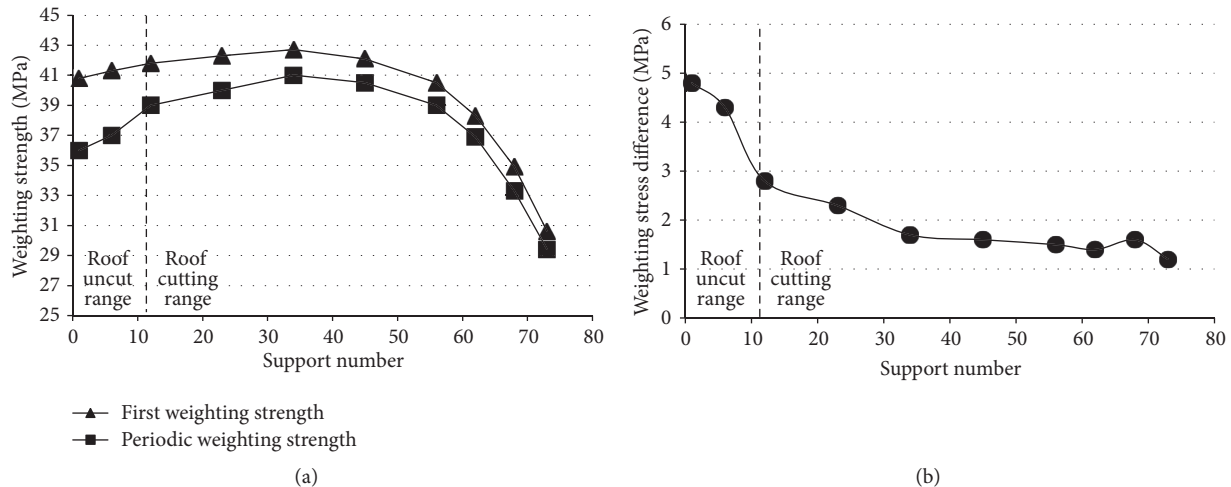


FIGURE 21: Monitoring result of weighting strength: (a) weighting strength statistics; (b) weighting strength difference.

OCRCPR can effectively shorten the first weighting step and reduce the first weighting strength and has a good pressure releasing effect.

## 6. Conclusions

- (1) Based on the entry retaining technology with roof cutting, the pressure releasing technology of open-off cut roof is put forward, namely, changing the roof structure of open-off cut actively by roof presplitting cutting, which can weaken the first weighting strength and shorten the first weighting step of working face artificially on the strike direction.
- (2) By means of mechanical calculation, the clamped beam structure of open-off cut roof under roof uncut condition and the cantilever beam structure under roof cutting condition are analyzed, respectively, and the roof cutting pressure releasing principle is explained from the first weighting step and strength about mining face. Besides, the stress evolution processes of surrounding rocks under the two conditions are deduced by numerical simulation to verify the roof cutting pressure releasing effect of open-off cut roof.
- (3) Taking the tested mine as an example, this paper summarizes the design, implementation process, and application effect of the OCRCPR test. Through the observation of roof collapse process at the initial stage of mining and the stress monitoring of hydraulic support in working face, it further verifies that the roof cutting technology of open-off cut can effectively shorten the first weighting step and weaken the first weighting strength of working face.

## Data Availability

All the data used to support the findings of this study are available from Xingen Ma upon request.

## Conflicts of Interest

The authors declare that they have no conflicts of interest.

## Acknowledgments

This research was financially supported by the State Key Laboratory for GeoMechanics and Deep Underground Engineering (SKLGDUEK2020), Guizhou Department of Education Youth Talent Growth Project of China (Grant no. [2019] 162), Bijie Science and Technology Bureau Joint Fund Project (Grant nos. G[2019] no. 26), and Higher Educational Scientific Research Projects of Inner Mongolia Autonomous Region (no. NJZY21291), which are gratefully acknowledged.

## References

- [1] Y. Xue, "From tradition to modern times: evolution of coal mining technology in China," *Journal of Hubei Polytechnic University (Humanities and Social Science)*, vol. 30, no. 05, pp. 7–15, 2013.
- [2] Q. Huang, "Structural analysis of main roof stability during first weighting in longwall face," *Chinese Journal of Rock Mechanics and Engineering*, vol. 17, no. 5, pp. 521–526, 1998.
- [3] X. Dai and M. Qian, "Limit analysis and calculation of first weighting interval of main roof," *Journal of China University of Mining and Technology*, vol. 22, no. 1, pp. 17–23, 1993.
- [4] J. Wang, J. Zhang, X. Gao et al., "Fracture mode and evolution of main roof stratum above longwall fully mechanized top coal caving in steeply inclined thick coal seam (I)—initial fracture," *Journal of China Coal Society*, vol. 40, no. 6, pp. 1353–1360, 2015.
- [5] Z. Song, "Roof deep-hole pre-blasting technology of first mining face in Suancigou colliery," *Coal Mining Technology*, vol. 15, no. 4, pp. 103–105, 2010.
- [6] Y. Wang, L. Wang, Z. Huang et al., "Preventing cock burst based on cutting hole and breaking roof blasting technology," *Safety in Coal Mine*, vol. 47, no. 12, pp. 133–136, 2016.
- [7] B. Junqi, "Study on deep hole pre-cracking blasting technology in open cut eyes of full mechanized caving face in

- special thick seam,” *Coal Mine Modernization*, vol. 147, no. 6, pp. 123–125, 2018.
- [8] M. He, Z. Song, A. Wang et al., “Theory of longwall mining by using roof cutting shortwall team and 110 method,” *Coal Science & Technology Magazine*, vol. 1, no. 1, pp. 1–9, 2017.
- [9] G. Pengfei, K. Ye, Z. Tao et al., “Experimental study on key parameters of bidirectional cumulative tensile blasting with coal-containing composite roof,” *KSCE Journal of Civil Engineering*, vol. 2, 2021.
- [10] M. Yun, H. Zheng, T. Li et al., “Support design and mine pressure measurement of 1102 working face in Qiuji Coal Mine,” *Safety in Coal Mines*, vol. 52, no. 3, pp. 127–132, 2021.
- [11] Z. Zhang, M. Deng, J. Bai, X. Yu, Q. Wu, and L. Jiang, “Strain energy evolution and conversion under triaxial unloading confining pressure tests due to gob-side entry retained,” *International Journal of Rock Mechanics and Mining Sciences*, vol. 126, Article ID 104184, 2020.
- [12] D. He, *Research on the Pre-splitting Blasting Weakening Mechanism of the Hard Roof under the Deep Environment*, China university of mining technology, Xuzhou, China, 2015.
- [13] X. Yang, Di Yuan, H. Xue et al., “Research on roof cutting and pressure releasing technology of cumulative blasting in deep and high stress roadway,” *Geotechnical and Geological Engineering*, vol. 39, 2021.
- [14] X. Sun, X. Liu, G. Liang et al., “Key Parameters of gob-side entry retaining formed by roof cut and pressure releasing in thin coal seams,” *Chinese Journal of Rock Mechanics and Engineering*, vol. 33, no. 7, pp. 1449–1456, 2014.
- [15] X. Ma, M. He, J. Sun, H. Wang, X. Liu, and E. Zhen, “Neural network of roof cutting blasting parameters based on mines with different roof conditions,” *Energies*, vol. 11, no. 12, p. 3468, 2018.
- [16] Z. Zhang, M. Deng, X. Wang, W. Yu, F. Zhang, and V. D. Dao, “Field and numerical investigations on the lower coal seam entry failure analysis under the remnant pillar,” *Engineering Failure Analysis*, vol. 115, p. 104638, 2020.
- [17] S. Zhang, *The Theory and Practice Research on Deep Hole Pre-split Blasting of Open-Off Cut of Fully Mechanized Caving Face*, Taiyuan University of Technology, Taiyuan, China, 2014.
- [18] G. Ramesh and R. Karpurapu, “Laboratory and numerical studies on the performance of geocell reinforced base layer overlying soft subgrade,” *International Journal of Geosynthetics and Ground Engineering*, vol. 7, 2021.
- [19] K. V. Amit and T. N. Singh, “Modeling of a jointed rock mass under triaxial conditions,” *Arabian Journal of Geosciences*, vol. 3, pp. 91–103, 2010.
- [20] M. He, X. Ma, J. Wang et al., “Feature analysis of working face strata pressure with roof cutting pressure releasing in medium-thick seam and compound roof condition,” *Chinese Journal of Rock Mechanics and Engineering*, vol. 37, no. 11, pp. 1–11, 2018.
- [21] J. Wang, Y. Liu, X. Ma et al., “Technology of roof cutting and entry retaining in fully-mechanized working face of Tashan Coal Mine,” *Coal Science and Technology*, vol. 47, no. 2, pp. 27–34, 2019.
- [22] C. Hu, X. Yang, R. Huang et al., “Presplitting blasting the roof strata to control large deformation in the deep mine roadway,” *Advances in Civil Engineering*, vol. 2020, Article ID 8886991, 15 pages, 2020.
- [23] S. Wang, “Experimental study on roof-cutting-and-pressure-relief technology with hydraulic fracturing in retaining roadway along goaf,” *Jiangxi Coal Technology*, vol. 1, pp. 25–30, 2021.
- [24] J. Hu, Y. Wang, Z. Ma et al., “Experimental and numerical analysis of rock burst tendency and crack development characteristics of tianhu granite,” *Geofluids*, vol. 2021, Article ID 6681261, 12 pages, 2021.
- [25] Z. Zhang, M. Deng, J. Bai, S. Yan, and X. Yu, “Stability control of gob-side entry retained under the gob with close distance coal seams,” *International Journal of Mining Science and Technology*, vol. 31, no. 2, pp. 321–332, 2021.
- [26] X. Ma, *Research on Key Technologies and Rock Pressure Law of 110 Mining Method with Compound Hard Roof in Tashan Coal Mine*, China University of Mining and Technology, Beijing, China, 2019.



## Research Article

# Large-Scale Model Test of a Micropile Group for Landslide Control

Xueling Liu,<sup>1</sup> Jinkai Yan ,<sup>2</sup> Lei Liu,<sup>3</sup> and Bing Han<sup>4</sup>

<sup>1</sup>School of Geological Engineering and Geomatics, Chang'an University, Xi'an 710054, China

<sup>2</sup>Chinese Academy of Geological Science, Beijing 100037, China

<sup>3</sup>Beijing City University, Beijing 100083, China

<sup>4</sup>China Institute of Geo-Environmental Monitoring, Beijing 100081, China

Correspondence should be addressed to Jinkai Yan; yanjinkaisw@163.com

Received 5 March 2021; Revised 27 March 2021; Accepted 7 April 2021; Published 23 April 2021

Academic Editor: Zhixiong Zeng

Copyright © 2021 Xueling Liu et al. This is an open access article distributed under the Creative Commons Attribution License, which permits unrestricted use, distribution, and reproduction in any medium, provided the original work is properly cited.

A large-scale model test on the interaction between a micropile group and a landslide was conducted, to investigate the effect of micropiles on the landsides prevention. The bearing mechanism, force condition, and failure mode of a micropile group for reinforcing landslide were analyzed in detail. The results showed that the thrust force over micropiles induced by landslide showed a trapezoidal distribution, with a higher Earth pressure near the sliding surface. The resistance from the sliding body behind the pile behaved in a parabolically trend. Meanwhile, the resistance force from the sliding bed was distributed unevenly along the height direction, with a higher resistance force near the sliding surface behind the pile. When a landslide occurred, micropiles were subjected to an increase in loading and displacement, eventually to the failure state. The load-bearing sections of the micropiles were all subjected to negative bending moments, with larger bending moments within the half length of pile range near the sliding surface. The maximum negative bending moment occurred at the height of seven times the diameter of the pile above the sliding surface. The damage mode along each row of micropiles was almost the same, showing a damage area within the range of three times the diameter of the pile above and below the sliding surface. The failure of micropile induced by landslides was mainly due to a combination effect of bending and shearing near the sliding surface.

## 1. Introduction

Micropiles refer to bored piles with the diameter is less than 300 mm, formed by pressure grouting after pores are drilled with strong reinforcement. Due to their convenient and rapid construction, flexible pile placement, and small disturbances to landslides, micropiles are increasingly used in landslide prevention projects [1–10]. Although micropiles have been used to prevent the landslides, the bearing mechanism of micropiles is not fully understood.

Experimental studies have been conducted on the horizontal load-bearing performance of micropiles. For example, through field tests, Zeng et al. [11] preliminarily studied the relationship between the lateral load acting on a single micropile and the required pile length. Richards et al. [12] investigated the lateral load-bearing performance of micropiles. Konagai et al. [13] carried out a detailed analysis on the performance of micropile groups with rigid caps

under lateral loading through model tests. However, the micropiles were taken as the pile foundation in the previous studies. The application of micropiles in landslide treatment remains rare and needs to be further studied. Several studies focused on the anti-sliding effect of micropiles via model test. For example, Liang [14] performed a model test and studied the ultimate flexural bearing capacity test of mini pile featuring steel tube and centered steel bar. Chen [15] presented an investigation into anti-sliding characteristics of high-pressure grouting steel-tube micropiles by model experiments. Zhang [16] carried out model tests to analyze the anti-sliding performance of multiple segmented grouting steel pile group from the aspects of soil pressure and bending of steel pipe. Grouting effect, pile group effect, and failure mode were also discussed. Hu [17] studied the stress deformation characteristics of micropile and the transmission law of a landslide through groups of experiments of different piles spacing under three rows of a micropile reinforcement

debris landslide. Although these researches provided valuable results on this area, the results were basically based on small-scale models. It is necessary to carry out large-scale model tests to study the force and deformation mechanism of micropiles under the action of landslide.

In this study, a large-scale model test regarding the interaction between landslide and micropile groups was conducted. The thrust force on a micropile induced by a landslide was monitored, along with the stress distribution and displacement of micropile. Accordingly, the bearing mechanism, force condition, and failure mode of a micropile group to reinforce a landslide were discussed in detail.

## 2. Testing Model

**2.1. Model Test Design.** A model of landslide was generated as a sliding bed and a sliding body above, which consisted of loess as shown in Figure 1. The sliding body was used to trigger the landslide by applying graded loads on the top of the slope. The micropiles were distributed along the slope foot, divided into 5 rows, a total of 23 piles. The top of micropiles was connected with a steel beam. By installing the pressure gauges in front of and behind the micropile, the variations of force on micropiles were monitored. The strain of the pile was tested using the strain gauge attached to the main reinforcement of the micropile. This value was also used to calculate the bending moment of the pile. The deformations of the micropile and the sliding body were recorded by the displacement meter installed at the top of the pile and the toe of landslide. The schematic diagram of the test model is shown in Figure 1.

**2.2. Similarity Ratio.** According to the test conditions, geometric similarity ratio  $C_L = 3$  and elastic modulus similarity ratio  $C_E = 1$  were adopted in this study. Based on the principle of similarity theory [10], the similarity ratio of physical quantities was determined as follows:  $C_q = 3$ ,  $C_P = 9$ ,  $C_\sigma = 1$ ,  $C_\epsilon = 1$ ,  $C_{Ac} = 9$ ,  $C_{As} = 9$ , where  $C_q$  denotes the similarity ratio of linear load on the pile body;  $C_P$  denotes the similarity ratio of concentrated force on the pile body;  $C_\sigma$  denotes the similarity ratio of stress of the pile body;  $C_\epsilon$  denotes the similarity ratio of strain of the pile body;  $C_{Ac}$  denotes the similarity ratio of cross-sectional area of the pile body; and  $C_{As}$  denotes the similarity ratio of cross-sectional area of reinforcement.

### 2.3. Materials

**2.3.1. Sliding Bed and Sliding Body.** Figure 2 shows the soil filling process. The slope was filled by layers of loess taken from the southern suburbs of Xi'an City. The weight of the compacted soil was  $18.3 \text{ kN/m}^3$ , and the moisture content was 15%. After layered filling, the sliding bed and sliding body were compressed to a target density. After the filling of slopes, the slope surface was made according to the designed shape, and the excess soil was removed. In order to reduce the boundary effect, three through grooves were designed in the sliding body and filled with sand.

**2.3.2. Sliding Surface.** Figure 3 depicts the photo of sliding surface. After filling the sliding bed soil, the sliding surface was made according to the shape of the designed sliding surface and double-layer plastic films were put on the sliding surface to simulate the sliding zone. On the basis of the no-pile test, we determined the load and the landslide thrust when the sliding body was in the ultimate equilibrium state using the reverse calculation:  $c = 3.5 \text{ kPa}$ , and  $\phi = 16^\circ$ .

**2.3.3. Model Pile and Connecting Beam.** Figures 4 and 5 show the precast reinforcement concrete and connecting beam of micropiles, respectively. To facilitate the burial of test instruments, the model piles used in this test were reinforced concrete prefabricated piles, and the micropiles were poured with fine aggregate concrete. The concrete strength grade was C25, and the cement strength grade was 42.5 R. The length of the pile was 4 m, the diameter of the pile was 60 mm, and the reinforcement method was  $4 \phi 6.5$ . The top of the piles was linked with the angle steel to simulate the connecting beam.

**2.4. Layout of Micropiles.** Figure 6 illustrates the layout of micropiles and pressure gauges. Five rows of micropiles were laid out with 0.5 m row spacing and 0.8 m row middle pile spacing.

### 2.5. Measurements

**2.5.1. Pressure Measurements for the Micropiles.** The pressure gauges were embedded along the piles in front of and behind piles to monitor the distribution and variation of landslide thrust of the micropiles, resistance from the sliding body behind the piles, and resistance from the sliding bed. Figure 7 depicts the position and number of pressure gauges.

**2.5.2. Strain Measurements of the Micropiles.** To test the bending moment of the micropile, strain gauges were pasted in pairs before and after the longitudinal bar of the tested piles. The spacing of the strain gauges is 10 cm. After measuring the strains of different parts of the micropile, the bending moments can be obtained by

$$M = \frac{EI(\epsilon_+ + \epsilon_-)}{h}. \quad (1)$$

In the formula,  $M$  is the bending moment,  $\text{N}\cdot\text{m}$ ;  $EI$  is the flexural rigidity of the micropile,  $\text{N}\cdot\text{m}^2$ ;  $\epsilon_+$ ,  $\epsilon_-$  are, respectively, the tensile and compressive strains of each measuring point; and  $h$  is the distance of the tensile and compressive strain gauges at the same section,  $m$ .

**2.5.3. Displacement Measurements.** The displacement gauges were placed on the top of the piles as well as at the toe of the landslide model, aiming to measure the displacement of the pile group and slope deformation.

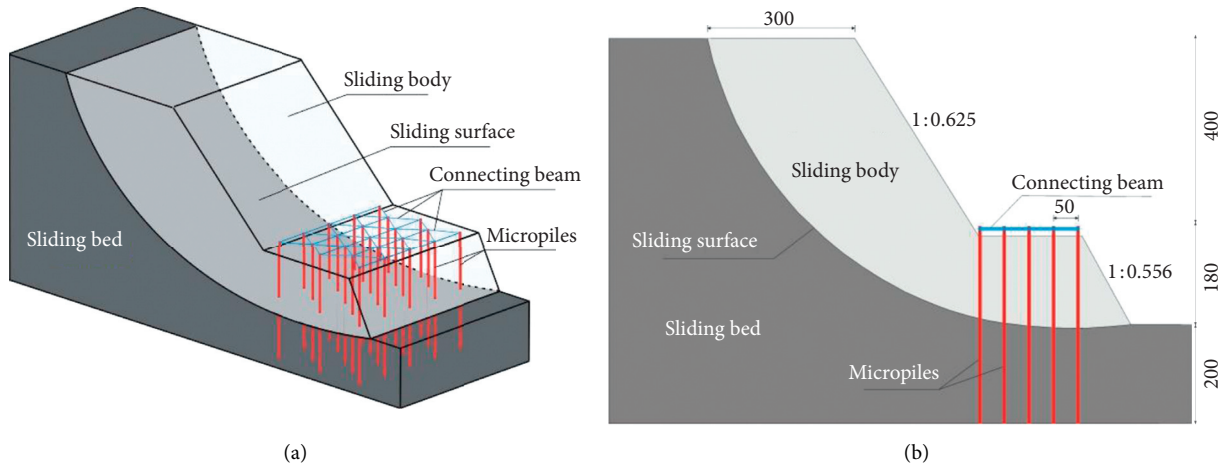


FIGURE 1: Schematic diagram of the test model. (a) Schematic diagram of the test model; (b) sectional view of the model (unit: cm).

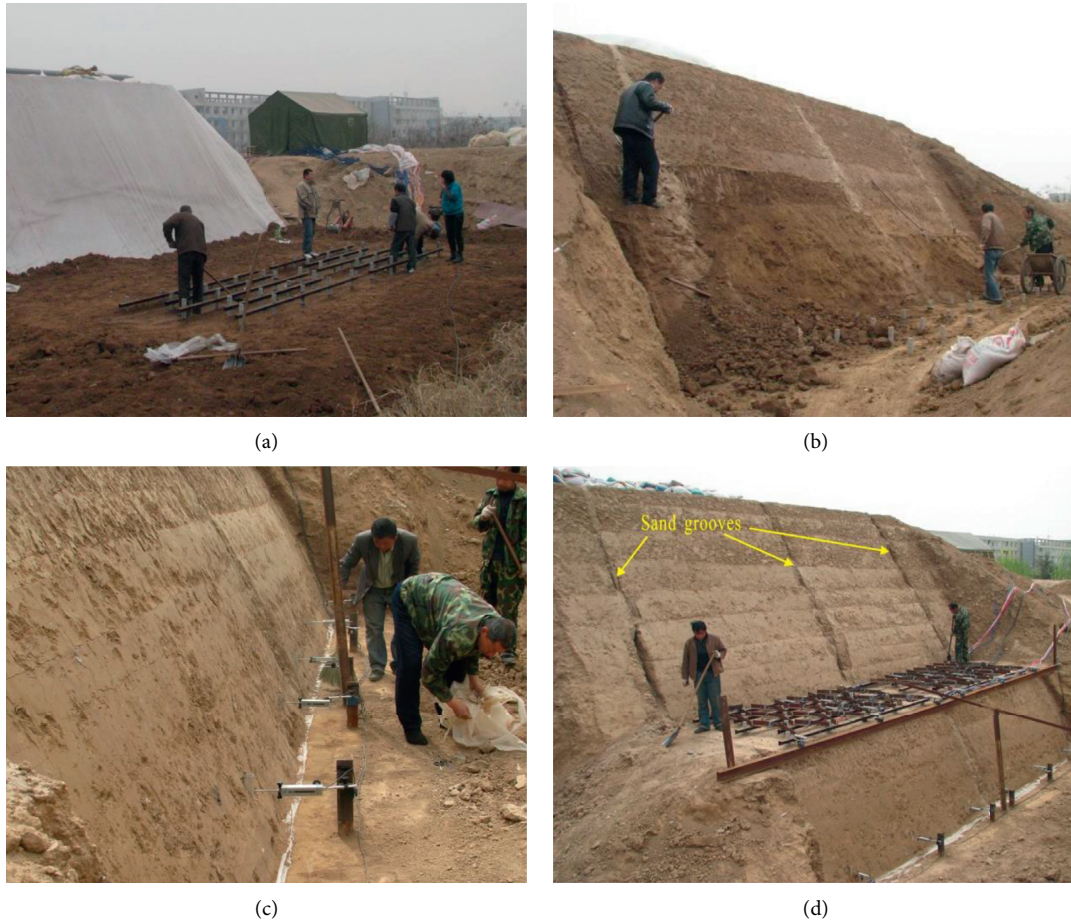


FIGURE 2: The manufacturing process of the sliding body. (a) Layered filling of soil; (b) removing excess soil; (c) excavating the landslide toe; (d) the completed test model.

2.6. *Loading Condition.* After model test was assembled and monitoring sensor was implemented, layers of sandbags used as the multi-stage loading were placed on the top of the landslide model. The photo of multi-stage loading is shown in Figure 8.

Each loading increment was 8 kPa. At each loading step, the recording of sensors was monitored [18, 19]. After reaching the stable value, the next step of load would be applied. A total of 48 kPa loads were applied in this test, as shown in Figure 8.



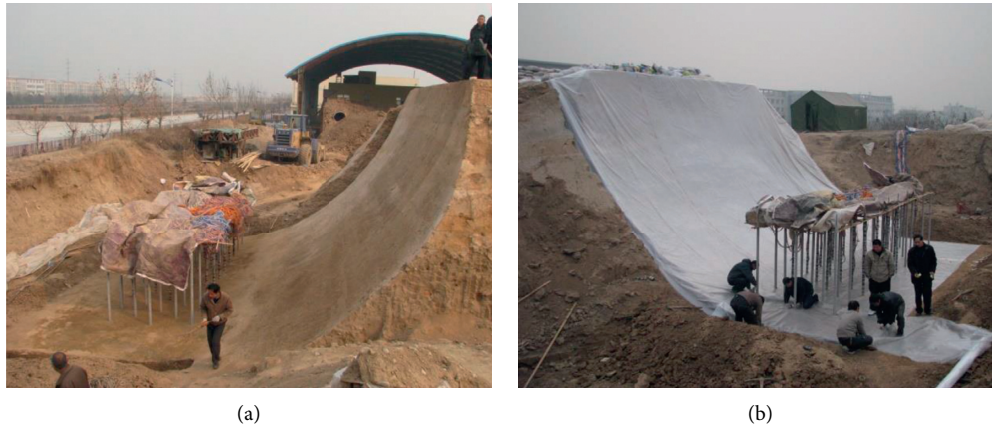


FIGURE 3: Schematic diagram of sliding surface. (a) The sliding surface; (b) double-layer plastic films were put on the sliding surface.



FIGURE 4: The precast reinforcement concrete micropiles: (a) Reinforcement; (b) micropiles.



FIGURE 5: The connecting beam on the top of micropiles.

### 3. Results and Analysis

**3.1. Failure Modes of Micropiles.** After the test, sectional excavation was conducted to observe the failure characteristic of micropile as shown in Figure 9. From the excavation section, it can be observed that the landslide completely slipped along the presupposed sliding surface

and no new fracture surface occurred. The damage zone of the micropiles in each row was almost the same. The damage zone of the pile was 12 cm under the sliding surface to 15 cm over the sliding surface. Within the range of the damage, the pile body was bent with several slanted cracks. Outside the range of the damage, the pile body was almost integrated. The load-bearing segment leaned slightly toward the front

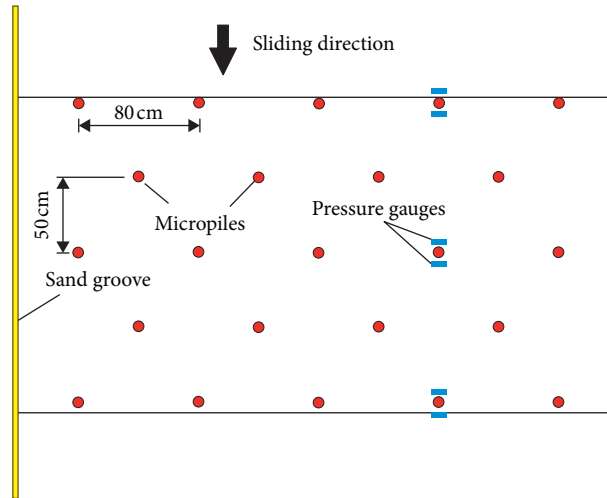


FIGURE 6: Layout of micropiles and pressure gauges (unit: cm).

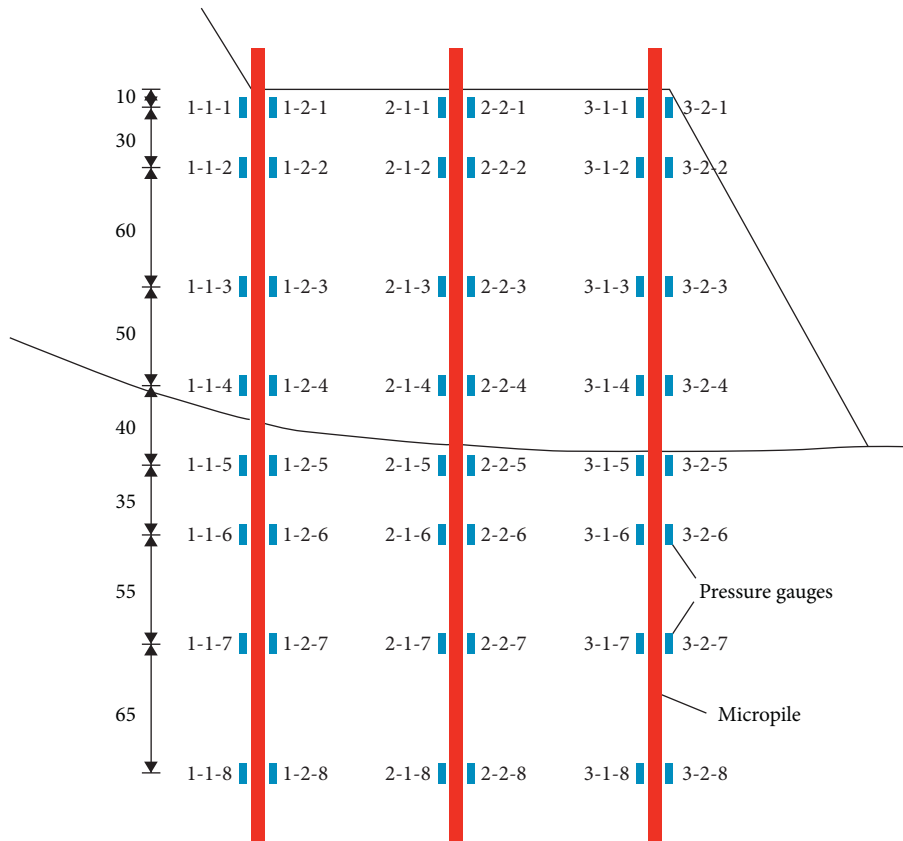


FIGURE 7: Distribution of the pressure gauges in vertical direction along the pile (unit: cm).

edge of the slide. Because of the deformation of the soil, there was a certain range of void area between the pile body around the sliding surface and surrounding soil. The void area around the sliding surface was located on the surface between the slide bed soil of the pile body and the slide bed soil behind the pile. By analyzing the damage conditions of the micropile, it was evident that the failure mode was composed of the bent and shear around the sliding surface.

**3.2. Force Condition of Micropiles.** Figure 10 shows the force distribution of the soil at each measurement point near the micropile.

Figure 11 shows the force distribution of the soil at each measurement point of the micropile. The pile section above the slipping surface was regarded as the anti-sliding segment of the pile. The pile section under the slipping surface was regarded as the anchoring section of the pile.





FIGURE 8: Multi-stage loading on the top of the landslide model.

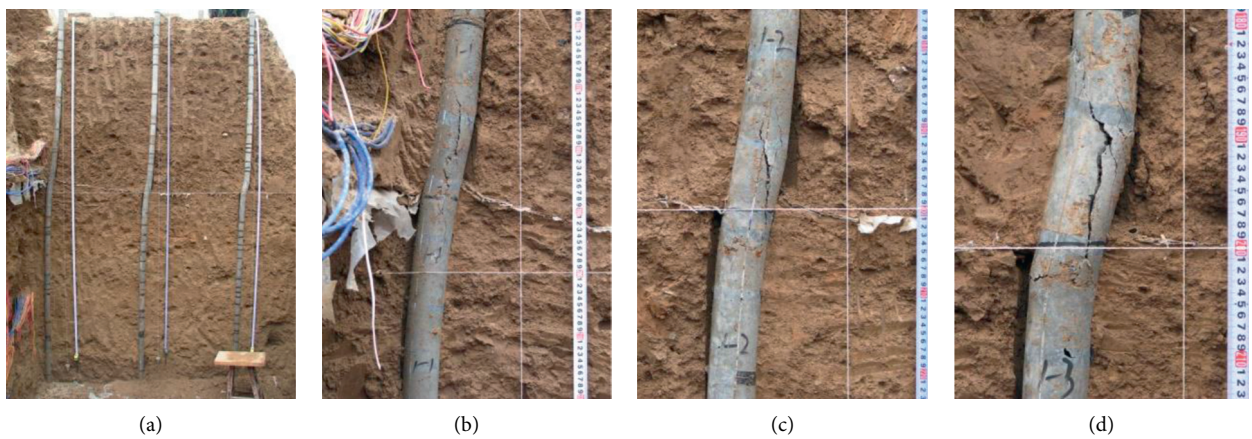


FIGURE 9: The damage of micropiles. (a) Overall damage of micropile groups; (b) breakage of the pile in first row near the slipping surface; (c) breakage of the pile in middle row near the slipping surface; (d) breakage of the pile in last row near the slipping surface.

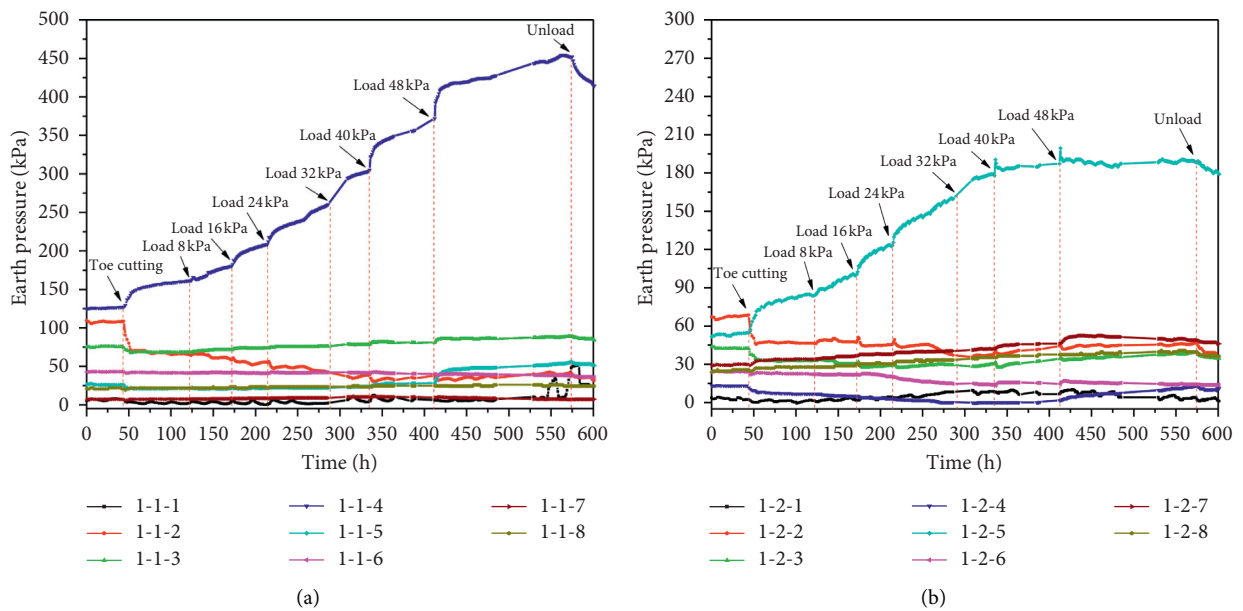


FIGURE 10: Continued.

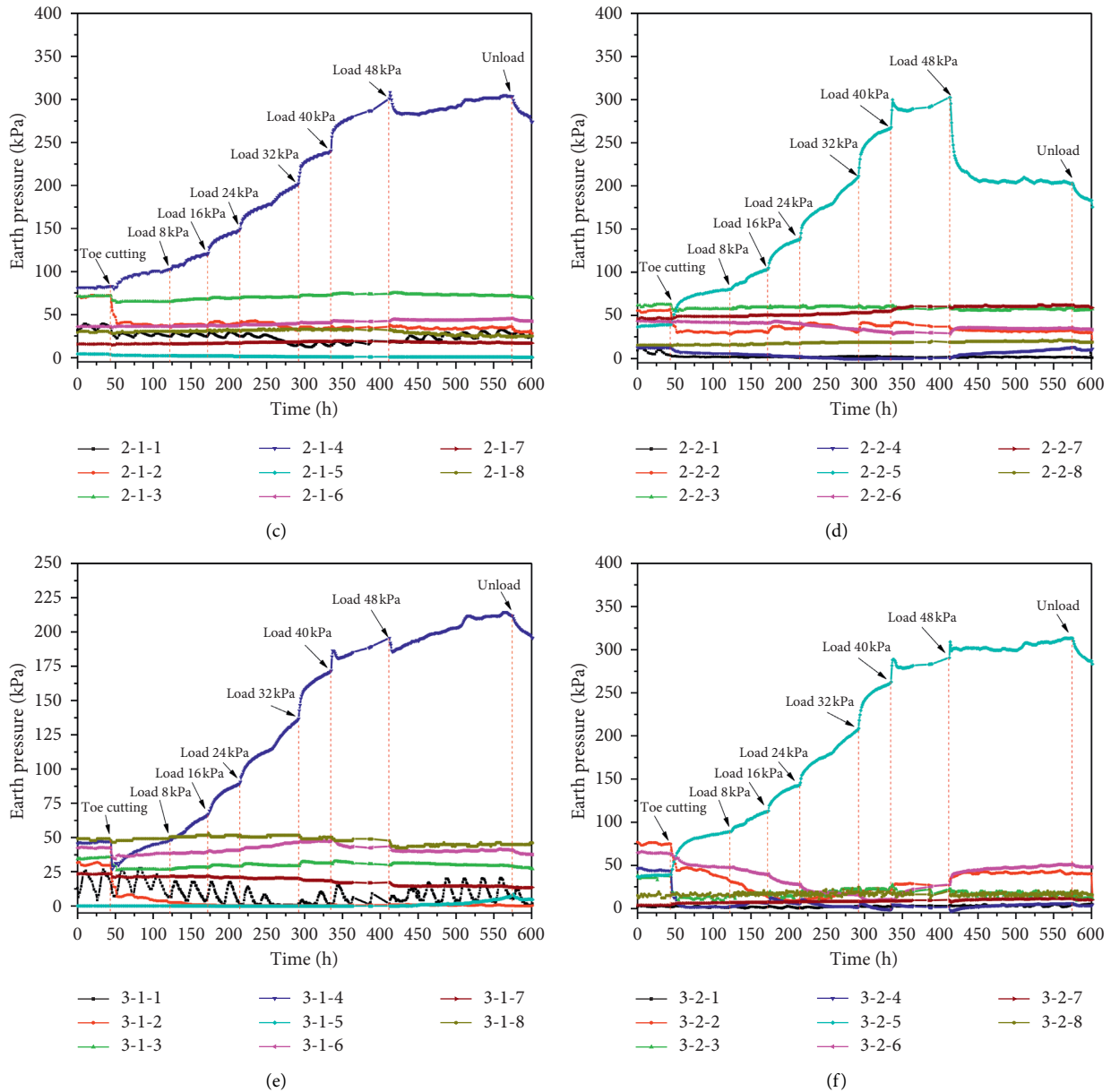


FIGURE 10: Earth pressure of micropiles. (a) Curves of earth pressure at measuring points before the pile in first row; (b) curves of earth pressure at measuring points behind the pile in first row; (c) curves of earth pressure at measuring points before the pile in middle row; (d) curves of earth pressure at measuring points behind the pile in middle row; (e) curves of earth pressure at measuring points before the pile in last row; (f) curves of earth pressure at measuring points behind the pile in last row.

**3.2.1. Distribution of the Landslide-Thrust Force of the Pile in the First Row.** Distribution of the landslide-thrust force of the pile in the first row is shown in Figures 11(a) and 12(a), including measuring points 1-1-1, 1-1-2, 1-1-3, and 1-1-4. After the filling stage, the landslide-thrust force was basically distributed in a polygonal line, which could be calculated according to trapezoid distribution in design phase. After the toe of the slope was excavated, the Earth pressure at 0.2 m over the sliding surface (1-1-4) enlarged and the Earth pressure of the other three points decreased, implying that the micropile was displaced at this time. The distribution mode of landslide thrust began to change and the point of resultant force moved close to the sliding surface. After

loading, at 0.2 m over the sliding surface (1-1-4), the Earth pressure enlarged continuously. While the Earth pressure at 0.7 m over the sliding surface (1-1-3) increased slightly, meanwhile the Earth pressure at 1.3 m over the sliding surface (1-1-2) decreased slowly. Finally, the landslide thrust was distributed approximately in a triangle shape and the Earth pressure near the sliding surface was relatively large.

**3.2.2. Resistance from the Sliding Body behind the Pile in the First Row.** Resistance from the sliding body behind the pile in the first row is shown in Figures 11(b) and 12(a), including measuring points 1-2-1, 1-2-2, 1-2-3, and 1-2-4.

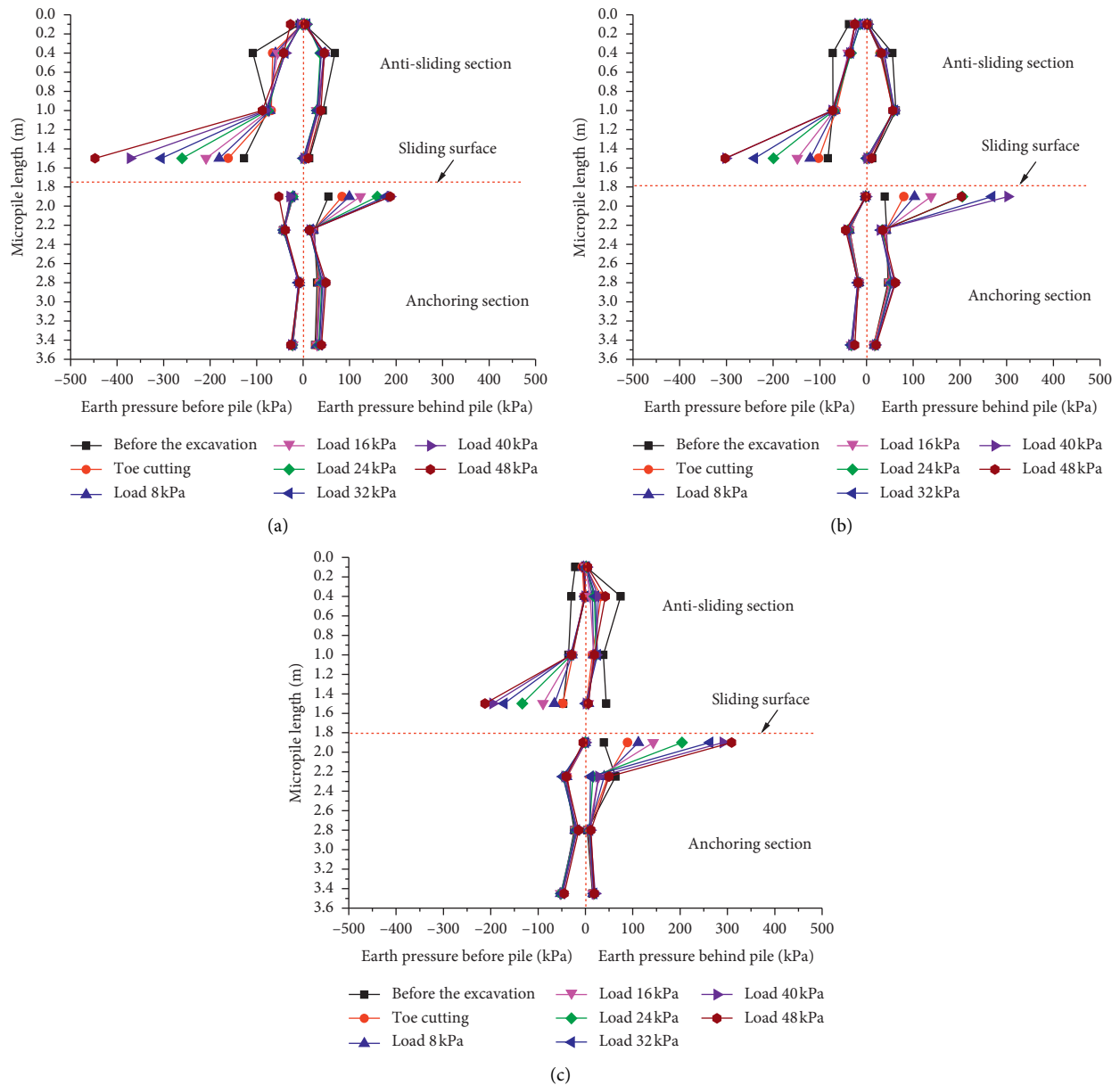


FIGURE 11: Distribution of the earth pressure on the micropiles. (a) Distribution of the earth pressure on the pile in first row; (b) distribution of the earth pressure on the pile in middle row; (c) distribution of the earth pressure on the pile in last row.

After excavating the toe of the slope, the Earth pressure of all four measurement points decreased. After loading, the Earth pressure at 0.2 m, 0.7 m, and 1.3 m over the sliding surface (1-2-4, 1-2-3, 1-2-2) kept decreasing, while loading to 40 kPa, the Earth pressure at the three points gradually grew larger. The Earth pressure at 1.6 m over the sliding surface (1-2-1) gradually enlarged in the loading process, and there were obvious fluctuations. Because this measurement point was close to the Earth surface, the fluctuation may have been related to the changing temperature. The anterior sliding mass resistance was basically distributed as a parabola.

**3.2.3. Resistance from the Sliding Bed in front of the Pile in the First Row.** Resistance from the sliding bed in front of the pile in the first row is shown in Figures 11(a) and 12(a),

including measuring points 1-1-5, 1-1-6, 1-1-7, and 1-1-8. Compared with the landslide-thrust force, the Earth pressure of each measurement point in front of the pile in the anchoring section was relatively small, and this pressure remained unchanged during the loading process. Sliding bed resistance in front of the pile was distributed in a polygonal line, which could be calculated according to rectangular distribution in design phase.

**3.2.4. Resistance from the Sliding Bed behind the Pile in the First Row.** Resistance from the sliding bed behind the pile in the first row is shown in Figures 11(b) and 12(a), including measuring points 1-2-5, 1-2-6, 1-2-7, and 1-2-8. Before completion of model filling and excavation of the slope foot, Earth pressures at each measurement point under the sliding

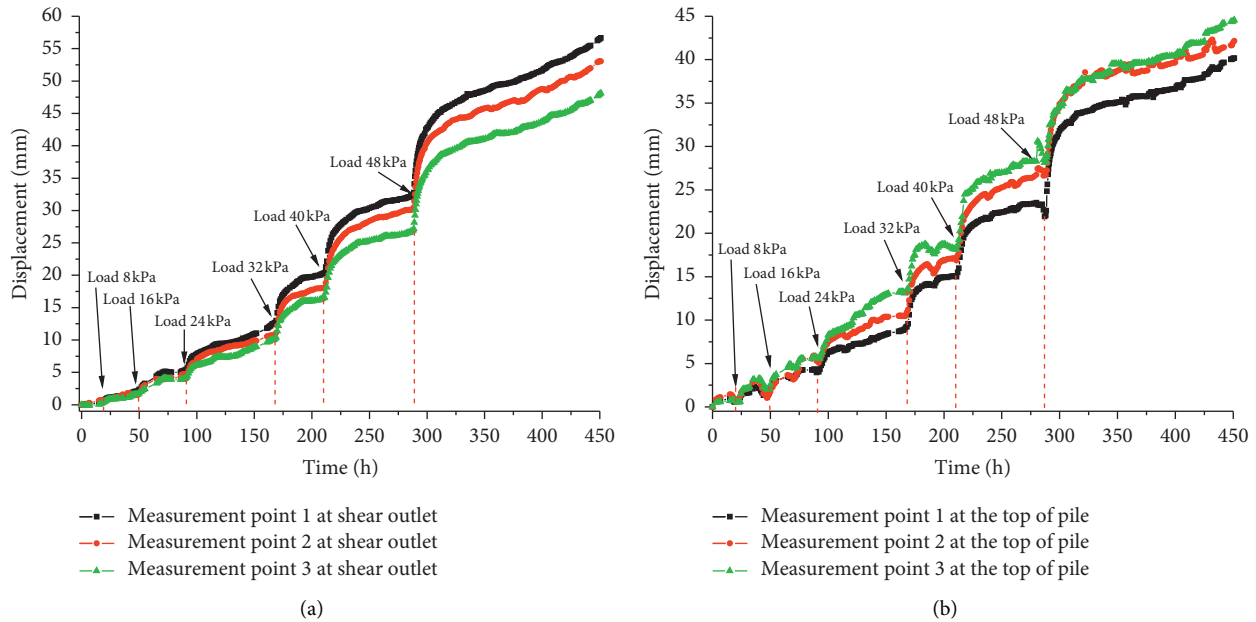


FIGURE 12: Displacement variation at the monitoring points. (a) Displacement curve at the toe of landslide; (b) displacement curve at the top of pile.

surface were basically equal, and resistance of the sliding bed behind the pile was distributed in a rectangular shape. Earth pressure at 0.2 m below the sliding surface (1-2-5) increased after the slope foot was excavated, and the Earth pressure at the remaining three measurement points under the sliding surface basically remained unchanged, indicating that the pile body in a certain range under the sliding surface deflected and squeezed the posterior soil body of the sliding bed. After the loading was applied, the Earth pressure at 0.2 m below the sliding surface continued to increase until the loading reached 40 kPa and then it began to be stable basically. The Earth pressure at other three measurement points was small relatively. The resistance from the sliding bed behind the pile was concentrated mainly near the sliding surface.

As shown in Figures 11 and 12, the piles in the middle row and last row behaved in a similar way to that of the pile in the first row. This distribution can be summarized as follows:

- (1) The landslide thrust of the micropiles was in an approximate trapezoid distribution, and the Earth pressure near the sliding surface was larger.
- (2) The landslide thrust of the first row of piles along the sliding direction was large, and the landslide thrusts of the remaining rows reduced successively.
- (3) The distribution of the resistance from sliding body behind the pile was basically parabolically distributed. The Earth pressure near the sliding surface and the pile top was small and the Earth pressure in the middle part of the landslide was large.
- (4) The resistance from the anterior sliding bed of the micropiles was small and changed little during the loading process. It was in a polygonal line

distribution and could be calculated as rectangular distribution in design.

- (5) In the early stage, the resistance from the posterior sliding bed was in a polygonal line or rectangular distribution. After loading, the Earth pressure near the sliding surface varied greatly, whereas the Earth pressure at the other measurement points varied slightly and resistance from anterior sliding bed was distributed mainly near the sliding surface.
- (6) The force variations of micropiles demonstrated good timeliness. Force was applied to the three rows of micropiles at the same time, and displacement and damage occurred simultaneously.

**3.3. Variation of Displacement at Measurement Points.** Figure 12 shows the displacement evolution during loading. The displacement at the top of pile and the shear outlet of landslide increased slowly in the early stage of loading. After the loading reached 32 kPa, the displacement of each measurement point increased rapidly. Hence, the pile entered a critical state when loading reached 32 kPa. Up to 40 kPa, the displacement at the top of micropiles was about 15 mm, corresponding to the failure stage.

Comparing Earth pressure variation and displacement evaluation, the results were consistent, showing the pile was damaged after 40 kPa loading.

**3.4. Bending Moment of Pile Body.** Based on strain gauge data, the bending moment distribution of each row of piles was obtained as shown in Figure 13.

Although the bending moments of each row of piles were slightly different, the variation mode along the pile was the

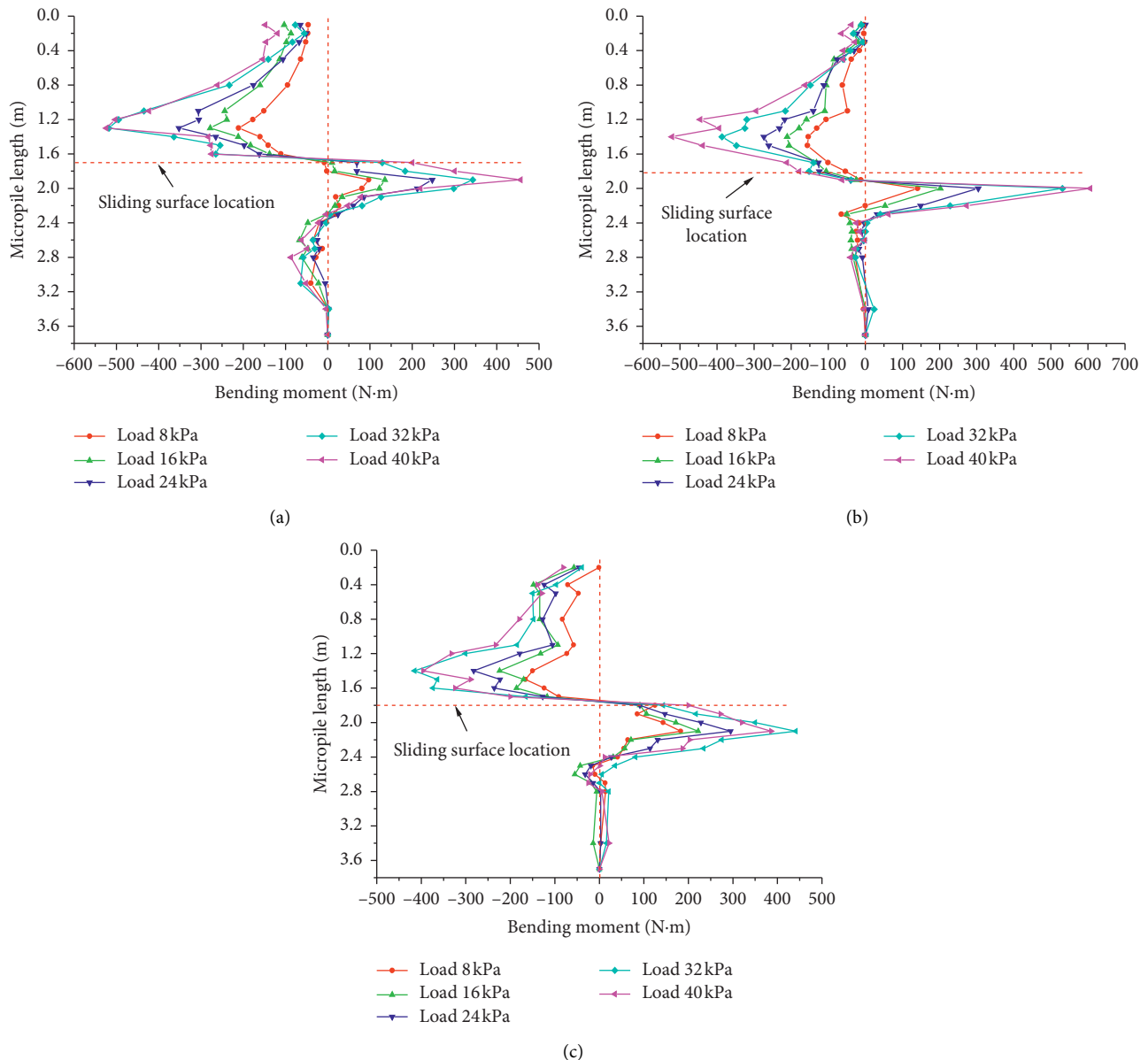


FIGURE 13: Bending moment of micropiles. (a) Bending moment of the pile in first row; (b) bending moment of the pile in middle row; (c) bending moment of the pile in last row.

same. The load-bearing sections of the pile body were all subjected to negative bending moments (positive tension on the sliding side and negative tension on the back side) and were distributed mainly within the pile length range of half of the load-bearing section on the sliding surface. The maximum negative bending moment was at 0.4 m above the sliding surface (about seven times the diameter of the pile). The pile body of the embedded section located in the range of 0.6 m below the sliding surface was subjected to a positive bending moment. The maximum positive bending moment occurred at 0.3 m below the sliding surface (five times the diameter of the pile). The pile body from 0.6 m below the sliding surface to the bottom of the pile was subjected to a negative bending moment, with a small magnitude. After loading, the bending moments of the load-bearing section and the embedded section increased

simultaneously, indicating that the load-bearing section and the embedded section of the micropiles deformed simultaneously.

#### 4. Conclusion

A large-scale model test was performed to simulate the interaction between the micropile group and landslide. The loading-induced deformation characteristics of the micropile group under the action of a landslide were investigated. The results provide a reference for the design of a micropile group preventing the landslide. The main conclusions can be drawn as follows:

- (1) When the landslide occurred, the micropiles at different rows were subjected to loads



simultaneously. Consequently, the displacement and the damage occurred simultaneously. The force distribution of micropiles of each row was basically the same.

- (2) The landslide thrust of micropiles was generally in a triangle distribution, with a larger Earth pressure near the sliding surface. The resistance from the sliding body behind the pile was parabolically distributed. The larger resistance was observed from the sliding bed behind the pile to the area near the sliding surface.
- (3) The load-bearing sections were all subjected to negative bending moments. The maximum negative bending moment occurred at a place seven times the diameter of the pile above the sliding surface. The pile body of the embedded section in the range of 0.6 m (10 times the diameter of the pile) below the sliding surface was subjected to a positive bending moment, with a maximum value at five times the diameter of the pile below the sliding surface.
- (4) The damage condition of each row of micropiles was basically the same. The damage area was within the range of three times the diameter of pile above and below the sliding surface each. The failure mode was a combination of effect of bending and shearing near the sliding surface.

## Data Availability

The data used to support the findings of this study are included within the article.

## Conflicts of Interest

The authors declare no conflicts of interest.

## Authors' Contributions

Xueling Liu and Jinkai Yan analyzed, wrote, and dealt with data; Jinkai Yan and Lei Liu conducted the model test; Bing Han modified the formats. All authors have read and agreed to the published version of the manuscript.

## Acknowledgments

The authors thank the funding agencies that supported this research. This work was supported by China Geological Survey Project (Grant nos. 1212010814016 and DD20190287) and the Fundamental Research Funds for the Chinese Academy of Geological Science (no. JKY201909).

## References

- [1] F. Lizzi, *Reticulated Root Piles to Correct Landslides*, ASCE Convention, Chicago, IL, USA, 1978.
- [2] R. Cantoni, T. Collotta, and V. Ghionna, "A design method for reticulated micropiles structure in sliding slopes," *Ground Engineering*, vol. 22, no. 4, pp. 41–47, 1989.
- [3] S. L. Pearlman, B. D. Campbell, and J. L. Withiam, "Slope stabilization using in-situ earth reinforcement," in *Proceedings of a Special Conference on Stability and Performance of Slopes and Embankment*, Berkeley, CA, USA, July 1992.
- [4] I. Juran, A. Benslimane, and D. A. Bruce, "Slope stabilization by micropile reinforcement," *Landslides*, vol. 5, pp. 1718–1726, 1996.
- [5] J. E. Loehr, J. J. Bowders, and J. W. Owen, "Slope stabilization with recycled plastic pins," *Transportation Research Record: Journal of the Transportation Research Board*, vol. 1714, no. 1, pp. 1–8.
- [6] B. LiewSommers, R. Mario, and A. Nadir, "Design and construction of a micropile wall to stabilize a railway embankment," in *Proceedings of the Deep Foundations Institute Annual Conference on Deep Foundations: Emerging Technologies*, Vancouver, British Columbia, Canada, October 2004.
- [7] L. L. Zeng, X. Bian, L. Zhao, Y. J. Wang, and Z. S. Hong, "Effect of phosphogypsum on physiochemical and mechanical behaviour of cement stabilized dredged soil from Fuzhou, China," *Geomechanics for Energy and the Environment*, vol. 25, Article ID 100195, 2021.
- [8] X. Bian, L. L. Zeng, X. Z. Li, X. S. Shi, S. M. Zhou, and F. Q. Li, "Fabric changes induced by super-absorbent polymer on cement and lime stabilized excavated clayey soil," *Journal of Rock Mechanics and Geotechnical Engineering*.
- [9] X. Bian, J. K. Yan, and W. Zhang, "Observed performance of highway embankment over soft marine clay: a case study in Wenzhou, China," *Advances in Civil Engineering*, vol. 2020, Article ID 8813832, 2020.
- [10] Y. B. Zhou, X. H. He, and M. Ma, "Study on the application of micro-group piles in highway cutting," *Journal of Anhui Jianzhu University*, vol. 26, no. 4, pp. 45–52, 2018.
- [11] L.-L. Zeng, Z.-S. Hong, and Y.-J. Cui, "On the volumetric strain-time curve patterns of dredged clays during primary consolidation," *Géotechnique*, vol. 65, no. 12, pp. 1023–1028, 2015.
- [12] J. R. Richards, D. Thomas, and J. Rothbauer Mark, "Lateral loads on pin piles (micropiles)," in *Proceedings of Sessions of the Geosupport Conference: Innovation and Cooperation in Geo*, Reston, VA, USA, January 2004.
- [13] K. Konagai, Y. Yin, and Y. Muroto, "Single beam analogy for describing soil-pile group interaction," *Soil Dynamics and Earthquake Engineering*, vol. 23, no. 3, pp. 31–39, 2003.
- [14] Z. Y. Liang, J. Y. Rao, Z. Q. Chen et al., "Study on ultimate flexural bearing capacity of mini pile featuring steel tube and centered steel bar," *Railway Engineering*, vol. 58, no. 11, pp. 99–102, 2018.
- [15] H. Chen, Y. F. Zhang, X. M. Zhang et al., "Full-scale model experiments on anti-sliding characteristics of high-pressure grouting steel-tube micropiles," *Rock and Soil Mechanics*, vol. 41, no. 2, pp. 428–436, 2020.
- [16] Y. F. Zhang, S. W. Wei, W. J. Zhou et al., "Model test study on anti-sliding behaviours of multiple segmented grouting steel pile group structure," *Chinese Journal of Rock Mechanics and Engineering*, vol. 38, no. 5, pp. 982–992, 2019.
- [17] S. Y. Hu, Q. Cai, and C. J. Li, "A study of the physical model test of debris landslide reinforcement with three row micropiles," *Hydrogeology & Engineering Geology*, vol. 45, no. 3, pp. 56–62, 2018.
- [18] X. Bian, Y.-J. Cui, L.-L. Zeng, and X.-Z. Li, "State of compacted bentonite inside a fractured granite cylinder after infiltration," *Applied Clay Science*, vol. 186, p. 105438, 2020.
- [19] X. Bian, Y.-J. Cui, and X.-Z. Li, "Voids effect on the swelling behaviour of compacted bentonite," *Géotechnique*, vol. 69, no. 7, pp. 593–605, 2019.

## Research Article

# Risk Early Warning Evaluation of Coal Mine Water Inrush Based on Complex Network and Its Application

Yanhui Li <sup>1,2</sup>, Jianbiao Bai <sup>2,3</sup>, Wei Yan <sup>4</sup>, Xiangyu Wang <sup>1,2</sup>, Bowen Wu <sup>1,2</sup>,  
Shuaigang Liu <sup>1,2</sup>, Jun Xu,<sup>5</sup> and Jiaxin Sun<sup>6</sup>

<sup>1</sup>School of Mines, China University of Mining & Technology, Xuzhou 221116, China

<sup>2</sup>State Key Laboratory of Coal Resources and Safe Mining, Xuzhou 221116, China

<sup>3</sup>College of Mining Engineering and Geology, Xinjiang Institute of Engineering, Urumqi 830023, China

<sup>4</sup>College of Energy and Mining Engineering, Shandong University of Science and Technology, Qingdao 266590, China

<sup>5</sup>School of Science, Yangzhou Polytechnic Institute, Yangzhou 225127, China

<sup>6</sup>Xuzhou Construction Machinery Co.,Ltd, Xuzhou 221000, China

Correspondence should be addressed to Jianbiao Bai; [baijianbiao@cumt.edu.cn](mailto:baijianbiao@cumt.edu.cn)

Received 20 March 2021; Revised 2 April 2021; Accepted 13 April 2021; Published 23 April 2021

Academic Editor: Xianjie Hao

Copyright © 2021 Yanhui Li et al. This is an open access article distributed under the Creative Commons Attribution License, which permits unrestricted use, distribution, and reproduction in any medium, provided the original work is properly cited.

As one of the five major coal mine disasters, the water inrush disaster poses a serious threat to the safety of the country and people, so the prevention work for that becomes very important. However, there is no perfect assessment system that can better solve the complex dependence relationships among disaster-causing factors of water inrush disasters. This study applied the knowledge of Complex Networks to research water inrush disaster, and based on that, the early warning evaluation system that combined ANP and Cloud model was established in order to solve the complex dependence problem and prevent the occurrence of water inrush. Moreover, this evaluation model was applied to the example Y coal mine to verify its superiority and feasibility. The results showed that the main cloud of goal was located at the yellow-strong warning level, and the first-level indicators were, respectively, at that the yellow-strong level of mining conditions, the yellow-strong warning level of hydrological factors, between the yellow-strong warning level and purple-general level of the geological structure, and among the blue-slightly weak warning level, purple-general level, and yellow-strong level of the human factor. The prediction results were consistent with the actual situation of the coal water inrush disaster in Y mine, which further proved that this early warning evaluation model is reliable. In response to the forecast results, the authors put forward relative improvements necessary to strengthen the prevention ability to disaster-causing factors among hydrological factors, mining conditions, and geological structure, which should comprehensively increase knowledge, technology, and management of workers to avoid leaving out disaster-causing factors. Meanwhile, the warning evaluation model also provides the relevant experience basis for other types of early warning assessment networks.

## 1. Introduction

With the rapid development of the Chinese market economy, the utilization rate of primary energy has generally increased. For example, the reserves of coal are about 90% [1–4]. Moreover, the usage amount of coal can still occupy an important position in future modern production. The most important mining method in China is underground mining [5–8]. Its advantages are large mining volume and wide mining range [9–11]. There are also many unsafe

factors, such as water inrush disasters. It is one of the most important five disasters in a coal mine. It is a water accident that occurred suddenly during the production process. The characteristics of water inrush disasters are rapid development and wide coverage [12]. Since the 1980s, more than 250 mines across the country have been flooded with more than 1700 deaths and economic losses of over 35 billion yuan [13, 14].

Therefore, the early warning work of coal mine water inrush is very important. Since the early 20th century,

scholars at home and abroad have already started exploring and researching this area. With the rapid development of computer technology, the different scientific systems have been merged to form many prediction methods for water inrush disasters. Yang et al. established the risk assessment model of floor water inrush through the GA-BP network model [15]. Wang used MATLAB to build a model for predicting the depth of floor damage [16]. Wang et al. proposed the risk assessment model of coal mine water inrush disaster based on a dynamic tree [17]. Qin et al. used D-S theory to evaluate the risk degree of coal mine water inrush disaster [18]. Wang et al. proposed the evaluation method of the accident tree model in coal mine water inrush disaster [19].

Water inrush disaster is a complex nonlinear problem [20, 21]. Its disaster-causing factors can interact with each other. Only by determining the relationship between disaster-causing factors can we better prepare for early warning assessment. The research status at home and abroad is still in the blank research stage on a complex relationship between disaster-causing factors. In addition, there is no study on using the Complex Network method combined with ANP and Cloud model to measure the important influencing factors of water inrush disaster. This study uses Complex Network model for the first time to deal with complex relationship problems between disaster-causing factors of water inrush to prevent the occurrence of water inrush disaster in coal mine. We also used ANP combined with Cloud model to calculate the early warning level of each factor accurately. Moreover, this study also offers a theoretical basis and practical guiding significance for other coal mines on the early warning work to water inrush disaster.

## 2. Theoretical Basis

### 2.1. Complex Network

**2.1.1. Composition of the Complex Network Model.** The Complex Network model is composed of nodes and connected edges [22, 23]. Each independent node in the network represents a disaster-causing factor. The impact of nodes on the occurrence, development, and results of disasters are clarified. The connected edges can reflect the connection relationship between all nodes in the network. If a certain factor can cause a new disaster to occur, a connected edge will be formed.

The connected edges include a single route and multiple route [24]. Single disaster route refers to factor A causing factor B to change, and thus, factor B can cause factor C to change. On the other hand, a multiple disaster route refers to factors A and B together causing factor C to change catastrophically. When the disaster-causing factors interact and feed back each other leading to the occurrence of disaster results, a multiple disaster route will be formed. It can produce a catastrophe that is quite complex and difficult to prevent. Moreover, combining all multiple disaster routes can form a Complex Network model.

**2.1.2. Expression of the Complex Network Model.** The Complex Network model is defined in the form of graph theory [25]. We can set up  $G = (V, E)$ , where  $V$  is the set of all nodes ( $V = \{v_1, v_2, \dots, v_n\}$ );  $E$  is the set of all connected edges ( $E = \{e_1, e_2, \dots, e_n\}$ ). Moreover, each edge can connect two different nodes expressed as  $e_{ij} = \{v_i, v_j\}$ . If  $e_{ij} = e_{ji}$ , it will mean that this network is undirected. Otherwise, the network is directed.

The method of recording a Complex Network is by constructing an adjacent matrix. If a connected edge between any two nodes exists, it will be recorded as 1 in an adjacent matrix; otherwise, it will be recorded as 0. The adjacent list is one of the most common ways to store the content of a Complex Network. It consists of many sets of numbers. There are two numbers in each row in the adjacent list, which represent two different numbered nodes. Moreover, the space between two numbers indicates that a connected relationship exists. Therefore, the adjacent matrix and adjacent list are interdependent, as shown in Figure 1.

### 2.2. ANP and the Cloud Model

**2.2.1. ANP.** Analytic Network Hierarchy Process (ANP) is a comprehensive and multiple objective decision-making method based on AHP, proposed by T. L. Saaty in 1996 [26, 27]. Its application range is very wide. It not only inherits the hierarchical characteristics from AHP but also considers nonindependent relationships such as feedback and dependence among internal elements [28, 29]. Therefore, ANP is more realistic than AHP.

Water inrush disaster is a Complex Network problem. There are many interdependent and feedback decision elements. Therefore, using ANP to calculate the weights of all elements in a water inrush disaster network can better solve the actual prevention problems.

**2.2.2. Cloud Model.** In 1995, academician D. Y. Li proposed the Cloud model concept based on the limitations of probability theory and fuzzy mathematics on the analysis of uncertainty problems [30], using three feature numbers to represent the ambiguity and randomness of the Cloud model. It can intuitively reflect the mathematical mapping of qualitative language [31, 32]. So far, it has been widely used in data analysis, decision judgment, intelligent control, and other fields [33, 34].

The three characteristic numbers of the Cloud model are Ex (Expected Value), En (Entropy), and He (Hyperentropy), which are expressed as C (Ex, En, He). Ex is the expectation of cloud drop  $x$  distributed in the domain  $U$ , which can reflect the central location of the Cloud model. En is the entropy of Ex that can represent the span and dispersed degree of Cloud model. He is the entropy of En, which can determine the thickness of cloud. The larger He indicates that the cloud image is more dispersed and larger in thickness.

$U$  is set to be the precise quantitative domain.  $C$  is a qualitative language in  $U$ . If the quantitative value  $x \in U$  and  $x$  is a random quantitative realization of  $C$ , then  $\mu(x)$  will be

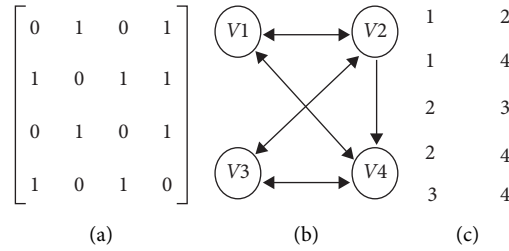


FIGURE 1: The nodes relationship of Complex Network for (a) adjacent matrix; (b) connected relationship; (c) adjacent list.

the certainty of  $x$  to  $C$ , which is a stable random number in  $[0, 1]$ . That is expressed as  $\mu:U \rightarrow [0, 1]$ . There are  $x \in U$  and  $x \rightarrow \mu(x)$ . All distribution forms of  $x$  on  $U$  are called clouds. Each  $x$  is a cloud drop [35].

The Cloud Generator is an algorithm to realize the mutual conversion between qualitative and quantitative in Cloud model [36]. It is also one of the most important steps in the uncertainty reasoning process in the entire Cloud model. It includes two types: Forward Cloud Generator and

Backward Cloud Generator. Forward Cloud Generator is the process of converting qualitative indicators into quantitative data. It is based on cloud numbers to form a cloud image, as shown in Figure 2(a). Backward Cloud Generator is to convert quantitative data into qualitative indicators, which can convert precise numerical values into cloud numbers, as shown in Figure 2(b). The calculation formulas of cloud numbers are as in

$$\left\{ \begin{array}{l} \text{Ex} = \bar{x} = \frac{1}{n} \sum_{i=1}^n x_i, \text{En} = \sqrt{\frac{\pi}{2}} \times \frac{1}{n} \sum_{i=1}^n |x_i - \text{Ex}|, \text{He} = \sqrt{S^2 - \text{En}^2} = \left[ \frac{1}{n-1} \sum (x_i - \bar{x})^2 - \text{En}^2 \right]^{1/2}. \end{array} \right. \quad (1)$$

### 3. Constructing the Complex Network Model

**3.1. Structural Analysis.** Through collecting a large amount of data of water inrush disaster from related papers and websites, we drew the network relationship of water inrush disaster, as shown in Figure 3. We can get the most important disaster-causing factors of coal mine water inrush disasters from all countries. It can provide a corresponding experience basis for the analysis of a specific coal mine water inrush disaster. There are 161 nodes and 149 connected edges in Figure 3. Nodes represent the disaster-causing factors and a connected edge indicates that there is a mutually influential relationship between two nodes.

The nodes with fewer connection relationships to other nodes in Figure 3 are all distributed on the outermost side of network. However, the nodes frequently influence other nodes that are located in the center of the network. In addition, all connected edges are directional. If the arrow points from node  $x$  to  $y$ , then it will mean that node  $x$  can cause catastrophe to node  $y$ , which is recorded as  $e_{xy}$ .

**3.2. Analysis of Topological Characteristics.** Topological characteristics are unique attributes of the Complex Network model [37]. By analyzing them, we can better understand the structure of the Complex Network model.

**3.2.1. Degree Centrality.** Degree centrality is a measured method to the importance of nodes, which includes in-degree and out-degree. Out-degree is from a certain node pointing to other nodes. The nodes with larger out-degree values are the

main factors leading to water inrush disasters. For example, the out-degree value of dynamic water pressure is 9, which indicates the dynamic water pressure can cause 9 nodes to be catastrophic. In-degree is directed by other nodes to a certain node. The factors with a larger in-degree value are the root cause of water inrush disaster.

However, there is not existing any relationship between out-degree and in-degree. A node with a larger out-degree value may not necessarily have a larger in-degree value. Therefore, when considering the degree centrality of the node, the out-degree and in-degree should be comprehensively analyzed.

**3.2.2. Closeness Centrality.** The closeness centrality of a node represents the distance to other nodes. The greater the closeness centrality of a node, the closer the distance to other nodes. For example, in shipping logistics network, if you need to select a transit center that is closer to all logistics points, you should select the node with the greatest closeness centrality [38, 39].

In the network of water inrush disaster, there are 102 nodes with closeness centrality not less than 1. It shows that the distances between nodes in the entire network are relatively closer. Moreover, it is more convenient for each node to influence others. In the network, the closeness centrality of coal body cementation degree is the largest, which is 2.125. It indicates that the coal body cementation degree is closest to other nodes in the entire network and it is easiest to activate other disaster-causing nodes.

**3.2.3. Intermediary Centrality.** The greater the intermediary centrality of a node, the larger the possibility of being a

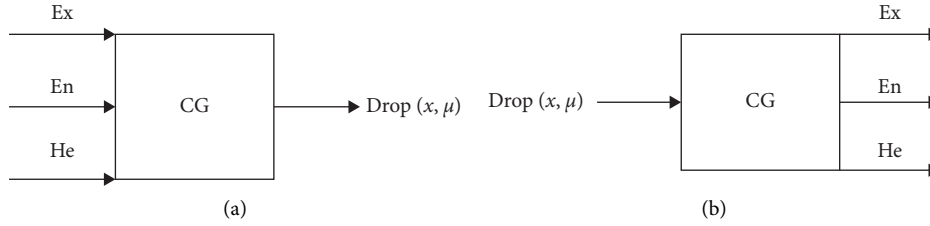


FIGURE 2: Cloud model generator. (a) Forward Cloud Generator and (b) Backward Cloud Generator.



FIGURE 3: Complex Network model diagram of the coal mine water inrush disaster.

transit center. If this transit node suddenly disappears, it will have a certain impact on the connected relationship between other nodes, making it difficult to spread the information between nodes and even paralyzing the entire network. In the network, the intermediary centrality of dynamic water pressure is the largest, with a value of 9. It shows that dynamic water pressure is the most important “transit center” in the entire network.

**3.2.4. Eigenvector Centrality.** Eigenvector centrality is an extended feature of degree centrality. Its main idea is that the importance of a node depends not only on the degree value but also on the characteristics of neighboring nodes. In the network, apart from the eigenvector centrality of the water inrush volume that is 1, others are less than 1. Therefore, the nodes adjacent to the water inrush volume are the most important in the entire network. In addition, the degree value of coal seam thickness is the largest, being 14, but its eigenvector centrality is not the largest.

**3.2.5. Selecting Important Disaster-Causing Nodes.** By analyzing the topological characteristics, understanding of the nature and overall structure of network has deepened. According to the requirements of different topological characteristics, the most important nodes are selected, as shown in Table 1.

#### 4. Construction of the ANP-Cloud Evaluation Model

Based on the Complex Network model of coal mine water inrush disasters, the “ANP-Cloud” early warning evaluation system was established in this article. The implementation steps are described in detail as follows.

**4.1. Establishing the Index System.** The constructed index system should meet comprehensiveness and scientificity. It takes the “coal mine water inrush disaster decision system” as the overall goal. Moreover, it divides 161 nodes obtained from the Complex Network model into four first-level



TABLE 1: The most important multiple nodes.

Nodes	Degree centrality	Closeness centrality	Intermediary centrality	Eigenvector centrality
Coal seam thickness	14	1	1	0.333150175
Depth of mining floor failure	12	0	3	0.285557293
Coal seam burial depth	9	1	2	0.21416797
Working surface length	6	1	0	0.630880426
Key position of the water barrier	8	0	1	0.190371529
Karst collapse column	5	0	6	0.320266341
Water inrush volume	1	0	1	1
Fault	5	0	3	0.231522494
Aquifer	3	0	2	0.559491103
Mining depth	3	1.333	0	0.183929612
Water barrier thickness	4	1	0	0.095185764
Karst fissure development degree	1	1.9	1	0.511898221
Dynamic water pressure	10	1	9	0.023796441
Collapse column	3	1	6	0.071389323
Ordovician water channel	2	0	1	0.160133171
Mining methods and processes	3	1.2	0	0.071389323
Reduce the strength of fractured rock mass	1	0	2	0.13633673
Complex geological conditions	2	1	1	0.047592882
Folds	3	1.6	5	0.023796441
Hidden troubles are not in place	1	1	0	0
Illegal production	1	1	1	0
Production organization management chaos	1	1	0	0
Production technology management chaos	1	1	2	0

indicators: geological structure, hydrological factors, mining conditions, and human factors. Then, the first-level indicators are correspondingly divided into the second-level indicators. According to the research requirements, the top 23 important second-level indicators are selected, as shown in Figure 4.

#### 4.2. Index Weights Based on ANP

**4.2.1. Constructing the ANP Model.** The ANP model is consists of a control layer and a network layer [40]. The control layer includes goal and dimensions and the control layer is a decision-making system for coal mine water inrush disaster. The goal is the final purpose of the system decision and dimensions are the first-level indicators whose numbers need to be set according to the specific model. It is affected by the next layer of factors. The four dimensions of mining conditions, hydrological factors, geological structure, and human factors are set as U1, U2, U3, and U4, respectively.

Factors of network layer contain the second-level indicators from Complex Network. The relationships of mutual feedback and dependence between the second-level indicators form a network system, as in Figure 5. The second-level indicators were, respectively, expressed as U1i ( $i = 1, 2, 3, 4, 5, 6$ ), U2i ( $i = 1, 2, 3, 4, 5, 6$ ), U3i ( $i = 1, 2, 3, 4, 5, 6$ ), and U4i ( $i = 1, 2, 3, 4, 5$ ).

**4.2.2. Calculating Weights.** The weights calculated process in ANP are extremely complicated. Thus, it is based on Super Decisions (SD) software for scientific weights calculation in this article [41]. It can clearly show the coupling relationship between various indicators. The calculation steps are as follows.

First of all, we need to build a network relationship model. It is very important to clarify the dependence and feedback relationship between indicators in the ANP model, which has a certain influence on the correctness of the decision. The connected relationship of all elements is entered, consulting related literature to the SD.

Secondly, it is necessary to collect expert evaluation data. There are connected relationships between elements in the same and different dimensions. The important influence degree of other elements that have a connection relationship with the certain element is judged. Ten experts in the relevant field were consulted by 1 ~ 9 scale scoring method [42]. The score rules are shown in Table 2. It is particularly important to note that the ANP model also requires consistency testing, which must be less than 0.1.

Then, unweighted matrix and weighted matrix of elements are obtained by inputting all scored data from 10 experts into SD. If the values of the unweighted matrix and weighted matrix are 0, then there is no dependent and feedback relationship between the two elements.

Finally, the comprehensive weights are calculated. We can obtain the normalized matrix from the unweighted matrix and weighted matrix in SD. Moreover, according to the academical abilities and experiences of 10 experts, we set weighted coefficients as shown in Table 3. Combining the normalized matrix and weighted coefficient to get the final comprehensive weights of elements, we obtain the following calculation formula as

$$\overline{\text{limiting}} = \sum_{k=1}^{10} (S_k \times P_k), \quad (2)$$

where  $P_k$  is the elements' normalized weights from 10 experts and  $S_k$  is the weighted coefficient of each expert.

4.3. *Building Cloud Models of Comment Sets.* Before constructing a risk early warning assessment model of water inrush disaster, the corresponding comment sets should be established. Moreover, the comment sets classified of early warning model should be based on the past examples of many coal mines water inrush disasters.

In this article, the influence degrees of disaster-causing factors in water inrush disaster are divided into five comment sets: weak, slightly weak, general, strong, and stronger. It is expressed as  $V = \{V_1, V_2, V_3, V_4, V_5\} = \{\text{weak, slightly weak, general, strong, stronger}\}$ .

The golden section method is used to generate a corresponding closed comment set as  $(C_{\min}, C_{\max})$ . In the golden section model, the closer the score to the center of domain, the smaller En and He. In addition, the cloud model parameters between two adjacent evaluation intervals are 0.618 times [43]. It can be represented by the corresponding cloud characteristic numbers, as follows:

$$\begin{cases} Ex = \frac{(C_{\max} + C_{\min})}{2}, \\ En = \frac{(C_{\max} - C_{\min})}{6}, \\ He = k. \end{cases} \quad (3)$$

In Equation (3),  $k$  is a constant that needs to be determined according to the ambiguity of comment.

In this article, the central cloud feature numbers are set  $Ex_3 = 0.5$  and  $He_3 = 0.005$ . The calculation formulas (4) to (6) are as follows:

$$\begin{cases} Ex_1 = 0, \\ Ex_2 = Ex_3 - \frac{(1 - 0.618)(C_{\max} + C_{\min})}{2} = 0.30, \\ Ex_3 = 0.5 \\ Ex_4 = Ex_3 + \frac{(1 - 0.618)(C_{\max} + C_{\min})}{2} = 0.69, \\ Ex_5 = 1, \end{cases} \quad (4)$$

$$\begin{cases} He_1 = \frac{He_2}{0.618} = 0.013, \\ He_2 = \frac{He_3}{0.618} = 0.008, \\ He_3 = 0.005, \\ He_4 = \frac{He_3}{0.618} = 0.008, \\ He_5 = \frac{He_4}{0.618} = 0.013, \end{cases} \quad (5)$$

$$\begin{cases} En_1 = \frac{0.618 \times (C_{\max} - C_{\min})}{6} = 0.103, \\ En_2 = \frac{(1 - 0.618)(C_{\max} - C_{\min})}{6} = 0.064, \\ En_3 = \frac{0.618 \times (1 - 0.618)(C_{\max} - C_{\min})}{6} = 0.039, \\ En_4 = \frac{(1 - 0.618)(C_{\max} - C_{\min})}{6} = 0.064, \\ En_5 = \frac{0.618 \times (C_{\max} - C_{\min})}{6} = 0.103. \end{cases} \quad (6)$$

All closed intervals  $(C_{\min}, C_{\max})$  are distributed in the theoretical domain  $[0, 1]$ . Moreover, the cover width of cloud model is  $[Ex - 3En, Ex + 3En]$ . The comment sets as shown in Table 4. We used the cloud feature numbers of different risk comment sets to generate the cloud image corresponding by MATLAB, as shown in Figure 6.

4.4. *Comprehensive Early Warning Assessment.* Ten experts in a related field were invited to conduct a questionnaire survey, which includes 2 second-level professors, 4 associate professors, 2 senior engineers, and 2 doctors. Moreover, the 23 important second-level indicators were scored reasonably, ranging from 0 to 100. The experts should give the highest and the lowest scores of indicators, respectively. Finally, the results to the domain  $[0, 1]$  are normalized.

4.4.1. *Comprehensive Cloud of First-Level Indicators.* The corresponding maximum and minimum cloud feature numbers  $C$  ( $Ex$ ,  $En$ ,  $He$ ) of indicators are obtained by a Backward Cloud Generator. According to the calculated formulas (7), the comprehensive cloud feature numbers of the second-level indicators are obtained by maximum and minimum cloud feature numbers fitted. However, the second-level indicators are used to calculate the comprehensive cloud, which is not considered as a relative influence on the first-level indicators. Therefore, it can not reflect the accurate prediction results.

Through formulas (8), we can obtain more accurate cloud characteristic numbers of the first-level indicators. We used MATLAB to generate the corresponding cloud image and compared it with the standard grades to clarify the early warning level of various first-level indicators.

4.4.2. *Comprehensive Cloud of Goal.* The comprehensive cloud feature number of goal is a summary for the evaluation model and its comprehensive degree is strongest because the correlations between the first-level indicators are much greater than those between the second-level indicators. We can use the integrated cloud algorithm to obtain the cloud feature number of goals, as in formula (9). Moreover, we compared it with standard grades to clarify disaster level of goal.

$$\begin{cases} Ex = \frac{Ex_{\max}En_{\max} + Ex_{\min}En_{\min}}{En_{\max} + En_{\min}}, \\ En = En_{\max} + En_{\min}, \\ He = \frac{He_{\max}En_{\max} + He_{\min}En_{\min}}{En_{\max} + En_{\min}}, \end{cases} \quad (7)$$

$$\begin{cases} Ex = \frac{Ex_1w_1 + Ex_2w_2 + \dots + Ex_nw_n}{w_1 + w_2 + \dots + w_n}, \\ En = \frac{w_1^2}{w_1^2 + w_2^2 + \dots + w_n^2} * En_1 + \frac{w_2^2}{w_1^2 + w_2^2 + \dots + w_n^2} * En_2 + \dots + \frac{w_n^2}{w_1^2 + w_2^2 + \dots + w_n^2} * En_n, \\ He = \frac{w_1^2}{w_1^2 + w_2^2 + \dots + w_n^2} * He_1 + \frac{w_2^2}{w_1^2 + w_2^2 + \dots + w_n^2} * He_2 + \dots + \frac{w_n^2}{w_1^2 + w_2^2 + \dots + w_n^2} * He_n, \end{cases} \quad (8)$$

$$\begin{cases} Ex = \frac{Ex_1En_1w_1 + Ex_2En_2w_2 + \dots + Ex_nEn_nw_n}{En_1w_1 + En_2w_2 + \dots + En_nw_n}, \\ En = En_1w_1 + En_2w_2 + \dots + En_nw_n, \\ He = \frac{He_1En_1w_1 + He_2En_2w_2 + \dots + He_nEn_nw_n}{En_1w_1 + En_2w_2 + \dots + En_nw_n}. \end{cases} \quad (9)$$

In Equations (7) and (8),  $w_i$  is comprehensive weights of second-level indicators;  $n$  is total number of second-level indicators;  $(Ex_i, En_i, He_i)$  are cloud characteristic numbers of second-level indicators;  $(Ex_{\max}, En_{\max}, He_{\max})$  and  $(Ex_{\min}, En_{\min}, He_{\min})$  are the corresponding maximum and minimum cloud feature numbers. In Equation (9),  $w_i$  is the comprehensive weights of first-level indicators;  $n$  is the total number of first-level indicators;  $(Ex_i, En_i, He_i)$  are the cloud characteristic numbers for first-level indicators.

## 5. Application

**5.1. Engineering Background.** This article takes Y coal mine as an example to verify the feasibility of the early warning assessment model; the mine position is shown in Figure 7. Y coal mine was constructed in 2005 and its reserve is 31.2 million tons. Moreover, the most mining depth is 680 m and the area of mine is 21.7 km<sup>2</sup>. The whole mining area is cut by faults with the compound fold structure. Small- and medium-sized seasonal rivers pass through the northeast of mine.

The inclination angle of the coal seam is 10~20°. The lithology of the floor is mainly medium and fine sandstone, with an average thickness of 19.80 m. There are some local vertical cracks and the sandstone fissure aquifer in the roof and floor of Y coal mine is a direct roadway water-filling source. The water-repellent layer is composed of sandy or calcareous clay with a thickness of 10–158 m, of which water blocking property is good. When encountering structures or karst collapse columns, Ordovician water directly filled roadway, which causes great harm to production.

**5.2. Constructing the Index System.** Based on the disaster-causing factors of water inrush in coal mine Y, the evaluation system was established. It includes 4 types of the first-level indicators: mining conditions, hydrological factors, geological structure, and human factors expressed as  $U = \{U1, U2, U3, U4\} = \{\text{mining conditions, hydrological factors, geological structure, human factors}\}$ . The disaster-causing factors of water inrush disasters in different coal mines may be inconsistent. Moreover, the second-level indicators of Y coal mine evaluation system are, respectively, expressed as  $U1 = \{U11, U12, U13, U14, U15, U16\}$ ,  $U2 = \{U21, U22, U23, U24, U25, U26\}$ ,  $U3 = \{U31, U32, U33, U34, U35, U36\}$ , and  $U4 = \{U41, U42, U43, U44, U45\}$ .

**5.3. Index Weights Based on ANP.** The index weights represent the contribution degree of each indicator to the entire evaluation system. Ten experts related to Y coal mine are invited to score indicators two by two according to the importance degree. The indicator's comprehensive weights are output, conforming Inconsistency <0.1," as shown in Figure 8.

**5.4. Cloud Model Early Warning Assessment.** Ten experts related to coal mine Y are invited to score 23 major second-level indicators; the rules are shown in Table 5. The highest and lowest scores are normalized to domain [0, 1]. Then, maximum and minimum cloud feature numbers are fitted to obtain comprehensive feature numbers, which are retained to three decimal places.

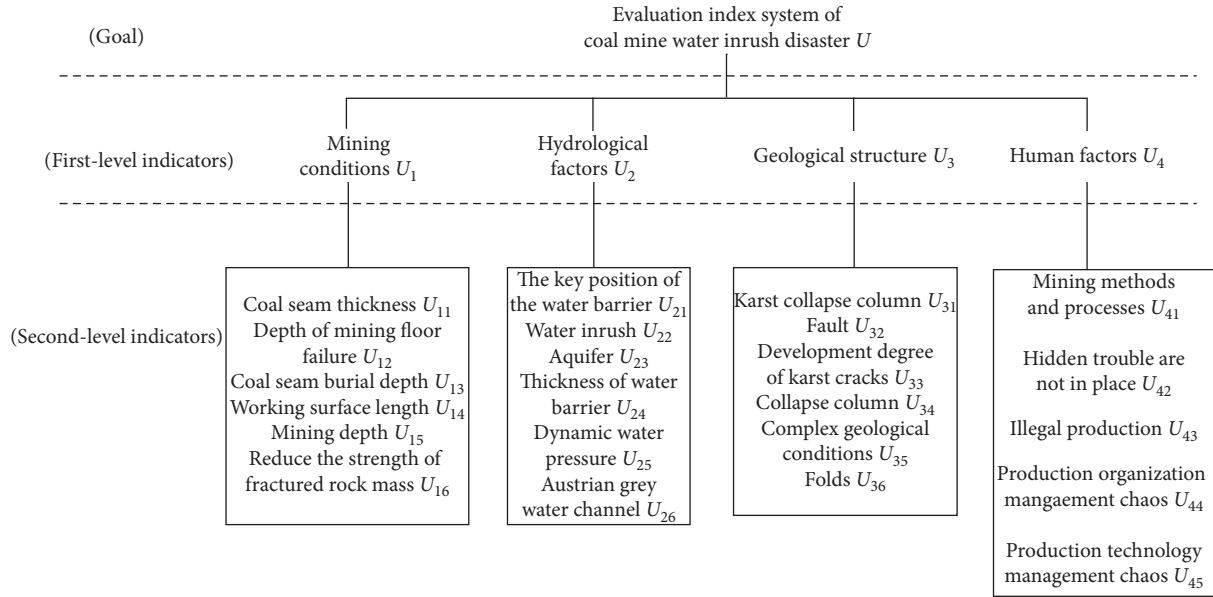


FIGURE 4: Network index system of the coal mine water inrush disaster.

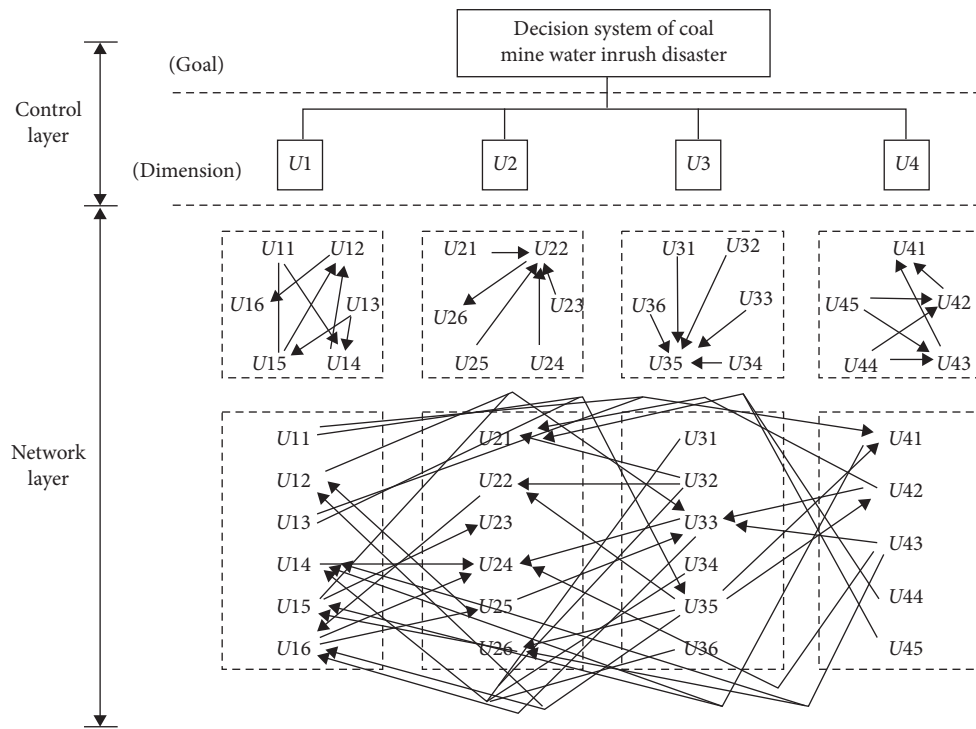


FIGURE 5: The network relationship diagram in ANP model.

TABLE 2: 1~9 scale scoring method.

Scale	Meaning
1	The two elements are of the same importance.
3	The former is slightly more important than the latter.
5	The former is significantly more important than the latter.
7	The former is more important than the latter.
9	The former is the most important than the latter.
2,4,6,8	The intermediate value of each scale.
Reciprocal (1,1/3, ..., 1/9)	The latter is more important than the former, with the same degree of importance as defined in 1~9.

TABLE 3: Expert rating weighted coefficients.

Experts	S1	S2	S3	S4	S5	S6	S7	S8	S9	S10
Weighted coefficients	0.09	0.07	0.14	0.09	0.011	0.09	0.14	0.09	0.11	0.07

TABLE 4: Five standard comment sets.

Language value	Weak	Slightly weak	General	Strong	Stronger
Cloud model	(0, 0.103, 0.013)	(0.309, 0.064, 0.008)	(0.50, 0.031, 0.005)	(0.069, 0.064, 0.008)	(1, 0.103, 0.013)
x-axis value interval	[0, 0.309]	[0.117, 0.501]	[0.407, 0.593]	[0.499, 0.883]	[0.691, 1]
Warning level color	Green	Blue	Purple	Yellow	Red

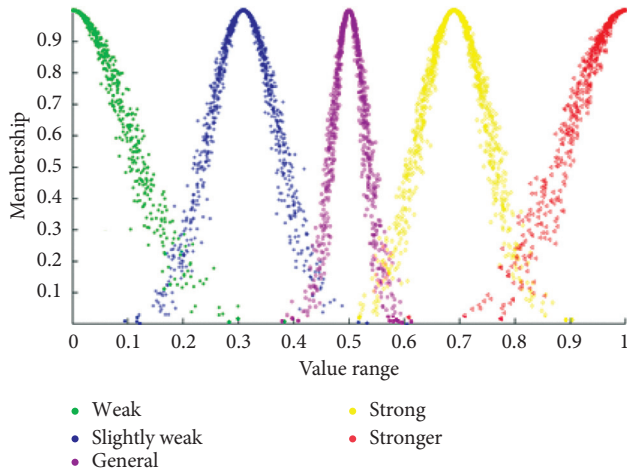


FIGURE 6: Standard evaluation cloud model.

5.4.1. *The Cloud Model Warning Results of First-Level Indicators.* Combining the cloud feature numbers and weights of second-level indicators can obtain comprehensive cloud feature numbers of first-level indicators, as shown in Table 6. They can be converted from qualitative to quantitative index through MATLAB, as shown in Figure 9. By comparing the black-circular cloud with the standard grades cloud model, we can obtain the corresponding risk level.

It can be seen from Figure 9 that the positions of four types of first-level indicators' clouds are generally at the moderate disaster level, which indicates they all can possibly cause water inrush disasters.

Figure 9(a) is the evaluation cloud map of mining conditions. It can be seen that the thickness and coverage of the main body of the black-circular cloud at the "yellow-strong" level are appropriate. It indicates that the mining conditions have strong prerequisites for disasters. So, it is necessary to strengthen the ability of prevention and control to all second-level indicators.

The evaluation cloud of hydrological factors is shown in Figure 9(b). It can be seen that the black-circular cloud image has a normal coverage and a suitable thickness, of which the main cloud basically meets with the "yellow-strong warning level." It shows that hydrological factors have a greater possibility of causing disaster. This is because hydrological factors include a series of conditions directly related to water inrush disasters, such as the aquifer and



FIGURE 7: The mine position of test Y coal mine.

hydrodynamic pressure. Thus, it should strengthen the rational prevention and control of hydrological factors.

Figure 9(c) is the evaluation cloud of geological structure. It can be seen that the black-circular cloud image has a normal coverage and thickness, of which the cloud location is between the "yellow-strong warning level" and "purple-general warning level." The geological structure can cause disaster, of which the risk rate is obviously lower than hydrological factors and mining conditions. Moreover, there are some structures with complex geological conditions and undetectable in mine, which may promote increasing the rock permeability, leading to water inrush disaster.

Figure 9(d) is the evaluation cloud of the human factor. It can be seen that the position of the black-circular cloud image is between three cloud images of "blue-slightly weak warning level," "purple-general warning level," and "yellow-strong warning level." It shows that human factors have little effect on water inrush disasters. However, its second-level indicators, such as "three violations of production," "hidden hazards can not be investigated," and other factors, will lead to inaccurate investigation on hidden dangers of water inrush disaster. It will have a certain impact on coal mine water inrush disaster. Therefore, we should focus on strengthening the quality and skills training of staff.

5.4.2. *The Cloud Model Warning Results of Goal.* The cloud feature numbers of goal are the inductive summary for the entire cloud model. In the early warning evaluation system of Y coal mine water inrush disaster, the comprehensive cloud characteristic numbers of goal are C (0.679, 0.086,



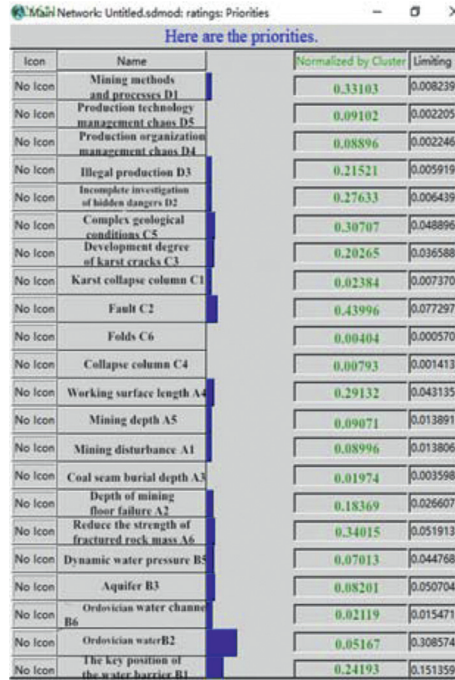


FIGURE 8: Index comprehensive weights chart.

TABLE 5: Scoring criteria for water inrush disaster indicators in Y coal mine.

Disaster level	Degree of disaster	Rating ranges
1	Weak	[0, 12.5]
2	Slightly weak	(12.5, 37.5]
3	General	(37.5, 62.5]
4	Strong	(62.5, 87.5]
5	Stronger	(87.5, 100]

TABLE 6: Comprehensive characteristic parameters and weights of each index cloud model.

First-level indicators	(Ex, En, He)	$w_i$	Second-level indicators	(Ex, En, He)	$w_i$
Mining conditions ( $U_1$ )	(0.682,0.100,0.006)	0.1707475	Mining disturbance $U_{11}$	(0.762,0.090,0.005)	0.09025
			Depth of mining floor failure $U_{12}$	(0.758,0.064,0.003)	0.17396
			Coal seam burial depth $U_{13}$	(0.730,0.044,0.003)	0.02349
			Working surface length $U_{14}$	(0.738,0.047,0.003)	0.28202
			Mining depth $U_{15}$	(0.655,0.084,0.005)	0.09082
			Reduce the strength of fractured rock mass $U_{16}$	(0.578,0.149,0.008)	0.33941
Hydrological factors ( $U_2$ )	(0.701,0.082,0.004)	0.610605	Key position of the water barrier $U_{21}$	(0.745,0.092,0.005)	0.23291
			Ordovician water $U_{22}$	(0.719,0.080,0.004)	0.47482
			Aquifer $U_{23}$	(0.654,0.075,0.004)	0.07802
			Water barrier thickness $U_{24}$	(0.669,0.073,0.004)	0.12155
			Dynamic water pressure $U_{25}$	(0.571,0.108,0.006)	0.06889
			Ordovician water channel $U_{26}$	(0.585,0.086,0.004)	0.02381
Geological structure ( $U_3$ )	(0.656,0.087,0.004)	0.1647225	Karst collapse column $U_{31}$	(0.746,0.077,0.004)	0.04282
			Fault $U_{32}$	(0.720,0.081,0.004)	0.44905
			Karst fissure development degree $U_{33}$	(0.601,0.076,0.004)	0.21256
			Collapse column $U_{34}$	(0.603,0.120,0.006)	0.00821
			Complex geological conditions $U_{35}$	(0.585,0.108,0.006)	0.28406
			Folds $U_{36}$	(0.575,0.106,0.005)	0.00331
Human factors ( $U_4$ )	(0.501,0.083,0.005)	0.05393	Mining methods and processes $U_{41}$	(0.641,0.076,0.004)	0.32893
			Incomplete investigation of hidden dangers $U_{42}$	(0.449,0.105,0.006)	0.25707
			Illegal production $U_{43}$	(0.423,0.071,0.004)	0.23631
			Production organization management chaos $U_{44}$	(0.427,0.065,0.004)	0.08967
			Production technology management chaos $U_{45}$	(0.417,0.089,0.005)	0.08803

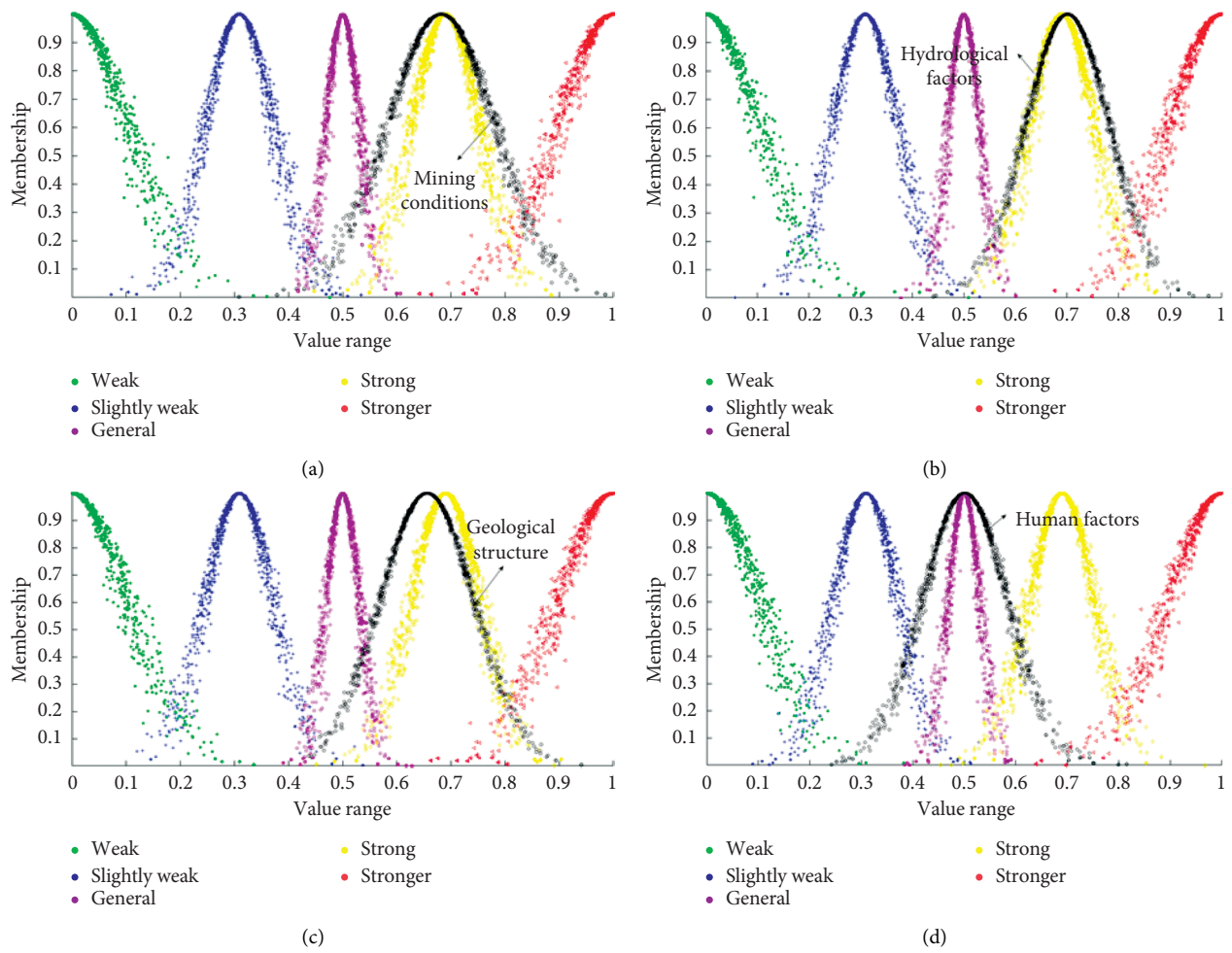


FIGURE 9: The cloud model evaluation results of first-level indicators. (a) Mining conditions evaluation cloud. (b) Hydrological factor evaluation cloud. (c) Geological structure evaluation cloud. (d) Human factors evaluation cloud.

0.004). The corresponding cloud image is shown in Figure 10.

It can be seen from Figure 10 that the cloud image of goal is a black-circular cloud, of which the coverage and thickness are appropriate. It is between three cloud images of “purple-general warning level,” “yellow-strong warning level,” and “red-strong warning level.” However, its main cloud is located at the yellow-strong warning level. It shows that there is a certain risk of water inrush in Y coal mine.

The predicted results are compared with actual disaster data of Y coal mine, which are consistent. It further proves that this early warning evaluation model of “ANP-Cloud” model based on Complex Network is reliable.

It is necessary to strengthen the prevented degree to hydrological factors, mining conditions, and geological structure. Moreover, we should comprehensively cultivate workers’ knowledge and technical capabilities. Moreover, construction technology management should be strengthened to avoid leaving out disaster-causing factors and eliminate illegal production.

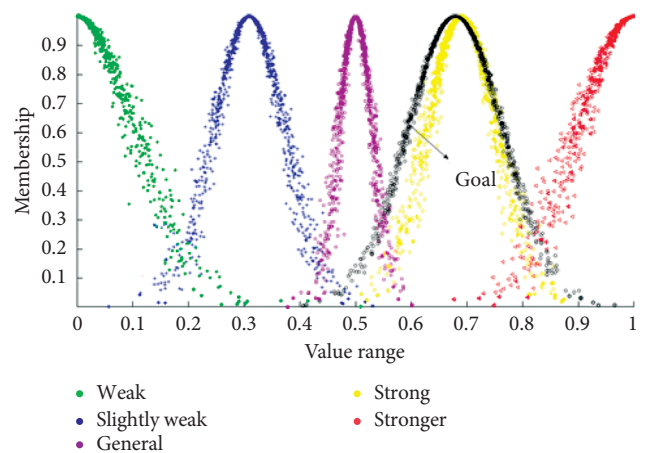


FIGURE 10: The cloud model evaluation results chart of goal.

## 6. Conclusions

In this article, the early warning evaluation system of the “ANP-Cloud” model based on Complex Network in water

inrush disaster was established to solve the problem of complex dependence relationship among disaster-causing factors and prevent water inrush disaster. Moreover, the usability and reliability of this warning evaluation model were verified in Y coal mine. The main conclusions are as follows:

- (1) The knowledge of the Complex Networks is used to establish a water inrush disaster network with 161 nodes and 149 connected edges. Through analyzing topological characteristics of the water inrush disaster network, 23 multiple importance nodes were obtained.
- (2) Based on the Complex Network model of water inrush disaster, the early warning evaluation system of the “ANP-Cloud” model was established. The main implementation steps include establishing index system, index weights based on ANP, building Cloud models of comment sets, and comprehensive early warning assessment.
- (3) Combining with the example of Y coal mine, the reliability and applicability of the evaluation model were further verified. The results show that the goal of the early warning evaluation system is a strong early warning level. Mining conditions, hydrological factors, and geological structures all belong to strong early warning levels. Moreover, human factors will have a certain effect on the other three first-level indicators. The predicted results are consistent with the actual situation of Y mine coal water inrush and the early warning evaluation system provides a base of experience for other types of network assessments.

## Data Availability

The data used to support the findings of this study are available from the corresponding author upon request.

## Conflicts of Interest

The authors declare that they have no conflicts of interest.

## Acknowledgments

This research was supported by the National Natural Science Foundation of China (Nos. 52074239, 51927807, and 51509149).

## References

- [1] L. Wang, J. S. Zhang, and S. H. Zou, “Study on basic reserves variation of China’s fundamental energy resources in recent 10 years,” *Advanced Materials Research*, vol. 1030-1032, pp. 616–619, 2014.
- [2] Z. Zhang, M. Deng, J. Bai, X. Yu, Q. Wu, and L. Jiang, “Strain energy evolution and conversion under triaxial unloading confining pressure tests due to gob-side entry retained,” *International Journal of Rock Mechanics and Mining Sciences*, vol. 126, p. 104184, 2020.
- [3] Z. Zhang, M. Deng, X. Wang, W. Yu, F. Zhang, and V. D. Dao, “Field and numerical investigations on the lower coal seam entry failure analysis under the remnant pillar,” *Engineering Failure Analysis*, vol. 115, p. 104638, 2020.
- [4] Z. Zhang, M. Deng, J. Bai, S. Yan, and X. Yu, “Stability control of gob-side entry retained under the gob with close distance coal seams,” *International Journal of Mining Science and Technology*, vol. 31, no. 2, pp. 321–332, 2021.
- [5] Z. Zhang, J. Bai, Y. Chen, and S. Yan, “An innovative approach for gob-side entry retaining in highly gassy fully-mechanized longwall top-coal caving,” *International Journal of Rock Mechanics and Mining Sciences*, vol. 80, pp. 1–11, 2015.
- [6] W. J. Yu, G. S. Wu, B. Pan, Q. H. Wu, and Z. Liao, “Experimental investigation of the mechanical properties of sandstone-coal-bolt specimens with different angles under conventional triaxial compression,” *International Journal of Geomechanics*, vol. 21, no. 6, 2021.
- [7] S. Liu, J. Bai, X. Wang, B. Wu, and W. Wu, “Mechanisms of floor heave in roadways adjacent to a goaf caused by the fracturing of a competent roof and controlling technology,” *Shock and Vibration*, vol. 2020, Article ID 5632943, 17 pages, 2020.
- [8] B. Wu, X. Wang, J. Bai, W. Wu, X. Zhu, and G. Li, “Study on crack evolution mechanism of roadside backfill body in gob-side entry retaining based on udec trigon model,” *Rock Mechanics and Rock Engineering*, vol. 52, no. 9, pp. 3385–3399, 2019.
- [9] W.-d. Wu, J.-b. Bai, X.-y. Wang, S. Yan, and S.-x. Wu, “Numerical study of failure mechanisms and control techniques for a gob-side yield pillar in the Sijiazhuang coal mine, China,” *Rock Mechanics and Rock Engineering*, vol. 52, no. 4, pp. 1231–1245, 2019.
- [10] B. W. Wu, X. Y. Wang, J. B. Bai et al., “An investigation on the effect of high energy storage anchor on surrounding rock conditions,” *Royal Society Open Science*, vol. 7, no. 10, 2020.
- [11] T. Li, G. Chen, Z. Qin, Q. Li, B. Cao, and Y. Liu, “The gob-side entry retaining with the high-water filling material in Xin’an Coal Mine,” *Geomechanics and Engineering*, vol. 22, pp. 541–552, 2020.
- [12] F. Cui, Q. Wu, Y. Lin, Y. Zeng, and K. Zhang, “Damage features and formation mechanism of the strong water inrush disaster at the daxing Co mine, guangdong province, China,” *Mine Water and the Environment*, vol. 37, no. 2, pp. 346–350, 2018.
- [13] Science Press, *Research on Unsafe Behavior in Major Accidents in Coal Mines in China*, Science Press, Beijing, China, 2016, pp. 15–18, (In Chinese).
- [14] S. Dong, L. Zheng, and S. Tang, “A scientometric analysis of trends in coal mine water inrush prevention and control for the period,” *Mine Water and the Environment*, vol. 39, no. 1, pp. 3–12, 2020.
- [15] Z. L. Yang, X. R. Meng, X. Q. Wang, and K. Y. Wang, “Nonlinear prediction and evaluation of coal mine floor water inrush based on GA-BP neural network model,” *Safety in Coal Mines*, vol. 44, no. 2, pp. 36–39, 2013, (In Chinese).
- [16] B. Wang, “Research on evaluation method of water inrush in coal floor with pressure and mining,” MSc thesis, Hebei University of Engineering, 2015, In Chinese.
- [17] Y. H. Wang, Z. X. Li, Y. Q. Zhao, W. Lei, and Y. Shu, “Probability evaluation of coal mine water inrush risk based on dynamic fault tree,” *China Mining Magazine*, vol. 25, no. 7, pp. 102–108, 2016, (In Chinese).

- [18] Z. C. Qin, G. B. Chen, and T. Li, "An improved evaluation method of water inrush risk in coal mines," *Mining Research and Development*, vol. 38, no. 2, pp. 53–58, 2018, (In Chinese).
- [19] C. S. Wang, Y. J. Sun, and Y. Hang, "Application of fault tree analysis to risk assessment of potential water-inrush hazards in coal mining," *Chinese Journal of Rock Mechanics and Engineering*, vol. 28, no. 2, pp. 298–305, 2009, (In Chinese).
- [20] Q. Gu, Z. Huang, S. Li, W. Zeng, Y. Wu, and K. Zhao, "An approach for water-inrush risk assessment of deep coal seam mining: a case study in Xinlongzhuang coal mine," *Environmental Science and Pollution Research*, vol. 27, no. 34, pp. 43163–43176, 2020.
- [21] Q. Lu, X. Li, W. Li, W. Chen, L. Li, and S. Liu, "Risk evaluation of bed-separation water inrush: a case study in the yangliu coal mine, China," *Mine Water and the Environment*, vol. 37, no. 2, pp. 288–299, 2018.
- [22] T. Liu, "Research on coal mine gas disaster network based on link prediction," MSc thesis, Xi'an University of Science and Technology, Xi'an, China, 2016, in Chinese.
- [23] Y. Xu and L. Cheng, "Review of logistics networks structure based on complex networks," in *Proceedings of the 2017 36th Chinese Control Conference (CCC)*, pp. 7535–7540, Dalian, China, July 2017.
- [24] X. H. Qin, B. N. Luo, and J. Q. Gong, "Uncertainty spread and control of complex supply chain networks in manufacturing industry," *Advanced Materials Research*, vol. 712–715, pp. 3161–3164, 2013.
- [25] T. T. Li, C. Luo, and R. Shao, "The structure and dynamics of granular complex networks deriving from financial time series," *International Journal of Modern Physics C*, vol. 31, no. 6, p. 2020, 2020.
- [26] D. Dudziak-Gajowiak and K. Juszczyszyn, "Complex networks modelling of supply chains in construction and logistics," *Central European Symposium on Thermophysics 2019 (Cest)*, vol. 2116, no. 1, 2019.
- [27] F. Y. Song, "Research on the evaluation of housing Industrialization Maturity Based on ANP-Gray Cluster Evaluation," MSc thesis, Zhengzhou University, Zhengzhou, China, 2018.
- [28] Y. Xie, "A study on the evaluation of competitiveness of tourism enterprise based on ANP Theory," MSc thesis, Dalian University of Technology, Dalian, China, 2010, in Chinese.
- [29] T. L. Saaty, "Decision making with dependence and feedback: the analytic network process," *Internationa*, vol. 95, no. 2, pp. 129–157, 2012.
- [30] X. Zhang, J. Zhang, and T. Chen, "An ANP-fuzzy evaluation model of food quality safety supervision based on China's data," *Food Science & Nutrition*, vol. 8, no. 7, pp. 3157–3163, 2020.
- [31] K. C. Di, D. Y. Li, and D. R. Li, "Cloud theory and its application in spatial data mining and knowledge discovery," *Journal of Image and Graphics*, vol. 4, no. 11, pp. 32–37, 1999, (In Chinese).
- [32] H. Dong, "Research on long-distance water diversion project operation safety risk assessment and countermeasures based on cloud model and social network analysis," MSc thesis, North China University of Water Resource and Electric Power, Zhengzhou, China, 2018, in Chinese.
- [33] L. Yun, "Study on crack control and quality evaluation of aerated concrete masonry filling wall based on cloud model," MSc thesis, Southwest Petroleum University, 2014, in Chinese.
- [34] L. G. Vargas, "Special issue on "AHP/ANP studies in technology, entrepreneurship and corporate social responsibility"," *Journal of Multi-Criteria Decision Analysis*, vol. 27, no. 1-2, pp. 3-4, 2020.
- [35] Q. Chen, Y. Yin, and A. Su, "Review of cloud modeling," in *Proceedings of the 2008 International Workshop on Education Technology and Training & 2008 International Workshop on Geoscience and Remote Sensing*, pp. 238–241, Shanghai, China, December 2018.
- [36] Q. W. Xu and K. L. Xu, "Evaluation of ambient air quality based on synthetic CLOUD model," *Fresenius Environmental Bulletin*, vol. 27, no. 1, pp. 141–146, 2018.
- [37] Y. Shi, A. Zhang, X. Gao, and Z. Tan, "Cloud model and its application in effectiveness evaluation," in *Proceedings of the 2008 International Conference on Management Science and Engineering 15th Annual Conference*, pp. 250–255, Long Beach, CA, USA, September 2018.
- [38] S. Onut, U. R. Tuzkaya, and E. Torun, "Selecting container port via a fuzzy ANP-based approach: a case study in the Marmara Region, Turkey," *Transport Policy*, vol. 18, no. 1, pp. 182–193, 2011.
- [39] F. Z. Zoubiri, R. Rihani, and F. Bentahar, "Golden section algorithm to optimise the chemical pretreatment of agro-industrial waste for sugars extraction," *Fuel*, vol. 266, p. 117028, 2020.
- [40] L.-P. Sun, Z. Liu, H. Shou, and Y.-H. Zhang, "Parameter optimization of gravity density inversion based on correlation searching and the golden section algorithm," *Applied Geophysics*, vol. 9, no. 2, pp. 131–138, 2012.
- [41] X. H. Wang, H. Yang, and Y. Chen, "Matlab realization of effectiveness evaluation based on cloud model," *Information Technology and Network Security*, vol. 31, no. 8, pp. 71–73, 2012, (In Chinese).
- [42] D. L. Xu, "Drawing the cloud model by Matlab," *Sci-tech Innovation and Productivity*, vol. 1, pp. 108–110, 2016, (In Chinese).
- [43] S. Gholam Abbas and N. Leila, "Evaluation of resilience engineering using super decisions software," *Health Promotion Perspectives*, vol. 9, pp. 191–197, 2019.

## Research Article

# Pile-Soil Stress Ratio and Settlement of Composite Foundation Bidirectionally Reinforced by Piles and Geosynthetics under Embankment Load

Binhui Ma <sup>1,2</sup>, Zhuo Li,<sup>1</sup> Kai Cai,<sup>1</sup> Meng Liu,<sup>3</sup> Minghua Zhao,<sup>3</sup> Bingchu Chen,<sup>1</sup> Qiunan Chen,<sup>1,2</sup> and Zhiyong Hu<sup>1</sup>

<sup>1</sup>School of Civil Engineering, Hunan University of Science and Technology, Xiangtan 411201, China

<sup>2</sup>Hunan Provincial Key Laboratory of Geotechnical Engineering for Stability Control and Health Monitoring, Hunan University of Science and Technology, Xiangtan 411201, China

<sup>3</sup>School of Civil Engineering, Hunan University, Changsha 410082, China

Correspondence should be addressed to Binhui Ma; mbh@hnust.edu.cn

Received 16 March 2021; Revised 4 April 2021; Accepted 15 April 2021; Published 23 April 2021

Academic Editor: Zhijie Zhu

Copyright © 2021 Binhui Ma et al. This is an open access article distributed under the Creative Commons Attribution License, which permits unrestricted use, distribution, and reproduction in any medium, provided the original work is properly cited.

The settlement calculation of composite foundation bidirectionally reinforced by piles and geosynthetics is always a difficult problem. The key to its accuracy lies in the determination of pile-soil stress ratio. Based on the theory of double parameters of the elastic foundation plate, the horizontal geosynthetics of composite foundation are regarded as the elastic thin plate, and the vertical piles and surrounding soil are regarded as a series of springs with different stiffness. The deflection equation of horizontal geosynthetics considering its bending and pulling action is obtained according to the static equilibrium conditions. The equation is solved by using Bessel function of complex variable, and the corresponding deflection function of horizontal geosynthetics is deduced. Then, the calculation formula of pile-soil stress ratio and settlement of composite foundation is derived by considering the deformation coordination of pile and soil. The results of engineering case analysis show that the theoretical calculation results are in good agreement with the measured values, which indicates that the proposed method is feasible and the calculation accuracy is good. Finally, the influence of composite modulus of horizontal geosynthetics, tensile force of geosynthetics, and pile-soil stiffness ratio on pile-soil stress ratio and settlement is further analyzed. The results show that the pile-soil stress ratio increases with the increase of the composite modulus of the horizontal geosynthetics, the tensile force of geosynthetics, and the pile-soil stiffness ratio, and the settlement decreases with the increase of the composite modulus of the horizontal geosynthetics, the tensile force of geosynthetics, and the pile-soil stiffness ratio. When the flexural stiffness of the horizontal geosynthetics is small, the influence of the tensile action of the geosynthetics on the pile-soil stress ratio and settlement of the composite foundation cannot be ignored.

## 1. Introduction

In recent years, with the rise of highway and railway construction in China, the problems of soft soil foundation have become increasingly prominent, the bearing capacity of the foundation is insufficient, the settlement is too large, and uneven settlement is particularly serious. The composite foundation reinforced by piles and geosynthetics, a new type of soft foundation treatment consisting of vertical piles and horizontal geosynthetics, has a good effect on the treatment

of the abovementioned foundation problems, and the foundation treatment method has simple construction and rapid progress. In recent years, it has been widely used in railway soft foundation treatment [1].

Research on the working mechanism of composite foundation has achieved many results so far [2–4]. Among them, the pile-soil stress ratio and settlement are important parameters reflecting the working behavior of composite foundation reinforced by piles and geosynthetics, and the research on its calculation method has also been a hot spot in



this field. Among them, Yang et al. [5] uses the helix to simulate the deformation shape of the cushion, taking into account the net effect of the cushion; Chen et al. [6] considered the tensile effect of the geosynthetics, assumed that the shape of the cushion after deformation is a rotating paraboloid, and deduced the calculation formula of pile-soil stress ratio based on Winkler foundation; Abusharar et al. [7] assumed that the stress of soil between piles is uniformly distributed, and a simple method for calculating the stress ratio of pile to soil is put forward by using the arc assumption of cushion deformation. For a considerable part of the project, single-layer grille cannot meet the needs of the project, geogrid, or multilayer grille should be installed in the cushion. At the same time, reference [2] points out that when this kind of structure is different from the single-layer grille, the geosynthetics and the contained bulk fillers can form a “flexible raft” with strong bending resistance. Obviously, the above method based on the thin film theory is not suitable for geogrid or multilayer grille because it cannot take into account the bending effect. Therefore, Rao and Zhao [8] assume that the geosynthetics is a thin plate, and the shape of the thin plate is a parabola in order to consider the “flexible raft effect.” The formula for calculating the stress ratio of pile to soil is derived; Zheng et al. [9] think that this kind of cushion not only has a “flexible raft effect” but also has “pulling membrane effect,” so it is assumed that the deformation of geosynthetics is in the form of heavy trigonometric function, and the geometric nonlinearity in the deformation process is considered. As a result, the pile-soil stress ratio and settlement calculation method considering both “flexible raft effect” and “pulling membrane effect” of cushion are obtained. Ma et al. [10, 11] have done some work in the calculation of soft soil settlement. He et al. [12] made some attempts to chemically improve special soils. In addition, it can be seen from the above literature that the deformation shape of geosynthetics is the premise and key to calculating the pile-soil stress ratio and settlement, and the pile-soil stress ratio and settlement obtained by different deformation shapes are also different. Therefore, the closer it is to the actual deformation of the geosynthetics, the more accurate the pile-soil stress ratio and settlement will be.

However, the above literature all assume the deformation of the geosynthetics in advance, which cannot really reflect the stress state of the geosynthetics, which can easily lead to a large error between the calculated results and the measured results. For this reason, Tan et al. [13] derived the flexure function of horizontal stiffened body in the three-dimensional case based on Winkler elastic foundation rectangular plate theory, but due to the complexity of rectangular plate boundary conditions, it is difficult to consider the influence of pile settlement on geosynthetics. After that, Zhao et al. [14] took the composite foundation within the influence area of a single pile as the research object, discretized the pile and soil into a series of springs with different stiffness, and with the aid of the circular plate theory of elastic foundation and the deformation coordination of cushion at the pile-soil interface, the deflection function of geosynthetics considering the common deformation of pile and soil is derived, and on this basis, the

calculation method of pile-soil stress ratio is put forward. However, the above two analysis methods still only consider the “flexible raft effect” of geosynthetics, but not the “pulling membrane effect” of the reinforcement.

From the above analysis, we can know how to comprehensively consider the flexible raft effect, net effect, and pile-soil joint deformation of cushion without assuming the deformation of geosynthetics is the key to accurately solve the pile-soil stress ratio and settlement of composite foundation reinforced by piles and geosynthetics. Therefore, on the basis of the above research work, based on the Filonenko–Borodich two-parameter foundation model [15], this paper comprehensively considers the “flexible raft effect” and net effect of the geosynthetics, considers the pile-soil deformation at the same time, deduces the analytical function of the flexural deformation of the geosynthetics according to the Bessel complex function, and then obtains the calculation expression of pile-soil stress ratio and settlement of composite foundation. In order to further improve the calculation method of pile-soil stress ratio and settlement of composite foundation.

## 2. Calculation Model

Take the typical unit within the influence range of the single pile as shown in Figure 1 for analysis. The diameter of the pile is  $d$ , the center distance is  $s_d$ , the diameter of single pile reinforcement range is  $d_e$ , square pile  $d_e = 1.13s_d$ , and piles are arranged as the shape of plum blossoms:  $d_e = 1.05s_d$ .

In order to further simplify the calculation, the following assumptions are made:

- (1) As shown in Figure 2, the geosynthetics within the range of single pile reinforcement is regarded as an elastic circular thin plate placed on the Filonenko–Borodich two-parameter foundation model [16], and among them, the tension  $T$  of the reinforcement can be obtained by the following formula:

$$T = E_g \cdot \varepsilon_g, \quad (1)$$

where  $\varepsilon_g$  is the average strain of the reinforcement and  $E_g$  is the tensile stiffness of the reinforcement.

- (2) It is assumed that the vertical supporting force  $P_p$  of the pile to the thin plate is uniformly distributed, and according to references [6, 13, 14], the deformation of pile and soil between piles accords with Winkler foundation model.
- (3) The distribution of embankment load caused by differential settlement is not considered, that is, the embankment load is uniformly distributed [7, 8, 14].

## 3. Analysis of Geosynthetics

Let  $w_1(r)$  represent the flexure function of the pile top reinforcement. According to the Filonenko–Borodich two-parameter foundation model, under the joint action of the embankment load  $q$  and the pile top reaction force  $p_p$ , the

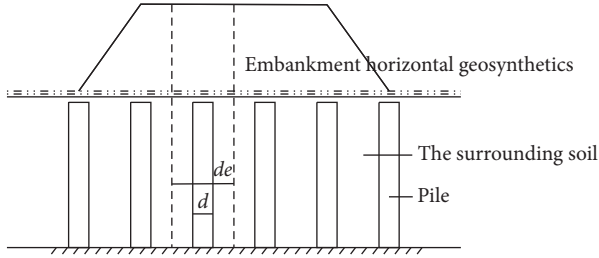


FIGURE 1: Sketch map of composite foundation.

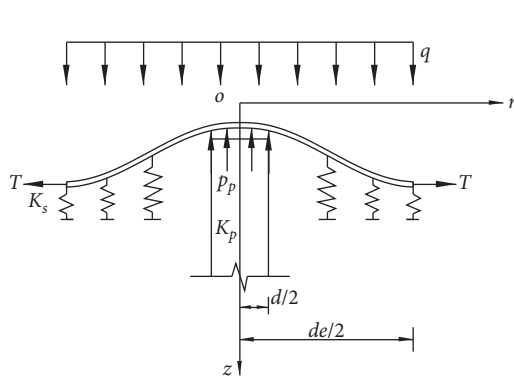


FIGURE 2: Calculation model for composite foundation.

control differential equation of the horizontal geosynthetics is as follows:

$$D\nabla^4 w_1(r) - T \cdot \nabla^2 w_1(r) = q - p_p, \quad (2)$$

where  $D$  is the bending stiffness of the thin plate.  $D = (E\delta^3/12(1-\nu^2))$ , where  $E$  is the elastic modulus of the plate,  $\nu$  is Poisson's ratio of the plate, and  $\delta$  is the thickness of the plate:  $\nabla^2 = (d^2/dr^2) + ((1/r)(d/dr))$ .

Let  $a_1 = \sqrt{-T/D}$ . Then, the homogeneous equation corresponding to equation (2) can be transformed into

$$\nabla^2 w_1(r) (\nabla^2 w_1(r) + a_1^2 w_1(r)) = 0. \quad (3)$$

The general solution of the homogeneous equation corresponding to equation (2) is

$$w_1(r) = C_1 J_0(a_1 r) + C_2 Y_0(a_1 r) + C_3 \ln r + C_4, \quad (4)$$

where  $J_N$  and  $Y_N$  are the first and second kinds of  $N$ -order Bessel functions and  $C_1, C_2, C_3,$  and  $C_4$  are undetermined constants.

Under the action of uniformly distributed load  $q$  and supporting force  $p_p$ , the special solution of equation (2) is  $w_1^* = -((q - p_p)r^2/4T)$ .

Combining formula (4), the flexural deformation function of the thin plate at the top of the pile is

$$w_1(r) = C_1 J_0(a_1 r) + C_2 Y_0(a_1 r) + C_3 \ln r + C_4 - \frac{(q - p_p)r^2}{4T}. \quad (5)$$

#### 4. Deformation Analysis of Thin Plate

Let  $w_2(r)$  denote the flexural function of the thin plate at the top of the pile, under the action of uniformly distributed load  $q$  and foundation soil support, the governing differential equation of thin plate at the top of interpile soil is as follows:

$$D\nabla^4 w_2(r) - T \cdot \nabla^2 w_2(r) + k_s w_2 = q, \quad (6)$$

where  $k_s$  is the spring coefficient of soil foundation between piles.

To simplify the calculation,

$$\begin{cases} a_{21} = \frac{1}{2} \left[ \frac{T}{D} + \sqrt{\left(\frac{T}{D}\right)^2 - \frac{4k_s}{D}} \right], \\ a_{22} = \frac{1}{2} \left[ \frac{T}{D} - \sqrt{\left(\frac{T}{D}\right)^2 - \frac{4k_s}{D}} \right]. \end{cases} \quad (7)$$

The homogeneous equation corresponding to equation (6) can be transformed into the following form:

$$(\nabla^2 w_2(r) + a_{21} w_2(r)) (\nabla^2 w_2(r) + a_{22} w_2(r)) = 0. \quad (8)$$

It can be seen from formula (7) that the values of  $a_{21}$  and  $a_{22}$  are divided into real and imaginary numbers according to the positive and negative of  $T^2 - 4Dk_s$ . The solution of equation (8) is different in the two cases, which are discussed as follows.

(1) When  $T^2 \geq 4Dk_s$ , order:

$$\begin{cases} l_{21} = \sqrt{a_{21}} \cdot i, \\ l_{22} = \sqrt{a_{22}} \cdot i. \end{cases} \quad (9)$$

The general solution of equation (8) is

$$w_2(r) = C_5 I_0(l_{21} r) + C_6 N_0(l_{21} r) + C_7 I_0(l_{22} r) + C_8 N_0(l_{22} r), \quad (10)$$

where  $N_n$  is the second kind of  $N$ -order virtual variable Bessel function and  $C_5, C_6, C_7,$  and  $C_8$  are undetermined constants.

Under the action of uniformly distributed load  $q$ , the special solution of equation (6) is  $w_2^* = q/k_s$ , and the combination formula (11) can be used to obtain the flexural deformation function of thin plate at the top of soil between piles at  $T^2 \geq 4Dk_s$ :

$$w_2(r) = C_5 I_0(l_{21} r) + C_6 N_0(l_{21} r) + C_7 I_0(l_{22} r) + C_8 N_0(l_{22} r) + \frac{q}{k_s}. \quad (11)$$

When  $T^2 < 4Dk_s$ , the general solution of equation (6) can be constructed as follows:

$$w_2(r) = C_5 u_0(r) + C_6 v_0(r) + C_7 f_0(r) + C_8 g_0(r) + \frac{q}{k_s}, \quad (12)$$

where  $u_n$  and  $v_n$  are the real parts of the first kind of Bessel function of order  $N$  and the real parts of Hankel function and  $f_n$  and  $g_n$  are the imaginary part of Bessel function of order  $N$  and the imaginary part of Hankel function, respectively.  $C_5$ ,  $C_6$ ,  $C_7$ , and  $C_8$  are undetermined constants.

$$\begin{cases} u_0(r) = \operatorname{Re}J_0(\sqrt{a_{21}}r) = \frac{1}{2}[J_0(\sqrt{a_{21}}r) + J_0(\sqrt{a_{22}}r)], \\ v_0(r) = \operatorname{Im}J_0(\sqrt{a_{21}}r) = \frac{1}{2i}[J_0(\sqrt{a_{21}}r) - J_0(\sqrt{a_{22}}r)], \\ f_0(r) = \operatorname{Re}H_0^{(1)}(\sqrt{a_{21}}r) = \frac{1}{2}[H_0^{(1)}(\sqrt{a_{21}}r) + H_0^{(2)}(\sqrt{a_{22}}r)], \\ g_0(r) = \operatorname{Im}H_0^{(2)}(\sqrt{a_{22}}r) = \frac{1}{2i}[H_0^{(1)}(\sqrt{a_{21}}r) - H_0^{(2)}(\sqrt{a_{22}}r)]. \end{cases} \quad (13)$$

## 5. Solution of Undetermined Coefficient

In order to determine the bending function of the thin plate, it is also necessary to compare the unknown parameters  $C_1$ ,  $C_2$ , ...,  $C_8$  and  $p_p$  in equations (5), (11), and (12), which are solved by boundary and continuous conditions.

As the turning angle of the thin plate at the center of the circular plate is 0,  $C_2 = C_3 = 0$  can be obtained. At the pile-soil junction, the continuity conditions of thin plate deflection, rotation angle, radial moment, and shear force are as follows:

$$\begin{cases} w_1\left(\frac{d}{2}\right) = w_2\left(\frac{d}{2}\right), \\ \theta_1\left(\frac{d}{2}\right) = \theta_2\left(\frac{d}{2}\right), \\ M_{r1}\left(\frac{d}{2}\right) = M_{r2}\left(\frac{d}{2}\right), \\ Q_{r1}\left(\frac{d}{2}\right) = Q_{r2}\left(\frac{d}{2}\right). \end{cases} \quad (14)$$

In addition, according to hypothesis (2), the deflection  $w_1(d/2)$  of the circular plate at the pile-soil interface is

$$w_1\left(\frac{d}{2}\right) = \frac{\pi d^2 p_p}{4K_p}. \quad (15)$$

The value of pile top reaction  $p_p$  is the sum of the upper embankment load and the load transferred from the cushion to the pile, that is,

$$p_p = \frac{4Q_{r1}(r=d/2)}{d} + q. \quad (16)$$

According to reference [2], the corner and shear boundary conditions at  $r = d_e/2$  of the element are as follows:

$$\begin{cases} \theta_2\left(\frac{d_e}{2}\right) = 0, \\ Q_{r2}\left(\frac{d_e}{2}\right) = 0. \end{cases} \quad (17)$$

At the same time, according to the bending functions (5), (11), and (12) of the thin plate, the expressions of the rotation angle, radial bending moment, and shear force of the thin plate can be obtained.

Within the range of the top of the pile, that is,  $0 \leq r \leq (d/2)$ ,

$$\begin{cases} \theta_{r1} = -C_1 a_1 J_1(a_1 r) - \frac{(q - p_p)r}{2T}, \\ M_{r1} = Da_1^2 \left\{ C_1 \left[ \frac{1-\nu}{a_1 r} J_1(a_1 r) - J_0(a_1 r) \right] + \frac{(1+\nu)(q - p_p)}{2T a_1^2} \right\}, \\ Q_{r1} = C_1 Da_1^3 \left[ \frac{J_2(a_1 r)}{r} + \frac{2-r^2}{r^2} J_1(a_1 r) - \frac{J_0(a_1 r)}{r} \right]. \end{cases} \quad (18)$$

Within the range of the top of the pile, that is,  $(d_e/2) \leq r \leq (d/2)$ ,

(1) When  $T^2 \geq 4Dk_s$ ,

$$\begin{cases} \theta_{r2} = l_{21}[C_5 I_1(l_{21}r) - C_6 N_1(l_{21}r)] + l_{22}[C_7 I_1(l_{22}r) - C_8 N_1(l_{22}r)], \\ M_{r2} = Dl_{21}^2 \left\{ C_5 \left[ \frac{1-\nu}{l_{21}r} I_1(l_{21}r) - I_0(l_{21}r) \right] - C_6 \left[ \frac{1+\nu}{l_{21}r} N_1(l_{21}r) + N_0(l_{21}r) \right] \right\} \\ \quad + Dl_{21}^2 \left\{ C_7 \left[ \frac{1-\nu}{l_{21}r} I_1(l_{22}r) - I_0(l_{22}r) \right] - C_8 \left[ \frac{1+\nu}{l_{22}r} N_1(l_{21}r) + N_0(l_{22}r) \right] \right\}, \\ Q_{r2} = C_5 Dl_{21}^3 \left[ \frac{I_2(l_{21}r)}{r} + \frac{2-r^2}{r^2} I_1(l_{21}r) - \frac{I_0(l_{21}r)}{r} \right] + C_6 Dl_{21}^3 \left[ \frac{N_2(l_{21}r)}{r} + \frac{2+r^2}{r^2} N_1(l_{21}r) + \frac{N_0(l_{21}r)}{r} \right] \\ \quad + C_7 Dl_{22}^3 \left[ \frac{I_2(l_{22}r)}{r} + \frac{2-r^2}{r^2} I_1(l_{22}r) - \frac{I_0(l_{22}r)}{r} \right] + C_8 Dl_{22}^3 \left[ \frac{N_2(l_{22}r)}{r} + \frac{2+r^2}{r^2} N_1(l_{22}r) + \frac{N_0(l_{22}r)}{r} \right]. \end{cases} \quad (19)$$

(2) When  $T^2 \geq 4Dk_s$ , in order to simplify the expression, order  $l_2 = \sqrt[4]{(k_s/D) \cos 2\varphi} = -(T/2\sqrt{(k_s D)})$ , according to Euler's formula:

$$\begin{aligned} a_{21} &= l_2^2 e^{2i\varphi}, \\ a_{22} &= l_2^2 e^{-2i\varphi}. \end{aligned} \quad (20)$$

Combining formula (20),

$$\begin{cases} \theta_{r2} = \sum_{M=1}^4 l_2 C_{M+4} \{Z_{M1}(r) [\cos \varphi - (-1)^M \sin \varphi]\}, \\ M_{r2} = D l_2^2 \sum_{M=1}^4 C_{M+4} \left\{ Z_{M0}(r) [\cos 2\varphi - (-1)^M \sin 2\varphi] - \frac{(1-\nu)}{l_2 r} Z_{M1}(r) [\cos \varphi - (-1)^M \sin \varphi] \right\}, \\ Q_{r2} = -D l_2^3 \sum_{M=1}^4 C_{M+4} \{Z_{M1}(r) [\cos 3\varphi - (-1)^M \sin 3\varphi]\}, \end{cases} \quad (21)$$

where  $Z_{MN}(r)$  (among them  $M=1, 2, 3, 4$ ) denotes  $u_n(r)$ ,  $v_n(r)$ ,  $f_n(r)$ , and  $g_n(r)$ , respectively.

According to the above analysis, the simultaneous equations (14)~(17) can be used to calculate  $C_1, C_4, \dots, C_8$  and  $p_p$ . Thus, the deflection expression of the plate is obtained.

## 6. Pile-Soil Stress Ratio and Settlement

From the above analysis, if the strain of the steel bar is known before the calculation, the tension of the steel bar can be calculated directly by using formula (1), and then the undetermined coefficient can be solved according to the steps in Section 5. However, in most projects, the deformation of reinforcement is not measured beforehand. In view of this situation [4] through field test and study, it is found that the relationship between average strain and settlement of reinforcement under embankment load is approximately as follows:

$$\varepsilon_g = \frac{\alpha}{50} S^\beta, \quad (22)$$

where  $\alpha$  and  $\beta$  are the relevant fitting parameters, respectively, which can be selected according to the settlement calculation position. According to the table listed in reference [4], 50 kN/m is the tensile stiffness of the grid used in the test.

According to the above research results, the maximum deflection  $w_2(d_e/2)$  of geosynthetics is selected as the settlement  $S$  in formula (22). Combined with the method in Section 5, when the tension of the reinforcement is unknown, the steps of solving the undetermined coefficient are as follows:

- (1) First of all, assuming an initial tension value  $T_0$  ( $T_0$  can be a very small value), it is substituted into equations (2) and (6) to solve the flexural function of geosynthetics, and the values of  $w_1(d/2)$  and  $w_2(d_e/2)$  are obtained.
- (2) Then, take the value of  $w_2(d_e/2)$  obtained before as  $S$ , replace (22), combine the formula (1) to obtain the tension  $T$ , then replace  $T$  into equations (2) and (6), solve the flexure function of geosynthetics, and get the values of  $w_1(d/2)$  and  $w_2(d_e/2)$ .
- (3) Select an error value and compare the obtained  $w_1(d/2)$  and  $w_2(d_e/2)$  with the previous one. If the comparison results are less than the error value, stop the calculation; otherwise, continue the iterative calculation according to the steps of second and third.

The flowchart of the above steps is shown in Figure 3 as follows.

After obtaining the flexure function and  $p_p$  of the geosynthetics, it can be seen from the calculation model shown in Figure 2 that, according to the stress balance in the  $z$  direction, the average vertical stress  $p_s$  at the top of the soil between piles can be obtained as follows:

$$p_s = \frac{(q\pi d_e^2/4) - (p_p \pi d_e^2/4)}{(\pi(d_e^2 - d^2)/4)}. \quad (23)$$

Then, the pile-soil stress ratio  $n$  can be calculated according to the following formula [16]:

$$n = \frac{p_p}{p_s}. \quad (24)$$

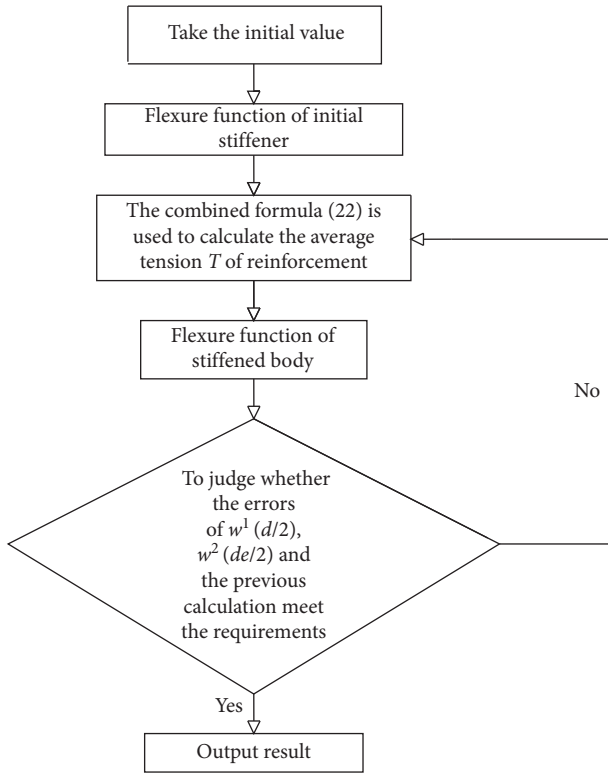


FIGURE 3: Flowchart of calculation.

Reference [8] thinks that, in the case of large area overloading, the settlement at the top of the pile is relatively small, and the settlement of soil between piles can be regarded as the settlement of the foundation.

$$S = w_2 \left( \frac{de}{2} \right). \quad (25)$$

## 7. Determination of Parameters

**7.1. Stiffness Coefficient of Pile  $k_p$ .** In order to comprehensively consider the nonlinearity in the process of pile deformation, the deformation stiffness of pile is taken as the secant slope of the load test  $q$ - $s$  curve of pile foundation.

**7.2. Spring Coefficient of Surrounding Soil  $k_s$ .** In order to comprehensively consider the nonlinearity in the process of soil deformation between piles, the coefficient of soil foundation between piles  $k_s$  takes the secant slope on the load test  $q$ - $s$  curve. If there is no measured data, it can also be taken in accordance with regional experience or determined according to the following formula [13]:

$$k_s = \frac{E_s}{H_s}, \quad (26)$$

where  $E_s$  is the deformation modulus of soil, the weighted average of multilayer soil is depth, and  $H_s$  is the thickness of soil layer.

**7.3. Calculated Thickness of Cushion  $\delta$ .** From the point of view of the joint action of the geosynthetics and the bulk material pile, the thickness of the composite structure formed by the geosynthetics and its wrapped filler is taken as the thin plate thickness if it is a multilayer grille, that is, the distance between the top layer and the bottom grille. If it is a geotechnical cell, the thickness of the geotechnical cell can be taken directly.

**7.4. Composite Elastic Modulus of Cushion  $E$ .** For the grid cushion, Zheng et al. [9] gave a method to determine its composite elastic modulus, that is, the weighted average value of the grid elastic modulus and the deformation modulus of the cushion filler. In the case of geotechnical cell, Yang et al. [17] gave the average elastic modulus of different types of geotechnical cell combined with various common fillers through stacked beam test.

## 8. Example and Parameter Analysis

**8.1. Example 1.** Technical treatment of soft soil foundation according to foundation reinforced by piles and geosynthetics in DK10+320 and DK10+336 test section of Suining-Chongqing railway [4], and the pile is powder injection pile, the diameter of the pile is 0.50 m, the center of the pile is 1.0 m, piles are arranged as the shape of plum blossoms and  $de = 1.05$  m, and powder injection pile is laid with a double-layer geogrid with 50 kN/m tensile stiffness and a distance of 30 cm. The foundation is quaternary alluvial soft soil, the bedrock is mudstone, the upper filling load is 20 kN/m<sup>3</sup>, the filling height of roadbed is 10 m, and the crushed stone cushion is 25 kN/m<sup>3</sup>. According to the static load test, the stiffness coefficient of pile is  $k_p = 2000$  kN/m. The thickness of the thin plate is 0.3 m, the composite elastic modulus  $E$  is 52 MPa, and Poisson's ratio  $\nu$  is 0.3. Other calculation parameters are shown in Table 1.

The comparison between the calculated and measured values of the central settlement of the embankment and the pile-soil stress ratio under the geogrid geosynthetics is shown in Table 2.

The development trend of foundation settlement  $S$  of DK10+336 test section with the increase of embankment filling height  $H$  is shown in Figure 4.

As can be seen from Tables 2 and 3, the pile-soil stress ratio and settlement of double-layer geogrid-reinforced composite foundation obtained by this method are close to the measured values.

**8.2. Example 2.** The test section of an expressway lying on soft soil foundation in Hunan is treated with geocell + mixing piles. The pile is arranged in the form of plum blossoms, and its diameter is 0.50 m with its spacing 1.2 m. The pile top is filled with a thick 30 cm sand cushion, and the center is equipped with a geotechnical cell with the thickness of 10 cm. The foundation is muddy clay, the load of the upper fill is 20 kN/m<sup>3</sup>, and the filling height of the roadbed in the test section is 4 m. The measured settlement value  $S$  is 5.3 cm, and the pile-soil stress ratio is  $n$ . The stiffness



TABLE 1: The parameters for calculation.

Station	Type of soils	Depth, $H_s$ (m)	Deformation modulus, $E_s$ (MPa)	Grid tension, $T$ (kN/m)	$T^2 - 4Dk_s$
DK10 + 320	Soft soil	7.0	3.1	60.3	<0
DK10 + 336	Soft soil	10.6	3.1	82.7	<0

TABLE 2: Results of settlement and pile-soil stress ratio.

Station	Settlement, $S$ (cm)		Pile-soil stress ratio, $n$	
	Calculated value	Measured value	Calculated value	Measured value
DK10 + 320	28.8	26.6	4.53	3.87
DK10 + 336	33.9	32.0	6.64	5.82

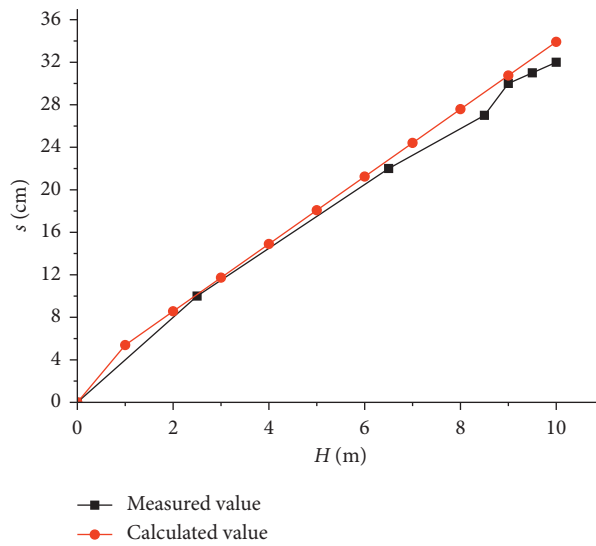


FIGURE 4: Comparison between calculated and measured results of embankment settlement.

TABLE 3: Results of settlement and pile-soil stress ratio.

Items	$T^2 - 4Dk_s$	Pile-soil stress ratio, $n$	Settlement, $S$ (cm)
Measured value	—	6.5	5.3
Method of literature [14]	—	5.8	—
The proposed method	<0	6.1	5.7

coefficient of pile  $k_p$  is 2355 kN/m. After treatment, the coefficient of soil foundation between piles  $k_s$  is 1024 kN/m<sup>3</sup>, the thickness of thin plate  $\delta$  is 0.10 m, the composite elastic modulus  $E$  is 40 MPa, and the composite Poisson's ratio  $\nu$  is 0.3.

The pile-soil stress ratio and settlement are calculated as shown in Table 3.

It can be seen from Table 3 that the pile-soil stress calculated in this paper is closer to the measured value than the method in reference [14]. In addition, the settlement is also close to the measured value. This is due to the fact that compared with the method in reference [14], the tensile effect of the cell body is considered in this paper.

**8.3. Parameter Analysis.** In order to further discuss and analyze the effects of geosynthetics composite elastic modulus, grille tension and pile-soil stiffness ratio on the settlement and pile-soil stress ratio of composite foundation reinforced by piles and geosynthetics, based on the parameters in example 2, the corresponding parameters are analyzed according to the abovementioned factors.

**8.3.1. Influence of Pile-Soil Stiffness Ratio on Settlement and Pile-Soil Stress Ratio.** Without considering the influence of tension of geosynthetics,  $k_p = 4K_p/(\pi d^2)$  is introduced to characterize the comprehensive influence of pile

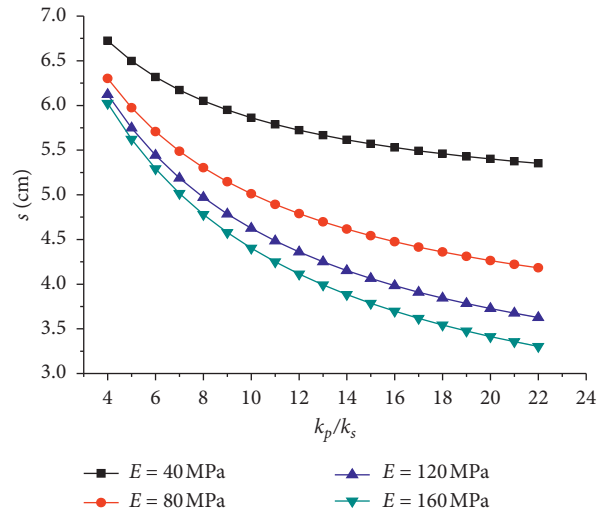


FIGURE 5: Relation between settlement and  $k_p/k_s$ .

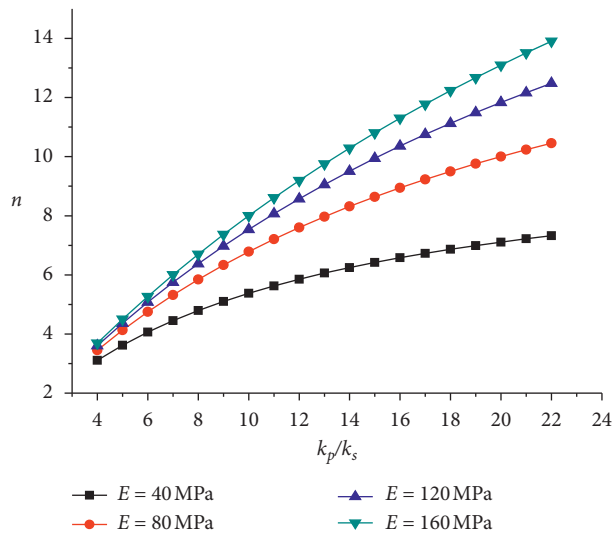


FIGURE 6: Relation between pile-soil stress and  $k_p/k_s$ .

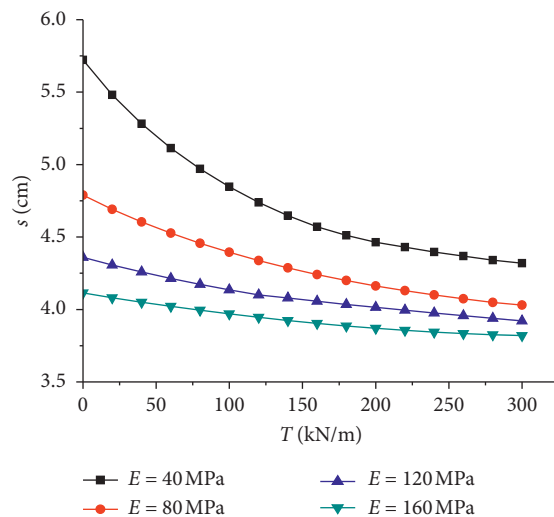


FIGURE 7: Relation between settlement and tension.

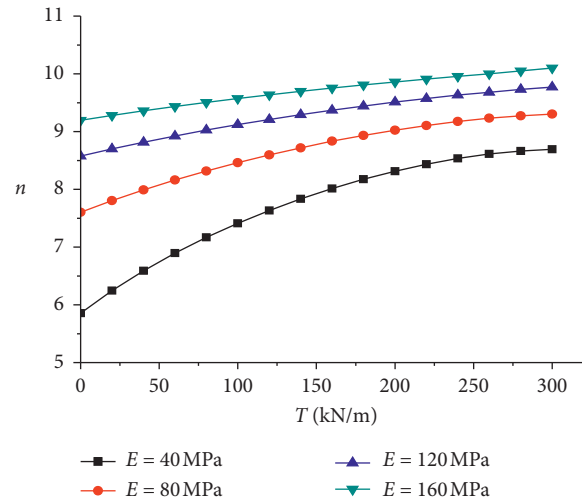


FIGURE 8: Relation between pile-soil stress and tension.

deformation stiffness and replacement ratio, and other parameters remain unchanged.

As shown in Figure 5, the influence of pile-soil stiffness ratio on settlement increases with the increase of elastic modulus  $E$ . At the same elastic modulus, the settlement of composite foundation decreases with the increase of pile-soil stiffness ratio. However, when the pile-soil stiffness ratio exceeds a certain value, continuing to increase the pile-soil stiffness ratio, it has little effect on reducing settlement.

As can be seen from Figure 6, the relationship between pile-soil stiffness ratio and pile-soil stress ratio is nonlinear under different elastic modulus, and the smaller the elastic modulus is, the more obvious the nonlinear phenomenon is. In addition, the larger the elastic modulus is, the more obvious the influence of pile-soil stiffness ratio on pile-soil stress ratio is.

**8.3.2. Effect of Reinforcement Tension on Settlement and Pile-Soil Stress Ratio.** As can be seen from Figures 7 and 8, for the same elastic modulus  $E$ , the settlement decreases with the increase of reinforcement tension  $T$ , while the pile-soil stress ratio  $n$  increases with the increase of tension  $T$ .

In addition, the effect of  $T$  on both pile-soil stress ratio and settlement decreases with the increase of  $E$ . It can be seen that when the elastic modulus of geosynthetics-reinforced cushion is small, using graded material and properly increasing the interface friction can effectively increase the pile-soil stress ratio and reduce the settlement.

## 9. Conclusions

Based on theory of the Filonenko–Borodich two-parameter elastic foundation model, the horizontal geosynthetics of composite foundation are regarded as the elastic thin plate, and the vertical piles and surrounding soil are regarded as a series of springs with different stiffness. The deflection equation of horizontal geosynthetics considering its bending and pulling action is obtained according to the static

equilibrium conditions. The equation is solved by using Bessel function of complex variable, and the corresponding deflection function of horizontal geosynthetics is deduced. The calculation method for pile-soil stress ratio and settlement of composite foundation is derived by considering the deformation coordination of pile and soil.

- (1) The settlement of composite foundation decreases with the increase of pile-soil stiffness ratio, geosynthetics tension, and composite elastic modulus of geosynthetics. The pile-soil stress ratio of composite foundation increases with the increase of pile-soil stiffness ratio, elastic modulus of geosynthetics, and its tension. When the bending stiffness of geosynthetics is small, the influence of tensile action of reinforcement on pile-soil stress ratio and settlement cannot be ignored.
- (2) The key to calculating with this method is to accurately measure the composite elastic modulus of geosynthetics-reinforced cushion, the strain of geosynthetics, and the stiffness of pile and soil.
- (3) Although this presented method does not rely on preassumed deformation when calculating the pile-soil stress ratio and settlement of composite foundation, the net effect of geosynthetics-reinforced cushion can be considered only when the strain of geosynthetics is known, which brings defects to the convenience of calculation. The proposed method still cannot consider the coupling relationship between deformation of geosynthetics-reinforced cushion and tension of geosynthetics, which can be carried out in the next work.

## Abbreviations

$T$ :	The tension of geosynthetics
$\varepsilon_g$ :	The average strain of geosynthetics
$E_g$ :	The tensile stiffness of geosynthetics
$D$ :	The bending stiffness of the thin plate

$E$ :	The elastic modulus of the thin plate
$\nu$ :	Poisson's ratio of the thin plate
$\delta$ :	The thickness of the thin plate
$J_N$ :	The first kind of N-order Bessel functions
$Y_N$ :	The second kind of N-order Bessel functions
$q$ :	The distributed load
$P_p$ :	The supporting force
$k_s$ :	The spring coefficient of surrounding soil
$N_N$ :	The second kind of N-order virtual variable Bessel function
$u_n$ :	The real part of the first kind of Hankel function of order N
$v_n$ :	The real part of the first kind of Bessel function of order N
$f_n$ :	The imaginary part of Hankel function of order N
$g_n$ :	The imaginary part of Bessel function of order N
$p_p$ :	The value of pile top reaction
$\alpha, \beta$ :	The relevant fitting parameters
$T_0$ :	The initial tension value
$S$ :	The settlement
$p_s$ :	The average vertical stress at the top of the soil between piles
$k_p$ :	The stiffness coefficient of pile
$E_s$ :	The deformation modulus of soil
$H_s$ :	The thickness of soil layer
$\delta$ :	The calculating thickness of cushion
$E$ :	The composite elastic modulus of cushion
$C_1, C_2, C_3$ :	The undetermined constants
$C_4$ :	
$C_5, C_6, C_7$ :	The undetermined constants.
$C_8$ :	

## Data Availability

The [Data Type] data used to support the findings of this study are available from the corresponding author upon request.

## Conflicts of Interest

The authors declare that they have no conflicts of interest.

## Acknowledgments

The work described in this paper was fully supported by these grants from the National Natural Science Foundation of China (award nos. 51778227, 51308208, and 41372303), the Provincial Natural Science Foundation of Hunan (award nos. 2015JJ3069 and 18C0311), the Youth Talent Plan Program of Hunan (award no. 2016RS3032), and the Postgraduate Scientific Research Innovation Project of Hunan Province (award no. CX20200992).







## References

- [1] B. Wang, *High-speed Railway Roadbed engineering*, China Railway Publishing House, Beijing, China, 2007.

- [2] J. Han and M. A. Gabr, "Numerical analysis of geosynthetic-reinforced and pile-supported earth platforms over soft soil," *Journal of Geotechnical and Geoenvironmental Engineering*, vol. 128, no. 1, pp. 44–53, 2002.
- [3] C. H. Abdullah and T. B. Edil, "Behaviour of geogrid-reinforced load transfer platforms for embankment on rammed aggregate piers," *Geosynthetics International*, vol. 14, no. 3, pp. 141–153, 2007.
- [4] X. Cao, S. Qing, and L. Zhou, "Experimental study on reinforcement effect of geogrid on composite foundation with dry jet mixing piles," *Chinese Journal of Rock Mechanics and Engineering*, vol. 25, pp. 3162–3167, 2006.
- [5] Y. Yang, *Study On Bearing Characteristics of Two-Way Reinforced Composite foundation*, Hunan University, Changsha, China, 2006.
- [6] C. Chen and Z. Zhou, "Analysis of pile-soil stress ratio for double reinforced composite ground," *Rock and Soil Mechanics*, vol. 30, no. 9, pp. 2660–2666, 2009.
- [7] S. W. Abusharar, J.-J. Zheng, B.-G. Chen, and J.-H. Yin, "A simplified method for analysis of a piled embankment reinforced with geosynthetics," *Geotextiles and Geomembranes*, vol. 27, no. 1, pp. 39–52, 2009.
- [8] W. Rao and C. Zhao, "The behavior of pile-soil composite foundation," *China Civil Engineering Journal*, vol. 35, no. 2, pp. 74–80, 2002.
- [9] J. Zheng, J. Zhang, and Q. Ma, "Three dimensional analysis of pile-earth ratio of biaxial reinforcement composite foundation," *Journal of Huazhong University of Science and Technology (Nature Science Edition)*, vol. 38, no. 2, pp. 83–86, 2010.
- [10] B. Ma, Z. Li, K. Cai et al., "An improved nonlinear settlement calculation method for soft clay considering structural characteristics," *Geofluids*, vol. 2021, Article ID 8837889, 7 pages, 2021.
- [11] B.-H. Ma, Z.-Y. Hu, Z. Li et al., "Finite difference method for the one-dimensional non-linear consolidation of soft ground under uniform load," *Frontiers in Earth Science*, vol. 8, pp. 1–9, 2020.
- [12] Y. He, M.-M. Wang, D.-Y. Wu, K.-N. Zhang, and W.-M. Ye, "Effects of chemical solutions on the hydromechanical behavior of a laterite/bentonite mixture used as an engineered barrier," *Bulletin of Engineering Geology and the Environment*, vol. 80, no. 2, pp. 1169–1180, 2021.
- [13] Y. Chen, H. Liu, and Q. Hou, "Theoretical analysis of cushion and embankment fills in pile-supported embankment," *Rock and Soil Mechanics*, vol. 29, no. 8, pp. 2271–2276, 2008.
- [14] M. Zhao, D. Liu, and L. Zhang, "Calculation for pile-soil stress ratio of two-direction reinforced composite foundation," *Engineering Mechanics*, vol. 26, no. 2, pp. 176–181, 2009.
- [15] A. P. S. Selvadurai, *Elastic Analysis of Soil-Foundation Interaction*, China Railway Press, Beijing, China, 1984.
- [16] X. Gong, *Theory and Application of Composite Foundation*, China Architecture and Building Press, Beijing, China, 2002.
- [17] M. Yang, Y. Deng, and M. Zhao, "Study of stiffness test method of geocell cushion based on the superposed beam theory," *China Civil Engineering Journal*, vol. 44, no. 11, pp. 87–92, 2011.

## Research Article

# Study on Dynamic Evolution of Roof Crack and Support Timing of Secondary Tunneling for Large Section Open-Off Cut in Deep Mines

Shuaigang Liu <sup>1,2</sup>, Jianbiao Bai <sup>2,3</sup>, Xiangyu Wang <sup>1,2</sup>, Bowen Wu <sup>1,2</sup>,  
Guanghui Wang <sup>1,2</sup>, Yanhui Li <sup>1,2</sup> and Jun Xu<sup>4</sup>

<sup>1</sup>School of Mines, China University of Mining and Technology, Xuzhou 221116, China

<sup>2</sup>State Key Laboratory of Coal Resources and Safe Mining, China University of Mining and Technology, Xuzhou 221116, China

<sup>3</sup>College of Mining Engineering and Geology, Xinjiang Institute of Engineering, Urumqi 830023, China

<sup>4</sup>School of Science, Yangzhou Polytechnic Institute, Yangzhou 225127, China

Correspondence should be addressed to Jianbiao Bai; [baijianbiao@cumt.edu.cn](mailto:baijianbiao@cumt.edu.cn)

Received 18 March 2021; Revised 29 March 2021; Accepted 5 April 2021; Published 21 April 2021

Academic Editor: Zhijie Zhu

Copyright © 2021 Shuaigang Liu et al. This is an open access article distributed under the Creative Commons Attribution License, which permits unrestricted use, distribution, and reproduction in any medium, provided the original work is properly cited.

The stability of large section open-off cut in deep mines (LODM) is the key factor affecting the normal equipment installation and safe mining in fully mechanized top-coal caving face. The mechanical model shows that the deflection of the roof of the LODM is proportional to the cubic of span. In this paper, UDEC Trigon model is established, and the parameters of different coal measures strata are modified in detail. The evolution law, failure mode, and damage degree of roof cracks in secondary tunneling are studied, and the roof support effect is analyzed. The numerical simulation results show that the process of roof crack evolution after the primary excavation section and the second excavation section can be divided into three stages according to microseismic activities, and the reasonable supporting time can control the propagation of roof microcracks and reduce the development height of macrocracks. The rock bridge existing in the roof rock stratum after the combined support of long and short anchor cables can effectively limit the formation of macrocracks and their interaction; especially the key support in the interface area can reduce the development height of roof cracks in secondary tunneling and weaken the damage degree of roof rock stratum in the LODM. The field test shows that the moved volume of rib-to-rib and roof-to-floor of the LODM is stable at about 350 mm and 550 mm, respectively. The numerical simulation in this paper is helpful to understand the failure mode of roof in LODM with large mining height and provides a method for the design of its control technologies.

## 1. Introduction

Open-off cut is the place for equipment installation and mining initiation in coal mining face. With the gradual improvement of mechanization degree in fully mechanized top-coal caving face, the width of open-off cut in fully mechanized top-coal caving face also gradually increases. At the same time, in recent years, with the depletion of shallow coal resources, many mines have begun to move to the deep part [1–5]. Compared with the open-off cut under conventional conditions, the LODM has the characteristics of high in situ stresses, high ground temperatures, high

permeability, large span, absciss layer, and easily separated and fell roof and low coal seam strength [6, 7]. There are many factors that affect the stability of the LODM, including section shape, geological conditions, ground stress, tunneling mode, supporting time, and supporting strength [8]. The service time of open-off cut is from the beginning of tunneling to the start of mining when the equipment is successfully installed and debugged in working face. Different from the shafts, main roadways, headgates, and tailgates, the service time of open-off cut is generally short and only a few months. If we pay attention to the support strength and density in order to control the deformation of



surrounding rock in the LODM, it will lead to excessive support, which will not only increase the cost, but also lead to serious consequences such as difficulty in preliminary roof caving and in roof management of working face for fully mechanized top-coal caving face. If the support strength and density are reduced in consideration of its short service time, it will lead to insufficient support, which will not only easily lead to roof falling accidents and threaten workers' life safety, but will also lead to serious deformation and damage of surrounding rock, thus making the equipment unable to be installed. And it is necessary to repair the roof or floor again; if not, it will affect the safety and efficient production of the mine [9–12].

A lot of research has been done on the failure mode and control technology of roof in the LODM. Yin [13] analyzes the mechanical structure of roof in large section roadway and derives differential equations based on elastic foundation beams to obtain the variation law of bending moment and roof subsidence with roof span. The structural characteristics of roof support by anchor truss and load distribution characteristics of anchor truss structure are studied, and the BP neural network active support design system for thick coal seam roadway of large section is developed to determine the key support parameters of large section roadway. Zhang et al. [14] obtained through physical similarity simulation that the roof of large section open-off cut with large mining height is easy to fall and the corner is easy to be damaged, and the roof sinks obviously after the open-off cut is expanded. According to the failure characteristics of the open-off cut, the treatment measures such as improving the stress state of the corner, supporting the roof in time, and reducing span support are put forward. He et al. [15] establish Hooke-Kelvin concatenation model of surrounding rock according to the failure characteristics of surrounding rock in large section open-off cut with large mining height, analyzes the key influencing factors of anchor cable tension, and reveals the interaction mechanism between roof pressure arch and anchor cable in open-off cut. Compared with the difference of action mechanism between single anchor cable and truss anchor cable, the control technology of truss surrounding rock with composite anchor cable is put forward, which achieved good results. Xie et al. [16] established FLAC<sup>3D</sup> numerical calculation model, analyzed the distribution characteristics of effective stress field of the roof of the LODM, constructed the load-bearing structure of anchored rock beam, obtained the analytical expression of maximum shear stress under compound influence function, and defined the cooperative control principle of the roof of the LODM as well as load-bearing structure of anchored rock beams of two sides of roadway. Peng et al. [17] put forward a support method combining double-layer I-bar closed support with grouting for large section roadway under the condition of high stress broken surrounding rock, and the field monitoring deformation is less than 25 mm. Zhang et al. [18] simulated the failure mechanism of a large section roadway with a depth of 1 km. The results show that the soft rock property and high original rock stress are the main factors leading to the instability of the deep roof and put forward the joint control

technologies such as long anchor rod and anchor cable, ring support, and grouting.

Many studies have discussed the influence of support schemes on roof failure control, but the continuum model usually underestimates the effectiveness of support units, because the continuum method can not simulate the inhibition of roof crack opening and sliding [19–25]. Using discontinuous or discrete elements to understand the failure mechanism of roof in the LODM and the interaction of support units is of great significance to guide the roadway support strategy [26]. Bai et al. [27] used UDEC Voronoi method to study the progressive failure process of roadway roof of large section, and the results showed that shear cracks dominated the roadway roof, and they put forward reasonable control technology. Gao et al. [28] used UDEC Trigon model to simulate the shear failure process of the roof in large section and successfully captured the shear failure of roof characterized by crack initiation and propagation. The results showed that the shear failure of roadway roof started at the corner of roadway, then gradually spread to the depth of roof, and finally formed a large-scale roof failure. Moreover, it simulated the role of anchor rod support in limiting the shear failure of roadway roof. Anchor rod support limited the expansion of roof rock, reduced the failure of rock bridge, and ensured the rock strength, thereby significantly reducing the subsidence of the roof of the large section roadway. Zhang et al. [29] analyzed the roof failure characteristics of large section roadway by using UDEC polygon method and put forward a support scheme involving key area reinforcement and high-strength anchor rod, and the deformation of large section roadway was controlled within 550 mm. Yin et al. [30] established a numerical simulation model of surrounding rock of large section roadway by using 3DEC. The results show that obvious cracks will occur at both ends of the roof under the action of shear stress. With the upward propagation of cracks at the roof abscissa layer and the extension of transverse cracks, the cracks above the large section roof run through a dangerous crack zone. On this basis, an optimized support scheme is given.

Although there are some understandings on the failure mechanism of roof in the LODM, it is relatively rare to study the failure process and control of roof by discrete element method [31–33]. The method of secondary tunneling is adopted in the LODM. The primary excavation section is affected by the secondary excavation section, and the start, slip and expansion of roof strata cracks are serious. How to control the roof in the interface area of the two excavations, the timing of reinforcement and support, and the support strength are the core points of the LODM. In this paper, discrete element model is used to study the failure process of roof in the LODM, to determine the reasonable support timing of two excavation sections, and to systematically study the laws of crack propagation, failure mode, and damage degree of roof in the LODM. On this basis, the control effects of three support schemes on roof in open-off cut are put forward. Finally, the support timing and key control points of the LODM are put forward, the control technical parameters of open-off cut in 5202 working face of

Xin'an coal mine are determined, and the effect of supporting is monitored and evaluated on site. The research provides reference and referential significance for open-off cut stability research and supporting design under similar engineering geological conditions.

## 2. Case Study

**2.1. Geological and Mining Conditions.** Xin'an coal mine is located in Pingliang City, Gansu Province, China, as shown in Figure 1(d). The mine adopts longwall mining method to exploit 5# coal, the mining height is 10 m, and the average buried depth of coal seam is about 800 mm. In this paper, the LODM is located in 5202 working face of Xin'an coal mine. The panel of 5202 working face includes three longwall working faces, namely, 5202, 5204, and 5206 working faces. The 5202 working face is the first mining working face in the panel, with an advancing length of about 1500 m and a width of about 200 m, as shown in Figure 1(c). The width and the height of open-off cut of the 5202 working face are, respectively, 7800 mm and 3200 mm, as shown in Figures 1(a) and 1(b). The roof consists of fine sandstone and sandy mudstone, while the floor consists of sandy mudstone and fine sandstone. The rock stratum histogram is shown in Figure 2.

**2.2. Mechanical Model of Roof Deformation in the LODM and Selection of Tunneling Mode.** With one-time tunneling mode, the load of the roof bearing the overlying rock gradually increases and the subsidence of the roof also increases. According to the simply supported beam model of material mechanics, the calculation model of the subsidence of the roof in large section open-off cut is established, as shown in Figure 3, and the deflections of the left and right hinge supports in the model are set to zero.

According to the bending moment equation of beam, the value of the following items can be known:

$$M(x) = \frac{1}{2}qlx - \frac{1}{2}qx^2, \quad (1)$$

where  $M$  is the bending moment of the beam,  $q$  is the load of overlying rock, and  $l$  is the span of the beam.

The differential equation of deflection curve of straight beam with uniform cross section is as follows:

$$EI\omega'' = -M(x), \quad (2)$$

where  $\omega''$  is the deflection of the beam,  $E$  is elastic modulus of roof, and  $I$  is moment of inertia of roof beam.

Then the approximate differential equation of the deflection curve of roof beam:

$$\omega = \frac{1}{24}qx(l^3 - 2lx^2 + x^3). \quad (3)$$

In the middle of the roof beam span  $x = l/2$ , and the deflection of the roof beam is the largest, namely:

$$\omega_{\max} = \frac{5ql^4}{384EI}. \quad (4)$$

When the height  $H$  of the roof beam is constant, its moment of inertia is proportional to its span  $l$ , and then:

$$I = \frac{H^3}{12}l. \quad (5)$$

Substitute equation (5) into equation (4) to get

$$\omega_{\max} = \frac{5ql^3}{32EH^3}. \quad (6)$$

It can be seen from Formula (6) that the maximum deflection of the roof of large section open-off cut is proportional to the cubic of span  $l$ . Therefore, a reasonable supporting method must be chosen for the roof and the support should be in time. The way of tunneling in two times is adopted, that is, to excavate an appropriate section through the open-off cut once. After releasing some energy and reasonably supporting the primary excavated section, then excavate to the designed section size. The primary excavated section and its reasonable support can reduce the span and avoid the roof deformation and crack expansion of the LODM from transferring to the deep.

## 3. Numerical Simulations of Roof Failure Process of the LODM

### 3.1. Model Setup

**3.1.1. UDEC Trigon Method.** In the trigon method, rock mass is expressed as a combination of triangular blocks bonded by internal contact to simulate brittle materials [28, 34]. It is assumed that each triangular block is an elastic material and is divided into triangular finite difference domains, which cannot fail. Damage caused by shear stress or tensile stress can only occur along the contact surface, which depends on the strength of the contact surface (see in Figure 4).

In the direction of vertical contact, the stress-displacement relationship is assumed to be linear and controlled by stiffness  $k_n$  [35]:

$$\Delta\sigma_n = -k_n\Delta u_n, \quad (7)$$

where  $\Delta\sigma_n$  is the effective normal stress increment and  $\Delta u_n$  is normal displacement increment. There is a limiting tensile strength,  $\tau_s^{\max}$ , for the contact. If the tensile strength is exceeded, then  $\Delta\sigma_n = 0$ .

In the shear direction, the response is governed by a constant shear stiffness. The shear stress,  $\tau_s$ , is determined by a combination of contact microproperties, cohesion and friction. Thus,

$$|\tau_s| \leq c + \sigma_n \tan \varphi = \tau_s^{\max}. \quad (8)$$

Then:

$$\Delta\tau_s = -k_s\Delta u_s^e. \quad (9)$$

Or else, if

$$|\tau_s| \geq \tau_s^{\max}, \quad (10)$$

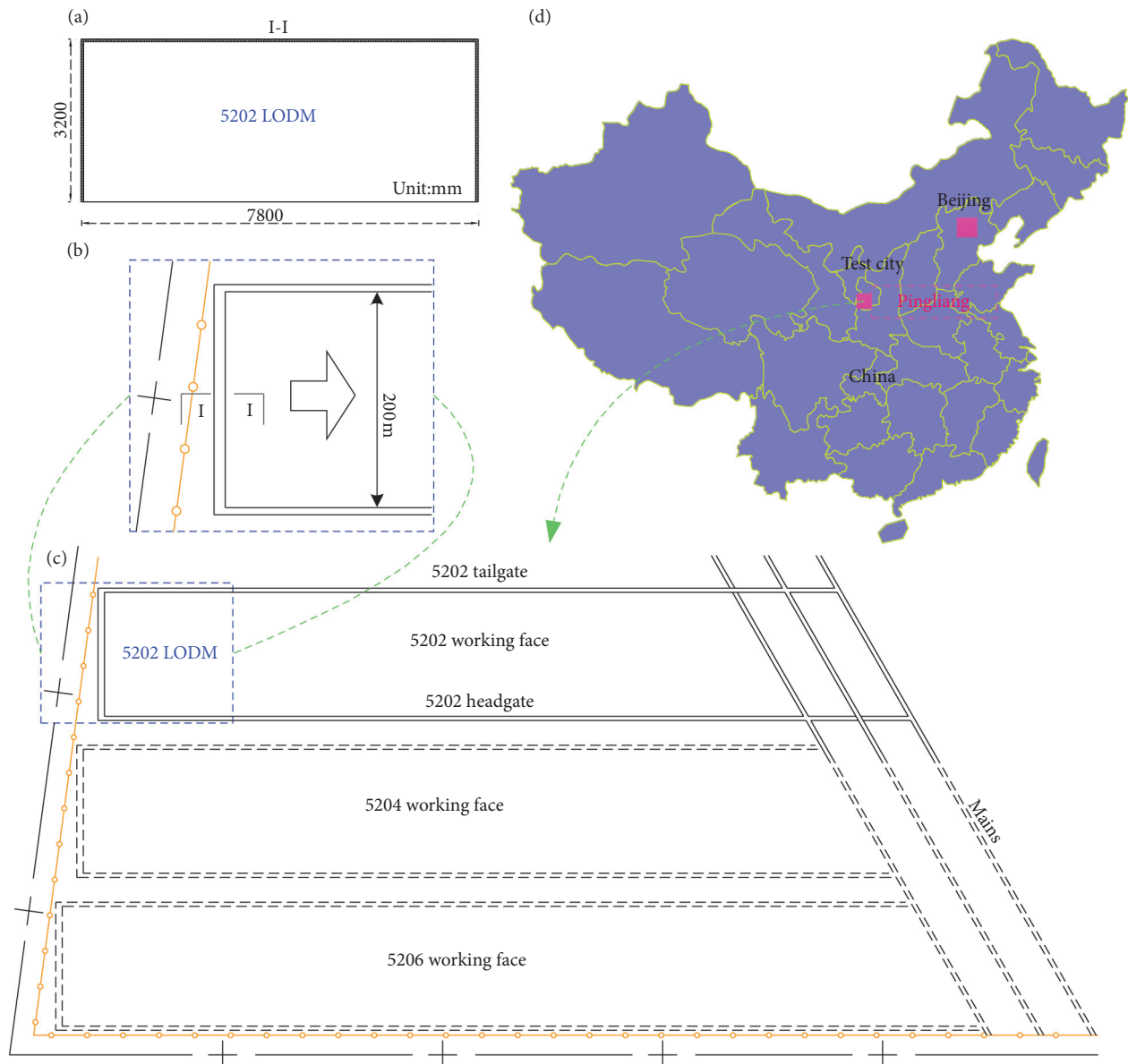


FIGURE 1: Coal mine location and the roadway site: (a) the LODM I-I section; (b) enlarged drawing of the 5202 LODM; (c) the LODM and working surface layout drawing of the research site; (d) location of the research site.

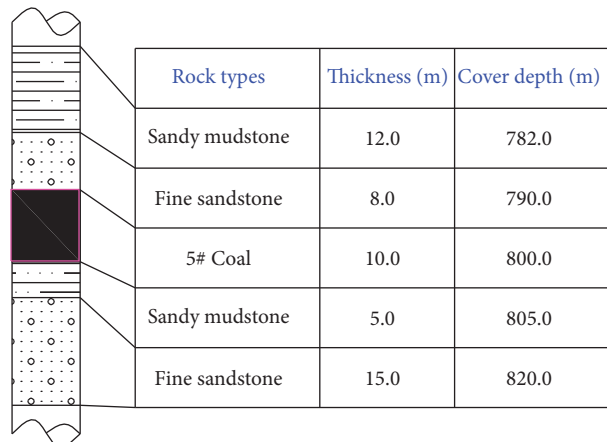


FIGURE 2: Nearby stratigraphic histogram of 5202 LODM.

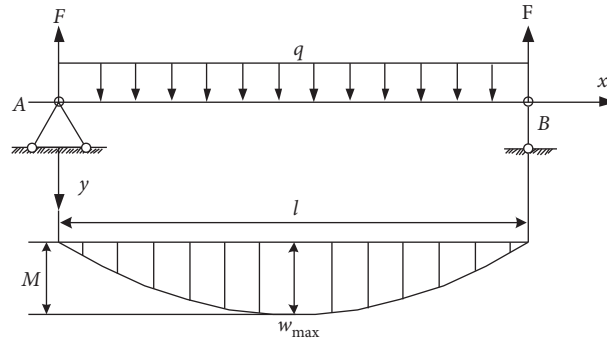


FIGURE 3: Mechanics model of simply supported beam in the LODM.

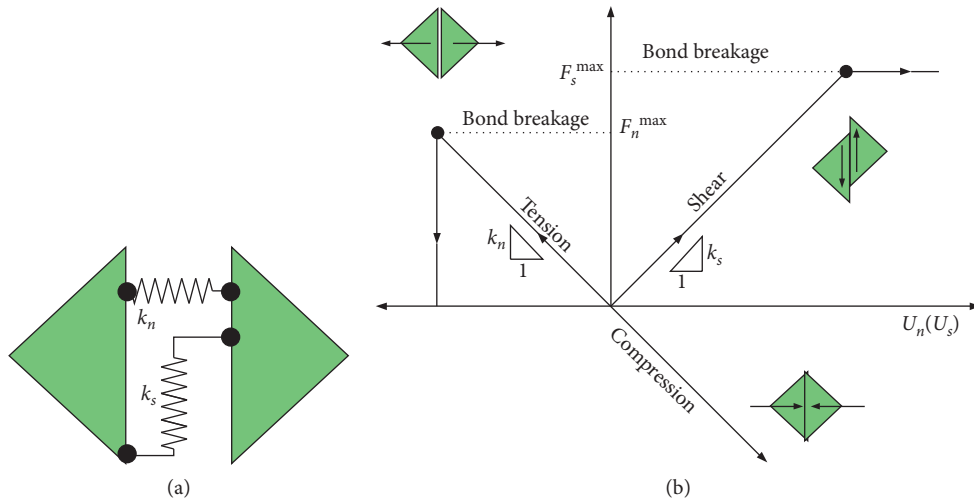


FIGURE 4: Using UDEC Trigon method to simulate the propagation process of rock mass fracture: (a) tangential and normal stiffness between blocks; (b) constitutive and failure behavior of tensile and shear strength between blocks.

then:

$$|\tau_s| = \text{sign}(\Delta u_s) \tau_{\max}, \quad (11)$$

where  $c$  is the cohesion,  $\varphi$  is the friction, and  $\Delta u_s^e$  is the elastic component of the incremental shear displacement, and  $\Delta u_s$  is the total incremental shear displacement.

Micromechanical parameters, such as polygonal block and contact surface, jointly determine rock mechanical properties [32]. In UDEC Trigon model, the polygonal block is an elastic body, and four micromechanical parameters such as elastic modulus of polygonal block, internal friction angle  $\varphi$ , cohesion  $C$ , and tensile strength  $T$  of contact surface should be determined for specific rocks.

**3.1.2. Model Configuration.** Two-dimensional UDEC model is established to simulate the failure mode of roof in the LODM and the effect analysis of supporting scheme. The numerical model is shown in Figure 5, with the width and the height of the model being, respectively, 70 m and 50 m. In order to improve the calculation efficiency of the model, only the area of interest, i.e., the direct roof, is discretized by UDEC Trigon logic. The average size of triangular blocks in

the study area is 0.2 m. The thicker polygonal Voronoi blocks with average block size of 0.5 m were used. The thicker polygonal Voronoi blocks with average block sizes of 1.0 m and 2.0 m are used to simulate the coal measures strata at the boundary of the model.

At the bottom of the model and the boundary of both sides of the model, the displacement is fixed in the vertical and horizontal directions, respectively. According to the field measurement, the vertical stress is 19.3 MPa, the axis value that the maximum principal stress is erecting to the LODM is 23.2 MPa, and the axis value that the minimum principal stress is erecting to the LODM is 15.8 MPa. This in situ stress state is applied to the model, and the vertical stress of 19.3 MPa is applied to the upper boundary of the model to simulate the overlying rock pressure.

Generally speaking, the simulation calculation of the model of the LODM is divided into four steps. The first step is to apply in situ stress conditions to the global model for calculation. The second step is to simulate the excavation process of the LODM. In the second step, the excavation method of the LODM is tunneling in two times, that is, two times of excavation. The first time, the section with a width of 4.8 m and a height of 3.2 m is excavated, and the anchor



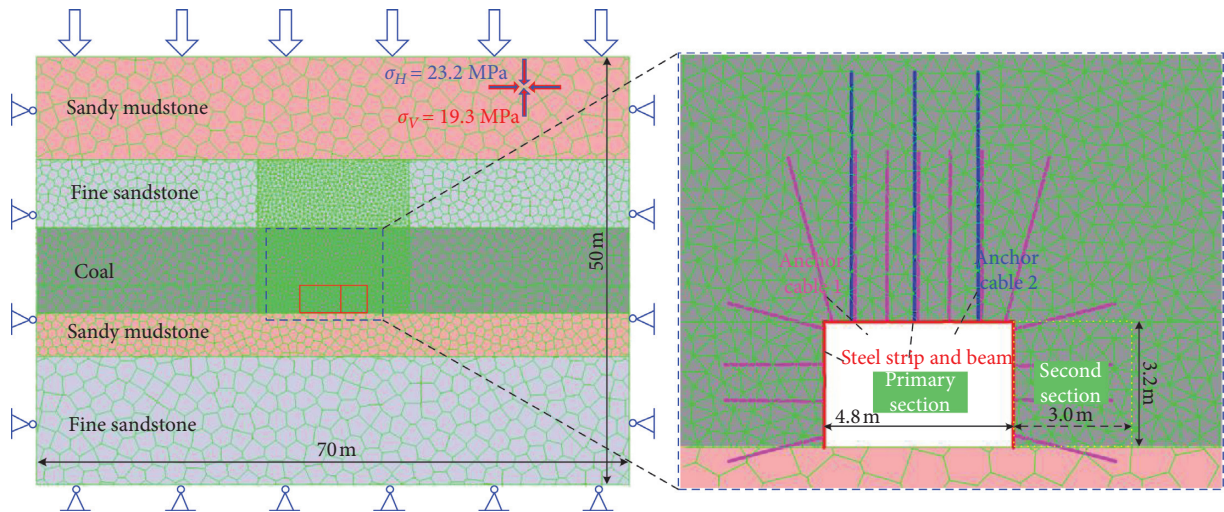


FIGURE 5: UDEC Trigon model of the LODM containing geometry and boundary conditions.

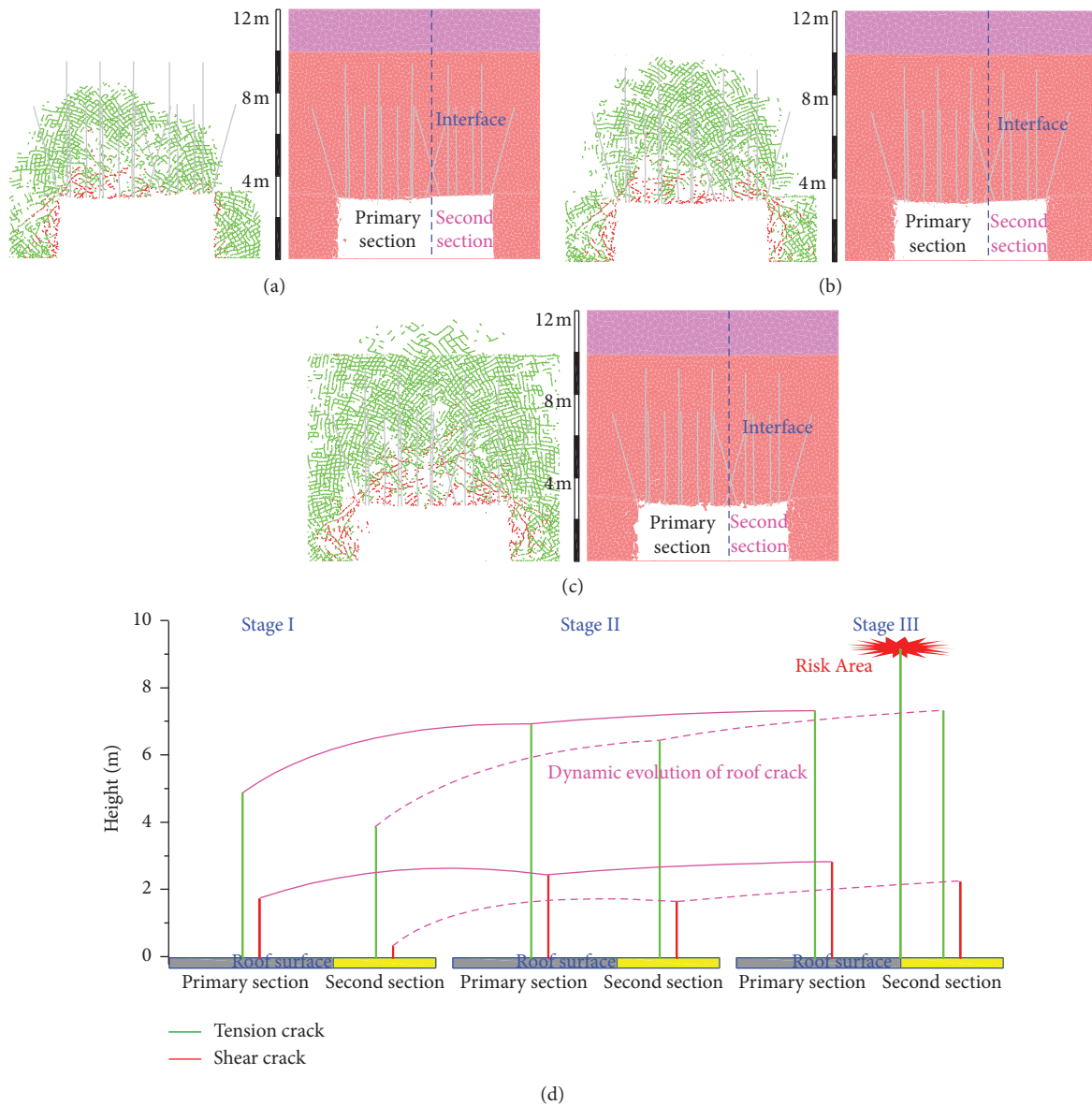


FIGURE 6: The development process of roof cracks in the full section and failure mode of roof: (a) Stage I; (b) Stage II; (c) Stage III; (d) dynamic evolution of roof crack after second excavation. (The green cracks represent tensile cracks, and the red cracks represent shear cracks.)



cable support is carried out. The specific support parameters are shown in Figure 6, and then the calculation is carried out. In second time, the excavation distance will be to open-off cut with the designed section size. In the third step, after the excavation of the LODM, the simulation calculation is done under different supporting parameters. The analysis of the failure process of the roof and the supporting effect of different supporting strengths during the two excavations is helpful to determine the supporting time of two times tunneling of the LODM and the roof control strategy of the supporting strength.

**3.2. Numerical Calibration.** Rock properties obtained from laboratory should be converted into rock mass properties. RQD is widely used to estimate the deformation modulus of rock mass. Based on a large number of field monitoring data, Zhang and Einstein [36] established the relational expression between RQD and  $E_m/E_r$  (3–6), so this relational expression was used to correct rock mass parameters. In our research, the RQD value of rock mass was observed by borehole camera:

$$\frac{E_m}{E_r} = 10^{0.0186RQD - 1.91}. \quad (12)$$

In the equation  $E_m$ ,  $E_r$  are the deformation modulus of rock mass and intact rock, respectively. Unconfined compressive strength (UCS) can be determined according to the ratio of  $E_m/E_r$  [37]:

$$\frac{\sigma_m}{\sigma_r} = \left( \frac{E_m}{E_r} \right)^n. \quad (13)$$

$\sigma_m$ ,  $\sigma_r$  are the strength of rock mass and intact rock, respectively. And the index  $n$  for splitting, shearing, sliding, and rotation modes is 0.56, 0.56, 0.66, and 0.72, respectively. Since the failure process of roof is complicated seriously, there are many failure models. The value of index  $n$  is 0.63 in this paper. Here, we also assume that the ratio of tensile strength ( $T_m$ ) of rock mass to tensile strength ( $T_r$ ) of intact rock follows the same relationship [37], so the properties of rock mass can be determined, and the results are listed in Table 1.

The rock mass property parameters of these data can not be directly applied to the model, and the mechanical parameters of the contact surface and polygon used to express the rock mass characteristics need to be obtained through numerical calibration. Therefore, UDEC Trigon logic correction models are established, which are UCS test block model with width of 2.0 m and height of 4.0 m and Brazilian disk test block model with diameter of 2.0 m. The input parameters of block and contact surface are calibrated by trial and error method to match the rock mass properties given in Table 1. The calibration results of rock and coal are shown in Figure 7, and the microparameter is shown in Table 2. It can be seen from Table 3 that the error between the uniaxial compressive strength and elastic modulus obtained by numerical simulation and the data obtained by laboratory test is within 10%. These parameters reproduce the rock mass properties in this study, so the micromechanical

TABLE 1: Intact rock properties and calculated rock mass properties.

Rock strata	Intact rock			RQD	Rock mass		
	(GPa)	(MPa)	(MPa)		(GPa)	(MPa)	(MPa)
Sandy mudstone	5.89	11.44	1.14	90	3.42	8.12	0.81
Fine sandstone	8.53	13.88	1.40	92	5.40	10.41	1.05
Coal	1.48	4.99	0.50	88	0.79	3.36	0.34

parameters of coal and rock mass determined in Table 2 are reasonable and usable.

**3.3. Validation of the Global Model.** In this section, the global model parameters are corrected for the primary section with a width of 4.8 m and a height of 3.2 m. In the process of numerical simulation, the excavation of the LODM is simulated by deleting the blocks in the profile of primary section of the LODM. However, sudden excavation may lead to unbalanced response of the model, which will lead to dynamic stress paths around the excavation boundary. This dynamic stress usually produces a larger failure range around the excavation than expected [38]. In the field excavation, the open-off cut is gradually and continuously excavated by a heading machine, and the boundary of the LODM produces a static stress path [39, 40]. In order to simulate this more realistic excavation effect, the *FISH* function is embedded into the UDEC model [35], and the equivalent force is decomposed into 10 stages to simulate the gradual excavation process. At each stage, the internal stress exerted on the excavation boundary is reduced by 10% of the original equivalent force, and enough numerical time step length is calculated to ensure the model reaches equilibrium. This method can minimize the impact of transient on material failure and provide a more static calculation scheme.

Adopting the abovementioned mechanical parameters of coal seam of the LODM and roof and floor rock in 5202 working face of Xin'an coal mine, and using the abovementioned "excavation" simulation method, the supporting parameters of primary excavated section are shown in Figure 5. Long and short anchor cables are both used for supporting. Short anchor cables with a diameter of 17.8 mm and a length of 4300 mm are used for basic support on the roof. The short anchor cables have a spacing of 800 mm and a row spacing of 800 mm, while long anchor cables with a diameter of 17.8 mm and a length of 6300 mm are used for reinforcing support. The long anchor cables have a spacing of 1600 mm and a row spacing of 800 mm. The two sides of the roadway are supported by anchor cables with a diameter of 17.8 mm and a length of 2700 mm. The anchor cables of two sides of the roadway have a spacing of 800 mm and a row spacing of 800 mm. The long and short anchor cables of the roof and the anchor cables of two sides of the roadway are made of reinforced ladder beam welded with round steel with a diameter of 14 mm. The reinforced ladder beam used for short anchor cables on roof has a width of 60 mm and a

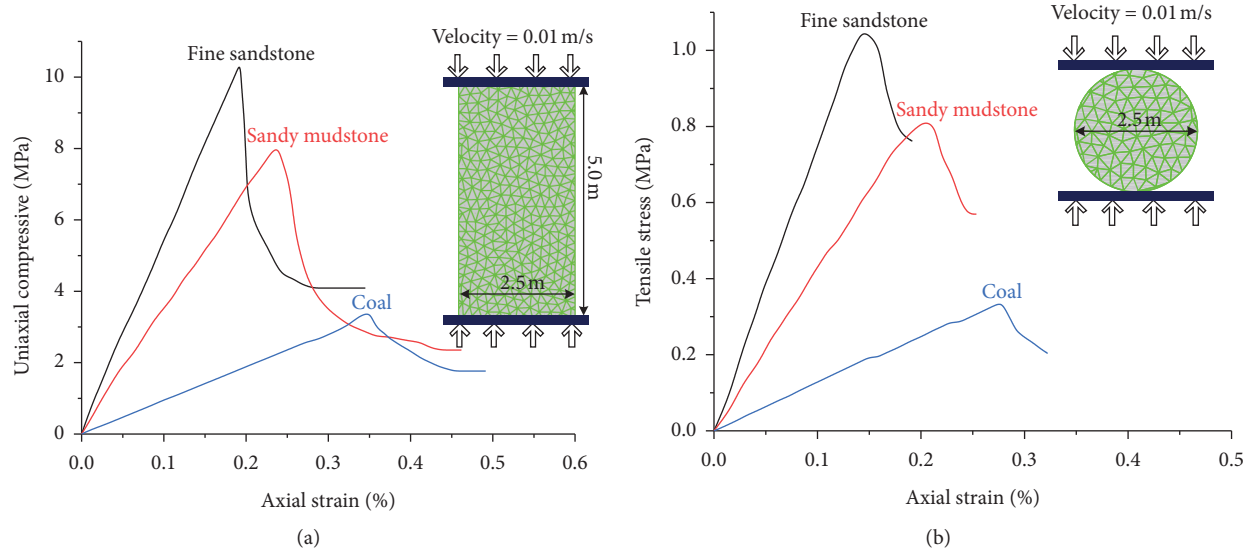


FIGURE 7: Calibration model using trigon logic: (a) calibrations for coal mass UCS; (b) Brazilian tensile test.

TABLE 2: Calibration of mechanical properties of rock strata and coal seams used in the model.

Rock strata	Matrix properties				Contact properties		
	Density ( $\text{kg/m}^3$ )	$E$ (GPa)	$k_n$ (GPa/m)	$k_s$ (GPa/m)	Cohesion (MPa)	Friction angle ( $^\circ$ )	Tensile strength (MPa)
Sandy mudstone	2450	3.42	180	54.2	2.7	32	1.23
Fine sandstone	2550	5.40	278.5	83.6	3.4	35	1.59
Coal	1400	0.79	150.2	46.1	1.4	30	0.52

TABLE 3: Comparison of theoretical and simulated values of elastic modulus, compressive strength, and tensile strength of rock mass.

Rock strata	$E$ (GPa)			UCS (MPa)			BTS (MPa)		
	Target	Calibrated	Error (100%)	Target	Calibrated	Error (100%)	Target	Calibrated	Error (100%)
Sandy mudstone	3.42	3.54	3.51	8.12	8.30	2.22	0.81	0.83	2.47
Fine sandstone	5.40	5.15	-4.63	10.41	10.85	4.23	1.05	0.98	-6.67
Coal	0.79	0.76	-3.78	3.36	3.23	3.87	0.34	0.36	5.88

length of 4500 mm, while that used for long anchor cables on roof is 60 mm and 3300 mm, respectively. The width and length of reinforced ladder beams used for the anchor cables on two sides of the roadway are 60 mm and 2500 mm, respectively. In the numerical simulation, the built-in “cable” element is used to simulate the long and short anchor cables of the roof and the anchor cables of the two sides of roadway, and the built-in “liner” element is used to simulate the roof and the reinforced ladder beams of the two sides of roadway. The parameters of the supporting unit are shown in Table 4 in this paper.

The deformation of the primary excavation section of the LODM of 5202 working face is numerically simulated. Figure 8 shows the comparison between the numerical simulation results and the field monitoring deformation results. Although the time of numerical simulation is not the actual time of field measurement, UDEC Trigon model reproduces a deformation process of excavation section in horizontal and vertical directions. At the same time, the numerical simulation also reproduces the roof failure mode

in the interface area of the two excavation sections after completion of the second section excavation, which will be studied in detail below. According to the results of numerical simulation, the maximum moved volume of the two sides of roadway of the primary excavation section is about 248 mm, and the maximum moved volume of the roof and floor is about 410 mm. The numerical calculation results are in good agreement with the field monitoring results, which verifies the rationality of UDEC Trigon model and the mechanical properties of rock mass used in this paper.

#### 4. Failure Mode of Roof in the LODM and Effect of Support Scheme

*4.1. Roof Failure Process and Support Timing of Primary Excavation Section.* The fracture of roof rock can be identified by microseismic activity. In recent years, microseismic system has been used to better understand the failure process of roadway and working face. In UDEC Trigon model, the damage of block contact is considered as the main source of

TABLE 4: Properties of support elements used in the model.

Contact properties		Value
Anchor cable	Elastic modulus (GPa)	200
	Tensile yield strength (kN)	380
	Stiffness of the grout (N/m/m)	2e9
	Cohesive capacity of the grout (N/m)	4e5
Structure	Elastic modulus (GPa)	200
	Tensile yield strength (MPa)	500
	Compressive yield strength (MPa)	500
	Interface normal stiffness (GPa/m)	10
	Interface shear stiffness (GPa/m)	10

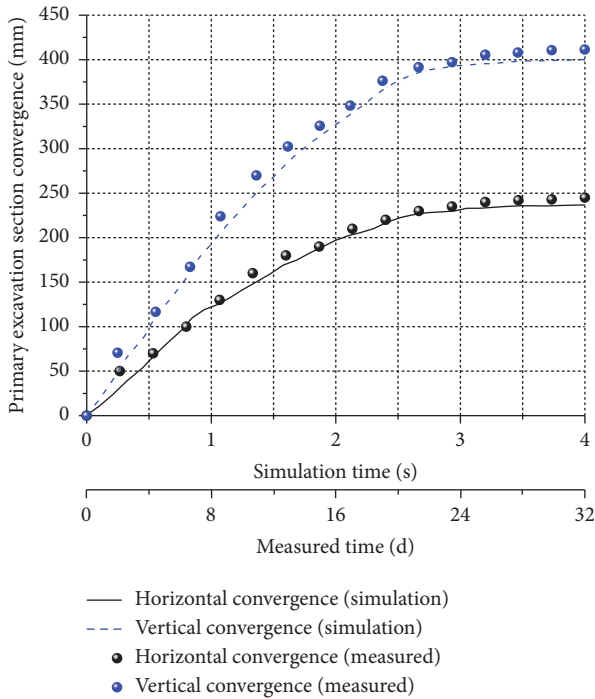


FIGURE 8: Comparison between the simulation and measured primary excavation section convergence in the Xin'an coal mine.

microseisms, so the microseismic activity can be simulated by counting the number of crack increments in a specific calculation time [40, 41]. In this paper, the contact failure of roof is related to microseismic activity [42, 43]. Therefore, the reasonable support timing can be determined through the development of microcracks.

Figure 9 shows the size of fracture and damage of roof in primary excavation section, and Figure 9 shows the height of fracture propagation and failure mode of roof in three different stages after primary section excavation. The term “damage” is defined as the ratio of the number of failure contacts (tensile strength or shear strength) to the number of all predefined contacts in the roof [34].

$$D = \frac{L_{SH} + L_{TE}}{L_{TC}} \times 100\%, \quad (14)$$

where  $L_{SH}$  is the total length of shear crack,  $L_{TE}$  is the total length of tensile crack, and  $L_{TC}$  is the total contact length.

It can be seen from Figures 9 and 10 that tensile fracture is the main mode leading to roof rock failure, and the process of roof rock failure and fracture propagation after primary excavation section is divided into three stages. In the first stage, the occurrence frequency of tensile cracks is 2.5 times that of shear cracks, the roof damage rapidly increases to 50%, the height of tensile cracks on the roof expands to about 1.8 m, and a small amount of shear cracks appears at the humeral angle of both sides of roadway in the primary excavation section. In the second stage, the occurrence frequency of tensile cracks and shear cracks on the roof gradually decreased, the damage of the roof slowly increased from 50% to 65%, the height of tensile cracks on the roof expanded to about 4.0 m, and the shear cracks at the humeral angle of the two sides of roadway gradually expanded to the central area of the roof, with the extension height of shear cracks about 1.5 m. In the third stage, the occurrence frequency of tensile cracks and shear cracks on the roof tends to low stable value, and the roof damage also keeps stable from 65% to 68%. The height of tensile cracks on the roof extends to about 4.8 m, and the expanded height of shear cracks is about 1.7 m, accompanied by a small amount of shear cracks in the deep part of the roof.

**4.2. Failure Process and Support Timing of Full Section Roof after Secondary Excavation.** The simulation method of secondary section excavation process is the same as that of primary section excavation process. The supporting parameters of secondary section excavation are shown in Figure 11(a). After the secondary section excavation, the failure mode and crack propagation process of roof of the full section open-off cut are shown in Figure 6. The development law of microcracks above the roof strata in the secondary section excavation process is similar to that in the primary section excavation process, so the development process of roof cracks in the secondary section excavation is also divided into three stages. It can be seen from Figure 6 that, in the first stage after secondary section excavation, the crack distribution of the full section roof is asymmetric, and the tensile crack propagation height of the primary section roof remains unchanged at 4.8 m, the shear crack propagation height remains unchanged at 1.7 m, the tensile crack propagation height of the secondary section roof reaches 3.8 m, the shear crack appears near the humeral angle of the secondary excavation section, and a few shear cracks appear in the middle of the roof. In the second stage after secondary section excavation, affected by secondary section excavation, the development height of roof cracks in primary section increased. The propagation height of the tensile cracks on the roof of the primary excavation section increased from 4.8 m to 6.8 m, while the propagation height of shear cracks increased from 1.7 m to 2.4 m. The propagation height of tensile crack on the roof of the secondary excavation section increased from 3.8 m to 6.3 m, and the propagation height of shear cracks increased from the humeral angle to 1.6 m above the roof of the secondary excavation section. In the third stage after the second section excavation, the crack propagation height of the full section roof continues to increase and tends to be stable, and the tensile crack height of the full section roof

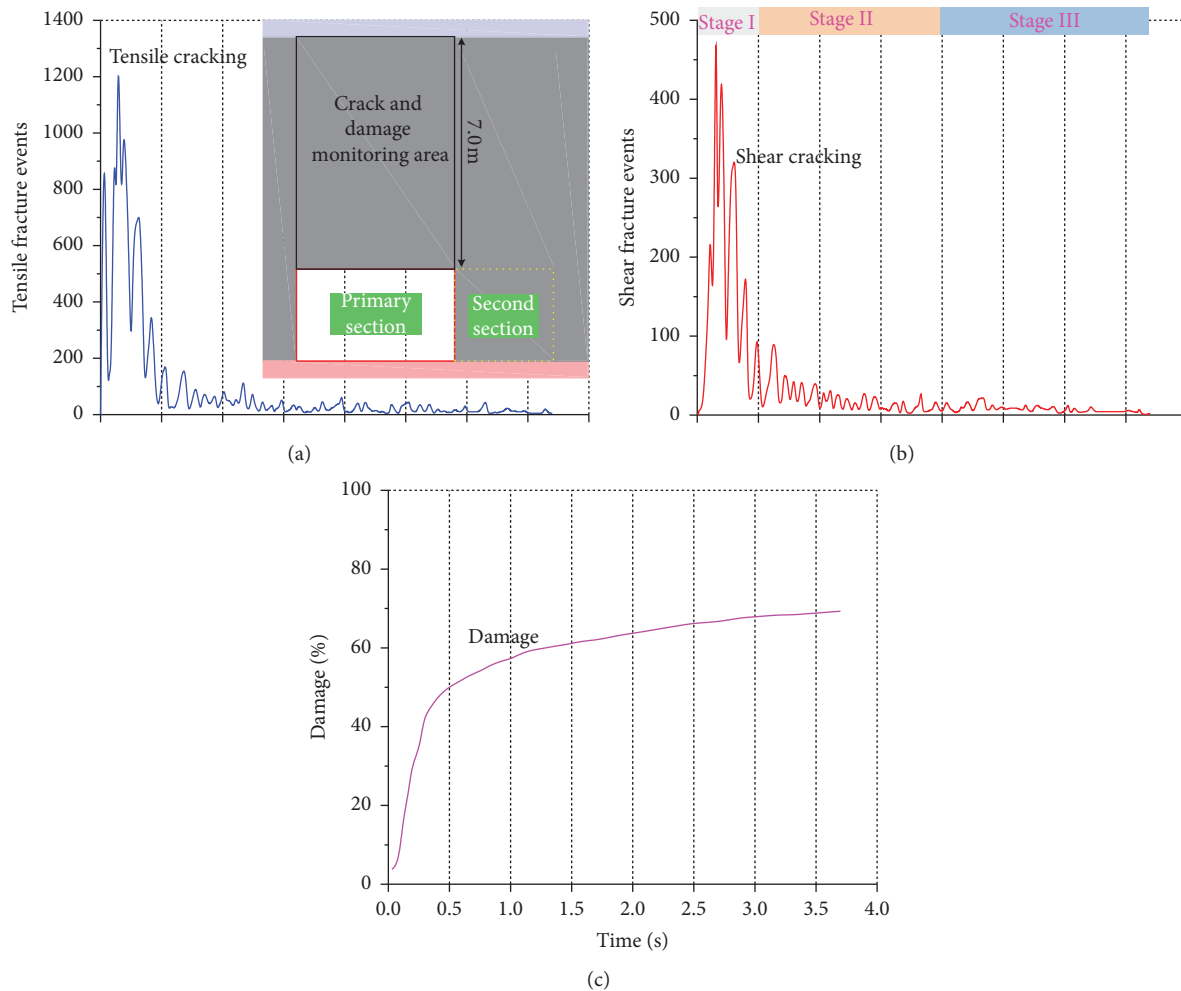


FIGURE 9: The change law of microcrack events and damage amount in the roof area after the primary section excavation.

extends to about 7.2 m. Among them, the tensile crack height of the interface area of the two excavated sections even reaches about 9.0 m. Compared with the previous two stages, the roof near the interface of the two excavated sections is seriously damaged, and the specific analysis is in Section 4.3.

Generally speaking, after the second section excavation, the failure mode of the full section roof is similar to that of the primary excavation section, which is mainly manifested in that the last two stages are accompanied by the deep expansion of roof cracks, and the tensile and shear cracks are changed from microcracks in the first stage to macrocracks in the last two stages. At the same time, along with the second section excavation, the cracks above the roof of the first excavation section are gradually transferred to the deep. In the full section, the failure mode of the roof mainly shows that the macrocracks of the roof in the interface area of the two excavations increase and extend to the deep. Therefore, after the second section excavation, the reasonable support timing should be chosen before the second stage, and the key control of the roof strata in the interface area of the second excavation must be considered.

#### 4.3. Analysis of Supporting Effect of the LODM

4.3.1. *Three Schemes for Roof Support.* Anchor rod and anchor cable support is the main method of rock stratum control in roadway roof. The main functions of pretension anchor cable are divided into two aspects: on the one hand, the anchor cable installed in the rock stratum can reinforce the strength of rock mass, limit the deformation of rock mass within the range of anchor cable action, and limit the sliding of preexisting microcracks in the roof rock mass. On the other hand, the support provided by the reinforced ladder beam, pallet, and steel mesh installed with anchor cable and the pretension exerted on anchor cable can provide constraint on the roof rock stratum surface through the extension of reinforced ladder beam, pallet, and steel mesh. Therefore, three schemes for roof support are proposed for the open-off cut of 5202 working face in Xin'an coal mine (see in Figure 11). Among the three support schemes, the support parameters of primary section are unchanged, and the support parameters of primary section and three support schemes for secondary section are as follows.



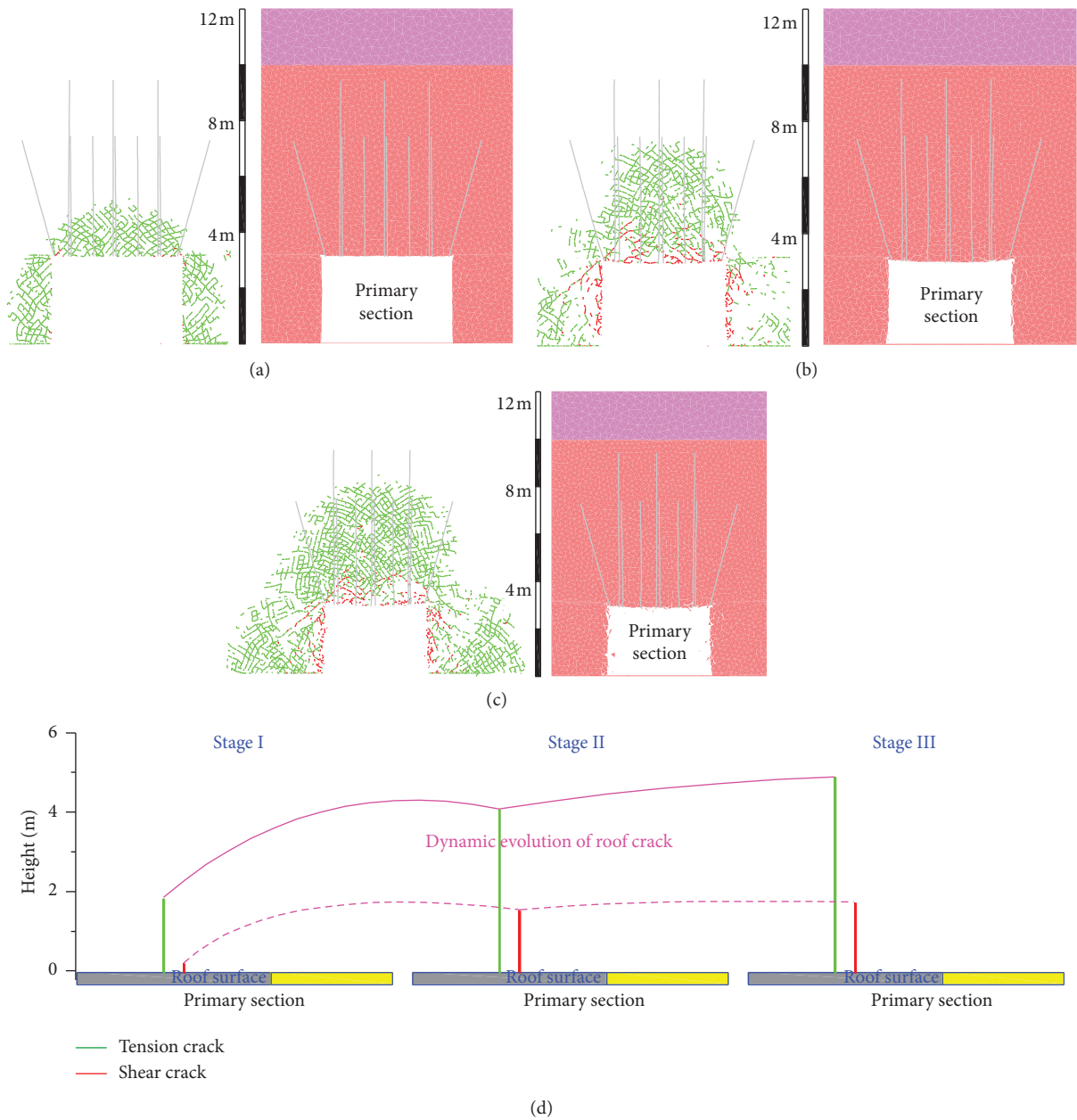


FIGURE 10: Crack development process and roof failure mode after primary excavation section supporting: (a) Stage I; (b) Stage II; (c) Stage III; (d) dynamic evolution of roof crack after primary excavation (green cracks represent tensile cracks, and the red cracks represent shear cracks).

4.3.2. *Failure Characteristics of Full Section Roof.* Scheme 1 is used in the simulation of roof failure process in Section 4.2. So in this section, the same UDEC Trigon model and simulation process are used to simulate Scheme 2 and Scheme 3. Figure 12 shows the variation law of cracks, damage, and failure modes of roof strata in the LODM under three kinds of support. In order to show the damage degree of roof in different areas above the roof more clearly, the rock strata within 9 m above the roof of full section open-off cut are divided into 1 m × 1 m square grids. The damage

calculation of each subgrid is calculated according to Formula (14)

## 5. Discussion

5.1. *Support Timing and Key Points of Control.* According to the analysis of roof failure mode, crack distribution, and damage characteristics of the LODM, the following measures are put forward about roof support timing and key points of control.



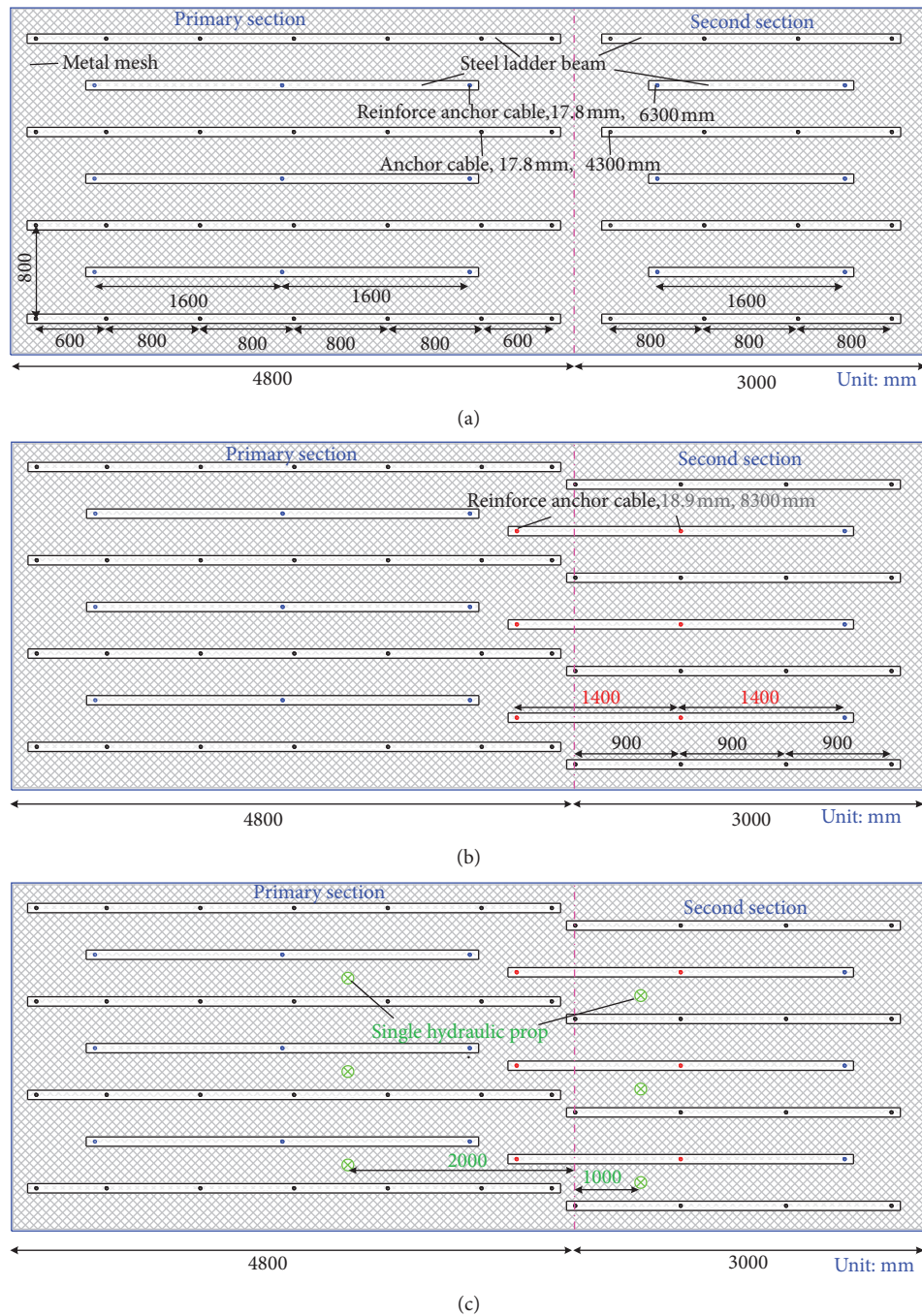


FIGURE 11: Plan view of three roof support schemes, (a) Scheme 1; (b) Scheme 2; (c) Scheme 3.

- (1) Excavation and open-off cut are the way of the two times tunneling. The primary excavation section should be supported in time. Before the second section excavation, in addition to the conventional long and short anchor cable support, a row of single hydraulic prop is installed in the primary excavation section together with the hinged top beam to actively bear and support the roof, ensuring the support strength of the primary excavation section.
- (2) After secondary section excavation, the roof should be supported in time, and the reinforcing long anchor cable should be installed in time after installing the short anchor cable. The interface area of the two excavation sections should be reinforced and supported to ensure the stability of roof strata in the interface area.
- (3) The high pretension anchor cable supports the roof with high-strength surface protection components such as reinforcing mesh, reinforced ladder beam, and pallet, controls the expansion of cracks on the surface and deep part of the roof, and improves the active support effect.

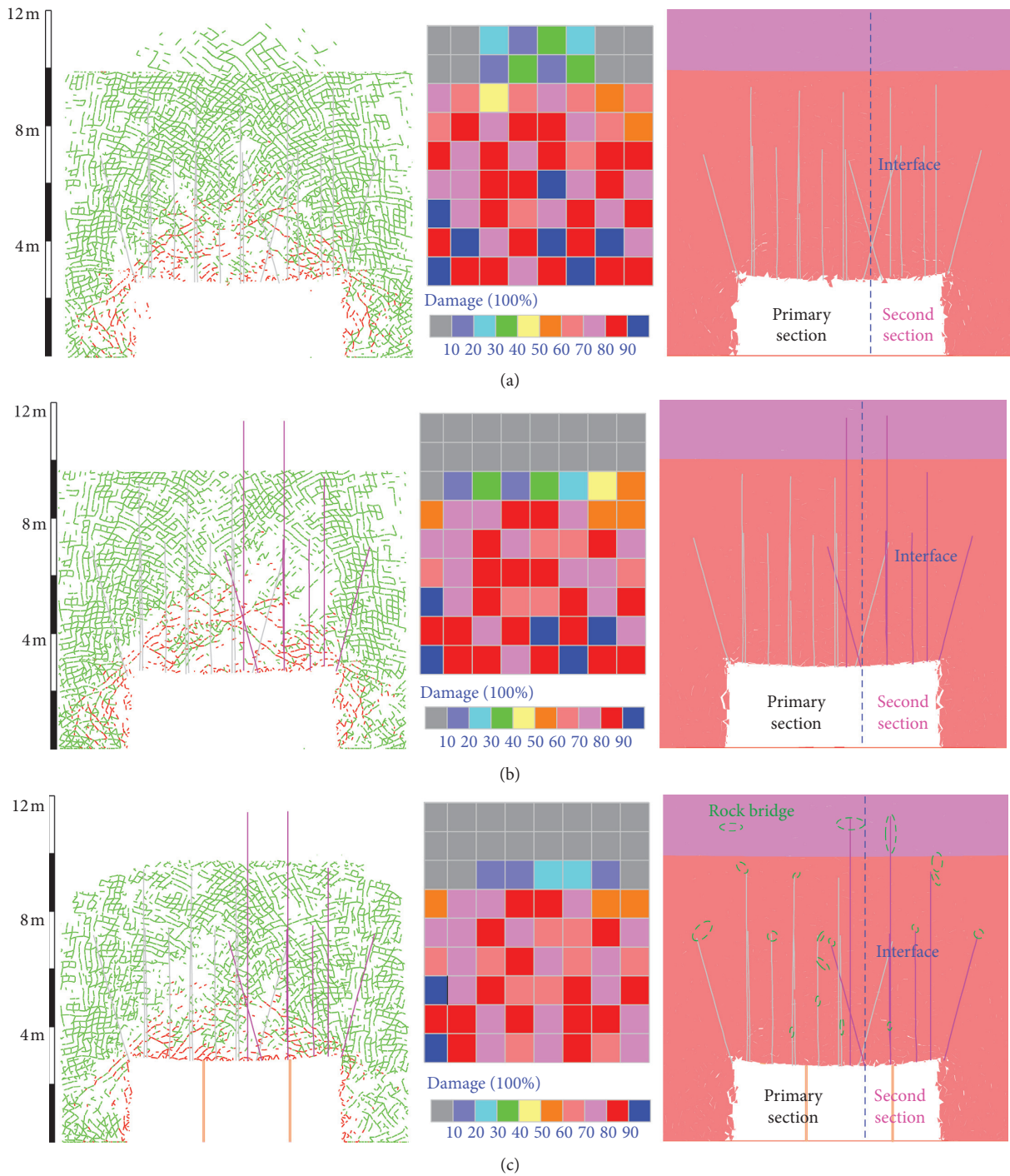


FIGURE 12: Distribution, damage, and failure modes of roof cracks in three support schemes, (a) Scheme 1; (b) Scheme 2; (c) Scheme 3. (The green cracks represent tensile cracks, and the red cracks represent shear cracks.)

5.2. *Control Technical Parameters.* After primary section excavation, the roof is supported by short anchor cables with a diameter of 17.8 mm and a length of 4300 mm, with a spacing of 800 mm and a row spacing of 800 mm, and reinforced by long anchor cables with a diameter of 17.8 mm and a length of 6300 mm, with a spacing of 1600 mm and a row spacing of 800 mm. Before the secondary section excavation, a row of DW-250/100 single hydraulic prop with

working resistance of 250 kN is arranged at 2000 mm away from the interface of the two excavation sections to match with DJB-1000 metal hinged roof beam. After secondary section excavation, the roof is supported by short anchor cables with a diameter of 17.8 mm and a length of 4300 mm, with a spacing of 900 mm and a row spacing of 800 mm. The two sides of roadway are supported by anchor cables with a diameter of 17.8 mm and a length of 2700 mm. Long anchor

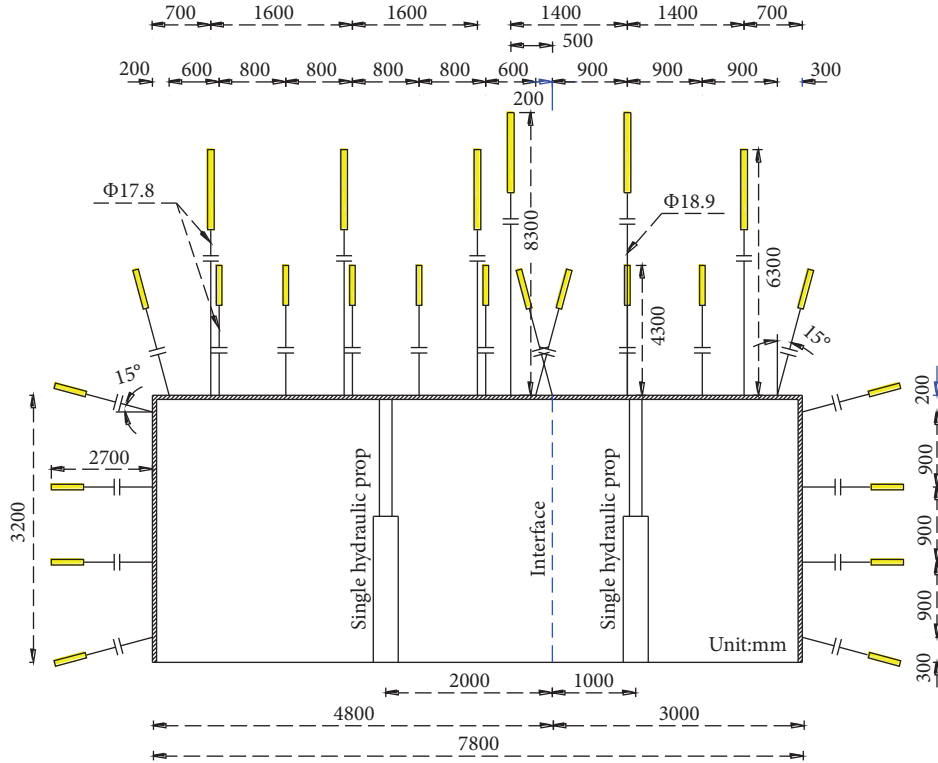


FIGURE 13: Parameter diagram of the LODM support in 5202 working face.

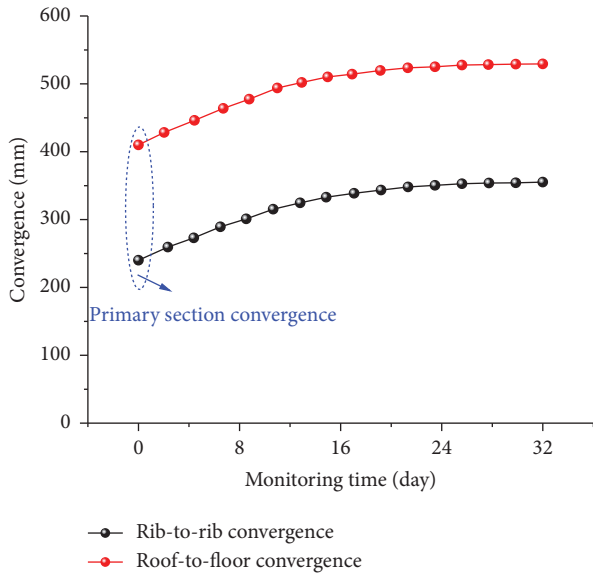


FIGURE 14: Field monitoring diagram of the LODM deformation of 5202 working face.

cables with a diameter of 18.9/17.8 mm and a length of 8300/6300 mm are used for reinforcement support, with a spacing of 1400 mm and a row spacing of 800 mm. Short anchor cables with a diameter of 17.8 mm and a length of 2700 mm are used on the two sides of roadway to support the two sides of roadway. The anchor cable spacing is 900 mm and the row spacing is 800 mm, and the pretension of both long and short

anchor cables is 250 kN. The supporting parameters of long and short anchor cables in the full section are shown in Figure 13.

5.3. *Field Test of Roof Support Effect.* After adopting the above optimized support scheme of the LODM, the roof deformation of the two excavation sections of the roof of 5202 open-off cut is shown in Figure 14. The monitoring results show that the deformation of the roof strata of the 5202 open-off cut is effectively controlled, the deformation of the roof of the two excavation sections is stable for a period of time, and the convergence deformation of the roof-to-floor and the rib-to-rib of the LODM is 550 mm and 350 mm, respectively. The field application shows that the surrounding rock of roof has been effectively improved under the action of support of high-strength long and short anchor cable and bearing structure of high working resistance hydraulic prop.

## 6. Conclusions

In order to solve the stability control problem of surrounding rock in the LODM, this paper systematically studies the evolution law of roof crack evolution, failure mode, and damage degree in secondary tunneling of the LODM by means of field investigation, theoretical calculation, numerical simulation, and engineering practice, compares and analyzes the control effect of roof crack and damage under three supporting conditions, and determines



the reasonable support timing and control technical parameters. The main conclusions are as follows.

- (1) The mechanical model of roof deformation of the LODM is established, and it is determined that the deflection of roof is directly proportional to the cubic of span. The secondary tunneling excavation method is selected for the LODM, so as to avoid large deflection deformation and instability of roof caused by primary excavation full section open-off cut.
- (2) A UDEC Trigon model is established to simulate the evolution characteristics, failure modes, and damage degree of roof cracks in secondary tunneling of the LODM, the input parameters are calibrated, the global model is verified according to the monitoring data, and the failure process of roof rocks in the LODM is studied. According to the microseismic activity of cracks in the simulation process, the failure process of roof rock stratum in the LODM is divided into three stages, and the reasonable support timing is determined.
- (3) The limiting effects of the three supporting schemes on the crack evolution of roof strata are evaluated, and the results show that the key supporting in the interface area can reduce the crack propagation height of roof strata in secondary tunneling and weaken the damage degree of roof strata in the deep.
- (4) The control timing and key points of control for surrounding rock of the LODM are put forward, and the technical parameters of the LODM in 5202 working face in Xin'an Coal Industry are determined. The field test shows that, after reinforcing and supporting by the lengthened anchor cable and single hydraulic props, the moved volumes of the LODM of rib-to-rib and roof-to-floor are about 350 mm and 550 mm, respectively. The results provide a basis for the control of surrounding rock of the LODM under similar conditions.

### Data Availability

The data used to support the findings of this study are available from the corresponding author upon request.

### Conflicts of Interest

The authors declare no conflicts of interest.

### Authors' Contributions

Conceptualization was performed by Shuaigang Liu, Yanhui Li, and Jianbiao Bai; methodology was developed by Xiangyu Wang; formal analysis and investigation were performed by Shuaigang Liu and Xiangyu Wang; software was provided by Shuaigang Liu; validation was performed by Bowen Wu and Guanghui Wang; reviewing and editing were performed by Shuaigang Liu, Jianbiao Bai, Xiangyu Wang, Bowen Wu, Guanghui Wang, Yanhui Li, and Jun Xu.

### Acknowledgments

This research was financially supported by the National Natural Science Foundation of China through contract no. 52074239. The authors thank Xin'an coal mine for their support during the field work.

### References

- [1] H. Xie, Y. Ju, S. Ren, F. Gao, J. Liu, and Y. Zhu, "Theoretical and technological exploration of deep in situ fluidized coal mining," *Frontiers in Energy*, vol. 13, no. 4, pp. 603–611, 2019.
- [2] J. Chen, J. Zhao, S. Zhang et al., "An experimental and analytical research on the evolution of mining cracks in deep floor rock mass," *Pure and Applied Geophysics*, vol. 177, no. 11, pp. 5325–5348, 2020.
- [3] S. Shreedharan and P. H. S. W. Kulatilake, "Discontinuum-equivalent continuum analysis of the stability of tunnels in a deep coal mine using the distinct element method," *Rock Mechanics and Rock Engineering*, vol. 49, no. 5, pp. 1903–1922, 2016.
- [4] K. Wang, L. Wang, B. Ren, and H. Fan, "Understanding the effect of cementitious grouting pressure on micro-fracture permeability for rock reinforcement underground: a lab study," *Energies*, vol. 13, no. 16, p. 4225, 2020.
- [5] Z. Zhang, J. Bai, Y. Chen, and S. Yan, "An innovative approach for gob-side entry retaining in highly gassy fully-mechanized long wall top-coal caving," *International Journal of Rock Mechanics and Mining Sciences*, vol. 80, pp. 1–11, 2015.
- [6] D. Zhu, Y. Wu, Z. Liu, X. Dong, and J. Yu, "Failure mechanism and safety control strategy for laminated roof of wide-span roadway," *Engineering Failure Analysis*, vol. 111, Article ID 104489, 2020.
- [7] G. Li, F. Ma, J. Guo, H. Zhao, and G. Liu, "Study on deformation failure mechanism and support technology of deep soft rock roadway," *Engineering Geology*, vol. 264, Article ID 105262, 2020.
- [8] J. G. Kan, N. Zhang, G. C. Li, W. Cheng, and D. H. Zhang, "Analysis of excavation method of large span open-off cut in deep mine," *Journal of Mining and Safety Engineering*, vol. 26, pp. 41–45, 2009, in Chinese.
- [9] Y. Yu, J. Bai, K. Chen, X. Wang, T. Xiao, and Y. Chen, "Failure mechanism and stability control technology of rock surrounding a roadway in complex stress conditions," *Mining Science and Technology (China)*, vol. 21, no. 3, pp. 301–306, 2011.
- [10] Y. Hu, Y. Liu, and L. Shi, "Research on supporting technology for surrounding rock of inclined large-span open-off cut roadway," *Geotechnical and Geological Engineering*, vol. 38, no. 2, pp. 1873–1884, 2020.
- [11] G. M. Chi, L. H. Zhang, and H. J. Tang, "Comprehensive control technology of ultra large section open-off cut surrounding rock," *Coal Science and Technology*, vol. 11, pp. 27–31, 2017, in Chinese.
- [12] Z. Z. Zhang, M. Deng, B. J. Bai, S. Yan, and X. Y. Yu, "Stability control of gob-side entry retained under the gob with close distance coal seams," *International Journal of Mining Science and Technology*, vol. 31, no. 2, pp. 321–332, 2020.
- [13] D. P. Yin, "Study on surrounding rock control and support system in a super large section roadway with thick fragmentation coal seam" Ph.D. thesis, China University of Mining and Technology, Beijing, China, 2011, in Chinese.
- [14] S. L. Zhang, "Study on bolt-net supporting technology of thick seam and large-section cut in Wangjialing coal mine,"

- M. A. thesis, China University mining and technology, Xuzhou, China, 2015, in Chinese.
- [15] F. L. He, L. Xu, H. K. Wu, and Y. F. Wang, "Fracture field evolution and stability analysis of surrounding rock in thick coal roof large-section," *Journal of China Coal Society*, vol. 39, no. 2, pp. 336–346, 2014, in Chinese.
- [16] S. Xie, Q. Zhang, D. Chen et al., "Research of roof anchorage rock beam bearing structure model of extra-large width open-off cut and its engineering application in a coal mine, China," *Advances in Civil Engineering*, vol. 2020, Article ID 3093294, 19 pages, 2020.
- [17] W.-q. Peng, H. Zhu, Q. Wang, and G. Peng, "Study on safety control of large-section roadway with high stress and broken surrounding rock," *Advances in Civil Engineering*, vol. 2021, Article ID 6686208, 12 pages, 2021.
- [18] G.-c. Zhang, F.-l. He, Y.-h. Lai, and H.-g. Jia, "Ground stability of underground gateroad with 1 km burial depth: a case study from Xingdong coal mine, China," *Journal of Central South University*, vol. 25, no. 6, pp. 1386–1398, 2018.
- [19] Z. Zhang, M. Deng, X. Wang, W. Yu, F. Zhang, and V. D. Dao, "Field and numerical investigations on the lower coal seam entry failure analysis under the remnant pillar," *Engineering Failure Analysis*, vol. 115, Article ID 104638, 2020.
- [20] S. Liu, J. Bai, X. Wang, B. Wu, and W. Wu, "Mechanisms of floor heave in roadways adjacent to a goaf caused by the fracturing of a competent roof and controlling technology," *Shock and Vibration*, vol. 2020, Article ID 5632943, 17 pages, 2020.
- [21] Z. Zhang, M. Deng, J. Bai, X. Yu, Q. Wu, and L. Jiang, "Strain energy evolution and conversion under triaxial unloading confining pressure tests due to gob-side entry retained," *International Journal of Rock Mechanics and Mining Sciences*, vol. 126, Article ID 104184, 2020.
- [22] N. Meng, Y. Chen, J. Bai, X. Wang, W. Wu, and B. Wu, "Numerical simulation of directional fracturing by shaped charge blasting," *Energy Science & Engineering*, vol. 8, no. 5, pp. 1824–1839, 2020.
- [23] S. Wang, W. Xu, M. Sun, and W. Wang, "Experimental investigation of the mechanical properties of fine-grained sandstone in the triaxial cyclic loading test," *Environmental Earth Sciences*, vol. 78, no. 14, 2019.
- [24] J. Chen, H. Zhao, F. He, J. Zhang, and K. Tao, "Studying the performance of fully encapsulated rock bolts with modified structural elements," *International Journal of Coal Science & Technology*, vol. 8, no. 1, p. 64, 2021.
- [25] J. Yang and M. Fall, "Coupled hydro-mechanical modelling of dilatancy controlled gas flow and gas induced fracturing in saturated claystone," *International Journal of Rock Mechanics and Mining Sciences*, vol. 138, Article ID 104584, 2021.
- [26] B. Wu, X. Wang, J. Bai, W. Wu, X. Zhu, and G. Li, "Study on crack evolution mechanism of roadside backfill body in gob-side entry retaining based on UDEC trigon model," *Rock Mechanics and Rock Engineering*, vol. 52, no. 9, pp. 3385–3399, 2019.
- [27] Q.-S. Bai, S.-H. Tu, C. Zhang, and D. Zhu, "Discrete element modeling of progressive failure in a wide coal roadway from water-rich roofs," *International Journal of Coal Geology*, vol. 167, pp. 215–229, 2016.
- [28] F. Gao, D. Stead, and H. Kang, "Simulation of roof shear failure in coal mine roadways using an innovative UDEC Trigon approach," *Computers and Geotechnics*, vol. 61, pp. 33–41, 2014.
- [29] S. Zhang, D. Zhang, H. Wang, and S. Liang, "Discrete element simulation of the control technology of large section roadway along a fault to drivage under strong mining," *Journal of Geophysics and Engineering*, vol. 15, no. 6, pp. 2642–2657, 2018.
- [30] J. Yin, B. Fu, and H. Zhang, "Failure mechanism and control technology for a large-section roadway under weakly cemented formation condition," *Geofluids*, vol. 2020, Article ID 6669060, 11 pages, 2020.
- [31] W.-d. Wu, J.-b. Bai, X.-y. Wang, S. Yan, and S.-x. Wu, "Numerical study of failure mechanisms and control techniques for a gob-side yield pillar in the Sijiazhuang coal mine, China," *Rock Mechanics and Rock Engineering*, vol. 52, no. 4, pp. 1231–1245, 2019.
- [32] C. Qi and A. Fourie, "Cemented paste backfill for mineral tailings management: review and future perspectives," *Minerals Engineering*, vol. 144, Article ID 106025, 2019.
- [33] B. Wu, X. Wang, J. Bai, W. Wu, N. Meng, and H. Lin, "An investigation on the effect of high energy storage anchor on surrounding rock conditions," *Royal Society Open Science*, vol. 7, no. 10, Article ID 201105, 2020.
- [34] F. Q. Gao, *Simulation of failure mechanisms around underground coal mine openings using discrete element modeling*, Ph.D. thesis, Simon Fraser University, Burnaby, Canada, 2013.
- [35] Itasca Consulting Group Inc, *UDEC (Universal Distinct Element Code), Version 6.0*, Itasca, Minneapolis, MN, USA, 2014.
- [36] L. Zhang and H. H. Einstein, "Using RQD to estimate the deformation modulus of rock masses," *International Journal of Rock Mechanics and Mining Sciences*, vol. 41, no. 2, pp. 337–341, 2004.
- [37] M. Singh and K. Seshagiri Rao, "Empirical methods to estimate the strength of jointed rock masses," *Engineering Geology*, vol. 77, no. 1-2, pp. 127–137, 2005.
- [38] M. Cai, "Influence of stress path on tunnel excavation response-numerical tool selection and modeling strategy," *Tunnelling and Underground Space Technology*, vol. 23, no. 6, pp. 618–628, 2008.
- [39] Q.-S. Bai, S.-H. Tu, and C. Zhang, "DEM investigation of the fracture mechanism of rock disc containing hole(s) and its influence on tensile strength," *Theoretical and Applied Fracture Mechanics*, vol. 86, pp. 197–216, 2016.
- [40] J. F. Hazzard and R. P. Young, "Dynamic modelling of induced seismicity," *International Journal of Rock Mechanics and Mining Sciences*, vol. 41, no. 8, pp. 1365–1376, 2004.
- [41] A. Lisjak, Q. Liu, Q. Zhao, O. K. Mahabadi, and G. Grasselli, "Erratum: numerical simulation of acoustic emission in brittle rocks by two-dimensional finite-discrete element analysis," *Geophysical Journal International*, vol. 196, no. 2, p. 1263, 2014.
- [42] J. Yang, M. Fall, and G. Guo, "A three-dimensional hydro-mechanical model for simulation of dilatancy controlled gas flow in anisotropic claystone," *Rock Mechanics and Rock Engineering*, vol. 53, no. 9, pp. 4091–4116, 2020.
- [43] E. Ghazvinian, M. S. Diederichs, and R. Quey, "3D random voronoi grain-based models for simulation of brittle rock damage and fabric-guided micro-fracturing," *Journal of Rock Mechanics and Geotechnical Engineering*, vol. 6, no. 6, pp. 506–521, 2014.



## Research Article

# Mining-Induced Redistribution of the Abnormal Stress under the Close Bearing Coal Pillar for Entry Design

Xudong Liu,<sup>1</sup> Wenlong Shen ,<sup>1,2,3</sup> Jianbiao Bai ,<sup>1,4</sup> Rui Wang ,<sup>1</sup> Jizhong Kang,<sup>1</sup> and Xiangyu Wang <sup>1</sup>

<sup>1</sup>Key Laboratory of Deep Coal Resource Mining Ministry of Education, State Key Laboratory of Coal Resources and Safe Mining, China University of Mining & Technology, Xuzhou 221116, Jiangsu, China

<sup>2</sup>School of Energy Science and Engineering, Henan Polytechnic University, Jiaozuo 454000, Henan, China

<sup>3</sup>Collaborative Innovation Center of Coal Work Safety and Clean High Efficiency Utilization, Jiaozuo 454000, China

<sup>4</sup>College of Mining Engineering and Geology, Xinjiang Institute of Engineering, Urumqi 830023, China

Correspondence should be addressed to Wenlong Shen; shenwenlong.888@163.com and Jianbiao Bai; baijianbiao\_cumt@163.com

Received 22 February 2021; Revised 8 March 2021; Accepted 23 March 2021; Published 8 April 2021

Academic Editor: Zhijie Zhu

Copyright © 2021 Xudong Liu et al. This is an open access article distributed under the Creative Commons Attribution License, which permits unrestricted use, distribution, and reproduction in any medium, provided the original work is properly cited.

Underground space is vulnerable to large deformation influenced by the abnormal stress induced by the bearing coal pillar. A numerical simulation model was established to determine the redistribution of the abnormal stress induced by the mining activities. The double-yield model, the strain softening model, the interface model, and the Mohr–Coulomb model were determined to simulate the gob compaction effect, the pillar strength reduction effect, the structure plane discontinuity effect, and the rock mechanical behavior, respectively. This numerical simulation model is reliable to predict the abnormal stress under the bearing coal pillar by the comparison of the abutment stress from this model and the existing theoretical model as well as the entry roof surface displacement from this model and the field measuring method. The results from the validated numerical model indicate that the abnormal stress including stress concentration coefficient, stress gradient, and lateral pressure coefficient will redistribute to another state that the stress concentration coefficient and stress gradient increase gradually and then decrease, and the lateral pressure coefficient decreases gradually, then increases, and finally decreases sharply with the approach of the mining working face. Their maximum increasing rates are calculated as 121.05%, 198.56%, and 236.82%, respectively. This predicted mining-induced redistribution of the abnormal stress is available for designing the underground entry layout in the determination of the entry position, determination of the driving operation time, mining disturbing range warning, and the prediction of the strengthening support area.

## 1. Introduction

Coal as one of the widely used energy resources in recent years will be used to accelerate the social development for a long time in the future. Its generation conditions play a significant role in the underground mining engineering, which are divided into shallow-buried condition, deep-buried condition, thin seam, thick seam, horizontal seam, dip seam, soft seam, hard seam, single seam, and multiple seams [1]. The underground mining engineering has to be carried out in multiple coal seams with the growth of the mining intensity and the reduction of the coal resources [2]. Numerous coal pillars will be left to bear the overburdens,

and the generated abutment stress will transfer into the close and unworked out coal seams, which generates an abnormal stress condition in the unworked out coal seam and threatens the stability of the underground entry, especially for the condition influenced by the mining operation of the longwall mining working face [3].

The precious achievements mainly concentrate on the stress distribution under the bearing coal pillar, which ignore the abnormal characteristics especially for the disturbing effect of the mining operation [4–7]. The CVISC rheological constitutive model was used to simulate the long-term creep behavior of the entry rock under bearing coal pillar and revealed that the stress concentration was not

large enough to damage this creep behavior rock under shallow-buried conditions [8]. The numerical simulation model with the Mohr–Coulomb criterion was used to reveal the distribution of the abutment stress around the mining working face near the bearing coal pillar and design the entry position for a special case [9]. However, this achievement just concentrates on the mining operation in one thick coal seam, which did not consider the lithology difference, gob compaction effect, and the pillar strength reduction effect. Deviatoric stress evolution under the bearing coal pillar was determined to predict the plastic zone around the entry and design its support technology with the advancement of the deviatoric stress-induced failure criterion [10]. However, this deviatoric stress ignores the volumetric strain of rock materials, which did not agree with the reality.

Entry layout has been widely used to protect this kind of entry from stress concentration disaster [11–13]. The pressure diffusion angle was used to design the entry layout below the bearing coal pillar, and the stress was divided into stress reducing area and stress increasing area, which ignored the influence of the abnormal stress condition [14]. Eight meters wide coal pillar was determined to layout the gob side entry under bearing coal pillar by the criterion of minimum plastic failure zone in the entry roof, which is a significant attempt for that geological and engineering condition [15]. Under the failure analysis of a typical case, it is demonstrated that the entry under the bearing coal pillar is vulnerable to stress concentration, and this entry can be arranged at a relative reasonable position, but this analysis ignored the influence of the abnormal stress [16]. Pressure bulb theory was used to determine the reasonable entry position at 71 m or 156 m away from the bearing coal pillar based on the maximum principle stress or the maximum shear stress predicted by a numerical simulation model, which is much larger than 30 m used in reality [17].

In this work, a numerical simulation model was established to reveal the mining-induced redistribution of the abnormal stress under the bearing coal pillar, which was validated by a theoretical model and a measuring method. After that, this validated model was used to predict the redistribution of the abnormal stress both in front and lateral sides of the mining working face. These predicted results are available for designing the entry layout under the bearing coal pillar with the disturbance of the mining operation. In fact, the abnormal stress is the stress state of rock below the bearing coal pillar, which is illustrated by the three key parameters of stress concentration coefficient, stress gradient, and lateral pressure coefficient.

## 2. Materials and Methods

Several factors were taken into consideration to make the numerical simulation model reliable such as the gob compaction effect, the pillar strength reduction effect, the structure plane discontinuity effect, and the rock mechanical behavior, respectively. This numerical model was established under the condition of the process as shown in Figure 1. The detailed process is demonstrated as the following section.

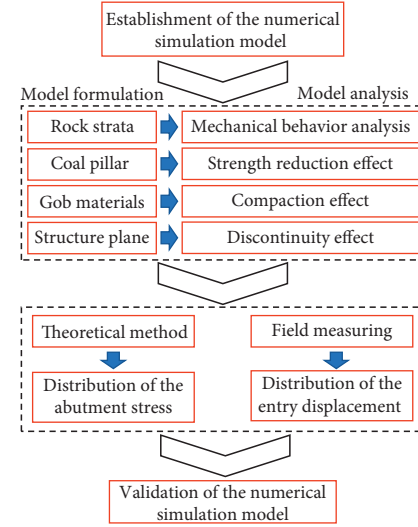


FIGURE 1: Formation process of the numerical simulation model.

### 2.1. Numerical Simulation Model

**2.1.1. Mohr–Coulomb Model for Rock Strata.** Rock materials will experience elastic deformation and plastic damage influenced with loadings, which can be simulated by the Mohr–Coulomb model expressed as equation (1) [18–20]. The rock materials are concentrated on a typical case from Xinrui coal mine in China. There are many bearing coal pillars left in coal seam 4 which was mined out several years ago. The entries of coal seam 5 will be influenced by these kinds of bearing coal pillars [3]. The average interlayer spacing between coal seams 4 and 5 is determined as 3.25 m, and the average stratigraphic dip angle is revealed as 6°. The detailed geological and engineering conditions are given in Table 1.

$$f = \sigma_1 - \sigma_3 \frac{(1 + \sin \varphi)}{(1 - \sin \varphi)} + 2c \sqrt{\frac{(1 + \sin \varphi)}{(1 - \sin \varphi)}}, \quad (1)$$

where  $f$  is the failure criterion;  $\sigma_1$  and  $\sigma_3$  are the principal stresses;  $\varphi$  is the frictional angle;  $c$  is the cohesion.

**2.1.2. Strain Softening Model for Coal Pillar.** One of the horizontal stresses is in the state of relief in the coal pillar due to the fact that both sides of the coal pillar are the workout area, and no objects apply stress along the rib sides of the coal pillar. However, the other horizontal stress is relatively stable, and the vertical stress varies, usually increases influenced by the abutment stress. Under the condition of the ultimate balance theory and plastic bearing characteristics [21, 22], the shallow coal bodies of the coal pillar will change into plastic deformation from elastic deformation with the increases of the vertical stress, which will result in the strength reduction of the coal pillar. And this mechanical behavior of the coal pillar has been demonstrated and described with the strain softening model [23–26]. The strength will decline rather than keeping stable after the coal is damaged. The reduction law of the strength parameters is

TABLE 1: Geological and engineering conditions of the research object.

Lithology	Thickness (m)	Bulk modulus (GPa)	Shear modulus (GPa)	Friction (°)	Cohesion (MPa)	Tension (MPa)
Sandstone	12.30	14.88	10.25	38	5.0	4.0
Coal seam 3	0.70	5.56	2.27	16	2.0	0.5
Mudstone	9.00	0.58	0.27	36	4.4	1.45
Coal seam 4	1.70	2.78	1.14	16	0.3	0.2
Sandy mudstone	3.25	8.33	4.76	35	3.5	0.65
Coal seam 5	2.76	5.56	2.27	9.5	1.6	0.5
Sandy mudstone	4.80	8.33	4.76	36	6.75	1.4
Sandstone	2.40	14.88	10.25	38	7.0	5.0
Mudstone	6.60	6.67	3.08	36	4.4	1.45
Limestone	4.50	23.02	11.24	42	10.0	8.0

TABLE 2: Parameters of the strain softening model for coal pillar.

	0	0.01	0.02	...	0.5
Plastic strain	0	0.01	0.02	...	0.5
Friction angle (°)	9.5	8.5	7.5	...	7.5
Cohesion (MPa)	1.6	1.2	0.9	...	0.9

given in Table 2 by the method of trial-and-error in terms of the peak vertical stress (18.8 MPa) and the width of plastic zone (5.5 m) beside the gob.

**2.1.3. Double-Yield Model for Gob Material.** The null model is widely used to simulate the gob material in longwall mining around the world [27], which ignored the consolidation of the caved rock strata. With the improvement of the numerical simulation technology and equivalence principle, the double-yield model gradually plays the main role to simulate the mechanical behavior of the gob material instead of the null model [28]. The key parameter is the cap pressure which usually follows a piecewise-linear law with the increases of the volumetric plastic strain. Salamon's model [29] (equation (2)) is used to calculate this cap pressure, and the result is given in Table 3. The basic properties of the double-yield model used for the gob material are given in Table 4.

$$\sigma = \frac{10.39\sigma_c^{1.042}h_{cav}^{7.7}h_m\epsilon}{(h_{cav} + h_m)^{7.7}[h_m - (h_{cav} + h_m)\epsilon]}, \quad (2)$$

where  $\sigma$  is the cap pressure;  $\epsilon$  is the plastic strain;  $\sigma_c$  is the in situ vertical stress;  $h_{cav}$  is the caving height;  $h_m$  is the mining height.

**2.1.4. Interface Model for Structure Plane.** Coal-bearing strata belong to sedimentary strata which contain structure plane located between coal seam and rock strata [30]. This kind of structure plane is so weak compared with the coal and rock materials that the separation and slippage damage always generate along this structure plane. The predicted results cannot be used to guide the operation of the engineering unless this structure plane is considered in the numerical simulation model [31]. The interface element follows the Mohr-Coulomb failure criterion illustrated as equation (3) [32]. When the shear stress is larger than the shear strength, the slippage will generate along the interface, and when the normal deformation capability is not

consistent for strata, the separation will generate along the interface. Jaeger and Cook's model [33] shown in equation (4) can be used to determine the parameters of the structure plane, and the results are illustrated in Table 5. The uniaxial compression strength of the structure plane is determined as 0.17 MPa.

$$F_{smax} = c_s A + \tan \varphi_s (F_n - pA), \quad (3)$$

where  $F_{smax}$  is the ultimate shear force;  $c_s$  is the cohesion of the interface;  $\varphi_s$  is the friction angle of the interface;  $A$  is the representative area touched with the interface node;  $F_n$  is the normal force;  $p$  is the pore pressure.

$$\sigma_1 = \sigma_3 + \frac{2(c_s + \sigma_3 \tan \varphi_s)}{(1 - \tan \varphi_s \cot \beta_s) \sin 2\beta_s}, \quad (4)$$

where  $\sigma_1$  is the compression strength;  $\sigma_3$  is the confining pressure;  $\beta_s$  is the angle between the major principal stress and the normal direction of the structure plane.

**2.2. Validation with the Theoretical Method.** The results of the distribution of the abutment stress under the two typical bearing coal pillars illustrated in Figure 2 indicate that this numerical simulation model is more reliable than the theoretical model to predict the distribution of the abnormal stress. Both of theoretical calculation and numerical simulation results indicate the abnormal characteristics of the stress along both the vertical and horizontal direction. The stress contour line presents a similar distribution in shape. However, the results have something different in distribution, especially for the influence range. For example, the influence depth of the abutment stress contour line of 12 MPa is less than 15 meters for the theoretical calculation result while it reaches more than 17 meters for the numerical simulation results. This theoretical model was established under the hypothesis of the isotropous and homogeneous rock materials, which ignores the influences of the lithology difference and the structure plane between adjacent rock strata [3].

**2.3. Validation with the Field Measuring Method.** Field measuring method of decussation [34] was conducted to validate the reliability of the numerical simulation model in terms of the roof surface displacement of the underground

TABLE 3: Cap pressure of the double-yield model.

Number	1	2	3	4	5	6	7	8	9	10
Strain/mm/m	0.00	0.02	0.04	0.06	0.08	0.10	0.12	0.14	0.16	0.18
Stress/MPa	0.00	0.29	0.64	1.09	1.66	2.44	3.53	5.21	8.09	14.21

TABLE 4: Basic properties of the gob material.

Density (kg/m <sup>3</sup> )	Bulk modulus (GPa)	Shear modulus (GPa)	Friction angle (°)	Dilation angle (°)
1200	5.56	2.27	8.96	6.28

TABLE 5: Structure plane properties used in the numerical model.

Shear stiffness (GPa/m)	Normal stiffness (GPa/m)	Friction angle (°)	Cohesion (MPa)	Tensile strength (MPa)
2	2	4.75	0.8	0.25

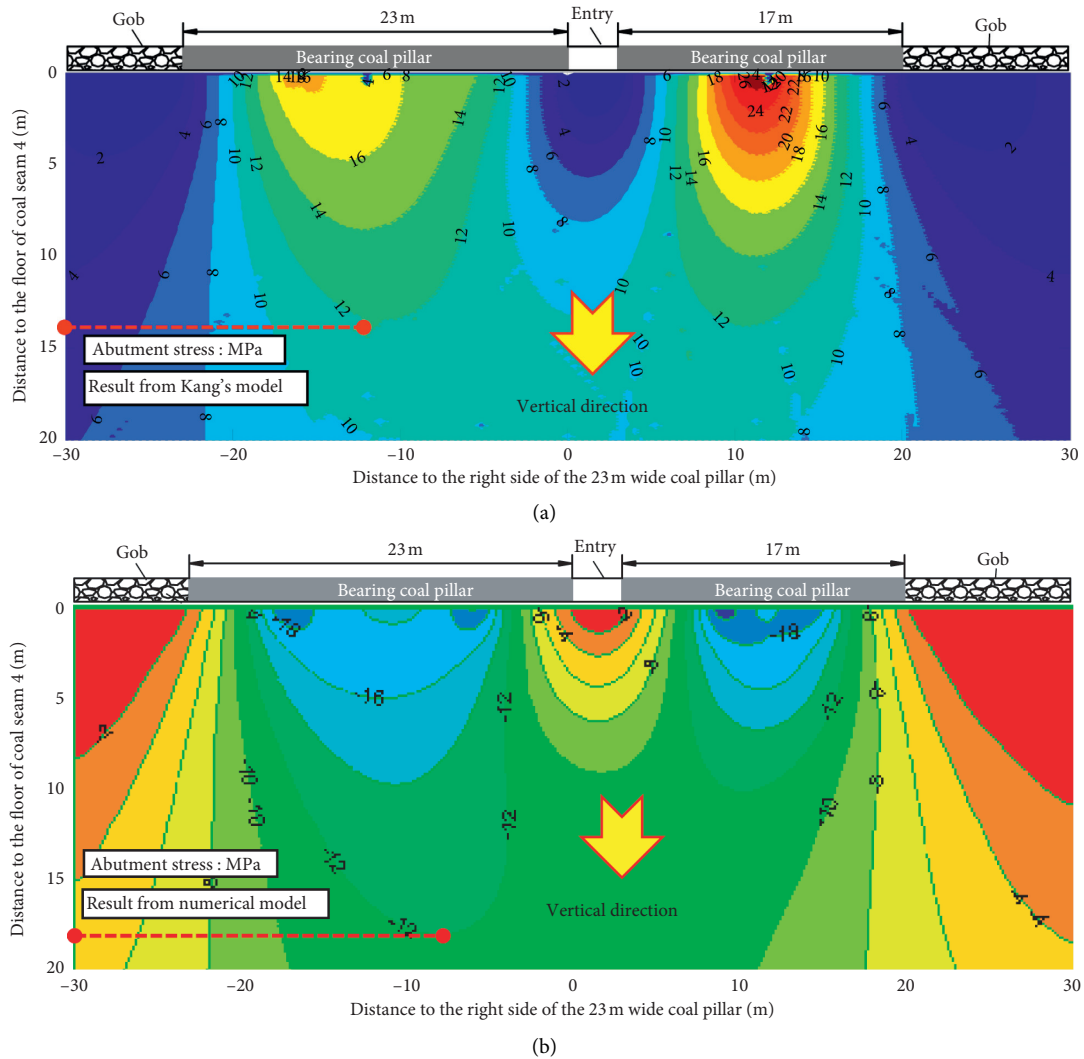


FIGURE 2: Distribution of the abutment stress under bearing coal pillars. (a) Theoretical calculation result; (b) numerical simulation result.

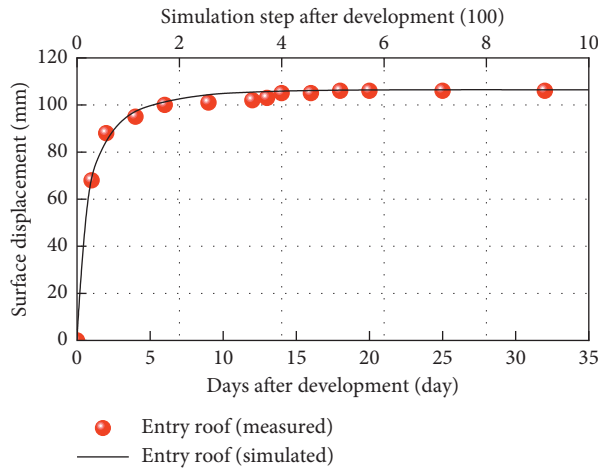


FIGURE 3: Comparison between the numerical simulation model and the field measuring method.

entry in coal seam 5. The results given in Figure 3 indicate that the numerical simulation model is reliable to predict the surface displacement of the entry roof since these results have a good agreement with each other. Actually, the surface displacement of underground space will present an increasing trend with the growth of the stress when the rock materials are determined [35]. The stress distribution, more reliable than the theoretical predicted result and the relative surface displacement of the entry consistent with the field measuring result together, demonstrated that the numerical simulation model is reliable to analyze the mechanical behavior of the coal and rock materials.

**2.4. Simulation Plans of the Redistribution of Abnormal Stress.** The numerical simulation process is divided into four steps to discover the redistribution of the abnormal stress under the bearing coal pillar to protect the underground space from large deformation. At the beginning, the three-dimensional numerical simulation model was established under the consideration of the geological and engineering conditions (Section 2.1). For the second step, the bearing coal pillars and gob material generalize by the mining operation in coal seam 4. The abnormal stress also generalizes in this step. Third, the mining entries including head entry and tail entry are established for the mining working face in coal seam 5 by the null model in FLAC3D software. Last but not least, the mining operation of the working face in coal seam 5 was carried out to calculate the redistribution of the abnormal stress.

Finding out the redistribution of the abnormal stress under bearing coal pillar with the retreating of the mining working face has a positive effect on the stability of the underground entry. Three indexes including stress concentration coefficient, stress gradient, and lateral pressure coefficient are determined to reveal the redistribution of the abnormal stress. Two typical areas are selected to layout the monitoring points including the area in front of the mining working face and the area in the side of the longwall panel as shown in Figure 4. And this bearing coal pillar is left in coal seam 4 while this mining working face is located in coal seam 5. This mining working face will pass across the coal below

the bearing coal pillar. There are three monitoring points in front of the mining working face, which are arranged below the gob, the interaction of the bearing coal pillar and the stable gob, and the bearing coal pillar. The region of the interaction is determined in the zone where the stress concentration coefficient is less than 1 and the stress gradient is larger than 1. In addition, three monitoring lines are arranged in side of the longwall panel to record the redistribution of the abnormal stress in the side of the gob.

### 3. Results

#### 3.1. Abnormal Stress in Front of the Mining Working Face

**3.1.1. Stress Concentration Coefficient.** The mining-induced redistribution of the stress concentration coefficient presents typical differences at different positions in front of the mining working face (Figure 5). It increases gradually with the approach of the mining working face, and its peak reaches 3.43 increasing by 50.44% compared with the starting value 2.28 in the point below the bearing coal pillar when the distance to the mining working face is less than 80 m. In the same time, it presents a similar increasing state with the decreasing of the distance to the mining working face, and the peak reaches 1.96, increasing by 96% compared with the starting value 1.00 in the point below the stable gob when the distance within 41 m. However, they are nearly kept stable and are less than 0.25 in the points below the interaction of the bearing coal pillar and the stable gob.

**3.1.2. Stress Gradient.** The mining-induced redistribution of the stress gradient is related to the distance from the mining working face and the relative location from the bearing coal pillar (Figure 6). It increases gradually and then reaches the peak value 1.20 MPa per meter increasing by 50% with the decrease of this distance for the area below the bearing coal pillar and the interaction of the bearing coal pillar and the stable gob when this distance is less than 80 m. In the same time, it increases relatively slowly for the area below the stable



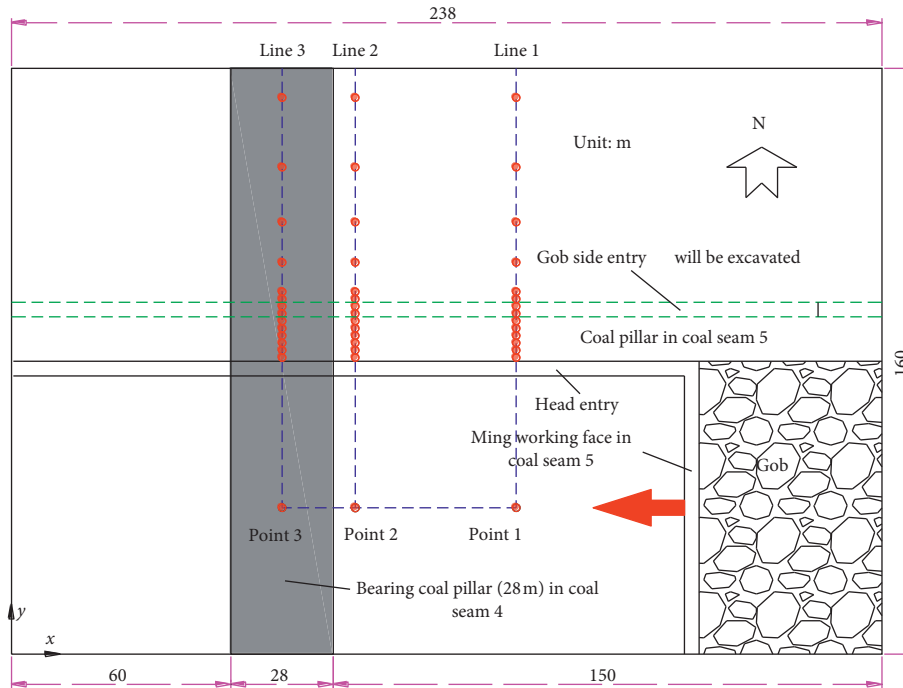


FIGURE 4: Monitoring scheme during the simulation step 4.

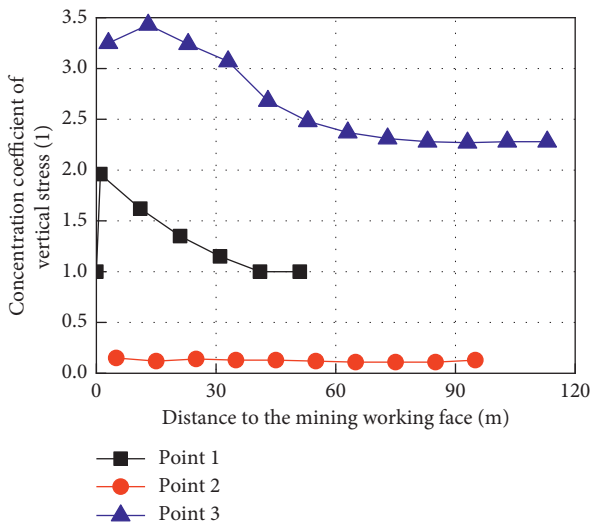


FIGURE 5: Concentration coefficient of abnormal stress in front of the mining working face.

gob with the maximum value of 0.31 MPa per meter and the growth rate of 107% when the distance is less than 50 m.

**3.1.3. Lateral Pressure Coefficient.** The mining-induced redistribution of the lateral pressure coefficient is influenced greatly by the distance to the mining working face (Figure 7). It decreases slowly in the area below the bearing coal pillar and the stable gob with the reduction of this distance when the distance is less than 80 m. However, it decreases first, increases slowly, then increases sharply to the peak, and finally decreases sharply in the area below the interaction of the bearing coal pillar and the stable gob with the reduction

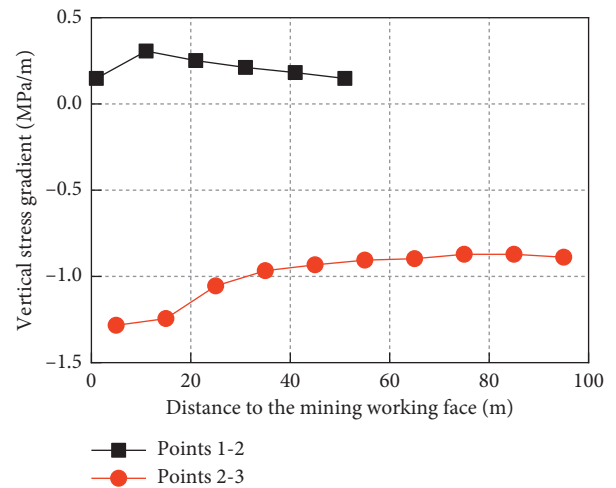


FIGURE 6: Stress gradient of abnormal stress in front of the mining working face.

of the distance to the mining working face. The maximum reaches 7.6 increasing by 52%.

**3.2. Abnormal Stress in Lateral of the Mining Working Face**

**3.2.1. Concentration Coefficient.** The mining-induced redistribution of the stress concentration coefficient also presents typical differences at different positions in lateral of the mining working face (Figure 8). First, in the area below the stable gob, it increases linearly to the peak value and then decreases gradually to a stable value with the growth of the distance to the side rib of the head entry. This peak increases from 1.64 to 3.26, and the influence range increases from

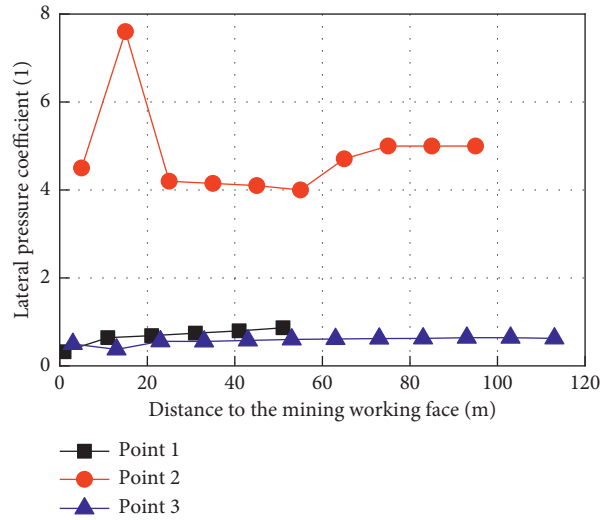


FIGURE 7: Lateral pressure coefficient of abnormal stress in front of the mining working face.

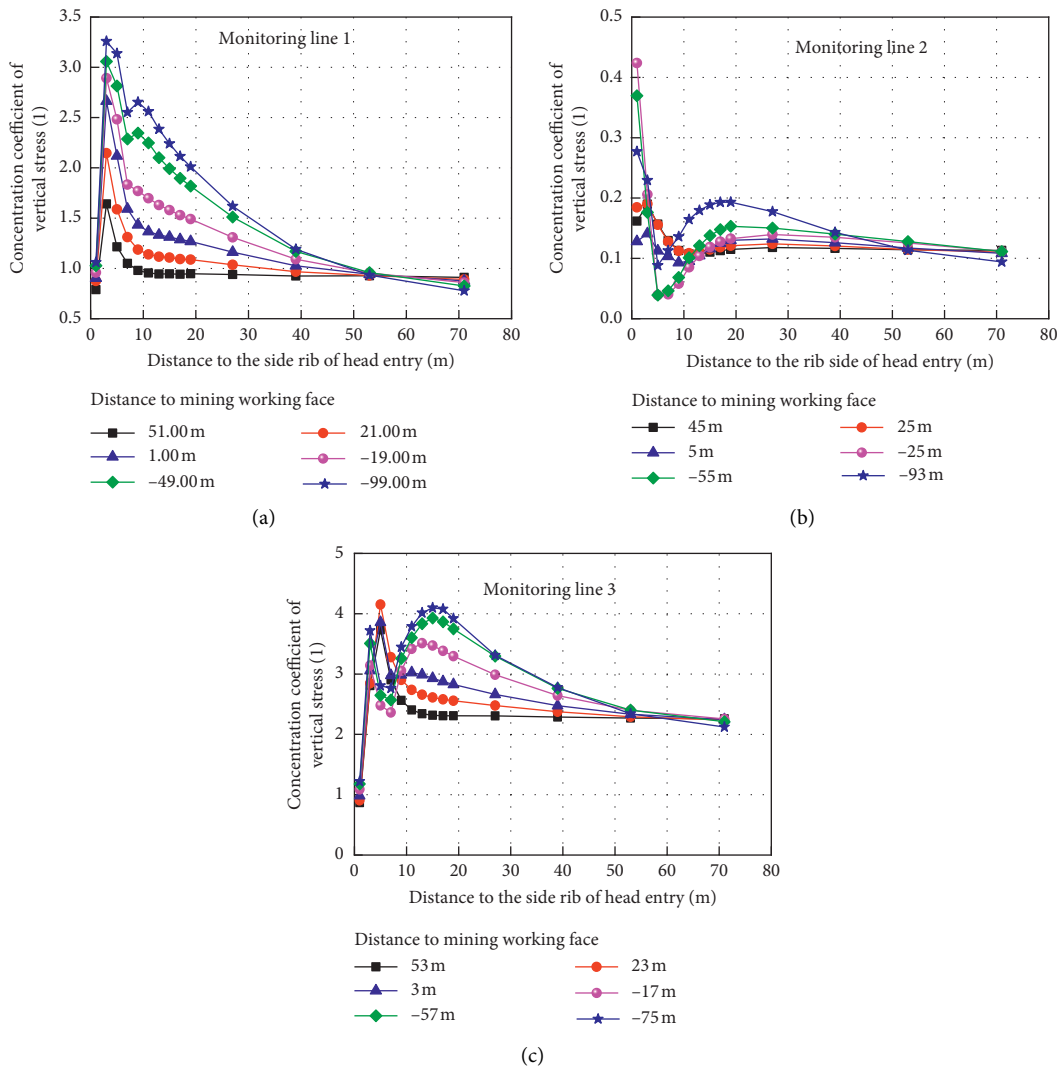


FIGURE 8: Concentration coefficient of abnormal stress in lateral of the mining working face. (a) Monitoring line 1, (b) monitoring line 2, and (c) monitoring line 3.

10 m to nearly 50 m with the reduction of the distance to the mining working face. Second, in the area below the interaction of the stable gob and the bearing coal pillar, it increases sharply to the peak value, decreases sharply to the valley, then increases gradually to the second peak, and finally decreases to a relatively stable value with the growth of the distance to the side rib of the head entry. The peak, second peak, and influence range increase from 0.19, 0.12, and 20 m to 0.42, 0.19, and 70 m, respectively, with the approach of the mining working face. Finally, in the area below the bearing coal pillar, it presents a similar variation to the concentration coefficient below the interaction area with the growth of the distance to the side rib of the head entry but differs in value and its change with the reduction of the distance to the mining working face. For example, the peak and second peak increase from 3.73 and 2.31 to 4.15 and 4.10, respectively, with the approach of the mining working face, which are very different from the values mentioned above.

**3.2.2. Stress Gradient.** The mining-induced redistribution of the stress gradient is related to the distance from the mining working face, the distance to the side rib of the head entry and the relative location from the bearing coal pillar (Figure 9). First, in the area below the stable gob, it decreases sharply to less than zero initially, increases closely to zero, then keeps stable or decreases slowly, and finally increases slowly close to zero again with the growth of the distance to the side rib of the head entry. The maximum of the variation amplitude reaches 5.04 MPa per meter with the approach of the mining working face. Second, in the area below the interaction of the bearing coal pillar and the stable gob, it is similar to that in the area below the bearing coal pillar in the variation trend with different values. For example, the maximum of the variation amplitude is just 0.92 MPa per meter with the approach of the mining working face. Finally, in the area below the bearing coal pillar, it also varies along the similar trend with that in the area below the stable gob but the values. For example, the maximum of the variation amplitude reaches 6.89 MPa per meter with the approaching of the mining working face.

**3.2.3. Lateral Pressure Coefficient.** The mining-induced redistribution of the lateral pressure coefficient is influenced greatly by the distance to the mining working face (Figure 10). It increases sharply initially, then decreases slowly, and finally increases gradually in the area below the stable gob with the distance to the side of the head entry. The maximum is 1.01, and the maximum of the amplitude is just 0.39 with the approach of the mining working face. In the area below the interaction of the bearing coal pillar and the stable gob, it presents a similar variation with that in the area below the stable gob, but it is much larger than that in the area below the stable gob. For example, the maximum reaches 10.00 and the maximum amplitude is 7.01 with the approach of the mining working face. However, in the area below the bearing coal pillar, it presents a very similar variation with that in the area below the stable gob, but it

differs in values. The maximum is limited into 0.74 which is less than 1.00, and the maximum amplitude is 0.25.

## 4. Discussion

**4.1. Contrastive Analysis.** The mining effects on the abnormal stress under the bearing coal pillar mainly concentrate on the stress concentration coefficient, stress gradient, and lateral pressure coefficient in their values and influence ranges. These mechanical behaviors are induced from the superposition of the bearing coal pillar and the mining operations due to the fact that the mining effects on the area below the bearing coal pillar are prior to and more intense than those on other areas below the stable gob and the interaction. For example, compared with the initial values, the stress concentration coefficient increases by 0.96 in the area below the stable gob, 0.00 in the area below the interaction, and 1.15 in the area below the bearing coal pillar, and the influence range increases by 41 m, 0 m, and 80 m, respectively, in front of the mining working face.

In the same time, the mining disrupted strength is larger in the lateral side of the mining working face than that in front of the mining working face. For example, the stress concentration coefficient increases by 1.62 in the area below the stable gob, 0.23 in the area below the interaction, and 1.79 in the area below the bearing coal pillar, and the influence range increases by 40 m, 50 m, and 45 m, respectively, in the lateral side of the mining working face. Obviously, the stress concentration coefficient keeps less than 0.50 all the time with the influence of the mining operation. The mining-induced stress gradient has a similar variation with the stress concentration coefficient.

Differently, the lateral pressure coefficient has slight relationship with the mining operation in the areas below the stable gob and the bearing coal pillar but has strong relationship with the mining operation in the area below the interaction. For example, the lateral pressure coefficient increasing the amplitude reaches 6.38 in the area below the interaction, but it is 0.39 in the area below the stable gob and is 0.25 in the area below the bearing coal pillar. The main reason is because of the stress relief effects for the area below the interaction and stress reinforcement for the area below the bearing coal pillar and the stable gob during the mining operation.

**4.2. Significance of the Results.** The theoretical model can be used to predict the abnormal stress under the bearing coal pillar for the design of the entry layout without disturbing mining operation below this coal pillar [3]. However, this abnormal stress is forced to redistribute to a new condition influenced by the mining operation of the longwall face. Under the condition of the redistribution of the abnormal stress predicted by the numerical simulation model, four key problems including determination of the entry position, determination of the driving operation time, mining disturbing range warning, and prediction of the strengthening support area can be solved to protect the underground entry

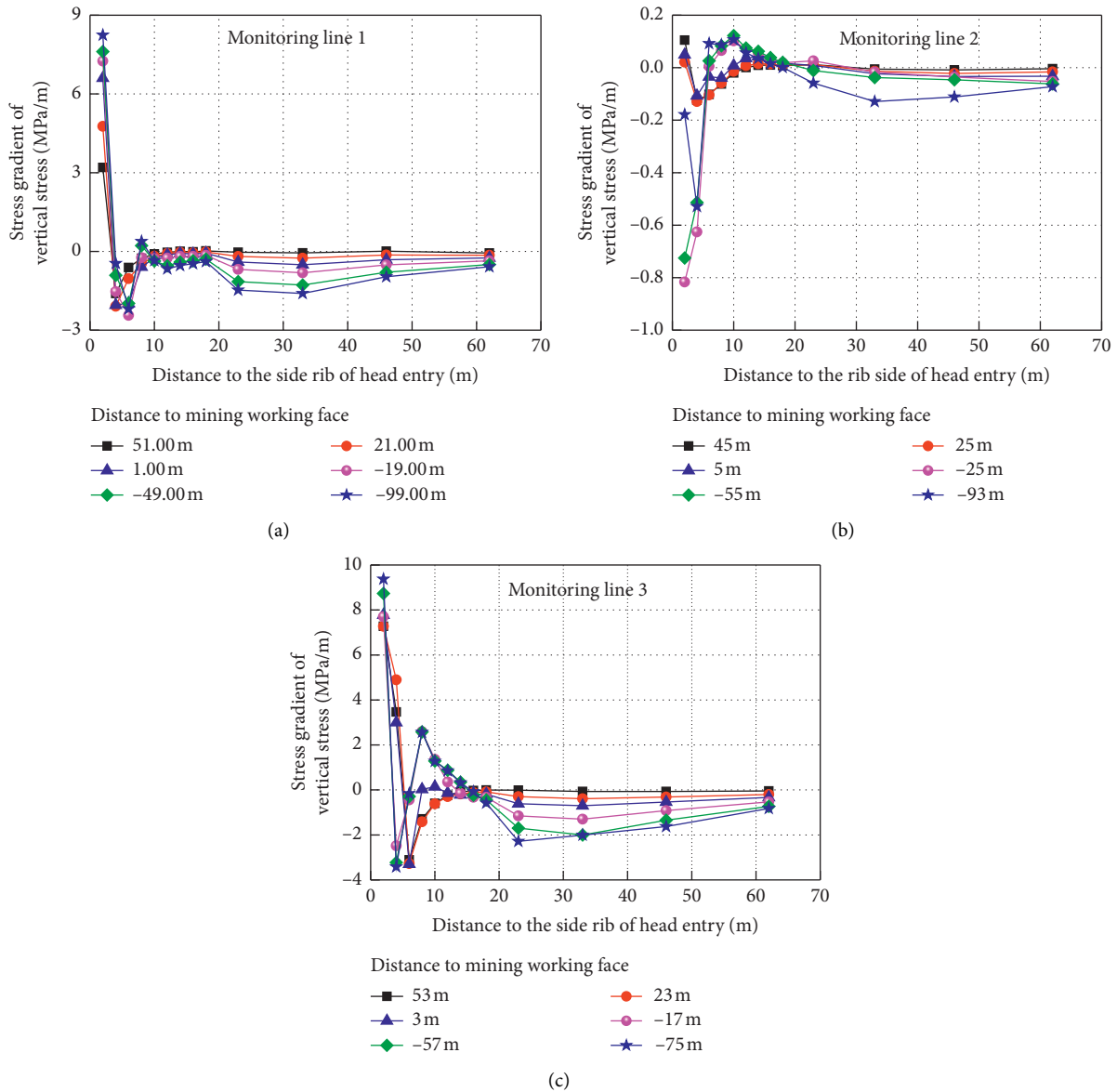


FIGURE 9: Stress gradient of abnormal stress in lateral of the mining working face. (a) Monitoring line 1, (b) monitoring line 2, and (c) monitoring line 3.

from mining-induced large deformation as shown in Figure 11.

The gob side entry under the bearing coal pillar can be layout at position I or position II with a coal pillar in coal seam 5. According to the typical judging criterion, this gob side entry should be arranged at position I where the stress concentration coefficient is less than 1 [36], and this position is determined as less than 2 m or more than 50 m away from the gob side rib. According to the judging criterion that the entry should layout in the zone where the stress concentration coefficient and the absolute value of the stress gradient are less than 1 and the lateral pressure coefficient is close to 1 [3], the position II can be determined at 50 m away from the gob side rib by the redistribution results of the abnormal stress.

If the gob side entry is excavated together with the head entry in the same time with a coal pillar, this entry system is called two-entry driving system [37]. Then, this gob side entry will suffer from the whole mining disturbing of the mining working face in coal seam 5. Determining the mining disturbing range has great significance to protect this kind of gob side entry. The numerical model results indicate that the mining disturbing range varies from 41 m in front of the mining working face to 99 m behind the mining working face in the area below the stable gob. While, it varies from 80 m in front of the mining working face to 75 m behind the mining working face in the area below the bearing coal pillar. For this warning area, the support of the gob side entry has to be strengthened to resist the influence of the mining disturbing.

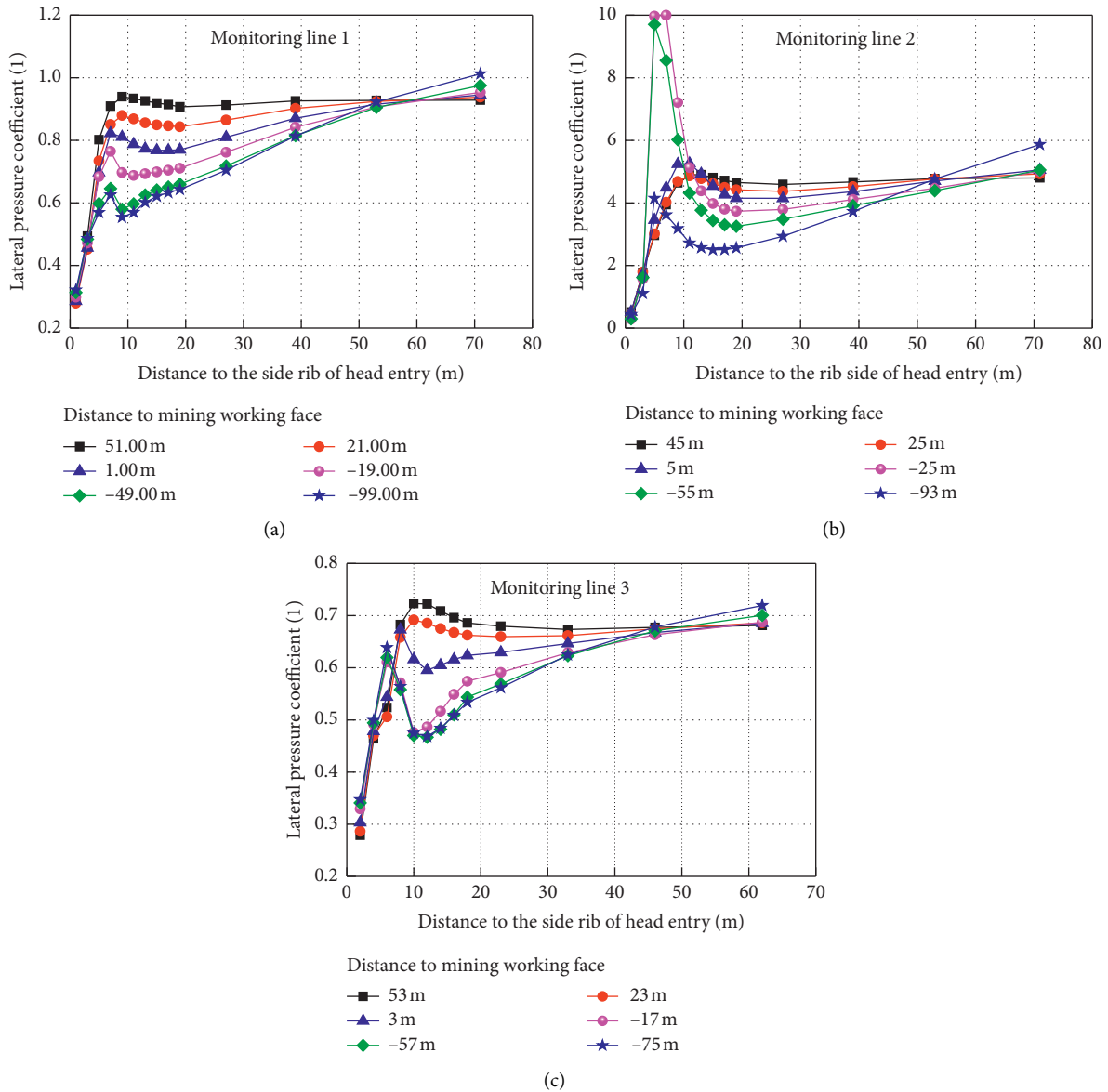


FIGURE 10: Lateral pressure coefficient of abnormal stress in lateral of the mining working face. (a) Monitoring line 1, (b) monitoring line 2, and (c) monitoring line 3.

If the gob side entry is excavated together with the retreating of the mining working face in coal seam 5, this entry system is called gob side entry driving heading adjacent to the advancing working face [38]. There are two key parameters to be determined before the driving operation of this gob side entry such as the driving stopping time and the driving starting time during this driving working face suffers from the mining disturbing. For example, the driving operation has to be stopped at 41 m in front of the mining working face and restart to drive at 99 m behind the mining working face in the area below the stable gob. While, the driving stopping time is determined as 80 m in front of the mining working face and the driving starting time is determined as 75 m behind the mining working face in the area below the bearing coal pillar.

**4.3. Limitation of This Model.** Though, in this numerical simulation model, the structure plane between the rock strata and the lithology differences of rock strata are considered to solve the limitation of the theoretical model, and this numerical simulation model has advantages to predict the mining-induced redistribution of the abnormal stress under the bearing coal pillar and ignores several problems. For example, the effects of the initial joints or cracks on the mechanical behaviors of the rock strata and the mining-induced development of these joints or cracks are not considered. In addition, for some typical geological conditions, dynamic stress wave will generate from the hard roof fracture or caving, which cannot be ignored to layout the entry [39].



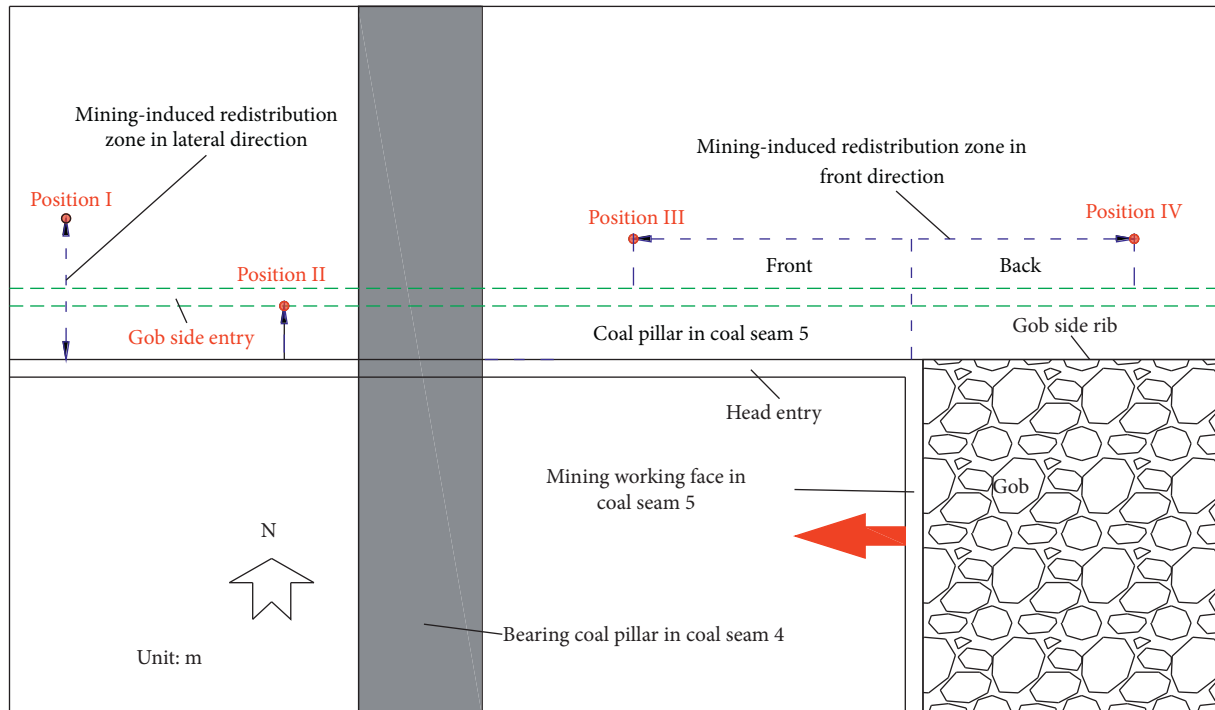


FIGURE 11: Key parameters to layout the entry under the bearing coal pillar.

## 5. Conclusion

The abnormal stress under the close bearing coal pillar plays a significant role in the control of the underground entry stability. A numerical simulation model was established to find out the mining-induced redistribution characteristics of this kind of abnormal stress. The double-yield model, the strain softening model, the interface model, and the Mohr–Coulomb model were determined to simulate the gob compaction effect, the pillar strength reduction effect, the structure plane discontinuity effect, and the rock mechanical behavior, respectively. This numerical mode was validated by comparing the abutment stress with the result of the theoretical method and surface displacement with the result of the measuring method.

The results of the validated numerical simulation model indicate that the mining operation mainly influence the stress concentration coefficient and stress gradient in the area below the bearing coal pillar and the stable gob and influence the lateral pressure coefficient in the area below the interaction of the bearing coal pillar and the stable gob. The stress concentration coefficient and stress gradient increase gradually and then decrease, and the lateral pressure coefficient decreases gradually, then increases, and finally decreases sharply with the approaching of the mining working face. Their maximum increasing rates are determined as 96%, 107%, and 52%, respectively, in front of the mining working face. In the same time, they are 121.05%, 198.56%, and 236.82%, respectively, in the lateral side of the mining working face.

The predicted mining-induced redistribution of the abnormal stress is available for designing the underground

entry layout under the bearing coal pillar with disturbance of the mining operation. The gob side entry has to be excavated at more than 50 m away from the gob side rib. The gob side entry support has to be strengthened in the area from 80 m in front of the mining working face to 99 m behind the mining working face in the two-entry driving system. Gob side entry driving heading adjacent to the advancing working face also has to stop at 80 m in front of the mining working face and restart at 90 m behind the mining working face.

## Data Availability

The data used to support the findings of this study are included within the article.

## Conflicts of Interest

The authors declare that they have no conflicts of interest.

## Acknowledgments

This work was supported by the National Natural Science Foundation of China (51804099 and 52074239), the Focus Research and Special Development for Scientific and Technological Project of Henan province (202102310542), the Fundamental Research Funds of the Central Universities (2017CXNL01), the Key Scientific Research Project Fund of Colleges and Universities of Henan Province (19A440011), and the Fundamental Research Funds for the Universities of Henan Province (NSFRF180328).

## References

- [1] M. G. Qian, P. W. Shi, and J. L. Xu, *Mining Pressure and Strata Control*, China University of Mining and Technology Press, Xuzhou, China, 2nd edition, 2010.
- [2] Y. Li, Y. Ren, S. S. Peng, H. Chen, N. Wang, and J. Luo, "Measurement of overburden failure zones in close-multiple coal seams mining," *International Journal of Mining Science and Technology*, vol. 31, no. 1, pp. 43–50, 2020.
- [3] J. Kang, W. Shen, J. Bai et al., "Influence of abnormal stress under a residual bearing coal pillar on the stability of a mine entry," *International Journal of Mining Science and Technology*, vol. 27, no. 6, pp. 945–954, 2017.
- [4] S. Lu, Y. Jiang, and Y. Sun, "The selection of vertical distance Z between roadway and its upper coal seam," *Journal of China University of Mining and Technology*, vol. 22, no. 1, pp. 4–10, 1993.
- [5] Z. Sun, Y. Wu, Z. Lu, Y. Feng, X. Chu, and K. Yi, "Stability analysis and derived control measures for rock surrounding a roadway in a lower coal seam under concentrated stress of a coal pillar," *Shock and Vibration*, vol. 2020, Article ID 6624983, 12 pages, 2020.
- [6] X. Wang, J. Bai, W. Li, B. Chen, and V. D. Dao, "Evaluating the coal bump potential for gateroad design in multiple-seam longwall mining: a case study," *Journal of the Southern African Institute of Mining and Metallurgy*, vol. 115, no. 8, pp. 755–760, 2015.
- [7] J.-X. Yang, C.-Y. Liu, B. Yu, and F.-F. Wu, "Calculation and analysis of stress in strata under gob pillars," *Journal of Central South University*, vol. 22, no. 3, pp. 1026–1036, 2015.
- [8] W. Ru, S. Hu, J. Ning et al., "Study on the rheological failure mechanism of weakly cemented soft rock roadway during the mining of close-distance coal seams: a case study," *Advances in Civil Engineering*, vol. 2020, Article ID 8885849, 20 pages, 2020.
- [9] H. Yang, Z. Guo, D. Chen, C. Wang, F. Zhang, and Z. Du, "Study on reasonable roadway position of working face under strip coal pillar in rock burst mine," *Shock and Vibration*, vol. 2020, Article ID 8832791, 21 pages, 2020.
- [10] D. Chen, E. Wang, S. Xie et al., "Roadway surrounding rock under multi-coal-seam mining: deviatoric stress evolution and control technology," *Advances in Civil Engineering*, vol. 2020, Article ID 9891825, 18 pages, 2020.
- [11] G. Wu, X. Fang, H. Bai, M. Liang, and X. Hu, "Optimization of roadway layout in ultra-close coal seams: a case study," *PLoS One*, vol. 13, no. 11, pp. 1–14, 2018.
- [12] H. Shang, J. Ning, S. Hu, S. Yang, and P. Qiu, "Field and numerical investigations of gateroad system failure under an irregular residual coal pillar in close-distance coal seams," *Energy Science & Engineering*, vol. 7, no. 6, pp. 2720–2740, 2019.
- [13] S. Lu, Y. Sun, and Y. Jiang, "Selection of horizontal distance X between roadway and the edge of its upper pillar," *Journal of China University of Mining and Technology*, vol. 23, no. 1, pp. 43–51, 1994.
- [14] L. Xinjie, L. Xiaomeng, and P. Weidong, "Analysis on the floor stress distribution and roadway position in the close distance coal seams," *Arabian Journal of Geosciences*, vol. 9, no. 2, p. 83, 2016.
- [15] X. Gao, S. Zhang, Y. Zi, and S.-K. Pathan, "Study on optimum layout of roadway in close coal seam," *Arabian Journal of Geosciences*, vol. 13, no. 15, p. 746, 2020.
- [16] Z. Zhang, M. Deng, X. Wang, W. Yu, F. Zhang, and V. Dao, "Field and numerical investigations on the lower coal seam entry failure analysis under the remnant pillar," *Engineering Failure Analysis*, vol. 115, p. 104638, 2020.
- [17] Z. Zhang, H. Shimada, D. Qian, and T. Sasaoka, "Application of the retained gob-side gateroad in a deep underground coalmine," *International Journal of Mining, Reclamation and Environment*, vol. 30, no. 5, pp. 371–389, 2016.
- [18] J.-B. Bai, W.-L. Shen, G.-L. Guo, X.-Y. Wang, and Y. Yu, "Roof deformation, failure characteristics, and preventive techniques of gob-side entry driving heading adjacent to the advancing working face," *Rock Mechanics and Rock Engineering*, vol. 48, no. 6, pp. 2447–2458, 2015.
- [19] J. F. Labuz and A. Zang, "Mohr-coulomb failure criterion," *Rock Mechanics and Rock Engineering*, vol. 45, no. 6, pp. 975–979, 2012.
- [20] F. Wu, B. Chen, Q. Zou et al., "Range estimation of horizontal stress of deep rock based on Mohr-Coulomb criterion," *Results in Physics*, vol. 12, pp. 2107–2111, 2019.
- [21] C. J. Hou and N. J. Ma, "Stress in in-seam roadway sides and limit equilibrium zone," *Journal of China Coal Society*, vol. 4, pp. 21–29, 1989.
- [22] X. Wang, J. Bai, R. Wang, and W. Sheng, "Bearing characteristics of coal pillars based on modified limit equilibrium theory," *International Journal of Mining Science and Technology*, vol. 25, no. 6, pp. 943–947, 2015.
- [23] E. Esterhuizen, C. Mark, and M. M. Murphy, "Numerical model calibration for simulating coal pillars, gob and overburden response," in *Proceedings of the Twenty-Ninth International Conference on Ground Control in Mining*, Morgantown, WV, USA, January 2010.
- [24] W. Li, J. Bai, S. Peng, X. Wang, and Y. Xu, "Numerical modeling for yield pillar design: a case study," *Rock Mechanics and Rock Engineering*, vol. 48, no. 1, pp. 305–318, 2015.
- [25] W. Shen, G. Shi, M. Wang et al., "Method of entry layout under synergistic effects of abutment stress and dynamic stress," *Shock and Vibration*, vol. 2020, Article ID 6655293, 16 pages, 2020.
- [26] S. Liu, X. Li, D. Wang, and D. Zhang, "Experimental study on temperature response of different ranks of coal to liquid nitrogen soaking," *Natural Resources Research*, vol. 30, no. 2, pp. 1467–1480, 2021.
- [27] X. Zhang, J. Hu, H. Xue et al., "Innovative approach based on roof cutting by energy-gathering blasting for protecting roadways in coal mines," *Tunnelling and Underground Space Technology*, vol. 99, p. 103387, 2020.
- [28] M. Shabanimashcool and C. Li, "Numerical modelling of longwall mining and stability analysis of the gates in a coal mine," *International Journal of Rock Mechanics and Mining Sciences*, vol. 51, pp. 24–34, 2012.
- [29] M. Salamon, "Mechanism of caving in longwall coal mining, presented at the in: rock mechanics contribution and challenges," in *Proceedings of the 31st US Symposium of Rock Mechanics*, Golden, CO, USA, 1990.
- [30] Y. J. Zhang, S. J. Liu, M. M. Kou, and Z. Q. Wang, "Mechanical and failure characteristics of fissured marble specimens under true triaxial compression: insights from 3-D numerical simulations," *Computers and Geotechnics*, vol. 127, Article ID 103785, 2020.
- [31] W.-L. Shen, J.-B. Bai, W.-F. Li, and X.-Y. Wang, "Prediction of relative displacement for entry roof with weak plane under the effect of mining abutment stress," *Tunnelling and Underground Space Technology*, vol. 71, pp. 309–317, 2018.
- [32] F. D. Itasca, *Fast Lagrangian Analysis of Continua in 3 Dimensions*, Itasca Consulting Group, Minneapolis, MN, USA, 2012.

- [33] J. C. Jaeger and N. Cook, *Fundamentals of Rock Mechanics*, Wiley, vol. 93, Hoboken, NJ, USA, Fourth edition, 1979.
- [34] W. Shen, T. Xiao, M. Wang, J. Bai, and X. Wang, "Numerical modeling of entry position design: a field case," *International Journal of Mining Science and Technology*, vol. 28, no. 6, pp. 985–990, 2018.
- [35] V. Kontogianni and S. Stiros, "Induced deformation during tunnel excavation: evidence from geodetic monitoring," *Engineering Geology*, vol. 79, pp. 115–126, 2005.
- [36] C. J. Hou, *Roadway Surrounding Rock Control*, China University of Mining and Technology Press, Xuzhou, Jiangsu, China, 2013.
- [37] W.-L. Shen, W.-B. Guo, H. Nan, C. Wang, Y. Tan, and F.-Q. Su, "Experiment on mine ground pressure of stiff coal-pillar entry retaining under the activation condition of hard roof," *Advances in Civil Engineering*, vol. 2018, Article ID 2629871, 11 pages, 2018.
- [38] G. Zhang, C. Zang, M. Chen, G. Tao, and D. Zhao, "Ground response of entries driven adjacent to a retreating longwall panel," *International Journal of Rock Mechanics and Mining Sciences*, vol. 138, Article ID 104630, 2021.
- [39] X. Li, Z. Cao, and Y. Xu, "Characteristics and trends of coal mine safety development," *Energy Sources, Part A: Recovery, Utilization, and Environmental Effects*, 2020.

## Research Article

# Instability Analysis and Reinforcement Support Technology of Coal-Rock Interbed Roadway in Gaojiazhuang Coal Mine

Chaolin Liu<sup>1,2</sup> and Guohua Zhang<sup>1</sup> 

<sup>1</sup>Heilongjiang University of Science and Technology, Haerbin, Heilongjiang 150022, China

<sup>2</sup>Information Institute of the Ministry of Emergency Management of the PRC, Chaoyang, Beijing 100029, China

Correspondence should be addressed to Guohua Zhang; 690349626@qq.com

Received 27 January 2021; Revised 6 March 2021; Accepted 16 March 2021; Published 30 March 2021

Academic Editor: Zhijie Zhu

Copyright © 2021 Chaolin Liu and Guohua Zhang. This is an open access article distributed under the Creative Commons Attribution License, which permits unrestricted use, distribution, and reproduction in any medium, provided the original work is properly cited.

In order to effectively solve a series of problems such as the difficulty of coal and rock interbed roadway support in Gaojiazhuang Coal Mine and get a scientific and reasonable optimization scheme of surrounding rock support, theoretical analysis, numerical simulation, ultrasonic detection, field-effect test, and other means are adopted to analyze the instability of coal and rock interbed roadway. The results show that the interbedded roadway has weak interbedded cementation, and its ore pressure is more intense due to the influence of its interbedded weak structural plane. Based on Mohr's strength envelope principle, it is proposed that horizontal stress is the main factor that causes a wide range of shear displacement, penetration crack, and surrounding rock failure of the roof of this kind of roadway. Through the finite element numerical simulation analysis, the deformation and failure law, stress distribution characteristics, and failure area distribution characteristics of coal and rock interbedding roadway surrounding rock are theoretically revealed, and the control effect of different support schemes on roadway surrounding rock deformation is greatly different. Based on the ultrasonic detection technology, it is proved that the roadway side failure has strong zoning characteristics, and the failure range and stress distribution range of the surrounding rock of the belt roadway in the 2103 working face of Gaojiazhuang Coal Mine are detected. Finally, the coupling strengthening support scheme combining prestressed anchor cable and bolt is proposed. The engineering application and the observation of surrounding rock deformation show that the reinforced support technology can effectively enhance the stability of the surrounding rock of the interbed roadway in Gaojiazhuang Coal Mine, and it has a good reference for the surrounding rock conditions of this kind of roadway.

## 1. Introduction

With the improvement of mechanization and intensification of coal mine mining, mining roadway section area is increasing, so in the construction of mining roadway, the way of breaking the bottom along the top or breaking the top along the bottom is often used to carry out the construction, resulting in the coal-rock interbed roadway proportion more and more. Interbed of coal and rock roadway surrounding rock is a thin layer of more than two of coal and rock, single layer thickness variation difference is not big, but each other between the layers of the coal-rock mechanical properties of the difference is very big, and the cementation between coal strata is weak, each layer has a certain thickness, but its relative development joint and bedding carry capacity of six to one. Due to the influence of the weak

structural surface of interbed coal and rock roadway, the mine pressure becomes more intense, and the instability phenomena such as roof sinking, roadway bulging, and floor heave often occur in the roadway, which brings great difficulties to the stability control of roadway surrounding rock [1–10].

A lot of research work has been carried out by scholars at home and abroad for coal-rock interlevel roadways. Zhang used field measurement, theoretical analysis, and numerical simulation to determine the reasonable width of coal pillars in the thin coal roof face section affected by high geostress and creep damage in deep wells [11]. Feng and Zhang used the finite element dynamic software ANSYS/LS-DYNA to simulate and analyze the propagation and attenuation law of pressure waves during the blasting of coal-rock interbed masses [12]. Zhong et al. used similar simulation tests and

numerical simulation tests to study the adaptability of the inclined trapezoidal and straight-walled semicircular arched roadway to the coal and rock interbed roadway; orthogonal simulation tests were conducted to obtain 6 coal rock instability factors of interlevel roadways [13, 14]. Wei et al. studied ultrasonic imaging recognition of coal-rock interface based on the improved variational mode decomposition [15]. Shou et al. studied experimental and analytical investigation on the coupled elastoplastic damage model of coal-rock [16]. Wu and Qin studied the loose and broken distribution of soft coal rock in deep coal roadway sidewall [17]. Yang revealed the intrinsic mechanism of the weakening of the thin layered interbed roof under the action of water [18]. Cui studied the deformation characteristics of the roof roadway in the interbed roof of the soft coal seam and the interaction mechanism between the two soft sides and the deformation process of the interbed roof [19]. Qin and Shi proposed the “two soft and one hard” coal gangue interbed composite difficult-to-mined fully mechanized top coal caving mining technology for composite coal roadway support [20]. However, due to the differences in the geological occurrence and mining technology conditions of coal seams in coal mines, the instability mechanism of coal-rock interbed roadway in different areas and its support technology still need to carry out theoretical and practical research according to local conditions [21–30].

In this study, the belt roadway at the 203 working face of Gaojiazhuang Coal Mine was taken as the research object. The ultrasonic wave and numerical simulation technology were used to study the failure characteristics of the surrounding rock, detect and simulate the range of surrounding rock loose zone, analyze the instability mechanism of the roadway, optimize the existing support scheme, and propose the design technology of strengthened support, which provides a reference for the subsequent support control of roadway under similar conditions.

## 2. Project Overview

The designed production capacity of Gaojiazhuang Coal Mine is 3 million tons/year. There are 4 layers of coal seams in the minefield, which are No. 2, No. 4, No. 8, and No. 9 + 10 seams from top to bottom. The 203 working face is located in the first plate area of the No. 2 coal seam. The thickness of the No. 2 coal seam is 1.65 m~1.85 m with an average of 1.75 m, and the average dip angle of the coal seam is 6°. The coal seam contains 0–3 layers of gangue, which is a typical interbedded structure of coal and rock. The direct roof of the coal seam is 2.5 m thick mudstone, and the basic roof is 5.2 m thick fine sandstone. The direct bottom is 1.8 m thick mudstone, and the basic bottom is 1.1 m thick No. 3 coal seam (nonmining). See Table 1 for the lithologic characteristics of No. 2 coal seam roof and floor.

The 203 working face adopts three roadway layouts, with a strike length of 972 m and dip length of 172 m, respectively. Tape lane width and height are 4.2 m × 2.8 m, the combined support with anchor, network, in the form of roof bolt arrangement in each row for roof is  $\Phi 20 \times 2500$  mm high strength metal bolt, the bolt between row spacing is

TABLE 1: Lithological characteristics of No.2 coal seam.

Horizon	Lithology	Thickness (m)
Roof	Fine sandstone	5.2
	Direct top mudstone	2.5
Coalbed	No. 2 coalbed	1.75
Floor	Direct bottom mudstone	1.8
	No. 3 coalbed	1.1

1200 mm × 1000 mm, the side bolt adopts  $\Phi 20 \times 2200$  mm right screw full thread and other strong metal bolts, the row spacing between bolts is 1100 × 1000 mm, the top steel belt is welded with  $\Phi 16$  mm round steel, the side steel belt is welded with  $\Phi 12$  mm round steel, the top anchor net adopts No. 10 spot welding metal net, the specification is 1000 × 2300 mm, the help net adopts No. 10 galvanized iron wire diamond net, and the specification is 1000 × 2500 mm.

Influenced by the occurrence condition of the coal seam, the interbedding arrangement of coal and rock along the top and bottom is adopted in the excavation of 203 working face, which brings great difficulties to roadway support. Figure 1 shows the layout of the roadway at the working face 203, and Figure 2 shows the support section of the belt roadway at the working face.

## 3. Research on the Failure Mechanism of Coal-Rock Interbed Roadway

The stress environment of the rock mass is a relatively balanced three-dimensional stress stable state before coal and rock interbedding roadway excavation. After the construction of the roadway, the stress in the surrounding rock is redistributed, and the stress environment is changed into a nearly two-dimensional stress state. The horizontal stress is transferred to the roof rock, and the vertical stress is transferred to the coal and rock in the two sides of the roadway. If the stress value caused by the stress concentration is greater than the rock strength, the surrounding rock will be damaged, and this failure zone is also the range of the surrounding rock loosening zone. On the contrary, the surrounding rock is in an elastoplastic state and remains stable. The intensity and stress state changes of surrounding rock before and after roadway excavation are shown in Figure 3.

As can be seen from the figure, the coal and rock mass were subjected to high primary rock stress before the roadway construction, the maximum and minimum principal stress were similar, the Mohr circle was far from the strength envelope, and the coal and rock mass in the roadway were in a stable state. After unloading, the lateral stress of the surrounding rock decreases in a certain range, and the lateral pressure drop of the surrounding rock surface is zero. At the same time, the stress is adjusted and transferred to the surrounding roadway, causing local stress concentration, increasing the maximum principal stress, and decreasing the minimum principal stress, which shows that the Mohr circle is cut by the strength envelope after roadway excavation construction, and the coal and rock mass are



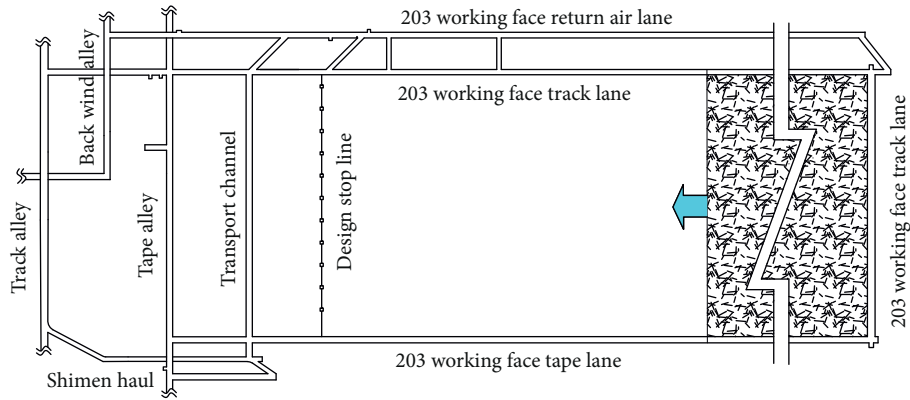


FIGURE 1: Roadway layout of the 203 working face.

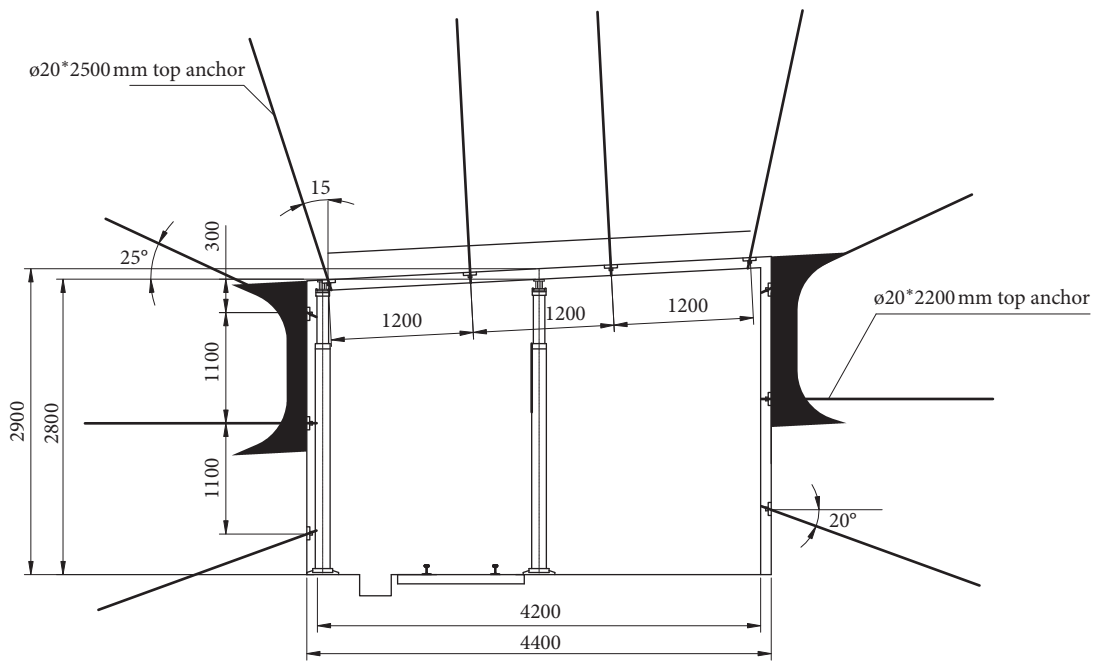


FIGURE 2: Sectional view of the original support of the belt lane.

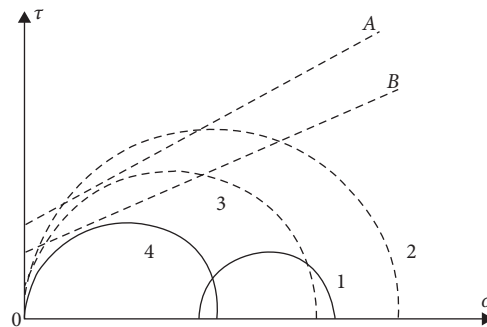


FIGURE 3: Changes in strength and stress of surrounding rock after the construction of the roadway. 1: raw rock stress circle; 2: deformation circle after roadway construction; 3: stress circle after roadway construction; 4: stress circle after roadway construction is stable; A: envelope line after roadway construction; B: long-term roadway stability package network.

destroyed. In order to maintain the stable state of the roadway, the first thing is to restore or improve the stress state of coal and rock mass as soon as possible after roadway construction. The timelier measures are taken; the smaller the degree of rock mass destruction, the better the integrity of coal and rock mass, and the more stable the rock mass.

According to the study, the roof of layered strata of coal measures is arched, and the failure formula of roadway surrounding rock according to the Platt pressure-free arch theory is as follows:

$$R = \left( \frac{k_c \cdot \gamma \cdot H \cdot B_c}{100\sigma_m} - 1 \right) \cdot h \cdot \tan\left(45^\circ - \frac{\phi}{2}\right). \quad (1)$$

In the formula,  $k_c$  is the stress concentration factor of the surrounding rock of the roadway, which is 2;  $\gamma$  is the average bulk density of the rock mass, which is 25 kN/m<sup>3</sup>;  $H$  is the coal seam depth, corresponding to the surface elevation of +100 m, and the coal seam elevation of +510 m, then  $H$  is 590 m;  $B_c$  is the mining influence coefficient, which is 0.5;  $\sigma_m$  is the uniaxial compressive strength of the roof rock mass, which is 30 MPa;  $h$  is the roadway height, which is 2.9 m;  $\phi$  is the internal friction angle of the coal seam, which is 64°.

The failure range of the surrounding rock of the interbedded roadway is calculated by using the data.  $R = 2.61$  m.

The maximum loosening range of the roof is  $b = (a + R)/f_m$ , where  $f_m$  is the firmness coefficient of the roof rock layer, taking 1.9;  $a$  is the half-lane width, taking 2.1 m. Substituting the data, it is calculated that the maximum loosening range of the roof of the coal-rock interlevel roadway is 2.48 m.

The above analysis shows that the direct roof rock layer is generally mainly affected by the effect of horizontal stress. The roof rock layer with relatively low local strength is damaged due to the stress reaching the limit of failure, resulting in a wide range of shear displacements or through fractures, resulting in collapse. Therefore, in order to ensure the safety of the roadway and the stability of the surrounding rock mass, the necessary support is usually required after the construction of the roadway to limit the continuous development of the deformation and damage of the surrounding rock of the roadway, and the stress imposed by the support on the surface of the roadway surrounding rock must reach sufficient amount. However, in terms of current roadway support technology and technical level, the stress that can be applied to the surrounding rock surface of the roadway by relying solely on the support method is relatively small compared to the original rock stress of the deep rock mass. This is the fundamental reason why the traditional existing support methods are not effective in the surrounding rock of deep roadways, and it is necessary to change the inherent properties of the surrounding rock by means of reinforcement. That is, the inherent strength of the surrounding rock (cohesion and internal friction angle) is increased by means of support and reinforcement, and the bearing capacity of the surrounding rock is enhanced.

Because the inherent strength of the surrounding rock belongs to shear properties, this requires that the support plus solid itself must have a sufficiently high shear strength, and because of the brittle nature of the surrounding rock

mass, it will fail as long as it undergoes small shear deformation cohesion. The supporting structure must have sufficient high shear strength and sufficient toughness to ensure that the inherent strength of the surrounding rock mass of the roadway can be significantly improved.

## 4. Numerical Simulation of Failure of Roadway between Coal and Rock

In this study, FLAC numerical simulation software was used for the theoretical calculation to simulate the surrounding rock failure, such as the supporting effect and stress state of coal and rock interbedding mining roadway, and theoretically reveal the deformation and failure law, stress distribution characteristics, and failure area distribution characteristics of surrounding rock of coal and rock interbedding mining roadway.

*4.1. Model Establishment and Parameter Selection.* The numerical simulation is based on the geological conditions of the coal seam in the 203 belt roadway. The model is 50 m in length, 54 m in height, and 30 m in width, with 118,200 units and 124,160 nodes in total, and 30 m boundaries are left around each. The numerical simulation calculation model is shown in Figure 4.

The constitutive model of numerical simulation is divided into seven layers, and the Moor-Coulomb failure criterion is selected. The physical and mechanical property parameters of each coal stratum are shown in Table 2.

*4.2. Comparative Analysis of Numerical Simulation Results.* As the roadway is constructed along the top and the bottom, the upper part is No. 2 coal seam with gangue layer, and the floor strata of the lower seam, the typical coal, and rock interbedding roadway conditions are formed. In order to deeply analyze the law of displacement, deformation, and stress distribution of the roadway and the supporting effect of the roadway, two cases of original support (original design) and strengthened support (follow-up design) of the roadway were, respectively, numerically simulated to provide a reference for the subsequent surrounding rock support control optimization of the roadway.

*4.2.1. Analysis of Maximum Principal Stress.* The cloud diagrams of the maximum principal stress distribution for numerical simulation under two different support conditions are shown in Figure 5. It can be seen from the figure that a low-stress area appears within a certain range around the excavation of the roadway, especially a large range of low-stress areas (or even a tensile stress area) in the floor of the two sides of the roadway. The tensile strength of the body is much smaller than the compressive strength, so the coal-rock mass in this area was considered to be seriously damaged. At the same time, it is worth noting that within a certain range of the roof of the roadway, a pressure arch that acts on the two sides of the roadway is formed, which also causes a local high-stress zone outside the roadway to a certain extent. In addition, it can be

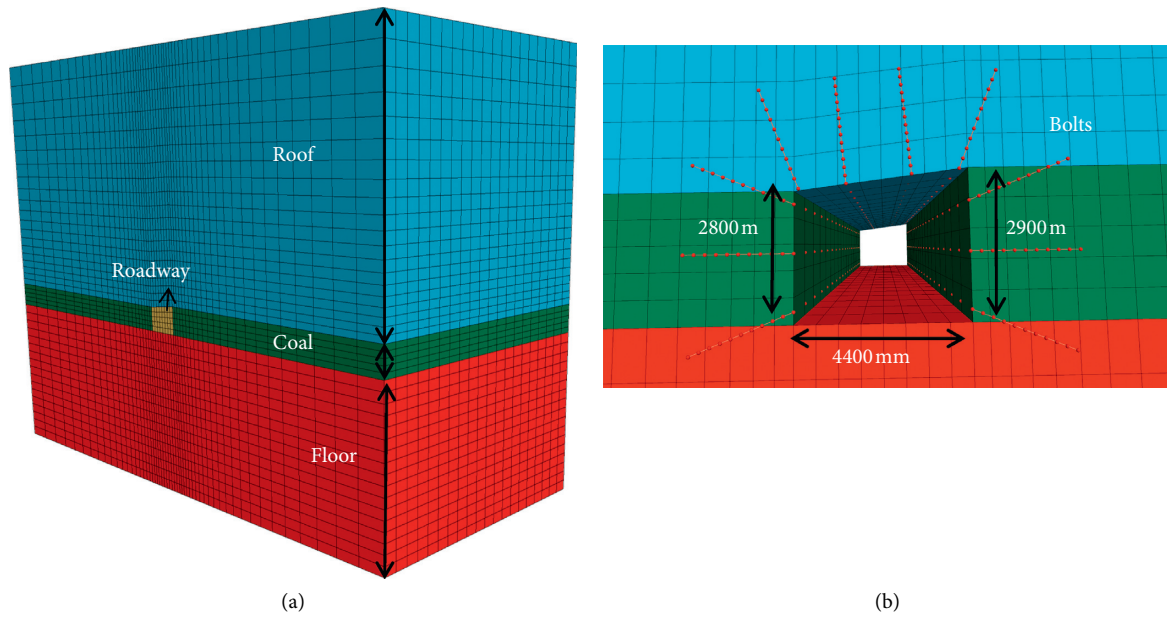


FIGURE 4: Numerical simulation calculation model: (a) model structure and (b) bolting parameter.

TABLE 2: Parameters of physical and mechanical properties of various coal and rock layers.

Model level (m)	Thickness (kg/m <sup>-3</sup> )	Density (MPa)	Adhesion (°)	Friction angle (GPa)	Bulk modulus (GPa)	Shear modulus (MPa)	Tensile strength
Sandstone	20	2500	16	36	16.3	13.5	2
Fine sandstone	5	2700	14	34	17.6	14.1	1.86
Direct top mudstone	4	2000	2	32	5.8	2.96	0.83
No. 2 coalbed	2	1400	0.35	18	1.15	0.33	0.15
Direct bottom mudstone	2	2000	0.86	28	3.8	1.96	0.45
No. 3 coalbed	1	1400	0.35	18	1.15	0.33	0.15
Sandstone	20	2500	16	36	16.3	13.5	2.2

seen that the roadway support measures have reduced the low-stress area of the roadway roof to a certain extent and have a small impact on the low-stress area of the roadway gang, and to a certain extent, the low-stress area of the roadway floor has been increased.

**4.2.2. Analysis of Deformation of Surrounding Rock of Roadway.** The vector diagram of the surrounding rock deformation of the roadway under two different support conditions is shown in Figure 6. The length of the arrow line in the figure indicates the magnitude of the displacement vector at that point, and the direction of the arrow indicates the vector direction of the point displacement. It can be seen from the figure that after the roadway is excavated, the two sides of the roadway have the largest continuous deformation of the coal and rock mass, followed by the roadway floor, and the continuous deformation of the roadway roof is relatively small. The reason for this analysis is that due to the hard lithology of the roof of the roadway, a pressure-bearing arch structure is formed above the roadway (the existence of the pressure arch can be seen from the above maximum

principal stress cloud diagram), so the absolute deformation of the roof is not large.

**4.2.3. Analysis on the Law of Roof Subsidence of Roadway.** See Figure 7 for the cloud subsidence of the roof of the roadway under two different support conditions, and see Figure 8 for the graph of roof subsidence and reduction rate. It can be seen that the subsidence curve of the roof of the roadway after the excavation of the roadway has an inflection point at the roof of 4 m, and the subsidence of the roof of the roadway within 4 m is significantly greater than that of the roof above 4 m. Strengthened support compared with the original support scheme, the original support is not as effective as strengthening support in reducing the roof subsidence rate within 2.5 m, and the original support is more powerful than the supporting roof when the rock layer is 2.5 m away. The sink reduction rate is large.

**4.2.4. Analysis of the Distribution Law of the Surrounding Rock Elastoplastic Zone.** The distribution of the elastoplastic zone of the surrounding rock of the roadway under two

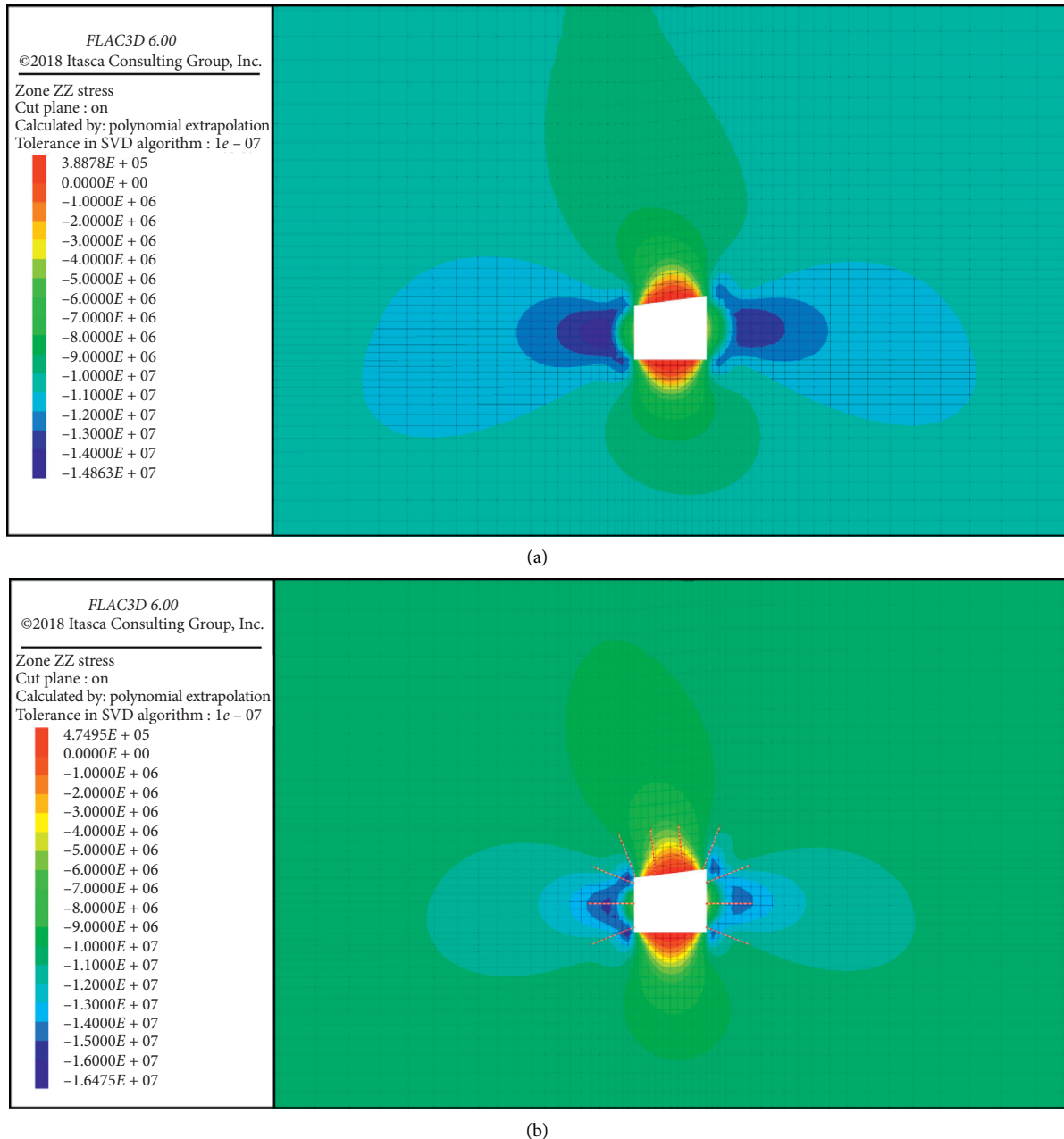
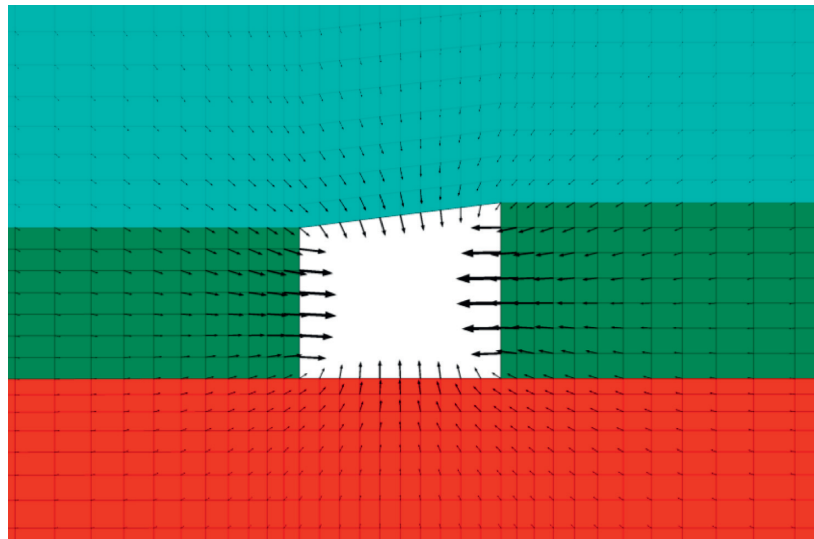


FIGURE 5: Cloud diagram of maximum principal stress distribution in numerical simulation: (a) original support and (b) reinforced support.

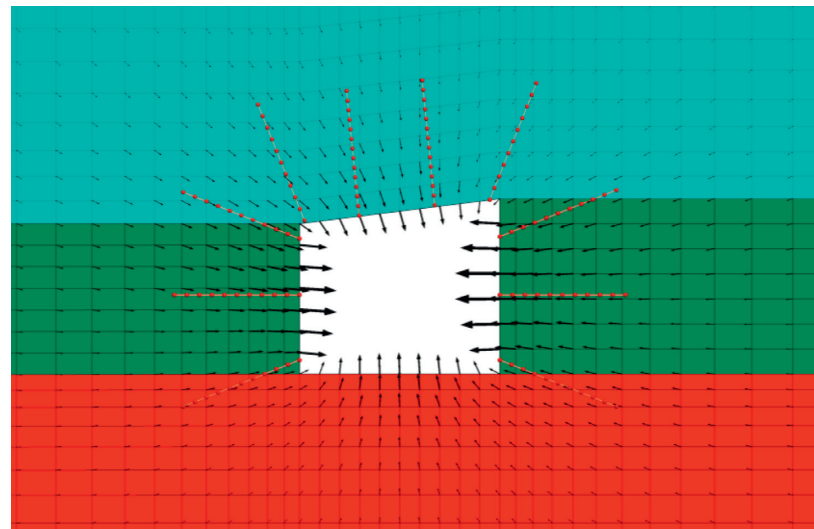
different support conditions is shown in Figure 9, where different colors indicate different plastic states (such as tensile plastic zone and shear plastic zone). It can be seen from the figure that after the excavation of the roadway, a large plastic area appears in the two corners of the roadway and a certain range of the roof, and the plastic area of the roof is arched. This is the same as the support pressure above the roof of the roadway obtained from the above-mentioned main stress distribution cloud diagram. Arch simulation wants to fit. This is also consistent with the lithological characteristics of the roof of the roadway mentioned above, but the brittleness of the roof due to the characteristics of the roof results in the local deformation of the roof under the

condition of a small amount of deformation, so that the entire large area of the pressure arch occurs.

*4.3. Analysis of Surrounding Rock Failure Characteristics Revealed by Numerical Simulation.* Compared with the rock strata, the coal seam is the weaker structure of the surrounding rock of the roadway, and its deformation is greater than that of the rock strata, which is also the reason for the large deformation of the coal body at the roadway side. Figure 10 shows the comparison of deformation distribution of different media in surrounding rock of interbedded roadway. For the interbedding coal and rock mining

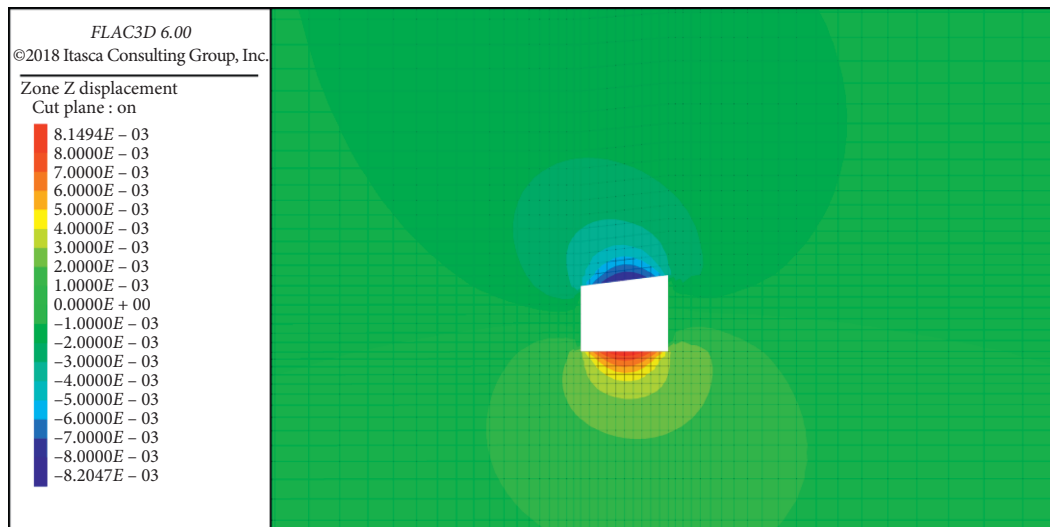


(a)



(b)

FIGURE 6: Vector diagram of deformation of surrounding rock: (a) original support and (b) reinforced support.



(a)

FIGURE 7: Continued.



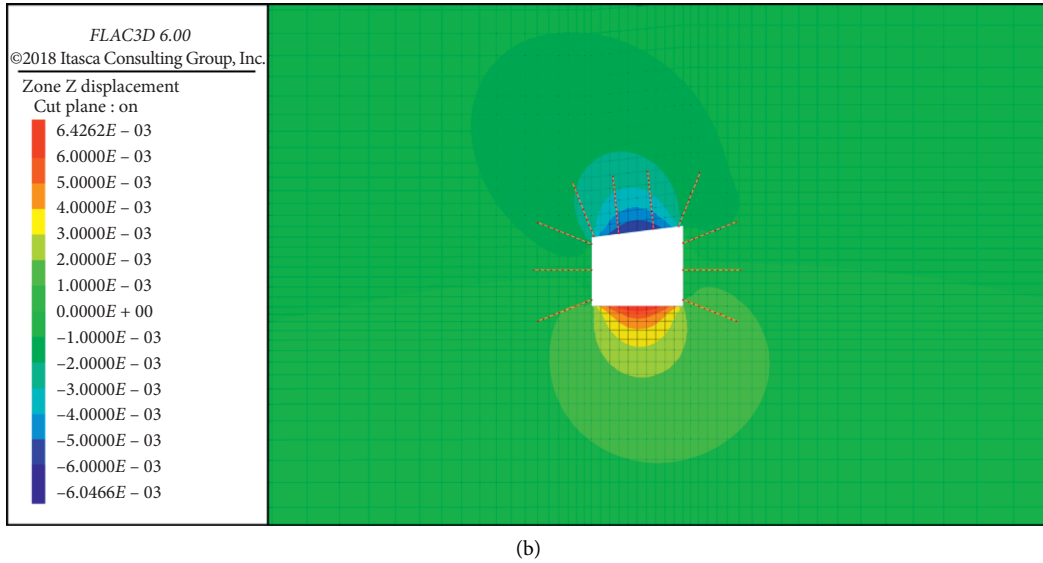


FIGURE 7: Sinking clouds on the roof under different support conditions: (a) original support and (b) reinforced support.

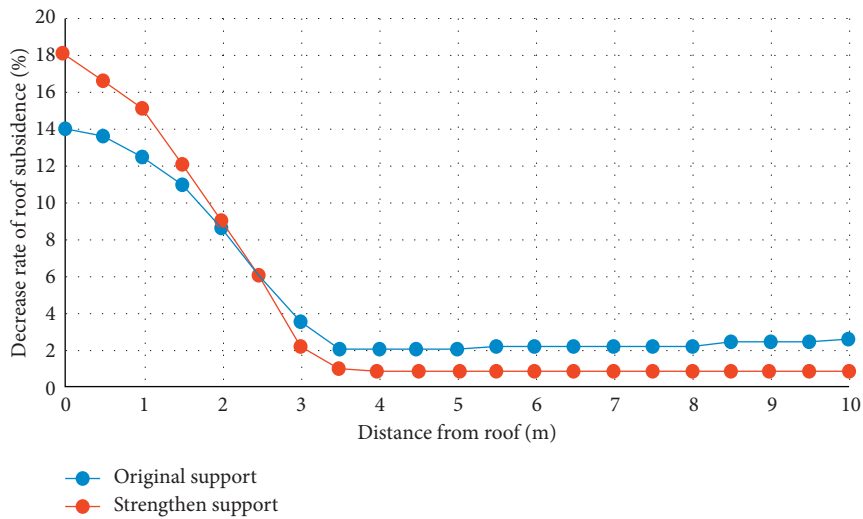
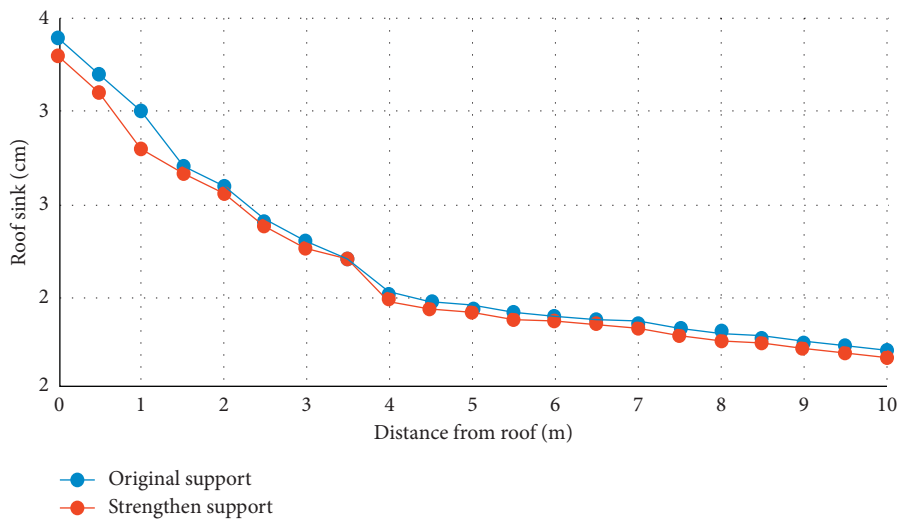


FIGURE 8: Curve of roof subsidence and reduction rate under different support conditions. (a) Graph of roof subsidence and (b) Graph of a reduction rate of roof subsidence.

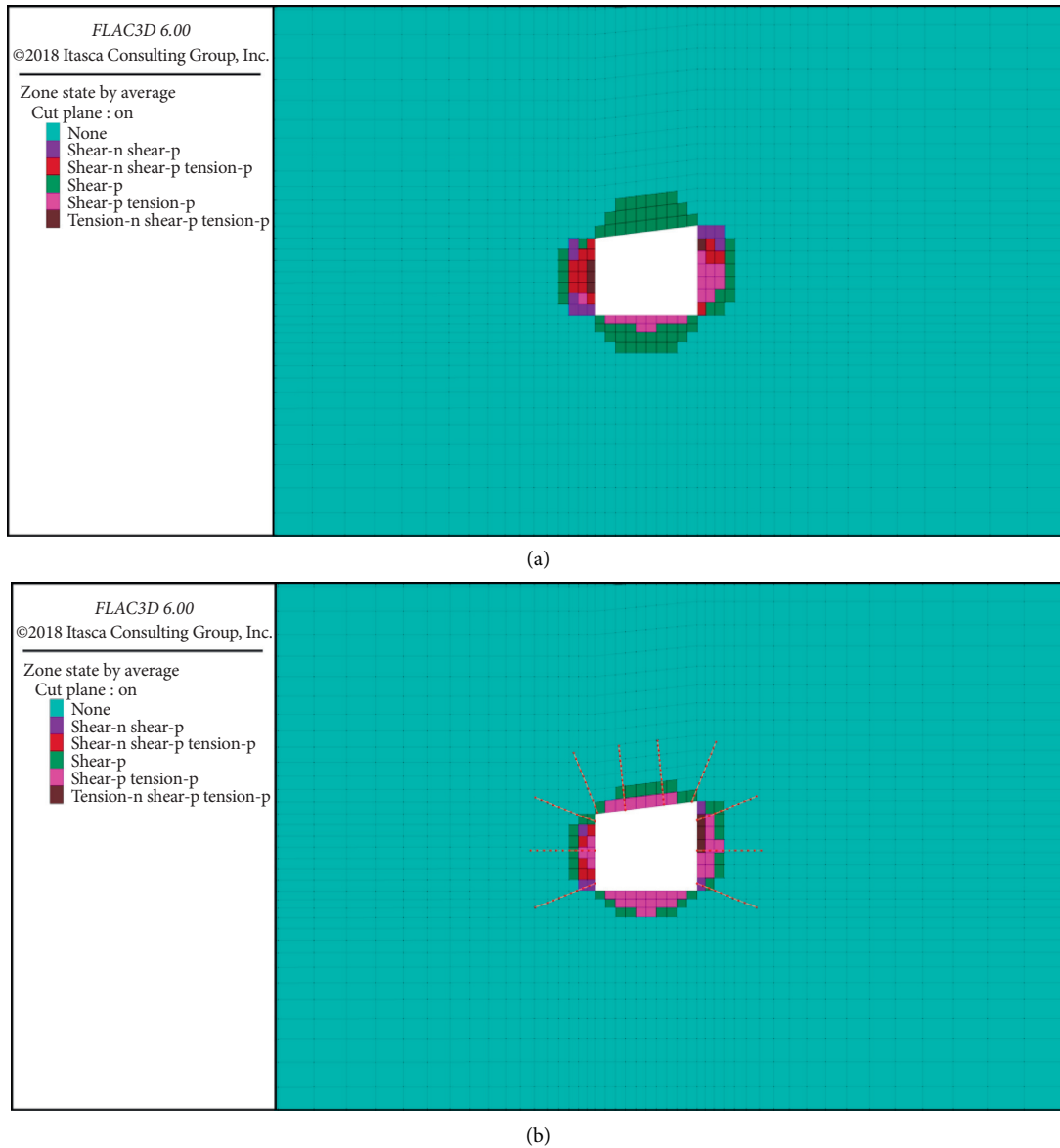


FIGURE 9: Distribution law of surrounding rock elastoplastic zone of the roadway with different support conditions: (a) original support and (b) reinforced support.

roadway at the 203 working face, different support schemes can control the deformation of surrounding rock to a certain extent. Compared with the original support scheme, the enhanced support has a more obvious control effect on the deformation of surrounding rock in the roadway to a certain extent, while the control effect of the shallow near field surrounding rock is not obvious.

### 5. Ultrasonic Detection of Coal-Rock Interbed Roadway Failure

5.1. *Technical Principles.* According to the rock mechanics theory, the integrity of the surrounding rock is good, its compressional wave velocity is high, the surrounding rock joints and fractures are more or more broken, and its compressional wave velocity is low. Therefore, the

characteristic parameters such as wave velocity, amplitude, and frequency of the ultrasonic longitudinal wave and their change rules are measured in the underground, so as to judge the lithology, density, cracks, weak interlayer, and other states and analyze the range of the loose zone of roadway surrounding rock.

A probe of a double-receiver transducer is placed in the borehole, and the transmitting transducer F emits ultrasonic waves in the borehole, generating gliding waves around the borehole wall to propagate along the borehole. Receiving transducers 1 (S1) and 2 (S2) receive the first wave of gliding wave, respectively. Therefore, the propagation velocity can be obtained according to the propagation time from the transmission to the receipt of the first wave recorded by the single-chip microcomputer and the fixed propagation distance between probes according to propagation

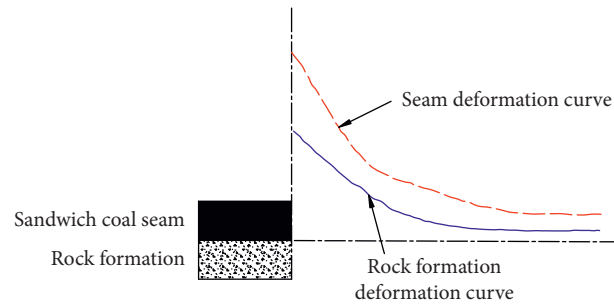


FIGURE 10: Comparison of deformation distribution of surrounding media in surrounding rock of coal-rock interbed roadway.

velocity = propagation distance/propagation time, and then the boundary of the loose circle can be determined by using it. The principle diagram of the ultrasonic crack tester for the surrounding rock is shown in Figure 11.

## 5.2. Ultrasonic Scene Detection Scheme

**5.2.1. Instrument and Detection Method.** The drill was drilled with a CLC1000 tester, with a diameter of 45 mm and a distance of 0.1 m between the transmitter and receiver. The drilling hole was tested in time after forming. The drilling hole was rinsed with pressure water before testing and the coal powder was cleaned. After the tester is connected with the probe, the probe is sent to the bottom of the hole with a push rod, and then the pushrod is pulled to record the sound wave outward at 10 cm for each block until the mouth of the hole. See Figure 12 for the layout of detection stations for surrounding rock failure of the roadway.

**5.2.2. Arrangement of Measuring Points in Underground Roadways.** Considering the current mining position of the working face and other influencing factors, the belt roadway of the 203 working face is selected as the object of underground exploration. The position of the detection points for surrounding rock failure is arranged at a distance of 70 m from the current position of the working face of the belt roadway. See Figure 13 for the layout plan of the detection points. A group of boreholes are arranged every 30 m for testing, consisting of 3 groups of measuring points, and 4 boreholes are arranged at each group of measuring points, which are, respectively, located in the middle of the waistline on both sides of the roadway and the floor. The two sides of the holes are arranged in the waistline position of the two sides of the roadway. The hole depth is 6-7 m, the diameter is 45 mm, and the bottom of the hole is inclined downward about 8-10°. The empty floor is arranged in the middle of the roadway floor, perpendicular to the roadway floor, with a hole depth of 6-7 m and a diameter of 45 mm. See Figure 14 for the horizontal section of the detection borehole at the detection point.

**5.3. Research on Ultrasonic Field Detection Results.** The purpose of underground ultrasonic detection is to find out the failure range and stress distribution range of

surrounding rock of interbedded roadway. See Figure 15 for ultrasonic detection results of cracks in surrounding rock of roadway at different leading positions from 203 working face.

The following can be seen from Figure 15:

- (1) The wave velocity at the side of the coal pillar at a distance of 70 m from the working face drops sharply in the range of 0.9 m-1.2 m in borehole depth, and the wave velocity decreases from 1085 m/s to 900 m/s. The wave velocity at the side of the coal pillar 100 m from the working face dropped sharply at the depth of 1.8-2.0 m, and the wave velocity dropped from 1148 m/s to 970 m/s. There is no significant change in the side wave velocity of the coal pillar at a distance of 130 m from the working face
- (2) The wave velocity of the solid coal side 70 m away from the working face drops sharply at a drilling depth of 0.9, and the wave velocity decreases from 1160 m/s to 1080 m/s; in addition, the range of 5.0-5.9 m also fluctuates violent fluctuations. The wave velocity of the solid coal side 100 m away from the working face drops sharply at a depth of 1.1 m, and the wave velocity drops from 1132 m/s to 1115 m/s. The wave velocity drops sharply at a depth of 3.1 m-3.6 m, and the wave velocity is s dropped to 1088 m/s; a sharp drop occurred in the borehole depth range of 4.2 m-4.5 m, and the wave velocity dropped from 1120 m/s to 1078 m/s. There is no significant change in the side wave velocity of the solid coal at a distance of 130 m from the working face
- (3) From the above analysis, it can be seen that the wave velocity of the coal pillar side is significantly lower than that of the solid coal side. The stress concentration range of the coal pillar side of the belt lane in the 203 working face is between 0.9 m and 2.0 m, the stress concentration range caused by the solid coal side is 0.9-1.1 m, and the range of 3.1-4.5 m on the side of the solid coal is also obvious

The schematic diagram of the surrounding rock failure stress distribution range of the coal-rock interbed roadway revealed by the detection of the belt lane in 203 working face is shown in Figure 16. The results of stress observation show that under the condition of the existing support system, about 0-2 m of the surrounding rock failure of the 203 belt lane is the loosening circle of the surrounding rock, and

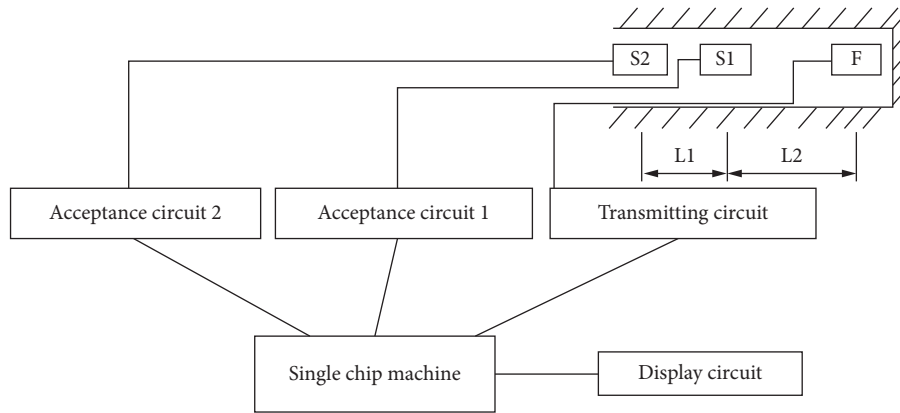


FIGURE 11: Schematic diagram of ultrasonic surrounding rock fracture tester.

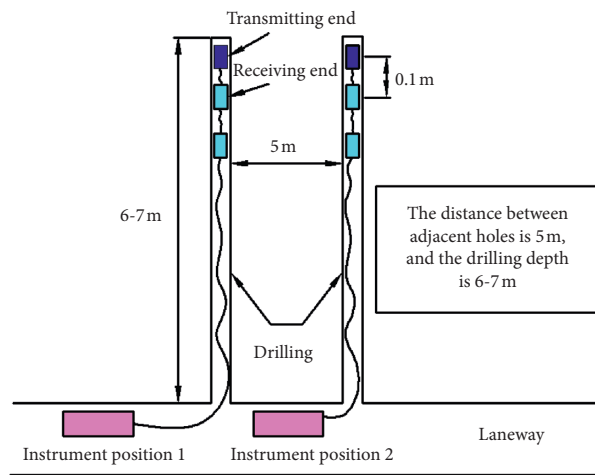


FIGURE 12: Arrangement of roadway surrounding rock damage detection stations.

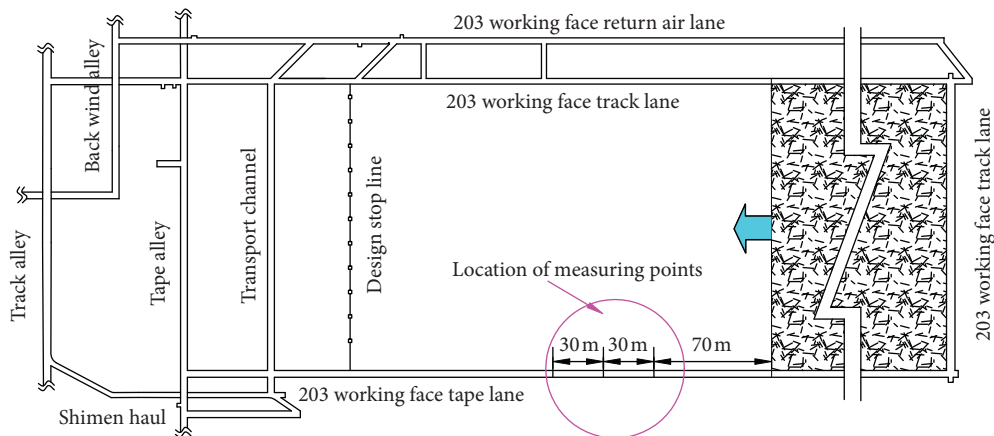


FIGURE 13: Plan view of measuring point arrangement position.

about 2.0–3.1 m of the surrounding rock failure of the laneway is the effect of the anchor to support the impact. In the region, the range of about 3.1–4.5 m destroyed by the surrounding rock of the roadway is the plastic zone, which is the influence range of the external stress field revealed by the foregoing numerical simulation results.

5.4. Analysis of Surrounding Rock Failure Characteristics Revealed by Ultrasonic Detection. Through the ultrasonic detection of the surrounding rock, the failure characteristics of surrounding rock revealed by the ultrasonic detection results of surrounding rock fractures are shown in Figure 17. The results show that the coal seam is affected by the internal

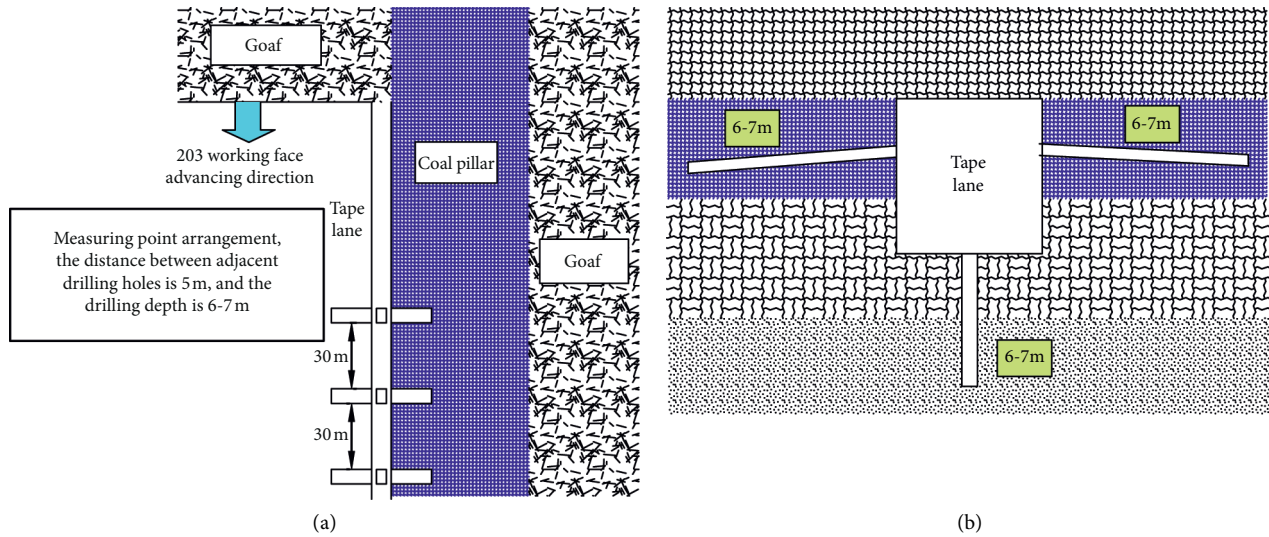


FIGURE 14: Plane section of borehole survey: (a) floor plan and (b) section.

and external stress field, and the failure range is large, with strong zoning characteristics. From near to far, the coal wall of the roadway is, respectively, the range of surrounding rock loose zone, the range of near field fracture under the control of bolt support, the range of far-field fracture without the influence of bolt support, and the stress area of the original rock. In the range of the above several fracture distribution areas, roadway bolt support can only control the range of near field fractures, and the development of the loose circle range is greatly affected by the support prestress, which is also the key range of bolt support control at present. In order to control the large deformation of surrounding rock, it is necessary to control the development of near field cracks, increase the strength of support, or strengthen the bearing capacity of the coal seam.

## 6. Design of Enhanced Support for Coal-Rock Interlevel Roadway

**6.1. Strengthening the Theoretical Basis of Support.** Through the above theoretical analysis, numerical simulation, ultrasonic detection, and other methods, it is obtained that the failure height of the 203 belt lane is 2.48 m, 2.5 m, and 2.0 m, respectively. The maximum value of 2.5 m is taken as the reference value of the surrounding rock failure support of the 203 belt roadway. Due to the small strength of the roof and easy destruction of the 203 belt roadway, the damage range of mudstone roof strata in the roadway is large, and the roof strata are the key point of the strengthened support design. The original rooftop anchor rod specifications for  $\Phi 20 \times 2500$  mm obviously cannot satisfy the need for safety and must strengthen the supporting design. See Figure 18 for the schematic diagram of roof rock instability under the control of original bolt support.

According to the site conditions, due to the use of the original design of the original anchor support in the 203 belt lane, the phenomenon of severe local roof sinking was

brought about, and the mine pressure was more obvious. According to the characteristics of this type of roof of coal and rock interbed, a prestressed anchor cable and anchor rod combined strengthening support scheme is adopted; that is, on the basis of ordinary anchor rod support, the roof is reinforced by installing anchor cables along appropriate sections. The mechanism is as follows: (1) the anchor cable strengthens the roof rock layer farther above into a peripheral load-bearing arch with a strong bearing capacity, that is, the “outer bearing arch”; (2) the “outer bearing arch” can not only maintain its own stability; it also becomes the foundation for the stability of the balanced arch supported by the lower anchor support; (3) through a certain spacing, the anchor cable will make the outer arches along the shape overlap each other and maintain the rock mass within the range of “outer bearing arch”. *Overall Stability.* A schematic diagram of the strengthening mechanism of the roof rock layer under the combined support of the anchor cable and anchor rod is shown in Figure 19.

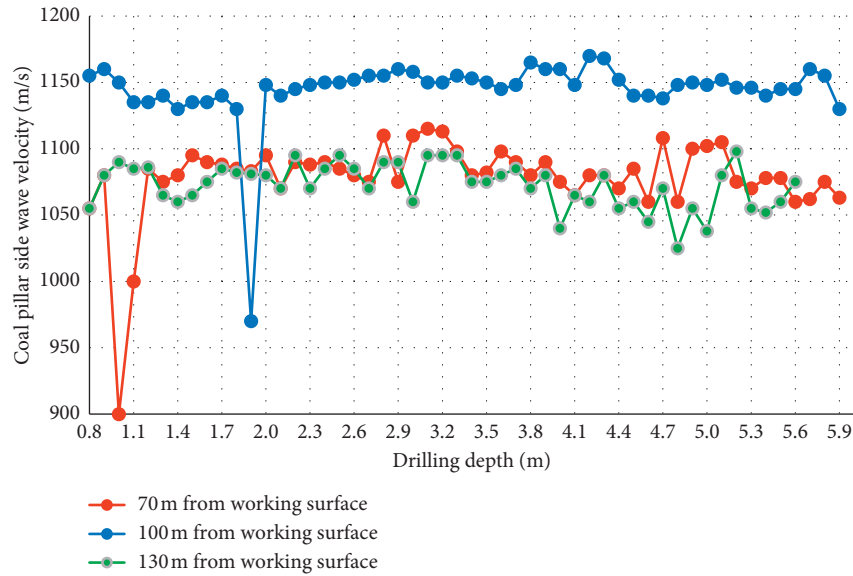
### 6.2. Anchor Cable Reinforced Support Design

**6.2.1. Anchor Cable Length Design.** The design length of the anchor cable should satisfy

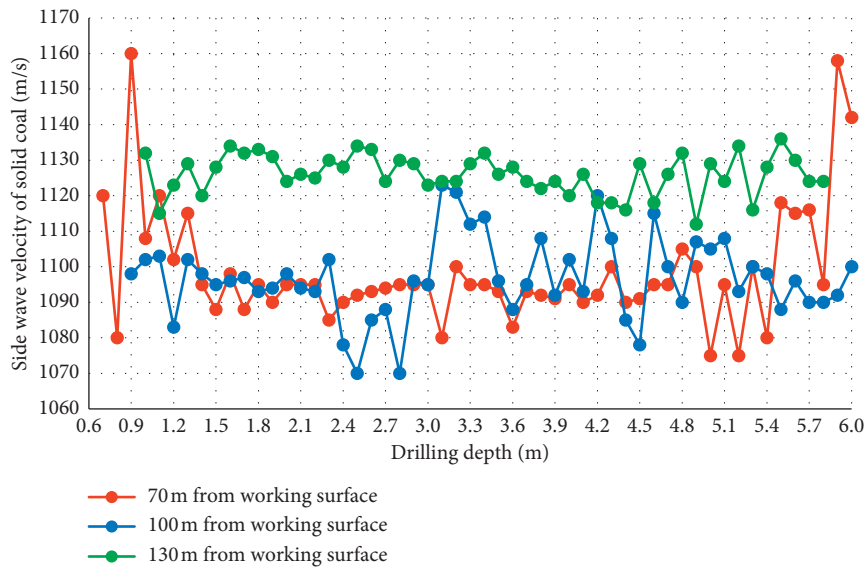
$$L = L_a + L_b + L_c + L_d, \quad (2)$$

where  $L$  is the total length of the anchor cable, m;  $L_a$  is the anchoring length of the anchor cable to the more stable rock formation,  $L_a \geq Kd_1f_a/4f_c$ , where  $K$  is the safety factor; taking 2,  $d_1$  which is the anchor diameter is 17.8 mm;  $f_a$  which is the anchor tensile strength is 1920 N/mm<sup>2</sup>;  $f_c$  is the adhesion strength of anchor cable and anchoring agent, N/mm<sup>2</sup>; taking 1. Substitute the data  $L_a = 2.56$  m,  $L_b$  is the thickness of the unstable rock layer to be suspended, 2.5 m;  $L_c$  is the thickness of the supporting plate and anchorage, taking 0.014 m;  $L_d$  is the exposed tensile length, generally 0.3 m; then, the total length of the anchor cable  $L = 5.1$  m.





(a)



(b)

FIGURE 15: Ultrasonic detection results of the surrounding rock cracks in the roadway at different advanced positions from the 203 working face: (a) coal pillar side and (b) solid coal side.

According to the common specifications of anchor cables, the 6.0 m anchor cable is selected to meet the length requirements.

6.2.2. Number of Anchor Cables. The number of anchor cables should satisfy

$$N \geq \frac{KW}{P}, \tag{3}$$

where  $N$  is the number of anchor cables and  $K$  is a safety factor of 1.2.

Break  $P$  is the minimum breaking force of the anchor cable, taking 355 kN.

$W$  is the dead weight of the suspended rock;  $W = B \times \Sigma h \times \Sigma \gamma \times D$ , where  $B$  is the lane width 4200 mm;  $D$  is the anchor spacing, 2000 mm;  $\Sigma h$  is the hanging rock thickness, 5.7 m;  $\Sigma \gamma$  is the hanging rock The average bulk density is  $12 \text{ kN/m}^3$ . Substitute the data  $W = 575 \text{ kN}$ .

Then, the number of anchor cables is  $N = 1.94$ , and two rows of anchor cables are arranged reasonably. Figure 20 shows the sectional drawing of the reinforced anchor cable support design.

### 7. Strengthening Support Effect Test

On the basis of the foregoing theoretical research results, combined with the roof and roof features of the 203 belt lane

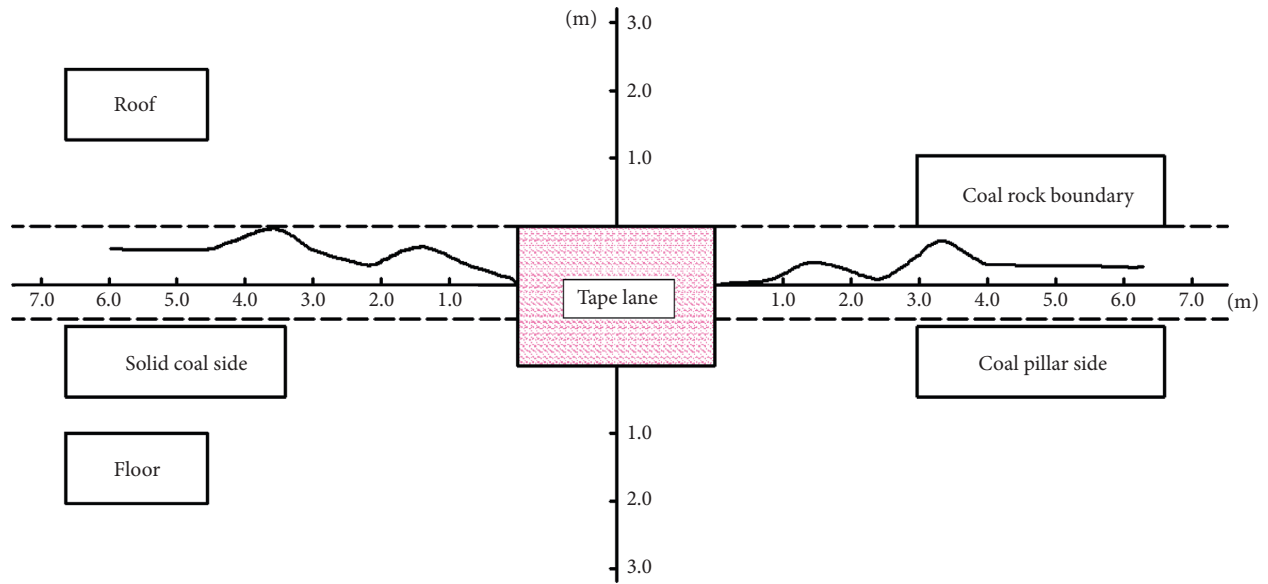


FIGURE 16: Schematic diagram of the surrounding rock failure stress distribution range of coal-rock interbed roadway.

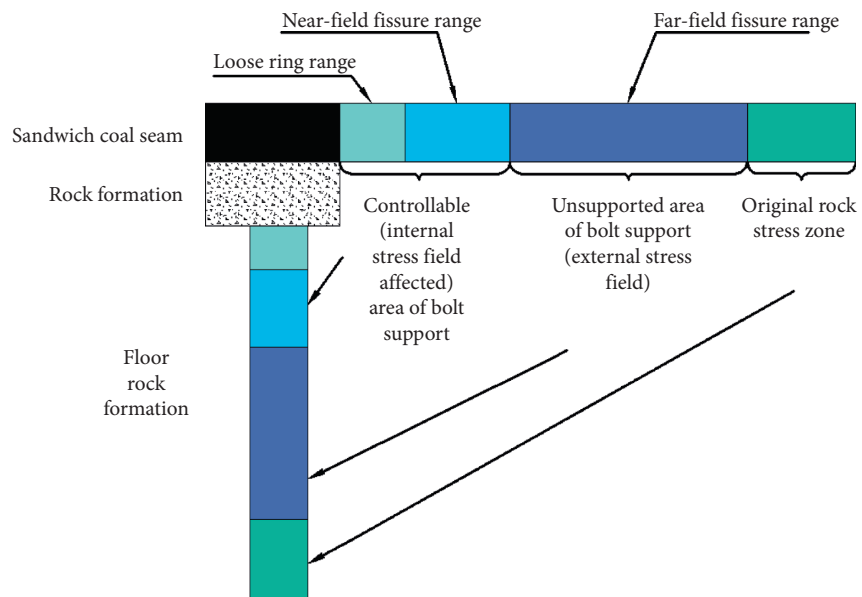


FIGURE 17: Schematic diagram of surrounding rock failure characteristics revealed by ultrasonic detection results.

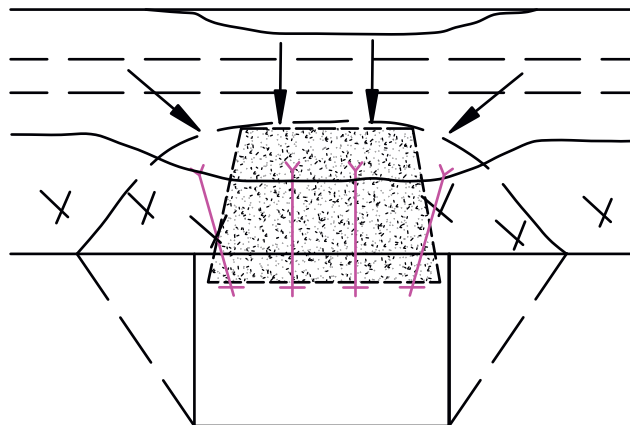


FIGURE 18: Schematic diagram of the instability of roof rock layer under original anchor support.

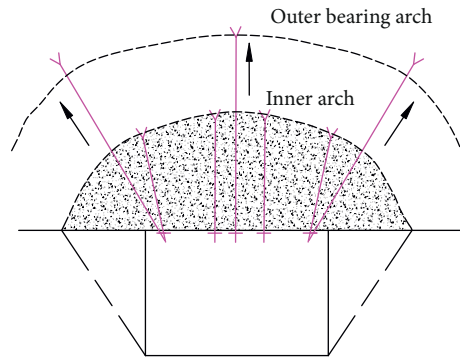


FIGURE 19: Schematic diagram of the strengthening mechanism of the roof rock layer under the combined support of the anchor cable and anchor rod.

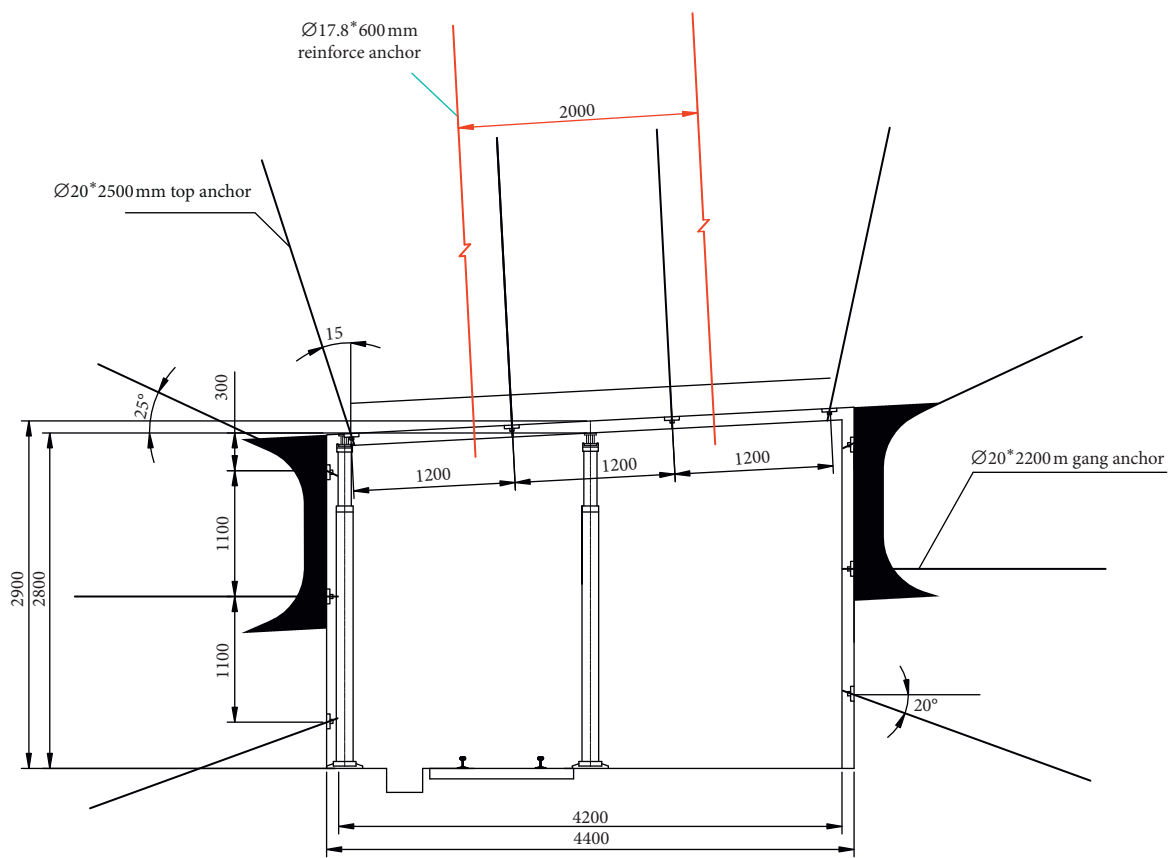


FIGURE 20: Sectional view of anchor cable reinforced support design.

in the field, the reinforced support design was carried out during the construction of the roadway, and the deformation of the roadway was observed. With the construction of the working face, an observation point is arranged at an interval of 50 m, and the deformation of the surrounding rock of the roadway is observed using the cross-point method. The observation period is 6 months, once a day for the first two months, and once a week for the next four months.

Observation results show that the approach distance of the roof and floor of the belt lane is 5.34 mm, which greatly improves the effective support strength of the coal-rock interbed roadway (compared with the approach distance of the roof and

floor of the roadway which is 56.2 mm), which has reached the expected goal, indicating that by strengthening the support the scheme significantly improves the effect of controlling the deformation of surrounding rocks to a certain extent.

### 8. Conclusion

Through the research of this paper, the main conclusions are as follows:

- (1) The excavation of the roadway disrupts the balance of the surrounding rock and forms the stress

concentration of the surrounding rock of the roadway. For the surrounding rock of the roadway with the characteristics of coal-rock interbed, the horizontal stress in the roof rock layer increases with the depth of the two groups of surrounding rocks. Transferring to the deep, there is a destruction of the top rock formation. Based on the analysis of Platts pressure-free arch theory, the maximum loosening range of the roof of the coal-rock interlevel roadway was obtained, which provided strong support for the rational design of the support process

- (2) The failure characteristics of the surrounding rock in the coal and rock interbedding roadway were analyzed by using the numerical simulation technology, and the deformation and failure law, stress distribution characteristics, and failure area distribution characteristics of the surrounding rock in the coal and rock interbedding roadway were theoretically revealed. Although the theory and hypothesis based on the numerical simulation are limited, and the simulation results are approximate numerical solutions, the research results can provide important references for in-depth analysis of the displacement, deformation, and stress distribution law of the roadway and the supporting effect of the roadway
- (3) The ultrasonic detection of the surrounding rock of the roadway shows that the coal seam is affected by the internal and external stress fields and has strong zoning characteristics. The damage range and stress distribution range of the surrounding rock of the coal-rock interbed roadway are reasonably analyzed to evaluate the surrounding rock of the roadway
- (4) Based on the methods of theoretical analysis, numerical simulation, and ultrasonic detection, the comprehensive development height of the roof of the coal-rock interlevel roadway is comprehensively obtained. Based on this, a reasonable anchor cable reinforcement support design is carried out, and the analysis of the anchor cable reinforcement support is analyzed. *Mechanism of Action*. After 6 months of mine pressure observation practice, the surrounding rock of the roadway has reached the expected stability target, and the enhanced support scheme has significantly controlled the deformation of the surrounding rock to a certain extent

### Data Availability

The data used to support the findings of this study are available from the submitting author upon request.

### Conflicts of Interest

The authors declare no conflicts of interest.

### Acknowledgments

The work was supported by the National Natural Science Foundation of China (Grant no. 51774122).

### References

- [1] J. Liu, N. Wu, G. Si, and M. Zhao, "Experimental study on mechanical properties and failure behaviour of the pre-cracked coal-rock combination," *Bulletin of Engineering Geology and the Environment*, vol. 11, pp. 1–15, 2020.
- [2] Y. Zhang, J. Panshi, and Y. Wu, "Study on deformation and failure mechanism and support technology of mining roadway in repeated mining of steeply inclined coal seam," *Coal Engineering*, vol. 2, pp. 91–95, 2020.
- [3] X. Liu, G. Yan, and Y. Zhang, "Research on failure mechanism of tunnel composite structure and control technology of bolt-grouting support," *Mining Safety and Environmental Protection*, vol. 6, pp. 102–106, 2020.
- [4] Y. Chu, G. Ren, C. Zou et al., "Research on instability analysis and control method of roadway in ore contact zone," *Journal of Wuhan University (Engineering Science Edition)*, vol. 11, pp. 975–980, 2019.
- [5] P. Wang, T. Feng, Y. Jiang et al., "Instability mechanism of surrounding rock in weakly reclaimed roof roadway and its control principle and technology," *Chinese Journal of Coal*, vol. 10, pp. 2953–2965, 2019.
- [6] J. Sun, "Failure mechanism and support technology of roadway with weak coal and rock composite roof," *Coal Mine Safety*, vol. 9, pp. 96–100, 2019.
- [7] Y. Peng, S. Zhang, and Y. Zhang, "Deformation and failure mechanism of surrounding rock in coal mine large cross section top coal roadway," *Coal Mine Safety*, vol. 5, pp. 263–268, 2019.
- [8] X. Liu, *Study on Failure Mechanism and Control Technology of Composite Roof in Medium-Thick and Weak Rock Layer Type*, Taiyuan University of Technology, Taiyuan, China, 2019.
- [9] B. Zhou, *Study on Instability Mechanism and Safety Control of Weak Structure on Roof of Roadway*, Anhui University of Science and Technology, Huainan, China, 2017.
- [10] L. He, *Stability Mechanism and Control of Roof Roadway in Weak Coal and Rock Interbed*, China University of Mining and Technology, Xuzhou, China, 2013.
- [11] Y. Zhang, "Numerical study on reasonable width of creep coal pillars in deep well and high geostressed coal-rock interbed thin roof section," *Mining Safety and Environmental Protection*, vol. 1, pp. 28–32, 2019.
- [12] F. Hui and H. Zhang, "Numerical simulation of coal-rock interbed blasting based on ANSYS/LS-DYNA," *Mining Technology*, vol. 5, pp. 128–130, 2017.
- [13] Z. Zhong, Y. Li, T. Wang et al., "Simulation test and control countermeasures of coal-rock interbed roadway," *Journal of Liaoning Technical University (Natural Science Edition)*, vol. 5, pp. 555–560, 2015.
- [14] Z. Zhong, X. Li, Q. Yao et al., "Study on instability factors of roof roadway in coal and rock interbed based on orthogonal test," *Journal of China University of Mining & Technology*, vol. 2, pp. 220–226, 2015.
- [15] W. Wei, L. Li, W. f. Shi, and J. p. Liu, "Ultrasonic imaging recognition of coal-rock interface based on the improved variational mode decomposition," *Measurement Volume*, vol. 170, Article ID 108728, 2020.
- [16] Y. Shou, J. Zhang, and F. Berto, "Experimental and analytical investigation on the coupled elastoplastic damage model of coal-rock," *Fracture and Structural Integrity*, vol. 14, no. 53, pp. 434–445, 2020.
- [17] D.-y. Wu and S. Qin, "Loose and broken distribution of soft coal-rock in deep coal roadway Sidewall," *Geotechnical and Geological Engineering*, vol. 5, pp. 1–10, 2020.

- [18] J. Yang, *Surrounding Rock Control Mechanism and Technology of Roof Tunnel in Thin-Bedded Coal-Rock Interbed*, China University of Mining and Technology, Xuzhou, China, 2013.
- [19] L. Cui, *Study on Underground Pressure Characteristics and Anchoring Scheme of Roof Roadway in Soft Coal Interbed*, Taiyuan University of Technology, Taiyuan, China, 2016.
- [20] X. Qin and Q. Shi, "Analysis of "two soft and one hard" coal gangue interbed composite coal roadway support technology," *Gansu Science and Technology*, vol. 13, pp. 56–59, 2014.
- [21] M. Guo, P. Gong, and P. Li, "Study on the parameters of reinforcement and support of the lower roadway in the goaf of an extremely close distance coal seam," *Coal Engineering*, vol. 1, pp. 54–58, 2020.
- [22] Z. Fu, X. Zeng, D. Ouyang et al., "Research on surrounding rock deformation and reinforcement support of coal mine roadway," *Coal Technology*, vol. 1, pp. 53–56, 2020.
- [23] T. Jing, "Research on strengthening support of roadway under complex geological conditions," *Energy and Energy Conservation*, vol. 12, pp. 84–85, 2019.
- [24] Y. Han and Z. Cai, "Research on surrounding rock reinforcement support technology in high ground pressure and three soft mining roadways," *Journal of Science & Technology and Economy*, vol. 29, pp. 47–49, 2018.
- [25] X. Wang, Y. Wang, and D. Zhang, "Research on strengthening support technology for key parts of roadway with large dip angle "three soft" coal seam," *Journal of Mining and Safety Engineering*, vol. 2, pp. 208–213, 2017.
- [26] B. Liu, "Technology and research on strengthening support of large-section soft rock composite roof," *Coal and Chemical Industry*, vol. 7, pp. 52–55, 2016.
- [27] G. Chen, T. Li, G. Zhang et al., "Experimental study on energy accumulation before coal rock mass failure," *Journal of China Coal Society*, vol. 11, 2020.
- [28] G. Chen, T. Li, L. Yang et al., "Mechanical properties and failure mechanism of different coal-rock ratios and combinations," *Journal of Mining And Strata Control Engineering*, vol. 1, 2021.
- [29] G. Zhang, C. Zang, M. Chen et al., "Ground response of entries driven adjacent to a retreating longwall panel," *International Journal of Rock Mechanics and Mining Sciences*, vol. 138, 2021.
- [30] G. C. Zhang, Z. J. Wen, S. J. Liang et al., "Ground response of a gob-side entry in a longwall panel extracting 17 m-thick coal seam: a case study," *Rock Mechanics and Rock Engineering*, vol. 53, no. 2, pp. 497–516, 2020.



## Research Article

# Distribution Law of Mining Stress of the Gob-Side Entry Retaining in Deep Mining Thin Coal Seam

Tao Qin <sup>1,2</sup>, Kai Ren <sup>1</sup>, Chen Jiang <sup>1</sup>, Yanwei Duan <sup>1</sup>, Zhi Liu <sup>1</sup> and Lei Wang <sup>1</sup>

<sup>1</sup>Heilongjiang Ground Pressure and Gas Control in Deep Mining Key Lab, Heilongjiang University of Science and Technology, Harbin 150022, China

<sup>2</sup>School of Resources and Civil Engineering, Northeastern University, Shenyang 110819, China

Correspondence should be addressed to Kai Ren; 978011787@qq.com

Received 9 January 2021; Revised 2 March 2021; Accepted 10 March 2021; Published 26 March 2021

Academic Editor: Zhijie Zhu

Copyright © 2021 Tao Qin et al. This is an open access article distributed under the Creative Commons Attribution License, which permits unrestricted use, distribution, and reproduction in any medium, provided the original work is properly cited.

In order to explore the mining pressure development rule of gob-side entry retaining during deep thin coal seam mining, FLAC<sup>3D</sup> numerical simulation is applied to analyze the stress distribution rule of gob-side entry retaining, observing the left third working face of 49# coal seam in No. 8 mining area of Xinxing Coal Mine as the research object. The results show that the working face stress field is asymmetrical which is caused by the reserved roadway and the over goaf. After roadway tunneling, features of obvious stress redistribution are formed. The vertical and horizontal stress in the coal seam develop a U-shaped distribution. The vertical stress in the roadway is less than that in the lower roadway, and the horizontal stress is half that in the lower roadway. The phenomenon of high stress “nucleation” appears and becomes more obvious in the process of working face advancing, and the nuclear body disappears after working face advanced to the boundary line. With the working surface advancing, the trend of horizontal stress of gob-side entry retaining decreases gradually and the vertical stress of gob-side entry retaining is less than the original rock stress. The research findings provide a basis for the supporting design of gob-side entry retaining in the deep thin coal seam and the stability control of surrounding rock.

## 1. Introduction

With the continuous process of coal mining, shallow coal resources are almost depleted, and mining is gradually accessing deep mining areas. Under the influence of high stress, the mechanical characteristics of surrounding rocks have changed substantially, and the occurrence of ore pressure induces more serious mine disasters [1]. China's thin coal seams are characterized by a diversified occurrence, large quantity, large distribution area, and large reserves. According to statistics, thin coal seams of the mining areas account for 84.2%, and reserves are about 6 billion tons [2, 3]. The gob-side entry retaining can maximize the recovery of resources and reduce the amount of drivage. The problem of surrounding rock control in thin coal mining the gob-side entry retaining brings severe challenges to coal mine safety mining; especially, the problem of stable gob-side entry retaining in Qitaihe thin coal mining area, which has already entered the process of deep mining, is becoming

increasingly prominent. It is of great significance for coal and rock stability control to explore the stress distribution of gob-side entry retaining in deep thin coal seam mining.

Scholars at home and abroad have done a lot of research on thin coal seam mining and the over goaf roadway retention, and they have achieved a series of successful results. According to the analysis of the plastic zone, stress distribution, supporting pressure, and deformation law of surrounding rock in thin coal seam mining by applying numerical simulation method, the finding obtained the ore pressure law of working face and proposed the supporting scheme [4–6]. Theoretical analysis is adopted to establish the mechanical deformation model of surrounding rock of thin coal seam under different geological conditions and to calculate the law of overburden movement and collapse and stress distribution [5–8]. Analyzing the support resistance, stress distribution, and surrounding rock deformation in the process of advancing the thin working face by on-site ore pressure monitoring method to evaluate whether the

existing support system meets the requirements provides a reference to similar working face support design [2, 9, 10]. Application of gob-side entry retaining technology is employed to study stress distribution and support scheme in heading stope [11–14]. However, due to the essential differences in the mechanical properties of the shallow and deep rock mass, there are a few studies on the stress distribution characteristics and control measures of the gob-side entry retaining in the thin coal seam. Besides, the existing studies have not explored the development law of the ore pressure of gob-side entry retaining in the deep thin coal seam.

Qitaihe mining area is one of the thin layers of oversize mine areas, with 0.86 m average thickness. At present, the average depth of three-level mining in the Xinxing Coal Mine is about 750 m. In the mining process, there are many problems to solve, such as large deformation of surrounding rocks, difficult roadway maintenance, and poor safety. In order to ensure the recovery of resources and production continuity, mining is mainly carried out by keeping the gob-side entry retaining [15]. Based on this, the author combines the actual situation of working face in 49<sup>#</sup> Xinxing Coal Mine, using FLAC<sup>3D</sup> numerical simulation of thin coal seam gob-side entry retaining in the mining process to analyze the working face stress distribution characteristics. The research results have theoretical guiding and reference significance for the surrounding rock control of deep thin coal seam gob-side entry retaining in similar working conditions.

## 2. Project Overview

The working face adopts the method of longwall coal mining. There are three working faces on the third left of 49<sup>#</sup> coal seam in No. 8 mining area of Xinxing Coal Mine. The strike of the coal seam gradually changes from N60W to EW direction. The dip angle of the coal seam is generally between 7° and 11°. The strike length is 565 m, while the cutting length is 135 m, and the inclined area is 7.63 m<sup>2</sup>. The thickness of the coal seam is 0.45~1.20 m and 0.65 m on average thickness. It belongs to the coal seam with a complex structure. The coal seam contains siltstone from one to six layers, and the interlayer thickness is generally 0.1~0.3 m. The left two pieces are located in the upper part of the left three pieces and have been stopped, as shown in Figure 1.

## 3. Numerical Analysis of the Development Law of Mine Pressure along Gob-Side Entry Retaining

**3.1. Simulation Scheme.** Given that the left three working faces use gob-side entry retaining to mine in Xinxing Coal Mine, the stress distribution, with stopped area of the left three working faces is affected by the left two mines the over goaf and the remaining roadway. Therefore, in order to truly reflect the stress conditions of the left three working faces and the roadway, it needs to simulate the tunneling and mining conditions of the working face in the area around the left three. According to the idea of treating the over goaf by

FLAC<sup>3D</sup>, the mechanical parameters of surrounding rocks are weak to simulate the left two goaves [16].

**3.2. Model Establishment.** On the basis of the borehole column chart and test data, the formation is simplified to address the needs of modeling. Therefore, fully considering the left three working faces of the over goaf, the stress distribution of roadway, and stope and its adjacent, the changes of model size for 450 m \* 200 m \* 96 m, selecting the model left three floors at the bottom right corner to zero, the width of the mined-out area is 30 m and the groove is 5 m, in view of the influence of stress, along the groove extend outward around 25 m for the border. The whole 3D model is divided into 11,187 units and 9,000 nodes. The model is shown in Figure 2. In order to analyze the stress distribution in the process of working face propulsion, single propulsion is applicable as the monitoring line, and the specific location is shown in Figure 3.

On account of the measured results of in situ stress in 49<sup>#</sup> coal seam, the maximum horizontal principal stress  $\sigma_{\max} = 31$  MPa and vertical principal stress  $\sigma_v = 15.89$  MPa. With the increase of the buried depth, the constraint force on the Z direction of the model presents an upward trend. Assuming that this point is at the floor of the coal seam roadway and combined with the excavation engineering plan, the average buried depth of the left three sections is  $h = 690$  m.

The horizontal principal stress of the model is

$$\begin{aligned}\sigma_{\max} &= \gamma_h * h = 31 \text{ MPa}, \\ \gamma_h &= 3.1e^4 \text{ N/m}^3.\end{aligned}\quad (1)$$

So,

$$\begin{aligned}\sigma_{h1} &= \sigma_h - \gamma_h * h_0 = 19.79 \text{ MPa}, \\ \sigma_{h2} &= \sigma_h + \gamma_h * h_0 = 25.37 \text{ MPa}.\end{aligned}\quad (2)$$

In light of the distribution of roof strata and rock density, the vertical stress on the roof surface of the model is

$$\sigma_{v1} = \sigma_v - \rho_2 h_2 g - \rho_3 h_3 g - \rho_4 h_4 g - \rho_5 h_5 g - \rho_6 h_6 g = 11.77 \text{ MPa}.\quad (3)$$

The front and rear boundaries of the model are fixed displacement constraints, and the left and right boundary conditions of the model are shown in Figure 4.

**3.3. Calculated Parameters.** Given the determination method of physical and mechanical properties of coal and rock, the coal and rock samples obtained in the field are processed and tested in the laboratory. Uniaxial compression deformation test, variable angle shear test, Brazilian splitting tensile test, and block density test are carried out, respectively. The experimental results are shown in Table 1, measured on the elastic modulus and shear modulus. The Mohr–Coulomb constitutive model is used for coal and rock mass.

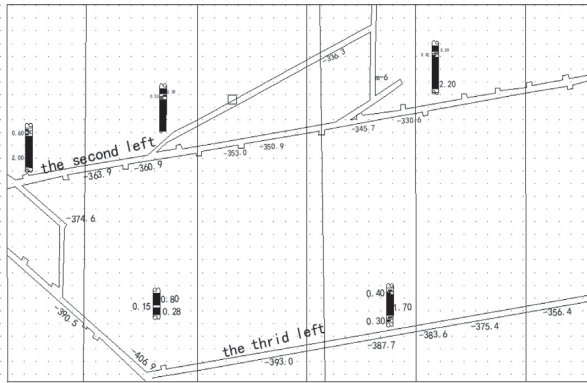


FIGURE 1: Roadway layout of the left third working face in the No. 8 mining area of 49 coal seams in Xinxing Coal Mine.

#### 4. Simulation Results and Analysis

The stress concentration area is divided into vertical stress concentration area and horizontal stress concentration area. When excavation is carried out in the stratum, the surrounding rock stress is redistributed, continuously transferred to the interior, and the middle part of the working face presents the phenomenon of stress concentration. The vertical stress concentration occurs at the two sides of the surrounding rock, while the horizontal stress concentration occurs at the top and bottom of the surrounding rock. This paper aims at analyzing the stress distribution of the left three pieces of the gob-side entry retaining driving face and studying the stress distribution characteristics in the process of the gob-side entry retaining to driving face and driving face.

By analyzing the stress distribution of the roadway driving model on the left three sections of the gob-side entry retaining (see Figures 5 and 6), it can be seen that the vertical stress concentration area of the coal seam is near the roof of the coal seam, and the horizontal stress concentration area of the coal seam is at the two sides of the upper and lower roadway. Therefore, in the following concentrated-area study, the vertical stress concentration adapts the roof along the coal seam trending roadway as the main research object, while the horizontal stress concentration regards the central plane of the coal seam as the main research object.

Numerical simulation is carried out for the tunneling and stopping process of the left three blocks of the gob-side entry retaining; furthermore, it obtains the stress cloud chart and stress distribution curve. Due to roadway tunneling, the surrounding rock stress will be redistributed. In spite of the quite small influence of thin coal seam tunneling on stress redistribution, the stress concentration zone is still formed in the middle of the coal seam. The residual roadway and the over goaf have a certain impact on the stress distribution, resulting in stress asymmetry.

##### 4.1. Analysis of Stress Distribution in the Over Goaf Roadway

**4.1.1. Vertical Stress Concentration Area Distribution.** Figure 7 shows that the vertical stress and the lower roadway stress in the middle of the coal seam are relatively large, and

the maximum stress near the middle of the coal seam is 19.2 MPa. This is because, after the mining of the left two working faces, the remaining roadway in the left three working faces is adjacent to the over goaf, the surrounding rock stress has been released, and the pressure is low and uniform around the remaining roadway. The crossheading tunneling in the coal seam results in the redistribution of surrounding rock stress at the mining area boundary, the mine pressure transfers to the solid coal side, and the internal abutment pressure increases obviously. The farther the distance from the over goaf, the less the stress is affected by the over goaf, and the stress in stope increases gradually. Since the left second stope faces have been stopped and the roof strata collapse is basically stable, there is little influence on the left third stope roadway and the stope face, and the relatively large stress concentration is at the whole stope of the left third faces. The vertical stress, which is extracted from the monitoring line in Figure 8, is consistent with the trend of cloud Figure 7, showing a feature of high in the middle and low on both sides, and the roadway pressure in the retention roadway is less than the vertical stress in the lower roadway.

##### 4.1.2. Horizontal Stress Concentration Area Distribution.

It can be seen from Figure 9 that horizontal stress concentration occurs in the middle of the coal seam, with the maximum value reaching 17.8 MPa. The horizontal stress is small in the whole length of the remaining roadway, and the end surface stress of the lower roadway is relatively large. Due to the effect of the left second goaf, the horizontal stress of the upper roadway has a large influent range. It extends to the interior of the coal seam, greatly increasing the concentration degree of horizontal stress, resulting in a rapid increase of horizontal stress, and the stress is the largest in the middle position. After roadway excavation, the horizontal stress of roof and floor in roadway increases sharply within a certain range, which is not conducive to the stability of surrounding rock. The horizontal stress is very high in the middle of the coal seam, and the concentration coefficient is very high, which easily leads to roof caving and floor uplift, and may induce rock burst disaster. Figure 10 presents the horizontal stress on the monitoring line. The horizontal stress in the coal seam presents an obvious “U” shaped distribution, with good symmetry on both sides, indicating the influence of the left second goaf area adjusted by the trough. The obvious difference between the two sides of the tunnel is mainly due to the impact of the left second goaf, which causes the horizontal pressure of the remaining roadway being half that of the lower side roadway.

##### 4.2. The Stress Concentration Area Distribution during Working Face Propulsion

**4.2.1. Vertical Stress Concentration Area Distribution.** Figure 11 demonstrates that, with the working faces advancing, the maximum vertical stress of the roof of the coal seam firstly increases and then decreases, with the working face advancing to 200–300 m, the maximum value is

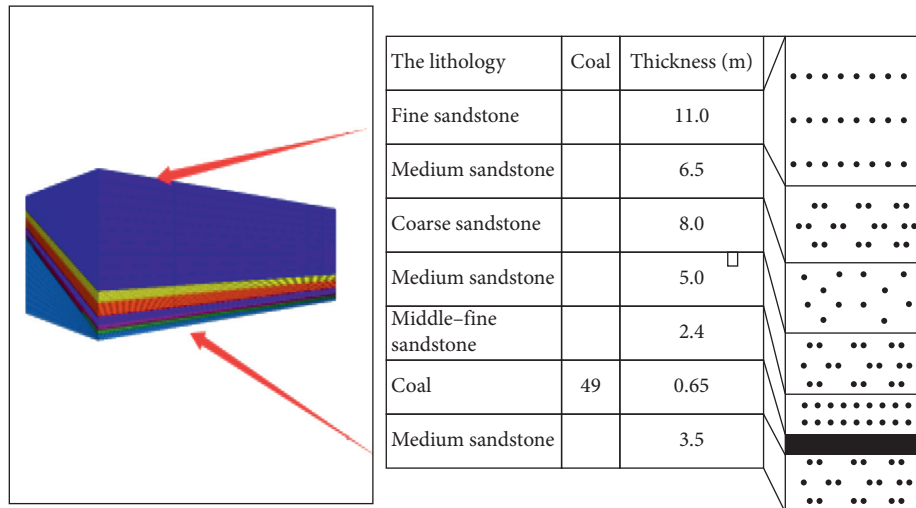


FIGURE 2: FLAC<sup>3D</sup> model of the third left mining face.

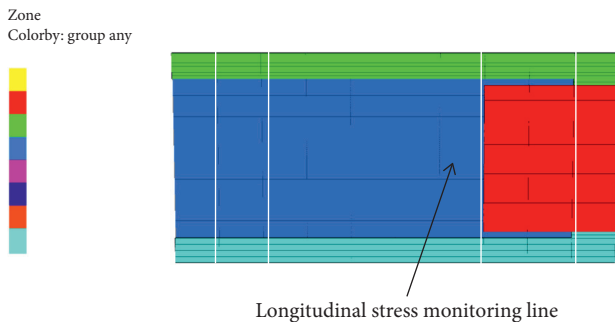


FIGURE 3: Monitoring lines of the third left mining face.

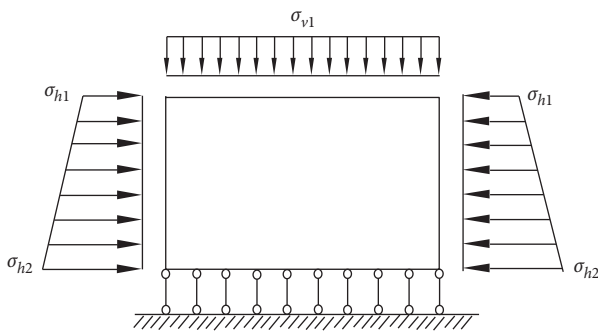


FIGURE 4: Boundary conditions of the model.

20.05 MPa, and the stress concentration coefficient is 1.20. When the working face is advanced to 400 m, the stress field is small and balanced in front of the working face. With the advance of the working face, the phenomenon of “nucleation” with high stress appearing on the working face becomes more growingly obvious, and the nuclear body disappeared after the working face is forward to the boundary line. Stress relief should be focused on the nuclear zone to prevent damage. Under the influence of the left second goaf, the average stress of the retaining roadway is less than the average stress of the lower roadway and less than the stress of the original rock, and the position of the

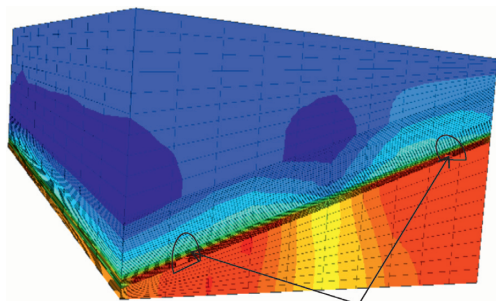
upper and lower roadway is relatively stable, which is conducive to the stability of the roadway and the prevention and control of rock burst. Figure 12 illustrates the vertical stress change curve of the monitoring line in the process of working face propulsion, and the analysis shows that the stress concentration in the middle of the coal seam is obvious during the initial propulsion with the maximum value around 19 MPa. In pace with the continuous release of the propulsive stress, the stress concentration becomes weaker. When the working face is advanced to 400 m, the vertical stress is around 17 MPa, which is close to the original rock stress. The inner part of the working face should pay attention to the initial pressure relief inside the coal body; especially, the stress nucleation area should be monitored.

4.2.2. Horizontal Stress Concentration Area Distribution.

The horizontal stress distribution is promoted to the left three working faces, as shown in Figure 13. It shows that the horizontal stress is mainly concentrated in the middle of the coal seam. As the working face advancing, the stress concentration becomes increasingly greater. The working face advances to 100 m and the maximum horizontal stress reaches 17.3 MPa. The working face advances to 200 m, and the maximum horizontal stress reaches 17.8 MPa. The working face advances to 300m and the maximum stress level reaches 17.9 MPa. The working face advances to 400 m and the horizontal maximum stress reaches 18.8 MPa. The horizontal stress of the upper and lower roadway is smaller than that of the original rock, the pressure of the gob-side entry retaining presents a trend of a gradual decline, and the floor pressure of the roadway is small. The pressure range and value of the upper roadway remain stable, and the pressure range of the upper roadway floor area gradually decreases, but the phenomenon of stress concentration appears obviously. Figure 14 shows the relationship between the monitoring line and the horizontal stress. According to the curve variation law, the horizontal stress in the middle reaches

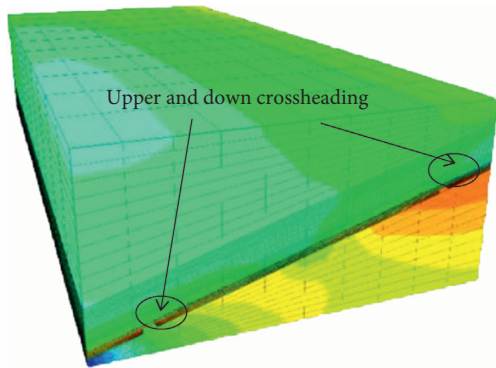
TABLE 1: Basically physical and mechanical parameters.

	The lithology	Volume modulus (GPa)	Shear modulus (GPa)	Cohesive force (MPa)	Tensile strength (MPa)	Within the angle of wipe (°)	Density (kg/m <sup>3</sup> )
1	Pulverous sandstone	6.53	3.92	16	2.6	42	2690
2	Coal seam	1.94	1.46	3	1.2	35	1400
3	Pulverous sandstone	11.0	6.60	15	2.7	38	2697
4	Medium sandstone	2.60	1.56	8	2.9	37	2688
5	Coarse sandstone	3.53	2.12	10	1.7	42	2741
6	Medium sandstone	2.60	1.56	13	2.9	48	2665
7	Fine sandstone	10.49	6.30	15	2.6	55	2690
8	Pulverous sandstone	6.53	3.92	16	2.6	42	2690
9	Goaf	0.5	0.3	0.1	0.1	35	2600



Upper and down crossheading

FIGURE 5: Model vertical stress cloud diagram.



Upper and down crossheading

FIGURE 6: Model horizontal stress cloud diagram.

about 9 MPa and presents a V-shaped distribution on both sides along the middle, and the pressure dropped in the gob-side entry retaining is greater than that of the other side roadway. The outside of the roadway presents the characteristics of two poles. Because the outside of the gob-side entry retaining is a goaf, the horizontal stress is less than 2 MPa. The stress outside the lower roadway increases sharply, reaching about 12 MPa. In summary, the pressure relief in the middle of the coal seam should be absorbed in ensuring the safety and stability in the mining process of the working face, and the floor of the lower roadway should be reinforced to prevent the occurrence of

Contour of ZZ-stress  
Calculated by: volumetric averaging

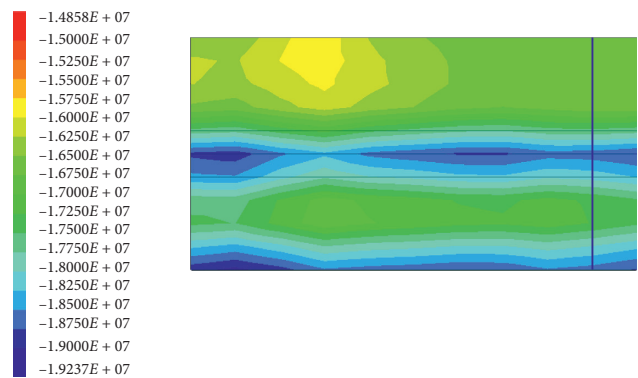


FIGURE 7: The vertical stress cloud diagram of the third left working face.

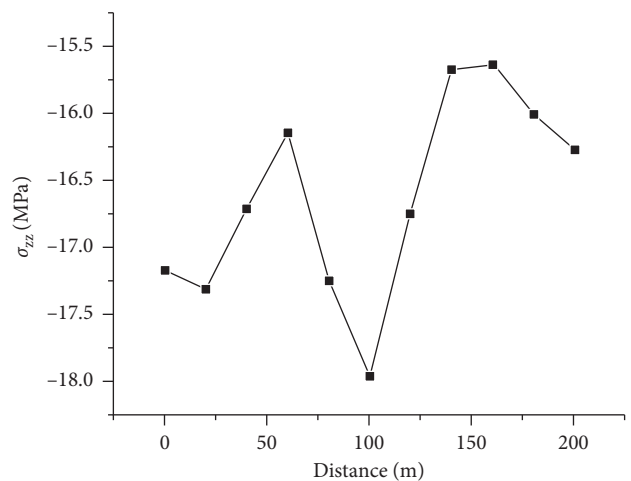


FIGURE 8: The vertical stress of monitoring points in the third left working face.

floor heave. The upper and lower sides of the roadway have low and stable pressure, which means safe and stable in the mining process.



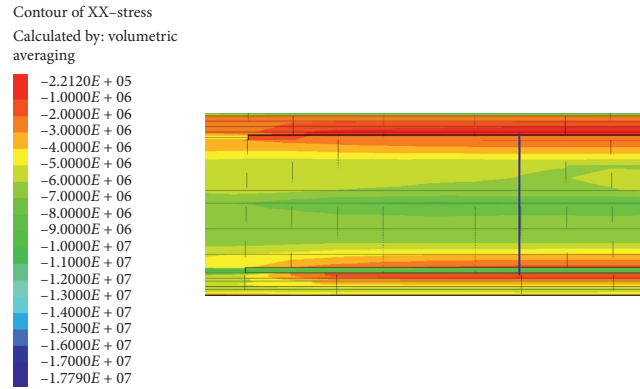


FIGURE 9: The horizontal stress cloud diagram of the third left working face.

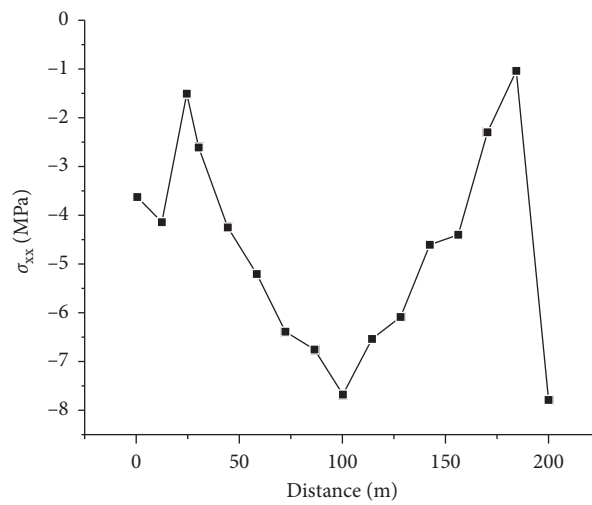


FIGURE 10: The horizontal stress of monitoring points in the third left working face.

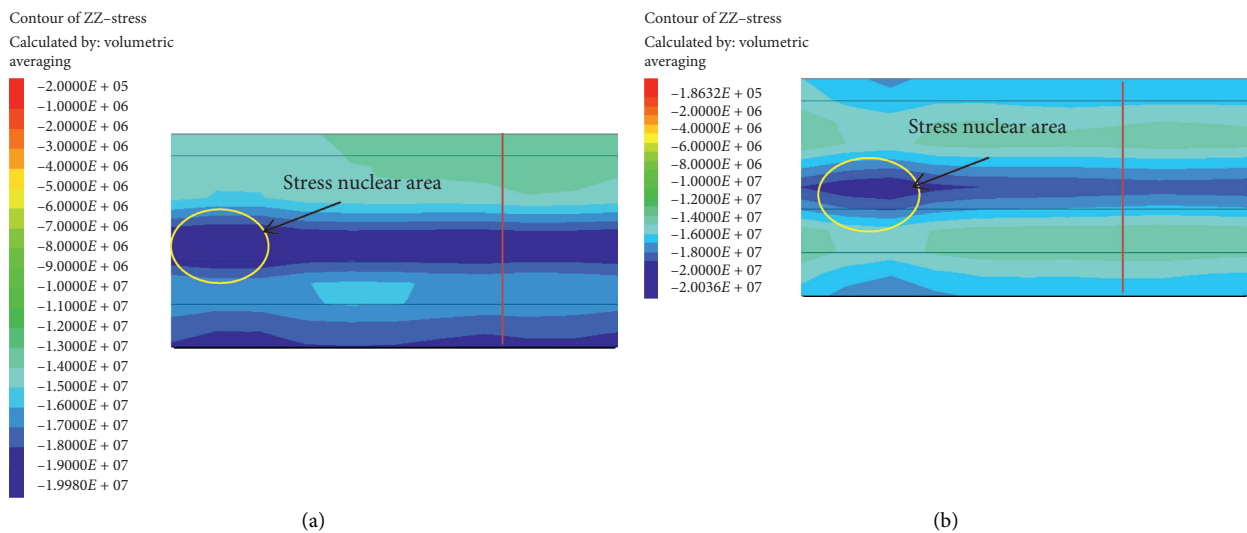


FIGURE 11: Continued.

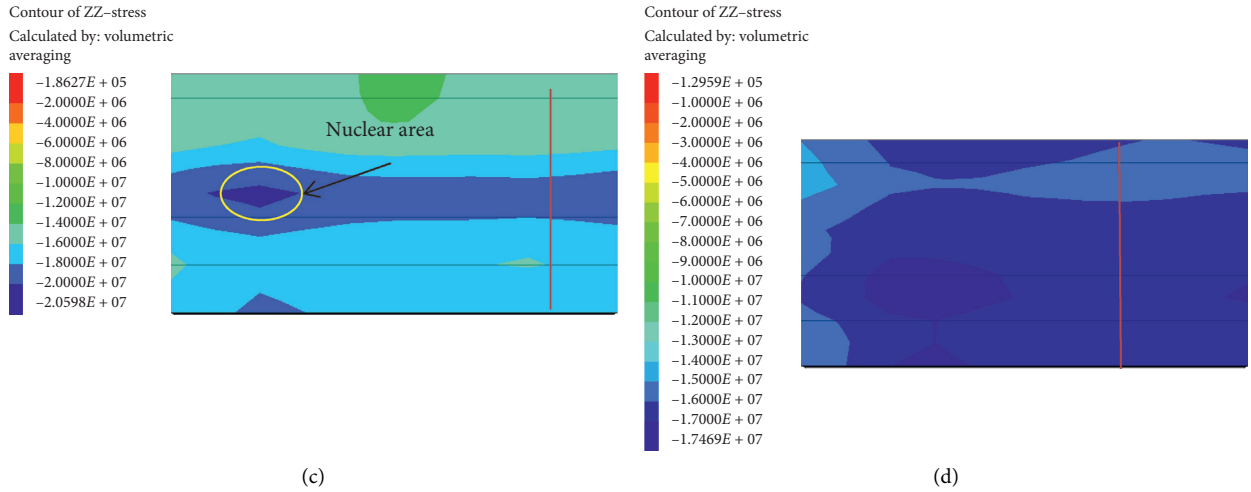


FIGURE 11: Advanced vertical stress cloud diagram of the third left working face. (a) The working face is advanced by 100 m. (b) The working face is advanced by 200 m. (c) The working face is advanced by 300 m. (d) The working face is advanced by 400 m.

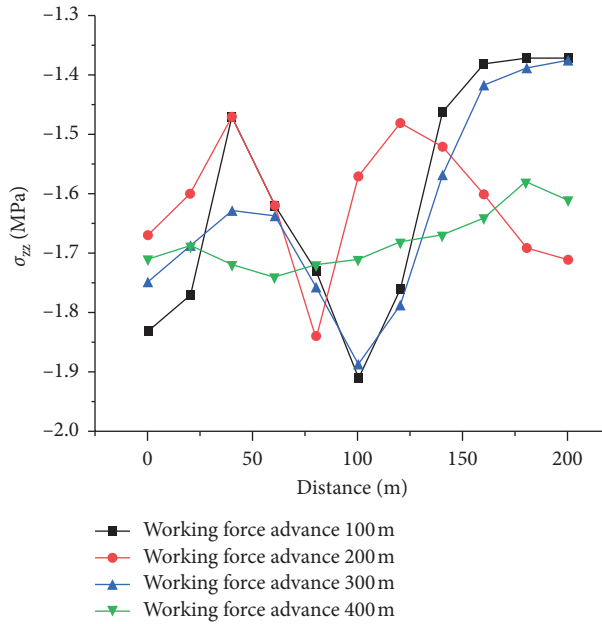


FIGURE 12: The vertical stress of monitoring points in the third left working face.

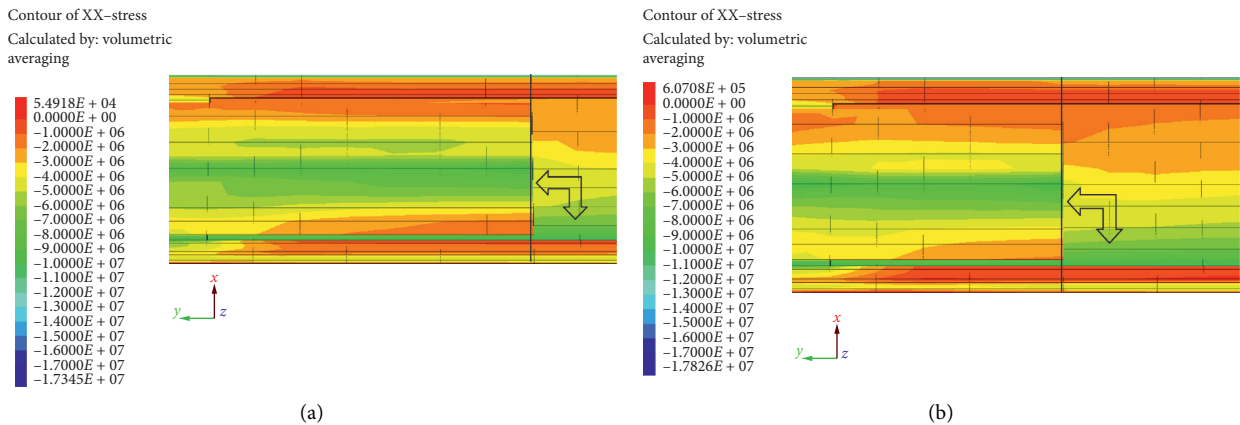


FIGURE 13: Continued.

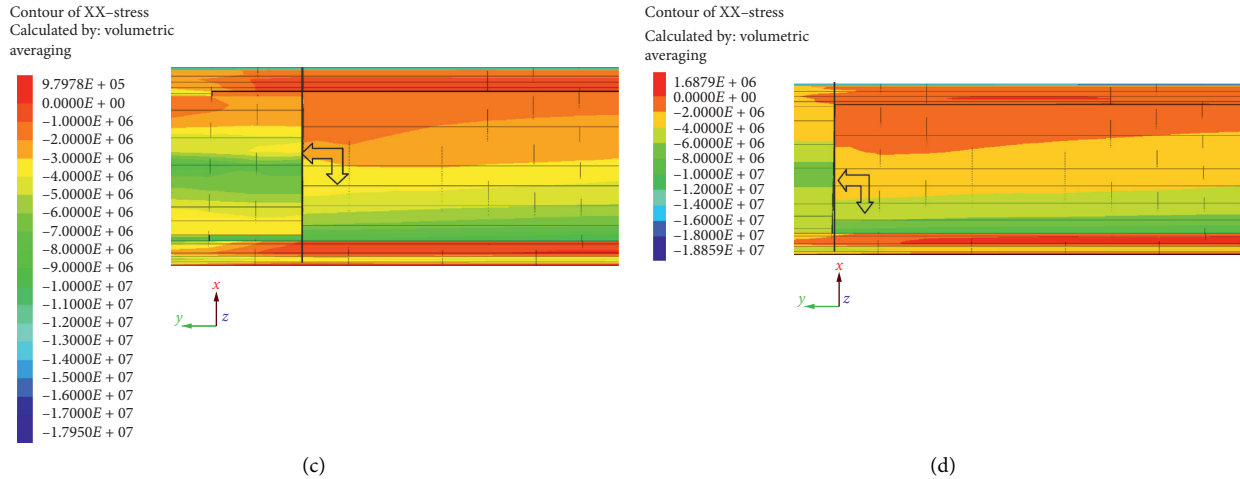


FIGURE 13: Advanced horizontal stress cloud diagram of the third left working face. (a) The working face is advanced by 100 m. (b) The working face is advanced by 200 m. (c) The working face is advanced by 300 m. (d) The working face is advanced by 400 m.

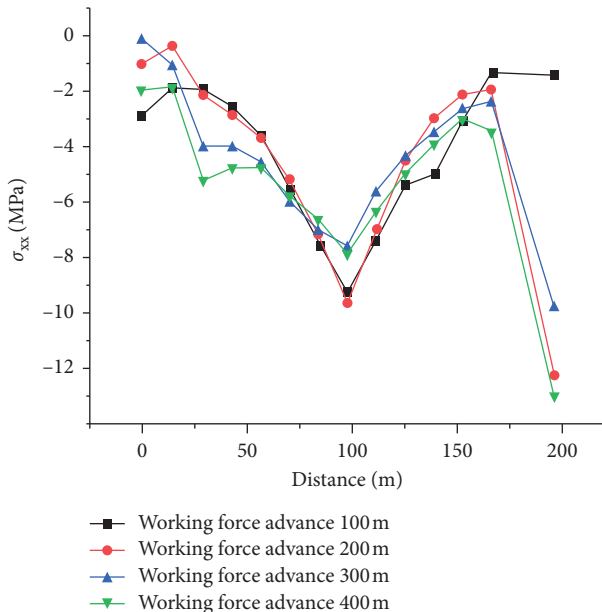


FIGURE 14: The horizontal stress of monitoring points in the third left working face.

## 5. Conclusion

By simulating the working face gob-side entry retaining of the left third working face of 49<sup>#</sup> coal seam in No. 8 mining area of Xinxing Coal Mine, the stress of remaining roadway is less than the vertical stress of lower roadway. The horizontal stress in the coal seam embodies an obvious “U” shaped distribution, with good symmetry on both sides. The horizontal stress in the remaining roadway is half that in the lower roadway. The phenomenon of high stress “nucleation” appears and becomes more progressively obvious in the process of working face advancing, and the nuclear body disappears after working face advancing to the boundary line. The average vertical stress of the remaining roadway is less than the original rock stress, and the horizontal stress of

the gob-side entry retaining presents a trend of gradual decrease. Corresponding pressure relief measures and actions should be taken to prevent the occurrence of disasters in the stress concentration area of deep thin coal seam during gob-side entry retaining driving and mining.

## Data Availability

The data used to support the findings of this study are available from the corresponding author upon request (e-mail: 19140270@qq.com).

## Conflicts of Interest

The authors declare that they have no conflicts of interest.

## Acknowledgments

The research presented in this paper was supported jointly by the Central Government supports the Reform and Development Fund for Local Universities, the National Natural Science Foundation of China (51774122), and the National Key Research and Development Program (Grant no. 2016YFC0600901).

## References

- [1] M. He, H. Xie, S. Peng et al., “Research on rock mechanics in deep mining,” *Journal of Rock Mechanics and Engineering*, vol. 24, no. 16, pp. 2803–2813, 2005.
- [2] W. Guo, “Analysis on the rule of coal pressure in fully mechanized coal face of two hard and thin coal seams,” *Coal Science and Technology*, vol. 44, no. 10, pp. 107–111, 2016.
- [3] Z. Guo, *Study on Highly Efficient Fully Mechanized Mining Technology of Extremely Thin Coal Seam in Huangsha Mine*, China University of Mining and Technology, Beijing, China, 2013.
- [4] S. Gu, Z. Sun, and S. Chen, “Numerical simulation analysis and support selection of steep thin coal seam roadway,” *Mine Pressure and Roof Management*, vol. 79, no. 1, pp. 76–77, 2005.

- [5] Q. Sun, F. Ju, J. Zhang et al., "Analysis on the development law of mine pressure of double soft thin coal seam working face at roof and floor," *Coal Science and Technology*, vol. 42, no. 11, pp. 29–32, 2014.
- [6] R. Zhu, K. Yang, and Z. Li, "Study on the occurrence law of ore pressure in fully mechanized coal face of deep well thin coal seam," *Coal Technology*, vol. 33, no. 5, pp. 159–162, 2014.
- [7] T. Qin and J. Feng, "Law of overburden movement of mining face of inclined thin coal seam," *Journal of Heilongjiang University of Science and Technology*, vol. 25, no. 2, pp. 119–123, 2015.
- [8] Q. Li, *Study on the Rule of Overburden Rock Movement in Shigetai Coal Mine with Thinner Shallow-Buried Coal Seam*, Shandong University of Science and Technology, Qingdao, China, 2009.
- [9] K. Shen, "Law of coal pressure development in stoping roadway of fully mechanized face of thin coal seam," *Coal Mine Safety*, vol. 49, no. 7, pp. 198–200+204, 2008.
- [10] W. Guo, Y. Cheng, Y. Gao, Z. Chen, Z. Zhang, and C. Wang, "Structural characteristics of Datong coalfield and coal bearing boundary of Taiyuan Formation," *Coal Geology and Exploration*, vol. 43, no. 5, pp. 1–7, 2015.
- [11] W. Wang, M. Gao, M. Wang et al., "Exploration on the deformation characteristics and stress distribution of deep buried roadway along the over goaf," *Journal of Rock Mechanics and Engineering*, vol. 38, no. S1, pp. 2955–2963, 2019.
- [12] G. Hou, T. Hu, Z. Li et al., "Effect of cutting top height on the stability of the over goaf retaining roadway along side support," *Journal of Mining and Safety Engineering*, vol. 36, no. 5, pp. 924–931, 2019.
- [13] Y. Ren, *Study on Stress Distribution and Deformation Characteristics of Backfill beside the over Goaf Retaining Roadway and Optimization of Roof Precrack Angle*, Taiyuan University of Technology, Taiyuan, China, 2019.
- [14] P. Wang, *Research on the Over Goaf Retention Technology of no. 6 Coal Seam Near the Xiangsheng Coal Mine*, Taiyuan University of Technology, Taiyuan, China, 2019.
- [15] W. Peng, "Research on the Over Goaf Retention Technology of No. 6 Coal Seam Near The Xiangsheng Coal Mine," Taiyuan University of Technology, Taiyuan, China, 2019.
- [16] Z. Liu, Q. Gao, X. Hua et al., "Aging characteristics of surrounding rock control for the over goaf roadway excavation," *Journal of Mining and Safety Engineering*, vol. 26, no. 4, pp. 465–469, 2009.

## Research Article

# An Innovative Elastoplastic Analysis for Soft Surrounding Rock considering Supporting Opportunity Based on Drucker-Prager Strength Criterion

Rui Wang <sup>1,2</sup>, Xu-dong Liu <sup>1,2,3</sup>, Jian-biao Bai <sup>1,4</sup>, Shuai Yan <sup>1,2</sup> and Jun Xu<sup>5</sup>

<sup>1</sup>State Key Laboratory of Coal Resources and Safe Mining, China University of Mining and Technology, Xuzhou 221116, Jiangsu, China

<sup>2</sup>Key Laboratory of Deep Coal Resource Mining, Ministry of Education of China, School of Mines, China University of Mining and Technology, Xuzhou 221116, Jiangsu, China

<sup>3</sup>Taiyuan Coal Gas Group Transportation and Marketing Branch, Taiyuan 030021, Shanxi, China

<sup>4</sup>Institute of Mining Engineering and Geology, Xinjiang Institute of Engineering, Urumqi 830091, China

<sup>5</sup>School of Science, Yangzhou Polytechnic Institute, Yangzhou 225127, China

Correspondence should be addressed to Xu-dong Liu; [lxdl118@126.com](mailto:lxdl118@126.com) and Jian-biao Bai; [baijianbiao@cumt.edu.cn](mailto:baijianbiao@cumt.edu.cn)

Received 7 February 2021; Revised 2 March 2021; Accepted 6 March 2021; Published 25 March 2021

Academic Editor: Zhijie Zhu

Copyright © 2021 Rui Wang et al. This is an open access article distributed under the Creative Commons Attribution License, which permits unrestricted use, distribution, and reproduction in any medium, provided the original work is properly cited.

In order to study the mechanism of excavation and supporting process of equivalent circular roadway, the model of soft roadway was established firstly. The elastoplastic solutions in excavation process were deduced based on Drucker-Prager strength criterion. Then, the elastoplastic solution under supporting condition was obtained based on homogenization method under the condition of rockbolts and liner supporting. Lastly, an example was analyzed to study the effect of different factors such as “space effect,” supporting opportunity, stresses, surrounding displacement, and the radius of plastic zone. Based on theoretical research case, the change rules of considering the “space effect” and the supporting opportunity when calculating the subarea of the roadway were discussed, the control of interval distance of rockbolts on the displacement of surrounding rock mainly reflecting in the plastic residual zone and the “space effect” in excavation, and the supporting time to control the displacement of surrounding rock not being ignored are revealed. The results can provide an important theoretical basis for the stability evaluation and quantitative support design of roadway surrounding rock. Therefore, the “space effect” and the supporting time to control the displacement and stresses of surrounding rock can not being ignored in underground engineering.

## 1. Introduction

Coal has long been the main energy source in China [1, 2]. In view of the exhaustion of shallow resources in recent years, the resource exploitation and space development gradually have been transferred to the deep earth [3, 4]. The complex mechanical environment of “three heights and one disturbance” in deep coal and rock body leads to many problems and challenges in deep mining [5, 6]. They lead to the strength degradation of rock mass, which affects the stability of underground engineering [7]. The development and establishment of new theories and methods are the theoretical

basis of surrounding rock control in deep underground engineering, which is of great significance to guide the surrounding rock control technology and engineering practice of kilometer deep roadway.

The stress and plastic zone distribution state of surrounding rock of deep roadway is an important basis for evaluating the stability of surrounding rock and the reliability of quantitative support design. In the past, many researchers [8–13] have done research on circular tunnel problems in an elastoplastic, elasto-brittle-plastic, and strain-softening way. Generally, the Mohr–Coulomb criteria, Hoek–Brown criteria, and generalized Hoek–Brown



criteria are employed as associated and nonassociated potential flow laws. On this basis, the surrounding rock stress and deformation distribution is analyzed by ideal elasto-plastic and elasto-brittle-plastic mechanical models. However, engineering practices show that, applying to the different strength criteria, the stress state and plastic zone of the surrounding rock are different. Therefore, choosing the appropriate strength criterion can make the mechanical state of surrounding rock closer to engineering practice. What is more, the elastic-plastic solution of surrounding rock under supporting condition could be obtained, and the deformation of surrounding rock may be too large in the process of soft rock roadway excavation, which affects the safety of chamber construction seriously.

At present, the supporting theory of surrounding rock after excavation has become mature, and many scholars have done a lot of research in this respect [14–20]. Although the elastic-plastic solution of surrounding rock under supporting condition is obtained, the deformation of surrounding rock may be too large in the process of soft rock chamber excavation, which affects the safety of roadway construction seriously. So, the supporting time should be considered, and it should be considered earlier than before. In summary, it is urgent to develop the theoretical study of supporting time in the process of roadway excavation. Due to the traditional elastic-plastic analysis of the roadway based on two-dimensional plane strain, considering the “space effect” can analyze the stress, displacement, and other analytical changes caused by three-dimensional excavation of the roadway. Both theory and practice have shown that, after roadway excavation, most of the rock mass is still in the state of three directions. In addition to the maximum and minimum principal stress, the magnitude of intermediate principal stress also has an important effect on the deformation and failure of roadway surrounding rock.

Based on the Drucker–Prager (D-P) strength criterion and noncorrelation flow rule, this paper analyzes the fact that brittle fracture zone exists obviously in deep roadway. The closed analytical solutions of stress field, displacement field, and plastic zone radius of roadway are derived. The influence of different parameters on the stress, deformation, and plastic zone radius of surrounding rock is studied. The results can provide important theoretical basis for the stability evaluation and support design of surrounding rock.

## 2. Theoretical Model

In the process of excavation, the excavation surface of roadway is within a certain range, and the development of elastoplastic deformation and stress redistribution of surrounding rock are restricted by its own constraints, which leads to the fact that the deformation of surrounding rock cannot be fully released. Stress redistribution cannot be completed quickly, called excavation “space effect.” Considering the “space effect” of excavation, the timely support of roadway has theoretical basis. With the advance of excavation facing forward, the virtual support force is

gradually released with the secondary deformation of surrounding rock, while the pretightening force of the actual support of roadway increases gradually, and the stability of surrounding rock is maintained.

According to the failure characteristics of the surrounding rock of the roadway, the zoning of the surrounding rock of the circular roadway is shown in Figure 1 and the following assumptions are made:

- (1) The roadway is considered to be infinite long, and the rock mass is isotropic approximately and homogeneous continuous medium;
- (2) The section of roadway is circular, and the radius of the roadway is  $R_0$ , and the radii of residual plastic zone, softening plastic zone, and elastic zone are  $R_r$ ,  $R_s$  and  $R_e$ ;
- (3) Before excavation, the surrounding rock of roadway is in the hydrostatic pressure field; that is, the original rock stress is  $\sigma_0$ , MPa. And supporting lining structure provides supporting resistance  $p_i$ ,  $\sigma_r$ ,  $\sigma_\theta$  are defined by the radial stress and the circumferential stress of the roadway, respectively, and  $\sigma_\theta > \sigma_r$  are satisfied.  $\varepsilon_\theta$ ,  $\varepsilon_r$  are defined by the radial and circumferential strain of the surrounding rock, respectively. In the following upper corner marks, “e”, “s” and “r” denote the amount of elastic zone, plastic softening zone, and plastic residual zone, respectively.

## 3. Drucker–Prager Strength Criterion

At present, the *Drucker–Prager* strength criterion has been applied to lots of finite element numerical modeling software; meanwhile, *Drucker–Prager* criterion is a linear expression of the generalized *Mises* criterion. The effects of the intermediate principal stress and the hydrostatic pressure on the yield characteristics of rock materials are considered. Hence, the *Drucker–Prager* criterion is adopted in this paper, and its form is given in the following equation [21]:

$$f(I_1, \sqrt{J_2}) = \sqrt{J_2} - \beta I_1 - k_f = 0, \quad (1)$$

where  $I_1$  is the first stress invariant, and  $J_2$  is the second stress deviation invariant.

Regarding the values of  $\beta$  and  $k_f$ , it is usually to associate the D-P criterion with the M-C criterion, that is, to think that the D-P criterion is a smooth approximate treatment method for the M-C criterion to remove angular points (also singular points) on the  $\pi$  plane, because the D-P criterion is a circle on the  $\pi$  plane. The characteristics of tensile resistance, different compressive strength, and the effect of the intermediate principal stress on the material need to be considered since the coal and rock mass are a strength differential (SD) material [22–27] with different compressive properties, and the elastic core zone is in a triaxial stress state.

If  $\sigma_1$ ,  $\sigma_2$  and  $\sigma_3$  are assumed to be maximum principal stress, intermediate principal stress, and minimum principal stress, and then the specific expressions of  $I_1$  and  $J_2$  are, respectively,

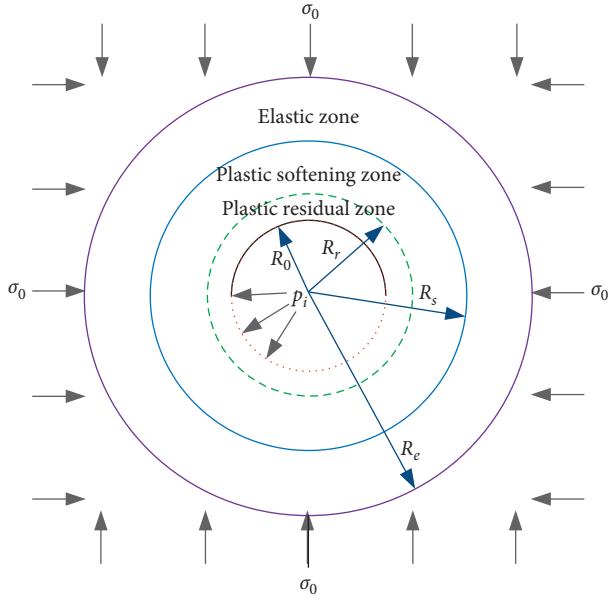


FIGURE 1: Elastoplastic deformation zones of surrounding rock around circular roadway.

$$I_1 = \sigma_1 + \sigma_2 + \sigma_3, \quad (2a)$$

$$J_2 = \frac{(\sigma_1 - \sigma_2)^2 + (\sigma_1 - \sigma_3)^2 + (\sigma_2 - \sigma_3)^2}{6}. \quad (2b)$$

To simplify the selection of the parameters in the *Drucker-Prager* criterion, the converted relationship between  $\beta$ ,  $k_f$ , the internal frictional angle ( $\varphi$ ), and the cohesion ( $c$ ) in the *Mohr-Coulomb* criterion with the plane strain assumption is provided in equation (3).

$$k_f = \frac{\sqrt{3}c \cos \varphi}{\sqrt{3 + \sin^2 \varphi}}, \quad (3a)$$

$$\beta = \frac{\sin \varphi}{\sqrt{9 + 3 \sin^2 \varphi}}. \quad (3b)$$

In practical engineering, the intermediate principal stress coefficient  $m$  is often introduced to indicate the relationship between the three principal stresses:

$$m = \frac{(\sigma_2 - \sigma_3)}{(\sigma_1 - \sigma_3)}, \quad (4)$$

where  $0 \leq m \leq 1$ , and the greater the  $m$ , the greater the effect of the intermediate principal stress, and the smaller the effect.

Equation (4) is simplified, then substituting in equations (2a) and (2b),

$$I_1 = (1 + m)\sigma_1 + (2 - m)\sigma_3, \quad (5a)$$

$$\sqrt{J_2} = \sqrt{\frac{m^2 - m + 1}{3}}(\sigma_1 - \sigma_3) = \lambda_m(\sigma_1 - \sigma_3), \quad (5b)$$

where  $\lambda_m = \sqrt{(m^2 - m + 1)/3}$ .

By substituting equations (5a), (5b) into equation (1), the expression of D-P criterion including to the parameters  $m$ ,  $\lambda_m$ ,  $\beta$ ,  $k_f$  is derived:

$$f = (\lambda_m - m\beta - \beta)\sigma_1 - (\lambda_m - m\beta + 2\beta)\sigma_3 - k_f = 0. \quad (6)$$

**3.1. Initial Bearing Capacity.** Elastic-plastic problem of surrounding rock of roadway can be regarded as plane strain problem. When the support resistance and original rock stress meet the  $p_i < \sigma_0$ , it is generally considered that the stress state of surrounding rock satisfies the following relationship:

$$\begin{cases} \sigma_1 = \sigma_\theta, \\ \sigma_3 = \sigma_r. \end{cases} \quad (7)$$

According to the finite element simulation results, it is pointed out that, due to the influence of "space effect" on the working surface of roadway, the released load acting on the roadway excavation section will not immediately reach the initial in situ stress state but has a time course. The release load varies with time,

$$p_0(t) = p_0 \left( 1 - 0.7e^{-(3.15V/2R_0)t} \right), \quad (8)$$

where  $R_0$  is the radius of circular roadway,  $m$ ;  $V$  is the average speed of roadway excavation, m/d;  $t$  is the starting time of the moment of excavation from section. The default value in this paper  $t = 1$  d, so different roadway velocities represent different distances between section and excavation surface.

The expression of "virtual support resistance" of "space effect" roadway is

$$p_i^* = p_0 - p_0(t) = 0.7p_0e^{-(3.15V/2R_0)t}. \quad (9)$$

At this point, the bearing capacity  $p_c$  of the initial support can be expressed as

$$p_c = p_i^* + p_i. \quad (10)$$

**3.2. Plastic Flow Equation (Definition of Dilatancy Coefficient).** Considering the dilatation of rock mass in plastic softening zone and plastic residual zone, the relationship between dilatancy coefficient and strain is shown in Figure 2.

The dilatation of rock mass in plastic softening zone and plastic residual zone is considered.

$$\Delta \varepsilon_r^s + \eta_1 \Delta \varepsilon_\theta^s = 0. \quad (11)$$

where  $\eta_1$  is the dilatancy coefficient of plastic softening zone, and its value is greater than 1.

The plastic deformation of rock is nonlinear and generally satisfies the noncorrelated flow rule, which can be determined by the plastic potential function ( $\varphi$ ). The yield function ( $f$ ) and  $\varphi$  have the same expression form. The internal friction angle ( $\varphi$ ) in  $f$  can be transformed into the

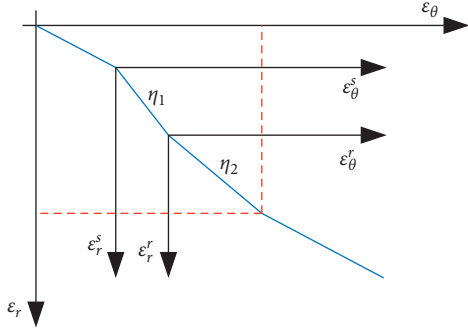


FIGURE 2: The strain model of soft rock [28].

shear dilatancy angle  $\psi$ . The expression of plastic potential function is

$$\phi = (\sigma_\theta, \sigma_r) = \sigma_\theta - A_{i,\psi} \sigma_r, \quad (12)$$

where  $A_{i,\psi}$  is the rock material parameter.

According to the plastic potential theory,

$$d\epsilon_{ij}^p = d\lambda (\partial\phi / \partial\sigma_{ij}), \quad (13)$$

where  $d\epsilon_{ij}^p, \sigma_{ij}$  are the plastic strain increment and stress tensor, respectively;  $d\lambda$  is a constant related to the plastic potential function.

According to the nonassociated flow rule of dilatation of rock mass in the plastic residual zone, we have

$$\Delta\epsilon_r^r + \eta_2 \Delta\epsilon_\theta^r = 0, \quad (14)$$

where  $\Delta\epsilon_r^r, \Delta\epsilon_\theta^r$  are the radial and circumferential strain increments in the plastic residual zone, respectively;  $\eta_2$  is the dilatancy coefficient in the plastic residual zone, and its range is 1.3–1.5 generally.

## 4. Elastoplastic Analysis of Surrounding Rock before Supporting Roadways

**4.1. Basic Equation.** According to the elastoplastic theory, the surrounding rock satisfies the equilibrium equation:

$$\frac{d\sigma_r}{dr} + \frac{(\sigma_r - \sigma_\theta)}{r} = 0. \quad (15)$$

Geometric equation:

$$\begin{cases} \epsilon_r = \frac{du}{dr}, \\ \epsilon_\theta = \frac{u}{r}, \end{cases} \quad (16)$$

where  $u$  is the radial displacement of the surrounding rock.

Constitutive equations satisfying the plane strain are shown:

$$\begin{cases} \epsilon_r = \frac{1-\mu^2}{E} \left( \sigma_r - \frac{1-\mu}{\mu} \sigma_\theta \right), \\ \epsilon_\theta = \frac{1-\mu^2}{E} \left( \sigma_\theta - \frac{1-\mu}{\mu} \sigma_r \right). \end{cases} \quad (17)$$

**4.2. Stresses and Displacement in Elastic Zone.** When considering the “space effect,” the stresses of elastic zone are

$$\begin{cases} \sigma_\theta^e = p_0 \left( 1 + r_0^2/r^2 \right) - \frac{p_c(t)r_0^2}{r^2}, \\ \sigma_r^e = p_0 \left( 1 - r_0^2/r^2 \right) + \frac{p_c(t)r_0^2}{r^2}. \end{cases} \quad (18)$$

Radial displacement is

$$u^e = \frac{(1+\mu)r}{E} \left[ p_0(1-2\mu) + p(t) \left( \frac{r_0}{r} \right)^2 \right], \quad (19)$$

where  $\mu$  is Poisson’s ratio of rock mass.

**4.3. Stress and Displacement in Plastic Softening Zone.** The total strains in plastic softening zone consist of elastic strain and plastic strain. The strains in plastic softening zone are

$$\begin{cases} \epsilon_r = (\epsilon_r^s)_{r=R_s} + \Delta\epsilon_r^s, \\ \epsilon_\theta = (\epsilon_\theta^s)_{r=R_s} + \Delta\epsilon_\theta^s. \end{cases} \quad (20)$$

The compatible equation of displacement in plastic softening zone can be obtained from eqs. (20), (16), and (14), and the displacement at the boundary condition  $r = R_s$  can be obtained continuously.

$$\begin{aligned} u^s &= \frac{R_s}{(1+\eta_1)(1+\eta_2)} [(\eta_2-1)I + (\eta_2+\eta_1)G] \left( \frac{R_s}{r} \right)^{\eta_2} \\ &+ \frac{r}{(1+\eta_1)(1+\eta_2)} [2I + (1-\eta_1)G], \end{aligned} \quad (21)$$

where  $G = (2(1+u)(p_0-p_c)/E)(r_0/R_e)^2(R_s/r)^{1+\eta_1}$ ,  $I = (1+u/E)[p_0(1-2u)(1+\eta_1) + p(t)(r_0/R_e)^2(\eta_1-1)]$ .

The radial stresses are derived by connecting eq. (15) when  $r = R_s$ ,

$$\begin{aligned} \sigma_r^s &= Q \left( \frac{r}{R_e} \right)^{k-1} - \frac{\sigma_c^m - \sigma_c^*}{1 - (R_e/R_s)^{1+\eta_2}} \left[ \frac{1}{1-k} + \frac{1}{\eta_2+k} \left( \frac{R_s}{r} \right)^{1+\eta_2} \right] \\ &+ \frac{\sigma_c^m}{1-k}, \end{aligned} \quad (22)$$

$$\sigma_\theta^s = k\sigma_r^s + \sigma_c^s, \quad (23)$$

where  $Q = (r/R_e)^{k-1} [p_0 - p(t)(r/R_e)^2 + (D/\eta_1 + k) - (\sigma_c^m - D(R_e/R_s)^{1+\eta_1}/(1-k)) - ((\eta_1+1)D/(\eta_1+k)(1-k))(R_e/R_s)^{1+\eta_1} + ((\sigma_c^m - \sigma_c^r)/1 - (R_e/R_s)^{1+\eta_2})(1+\eta_2/(\eta_2+k)(1-k))$ ,  $\sigma_c^s = \sigma_c^m - ([1 - (R_s/r)^{1+\eta_2}](\sigma_c^m - \sigma_c^r)/1 - (R_s/R_r)^{1+\eta_2})$ ,  $D = (2(\sigma_c^m - \sigma_c^r)p(t)(r_0/R_e)^2/p_0(1-2\mu)\eta_1 + p(t)(r_0/R_e)^2[\eta_1 - 2 + 2(R_e/R_s)^{1+\eta_1}])$ .  $\varphi$  is the internal friction angle of rock mass.  $\sigma_c, \sigma_c^m$ , and  $\sigma_c^r$  are the yield strength, peak strength, and residual strength of rock mass, respectively.

4.4. *Stress and Displacement in Plastic Residual Zone.* The strains in plastic residual zone are

$$\begin{cases} \varepsilon_r = (\varepsilon_r^p)_{r=R_r} + \Delta\varepsilon_r^r, \\ \varepsilon_\theta = (\varepsilon_\theta^p)_{r=R_r} + \Delta\varepsilon_\theta^r. \end{cases} \quad (24)$$

The displacement solution process is consistent with the plastic softening zone, and the differential equation can be obtained:

$$\frac{du}{dr} + \eta_2 \frac{u}{r} = A, \quad (25)$$

where  $A = M - Np_i^*$ ,  $M = [(1 + \mu)(1 + \xi_2)(1 - 2\mu)/E + 1]p_0$ ,  $N = ((1 + \mu)(1 + \xi_2)(r_0/R_r)[(\xi_1 - 1) + (2(\xi_2 - \xi_1)/1 + \xi_2)(R_s/R_r)^{(1+\xi_1)}]/E + (1 + \xi_1))$ .

The compatible equation of displacement in this zone can be obtained from eqs. (25), (15), and (13), and the displacement at the boundary condition  $r = R_r$  can be obtained continuously.

$$u^r = r \left[ \frac{A}{1 + \eta_2} + \frac{2(1 + \mu)(p_0 - p_c)(r_0/R_s)^2 (R_s/R_r)^{1+\eta_1} (R_r/r)^{1+\eta_2}}{E(1 + \eta_2)} \right]. \quad (26)$$

The radial stresses can be obtained by combining eq (15) when  $r = R_r$ ,

$$\begin{aligned} \sigma_r^r = & \left\{ Q \left( \frac{R_r}{R_c} \right)^{k-1} - \frac{\sigma_c^m - \sigma_c^b}{1 - (R_c/R_s)^{1+\eta_2}} \left[ \frac{1}{1-k} + \frac{1}{\eta_2 + k} \left( \frac{R_s}{R_r} \right)^{1+\eta_2} \right] \right. \\ & \left. + \frac{\sigma_c^m - \sigma_c^b}{1-k} \right\} \cdot \left( \frac{r}{R_r} \right)^{k-1} + \frac{\sigma_c^r}{1-k}, \end{aligned} \quad (27)$$

$$\sigma_\theta^r = k\sigma_r^r + \sigma_c^r. \quad (28)$$

4.5. *Plastic Softening Zone and Plastic Residual Zone.* At the boundary of the plastic softening zone and the plastic residual zone (i.e.,  $r = R_r$ ), the strength parameter of plastic softening zone softens to the residual strength value. So the ratio of radius of plastic residual zone to radius of plastic softening zone is

$$\begin{cases} \frac{R_s}{R_r} = \left[ \frac{c_0 - c_r + J \left( \frac{R_s}{r_0} \right)^2}{J} \right]^{(1/1+\eta_1)}, \\ J = \frac{2F(1 + \mu)(p_0 - p_c)}{E(1 + \eta_1)}. \end{cases} \quad (29)$$

At the boundary of the elastic zone and the plastic softening zone (i.e.,  $r = R_s$ ), the radius of the plastic softening zone can be obtained:

$$R_s = r_0 \sqrt{\frac{(p_0 - p_c)(1 + k_\varphi)}{(k_\varphi - 1)p_0 + \sigma_c}}. \quad (30)$$

The radius of the plastic residual zone can be obtained by combining eqs. (29) and. (30):

$$R_r = r_0 \sqrt{\frac{(p_0 - p_c)(1 + k_\varphi)}{(k_\varphi - 1)p_0 + \sigma_c} \left[ \frac{J}{c_0 - c_r + J \left( \frac{r_0}{R_s} \right)^2} \right]^{(1/1+\eta_1)}}. \quad (31)$$

## 5. Coupling Effect between Supporting Structures and Surrounding Rock

Assuming that the bolts and liners of the supporting structure are contacting with the surrounding rock closely, the coupling between the bolt and the surrounding rock is considered as a composite bearing body, and the time difference between bolts and liners is 0 approximately. In addition, considering the timeliness of concrete strength hardening, rockbolts and liners bear the load of surrounding rock together.

5.1. *Equivalent Material Parameters under Coupling Effect of Surrounding Rock and Rockbolts.* Because of the supporting force between rockbolts and surrounding rock acting on the surrounding rock in the form of equivalent volume force, the stresses and the displacement of plastic softening zone change nonlinearly. When the rockbolt anchoring acts on these two sections, it is more complicated to solve the stresses and displacement of surrounding rock.

According to reference [29], using homogenization method, bolts are uniformly arranged. Bolts and surrounding rock are regarded as equivalent materials, and its elastic modulus expression is as follows

$$E^* = \frac{E_b \pi r_b^2 + E(f_1 f_2 - \pi r_b^2)}{f_1 f_2}, \quad (32)$$

where  $E_b$  is the elastic modulus of bolt;  $r_b$  is the diameter of bolt;  $E$  is the elastic modulus of surrounding rock;  $f_1$  is the row spacing of bolt,  $f_2$  is the hoop spacing of bolt.

When the plastic zone is formed after the excavation of the surrounding rock, the internal friction angle changes to be smaller than that of the elastic zone. When the bolt is applied in the plastic zone, the internal friction angle will be close to the elastic zone. According to reference [30], the equivalent material cohesive force of bolt pretightening force should be considered, and the equivalent material cohesive force is

$$c^* = c_i + c_j + c_t. \quad (33)$$

where  $c_i$  is the cohesion of each zone, and the cohesion of the elastic zone, the plastic softening zone, and the plastic residual zone is  $c_0$ ,  $c_s$  and  $c_r$ , respectively;  $c_j$  is the cohesion force of the rockbolt and  $c_j = \sigma_s \pi r_b^2 / 4 \sqrt{3} f_1 f_2 \cos(45^\circ - \varphi)$ . In this equation,  $\sigma_s$  is the yield strength of the rockbolt;  $c_t$  is the additional cohesion force formed by the pretightening force of rockbolt and  $c_t = (F_0 / f_1 f_2) \cos(45^\circ - \varphi) \tan \varphi$ . In this equation,  $F_0$  is the pretightening force of rockbolt.

The stresses, displacement, and the zoning range of surrounding rock after rockbolt supporting can be obtained by substituting the equivalent material parameters  $E^*$  and  $c^*$  into the above equations.

### 5.2. Displacement Analysis of Concrete Shotcrete Supporting.

The supporting resistance is provided by passive compression after spraying, but the strength required for the bearing capacity of the spraying layer needs a time course. The strength is mainly related to the elastic modulus.

According to reference [31], the elastic modulus can be obtained:

$$E(t) = \begin{cases} E_0 \left[ \alpha + \beta \lg \left( 1 + \frac{t}{t_1} \right) \right], & (t_0 < t < t_1), \\ E_0, & (t \geq t_1), \end{cases} \quad (34)$$

where  $E_0$  is the ultimate elastic modulus of concrete shotcrete layer;  $t_1$  is the time of concrete shotcrete layer achieving the design strength.

When the rockbolts and surrounding rock are regarded as composite bearing body, the load of composite bearing body is assumed by lining supporting resistance and virtual supporting force. The radial displacement of the plastic residual zone is expressed as follows:

$$u^r|_{r=r_0} = r_0 h_3 [p_i(t) + p_1(t)]. \quad (35)$$

For a given time increment  $\Delta t$ , the radial displacement increment of the plastic residual zone is

$$\Delta u^r|_{r=r_0} = r_0 h_3 \left[ \frac{dp_i(t)}{dt} \Delta t + \frac{dp_1(t)}{dt} \Delta t \right]. \quad (36)$$

The concrete spray layer is equivalent to the curved beam with stiffness  $K_c$  as the incremental constitutive equation of the roadway. The equation is

$$\frac{\Delta u^r|_{r=r_0}}{r_0} = \frac{\Delta t}{K_c} \frac{dp_i(t)}{dt}, \quad (37)$$

where  $K_c = (E(t)(r_0^2 - a^2))/((1 + \mu_0)[(1 - 2\mu_0)r_0^2 + a^2])$ ,  $\mu_0$  is Poisson's ratio of the concrete sprayed layer, and  $a$  is the inner diameter of the concrete sprayed layer.

According to eq. (37), we can obtain

$$\Delta u^r|_{r=r_0} = \frac{r_0 h_3}{1 - K_c h_3} \int_{t_0}^t \frac{dp_1(s)}{ds} ds. \quad (38)$$

## 6. Example Analysis

The basic parameters of circular roadway design are as follows: radius of roadway  $r_0 = 3$  m, elastic modulus  $E = 2.0$  GPa, Poisson's ratio  $\mu = 0.32$ , crustal stress  $p_0 = 20$  MPa, initial cohesion  $c_0 = 0.8$  MPa, peak hardening cohesion  $c_m = 1.6$  MPa, residual cohesion  $c_r = 0.4$  MPa, internal friction angle  $= 30^\circ$ , and initial support force  $p_i = 0$  MPa. The rockbolts cover the plastic zone, and the specific parameters are as follows: modulus of elasticity  $E_b = 210$  GPa, yield

strength  $\sigma_b = 345$  MPa, pretightening force  $F = 60$  kN,  $r_b = 20$  mm, row spacing, and hoop spacing  $f_1 = f_2 = 800$  mm. The lining parameters are as follows: elastic modulus  $E_0 = 2.8 \times 10^4$  MPa,  $r_0 - a = 0.25$  m. When considering the supporting time, the excavation progress is  $V = 5$  m/d, and the excavation section follows the principle of excavation to support. Before and after supporting, the roadway area is shown in Table 1 [13, 25, 28].

As shown in Table 1, the thickness of plastic residual zone is 1.87 m under high crustal stress and only 0.96 m under the supporting. The supporting can reduce the range of plastic zone effectively. When considering the "space effect," the range of plastic zones is further reduced. In addition, the more nearer the distance between the excavation face and the supporting surface, the more obvious the "space effect."

**6.1. The Influence of Spacing-Row of Rockbolts between the Stresses and Displacement.** As shown in Figure 3, the larger the distance between rows, the smaller the circumferential stress and radial stress, and the peak value of circumferential stress moves away from the center of the roadway, which is not conducive to the safety of the roadway. The radial stress has an inflection point at the radius of the plastic softening zone, developing faster in the plastic softening zone. In the plastic softening zone, the circumferential stress increases sharply, while the elastic zone tends to be stable. Although the reduction of row spacing between rockbolts can increase the stress of surrounding rock and strengthen the bearing capacity of plastic zone, the increasement is not obvious.

Figure 4 shows that the displacement of surrounding rock increases with the distance increasement of spacing-row of rockbolts. The displacement of plastic zone is mainly affected by the distance of spacing-row of rockbolts. But the displacement of elastic zone is almost negligible. When the distance between spacing-row of rockbolts is 1.2 m, the displacement of surrounding rock is compared with that of the spacing-row of rockbolts, which is 0.4 m. The displacement of the latter is 35.6% less than that of the former. The influence of spacing-row of rockbolts is mainly reflecting in the displacement of surrounding rock.

**6.2. Effect of "Space Effect" and Support Time on Displacement of Surrounding Rock in Roadway.** The distance between the excavation face and the supporting surface is defined as  $x$  and  $x = Vt_0$ . So,  $x$  is related to the "space effect." The influence of "space effect" on the displacement of surrounding rock is shown in Figure 5. The smaller the value  $x$  is, the greater the virtual supporting resistance is, and the shorter the distance between the supporting surface and the excavation surface is. So, the smaller the radial displacement of the tunnel wall is, the more favorable the stability of the roadway is. The displacement of the surrounding rock at  $x = 15$  m is compared with the displacement without considering the "space effect" and the supporting time, and the displacement of the former is 95.9% of that of the latter when the displacement of surrounding rock is equal to  $r = 3$  m. Therefore, when the displacement of surrounding rock is



TABLE 1: The zones' ranges of surrounding rock of roadway.

Consideration of factors	Plastic residual zone (m)	Plastic softening zone (m)	Elastic zone (m)
No- supporting	4.77	6.58	$\infty$
Supporting	3.86	5.60	$\infty$
Supporting (considering "space effect" $V = 10$ m/d)	3.83	5.55	$\infty$
Supporting (considering "space effect" $V = 6$ m/d)	3.79	5.48	$\infty$
Supporting (considering "space effect" $V = 3$ m/d)	3.71	5.32	$\infty$

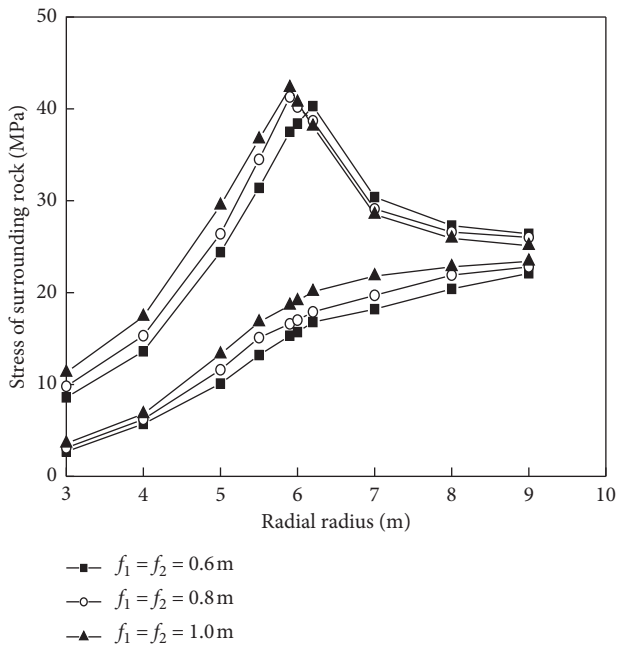


FIGURE 3: The influence of spacing-row of rockbolts to stress of surrounding rock.

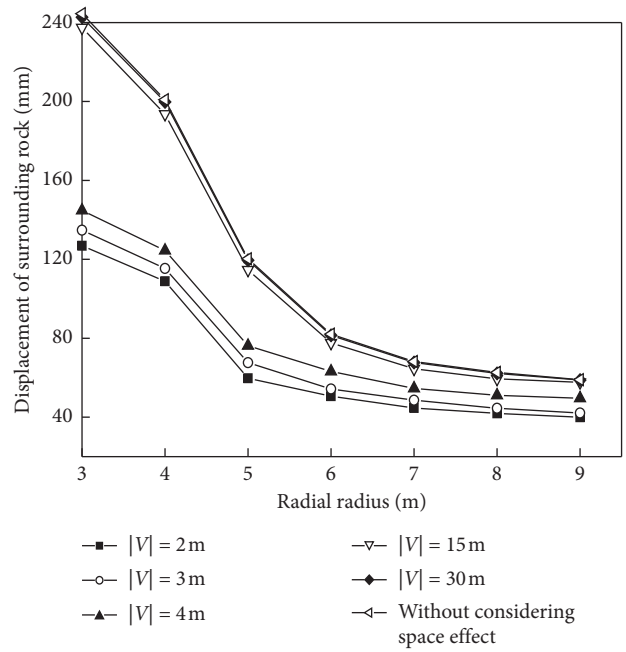


FIGURE 5: The influence of space effect on surrounding rock displacement of roadway.

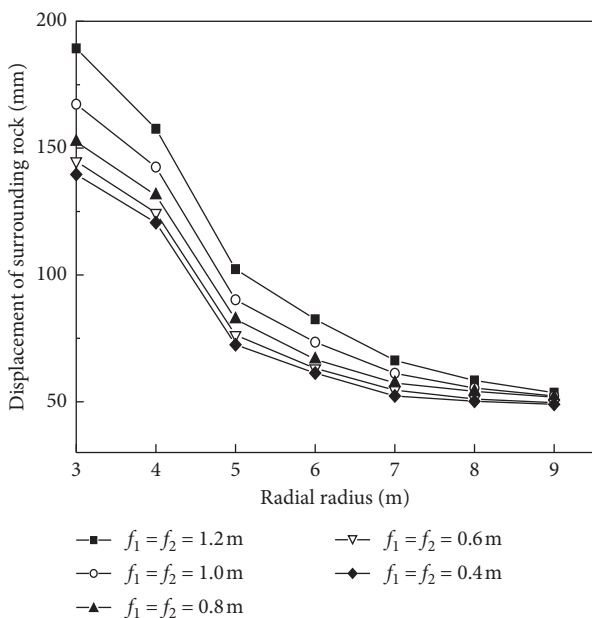


FIGURE 4: The influence of spacing-row of rockbolts to displacement of surrounding rock.

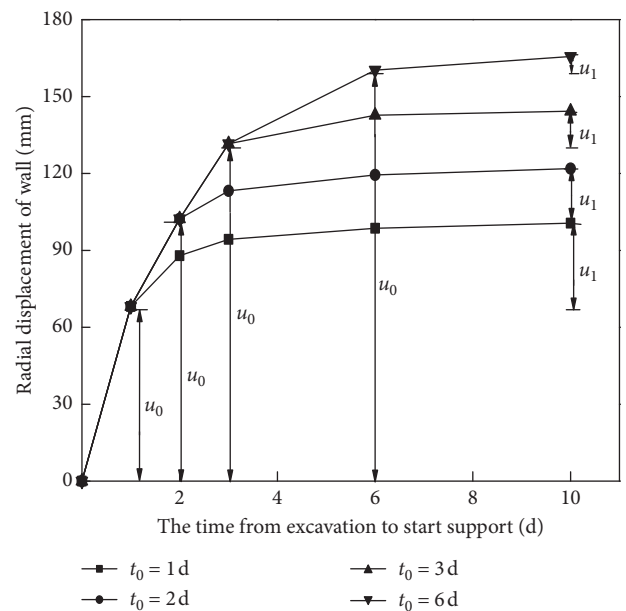


FIGURE 6: The influence of supporting opportunity on surrounding rock displacement of roadway.

greater than 15 m, the influence of the “space effect” on the displacement of surrounding rock can be neglected.

In the process of soft rock roadway excavation, a layer of concrete is sprayed on the excavated part to restrain the deformation of surrounding rock, and then the bolt is applied. The influence of supporting time on surrounding rock displacement is shown in Figure 6. Before the supporting is applied, a section of displacement has been produced on the wall of the roadway, which can be recorded as  $u_0$ . The displacement after the supporting is applied, which can be recorded as  $u_1$ . When the driving speed is constant,  $x$  is correlated with  $t_0$  positively. The bigger the  $t_0$ , the bigger the  $u_0$ , and the smaller the  $u_1$ . But the increase of  $u_0$  is far greater than the reduction of  $u_1$  and the total deformation of the tunnel wall is increasing. This is a result of the larger displacement of the roadway wall before supporting, and the limited displacement of the surrounding rock is restrained by supporting. For example, when  $t_0$  is 6 d,  $u_1$  is only 47.4% of  $u_0$ . On the contrary, when  $t_0$  is 1 d,  $u_1$  is only 28.8% of  $u_0$ . The total displacement is only 60.7% when  $t_0$  is 6 d, and the supporting effect is obvious.

## 7. Conclusions

In this paper, based on D-P strength criterion and the noncorrelation flow rule, an equivalent circular roadway solution method is proposed. The stress and deformation of surrounding rock of underground roadways are obtained by the elastoplastic theory. Then, the failure mechanism of roadway with soft rock is analyzed. Based on the D-P strength criterion, considering the softening and dilatation of surrounding rock, the surrounding rock of the roadway is divided into three zones, and the “space effect” is introduced. The analytical expressions of stress, displacement, and partition range of surrounding rock without rockbolt and lining supporting are obtained. In the process of supporting, the rockbolt is evenly arranged in the roadway, and the composite bearing body is composed of the rockbolt and the surrounding rock. The equivalent material parameters are calculated reasonably, and the elastoplastic solution of surrounding rock under the supporting condition is obtained. Therefore, considering the aging characteristics of the concrete shotcrete layer, the theoretical calculation is closer to the field engineering practice. Under the support condition, the plastic softening zone can be effectively reduced, and the plastic residual zone can be mainly reduced. Considering the “space effect” and the supporting time, the zones can be calculated more accurately. By analyzing the influencing factors of the stress and displacement of the surrounding rock, it is concluded that the spacing-row between rockbolts has little effect on the surrounding rock stress, while the influence on the displacement of surrounding rock is mainly reflected in the plastic residual zone.

## Data Availability

The data used to support the findings of this study are available from the corresponding author upon request.

## Conflicts of Interest

The authors declare no conflicts of interest.

## Acknowledgments

This research has been supported by the National Natural Science Foundation of China (grant no. 51927807), a Project Funded by the Priority Education Academic Program Development of Jiangsu Higher Education Institutions (PAPD), National Natural Science Foundation of China (General Program: 52074239), and Independent Research Project of State Key Laboratory of Coal Resources and Safe Mining, CUMT (SKLCRSM18X08).


## References

- [1] S. S. Peng, “Topical areas of research needs in ground control - a state of the art review on coal mine ground control,” *International Journal of Mining Science and Technology*, vol. 25, no. 1, pp. 1–6, 2015.
- [2] R. Wang, S. Yan, J. B. Bai et al., “Theoretical analysis of damaged width & instability mechanism of rib pillar in open-pit highwall mining,” *Advance in Civil Engineering*, vol. 2019, Article ID 6328702, 15 pages, 2019.
- [3] G. Silva, P. G. Ranjith, M. S. A. Perera, and B. Chen, “Effect of bedding planes, their orientation and clay depositions on effective re-injection of produced brine into clay rich deep sandstone formations: implications for deep earth energy extraction,” *Applied Energy*, vol. 161, pp. 24–40, 2016.
- [4] Z. Zhang, M. Deng, X. Wang, W. Yu, F. Zhang, and V. D. Dao, “Field and numerical investigations on the lower coal seam entry failure analysis under the remnant pillar,” *Engineering Failure Analysis*, vol. 115, Article ID 104638, 2020.
- [5] J. A. Bay and K. H. Stokoe, “Field determination of stiffness and integrity of PCC members using the SASW method,” in *Proceedings of the Nondestructive Evaluation of Civil Structures and Materials Conference*, Colorado, CO, USA, October 2000.
- [6] E. T. Brown, J. W. Bray, B. Ladanyi, and E. Hoek, “Ground response curves for rock tunnels,” *Journal of Geotechnical Engineering*, vol. 109, no. 1, pp. 15–39, 1983.
- [7] W. Zhu, H. Jing, L. Yang, B. Pan, and H. Su, “Strength and deformation behaviors of bedded rock mass under bolt reinforcement,” *International Journal of Mining Science and Technology*, vol. 28, no. 4, pp. 593–599, 2018.
- [8] K.-H. Park and Y.-J. Kim, “Analytical solution for a circular opening in an elastic-brittle-plastic rock,” *International Journal of Rock Mechanics and Mining Sciences*, vol. 43, no. 4, pp. 616–622, 2006.
- [9] C. Carranza-Torres, “Elasto-plastic solution of tunnel problems using the generalized form of the hoek-brown failure criterion,” *International Journal of Rock Mechanics and Mining Sciences*, vol. 41, no. 3, pp. 480–481, 2004.
- [10] Y.-K. Lee and S. Pietruszczak, “A new numerical procedure for elasto-plastic analysis of a circular opening excavated in a strain-softening rock mass,” *Tunnelling and Underground Space Technology*, vol. 23, no. 5, pp. 588–599, 2008.
- [11] T. C. Carranza and C. Fairhurst, “The elasto-plastic response of underground excavations in rock masses that satisfy the Hoek-Brown failure criterion,” *International Journal of Rock Mechanics and Mining Sciences*, vol. 36, no. 6, pp. 777–809, 1999.

- [12] T. C. Carranza and C. Fairhurst, "Application of the convergence-confinement method of tunnel design to rock masses that satisfy the Hoek-Brown failure criterion," *Tunnelling and Underground Space Technology*, vol. 15, no. 2, pp. 187–213, 2000.
- [13] A. Fahimifar and M. Ranjbaria, "Analytical approach for the design of active grouted rockbolts in tunnel stability based on convergence-confinement method," *Tunnelling and Underground Space Technology*, vol. 24, no. 4, pp. 363–375, 2009.
- [14] Z. Guan, Y. Jiang, Y. Tanabasi, and H. Huang, "Reinforcement mechanics of passive bolts in conventional tunnelling," *International Journal of Rock Mechanics and Mining Sciences*, vol. 44, no. 4, pp. 625–636, 2007.
- [15] F. Nagel and G. Meschke, "An elasto-plastic three phase model for partially saturated soil for the finite element simulation of compressed air support in tunnelling," *International Journal for Numerical and Analytical Methods in Geomechanics*, vol. 34, no. 6, pp. 605–625, 2010.
- [16] C. H. Tan, "Passive bolts reinforcement around a circular opening in strain-softening elastoplastic rock mass," *International Journal of Rock Mechanics and Mining Sciences*, vol. 88, pp. 221–234, 2016.
- [17] P. P. Oreste and D. Pella, "Modelling progressive hardening of shotcrete in convergence-confinement approach to tunnel design," *Tunnelling and Underground Space Technology*, vol. 12, no. 3, pp. 425–431, 1997.
- [18] S. Ding, H. Jing, K. Chen, G. a. Xu, and B. Meng, "Stress evolution and support mechanism of a bolt anchored in a rock mass with a weak interlayer," *International Journal of Mining Science and Technology*, vol. 27, no. 3, pp. 573–580, 2017.
- [19] Y.-W. Pan and J.-J. Dong, "Time-dependent tunnel convergence-I. formulation of the model," *International Journal of Rock Mechanics and Mining Sciences & Geomechanics Abstracts*, vol. 28, no. 6, pp. 469–475, 1991.
- [20] G. Wang, Y. Zhang, Y. Jiang et al., "Shear behaviour and acoustic emission characteristics of bolted rock joints with different roughnesses," *Rock Mechanics and Rock Engineering*, vol. 51, no. 6, pp. 1885–1906, 2018.
- [21] L. Chen, X. B. Miao, M. Li et al., "Elastoplastic analysis of cracked surrounding rock in deep roadway based on drucker-prager criterion," *Journal of China Coal Society*, vol. 42, no. 2, pp. 484–491, 2017.
- [22] M. H. Yu, G. W. Ma, and J. C. Li, *Structural Plasticity*, Zhejiang University Press, Hangzhou, China, 2009, in Chinese.
- [23] R. Chait, "Factors influencing the strength differential of high-strength steels," *Metallurgical and Materials Transactions B*, vol. 3, pp. 365–371, 1972.
- [24] D. C. Drucker, "Plasticity theory strength-differential(SD) phenomenon, and volume expansion in metals and plastics," *Metallurgical Transactions*, vol. 4, no. 3, pp. 667–673, 1973.
- [25] G. C. Rauch and W. C. Leslie, "The extent and nature of the strength-differential effect in steel," *Metal Trans*, vol. 3, pp. 365–371, 1972.
- [26] M. H. Yu, *Twin Shear Theory and its Application*, Science Press, Beijing, China, 1991, in Chinese.
- [27] M. H. Yu and L. N. He, "A new model and theory on yield and failure of materials under the complex stress state," in *Mechanical Behavior of Materials, International Series of the Strength and Fracture of Materials and Structures*, M. Jono and T. Inoue, Eds., pp. 841–846, Pergamon Press, Oxford, UK, 1991.
- [28] G. M. Zhao, R. Peng, X. R. Meng et al., "Stability of bearing structure during soft roadway excavation-supporting," *Journal of China University of Mining & Technology*, vol. 46, no. 4, pp. 792–802, 2017.
- [29] C. Yuan, W. J. Wang, and Y. L. Zhao, "Theoretical analysis on roadway surrounding rock deformation based on the properties of rock plastic hardening and softening," *Journal of the China Coal Society*, vol. 40, no. S2, pp. 311–319, 2015.
- [30] J. W. Zhang, "Theoretical analysis on failure zone of surrounding rock in deep large-scale soft rock roadway," *Journal of China University of Mining and Technology*, vol. 46, no. 2, pp. 292–299, 2017.
- [31] Y. Zhang, X. Zhuang, and R. Lackner, "Stability analysis of shotcrete supported crown of NATM tunnels with discontinuity layout optimization," *International Journal for Numerical and Analytical Methods in Geomechanics*, vol. 42, no. 11, pp. 1199–1216, 2018.

## Research Article

# Theoretical Analysis on Distribution Pattern of Plastic Zone in Surrounding Rock of High-Gas-Coal Roadway

Chao Yuan <sup>1,2,3</sup>, Liming Cao,<sup>3</sup> Lei Fan,<sup>3</sup> and Jianqiang Guo<sup>3</sup>

<sup>1</sup>Work Safety Key Lab on Prevention and Control of Gas and Roof Disasters for Southern Coal Mines, Hunan University of Science and Technology, Xiangtan 411201, China

<sup>2</sup>Hunan Provincial Key Laboratory of Safe Mining Techniques of Coal Mines, Hunan University of Science and Technology, Xiangtan 411201, China

<sup>3</sup>School of Resources, Environment and Safety Engineering, Hunan University of Science and Technology, Xiangtan 411201, China

Correspondence should be addressed to Chao Yuan; [yuanchaozh1@126.com](mailto:yuanchaozh1@126.com)

Received 8 December 2020; Revised 3 January 2021; Accepted 26 February 2021; Published 9 March 2021

Academic Editor: Alessandro Palmeri

Copyright © 2021 Chao Yuan et al. This is an open access article distributed under the Creative Commons Attribution License, which permits unrestricted use, distribution, and reproduction in any medium, provided the original work is properly cited.

The formation and expansion of the plastic zone is always accompanied by the deformation and failure of the roadway-surrounding rock. Based on elastoplastic theory, this paper considers the gas pressure parameters and uses the Mohr–Coulomb strength criterion to derive the implicit equation of the plastic zone boundary in the rock surrounding gas-coal roadways. The distribution characteristics of the plastic zone of gas-coal roadway-surrounding rock are studied, and the sensitivity to the gas pressure, cohesion, internal friction angle, and support strength of the roadway free face on the plastic zone of the surrounding rock is analyzed. The research results show that the plastic zone of the surrounding rock has four distribution patterns: circular, elliptical, rounded rectangle, and butterfly. Additionally, the lateral pressure coefficient, gas pressure, cohesion, and internal friction angle are found to jointly determine the distribution and range of the plastic zone. However, the support strength of the roadway free face does not change the distribution of the plastic zone but only affects its range. The circular and elliptical plastic zones are less sensitive to gas pressure, cohesion, and internal friction angle, whereas butterfly-shaped plastic zones are highly sensitive to these factors. The main manifestation of this sensitivity is that the four butterfly leaves degenerate rapidly with any decrease in the gas pressure or increase in the cohesion and internal friction angle. Larger butterfly leaves are prone to faster degeneration. The research results presented in this paper have important theoretical guiding significance and engineering application value for the design of high-gas-coal roadway support and gas drilling.

## 1. Introduction

Gas-rich coal has an unstable structure, low degree of cementation, and significant variations in particle size and adsorption characteristics. These characteristics lead to a decrease in the overall strength and stability of the surrounding rock of gas-coal roadways, leaving them vulnerable to disturbances such as mining activities. Part of the coal body enters a pressurized state from the original stress state, and its internal cracks shrink and close, causing the gas pressure to increase [1–3]. Under the influence of multiple factors (e.g., high ground stress, mining, and gas pressure), the surrounding rock of gas-coal roadways exhibits a series of engineering response characteristics

during service periods, such as asymmetry and large-scale instability failures. Roof and patchwork disasters frequently occur. This represents a great threat to safe production, and so the prevention and control of deformation and instability of surrounding rock in gas-coal roadways are of great importance. However, the increasing complexity of the coal seam environment and the increasing intensity of mining make the control of gas-coal roadway stability more difficult. Therefore, we need to fully understand the mechanism of the deformation and failure of surrounding rock in gas-coal roadways. This is the basis and key to the scientific design of roadway-surrounding rock and the prevention and control of various geological disasters.

There has been considerable research on the deformation and failure mechanism of surrounding rock in roadways. The formation and expansion of the plastic zone is always accompanied by the deformation and failure of the surrounding rock of the roadway, and the plastic zone is used as the main basis for analyzing the deformation and failure mode of the roadway-surrounding rock [4]. Zareifard and Fahimifar derived analytical solutions for the stress and displacement of the surrounding rock of a circular roadway-surrounding rock and found that the distribution of the plastic zone under a uniform stress field has a significant influence on its stability [5]. Based on the deviatoric stress theory of elastoplastic mechanics, Ma et al. found analytical solutions for the deviatoric stress of the rock surrounding a circular roadway under a nonuniform stress field and developed a calculation method for the radius of the plastic zone, which showed that the distribution of the plastic zone is closely related to the deviator correlation and irregular distribution [6]. Using the Hoek–Brown strength criterion, Xia et al. derived an analytical expression for the plastic zone of the surrounding rock of a circular roadway considering the strain-softening characteristics [7]. Zhao et al. derived theoretical calculation formulas for the radius and stress field of the plastic zone of a circular roadway-surrounding rock based on the humidity stress field and elastoplastic theory. The influence of the roadway-surrounding rock humidity and support strength on the plastic zone of the surrounding rock was analyzed, and the accuracy of the humidity distribution function and radius of the plastic zone was verified by field tests [8]. Liu et al. analyzed the plastic zone range of the surrounding rock in shallow tunnels from an energy perspective and divided the development process of the plastic zone into three stages: (1) formation and expansion of the plastic zone; (2) connection of the plastic zone; and (3) extension of the plastic zone to the surface [9]. Zhou and Li used the nonlinear Hoek–Brown failure criterion to derive analytical solutions for the plastic zone of circular roadway-surrounding rock considering the magnitude of ground stress. The influence of horizontal in situ stress, vertical in situ stress, and rock mass strength parameters on the distribution of the plastic zone in the surrounding rock was analyzed [10]. Ma et al. studied the shape and size of the plastic zone around a deeply buried double circular tunnel and analyzed the effects of tunnel spacing, ground stress, cohesion, and internal friction angle on the plastic zone [11]. Zhou et al. found that the plastic zone enhances the effective permeability of gas-rich coal seams through engineering field investigations [12]. Zhao et al. used COMSOL to simulate the gas pressure distribution around a roadway and found that the plastic zone is the main channel for gas flow [13]. Liu et al. investigated the effect of the plastic zone on the quality of gas extraction and found that a larger plastic zone can significantly improve gas extraction, thus preventing spontaneous coal combustion, gas explosion, and other disasters [14]. Zhang et al. used FLAC 3D software to analyze the stress state and deformation law of a coal body after roadway excavation and drilling. They determined the distribution range of the plastic and elastic zones and studied the permeability of the

coal near the drilling site [15]. Zhang et al. combined the noncorrelated flow law and the Hoek–Brown criterion and used an FVP model to derive an analytical solution for the viscoplastic deformation of a circular roadway-surrounding rock. The variation of the displacement of the viscoplastic zone with respect to depth has been analyzed, providing a rapid evaluation of the viscoplastic deformation of the roadway-surrounding rock in the early design process [16]. Xu et al. derived an analytical solution for the plastic zone around a noncircular tunnel based on the Mohr–Coulomb criterion and the theory of complex variables. The influence of the lateral pressure coefficient and the depth of the pressure relief hole on the plastic zone of the tunnel-surrounding rock was discussed [17]. Kabwe et al. derived an elastoplastic analytical solution for noncircular tunnel-surrounding rock considering the intermediate principal stress based on the equivalent radius function and the Drucker–Prager yield criterion. The analytical solution can better predict the plastic zone range of the rock surrounding the tunnel and the degree of convergent deformation of the tunnel, enabling the design of an appropriate tunnel support structure [18].

Analysis of the above results shows that researchers have generally used the plastic zone as an important indicator for theoretical analysis, numerical simulations, and engineering test results when evaluating the rock surrounding a roadway. However, little research has focused on the plastic zone itself, and the influence of the gas pressure, original rock stress, rock mass strength, and support strength on the plastic zone of coal roadway-surrounding rock has rarely been considered. Thereby, it is impossible to truly reflect the deformation and failure instability mechanism of the surrounding rock of gas-coal roadways, making it impossible to propose an effective surrounding-rock support strategy. Therefore, based on elastoplastic theory and Mohr–Coulomb strength theory, this paper derives the implicit equation for the boundary of the plastic zone of the roadway-surrounding rock considering the gas pressure. Using theoretical analysis, the influence of the lateral pressure coefficient, gas pressure, cohesion, internal friction angle, and support strength of the roadway's free face on the distribution morphology of the plastic zone of the roadway-surrounding rock is examined. The research results have important theoretical guiding significance for the reinforcement of the surrounding rock of gas-coal roadways.

## 2. Description and Hypothesis of Mechanical Model of Surrounding Rock in Coal Roadway

In the vertical direction, the original rock stress is  $P_1$ , the horizontal direction of the original rock stress is  $P_3$ , and the pore gas pressure is  $P_g$ , and the excavation radius is a circular section of roadway. The supporting force acting on the roadway wall is  $P_b$ , and the gas pore pressure is  $P_a$ . Taking the unit length along the axis of the roadway, we have an axisymmetric plane strain problem, assuming that the physical strength can be ignored.

To analyze the stress state of the surrounding rock in a disequilibrium circular roadway, the mechanical model of



the surrounding rock of the roadway must be simplified accordingly. Thus, the bidirectional stress field is regarded as a uniform load, and the following basic assumptions are made:

- (1) The section of the roadway is circular, with radius  $a$  and buried depth  $H \geq 20a$ , and is an infinitely long flat roadway.
- (2) The surrounding rock mass of the roadway is an isotropic medium, forming an ideal elastic-plastic body.
- (3) The surrounding rock of the roadway is in a non-uniform high-stress environment.
- (4) The external boundary condition of the calculation model is the vertical principal stress  $P_1$  and the horizontal principal stress  $P_3$ , both of which are parallel to the Cartesian coordinate axes.

Based on this, the mechanical model of the surrounding rock of circular roadway is established as shown in Figure 1.

### 3. Gas Pressure Distribution in Rock Surrounding a Coal Roadway

After the excavation of the roadway, the gas flow in the surrounding rock has the form of axisymmetric radial seepage. The gas flow rate  $Q$  through a cylindrical area of unit length and radius  $r$  per unit time is

$$Q = -2\pi rK \frac{dp}{dr}, \quad (1)$$

where  $p$  is the pore gas pressure at radius  $r$  and  $K$  is the permeability coefficient.

Integrating equation (1) gives

$$p(r) = c_1 - \frac{Q}{2\pi K} \ln r. \quad (2)$$

From equation (2) and the boundary conditions  $p(a) = P_a$ ,  $p(b) = P_g$ , we have

$$c_1 = P_a + \frac{Q}{2\pi K} \ln a, \quad (3a)$$

$$\frac{Q}{2\pi K} = \frac{P_g - P_a}{\ln(a/b)}. \quad (3b)$$

Substituting equations (3a) and (3b) into equation (2) for the gas pressure distribution leads to

$$p(r) = P_a + \frac{(P_g - P_a) \ln(a/r)}{\ln(a/b)}, \quad (4a)$$

$$\frac{dp}{dr} = -\frac{(P_g - P_a)}{r \ln(a/b)}. \quad (4b)$$

### 4. Theoretical Solution of Plastic Zone around a Coal Roadway

The circular roadway model in Figure 2 is decomposed into two parts under the action of the initial ground stress and gas pressure: the first part is the uniform stress field condition, which bears the gas pressure effect, as shown in Figure 2(a); the second part does not consider the gas pressure, but the vertical and horizontal directions are subjected to equal compression and tensile stress, respectively, as shown in Figure 2(b).

#### 4.1. Theoretical Solution of Stress Field in Elastic Zone of Rock Surrounding a Coal Roadway

4.1.1. *First Part of the Theoretical Solution of the Surrounding Rock under the Uniform Stress Field (Figure 2(a)).* For rock materials, the modified Terzaghi effective stress principle indicates that the relationship between the effective stress  $\sigma'_{ij}$  acting on the coal skeleton and the pore gas pressure  $p$  is

$$\sigma'_{ij} = \sigma_{ij} - \nu p \delta_{ij}, \quad (5)$$

where  $\sigma'_{ij}$  is the effective stress tensor,  $\sigma_{ij}$  is the stress tensor generated by the external load,  $p$  is the pore gas pressure,  $\nu$  is the effective stress coefficient, and  $\delta_{ij}$  is the Kronecker delta function.

$$\left. \begin{aligned} \sigma'_r &= \sigma_r - \nu p \\ \sigma'_\theta &= \sigma_\theta - \nu p \end{aligned} \right\} \quad (6)$$

The equilibrium equation for the axisymmetric plane strain problem under the condition of neglecting the surrounding rock mass of the roadway is

$$\frac{d\sigma_r}{dr} + \frac{\sigma_r - \sigma_\theta}{r} = 0. \quad (7)$$

Substituting Equations (4b) and (6) into Equation (7) gives

$$\frac{d\sigma'_r}{dr} - \frac{\nu(P_g - P_a)}{r \ln(a/b)} + \frac{\sigma'_r - \sigma'_\theta}{r} = 0. \quad (8)$$

Setting

$$\frac{\nu(P_g - P_a)}{\ln(a/b)} = A, \quad (9)$$

allows equation (8) to be expressed as

$$\frac{d\sigma'_r}{dr} + \frac{\sigma'_r - \sigma'_\theta}{r} - A = 0. \quad (10)$$

Let the radial strain component be  $\varepsilon_r$ , the hoop strain component  $\varepsilon_\theta$ , and the radial displacement  $u$ . Then, the geometric equation is

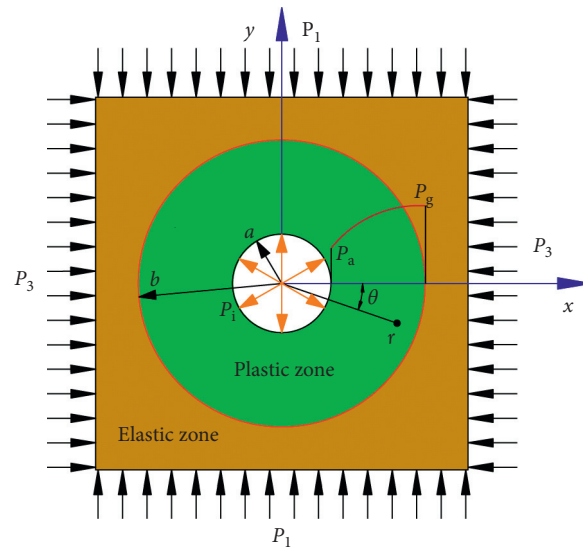


FIGURE 1: Mechanical model of roadway.

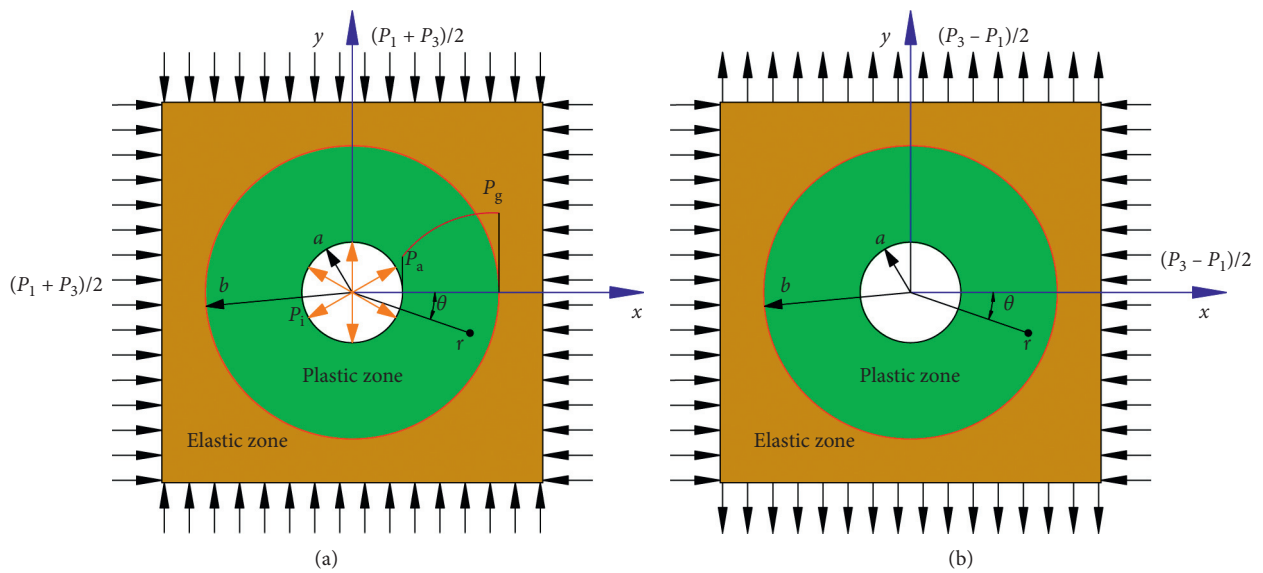


FIGURE 2: Decomposition of surrounding rock pressure for roadway.

$$\left. \begin{aligned} \varepsilon_r &= \frac{du}{dr} \\ \varepsilon_\theta &= \frac{u}{r} \\ \gamma_{r\theta} &= 0 \end{aligned} \right\} \quad (11)$$

In the elastic region, the stress-strain relationship is

$$\left. \begin{aligned} \varepsilon_r &= \frac{1-\mu^2}{E} \left( \sigma'_r - \frac{\mu}{1-\mu} \sigma'_\theta \right) \\ \varepsilon_\theta &= \frac{1-\mu^2}{E} \left( \sigma'_\theta - \frac{\mu}{1-\mu} \sigma'_r \right) \\ \gamma_{r\theta} &= \tau_{r\theta} = 0 \end{aligned} \right\} \quad (12)$$

Set

$$\left. \begin{aligned} m &= \frac{1 - \mu^2}{E} \\ n &= \frac{\mu}{1 - \mu} \end{aligned} \right\}. \quad (13)$$

We can write Equation (12) as

$$\left. \begin{aligned} \sigma'_r &= \frac{1}{m - mn^2} (\varepsilon_r + n\varepsilon_\theta) \\ \sigma'_\theta &= \frac{1}{m - mn^2} (n\varepsilon_r + \varepsilon_\theta) \end{aligned} \right\}. \quad (14)$$

Taking the derivative of Equation (14) gives

$$\left. \begin{aligned} \frac{d\sigma'_r}{dr} &= \frac{1}{m - mn^2} \left( \frac{d\varepsilon_r}{dr} + \frac{nd\varepsilon_\theta}{dr} \right) \\ \frac{\sigma'_r - \sigma'_\theta}{r} &= \frac{\varepsilon_r - n\varepsilon_r + n\varepsilon_\theta - \varepsilon_\theta}{r(m - mn^2)} \end{aligned} \right\}. \quad (15)$$

Substituting Equation (15) into Equation (11) yields

$$\left. \begin{aligned} \frac{d\sigma'_r}{dr} &= \frac{1}{m - mn^2} \left( \frac{d^2u}{dr^2} + \frac{ndu}{rdr} - \frac{mu}{r^2} \right) \\ \frac{\sigma'_r - \sigma'_\theta}{r} &= \frac{(1 - n)}{r(m - mn^2)} \frac{du}{dr} + \frac{(n - 1)u}{r^2(m - mn^2)} \end{aligned} \right\}. \quad (16)$$

And substituting Equation (16) into Equation (8) gives

$$\frac{d^2u}{dr^2} + \frac{1}{r} \frac{du}{dr} - \frac{u}{r^2} - \frac{A(m - mn^2)}{r} = 0. \quad (17)$$

Solving this differential equation, we obtain

$$u = c_1 r + \frac{c_2}{r} + \frac{A(m - mn^2)r \ln r}{2}. \quad (18)$$

Substituting Equation (18) into Equation (11), we then have that

$$\left. \begin{aligned} \varepsilon_r &= c_1 - \frac{c_2}{r^2} + \frac{A(m - mn^2) \ln r}{2} + \frac{A(m - mn^2)}{2} \\ \varepsilon_\theta &= c_1 + \frac{c_2}{r^2} + \frac{A(m - mn^2) \ln r}{2} \end{aligned} \right\}, \quad (19)$$

which can be substituted into Equation (14) to give

$$\left. \begin{aligned} \sigma'_r &= \frac{1}{m - mn^2} \left[ (1 + n)c_1 + (n - 1) \frac{c_2}{r^2} + \frac{A(1 + n)(m - mn^2) \ln r}{2} + \frac{A(m - mn^2)}{2} \right] \\ \sigma'_\theta &= \frac{1}{m - mn^2} \left[ (n_1 + 1)c_1 + \frac{(1 - n)c_2}{r^2} + \frac{A(n + 1)(m - mn^2) \ln r}{2} + \frac{An(m - mn^2)}{2} \right] \end{aligned} \right\}. \quad (20)$$

For  $r = a$  and  $r = b$ , we can write

$$\left. \begin{aligned} \sigma_r|_{r=a} &= P_i - \nu P_a \\ \sigma_r|_{r=b} &= \frac{P_3 + P_1}{2} - \nu P_g \end{aligned} \right\}. \quad (21)$$

Substituting Equation (20) into Equation (21) then yields

$$\left. \begin{aligned} c_2 &= \frac{T(m - mn^2)a^2b^2}{(b^2 - a^2)(n - 1)} - \frac{S(m - mn^2)a^2b^2}{(b^2 - a^2)(n - 1)} - \frac{Aa^2b^2(1 + n)(m - mn^2) \ln(a/b)}{2(b^2 - a^2)(n - 1)} \\ c_1 &= \frac{T(m - mn^2)}{(1 + n)} - \frac{T(m - mn^2)b^2}{(b^2 - a^2)(1 + n)} + \frac{S(m - mn^2)b^2}{(b^2 - a^2)(1 + n)} - \frac{A(m - mn^2) \ln a}{2} - \frac{A(m - mn^2)}{2(1 + n)} + \frac{Ab^2(m - mn^2) \ln(a/b)}{2(b^2 - a^2)} \end{aligned} \right\}. \quad (22)$$

where

$$\left. \begin{aligned} T &= P_i - \nu P_a \\ S &= \frac{P_3 + P_1}{2} - \nu P_g \end{aligned} \right\}. \quad (23)$$

Substituting Equation (22) into Equation (20), the stress expression in the elastic phase is

$$\left. \begin{aligned} \sigma'_r &= \frac{(b^2 - r^2)Ta^2}{(b^2 - a^2)r^2} + \frac{(r^2 - a^2)Sb^2}{(b^2 - a^2)r^2} + \frac{A(1+n)}{2} \left[ \frac{(r^2 - a^2)b^2 \ln(a/b)}{(b^2 - a^2)r^2} + \ln r - \ln a \right] \\ \sigma'_\theta &= \frac{(r^2 + b^2)Ta^2}{(b^2 - a^2)r^2} + \frac{(a^2 + r^2)Sb^2}{(b^2 - a^2)r^2} + \frac{A(n+1)}{2} \left[ \frac{(r^2 + a^2)b^2 \ln(a/b)}{(b^2 - a^2)r^2} + \ln r - \ln a \right] \end{aligned} \right\}. \quad (24)$$

If  $b$  is much larger than  $a$ , Equation (24) can be approximated as

$$\left. \begin{aligned} \sigma'_r &= \frac{Ta^2}{r^2} + \left(1 - \frac{a^2}{r^2}\right)S + \left[ \frac{a(1+n)(P_g - P_a)}{2} \left(1 - \frac{a^2}{r^2}\right) \right] \\ \sigma'_\theta &= -\frac{Ta^2}{r^2} + \left(1 + \frac{a^2}{r^2}\right)S + \left[ \frac{a(1+n)(P_g - P_a)}{2} \left(1 + \frac{a^2}{r^2}\right) \right] \end{aligned} \right\}. \quad (25)$$

4.1.2. *Second Part of the Theoretical Solution for the Surrounding Rock Stress Field of the Roadway under Pressure and Tensile Stress Field (Figure 2(b)).* When  $r=b$ , we can write

$$\left. \begin{aligned} \sigma_r|_{r=b} &= \frac{P_3 - P_1}{2} \cos 2\theta \\ \tau_{r\theta}|_{r=b} &= \frac{P_3 - P_1}{2} \sin 2\theta \end{aligned} \right\}. \quad (26)$$

Obviously, the stress solution is related to  $r$  and  $2\theta$ , and the stress function is

$$y = f(r) \cos 2\theta. \quad (27)$$

Substituting Equation (27) into the biharmonic equation, and recalling the boundary conditions  $r=a$ ,  $\sigma_r=0$ ,  $\tau_{r\theta}=0$ , the elastic phase stress expression is

$$\left. \begin{aligned} \sigma_r &= W \cos 2\theta \left(1 - \frac{a^2}{r^2}\right) \left(1 - \frac{3a^2}{r^2}\right) \\ \sigma_\theta &= -W \cos 2\theta \left(1 + \frac{3a^4}{r^4}\right) \\ \tau_{r\theta} &= -W \sin 2\theta \left(1 - \frac{a^2}{r^2}\right) \left(1 + \frac{3a^2}{r^2}\right) \end{aligned} \right\}, \quad (28)$$

where

$$W = \frac{(P_3 - P_1)}{2}. \quad (29)$$

In the above expressions,  $\tau_{r\theta}$  is the shear stress of a point in the surrounding rock of the roadway in polar coordinates, and  $\theta$  is the polar coordinate of this point.

4.1.3. *Theoretical Solution of Surrounding Rock Stress Field in Gas-Coal Roadway.* The first and second partial stress components are superimposed; that is, Equations (25) and (28) are added together to obtain the theoretical solution for

$$\left. \begin{aligned} \sigma'_r &= W \cos 2\theta \left(1 - \frac{a^2}{r^2}\right) \left(1 - \frac{3a^2}{r^2}\right) + \left(1 - \frac{a^2}{r^2}\right) S + \frac{Ta^2}{r^2} + \left[ \frac{v(1+n)(P_g - P_a)}{2} \left(1 - \frac{a^2}{r^2}\right) \right] \\ \sigma'_\theta &= -W \cos 2\theta \left(1 + \frac{3a^4}{r^4}\right) + \left(1 + \frac{a^2}{r^2}\right) S - \frac{Ta^2}{r^2} + \left[ \frac{v(1+n)(P_g - P_a)}{2} \left(1 + \frac{a^2}{r^2}\right) \right] \\ \tau_{r\theta} &= -W \sin 2\theta \left(1 - \frac{a^2}{r^2}\right) \left(1 + \frac{3a^2}{r^2}\right) \end{aligned} \right\}. \quad (30)$$

4.2. *Theoretical Solution of Stress Field in Plastic Zone of Rock Surrounding a Coal Roadway.* When the stress in the surrounding rock of the roadway is greater than the strength of the rock mass, the surrounding rock undergoes plastic

the elastic stress field of the surrounding rock of a gas-coal roadway under the condition of a nonuniform stress field. The specific expression is as follows:

deformation, and a plastic deformation zone appears in the surrounding rock from the free face of the roadway. At this time, the surrounding rock stress satisfies the Mohr-Coulomb yield criterion [19], namely,

$$\frac{(\sigma'_r - \sigma'_\theta)^2}{4} + \tau_{r\theta}^2 = \left[ \frac{(\sigma'_r + \sigma'_\theta)^2}{4} - c^2 \right] \frac{(1 - \cos 2\varphi)}{2} + \frac{(\sigma'_r + \sigma'_\theta)}{2} c \sin 2\varphi + c^2, \quad (31)$$

where  $c$  is the cohesion [MPa] and  $\varphi$  is the internal friction angle [°].

Let the boundary of the plastic zone be  $r$ , and set  $P_3 = \lambda P_1$ . Now, bringing Equation (31) into Equation (30), we can

derive the boundary stealth equation of the plastic zone of the circular roadway-surrounding rock around  $r, \theta$ , namely,

$$\begin{aligned} f(r, \theta) &= \left\{ P_1(\lambda - 1) \cos 2\theta \left(1 - \frac{2a^2}{r^2} + \frac{3a^4}{r^4}\right) - \frac{a^2(\lambda P_1 + P_1 - 2vP_g)}{r^2} + \frac{2a^2(P_i - vP_a)}{r^2} - \frac{a^2[(v(P_g - P_a)/1 - \mu) - 2vP_g]}{r^2} \right\}^2 \\ &+ \left[ P_1(\lambda - 1) \sin 2\theta \left(1 + \frac{2a^2}{r^2} - \frac{3a^4}{r^4}\right) \right]^2 - \frac{(1 - \cos 2\varphi)}{2} \left\{ \left[ P_1(\lambda + 1) - \frac{2P_1(\lambda - 1)a^2 \cos 2\theta}{r^2} - 4vP_g + \frac{v(P_g - P_a)}{1 - \mu} \right]^2 - 4c^2 \right\} \\ &- 2c \sin 2\varphi \left[ P_1(\lambda + 1) - \frac{2P_1(\lambda - 1)a^2 \cos 2\theta}{r^2} - 4vP_g + \frac{v(P_g - P_a)}{1 - \mu} \right] - 4c^2. \end{aligned} \quad (32)$$

The point at which  $f(r, \theta) = 0$  is the boundary line between the elastic zone and the plastic zone of the surrounding rock of the circular roadway, that is, the boundary equation of the plastic zone. If  $\lambda = 1$ , then the radius of the

plastic zone of the circular roadway-surrounding rock under the normal uniform stress field can be obtained from Equation (32) as

$$\begin{aligned} f(r, \theta) &= \left\{ \frac{2a^2(P_i - vP_a)}{r^2} - \frac{2a^2(P_1 - vP_g)}{r^2} - \frac{a^2[(v(P_g - P_a)/1 - \mu) - 2vP_g]}{r^2} \right\}^2 \\ &- \frac{(1 - \cos 2\varphi)}{2} \left\{ \left[ 2P_1 - 4vP_g + \frac{v(P_g - P_a)}{1 - \mu} \right]^2 - 4c^2 \right\} - 2c \sin 2\varphi \left[ 2P_1 - 4vP_g + \frac{v(P_g - P_a)}{1 - \mu} \right] - 4c^2. \end{aligned} \quad (33)$$



## 5. Factors Affecting the Theoretical Solution for the Plastic Zone Surrounding a Coal Roadway

We now analyze the influence of the lateral pressure coefficient, gas pressure, support strength, surrounding rock cohesion, and internal friction angle on the plastic zone boundary. According to Equation (32), the circular roadway is calculated using MATLAB, and the boundary of the surrounding rock plastic zone approximates a curve.

*5.1. Influence of Lateral Pressure Coefficient on Plastic Zone of Rock Surrounding a Coal Roadway.* Figure 3 shows the approximate curve of the plastic zone boundary of the circular roadway-surrounding rock under different lateral pressure coefficients, where  $P_1 = 19$  MPa,  $c = 3$  MPa,  $\varphi = 25^\circ$ ,  $\mu = 0.3$ ,  $a = 2$  m,  $P_i = 0$  MPa,  $P_a = P_g = 0$  MPa, and  $\nu = 0$ .

It can be seen from Figure 3 that when the lateral pressure coefficient is equal to 1, the distribution pattern of the surrounding plastic zone of the circular roadway-surrounding rock under the uniform stress field is circular. As the lateral pressure coefficient increases, the distribution pattern of the plastic zone changed from circular to elliptical, and then a rounded rectangle, before finally forming a butterfly shape with four symmetrical butterfly leaves. Once the plastic zone of the roadway forms a butterfly shape, further increases in the lateral pressure coefficient cause the four butterfly leaves in the plastic zone to expand.

To describe the relationship between the lateral pressure coefficient and the plastic zone range of the roadway-surrounding rock, the relationship between the lateral pressure coefficient  $\lambda$  and the effective radius (maximum radius, see Figure 4)  $R$  of the plastic zone is plotted in Figure 5. Larger values of the effective radius  $R$  result in more severe plastic failure of the surrounding rock in the direction of the radius. For ease of description, the plastic zone radii discussed below all refer to the effective radius.

It can be seen from Figure 5 that increasing the lateral pressure coefficient causes the radius of the plastic zone to increase. According to the difference in the growth rate of the radius of the plastic zone, the process can be divided into two stages. In the first stage, when the lateral pressure coefficient is small, the radius of the plastic zone increases slowly with respect to the lateral pressure coefficient in an approximately linear manner. The growth rate at this stage is less sensitive to changes in the lateral pressure coefficient. For example, when the lateral pressure coefficient increases from 1.6 to 1.9, the radius of the plastic zone only increases by 0.5 m. The distribution of the plastic zone at this stage mainly transitions from circular  $\rightarrow$  ellipse  $\rightarrow$  rounded rectangle.

As the lateral pressure coefficient continues to increase, the sensitivity of the plastic zone radius to the lateral pressure coefficient increases rapidly, and the growth rate of the plastic zone radius increases rapidly, entering the second stage. The growth mode of the radius of the plastic zone in the second stage is mainly manifested in the nonlinear growth of the butterfly leaves in the plastic zone, with the distribution of the plastic zone rapidly expanding in a

butterfly shape. For example, when the lateral pressure coefficient increases from 2.5 to 2.8, the radius of the plastic zone increases from 6.4 to 12.5 m. This demonstrates that the plastic yield failure of the surrounding rock mass in this range is extremely sensitive to the lateral pressure coefficient—even if the lateral pressure coefficient does not change by much, it may cause localized deformation and failure of the surrounding rock. Through field investigations and a literature search [20, 21], it is apparent that many underground roadways are in high-ground-stress areas with relatively large lateral pressure coefficients, leading to butterfly plastic zones around the roadways. The formation and nonlinear expansion of the butterfly plastic zone also theoretically proves that the two top and bottom corners of the roadway obtained from field investigations often suffer from shear deformation and failure. At the same time, it is clear that this type of roadway undergoes greater deformation than ordinary roadways and has features that are more difficult to control.

*5.2. Influence of Gas Pressure on Plastic Zone of Rock Surrounding a Coal Roadway.* Figure 6 shows approximate curves of the plastic zone boundary of the circular roadway-surrounding rock under different gas pressures, where  $P_1 = 19$  MPa,  $c = 3$  MPa,  $\varphi = 25^\circ$ ,  $\mu = 0.3$ ,  $a = 2$  m,  $P_i = 0$  MPa,  $P_a = 0$  MPa, and  $\nu = 0.5$ ; the other parameters are unchanged from the previous subsection.

It can be seen from Figures 6(a) and 6(b) that when the plastic zone of the surrounding rock of the roadway is circular or elliptical, that is, when the lateral pressure coefficient is small, changes in the gas pressure have little effect on the distribution pattern of the plastic zone. As shown in Figure 6(c), when the gas pressure is 7.0 MPa, the plastic zone of the roadway-surrounding rock presents an approximate butterfly shape, while the shape of the plastic zone when the gas pressure is reduced to 0.0 MPa is a rounded rectangle. That is, a reduction in the gas pressure can promote the transformation of the distribution form of the plastic zone from an approximate butterfly shape to a rounded rectangle. The plastic zone expands slightly in the horizontal direction as the gas pressure decreases, while the plastic zone remains almost unchanged in the vertical direction.

For the butterfly-shaped plastic zone, when the gas pressure is large, the four butterfly leaves are extremely sensitive to the gas pressure and rapidly degrade as the gas pressure decreases. The sensitivity of the butterfly leaves to the gas pressure in the plastic zone gradually weakens, and the nonlinear relationship between the two gradually changes to an approximately linear relationship, as shown in Figure 6(d). If the gas pressure decreases from 6.75 to 5.75 MPa, the radius of the plastic zone decreases rapidly from 10.3 m to 9.1 m. When the gas pressure decreases from 1.75 to 0.75 MPa, the plastic zone radius only decreases by 0.3 m, as shown in Figure 7.

*5.3. Influence of Cohesion on the Plastic Zone of Rock Surrounding a Coal Roadway.* Figure 8 shows approximate curves of the plastic zone boundary of the circular roadway-

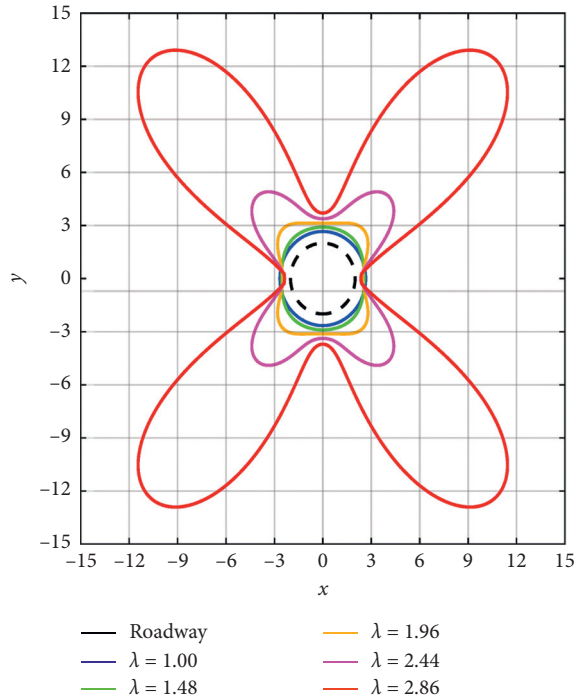


FIGURE 3: Distribution characteristics of plastic zone for various lateral pressure coefficients.

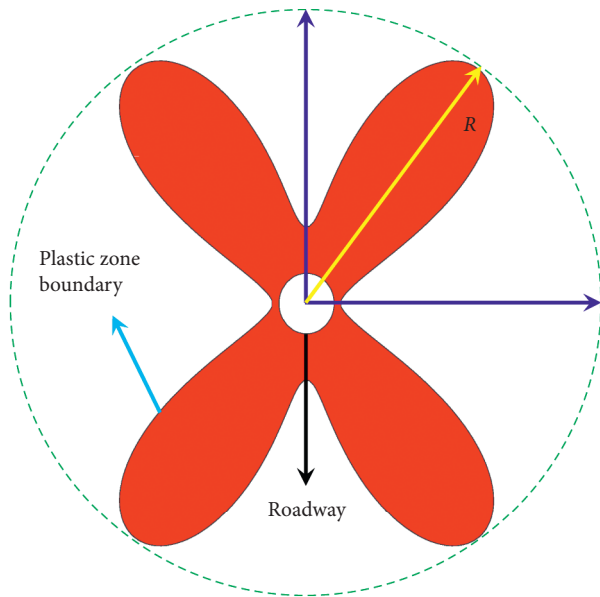


FIGURE 4: Effective radius of plastic zone.

surrounding rock under different cohesion forces, where  $P_1 = 19$  MPa,  $\varphi = 25^\circ$ ,  $\mu = 0.3$ ,  $a = 2$  m,  $P_i = 0$  MPa,  $P_a = P_g = 0$  MPa, and  $\nu = 0$ ; the other parameters remain unchanged.

Figures 8(a) and 8(b) indicate that the plastic zone of the surrounding rock of the roadway is circular or elliptical when the lateral pressure coefficient is small. In this case, the cohesion force has little influence on the distribution of the plastic zone, and the plastic zone maintains its original shape and slowly decreases in size as the cohesion increases. It is

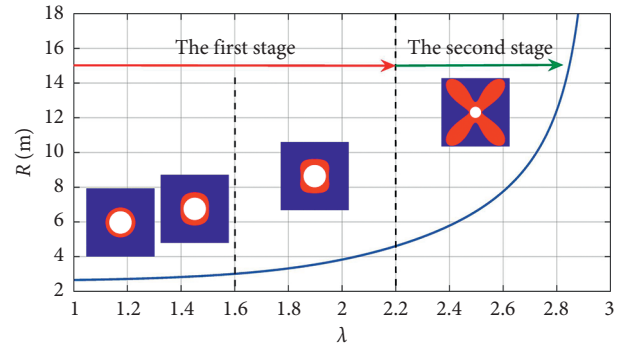


FIGURE 5: Variation of plastic zone radius with respect to the lateral pressure coefficient.

also clear from Figure 9 that the sensitivity of the plastic zone radius to cohesion is relatively weak, with an approximately linear decrease as the cohesion increases. For example, when the cohesion increases from 0.25 to 1.00 MPa, the radius of the plastic zone only decreases by 0.16 m.

Figure 8(c) shows that the plastic zone of the surrounding rock of the roadway exhibits an approximate butterfly shape when the cohesion is 0.25 MPa. The plastic zone shape when the cohesion increases to 4.00 MPa is a rounded rectangle; that is, an increase in the cohesive force promotes the transformation of the plastic zone from an approximate butterfly to a rounded rectangle. At this stage, the rate of decrease of the plastic zone distribution is different. The four sharp corners of the plastic zone exhibit the fastest rate of decrease, followed by the vertical extent of the plastic zone, with the horizontal extent of the plastic zone exhibiting the smallest rate of decrease.

When the surrounding rock of the roadway presents a butterfly-shaped plastic zone, as shown in Figure 8(d), the four butterfly leaves in the plastic zone are extremely sensitive to cohesion, when the cohesive force is small, and rapidly degrade as the cohesion increases. As the cohesive force continues to increase, the sensitivity of the butterfly leaves to the cohesive force in the plastic zone gradually weakens, and the nonlinear relationship between the two gradually changes to an approximately linear relationship. If the cohesion increases from 0.25 to 1.00 MPa, the radius of the plastic zone decreases rapidly from 18.04 m to 12.86 m. When the cohesion increases from 10.00 to 10.75 MPa, the plastic zone radius only decreases by 0.08 m, as shown in Figure 9.

**5.4. Influence of Internal Friction Angle on Plastic Zone of Rock Surrounding a Coal Roadway.** Figure 10 shows approximate curves of the plastic zone boundary of the circular roadway-surrounding rock under different internal friction angles, where  $P_1 = 19$  MPa,  $c = 3$  MPa,  $\mu = 0.3$ ,  $a = 2$  m,  $P_i = 0$  MPa,  $P_a = P_g = 0$  MPa, and  $\nu = 0$ ; the other parameters remain unchanged.

Figure 10 has a similar pattern to that in Figure 8. As shown in Figures 10(a) and 10(b), the internal friction angle has little effect on the distribution of the circular or elliptical plastic zone, and the plastic zone maintains its original shape

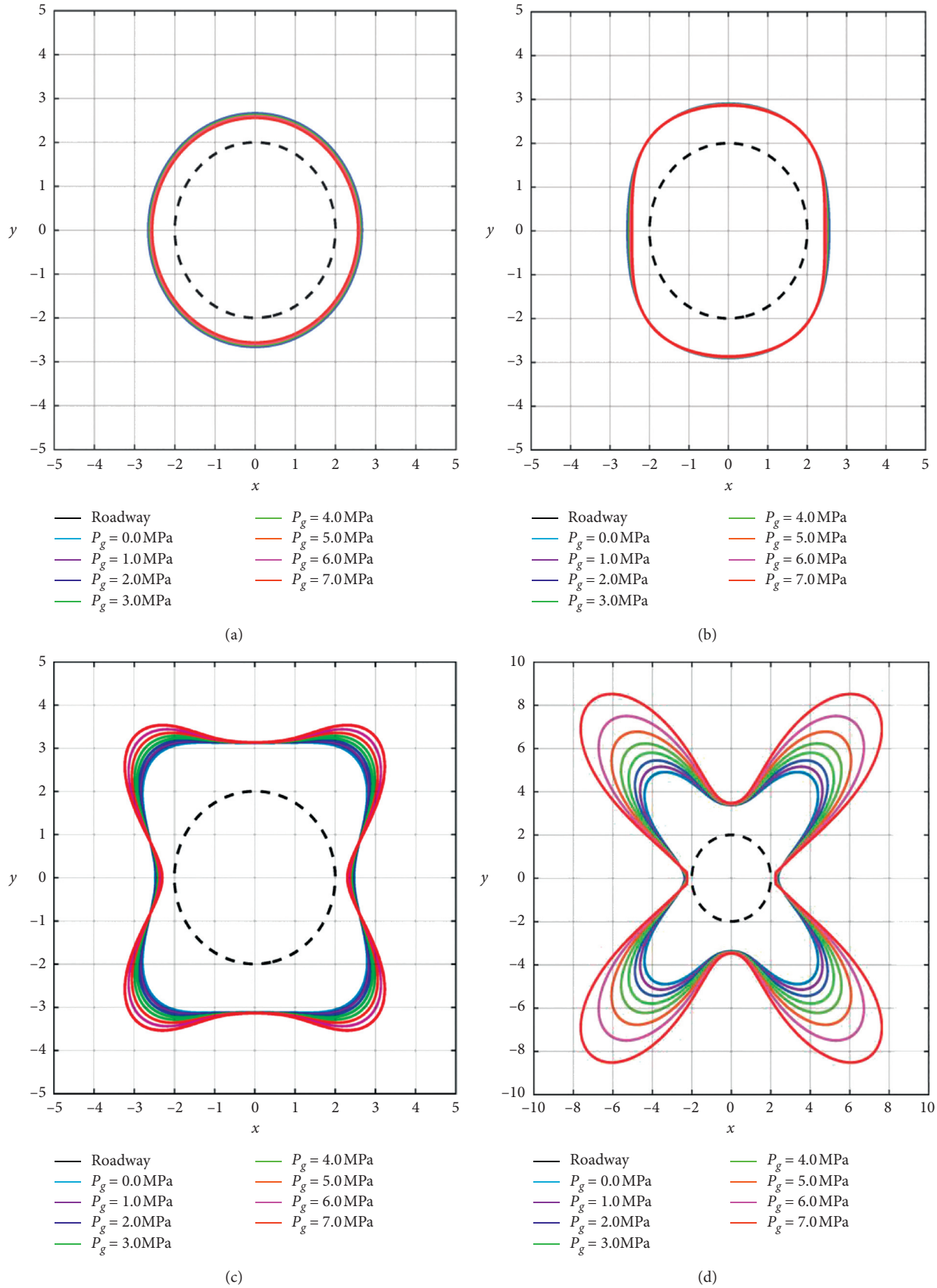


FIGURE 6: Distribution of plastic zone for various gas pressures. (a)  $\lambda = 1.00$ . (b)  $\lambda = 1.48$ . (c)  $\lambda = 1.96$ . (d)  $\lambda = 2.44$ .

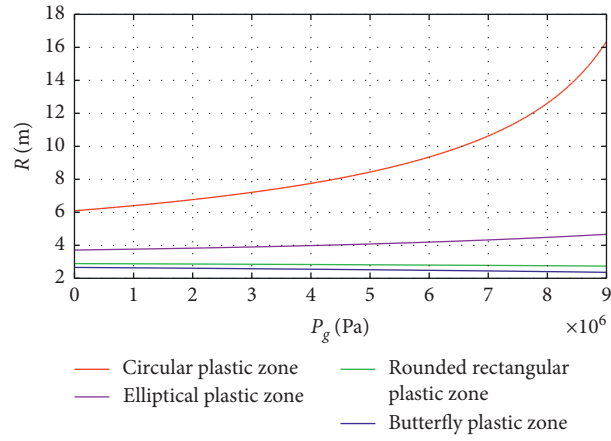


FIGURE 7: Variation of plastic zone radius with respect to gas pressure.

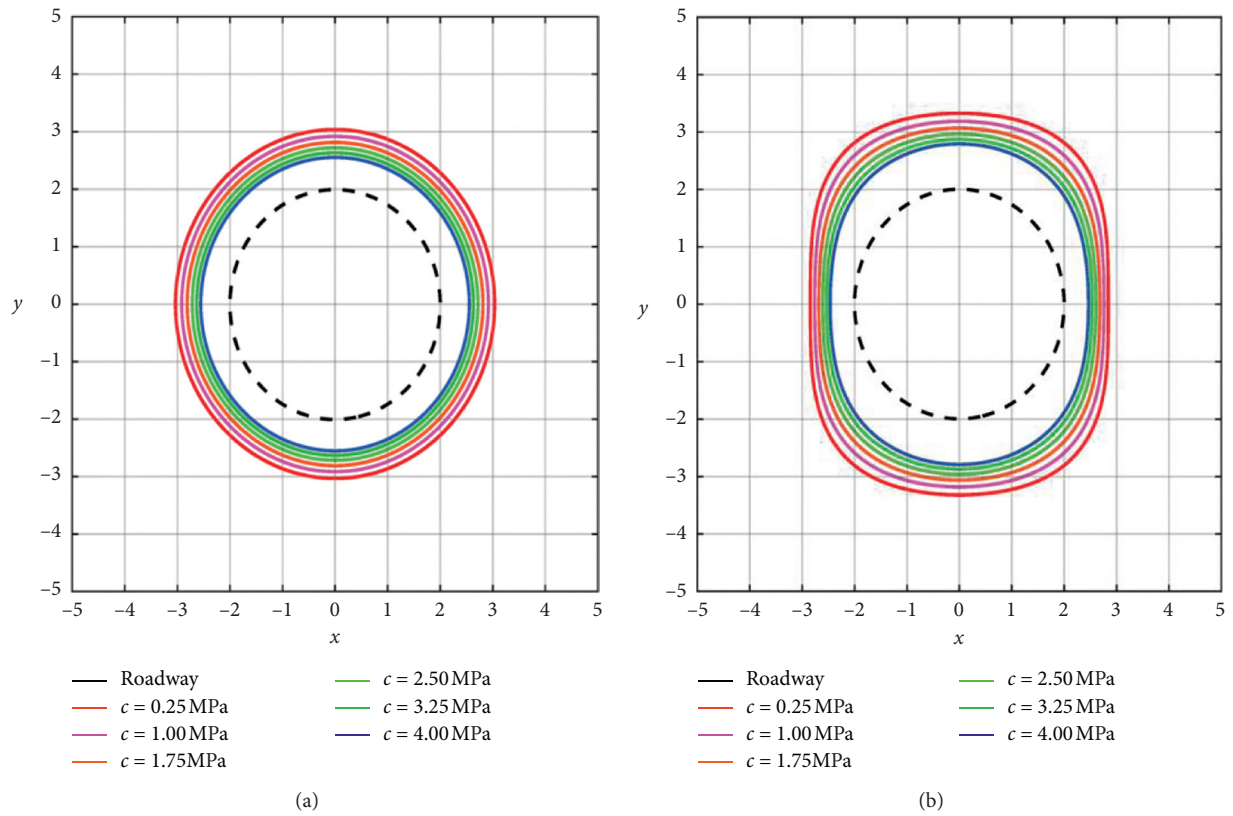


FIGURE 8: Continued.

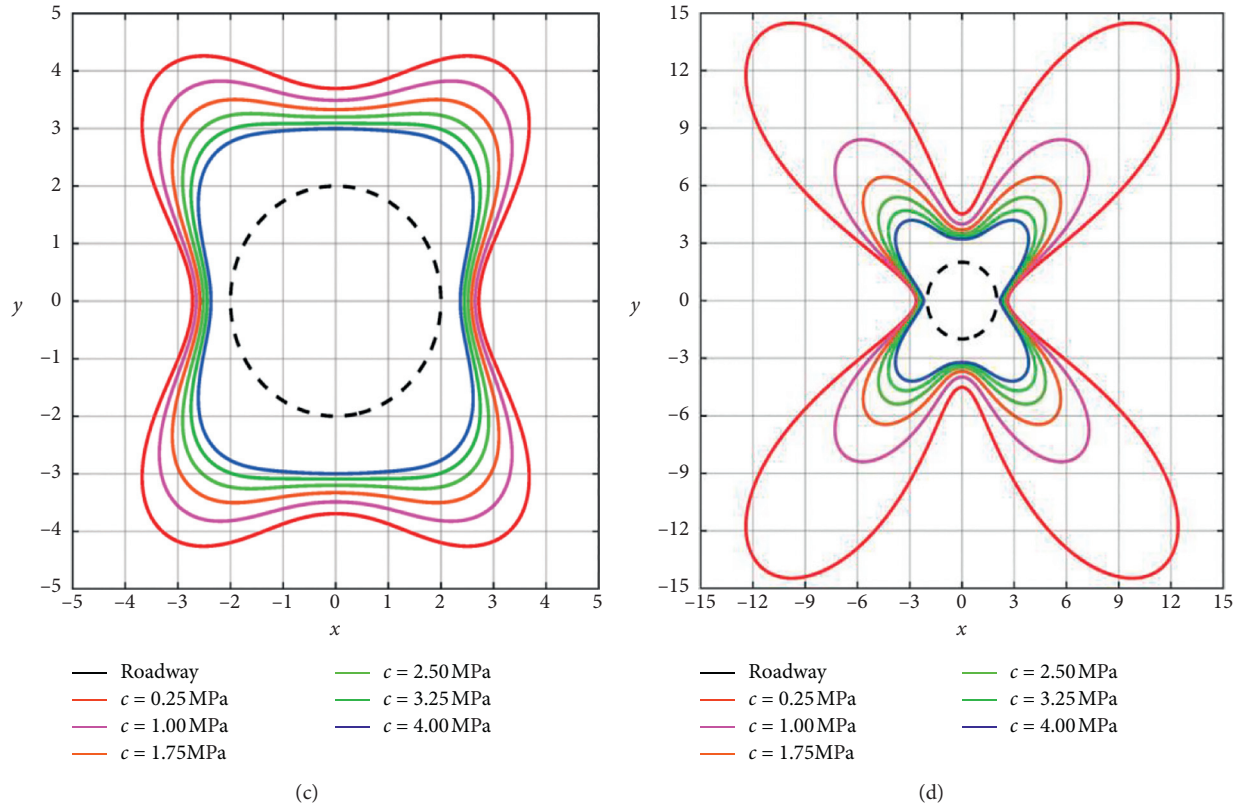


FIGURE 8: Distribution of plastic zone for various cohesive forces. (a)  $\lambda = 1.00$ . (b)  $\lambda = 1.48$ . (c)  $\lambda = 1.96$ . (d)  $\lambda = 2.44$ .

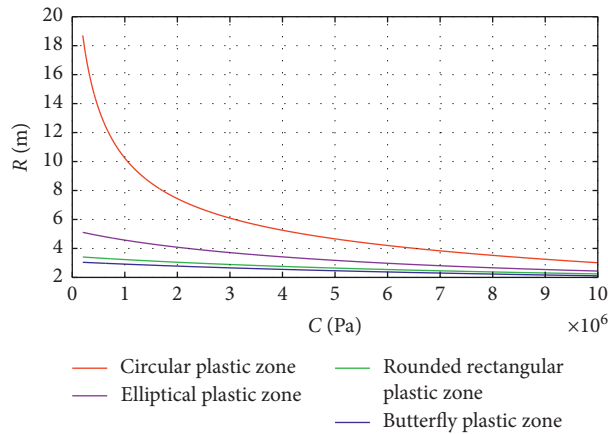


FIGURE 9: Change of radius of plastic zone with respect to cohesion.

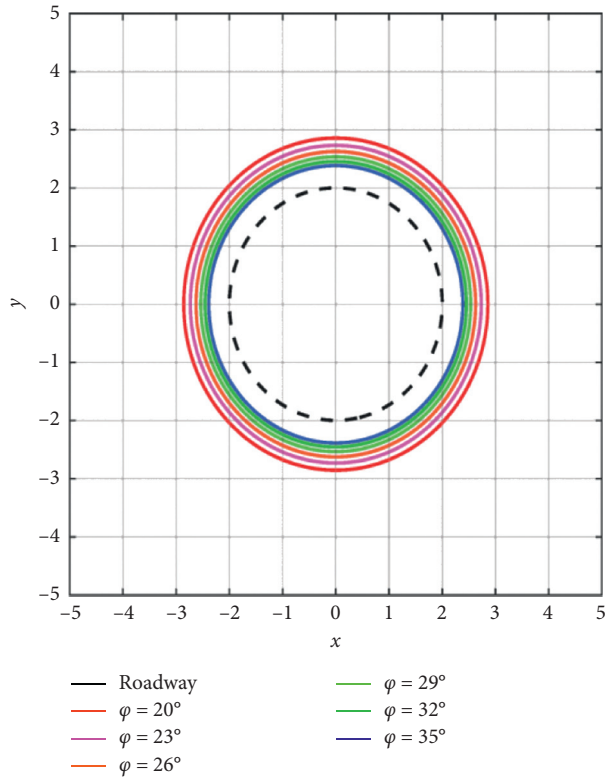
and slowly decreases in size as the internal friction angle increases. The sensitivity of the radius of the plastic zone to the internal friction angle is also relatively weak and tends to decrease linearly as the internal friction angle increases. For example, with  $\lambda = 1.48$ , the radius of the plastic zone only decreases by 0.20 m when the internal friction angle increases from 20 to 23°, as shown in Figure 11.

It is apparent from Figure 10(c) that when the plastic zone of the surrounding rock of the roadway is rectangular with rounded corners, a continuous increase in the internal friction angle promotes the transformation to an elliptical plastic zone, whereas a continuous reduction promotes the

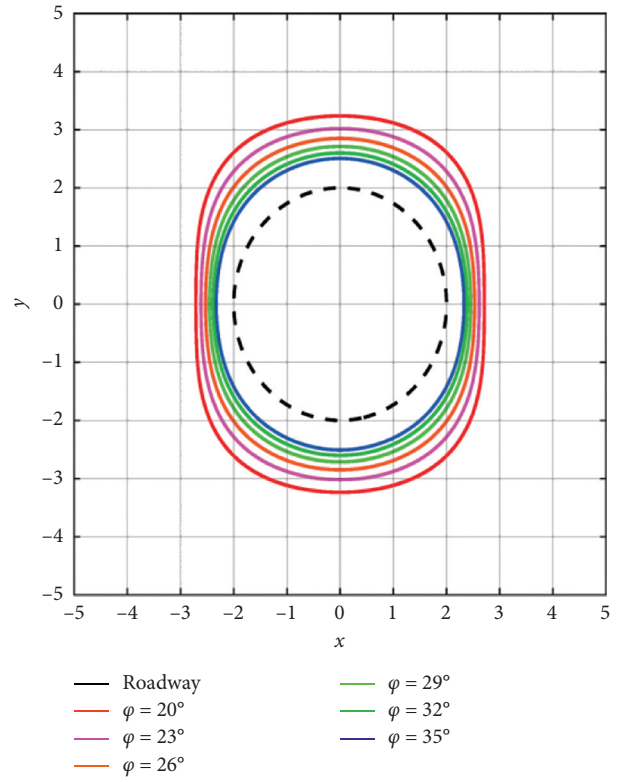
transformation to an approximate butterfly shape. For example, when the internal friction angle is 26°, the plastic zone is rectangular with rounded corners. When this value increases to 35°, the shape of the plastic zone becomes elliptical, and when it decreases to 20°, the shape of the plastic zone is an approximate butterfly. In addition, the rate of change of each part of the plastic zone distribution is different. The four sharp corners change the fastest, followed by the vertical extent of the plastic zone, and finally the horizontal extent of the plastic zone.

When the surrounding rock of the roadway presents a butterfly-shaped plastic zone, as shown in Figure 10(d), the

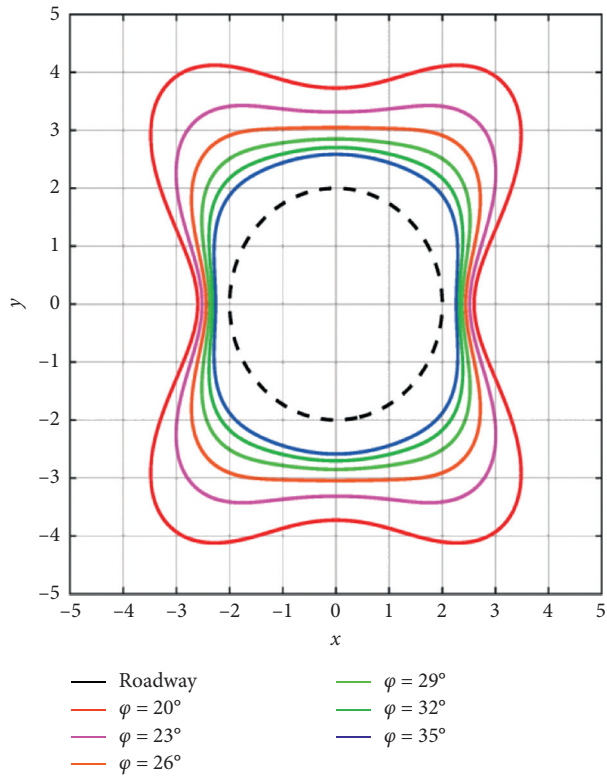




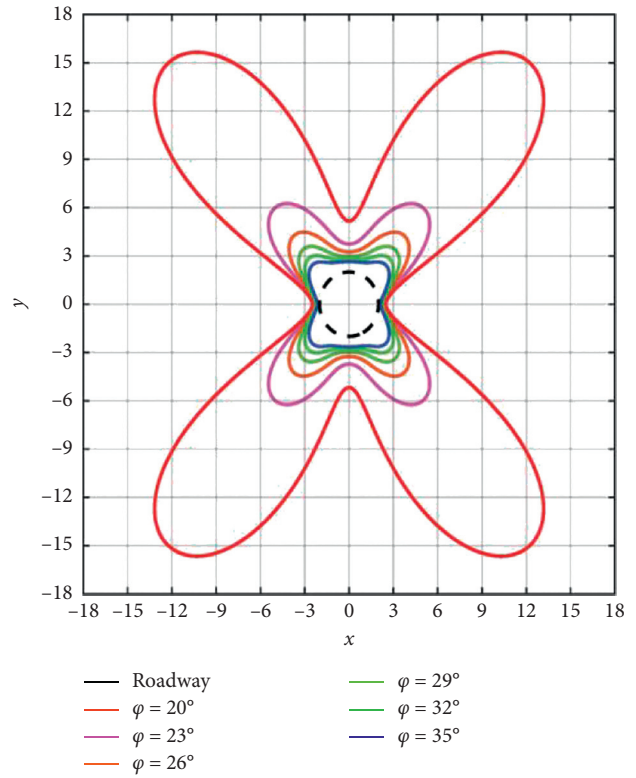
(a)



(b)



(c)



(d)

FIGURE 10: Plastic zone distribution characteristics for various internal friction angles. (a)  $\lambda = 1.00$ . (b)  $\lambda = 1.48$ . (c)  $\lambda = 1.96$ . (d)  $\lambda = 2.44$ .

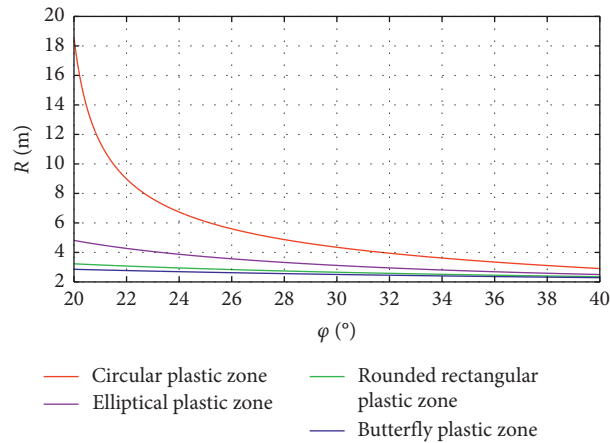


FIGURE 11: Variation of the radius of the plastic zone with respect to the friction angle.

four butterfly leaves in the plastic zone are extremely sensitive to the internal friction angle, when this angle is small, and degrade rapidly as the internal friction angle increases. With the continuous increase of the internal friction angle, the sensitivity of the butterfly blades in the plastic zone to the internal friction angle gradually weakens, and the nonlinear relationship between the two gradually becomes an approximately linear relationship. If the internal friction angle increases from 20 to 23°, the radius of the plastic zone decreases from 19.35 m to 7.80 m, whereas an increase from 45 to 48° only reduces the radius by 0.16 m, as shown in Figure 11.

**5.5. Influence of Support Strength on Plastic Zone of Rock Surrounding a Coal Roadway.** Figure 12 shows approximate curves of the plastic zone boundary of the circular roadway-surrounding rock under different supporting strengths, where  $P_1 = 19$  MPa,  $c = 3$  MPa,  $\mu = 0.3$ ,  $a = 2$  m,  $\phi = 25^\circ$ ,  $P_a = P_g = 0$  MPa, and  $\nu = 0$ ; the other parameters remain unchanged.

Figures 12 and 13 show that when the mechanical properties and stress environment of the surrounding rock of the roadway are constant, increasing the support strength at the free face of the roadway has a limited effect on the distribution and range of the plastic zone. The radius of the plastic zone decreases as the support strength increases, but the rate of decrease is extremely slow. For example, when  $\lambda = 2.44$ , the radius of the plastic zone only decreases by 0.1 m when the support strength increases from 0.0 to 5.0 MPa. It must be emphasized that the support strength discussed in this article refers to the support strength for the free face of the roadway. Its function is mainly to prevent the deformation of the roadway-surrounding rock and the expansion of the plastic zone, rather than to change the strength of the roadway-surrounding rock mass. The main functions in underground engineering are for shotcrete support, masonry support, steel arch support, and so on. Therefore, for

the control of gas-coal roadways, it is necessary to increase the support strength and to increase the strength of the surrounding rock mass, thereby restraining the expansion of the plastic zone and ensuring the normal use of gas-coal roadways.

## 6. Discussion

The theoretical analysis presented in the previous section has found that the plastic zone of the surrounding rock of a roadway mainly has four distribution patterns: circular, elliptical, rounded rectangle, and butterfly. The lateral pressure coefficient, gas pressure, surrounding rock cohesion, and internal friction angle all affect the distribution and range of the plastic zone of the surrounding rock of the roadway. For the support problem of high-gas-coal roadway-surrounding rock, targeted support should be designed according to the shape and range of the plastic zone. The length of the anchor rod and the anchor cable must be greater than the range of the plastic zone, thus reinforcing the support of the leaves of butterfly-shaped plastic zones, reducing the gas pressure, and improving the strength and overall stability of the surrounding rock mass.

The research results presented in this paper will contribute to the improvement of gas drainage efficiency. The plastic zone effectively increases the permeability of high-gas-coal seams, and the plastic zone is the main channel for gas flow. When there is a butterfly-shaped plastic zone in the coal seam, the distance between the drainage boreholes should be designed scientifically and reasonably. The butterfly blades in the plastic zone between the drainage boreholes should be connected to each other to avoid the appearance of blind areas. When there is a nonbutterfly plastic zone in the coal seam, its range can be expanded by means of hydraulic fracturing and blasting fracturing, thereby increasing the permeability of the coal seam and increasing the gas drainage rate.

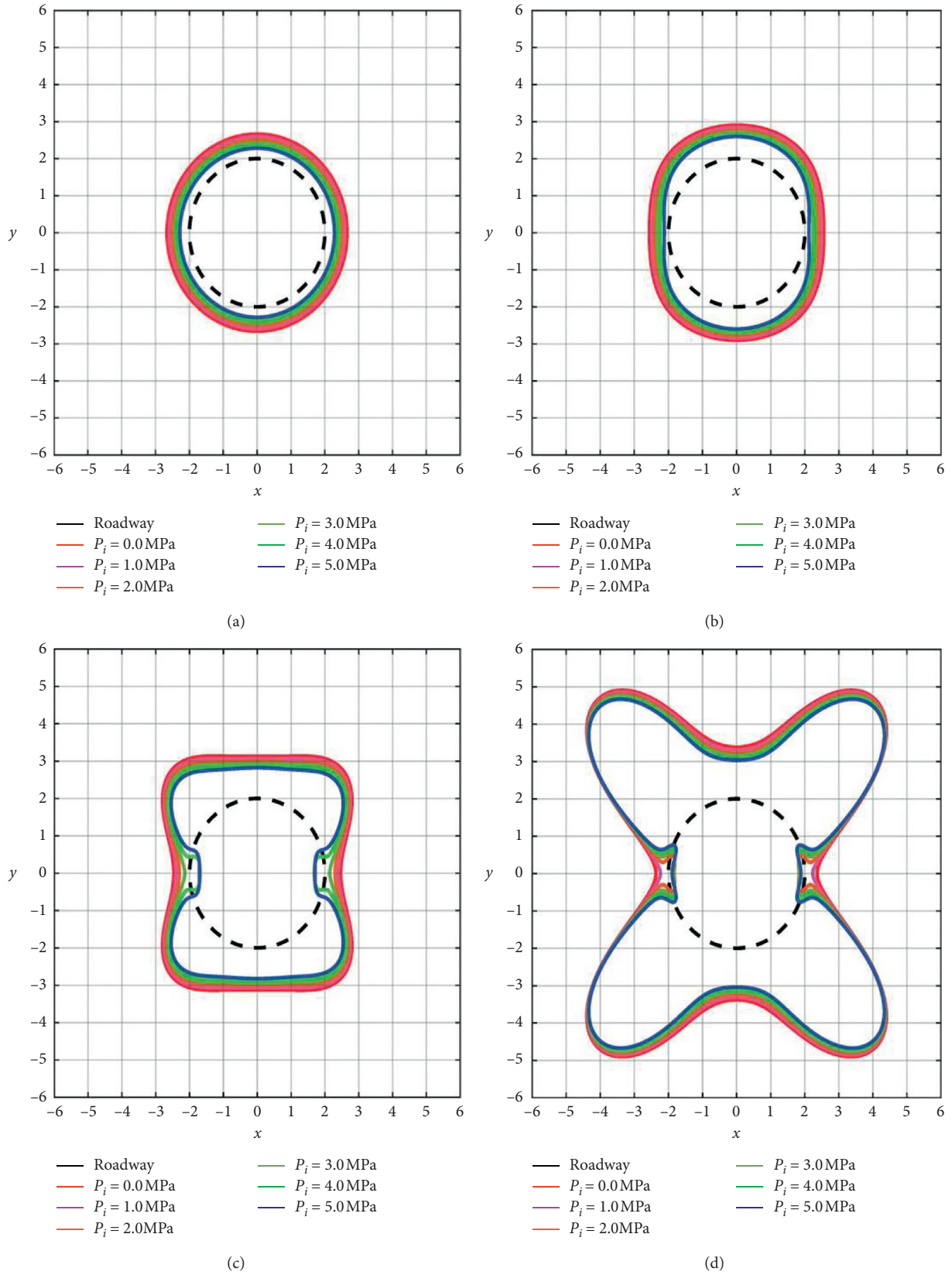


FIGURE 12: Relationship between tunnel radius and shape of plastic zone. (a)  $\lambda = 1.00$ . (b)  $\lambda = 1.48$ . (c)  $\lambda = 1.96$ . (d)  $\lambda = 2.44$ .

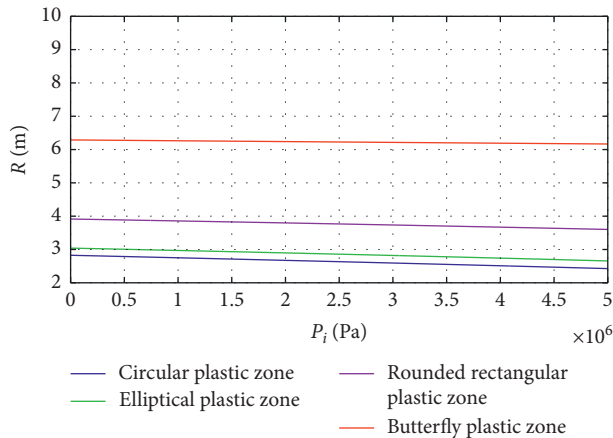


FIGURE 13: Relationship between tunnel radius and radius of plastic zone.

## 7. Conclusions

- (1) The implicit equation for the boundary of the plastic zone in the surrounding rock of a gas-coal roadway has been obtained, and the plastic zone was found to have four main distribution patterns: circular, elliptical, rounded rectangle, and butterfly.
- (2) Circular and elliptical plastic zones are less sensitive to gas pressure, cohesion, and internal friction angle, whereas butterfly-shaped plastic zones are extremely sensitive to these variables. The main manifestation is that the four butterfly leaves rapidly degenerate as the gas pressure decreases or as the cohesion and internal friction angle increase; larger butterfly leaves tend to degenerate faster.
- (3) The rounded rectangle is a transitional plastic zone between the butterfly and elliptical plastic zones. Changes in gas pressure, cohesion, and internal friction angle can all promote the transformation of the rounded rectangular plastic zone to the butterfly-shaped plastic zone or the elliptical plastic zone.
- (4) The support strength at the roadway free face has a limited impact on the plastic zone. The support strength does not change the distribution of the plastic zone but does affect its range.

## Data Availability

All the data generated or published during the study are included within the article; no other data were used to support this study.

## Conflicts of Interest

The authors declare that they have no conflicts of interest regarding the publication of this paper.

## Acknowledgments

This work was financially supported by the National Natural Science Foundation of China (Grant nos. 51804109,

51874130, 51974118, and 51774133). The authors are grateful for this financial support.

## References

- [1] J. F. Cui, W. J. Wang, C. Yuan, L. M. Cao, Y. N. Guo, and L. Fan, "Study on deformation mechanism and supporting countermeasures of compound roofs in loose and weak coal roadways," *Advances in Civil Engineering*, vol. 2020, Article ID 8827490, 13 pages, 2020.
- [2] C. Yuan, Y. N. Guo, W. J. Wang, L. M. Cao, L. Fan, and C. Huang, "Study on "triaxial loading-unloading-uniaxial loading" and microscopic damage test of sandstone," *Frontiers in Earth Science*, vol. 8, p. 11, 2020.
- [3] L. Jiang, A. Sainoki, H. S. Mitri, N. Ma, H. Liu, and Z. Hao, "Influence of fracture-induced weakening on coal mine gateroad stability," *International Journal of Rock Mechanics and Mining Sciences*, vol. 88, pp. 307–317, 2016.
- [4] C. Yuan, L. Fan, J. F. Cui, and W. J. Wang, "Numerical simulation of the supporting effect of anchor rods on layered and nonlayered roof rocks," *Advances in Civil Engineering*, vol. 2020, Article ID 4841658, 14 pages, 2020.
- [5] M. R. Zareifard and A. Fahimifar, "Analytical solutions for the stresses and deformations of deep tunnels in an elastic-brittle-plastic rock mass considering the damaged zone," *Tunnelling and Underground Space Technology*, vol. 58, pp. 186–196, 2016.
- [6] N. J. Ma, J. Li, and Z. Q. Zhao, "Distribution of the deviatoric stress field and plastic zone in circular roadway surrounding rock," *Journal of China University of Mining and Technology*, vol. 44, no. 2, pp. 206–213, 2015.
- [7] C. C. Xia, C. Xu, Y. P. Liu, and C. L. Han, "Elastoplastic solution of deep buried tunnel considering strain-softening characteristics based on GZZ strength criterion," *Chinese Journal of Rock Mechanics and Engineering*, vol. 37, pp. 2468–2477, 2018.
- [8] Z. H. Zhao, Y. L. Tan, S. J. Chen, Q. Ma, and X. J. Gao, "Theoretical analyses of stress field in surrounding rocks of weakly consolidated tunnel in a high-humidity deep environment," *International Journal of Rock Mechanics & Mining Sciences*, vol. 122, p. 11, Article ID 104064, 2019.
- [9] X. Liu, Q. Fang, D. L. Zhang, and Y. Liu, "Energy-based prediction of volume loss ratio and plastic zone dimension of shallow tunnelling," *Computers and Geotechnics*, vol. 118, p. 13, Article ID 103343, 2020.
- [10] X. P. Zhou and J. L. Li, "Hoek-Brown criterion applied to circular tunnel using elastoplasticity and in situ axial stress," *Theoretical and Applied Fracture Mechanics*, vol. 56, no. 2, pp. 95–103, 2011.
- [11] Y. C. Ma, A. Z. Lu, X. T. Zeng, and H. Cai, "Analytical solution for determining the plastic zones around twin circular tunnels excavated at great depth," *International Journal of Rock Mechanics & Mining Sciences*, vol. 136, p. 14, Article ID 104475, 2020.
- [12] H. Zhou, J. Gao, K. Han, and Y. Cheng, "Permeability enhancements of borehole outburst cavitation in outburst-prone coal seams," *International Journal of Rock Mechanics and Mining Sciences*, vol. 111, pp. 12–20, 2018.
- [13] W. Zhao, K. Wang, Y. Ju et al., "Influence of the roadway exposure time on the accuracy of gas content measurements in reconstructed and extended mines," *Process Safety and Environmental Protection*, vol. 142, pp. 109–117, 2020.
- [14] T. Liu, B. Lin, X. Fu, and C. Zhu, "Modeling air leakage around gas extraction boreholes in mining-disturbed coal

- seams,” *Process Safety and Environmental Protection*, vol. 141, pp. 202–214, 2020.
- [15] Y. Zhang, Q. Zou, and L. Guo, “Air-leakage model and sealing technique with sealing-isolation integration for gas-drainage boreholes in coal mines,” *Process Safety and Environmental Protection*, vol. 140, pp. 258–272, 2020.
- [16] J.-Z. Zhang, X.-P. Zhou, and P. Yin, “Visco-plastic deformation analysis of rock tunnels based on fractional derivatives,” *Tunnelling and Underground Space Technology*, vol. 85, pp. 209–219, 2019.
- [17] M.-F. Xu, S.-C. Wu, Y.-T. Gao, J. Ma, and Q.-L. Wu, “Analytical elastic stress solution and plastic zone estimation for a pressure-relief circular tunnel using complex variable methods,” *Tunnelling and Underground Space Technology*, vol. 84, pp. 381–398, 2019.
- [18] E. Kabwe, M. Karakus, and E. K. Chanda, “Proposed solution for the ground reaction of non-circular tunnels in an elastic-perfectly plastic rock mass,” *Computers and Geotechnics*, vol. 119, p. 15, Article ID 103354, 2019.
- [19] Z. L. Xu, *Concise Course of Elasticity*, Higher Education Press, Beijing, China, 4th edition, 2013.
- [20] P. Li and S. J. Miao, “Analysis and application of in-situ stress in metal mining area of Chinese mainland,” *Chinese Journal of Engineering*, vol. 39, no. 3, pp. 323–334, 2017.
- [21] W. Yu, B. Pan, F. Zhang, S. Yao, and F. Liu, “Deformation characteristics and determination of optimum supporting time of alteration rock mass in deep mine,” *KSCE Journal of Civil Engineering*, vol. 23, no. 11, pp. 4921–4932, 2019.



## Research Article

# Study on Pressure Relief Effect of Rock Mass with Different Borehole Parameters

Chao Peng <sup>1,2</sup> and Wanrong Liu <sup>1</sup>

<sup>1</sup>School of Architecture & Civil Engineering, Liaocheng University, Liaocheng, Shandong 252059, China

<sup>2</sup>School of Emergency Management and Safety Engineering, China University of Mining & Technology (Beijing), Haidian, Beijing 100083, China

Correspondence should be addressed to Wanrong Liu; wanrongliu1989@163.com

Received 1 February 2021; Revised 15 February 2021; Accepted 22 February 2021; Published 8 March 2021

Academic Editor: Zizheng Zhang

Copyright © 2021 Chao Peng and Wanrong Liu. This is an open access article distributed under the Creative Commons Attribution License, which permits unrestricted use, distribution, and reproduction in any medium, provided the original work is properly cited.

Rock burst is one of the disaster accidents that can easily happen in rock cavern engineering. At present, one of the most commonly used methods to control rock burst is borehole pressure relief technology. In this paper, the influence of drilling layout schemes on the pressure relief effect of surrounding rock mass is systematically studied. The research results show that the strength reduction degree, AE evolution characteristics, failure modes of rock samples with different borehole positions, boreholes spacing, boreholes dip angles, and boreholes layout forms are different. The strength reduction degree of rock sample with an inclined arrangement form is the largest, followed by the arrangement form being up three-flower layout or down three-flower layout. Using the inclined layout and three-flower layout can achieve better pressure relief effect of the surrounding rock mass. The research results are beneficial to the rock burst of surrounding rock of the cavern. The acoustic emission can effectively monitor the stability of the surrounding rock of the cavern. However, the threshold value and the occurrence time of the acoustic emission of the cavern instability changed after the cavern surrounding rock is drilled holes. If the borehole is arranged at the surrounding rock mass, the occurrence time of the cavern instability may be advanced.

## 1. Introduction

With the rapid development of economy and technology as well as the increase of population, the underground rock cavern engineering has made great progress. However, as the development scale and depth increase, the frequency and intensity of rock burst and other surrounding rock dynamic disasters are also increasing, which seriously affects the safety construction and operation of cavern engineering. For the deep surrounding rock with rockburst tendency, one of the most commonly used methods to control rockburst risk is borehole pressure relief technology [1–5]. The borehole pressure relief technology is to form a weakening area in the deep part of the rock mass by means of the boreholes, to provide a release space for the accumulated energy in the rock mass, and to promote the peak value of stress concentration to transfer to the deep part of the rock mass, so as to reduce the risk of rock burst.

In the aspect of drilling pressure relief technology research, Liu et al. [3] used laboratory test, numerical simulation, and theoretical method and analyzed the mechanism of boreholes to prevent rockburst, and the research results show that the borehole spacing is a function of borehole diameter, thickness of coal seam, increasing overflow coefficient, and safety increasing variables and is also related to increasing overflow coefficient and borehole diameter. Yi et al. [6] used FLAC numerical simulation to analyze the pressure relief effect of large-diameter drilling in soft and hard coal seam; the research results show that the pressure relief effect of drilling in soft rock is better than that in hard rock. Li et al. [7] analyzed the safety parameters of the pressure relief drilling in the dangerous coal seam and found that the larger the hole diameter of the pressure relief drilling, the better the pressure relief effect. There is a critical value for the spacing of the pressure relief drilling; when the holes spacing is less than the critical value, the coal body between the two holes will be

damaged and deformed to a greater extent, and the pressure relief effect will be good. Zhang et al. [8], based on actual geologic conditions in the area of a rock burst that occurred in the Yangcheng Mine, conducted a series of experimental studies on mechanical properties using gypsum-type coal-like materials with different numbers and configurations of pressure relief boreholes. Other scholars also conducted drilling holes to relieve pressure on coal and rock and guided certain engineering practices [9–11]. The results show that the larger the drilling density, the more the rock fracture development around the boreholes, and the greater the energy release and, hence, the more effective the relief effect. These researches are of great significance to alleviate the rock burst risk of surrounding rock of cavern; however, there are few systematic researches on the influence of drilling layout schemes on the pressure relief effect.

Based on the above research, this paper studies the influence of drilling layout schemes on the pressure relief effect of surrounding rock mass. Firstly, the rock models of different drilling layout schemes are established by means of particle flow code (PFC); secondly, the influences of different borehole positions, boreholes spacing, boreholes dip angles, and boreholes layout forms on the strength reduction characteristics, acoustic emission evolution characteristics, and failure modes of rock samples are analyzed. The research results are beneficial to the rock burst of surrounding rock of the cavern.

## 2. Numerical Test Scheme

**2.1. Particle Flow Code (PFC) Theory.** The particle flow code theory was firstly introduced by Cundall and Strack [12] based on discrete element method. The basic compositions of the PFC model are particles and bonds, and the geometrical and mechanical properties of the particles and bonds determined the macroscopic mechanical properties of the models [13]. The bonded contact constitutive model was widely used in numerical simulation of rock and soil materials [14–17]. There are two kinds of modes of the bonds, named contact bond and parallel bond. The contact bonding is point contact; it can only transfer force, but not force moment. The contact position of the parallel bond model is a rectangular section, as shown in Figure 1, which can transfer both force and moment. Therefore, the parallel bond model is more suitable for the simulation of rock materials.

The contact force of parallel bond particles can be expressed by the following formula:

$$\bar{F}_i = \bar{F}_i^n + \bar{F}_i^s, \quad (1)$$

where  $\bar{F}_i^s$  is the shear contact force and  $\bar{F}_i^n$  is the normal contact force.

In the process of calculation, no matter it is normal force, shear force, or moment, the increment will be generated. The increment in each time step is expressed as [13]

$$\begin{cases} \Delta \bar{F}_i^n = (-\bar{k}^n A \Delta U^n) n_i, \\ \Delta \bar{F}_i^s = -\bar{k}^s A \Delta U_i^s, \\ \Delta \bar{M}_3 = -\bar{k}^n I \Delta \theta_3, \end{cases} \quad (2)$$

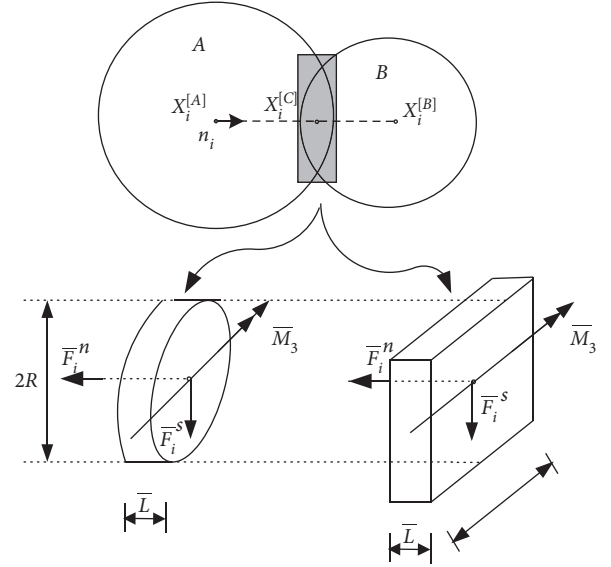


FIGURE 1: Parallel bond models [13].

where  $\bar{k}^n$  is the normal stiffness and  $\bar{k}^s$  is the shear stiffness.  $n_i$  is the normal vector of the contact point.  $A$  is the area of the parallel bond surface.  $\bar{M}$  is the moment. During the calculation, the force and moment are continuously updated for each iteration, until the specified balance condition is reached, the calculation stopped, and the new force and moment expressions are as follows:

$$\begin{cases} \bar{F}_i^n \leftarrow \bar{F}_i^n + \Delta \bar{F}_i^n, \\ \bar{F}_i^s \leftarrow \bar{F}_i^s + \Delta \bar{F}_i^s, \\ \bar{M}_3 \leftarrow \bar{M}_3 + \Delta \bar{M}_3. \end{cases} \quad (3)$$

During the calculation process, when the external force exceeds the normal bond strength or the shear bond strength of the parallel bond, the parallel bond will break, and then tension or shear crack will occur.

**2.2. Model Parameter Checking.** Usually, the micro-parameters of PFC rock models are calibrated by simulating the uniaxial compression experiments [14]. During the process of calibration, the microparameters of the particles and bonds are adjusted many times through “trial-and-error” method [13] until these parameters can better reflect the mechanical properties of the real rocks. In this manuscript, the model parameters were checked with a sandstone based on “trial-and-error” method. Through repeated trial and error, the parameters in Table 1 can simulate the sandstone well, as shown in Figures 2 and 3. It can be seen that the elastic modulus ( $E$ ) and uniaxial compressive strength (UCS) of the numerical simulation are basically consistent with the experimental test of the sandstone. However, the stress-strain curves of laboratory tests and numerical simulations showed a certain deviation at the beginning. The main reason is that the indoor samples contain original cracks.

TABLE 1: Physicomechanical parameters of numerical test model.

Parameter	Value
Minimum particle diameter (mm)	0.3
Maximum particle diameter (mm)	0.5
Parallel bond tensile strength (MPa)	22
Parallel bond cohesive force (MPa)	56.5
Stiffness ratio	1.51
Contact bond gap (mm)	0.05
Density ( $\text{kg/m}^3$ )	2500
Contact modulus of the particle (GPa)	10.2
Parallel bond deformation modulus (GPa)	16.2
Porosity	0.1

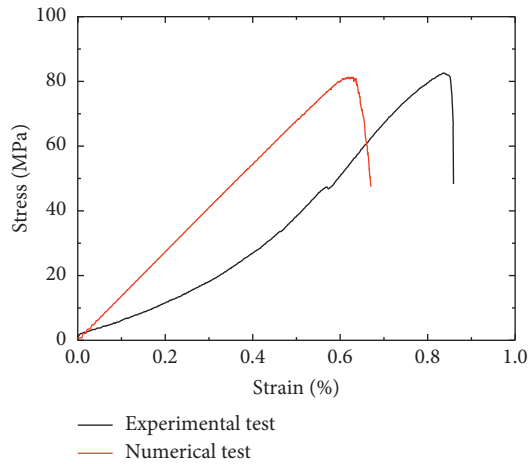


FIGURE 2: Stress-strain curves of sandstone based on experimental and numerical tests.

**2.3. Test Schemes.** In order to systematically explore the influence of drilling layout schemes on the pressure relief effect of rock burst prone surrounding rock mass, this paper considered the following four simulation schemes according to the actual drilling characteristics. The size of these models is 50 mm (width)  $\times$  100 mm (height) and the parameters of them is the same as in Table 1. The process of establish the models is as follows: (1) establish complete rock models, which have the same particle distribution form and the same mechanical properties; (2) according to the test schemes, delete some particles to simulation drilling holes, and all the drilling holes have the same diameter of 6 mm.

**2.3.1. Models of Different Borehole Locations.** Because the height of the cavern is known in the actual engineering, the ratio ( $R$ ) of the borehole height ( $h$ ) to the tunnel height ( $H$ ) is used to determine the location of the borehole quantitatively, and it is defined as borehole height ratio. In order to study the influence of borehole location on the pressure relief effect of cavern surrounding rock mass, numerical models of different borehole location are established, as shown in Figure 4. The borehole height ratio  $R$  ( $=h/H$ ) are considered as 0.1, 0.3, 0.5, 0.7, and 0.9, respectively.

**2.3.2. Models of Different Boreholes Spacing.** In order to study the influence of boreholes spacing  $S$  on the pressure relief effect of cavern surrounding rock mass, rock models with double boreholes were established (as shown in Figure 5) and the  $S$  are considered as  $1D$ ,  $2D$ ,  $4D$ ,  $6D$ , and  $8D$ , respectively.  $D$  is the diameter of boreholes.

**2.3.3. Models of Different Boreholes Dip Angles.** In order to study the influence of boreholes dip angle  $\alpha$  on the pressure relief effect of cavern surrounding rock mass, rock models with double boreholes were established (as shown in Figure 6) and  $\alpha$  are considered as  $0^\circ$ ,  $20^\circ$ ,  $40^\circ$ ,  $60^\circ$ , and  $80^\circ$ , respectively.

**2.3.4. Models of Different Boreholes Arrangement Forms.** In order to study the influence of boreholes arrangement form on the pressure relief effect of cavern surrounding rock mass, rock models with three boreholes were established (as shown in Figure 7) and the arrangement form are considered as vertical layout ( $V$ ), horizontal layout ( $H$ ), inclined layout ( $I$ ), up three-flower layout ( $U$ ), and down three-flower layout ( $D$ ), respectively.

After the models are built, the uniaxial compression tests are carried out through the wall set at the top of the models. The displacement control model is used for loading. During the loading process, the stress, strain, and crack growth characteristics of the models are monitored by fish language.

### 3. Analysis of Test Results

**3.1. Strength Reduction Characteristics.** The peak stress intensity can well reflect the pressure relief effect of the rock mass. Therefore, the peak stress is used to analyze the pressure relief effect.

**3.1.1. Influence of Borehole Locations.** Figures 8 and 9 are stress-strain curves and strength reduction curves of rock samples with different drilling positions. From the figures it can be seen that, in addition to the sample that the drill hole is at the end face of the rock bottom ( $R=0.1$ ), the closer the drilling hole is to the top of the rock sample, that is, the larger  $R$  value is, the lower the strength of the rock is, and the higher the strength reduction degree of the rock sample is. When  $R$  increase from 0.3 to 0.9, the strengths of rock samples are 77.07 MPa, 74.24 MPa, 70.49 MPa, and 57.87 MPa and the corresponding strength reduction degrees are 4.9%, 8.4%, 13%, and 28.6%. The reason is that the upper and lower end faces of rock sample are prone to producing stress concentration in the process of loading, which makes drilling at the end easy to damage the rock sample. Therefore, it is easy to reduce the stress concentration of surrounding rock mass by drilling at the top and bottom of the cavern, which can effectively prevent rock burst.

**3.1.2. Influence of Boreholes Spacing.** Figures 10 and 11 are stress-strain curves and strength reduction curves of rock samples with different boreholes spacing. From the figures it

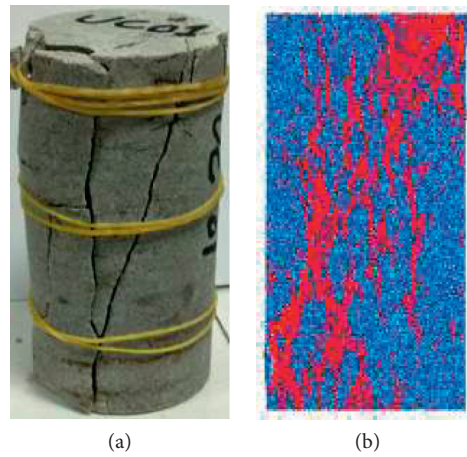


FIGURE 3: Failure modes of sandstone based on experimental and numerical tests: (a) experimental test; (b) numerical test.

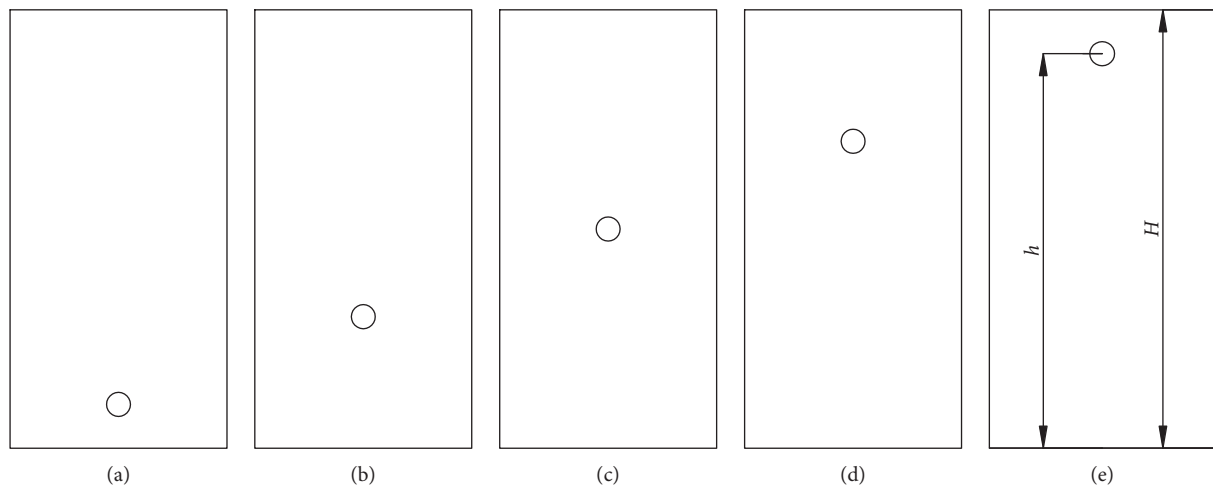


FIGURE 4: Numerical test samples with different borehole height ratio. The  $R$  of (a), (b), (c), (d), and (e) are 0.1, 0.3, 0.5, 0.7, and 0.9, respectively.

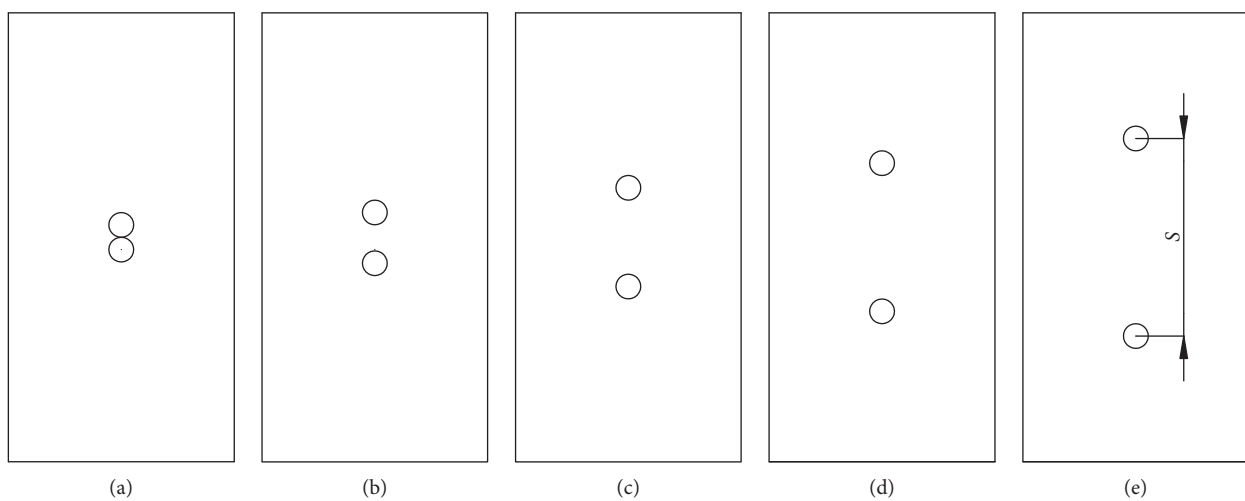


FIGURE 5: Numerical test samples with different boreholes spacing. The  $S$  of (a), (b), (c), (d), and (e) are  $1D$ ,  $2D$ ,  $4D$ ,  $6D$ , and  $8D$ , respectively.

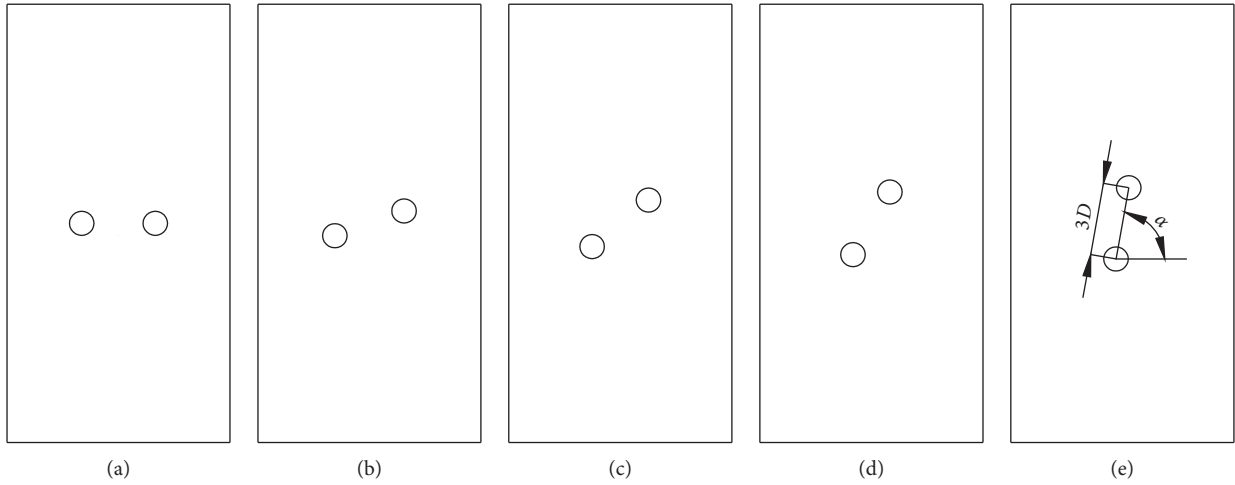


FIGURE 6: Numerical test samples with different boreholes dip angle.  $\alpha$  of (a), (b), (c), (d), and (e) are  $0^\circ$ ,  $20^\circ$ ,  $40^\circ$ ,  $60^\circ$ , and  $80^\circ$ , respectively.

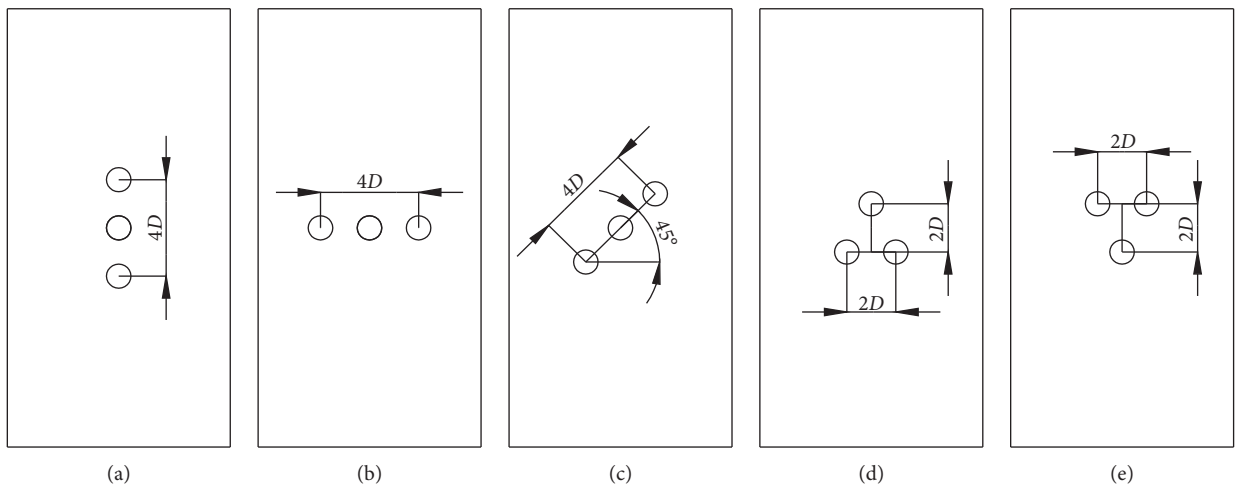


FIGURE 7: Numerical test samples with different boreholes arrangement form. The arrangement form of (a), (b), (c), (d), and (e) are vertical layout, horizontal layout, inclined layout, up three-flower layout, and down three-flower layout, respectively.

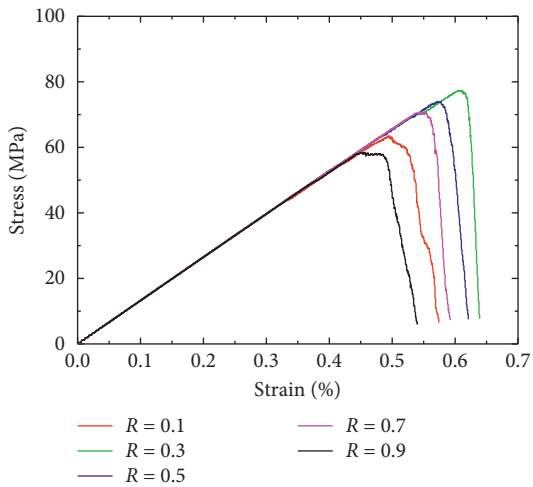


FIGURE 8: Stress-strain curves of rock samples with different drilling positions.

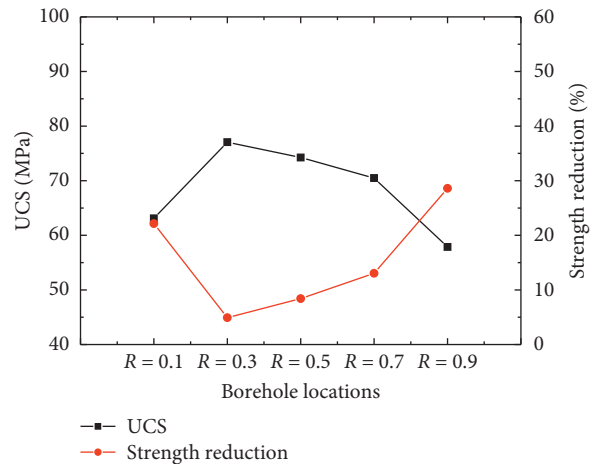


FIGURE 9: Strength reduction curves of rock samples with different drilling positions.



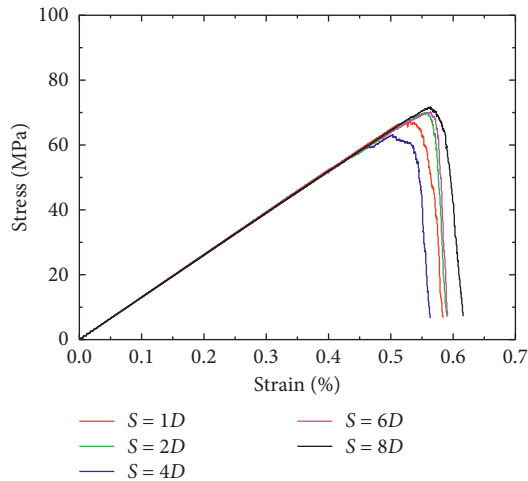


FIGURE 10: Stress-strain curves of rock samples with different boreholes spacing.

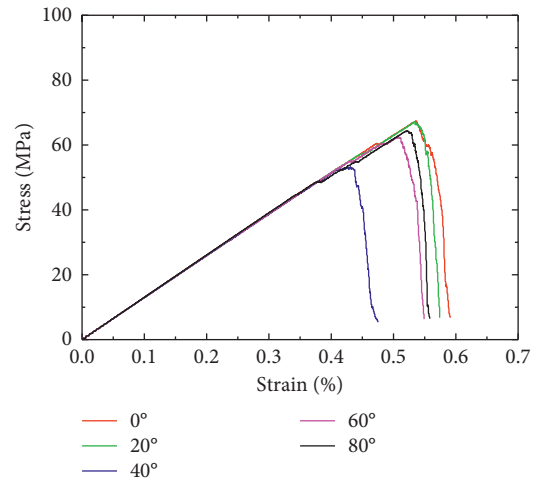


FIGURE 12: Stress-strain curves of rock samples with different boreholes dip angles.

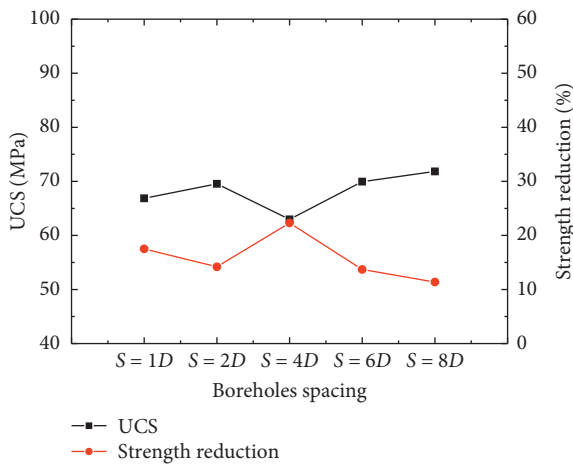


FIGURE 11: Strength reduction curves of rock samples with different boreholes spacing.

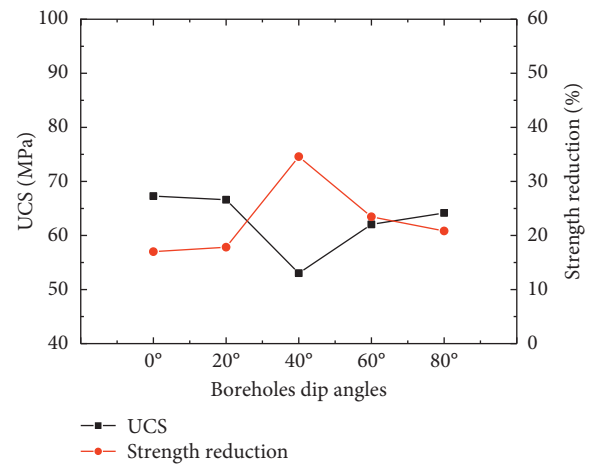


FIGURE 13: Strength reduction curves of rock samples with different boreholes dip angles.

can be seen that the compressive strength of rock samples shows an increase-decrease-increase trend with the increase of boreholes spacing. The compressive strengths of the rock samples are 66.87 MPa, 69.55 MPa, 62.97 MPa, 69.95 MPa, and 71.84 MPa as the drilling spacing increases from 1D to 8D. The corresponding strength reduction degree of these rock samples shows the trend of decrease-increase-decrease. With the increase of the drilling distance, the strength reduction degrees are 17.5%, 14.2%, 22.3%, 13.7%, and 11.4%, respectively. Therefore, the notion that the larger the boreholes spacing is, the better the pressure relief effect does not apply. The boreholes spacing with the best pressure relief effect is about 4 times of the borehole diameter.

**3.1.3. Influence of Boreholes Dip Angles.** Figures 12 and 13 are stress-strain curves and strength reduction curves of rock samples with different boreholes dip angle. From the figures it can be seen that the compressive strength of rock samples shows a trend of increases firstly and then decreases with the

increase of boreholes dip angle. The compressive strengths of the rock samples are 67.28 MPa, 66.61 MPa, 53.03 MPa, 62.04 MPa, and 64.17 MPa. The corresponding strength reduction degree of these rock samples shows the trend of decrease firstly and then increase. With the increase of the boreholes dip angles, the strength reduction degrees are 17%, 17.8%, 34.56%, 23.5%, and 20.8%, respectively. The reason why the strength of the rock sample with the boreholes dip angle is 40° the lowest is that the failure mode of the complete rock sample is mostly splitting failure along the 45° angle, and the 40° boreholes dip angle is the closest to the failure angle of the intact rock sample. It can be seen that the best way to reduce the pressure of surrounding rock is to arrange the boreholes at about 45°.

**3.1.4. Influence of Boreholes Arrangement Forms.** Figures 14 and 15 are stress-strain curves and strength reduction curves of rock samples with different boreholes arrangement forms. From the figures it can be seen that the compressive strength

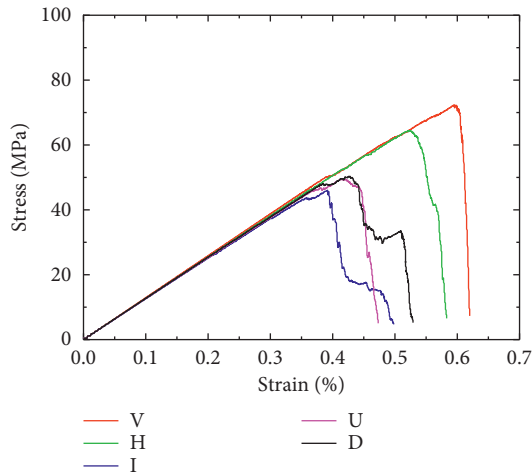


FIGURE 14: Stress-strain curves of rock samples with different boreholes arrangement forms.

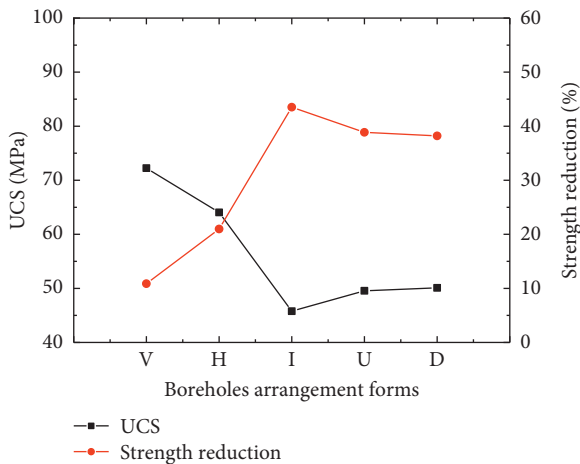


FIGURE 15: Strength reduction curves of rock samples with different boreholes arrangement forms.

of rock sample with an inclined arrangement form is the lowest, 45.78 MPa (corresponding strength reduction degree is 43.5%). When the arrangement form is up three-flower layout or down three-flower layout, the compressive strength of the rock sample is similar, about 50 MPa (corresponding strength reduction degree is about 38%). In addition, when the boreholes arrangement forms are vertical layout and horizontal layout, the compressive strength of the rock samples are 72.25 MPa (corresponding strength reduction degree is 10.9%) and 64.05 MPa (corresponding strength reduction degree is 21%). Therefore, using the inclined layout and three-flower layout can achieve better pressure relief effect of the surrounding rock mass of the caverns.

**3.2. AE Characteristics.** When the material receives an external force, the elastic energy stored in the material is quickly released to generate elastic waves and sound, which is called acoustic emission (AE) [18]. For the PFC numerical

simulation, the fracture of the parallel bond will release a certain amount of elastic energy. Therefore, the fracture of the bond can be used to reflect the acoustic emission characteristics [19–21]. The numerical acoustic emission of PFC simulation is different from the acoustic emission monitored by the actual test, but there are similarities, which can reflect the characteristics of internal crack damage in rock materials. In this paper, the AE characteristics of different drilling schemes are analyzed based on the number of AE counts (the number of bonds breakages).

**3.2.1. Influence of Borehole Locations.** Figure 16 shows the stress-time-AE counts of samples with different borehole height ratio. The  $R$  of (a), (b), (c), (d), and (e) are 0.1, 0.3, 0.5, 0.7, and 0.9, respectively. It can be seen from the figures that the position of the borehole has little influence on the evolution law of acoustic emission, and all go through silent emission stage, slow increase stage, and rapid increase stage. However, the maximum value of acoustic emission counts and the corresponding occurrence time of the rock samples are changed under different drilling positions. As the  $R$  increase from 0.1 to 0.9, the maximum values of the acoustic emission counts are 20 times, 28 times, 22 times, 35 times, and 17 times and the corresponding occurrence time are 54343 steps, 59918 steps, 57138 steps, 55675 steps, and 51929 steps. As  $R$  increase, the maximum value of the acoustic emission counts of the samples shows a state of fluctuation. However, the corresponding occurrence time shows a trend of increase firstly and then decrease, which are consistent with the change of the UCS. This shows that the acoustic emission can effectively monitor the stability of the surrounding rock of the caverns. However, the threshold value and the occurrence time of the acoustic emission of the cavern instability changed after the cavern surrounding rock is drilled holes. If the borehole is arranged at the upper part of the cavern, the occurrence time of the cavern instability will be advanced.

**3.2.2. Influence of Boreholes Spacing.** Figure 17 shows the stress-time-AE counts of samples with different boreholes spacing. The  $S$  of (a), (b), (c), (d), and (e) are  $1D$ ,  $2D$ ,  $4D$ ,  $6D$ , and  $8D$ , respectively. Similar to the influence of drilling positions, the boreholes spacing also has little influence on the evolution law of acoustic emission, and all go through silent emission stage, slow increase stage, and rapid increase stage. In addition, the maximum value of acoustic emission counts and the corresponding occurrence time of the rock samples are changed as the boreholes spacing increase. As the boreholes spacing  $S$  increases from  $1D$  to  $8D$ , the maximum values of the acoustic emission counts are 21 times, 28 times, 25 times, 26 times, and 21 times and the corresponding occurrence times are 54475 steps, 55075 steps, 53378 steps, 55675 steps, and 57987 steps. Similar to the influence of drilling positions, as  $S$  increases, the maximum value of the acoustic emission counts of the samples shows a state of fluctuation. However, the corresponding occurrence time shows a consistent trend (increase-decrease-increase) with the change of the UCS.

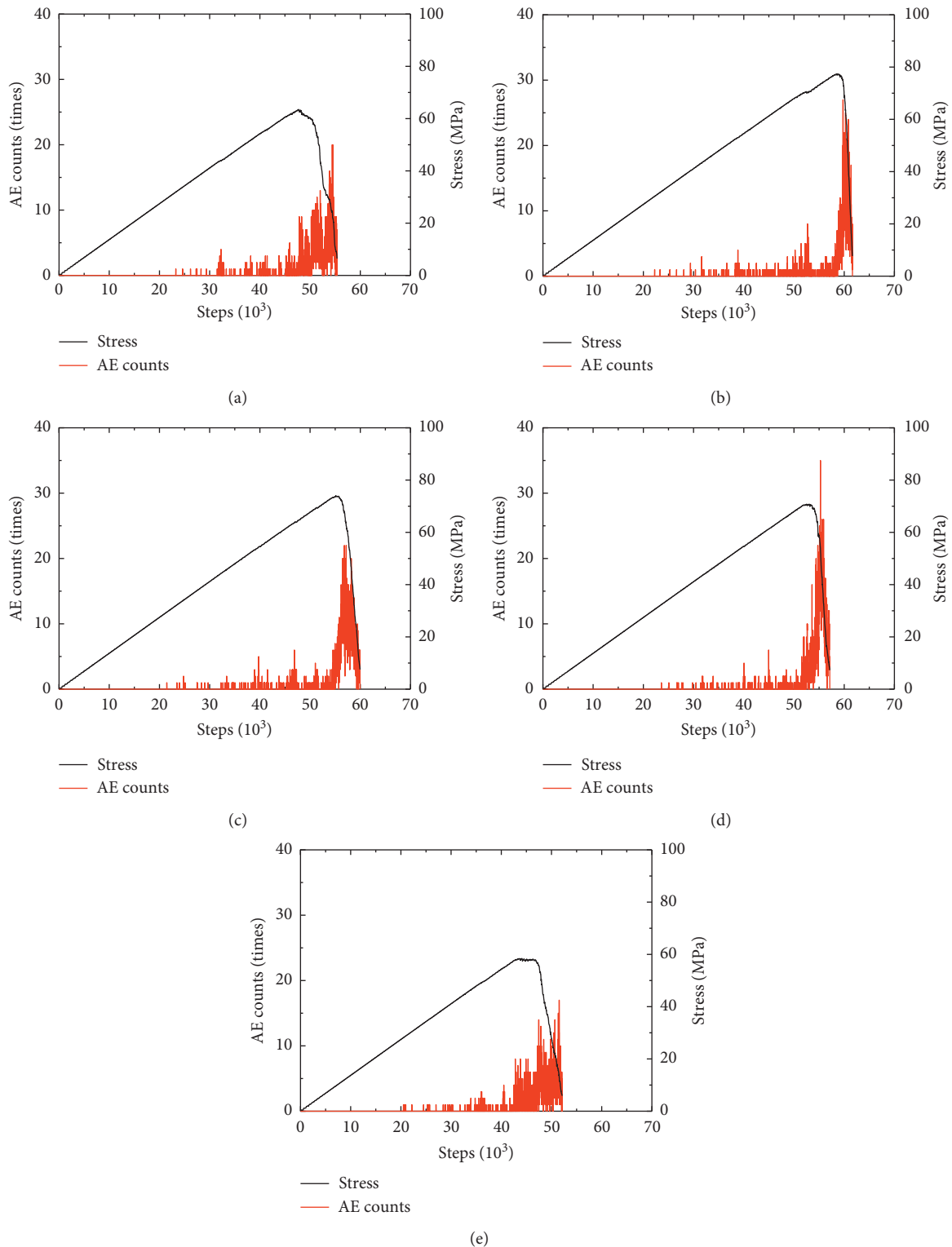


FIGURE 16: Stress-time-AE counts of samples with different borehole height ratio. The  $R$  of (a), (b), (c), (d), and (e) are 0.1, 0.3, 0.5, 0.7, and 0.9, respectively.

3.2.3. *Influence of Boreholes Dip Angles.* Figure 18 shows the stress-time-AE counts of samples with different boreholes dip angles. The dip angles  $\alpha$  of (a), (b), (c), (d), and (e) are  $0^\circ$ ,  $20^\circ$ ,  $40^\circ$ ,  $60^\circ$ , and  $80^\circ$ , respectively. Similar to

the influence of drilling positions and boreholes spacing, the boreholes dip angle also has little influence on the evolution law of acoustic emission, and all go through silent emission stage, slow increase stage, and rapid

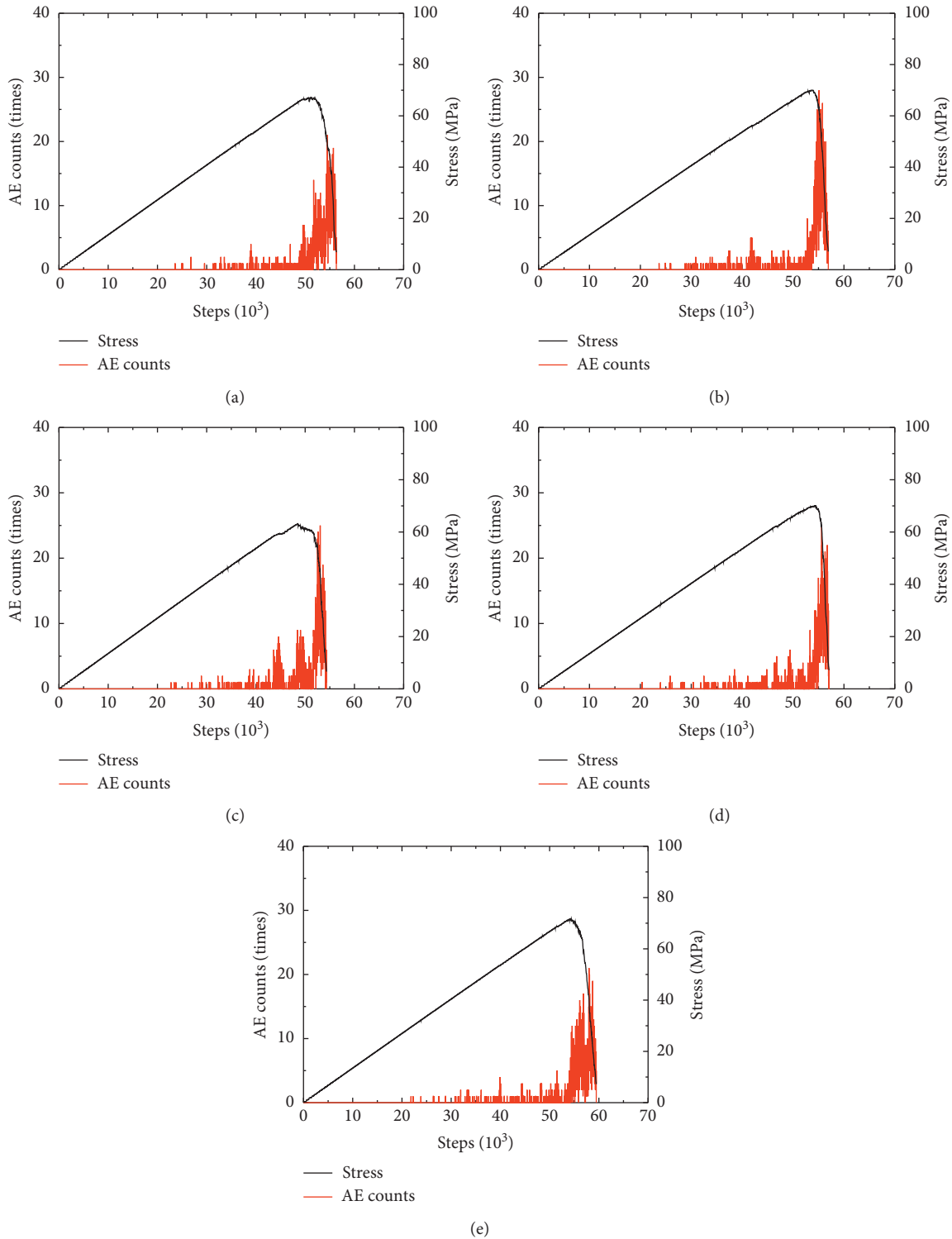


FIGURE 17: Stress-time-AE counts of samples with different boreholes spacing. The S of (a), (b), (c), (d), and (e) are 1D, 2D, 4D, 6D, and 8D, respectively.

increase stage. In addition, the maximum value of acoustic emission counts and the corresponding occurrence time of the rock samples are changed as the boreholes dip angles increase. As the boreholes dip angle increase from 0° to 80°, the maximum value of the acoustic emission counts are 30 times, 33 times, 12 times, 23 times, and 21

times and the corresponding occurrence times are 55924 steps, 53744 steps, 43808 steps, 52295 steps, and 52646 steps. Similar to the influence of drilling positions and boreholes spacing, as the dip angle  $\alpha$  increase, the maximum value of the acoustic emission counts of the samples shows a state of fluctuation.

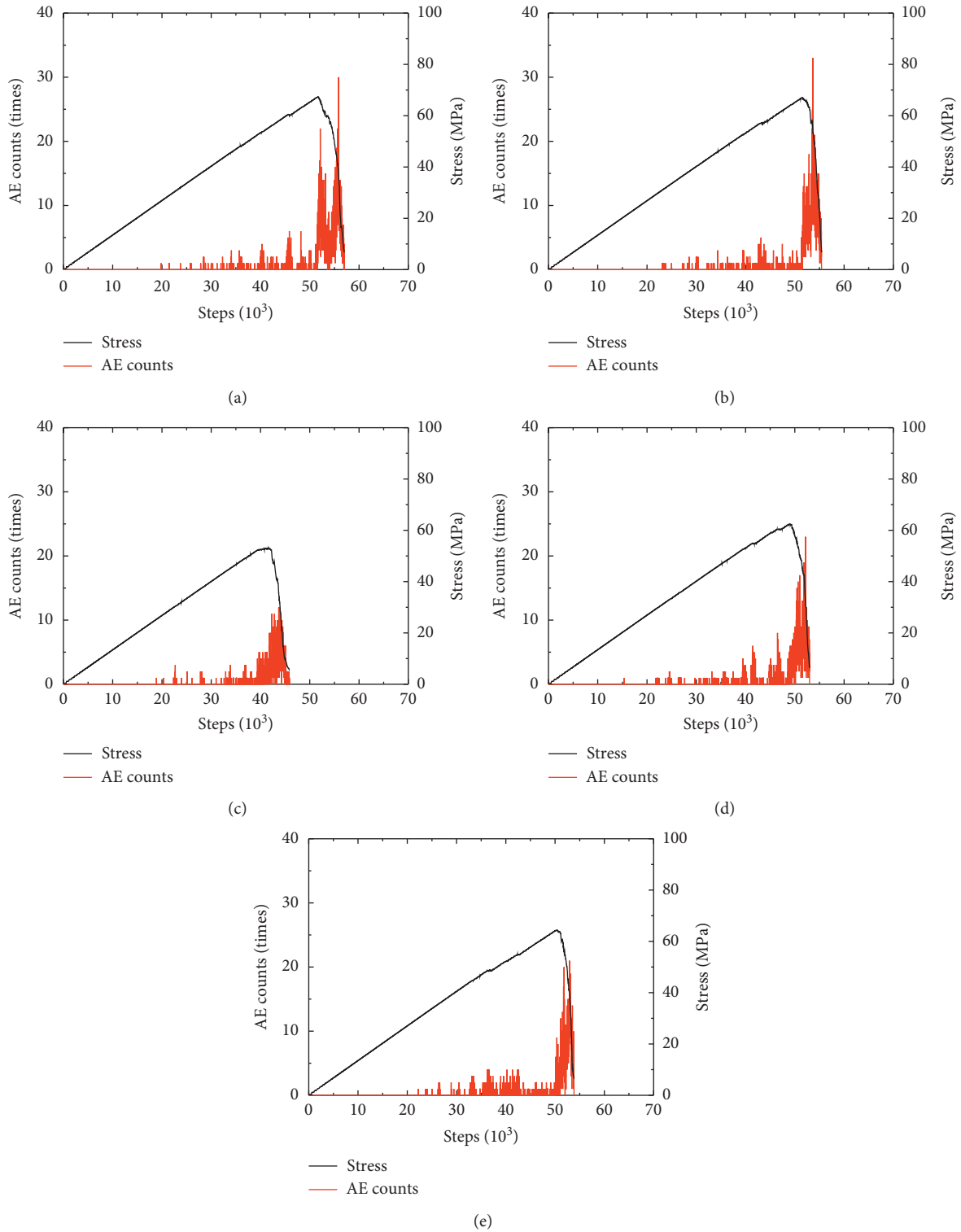


FIGURE 18: Stress-time-AE counts of samples with different boreholes dip angle. The  $\alpha$  of (a), (b), (c), (d), and (e) are  $0^\circ$ ,  $20^\circ$ ,  $40^\circ$ ,  $60^\circ$ , and  $80^\circ$ , respectively.

3.2.4. *Influence of Boreholes Arrangement Forms.* Figure 19 shows the stress-time-AE counts of samples with different boreholes arrangement forms. The arrangement forms of (a), (b), (c), (d), and (e) are vertical layout, horizontal layout, inclined layout, up three-flower layout,

and down three-flower layout, respectively. Similar to the influence of drilling positions, boreholes spacing, and borehole dip angles, the boreholes arrangement forms also have little influence on the evolution law of acoustic emission, and all go through silent emission stage, slow



increase stage, and rapid increase stage. The difference is that there are two or more peaks in the third stage of acoustic emission rapid increase. This is because the number of drilling holes is three, more than one and two, which makes the mechanical properties of rock samples changed to serious, leading to the stress of rock samples before and after the peak is in a state of fluctuation. Similar to the influence of drilling positions, boreholes spacing, and boreholes dip angles, as the boreholes arrangement forms change, the maximum value of the acoustic emission counts of the samples shows a state of fluctuation. However, the corresponding occurrence time shows a consistent trend with the change of the UCS. When the boreholes arrangement form is vertical layout, the maximum value of the acoustic emission counts and its occurrence time are 27 times and 58586 steps; when the boreholes arrangement form is horizontal layout, the maximum value of the acoustic emission counts and its occurrence time are 26 times and 55675 steps; when the boreholes arrangement form is inclined layout, the maximum value of the acoustic emission counts and its occurrence time are 13 times and 38716 steps; when the boreholes arrangement form is up three-flower layout, the maximum value of the acoustic emission counts and its occurrence time are 17 times and 43559 steps; when the boreholes arrangement form is down three-flower layout, the maximum value of the acoustic emission counts and its occurrence time are 17 times and 49749 steps.

**3.3. Failure Modes.** It can be seen from Figure 3 that the failure mode of intact rock is inclined split failure with two large fracture face, which is taken as a reference when analyzing the influence of drilling layout on the failure modes of surrounding rock samples.

**3.3.1. Influence of Borehole Locations.** Figure 20 shows the failure modes of rock samples with different borehole height ratio. The  $R$  of (a), (b), (c), (d), and (e) are 0.1, 0.3, 0.5, 0.7, and 0.9, respectively. It can be seen from the figures that the failure modes of rock samples with different drilling positions are different from the of intact rock sample. When  $R=0.1$ , the failure mode of rock sample is mainly at the bottom of the rock sample, which is similar to “V” shape; when  $R=0.3$ , the failure mode of rock sample is also mainly concentrated at the bottom of the rock sample, which is similar to “W” shape; when  $R=0.5$ , the failure mode of rock sample is approximately X-shaped; when  $R=0.7$ , the failure mode of rock sample is approximately Y-shaped; when  $R=0.9$ , the failure mode of rock sample is approximately inverted “√” shape. The failure of rock samples is caused by cracks (stress concentration) near the borehole first, and then the whole rock samples are damaged. Drilling can not only lead to the strength reduction of rock mass but also control the failure mode of rock mass. The actual project can control the pressure relief range of drilling with this advantage.

**3.3.2. Influence of Boreholes Spacing.** Figure 21 shows the failure modes of rock samples with different boreholes spacing. The  $S$  of (a), (b), (c), (d), and (e) are  $1D$ ,  $2D$ ,  $4D$ ,  $6D$ , and  $8D$ , respectively. From the figures it can be obtained that the failure modes of rock samples with different boreholes spacing are different from those of intact rock sample. When  $S=1D$  and  $2D$ , the failure modes of rock samples are similar to “X” shape; when  $S=4D$  and  $6D$ , the failure modes of rock samples are inclined split failure, similar to “/” shape; when  $S=8D$ , the failure mode of rock sample is approximately n-shaped. The smaller the distance between the boreholes is, the more obvious the coupling effect between the boreholes is, and the stronger the damage degree near the boreholes is. However, there is also a waste of drilling. Therefore, the drilling spacing should be reasonably arranged in the actual project. This study shows that when the boreholes spacing is 4 times the hole diameter, the pressure relief effect is the best.

**3.3.3. Influence of Boreholes Dip Angles.** Figure 22 shows the failure modes of rock samples with different boreholes dip angles. The dip angle  $\alpha$  of (a), (b), (c), (d), and (e) are  $0^\circ$ ,  $20^\circ$ ,  $40^\circ$ ,  $60^\circ$ , and  $80^\circ$ , respectively. From the figures it can be obtained that the failure modes of rock samples with different boreholes dip angle are also different from those of intact rock sample. When  $\alpha=0^\circ$ , the failure mode of the rock sample is approximately inverted “V” shape; when  $\alpha=20^\circ$ , the failure mode of the rock sample is approximate to “H” shape; when  $\alpha=40^\circ$  and  $80^\circ$ , the failure modes of the rock samples are similar to “y” shape; when  $\alpha=60^\circ$ , the failure modes of the rock samples are similar to “X” shape. The smaller the boreholes dip angle is, the more likely the failure mode of the rock sample concentrated in the middle of the sample is; the larger the boreholes dip angle is, the more likely it can lead to splitting failure of rock samples.

**3.3.4. Influence of Boreholes Arrangement Forms.** Figure 23 shows the failure modes of rock samples with different boreholes arrangement forms. The arrangement forms of (a), (b), (c), (d), and (e) are vertical layout, horizontal layout, inclined layout, up three-flower layout, and down three-flower layout, respectively. From the figures it can be obtained that the failure modes of rock samples with different boreholes arrangement forms are also different from those of intact rock sample. When the boreholes arrangement form is vertical layout, the failure mode of the sample is similar to “√” shape; when the boreholes arrangement form is horizontal layout, the failure mode of the sample is similar to “H” shape; when the boreholes arrangement form is inclined layout, the failure mode of the sample is similar to symmetrical “h” shape; when the boreholes arrangement form is up three-flower layout, the failure mode of the sample is similar to inverted “Y” shape; when the boreholes arrangement form is down three-flower layout, the failure mode of the sample is similar to “Y” shape. In addition, the inclined drill holes are more likely to lead to the propagation and penetration of rock cracks, even if the number of cracks is less.

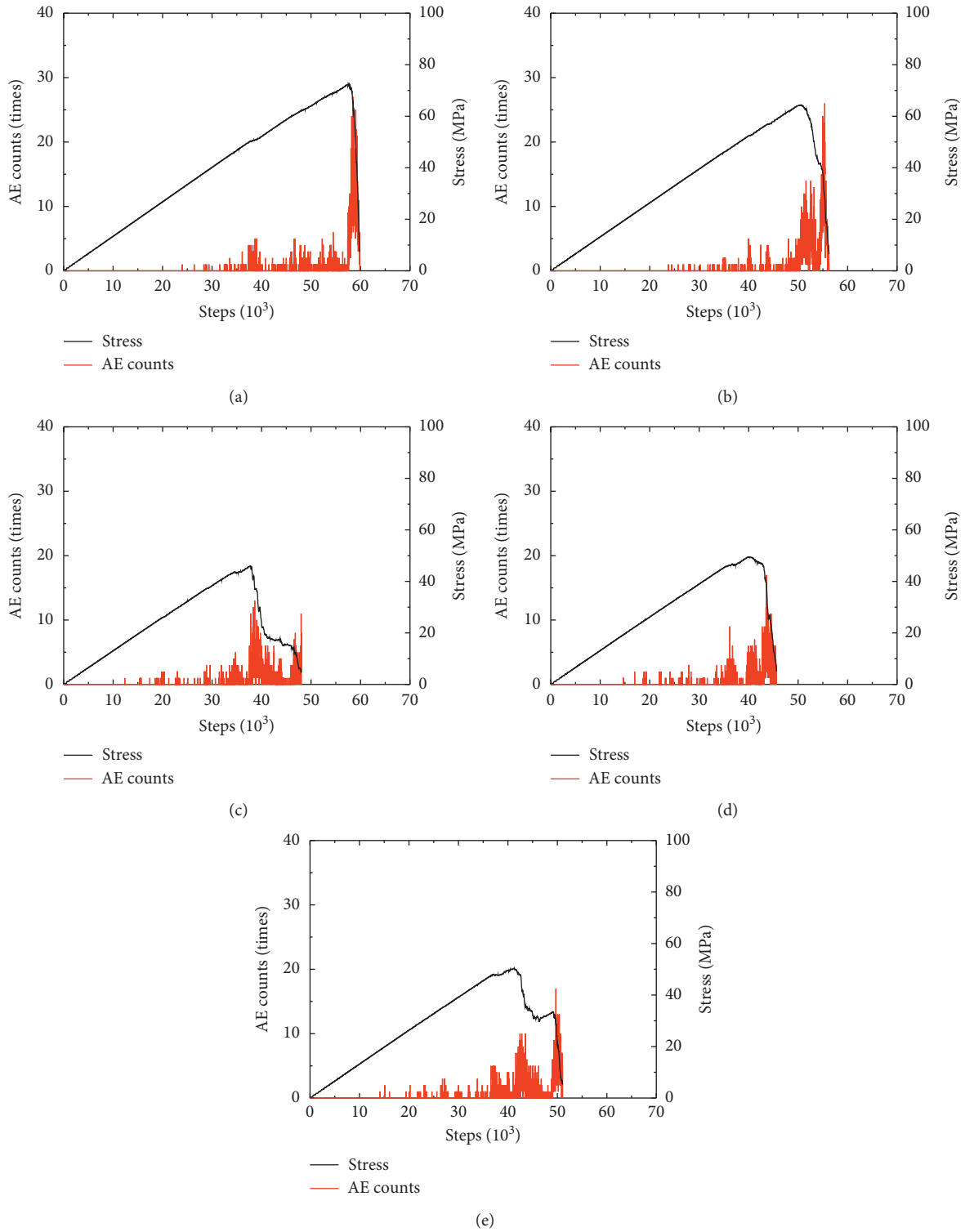


FIGURE 19: Stress-time-AE counts of samples with different boreholes arrangement form. The arrangement forms of (a), (b), (c), (d), and (e) are vertical layout, horizontal layout, inclined layout, up three-flower layout, and down three-flower layout, respectively.



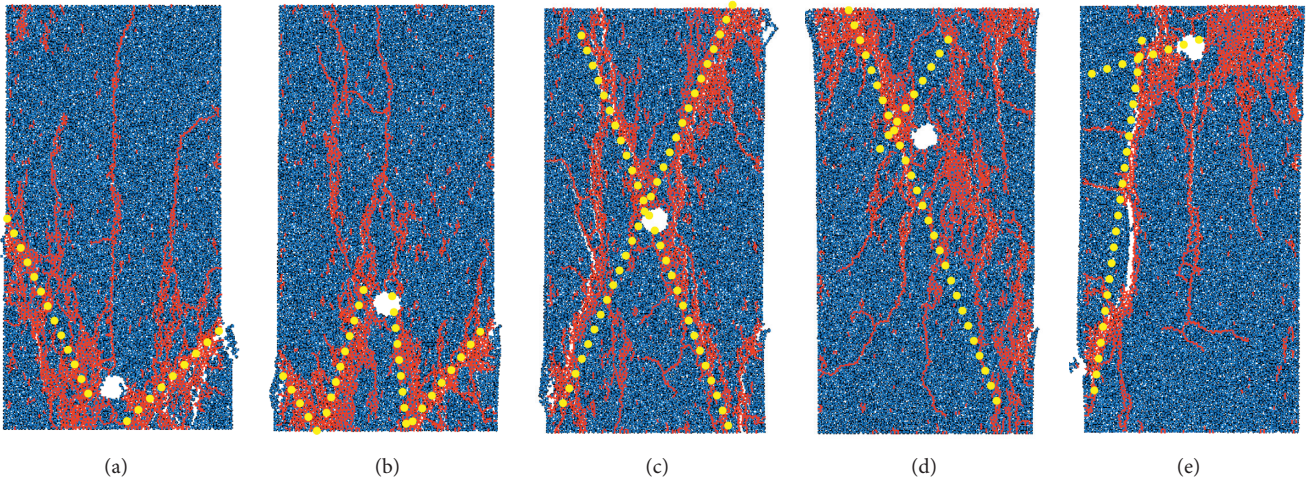


FIGURE 20: Failure modes of samples with different borehole height ratio. The  $R$  of (a), (b), (c), (d), and (e) are 0.1, 0.3, 0.5, 0.7, and 0.9, respectively.

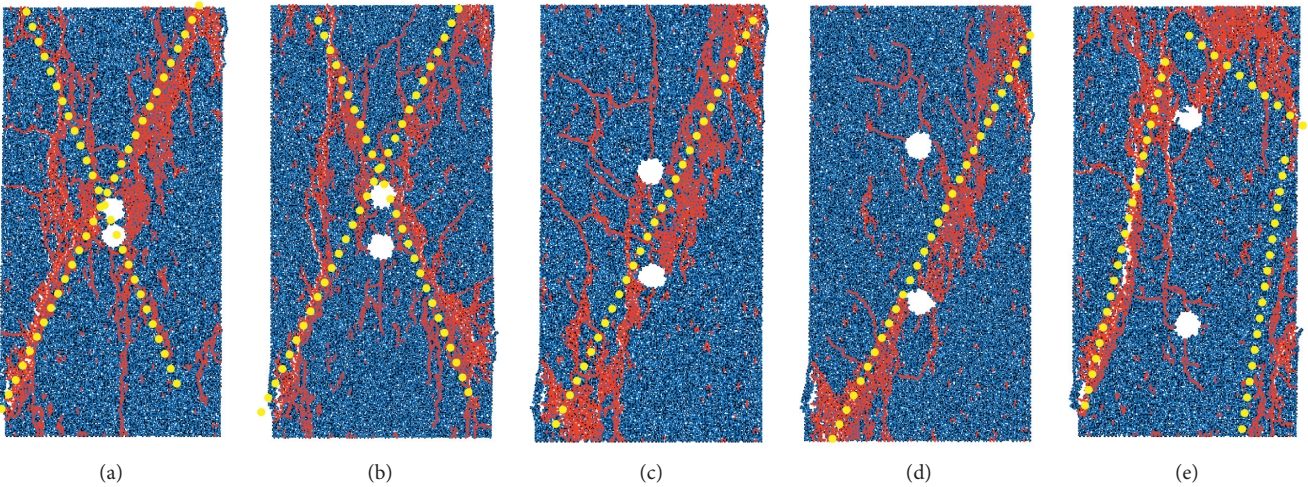


FIGURE 21: Failure modes of samples with different boreholes spacing. The  $S$  of (a), (b), (c), (d), and (e) are  $1D$ ,  $2D$ ,  $4D$ ,  $6D$ , and  $8D$ , respectively.

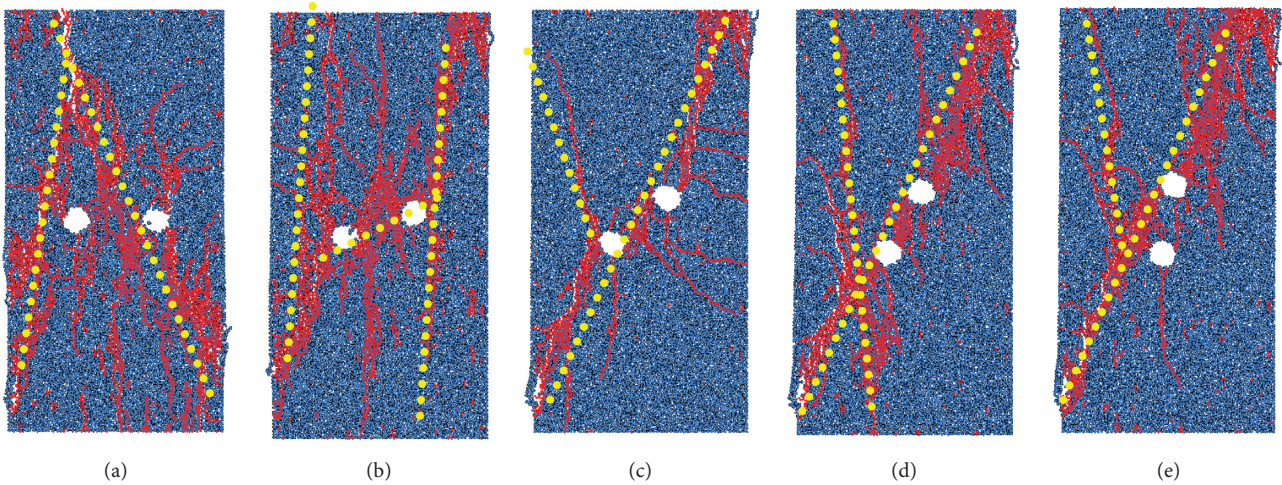


FIGURE 22: Failure modes of samples with different boreholes dip angle. The  $\alpha$  of (a), (b), (c), (d), and (e) are  $0^\circ$ ,  $20^\circ$ ,  $40^\circ$ ,  $60^\circ$ , and  $80^\circ$ , respectively.



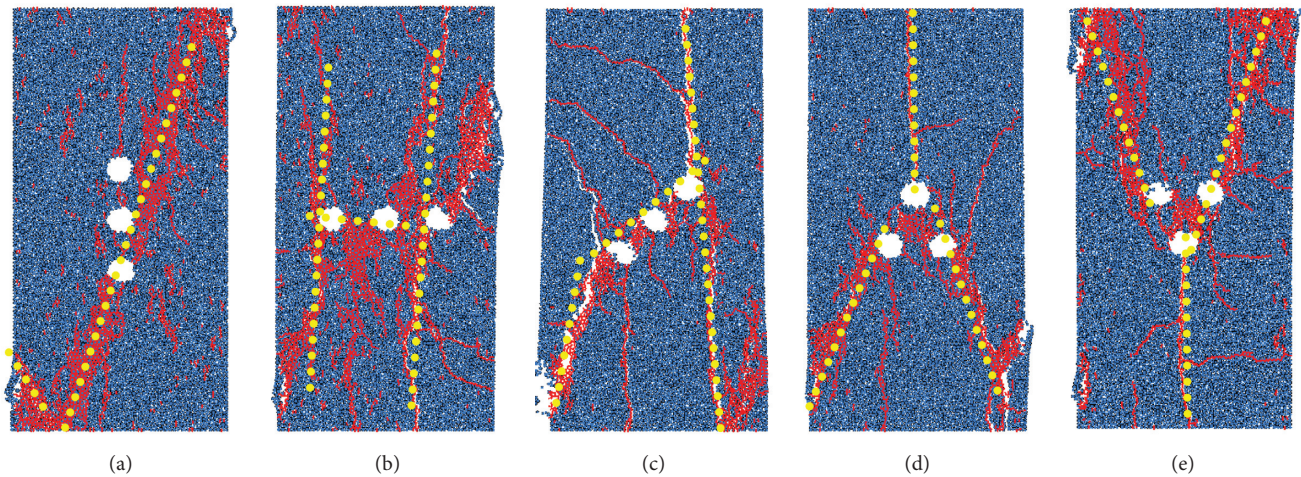


FIGURE 23: Failure modes of samples with different boreholes arrangement forms. The arrangement forms of (a), (b), (c), (d), and (e) are vertical layout, horizontal layout, inclined layout, up three-flower layout, and down three-flower layout, respectively.

#### 4. Conclusions and Suggestions

The strength reduction degrees of rock samples with different drilling layout schemes are different. In addition to the sample that the drill hole is at the end face of the rock bottom ( $R = 0.1$ ), the closer the drilling hole is to the top of the rock sample, that is, the larger the  $R$  value is, the higher the strength reduction degree of the rock sample is. It is easy to reduce the stress concentration of surrounding rock mass by drilling at the top and bottom of the cavern. The strength reduction degree of rock samples shows a decrease-increase-decrease trend with the increase of boreholes spacing. The boreholes spacing with the best pressure relief effect is about 4 times of the borehole diameter. The strength reduction degree of rock samples shows a trend of decrease firstly and then increase with the increase of boreholes dip angle. The best way to reduce the pressure of surrounding rock is to arrange the boreholes at about  $45^\circ$ . The strength reduction degree of rock sample with an inclined arrangement form is the largest, followed by the arrangement form being up three-flower layout or down three-flower layout. Using the inclined layout and three-flower layout can achieve better pressure relief effect of the surrounding rock mass of the caverns.

The rock samples with different drilling layout schemes have little influence on the evolution law of acoustic emission, and all go through silent emission stage, slow increase stage, and rapid increase stage. However, the maximum value of acoustic emission counts and the corresponding occurrence time of the rock samples are changed. As the drilling layout schemes change, the maximum value of the acoustic emission counts of the samples shows a state of fluctuation. However, the changed trend of the occurrence time of the maximum value of the acoustic emission counts is consistent with the change of the UCS. The acoustic emission can effectively monitor the stability of the surrounding rock of the caverns. However, the threshold value and the

occurrence time of the acoustic emission of the cavern instability changed after the cavern surrounding rock is drilled holes. If the borehole is arranged at the surrounding rock mass, the occurrence time of the cavern instability may be advanced.

The failure modes of rock samples with different drilling layout schemes are different. The shapes of the failure modes of the rock samples with different borehole location are “V” ( $R = 0.1$ ), “W” ( $R = 0.3$ ), “X” ( $R = 0.5$ ), “Y” ( $R = 0.7$ ), and “√” ( $R = 0.9$ ). The shapes of the failure modes of the rock samples with different boreholes spacing are “X” ( $S = 1D$  or  $2D$ ), “/” ( $S = 4D$  or  $6D$ ), and “n” ( $S = 8D$ ). The shapes of the failure modes of the rock samples with different boreholes dip angles are “V” ( $\alpha = 0^\circ$ ), “H” ( $\alpha = 20^\circ$ ), “y” ( $\alpha = 40^\circ$  or  $80^\circ$ ), and “X” ( $\alpha = 60^\circ$ ). The shapes of the failure modes of the rock samples with different boreholes arrangement forms are “√” (vertical layout), “H” (horizontal layout), symmetrical “h” (inclined layout), inverted “Y” (up three-flower layout), and “Y” (down three-flower layout). The failure of rock samples is caused by cracks near the borehole first, and then the whole rock samples are damaged. Drilling can not only lead to the strength reduction of rock mass but also control the failure mode of rock mass. The actual project can control the pressure relief range of drilling with this advantage.

#### Data Availability

All the data generated or analyzed during this study are included in this published article.

#### Conflicts of Interest

The authors declare that they have no conflicts of interest.

#### Acknowledgments

The research described in this paper was financially supported by Liaocheng University Research Fund (no. 318051703).

## References

- [1] Y. Pan, Z. Li, and M. Zhang, "Distribution, type mechanism and prevention of rockburst in China," *Chinese Journal of Rock Mechanics and Engineering*, vol. 22, no. 11, pp. 1844–1851, 2003.
- [2] P. Konicek, K. Soucek, L. Stas, and R. Singh, "Long-hole destress blasting for rockburst control during deep underground coal mining," *International Journal of Rock Mechanics and Mining Sciences*, vol. 61, pp. 141–153, 2013.
- [3] J. H. Liu, F. X. Jiang, G. J. Sun et al., "Mechanism of intensive venting pulverized coal to prevent coal burst and its application," *Chinese Journal of Rock Mechanical Engineering*, vol. 33, no. 4, pp. 747–754, 2014.
- [4] X. Zhang and F. Meng, "Statistical analysis of large accidents in China's coal mines in 2016," *Natural Hazards*, vol. 92, no. 1, pp. 311–325, 2018.
- [5] Z. Zhang, M. Deng, X. Wang et al., "Field and numerical investigations on the lower coal seam entry failure analysis under the remnant pillar," *Engineering Failure Analysis*, vol. 115, 2020.
- [6] E. B. Yi, Z. L. Mu, L. M. Dou et al., "Study on comparison and analysis on pressure releasing effect of boreholes in soft and hard seam," *Coal Science and Technology*, vol. 39, no. 6, pp. 1–5, 2011.
- [7] Y. Li, H. Zhang, Z. Zhu et al., "Study on safety parameters of pressure relief borehole in rockburst coal seam," *China Safety Science Journal*, vol. 28, no. 11, pp. 122–128, 2018.
- [8] S. Zhang, Y. Li, B. Shen, X. Sun, and L. Gao, "Effective evaluation of pressure relief drilling for reducing rock bursts and its application in underground coal mines," *International Journal of Rock Mechanics and Mining Sciences*, vol. 114, pp. 7–16, 2019.
- [9] S. Zhu, F. Jiang, X. Shi et al., "Energy dissipation index method for determining rockburst prevention drilling parameters," *Rock and Soil Mechanics*, vol. 36, no. 8, pp. 2270–2276, 2015.
- [10] C. Jia, Y. Jiang, X. Zhang et al., "Laboratory and numerical experiments on pressure relief mechanism of large-diameter boreholes," *Chinese Journal of Geotechnical Engineering*, vol. 39, no. 6, pp. 1115–1122, 2017.
- [11] Q. Zhang, G. Sun, J. Suo et al., "The 3D numerical simulation of deep granite borehole unloading," *Chinese Journal of Applied Mechanics*, vol. 34, no. 5, pp. 988–994, 2017.
- [12] P. A. Cundall and O. D. L. Strack, "A discrete numerical model for granular assemblies," *Géotechnique*, vol. 29, no. 1, pp. 47–65, 1979.
- [13] Itasca Consulting Group, *PFC Users' Manual (Version 5.0)*, Itasca Consulting Group, Minneapolis, MN, USA, 2014.
- [14] U. Castro-Filgueira, L. R. Alejano, J. Arzúa, and D. M. Ivars, "Sensitivity analysis of the micro-parameters used in a PFC analysis towards the mechanical properties of rocks," *Procedia Engineering*, vol. 191, pp. 488–495, 2017.
- [15] X. Zhang, N. Louis, and W. Yuen, "Cracking processes in rock-like material containing a single flaw under uniaxial compression: a numerical study based on parallel bonded-particle model approach," *Rock Mechanics and Rock Engineering*, vol. 45, no. 5, pp. 711–737, 2012.
- [16] Y. Xiang, H. Liu, W. Zhang, J. Chu, D. Zhou, and Y. Xiao, "Application of transparent soil model test and DEM simulation in study of tunnel failure mechanism," *Tunnelling and Underground Space Technology*, vol. 74, pp. 178–184, 2018.
- [17] W. Liu, J. Liu, and C. Zhu, "Multi-scale effect of acoustic emission characteristics of 3D rock damage," *Arabian Journal of Geosciences*, vol. 12, no. 22, 2019.
- [18] Y. Cao, J. Wu, L. Chen, P. Wu, and F. Shaikh, "Experimental study on granite acoustic emission and micro-fracture behavior with combined compression and shear loading: phenomenon and mechanism," *Scientific Reports*, vol. 10, no. 1, 2020.
- [19] M. Cai, P. K. Kaiser, H. Morioka et al., "FLAC/PFC coupled numerical simulation of AE in large-scale underground excavations," *International Journal of Rock Mechanics and Mining Sciences*, vol. 44, no. 4, pp. 550–564, 2007.
- [20] X.-P. Zhang, Q. Zhang, and S. Wu, "Acoustic emission characteristics of the rock-like material containing a single flaw under different compressive loading rates," *Computers and Geotechnics*, vol. 83, pp. 83–97, 2017.
- [21] W. Liu, W. Yuan, Y. Yan et al., "Analysis of acoustic emission characteristics and damage constitutive model of coal-rock combined body based on particle flow code," *Symmetry*, vol. 11, no. 8, 2019.



## Research Article

# Numerical Analysis of the Width Design of a Protective Pillar in High-Stress Roadway: A Case Study

FuZhou Qi <sup>1</sup>, ZhanGuo Ma,<sup>2</sup> Ning Li <sup>2</sup>, Bin Li,<sup>1</sup> Zhiliu Wang,<sup>1</sup> and WeiXia Ma<sup>3</sup>

<sup>1</sup>School of Civil & Architecture Engineering, Zhongyuan University of Technology, Zhengzhou 450007, Henan, China

<sup>2</sup>State Key Laboratory for Geomechanics and Deep Underground Engineering, China University of Mining and Technology, Xuzhou 221116, Jiangsu, China

<sup>3</sup>Earthquake Administration of Henan, Zhengzhou 450016, Henan, China

Correspondence should be addressed to FuZhou Qi; 18255416386@163.com

Received 8 January 2021; Revised 27 January 2021; Accepted 10 February 2021; Published 28 February 2021

Academic Editor: Zizheng Zhang

Copyright © 2021 FuZhou Qi et al. This is an open access article distributed under the Creative Commons Attribution License, which permits unrestricted use, distribution, and reproduction in any medium, provided the original work is properly cited.

The width design of protective pillars is an important factor affecting the stability of high-stress roadways. In this study, a novel numerical modeling approach was developed to investigate the relationship between protective pillar width and roadway stability. With the 20 m protective pillar width adopted in the field test, large deformation of roadways and serious damage to surrounding rocks occurred. According to the case study at the Wangzhuang coal mine in China, the stress changes and energy density distribution characteristics in protective pillars with various widths were analysed by numerical simulation. The modeling results indicate that, with a 20 m wide protective pillar, the peak vertical stress and energy density in the pillar are 18.5 MPa and 563.7 kJ/m<sup>3</sup>, respectively. The phenomena of stress concentration and energy accumulation were clearly observed in the simulation results, and the roadway is in a state of high stress. Under the condition of a 10 m wide protective pillar, the peak vertical stress and energy density are shifted from the pillar to roadway virgin coal region, with peak values of 9.5 MPa and 208.3 kJ/m<sup>3</sup>, respectively. The decrease in vertical stress and energy density improves the stability of the protective pillar, resulting in the roadway being in a state of low stress. Field monitoring suggested that the proposed 10 m protective pillar width can effectively control the large deformation of the surrounding rock and reduce coal bump risk. The novel numerical modeling approach and design principle of protective pillars presented in this paper can provide useful references for application in similar coal mines.

## 1. Introduction

With increased mining depth, the failure of protective pillars in deep high-stress roadways has received much attention [1]. The influence of the protective pillar design on the stability of roadways has a bearing on worker safety and the effective mining of coal resources. Protective pillar around the gob provides a safe and stable production environment for the roadway and decreases disturbance to the roadway from high external stress. An improper protective pillar design can cause frequent roof sagging, pillar rib bulging, and severe coal bump to occur in a roadway, which will eventually cause the collapse of the surrounding rock structure [2, 3]. Therefore, protective pillar width design is a necessity for maintaining

the stability of the surrounding rock. Many methods of designing an appropriate protective pillar width have been proposed, including theoretical analysis calculations and numerical simulations.

A variety of calculation models have been established to analyse the proper width of a protective pillar and decrease the risk of pillar failure [4, 5]. Ghasemi et al. [6] used limit equilibrium analysis to explore the relationship between the range of elastic area and the stability of the protective pillar. Cao and Zhou [7] investigated the influence of movement in key blocks of broken strata above the roadway on the stability of the protective pillar and defined a reasonable width for the pillar. Yang et al. [8] showed the scope of stress distribution in the upper and lower strata of a protective pillar by analysing the influence of roof failure on the bearing capacity of the pillar.

In reality, many factors, such as the protective pillar's form, the rock mechanical properties, the stress state, and the panel mining methods, should be considered in designing the width of the protective pillar. Since some of these factors are not considered in theoretical analysis calculations, they are limited in application. Various numerical simulations have been adopted to analyse the effect of the protective pillar width on the roadway stability because of their low cost and high efficiency [9]. Moreover, as numerical simulation includes numerous factors during modeling, the results are often more reliable than those of theoretical calculations. Shabanimashcool and Li [10] established local and global numerical models to study the influence of falling strata on the stress and breaking range of a protective pillar during panel retreat. Bai et al. [11] investigated roof failure characteristics and stress change rules of gob-side entry driving by stages, noting that a rational protective pillar width could enhance the roadway stability. Ma et al. [12] analysed the shear failure behavior for protective pillars and found that the failure mode varied with the pillar width and inclination of the coal seam. Wang et al. [13] adopted FLAC3D software to study the dynamic response and failure mechanism of protective pillars; the results showed that enlarging the elastic core in the pillar increased the risk of coal bump. However, based on previous studies, we found that the numerical simulations seldom considered the following: (1) When the overlying strata in a gob are cut off along a preexisting fissure, the caving materials will fill the gob and provide supporting resistance to the roof strata, which will relieve stress on the protective pillar and decrease its width. (2) The energy stored in the rock mass is closely related to its stress state. The stored energy will vary as the stress changes. Thus, the evolution laws of energy stored in a rock mass can be inferred by the change in stress, decreasing or avoiding the deformation failure of the surrounding rock and the occurrence of coal bump. In view of these limitations in current simulations and considering the supporting feature of gob caving materials and the relationship between the stress and energy of the rock mass, a numerical modeling is developed to analyse failure mechanism for protective pillars.

In this paper, the relationship between roadway stability and protective pillar width is investigated based on numerical simulations and field tests. First, the failure characteristics of high-stress roadways are studied when the width of protective pillar is 20 m. Next, a novel modeling approach is proposed. In this modeling, a strain-softening model is adopted to describe the mechanical behaviour of protective pillars, and a double-yield model is used to simulate the gob materials mechanical behaviour. The stress changes and energy density distribution characteristics of roadways with five different widths are analysed. Finally, the effect of the optimal protective pillar on controlling the deformation of the surrounding rock is evaluated by a field

test. The modeling approach and design principle presented in this paper can be used to analyse the protective pillar design of high-stress roadways at other similar sites.

## 2. Engineering Background

*2.1. Geology Conditions.* As shown in Figure 1, the selected study site is in the Wangzhuang coal mine, Shanxi Province, China. The average depth and thickness of coal seam are 300 m and 4 m. Roadway roof and floor mainly include mudstone, siltstone, and sandy mudstone. A detailed stratigraphic column is shown in Figure 2.

Panels 8101, 8102, and 8103 are located in mining area #8 of the test coal mine, with a strike length of 1088 m and dip length of 210 m, as shown in Figure 3. Panel 8101 is located to the north of panel 8102, where the coal seam has been exploited. Panel 8103 is located to the south of panel 8102, which is unexploited. At present, the width of the protective pillar between the 8101 tailgate and 8102 headgate is 20 m (Figure 3).

*2.2. Field Monitoring.* In order to evaluate the current protective pillar stability, the roadway deformation for 8102 headgate was measured in the process of roadway excavation and panel retreat. Four measuring stations (solid magenta circles in Figure 3) were arranged in the 8102 headgate. The distance between measuring stations was 50 m. The field measuring process included the following work:

- (1) The pins (red solid circle in Figure 4(a)) were fixed to the corresponding regions of the roadway at each measuring station. Floor and roof pins were fixed in the midspan; the distance of pins in two ribs from the roof was 1.7 m.
- (2) In the observation process, the convergence of the roof, floor, and two ribs was measured by using a digital deformation instrument and measuring line (Figure 4(b)). The digital deformation instrument was accurate to 0.01 mm, which satisfied the needs of deformation observation.
- (3) During the measuring period, the field data were measured once every 3 days.

The results of the 8102 headgate displacements at different stages are shown in Figure 5. Note that the displacement of the 8102 headgate in Figure 5 is the average displacement of the four measuring stations in the field. The roadway deformation tended to be stable after excavation of 57 days, with a rate of deformation close to zero (Figure 5(a)). The total convergence of the roof, protective pillar rib, and virgin coal rib reached 286 mm, 206 mm, and 158 mm, respectively. As shown in Figure 5(b), compared with the convergence during excavation, the roadway displacement grew rapidly in the panel retreat period. The



FIGURE 1: Location of the Wangzhuang coal mine.

	Lithology	Thickness (m)	Cover depth (m)	Remarks
	Fine sandstone	5.4	268.7	
	Mudstone	9.6	278.3	
	Sandy mudstone	6.4	284.7	
	Siltstone	7.8	292.5	Main roof
	Mudstone	3.6	296.1	Immediate roof
	Coal seam	4.0	300.1	Coal
	Mudstone	4.2	304.3	Immediate floor
	Fine sandstone	6.4	310.7	Main floor
	Siltstone	4.5	315.2	

FIGURE 2: Detailed stratigraphic column for the test site.

convergence of roadway roof increased to 991 mm, and the protective pillar rib and virgin coal rib convergence reached 661 mm and 396 mm, respectively. More than 80% of the

roadway deformation occurred in a location where measuring stations advanced approximately 40 m from the longwall face. The results show that the deformation of the

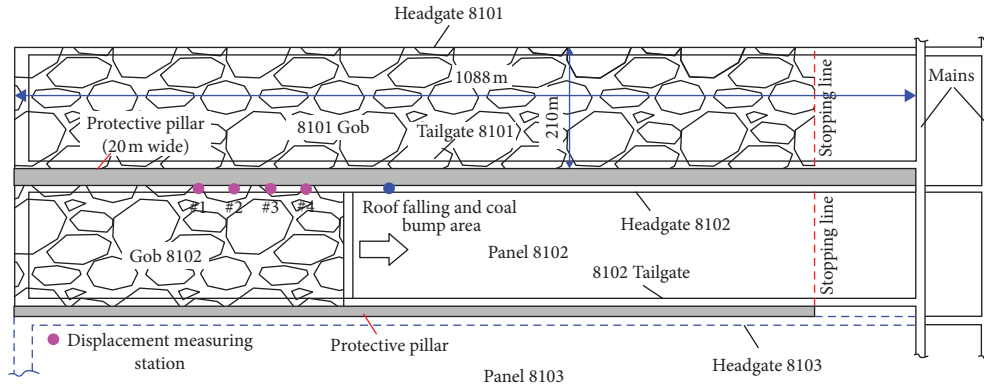


FIGURE 3: Layout of roadway and panel at the test site.

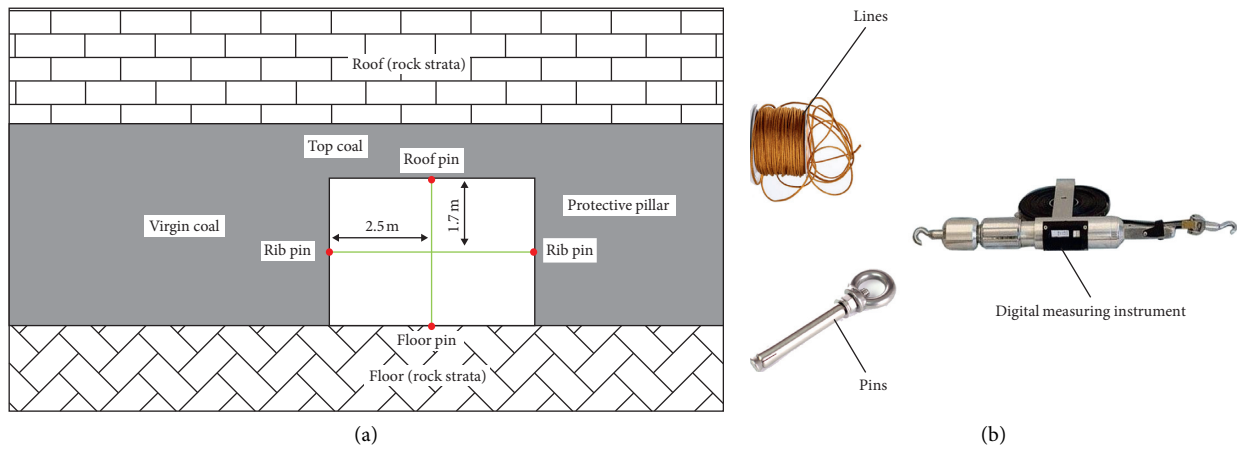


FIGURE 4: Roadway convergence measurement in field. (a) Layout of the measurement station. (b) Measurement devices.

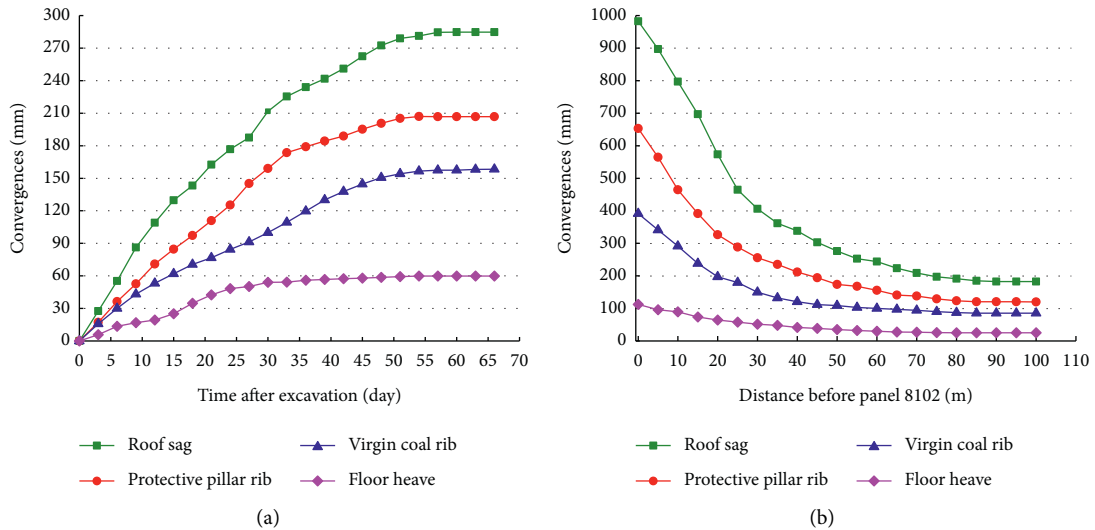


FIGURE 5: Measured convergences in 8102 headgate. (a) During 8102 headgate excavation. (b) During panel 8102 retreat.

roof was the largest and that the deformation in the protective pillar rib was the next largest; the deformation on the floor was considerably smaller than that of the roof and ribs.

The immediate roof and two ribs of headgate 8102 were located in the coal seam with low strength, and the floor was located in mudstone with relatively high strength. This

special engineering geological condition led to a great amount of deformation in the roof and the two ribs once the roadway was excavated.

Severe roof sagging and pillar rib bulging (Figures 6(a) and 6(b)) occurred frequently in the process of panel 8102 retreat. Approximately 30 m in front of panel 8102, roof fall and small-scale coal bump accidents (solid blue circle in Figure 3) occurred, as shown in Figures 6(c) and 6(d). Fortunately, no injuries occurred in the accidents; however, the production efficiency was affected. It took about 20 days to repair the roadway, wasting large amounts of time and money. Professionals did not find the cause of the roof caving and coal bump. It was presumed that the coupling action of high mining-induced stress and low coal strength led to instability of the protective pillar, resulting in the accidents. Therefore, the roof stratum and protective pillar rib were the areas that received attention in panel retreat process.

### 3. Protective Pillar Design Principle

**3.1. Stress Distribution Laws of Protective Pillars.** With roadway excavation, roof strata loads, initially borne by solid coal, are transferred to the two roadway ribs. The distribution of vertical stress in the protective pillar varies greatly with the variation in the pillar width. With a protective pillar width of 5–20 m, the vertical stress distribution characteristics are described by a “single peak,” while the vertical stress distribution characteristics are described by a “double peak” with a 20–40 m wide protective pillar, as shown in Figure 7.

**3.2. Relationship between Protective Pillar Width and Roadway Stability.** The relationship between the width of protective pillar and roadway convergence was used to evaluate the stability of the roadway, as shown in Figure 8.

For determining a rational pillar width for a high stress roadway, the following considerations could be made:

- (1) The width of the protective pillar could not be too thin, such as the left side of point A in Figure 8. Because of its weak bearing capacity, the protective pillar could not maintain roadway stability in this case.
- (2) The protective pillar width could not be too wide, indicated by the curve between points B and D. On account of the strain energy accumulation, the protective pillar may lead to coal bumps in this situation.
- (3) The width of the protective pillar could not reach the critical width, such as point B. Under this condition, the peak stress would be shifted from the solid coal region to the protective pillar. The bearing strength of the protective pillar could not resist the peak stress effectively, and the roadway was in a state of high stress.

A suitable width for protective pillars should provide enough capacity to bear roof strata loads while maintaining

the pillar integrity, reducing the pillar width, and increasing coal recovery rate. Therefore, a thin pillar could be chosen, corresponding to the left side of point B (Figure 8). The roadway could undertake a certain degree of large deformation in this condition, and its integrity could be maintained.

**3.3. Determination of the Cutting Height for the Overlying Strata in the Gob.** During mining, as the working face constantly moved forward, the strata behind the working face were cut off along the preexisting fissure. The gob caving material had a certain bearing capacity when compressed by the upper strata. The gob caving material could support the overlying strata and reduce the pressure on the pillars. Therefore, when designing protective pillars, it is necessary to account for the supporting characteristics of the caving materials.

To effectively utilize the supporting characteristics of the caving materials, it is important to determine the cutting height of the overlying strata in the gob. After roof stratum caving, the volume of caving materials expands. In other words, the pile height of the caving rock mass will be larger than the original height. The volume expansion of the caving materials can be fully described with the bulking factor  $K_p$ . The intact rock original height is  $\Sigma h$ , and the rock mass pile height after roof strata collapse is  $K_p \Sigma h$ . The stratum void height  $\Delta$  between the piled rock and the overlying stable rock will be

$$\Delta = \sum h + M - K_p \sum h = M - \sum h(K_p - 1), \quad (1)$$

where  $M$  denotes the coal seam height and  $K_p$  denotes the bulking factor.

According to equation (1), when  $\Delta = 0$ , the cutting height of the roof strata is calculated by the following equation [15, 16]:

$$\sum h = \frac{M}{K_p - 1}. \quad (2)$$

Based on a number of field observations, the caving height is 4 to 8 times of the coal seam height [17, 18]. For panel 8102, the coal seam height is 4 m, and the bulking factor is determined to be 1.25 [19, 20]. Therefore, the cutting height of the strata above the gob is 16 m.

## 4. Establishment of Numerical Model

**4.1. Modeling Scheme.** To analyse the relationship between the roadway stability and protective pillar width, a numerical model was established based on FLAC3D software. The dimensions of the model were 160 m  $\times$  59.1 m  $\times$  2 m. The model consisted of panels 8101 and 8102 and their roadway system (Figure 9). A vertical stress of 7.5 MPa, representing the loads of overlying rock, is applied to the model top boundary. Based on the in situ stress monitoring data, the ratio of horizontal to vertical stress was determined to be 1.1. For the four vertical model planes, the horizontal displacement was constrained. The displacements in the horizontal and vertical directions were restrained in bottom



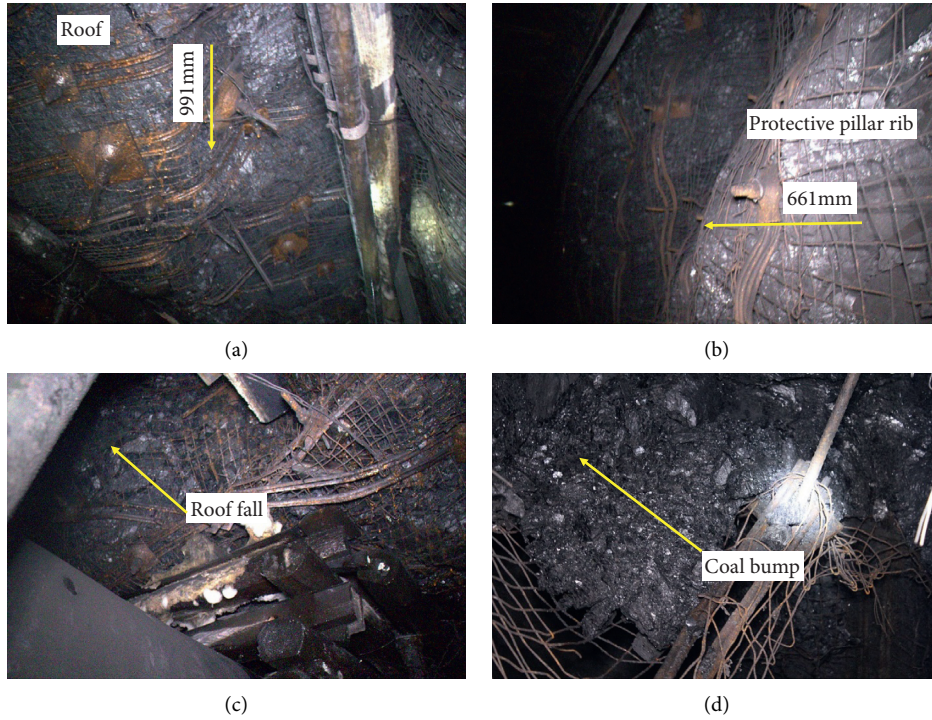


FIGURE 6: Failure characteristics of 8102 headgate. (a) Roof sagging. (b) Protective pillar bulging. (c) Roof fall. (d) Coal bump.

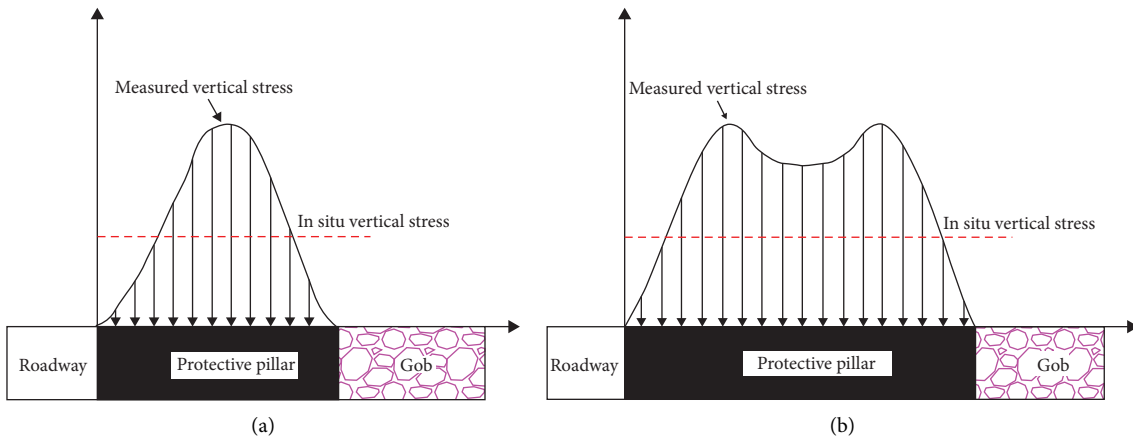


FIGURE 7: Stress distribution of the protective pillar [35]. (a) Single-peak distribution. (b) Double-peak distribution.

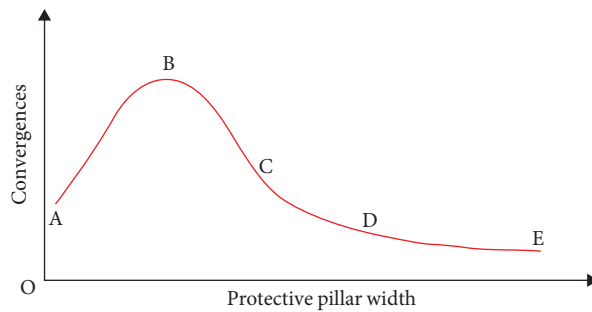


FIGURE 8: The protective pillar width and roadway convergence.

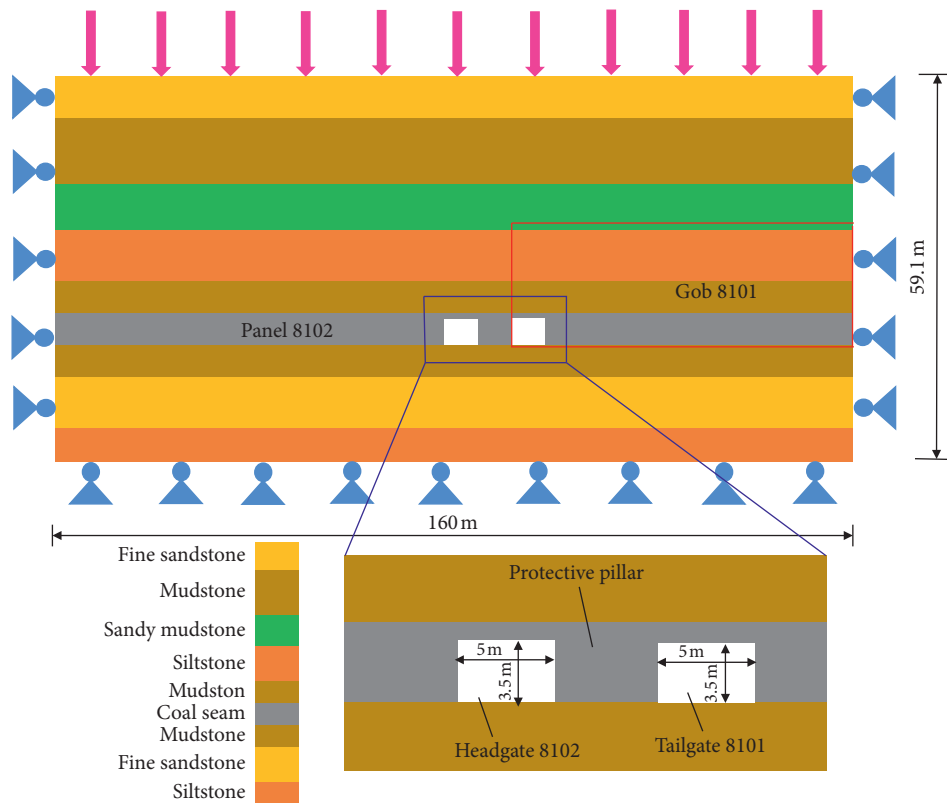


FIGURE 9: Numerical simulation model.

boundary. The Mohr–Coulomb model was adopted to simulate the rock mass, except for the protective pillar and gob caving materials. Table 1 shows the mechanical properties of the rock mass.

The numerical simulation comprised five steps: (1) model establishment and application of in situ stress, (2) initial stress balance in the model, (3) 8101 tailgate excavation, (4) retreat of panel 8101 and equivalent gob materials simulation, and (5) 8102 headgate excavation with five different pillar widths. On the basis of the 8102 headgate conditions, the protective pillar height was maintained at 3.5 m, and the protective pillar width was simulated at 5, 10, 15, 20, and 25 m, as shown in Figure 10.

**4.2. The Constitutive Model of Protective Pillars.** There are elastic phase, plastic softening phase, and residual phase in the process of protective pillar failure. With pillar yielding, plastic softening phases occur until a residual strength level is obtained. At present, the widely used constitutive model of simulating protective pillar failure is the Mohr–Coulomb strain-softening model, in which pillars are considered to be materials with softening properties [21, 22]. After yielding, the friction angle and cohesion soften with the change in plastic strain. To simulate the strain-softening behaviour of protective pillar, a pillar submodel is established and includes the roof, pillar, and floor, as shown in Figure 11. The mechanical behaviour of the pillar is simulated by the strain-softening model, and the mechanical behaviour of the roof and floor is simulated by the Mohr–Coulomb model.

Many strength formulas of pillar have been put forward in the recent decades [23–25]. It is noted that Salamon–Munro proposed the following empirical formula, with pillar  $W/H$  (width-to-height) ratios from 2 to 20 [23].

$$\text{Pillar Strength} = 7.716 \frac{w^{0.46}}{h^{0.66}}, \quad (3)$$

where  $w$  and  $h$  indicate the width and height of pillar, respectively.

The empirical strength formula of the pillar has good consistency with developed average strength formulas. Therefore, the Salamon–Munro strength formula was adopted in this study to verify the pillar numerical model. A commonly used iterative method is adopted [21, 26]. The parameters of the strain-softening model are determined by matching the strength of the pillar acquired by numerical simulation with that determined by the Salamon–Munro formula. Table 2 shows the input parameters for calibrating the pillar strain-softening model. The simulated and calculated strengths of pillar are displayed in Figure 12. The results show that the simulated strength of the pillar matches with the calculated strength of pillar from the Salamon–Munro empirical formula very well, suggesting that the parameters can be adopted to accurately simulate the mechanical behaviour of a protective pillar.

**4.3. Modeling of the Caving Materials in the Gob.** After panel retreat, the roof strata behind the panel collapse, and the caving rock in the gob is compacted and consolidated.

TABLE 1: Mechanical properties of the rock mass.

Lithology	Density (kg/m <sup>3</sup> )	Compressive strength (MPa)	Elasticity modulus (GPa)	Poisson's ration ( $\nu$ )	Cohesion (MPa)	Friction (°)
Fine sandstone	2750	57.2	12.5	0.22	2.6	29
Mudstone	1900	13.1	5.0	0.29	1.4	25
Sandy mudstone	2450	27.8	7.1	0.26	1.8	27
Siltstone	2680	47.6	9.8	0.24	2.3	31
Mudstone	1900	13.1	5.0	0.29	1.4	25
Coal seam	1600	9.8	1.5	0.32	0.8	22
Mudstone	1900	13.1	5.0	0.29	1.4	25
Fine sandstone	2750	57.2	12.5	0.22	2.6	29
Siltstone	2680	47.6	9.8	0.24	2.3	31

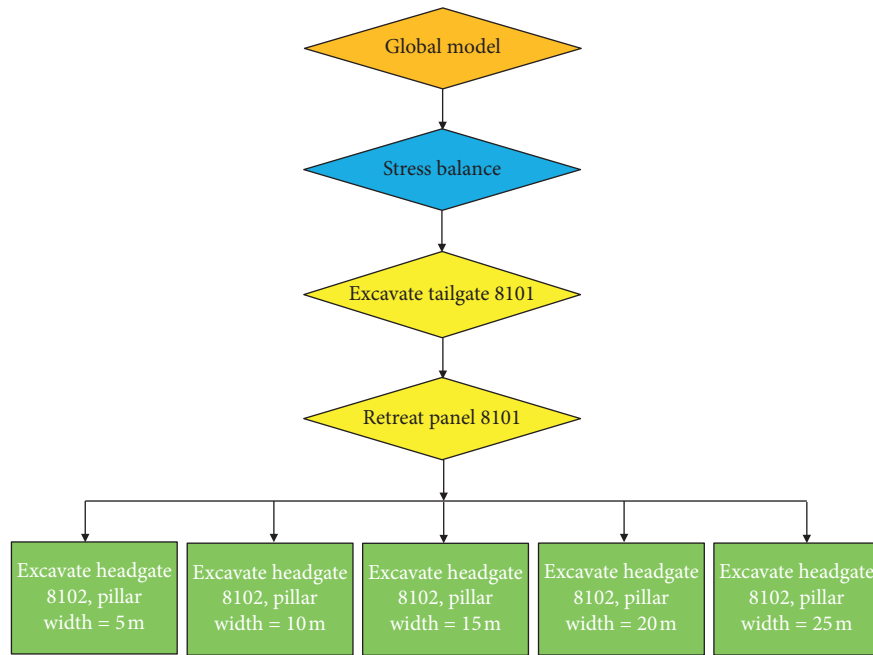


FIGURE 10: The FLAC3D numerical simulation steps.

TABLE 2: Strain-softening properties of pillar with plastic strain.

Strain	0	0.0025	0.005	0.0075	0.01
Cohesion (MPa)	0.8	0.68	0.54	0.4	0.28
Friction angle (°)	24	23	22	21	21

Regarding the influence of the gob caving rock on the protective pillars, the mechanical behaviour of the gob caving materials was simulated by the double-yield model [21, 27]. The input parameters of the double-yield model included material properties and cap pressure [28]. The cap pressure parameters were determined by the following equation proposed by Salamon:

$$\sigma = \frac{E_0 \varepsilon}{1 - \varepsilon/\varepsilon_m}, \quad (4)$$

where  $\sigma$  denotes the vertical stress applied to the gob caving materials;  $\varepsilon$  denotes the volumetric strain and maximum strain  $\varepsilon_m$ , respectively;  $E_0$  denotes the initial modulus of the

gob materials. Parameters  $E_0$  and  $\varepsilon_m$  could be obtained by the two following equations:

$$\varepsilon_m = \frac{(K_p - 1)}{K_p}, \quad (5)$$

$$E_0 = \frac{10.39 \sigma_c^{1.042}}{K_p^{7.7}}, \quad (6)$$

Where  $K_p$  denotes the bulking factor; and  $\sigma_c$  denotes the compressive strength of the caving materials in gob. Based on equation (2), the bulking factor  $K_p$  and compressive strength  $\sigma_c$  were determined to be 1.25 and 12 MPa,

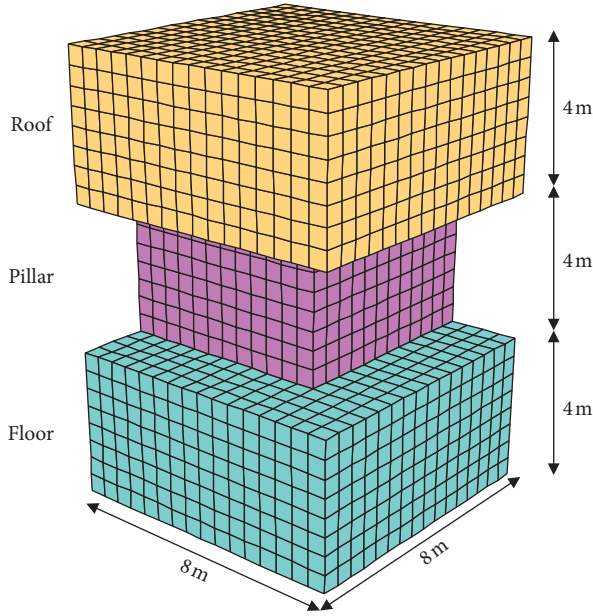


FIGURE 11: A pillar submodel.

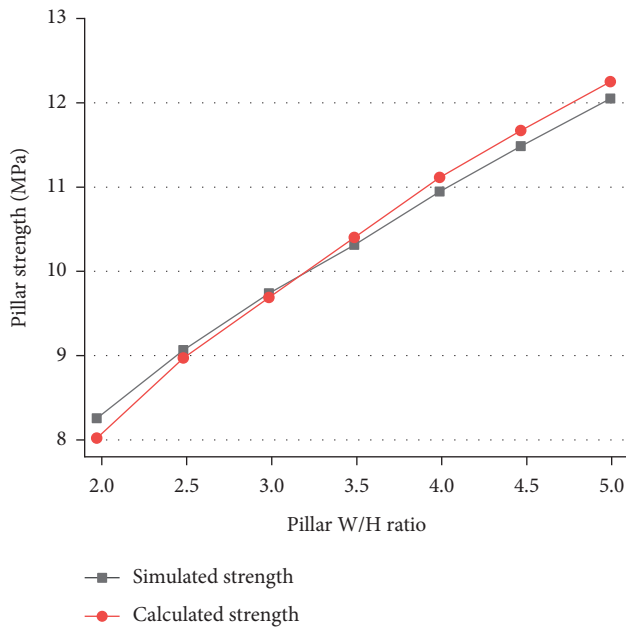


FIGURE 12: The simulated and calculated strengths of pillar.

respectively. According to equations (5) and (6), the maximum strain  $\epsilon_m$  and initial tangent modulus  $E_0$  are 0.2 and 24.8 MPa, respectively. The cap pressure parameters of the numerical model are shown in Table 3.

To obtain the material parameters of the double-yield model (bulk modulus, shear modulus, friction angle, and dilation angle), a gob element (Figure 13) was selected. A  $10^{-5}$  m/s vertical velocity was used to represent the load and apply to the element top. The horizontal deformation of four vertical faces of the element was restrained, while the vertical deformation at the element bottom was set to zero. A fitting method in previous related research was adopted to match

the gob element stress-strain curve with Salamon's model [21, 29]. Figure 14 compares the stress-strain curves of two models, and they match very well. Based on the comparison result, the final parameters of the gob material in the double-yield model were obtained and used in FLAC3D (Table 4).

**4.4. The Relationship between the Stress and Energy Density of the Surrounding Rock Element.** The stress state of the surrounding rock structure is closely related to its stored energy. During excavation, the stress of the rock mass is adjusted with changes of the energy storage structure. As the essential attribute of the deformation and destruction of surrounding rock, the energy change reflects the continuous development of defects, weakening, and loss of strength in the surrounding rock mass [30]. Therefore, failure of the surrounding rock structure is reflected by internal energy change.

An element of the surrounding rock structure was chosen, and the size and shape of the element changed with the external forces. Figure 15 shows the 3D stress state of the element, which can be considered the superposition of two stress states. On the one hand, it can be described by the average stress  $\sigma_m$  of the element in three directions:

$$\sigma_m = \frac{\sigma_1 + \sigma_2 + \sigma_3}{3}, \quad (7)$$

where  $\sigma_1$ ,  $\sigma_2$ , and  $\sigma_3$  are the maximum, intermediate, and minimum principal stress, respectively.

On the other hand, it can be considered that stresses  $\sigma_1^- = \sigma_1 - \sigma_m$ ,  $\sigma_2^- = \sigma_2 - \sigma_m$ , and  $\sigma_3^- = \sigma_3 - \sigma_m$  are applied in the three directions of the element, where  $\sigma_1^-$ ,  $\sigma_2^-$ , and  $\sigma_3^-$  are considered to be the deviations in stress from the principal stresses  $\sigma_1$ ,  $\sigma_2$ , and  $\sigma_3$  [31].

$$\sigma_1^- = \frac{2\sigma_1 - \sigma_2 - \sigma_3}{3}, \sigma_2^- = \frac{2\sigma_2 - \sigma_3 - \sigma_1}{3}, \sigma_3^- = \frac{2\sigma_3 - \sigma_1 - \sigma_2}{3}. \quad (8)$$

Under the action of the average stress  $\sigma_m$ , the volume of the element changes, while its shape is invariant. The strain energy density was calculated according to the following formula:

$$v_v = \frac{1 - 2\mu}{6E} (\sigma_1 + \sigma_2 + \sigma_3)^2, \quad (9)$$

where  $v_v$  denotes the strain energy density under the action of average stress  $\sigma_m$ ; and  $\sigma_1$ ,  $\sigma_2$ , and  $\sigma_3$  are the maximum, intermediate, and minimum principal stress, respectively.

Under the action of the deviatoric stresses  $\sigma_1^-$ ,  $\sigma_2^-$ , and  $\sigma_3^-$ , the shape of the element changes, while its volume is invariant. Thus, the strain energy density was calculated according to the following formula:

$$v_d = \frac{1 + \mu}{6E} [(\sigma_1 - \sigma_2)^2 + (\sigma_2 - \sigma_3)^2 + (\sigma_3 - \sigma_1)^2], \quad (10)$$

where  $v_d$  denotes strain energy density under the action of the deviatoric stresses  $\sigma_1^-$ ,  $\sigma_2^-$ , and  $\sigma_3^-$ .

The element strain energy density includes the volume-changed and shape-changed strain energy density. Therefore,

TABLE 3: The double-yield model cap pressures.

Strain	0	0.01	0.02	0.03	0.04	0.05	0.06	0.07	0.08	0.09
Stress (MPa)	0	0.26	0.55	0.88	1.24	1.65	2.13	2.67	3.31	4.06
Strain	0.10	0.11	0.12	0.13	0.14	0.15	0.16	0.17	0.18	0.19
Stress (MPa)	4.96	6.06	7.44	9.21	11.57	14.88	19.84	28.10	44.64	94.24

the strain energy density of the element can be expressed [32, 33]:

$$v = v_v + v_d = \frac{1-2\mu}{6E}(\sigma_1 + \sigma_2 + \sigma_3)^2 + \frac{1+\mu}{6E}[(\sigma_1 - \sigma_2)^2 + (\sigma_2 - \sigma_3)^2 + (\sigma_3 - \sigma_1)^2], \quad (11)$$

where  $v$  denotes the sum of the strain energy density caused by the changes in volume and shape of the element.

According to equation (11), it can be clearly seen that energy stored in the surrounding rock element is closely related to its own stress state. A coupled program of the strain energy density and stress of a surrounding rock element was developed in this study, which was used to investigate the relationship between the internal energy and stress of the rock mass.

**4.5. Verification of the Gob Caving Materials Supporting Capacity.** To validate the effectiveness of the supporting capacity of caving materials in gob 8101, Figure 16 displays the vertical stress evolution law in the caving area. There is 0.42 MPa of vertical stress at the gob edge. Meanwhile, the vertical stress increases gradually with distance increase from the gob edge. The maximal vertical stress reaches 7.45 MPa at an approximately 73.6 m distance from the gob edge and remains relatively steady. The caving materials in the gob bear 99% of the initial vertical stress (7.45/7.5 MPa). With increasing distance from the gob edge, the caving materials are compressed and the vertical stress in the caving area increases gradually. The vertical stress of the gob reaches the initial stress (7.5 MPa) at approximately 73.6 m from the gob edge, that is, 25% (73.6/300) of the overlying depth. Through extensive field tests, Wilson and Carr [34] and Campoli et al. [35] proposed that the gob vertical stress could reach the initial stress of the rock mass at a distance of 0.2–0.38 times the buried depth of coal seam. In this study, the obtained vertical stress distribution agrees well with the related conclusions [14, 25, 36], indicating that the simulation result of the supporting capacity of the gob caving materials is reliable.

## 5. Modeling Results and Discussion

**5.1. Modeling Results.** The simulation results of the vertical stress and energy density of the two ribs in the 8102 headgate are shown in Figure 17. To analyse the simulation results in detail, Figure 17(a) is taken as an example. The upper diagram indicates vertical stress distribution and the lower diagram shows the energy density distribution of two

roadway ribs. The blue and yellow areas in the middle represent elements of surrounding rock in the elastic and yielded states, respectively. The curves on the two sides of the roadway represent the changes of vertical stress and energy density. Note that all the data come from the mid-height on the two roadway ribs. The peak values of the vertical stress and energy density in the protective pillar are designated as  $\sigma_{cs}$  and  $v_{cd}$ , respectively, while the peak values of the vertical stress and energy density in the virgin coal rib are designated as  $\sigma_{vs}$  and  $v_{vd}$ , respectively.

With a 5 m width, the protective pillar is damaged completely and could not keep the stability of the 8102 headgate, as shown in Figure 17(a). Stress concentration and energy accumulation occur in a position 4.6 m from the edge of the protective pillar rib, with  $\sigma_{cs}$  of 8.6 MPa and  $v_{cd}$  of 176.1 kJ/m<sup>3</sup>, while at a position 14.3 m from the virgin rib edge,  $\sigma_{vs}$  and  $v_{vd}$  are 16.7 MPa and 461.5 kJ/m<sup>3</sup>, respectively. The peak values of the vertical stress and energy density for the virgin coal rib are obviously greater than those of the protective pillar. When the pillar width reaches 10 m, protective pillar is in yield state but is not crushed. The virgin coal rib yield range decreases. Moreover,  $\sigma_{cs}$  increases gradually from 8.6 MPa to 9.5 MPa with  $v_{cd}$  increasing from 176.1 kJ/m<sup>3</sup> to 208.3 kJ/m<sup>3</sup>, remaining lower than the vertical stress (16.2 MPa) and energy density (434.8 kJ/m<sup>3</sup>) of the virgin coal rib (Figure 17(b)), showing that the roof strata loads are mainly on the solid coal region. When the protective pillar is 15 m and 20 m wide, the vertical stress and energy density increase sharply and exceed the virgin rib (Figures 17(c) and 17(d)), showing that mining pressure is transferred rapidly to the protective coal pillar, sharply changing the energy density. The excess stress and elastic energy result in severe roadway deformation and the occurrence of coal bumps, which are identical to the failure characteristics of 8102 headgate in the field test. With condition of 25 m wide protective pillar, there is a 6 m elastic zone in the pillar (Figure 17(e)). The yielded range of the two roadway ribs shrinks significantly. A stable elastic energy storage structure is formed in the protective pillar, which is capable of absorbing substantial stress and elastic energy. The distribution of the vertical stress and energy density exhibits a double peak,



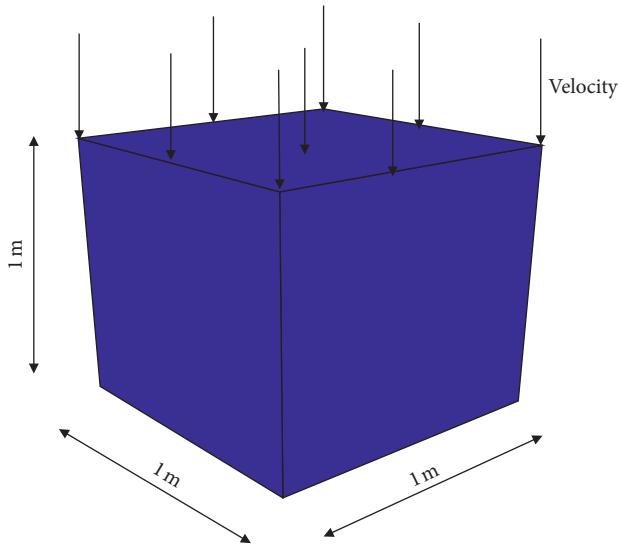


FIGURE 13: An element of the gob.

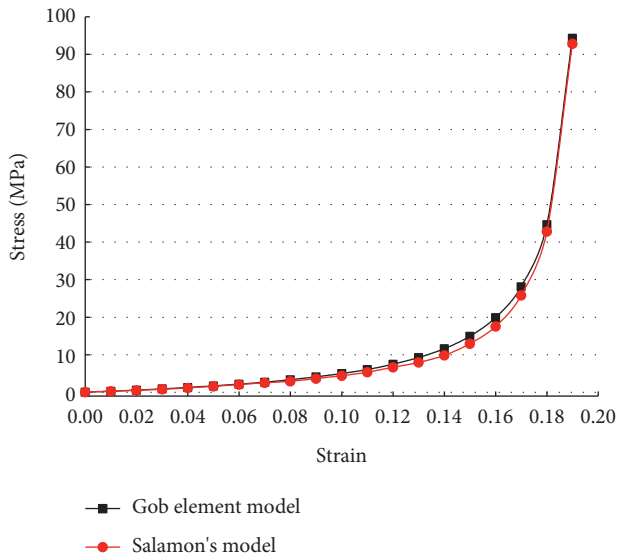


FIGURE 14: The stress-strain curve comparison of simulated and calculated model.

which is consistent with the conclusion based on Figure 7(b). The modeling results illustrate that adjusting the pillar width improves the stability of the surrounding rock.

For the different protective pillar widths, the roadway deformation laws are shown in Figure 18. The displacement of two ribs in roadway is obviously larger than that of the roof and floor. The effect of the protective pillar width on the stability of the two ribs is greater than that of the roadway roof and floor. Meanwhile, the roadway deformation of 10 m pillar width is similar to that of 25 m wide protective pillar.

The results (Figures 17 and 18) show that the protective pillar width influences greatly the pillar load-bearing capacity and roadway deformation. Most surprisingly, when the protective pillar widths are 10 m and 25 m, the difference in roadway deformation is not

obvious. This demonstrates that the existence of an elastic intact zone enhances the stability of the protective pillar. Consequently, increasing the protective pillar width could enhance the reliability of the pillar load-bearing capacity and improve the roadway stability.

5.2. Discussion of the Rational Width for a Protective Pillar.

The original balanced state of the main roof above the roadway is strongly disturbed during the panel retreat period. The main roof is broken [37–39], as shown in Figure 19(a). Rock masses A, B, and C interact, which influences the stability of the 8102 headgate. During the roof fracture period, rock mass B above the roadway begins to rotate and subside. The rotation and subsidence have a great impact on the stability of the protective pillar. The rock B fracture position and rotating speed are closely related to the pillar width. According to the ultimate balance theory, the geometry size  $l$  of rock B can be derived from the panel dip length  $S$  and periodic breakage length  $L$  of the main roof, as in the following formula [40, 41]:

$$l = \frac{2L}{17} \left[ \sqrt{\left(10 \frac{L}{S}\right)^2 + 102} - 10 \frac{L}{S} \right], \quad (12)$$

where  $S$  is the dip length of the panel and  $L$  is the periodic breakage length of the main roof. From field measurements, the periodic breakage length of the main roof is 23 m. The dip length of panel 8102 was 210 m. From equation (12), the geometry size  $l$  of rock B was 24.5 m.

From the results of the numerical simulation, in the case of a 5 m wide protective pillar, the peak vertical stress of the virgin coal rib occurs 14.3 m from the rib edge. The length between the peak vertical stress location in the virgin rib and the rib edge plus the width of the protective pillar and the roadway equals the geometry size of rock B, indicating that rock mass B will fracture at the location where the peak vertical stress of the virgin coal rib occurs (Figure 19(a)). A 5 m wide protective pillar cannot withstand the loads of the overlying strata. Rock mass B rotates violently and the protective pillar is crushed. With a 20 m wide protective pillar, the vertical stress peak in the virgin rib is transferred to the pillar. Based on the geometry size of rock B, it could be concluded that its fracture position is located at the junction of the roof and the virgin coal rib (Figure 19(b)), which is consistent with the field result showing that roof sagging and falling often occur at the place close to the junction between the roof and the virgin coal rib. In the panel retreat period, the superimposed effect of mining stress and high in situ stress surpasses the bearing strength of the protective pillar, and the continued pillar deformation leads to the fracture and rotation movement of rock mass B in the main roof. Finally, the protective pillar is crushed and fails. With a 10 m wide protective pillar, the vertical stress peak is still located in the virgin coal rib; that is, the area of virgin rib is subjected to the main load of the overlying strata. The pillar bears relatively less load, which puts the roadway in a state of low stress. Meanwhile, the protective pillar could provide support to the fractured rock mass B and prevent it from rotary movement, which maintains the stability of the roadway. When the width of protective pillar is 25 m, the

TABLE 4: The caving material parameters in gob.

Parameters	Density (kg/m <sup>3</sup> )	Bulk modulus (GPa)	Shear modulus (GPa)	Friction (°)	Dilation (°)
Value	1200	4.8	2.7	25	5

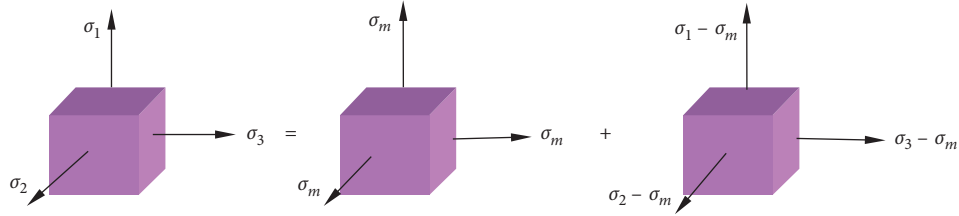


FIGURE 15: Three-dimensional stress state of surrounding rock element.

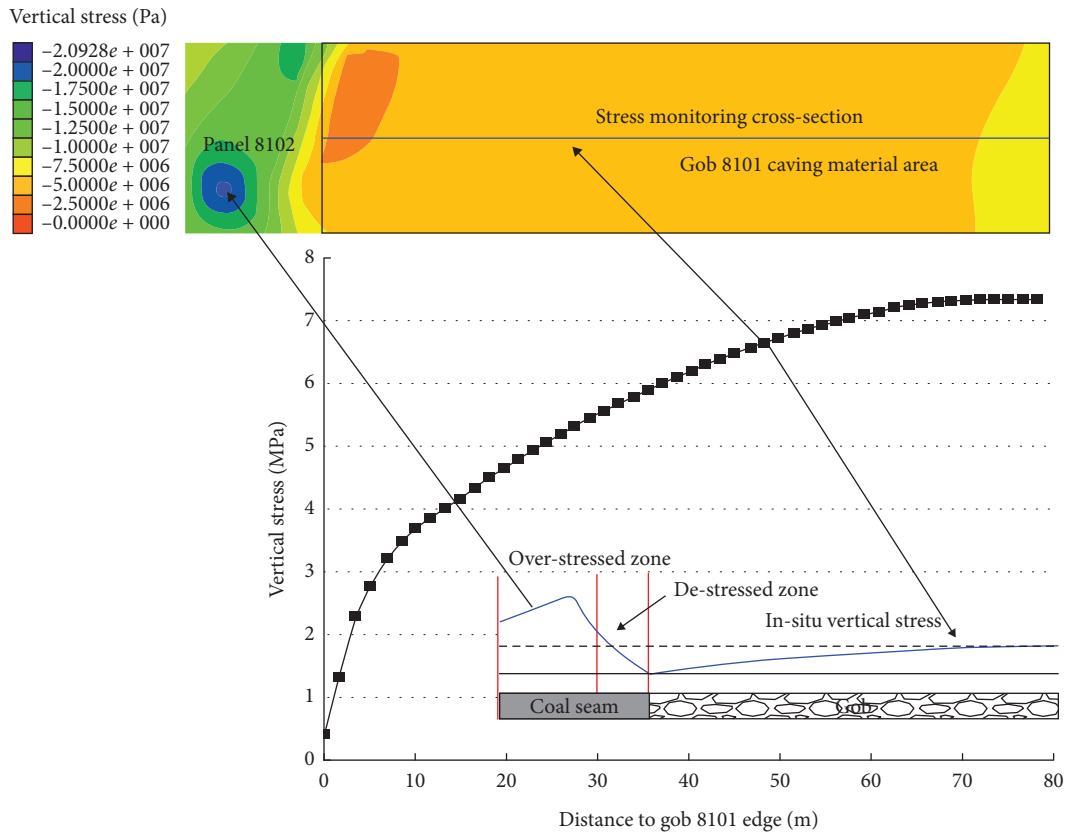


FIGURE 16: The vertical stress distribution in gob 8101.

bearing capacity is improved due to the expansion of the elastic area in the pillar. The protective pillar can not only maintain its own stability but also prevent the fractured rock mass B of the main roof from rotating, transitioning the roadway to a stable state. However, a greater pillar width wastes more coal resources.

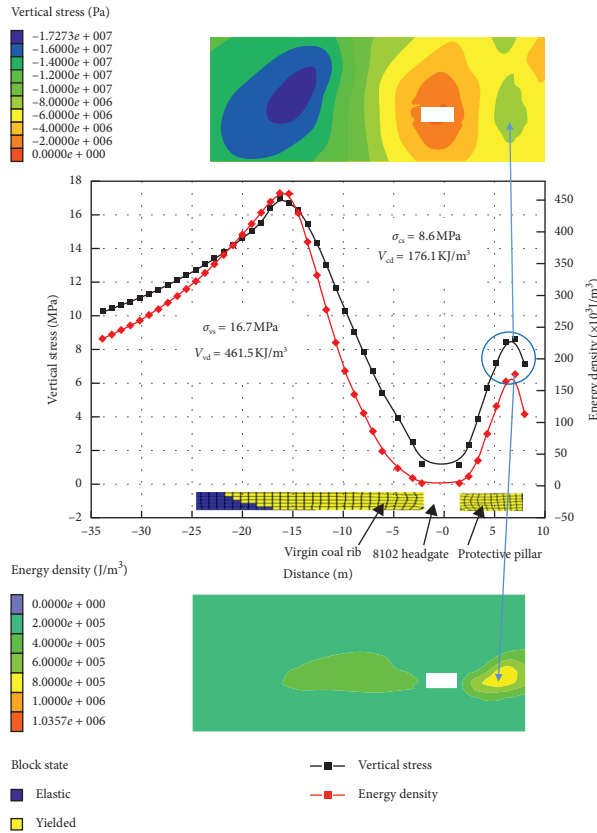
A rational pillar width should have the capacity to withstand abutment pressure and maintain a stable roadway, while maximizing the recovery of coal resources. Based on the above discussion, the recommended 10 m wide protective pillar may be more conducive to improving the roadway stability and coal recovery rate, while reducing economic loss due to large deformation and coal bump failure.

## 6. Field Test

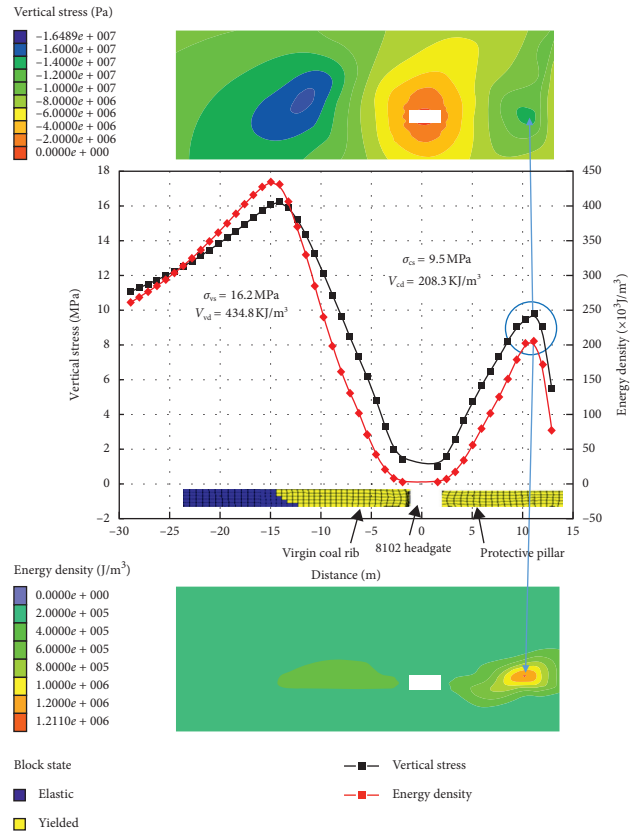
A protective pillar width of 10 m was applied in field to maintain the stability of the surrounding rock 8103 headgate. The protective pillar stress distribution and deformation of the 8103 headgate were measured to validate the reliability of the simulation results.

### 6.1. Stress Measurement of the Protective Pillar in the Field.

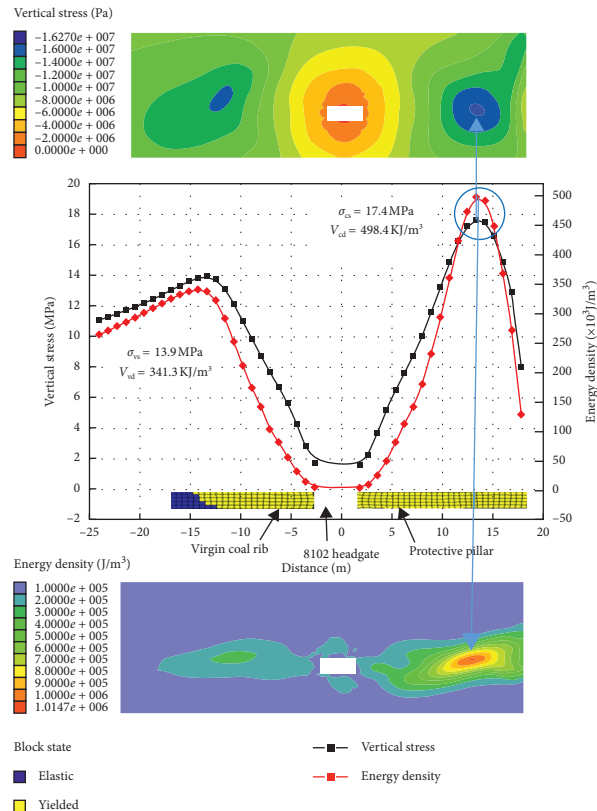
The vertical stress at different distances from the protective pillar rib of the 8103 headgate is plotted in Figure 20. The field data are also displayed for comparison with the



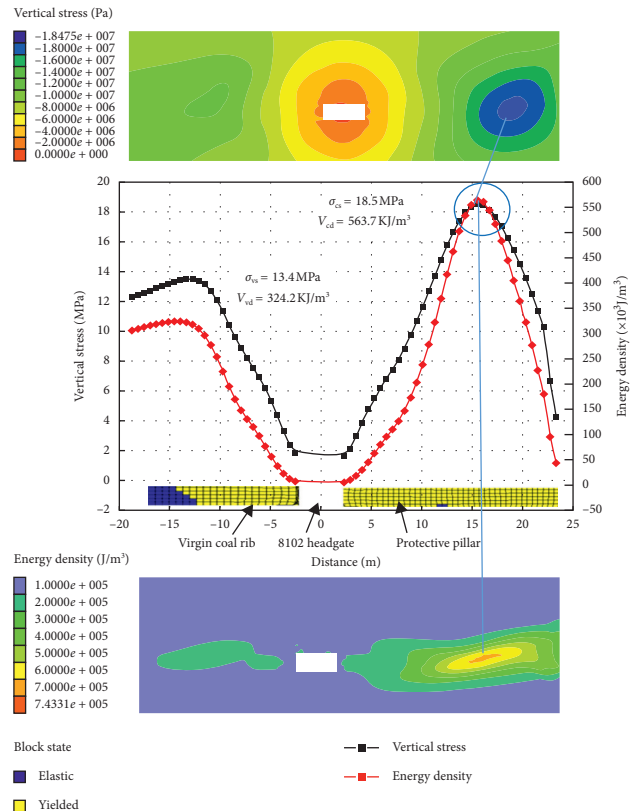
(a)



(b)

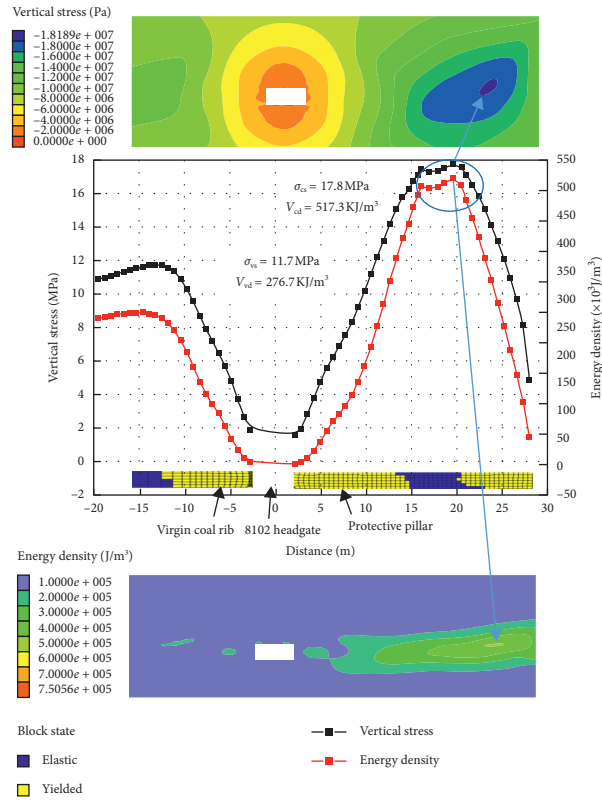


(c)



(d)

FIGURE 17: Continued.



(e)

FIGURE 17: Vertical stress and energy density distribution on two ribs of 8102 headgate with different pillar widths. (a) The width of 5 m. (b) The width of 10 m. (c) The width of 15 m. (d) The width of 20 m. (e) The width of 25 m.

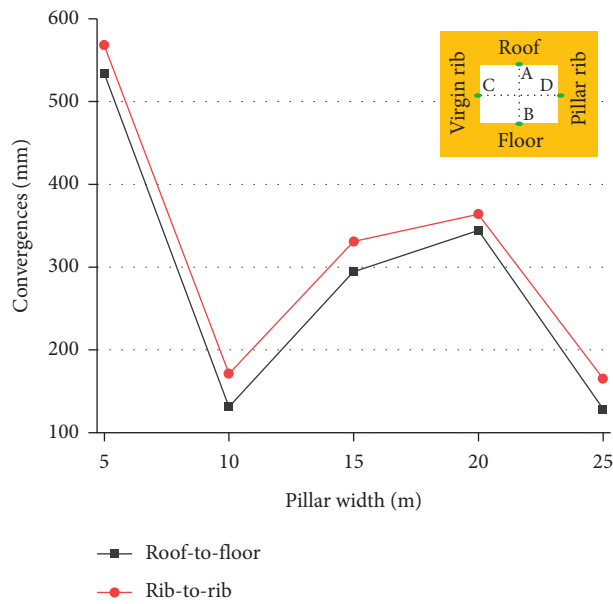


FIGURE 18: Roadway deformation with different pillar width.

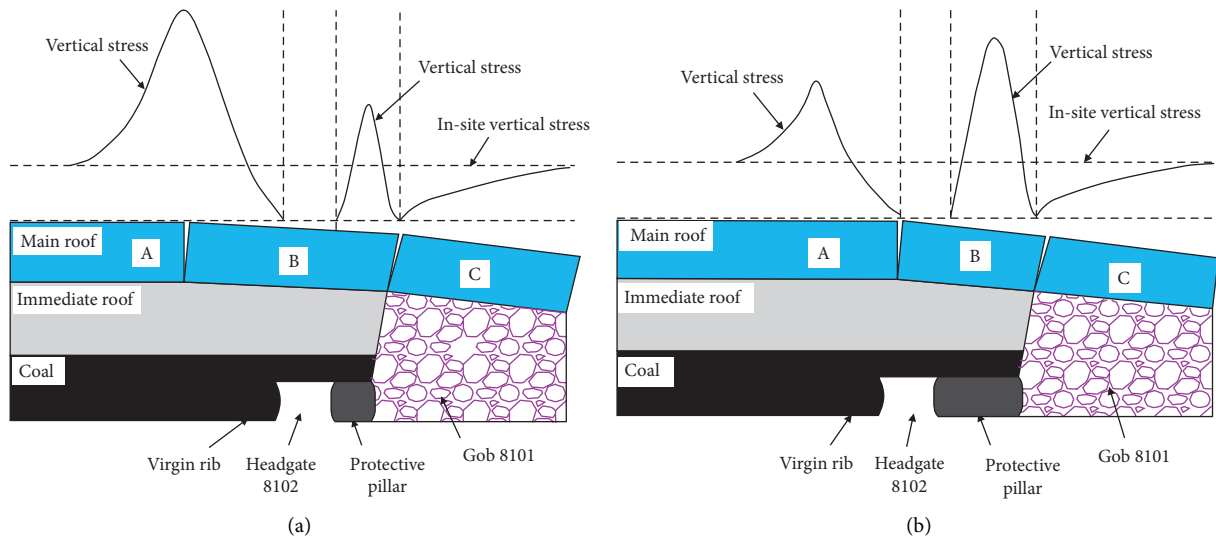


FIGURE 19: Failure modes of the protective pillar. (a) 5 m wide. (b) 20 m wide.

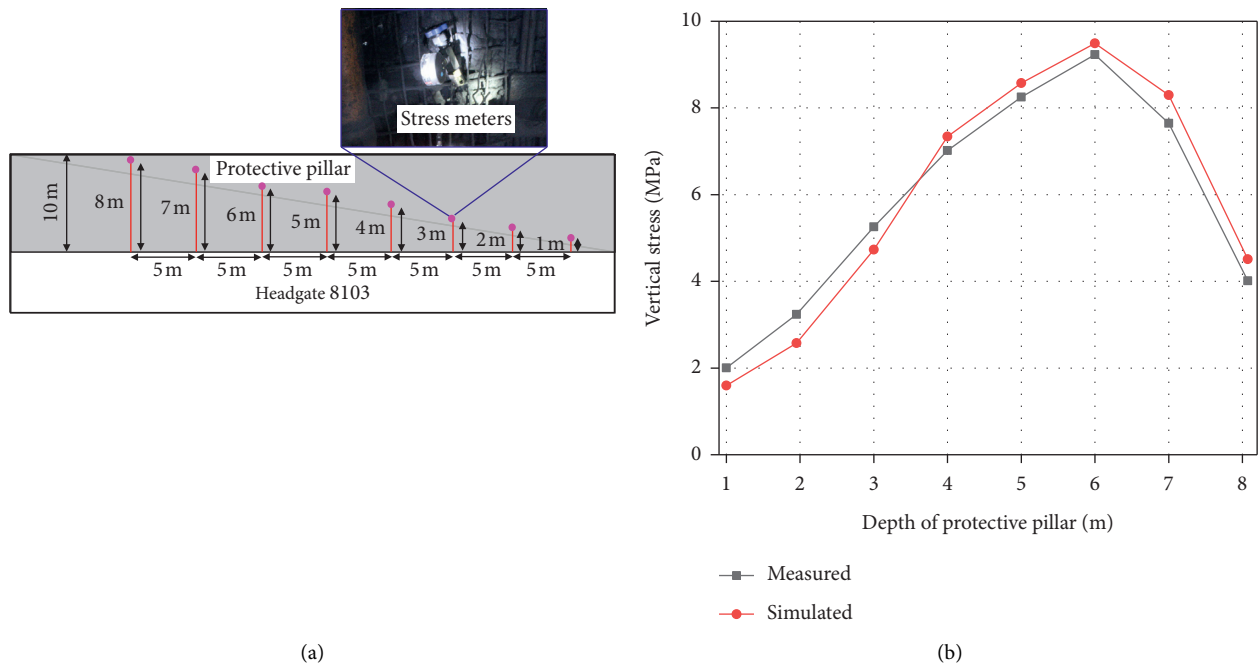


FIGURE 20: Stress measurement of protective pillar. (a) Layout of stress meters. (b) Distribution law of vertical stress after roadway excavation.

modeling results. The measured results and simulated results have good agreement, verifying the numerical modeling accuracy.

6.2. Roadway Deformation Laws. The measured roadway deformation results at different stages are shown in Figure 21. The deformation of the roadway became stable after 50 days of excavation. The convergences of the roof, virgin coal rib, protective pillar rib, and floor were

115 mm, 74 mm, 87 mm, and 16 mm, respectively. During the panel 8103 retreat period, the roadway deformation mainly occurred 60 m in front of the working face; the total convergences at the roof, virgin coal rib, protective pillar rib, and floor were 301 mm, 162 mm, 214 mm, and 24 mm, respectively, which represented reductions of 70%, 59%, 68%, and 77% (Figure 22), compared with the deformation that occurred under the previous protective pillar width. The stability of the surrounding 8103 headgate is improved, as shown in Figure 23. The field



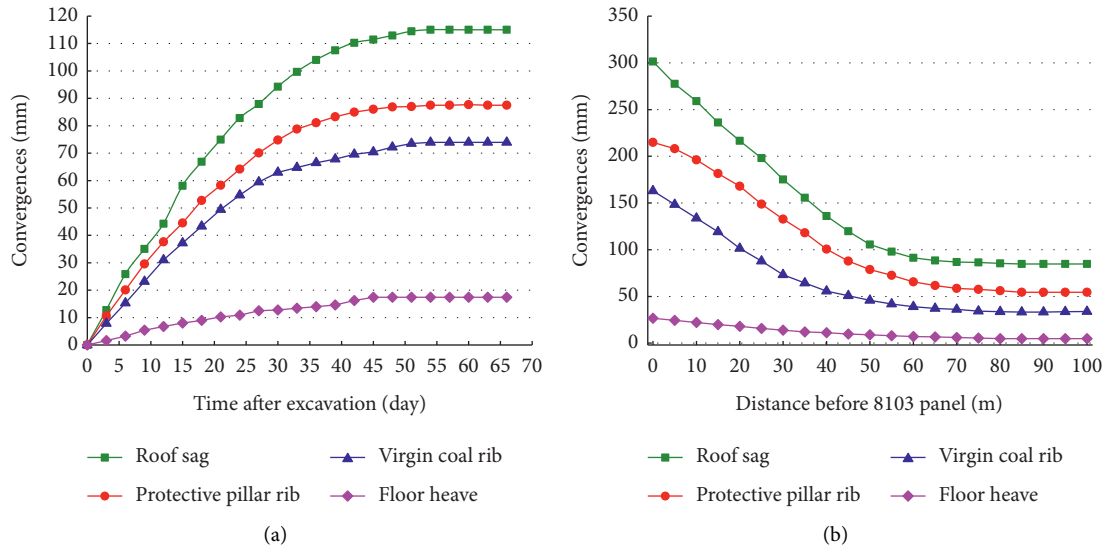


FIGURE 21: Measured convergences in 8103 headgate. (a) During 8103 headgate excavation. (b) During panel 8103 retreat.

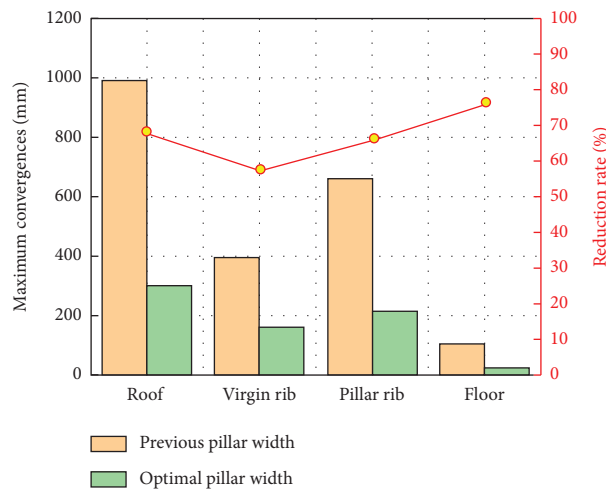


FIGURE 22: Comparison of roadway convergences during panel 8103 retreat.



FIGURE 23: The stable environment of surrounding rock in 8103 headgate.

observation results indicate that the proposed protective pillar width is feasible for maintaining the stability of the roadway.

## 7. Conclusions

This study was mainly focused on analysing the effect of protective pillar width on the roadway stability to identify a pillar design principle based on field tests and numerical simulations. The main conclusions in this paper are summarized as follows:

- (1) A novel numerical model was established to analyse the failure mechanism of the protective pillar. As an innovative design method of protective pillars, the supporting features of the gob caving materials on overlying strata and the relationship between the internal stress and stored energy of the rock mass were considered in the modeling process. The stress change and distribution characteristics of the energy density are regarded as important conditions in designing the width of a protective pillar and evaluating the stability of the roadway.
- (2) The modeling results showed that, with a 20 m wide pillar, the peak vertical stress and energy density in the protective pillar were 18.5 MPa and 563.7 kJ/m<sup>3</sup>, respectively. Excessive stress and elastic energy resulted in considerable deformation and coal bump failure in headgate 8102. With a pillar width of 10 m, the location of the peak vertical stress and energy density moved from the protective pillar to the virgin rib. The main loads of the overlying strata were borne by the virgin rib, and the pillar was subjected to a relatively low load. The roadway was in a state of low stress and could maintain its stability.
- (3) The results of the field measurements showed that a 10 m wide protective pillar was able to effectively control the roadway deformation and release most of the storing energy in protective pillar. Meanwhile, the proposed modeling approach and protective pillar design principles in this study can provide a useful basis for application in similar coal mines.

## Data Availability

The data used to support the findings of this study are included within the article.

## Conflicts of Interest

The authors declare that they have no conflicts of interest to report regarding the present study.

## Acknowledgments

This study was supported by the National Natural Science Foundation of China (no. 51674250) and the State Key

Program of the National Natural Science Foundation of China (no. 50834005). In addition, the authors are very grateful for the linguistic assistance of AJE (American Journal Experts) in the manuscript preparation period.

## References

- [1] S.-Q. Yang, M. Chen, H.-W. Jing, K.-F. Chen, and B. Meng, "A case study on large deformation failure mechanism of deep soft rock roadway in Xin'An coal mine, China," *Engineering Geology*, vol. 217, pp. 89–101, 2017.
- [2] R. Gu and U. Ozbay, "Numerical investigation of unstable rock failure in underground mining condition," *Computers and Geotechnics*, vol. 63, pp. 171–182, 2015.
- [3] Z. Zhang, M. Deng, X. Wang, W. Yu, F. Zhang, and V. D. Dao, "Field and numerical investigations on the lower coal seam entry failure analysis under the remnant pillar," *Engineering Failure Analysis*, vol. 115, Article ID 104638, 2020.
- [4] W. Gao and M. Ge, "Stability of a coal pillar for strip mining based on an elastic-plastic analysis," *International Journal of Rock Mechanics and Mining Sciences*, vol. 87, pp. 23–28, 2016.
- [5] H. Wu, X. Wang, W. Wang, G. Peng, and Z. Zhang, "Deformation characteristics and mechanism of deep subscale coal pillar of the tilted stratum," *Energy Science & Engineering*, vol. 8, no. 2, pp. 544–561, 2020.
- [6] E. Ghasemi, M. Ataei, and K. Shahriar, "Prediction of global stability in room and pillar coal mines," *Natural Hazards*, vol. 72, no. 2, pp. 405–422, 2014.
- [7] Z. Z. Cao and Y. J. Zhou, "Research on coal pillar width in roadway driving along goaf based on the stability of key block," *CMC-Computers, Materials Continua*, vol. 48, pp. 77–90, 2015.
- [8] J. X. Yang, C. Y. Liu, B. Yu, and F. F. Wu, "The effect of a multi-gob, pier-type roof structure on coal pillar load-bearing capacity and stress distribution," *Bulletin of Engineering Geology and the Environment*, vol. 74, no. 4, pp. 1267–1273, 2015.
- [9] M. Chen, S.-Q. Yang, Y.-C. Zhang, and C.-W. Zang, "Analysis of the failure mechanism and support technology for the Dongtan deep coal roadway," *Geomechanics and Engineering*, vol. 11, no. 3, pp. 401–420, 2016.
- [10] M. Shabanimashcool and C. C. Li, "A numerical study of stress changes in barrier pillars and a border area in a longwall coal mine," *International Journal of Coal Geology*, vol. 106, pp. 39–47, 2013.
- [11] J.-B. Bai, W.-L. Shen, G.-L. Guo, X.-Y. Wang, and Y. Yu, "Roof deformation, failure characteristics, and preventive techniques of gob-side entry driving heading adjacent to the advancing working face," *Rock Mechanics and Rock Engineering*, vol. 48, no. 6, pp. 2447–2458, 2015.
- [12] T. Ma, L. Wang, F. T. Suorineni, and C. Tang, "Numerical analysis on failure modes and mechanisms of mine pillars under shear loading," *Shock and Vibration*, vol. 2016, Article ID 6195482, 14 pages, 2016.
- [13] H. Wang, Y. Jiang, Y. Zhao, J. Zhu, and S. Liu, "Numerical investigation of the dynamic mechanical state of a coal pillar during longwall mining panel extraction," *Rock Mechanics and Rock Engineering*, vol. 46, no. 5, pp. 1211–1221, 2013.
- [14] Z. Zhang, J. Bai, Y. Chen, and S. Yan, "An innovative approach for gob-side entry retaining in highly gassy fully-mechanized longwall top-coal caving," *International Journal of Rock Mechanics and Mining Sciences*, vol. 80, pp. 1–11, 2015.
- [15] V. Palchik, "Bulking factors and extents of caved zones in weathered overburden of shallow abandoned underground

- workings,” *International Journal of Rock Mechanics and Mining Sciences*, vol. 79, pp. 227–240, 2015.
- [16] F. Z. Qi and Z. G. Ma, “Investigation of the roof presplitting and rock mass filling approach on controlling large deformations and coal bumps in deep high-stress roadways,” *Latin American Journal of Solids and Structures*, vol. 190, pp. 1–24, 2019.
- [17] S. S. Peng, *Longwall Mining*, pp. 46–53, Peng SS publisher, Morgantown, WV, USA, 2nd edition, 2006.
- [18] M. G. Qian, W. C. Shi, and J. L. Xu, *Ground Pressure and Strata Control*, China University of Mining and Technology Press, Xuzhou, China, 2010.
- [19] B. X. Huang, Y. Z. Wang, and S. G. Cao, “Cavability control by hydraulic fracturing for top coal caving in hard thick coal seams,” *International Journal of Rock Mechanics and Mining Sciences*, vol. 74, pp. 75–57, 2015.
- [20] S. Yan, T. Liu, J. Bai, and W. Wu, “Key parameters of gob-side entry retaining in a gassy and thin coal seam with hard roof,” *Processes*, vol. 6, no. 5, pp. 51–65, 2018.
- [21] W. Li, J. Bai, S. Peng, X. Wang, and Y. Xu, “Numerical modeling for yield pillar design: a case study,” *Rock Mechanics and Rock Engineering*, vol. 48, no. 1, pp. 305–318, 2015.
- [22] Z. Z. Zhang, W. J. Wang, S. Q. Li et al., “An innovative approach for gob-side entry retaining with thick and hard roof: a case study,” *Technical Gazette*, vol. 25, no. 4, pp. 1028–1036, 2018.
- [23] M. D. G. Salamon and A. H. Munro, “A study of the strength of coal pillars,” *Journal of the Southern African Institute of Mining and Metallurgy*, vol. 68, pp. 55–67, 1967.
- [24] X. Du, J. Lu, K. Morsy, and S. S. Peng, “Coal pillar design formulae review and analysis,” in *Proceedings of the 27th International Conference on Ground Control in Mining*, pp. 153–160, West Virginia University, Morgantown, WV, USA, July 2008.
- [25] G. Feng, P. Wang, and Y. P. Chugh, “Stability of gate roads next to an irregular yield pillar: a case study,” *Rock Mechanics and Rock Engineering*, vol. 52, no. 8, pp. 2741–2760, 2019.
- [26] G. Zhang, S. Liang, Y. Tan, F. Xie, S. Chen, and H. Jia, “Corrigendum to: numerical modeling for longwall pillar design: a case study from a typical longwall panel in China,” *Journal of Geophysics and Engineering*, vol. 16, no. 3, p. 666, 2019.
- [27] M. Shabanimashcool and C. C. Li, “Numerical modelling of longwall mining and stability analysis of the gates in a coal mine,” *International Journal of Rock Mechanics and Mining Sciences*, vol. 51, pp. 24–34, 2012.
- [28] M. Salamon, “Mechanism of caving in longwall coal mining,” *Rock mechanics contributions and challenges*, in *Proceedings of the 31st US Symposium on Rock Mechanics*, pp. 161–168, Colorado, CO, USA, January 1990.
- [29] G.-E. Zhang, F.-L. He, H.-G. Jia, and Y.-H. Lai, “Analysis of gateroad stability in relation to yield pillar size: a case study,” *Rock Mechanics and Rock Engineering*, vol. 50, no. 5, pp. 1263–1278, 2017.
- [30] Z. Z. Zhang and F. Gao, “Research on nonlinear characteristics of rock energy evolution under uniaxial compression,” *China Journal of Rock Mechanics and Engineering*, vol. 31, pp. 1198–1207, 2012.
- [31] D. Song, E. Wang, Z. Liu, X. Liu, and R. Shen, “Numerical simulation of rock-burst relief and prevention by water-jet cutting,” *International Journal of Rock Mechanics and Mining Sciences*, vol. 70, pp. 318–331, 2014.
- [32] Q. B. Meng, M. W. Zhang, Han et al., “Effects of acoustic emission and energy evolution of rock specimens under the uniaxial cyclic loading and unloading compression,” *Rock Mechanics and Rock Engineering*, vol. 49, pp. 3873–3886, 2016.
- [33] C. Q. Zhu, L. Wang, and X. G. Han, “State judgement model of the coal and rock medium and its engineering application,” *Advances in Civil Engineering*, vol. 2020, Article ID 4670876, 11 pages, 2020.
- [34] A. H. Wilson and F. Carr, “A new approach to the design of multientry developments of retreat longwall mining,” in *Proceedings of the 2nd International Conference on Ground Control in Mining*, pp. 1–21, Morgantown, WV, USA, June 1982.
- [35] A. A. Campoli, T. M. Barton, F. C. Dyke, and M. Gauna, “Gob and gate road reaction to longwall mining in bump-prone strata,” *Bureau of Mines*, vol. 9445, pp. 48–56, 1993.
- [36] Z. Z. Zhang, M. Deng, Bai et al., “Stability control of gob-side entry retained under the gob with close distance coal seams,” *International Journal of Mining Science and Technology*, vol. 11, pp. 234–249, 2020.
- [37] J. N. Liu, M. C. He, Y. J. Wang et al., “Stability analysis and monitoring method for the key block structure of the basic roof of non-coal pillar mining with automatically formed gob-side entry,” *Advances in Civil Engineering*, vol. 2019, Article ID 5347683, 14 pages, 2019.
- [38] Z. Li, S. Yu, W. Zhu et al., “Dynamic loading induced by the instability of voussoir beam structure during mining below the slope,” *International Journal of Rock Mechanics and Mining Sciences*, vol. 132, Article ID 104343, 2020.
- [39] Z. Tian, Z. Zhang, M. Deng, S. Yan, and J. Bai, “Gob-side entry retained with soft roof, floor, and seam in thin coal seams: a case study,” *Sustainability*, vol. 12, no. 3, pp. 1197–1214, 2020.
- [40] S. Yan, J. Bai, X. Wang, and L. Huo, “An innovative approach for gateroad layout in highly gassy longwall top coal caving,” *International Journal of Rock Mechanics and Mining Sciences*, vol. 59, pp. 33–41, 2013.
- [41] H. Wu, X. K. Wang, Yu et al., “Analysis of influence law of burial depth on surrounding rock deformation of roadway,” *Advances in Civil Engineering*, vol. 2020, Article ID 8870800, 13 pages, 2020.

## Research Article

# Properties of Gobi Aggregate and Sulfide-Rich Tailings Cemented Paste Backfill and Its Application in a High-Stress Metal Mine

D. Q. Deng <sup>1,2</sup>, Y. H. Liang <sup>3</sup> and F. C. Huangfu<sup>4</sup>

<sup>1</sup>School of Civil Engineering and Mechanics, Xiangtan University, Xiangtan, Hunan 411105, China

<sup>2</sup>Institute of Mining Engineering, Guizhou Institute of Technology, Guiyang, Guizhou 550003, China

<sup>3</sup>Planning and Finance Division, Guizhou Institute of Technology, Guiyang, Guizhou 550003, China

<sup>4</sup>Xinjiang Ashele Copper Co., Ltd., Habahe, Altay, Xinjiang 836700, China

Correspondence should be addressed to D. Q. Deng; [ustbb20070025@126.com](mailto:ustbb20070025@126.com) and Y. H. Liang; [81036423@qq.com](mailto:81036423@qq.com)

Received 4 January 2021; Revised 21 January 2021; Accepted 30 January 2021; Published 16 February 2021

Academic Editor: Zizheng Zhang

Copyright © 2021 D. Q. Deng et al. This is an open access article distributed under the Creative Commons Attribution License, which permits unrestricted use, distribution, and reproduction in any medium, provided the original work is properly cited.

This experiment studied the influence law of the strength of CPB affected by tailings content, Gobi aggregate content, cement content, and slurry concentration. The results show, for the CPB with concentration of 77%, when the addition amount of cement reaches 20%, the addition amounts of tailings and Gobi aggregate change within the ranges of 12~24% and 56~68%, respectively. The strength of CPB has been gradually improved when the addition amount of Gobi aggregates decreases and the addition amount of tailings increases. In this case, the slump of CPB changes within the range of 26.5 cm~26.9 cm while the strength of CPB changes within the range of 4.021~6.845 MPa. Considering future utilization value of tailings, the addition amount is finally set at 16% in production, and the addition amount of Gobi aggregate is set at 64%; namely, tailings: Gobi aggregate = 20:80. When the addition amount of cement is 20% (cement/(tailings + Gobi aggregates) = 1:4), the strength of CPB reaches 5.62 MPa which meets the production requirement. When the heading machine is used for tunnelling mine roadway in bottom backfill of VCR stope, no collapse or delamination occurs without support, showing good stability and integrity of backfill. When the adjacent stope ore is mined, the backfill with cement content of 11.1%, 14.3%, 20%, and 25% is exposed. In the process of mining, no collapse or delamination occurs. Therefore, the proportion of various backfill materials applied in production is reasonable, being verified by the experiment and field test.

## 1. Introduction

Over the course of past 20 to 30 years, the China mining has gradually developed tending to stricter and perfect eco-environment protection. Especially in recent 10 years, some provinces have introduced corresponding environmental protection policies and regulations in succession, requiring the mining enterprises to have sound tailing disposal systems and preventing the land from collapse. With the development of mining, the strata and rocks show some corresponding mechanical changes and have a certain impact on the stability of rock mass [1–5]. This means that mine enterprises are not only required to build safe and reliable tailing ponds with proper scale, but also required to keep the maximum discharge reduction of the tailings, to remove the

hidden dangers including dam break and leakage of tailing ponds. In general, the tailings are discharged to tailing ponds. For mines with less tailings produced, some tailings will be used for the preparation of building materials if tailings meet the requirements of building materials. If the tailings contain some useful minerals, the tailings can be sold to other enterprises for refining useful minerals. Among the tailing disposal methods, the best way is to use tailings as filling material in the underground goaf so as to achieve objectives such as maximum use of tailings, safety and environmental protection of mine, ground pressure controlling, and resource recycling as well as maintaining the sustainable development. In backfilling of underground goaf, a lot of tailings from ore-dressing can be used; in this process, tailing discharge is reduced and the pollution

discharge cost is decreased. Meanwhile, the backfill plays a great supportive role in the rock strata movement, makes the surrounding rocks in the goaf stabler, and completely restrains the potential damage. Thus, it creates safer environment for surrounding mining, improves the mineral recovery, and reduces the dilution rate of mines simultaneously. Therefore, it contributes to the significant economic and environmental benefits. For deep filling technology in coal mine and roof maintenance in high-stress stope, relevant researchers have done a series of tests and developed a good way of retaining roadway along goaf according to the maintenance of thick and hard roof; it has been used in production, and the mechanism of roof dilatancy and bolt support in filling area of gob-side entry retaining is analyzed [6–9].

The backfill technology of filling the underground goaf with tailings was adopted earlier in foreign countries. In early phase, water and sand were widely used in filling. With the development of technology and equipment, the cemented filling and high concentration paste backfill gradually came into being. The paste backfill presents superior mechanical property in production and plays an important role in recycling resources. By virtue of the advanced pump pressure transport equipment, and strict operation and management mode, the foreign research on the paste backfill technology once took the leading position. The related research is active; for instance, the international paste backfill conference is held regularly once every few years and provides better target and development to the relevant international research. Among these countries, America, Canada, Australia, and South Africa are relatively representative. On preparation and hydrological characteristics of paste tailings, literature illustrates the concentration of sulfide tailings paste as well as field test of LaRonde polymetallic ore in Abitibi, Quebec, and the analysis on mechanics and hydrologic features of cemented and uncemented paste [10]. In addition, there is a study on mixed characteristics of the sulfide tailings backfill and the influence of the mixing and stirring on the mechanical property, which can be referred to by the similar analysis [11], while in literature, the performance of CPB is predicted and the cost is analyzed, which could be a guidance to production and application [12]. In literature, the paste backfill technology of the underground hard-rock mine is analyzed, the mechanical property of CPB in the stope is studied, the importance of the horizontal stress towards the acting force of backfill is pointed out, and the influence characteristic of the initial concentration of tailings on the paste preparation, shear yield stress, and viscosity of pipeline transport is emphasized. That is of great importance to guide production [13].

Literature shows the strength test on cementing materials of CPB including the ordinary Portland cement (OPC), Portland composite cement (PCC), and sulphate resistant cement (SRC) separately, presenting the influence of cementing agent type and dosage on the short-term and long-term mechanic performance of CPB, which can be reference for the mine backfill in selecting proper cementing agent [14]. Literature studies the influence of 3 water reducing agents on the rheological property of the paste filling slurry and the mechanical strength of the CPB and also analyzes the mechanical property of CPB when the mass percentage of OPC and PCC is 5%, which can be regarded as

the design basis of related engineering [15]. The paste backfill technology of Kidd Creek ore is examined and the technical characteristics are analyzed, which is helpful for production [16]. The hydrological property and geomechanics property of CPB under different curing conditions and stress conditions are investigated, which is quite important for further study on the property of CPB [17]. With regard to the application of CPB in the ore site of Cayeli, literature measures the mechanics property of CPB, which can provide relative, useful information for safe production [18].

With the development of rock mechanics analysis and testing technology, some new methods and laws have been applied well, and positive results have been obtained, which can be used for reference in filling engineering [19–23]. Among the related research in China, literature shows slump test of paste backfill slurry and analyzes the rheological property of the paste, which could be better basis for the study on the flow and diffusion property of backfill slurry [24]. Literature illustrates a series of tests aiming at the paste backfill of Chihong ore and analyzes the relationship between the solid content of paste backfill slurry and its rheological property as well as mechanical property, which plays a vital role in better application of production [25]. With regard to mining under villages, as tests have shown in the literature, solid wastes are used to prepare backfill [26, 27]. The strength change of CPB and its influential factors are analyzed. In field application, the high-quality CPB effectively controls the ground pressure, restricts the sinking of the rock stratum, and successfully realizes the target of coal mining without relocating the village. Literature shows application of crude tailings to prepare the CPB that achieves good result in Lame Zinc Mine, in which the paste backfill technology is relatively early applied in Southwest China [28]. The literature analyzes the rheological property of the crude tailings paste slurry and the inspection optimization test of its yield stress, which provides reference for analyzing the pipeline transportation efficiency [29, 30]. Literature states the change and development of the paste backfill and tailing disposal technology, performs fluidity test on the paste prepared by crude tailings and water-quenched slag, and analyzes and optimizes the pumping performance of the paste [31, 32].

At the present stage, because of the influence of labor cost and raw material price, the production cost of filling engineering is rising constantly; in order to reduce the production cost, various related research works also become more and more [33–37]. In the research on slag cementitious materials, some scholars have optimized the slag powder and its properties so that solid waste such as slag can be reused and the environment can be protected, thus laying a foundation for the operation of the filling system [38–42]. For large-scale industrial solid waste treatment, the researchers conducted feasibility analysis on solid waste resource utilization based on laboratory tests. Based on the macroscopic and microscopic characteristic tests, the physicochemical properties of solid waste were optimized to meet the technical requirements of mined-out voids backfilling, thus creating conditions for large-scale industrial treatment of solid waste and effectively protecting the overburden strata of mined-out voids in the area of high in situ stress [43–45]. Based on the method of soil mechanics,



some researchers have studied the stability of rock mass, the triaxial force of filling body, and the law of stress and strain of filling body, to create the conditions for engineering applications [46–49].

As for the high concentration cemented backfill technology of Gobi aggregate, tailings, and cement, the basic test of the property of backfill material was done based on multiple-material additive technology of Ashele Copper Mine. According to the test result, the study could be used for the guidance of production. As one of the main mines of Fujian Zijin Group, focusing on technical research and development as well as technology innovation, Ashele Copper Mine has already become a typical scientific and technological manufacturer of Zijin Group and even Northwest China with constant development. At present, it has become a large nonferrous mine with mining capacity of 6000 t/d. The mine locates in south hilly land of Altay, the northwestern part of Xinjiang. There, the winter is cold and long with heavy snowfalls. The terrain of the mine is high in north and east with a relative height difference of 30–50 cm and maximum height difference of 100–300 cm, while the southwestern part of the mine is flat, and the relative height difference is about 10 m. Ashele Copper Mine has high copper and zinc grade of 2.46% and 1.98%, respectively. The subterranean mine is divided into three mining parts: the upper, the middle, and the lower. The ore rock of the upper part is relatively broken, so the downward access method is adopted. While the ore rock of the middle part is relatively better than that of the upper, so the upward slicing is applied. For the lower part with good ore rock conditions, VCR mining method is adopted.

In order to make full use of ore resources, avoid the surface subsidence, and create safe and clean working environment for the borehole operation, the cemented paste backfill is applied in Ashele Copper Mine using Gobi aggregates and tailings as coarse and fine aggregates together with locally produced PC32.5 composite slag cement as cementing material. The applied Gobi aggregates are produced around the mine. To collect the Gobi aggregates, the surface soil layer of the ancient river bed is peeled off. Then, Gobi aggregates are screened to remove the blocks and fine silts and keep particles with the size of 48–25,000  $\mu\text{m}$ , while the content of the particles  $<48 \mu\text{m}$  is less than 7–12% according to technical requirements. The tailings for backfill are discharged by ore treatment plant. Some useful substances are contained in tailings and they are difficult to recycle with current ore-dressing technique. Considering the possible use of minerals in future, we discharge most tailings into the tailing pond for stock and piling while only a small amount of tailings is used for underground backfill. During the blending process of backfill, the proportions of the tailings and Gobi aggregates are 30 : 70, 25 : 75, 20 : 80, and 15 : 85. Based on the strength test of backfill, the ratio of tailings and Gobi aggregates with best strength performance is 30 : 70. To reduce the use of tailings and meet the strength performance requirement of backfill, the actual proportion of tailings and Gobi aggregates is generally set to 20 : 80 in production. Over 10 years, since the Ashele Cooper mine has been built and put into production, the cemented backfill

mining plays an active role in production. Namely, it is of great importance to the stability of rock stratum with rock bump tendency and full recycling of the ore.

## 2. Materials and Methods

*2.1. Characteristics of Tailings.* The coarse aggregate cemented paste preparation system of Ashele Copper Mine is composed of 2 vertical sand tanks, 2 cement bins, and 2 sets of Gobi aggregate belt conveyor. In the backfill process of paste preparation in station, tailings slurry with the concentration of 26–33% is transported from the ore-dressing plant to the vertical sand tanks and material blending house through the pipeline. Gobi aggregates are transported by the forklift to the belt conveyor room. Then, big Gobi aggregate blocks with size of  $>25 \text{ mm}$  are removed by screening, while materials with size of  $\leq 25 \text{ mm}$  will travel to the material blending house through the belt conveyor. The cement is transported to the material blending house through the spiral conveyor, located at the bottom of cement bin. In the blending material house, the tailings, Gobi aggregates, and cement are put into the mixer after preliminary mixing. After complete stirring in two-stage horizontal mixer, the paste backfill slurry with the concentration of 75–81% is transported to the goaf for backfill through the backfill pipeline.

Results of the chemical composition analysis for tailings and Gobi aggregates are shown in Table 1. As data show, tailings consist of sulfur (S) accounting for 48%, total iron (TFe) accounting for 43.38%,  $\text{SiO}_2$  accounting for 1.77%, phosphorus (P) accounting for 0.0097%, and  $\text{Al}_2\text{O}_3$  and CaO with MgO totally accounting for 0.86%. The current mineral processing technology applied in Ashele Copper Mine is fine grinding of the tailings after copper and zinc selection are finished, and then selecting copper and zinc in sequence. In view of low price of S and Fe, the selection of both elements has not been carried out in recent years, and some tailings are used for backfill in the pit. Therefore, the contents of S and Fe are high in tailings. Furthermore, the content of fine particles in tailings is high after 2 times of grinding. In general, Fe is favorable for the strength performance of backfill, while the excessive content of S is unfavorable for the strength. Although the contents of S and Fe are high in tailings, there will not be negative impact on the strength of backfill as tailings are only used as auxiliary additives.

As shown in Table 2, the proportion of tailings is 4.39, the loose volume weight and dense volume weight are 1.55  $\text{t/m}^3$  and 2.23  $\text{t/m}^3$ , and the porosity is 49.2%. On the basis of mineral process of Ashele Copper Mine and the chemical composition analysis of tailings, it is known that the relatively high content of Fe leads to the high proportion of tailings. As for loose stack and dense stack, the porosity is relatively big. When tailings are used for backfill, it is easy to form relatively dense backfill. Hence, they are helpful for improving the strength of backfill.

shown in Table 3, the test data indicates that the average particle size of tailings in Ashele Copper Mine is 34.4  $\mu\text{m}$ , of which the percentage of fines (particle size  $<29.6 \mu\text{m}$ ) is 18.33% and the content of the particles

TABLE 1: Chemical composition of tailings and Gobi aggregates.

Material	Content of chemical composition (%)						
	SiO <sub>2</sub>	Al <sub>2</sub> O <sub>3</sub>	MgO	CaO	S	P	Fe
Tailings	1.77	0.44	0.06	0.36	48.0	0.0097	43.38
Gobi aggregates	85.61	3.92	0.41	1.91	0.095	0.013	2.06

TABLE 2: Physical properties of filling materials.

Material	Proportion	Loose volume weight (t/m <sup>3</sup> )	Dense volume weight (t/m <sup>3</sup> )	Porosity (%)	Slope angle (°)
Tailings	4.39	1.55	2.23	49.2	41.5
Gobi aggregates	2.56	1.26	1.75	31.6	36
PC32.5 cement	3.11	1.02	1.61	48.2	39

TABLE 3: Particle size distribution of tailings and PC32.5 cement.

Material	Particle size cumulative passing (%)								
	5 $\mu\text{m}$	10 $\mu\text{m}$	20 $\mu\text{m}$	50 $\mu\text{m}$	75 $\mu\text{m}$	100 $\mu\text{m}$	150 $\mu\text{m}$	200 $\mu\text{m}$	300 $\mu\text{m}$
Tailings	4.13	9.10	18.33	82.28	99.47	100	100	100	100
PC32.5 cement	14.77	28.73	48.31	81.58	92.53	97.00	99.51	99.86	100

(particle size  $< 75 \mu\text{m}$ ) is 99.47%. Compared with that of other mines, the particle size of tailings is really fine, and the content of coarse particles is low. Moreover, the mean particle size of PC32.5 cement used for Ashele Copper Mine backfill is  $29.6 \mu\text{m}$ , of which the percentage content of the fines (particle size  $< 20 \mu\text{m}$ ) is 48.31%, while that of particles (particle size  $< 75 \mu\text{m}$ ) is 92.53%. Compared with tailings of Ashele Copper Mine, the mean particle sizes of cement and tailings are basically of the same order of magnitude. Sufficient superfine cement and tailings particles are necessary for pipeline transportation of coarse aggregate paste slurry.

**2.2. Characteristics of Gobi Aggregates.** Table 1 shows that the main component of Gobi aggregates is SiO<sub>2</sub> accounting for 85.61%, while S and Fe are quite low accounting for only 0.095% and 2.06%, respectively. Besides, the total content of Al<sub>2</sub>O<sub>3</sub>, CaO, and MgO accounts for 6.24%, the content of P is 0.013%, and the content of other chemical compositions is quite low. According to the chemical composition analysis of Gobi aggregates, the content of SiO<sub>2</sub> is relatively high in Gobi aggregates. As the content of Gobi aggregates (the most important backfill material) is high, it can be used to make up for insufficient SiO<sub>2</sub> and improve the strength of paste backfill.

As shown in Table 2, the proportion of tailings is 2.56, the loose volume weight and dense volume weight are 1.26 t/m<sup>3</sup> and 1.75 t/m<sup>3</sup>, and the porosity is 31.6%. Compared with the backfill of other mines, the proportion and porosity of Gobi aggregates are both small relatively. When used as the backfill, they can match well the physical and mechanical property of tailings. When the tailings particles are filled in the Gobi aggregates, it is easy to form stable mechanical structure, which is helpful for mechanical property of the backfill.

As shown in Table 4, the particle size of Gobi aggregates, the maximum particle size of Gobi aggregates for backfill of Ashele Copper Mine is  $25000 \mu\text{m}$ , of which the proportion of fines (particle size  $< 20 \mu\text{m}$ ) is 9.74%, and that of the particles ( $< 1,000 \mu\text{m}$ ,  $< 2,000 \mu\text{m}$ , and  $< 10,000 \mu\text{m}$ ) is 59.45%, 64.26%, and 88.46%, respectively. Thus, the particle sizes of Gobi aggregates, tailings, and PC32.5 cement are not of the same order of magnitude. The Gobi aggregates are coarse, which can well match the fine particles and is helpful for improving the gradation of the backfill.

**2.3. Cementing Agent.** Generally, the cement is widely used as cementing material in mines. For the filling project of high-stress underground GOAF in Ashele Copper Mine, the way to obtain cement is convenient because of the good highway traffic condition in the enterprise's geographical location; therefore, on the premise of obtaining good mechanical properties of paste filling materials, the price of PC32.5 cement is also cheaper than that of PO42.5 cement and slag cement; the filling cementitious material was determined to be of grade PC32.5 cement produced by a nearby cement plant. Owing to small particle size, some cement in the mixing material together with slurry of other particles can form argillaceous layer during the process of backfill slurry pipeline transportation. When the paste flows in the pipeline, the argillaceous layer can lubricate the inner wall of pipeline. This greatly helps to reduce the transportation resistance and makes the paste backfill slurry stably flow with high concentration. Locally produced PC32.5 cement is used as backfill cementing agent in Ashele Copper Mine. As data of Table 2 show, the proportion of PC32.5 cement is 3.11, the loose volume weight and dense volume weight are 1.02 t/m<sup>3</sup> and 1.61 t/m<sup>3</sup>, and the porosity is 48.2%.

TABLE 4: Particle size distribution of the Gobi aggregates.

Particle size ( $\mu\text{m}$ )	5	20	75	200	500	1000	2000
Accumulative passing (%)	2.089	9.74	19.67	27.71	44.97	59.45	64.26
Particle size ( $\mu\text{m}$ )	2500	5000	8000	10000	12000	14000	25000
Accumulative passing (%)	64.77	80.75	85.48	88.46	91.75	94.08	100

The cement can be used not only as a cementing agent but also as fine particle backfill. Like tailings particles, the cement particles are evenly distributed in the gap of Gobi aggregates particles. The cementation of cement consolidates tailings and Gobi aggregates as a whole, forms the even distribution structure of coarse and fine particles, and finally constitutes a relatively stable mechanical structure. That is the reason why coarse aggregates particles are added to the backfill, resulting in higher strength compared with the cemented tailings backfill.

**2.4. Water.** The tap water is used to mix the cementing agents, tailings, and Gobi aggregates uniformly. The amount of water is determined by the concentration of paste backfill slurry that needs to be prepared.

**2.5. Preparation of the Paste Backfill.** In practical application, when the paste preparation concentration is low, such as 75% or 77%, the coarse aggregate in the paste will be faster than the previous sedimentation rate, but there is no serious stratification or segregation, and the way to overcome the rapid sedimentation rate of coarse aggregate in paste is to increase the flow rate properly to ensure that the paste can continue to advance steadily under high pipe pressure. According to the concentration of the paste backfill slurry in field investigation and actual production, the factors influencing the strength of backfill are analyzed. As the result shows, the content of cementing agents, the proportion of tailings and Gobi aggregates, and slurry concentration have significant influence on the strength performance of backfill. Thus, the proportions of tailings and Gobi aggregates are 30 : 70, 25 : 75, 20 : 80, and 15 : 85. The proportions for the cement/(tailings + Gobi aggregates) are 1 : 3, 1 : 4, 1 : 6, 1 : 8, and 1 : 10. To make the paste backfill test specimens with the concentration of 75~83%, mix the tailings, Gobi aggregates, and PC32.5 cement with a certain proportion; add water; and mix them uniformly. Then, pour the uniformly mixed paste backfill slurry into the steel tool with specification of  $7.07 \text{ cm}^3$ . (After the tool is disassembled, the volume of specimen is  $7.07 \text{ cm}^3$ .) Then put the test specimen into conservation cabinet with constant temperature and humidity, and test its uniaxial comprehensive strength on the 3<sup>rd</sup>, 7<sup>th</sup>, 28<sup>th</sup>, and 60<sup>th</sup> days, respectively.

**2.6. Mechanical Test.** Generally, in underground mining, it is necessary to test the independence of the disclosed backfill after the adjacent ores in the stope are mined. This means that the unconfined compressive strength of the backfill, namely, uniaxial compressive strength, needs to be tested. In this experiment, the uniaxial compressive strength of the

backfill is tested by NYL-300 press machine, which is equipped with microprocessor control and record system. Two relatively flat opposites are selected as compression faces for the test, and the regulation together with loading is carried by the pressure sensor. By controlling the loading with the displacement at the speed of 1.5–2 mm/min, the uniaxial compressive strength is recorded till the test specimen is damaged, the stress is no longer increased, and press machine stops loading automatically. Thus, the final value is the average value of data while the uniaxial compressive strength of all backfill can be recorded and kept by the testing system.

### 3. Results

**3.1. Effect of Tailings Content on the Strength of CPB.** The specimens of the first group are used to study the influence of tailings content on the strength of CPB. The concentration is 77%, the proportion of cement/(tailings + Gobi aggregates) is 1 : 4; the proportion of tailings and Gobi aggregates is 5 : 85, 20 : 80, 25 : 75, and 30 : 70, respectively. Namely, in the dried materials without water, the percentage content of cement is 20% all along while that of Gobi aggregates is 68%, 64%, 60%, and 56%, respectively; the percentage content of tailings is 12%, 16%, 20%, and 24%, respectively. Figure 1—the curve of the effect of the tailings content on the strength of CPB—shows the rule that the strength of the CPB changes with the percentage content of tailings. Based on the slump test, it is known the slump of the above four types of paste backfill slurry changes from 26.9 cm to 26.5 cm with increasing of tailings and decreasing of Gobi aggregates. This means that the more the tailings (as fine particles) added, the more the water that can be absorbed by the paste to reduce the slump of backfill slurry. As Figure 1 shows, the strength of the CPB specimen in different curing periods is increased along with the increase in tailings addition correspondingly. The strength amplification of the specimen with curing period of 3 days and 7 days is relatively small. Along the extension of the curing period, when it reaches 28 days and 60 days, the strength amplification of the specimen increases greatly. This indicates that, in a certain range, the addition of tailings is helpful to improve the strength of the specimen. As the tailings particles are relatively fine, they can be uniformly dispersed in the gap of Gobi aggregates with coarse particles and form dense structure. When affected by the external force, the coarse particles are not easy to dislocate. If there are more tailings particles with the percentage content of tailings reaching 20% and 24%, the particles of Gobi aggregates will be more tightly encapsulated. Therefore, macroscopically, this shows that

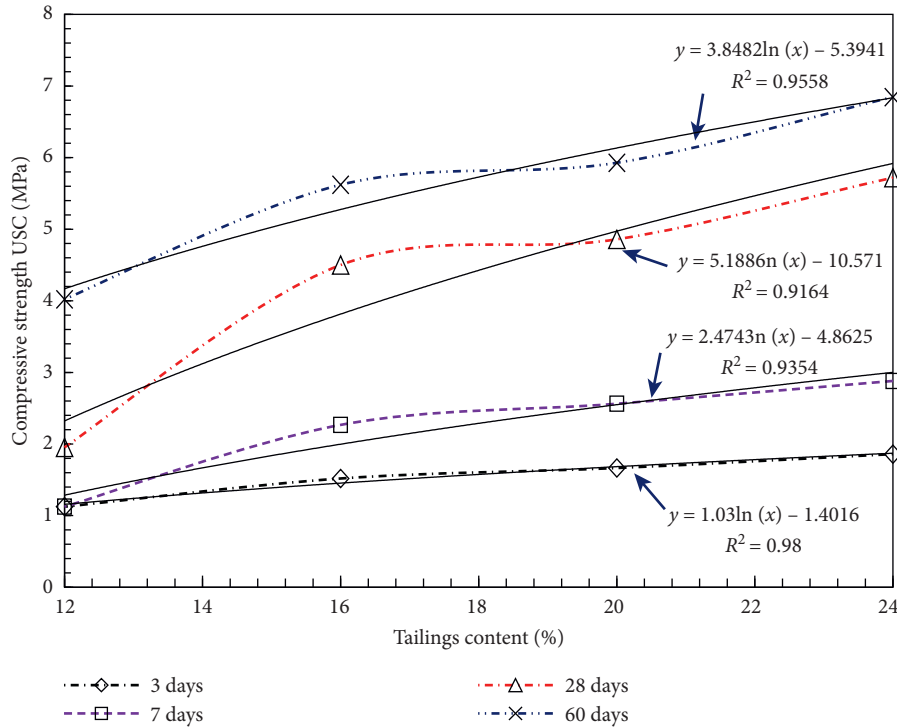


FIGURE 1: Effect of the tailings content on the strength of CPB.

the specimens have relatively high uniaxial compressive strength.

According to the data and the trend of the curve, we analyze the change of paste filling strength with the tailings content, use statistical software for fitting test curve, and can get relations between tailings content ( $x$ ) and paste filling strength ( $y$ ). From Figure 2, we can see that the correlation coefficient is 0.9164~0.98 when the logarithm character is used to describe the effect of the tailings content on the strength of the paste filling body at times of 3 d, 7 d, 28 d, and 60 d, which shows that the fitting effect is good, meeting the requirements. The common logarithmic expression is shown in (1), and the coefficient  $a_1, b_1$  ranges are shown in Figure 1.

$$y = a_1 * \ln(x) - b_1. \quad (1)$$

**3.2. Effect of the Gobi Aggregates Content on the Strength of CPB.** To study the effect of Gobi aggregates content on the strength of CPB, the specimens of the first group with the proportion and content of all materials as mentioned above are analyzed. The percentage content of Gobi aggregates is 56%, 60%, 64%, and 68%, respectively. Figure 2—the effect of Gobi aggregates content on the strength of PCB—shows the rule that the strength of CPB changes with the change of Gobi aggregate content. As shown in Figure 2, as Gobi aggregates addition increases, the strength of CPB specimens in different curing periods decreases. The amplification of the test specimens with

curing periods of 3 days and 7 days is relatively small. With the extension of the curing period, when it reaches 28 days and 60 days, the strength of the specimen increases rapidly. This indicates that, in a certain range, the addition of Gobi aggregates is unfavorable for the strength of the specimens. As Gobi aggregates particles are relatively coarse, proper addition of Gobi aggregates can improve the mechanical structure of particles in the backfill as well as the strength of CPB. However, with increase of addition, the structure will become relatively loose with less density due to the lack of fine particles to backfill the gap between the particles of Gobi aggregates. When affected by the external force, the coarse particles of Gobi aggregates will be dislocated mutually owing to the lack of fine particles for encapsulating. When the percentage content of Gobi aggregates reaches 64% and 68%, with relatively big external force, the fine particles cannot form dense structure to maintain the stability of the coarse particles of Gobi aggregates. Therefore, macroscopically, this shows that the specimens have relatively weak uniaxial comprehensive strength.

According to the data and the trend of the curve, we analyze the law of the paste filling body strength with the Gobi content changes. By using statistical software and getting fitting test curve, it is easy to get relationship between Gobi aggregate content ( $x$ ) and paste filling body strength ( $y$ ). It can be seen from Figure 3 that the correlation coefficient ranges from 0.954 to 0.9849 when quadratic polynomials are used to characterize the effect of Gobi aggregate content on the strength of paste filling body at times of 3 d, 7 d, 28 d, and 60 d, which means that the fitting

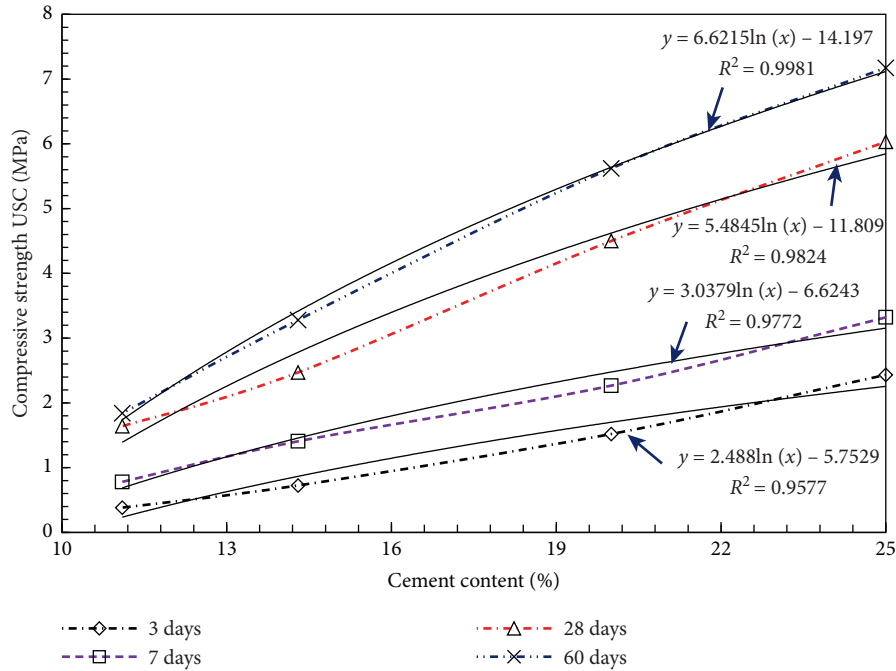


FIGURE 2: Effect of cement content on the strength of CPB.

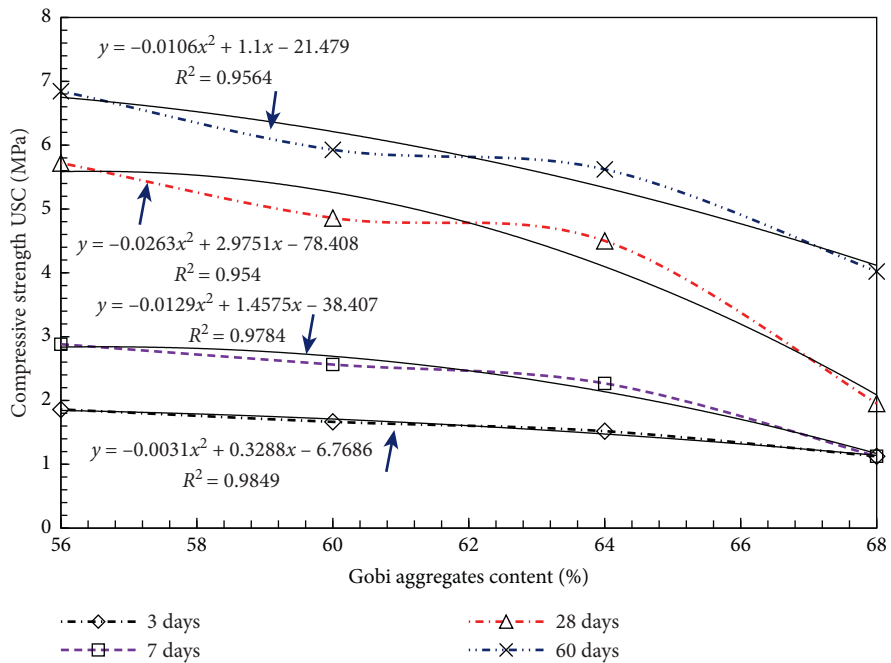


FIGURE 3: Effect of the Gobi aggregates content on the strength of CPB.

effect is good. The common expression is shown in (2), and the coefficients ranges of  $a_2, b_2, c_2$  are shown in Figure 2.

$$y = -a_2 * x^2 + b_2 * x - c_2. \quad (2)$$

3.3. Effect of the Cement Content on the Strength of CPB. The specimens of the second group are used to study the effect of cement content on the strength of CPB. The

concentration is 77%, the proportion of tailings and Gobi aggregates is 20:80, and the proportion of cement/(tailings + Gobi aggregates) is 1:3, 1:4, 1:6, and 1:8, respectively. Namely, in the dried materials without water, the percentage content of tailings is 17.8%, 17.1%, 16%, and 15% while that of Gobi aggregates is 71.1%, 68.6%, 64%, and 60%, respectively; the percentage content of cement is 11.1%, 14.3%, 20%, and 25%, respectively. The curve of Figure 3—the effect of the cement content on the strength of



CPB—shows the rule that the strength of CPB changes with the percentage content of cement.

Based on the slump test, it is known the slump of the above four types of paste backfill slurry changes from 26.2 cm to 26.9 cm with the increase of tailings and decrease of Gobi aggregates. This means that the more the cement (as fine particles) added, the more the water that can be absorbed by the paste to reduce the slump of backfill slurry. As Figure 3 shows, the strength of the CPB specimen in different curing periods is increased with the increase of cement addition correspondingly. The strength amplification of the specimen with curing period of 3 days, 7 days, 28 days, and 60 days is relatively small with low cement content of 11.1% and 14.3%. With the increase of cement content reaching 20% or 25%, the strength amplification of the specimen increases greatly. This indicates that, in a certain range, the addition of cement is helpful to improve the strength of the specimen. As the cement particles are relatively fine, they can be uniformly dispersed in the gap of Gobi aggregates with coarse particles and form dense structure. The more the cement added, the more tighter the connection between coarse and fine particles. The coarse particles are not easy to dislocate even when affected by the external force. Therefore, macroscopically, this shows that the specimens have relatively high uniaxial comprehensive strength.

According to the trend of data and curves, we analyze the law of paste filling strength with the change of cement content. By using statistical software, we get fitting test curve, and it is easy to get the function relation between cement content ( $x$ ) and paste filling body strength ( $y$ ). From Figure 3, we know that when the logarithmic function is used to characterize the effect of cement content on the strength of paste filling body at times of 3 d, 7 d, 28 d, and 60 d, the correlation coefficients range from 0.9577 to 0.9981, which indicates that the fitting effect is good and the accuracy meets the requirements. The logarithmic function expression is expressed by (3), and the range of the coefficients  $a_3, b_3$  is shown in Figure 2.

$$y = a_3 * \ln(x) - b_3. \quad (3)$$

### 3.4. Effect of the Slurry Concentration on the Strength of CPB.

The specimens of the third group are used to study the effect of slurry concentration on the strength of CPB. The proportion of cement/(tailings + Gobi aggregates) is 1 : 6, and the proportion of tailings and Gobi aggregates is 20 : 80. The slurry concentration is 75%, 77%, 79%, 81%, and 83%, respectively. The curves in Figure 4—the effect of the slurry concentration on the strength of CPB—show the rule that the strength of the CPB changes with the slurry concentration. As the result of the slump test shows, the slump of the above four types of paste backfill slurry decreases from 27.5 cm to 24.5 cm with the increase of the slurry concentration. This shows that the decrease of water addition leads to the decrease of the water contained in the paste, increase of the viscosity, weak liquidity, and relatively small slump. As Figure 4 shows, with the increase of the concentration, the

strength of CPB specimens in different curing periods is improved correspondingly. When the concentration is 75% or 77%, the strength of the specimens in different curing periods increases slowly. With the increase of the concentration, reaching 79%, 81%, and 83%, the strength of the specimens increases rapidly. With the slope increase of curve, shown in Figure 4, in a certain range, there is a proportional relation between the specimen strength and slurry concentration. In other words, the strength of the specimen increases with the increase of content of solid material. On the other hand, from the micro perspective, when the concentration is relatively low, the backfill formed by the solidification of the backfill slurry contains much water that occupies space. When some free water leaves the backfill, the space will become tiny holes. Compared with the backfill with high concentration, the backfill specimens with low concentration have relatively more tiny holes. This leads to low volume weight. Because of loose connection between coarse particles, there is big compressibility and the integrity is easy to damage when affected by the external force. Macroscopically, the higher the concentration of the slurry is, the higher the uniaxial compressive strength of the specimens will be.

According to the data and the trend of the curve, we analyze the law of paste filling strength with the filling slurry concentration change. By using statistical software, we get fitting test curve, and it is easy to get the function relation between paste concentration ( $x$ ) and paste filling body strength ( $y$ ). It can be seen from Figure 4 that when the linear function is used to characterize the effect of filling slurry concentration on the strength of paste filling bodies at times of 3 d, 7 d, 28 d, and 60 d, the correlation coefficients range from 0.9777 to 0.9959, which indicates that the fitting effect is good. The function expression is expressed by (4), and the range of coefficients  $a_4, b_4$  is shown in Figure 4.

$$y = a_4 * x - b_4. \quad (4)$$

## 4. Application of Paste Backfill in Production

In production of Ashele Copper Mine, the tailings, Gobi aggregates, and cement are premixed by horizontal mixer in the first phase and discharged through discharge outlet into the second-phase horizontal mixer for intensive mixing. Then, the paste backfill slurry with better homogeneity and high viscosity is ready, presenting the significant characteristics of the paste. During the preparation of paste filling slurry, when the concentration of paste reaches 81% or so, the paste will become more viscous, and sometimes it will adhere to the surface of the mixing equipment and the flowing parts, resulting in scaling, thus affecting the normal production. In this process, paste preparation station is usually equipped with production inspectors, using tools such as high-pressure water gun or drill rod, cleaning up the paste materials bonded on the equipment in time to enable the normal operation of the relevant equipment. The uniform paste backfill slurry is transported into the drilling hopper after screening and then sent to the goaf for backfill through the borehole and underground backfill pipeline.

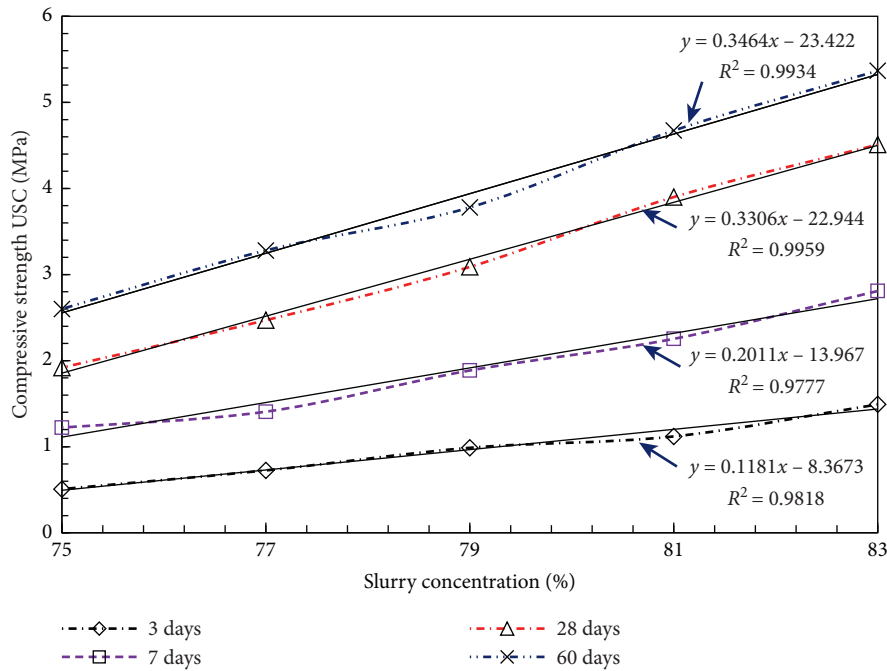


FIGURE 4: Effect of the slurry concentration on the strength of CPB.

Figure 5 shows the preparation process of the paste backfill slurry with Gobi aggregates as the main component. The paste backfill slurry in mushy state shows good performance. Figure 6 shows the status of paste backfill slurry in the boreholes after screening.

As the paste backfill slurry of Ashele Copper Mine has high concentration and little water content, the dehydration is unnecessary after it enters into the stope. Therefore, there is no need to install the filter in stope and decrease the backfill cost. In general, the water in the backfill slurry can be consumed in two ways. First, the hydration of cement can consume some water that exists in the form of molecule bound water. Meanwhile, the water inside the backfill is generally kept for a long time if it is not high or dry. Second, some water is derived from fractures of the ore rock; namely, we can use the fracture and boreholes in the ore rock as the channel and enable the ore rock to absorb some free water.

The paste backfill slurry of Ashele Copper Mine contains less water. Besides, there is little underground water, so it is dry. Therefore, when the slurry enters into the stope, some water is rapidly absorbed by the ore rock. Therefore, the concentration of the paste backfill slurry increases. The solidification and hardening of the paste in stope are faster than those in the laboratory. The strength of the backfill increases rapidly. In general, on the second day after backfill, the backfill surface has relatively high strength. Regarding the stope of Ashele Copper Mine with VCR mining, the paste [cement/(tailings + Gobi aggregates) = 1 : 4] is used at the bottom, the paste [the cement/(tailings + Gobi aggregates) = 1 : 4, 1 : 6, and 1 : 8] is used in the middle part. Before mining the ore pillar in the second step, it is necessary to excavate the tunnels at the bottom of the backfill in the ore house. This requires the backfill to have high strength to prevent the backfill from collapse when excavating tunnels



FIGURE 5: Preparation of paste filling slurry.

in the paste backfill ([cement/(tailings + Gobi aggregates)] = 1 : 4). During excavating tunnels in the backfill, the backfill has good integrity. The cross section of the tunnel is regular. The back and both sides of backfill have dense structures without any loosening or delaminating. When the backfill around the roadway is beaten by the rock, the echo is clear, and the mechanic performance is good. The tunnel excavating process inside the big backfill by heading machine is shown in Figure 7. As we can see, the ore removal roadway formed by excavating has good and complete structure. The imprinting grinded by the cone of the heading machine is clearly distributed in the roof and both sides, indicating good strength and integrity of backfill. Figure 8 shows the status of tunnel after excavation.

From Figures 7 and 8 and long-term observation in the field, it can be seen that the performance of paste filling material can keep stable for a long time in the later period of use, and with the extension of time, the strength of the exposed paste also increased to a certain extent. During the



FIGURE 6: Paste filling slurry flowing into borehole.



FIGURE 7: Excavating tunnel in paste backfill.



FIGURE 8: Completed tunnel in paste backfill.

course of transporting ore by LHD, the paste did not collapse and fall. As the performance of paste filling material is uniform, the high stress in the stratum has not destroyed the paste filling material. From the surface of the roadway in the paste, it can be seen that after the extrusion of the roadheader, the surface of the paste has been squeezed more densely, as if a layer of thick crust is formed, with basically no cracks, so the high-stress areas of the tunnel provided a better protection.

## 5. Conclusion

Ashele Copper Mine is the first copper mine that successfully uses Gobi aggregates with coarse particles as main composition to prepare the paste in China. As Ashele Copper Mine has rich Gobi aggregates, they are convenient to get

with low price which creates conditions for effective utilization. In general, adding proper coarse materials can not only improve the size grading combination of backfill, but also promote the strength of backfill. Adding proper tailings is favorable for preparing paste with good performance, reducing the abrasion on the pipeline, improving the strength of backfill, and forming dense and stable structure. This helps to maintain mechanical framework of inner particles in backfill and provides safe environment for production. Even though we have achieved success by using Gobi aggregates with coarse particles as main composition to prepare the backfill, Ashele Copper Mine still faces challenges in other aspects. For instance, when we use the coarse aggregate to prepare the backfill slurry, the bend is quite easy to wear, and the cost of pipeline maintenance and change is relatively high. The abrasion on the pipeline can be reduced with more tailings, which has negative impact on the strength of CPB.

In the process of preparing paste with coarse aggregate, it is very important to prevent the deposition and segregation of the granular materials in the paste, which often restricts the daily production schedule. In view of the effect of using tailings with high sulfur and iron content as filling materials to prepare cemented paste filling materials, in the process of large-scale underground mining in Ashele Copper Mine, the self-supporting ability of paste filling materials is better, there is no collapse or flake falling and, the proportion of all kinds of filling materials used in production is reasonable through test and field verification.

This research reveals the rule about the effect of tailings content, Gobi aggregates content, cement content, and slurry concentration on the strength of CPB. As the results show, when the addition amount of Gobi aggregates is within 56%~68%, the strength of CPB tends to decrease as addition amount of Gobi aggregates increases. When the addition amount of tailings is within the range of 12%~24%, the strength of CPB increases with the increase of tailings. The addition of both backfill materials plays different roles in maintaining the pipeline. As tailings of Ashele Copper Mine are valuable in use, under the premise of ensuring the strength of CPB, it is suggested that tailings are used as backfill material as little as possible. Even though the backfill with good performance is formed when the proportion of tailings and Gobi aggregates is 30:70, the proportion for both materials is finally confirmed at 20:80 in production in consideration of the usage value of tailings. When the addition amount of cement is 20% [cement/(tailings + Gobi aggregates) = 1:4] and the concentration is 77%, the strength of CPB reaches 5.62 MPa. According to tunnels excavating by heading machine in the backfill at the bottom of VCR stope, the backfill [cement/(tailings + Gobi aggregates) = 1:4] has good stability and integrity. No collapse or delamination occurs even without support in roadway. When the ores of adjacent stopes are mined, the backfill with cement content of 11.1%, 14.3%, 20%, and 25% is exposed. During the whole mining process, no collapse or delamination occurs presenting good independence of the backfill. Therefore,

the proportion of the backfill used in production is rational according to the test and field validation.

### Data Availability

The data used to support the findings of this study are available from the corresponding author upon request.

### Conflicts of Interest

The authors declare no conflicts of interest.

### Authors' Contributions

D. Q. Deng wrote the main text of the manuscript. Y. H. Liang and F. C. Huangfu collected and analyzed the data. All authors reviewed and commented on the manuscript.

### Acknowledgments

The authors gratefully acknowledge the support for this research from the National Natural Science Foundation of China (51764009), the Guizhou Province Science and Technology Support Plan Project (Grant No. [2018]2836), the Scientific Research Fund of Hunan Province Education Department (20A475), and the High-level Talent Gathering Project in Hunan Province (2019RS1059).

### References

- [1] Y. Zhao, Y. Wang, W. Wang, L. Tang, Q. Liu, and G. Cheng, "Modeling of rheological fracture behavior of rock cracks subjected to hydraulic pressure and far field stresses," *Theoretical and Applied Fracture Mechanics*, vol. 101, pp. 59–66, 2019.
- [2] Y. L. Zhao, L. Y. Zhang, J. Liao, W. J. Wang, Q. Liu, and L. Tang, "Experimental study of fracture toughness and subcritical crack growth of three rocks under different environments," *International Journal of Geomechanics*, vol. 20, no. 8, Article ID 04020128, 2020.
- [3] W. Yu, G. Wu, and B. An, "Investigations of support failure and combined support for soft and fractured coal-rock tunnel in tectonic belt," *Geotechnical and Geological Engineering*, vol. 36, no. 6, 2018.
- [4] W. Yu, W. Wang, G. Wu, X. Yu, and W. Peng, "Three zones and support technique for large section incline shaft crossing goaf," *Geotechnical and Geological Engineering*, vol. 35, no. 5, pp. 1921–1931, 2017.
- [5] Y. L. Zhao, L. Y. Zhang, W. J. Wang, Q. Liu, L. M. Tang, and G. Cheng, "Experimental study on shear behavior and a revised shear strength model for infilled rock joints," *International Journal of Geomechanics*, vol. 20, no. 9, Article ID 04020141, 2020.
- [6] Z. Zhang, W. Wang, S. Li, and X. Yu, "Analysis on rockbolt support interaction with roof dilatancy above roadside backfill area in gob-side entry retaining," *Geotechnical and Geological Engineering*, vol. 36, no. 4, pp. 2577–2591, 2018.
- [7] X. Wang, R. Wang, and Z. Zhang, "Numerical analysis method of shear properties of infilled joints under constant normal stiffness condition," *Advances in Civil Engineering*, vol. 2018, p. 13, 2018.
- [8] Z. Zhang, W. Wang, S. Li et al., "An innovative approach for gob-side entry retaining with thick and hard roof: a case study," *Technical Gazette*, vol. 25, no. 4, pp. 1028–1036, 2018.
- [9] W. J. Yu, S. H. Du, and W. J. Wang, "Prediction of instability and mechanism of multi-factor comprehensive action on mine goaf," *International Journal of Engineering Research in Africa*, vol. 13, no. 2, pp. 39–48, 2014.
- [10] E. Yilmaz, M. Benzaazoua, B. Bussière, and S. Pouliot, "Influence of disposal configurations on hydrogeological behaviour of sulphidic paste tailings: a field experimental study," *International Journal of Mineral Processing*, vol. 131, no. 131, pp. 12–25, 2014.
- [11] M. Benzaazoua, T. Belem, and B. Bussière, "Chemical factors that influence the performance of mine sulphidic paste backfill," *Cement and Concrete Research*, vol. 32, no. 7, pp. 1133–1144, 2002.
- [12] M. Fall and M. Benzaazoua, "Advances in predicting performance properties and cost of paste backfill," in *Proceedings of the On Tailings and Mine Waste'03*, pp. 73–85, Vail, CO, USA, October 2003.
- [13] T. Belem and M. Benzaazoua, "Design and application of underground mine paste backfill technology," *Geotechnical and Geological Engineering*, vol. 26, no. 2, pp. 147–174, 2008.
- [14] B. Ercikdi, A. Kesimal, F. Cihangir, H. Deveci, and I. Alp, "Cemented paste backfill of sulphide-rich tailings: importance of binder type and dosage," *Cement Concrete Composites*, vol. 31, no. 1, pp. 268–274, 2009.
- [15] B. Ercikdi, F. Cihangir, A. Kesimal, H. Deveci, and I. Alp, "Utilization of water-reducing admixtures in cemented paste backfill of sulphide-rich mill tailings," *Journal of Hazardous Materials*, vol. 179, no. 1–3, 2010.
- [16] D. A. Landriault, R. E. Brown, and D. Counter, "Paste backfill study for deep mining at Kidd creek," *CIM Bulletin*, vol. 93, no. 1036, pp. p156–161, 2000.
- [17] E. Yilmaz, T. Belem, and M. Benzaazoua, "Effects of curing and stress conditions on hydromechanical, geotechnical and geochemical properties of cemented paste backfill," *Engineering Geology*, vol. 168, pp. 23–37, 2014.
- [18] B. D. Thompson, W. F. Bawden, and M. W. Grabinsky, "In situ measurements of cemented paste backfill at the Cayeli mine," *Canadian Geotechnical Journal*, vol. 49, no. 7, pp. 755–772, 2012.
- [19] Y. L. Zhao, C. S. Zhang, Y. X. Wang, and H. Lin, "Shear-related roughness classification and strength model of natural rock joint based on fuzzy comprehensive evaluation," *International Journal of Rock Mechanics and Mining Sciences*, vol. 137, Article ID 104550, 2020.
- [20] Y. Zhao, C. L. Wang, and J. Bi, "Analysis of fractured rock permeability evolution under unloading conditions by the model of elastoplastic contact between rough surfaces," *Rock Mechanics and Rock Engineering*, vol. 53, 2020.
- [21] R. Rankine, M. Pacheco, and N. Sivakugan, "Underground mining with backfills," *Soils and Rocks*, vol. 30, no. 2, pp. 93–101, 2007.
- [22] M. Fall, M. Benzaazoua, and E. G. Saa, "Mix proportioning of underground cemented tailings backfill," *Tunnelling and Underground Space Technology*, vol. 23, no. 1, pp. 80–90, 2008.
- [23] B. Tikov and B. Mostafa, "Design and application of underground mine paste backfill technology," *Geotechnical and Geological Engineering*, vol. 26, no. 2, pp. 147–174, 2008.
- [24] J. Zhao and L. Liu, "Research into rheological properties of backfill paste based on the slump test," *Journal of Xi'an University of Architecture & Technology (Natural Science Edition)*, vol. 47, no. 2, 2015.

- [25] S. Yin, A. Wu, K. Hua, Y. Wang, and Y. Zhang, "The effect of solid components on the rheological and mechanical properties of cemented paste backfill," *Minerals Engineering*, vol. 35, pp. 61–66, 2012.
- [26] H. Zhou, C. Hou, X. Sun, Q. Qu, and D. Chen, "Solid waste paste filling for none-village-relocation coal mining," *Journal of China University of Mining & Technology*, vol. 33, no. 2, pp. 154–158, 2004.
- [27] C. Zhao, H. Zhou, J. Bai, Q. Hui, and J. B. Qiang, "Influence factor analysis of paste filling material strength," *Journal of Liaoning Technical University*, vol. 25, no. 6, pp. 904–906, 2006.
- [28] Z. Li, "Full tailing paste filling in the research and application of Lame zinc mine," *Mining Technology*, vol. 15, no. 1, pp. 6–13, 2015.
- [29] Y. Zhai, A. Wu, and H. Wang, "Study on rheological properties of the unclassified-tailings paste," *Metal Mine*, vol. 39, no. 12, pp. 30–32, 2010.
- [30] A. Wu, H. Jiao, and H. Wang, "Yield stress measurements and optimization of paste tailings," *Journal of Central South University (Science and Technology)*, vol. 8, pp. 3370–3376, 2013.
- [31] A. Wu, "Review on paste filling with tailings disposal technology," *Mining Equipment*, vol. 36, no. 4, pp. 32–35, 2011.
- [32] H. Wang, A. Wu, and J. Chen, "Full tailings-slag paste material pumping index optimization," *Mining Technology*, vol. 7, no. 3, pp. 15–17, 2007.
- [33] Z. A. Glaser, J. A. Fougereuse, S. J. Galgano et al., "High-volume concurrent polypoid ureteritis and ureteritis cystica manifesting with ureteral obstruction," *Urology*, vol. 136, 2020.
- [34] M. Benzaazoua, M. Fall, and T. Belem, "A contribution to understanding the hardening process of cemented pastefill," *Minerals Engineering*, vol. 17, no. 2, pp. 141–152, 2004.
- [35] W. S. Aaron, M. J. Hamlin, and P. S. Surendra, "A generalized approach for the determination of yield stress by slump and slump flow," *Cement and Concrete Research*, vol. 34, no. 3, pp. 363–371, 2004.
- [36] S. Kwan, J. LaRosa-Thompson, and M. W. Grutzeck, "Structures and phase relations of aluminum-substituted calcium silicate hydrate," *Journal of the American Ceramic Society*, vol. 79, no. 4, p. 967, 1996.
- [37] J. Rutqvist, "Thermal management associated with geologic disposal of large spent nuclear fuel canisters in tunnels with thermally engineered backfill," *Tunnelling and Underground Space Technology Incorporating Trenchless Technology Research*, vol. 102, Article ID 103454, 2020.
- [38] P. M. Keeley, N. A. Rowson, T. P. Johnson, and D. E. Deegan, "The effect of the extent of polymerisation of a slag structure on the strength of alkali-activated slag binders," *International Journal of Mineral Processing*, vol. 164, p. 37, 2017.
- [39] S. Clayton, T. G. Grice, and D. V. Boger, "Analysis of the slump test for on-site yield stress measurement of mineral suspensions," *International Journal of Mineral Processing*, vol. 70, no. 1–4, pp. 3–21, 2003.
- [40] B. Ercikdi, H. Baki, and M. Izki, "Effect of desliming of sulphide-rich mill tailings on the long-term strength of cemented paste backfill," *Journal of Environmental Management*, vol. 115, pp. 5–13, 2013.
- [41] H. Alhassan, P. Adjei Kwakwa, and E. Owusu-Sekyere, "Households' source separation behaviour and solid waste disposal options in Ghana's Millennium City," *Journal of Environmental Management*, vol. 259, 2020.
- [42] F. W. Brackebusch, "Basics of paste backfill systems," *Mining Engineering*, vol. 46, no. 10, pp. 1175–1178, 1994.
- [43] M. A. Khairul, J. Zanganeh, and B. Moghtaderi, "The composition, recycling and utilisation of Bayer red mud," *Resources, Conservation and Recycling*, vol. 141, p. 483, 2019.
- [44] S. K. Nath and S. Kumar, "Role of particle fineness on engineering properties and microstructure of fly ash derived geopolymer," *Construction and Building Materials*, vol. 233, Article ID 117294, 2020.
- [45] P. Kandiah and S. Nagaratnam, "Arching within hydraulic fill stopes," *Geotech Geological Engineering*, vol. 25, no. 1, pp. 25–35, 2007.
- [46] D. F. McCarthy, *Essentials of Soil Mechanics and Foundations: Basic Geotechnics*, Prentice-Hall, Upper Saddle River, NJ, USA, 1998.
- [47] M. Aubertin, L. Li, and S. Arnoldi, "Interaction between backfill and rock mass in narrow stopes," *Soil and Rock Mechanics America*, vol. 2, pp. 1157–1164, 2003.
- [48] L. Li, M. Aubertin, and T. Belem, "Formulation of a three dimensional analytical solution to evaluate stresses in back-filled vertical narrow openings," *Canadian Geotechnical Journal*, vol. 42, no. 5, pp. 1705–1717, 2005.
- [49] L. Li and M. Aubertin, "An improved analytical solution to estimate the stress state in subvertical backfilled stopes," *Canadian Geotechnical Journal*, vol. 45, no. 10, pp. 1487–1496, 2008.



## Research Article

# A Study of the Anchorage Body Fracture Evolution and the Energy Dissipation Rule: Comparison between Tensioned Rock Bolts and Torqued Rock Bolts

Bowen Wu <sup>1,2</sup>, Xiangyu Wang <sup>1,2</sup>, Jianbiao Bai <sup>2</sup>, Shuaigang Liu <sup>1,2</sup>,  
Guanghui Wang<sup>1,2</sup> and Guanjun Li<sup>1,2</sup>

<sup>1</sup>School of Mines, China University of Mining & Technology, Xuzhou 221116, China

<sup>2</sup>State Key Laboratory of Coal Resources and Safe Mining, Xuzhou 221116, China

Correspondence should be addressed to Xiangyu Wang; wangxiangyu\_cumt@163.com

Received 12 January 2021; Revised 19 January 2021; Accepted 4 February 2021; Published 15 February 2021

Academic Editor: Jian Ji

Copyright © 2021 Bowen Wu et al. This is an open access article distributed under the Creative Commons Attribution License, which permits unrestricted use, distribution, and reproduction in any medium, provided the original work is properly cited.

Rock bolt support is an effective technique for controlling surrounding rock of deep roadway. The stability of the anchorage body composed of rock bolts and surrounding rock mass is the core in keeping the stability of roadways. In this paper, the UDEC Trigon model was used in simulating uniaxial compressive test on the anchorage body under different pretension loads. The energy equilibrium criterion of the anchorage body under the uniaxial compressive state was proposed. Furthermore, the fracture evolution and the energy dissipation during the failure process of the anchorage body were analyzed. Results showed that before the peak strength, the external work was stored in the anchorage body in the form of the elastic strain energy ( $U^e$ ). After the peak, energy dissipated through three ways, including the fracture developing friction ( $W_f$ ), plastic deformation ( $W_p$ ), and acoustic emission ( $U^a$ ). Based on the simulation results, the high pretensioned rock bolts can eliminate the continuous tensile fractures in the anchorage body, decreasing the damaging extent of the anchorage body and the energy that was consumed by the following two main approaches: fracture developing friction ( $W_f$ ) and plastic deformation ( $W_p$ ). Moreover, the surplus of the elastic strain energy ( $U^e$ ) and the strength of the anchorage body can be improved. The pretension load had a positive relationship with elastic strain energy and a negative relationship with the anchorage body damage degree. Based on the above research, the transport roadway of the working face 6208 in the Wangzhuang Coal Mine selected tensile rock bolts to establish the high-performance anchorage body. The monitoring data showed that this reinforcement method effectively managed the serious deformation issue of the roadway surrounding the rock masses.

## 1. Introduction

In recent years, the depth of coal mining has been increasing at an annual rate of 6–10 m [1]. Under the superposition of the high in situ stress and the strong mining stress in the surrounding rock of the deep roadway, the surrounding rock of the roadway is prone to unsteady failure characteristics, and it may cause disasters in severe cases. The stability control of the surrounding rock of the roadway is one of the major problems to be solved in deep mining [2–4]. Massive engineering practices demonstrated that rock bolt reinforcement can effectively improve the stability of the surrounding rock mass [5–7]. Therefore, the rock bolt reinforcement technology,

regarded as an active reinforcement method, has been widely implemented in mining engineering in China. The anchorage body composed of rock bolts and the surrounding rock mass is the core to measure the stability of the roadway surrounding the rock mass. This is because it can control the volume expanding, deformation, and failure of the rock mass in the anchorage area [8–10]. To date, researchers have conducted substantial research regarding the anchorage body [11–13]. Wei and Gou [14] used the numerical simulation method to study the parameters of the anchorage body under the effect of pretensioned rock bolts and the instability condition of the anchorage body under in situ stresses. Results suggested that in the in situ stress environment, influence of the surrounding

rock mass strength around the roadway, the rock bolt pretension load, the lateral pressure coefficient of the in situ stress, the depth of the cover, the rock bolt interval, and the rock bolt spacing decreased successively. Wang et al. [15] deduced the theoretical equation of the shear strength for the anchorage body before and after grouting. The analysis illustrated that after grouting and reinforcing, with the greater mechanical parameters of the surrounding rock mass (elastic modulus, cohesion, internal friction angle and dilation angle), shear strength of the anchorage body increased significantly. Wu et al. [16] analyzed the acting response of the anchored surrounding rock mass under the dynamic loading impact. It was found that under the dynamic loading impact, the anchored surrounding rock mass of the roadway was subjected to repeated compression and tension. This resulted in the development of joints and fractures, which in turn led to the failure of the anchorage system. Wang et al. [17] investigated the effect of the anchoring length of the rock bolts and the pretension force on the stability of the anchorage body. It indicated that increasing the pretension force more effectively control the surrounding rock masses. When the anchorage length of the rock bolt was constant, the effective compressive stress area of the surrounding rock mass in the nonanchored section increased with the pretension force. Liu et al. [18] proposed the concept of the coordinated effect of the anchorage system. They believed that high pretension force was the major factor to develop the effect of the anchorage system.

It can be found that the research on the anchorage body conducted by predecessors mainly focused on the anchorage technology, the anchorage material, the coordinated effect, the stress transfer rule, and the dynamic loading character. As for the theoretical analysis, the traditional elastic–plastic mechanics was usually used. The stress-strain relationship was used to depict the mechanical acting character in the deformational failure process of the anchorage body. Based on this, the strength theory was established. However, the theory cannot truly reflect the deformational failure rule of the anchorage body.

In fact, the anchorage body in underground engineering is a highly nonlinear, complicated system. Furthermore, it is in the dynamic irreversible evolution period. Therefore, the deformational failure process of the anchorage body is the complicated conversion process of the energy, which is a status instability phenomenon driven by energy. The core of the damaging evolution of the anchorage body is the process of energy dissipation and release. The evolution rule of energy is the core expression of the deformational failure for the anchorage body [19–21]. Using the perspective of energy to analyze and explain the mechanical responding characters of the deformational failure in the anchorage body is an effective method.

Moreover, researchers have already used theoretical analysis and laboratory experiments to conduct research on the energy dissipating and releasing mechanism of the rock failure [22–25]. Meng et al. [26] analyzed the acoustic emission and the energy evolution character of the rock samples under the uniaxial cyclic unloading compression condition. The results showed that the energy evolution of rock masses had a close relationship with the axial loading stress, rather than the axial

displacement rate. Before the axial load reached its peak strength, the energy accumulation accounted for the leading role. After that, the energy dissipation accounted for the leading role. The input energy led to generation of microfractures in the rock mass and irreversible development. The releasing of the elastic energy resulted in the instability of the rock mass. Moreover, this induced damage to rock mass. Dong et al. [27] studied the energy evolution process of the rock masses in the mining process. According to the variation tendency of energy, the dissipating process was divided into the initiating stage, the stable increasing stage, the dramatic increasing stage, and the stable stage. However, limited research has been conducted on studying the energy dissipation in the failure process of the anchorage body via the numerical simulation method. Previous studies found that the fracture development was the internal reason leading to the instability of the anchorage body [28, 29]. However, the pretension force was the primary external influencing parameter in affecting the stability of the anchorage body [12]. Therefore, in this study, the UDEC Trigon method was used to carry out the Uniaxial Compressive Strength (UCS) test on the anchorage body under various pretension forces. The energy evolution and the fracture development of the anchorage body with different pretension forces were monitored. The relationship between the pretension force, the fracture development of the anchorage body, and the energy in the anchorage body was studied. The failure character of the anchorage body was analyzed from the perspective of energy. It is expected that the research results can be more representative of the deformational failure rule of the anchorage body.

## 2. Energy Balance and Components

Since the 1960s, scholars have conducted a significant body of research on the theory of energy equilibrium in rock mechanics [30–34]. From the initial rough studying of the energy variation in the underground mining process, these energy concepts gradually developed to a detailed study of the energy evolution of the rock masses under the conditions of the different buried depth, the loading and the unloading method, and the confining pressure. Based on summarizing the previous scholars' work, this study combined the simulation condition to determine the energy equilibrium criteria.

During the UCS process, the applied work by the external force was expressed with  $W$ . Due to the elastic deformation of the anchorage body, certain forces were stored in the internal area of the anchorage body in the form of elastic strain energy. The energy of this section was expressed with  $U^e$ . The difference between the applied work by the model boundary and the elastic strain energy was the dissipating energy ( $U^d$ ). Therefore, the total input energy ( $W$ ) induced by the applied work of the external forces can be expressed with

$$W = U^d + U^e. \quad (1)$$

Energy was mainly dissipated through three approaches. The first approach was generating, developing, closing, and fracture friction in the rock masses. The dissipated energy by

them was  $W_f$ . The second approach was the plastic deformation of the rock masses ( $W_p$ ). When the rock block generated irreversible deformation, energy was dissipated through the plastic work. The residual section was commonly released through acoustic emission, which can be expressed with  $U^r$ . Therefore, the dissipated energy  $U^d$  can also be defined as

$$U^d = W_f + W_p + U^r. \quad (2)$$

In UDEC, the increment variation of this energy was determined and accumulated in each timestep [35]. Combining equations (1) and (2), in this study, the energy equilibrium equation that was used to calculate the energy releasing can be written as

$$W = W_f + W_p + U^r + U^e. \quad (3)$$

Then, this energy equilibrium concept was used to discuss the energy dissipation of the complicated anchorage body.

### 3. Parameter Calibration

**3.1. The UDEC Trigon Approach.** The UDEC Trigon model was proposed by Gao et al. [36] to simulate brittle fracture of the rock. In this model, a rock is represented by an assembly of triangular blocks bonded together via their grain contacts. Each block is made elastic by dividing them into triangular finite difference zones. Hence, the block does not fail by plastic yielding. Failure can only occur along the contacts in shear or tension, depending on the stress state and the properties of the contact surface [35]. In the direction normal to a contact, the stress-displacement relation is assumed to be linear and governed by the stiffness  $k_n$ :

$$\Delta\sigma_n = -k_n\Delta u_n, \quad (4)$$

where  $\Delta\sigma_n$  is the effective normal stress increment and  $\Delta u_n$  is the normal displacement increments. A limiting tensile strength ( $T$ ) is assumed for the contact. If this value is exceeded, then  $\sigma_n = 0$ .

Along the shear direction, the response is governed by constant shear stiffness. The shear stress ( $\tau_s$ ) is determined by a combination of contact properties: cohesion ( $c$ ) and friction ( $\varphi$ ).

$$|\tau_s| \leq c + \sigma_n \tan \varphi = \tau_{\max}. \quad (5)$$

Then,

$$\tau_s = -k_s u_s^e. \quad (6)$$

However, if  $|\tau_s| \geq \tau_{\max}$ , then,

$$\tau_s = \text{sign}(\Delta u_s^e) \tau_{\max}. \quad (7)$$

where  $\Delta u_s^e$  is the elastic component of the incremental shear displacement and  $\Delta u_s^s$  is the total incremental shear displacement.

The proposed modeling approach has been implemented within UDEC [35].

**3.2. Mechanical Parameters of the Anchorage Body.** As the UDEC Trigon model defines the block as the elastic material, plastic failure cannot be generated. However, in the anchorage body, failure is elastoplastic. Therefore, to accurately simulate the physical and mechanical characters and the energy dissipating rule after the anchorage body fails, based on the UDEC Trigon block, this study used the strain-softening model for the block. The strain-softening model is based on the UDEC Mohr-Coulomb model with nonassociated shear and associated tension flow rules.

The intact properties of the coal are listed in Table 1. These properties were obtained through laboratory tests and were provided by the Wangzhuang Coal Mine. The RQD values of the coal masses were evaluated from borehole televiewer images.

The rock mass elastic modulus was calculated using the relationship between RQD and the elastic modulus ratio [37], as shown in equation (7), where  $E_m$  is the elastic modulus of the rock mass and  $E_r$  is the elastic modulus of the rock sample.

$$\frac{E_m}{E_r} = 10^{0.0186RQD - 1.91}. \quad (8)$$

The rock mass strength was calculated using the relation between the UCS ratio  $\sigma_{cm}/\sigma_c$  and the deformation modulus ratio  $E_m/E_r$  [38]. The value of  $q$  is 0.63 [39]:

$$\frac{\sigma_{cm}}{\sigma_c} = \left( \frac{E_m}{E_r} \right)^q. \quad (9)$$

To represent the coal by using an assembly of triangular blocks, the properties of the blocks and contacts were calibrated against the coal properties listed in Table 2. This was achieved by simulating UCS tests in a numerical model created using the Trigon logic. The size of the rock sample is 2 m (in width)  $\times$  4 m (in height) [38] (Figure 1). The bottom of the numerical model was fixed and a displacement rate of 0.02 m/s was applied at the top. The calibrated properties of the UDEC model are illustrated in Table 3.

The UCS and elastic modulus data derived by numerical simulation are consistent with laboratory tests (within an error of 7%). Hence, the reasonable availability of the micromechanical parameters of the coal mass and the rock mass was verified.

**3.3. Rock Bolt Parameters.** The ‘‘cable’’ structural element in UDEC was adopted to simulate the rock bolts. The parameters of the ‘‘cable’’ element are presented in Table 4. A detailed description of the support elements in UDEC is provided by the Itasca Consulting Group Inc. For resin-grouted rock bolts, two key properties governing the anchor characteristics are the stiffness ( $K_{\text{bond}}$ ) and the cohesive strength ( $S_{\text{bond}}$ ) of the grout. A practical estimation of  $K_{\text{bond}}$  was provided in the UDEC manual [36] as

$$K_{\text{bond}} \cong \frac{2\pi G}{10 \ln(1 + 2t/D)}, \quad (10)$$

TABLE 1: Intact rock properties and scaled rock mass properties of coal from the Wangzhuang Coal Mine.

Coal measures	Intact rock		RQD (%)	Rock mass		
	$E_r$ (GPa)	$\bar{\sigma}_r$ (MPa)		$E_m$ (GPa)	$\bar{\sigma}_{cm}$ (MPa)	$\bar{\sigma}_{tm}$ (MPa)
Coal	2.6	10.8	75	0.79	5.1	0.51

TABLE 2: Calibrated mechanical parameters of blocks and joints of the coal.

	Density (kg/m <sup>3</sup> )	Young's modulus (GPa)	Cohesion (MPa)	Friction (°)	Tensile strength (MPa)
Block	1400	0.79	1.6 ( $\epsilon=0$ ) 1.1 ( $\epsilon=0.04$ ) 0.6 ( $\epsilon=0.15$ )	27	0.9
Joint	Normal stiffness (GPa/m)	Tangential stiffness (GPa/m)	Cohesion (MPa)	Friction (°)	Tensile strength (MPa)
	113	45.2	1.3	18	0.4

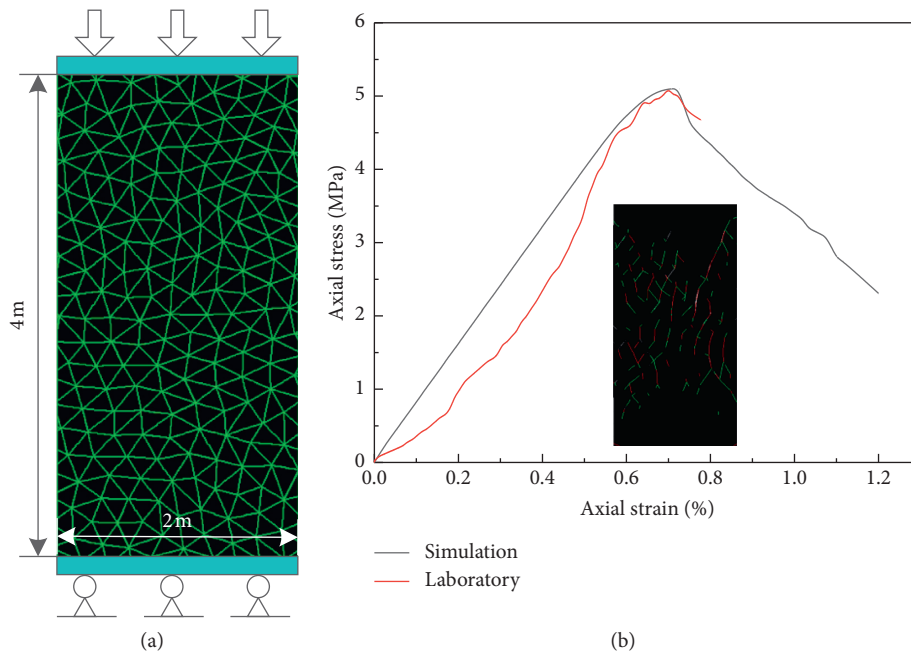


FIGURE 1: Results of UCS testing: (a) numerical simulation of uniaxial compression and (b) stress-strain curve of coal.

TABLE 3: Calibrated microproperties in the UDEC Trigon model to represent the coal.

Coal measures	Young's modulus (GPa)			Compressive strength (MPa)		
	Target	Calibrated	Error (%)	Target	Calibrated	Error (%)
Coal	0.79	0.73	7	5.1	5.1	0

TABLE 4: Properties of support elements in UDEC.

Contact properties	Value
Elastic modulus (GPa)	200
Tensile yield strength (kN)	390
Stiffness of the grout (N/m/m)	2e9
Cohesive capacity of the grout (N/m)	4e5



where  $G$ : the grout shear modulus;  $D$ : the bolt diameter, and  $t$ : the annulus thickness. Zipf [40] provided practical values of  $S_{\text{bond}}$  for simulating resin-grouted rock bolts installed in varying Coal Measures. A value of 400 kN/m of  $S_{\text{bond}}$  was adopted in this study.

#### 4. Fracture Evolution and Energy Dissipating Rule of the Anchorage Body

**4.1. Simulation Method and the Model Building.** According to the physical and the mechanical characters of the in situ anchorage body, the UDEC Trigon simulation method was used to conduct research on the fracture evolution and energy dissipating rule of the anchorage body (Figure 2). The supporting resistance of the rock bolts to the surrounding rock is far from the in situ stress, so that the influence of the rock bolt supporting effect on the surrounding rock cannot be effectively displayed, and hence, the effect of in situ stress is ignored in the simulation. In the model, for the zone and the interface, the strain-softening model and the coulomb slip model were used, respectively. The model was a rectangle with the width–height ratio of 1 : 2. The dimension was 2 m in width and 4 m in height. At the middle of the model bottom boundary, a rock bolt with a length of 2.4 m was installed. At the top of the model, a loading velocity of 0.02 m/s was applied. The bottom boundary of the model was fixed. During the loading process of the model, the FISH function was used to monitor the stress in the anchorage body, the quantity of shearing fractures, the length of shearing fractures, the quantity of tensile fractures, and the length of tensile fractures. The energy module in UDEC was used to monitor parameters such as the applied work by the boundary forces, the applied work by friction, and the applied work by plasticity. Based on whether it was anchored and the difference of the rock bolt pretension forces, three simulation schemes were established: (1) no rock bolt; (2) rock bolts with low pretension forces; and (3) rock bolts with high pretension forces. Table 5 shows the specific parameters of each scheme. In the field, the pretensioned torque that was applied on rock bolts commonly ranged from 300 to 400 Nm. The corresponding pretension forces ranged from 40 kN to 50 kN [41]. Therefore, in this study, in the simulation scheme, the low pretension force was 40 kN.

For rock bolts, the other parameters were equal except that the pretension force was different.

Attention should be paid that when energy was monitored, the command of “SET energy on” should be used to activate the energy monitoring module. In addition, the mass-scaling option was shut down. Because in this study, the nonsticky boundary was used and the dynamic calculating analysis was not involved, the damping was set as “Damping auto.” The modeling processes were described as: (a) establishing the model and applying the calibrated parameters on the model; (b) according to the simulated scheme, conducting loading simulation on the anchorage body; and (c) finally, according to the monitored data, analyzing the energy dissipating rule of the anchorage body. Figure 2 shows the schematic diagram of the model.

**4.2. Deformational Failure Character and Energy Dissipating Rule of the Anchorage Body.** Figure 3 shows that when there was no rock bolt, there were massive continuous fractures distributed in the anchorage body. In particular, at the upper right of the anchorage body, there were coalescence of shear and tensile fractures. In the anchorage body with low pretensioned rock bolt installed, fractures developed in the body were lower than that shown in Figure 3(a), indicating that pretension has an impact on the fracture distribution. Thereby, the number of cracks was also reduced compared to that of no rock bolt. In the anchorage body with high pretensioned rock bolts installed, most fractures were shear and a substantial decrease in the total fractures can be observed. It is noted that there were only a small number of discontinuous tensile fractures at the corner of the top and the bottom. Therefore, high pretensioned rock bolts can effectively reduce the quantity of the continuous tensile fractures in the anchorage body. Also, the condition of the anchorage body can be improved, which was beneficial for ensuring the integrity and stabilization of the anchorage body.

Figure 4 shows the processing results of the monitored data. These nine figures were classified into groups along the vertical direction according to the simulation scheme. From the left to the right, they were anchorage body without the rock bolt, anchorage body with low pretensioned rock bolts, and anchorage body with high pretensioned rock bolts. Along the horizontal direction, they were classified into groups, according to the anchorage body strength, fracture developing, and energy variation. The damaging extent of the anchorage body was determined by the ratio of damage length of the contact surface (including both shear cracks and tensile cracks) to the total length [37]. From the top to bottom, they were stress-strain curves, fracture-strain curves, and energy-strain curves. The fracture-strain curves include shearing fractures, tensile fractures, total damaging extent, shearing damaging extent, and tensile damaging extent. The energy-strain curves include the applied work by the boundary, the elastic strain energy, applied work by friction, applied work by plasticity, and released energy.

First, analysis was conducted on Figure 4 along the vertical direction. According to the tendency of the fracture curve and the energy curve, and the relationship between them and the stress curve, the whole failure process of the anchorage body was divided into three stages: fracture initiating stage (Phase I), rapid developing stage of fractures (Phase II), and the post-peak stage (Phase III).

The fracture initiating stage (Phase I) started from zero to around 80% of the peak strength. In this stage, the fractures and the damaging extent were at a relatively low level. The anchorage body was in the elastic strain stage. The externally imported energy was almost all transferred to the elastic strain energy, which was stored in the anchorage body. In this stage, there was very minor energy dissipation induced by the anchorage body failure.

The rapid developing stage of fractures (Phase II) started from around 80% of the peak strength to the peak strength. In this stage, the shearing fractures developed rapidly, leading to the damage of the anchorage body. However, the tensile fractures were still at a relatively low level. Therefore,



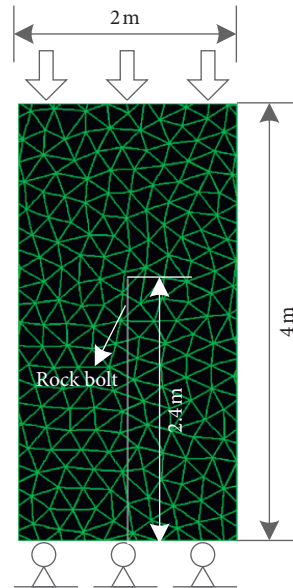


FIGURE 2: Model overview and dimensions.

TABLE 5: Numerical simulation scheme.

	Whether there are rock bolts	Rock bolt pretension force	Displacement rate
Scheme I	No	—	0.02 m/s
Scheme II	Yes (torqued rock bolts)	Low (40 kN)	0.02 m/s
Scheme III	Yes (tensile rock bolts)	High (90 kN)	0.02 m/s

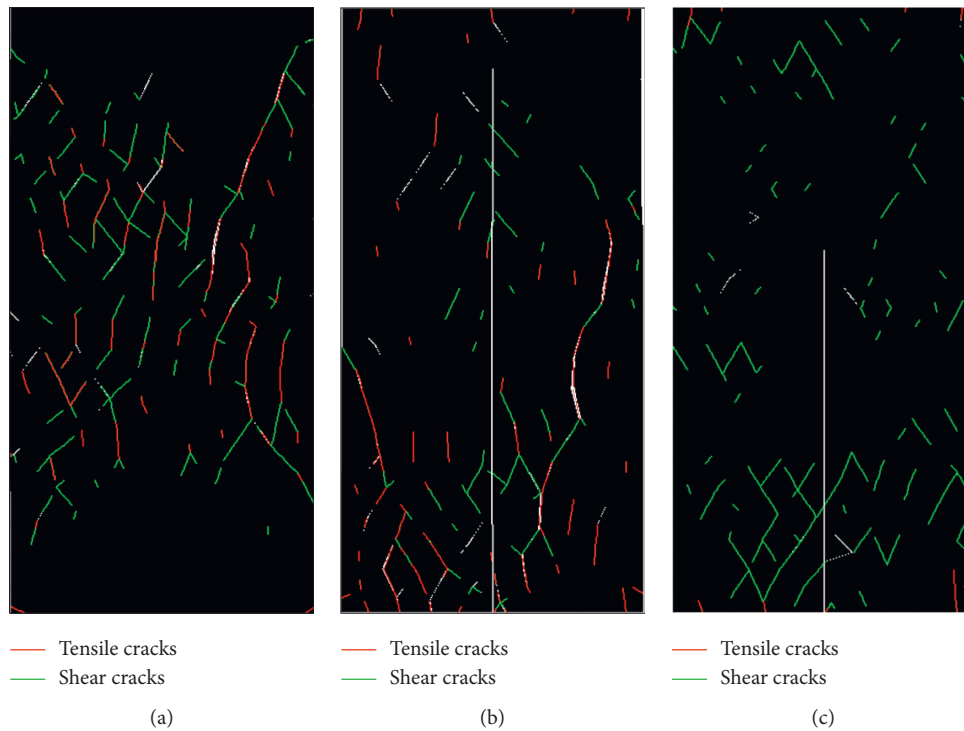


FIGURE 3: Failure of anchorage body: (a) no rock bolt; (b) a rock bolt with low pretension; (c) a rock bolt with high pretension.

in this stage, the developing and propagation of shearing fractures were the principal factors leading to the failure of the anchorage body. In this stage, a small amount of energy was dissipated through applying work with fracture friction and applying work with plastic deformation. However, more energy was still stored in the anchorage body in the form of the elastic strain energy. Furthermore, around the peak strength, it reached the peak of the elastic strain energy.

The post-peak stage (Phase III) indicated the section that was after the peak. In this stage, the development of the shearing fractures in the anchorage body became stable. However, at this time, the tensile fractures in the low level in previous two stages showed increasing tendency in this stage. Not only the quantity but also the extent of damage resulted by tension increased. In this stage, a quantity of energy was dissipated through applying work via fracture friction and applying work via plastic deformation. The energy released by acoustic emission also increased rapidly. The anchorage body gradually entered the plastic strain. The internal elastic strain energy decreased from the peak. All dissipated energy became stable after a period of time. This was probably the result of the continuous dissipation of the energy, which lead to further developing of the fractures in the anchorage body and the shearing deformation along the sliding plane [42].

To monitor the degree of damage to the anchorage body, the total fracture length as well as the shear and tensile fracture lengths during uniaxial compression were measured. The degree of damage ( $D$ ) can be calculated as follows [36]:

$$D = \frac{L_S + L_T}{L_C} \times 100\%, \quad (11)$$

where  $L_C$  is the total fracture length, and  $L_S$  and  $L_T$  are the total shear and tensile fracture lengths, respectively.

Then, analysis was conducted on Figure 4 along the horizontal direction. The evolution characters of the stress, fracture, and energy in the anchorage body under different simulation schemes were compared and analyzed. Table 6 shows the specific data comparison of the stress and fractures in the anchorage body. The variation rate in the table was obtained by comparing with the data in Group 1.

With regard to the aspect of stress, the pretensioned rock bolts not only improve the elastic modulus of the anchorage body to improve its peak strength but also improve the post-peak character of the anchorage body (Figures 4(a)–4(c)). Then, the decreasing of the anchorage body strength can be reduced. The peak strength of the anchorage body with high pretensioned rock bolts installed reached 5.8 MPa, improving by 13.7% compared with the coal mass that was not installed with the rock bolts. When there was no rock bolt installed, after the coal mass reached the peak, the stress curve decreased rapidly, with the strength decreasing from 5.1 MPa to 2.3 MPa (Figure 4(a)). After the pretensioned rock bolts were installed, the post-peak stresses were all above 4 MPa.

With regard to the aspect of fracture and damage, pretensioned rock bolts can effectively decrease the whole extent of damage of the anchorage body. After the low pretensioned rock bolts and high pretensioned rock bolts were installed, the whole

extent of damage of the anchorage body decreased by 8.6% and 16.6%. Besides, the quantity of the shearing fractures, the quantity of tensile fractures, and the tensile damaging extent showed a tendency to decrease. However, when the low pretensioned rock bolts were installed, the fracture evolution situation was different from the other two groups. Compared with the coal body without the rock bolts, the damage starting point of the anchorage body with low pretension bolts has not changed, and the tensile cracks and tensile damage increase rapidly and greatly between the strain of 0.5%–0.6%. Moreover, the ultimate tensile fractures and the extent of tensile damage were higher compared with the coal mass that was not installed with the rock bolts (Figures 4(d) and 4(e)). The increasing rate reached 25.8% and 34%, respectively. This was probably because the pretension applied on the rock bolt was relatively low. At the initial loading stage, the active reinforcing effect of the rock bolts was not apparent. Therefore, at the initial loading stage, the microfailure of the anchorage body occurred (with the strain ranging between 0.5% and 0.6%). Furthermore, tensile failure occurred. This led to an increase in the ultimate fractures and the extent of tensile damage. When the strain was 0.6%, the rock bolts started developing the active reinforcement effect. The tensile fractures became stable when the strain ranged from 0.6% to 0.76% (the corresponding strain for the peak strength). Based on the above analysis, the low pretensioned rock bolts cannot develop the active reinforcement effect at the initial reinforcing stage, which leads to an increase of tensile damage of the anchor body.

For energy, when plotting Figures 4(g)–4(i), energy dissipated by acoustic emission was plotted individually. The tendency of the acoustic emission energy curve was basically consistent with the tendency of the acoustic emission count curve. This was the important appearance of the anchorage body failure [31]. Figure 5 shows the specific data of each energy component after the simulation was finished. From the development tendency of the elastic strain energy curve, it can be seen that the whole process of the anchorage body failure was composed of energy charging and releasing. Therefore, the fracture initiating stage (Phase I) and the rapid developing stage of fractures (Phase II) were combined and called as the energy charging stage. The post-peak stage (Phase III) was called as the energy releasing stage. After the rock bolts were installed in coal strata, with the increasing of the pretension, the peak energy in the energy charging stage increased and the position of peak energy moved behind. Furthermore, under the situation of equal strain, the residual elastic strain energy is increased. At the peak position of the elastic strain energy, it entered the energy-releasing stage and massive energy was released. Energy was mainly dissipated through the developing of fractures and friction. Then, the energy was dissipated through the plastic applied work of the anchorage body. The dissipated energy by acoustic emission was minimal. The acoustic emission energy in three groups accounted for 5.7%, 14.4%, and 16.9% of the released energy in each group. With an increase in the pretension, the dissipated energy through the fracture developing, friction, and the plastic applied work of the anchorage body showed a decreasing tendency. The acoustic emission energy and the residual elastic strain energy increased (Figure 5). This was mainly because when the rock bolt developed an active

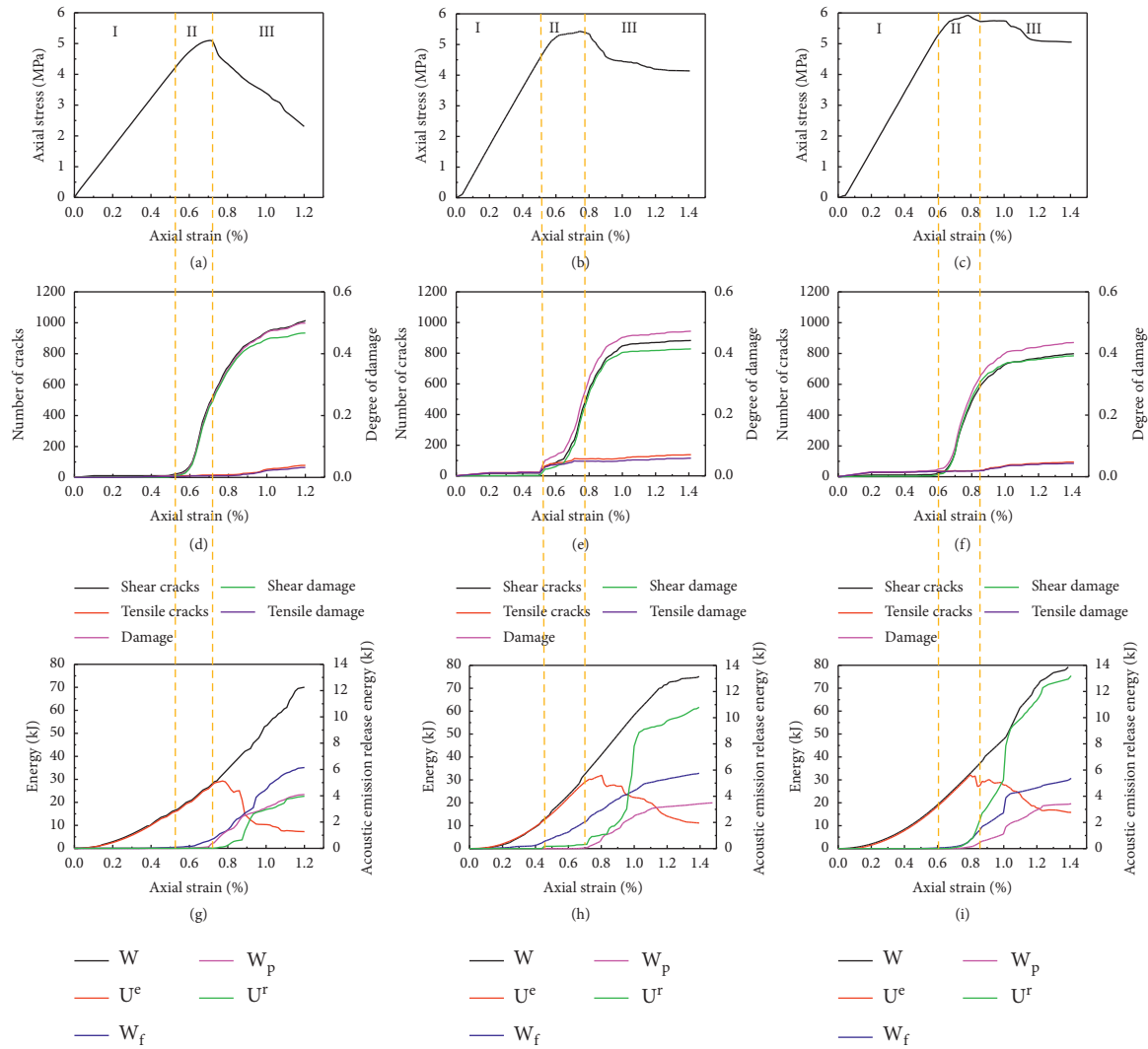


FIGURE 4: Strength, fracture, and energy evolution of the anchorage body under uniaxial compression: (a) stress-strain curve (no rock bolt); (b) stress-strain curve (low pretensioned rock bolt); (c) stress-strain curve (high pretensioned rock bolt); (d) crack and damage curve (no rock bolt); (e) crack and damage curve (low pretensioned rock bolt); (f) crack and damage curve (high pretensioned rock bolt); (g) energy curve (no rock bolt); (h) energy curve (low pretensioned rock bolt); and (i) energy curve (high pretensioned rock bolt).

TABLE 6: Comparison of the stress and fractures in the anchorage body.

	Group 1	Group 2	Group 3	Rate of change
Peak strength	5.1 MPa	5.4 MPa	5.8 MPa	5.9% 13.7%
Quantity of the shearing fractures	1068	887	800	-16.9% -25.1%
Quantity of tensile fractures	116	146	95	25.8% -18.1%
Total damaging extent	52.4%	47.9%	43.7%	-8.6% -16.6%
Shearing damaging extent	47.7%	41.6%	39.4%	-12.8% -17.4%
Tensile damaging extent	4.7%	6.3%	4.3%	34.0% -8.5%

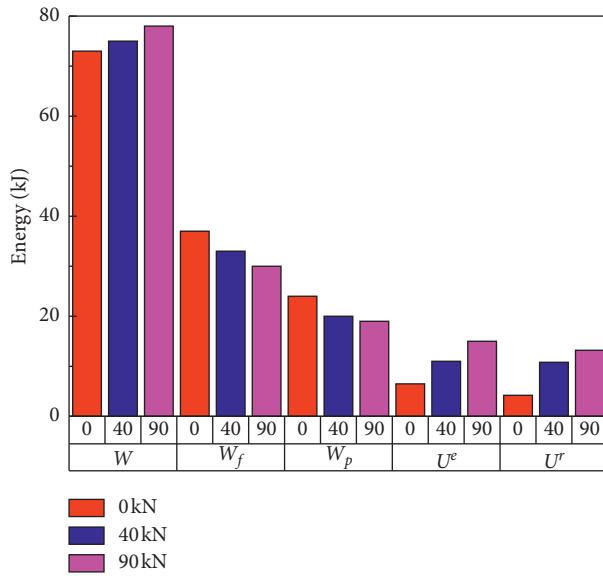


FIGURE 5: Data of each energy component.

reinforcing effect, it changed the physical and mechanical characters of the anchorage body. This improved the parameters such as the elastic modulus of the anchorage body. Also, this improved the ability of the anchorage body in resisting the developing of fractures and plastic deformation. Under the low pretensioned situation, in the energy charging stage, fracture developing and energy dissipating via friction occurred (Figure 4(h)). This was because in the initial reinforcement stage, the rock bolt reinforcement effect was poor. This led to the initiating and developing of tensile fractures. This was consistent with the fracture evolution curve (Figure 4(e)). Improving the rock bolt pretension can effectively improve this situation (Figure 4(i)). At the initial reinforcement stage, it developed the active reinforcement effect, ensuring the stability of the anchorage body.

**4.3. Strengthening of the High-Performance Anchorage Body Strength.** The rock bolt surrounding rock mass strength strengthening theory assumed that installing the high pretensioned rock bolts can effectively improve the mechanical parameters of the anchorage body. Also, the strength of the anchorage body can be improved. The plastic area, radius of the fractured zone, and the surface displacement can effectively be reduced. The stability of the surrounding rock mass can be maintained [1, 43]. Based on the deformational failure character of the anchorage body and the energy dissipating rule in section 4.2, this section explained the strength strengthening theory from the perspective of energy. Figure 6 shows the comparison between the peak strength, residual elastic strain energy, and the damaging extent of the anchorage body with different pretension forces after the simulation was finished.

The residual strain energy was the residual energy in the anchorage body after the simulation was finished. Figure 6 shows that applying high pretension forces can improve the residual strain energy of the anchorage body. This was because installation of high pretensioned rock

bolts improved the mechanical parameters of the anchorage body. Meanwhile, the development of the fractures in the anchorage body was restricted. Then, the energy was dissipated by using two main approaches: fracture developing friction and plastic deformation. The residual strain energy had a positive relationship with the peak strength and a negative relationship with the damaging degree. Therefore, it can be assumed that the high-performance anchorage body constructed with high pretension has a high strength anchorage body with a low extent of damage. This was consistent with the rock bolt surrounding the rock mass strength strengthening theory. Therefore, constructing the high-performance anchorage body can effectively reduce the surface displacement of the surrounding rock masses.

## 5. In Situ Tests and Observations

**5.1. Profile of Tensile Rock Bolts.** Our research group developed a new rock bolt locking instrument, which changed the traditional rock bolt locking method. This solved the problem of low transferring efficiency in the torque and pretension, which occurred in the traditional torqued pretensioned rock bolts in essence. This effectively improved the rock bolt pretension and fully developed the active reinforcement effect of the rock bolts. The rock bolt locking instrument was composed of barrel and wedge. The barrel and wedge was a circular structure. At the middle of it, there was a cone hole. As for the clamping, there were multiple pieces. Its external surface radian dimension was matched with the cone hole. Meanwhile, its internal surface radian dimension was matched with the outside diameter of the rock bolts. The clamping was installed between the internal surface of the anchoring ring cone hole and the rock bolt (Figures 7(a) and 7(b)). A specially manufactured hydraulic jack was used to apply pretension. It can apply a pretension force of 90 kN on threaded rock bolts (HRB 335) with a diameter of 22 mm without damaging, as shown in Figure 7(d). It reached about 70% of the yielding capacity.

**5.2. In Situ Observations.** To verify the accuracy of the numerical simulation, experiments were conducted in the field. The location of the experiment was the transport roadway of the working face 6208 in the Wangzhuang Coal Mine in the city of Changzhi, Shanxi Province, China. The Working face 6208 was located in the coal seam 3#, with an average thickness of 6.9 m. The transport roadway of 6208 was tunneled along the gob. The excavation was conducted along the floor. Two sides of the roadway and the immediate roof were coal (Figure 8(a)). The head entry of the working face 6208 was excavated along the floor with a cross section of 5.0 m (in width)  $\times$  3.2 m (in height), as shown in Figure 8(b). In the working face 6208, the traditional torqued HRB 335 threaded rock bolts were used to perform the roadway reinforcement. The rock bolt diameter was 22 mm and the length was 2400 mm, with 300 Nm applied to provide the pretension. During the excavation period, the serious problem of surrounding the



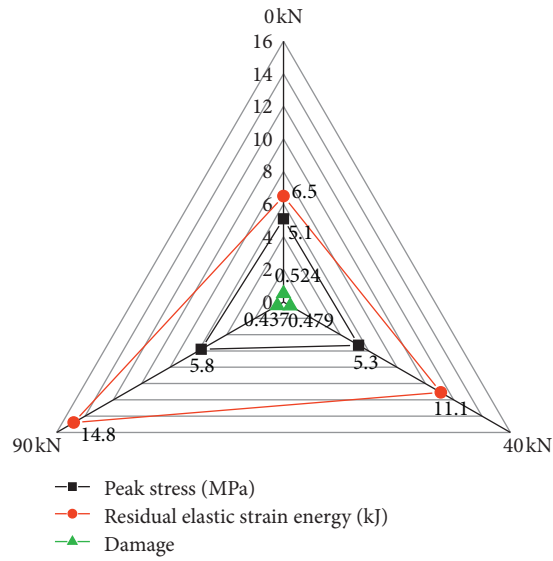


FIGURE 6: Comparison of peak strength, residual elastic strain energy, and damaging extent of anchorage body under different pretensions after the simulation was finished.



FIGURE 7: The anchoring system components: (a) barrel and wedge; (b) separated barrel and wedge; (c) barrel and wedge installed in the rock bolt; (d) barrel and wedge installation.



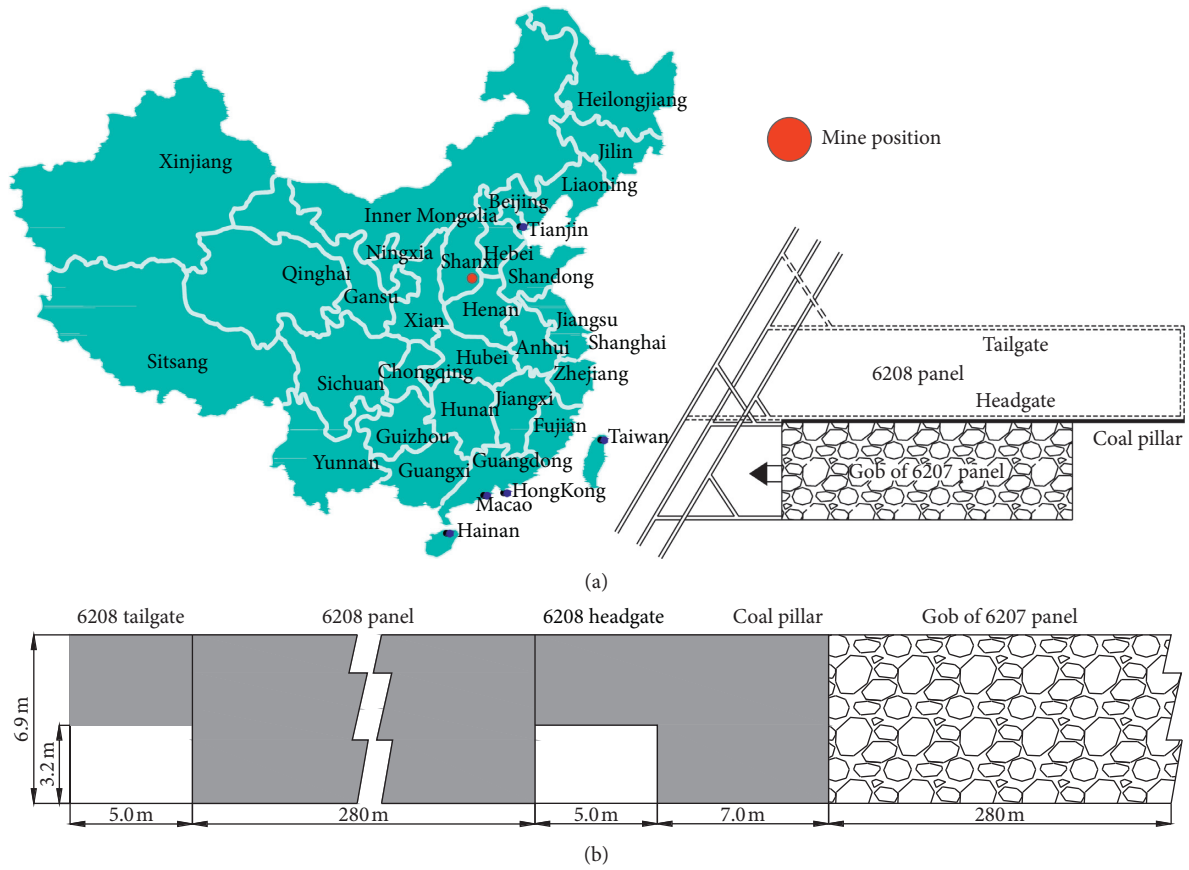


FIGURE 8: The panel introduction of sampling site: (a) mine position and plan view and (b) section view.

rock mass deformation at two sides of the roadway occurred, as shown in Figure 9. In this roadway, a length of 200 m was selected as the test section. Tensile rock bolts were installed. The rock bolt locking instrument was matched with the particularly manufactured hydraulic Jack to apply pretension on the HRB 335 threaded rock bolts with a diameter of 22 mm. In the test, a pretension of 90 kN was applied without damaging the rock bolt. In the torqued rock bolt section and the tensile rock bolt section, the surface displacement observation stations were installed to monitor the convergence of the two sides of the roadway during the tunneling period. Figure 10 shows the convergence of the two sides of the roadway in the torqued

rock bolt test section and the tensile rock bolt test section during the tunneling period. With the tunneling face advancing, the deformation of the roadway surrounding the rock masses gradually increased. After the distance to the tunneling face was 100 m, the convergence of the two sides of the roadway became stable. The maximum convergence of the two sides of the roadway for the torqued rock bolt test section was 527 mm. As for the tensile rock bolt test section, the maximum convergence of the two sides of the roadway was 210 mm. The maximum convergence of the two sides of the roadway was reduced by 60%. Therefore, the tensile anchorage body constructed with tensile rock bolts can effectively reduce the



FIGURE 9: Deformation of the roadway surrounding the rock masses.

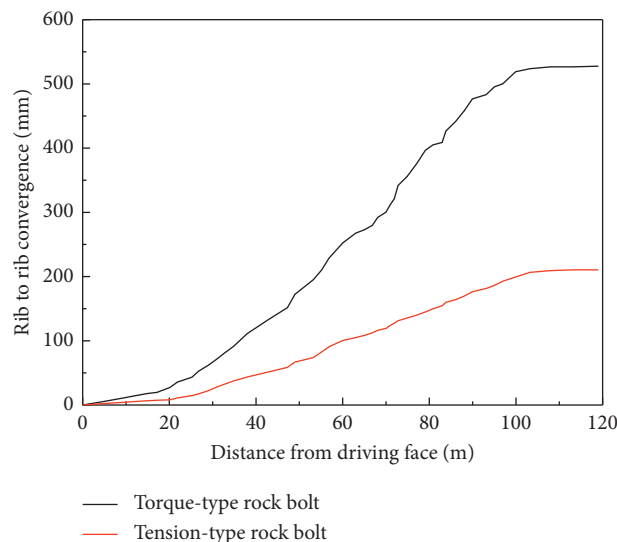


FIGURE 10: Convergence of head entry of the working face 6208 during tunneling.

deformation of the rock masses surrounding the roadway. Furthermore, the roadway surrounding the rock masses can be guaranteed to be stable.

## 6. Conclusions

In this study, the UDEC Trigon method was used to study the influence of pretension on the anchorage body strength and energy. The anchorage body model was composed of triangle deformable blocks. According to the standard calibration procedures, rigid calibration and validation were conducted on the input character of the anchorage body and the rock bolts. Then, through the UCS test, the anchorage body, and the influence of pretension force was studied. The following conclusions were acquired:

- (1) High pretension rock bolts can reduce the extent of fractures in the anchorage body, especially the tensile fractures. The damage extent of the anchorage body was reduced, with a reduction of 16.6% with 90 kN.

Meanwhile, the anchorage body strength can be improved by 13.7%, which effectively improved the stability of the anchorage body.

- (2) According to the fracture development and energy dissipation character, the whole failure process of the anchorage body was composed of three stages: fracture initiating stage (Phase I), rapid developing stage of fractures (Phase II) and the post-peak stage (Phase III). The externally applied work was stored in the internal area of the anchorage body in the form of the elastic strain energy. Energy was dissipated through three approaches: fracture friction, plastic deformation, and acoustic emission. At the initial reinforcing period, the active reinforcement effect of the low pretensioned rock bolts was not apparent. At the initial reinforcing period, tensile fractures occurred. The energy was dissipated through applying work via fracture friction. With the increasing pre-tension, rock bolts can restrict the fracture

friction and plastic deformation. This means that more elastic strain energy was stored in the anchorage body, forming the high-performance anchorage body.

- (3) In the transport roadway of the Working face 6208 in the Wangzhuang Coal Mine in the city of Changzhi, Shanxi Province, China, an in situ experiment was conducted. The monitoring data showed that for the torqued rock bolt section, the maximum convergence of the two sides of the roadway was 527 mm. As for tensile rock bolts, the maximum convergence of the two sides of the roadway was 210 mm. The maximum convergence of the two sides of the roadway was reduced by 60%. Therefore, through constructing high-performance anchorage body, the surface displacement of the surrounding rock mass can be effectively reduced.

## Data Availability

The data used to support the findings of this study are available from the corresponding author upon request.

## Conflicts of Interest

The authors declare that they have no conflicts of interest regarding the publication of this paper.

## Acknowledgments

The authors are grateful for the support from the Fundamental Research Funds for the Central Universities (2018ZDPY02).

## References

- [1] H. Wu, X. K. Wang, W. Wang et al., "Deformation characteristics and mechanism of deep subsized coal pillar of the tilted stratum," *Energy Science and Engineering*, vol. 8, no. 2, pp. 544–561, 2020.
- [2] C. J. Hou, X. Y. Wang, J. B. Bai et al., "Basic theory and technology study of stability control for surrounding rock in deep roadway," *Journal of China University of Mining and Technology*, vol. 50, no. 1, pp. 1–10, 2021.
- [3] H. Jing, J. Wu, Q. Y. Qian, and K. Wang, "Deformation and failure characteristics of anchorage structure of surrounding rock in deep roadway," *International Journal of Mining Science and Technology*, vol. 30, no. 5, pp. 593–604, 2020.
- [4] J. B. Yin and C. J. Hou, "Control principle of surrounding rocks in deep roadway and its application," *Journal of China University of Mining and Technology*, vol. 35, no. 2, pp. 145–148, 2006.
- [5] A. Mirzaghobanali, H. Rasekh, N. Aziz, G. Yang, S. Khaleghparast, and J. Nemcik, "Shear strength properties of cable bolts using a new double shear instrument, experimental study, and numerical simulation," *Tunnelling and Underground Space Technology*, vol. 70, pp. 240–253, 2017.
- [6] Z. Wen, E. Xing, S. Shi, and Y. Jiang, "Overlying strata structural modeling and support applicability analysis for large mining-height stopes," *Journal of Loss Prevention in the Process Industries*, vol. 57, pp. 94–100, 2019.
- [7] J. P. Zuo, J. H. Wen, Y. D. Li et al., "Investigation on the interaction mechanism and failure behavior between bolt and rock-like mass," *Tunnelling and Underground Space Technology*, vol. 93, Article ID 103070, 2019.
- [8] J. K. Jiao, *Burst failure mechanism and control technology of roadway anchorage bearing structure under dynamic load disturbance*, Ph.D. thesis, China Coal Research Institute, Beijing, China, 2018.
- [9] Z. Z. Zhang, M. Deng, X. Y. Wang et al., "Field and numerical investigations on the lower coal seam entry failure analysis under the remnant pillar," *Engineering Failure Analysis*, vol. 115, 2020.
- [10] Z. Z. Zhang, M. Deng, J. B. Bai et al., "Stability control of gob-side entry retained under the gob with close distance coal seams," *International Journal of Mining Science and Technology*, 2020.
- [11] C. A. You, *Theory and application study on stress-transfer mechanism of anchoring system*, Ph.D. thesis, Shandong University of Science and Technology, Qingdao, China, 2004.
- [12] H. P. Kang, T. M. Jiang, and F. Q. Gao, "Effect of pretension stress to rock bolting," *Journal of China Coal Society*, vol. 32, no. 7, pp. 680–685, 2007.
- [13] K. Zhang, G. Zhang, R. Hou, Y. Wu, and H. Zhou, "Stress evolution in roadway rock bolts during mining in a fully mechanized longwall face, and an evaluation of rock bolt support design," *Rock Mechanics and Rock Engineering*, vol. 48, no. 1, pp. 333–344, 2015.
- [14] S. J. Wei and P. F. Gou, "Analogy simulation test on strengthening effect for pretension of bolts on anchorage body," *Journal of China Coal Society*, vol. 37, no. 12, pp. 1987–1993, 2012.
- [15] Q. Wang, Q. Qin, B. Jiang, H. C. Yu, R. Pan, and S. C. Li, "Study and engineering application on the bolt-grouting reinforcement effect in underground engineering with fractured surrounding rock," *Tunnelling and Underground Space Technology*, vol. 84, pp. 237–247, 2019.
- [16] Y. Z. Wu, J. Y. Chen, J. K. Jiao et al., "Damage and failure mechanism of anchored surrounding rock with impact loading," *Journal of China Coal Society*, vol. 43, no. 9, pp. 2390–2397, 2018.
- [17] Q. Wang, R. Pan, S. C. Li et al., "The control effect of surrounding rock with different combinations of the bolt anchoring lengths and pre-tightening forces in underground engineering," *Environmental Earth Sciences*, vol. 77, no. 13, pp. 501–514, 2018.
- [18] G. Liu, J. K. Long, H. D. Cai et al., "Design method of synergistic support for coal roadway," *Procedia Earth and Planetary Science*, vol. 1, no. 1, pp. 524–529, 2009.
- [19] H. P. Xie, Y. Ju, and L. Y. Li, "Criteria for strength and structural failure of rocks," *Chinese Journal of Mechanical Engineering*, vol. 24, no. 17, pp. 3003–3010, 2005.
- [20] H. P. Xie, Y. Ju, L. Y. Li et al., "Energy mechanism of deformation and failure of rock masses based on energy dissipation and energy release principles," *Chinese Journal of Mechanical Engineering*, vol. 27, no. 9, pp. 1729–1938, 2008.
- [21] Y. Zhang, X.-T. Feng, X. Zhang, Z. Wang, M. Sharifzadeh, and C. Yang, "A novel application of strain energy for fracturing process analysis of hard rock under true triaxial compression," *Rock Mechanics and Rock Engineering*, vol. 52, no. 11, pp. 4257–4272, 2019.
- [22] V. P. Efimov, "Estimate of initial energy of rock failure activation by measuring rock resistance," *Journal of Mining Science*, vol. 40, no. 5, pp. 503–507, 2004.

- [23] J. A. Sanchidrián, P. Segarra, and L. M. López, "Energy components in rock blasting," *International Journal of Rock Mechanics and Mining Sciences*, vol. 44, no. 1, pp. 130–147, 2007.
- [24] R. Peng, Y. Ju, J. G. Wang, H. Xie, F. Gao, and L. Mao, "Energy dissipation and release during coal failure under conventional triaxial compression," *Rock Mechanics and Rock Engineering*, vol. 48, no. 2, pp. 509–526, 2015.
- [25] F.-Q. Gong, S. Luo, and J.-Y. Yan, "Energy storage and dissipation evolution process and characteristics of marble in three tension-type failure tests," *Rock Mechanics and Rock Engineering*, vol. 51, no. 11, pp. 3613–3624, 2018.
- [26] Q. Meng, M. Zhang, L. Han, H. Pu, and T. Nie, "Effects of acoustic emission and energy evolution of rock specimens under the uniaxial cyclic loading and unloading compression," *Rock Mechanics and Rock Engineering*, vol. 49, no. 10, pp. 3873–3886, 2016.
- [27] X. Dong, A. Karrech, H. Basarir, M. Elchalakani, and A. Seibi, "Energy dissipation and storage in underground mining operations," *Rock Mechanics and Rock Engineering*, vol. 52, no. 1, pp. 229–245, 2019.
- [28] B. Wu, X. Wang, J. Bai, W. Wu, X. Zhu, and G. Li, "Study on crack evolution mechanism of roadside backfill body in gob-side entry retaining based on UDEC Trigon model," *Rock Mechanics and Rock Engineering*, vol. 52, no. 9, pp. 3385–3399, 2019.
- [29] Q. H. Wu, L. Weng, Y. L. Zhao et al., "Deformation and cracking characteristics of ring-shaped granite with inclusion under diametrical compression," *Arabian Journal of Geosciences*, vol. 13, pp. 681–692, 2020.
- [30] N. G. W. Cook, E. Hoek, and J. P. G. Pretorius, "Rock mechanics applied to the study of rockbursts," *Journal of the South African Institute of Mining and Metallurgy*, vol. 66, no. 10, pp. 435–528, 1966.
- [31] J. B. Walsh, "Energy changes due to mining," *International Journal of Rock Mechanics and Mining Sciences & Geomechanics Abstracts*, vol. 14, no. 1, pp. 25–33, 1977.
- [32] M. D. G. Salamon, "Energy considerations in rock mechanics: fundamental results," *Journal of the South African Institute of Mining and Metallurgy*, vol. 84, no. 8, pp. 233–246, 1984.
- [33] J. A. L. Napier, "Energy changes in a rockmass containing multiple discontinuities," *Journal of the Southern African Institute of Mining and Metallurgy*, vol. 91, no. 5, pp. 145–157, 1991.
- [34] V. Onur, C. G. Zhang, C. Ismet et al., "Numerical modelling of strength and energy release characteristics of pillar-scale coal mass," *Journal of Rock Mechanics and Geotechnical Engineering*, vol. 11, pp. 935–943, 2019.
- [35] Itasca Consulting Group Inc., *UDEC (Universal Distinct Element Code)*, Itasca Consulting Group Inc., Minneapolis, Min, USA, Version 6.0, 2014.
- [36] F. Gao, D. Stead, and J. Coggan, "Evaluation of coal longwall caving characteristics using an innovative udec trigon approach," *Computers and Geotechnics*, vol. 55, no. 55, pp. 448–460, 2014.
- [37] L. Zhang and H. H. Einstein, "Using RQD to estimate the deformation modulus of rock masses," *International Journal of Rock Mechanics and Mining Sciences*, vol. 41, no. 2, pp. 337–341, 2004.
- [38] M. Singh and K. Seshagiri Rao, "Empirical methods to estimate the strength of jointed rock masses," *Engineering Geology*, vol. 77, no. 1–2, pp. 127–137, 2005.
- [39] B. W. Wu, X. Y. Wang, J. B. Bai et al., "An investigation on the effect of high energy storage anchor on surrounding rock conditions," *Royal Society Open Science*, vol. 7, no. 10, 2020.
- [40] R. K. Zipf, "Numerical modeling procedures for practical coal mine design," in *Proceedings of the 41st US Rock Mechanics Symposium*, no. 1–11 Golden, CO, USA, June 2006.
- [41] H. Kang, Y. Wu, F. Gao et al., "Mechanical performances and stress states of rock bolts under varying loading conditions," *Tunnelling and Underground Space Technology*, vol. 52, pp. 138–146, 2016.
- [42] Z. Z. Zhang, M. Deng, J. B. Bai et al., "Strain energy evolution and conversion under triaxial unloading confining pressure tests due to gob-side entry retained," *International Journal of Rock Mechanics and Mining Science*, vol. 126, 2020.
- [43] C. J. Hou and P. F. Gou, "Study on the strengthening mechanism of surrounding rock strength with bolting support," *Chinese Journal of Mechanical Engineering*, vol. 19, no. 3, pp. 342–345, 2000.



## Research Article

# Study on Safety Control of Large-Section Roadway with High Stress and Broken Surrounding Rock

Wen-qing Peng , Hao Zhu, Qi Wang, and Gang Peng

China School of Resource Environment and Safety Engineering, Hunan University of Science and Technology, Xiangtan 411201, China

Correspondence should be addressed to Wen-qing Peng; pengwenqing@163.com

Received 25 December 2020; Revised 6 January 2021; Accepted 9 January 2021; Published 29 January 2021

Academic Editor: Zhijie Zhu

Copyright © 2021 Wen-qing Peng et al. This is an open access article distributed under the Creative Commons Attribution License, which permits unrestricted use, distribution, and reproduction in any medium, provided the original work is properly cited.

In order to solve the problem of difficult support of the roadway with high stress and large-section broken surrounding rock, this paper takes the subinclined shaft in Gaokeng mine of Jiangxi Province as the engineering background, analyzes the deformation mechanism and support mode of the roadway under the influence of mining through field investigation and mechanical derivation, and concludes that the stress concentration point of the roadway is in the middle point of roof and floor and the middle point of left and right sides. Through the modeling analysis of FLAC3D numerical software and the comparison of various support schemes, it is concluded that, after the combined support method of “anchor, net, and spray + grouting + full-section anchor cable + floor anchor cable” is adopted, the convergence of roof and floor is reduced by 508 mm, and the convergence of two sides is reduced by 663 mm. And, it is applied in engineering practice. The results show that the combined support scheme can effectively control the stability of the surrounding rock.

## 1. Introduction

Although China's coal mine mortality rate is decreasing year by year, the number of deaths by 2017 is as high as 375, with a million-ton mortality rate higher than that in developed countries, as shown in Figure 1. With the increase of mining depth and intensity of coal resources, mine roof accidents are increasing, which seriously threaten the safety of coal mining. In the past five years, there have been 9009 coal mine deaths due to roof accidents in China, accounting for 38 percent. Therefore, strengthening the research of the coal mine roadway support is the focus of coal mine safety.

According to statistics, the mining depth of many mining areas in China has exceeded 600~800 m, and many coal mines in China are expected to enter the mining depth of 1000~1500 m in the next 20 years. In recent years, with the improvement of heavy mining equipment and the promotion of the large mining-height working face, the roadway section increases from 10 m<sup>2</sup>~15 m<sup>2</sup> to 18 m<sup>2</sup>~20 m<sup>2</sup> and even larger, and the large-section roadway becomes the development trend of the modern mine. However, the large-

section roadway has the disadvantages of easy settlement, easy instability, and difficult support. These factors affect the safety of the roadway, so how to take protective measures has always been a research topic of the industry. At present, there are many research results in the research of roadway safety control, such as Zhu et al. [1] through the on-site roof exploration test, using numerical simulation to analyze the failure process of the roadway roof, so as to elaborate the failure mechanism of the roadway roof, put forward bolt + wood combined support technology, and achieve good support effect. Yang et al. [2] analyzed the stress characteristics and crack evolution process of the roadway under different supporting forms for the soft-rock roadway and thus proposed the “bolt-mesh-spraying concrete + shell” combined support scheme, which effectively controlled the large deformation of the roadway. And, many scholars [3–6] proposed various combined support methods for complex geological conditions. Wang et al. [7] and Bai and Hou [8] believe that stress is an important factor in roadway deformation, and the former thinks that the causes of roadway safety are excessive pressure and stress concentration of the



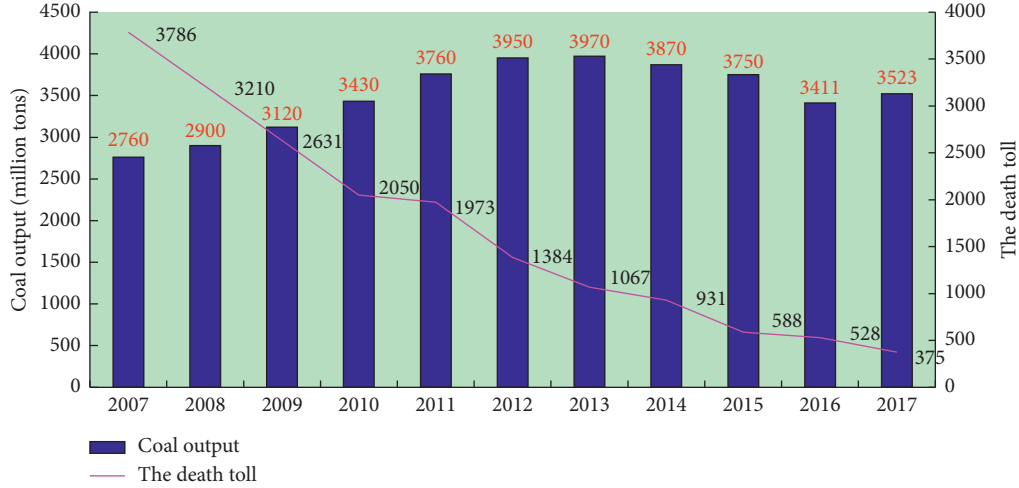


FIGURE 1: The death toll and coal output of coal mines in China.

surrounding rock. They optimized the optimal setting position of the pressure relief groove on the existing basis and effectively controlled the deformation of the surrounding rock. The latter thinks that the supporting technology of controlling the stress of the deep surrounding rock should start with controlling the stress and improving the strength of the broken zone of the surrounding rock. However, in the aspect of high stress and large-section roadway, the current research results are still relatively scarce. Zhang et al. [9] supported the concrete-filled steel tube in the high and deep stress roadway. Ping et al. [10] and many scholars [11–15] proposed that the main reason of the roadway broken ring is the instability of the structure under high stress, so it is particularly important to improve the stability and bearing capacity of the supporting structure. Therefore, on the basis of these methods, taking Gaokeng coal mine in China as the background, the failure mechanism of the subinclined shaft under the mining influence was analyzed in this paper, and the “anchor, mesh, and spray + grouting + full-section anchor cable + floor anchor cable” supporting scheme was put forward. Through the numerical simulation and field application, the results show that the combined support method can effectively complete the safety control of the large-section roadway.

## 2. Stress Analysis of the Roadway Surrounding Rock under Mining Influence

In practice, the characters of the roadway are complex and diverse, and the surrounding rock of the roadway is heterogeneous and discontinuous. There are many difficulties in establishing the mathematical model. Therefore, it is necessary to make some reasonable assumptions. Firstly, the roadway is assumed to be a circular roadway, and then, the surrounding rock is analyzed as a homogeneous and continuous elastic body, and the model is shown in Figure 2:

From elastic mechanics, the stress solution of the circular hole is as follows:

$$\sigma_r = \frac{1}{2}(\sigma_x + \sigma_y) \left(1 - \frac{r^2}{R^2}\right) - \frac{1}{2}(\sigma_y - \sigma_x) \left(1 - 4\frac{r^2}{R^2} + 3\frac{r^4}{R^4}\right) \cos 2\theta, \quad (1)$$

$$\sigma_\theta = \frac{1}{2}(\sigma_x + \sigma_y) \left(1 + \frac{r^2}{R^2}\right) + \frac{1}{2}(\sigma_y - \sigma_x) \left(1 + 3\frac{r^4}{R^4}\right) \cos 2\theta, \quad (2)$$

where  $\sigma_r$  is the radial stress,  $\sigma_\theta$  is the hoop stress,  $\sigma_x$  is the horizontal stress,  $\sigma_y$  is the normal stress,  $r$  is the tunnel radius,  $R$  is the radial distance from point A to roadway center, and  $\theta$  is the angle between the OA direction and horizontal line.

It can be concluded from formulas (1) and (2) that the stress value has nothing to do with the mechanical parameters of the surrounding rock, but only with the horizontal stress  $\sigma_x$  and vertical stress  $\sigma_y$ , and they are as follows:

$$\begin{aligned} \sigma_y &= \gamma H, \\ \sigma_x &= \lambda \sigma_y. \end{aligned} \quad (3)$$

In the formula,  $\gamma$  is the average bulk density of rock mass,  $H$  is the burial depth, and  $\lambda$  is the lateral pressure coefficient.

When the roadway design is completed, its  $\gamma$ ,  $H$ , and  $r$  have been determined, so the unknown quantities in equation (2) are  $\lambda$ ,  $R$ , and  $\theta$ ; when  $R=r$  is considered, equation (2) can be expressed as follows:

$$\sigma_\theta = \gamma H(1 + \lambda) + 2\gamma H(1 - \lambda)\cos 2\theta. \quad (4)$$

The function graph of equation (5) is drawn by Matlab, as shown in Figure 3.

It can be seen from Figure 3 that when it is about  $0^\circ$ ,  $90^\circ$ ,  $180^\circ$ , and  $270^\circ$ , the function has extreme points, that is, the midpoint of the roof and floor of the roadway and

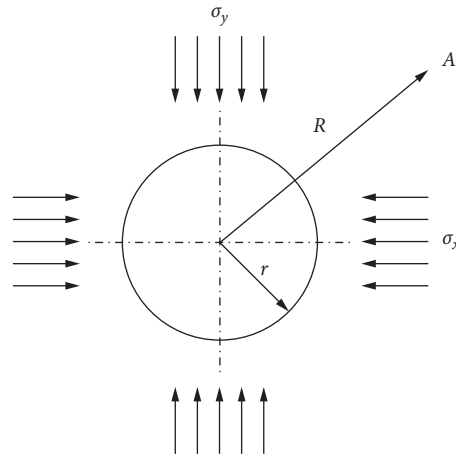


FIGURE 2: The computational mechanics model.

the midpoint of the left and right sides, so the most unfavorable position of the roadway is in the midpoint of the roof and floor and the midpoint of the left and right sides.

### 3. Numerical Simulation of Stability Analysis of Bottom Dark Inclined Well under Mining Influence

This simulation is based on the engineering geological conditions of the subinclined shaft in the Gaokeng Mine, Jiangxi Province. The subinclined shaft is arranged in the coal seam 3 floor, and the roadway section is  $4.2\text{ m} \times 3.9\text{ m}$ . The anchor net ladder spray, arch shed, reticulated shell, and other supporting methods are adopted, which are the main coal transportation systems at the three levels and below. The roadway is arranged in the coal seam 3 floor and bottom conglomerate layer from top to bottom, and the roadway is arranged in the bottom conglomerate, as shown in Figure 4.

In order to determine the loose range of the surrounding rock of the inclined shaft in the dark belt, the surrounding rock detection test was carried out. It can be seen that, in the surrounding rock of the inclined shaft roof in the dark belt, the cracks at 5 m–10 m are more developed, the surrounding rock is broken seriously, and there are obvious longitudinal cracks at 5 m. In the wall rock, the most developed part of the crack is within 8 m, and the other parts are relatively complete.

The roof and support of the roadway subsided as a whole. The roof fall occurred in many places from  $-140\text{ m}$  to  $-160\text{ m}$  elevation and showed the form of sharp tops, which indicated that the roof had a high horizontal stress state. And, at the elevation of  $-160\text{ m}$  and the area below, it can be seen that there is an obvious fracture area in the part of the roof surrounding rock with the depth of 500 mm. When drilling the anchor rod, the two sides bulge out into the roadway, spray layer falls off, phenomenon of spalling occurs, and damage is asymmetric. The damage of the side near the advancing direction of the working face is clearly serious. The most serious damage is found in the coal seam section

where the underground inclined shaft passes through the bottom groove, and the spalling depth of the right-side slope is more than 1400 mm, as shown in Figure 5. The floor heave is obvious, and the extrusion converges at the bottom corner.

The lithology classification and mechanical parameters of this simulation model are shown in Table 1. The specific model is shown in Figure 6.

Cyclic excavation of coal seam 3 is carried out during the calculation because the influence of coal seam excavation on the subinclined shaft is a dynamic process. In order to describe the cross mining process, considering the advance abutment pressure in front of the work 5~10 m, so taking the overlying coal seam working face and the bottom plate at the horizontal distance of 40 m and 10 m, the stress and plastic zone of the dark inclined shaft are analyzed.

It can be seen from Figures 7 and 8 that, during the whole excavation process, the vertical stress changes of the two sides are greater than the horizontal stress changes of the roof and floor. In the process of advancing, the vertical stress is mainly concentrated in the deep left side, and after the working face is pushed, the vertical stress changes to be concentrated in the deep right side. The shear stress has also changed greatly in the process of advancing. The shear stress of the bottom corner of the left side and the top corner of the right side increases at the beginning of the advancing process. After the working face is pushed, the shear stress of the top corner of the left side and the bottom corner of the right side increases, and the maximum value is larger than before. The change of the plastic zone reveals the process of roadway failure and is closely related to the change of stress. The first failure area is at the bottom corner of the left side and the top corner of the right side. With the advance of the working face and shortening of the horizontal distance from the dark inclined shaft, the two sides continue to damage. The top angle of the left side and the bottom angle of the right side are also seriously damaged, which leads to the increase of the hanging length of the roof and floor, and finally, the roof and floor begin to be seriously damaged.

In the process of excavation, the displacement measuring points are arranged at the midpoint of the roof and floor and the midpoint of the two sides, and the monitoring results are

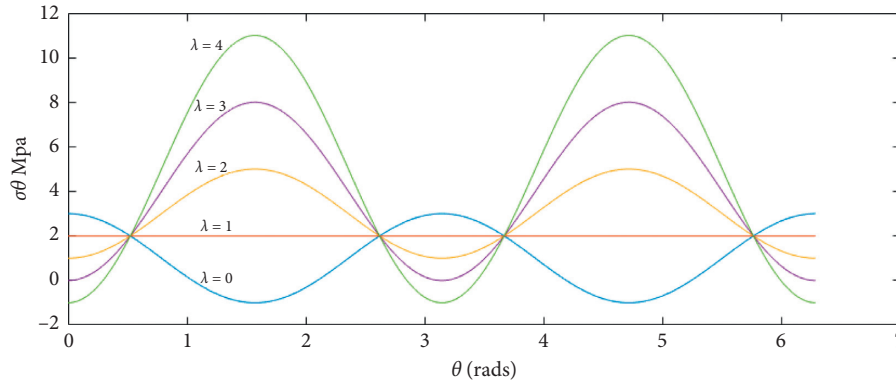


FIGURE 3:  $\sigma_\theta$  stress distribution of the surrounding rock when  $\lambda = 0 \sim 4$ ,  $\theta = 0 \sim 2\pi$ , and  $R = r$ .

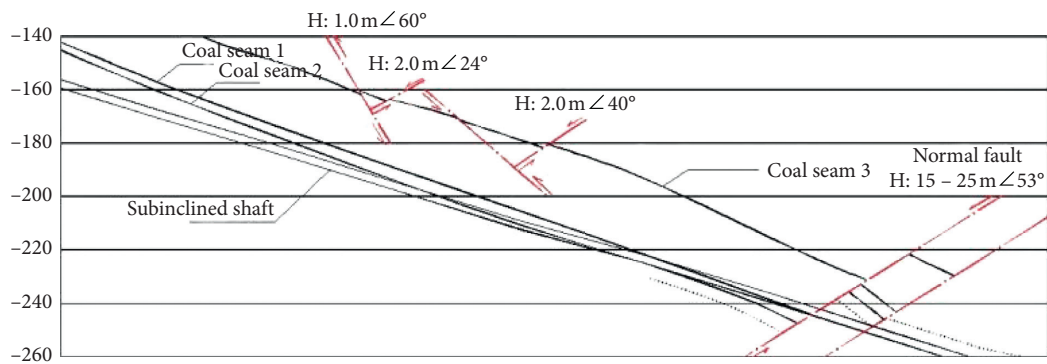


FIGURE 4: The space position relationship between the subinclined shaft and coal seam.



FIGURE 5: The damage of the surrounding rock. (a) Left side. (b) Right side.

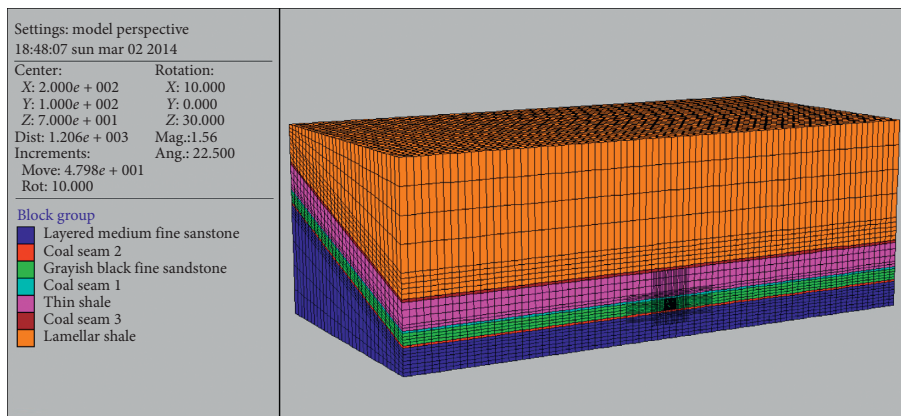


FIGURE 6: The model mesh map.

TABLE 1: Mechanics calculation parameters of strata.

Name	Bulk modulus B (GPa)	Shear modulus S (GPa)	Cohesion C (MPa)	Internal friction angle $\Phi$ (°)	Tensile strength $R_t$ (MPa)	Density $\gamma$ (g·cm <sup>-3</sup> )
Lamellar shale	6.79	4.47	2.65	31	1.20	2.50
Sweeping groove coal seam	4.15	1.36	1.10	19	0.60	1.40
Thin shale	6.79	4.47	2.65	31	1.20	2.50
Coal seam 1	4.15	1.36	1.10	19	0.60	1.40
Grayish-black fine sandstone	21.00	10.23	4.25	39	1.85	2.64
Coal seam 2	4.15	1.36	1.10	19	0.60	1.40
Layered medium-fine sandstone	21.00	10.23	4.25	37	1.85	2.64

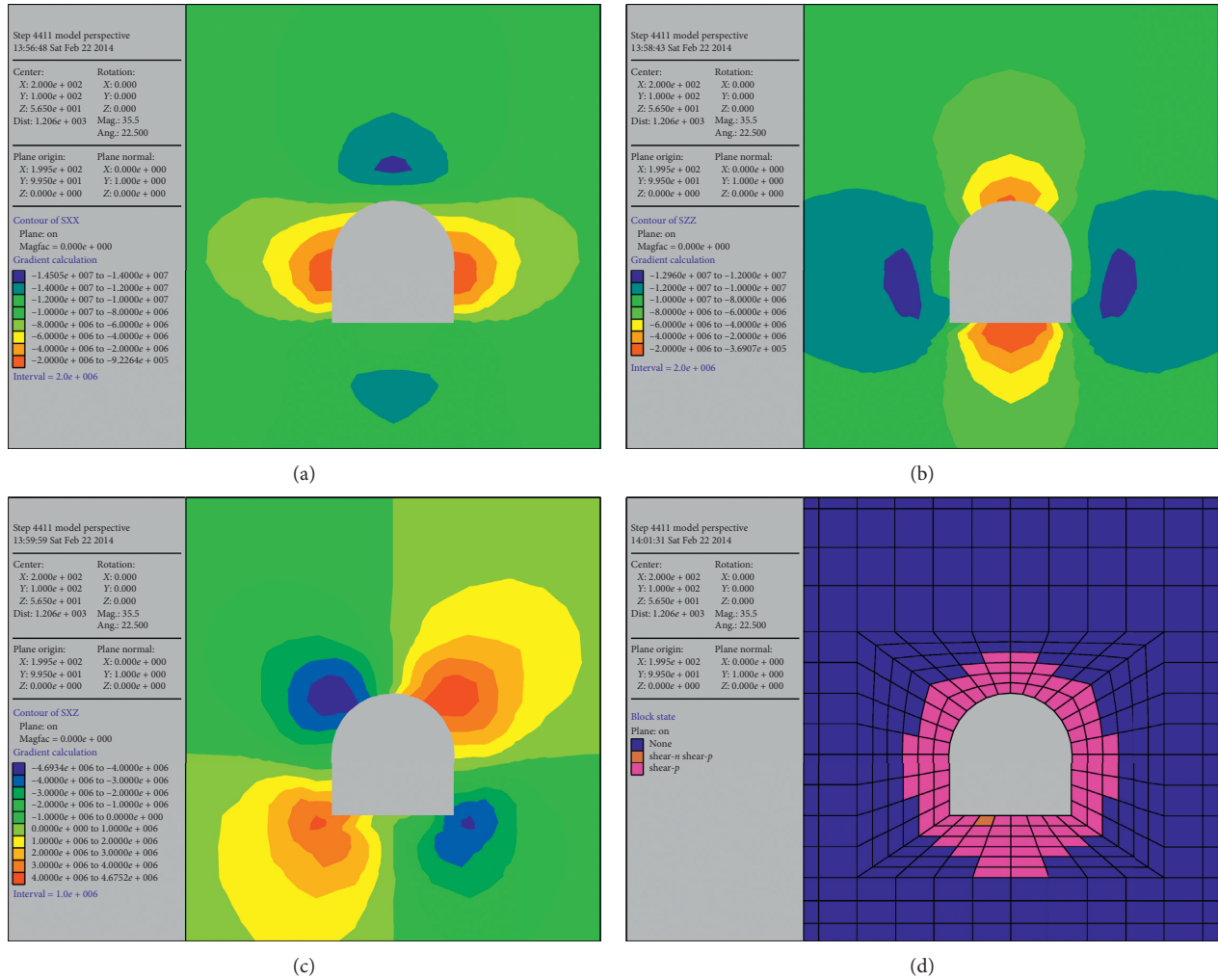


FIGURE 7: The stress state of the roadway after initial excavation. (a) Horizontal stress nephogram. (b) Vertical stress nephogram. (c) Shear stress nephogram. (d) Distribution of the plastic area.

calculated to obtain the deformation of the surrounding rock of each excavation roadway. In the process of working face advancing, the destruction of the two sides is prior to the destruction of the roof and floor, so the deformation of the two sides in the process of working face pushing close to the subinclined shaft is greater than that of the roof and floor. When the working face is pushed above the subinclined shaft because the two sides have been destroyed, the roof and floor

begin to be seriously damaged due to the increase of the hanging length. In order to investigate the circumferential stress variation process around the inclined shaft in detail, measuring points are arranged at 3 m depth of the two sides to monitor the vertical stress variation, and the monitoring results are shown in Figure 9.

It can be seen from Figure 10 that the vertical stress of the two sides is greatly affected by mining and changes rapidly. It

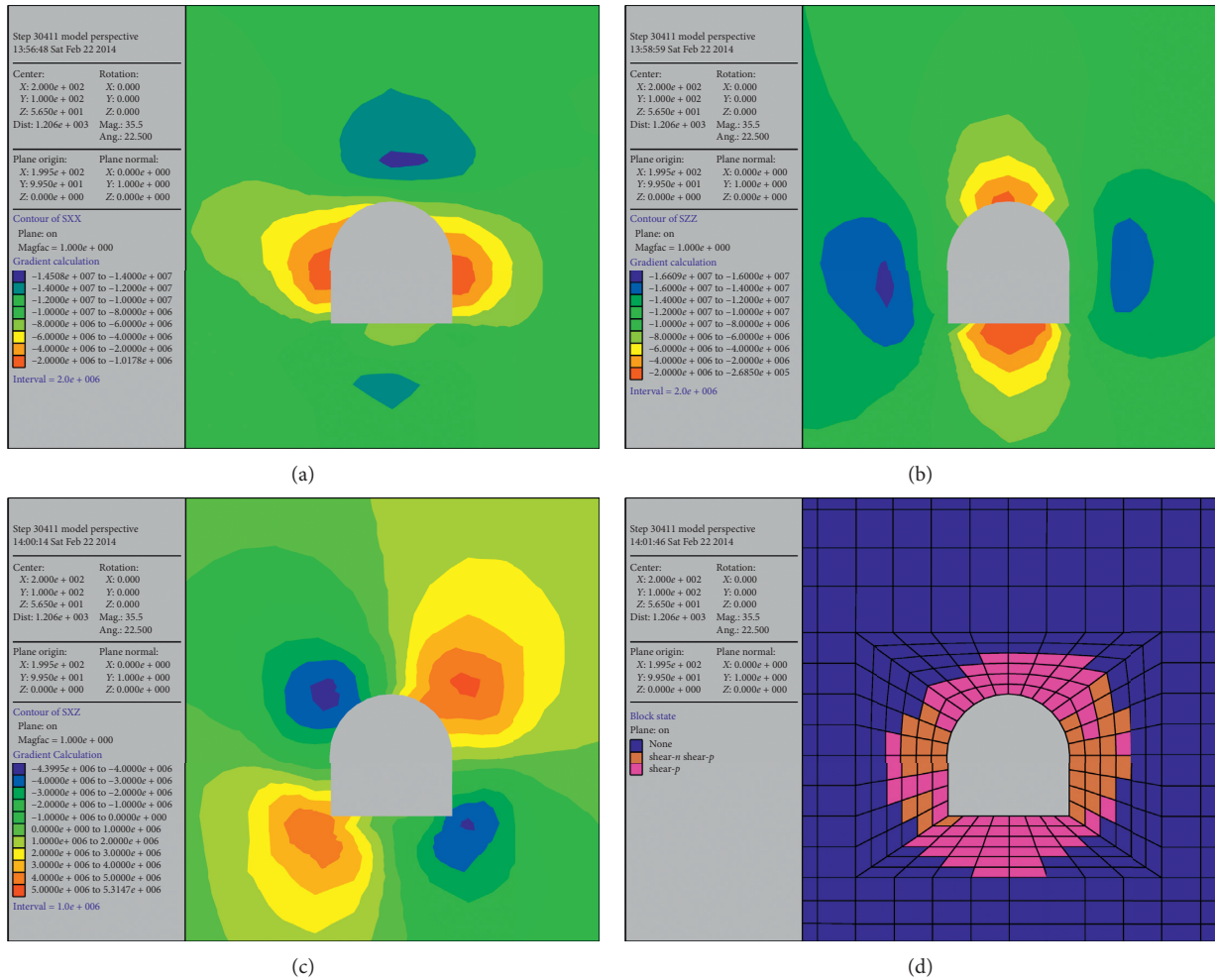


FIGURE 8: The stress state of the roadway. (a) Horizontal stress nephogram. (b) Vertical stress nephogram. (c) Shear stress nephogram. (d) Distribution of the plastic area.

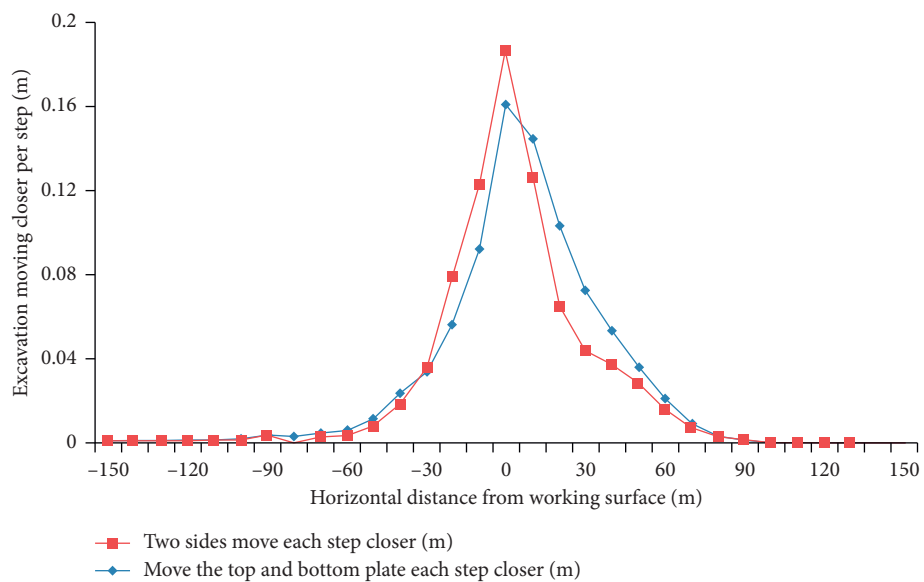


FIGURE 9: Deformation of roof and floor and sides per mining step.



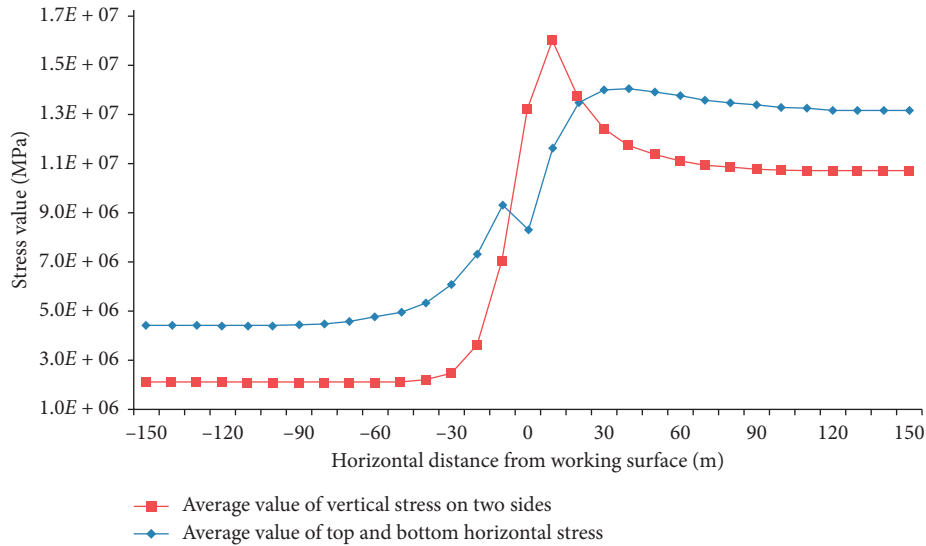


FIGURE 10: Circumferential stress distribution in 3 meters deep surrounding rock.

begins to rise rapidly at 30 m and reaches the peak of 16 MPa at 10 m. The horizontal stress of the roof and floor is less affected, which has reached the peak of 14 MPa and then began to decline, and there is a rebound at 15 m. The biggest difference is that the horizontal stress of the roof and floor and the vertical stress of the two sides did not rise back to the initial state after the working face was pushed. The main reason is that the surrounding rock enters the plastic zone due to the influence of high stress, and the rock enters the postpeak strength stage, which has lost its bearing capacity.

#### 4. Study on Surrounding Rock Control Technology of the Dark Inclined Shaft under Mining Influence

**4.1. Conceptual Design.** This numerical simulation mainly analyzes the numerical calculation models of different supporting methods in the process of coal seam 3. The model still uses the numerical calculation model established above. For comparison, four schemes are determined in this simulation, as shown in Table 2.

**4.2. Numerical Simulation Result Analysis.** It can be seen from Figures 11–15 that, in the case of no support, the roadway deformation is serious, the roadway roof and floor convergence is 792 mm, and the two sides' convergence is 850 mm. After using “anchor, net, and spray+grouting” support, the roof and floor movement is reduced by 223 mm, and the two sides' movement is reduced by 414 mm. It can be seen that the surrounding rock of the two sides of the roadway is under certain control, but the control effect of floor heave is not obvious. At this time, the floor heave of the roadway is 334 mm, which becomes the main part of the roadway deformation. After adopting “anchor, net, and spray+grouting+full-section anchor cable” support, the displacement of the roof and floor is reduced by 427 mm, and the displacement of two sides is reduced by 642 mm. The

TABLE 2: The table of support schemes.

Serial number	Support mode
Scheme 1	No support
Scheme 2	Bolt + metal mesh + shotcrete support
Scheme 3	Bolt + anchor cable + metal mesh + shotcrete support
Scheme 4	Bolt + anchor cable + metal mesh + shotcrete + floor-anchor cable support

deformation of the surrounding rock of the roadway is controlled effectively. After adopting supporting scheme 4, the deformation was further controlled, in which the displacement of the roof and floor was reduced by 508 mm, the displacement of the two sides was reduced by 663 mm, and the surrounding rock of the roadway remained stable. Therefore, it was reasonable to adopt the support method of “anchor, net spray+grouting+full-section anchor cable+ floor anchor cable.”

#### 5. Engineering Application

In the subinclined shaft with the elevation of  $-205\text{ m}$ – $-240\text{ m}$ , because it has entered the floor of coal seam 3, the surrounding rock is relatively complete, but the vertical distance from coal seam 3 is small, so it is still necessary to strengthen the support. The specific layout is shown in Figure 16.

The cross method is used to monitor the surface deformation of the roadway. In order to analyze the supporting effects of three different supporting schemes, the observation results are shown in Figures 17 and 18.

It can be seen from the displacement monitoring map that the deformation of the dark inclined shaft changes greatly between the 25th day of monitoring and the 50th day of monitoring. At this time, the horizontal distance between the working face and floor roadway is 40 m to  $-10\text{ m}$ , and the working face has no effect on the stability of the surrounding rock of the dark inclined shaft. The deformation of station 2 is

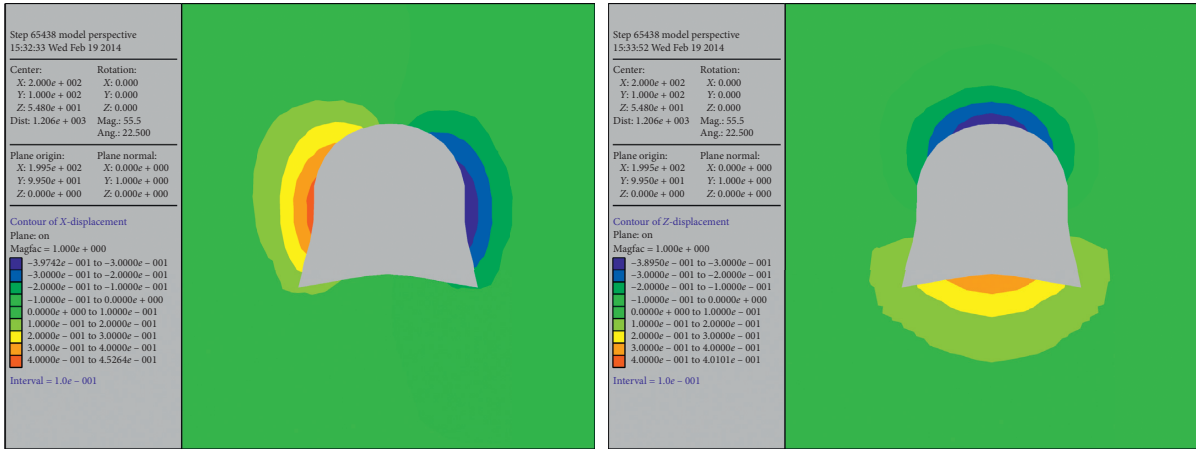


FIGURE 11: The nephograms of displacement (Scheme 1).

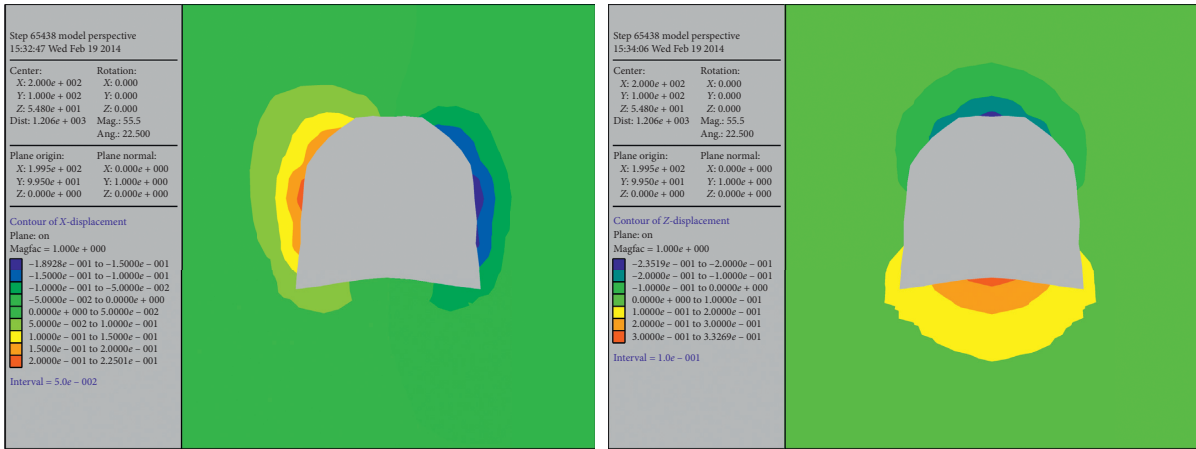


FIGURE 12: The nephograms of displacement (Scheme 2).

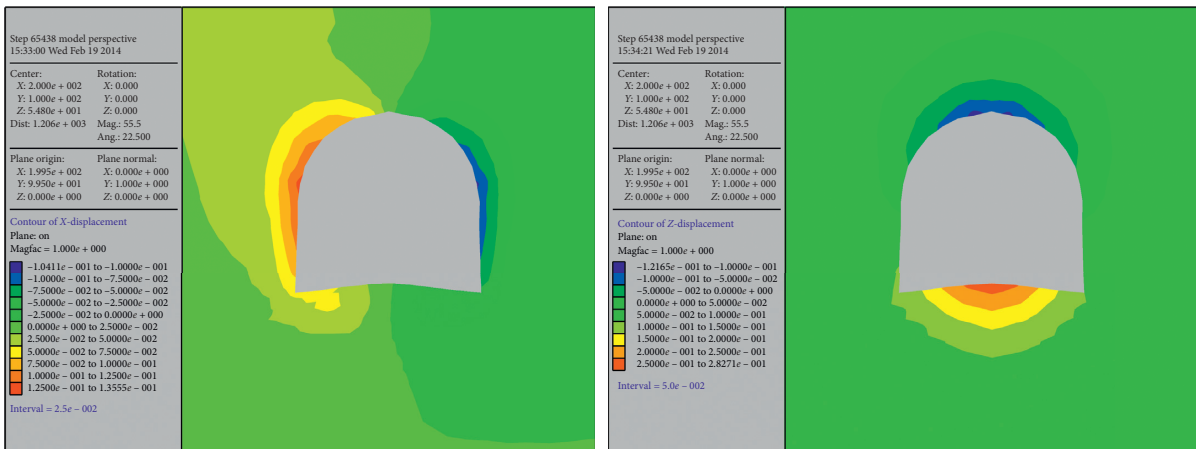


FIGURE 13: The nephograms of displacement (Scheme 3).

less than the other two, which shows that grouting has a significant effect on improving the stability of the roadway. The deformation rate of station 3 is faster, which is related to the small vertical distance between the measuring point

position and overlying coal seam. However, because the spacing between the anchor cables is encrypted in the support scheme, the cumulative deformation is still close to that of station 1. In short, according to the monitoring results, the

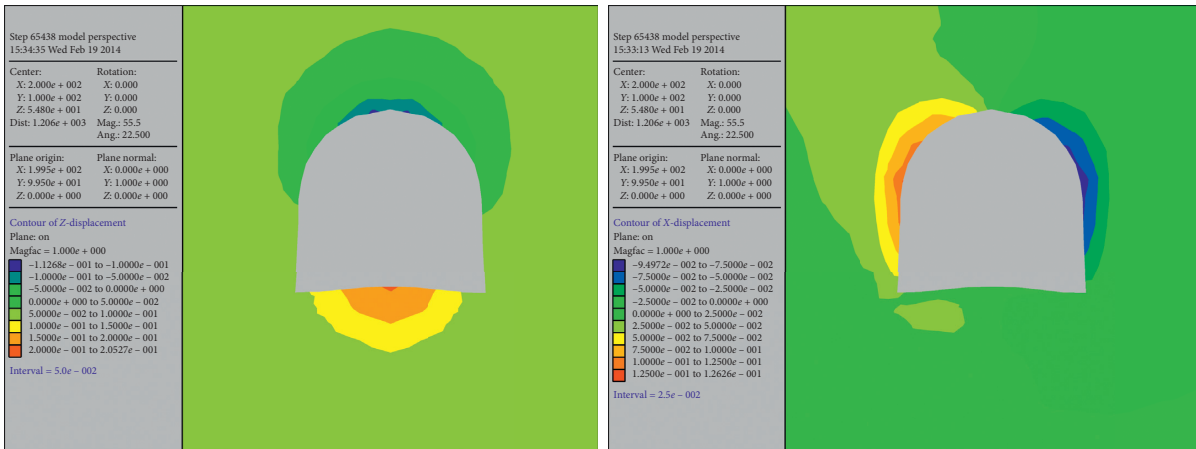


FIGURE 14: The nephograms of displacement (Scheme 4).

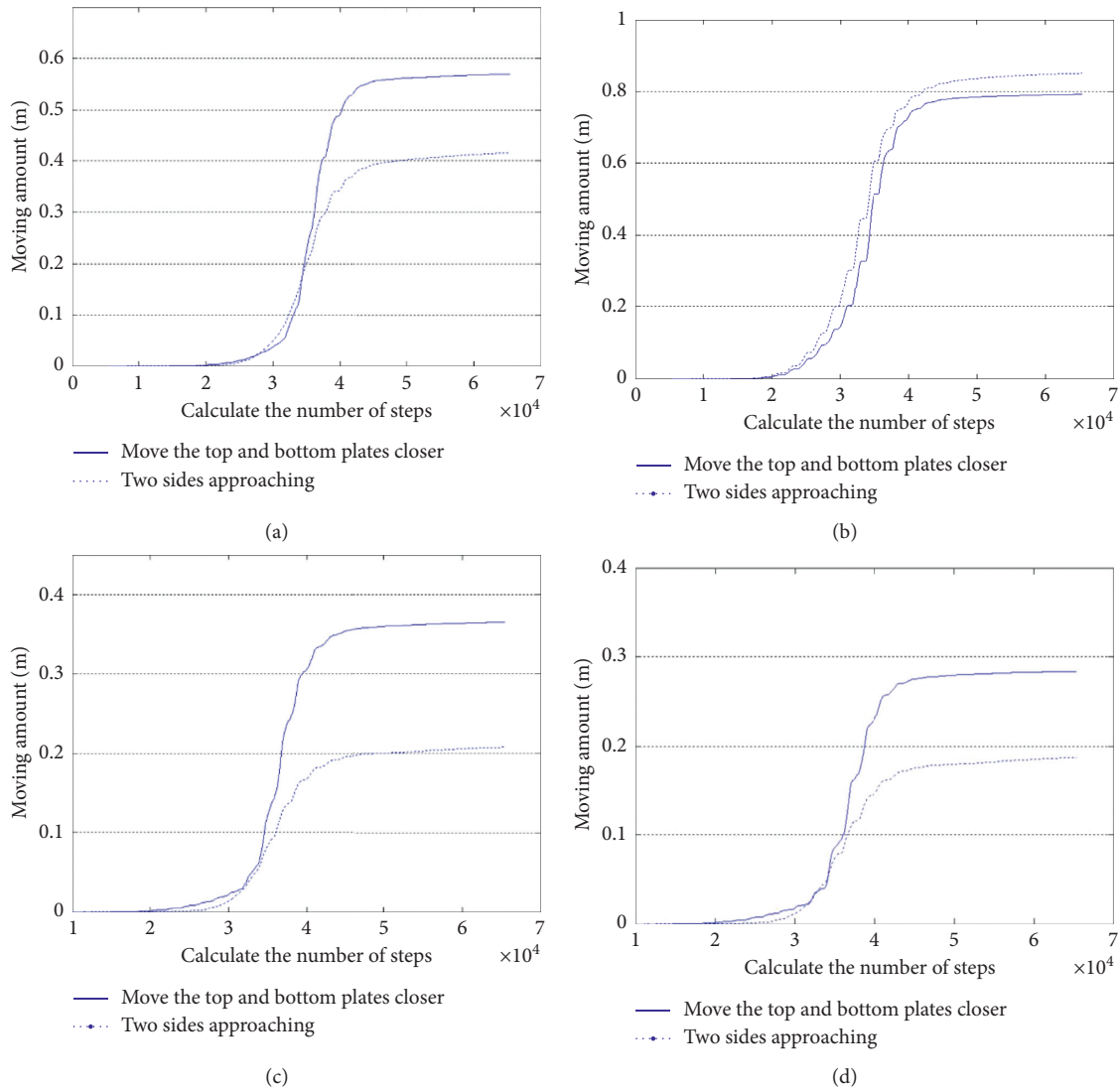


FIGURE 15: The displacement curve with each scheme. (a) No support. (b) Bolt-mesh shotcreting support. (c) Anchor mesh shotcreting + anchor cable. (d) Anchor mesh shotcreting + anchor cable + bottom anchor cable.

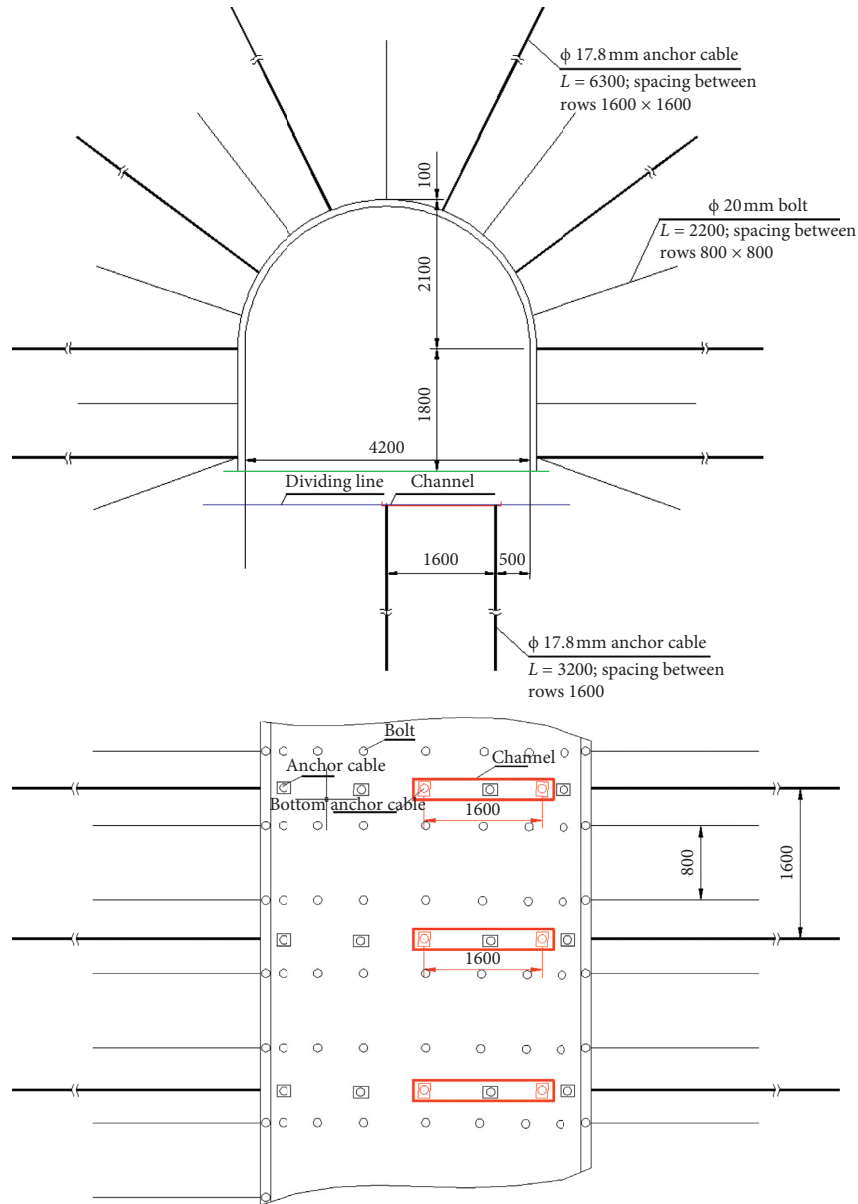


FIGURE 16: The diagram of the section support.

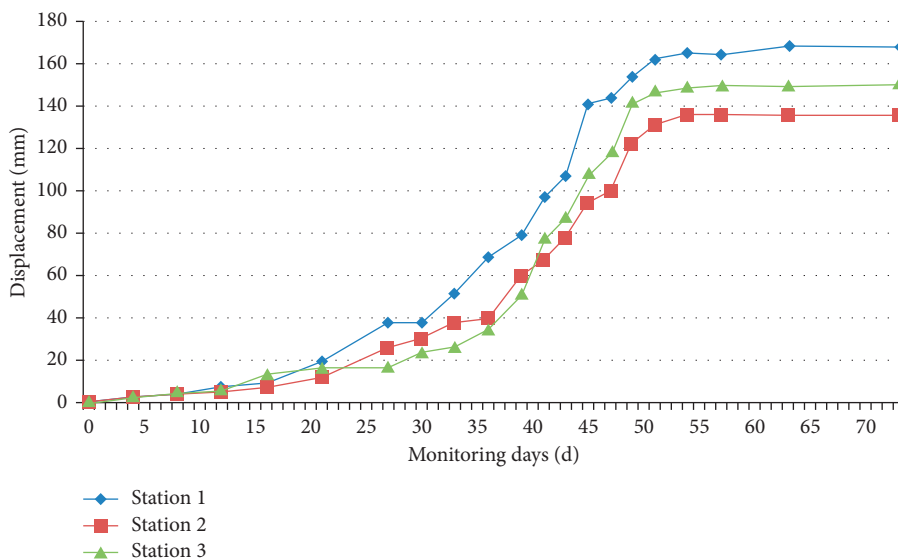


FIGURE 17: The displacement monitor of the roof and floor.

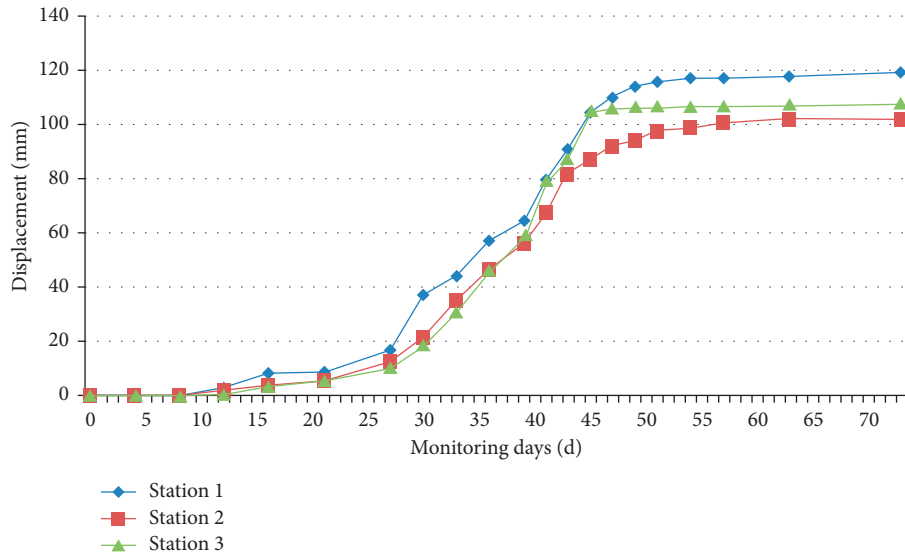
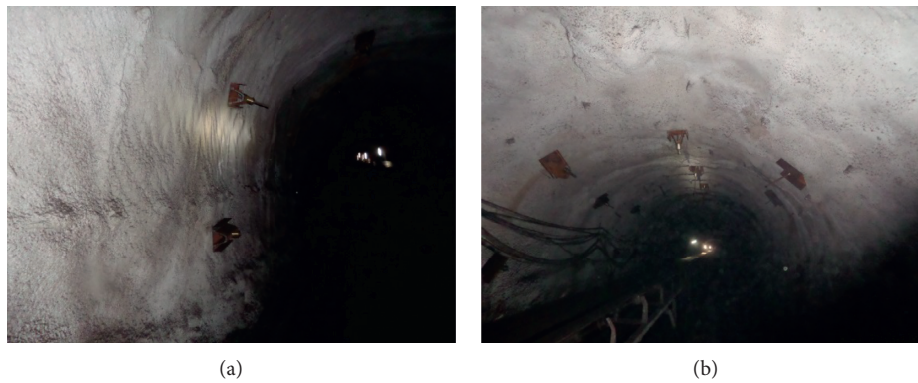


FIGURE 18: The displacement monitor of sides.



(a)

(b)

FIGURE 19: Support graphs.

maximum displacement of the roof and floor is 168.5 mm, the displacement of left and right sides is 119.3 mm, and the deformation of the surrounding rock is within the allowable range, which fully proves that the combined support technology of anchor, net, and spray + grouting + full-section anchor cable is feasible and can maintain the long-term stability of the floor dark inclined shaft. The support for the actual project is shown in Figure 19.

## 6. Conclusions

- (1) The failure of the roadway supporting structure and the serious deformation of the roadway itself are due to the high stress level of the surrounding rock in the roadway, so floor heave, spalling, and tipping are produced.
- (2) Under the influence of disturbance in the process of excavation, the dark inclined shaft begins to deform at 60 m away from the working face, and the deformation is the largest at 10 m to -10 m away from

the working face, and the influence is the deepest, but the working face is pushed over 60 m and out of the influence range.

- (3) Using the combined support method of “anchor, mesh, and shotcreting + grouting + full-section anchor cable,” the maximum displacement of the top and bottom plate is 168.5 mm, which is reduced by 64%, and the displacement of the left and right side is 119.3 mm, which is about 78% less, which shows that this support method plays a good role

## Data Availability

The data used to support the findings of this study are available from the corresponding author upon request.

## Conflicts of Interest

The authors declare that they have no conflicts of interest regarding the publication of this paper.



## Acknowledgments

This work was supported by the National Natural Science Foundation of China (51974118), Hunan Provincial Natural Science Foundation of China (2020JJ4305), and Scientific Research Fund of Hunan Provincial Education Department (18B226).

## References

- [1] D. Zhu, Y. Wu, Z. Liu, X. Dong, and Yu Jin, "Failure mechanism and safety control strategy for laminated roof of wide-span roadway," *Engineering Failure Analysis*, vol. 111, Article ID 104489, 2020.
- [2] S.-Q. Yang, M. Chen, H.-W. Jing, K.-F. Chen, and B. Meng, "A case study on large deformation failure mechanism of deep soft rock roadway in Xin'An coal mine, China," *Engineering Geology*, vol. 217, pp. 89–101, 2017.
- [3] F. He, B. Yang, S. Yin, X. Wang, and C. Tian, "Study on safety technology of anti-caving at a super-large section roadway with thick and fractural coal roof," *Procedia Engineering*, vol. 26, pp. 545–553, 2011.
- [4] S. Du, D. Li, W. Yu, J. Zhang, and F. Liu, "Stability analysis and support control for a jointed soft rock roadway considering different lateral stresses," *Geotechnical and Geological Engineering: An International Journal*, vol. 38, no. 12, 2020.
- [5] Q. Meng, L. Han, Y. Chen et al., "Influence of dynamic pressure on deep underground soft rock roadway support and its application," *International Journal of Mining Science and Technology*, vol. 26, no. 5, 2016.
- [6] J. Kong, P. Chen, J. Chen, Q. S. Liu, and Z. Ma, "Research on support technology in deep roadway of huafeng mine," *Advanced Materials Research*, vol. 753–755, 2013.
- [7] X. Wang, W. Luo, L. Qiu et al., "Unloading mechanism and design analysis of surrounding rock in deep high stress roadway," in *IOP Conference Series: Earth and Environmental Science*, vol. 428, no. 1, IOP Publishing, Article ID 012056, 2020.
- [8] J.-B. Bai and C.-J. Hou, "Control principle of surrounding rocks in deep roadway and its application," *Journal-China University of Mining and Technology-Chinese Edition*, vol. 35, p. 145, 2006.
- [9] J. Zhang, L. Liu, J. Cao, X. Yan, and F. Zhang, "Mechanism and application of concrete-filled steel tubular support in deep and high stress roadway," *Construction and Building Materials*, vol. 186, pp. 233–246, 2018.
- [10] Z. Ping, M. Nianjie, J. Wei, and R. Jianju, "Combined support technology of large section roadway in high-stress fractured surrounding rock," *Procedia Engineering*, vol. 26, pp. 1270–1278, 2011.
- [11] W.-Q. Peng, W.-J. Wang, and C. Yuan, "Supporting technology research in deep well based on modified terzaghi formula," *Advances in Civil Engineering*, vol. 2018, no. 10, pp. 1–6, 2018.
- [12] S. Liu, Q. Zhu, H. Jia, and X. Li, "Characteristics and recognition of the dynamic response of strata interfaces to anchorage hole drilling in coal roadway roof," *Journal of Mining & Safety Engineering*, vol. 34, no. 4, pp. 748–759, 2017.
- [13] Y. Li, D. Zhang, Y. Song et al., "Experimental research of progressive damage of surrounding rock for soft fractured deep tunnel," *Chinese Journal of Rock Mechanics and Engineering*, vol. 31, no. 6, pp. 1138–1147, 2012.
- [14] S.-Q. Yang, Y.-H. Huang, Y.-Y. Jiao, W. Zeng, and Q.-L. Yu, "An experimental study on seepage behavior of sandstone material with different gas pressures," *Acta Mechanica Sinica*, vol. 31, no. 6, pp. 837–844, 2015.
- [15] R. Porras, J. R. Carmona, R. C. Yu, and G. Ruiz, "Experimental study on the fracture of lightly reinforced concrete elements subjected to eccentric compression," *Materials and Structures*, vol. 49, no. 1-2, pp. 87–100, 2016.

## Research Article

# Partitioning Control Mechanism and Engineering Practice of Rebuilding Bearing Arch in Surrounding Rock under High Ground Stress

Mengtang Xu <sup>1</sup>, Ke Li <sup>1,2</sup> and Youlin Xu<sup>1</sup>

<sup>1</sup>College of Mining, Guizhou Institute of Technology, Guiyang, Guizhou 550003, China

<sup>2</sup>School of Resource & Environment and Safety Engineering, Hunan University of Science and Technology, Xiangtan, Hunan 411201, China

Correspondence should be addressed to Ke Li; 20120016@git.edu.cn

Received 3 December 2020; Revised 6 January 2021; Accepted 12 January 2021; Published 19 January 2021

Academic Editor: Xianjie Hao

Copyright © 2021 Mengtang Xu et al. This is an open access article distributed under the Creative Commons Attribution License, which permits unrestricted use, distribution, and reproduction in any medium, provided the original work is properly cited.

The mining of coal seam has a significant influence on the stability of the roadway near it, especially under the condition of high ground stress. To study the control mechanism of the surrounding rock under the influence of high ground stress, a general idea for the partition control of the rebuilding bearing arch (RBA) was proposed in this paper. Based on the basic mechanical performance test of the bearing arch, this paper built a mechanical model of the RBA based on Protodyakonov's pressure arch theory, analyzed the influence of the strength of the bearing arch on the surrounding rock failure, and obtained the ultimate thickness of the bearing arch failure under high ground stress. The results show that the RBA's damage is closely related to the overburden load and RBA's thickness. The tensile stress and shear stress of RBA increase linearly with the overburden load increase and increase sharply with the load-bearing arch's thickness, showing a nonlinear relationship. To maintain the surrounding rock's stability, it is necessary to ensure that the RBA's thickness is within a specific range. The results are applied to the Wantian coal mine. The theoretically determined load-bearing thickness is 10 m, which can effectively control the surrounding rock deformation and significantly reduce the roadway's repair rate.

## 1. Introduction

The problem of surrounding rock control of roadways under the influence of high ground stress has always been problematic in underground mine engineering. Especially in multi-coal mining, the roadways near the coal seams are affected by high ground stress, and the problem of nonlinear considerable deformation control is particularly prominent [1, 2]. Under the influence of high ground stress, the surrounding rock's stress environment has deteriorated, and the surrounding rock is easy to show a nonlinear and uneven massive deformation phenomenon. The roadway support structure's stability is reduced, and the repair rate is significantly increased [3, 4]. It is not easy to control the continuous deformation of roadway surrounding rock only by

strengthening conventional support. Improving the structure and mechanical properties of the surrounding rock is the fundamental way to control roadway deformation surrounding rock [5]. Rebuilding the bearing arch through grouting can effectively improve the bearing capacity of the surrounding rock of the roadway, leave a pressure relief space for high ground stress, and decompose and alleviate the impact of mining stress. For roadways affected by high ground stress, proper grouting to save material costs while ensuring the grouting effect and improving the surrounding rock's self-carrying capacity has become an urgent problem in controlling the roadway's surrounding rock [6, 7]. Therefore, it has important theoretical significance and engineering practical value to study the control mechanism of RBA of the surrounding rock affected by high ground stress.

Some scholars have done some sufficient research work on the surrounding rock control theory and the high-pressure roadway technology in recent years. Meng et al. [8, 9] studied the displacement, plastic zone, and distribution law of principal stress difference with different support schemes under the influence of mining disturbance on the bottom extraction roadway and proposed a U-shaped steel reinforced support scheme. Wang et al. [10] found that the width of excavation damaged zone around roadways under dynamic pressure was larger than that under static pressure, and they proposed that the bolt length should be larger than the width of excavation damaged zone. Tian and Gao [11] established a mechanical model of adjacent rock strength, mining stress, and supporting resistance based on an elastic-plastic theory of mechanics, and they obtained an analytical solution for stress and displacement distribution of elastic and plastic regions in surrounding rock of dynamic pressure roadway. Yan and He [12] proposed a new cable truss support system for coal roadways affected by dynamic pressure, established a theoretical formula for the pretightening force required for the truss cables, and deduced the lowest anchoring force between the roof surrounding rock and the cable bolt. Wang et al. [13] put forward a dynamic pressure roadway supporting scheme under the surrounding rock condition and stress environment and proved that the length of small aperture cable hole has a more significant impact on anchoring effect. Zhang et al. [14] analyzed the asymmetry characteristics of surrounding rock structure and stress distribution in dynamic pressure roadway and proposed an asymmetrical support scheme. Yang et al. [15] examined the technology of directional fracturing blasting for pressure relief of dynamic pressure roadway. Zuo et al. [16, 17] theoretically derived the Hoek–Brown rock failure criterion based on the linear elastic fracture theory and established the analogous hyperbola movement model of overlying strata. Wu et al. [18, 19] proposed an improved support scheme for the roadway in steeply inclined geological formations. Zhang et al. [20] studied the change laws of the maximum principal stress and the minimum one for the floor roadway surrounding rock when mining the upper working face, and they built the mechanical model of roadway stress based on the nonconstant pressure force state and the cracks revolution mechanisms of floor roadway surrounding rock. Xie et al. [21, 22] deduced the equation of maximum shear stress in the deep beam structure based on the stress superposition criterion. Zhang et al. [23–25] investigated the lower coal seam entry failure mechanism's characteristics under the remnant pillar by means of numerical simulations and in situ observations. Yu et al. [5, 26–29] established the mechanical model of overlap arch bearing body in allusion to the united supporting characteristics of anchor, spray net, and cable bolt of deep wall rock, which are composed of the main compression arch (bolt supporting) and the second compression arch (intensive cable bolt supporting), and deduced neutral point theory of bolt and force transferring mechanism of cable bolt, strength equations

of the bearing body of primary supporting and second supporting. Huang et al. [30] proposed the concept of strong mining and large deformation of roadway from mechanical essence and engineering application, established the quantitative evaluation method of intense mining and large deformation, and considered that the large deformation of the surrounding rock structure of the roadway includes the large deformation of the whole movement caused by the large structure instability of the overlying strata and the large deformation of the movement of the fractured rock mass in the loosening circle. Zhu et al. [31] established the roadway's numerical model by combining the results of exploration test, micro-properties calibration, tension and shear test of rock bolt, and bearing characteristics of timber. Yang et al. [32, 33] proposed a support technology focusing on cutting off the water, strengthening the rock's small structure, and transferring its immense structure.

However, due to the complexity and difference of the geological environment and production conditions in deep coal seam mining, the instability and control problems of deep dynamic pressure mining roadways have not been completely solved. The deformation and failure mechanism of the surrounding rock under the influence of high ground stress needs to be further studied. [34, 35]. Based on Protodyakonov's pressure arch theory and field investigation and analysis, this paper establishes a mechanical model for reconstructing the bearing arch of the roadway's surrounding rock under high ground stress conditions. The ultimate thickness of failure provides a scientific basis for controlling surrounding rock in this type of roadway.

## 2. Research Engineering Background

*2.1. The Condition of the Roadway Studied.* This paper is based on the engineering background of the crossheading 1433 restoration project of Wantian coal mine, Panzhou city, Guizhou Province, China. Its depth is about 820 m. The surrounding rock of crossheading 1433 is dominated by mudstone and siltstone, and overlying 10#, 12#, 15#, 17#, and 18# coal seam. The crossheading is affected by high ground stress, causing large deformation and severe damage. After many repairs, the effect gets worse with the repair. The damage of the crossheading supporting structure is shown in Figure 1.

The roadway damage characteristics affected by high ground stress are considerable damage depth, high damage degree, and lacking integrity of surrounding rock. In recent years, the original support adopts U29 U-steel support, the row spacing is 700 mm, and the cable bolt and iron channel are used as reinforcement support. However, due to high ground stress, U-steel's damage in the roadway has become more and more serious. The maximum deformation of the sidewalls reached 2.5 m. The severe floor heave section reached 2.7 m in 3 quarters, and the local roof subsidence reached 1.0 m, which seriously affected the normal production of the mine. It could not meet the regular transportation and ventilation requirements of the roadway. It needs to be repaired 2-3 times every year.

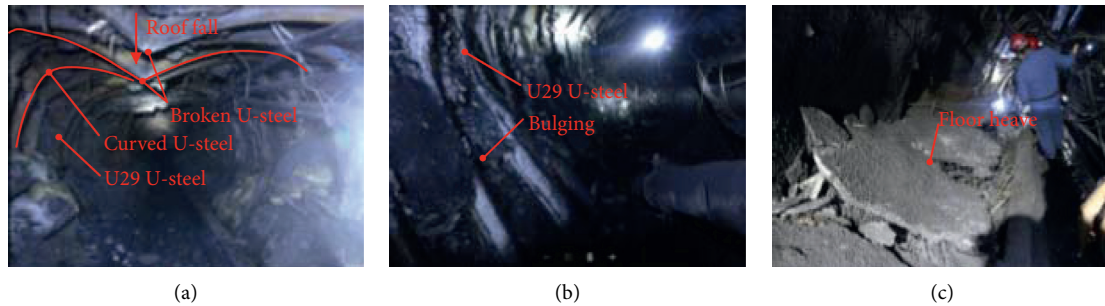


FIGURE 1: The damage of the crossheading supporting structure.

**2.2. Stress Monitoring of Bolts and Cable Bolts.** During the mining period of 11502 working face in the upper part of crossheading 1433, roof subsidence and floor heave occurred in the surrounding rock of roadway. During the mining period of the upper 11502 working face, the roof subsidence and floor heave occurred in crossheading 1433 surrounding rock. To monitor the change of bearing capacity of roadway supporting structure (bolts and cable bolts) affected by mining, SHH-60 hydraulic dynamometer was used to monitor three bolts and two cable bolts at the sidewalls, arch, and top. The monitoring time was 42 days. The stress variation curve of bolts and cable bolts is shown in Figure 2. It can be seen that, during the mining process of the working face, the load-bearing capacity of the sidewalls and arch bolts does not change much. During the monitoring period of 20–30 days, under the influence of heavy mining, the anchor cable bolt's bearing capacity increases, and the maximum bearing capacity of the bolt is 66 kN. After the end of mining, the cable bolt's stress gradually decreases and tends to be stable at 40–48 kN. Compared with the side bolt and arch bolt, the roof bolt bearing capacity is more extensive, with a maximum of 82 kN. After being affected by heavy mining, the ultimate stability value is 72–75 kN.

The anchorage depth of the cable bolt is 6.0 m. At the initial stage of monitoring, the cable bolt load at the top and arch is 70 kN and 56 kN, respectively. When the distance is about 30 m from the stoppage line, the cable bolt's bearing capacity reaches 120 kN and 93 kN, respectively. During the upper working face's mining period, the cables' bearing capacity had not changed significantly.

Under the influence of high ground stress, the roof bolt's maximum bearing capacity is 82 kN, and the maximum bearing capacity of the top cable bolt is 126 kN. Therefore, it is difficult to restrain the continuous deformation of roadway surrounding rock only by strengthening conventional roadway support. It is imperative to improve the structure and mechanical properties of surrounding rock.

### 3. General Idea of Partition Control of RBA

Taking the support system's integrity as the basic idea, the zoning control method from the whole to the local and from the external field to the internal field is proposed. The integrity of the roadway's surrounding rock is restored by grouting the surrounding rock in the roadway's shallow part. Then, the high preload is applied to the surrounding rock to

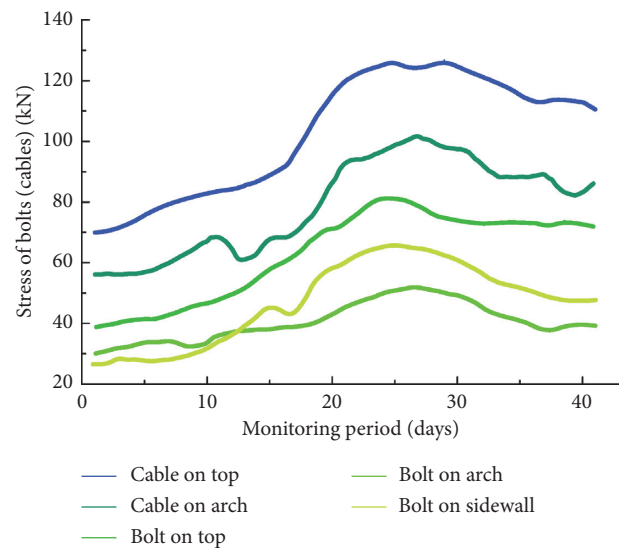


FIGURE 2: Stress variation curve of bolt and cable bolt under the influence of high ground stress.

give full play to the role of active support, so that a bearing arch “shell” with strong bearing capacity is formed in the shallow part of the surrounding rock of the roadway. The broken surrounding rock outside the bearing arch is used to decompose the upper mining stress, so that the mining stress can be digested and absorbed for the first time in the pressure relief area of the deep broken surrounding rock. The destructive force of the mining stress transferred to the surrounding rock of the roadway is reduced. The reinforced bearing arch can effectively resist the destructive force transmitted by the “digestion and absorption” of mining stress, to control the stability of surrounding rock. In the actual control process, the bearing arch's mechanical properties and the radius of the arch body are the key to the success of the zoning control. In the actual coal mine engineering, the grouting cannot be unlimited, which not only causes material waste, but also reduces the buffer effect of the broken zone, which provides a continuous path for the propagation of mining stress and leads to roadway damage.

### 4. Control Mechanism of RBA

**4.1. Mechanical Properties of RBA.** Through the uniaxial compression test, uniaxial tensile test, and shear test, RBA's

mechanical parameters are obtained, which can be used to calculate the ultimate arch thickness without breaking. The grouting material is high water quick-setting material divided into material A and material B. The ratio of material A to material B is 1:1. The gangue is taken from the top of crossheading 1433. The lithology is siltstone, and the ratio of water: Ash: gangue is 1.2:1:1. The uniaxial compressive strength, tensile strength, and shear strength of RBA are 8.62 MPa, 1.12 MPa, and 2.08 MPa. The experimental process is shown in Figure 3.

**4.2. Mechanical Model of RBA.** According to the field measurement of roadway surrounding rock deformation, the roadway surrounding fracture zone's scope increases rapidly due to high ground stress, which makes the roadway support scope increase. RBA construction around the roadway can reduce the roadway deformation and overlying roof pressure, which plays an essential role in the maintenance of roadway deformation. It is necessary to establish a new mechanical model to determine the surrounding rock pressure of the roadway. The calculation of surrounding rock pressure under the condition of loose body accords with the basic assumption of Protodyakonov's pressure arch theory. The surrounding rock pressure is calculated by Protodyakonov's pressure arch theory, as shown in Figure 4, where  $Q$  is the in situ stress,  $R$  is the radius of bearing arch,  $a_1$  is the maximum span of natural balance arch,  $b$  is the maximum height of natural balance arch, and  $\varphi$  is internal friction angle of the rock.

Loose rock mass itself can form a natural balance arch structure, and the vertical pressure transmitted above the working face is the weight of loose rock mass in the natural balance arch. The stability of the natural balance arch under the influence of high ground stress is the core of the roadway's rock stability. The overall performance of rock mass in the natural balance arch needs to be improved.

According to Protodyakonov's pressure arch theory, the maximum span of a natural balanced arch is as follows:

$$a_1 = R + R \tan\left(45^\circ - \frac{\varphi}{2}\right). \quad (1)$$

The upper part of the RBA is a natural balance arch, and its height increases with the increase of the RBA height. The maximum compressive stress  $q_{\max}$  in the natural equilibrium arch can be obtained as follows:

$$q_{\max} = \frac{a_1 \gamma}{f}, \quad (2)$$

where  $f$  is the firmness coefficient of the rock mass, and  $\gamma$  is the density of rock mass.

### 4.3. Tensile Failure Analysis of RBA

**4.3.1. Establishment of Tensile Failure Mechanical Model of RBA.** The stress model of the roadway is simplified as a plane half-cylinder stress model. The semicircular arch is subjected to uniform load  $q$ , and both ends of the semicircular arch are constrained by simply supported beams, as

shown in Figure 5, where  $R$  is the radius of the arch, and  $h$  is the thickness of the arch.

Considering that the arch's failure mode is caused by the semicircular arch's tensile failure, the maximum bending moment  $M_{\max}$  of the semicircular arch beam needs to be solved. Because the beam's shape and force take the  $y$ -axis as the symmetry axis, the semicircular arch beam's bending moment also takes the  $y$ -axis as the symmetry axis. So, it is only needed to solve half of the solution of the semicircle arch.

If the bending moment of any angle  $\alpha$  is  $M_\alpha$ , as shown in Figure 6, the calculation formula of bending moment  $M_\alpha$  can be expressed as follows:

$$M_\alpha = q^2 - qR^2 \cos \alpha - M_q, \quad (3)$$

where  $M_q$  is the end bending moment of overlying strata load  $q$  to  $\alpha$  angle.

By comparing the change of unit stress gradient  $\Delta\sigma_{n,b}$ , the impact risk and impact risk area can be evaluated.

Then, the expression of bending moment  $M_\alpha$  is

$$M_\alpha = -3qR^2 - qR^2 \cos \alpha + 4qR^2 \cos\left(\frac{\alpha}{2}\right), \quad (4)$$

The value range of  $\alpha$  is  $[0, \pi/2]$ .

As the bending moment of the semicircular arch, the beam is symmetrically distributed with  $\alpha = \pi/2$ , and the variation relationship of bending moment in the arch is as shown in Figure 7.

The relationship between bending moment and the angle of the semicircular arch is shown in Figure 8.

Therefore, when the angle of  $\alpha$  is  $\pi/2$ ,  $M_\alpha$  reaches the maximum value, then

$$M_{q_{\max}}^2 = 0.17qR^2. \quad (5)$$

The maximum tensile stress  $\sigma_{\max}$  of the semicircular arch beam can be calculated as follows:

$$\sigma_{\max} = \frac{1.02qR^2}{h}. \quad (6)$$

- (1) If the radius  $R$  of the semicircular arch is 14 m, the relationship between the stress of the beam and the load of the overlying strata and the arch thickness is shown in Figure 9
- (2) If the arch thickness  $h$  of the semicircular arch is 6 m, the relationship between the arch's stress and the overlying strata's load and the arch radius is shown in Figure 10.

It can be seen from Figures 9 and 10 that the maximum tensile stress of semicircular arch is related to the load of overburden rock, the thickness of the arch, and the radius of semicircular arch. The maximum tensile stress increases with overburden rock load and decreases sharply with the increase of arch thickness, showing a nonlinear relationship. Therefore, it is necessary to increase the thickness of the semicircular arch to ensure that the semicircular arch does not break.



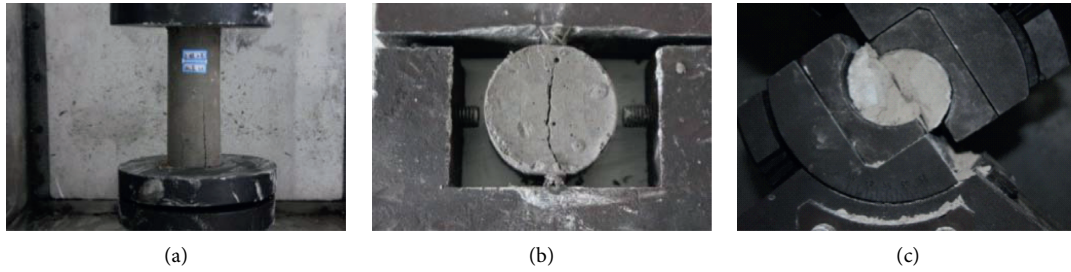


FIGURE 3: Experimental process of mechanical properties of RBA. (a) Uniaxial compression test. (b) Uniaxial tensile test. (c) Shear test.

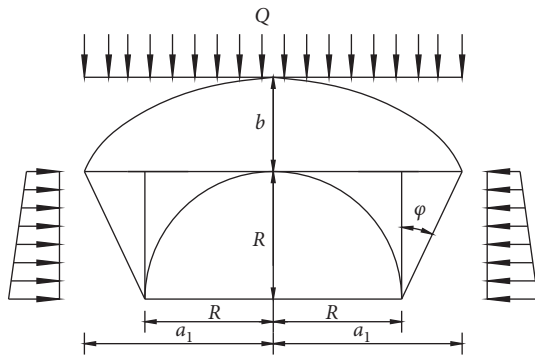


FIGURE 4: Mechanical model of RBA.

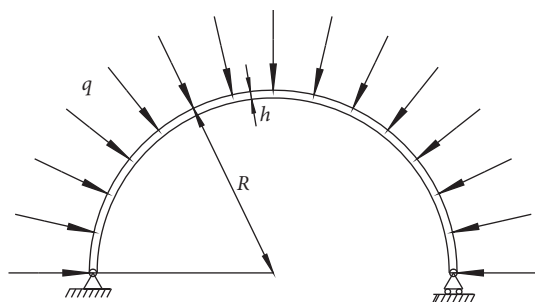


FIGURE 5: Simplified stress model of half-cylinder arch.

(3) The thickness of RBA

The grouting radius  $r$  of crossheading 1433 is 12 m. The stable internal friction angle and tensile strength of high water-cement are  $45^\circ$  and 1.12 MPa, respectively. Put them into equation (2), then  $\gamma \approx 2.2 \times 10^4 \text{ N/m}^3$ ,  $f=0.86$ . The maximum load of overburden rock is 0.434 MPa, the dead weight of semicircular arch is 0.264 MPa, and the maximum load of the semicircular arch beam is 0.698 Mpa.

According to equation (6), the thickness of RBA must meet the following equation's requirements.

$$h_{\text{arch}} = \sqrt{\frac{1.02q}{\sigma_{\text{max}}}}R = 9.57 \text{ m.} \quad (7)$$

The actual semicircular arch thickness of crossheading 1433 is 10 m, which meets the requirements of tensile strength.

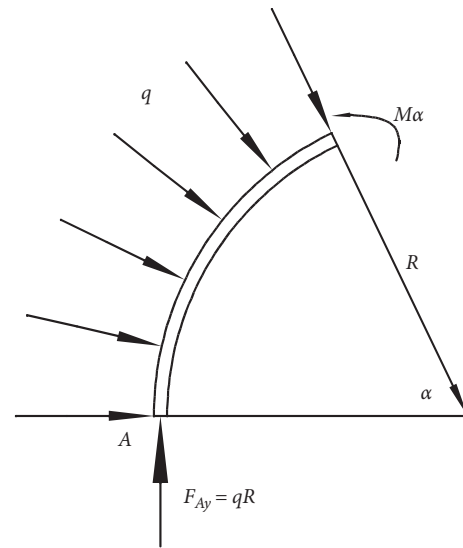


FIGURE 6: Bending moment of a semicircular arch.

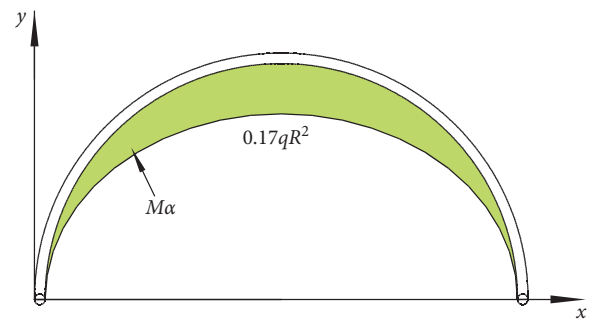


FIGURE 7: Bending moment of a semicircular arch.

4.3.2. Shear Failure Analysis of RBA.

(1) Calculation of maximum shear stress of RBA

It can be seen from the RBA stress model in Figure 4 that the shear force of the bearing arch is the largest in the middle of the semicircular arch, as shown in Figure 10. The inner radius of the circular arch is  $a$ . The outer radius is  $b$ , and the edge of the outer radius is affected by the uniformly distributed load  $q$ , as shown in Figure 11.

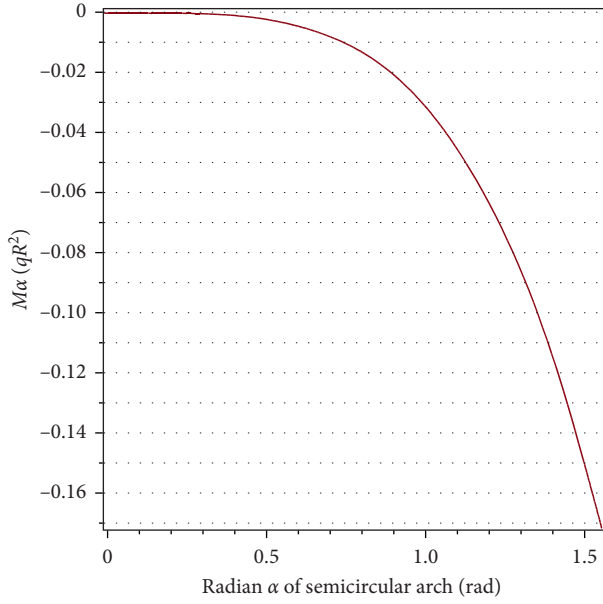


FIGURE 8: Relationship between bending moment and angle of a semicircular arch.

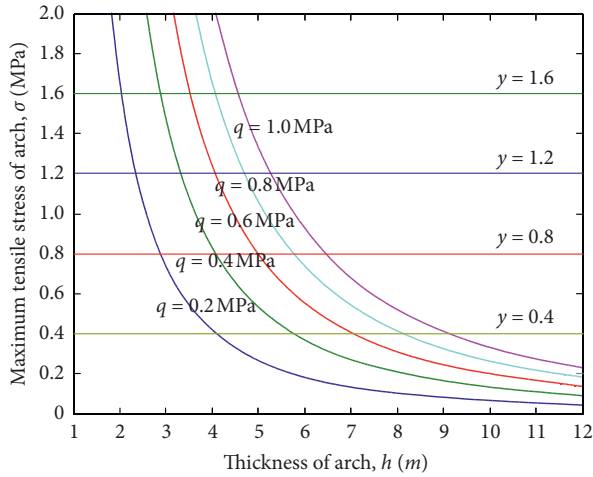


FIGURE 9: Relationship between beam stress and overburden rock layer load and arch thickness.

Therefore, the maximum shear force  $F_{smax}$  can be obtained as follows:

$$F_{smax} = \int_0^{(\pi/2)} q \sin \theta R d\theta = qR. \quad (8)$$

When the maximum shear stress on the rectangular section is 1.5 times of the average shear stress [36], the maximum shear stress of the semicircular arch is obtained as follows:

$$\tau_{max} = \frac{1.5qR}{h}. \quad (9)$$

(2) Determination of shear strength of RBA

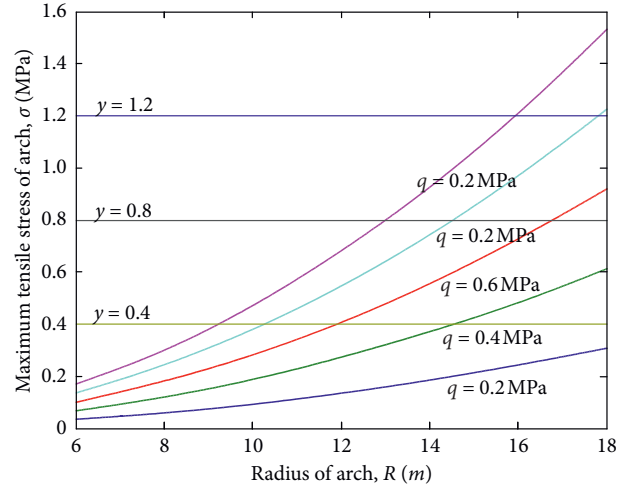


FIGURE 10: Relationship between arch stress, overburden rock load, and arch radius.

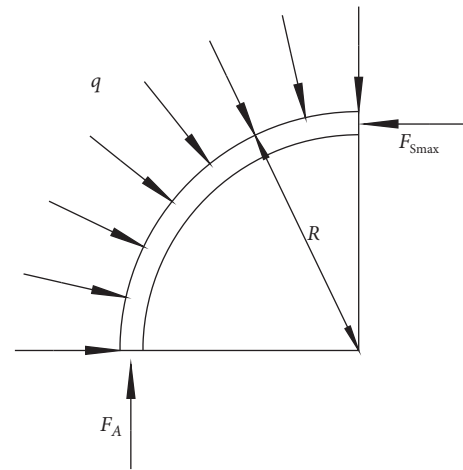


FIGURE 11: Maximum shear force of RBA.

The actual radius  $R$  of the semicircular arch is 12 m, the thickness  $h$  is 10 m, and the maximum load on the semicircular arch is 0.698 MPa. According to equation (9), the shear strength of the semicircular arch must meet the following requirement:

$$\tau_{max} = 1.256 \text{ MPa}. \quad (10)$$

The shear strength of RBA is 2.08 MPa, which meets the requirement.

## 5. Engineering Practice Verification

The RBA thickness of crossheading 1433 is determined to be 10 m by theoretical mechanical analysis. The field grouting industrial test was carried out in the coal mine, and the grouting material was high water material. The engineering practice shows that the actual compressive, tensile, and shear strength of the high water material and the roadway's

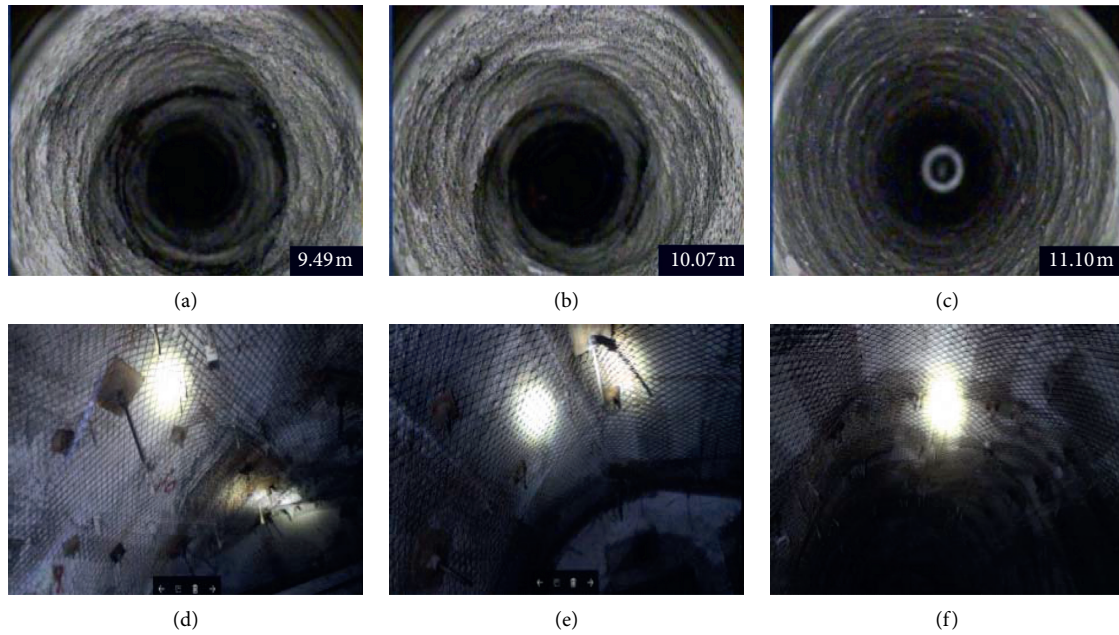


FIGURE 12: Photos of the project site after the completion of support. (a–c) Internal conditions after grouting. (d–f) Surface after grouting.

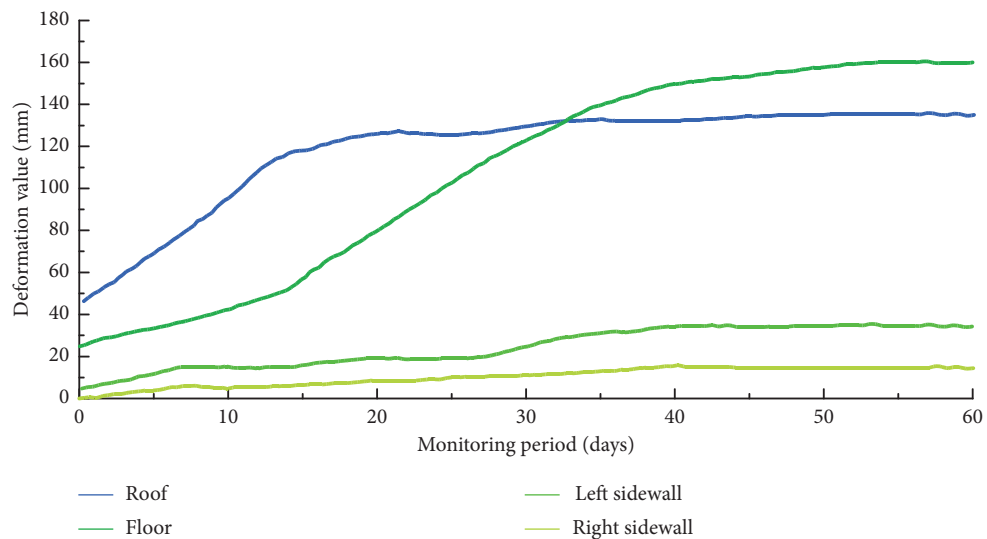


FIGURE 13: Monitoring data of roadway surface displacement after grouting.

surrounding rock cement can be calculated to meet the engineering needs. The reconstructed bearing arch can effectively control the surrounding rock deformation. The stability of surrounding rock before and after engineering practice is prominent, and the deformation of roadway surrounding rock is effectively controlled. The deformation of roadway monitored on-site is shown in Figures 12 and 13. During the monitoring period, the maximum subsidence of roadway roof is 135 mm, and the maximum value of roadway floor heave is 160 mm. The deformation of both sides is small, and the cumulative displacement is 30 mm. The deformation of surrounding rock in-field measurement is significantly reduced, especially floor heave. The deformation of surrounding rock is effectively controlled, and the

repair rate is significantly reduced. This proves that the RBA model established in this paper is reliable.

### 6. Conclusion

- (1) Given the difficulties of surrounding rock control of roadway with considerable failure depth and high damage degree under the influence of high ground stress, the RBA zoning control method from the whole to the local and from the external field to the internal field is proposed.
- (2) The mechanical model of surrounding rock pressure of “RBA-roadway” is constructed, and the expression of the minimum arch thickness of the bearing arch is

obtained by theoretical calculation. Based on the basic mechanical parameters experiment of bearing arch, the strength of bearing arch is checked.

- (3) The results show that the failure of the reconstructed bearing arch is closely related to the overburden load and the thickness of the bearing arch; all the tensile stress and shear stress of the bearing arch increase linearly with the increase of the overburden load and decrease sharply with the increase of the bearing arch thickness, showing a nonlinear relationship.
- (4) When the research results are applied to the Wantian coal mine, the deformation of roadway surrounding rock is reduced, and the repair rate is significantly reduced.

## Data Availability

The data used to support the findings of this study are included within the article.

## Conflicts of Interest

All the authors declare that they have no known conflicts of interest that could influence the work reported in this paper.

## Acknowledgments

This research was supported by National Natural Science Foundation of China (Nos. 51764010 and 51874109), Guizhou Province Science and Technology Support Plan Project (No. qiankehezhicheng[2019]2861), New Talent Training Project of Guizhou Institute of Technology (Nos. qiankehepingtairencai [2017]5789-14 and GZLGM-02), and Guizhou Province Safety Production Major Accident Prevention Key Technology Science and Technology Project (No. guizhou-0004-2017AQ).

## References

- [1] X. T. Feng, *Rock Mechanics and Engineering Volume 4, Excavation, Support and Monitoring*, CRC Press, England, UK, 2016.
- [2] H. Kang, "Support technologies for deep and complex roadways in underground coal mines: a review," *International Journal of Coal Science & Technology*, vol. 1, no. 3, pp. 261-277, 2014.
- [3] J. A. Hudson and X. T. Feng, *Rock Engineering Risk*, CRC Press, Great Britain, UK, 2015.
- [4] J. M. Galvin, *Ground Engineering*, Springer, Cham, Switzerland, 2016.
- [5] W. Yu, B. Pan, F. Zhang, S. Yao, and F. Liu, "Deformation characteristics and determination of optimum supporting time of alteration rock mass in deep mine," *KSCE Journal of Civil Engineering*, vol. 23, no. 11, pp. 4921-4932, 2019.
- [6] M. T. Xu, D. S. Zhang, and W. Zhang, "Deformation and fracture evolution of surrounding rock for shallow underground projects," *Electronic Journal of Geotechnical Engineering*, vol. 18, pp. 3895-3908, 2013.
- [7] Y. L. Xu, R. K. Pan, and H. Zhang, "Investigation of key techniques on floor roadway support under the impacts of superimposed mining: theoretical analysis and field study," *Environmental Earth Sciences*, vol. 78, p. 15, 2019.
- [8] Q. Meng, L. Han, Y. Chen et al., "Influence of dynamic pressure on deep underground soft rock roadway support and its application," *International Journal of Mining Science and Technology*, vol. 26, no. 5, pp. 903-912, 2016.
- [9] Q. Meng, L. Han, Y. Xiao, H. Li, S. Wen, and J. Zhang, "Numerical simulation study of the failure evolution process and failure mode of surrounding rock in deep soft rock roadways," *International Journal of Mining Science and Technology*, vol. 26, no. 2, pp. 209-221, 2016.
- [10] H. Wang, Y. Jiang, S. Xue et al., "Assessment of excavation damaged zone around roadways under dynamic pressure induced by an active mining process," *International Journal of Rock Mechanics and Mining Sciences*, vol. 77, pp. 265-277, 2015.
- [11] J. Tian and S. Gao, "Deformation and failure study of surrounding rocks of dynamic pressure roadways in deep mines," *Mining Science and Technology (China)*, vol. 20, no. 6, pp. 850-854, 2010.
- [12] H. Yan and F. L. He, "A new cable truss support system for coal roadways affected by dynamic pressure," *International Journal of Mining Science and Technology*, vol. 22, no. 5, pp. 613-617, 2012.
- [13] W.-J. Wang, L.-Q. Luo, W.-J. Yu, H. Wu, Y.-S. Qu, and Y. S. Qu, "Study of dynamic pressure roadway supporting scheme under condition of thick composite roof," *Journal of Coal Science and Engineering (China)*, vol. 19, no. 2, pp. 119-125, 2013.
- [14] J. Zhang, L. Liu, X. Yan, and Y. Li, "Asymmetrical support technology for dynamic pressure roadway: a case study from guotun coal mine in China," *Geotechnical and Geological Engineering*, vol. 37, no. 2, pp. 823-832, 2019.
- [15] X. Yang, C. Liu, Y. Ji, X. Zhang, and S. Wang, "Research on roof cutting and pressure releasing technology of directional fracture blasting in dynamic pressure roadway," *Geotechnical and Geological Engineering*, vol. 37, no. 3, pp. 1555-1567, 2019.
- [16] J. Zuo, J. Wang, and Y. Jiang, "Macro/meso failure behavior of surrounding rock in deep roadway and its control technology," *International Journal of Coal Science & Technology*, vol. 6, no. 3, pp. 301-319, 2019.
- [17] J. Zuo, Z. Wang, H. Zhou, J. Pei, and J. Liu, "Failure behavior of a rock-coal-rock combined body with a weak coal interlayer," *International Journal of Mining Science and Technology*, vol. 23, no. 6, pp. 907-912, 2013.
- [18] G. Wu, W. Chen, S. Jia et al., "Deformation characteristics of a roadway in steeply inclined formations and its improved support," *International Journal of Rock Mechanics and Mining Sciences*, vol. 130, Article ID 104324, 2020.
- [19] G. Wu, S. Jia, W. Chen, J. Yuan, H. Yu, and W. Zhao, "An anchorage experimental study on supporting a roadway in steeply inclined geological formations," *Tunnelling and Underground Space Technology*, vol. 82, pp. 125-134, 2018.
- [20] H. Zhang, J. Cao, and M. Tu, "Floor stress evolution laws and its effect on stability of floor roadway," *International Journal of Mining Science and Technology*, vol. 23, no. 5, pp. 631-636, 2013.
- [21] S. R. Xie, M. M. Gao, D. D. Chen et al., "Stability influence factors analysis and construction of a deep beam anchorage structure in roadway roof," *International Journal of Mining Science and Technology*, vol. 28, no. 3, pp. 445-451, 2018.
- [22] S. Xie, E. Li, S. Li, J. Wang, C. He, and Y. Yang, "Surrounding rock control mechanism of deep coal roadways and its

- application,” *International Journal of Mining Science and Technology*, vol. 25, no. 3, pp. 429–434, 2015.
- [23] Z. Zhang, M. Deng, J. Bai, X. Yu, Q. Wu, and L. Jiang, “Strain energy evolution and conversion under triaxial unloading confining pressure tests due to gob-side entry retained,” *International Journal of Rock Mechanics and Mining Sciences*, vol. 126, Article ID 104184, 2020.
- [24] Z. Zhang, M. Deng, X. Wang, W. Yu, F. Zhang, and V. D. Dao, “Field and numerical investigations on the lower coal seam entry failure analysis under the remnant pillar,” *Engineering Failure Analysis*, vol. 115, Article ID 104638, 2020.
- [25] Z. Zhang, J. Bai, Y. Chen, and S. Yan, “An innovative approach for gob-side entry retaining in highly gassy fully-mechanized longwall top-coal caving,” *International Journal of Rock Mechanics and Mining Sciences*, vol. 80, pp. 1–11, 2015.
- [26] G. S. Wu, W. J. Yu, J. P. Zuo, C. Y. Li, J. H. Li, and S. H. Du, “Experimental investigation on rockburst behavior of the rock-coal-bolt specimen under different stress conditions,” *Scientific Reports*, vol. 10, p. 1, 2020.
- [27] W. Yu and K. Li, “Deformation mechanism and control technology of surrounding rock in the deep-buried large-span chamber,” *Geofluids*, vol. 2020, Article ID 8881319, 22 pages, 2020.
- [28] G. Wu, W. Yu, J. Zuo, and S. Du, “Experimental and theoretical investigation on mechanisms performance of the rock-coal-bolt (RCB) composite system,” *International Journal of Mining Science and Technology*, vol. 30, no. 6, pp. 759–768, 2020.
- [29] W. J. Yu, G. S. Wu, B. Pan, Q. H. Wu, and Z. Liao, “Experimental investigation of the mechanical properties of sandstone-coal-bolt specimens with different angles under conventional triaxial compression,” *International Journal of Geomechanics*, vol. 7556, 10 pages, 2020.
- [30] B. X. Huang, N. Zhang, H. W. Jing et al., “Large deformation theory of rheology and structural instability of the surrounding rock in deep mining roadway,” *Journal of China Coal Society*, vol. 45, no. 03, pp. 911–926, 2020.
- [31] D. Zhu, Y. Wu, Z. Liu, X. Dong, and J. Yu, “Failure mechanism and safety control strategy for laminated roof of wide-span roadway,” *Engineering Failure Analysis*, vol. 111, Article ID 104489, 2020.
- [32] R. Yang, Y. Li, D. Guo, L. Yao, T. Yang, and T. Li, “Failure mechanism and control technology of water-immersed roadway in high-stress and soft rock in a deep mine,” *International Journal of Mining Science and Technology*, vol. 27, no. 2, pp. 245–252, 2017.
- [33] R. S. Yang, Y. L. Li, D. M. Guo et al., “Deformation reasons and support technology of deep and high-stress soft rock roadway,” *Journal of Mining and Safety Engineering*, vol. 34, no. 6, pp. 1035–1041, 2017.
- [34] M. Kanji, M. C. He, and L. R. Sousa, *Soft Rock Mechanics and Engineering*, Springer, Chem, Switzerland, 2020.
- [35] X. T. Feng, *Rock Characterisation, Modelling and Engineering Design Methods*, CRC Press, Boca Raton, FL, USA, 2013.
- [36] H. W. Liu, *Concise Materials Mechanics*, Higher Education Press, Beijing, China, 2008.